

Lecture Notes in Mechanical Engineering

Krishna Mohan Singh

Sushanta Dutta

Sudhakar Subudhi

Nikhil Kumar Singh *Editors*

Fluid Mechanics and Fluid Power, Volume 2

Select Proceedings of FMFP 2022



Springer

Lecture Notes in Mechanical Engineering

Series Editors


Fakher Chaari, National School of Engineers, University of Sfax, Sfax, Tunisia

Francesco Gherardini , Dipartimento di Ingegneria “Enzo Ferrari”, Università di Modena e Reggio Emilia, Modena, Italy

Vitalii Ivanov, Department of Manufacturing Engineering, Machines and Tools, Sumy State University, Sumy, Ukraine

Mohamed Haddar, National School of Engineers of Sfax (ENIS), Sfax, Tunisia

Editorial Board

Francisco Cavas-Martínez , Departamento de Estructuras, Construcción y Expresión Gráfica Universidad Politécnica de Cartagena, Cartagena, Murcia, Spain

Francesca di Mare, Institute of Energy Technology, Ruhr-Universität Bochum, Bochum, Nordrhein-Westfalen, Germany

Young W. Kwon, Department of Manufacturing Engineering and Aerospace Engineering, Graduate School of Engineering and Applied Science, Monterey, CA, USA

Justyna Trojanowska, Poznan University of Technology, Poznan, Poland

Jinyang Xu, School of Mechanical Engineering, Shanghai Jiao Tong University, Shanghai, China

Lecture Notes in Mechanical Engineering (LNME) publishes the latest developments in Mechanical Engineering—quickly, informally and with high quality. Original research reported in proceedings and post-proceedings represents the core of LNME. Volumes published in LNME embrace all aspects, subfields and new challenges of mechanical engineering.

To submit a proposal or request further information, please contact the Springer Editor of your location:

Europe, USA, Africa: Leontina Di Cecco at Leontina.dicecco@springer.com

China: Ella Zhang at ella.zhang@springer.com

India: Priya Vyas at priya.vyas@springer.com

Rest of Asia, Australia, New Zealand: Swati Meherishi at swati.meherishi@springer.com

Topics in the series include:

- Engineering Design
- Machinery and Machine Elements
- Mechanical Structures and Stress Analysis
- Automotive Engineering
- Engine Technology
- Aerospace Technology and Astronautics
- Nanotechnology and Microengineering
- Control, Robotics, Mechatronics
- MEMS
- Theoretical and Applied Mechanics
- Dynamical Systems, Control
- Fluid Mechanics
- Engineering Thermodynamics, Heat and Mass Transfer
- Manufacturing Engineering and Smart Manufacturing
- Precision Engineering, Instrumentation, Measurement
- Materials Engineering
- Tribology and Surface Technology

Indexed by SCOPUS, EI Compendex, and INSPEC.

All books published in the series are evaluated by Web of Science for the Conference Proceedings Citation Index (CPCI).

To submit a proposal for a monograph, please check our Springer Tracts in Mechanical Engineering at <https://link.springer.com/bookseries/11693>.

Krishna Mohan Singh · Sushanta Dutta ·
Sudhakar Subudhi · Nikhil Kumar Singh
Editors

Fluid Mechanics and Fluid Power, Volume 2

Select Proceedings of FMFP 2022

 Springer

Editors

Krishna Mohan Singh
Department of Mechanical and Industrial
Engineering
Indian Institute of Technology Roorkee
Roorkee, Uttarakhand, India

Sushanta Dutta
Department of Mechanical and Industrial
Engineering
Indian Institute of Technology Roorkee
Roorkee, Uttarakhand, India

Sudhakar Subudhi
Department of Mechanical and Industrial
Engineering
Indian Institute of Technology Roorkee
Roorkee, Uttarakhand, India

Nikhil Kumar Singh
Department of Mechanical and Industrial
Engineering
Indian Institute of Technology Roorkee
Roorkee, Uttarakhand, India

ISSN 2195-4356

ISSN 2195-4364 (electronic)

Lecture Notes in Mechanical Engineering

ISBN 978-981-99-5751-4

ISBN 978-981-99-5752-1 (eBook)

<https://doi.org/10.1007/978-981-99-5752-1>

© The Editor(s) (if applicable) and The Author(s), under exclusive license to Springer Nature Singapore Pte Ltd. 2024

This work is subject to copyright. All rights are solely and exclusively licensed by the Publisher, whether the whole or part of the material is concerned, specifically the rights of translation, reprinting, reuse of illustrations, recitation, broadcasting, reproduction on microfilms or in any other physical way, and transmission or information storage and retrieval, electronic adaptation, computer software, or by similar or dissimilar methodology now known or hereafter developed.

The use of general descriptive names, registered names, trademarks, service marks, etc. in this publication does not imply, even in the absence of a specific statement, that such names are exempt from the relevant protective laws and regulations and therefore free for general use.

The publisher, the authors, and the editors are safe to assume that the advice and information in this book are believed to be true and accurate at the date of publication. Neither the publisher nor the authors or the editors give a warranty, expressed or implied, with respect to the material contained herein or for any errors or omissions that may have been made. The publisher remains neutral with regard to jurisdictional claims in published maps and institutional affiliations.

This Springer imprint is published by the registered company Springer Nature Singapore Pte Ltd.

The registered company address is: 152 Beach Road, #21-01/04 Gateway East, Singapore 189721, Singapore

Paper in this product is recyclable.

Contents

Instability, Transition and Turbulence

Flux Enhancement Due to the Modification of the Large Scales in an Axially Homogeneous Turbulent Convection	3
Adhitya Krishnan and Murali R. Cholemani	
Comparative Study of Turbulent Heat Transfer in Plane Wall Jet Using Different $k-\epsilon$ RANS Models	15
Animesh Patari, Shantanu Pramanik, and Tanmoy Mondal	
Linear Instability Analysis of Natural Convection in a Heated Vertical Porous Annulus	29
A. Khan, P. Chokshi, and P. Bera	
Response of a Partially Submerged Pendulum Under Gravity Waves ...	39
Md. Shadab Hasan, Kamlesh Kumar, and P. Deepu	
The Nature of Probability Density Functions in Turbulent Channel Flow	49
S. Raghuram	
Optimal Perturbations of Flat-Plate Boundary Layer with Suction and Injection	59
Mayank Thummar, Ramesh Bhoraniya, Ravi Kant, and Vinod Narayanan	
Linear Stability Analysis of Two-Dimensional Mixed Convective Flow Past a Square Cylinder	75
Rudram Dushe, Basheer A. Khan, and Arun K. Saha	
Characteristics of Transitional Separation Bubble Formed Over Negatively and Positively Skewed Anisotropic Rough Surface	89
K. T. Ganesh and K. Anand	

Numerical Study on Effect of Inclination of a Plane on Flow and Heat Transfer by Turbulent Wall Jet	103
Amiruzzahan Mondal and Animesh Patari	
Pattern Formation and Evolution of Viscous and Non-viscous Liquids on a Vertical Vibrating Surface: An Experimental Investigation	117
Prashant Narayan Panday, Anushka, Prasanta Kumar Das, and Aditya Bandopadhyay	
Activity-Induced Mixing in a Stratified Binary Passive System	129
Thomas Jacob, Siddhant Mohapatra, and Pallab Sinha Mahapatra	
Spatio-temporal Stability Analysis of Falling Film Over Heated Inclined Plane	141
Arnab Choudhury and Arghya Samanta	
Thermal Gradient-Mediated Instability in a Bilayer Flow Over a Porous Medium	153
Saurabh Dubey, Vinod B. Vanarse, Prathu Raja Parmar, Omkar S. Deshmukh, and Dipankar Bandyopadhyay	
Compound Matrix Method for Linear Stability Analysis of Flow Over a Flat Plate	165
Rituparn Somvanshi, Neha Chaturvedi, and Swagata Bhaumik	
Wavy Dynamics of Confined and Inclined Falling Liquid Films	179
Saurabh Dhopeswar, Ujjwal Chetan, Toshan Lal Sahu, Prabir Kumar Kar, Suman Chakraborty, and Rajaram Lakkaraju	
Co-existence of Multiple Steady States in Bottom Heated Trapezoidal Closed Cavities	191
Govind Maurya, Alok Kumar, Nadeem Ahmed, and Suneet Singh	
Jet Noise Prediction Using Turbulent Scales from LES and RANS	201
N. P. Shabeeb and Aniruddha Sinha	
Reduction in Turbulence-Induced Non-linear Dynamic Vibration Using Tuned Liquid Damper (TLD)	215
Ananya Majumdar, Biplab Ranjan Adhikary, and Partha Bhattacharya	
Transition of the Boundary Layer Subjected to Freestream Turbulence	231
Ravi Kumar and S. Sarkar	
Introduction of Critical Filling Parameter on Faraday Instability and Its Dependencies on Fluid Densities	241
K. P. Choudhary, S. P. Das, and Shaligram Tiwari	

Surface Roughness Heterogeneity Effects on Five Turbine Wind Farm Evaluated Using Large Eddy Simulation 253
 Naveen N. Kethavath, Kingshuk Mondal, and Nirranjan S. Ghaisas

Resonant Three-Wave Interactions in a Shear Flow with Density Stratification 263
 Lima Biswas and Priyanka Shukla

The Differences in the Near Wall Turbulent Structure Between a Uniform Flow and a Wall Jet with Co-Flow—A Numerical Study 275
 Prithwisha Nath and Animesh Patari

Linear Stability Analysis of Phase Inversion-Induced Viscous Fingering 289
 Vinod B. Vanarse, Siddharth Thakur, Prathu Raja Parmar, Saurabh Dubey, Tapas Kumar Mandal, and Dipankar Bandyopadhyay

Stability Characteristics of Linear Unstable Modes in Flow Past Elliptic Cylinders 301
 Deepak Kumar and Bhaskar Kumar

Linear Stability Analysis of Open Cavity Flow Using OpenFOAM® 313
 Ravi Kant, Samarth Acharya, and Ramesh Bhoraniya

Aerodynamics

Impact of Roughness Strip Location on Improving Aerodynamic Characteristics of Circular Cylinder 329
 A. N. S. Prakash Kurakula, Sk Abdul Zakaria, B. Avinash Reddy, and Tamal Jana

Chaotic Onset in the Flow Past a Flapping Foil Depends on the Free-Stream Reynolds Number 339
 Sourav Dey, Dipanjan Majumdar, and Sunetra Sarkar

Wake Interactions Around a Pair of Porous Cylinders in a Side-By-Side Arrangement in Channel Flow 349
 Saqib Jamshed and Amit Dhiman

A Study on the Aerodynamic Characteristics and the Flow Separation of a Circular Cylinder with Longitudinal Ridges 361
 B. Kailashnath, J. Harisankar, Anirudh Renganathan, E. Karthik Vel, G. Vinayagamurthy, and S. Nadaraja Pillai

Effect of Surface Roughness on Boundary Layer Thickness 371
 Saurabh Powar, Neha Chitrakar, Lalit Chacharkar, Prakhar Adarsh, Shankar Karhale, Rohan Patil, and Pramod Kothmire

Effect of Secondary Swirl Strength on the External Aerodynamics of a Gas Turbine Fuel Injector	381
Vivek Sahu, Devin Chugh, Deepanshu Mittal, and K. P. Shanmugas	
Effects of Flapping Frequency on the Aerodynamic Performance of the Elliptical Tandem Flapping Wings	395
Rahul Ranjan, Akashdeep Singh, Jit Sinha, and Sunil Manohar Dash	
Aerodynamic Performance of a Tandem Wing Configuration Inspired from Dragonfly Gliding Flight for MAV Application	409
Rajosik Adak, Arindam Mandal, and Sandeep Saha	
Aeroacoustic Characteristics of the Supersonic Free Jet at Mach Number 1.6	419
K. Manikandan, Jeevitha Jagajeevan, M. Aruna Priyadharshini, Rajarshi Das, and P. Booma Devi	
Aerodynamic and Thermal Optimization of Plate Heat Exchanger Fin Arrangements	431
Pratyush Padmanabhan, Sanatkumar Samvit Rajagopalan, and Chennu Ranganayakulu	
Computational Study on Wingtip Fluid Injection for Enhancing Wing Performance	447
Vishwanath Nagaraj, Darshan Purushan, Ashish Patra, Nimal Prakash, and V. Krishna	
Numerical Studies of the Influence of Strouhal Number on the Flow Characteristics of Synthetic Jet Impingement	461
Pawan Sharma, Dnyanesh Mirikar, Jitendra K. Choudhary, Raghuvamsi Bokka, Jay Joshi, Santosh K. Sahu, and Harekrishna Yadav	
Aerodynamic Analysis of Stretched Trailing Edge Over NACA 0020 Airfoil at Various Turbulence Intensities	475
E. Livya and S. Nadaraja Pillai	
Control of Flow Separation Using Hemispherical Protuberance on the Leading Edge	489
Pradeep Singh, Ravi Kumar, and S. Sarkar	
Numerical Investigation to Study the Effects of Wing Flexibility on the Store Trajectory Using MSC CoSim	501
Varun Palahalli, R. Ganesh Pawar, Nuza Nigar, and T. Praphul	
Aerodynamics of Flapping Fin Inspired from Manta Ray	513
Dharambir Poddar, Nitin Kumar, Javed Mohd., and Debopam Das	

Internal and External Aerodynamics of a Lean Burn Gas Turbine Fuel Injector 525
 Preetam Jamod, Ayush Divyansh, Harish Pothukuchi, and K. P. Shanmugas

Aero-Thermal Investigation on Commuter Category Turboprop Aircraft Engine Nacelle 539
 C. A. Vinay, G. N. Kumar, S. Venkat Iyengar, and T. Pugazhendhi

Design, Analysis and Manufacturing of Twist Morphing Wing for UAV Purpose 553
 Shivang Patni, Kaushal Mahant, Saumya Shah, Anand Makwana, and Jignesh Vala

Experimental Validation for Vortex-Induced Vibration of Circular and Square Cylinders of Low and High Mass Damping 569
 Parth Patel, Amit Agrawal, Atul Sharma, and Rajneesh Bhardwaj

Experimental Investigation of Vortex-Induced Vibration of a Circular Cylinder Mounted on a Cantilever Beam 579
 Deepak Kumar Rathour and Atul Kumar Soti

Effect of Crosswind on Vehicle Dynamics 593
 P. M. Vamsi Krishna and B. Ravindra

Proposal of a Mutual Inertia Force Coupling on the Wake Oscillator Model for Vortex-Induced Vibrations 605
 Adithya Krishna Menon and V. Vinod

Kinematics of a Low Aspect Ratio Pitching Flexible Panel—A New Insight 619
 Kakulambarri S. N. Abhinav Kumar, Parag J. Deshpande, Ravi Dodamani, and Geetanjali N. Alle

The Effect of Riblet Shapes on Flow Characteristics 631
 Ishita Jain, Issam Wajih, and S. Sarkar

Development of New Technology and Design Framework for Supersonic Transport Aircraft 641
 Aravind Seeni

Numerical Study of Impulsive Motion Past a Rotating Cylinder for Newtonian and Non-newtonian Fluid 655
 Sibashish Panda, Pratyush Kumar Mohanty, Prateek Gupta, and Chinu Routa

Dynamic Response of a Cantilevered Flexible Vertical Plate in a Uniform Inflow at $Re = 100$ 667
 Avinash Kumar Pandey, Gaurav Sharma, and Rajneesh Bhardwaj

Numerical Investigations of Forced Oscillating Circular Cylinder in Uniform Flow	681
Ravikant Roy and Simon Peter	
Wake Dynamics of a Longitudinally Oscillating Cylinder at Low Reynolds Number	697
N. David	
Effect of Wind Gust on Flow Past Pitching Seagull Wing	707
Jay Rana and Shaligram Tiwari	
Aerodynamic Characteristics of Finite Rectangular Wings in Formation Flight with Ground Effect	723
Ravindra A. Shirsath and Rinku Mukherjee	
Compressible Flow	
Experiments on Compressible Vortex Ring Interaction with a Cone Mounted on a Flat Plate	739
Praveen K. Nuvvula, Amar Yadav, Pawan Kumar Karn, Rijin Rajan, Mohd Javed, and Debopam Das	
Numerical and Experimental Studies on Supersonic Free Jet with Various Cross-Sectional Tab Configuration	747
Srinivasa Rao Lavala, Partha Mondal, and Sudip Das	
Effect of Viscosity on Air Entrapment and Spreading of Molten Droplet in Thermal Spray Coating Deposition	759
Surendra Kumar, Rajesh Kumar Shukla, and Sayan Sadhu	
Effects of Operating Conditions and Geometry in Augmentation of Initial Transients and Hysteresis in Supersonic Vacuum Ejector	771
Darshan Gohel and M. Deepu	
The Effects of Shock Waves on OFHC Copper	785
M. K. Singh and R. K. Anand	
Supersonic Flow Field Characteristics of a Sharp Spiked Blunt Body Having Various Nose Cone Fairings	797
MD. G. Sarwar, P. Kumar, and S. Das	
Pressure Drop Prediction Using CFD for a Launch Vehicle Payload Fairing Separation Ground Test	811
Ankur Nagpal and G. Vidya	
Effect of Upstream Energy Deposition Rate on Flow Characteristics of a Scramjet Engine	825
Amrita Pathak, Pranjal Khare, Ali Jraisheh, and Vinayak Kulkarni	

Effect of Geometric Parameters on Steady-State Supersonic Film Cooling of the Basic Conical Rocket Nozzle 841
 V. M. Rahul and N. Gnanasekaran

Effect of Nozzle Internal Shape on Near-Field Characteristics of Transverse Liquid Jet in a Supersonic Crossflow 857
 Chandrasekhar Medipati, S. Deivandren, and R. N. Govardhan

Effect of Reduced Mass on Two-Dimensional Compressible Flow Past Circular Cylinder 867
 Sawant Omkar Deepak, Chandan Kumar Bhardwaj, Saurav Sharma, and Swagata Bhaumik

Effect of Overtaking Disturbances on the Motion of Strong Cylindrical MHD Shock Waves in a Self-Gravitating Van Der Waals Gas 883
 Sewa Singh and R. K. Anand

An Investigation on the Effect of Changing Bump Geometry on a 2D Supersonic Inlet 897
 Pranav Joshi, Om Kolhatkar, and Prithviraj Ghule

Laminar Shear Layer Growth in Supersonic Underexpanded Flows 907
 Ali Jraisheh, Jubajyoti Chutia, Amrita Pathak, and Vinayak Kulkarni

Numerical Investigation on Shock-Wave and Boundary-Layer Interactions Inside the Axisymmetric and Planar Scramjet Intakes with Different Cowl Orientations 919
 S. Sharath and Tamal Jana

Accurate Compressible Flow Modelling of Liquid Shock Tube Problems 931
 R. Jishnu Chandran, Risha Raju, A. Salih, and Senthil Kumar Arumugam

Numerical Simulation of Compressible Multiphase Flows with Phase Change Using Two-Fluid Approach 947
 Mansu Navaneethan, T. Sundararajan, and T. Jayachandran

About the Editors

Prof. Krishna Mohan Singh is Professor in the Department of Mechanical and Industrial Engineering at Indian Institute of Technology (IIT) Roorkee. His research interests include the areas of computational mechanics, development of novel parallel algorithms, meshfree methods, shape and topology optimization, fluid dynamics, DNS/LES of turbulent flows, CAE, computer-aided analysis and design of thermo-fluid and multi-physics systems, computational fluid dynamics, modeling and simulation of flow and heat transfer in turbomachines, transport and energy systems.

Prof. Sushanta Dutta is Professor in the Department of Mechanical and Industrial Engineering at Indian Institute of Technology (IIT) Roorkee. His research interests are in the areas of experimental fluid mechanics, experimental heat transfer, optical measurement techniques, active and passive control of flow field, wake dynamics, turbulence study, Schlieren, HWA, PIV, LCT, PSP, microfluidics and heat transfer augmentation using phase change material.

Prof. Sudhakar Subudhi is Professor in the Department of Mechanical and Industrial Engineering at Indian Institute of Technology (IIT) Roorkee. His research interests are in the area of experimental heat transfer and fluid mechanics, heat transfer enhancement of natural and forced convection in water/nanofluids, natural ventilation and unconventional energy systems.

Dr. Nikhil Kumar Singh is Assistant Professor in the Department of Mechanical and Industrial Engineering at Indian Institute of Technology (IIT) Roorkee. His broad research interests include direct numerical simulations of two-phase flows and phase change, computational fluid dynamics and heat transfer, numerical methods and turbulent flows.

Instability, Transition and Turbulence

Flux Enhancement Due to the Modification of the Large Scales in an Axially Homogeneous Turbulent Convection



Adhitya Krishnan and Murali R. Cholehari

Abstract An experimental study reporting the enhancement of turbulent flux of a scalar due to the modification of the large scales of a turbulent convective flow is reported. The control flow considered is an axially homogeneous, zero mean shear turbulent convection. The effect of stationary surfaces (cylindrical rod inserts) introduced into the flow is reported here. The characteristics of turbulence are significantly affected by the introduction of these surface(s) which includes the increase in the buoyant flux. The placement and the number of inserts in relation to the quantum of flux enhancement is studied. Directions of study and the context of the study in relation to turbulence control are discussed.

Keywords Turbulent convection · Kinematic wall blocking · Flux enhancement

1 Introduction

The control of turbulence by active or passive means has been a topic of continued and considerable interest. In particular, the modification of drag of a turbulent flow is of considerable theoretical and practical relevance. A large body of work elucidates the mechanisms of drag reduction by additives, in which theories have been developed explaining the mechanisms. The novel passive turbulence control mechanism discussed in this paper involves a phenomenon theoretically discussed by Hunt and Graham [1]. The thought experiment devised by Hunt and Graham involves the introduction of rigid surfaces, without relative mean motion (oriented in the stream-wise direction) into a pre-existing homogeneous isotropic turbulent flow field generating an analogue, wherein the mean velocity boundary layer is eliminated and the interaction between turbulence and the surface becomes the primary phenomenon of concern. The experimental validation of the above case by Thomas and Hancock suggests the presence of an outer kinematic region with zero shear that scales with

A. Krishnan · M. R. Cholehari (✉)
Department of Applied Mechanics, IIT Delhi, New Delhi 110016, India
e-mail: murali@am.iitd.ac.in

the external turbulence flow parameters. This region is characterized by the attenuation of the wall-normal component of velocity fluctuation v' and the amplification of the stream-wise component of the velocity fluctuation u' , i.e. there occurs an inviscid blocking of v' in a region considerably distant from the wall.

This attenuation of wall-normal momentum transport due to kinematic wall blocking can bring about drag reduction. These drag reduction effects become predominant and visible upon the elimination of the shear boundary layer, which increases production (due to increase in $\partial_i \langle U_j \rangle$). The contribution of such 'Shear Free Surfaces' in wall-bounded turbulent flows towards global turbulence control has been studied experimentally by Kathuria and Shukla [2], Raja Vamsi [3], Sahoo [4], Snigdha Lal [5] and Cholehari and Srinivasan [6].

The attenuation of wall-normal velocity due to kinematic wall blocking is also expected to weaken other wall-normal/ lateral turbulent transport processes similar to wall-normal momentum transport. To test this hypothesis, a control flow involving buoyancy driven turbulent convection as described by Cholehari and Arakeri [7] is chosen. The flow is driven by an unstable density gradient, using brine and water across the ends of a long vertical pipe ($l/D = 10$). The Schmidt number $Sc = \nu/\alpha$ is 670 and the Rayleigh number $Ra = g(\Delta\rho/\rho_0)Ld^4/\nu\alpha$ achieved (based on density gradient and aspect ratio of pipe) is of the order of 10^9 (initial Ra at the start of the flow). Under these conditions, the convection is turbulent and the time averaged velocity at any point is zero. The pipe is long enough that there is an axially homogeneous region with a linear density gradient of about 6–7 diameters long in the mid-length of the pipe. In the absence of mean flow and therefore mean shear, turbulence is sustained only by buoyancy. The flow can thus be considered a turbulent natural convection driven by an unstable density gradient. The flow in the central zone of the pipe cross section, mainly affected by buoyancy consists of vertically moving fluid masses colliding and interacting, while the flow near the wall appears similar to that in wall-bounded shear-free turbulence. The flow is anisotropic, with the anisotropy increasing to large values near the wall. A mixing length model (as reported by Cholehari [8]) incorporating the diameter of the pipe as the length scale predicts well the scaling for velocity fluctuations and the flux. This flow, without any modification of the turbulence, is referred to as the base configuration in this study.

The attenuation of wall-normal/ lateral velocity components (u', v') due to the presence of shear-free surface(s), weakens the turbulent diffusivity in the lateral directions and in turn reduces turbulent energy and mixing. This reduction in turbulent energy results in attenuation of lateral turbulent transport and mixing processes. Coherent structures in the flow are thus able to maintain their coherence over longer time and length scales which in turn helps in enhanced transport in the axial direction.

Thus, in this study, the attenuation of wall-normal/ lateral scalar (salt concentration) transport due to the presence of the shear-free surface(s) manifests itself as an enhancement in the salt flux across the pipe. This enhancement is driven by an increase in the turbulent transport of salt concentration in the axial direction. In the base configuration flow discussed above, it is noted that the flow is free of mean shear and hence any surface in the bulk of the flow could possibly be used to test the hypothesis. In this study, smooth cylindrical glass rods of various diameters axially

aligned along the length of the pipe and placed in different configurations are used as shear-free surfaces.

2 Methodology

An unstable linear density gradient created using brine and water across the ends of a vertical pipe (50 cm in length and 50 mm in diameter) is used to generate the turbulence. The pipe connects two tanks, with the top tank containing brine and the bottom tank, water. The fluids in the respective tanks are mixed thoroughly using small aquarium pumps (as shown in Fig. 1) to remove stratification and thus provide uniform boundary condition at the ends of the pipe. This mixing to remove stratification is achieved by pumping the heavier fluid that stratifies at the bottom of the tanks to the top of the respective tanks using the pump and diffuser set-up. The diffuser is used to minimize the influence of pumping on the primary flow. The hypothesis of flux enhancement upon introduction of shear-free surfaces in such flows is validated through the placement of rigid rod inserts (of desired diameter) concentric to the pipe or in preferred configuration at the periphery (at the location of peak turbulence production) of the pipe. The experimental procedure is as follows. The pipe is placed in configuration with respect to the bottom and top tanks (as shown in Fig. 1) and is aligned vertically. First the bottom tank and the pipe are filled with distilled water and a stopper is used to block the top end of the pipe. The top tank is then filled with brine. Typically, the initial salt concentration in the top tank is about 0.02 g/cc. In the case of the base configuration (without rod inserts in any configuration), the stopper is removed from the top end of the pipe to start the turbulent buoyant convection along the length of the pipe.

The main measure of the effect on turbulence in base and rod inserts configurations is the altered flux of salt in the pipe, which is inferred through time resolved conductivity measurements of the top tank fluid. The salt concentration in the top tank is measured using a conductivity metre probe (ORION 3-Star Metre).

The salt concentration measurements are indirectly derived from the conductivity measurements (κ) which are compensated for temperature variations ($\kappa_T = \kappa_{25} (1 + \alpha(T - 25))$); and through calibration $\alpha = 2.1\%/C$) and salt purity. The probe is also calibrated for its cell-constant before every run using standard saline solutions. The time-series data (collected every 5 s) for conductivity and temperature of top tank fluid are logged to a computer through a serial interface. The initial salt concentration in the top tank is measured and the pumps are allowed to mix the fluids in the top and bottom tanks thoroughly before the start of the experiment. The experiment runs for about 120 min, before the concentration difference between the top and bottom tanks driving the flow becomes negligible and the flow transitions to become laminar. At the end of the experiment, the concentration of the mixed fluid is measured. Using the acquired time rate of variation of salt concentration in the top tank and integral mass balance, the concentration difference and the flux of salt as functions of time are calculated. Note that, from continuity considerations and incompressibility

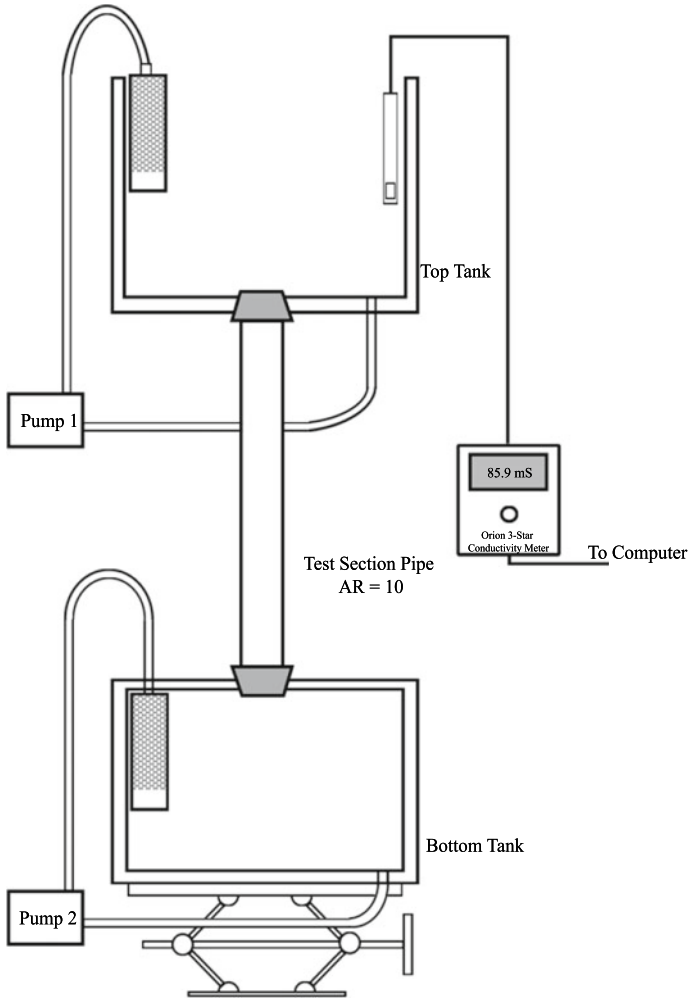


Fig. 1 Schematic of experimental set-up

assumption at any instant of time, the axial velocity averaged over the cross section of the pipe is,

$$\int_A \tilde{w} dA = 0 \quad (1)$$

where \tilde{w} is the velocity in the vertically upward (axial), z direction. The tilde represents the total velocity. In the following analysis, the top and bottom tank concentrations are denoted as C_T and C_B , respectively. V_T , V_B and V_P refer to the volumes of the top tank, bottom tank and the pipe respectively; A_P the cross-sectional area of

the pipe; M_S the total mass of the salt in the set-up and F the mass flux of salt in the pipe. From mass conservation of salt, we have,

$$V_T C_T + V_B C_B + A_P \int_0^L \bar{c} dz = M_S \quad (2)$$

assuming the average concentration in the pipe $\bar{C} = \frac{C_T + C_B}{2}$,

$$C_B(t) = \frac{M_S - C_T(t)(V_T + \frac{V_P}{2})}{\frac{V_P}{2} + V_B} \quad (3)$$

$$\Delta C = C_T - C_B = \frac{C_T(t)(V_T + V_B + V_P) - M_S}{\frac{V_P}{2} + V_B} \quad (4)$$

It is assumed that in the experiments,

$$m_{sT} = m_{sB} = m_s = V_T \frac{dC_T}{dt} \quad (5)$$

Then flux, mass flow rate of salt going down per unit cross-sectional area of the tube is,

$$F = -\overline{c'w'} = \rho_0 V_T \frac{dC_T}{dt} \quad (6)$$

Salt concentration is related to density by,

$$\frac{\partial \rho}{\partial c} = \rho_0 \beta \quad (7)$$

where ρ_0 is the density of water and $\beta = 0.72$ for the salt concentration range encountered in the experiments. Thus,

$$\Delta \rho = \rho_0 \beta \Delta C \quad (8)$$

$$\rho = \rho_0 + \Delta \rho = \rho_0 + \rho_0 \beta \Delta C \quad (9)$$

Thus, from the measurement of the top tank concentration with time, we can determine the instantaneous concentration difference between the top tank and bottom tank fluids as well as flux.

2.1 Modelling the Base Configuration

The theoretical flux for the base configuration (without rod inserts) has been modelled by Cholehari and Arakeri [8]. They report that the large-scale energy containing structures of the flow, scale with the pipe diameter: d (dominant length scale). For pipes with high aspect ratio ($L/d \ll 1$), the flow is homogeneous (away from the entrance) in the axial direction and driven by a linear, unstable axial density gradient.

In the central homogeneous region of the pipe, the only relevant parameters are the pipe diameter d , the density gradient $\partial\rho/\partial z$ and g . The two molecular diffusivities ν (momentum diffusivity) and α (salt concentration scalar diffusivity) are not expected to be relevant for scaling in the energy containing scales. The dimensional analysis gives the scales for density fluctuations ρ' , axial velocity fluctuations w' and salt flux— $\langle w'c' \rangle$ as,

$$w' \sim \sqrt{g \frac{\partial\rho}{\partial z} \frac{d^2}{\rho_0}} = w_m \quad (10)$$

$$\rho' \sim \frac{\partial\rho}{\partial z} \cdot d = \rho_m \quad (11)$$

$$-\langle w'c' \rangle \sim \frac{w_m \rho_m}{\beta \rho_0} = F_m \quad (12)$$

Physically, the above relations imply that a fluid packet (a coherent region of fluid) heavier (or lighter) than the surrounding fluid by an amount ρ' attains a ‘free fall’ velocity w_m as it falls through the mixing length $\sim d$ before it interacts and mixes. The implicit assumption is that the flow becomes de-correlated over distances scaling with d .

The modelled flux (compensated for the nonlinear pipe end effects) is given by,

$$F_T = C_m F_m = \frac{C_r \left(\frac{g}{\rho_0}\right)^{\frac{1}{2}} d^2}{\beta \rho_0} \left(\frac{\Delta\rho}{L}\right)^{\frac{3}{2}} \quad (13)$$

$$C_r = \frac{C_m}{(1 + 2(\kappa_p - \kappa_L)/AR)^{3/2}} = \frac{0.88}{(1 + 4.2/AR)^{3/2}} \quad (14)$$

The Nusselt (non-dimensional flux) and the Reynolds number scale with the Rayleigh number as (using $w' \sim w_m$ and d):

$$Nu = \frac{-\langle flux \rangle}{\alpha \Delta C / L} = C_r Ra^{1/2} Sc^{1/2} \quad (15)$$

$$Re = \frac{w'd}{\nu} \sim Ra^{\frac{1}{2}} Sc^{-\frac{1}{2}} \quad (16)$$

2.2 Placement of Inserts

The SFS insert configuration cases involved the placement of rod inserts into the flow either concentric to the pipe or in a circular pattern about the periphery of the pipe. The peripheral placement of the inserts is to attenuate $\langle w'c' \rangle$ at its region of peak production. This region of peak production has been identified using PIV data from Cholemani et. al. [7] for buoyancy driven turbulent convection in the same range of Ra . It is noted from this above study that the profile of w_{rms} is double-peaked with the peaks present near the wall of pipe. Since the profile of c'_{rms} can be safely assumed to have a uniform distribution at any cross section in the homogeneous region of the flow, it can be concluded that the profile of the buoyancy production term: $\langle w'c' \rangle$ follows a similar trend, with the same region of peak production as w_{rms} . From this data, the pitch diameter for the placement of the inserts in the peripheral configuration is found to be at 45 mm. The length scale of the insert (diameter of insert – 6.5 mm) fairly corresponds to half-peak width. The experiments with the peripheral inserts were conducted with 4, 6 and 8 inserts configurations. The profile of $\langle w'c' \rangle$ despite having its double peaks near the wall, has significant magnitude at the central region of the pipe. Thus, the experiments involving the central placement of SFS are also done, with inserts of diameters: 4 mm, 6.5 mm, 8 mm, 10 mm, 12 mm and 17 mm. The rod inserts were held in respective configurations and vertically aligned using mounts. 10 sets of observations are taken for the each of the above described cases. The flux measured and calculated based on Eq. (6) is normalized with the modelled/theoretical flux F_T discussed in subsection A. The flux calculated from the raw data was found to be extremely noisy. Therefore, an exponential polynomial of the form: $e^{\sum a_n t^n}$ is fit to the raw data before flux is evaluated. [7, 8] (Typically $n = 5$ is chosen for proper conditioning of the fit).

3 Results and Discussion

3.1 Results

The results from the experiments conducted with the centrally placed and peripherally placed inserts are presented in Tables 1 and 2, respectively. The Ra ranges for the studies with the centrally placed inserts was $(0.4-1.2) \cdot 10^9$ and for the peripherally placed inserts $(0.8-1.7) \cdot 10^9$. At the lower Ra ranges, the flow transitions to become laminar and thus does not conform to the model discussed in the previous section. Therefore, the flux measurements in the lower Ra ranges are truncated. The values reported here for the various configurations are first averaged over the $n (=10)$ sets of observations for each case (over the entire Ra range) and then averaged over the Ra range. The (F/F_t) calculated from the measurements are normalized with respect to their respective baseline configurations and further compensated for the area blockage.

$$\left(\frac{F}{F_T}\right)_n = \frac{(F/F_T)_{\text{observed}}}{(F/F_T)_{\text{baseline}}} \quad (17)$$

$$\left(\frac{F}{F_T}\right)_a = \frac{\left(\frac{F}{F_T}\right)_n A_P}{A_P - m \cdot A_{SFS}} \quad (18)$$

In the case of the centrally placed inserts, an increasing trend in $(F/F_T)_a$ exists up to the case of the 6.5 mm centrally placed insert, where a maximum of 41.4% increase in $(F/F_T)_a$ (w.r.t. base configuration) is observed. The decreasing trend after this point reaches a steady value of about 26% increase in $(F/F_T)_a$, as seen in the cases of 12mm and 17mm centrally placed inserts (see Fig. 2). It is evident from the above observations that there is significant flux enhancement even for the central placement of the inserts, which is not the region of peak production of $\langle w'c' \rangle$. In the experiments conducted with the peripherally placed 6.5mm inserts, an increasing trend in $(F/F_T)_a$ is observed for increase in the number of inserts. The maximum enhancement was observed in the case of 8 peripherally placed inserts with an increase of about 163% in $(F/F_T)_a$.

Table 1 Means and standard errors for F/F_t in the centrally placed SFS configuration

$dSFS$	ABR	F/F_t	$(F/F_t)_n$	$(F/F_t)_a$	ϵ
0.0	0	0.745	1	1	0.039
4.0	1.006	0.842	1.129	1.136	0.041
6.5	1.017	1.0362	1.389	1.414	0.042
8.0	1.026	0.961	1.289	1.323	0.038
10.0	1.042	0.909	1.219	1.271	0.046
12.0	1.061	0.890	1.193	1.266	0.071
17.0	1.131	0.834	1.120	1.267	0.038

Table 2 Means and standard errors for F/F_t in the peripherally placed SFS configuration

$NSFS$	ABR	F/F_t	$(F/F_t)_n$	$(F/F_t)_a$	ϵ
0	0	0.835	1	1	0.067
4	1.072	1.114	1.334	1.429	0.082
6	1.113	1.407	1.686	1.845	0.174
8	1.156	1.907	2.284	2.639	0.225

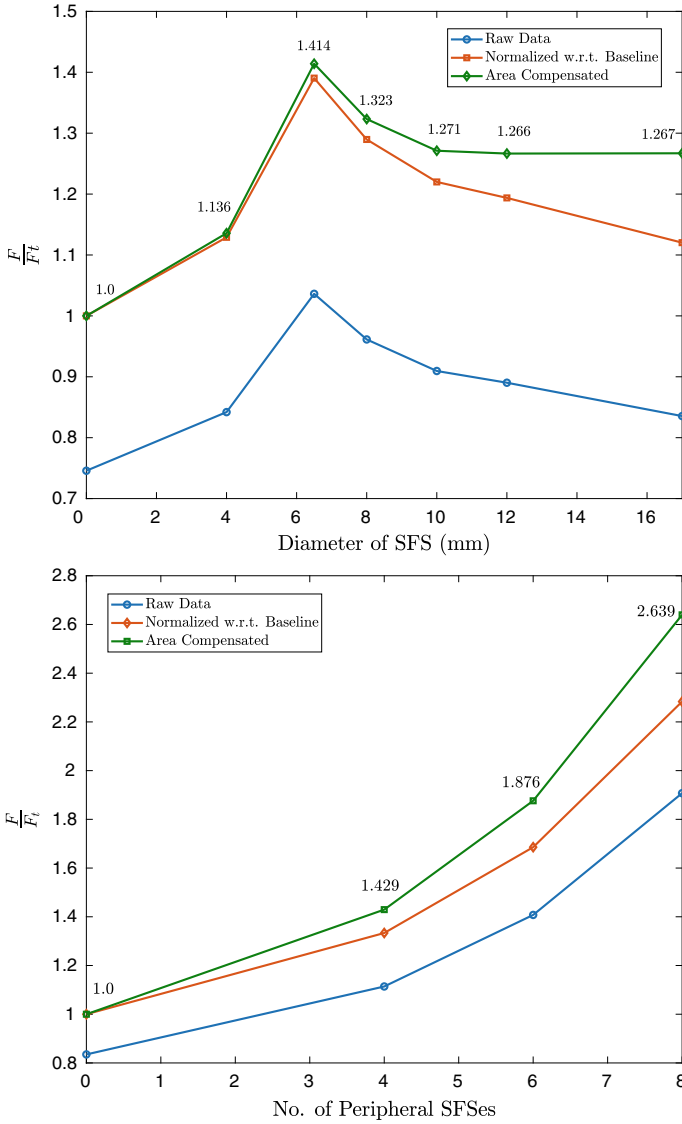


Fig. 2 Comparative charts for the cases of centrally placed (top) and peripherally placed inserts (bottom)

3.2 Uncertainties in Measurements

Internal errors (ϵ) in the measurements of $(F/F_t)_a$ are reported in Tables 1 and 2 as standard deviations ($\pm\sigma$) in the data. The standard deviations reported here are means of the standard deviations over the entire Ra range.

3.3 Discussion

The enhancement in salt flux across the pipe suggests that there is an enhancement of axial salt transport due to the presence of the shear-free surface(s). Though this enhancement of axial transport has been directly observed, the causality between this observation and attenuation of wall-normal and lateral transport process is not firmly established. To this end, future studies will incorporate flow visualization involving Particle Image Velocimetry (PIV) and Planar Laser-Induced Fluorescence (PLIF) techniques to investigate the scalar (salt concentration) and velocity fields.

4 Conclusions

The flux enhancement observed from the experimental studies reported here provides for a strong validation of the proposed hypothesis, i.e. the placement of shear-free surface(s) in various configurations in a buoyancy driven zero mean shear turbulent convection results in attenuation of wall-normal/ lateral turbulent scalar transport whose global effects are visible as enhanced flux.

Nomenclature

C_T, C_B	Salt Concentration in the top and bottom tanks, respectively
V_T, V_B, V_P	Volumes of top tank, bottom tank and pipe, respectively
F	Measured Salt Flux
F_T	Modelled/ Theoretical Salt Flux
$(F/F_T)_n$	F/F_T Normalized w.r.t. baseline
$(F/F_T)_a$	$(F/F_T)_n$ Compensated for area blockage
ABR	Area Blockage Ratio $\frac{A_{pipe}}{A_{pipe} - m * A_{SFS}}$

References

1. Hunt JCR, Graham JMR (1978) Free stream turbulence near plane boundaries. J Fluid Mech 84(2):209–235
2. Kathuria A, Shukla G (2008) Experimental Investigation of drag reduction by macro additives in a turbulent pipe flow. Technology Report, Indian Institute of Technology, Delhi
3. Vamsi R (2009) Drag Reduction by modifying the large scales of turbulent channel flow, Ph.D. Thesis, Indian Institute of Technology, Delhi
4. Sahoo TK (2010) Drag Reduction by modifying large scales of a turbulent flow, Ph.D Thesis, Indian Institute of Technology, Delhi
5. Lal S (2013) Flux enhancement by shear free surfaces in turbulent convection, Ph.D. Thesis, Indian Institute of Technology, Delhi

6. Cholehari MR, Srinivasan B (2011) Investigation of novel drag reduction strategies. Technology Report, Indian Institute of Technology, Delhi
7. Cholehari MR, Arakeri JH (2009) Axially homogeneous, zero mean flow buoyancy driven turbulence in a vertical pipe. *J Fluid Mech* 621:69–102
8. Cholehari MR, Arakeri JH (2005) Experiments and model of turbulent exchange flow in a vertical pipe. *Int J Heat Mass Transfer* 48(21–22):4467–4473

Comparative Study of Turbulent Heat Transfer in Plane Wall Jet Using Different k - ϵ RANS Models



Animesh Patari, Shantanu Pramanik, and Tanmoy Mondal

Abstract The turbulent mechanism of heat transfer from an isothermal flat surface by a wall jet has been numerically investigated using three varieties of k - ϵ models such as Realizable, RNG and Standard k - ϵ models. Enhanced Wall Treatment (EWT) has been implemented with all of them as near wall treatments to capture the near wall more accurately. The primary objective of this work is to find the best performing model among these three which predicts the thermal behavior of wall jet with highest accuracy. Commercial CFD package ANSYS-Fluent solver has been used to perform the numerical simulation under a fixed jet exit Reynolds number of 9600. This study reveals that the Realizable k - ϵ model has the better potential to predict the near wall thermal characteristics of wall jet in terms of heat transfer coefficient, turbulent heat flux and near wall temperature distribution with reasonable accuracy than the others, if the near wall mesh elements are properly structured.

Keywords Turbulence · Heat transfer · RANS models · Wall treatments · Wall jet

1 Introduction

When a turbulent jet is issued tangentially to a wall, the outer portion of the jet promotes strong momentum exchange with the surrounding fluid and set it in motion due to the effect of shear, which is further augmented by turbulent mixing. This region is known as free shear or outer layer. In contrast to that, the portion of the jet closed to the wall creates a very thin inner layer of thickness δ_x , as shown schematically

A. Patari (✉) · S. Pramanik
Department of Mechanical Engineering, NIT Durgapur, Durgapur 713209, India
e-mail: apatari.me@nitdgp.ac.in

S. Pramanik
e-mail: spramanik.me@nitdgp.ac.in

T. Mondal
Department of Mechanical Engineering, NIT Patna, Patna 800005, India
e-mail: tanmoy.me@nitp.ac.in

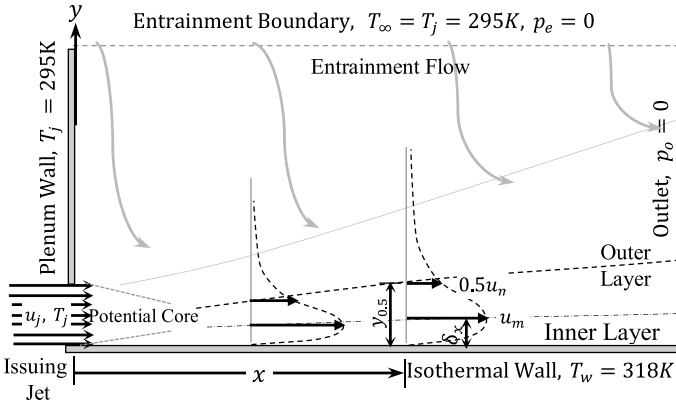


Fig. 1 Schematic of wall jet flow domain

in Fig. 1, across which the velocity changes from zero to maximum value u_m , quite similar to a boundary layer. This is called inner layer. The velocity starts decreasing thereon and reaches to a half of the maximum value at a wall normal distance known as half thickness. Velocity further decreases and attains the far field condition asymptotically at some distance. The flow and thermal characteristic in this two layers are completely different. The inner layer resembles a boundary layer over a flat surface but with certain disparities. Therefore, the presence of any wall adjacent to the jet makes its near wall features much more complicated and challenging. Moreover, there are vast applications of wall jet in heat transfer engineering such as, cooling of turbine blades, electronic cooling, defrosting of wind shield and many more. That is why, the turbulent wall jet in particular has been very interesting topic for many researchers since last few decades.

2 Literature Review and Objective

Several studies with measurements and simulations on the investigation of wall jet flow with different wall configurations and with or without co-flow and concurrent heat transfer are available. Most significant among the experimental investigations are those of Wygnanski [1], Eriksson [2] and Dakos [3], which revealed different aspects of the mean flow as well as the turbulent structure of wall jet. The early researches on wall jet heat transfer include the work of Seban [4], who performed experimental estimation along with theoretical correlation of the temperature and heat transfer coefficient for turbulent jet of hot air injected tangentially to an adiabatic wall. Nizou [5] conducted an experiment on turbulent wall jet with iso-flux wall for a range of $Re = 9000-60,000$ to underline the differences between the correlations of skin friction with heat transfer coefficient of a wall jet and turbulent boundary layer. Later on, experiment with analytical treatment on wall jet heat transfer characteristics was

performed by Mabuchi [6]. The effect of curvature of wall on heat transfer in wall jet was experimentally studied by Dakos [3]. AbdulNour [7] studied heat transfer characteristics of wall jet experimentally with both isothermal and iso-flux wall in the developing region of flow. The thermal characteristics of wall jet were simulated also by using several numerical tools. A meticulous analysis with the budget of turbulent heat flux and temperature variance was presented by Naqavi [8] using Direct Numerical Simulation (DNS) of plane wall jet on an isothermal wall with jet $Re = 7500$. The Standard $k-\varepsilon$ model [9, 10] was tested by Singh [11] to study the heat transfer enhancement on a wavy surface using wall jet. Recently, the transition of boundary layer of turbulent jet on an isothermal wall has been numerically simulated by Nie [12] using six different low- Re $k-\varepsilon$ models, however, they reported only the mean flow and heat transfer features over a short span of wall.

A comprehensive literature survey reveals that there are very limited number of numerical works which simulate particularly the near wall heat transfer characteristics of a wall jet. A wide range of numerical methods have been implemented for the same. It is observed that the DNS can simulate the turbulent features of wall jet with greater accuracy but at the cost of huge computational overhead and time. So, DNS is a costly affair for large domain size and high Re . Self-similar features and detail interaction between inner and outer layers in wall jet can be accurately simulated with LES [13] at reasonable Re , but the domain extent must be at least 40 slot distance downstream with a very high mesh resolution, which imposes a constraint to the computational resource similar to DNS. But with sufficiently large 2D domain, the RANS model can simulate the same with lower grid resolution and limited resource.

Therefore, the purpose of this numerical work is to search for a low cost alternative to LES or DNS, in the $k-\varepsilon$ models coupled with suitable near wall treatment like EWT which can simulate the heat transfer characteristics as well as the behavior of turbulent heat flux of any wall jet with acceptable accuracy and sufficient details.

3 Mathematical Formulation and Numerical Methodology

An incompressible jet of air is discharged through a rectangular slot of gap $w = 10\text{mm}$ tangentially to a flat isothermal wall having temperature $T_w = 318\text{K}$. The velocity of jet at the exit is $u_j = 15.606\text{m/s}$, issuing under zero gauge pressure and the temperature same as that of the ambient $T_j = 295\text{K}$. An adiabatic plenum wall is placed immediately above the slot and perpendicular to the wall to restrict any co-flow. In order to investigate the interaction of the jet with surrounding fluid medium, a rectangular domain is assumed, with sufficient separating distance between the wall and the entrainment or the top boundary to ensure negligible influence of the jet on the top boundary, where the local ambient condition is assumed to persist. Reynolds Averaged Navier–Stokes (RANS) equations which are needed to be solved for steady incompressible flow without volumetric heat source are, respectively

$$\text{Continuity : } \frac{\partial u_j}{\partial x_j} = 0 \quad (1)$$

$$\text{Momentum : } \frac{\partial u_i u_j}{\partial x_j} = \frac{1}{\rho} \frac{\partial}{\partial x_j} \left[\tau_{ij} - \overline{\rho u'_i u'_j} \right] + g_i \quad (2)$$

$$\begin{aligned} \text{Energy : } \frac{\partial u_j (\lambda + \frac{1}{2} u_i u_i + k)}{\partial x_j} &= \frac{\partial}{\partial x_j} \left(\frac{k_f}{\rho} \frac{\partial T}{\partial x_j} - \overline{u'_j \lambda'} \right) \\ &+ g_i u_i + \frac{1}{\rho} \frac{\partial}{\partial x_j} \left[u_i (\tau_{ij} - \overline{\rho u'_i u'_j}) \right] \\ &+ \frac{1}{\rho} \frac{\partial p u_j}{\partial x_j} \end{aligned} \quad (3)$$

The stress tensor, τ_{ij} , for the mean flow is defined as

$$\tau_{ij} = - \left(p + \frac{2}{3} \rho \nu \frac{\partial u_j}{\partial x_j} \right) \delta_{ij} + \rho \nu \left(\frac{\partial u_j}{\partial x_i} + \frac{\partial u_i}{\partial x_j} \right) \quad (4)$$

According to the gradient diffusion hypothesis [9, 10], the fluctuating stress $-\overline{\rho u'_i u'_j}$ is correlated with the mean velocity gradient and eddy viscosity ($\nu_t = C_\mu k^2 / \varepsilon$) as follows-

$$-\overline{\rho u'_i u'_j} = -\frac{2}{3} \rho \left(k + \nu_t \frac{\partial u_k}{\partial x_k} \right) \delta_{ij} + \rho \nu_t \left(\frac{\partial u_j}{\partial x_i} + \frac{\partial u_i}{\partial x_j} \right) \quad (5)$$

Therefore, to deal with this term, some closure models in the form of transport equation of turbulent kinetic energy, k and the dissipation of turbulent kinetic energy, ε , are additionally solved. Three varieties of k - ε models such as the Standard, RNG and the Realizable [9, 14] models in combination with Enhanced Wall Treatments have been employed to simulate the same problem. The steady state transport equations for k and ε are, respectively-

$$\frac{\partial k u_j}{\partial x_j} = \frac{\partial}{\partial x_j} \left\{ \left(\nu + \frac{\nu_t}{\sigma_k} \right) \frac{\partial k}{\partial x_j} \right\} + P_k + P_b - \varepsilon \quad (6)$$

$$\frac{\partial \varepsilon u_j}{\partial x_j} = \frac{\partial}{\partial x_j} \left\{ \left(\nu + \frac{\nu_t}{\sigma_\varepsilon} \right) \frac{\partial \varepsilon}{\partial x_j} \right\} + C_{1\varepsilon} \varepsilon \left(\frac{P_k + C_{3\varepsilon} P_b}{k} \right) - C_{2\varepsilon} \frac{\varepsilon^2}{k} \quad (7)$$

Here, P_k and P_b are two production terms appear due to turbulent fluctuation and buoyancy. However, the shape of the above equations slightly differs for the RNG model [9, 10]. ANSYS-Fluent solver version 17.1 is used for all the simulation keeping the standard values of the model constants like, $C_{1\varepsilon}$, $C_{2\varepsilon}$, α , etc., as assigned in the Fluent set up. The SIMPLE algorithm [15] is adopted as pressure-velocity coupling with second-order scheme for pressure and second-order upwind scheme for all other

transport equations. The numerical solutions are assumed to have been converged when the residues for energy and other transport equations reached 10^{-9} and 10^{-6} , respectively.

3.1 Enhanced Wall Treatment

Mainly two different wall treatments such as the Standard Wall Function [16] and the EWT are most suitable for non-reattaching flow without any pressure gradient.

The EWT is a two layer-based approach [9], in which the improved values of turbulent viscosity, dissipation, etc., are calculated in the near wall region by employing some blending functions depending upon the value of turbulent Reynolds number $Re_t = y\sqrt{k}/\nu$. For example, the dissipation is expressed as $\varepsilon = C_\mu^{3/4} k_p^{3/2} / \left[\chi y \left\{ 1 - \exp\left(-Re_t / 2\chi C_\mu^{-3/4}\right) \right\} \right]$. In the viscosity dominated near wall region ($Re_t < 200$) only the turbulent kinetic energy equation is solved along with the mean flow equations. The near wall gradient of any mean flow parameter as well as the turbulence structure can be captured very accurately using this wall treatment approach. But it can be achieved only if the near wall region of the flow domain be resolved into very fine meshes so as to have the y^+ value of the wall attached cell centers less than unity as recommended in the literatures [9]. But this dense grid structure generally delays the solution convergence. However, this difficulty can be avoided if the grid distribution particularly in the wall attached zone are done in a proper manner.

A typical mesh distribution for a wall jet domain as explained earlier is shown in Fig. 2. The mesh distribution is non-uniform but structured. The number of elements for the finer mesh used for computation is $735 \times 290 = 213150$.

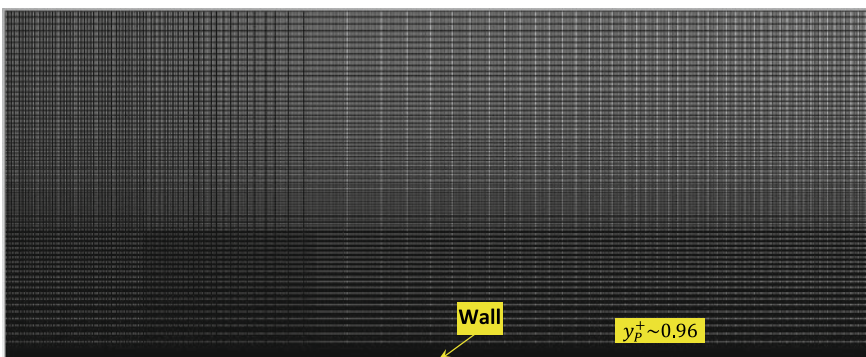


Fig. 2 Typical mesh structure of the flow domain

3.2 Grid Independence Study

A grid dependence study is performed in order to find the optimum number of mesh elements to ensure the accuracy and independency of the numerical results on further mesh refinement.

This is done by estimating the Grid Convergence Index (GCI) for any variable ϕ , a detailed study based on Richardson extrapolation method as systematically explained in the literature [17].

For particular model a coarse (c), a medium (m) and a fine (f) grid have been generated through systematic refinement technique with number of elements N_c , N_m and N_f , respectively. The grid refinement ratio becomes $r_{fm} = \sqrt{N_f/N_m}$ between the fine and medium grid, etc. The difference in numerically computed values of ϕ from the fine and the medium grids at any particular grid point is $\epsilon_{fm} = \phi_f - \phi_m$ with the relative error $\epsilon_{r_{fm}} = |100\epsilon_{fm}/\phi_f|\%$. The resulting apparent order of accuracy of the numerical scheme is then calculated using the iterative formulation as expressed below

$$\hat{p} = \left| \ln|\epsilon_{mc}/\epsilon_{fm}| + \ln\left(r_{fm}^{\hat{p}} - s\right) / \left(r_{mc}^{\hat{p}} - s\right) \right| / \ln r_{fm}$$

where, $s = \text{sign}(\epsilon_{mc}/\epsilon_{fm})$. The extrapolated value of the variable ϕ and the corresponding extrapolated error on that particular point are calculated, respectively, using the relations

$\phi_{ex_{fm}} = \left(r_{fm}^{\hat{p}}\phi_f - \phi_m\right) / \left(r_{fm}^{\hat{p}} - 1\right)$ and $\epsilon_{ex_{fm}} = |100(1 - \phi_f/\phi_{ex_{fm}})|$. Finally, the GCI of fine grid is estimated to be $GCI_f = 1.25\epsilon_{r_{fm}} / \left(r_{fm}^{\hat{p}} - 1\right)$.

The GCI of the fine grid solutions for the local shear stress τ_{wx} obtained using the Realizable $k-\epsilon$ model has been calculated. For this purpose, total 23 data points at convenient locations along the length of the wall are chosen. The apparent order of accuracy \hat{p} varies within a range of 0.2145–10.338, giving a global average of 1.945 based on which the numerical uncertainties are estimated at each of those points and plotted as error bar associated to the fine grid results (refer to the Fig. 3). The medium and coarse grid solutions are also plotted together. The maximum uncertainty in τ_{wx} values is found to be 1.14%.

Similar analysis has been conducted for the turbulent kinetic energy at 30 slot distance downstream for realizable $k-\epsilon$ model considering 24 points across the flow (as depicted in Fig. 4). The range of values of \hat{p} and its global average have been estimated to be 0.870–12.547 and 2.093, respectively. The maximum uncertainty in this case is 60.68% but corresponding to a very low k -value of 0.000373.

It is evident from the GCI analysis for both the cases that the fine grid solutions are in the asymptotic convergence state. Therefore, this fine grid with number of elements $735 \times 290 = 213150$ can be finalized to perform all the simulations.

Fig. 3 Wall shear stress variation with grid and discretization error bar for the fine grid solution

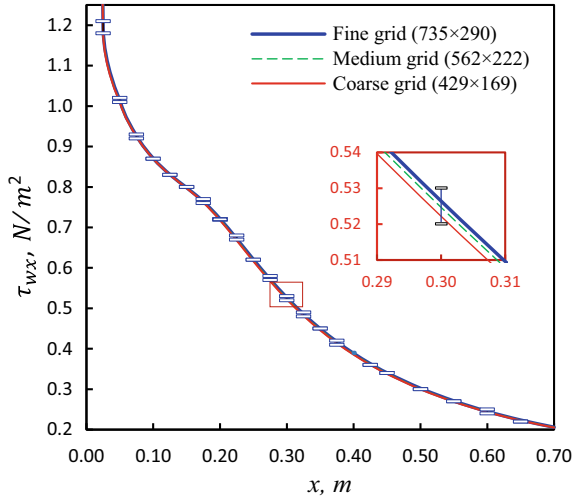
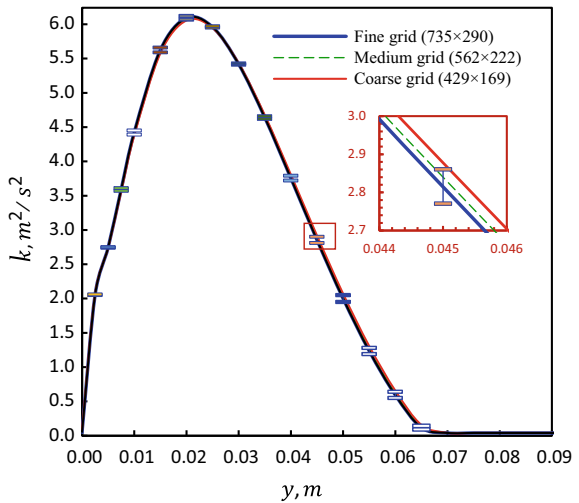


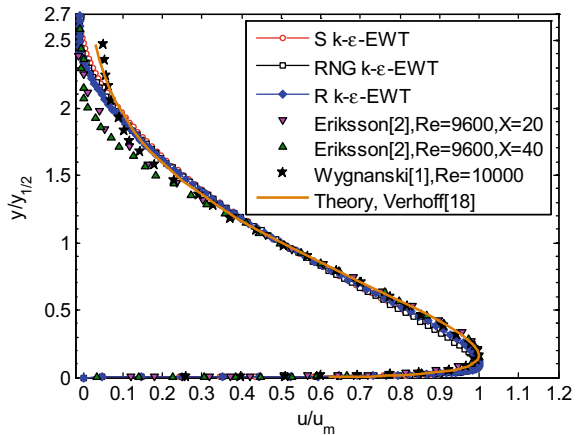
Fig. 4 Variation of turbulent kinetic energy for different grids and discretization error bar for the fine grid solution at $X = 30$



4 Results and Discussion

Following the grid independence test, the numerical data for several field variables are systematically compared with some benchmark experimental data to check the accuracy and hence the validity of the numerical simulations.

Fig. 5 Similarity of velocity profiles at $X = 40$



4.1 Validation of the Mean Flow Field

Firstly, the non-dimensional stream-wise velocity, u/u_m , for all the schemes is chosen to plot against non-dimensional wall normal distance $y/y_{1/2}$ at downstream position $X = 40$. Here, $y_{1/2}$ is the wall normal distance, where the stream-wise velocity in the outer layer reaches fifty percent of the local maximum velocity. This is called outer scale representation. The velocity profiles are compared with experimental finding of Eriksson [2], Wygnanski [1] as well as Verhoff's theoretical expression given in literature [18]. As seen from Fig. 5, the numerically computed data are in excellent conformity with the respective experimental data for all three numerical schemes. Maximum velocity occurs at 9–10% of the $y_{1/2}$, a little lower than the experimental value of 13–17% [1–3].

4.2 Variation of the Mean Temperature

The non-dimensional temperature, θ at $X = 40$, is plotted in Fig. 6 in the outer coordinate along with the experimental temperature profiles of Dakos [3] and AbdulNour [7] as well as with the DNS temperature profile of Naqavi [8]. A complete similarity can also be achieved if the temperature is plotted in a scale y/δ_T (Fig. 7). To test the mean temperature in inner scale, $y^+ = yu_\tau/\nu$, the non-dimensional temperature $T^+ = (T_w - T)/T_\tau$ at $X = 20$ is plotted alongside the corresponding data experimentally determined by Nizou [5] as shown in Fig. 8. Here, u_τ is the local friction velocity and defined as $u_\tau = \sqrt{\tau_w/\rho}$, whereas $T_\tau = q_w/(\rho C_p u_\tau)$ is termed as the friction temperature. The temperature in the inner layer (y^+ upto 120 around) is correctly represented by all the models. The RNG model precisely obeys the log-law proposed by Nizou based on his experimental findings. But the Realizable and

Fig. 6 Non-dimensional mean temperature variation at stream-wise location $X = 40$

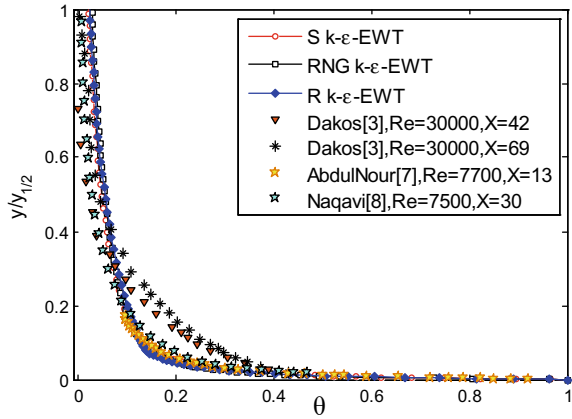
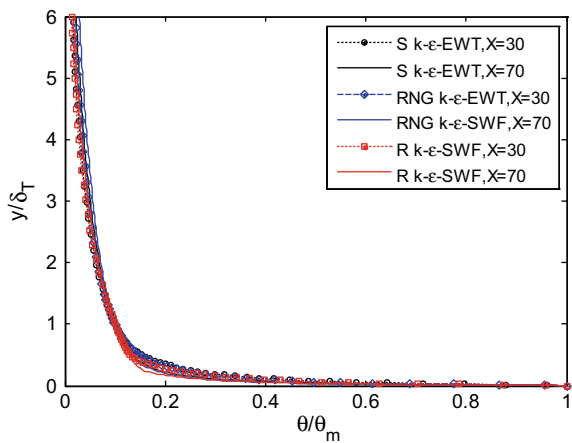


Fig. 7 Similarity profile of temperature in thermal boundary layer scale



Standard $k-\epsilon$ model deviate a little from the measure data in the logarithmic layer (Fig. 8).

4.3 Thermal Boundary Layer Growth

If a thermal boundary layer thickness δ_T is defined as the wall normal distance where the dimensionless temperature attains a value of $\theta = 0.1$, the thermal growth of the jet can be determined over the length of the plate. When compared with the experimental data of AbdulNour [7] and DNS data of Naqavi [8], the thermal boundary layer growth exhibited by all the schemes are found to be very close, as exhibited in Fig. 9. Particularly in the developed zone, the Standard $k-\epsilon$ model shows excellent agreement with the DNS data. The experimental data of AbdulNour [7]

Fig. 8 Mean temperature variation in inner scale

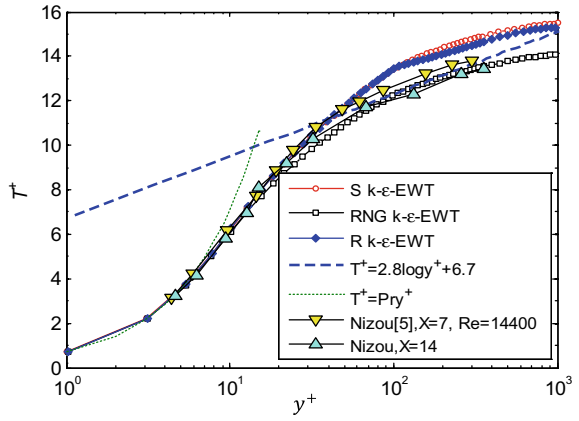


Fig. 9 Growth of thermal boundary layer

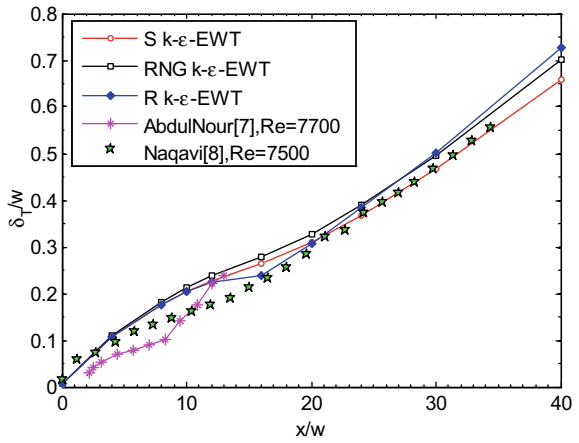
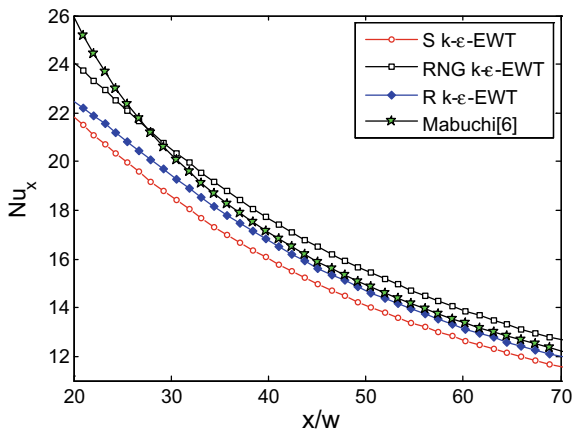


Fig. 10 Nusselt number variation over the wall



is limited within the developing region of the flow, where the present data as well as the DNS data [8] are found to be in a bit different alignment. However, it is also found that the thermal boundary layer grows almost linearly in the developed region. A little higher growth rate (around 5–8%) is shown by the Realizable k - ε model.

4.4 The Nusselt Number Variation

A local Nusselt number at any stream-wise location x on the wall can be defined based on the slot thickness w as $Nu_x = \frac{h_x w}{k_f}$. The dependency of the local Nusselt number on the jet exit Reynolds number and Prandtle number (Pr) for wall jet was determined by Mabuchi [6] through experimentation and theoretical analysis. The proposed correlation is written as $Nu_x = 0.118 Pr^{0.43} Re_j^{0.8} (x/w)^{-0.6}$, which was tested for 30 to 200 slot distance region over the plane and for the Reynolds number range of 7170 to 25,600. The numerically found data of the Nusselt number from the present simulations are plotted in Fig. 10 along with the above correlation. The plot shows that the Realizable model executes the result with very high accuracy beyond 30 slot distance, whereas the Standard k - ε model predicts the Nusselt number around 5% to 9% less than the reference data. The accuracy of RNG model is within 3–4%.

4.5 The Turbulent Heat Flux

The transport of any physical quantity like, mass, energy, heat, etc., occurs in a turbulent flow through molecular motions as well as through turbulence fluctuation of the bulk motion of the fluid within the given geometry. This turbulent fluctuation is suppressed in the vicinity of any wall and the molecular motion dominates over there. As per the eddy viscosity formulation, ν_t acquires a very low value in the sublayer with zero value at the wall. Hence, the turbulent heat flux therein appears to be zero. However, a little distance away from the wall, the transport process occurs mainly due to turbulent mixing. By gradient diffusion hypothesis, the turbulent heat flux can be expressed as

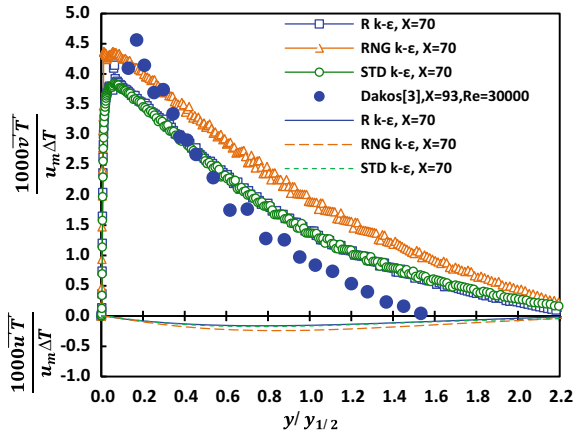
$$-\overline{u'_j \lambda'} = -C_p \overline{u'_j T'} = \frac{C_p \nu_t}{Pr_t} \frac{\partial T}{\partial x_j} \quad (8)$$

The stream-wise and cross-stream components are given as.

$$-C_p \overline{u' T'} = \frac{C_p \nu_t}{Pr_t} \frac{\partial T}{\partial x} \text{ and } -C_p \overline{v' T'} = \frac{C_p \nu_t}{Pr_t} \frac{\partial T}{\partial y} \quad (9)$$

where Pr_t is the turbulent Prandtle number assigned with a value of 0.85 in all varieties of the k - ε models except in the RNG model, where an inverse turbulent Prandtl

Fig. 11 Turbulent heat flux



number is calculated based on the turbulent viscosity ratio [9]. The normalized turbulent heat flux at $x = 70w$ are presented in Fig. 11. These values were normalized by $C_p u_m (T_w - T_j)$ and compared with the corresponding experimental data of Dakos[3], reported for the downstream location $x = 93w$ with jet exit Reynolds number of 30,000. As $\left| \frac{\partial T}{\partial x} \right| \ll \left| \frac{\partial T}{\partial y} \right|$, the eddy viscosity model shows that the turbulent heat flux due to the stream-wise fluctuation of velocity is much lesser than that due to cross-stream velocity fluctuation. It is also found that in the near wall region the turbulent flux of heat acquires a very high magnitude (typically the maximum value around 80% of the wall flux). The maximum value appears a little earlier than the point of maximum velocity. The turbulent heat flux is represented quite appreciably by the Standard and Realizable models with EWT schemes particularly up to the jet half thickness. But the RNG model doesn't stand up to the mark.

5 Conclusions

The thermal transport characteristics of a steady incompressible wall jet have been numerically investigated using different $k-\epsilon$ models using EWT approach at a slot Reynolds number of 9600. The analysis on the numerical results was done and presented graphically alongside corresponding benchmark experimental data. Similarity profiles of velocity and temperature are achieved in the developed zone 30 slot distance onward. The near wall velocity in inner scale is very accurately predicted by the Realizable model, whereas the RNG model stands better than others in predicting the local skin friction coefficient. The inner layer thickness is found to be about 20–30% lower than the experimental value as also evident in the RANS simulation by Yan et. al. [19]. About 8–10% over prediction of the inner scale temperature (under prediction of absolute temperature) in the fully turbulent region is obtained from both the Realizable and Standard models. Though, the near wall temperatures are

very accurately calculated by all the models. The growth of the thermal boundary layer as simulated by the Standard $k-\varepsilon$ model is very close to the DNS data. As far as the wall heat transfer is concern, the Realizable model provides the highest accuracy, whereas the Standard $k-\varepsilon$ model under predicts heat transfer by around 5–9%. The near wall turbulent heat flux is also given quite correctly by Realizable model.

Therefore, none of the three $k-\varepsilon$ models can be certified to be better than the other options to predict wall jet heat transfer characteristics. However, the Realizable $k-\varepsilon$ model is found to be more optimistic than the other models, hence it can be employed with acceptable accuracy to simulate the heat transfer characteristics of a plane wall jet.

Nomenclature

ρ	Fluid density [kg/m ³]
ν	Fluid kinematic viscosity [m ² /s]
C_p	Specific heat of the fluid [J/kg-K]
k_f	Thermal conductivity of the fluid [W/m-K]
X	Non-dimensional stream-wise distance from the nozzle exit, = x/w
θ	Non-dimensional temperature, = $\frac{T-T_j}{T_w-T_j}$
λ	Specific enthalpy [J/kg]
δ_x	Normal distance from the wall at location x where the stream-wise velocity reaches its maximum value u_m [m]
$y_{1/2}$	Wall normal distance where the local stream-wise velocity (u) is half the u_m [m]
Re_j	Reynolds number at nozzle exit, = $\frac{\rho u_j w}{\mu}$
C_f	Local skin friction coefficient, = $\frac{\tau_w}{0.5\rho u_m^2}$

References

1. Wagnanski I, Katz Y, Horev E (1992) On the applicability of various scaling laws to the turbulent wall jet. *J Fluid Mech* 234:669–690
2. Eriksson JG, Karlsson RI, Persson J (1998) An experimental study of a two-dimensional plane turbulent wall jet. *Exp Fluids* 25:50–60
3. Dakos T, Verriopoulos CA, Gibson MM (1984) Turbulent flow with heat transfer in plane and curved wall jets. *J Fluid Mech* 145:339–360
4. Seban RA, Back LH (1961) Velocity and temperature profiles in a wall jet. *Int J Heat Mass Transfer* 3:255–265
5. Nizou PY (1981) Heat and momentum transfer in a plane turbulent wall jet. *ASME J Heat Trans* 103(1):138–140
6. Mabuchi I, Kumada M (1972) Studies on heat transfer to turbulent jets with adjacent boundaries. *Bull JSME* 15(88):1236–1245

7. AbdulNour RS, Willenborg K, McGrath JJ, Foss JF, AbdulNour BS (2000) Measurements of the convection heat transfer coefficient for a planar wall jet: uniform temperature and uniform heat flux boundary conditions. *Exp Therm Fluid Sci* 22(3):123–131
8. Naqavi IZ, Tyacke JC, Tucker PG (2017) A numerical study of a plane wall jet with heat transfer. *Int J Heat Fluid Flow* 63:99–107
9. ANSYS Inc, ANSYS fluent theory guide 12.0 (2015)
10. Biswas G, Eswaran V (2002) *Turbulent flows: fundamentals, experiments and modeling*. Narosa Publishing House, New Delhi
11. Singh TP, Kumar A, Satapathy AK (2020) Enhancement of heat transfer using turbulent wall jet. *Proc IMechE, Part E J Process Mech Eng* 234(1):123–136
12. Nie X, Zhu Z, Liao H, Lü M, Xu J (2021) A comparative study of heat transfer characteristics of wall jet with boundary layer transition using six low-Reynolds number $k-\epsilon$ models. *AIP Adv* 11:025025
13. Dejoan A, Leschziner MA (2005) Large eddy simulation of a plane turbulent wall jet. *Phys Fluids* 17(2):1–16
14. Yang Z, Shih TH (1991) A $k-\epsilon$ modeling of near wall turbulence. NASA TM-105238
15. Patankar SV (1980) *Numerical heat transfer and fluid flow*. Hemisphere, Washington D.C.
16. Amano RS (1984) Development of a turbulence near wall model and its application to separated and reattached flows. *Numer Heat Transfer* 7(1):59–75
17. Celik IB, Ghia U, Roache PJ, Freitas CJ, Coleman H, Raad PE (2008) Procedure for estimation and reporting of uncertainty due to discretization in CFD applications. *J Fluids Eng* 130(7):078001. <https://doi.org/10.1115/1.2960953>
18. Rajaratnam N (1976) *Turbulent jets*. Elsevier Scientific Pub Company
19. Yan Z, Zhong Y, Lin WE, Savory E, You Y (2018) Evaluation of RANS and LES turbulence models for simulating a steady 2-D plane wall jet. *Eng Comput* 35(1):211–234

Linear Instability Analysis of Natural Convection in a Heated Vertical Porous Annulus



A. Khan, P. Chokshi, and P. Bera

Abstract The stability analysis of non-isothermal annular parallel flow through a highly permeable porous medium is studied. The flow is governed by the buoyancy force induced due to the different temperature conditions on the surface of inner and outer cylinders. A linear stability analysis subjected to normal mode analysis has been considered to investigate the influence of gap between cylinders (defined by the curvature parameter, C), Darcy number (Da , which is defined in terms of permeability of the porous medium) as well as Prandtl number (Pr) on the flow instability characteristics. The existence of the inflection point in the laminar base flow profile is checked. Depending on the value of controlling parameters (C , Pr , and Da), the least stable disturbance is found to be axisymmetric for smaller gap and non-axisymmetric for a larger gap between cylinders. The physical mechanism of the flow instability has been examined through kinetic energy analysis.

Keywords Natural convection · Porous media flow · Linear stability theory

1 Introduction

The natural convection in a vertically oriented porous slab/duct has been thoroughly explored due to its practical relevance appeared in electronic industry, thermal-hydraulics of nuclear reactors [1], chemical processing equipment [2], geothermal engineering [3] and building engineering [4]. Knowledge of the heat transfer characteristics and fluid flow mechanism for duct flow systems can guide in optimization of the thermal design and ensure a high degree of safety in the devices used in these applications. As a result, understanding the flow dynamics and heat transfer mechanism under different geometry is crucial before initializing the duct flow through

A. Khan (✉) · P. Chokshi
Department of Chemical Engineering, IIT Delhi, New Delhi 110016, India
e-mail: arshan.khan792@gmail.com

P. Bera
Department of Mathematics, IIT Roorkee, Roorkee 247667, India

porous media in any appliance. The storage of nuclear wastes is another significant application of the flow through vertical porous slab, and it is essential to determine the insulating impact of the annular air gap surrounding a cylindrical nuclear waste canister implanted in a geologic repository. In such a situation, the temperature of the canister is critical because it is the primary factor that determines the life span of the metal containers. To determine if heat will be transferred through the air gap by conduction or convection, the stability of the parallel motion must be investigated.

Generally, the flow through porous medium can be show to depend on the Prandtl number (Pr), Grashof number (Gr), permeability of the porous medium and geometry of the porous enclosure. There are numerous studies that explore the influence of Pr and the media permeability on the instability characteristics of natural convection in a rectangular channel saturated with porous material, which are well documented in refs. [5, 6] and references therein. The annular flow is unlike the conventional channel flow in terms of heat transfer mechanism and the flow instability characteristic [7]. Based on the gap between circular coaxial cylinders, the study of the annular flow provides a more general overview of the duct flow (including channel flow as well as flow through a circular pipe with a thin rod its center) dynamics. Therefore, motivated by the strikingly different stability characteristics of the flow in annular configuration compared to the flow in channel and the use of annular set up in many industrial situations [8], an extension of the work of Khan and Bera [9] to the natural convection case is established in the present study. From the best of our knowledge, there are only two studies [10, 11] on the stability of a natural convection in a vertical annulus filled with porous media. These studies are restricted to the stationary base flow. They have only looked into the effect of radius ratio (or curvature parameter), ignoring the effects of the permeability of the porous medium and the type of fluid in terms of Prandtl number. In a tall vertical slot, if the flow is assumed to be parallel, the velocity profile persists a nonlinear shape, with the fluid moving downward near the cooler wall and upward near the warmer wall [12]. It has been observed for the purely viscous media flow through vertical annulus. In a parallel flow, the flow is said to be in the conduction regime since heat is only carried across the duct by conduction between the fluid layers. The conduction regime when Gr is small was also validated by the experimental data [13]. However, as Gr rises, the flow becomes unstable, first giving rise to multicellular secondary flow patterns and then, as Gr rises even higher, turbulence. It has also been studied into whether the natural convection conduction regime is stable [14]. The Pr effects on the flow instabilities of natural convection in annular geometry filled with isotropic porous material have never been studied. Therefore, a step has been taken in the present work to understand such instability characteristics. Here, we have focused on the Prandtl number, curvature parameter (characterized in terms of the gap between cylinders), and media permeability on the type of instability and have been shown that these parameters are also responsible for the resulting type of insatiability and heat transport in the annular domain.

2 Methodology

The problem under consideration is the natural convection in a vertically oriented annular passage filled with isotropic porous material. The annulus is delimited by homogeneous and isotropic porous layers. The inner wall of the annulus is kept at constant heat flux and the outer wall is insulated. The fluid's thermo-physical properties are considered to be constant except for the dependence of the buoyancy force term in the momentum equation on the fluid density, which is satisfied by the Boussinesq approximation. For the present theoretical investigation, we consider the Darcy-Brinkman model including the local time derivative based on the volume-averaged Navier–Stokes equations developed by Whitaker [15].

After scaling the dimensional variables, the non-dimensional space coordinates (n, ψ, z) , dependent variables (u, v, w, θ, p) and time t are determined as follows:

$$(u, v, w) = \frac{(u^*, v^*, w^*)}{w_s^*}, z = \frac{z^*}{(r_o - r_i)}, \eta = \frac{(r^* - r_i)}{(r_o - r_i)},$$

$$\theta = \frac{(T_w - T^*)v}{k(r_o - r_i)^2}, P = \frac{p^*}{\rho_f w_s^{*2}}, t = \frac{t^* w_s^*}{(r_o - r_i)^2},$$

here w_s^* is defined as $g\beta k(r_o - r_i)^4/v^2$, which can be obtained by balancing the buoyancy force and viscous force in the vertical momentum equation. The non-dimensional governing equations for continuity, momentum and energy, after dropping asterisks, in cylindrical coordinate (n, ψ, z) , are given as

$$\frac{\partial u}{\partial \eta} + \frac{u}{(\eta + C)} + \frac{1}{(\eta + C)} \frac{\partial v}{\partial \psi} + \frac{\partial w}{\partial z} = 0, \quad (1)$$

$$\frac{1}{\epsilon} \frac{\partial u}{\partial t} = -\frac{\partial p}{\partial \eta} + \frac{1}{Gr} \left[D^2 u - \frac{2}{(\eta + C)^2} \frac{\partial v}{\partial \psi} - \frac{u}{(\eta + C)^2} \right] - \frac{1}{Gr Da} u, \quad (2)$$

$$\frac{1}{\epsilon} \frac{\partial v}{\partial t} = -\frac{1}{\eta + C} \frac{\partial p}{\partial \psi} + \frac{1}{Gr} \left[D^2 v + \frac{2}{(\eta + C)^2} \frac{\partial u}{\partial \psi} - \frac{v}{(\eta + C)^2} \right] - \frac{1}{Gr Da} v, \quad (3)$$

$$\frac{1}{\epsilon} \frac{\partial w}{\partial t} = -\frac{\partial p}{\partial z} + \frac{1}{Gr} \left[D^2 w - \frac{1}{Da} w - \theta \right], \quad (4)$$

$$\sigma \frac{\partial \theta}{\partial t} + u \frac{\partial \theta}{\partial \eta} + \frac{v}{\eta + c} \frac{\partial \theta}{\partial \psi} + w \frac{\partial \theta}{\partial z} = \frac{1}{Gr Pr} [D^2 \theta + \sigma], \quad (5)$$

where,

$$D^2 = \frac{\partial^2}{\partial \eta^2} + \frac{1}{\eta + C} \frac{\partial}{\partial \eta} + \frac{1}{(\eta + C)^2} \frac{\partial^2}{\partial \psi^2} + \frac{\partial^2}{\partial z^2}.$$

The used dimensionless parameters in the governing equations are the curvature parameter, $C = \frac{r_i}{r_o - r_i}$, porosity, ε , the Grashof number, $Gr = \frac{w_s(r_o - r_i)}{\nu}$, the Darcy number, $Da = \frac{K}{(r_o - r_i)^2}$, ratio of specific heat capacities, $\sigma = \frac{c_p}{c_v}$ and the Prandtl number, $Pr = \frac{\nu}{\alpha}$. Here r_i , r_o , ν , K , c_p , c_v , α and ρ are the radius of inner cylinder, radius of outer cylinder, kinematic viscosity, permeability of the porous medium, specific heat capacity at constant pressure, specific heat capacity at constant volume, thermal diffusivity and the density of the fluid phase, respectively. To avoid too many parametric studies, we have fixed the heat capacity ratio at 1.

2.1 Basic Flow Equations

The basic flow, whose stability will be analyzed, is a steady, unidirectional and fully developed flow. Using these assumptions to Eqs. (2)-(6), the basic flow becomes independent of the axial and azimuthal coordinates and the simplified governing equations are

$$W'' + \frac{1}{\eta + C}W' - \frac{1}{Da}W - \Theta = Gr \frac{dP}{dz} \quad (6)$$

$$\Theta'' + \frac{1}{\eta + C}\Theta' = -1 \quad (7)$$

where W , P and Θ are the basic velocity, pressure and temperature, respectively. The prime ($'$) denotes the derivative with respect to η . The corresponding boundary conditions are

$$W = \Theta = 0 \text{ at } \eta = 0 \text{ and } W = \Theta' = 0 \text{ at } \eta = 1$$

The axial pressure gradient can be determined by the requirement of global mass conservation:

$$\int_0^1 (\eta + C)W d\eta = 0$$

2.2 Linear Stability Analysis

The normal mode analysis [16] is employed to investigate the stability of the above considered basic flow. The dependent field variables are decomposed into a basic state variables and an infinitesimal disturbance. The velocity field, temperature and pressure are written as:

$$(u, v, w, \theta, p) = (\tilde{u}, \tilde{v}, W(\eta) + \tilde{w}, \Theta(\eta) + \tilde{\theta}, P(z) + \tilde{p})$$

These infinitesimal disturbances of corresponding field variables are split into the following normal mode form as:

$$(\tilde{u}, \tilde{\theta}, \tilde{p}) = (\hat{u}(\eta), \hat{\theta}(\eta), \hat{p}(\eta))e^{i(\alpha(z-ct)+n\psi)} \quad (9)$$

where $\mathbf{u} = (u, v, w)$, $\alpha, c = \hat{c}_r + i\hat{c}_i$, and n are the velocity field, axial wavenumber, complex disturbance wave speed, and azimuthal wavenumber, respectively. Upon substitution of equations above decomposition into the non-dimensional governing equations and neglecting the nonlinear terms, the linearized perturbation equations are given as follows:

$$\begin{aligned} \hat{u}' + \frac{\hat{u}}{\eta + C} + \frac{in\hat{v}}{\eta + C} + i\alpha\hat{w} &= 0, \\ Gr[i\alpha(W - c)\hat{u} + \hat{p}'] - \hat{u}'' - \frac{\hat{u}'}{\eta + C} + \frac{(1 + n^2)\hat{u}}{(\eta + C)^2} + \left(\alpha^2 + \frac{1}{Da}\right)\hat{u} \\ &\quad + 2in\frac{\hat{v}}{(\eta + C)^2} = 0, \\ iGr\left[\alpha(W - c)\hat{v} + \frac{n\hat{p}}{\eta + C}\right] - \hat{v}'' - \frac{\hat{v}'}{\eta + C} + \frac{(1 + n^2)\hat{v}}{(\eta + C)^2} + \left(\alpha^2 + \frac{1}{Da}\right)\hat{v} \\ &\quad - 2in\frac{\hat{u}}{(\eta + C)^2} = 0, \\ Gr[i\alpha\{(W - c)\hat{w} + \hat{p}\} + W'\hat{u}] - \hat{w}'' - \frac{\hat{w}'}{\eta + C} + \frac{n^2\hat{w}}{(\eta + C)^2} \\ &\quad + \left(\alpha^2 + \frac{1}{Da}\right)\hat{w} + \hat{\theta} = 0, \\ -GrPr[i\alpha(W - c)\hat{\theta} - \Theta'\hat{u}] + \hat{\theta}'' + \frac{\hat{\theta}'}{\eta + C} - \frac{n^2\hat{\theta}}{(\eta + C)^2} \\ &\quad - \alpha^2\hat{\theta} = 0. \end{aligned}$$

Here, prime ($'$) denotes the first order derivative of a field variable with respect to η . The boundary conditions required to solved of the perturbation equations are

$$\begin{aligned} \hat{u}(0) = \hat{v}(0) = \hat{w}(0) = \hat{\theta}(0) &= 0 \quad \text{and} \\ \hat{u}(1) = \hat{v}(1) = \hat{w}(1) = \hat{\theta}'(1) &= 0. \end{aligned}$$

Table 1 Validation of present results with the published results of Rogers and Yao [12] for different values of Pr , C and n

(Pr, C, n)	Published results [12]	Present results
	(Gr_c, α_c, c_r)	(Gr_c, α_c, c_r)
(0.01, 0.6, 1)	$(13900, 2.5, 0.19 \times 10^{-2})$	$(13913.2, 2.5, 0.20 \times 10^{-2})$
(0.01, 10, 0)	$(15140, 2.73, 0.42 \times 10^{-2})$	$(15135.4, 2.73, 0.42 \times 10^{-2})$
(10, 10, 0)	$(5526, 1.58, 0.43 \times 10^{-2})$	$(5520.6, 1.58, 0.43 \times 10^{-2})$
(10, 100, 1) and (10, 100, 0)	(6100, 1.52,)	(6086.6, 1.52,)

The basic flow equations as well as linear disturbance equations are solved by using spectral collocation method. The Chebyshev polynomials are used to approximate the dependent field variables. The domain $[0, 1]$ is transformed to the canonical domain of Chebyshev polynomials by using transformation, $\xi = 2\eta - 1$. The highest order of Chebyshev polynomial used in the approximation of velocity, temperature and pressure fields is 80. The procedure of solving the linear disturbance equations and finding the critical value of controlling parameters is well explained in ref. [17]. To validate the presented numerical results, we have computed the critical value of Grashof number, the critical value of axial wavenumber, and critical wave speed for different values of C and Pr to the special case of purely viscous media flow [12] by setting $Da = 10^{12}$. Table 1 provides good support for the present results.

3 Results and Discussion

The parameters in this problem are Gr , Pr , C and Da . For a fixed Pr , C and Da , the flow becomes unstable as Gr increases and a complete linear instability map is obtained by considering the effect of Pr , C and Da on Grashof number. In this article, the impact of Pr on Gr is examined for two values (0.1 and 10) of C , three values (10^{-1} , 10^{-2} and 10^{-3}) of Da and a wide range [10^{-3} , 10^2] of Prandtl number. The current choice of Pr provides a complete picture of the instabilities present in the considered physical scenario. It is worthwhile to note that the ideal gases will have Prandtl numbers greater than 0.4, which is known from kinetic theory, while most common liquids have Prandtl numbers greater than 1. The exceptions are liquid metals, whose Prandtl numbers are less than 0.1. Consequently, no common fluids will have Prandtl numbers in the intermediate range. However, data are presented for a continuous range of Prandtl number to demonstrate the results of the instability calculations.

It is crucial to understand how controlling parameters C and Da affect the point of inflection's appearance since the point of inflection on the basic flow velocity profile acts as a possibility for the flow instability [18]. In this connection, we have shown the basic flow velocity (W) for different value of both curvature parameter and Rayleigh number, as shown in Fig. 1a. The corresponding basic flow temperature (Θ) profile

displayed in Fig. 1b. The velocity profile for $C = 10$ is almost symmetric about $\eta = 0.5$, while the profile for $C = 0.1$ is asymmetric. This is because $C = 10$ corresponds to an annulus with a narrow gap, approaching a two-dimensional slot, while $C = 0.1$ represents an annulus with a much more pronounced curvature effect. Both of these velocity profiles contain inflection points, which suggests a potential for inviscid instability. Moreover, it can be seen from the velocity profiles that on changing the value of curvature parameter from 0.1 to 10, the point of inflection shifts from the inner cylinder to the center of the annular domain. However, on decreasing the media permeability, the same shifts from the center to the inner cylinder. On increasing the value of C , the maximum magnitude of the velocity decreases representing the stabilizing nature of C . The media permeability played just a reverse role in the stability of the flow. The temperature profile does not influence by the media permeability for a fixed gap between cylinders, whereas a significant impact of C is visible in Fig. 1b.

The linear instability boundary for the considered set of parameters is shown in Fig. 2a and b. Figure 2a represents the graph of critical value of Gr (i.e., Gr_c) as a function of Pr for $C = 0.1$ and Fig. 2b represents the same for $C = 10$. The solid line in each figure demonstrates the Gr_c -profile for two-dimensional axisymmetric disturbance, whereas the dashed line demonstrate the Gr_c -profile for three-dimensional non-axisymmetric disturbance. It can be seen that the least stable disturbance may be axisymmetric or non-axisymmetric depending on the value of C . For smaller value of C , the least stable disturbance are always three-dimensional, i.e., non-axisymmetric (see Fig. 2a). However, for larger value of C , the least stable disturbance are always

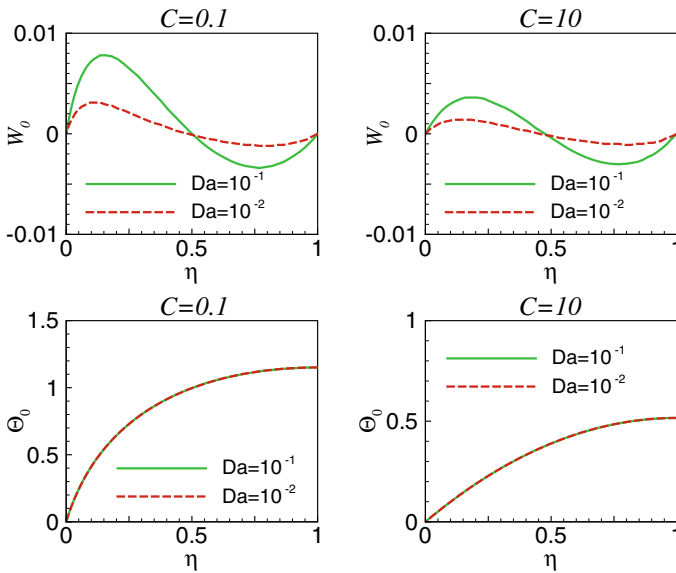


Fig. 1 Base flow velocity and temperature profile for different values of C and Da . The green solid line and red dashed line correspond to $Da = 10^{-1}$ and $Da = 10^{-2}$

two-dimensional, i.e., axisymmetric (see Fig. 2b). The solid and dashed lines in the same figure appear to overlap, but after closely examining the data, we found that the solid line is always lower than the dashed line, signifying that the axisymmetric disturbance is most unstable. On decreasing the media permeability in terms of Da , the critical value of the Grashof number increases for both values of C . Further, an increase in the curvature parameter results in an increase in the critical value of Grashof number, demonstrating the stabilizing nature of C . In general, it can be seen from both figures that on increasing the value of Pr , the critical value of Gr decreases rapidly up to a threshold value of Prandtl number, and above that threshold value of Prandtl number the change in Gr_c is smooth and gradual. To get a greater understanding of the variation of instability boundary, we have taken the help of kinetic energy budget [17]. To derive the balance of kinetic energy, the disturbed velocity field is multiplied on both sides of the disturbed momentum equations (before substituting the normal mode form of the disturbance), which are then integrated over the volume: $[0, 1] \times [0, 2\pi/\alpha] \times [0, 2\pi/n]$ of the disturbance cell. Thus, the rate of change of kinetic energy balance is given as

$$\begin{aligned} \frac{Gr}{\varepsilon} \frac{\partial}{\partial t} \frac{1}{2} (\tilde{u}^2 + \tilde{v}^2 + \tilde{w}^2) &= -\tilde{w}\tilde{\theta} - \frac{1}{Da} (\tilde{u}^2 + \tilde{v}^2 + \tilde{w}^2) - (\nabla\tilde{u})^2 \\ &+ (\nabla\tilde{v})^2 + (\nabla\tilde{w})^2 = E_b + E_D + E_d \end{aligned}$$

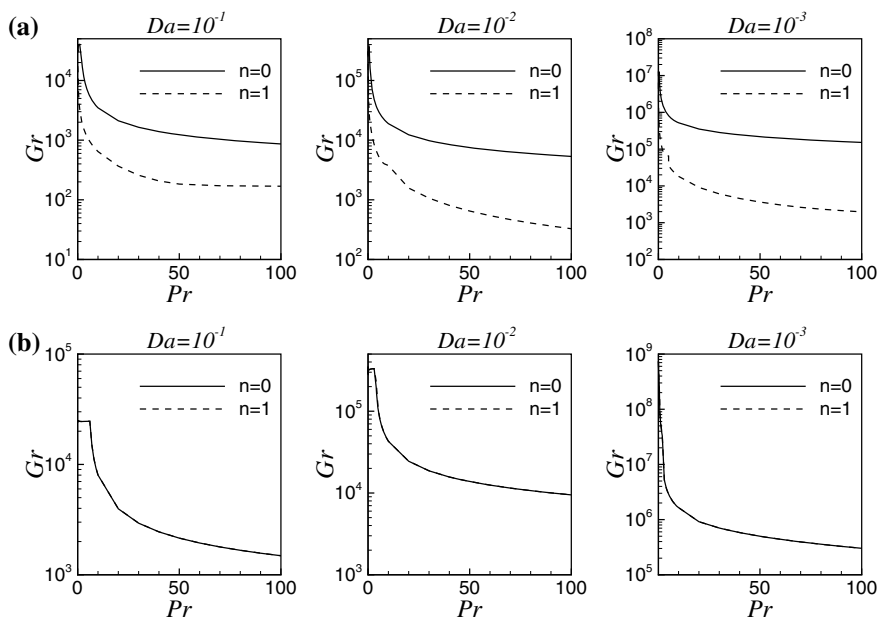


Fig. 2 Linear instability boundary as a function of Prandtl number in (Pr, Gr) -plane for **a** $C = 0.1$ and **b** $C = 10$

In the above equation, the symbol $\langle \rangle$ indicates the integration over the volume of a disturbance cell. In Eq. (20), the integrands in the above equation can be calculated by using the eigenvectors from the linear stability theory. The left-hand side of the Eq. (20) is zero at the critical values of controlling parameter because the disturbances neither grow nor decay along neutral-stability boundary. On the right side of the Eq. (20), the three terms E_D , E_d , and E_b stand for the dissipation of kinetic energy due to work done by surface drag, the dissipation of kinetic energy due to viscous effects, and the production of kinetic energy through work done by the fluctuating body force, respectively. Overall, KE balance Eq. (20) depicts a balance between the dissipation of disturbance kinetic energy caused by viscous force and surface drag and the production of disturbance kinetic energy caused by the buoyant mechanism. Figure 2 clearly indicates that at larger values of Pr , the dominant instability is insensitive to changes in Pr for both values of C . Moreover, the critical value of axial wavenumber shows an asymptotic nature (figure not shown). On the other hand, at smaller values of Pr , instability appears which is strongly dependent on Pr , with Gr , decreasing with increasing Pr . Moreover, in the case of purely viscous media [12], at larger values of the Prandtl number, the flow instability is strongly dependent on Pr , with Gr , decreasing with increasing Pr ; whereas at small values of Pr , the dominant instability is insensitive to changes in Pr . In the present case, at a large value of Pr , the buoyant production is balanced by the dissipation of disturbance kinetic energy, which is due to the effect of viscosity as well as surface drag. Therefore, for all considered values of Da and C , the type of instability is thermal-buoyant. In this instance, for a high value of Pr , the buoyant production is counterbalanced by the dissipation of disturbance kinetic energy, which is caused by the impact of viscosity as well as surface drag. In all cases when Da and C are taken into consideration, the kind of instability is thermal-buoyant. Additionally, the buoyant, viscous and surface drag disturbance forces acting on the flow through the porous material cause the point of inflection in the basic velocity profile to exist or not appear.

4 Conclusions

The present work considered the linear stability analysis of stably stratified non-isothermal parallel flow through a vertically oriented annular domain filled with porous material. The point of inflection in the considered stable laminar flow results in flow instability. The flow is stabilized by the curvature parameter, which is described in terms of the space between the coaxial circular cylinders. The media permeability has a destabilizing impact on the flow. The fluid with a relatively low Prandtl number is linearly most stable against non-axisymmetric disturbance whereas the fluid with relatively high Pr is linearly most stable against axisymmetric disturbance. When the Prandtl number is comparatively bigger, the kinetic energy budget shows that the dominating instability predominantly derives its energy through buoyant production.

To acquire a comprehensive view of the transition to turbulence, the influence of the Prandtl number on the type of bifurcation and secondary flow pattern may also

be studied via nonlinear stability analysis of the same problem. These analyses are left for our future study.

Acknowledgements The author A.K. is grateful to *IIT Delhi*, India for providing the *institute postdoctoral research fellowship* to carry the present work.

References

1. Venugopal G, Balaji C, Venkateshan SP (2010) Experimental study of mixed convection heat transfer in a vertical duct filled with metallic porous structures. *Int J Therm Sci* 49:340–348
2. Nield DA, Bejan A (2013) *Convection in porous media*. Springer, New York
3. Orr FM (2010) Onshore geologic storage of CO₂. *Science* 325:1656–1658
4. Lorente S, Petit M, Javelas R (1998) The effects of temperature conditions on the thermal resistance of walls made of different shapes vertical hollow bricks. *Energy Build* 28:237–240
5. Shankar BM, Kumar J, Shivakumara IS (2017) Stability of natural convection in a vertical layer of brinkman porous medium. *Acta Mech* 228:1–19
6. Sharma AK, Bera P (2018) Linear stability of mixed convection in a differentially heated vertical channel filled with high permeable porous-medium. *Intl J Therm Sci* 134:622–638
7. Choueiri GH, Tavoularis S (2015) Experimental investigation of flow development and gap vortex street in an eccentric annular channel. Part 2. Effects of inlet conditions, diameter ratio, eccentricity and Reynolds number. *J Fluid Mech* 768:294–315
8. Orihuela MP, Anuar FS, Abdi IA, Odabae M, Hooman K (2018) Thermohydraulics of a metal foam-filled annulus. *Intl J Heat Mass Transfer* 117:95–106
9. Khan A, Bera P (2022) Weakly nonlinear analysis of non- isothermal parallel flow in a vertical annulus filled with porous medium. Available at SSRN: <https://ssrn.com/abstract=4210152> or <https://doi.org/10.2139/ssrn.4210152>
10. Bringedal C, Berre I, Nordbotten JM, Rees DAS (2011) Linear and nonlinear convection in porous media between coaxial cylinders. *Phys Fluids* 23:094109–094111
11. Barletta A, Celli M, Rees DAS (2020) Buoyant flow and instability in a vertical cylindrical porous slab with permeable boundaries. *Intl J. Heat Mass Transf* 157:119956
12. Rogers BB, Yao LS (1993) Natural convection in a heated annulus. *Intl J Heat Mass Transfer* 36:35–47
13. Elder JW (1965) Turbulent free convection in a vertical slot. *Intl J Fluid Mech* 23:99–111
14. Choi G, Korpela SA (1980) Stability of the conduction regime of natural convection in a tall vertical annulus. *J Fluid Mech* 99:725–738
15. Whitaker S (1996) The forchheimer equation: a theoretical development. *Transp Porous Media* 25:27–61
16. Drazin PG, Reid WH (2004) *Hydrodynamic stability*. Cambridge University Press
17. Khan A, Bera P (2020) Linear instability of concentric annular flow: effect of Prandtl number and gap between cylinders. *Int J Heat Mass Transf* 152:119530
18. Khan A, Bera P, Khandelwal MK (2019) Bifurcation and instability of mixed convection in a vertical annulus: dependence on curvature parameter. *Phys Fluids* 31:104105-1–104120

Response of a Partially Submerged Pendulum Under Gravity Waves



Md. Shadab Hasan, Kamlesh Kumar, and P. Deepu

Abstract In this paper, an experimental investigation is conducted to study the hydrodynamic interaction between a partially submerged pendulum. The pendulum is made by fixing a spherical ball at one end of a small diameter rigid rod, whose other end is hinged. The pendulum is hinged to the bottom of a water wave tank. Particle image velocimetry and high-speed imaging measurements are applied here to investigate the oscillation properties of the pendulum placed transversely in the waterway, which is induced due to gravity waves in a water channel. Using image analysis tools, we obtain the time series of the angle of the pendulum from the equilibrium position. Their frequency spectra reveal a subharmonic response in addition to the primary resonance. The instantaneous velocity field is also shown with the help of particle image velocimetry.

Keywords Fluid–structure · Interaction · Particle image velocimetry · Frequency response · Subharmonic resonance

1 Introduction

Structure partially submerged in a fluid behaves in such a way that it shows some unique characteristics that have very wide applications. Due to this, it has attracted the attention of researchers, and it is also due to its presence in various industrial and biological systems. Numerous applications exist for structures embedded in oscillatory flow fields, such as oceanic offshore structures. References [1–3], and various energy harvesters [4–6]. Applications such as offshore oceanic structures and towers that are actuated by any means, to prevent structural or operational failure, the response of the structure is to be kept as low as possible. On the other hand, for given wave energy, to harvest optimum energy from any energy harvesting applications, a very high amplitude response of the structure is highly desirable. Therefore, modeling the response of structures, especially those that are embedded in or interact with

Md. S. Hasan (✉) · K. Kumar · P. Deepu
Department of Mechanical Engineering, IIT Patna, Bihta 801106, India
e-mail: shadab_2121me09@iitp.ac.in

© The Author(s), under exclusive license to Springer Nature Singapore Pte Ltd. 2024
K. M. Singh et al. (eds.), *Fluid Mechanics and Fluid Power, Volume 2*, Lecture Notes in Mechanical Engineering, https://doi.org/10.1007/978-981-99-5752-1_4

an oscillatory flow field, is very critical in developing control strategies for these applications.

We made an effort to explore how a buoyant pendulum responded to a surface gravity water wave (simulating oceanic structures like actuated towers excited by ocean waves). Particle image velocimetry and high-speed imaging are both used in the investigation. Findings demonstrate conditions for both primary and subharmonic resonance. We have investigated here how the system's characteristics, like the water wave's frequency and amplitude, affect the response of the structure. The current results will make it possible to select the parameters that will best utilize the wave energy available, such as wave frequency, installation depth, and geometrical property of the structure, in order to maximize energy in the case of an energy harvester or to avoid malfunctioning or prevent any kind of failure for an oceanic structure. In the current piece, analysis has been done for the situation where one end is free and the other is hinged. Section 3 discusses the experimental design that was used, and Sect. 4 discusses the findings of the current study before coming to a conclusion.

2 Literature Review and Objective

Kumar et al. [7] evaluated the interaction of a deformable structure under a gravity wave using both experimental and analytical methods. The system exhibits resonance in the inertia-dominated zone, but the frequency response of oscillations displays no resonance in the drag-dominated regime, according to the study, in which particle image velocimetry and high-speed imaging are used.

For the motion of a rigid body near a free surface, Andersen et al. [8] used the components of a Lagrangian mechanical system model. They discovered that altering the water level relative to the equilibrium state causes a modification in the depth-dependent hydrodynamic effects, such as added mass and radiative damping. Secondary local maxima in the signal of the pendulum position were detected for a wave period that was significantly larger than the dry natural period. Bos et al. [9] noted that the behavior of the resonant motion with a wave period greater than the dry natural period particularly for sessile plants, the relative motion of the water places fluid stresses on the plants, causing hydrodynamic forces to operate on the plant. In response, the plant modifies its morphology to reduce the drag force and save themselves from uprooting [10]. According to the findings of Jung et al. [11], an oscillating bluff body-like wake structure can be seen behind an oscillating elastic loop in a fast-flowing soap film. The intricate interaction of rigidity, structural inertia, and pressure forces is what causes the flapping instability seen in these investigations. Bos et al. [12] experimentally examine how a focused, breaking wave affects a one-degree-of-freedom pendulum in order to determine how structural deformation is brought on by an intense wave load on a marine structure. When initial clearance and focus location are altered, the pendulum behaves in a consistent manner. The substantial range of the pendulum reactions was detected even when the initial

clearance and focus location were held constant between different testing. It is also indicating that the impulse of wave must have varied.

In a flow field that is sinusoidally variable in time but homogeneous in space, Leclercq and de Langre [13] explored two-dimensional polymer blades. Based on the amplitude and frequency of the oscillating flow in relation to the dimensions and natural frequencies of the blade, respectively, they identified four distinct kinematic regimes of the structure response. In the area where drag predominated, the internal tensions were seen to decrease (when the drag dominates the fluid inertia). In the absence of structural inertia, they also talked about the resonant excitation of the blade in this domain.

3 Experimental Set-Up

A rectangular wave-generator plate was attached to one end of a water channel that was formed of glass sheets and was 1500 mm long, 240 mm wide, and 240 mm high. A servo-actuator was used to regulate the frequency and amplitude of the plate's stroke (see Fig. 1). A rack and pinion setup was used to translate the rotating motion of two Nema 17 motors, each of which had a holding torque of 4.2 kg/cm, into the reciprocating action of the wave generator. At the opposite end of the tank, a damper constructed of stone pellets was put in place to reduce wave reflections and ensure the creation of moving surface waves. The bob's diameter is 4 cm, and the length of the pendulum, $L = 16.8$ cm, was fixed at the center of the tank vertically. A pendulum with a density of 910 kg/m^3 for the bob and 7800 kg/m^3 for the rod was the subject of experiments here. They are merely an iron rod and a plastic ball assembled, respectively. The photographs of the water wave and the movements of the structure were captured at 100 frames per second by a high-speed camera (Phantom v7.3). To calculate the displacement of the pendulum and water wave characteristics such wave number ($k = 2\pi/\lambda$; λ is the wavelength), angular frequency ($\Omega = 2\pi f$, with f denoting the frequency), and amplitude, image analysis was done by using the custom-written MATLAB programmer (A). Using a gray threshold, each grayscale frame of the recorded films was transformed into a binary image. The MATLAB programs take the time-series data of the desired parameters and extract them from the subsequent frames of the video. The spatial resolution of the images used to measure the bob displacement ranged from 3.5×10^{-5} to 4.9×10^{-4} m/pixel. However, in order to achieve a larger field of view for wave surface elevation, the tests had to be recorded at spatial resolution in the range of 2.9×10^{-4} to 4.9×10^{-4} m/pixel. The PIV technique was used to determine the instantaneous 2D the reconfiguration and the associated internal stress of two-velocity field of the fluid, $\mathbf{U}(x, y, t) \equiv u \hat{i} + v \hat{j}$, Here, the unit vector in the x direction (the direction of a traveling wave) is represented by (\hat{i}) and the unit vector in the y direction is represented by (\hat{j}) (measured from the bottom of the liquid layer). A double-pulsed Nd-YAG laser was used to illuminate the vertical longitudinal plane (field of view $228.8 \text{ mm} \times 228.8 \text{ mm}$) containing the fiber after it had been seeded with neutrally buoyant

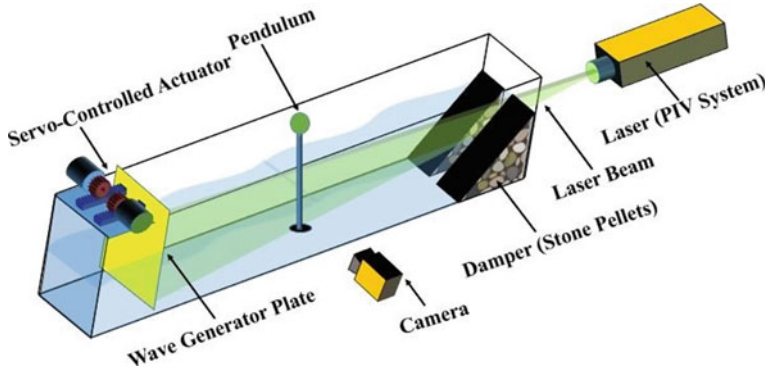


Fig. 1 Schematic of the experimental setup showing the wave generator with water channel

silver-coated tracer particles (diameter: $14 \mu\text{m}$) in the fluid (water) (pulse frequency 15 Hz). The particle images were captured using a charge-coupled device camera with a resolution of 2048×2048 pixels. The fluid velocity field was then acquired using the PIV programmed INSIGHT 4G (TSI Inc.) using interrogation windows of $104 \text{ pixels} \times 104 \text{ pixels}$. The tests' average surface wave had a wavelength of around 10 cm, which is substantially bigger than the capillary length scale. As a result, the waves seen in the current investigation are gravity waves. A variety of wavelength, forcing frequency, amplitude, and water layer height (H) parameters were used in the experiments. The parameter range was chosen to allow for the realization of linear, traveling, and sinusoidal gravity waves in the experiments. Only waves with the ratio of wave amplitude and total depth, which is $\frac{\Delta}{H} < 0.10$ are taken into consideration, we are ensuring that the waves are linear.

However, waves of very small amplitudes were avoided because the pendulum only responded insignificantly to them. Also take note that the pendulum response is anticipated to be in the static reconfiguration regime since the ratio of wave amplitude and total length of the structure $\frac{\Delta}{H} < 1$ in our tests, according to the amplitude-frequency space. At 1.3 Hz and 2.5 Hz, the experiment is run at the forcing frequency. The water level of the channel is 155 mm, and the overall length of the pendulum is 168 mm. After the transients had time to fade, the data collection process began. The pendulum was observed to oscillate in its initial mode under steady-state circumstances. The movement of the pendulum's bob and the observed water wave height's Fast Fourier transform (FFT) spectra demonstrate that both data have the same dominant frequency. This indicates that a periodic force is applied to the bob by the oscillatory velocity field that is being produced due to the moving water wave, and that the pendulum can be described as a forced harmonic continuous system.

4 Results and Discussion

The amplitude response against frequency and the angular position of the pendulum with respect to time are discussed. The frequency response of the pendulum excited by the gravity wave is presented in this section. Instantaneous velocity fields and streamlines are shown using particle image velocimetry.

4.1 Low-Frequency Response

The pendulum's angular position over time and frequency spectrum have been presented in Fig. 2a and b, respectively, at a forcing frequency of 1.3 Hz. As it can be seen, the amplitude of the angular position shows no variation for the given time period; hence, a steady-state condition can be seen here. From Fig. 2b, it can be seen that two peaks of different magnitudes are observed in the frequency domain. Here, natural frequency (f_n) of the pendulum is 1.3 Hz and the forcing frequency (f_d) is 1.3 Hz. The amplitude of oscillation is much larger than in other driving frequency cases; hence, the system is in its primary resonance condition. Also, note that there is a peak at a subharmonic frequency of around 0.6 Hz, indicating the nonlinearity in the system.

Figure 2c shows the instantaneous velocity field captured using particle image velocimetry. There is no vortex shedding observed around the pendulum in the velocity field; hence, it is clear that the oscillations are not vortex-induced. The pendulum motion is induced only due to fluid motion. The local velocity vectors oscillate at the driving frequency, and hence the drag force on the pendulum bob also oscillates once in a cycle of the gravity wave, exciting the primary resonance condition. There is no effect of the pendulum motion on the gravity wave.

4.2 High-Frequency Response

The angular position over time of the pendulum and frequency spectrum have been presented in Fig. 3a and b, at a forcing frequency of 2.5 Hz. As can be seen, the amplitude of the angular position is showing no variation here, and steady-state conditions can also be seen. From Fig. 3b, It can be seen that the major response is at the driving frequency of 2.5 Hz. Small subharmonic and super-harmonic responses can also be seen in the frequency spectrum, indicating the inherent nonlinearities in the system.

Figure 3c shows the instantaneous velocity field captured at the same driving frequency. Here also, no vortex shedding is observed, and the pendulum is purely driven by the oscillatory velocity fields and drag force.

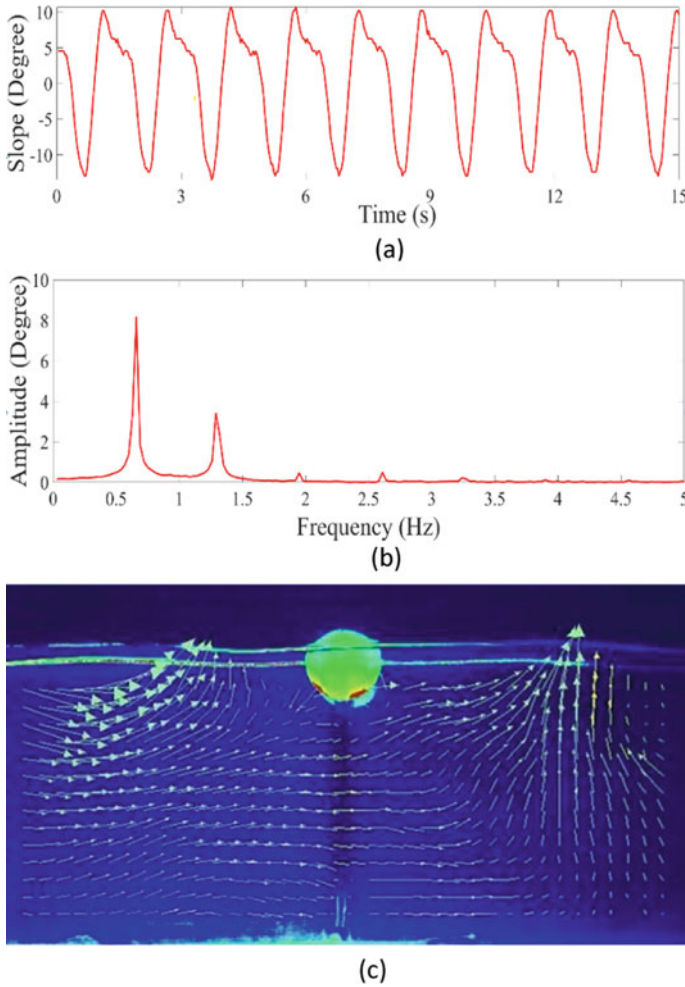


Fig. 2 **a** Time series of the angle of the pendulum from the equilibrium position. **b** The frequency spectrum of the time series is shown in **a**. **c** Streamlines and Instantaneous 2D velocity field measured using the PIV technique at a driving frequency of 1.3 Hz

4.3 Root Mean Square

Here, Fig. 4 is presenting the RMS value of the angular displacement of the pendulum versus the frequency ratio, f_d/f_n .

As can be seen from Fig. 4, two peaks are observed in the frequency ratio range considered in the study. The first peak is absorbed at a frequency ratio slightly greater than unity, indicating the primary resonance condition. The second, smaller peak at a frequency ratio of 2 indicates a subharmonic resonance condition. A detailed

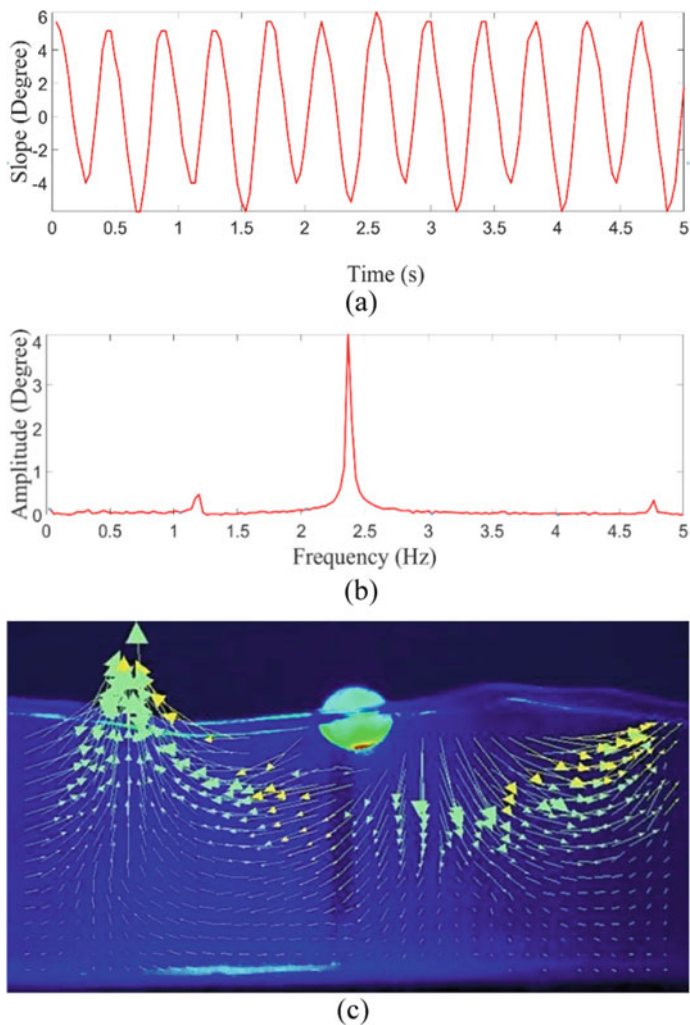
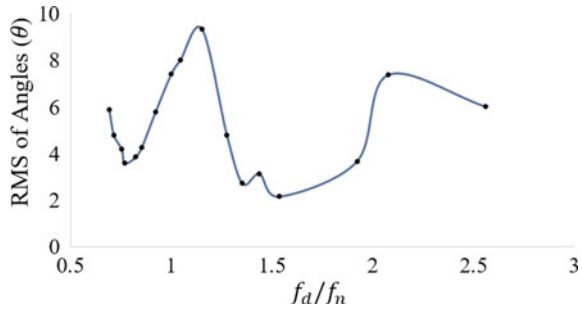


Fig. 3 **a** Time series of the angle of the pendulum from the equilibrium position. **b** The frequency spectrum of the time series is shown in **a**. **c** Streamlines and Instantaneous 2D velocity field measured using the PIV technique at a driving frequency of 2.5 Hz

parametric study and theoretical modeling of the system are underway and will be the subject of a future paper.

Fig. 4 Root mean square of theta with respect to frequency ratio



5 Conclusions

The dynamic behavior of a partially submerged pendulum under a surface gravity wave is examined in this study using particle image velocimetry and high-speed imaging. The steady-state oscillation in the angular displacement of the pendulum is measured. Frequency response at different driving frequencies are compared, and primary as well as secondary resonances are observed. The instantaneous velocity field and streamline around the oscillating pendulum show no vortex shedding, showing that the oscillations are not vortex shedding induced, rather that the oscillatory drag is responsible for them.

References

1. Correia JA, Mendes P, Fazerres-Ferradosa T, Zhu S-P (2020) Renewable energy and oceanic structures: part III. In: Proceedings of the institution of civil engineers-maritime engineering, vol 173, pp 1–2
2. Akcabay DT, Young YL (2012) Hydroelastic response and energy harvesting potential of flexible piezoelectric beams in viscous flow. *Phys Fluids* 24(5):054106
3. Bao B, Wang Q, Wu Y, Li P (2021) Experimental study on hydroelectric energy harvester based on a hybrid wiki and turbine structure. *Energies* 14(22):7601
4. Lan C, Hu G, Liao Y, Qin W (2021) A wind-induced negative damping method to achieve high-energy orbit of a nonlinear vibration energy harvester. *Smart Mater Struct* 30(2):02–02
5. Yang W, Towfighian S (2017) A hybrid nonlinear vibration energy harvester. *Mech Syst Signal Process* 90:317–333
6. Zhang L, Abdelkefi A, Dai H, Naseer R, Wang L (2017) Design and experimental analysis of broadband energy harvesting from vortex induced vibrations. *J Sound Vib* 408:210–219
7. Kumar K, Kumar V, Deepu P, Ramya P (2021) Oscillations of a flexible filament under surface gravity waves. *Phys Rev Fluids* 6(11):114004
8. Bos RW, Wellens PR (2021) Fluid–structure interaction between a pendulum and monochromatic waves. *J Fluids Struct* 100:103191
9. Bruce A et al (2018) An immersed spheroidal pendulum oscillating near a free surface. *Oceans 2018 MTS/IEEE Charleston*. IEEE
10. Vogel S (1994) *Life in moving fluids: the physical biology of flow*. Princeton University Press, Princeton

11. Bos RW, Wellens PR (2021) Fluid structure interaction between a pendulum and focused breaking waves. *Phys Fluids* 33(6):062118
12. Jung S, Marek K, Shelley M, Zhang J (2006) Dynamics of a deformable body in a fast-flowing soap film. *Phys Rev Lett* 97:134502
13. Leclercq T, De Langre E (2018) Reconfiguration of elastic blades in oscillatory flow. *J Fluid Mech* 838:606–630. <https://doi.org/10.1017/jfm.2017.910>

The Nature of Probability Density Functions in Turbulent Channel Flow



S. Raghuram

Abstract The nature of probability density functions of streamwise velocity, wall-normal velocity and Reynolds shear stress fluctuations is analysed for a turbulent channel flow using hotwire anemometry and particle image velocimetry measurements. The hotwire measurements are validated with data from literature. The particle image velocimetry measurements capture the probability density functions well albeit at a smaller acquisition sampling rate when compared to hotwire. The probability density functions of the streamwise and the wall-normal velocity fluctuations exhibit Gaussian behaviour close to the wall at least till the end of the inertial sublayer, while the probability density functions of Reynolds stress fluctuations exhibit non-Gaussian, peaky behaviour throughout the channel, depicting the episodic nature of turbulence production.

Keywords Turbulent channel flow · Probability density function · Gaussian distribution · Log region

1 Introduction

Probability density function (PDF) of fluctuating quantities is an important statistical property of turbulence. Quantities computed from PDFs have the same value if the PDF profiles are identical. A new definition for the logarithmic region was defined by ref. [1] to be the wall-normal extent, in which the PDF profiles of streamwise velocity fluctuations are invariant, using hotwire (HW) measurements in a low Reynolds number zero pressure gradient (ZPG) turbulent boundary layer (TBL). They also find the PDF profiles of streamwise velocity fluctuations to be close to Gaussian distribution in the logarithmic region. This invariance is later tested for higher Reynolds numbers using KTH database for ZPGTBL by ref. [2]. It is found that the region of self-similarity extends from 160 wall units to 0.3 BL thicknesses. This region is

S. Raghuram (✉)

Department of Aerospace Engineering, Indian Institute of Science Bangalore, Bengaluru 560012, India

e-mail: ssrinivasan@iisc.ac.in

larger than and includes the universal overlap region. While the self-similarity of the PDF of streamwise fluctuations has been studied in detail, not much has been reported on the nature of PDF of the wall-normal and shear stress fluctuations.

From detailed experiments in a neutrally stable atmospheric boundary layer, [3] distinguished between productive and counter-productive momentum flux events and periods in the time domain. They contended that these productive/counter-productive events and idle events (that produce no momentum flux) are, respectively, similar to the concept of active and inactive motions introduced by Townsend. They noted that low-flux fluctuations (typically less than a standard deviation in the flux) make little net contribution to the mean flux, and so could perhaps be termed passive motion. The more intense fluctuations are ‘active’ in the generation of flux. It was suggested therein that the passive motion is best described in the language of waves and harmonic analysis, whereas the active motions (productive or counter-productive)—could usefully be viewed as a series of events, possibly related to certain strongly coherent motions.

Episodic nature of the signals can be analysed using PDFs. The signals can be characterized to be episodic if the PDF exhibits a peaky behaviour. In particular, if the most probable value or the mean value is zero and centred at the peak and nonzero values are lot less frequent. An example of a similar distribution for $u'v'$ was noticed by ref. [4] and such a peaky non-Gaussian distribution was deemed therein to be transitional. In this paper, the Gaussian nature of the streamwise velocity fluctuations in the logarithmic region is confirmed using particle image velocimetry (PIV) data for a turbulent channel flow. Further, the nature of PDFs of wall-normal and Reynolds shear stress fluctuations is analysed, their Gaussian-ness in the log region explored. The paper is organized into four sections. The Sect. 2 deals with details of the measurements made, Sect. 3 discusses the main results in the paper and the final Sect. 4 summarizes the findings of the study.

2 Experimental Details

Data from measurements conducted in a TCF using HW (at $Re_\tau = 1537$) and PIV (at $Re_\tau = 1400, 1559$) are used in the present study. The inflow to the channel is through a wind tunnel section and connects to the channel through a contraction with high area contraction ratio (CR) as shown in Fig. 1. The effective CR of the contractions C1 (CR of 8.3) and C2 (CR of 13) connected in series is 108, thereby making the flow in the tunnel very quiet. The details of the tunnel design and the measurement techniques used can be found from [5].

Two-dimensional instantaneous velocity field is measured (in the streamwise wall-normal plane) using a LaVision FlowMaster PIV system, consisting of a double-pulsed Nd:YAG laser (Litron Lasers—Nano L PIV Series) with repetition rate of 15 Hz. A CCD camera (Imager SX) with 4 megapixel resolution fitted with a Nikon macro lens having a focal length of 105 mm (AF-S VR MICRO-NIKKOR 105MM F/2.8G IF-ED) is used to capture the images of the seeded particles, introduced at the

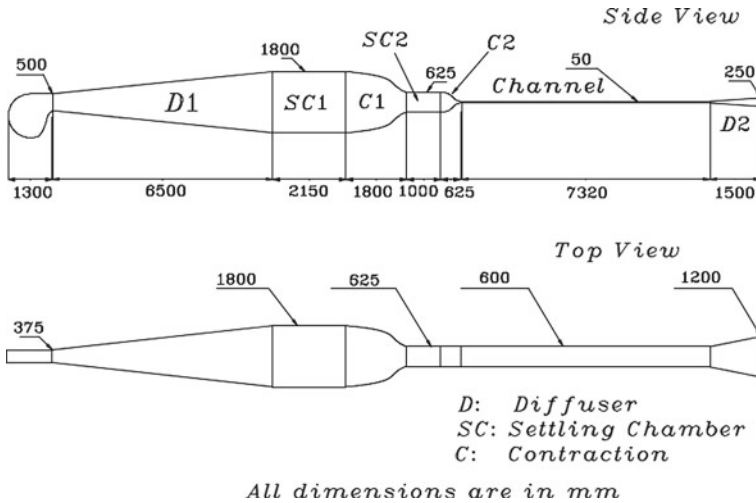


Fig. 1 Channel tunnel design drawing

blower inlet. The experiments were carried out and post-processed using the Davis 8.4.0 commercial software. The PIV measurements (at $Re_\tau = 1400, 1559$) used in the present study have been acquired and processed for 5 min (4500 images).

Hot wire anemometer is used to measure streamwise velocity fluctuations using a probe built in-house. The probe consists of two steel prongs (10 mm long, spaced at 0.8 mm from each other), where the sensor element is soft-soldered onto its tips. The sensor element is a Wollaston wire (manufactured by Sigmund Cohn Corp., USA) with a Pt-Rh core wire of diameter 5 microns protected by a silver outer coating. The active length of the sensor is kept typically around 0.5 mm. The viscous-scaled wire length $l^+ = lu_\tau/\nu \approx 30$ in this study for the highest speed case and $l/d \approx 100$. The prongs are inclined at an angle of 45° with the axis of the tube, so that the measurement is free from disturbance due to a part of the probe being in the downstream of the sensor, especially in the same wall-normal plane. The hot wire is operated by DANTEC DYNAMICS miniCTA (constant temperature anemometer) unit with a sampling frequency of 10 kHz. The unit was operated with a constant overheating ratio of 1.5. A National Instruments M Series NI PCI-6251 A/D card (16-bit resolution) was used for converting the analogue signals to digital voltage data. The HW is connected to a Mitutoyo height gauge, which is used as a traverse in the wall-normal direction and has a least count of 0.01 mm.

The probe is calibrated in situ to avoid drifts associated with moving the probe between tunnels and re-inserting. This is done by taking measurements at various y-locations and comparing them with measurements from Pitot tube at the same locations. Hence, separate measurements are not performed exclusively for the calibration. The probe is then calibrated using the standard King's law $V^2 = A + BU^n$, $n = 0.5$. The near-wall measurements using HW are disturbed by the conduction or convection heat loss to the wall, leading to velocities higher than the actual value.

This is corrected by employing a heat transfer correction to the acquired signal given by ref. [6]. The HW measurements (at $Re_\tau = 1537$) used in the present study has been acquired and processed for 1 min (600,000 data points). The velocity obtained from HW measurements is plotted in semilog scale in Fig. 2a for $Re_\tau = 1537$ along with Pitot measurements at the same speed. The curves follow the standard log-law shown by dashed lines in the inertial sublayer (ISL) with a slope, $\kappa = 0.37$. The quality of the velocity data in the near-wall region is excellent, follows $u^+ = y^+$ variation faithfully in the viscous sublayer (linear region) as expected. HW data from [7] is also plotted at $Re_\tau = 1543$ and has nearly the same slope, with slightly lower intercept. Streamwise intensity is next plotted in Fig. 2b along with HW data of [7] at $Re_\tau = 1543$ and that of [8] at $Re_\tau = 1524$ and the agreement with the present data is good. The peak of present data matches with that of [7], while the peak of [8] is slightly higher.

The PDF of fluctuating streamwise velocity for $Re_\tau = 1559$ using present PIV data (denoted by dashed lines) is plotted with corresponding HW data for $Re_\tau = 1537$ (denoted by solid lines) at various heights from the wall in Fig. 3. It can be seen that the PDF of u from PIV measured with sampling rate of 15 Hz compares well at various heights throughout the channel with u PDF of HW at similar heights measured with sampling rate of 10 kHz. This shows that the PDF of u is captured well by PIV measurements despite its lower sampling rate.

3 Results and Discussion

The PDFs of streamwise and wall-normal velocity fluctuations are, respectively, shown in Figs. 4 and 5 for $Re_\tau = 1400$ using the PIV data. While the solid lines denote the PDF of the fluctuations, the dashed lines denote the corresponding Gaussian curves with the same mean and standard deviation as the fluctuations at a given wall-normal location. The PDF of streamwise velocity fluctuations looks closely Gaussian, especially at small values of y^+ and there is departure from that trend as one moves to the outer region as shown in Fig. 4. The PDFs of streamwise velocity are also positively skewed and the skewness decreases with y^+ . In Fig. 5, again the wall-normal velocity looks closely Gaussian at small values of y^+ but looks more negatively skewed as one moves outward towards the core region. The wall-normal velocity fluctuations exhibit less skewness than the streamwise velocity fluctuations.

The PDF of the Reynolds stress is shown for the same Reynolds number in Fig. 6. The profiles look less Gaussian and a more peaky kind of distribution is observed centred around a zero mean value, though u' and v' are themselves Gaussian. It is interesting to note the observation of [4] who got such peaky PDFs of Reynolds stress with zero mean and was seen to correspond to intermittent behaviour. In other words for most of the duration, the Reynolds stress is hovering around a zero value and every once in a while due to a strong event a large value of $-u'v'$ may be produced. This would be called a productive or episodic event according to [3].

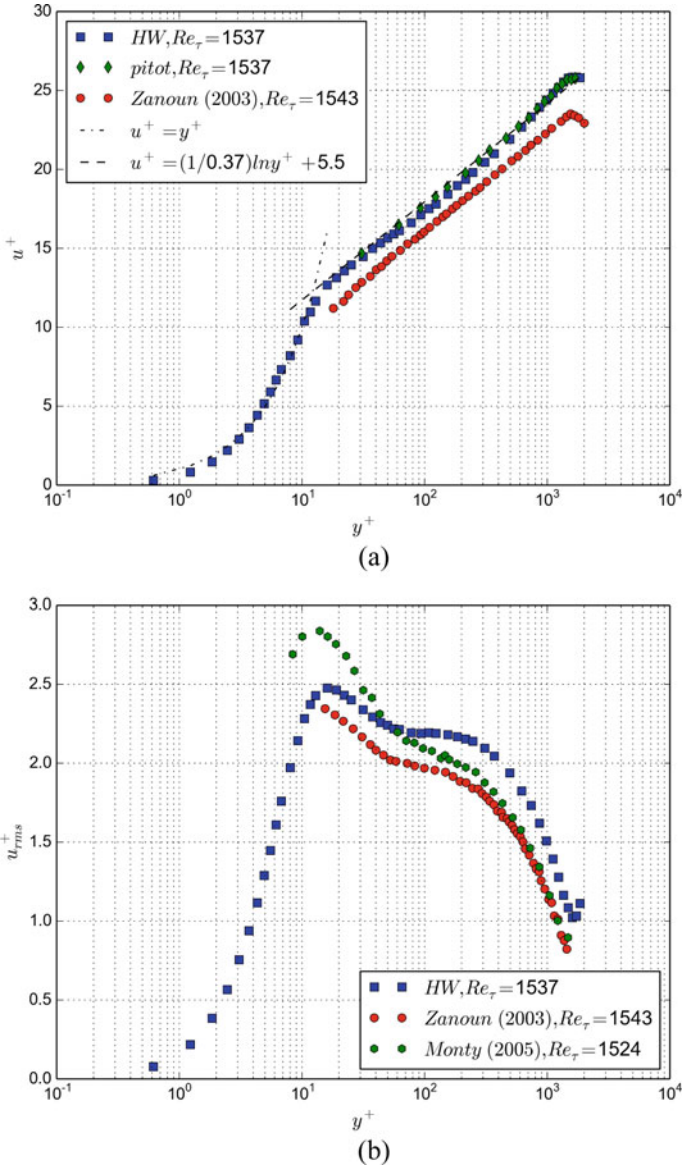


Fig. 2 Comparison of present HW data at $Re_\tau = 1537$ along with HW data of [7] at $Re_\tau = 1543$ for **a** mean velocity, **b** u_{rms} . The present mean velocity measured using Pitot at $Re_\tau = 1537$ is also included in **a**, HW data of [8] at $Re_\tau = 1524$ included in **b**

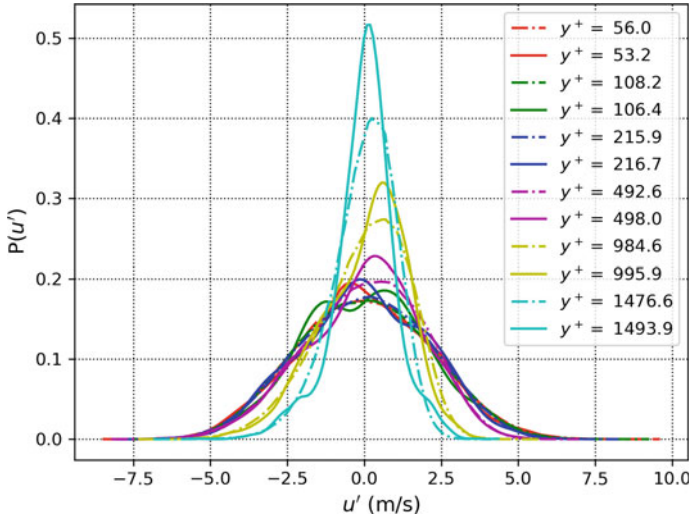


Fig. 3 PDF of fluctuating streamwise velocity for $Re_{\tau} = 1559$ using present PIV data (dashed lines) at various heights from the wall, plotted with PDF of fluctuating streamwise velocity from HW data for $Re_{\tau}=1537$ (solid lines) at similar wall-normal heights

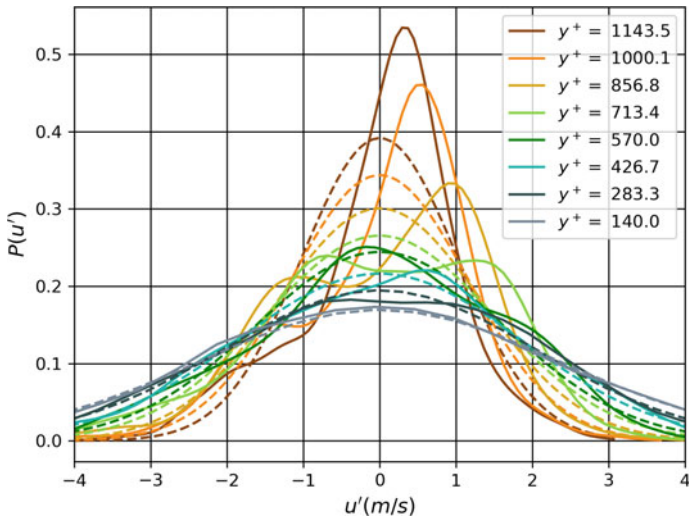


Fig. 4 PDF of fluctuating streamwise velocity for $Re_{\tau} = 1400$ at various heights from the wall plotted using PIV data (solid lines). The dashed lines denote the respective Gaussian curves with the same mean and standard deviation as the fluctuations at a given wall-normal location

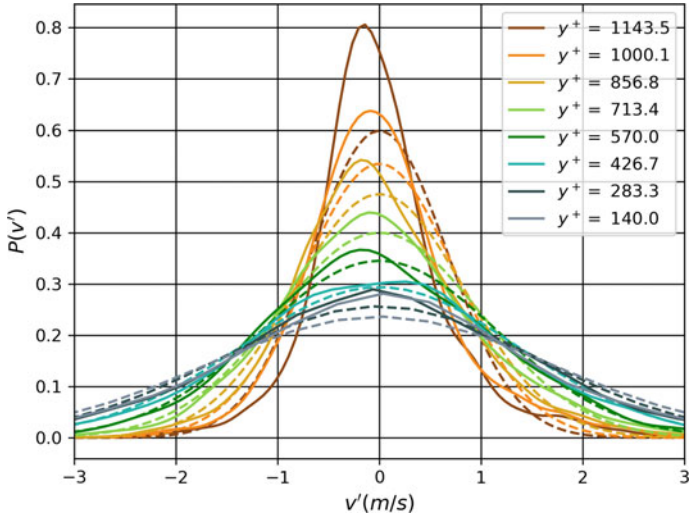


Fig. 5 PDF of fluctuating wall-normal velocity for $Re_\tau = 1400$ at various heights from the wall plotted using PIV data (solid lines). The dashed lines denote the respective Gaussian curves with the same mean and standard deviation as the fluctuations at a given wall-normal location

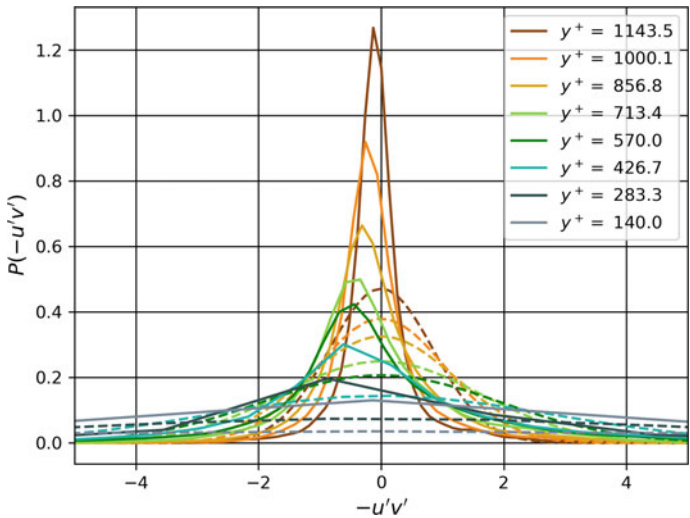


Fig. 6 PDF of fluctuating Reynolds stress for $Re_\tau = 1400$ at various heights from the wall plotted using PIV data (solid lines). The dashed lines denote the respective Gaussian curves with the same mean and standard deviation as the fluctuations at a given wall-normal location

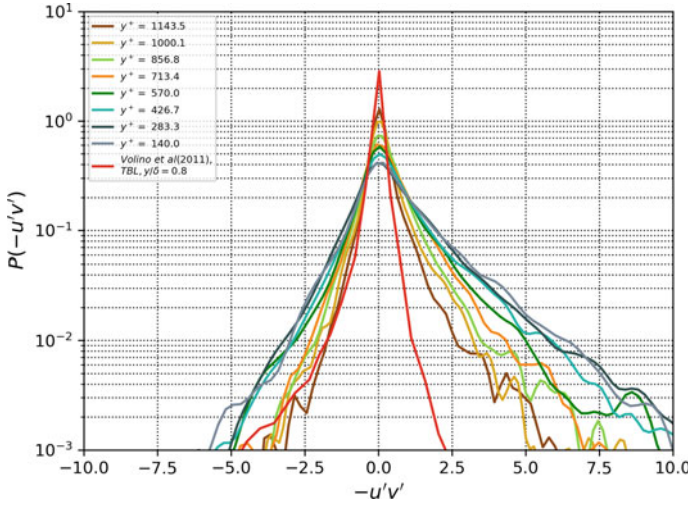


Fig. 7 PDF of fluctuating Reynolds stress for $Re_\tau = 1400$ at various heights from the wall plotted in loglog scale and compared with TBL data of [9] at $Re_\tau = 1772$, $y/\delta = 0.8$

The same PDF of $-u'v'$ is also plotted in semilog scale along with the result of [9] at a Reynolds number of $Re_\tau = 1772$ in Fig. 7. The peaky nature of the curve is more evident from this plot. The comparison with the data of [9] is fair. This also validates the use of PIV data to analyse PDFs.

4 Conclusions

The nature of PDFs of streamwise velocity, wall-normal velocity and Reynolds stress fluctuations is analysed for a turbulent channel flow using HW and PIV measurements. The HW measurements are validated with data from literature. The PDF calculated using the PIV data are in agreement with data from literature as well as with PDF calculated using present HW data. The PIV measurements capture the PDFs well albeit at a smaller acquisition sampling rate when compared to that of the HW. The PDFs of streamwise and wall-normal velocity fluctuations exhibit Gaussian behaviour close to the wall at least till the end of ISL, while the PDFs of Reynolds stress fluctuations exhibit non-Gaussian peaky behaviour throughout the channel, depicting the episodic description of bursting and turbulence production by ref. [3].

Acknowledgements The author wishes to profusely thank his research advisor, Prof. O. N. Ramesh of Indian Institute of Science Bangalore, India for the insightful and valuable discussions throughout the course of preparing this manuscript and the meticulous editing of the manuscript. The author expresses his sincere thanks to Defence Research and Development Organisation (DRDO), Ministry of Defence, Government of India and the Department of Science and Technology (DST), Ministry

of Science and Technology, Government of India for the PIV systems and the computers for data acquisition, which have been used extensively to obtain the data presented in this research article.

Nomenclature

CR	Contraction Ratio
d	Hotwire diameter [m]
HW	Hotwire
l	Hotwire active length [m]
κ	Karman constant
PDF	Probability Density Function
PIV	Particle Image Velocimetry
TBL	Turbulent Boundary Layer
TCF	Turbulent Channel Flow
Re_τ	Friction Reynolds number
u_τ	Friction Velocity [m/s]
U	Mean Streamwise Velocity [m/s]
u'	Fluctuating Streamwise Velocity [m/s]
v'	Fluctuating Wall-normal Velocity [m/s]
V	Voltage [V]
ν	Kinematic viscosity [m ² /s]
y	Wall-normal coordinate [m]
ZPG	Zero Pressure Gradient

References

1. Tsuji Y, Nakamura I (1999) Probability density function in the log-law region of low Reynolds number turbulent boundary layer. *Phys Fluids* 11(3):647–658
2. Lindgren B, Johansson AV, Tsuji Y (2004) Universality of probability density distributions in the overlap region in high Reynolds number turbulent boundary layers. *Phys Fluids* 16(7):2587–2591
3. Narasimha R, Kumar SR, Prabhu A, Kailas SV (2007) Turbulent flux events in a nearly neutral atmospheric boundary layer. *Philos Trans Royal Soc A: Math, Phys Eng Sci* 365(1852):841–858
4. Willmarth WW, Lu SS (1972) Structure of the Reynolds stress near the wall. *J Fluid Mech* 55(1):65–92
5. Raghuram S, Ramesh ON (2021) Delayed transition in a plane channel flow with high contraction ratio. *Exp Fluids* 62(7):1–9
6. Durst F, Zanoun E-S, Pashtropanska M (2001) In situ calibration of hot wires close to highly heat-conducting walls. *Exp Fluids* 31(1):103–110
7. Zanoun E-S (2003) Answers to some open questions in wall-bounded laminar and turbulent shear flows, Ph.D. thesis
8. Monty JP (2005) Developments in smooth wall turbulent duct flows, Ph.D. thesis, p 272
9. Volino RJ, Schultz MP, Flack KA (2011) Turbulence structure in boundary layers over periodic two-and three-dimensional roughness. *J Fluid Mech* 676:172–190

Optimal Perturbations of Flat-Plate Boundary Layer with Suction and Injection



Mayank Thummar, Ramesh Bhoraniya, Ravi Kant, and Vinod Narayanan

Abstract This paper presents the effect of suction and injection on the non-modal stability analysis of the boundary layer flow. The base flow solution is obtained by OpenFOAM software. The 3D governing stability equations are derived in terms of normal velocity and vorticity. The spectral collocation method is used for spatial discretization of the stability equations. The QZ algorithm solves the formulated eigenvalue problem with appropriate boundary conditions. Transient amplification is achieved by linear superposition of non-orthogonal eigenvectors. The optimal energy growth and associated perturbations are computed for different parameters such as Reynolds number (Re), streamwise and spanwise wave numbers (α , β), and time horizon (t). A detailed description of it is mentioned in the results and discussion section. A harmonically driven input–output framework is also considered in a general fluid system to study receptivity analysis. In a case of injection, strong resonant peak is detected at resonant frequency, $\omega = 0.07143$ and 0.602 for $\alpha = 0.15$, $\beta = 0.96$ and $\alpha = 0.86$, $\beta = 1.7$, respectively. Similarly for suction, peak response in energy is found at $\omega = 0.1122$ and 0.8469 for $\alpha = 0.15$, $\beta = 0.96$ and $\alpha = 0.86$, $\beta = 1.7$, respectively.

Keywords Transient growth · Suction · Injection · Stability · Receptivity

M. Thummar (✉) · R. Bhoraniya

Department of Mechanical Engineering, Marwadi University, Rajkot, Gujarat 360003, India
e-mail: mayank.thummar@marwadieducation.edu.in

R. Kant

Department of Mechanical Engineering, PDEU Gandhinagar, Gandhinagar, Gujarat 382007, India

V. Narayanan

Department of Mechanical Engineering, IIT Gandhinagar, Gandhinagar, Gujarat 382355, India

1 Introduction

The boundary layer control through suction and injection falls under Active or Laminar Flow Control (LFC) techniques. Suction reduced the drag force exerted by the viscous fluid onto the surface of aircraft wings or propelling bodies, about 50% of total drag [1]. Thus, it reduces environmental pollution and saves an enormous amount of fuel [1]. The suction and injection having a significant impact in the fields of aerodynamics or hydrodynamics such as boundary layer control, biological areas like blood flows in tumours and brain tissues, chemical vapour deposition on the solid surface, and transpiration cooling of turbine blades.

2 Literature Review and Objective

The stability of laminar boundary layer flows with uniform suction or injection was first experimentally investigated by Labby et al. [2]. They found that experimental results closely match the theoretical results of an ideal porous wall, and the velocity profile is an exact match with the theoretical ones. Similar, experiments were also performed by Reynolds et al. [3, 4]. They found that due to suction, a profile of disturbances moves towards the wall into the region of higher dissipation and stabilizes the T-S wave. The suction increased the transition Reynolds number while injection reduced it. Haung and Wu [5] studied the stability of the boundary layer flow with local suction using linear stability theory. They found that local weak suction at a rate of 10^{-4} m³/s reduced an amplitudes of T-S waves by about 90%. Several authors [6–10] studied the effect of suction or injection with cooling or heating on the characteristics of laminar boundary layers. Suction increased heat transfer and skin-friction coefficient while injection produced a reverse effect [6]. The suction with wall cooling improved the flow stability and delayed the flow transition [7]. The flow becomes more stable by increasing the suction parameters [8]. Due to suction, boundary and momentum thickness reduced, while reverse trends have been observed for injection [9]. The flow velocity and temperature decreased with increasing Re and Pr [10].

The energy growth of disturbances in viscous flows was studied by several authors [11–15] via non-modal analysis. Reddy and Henningson [11] studied substantial energy amplification of small perturbations for plane Poiseuille and Couette flow. They derived the condition of no energy growth using the Hille-Yosida theorem. The transient growth of the asymptotic suction boundary layer (ASBL) was studied by Kurian and Fransson [12]. They found that the energy growth theory completely failed to predict the energy evolution of the small perturbations for ASBL. For ASBL, the critical Re was found to be two orders higher magnitudes than the Blasius boundary layer (BL) [13]. Similarly, transient growth analysis has been performed by Byström et al. [14] for the semi-suction boundary layer (SSBL) and ASBL. They found that both boundary layers produced streamwise vortices resulting in streamwise streaks, which are found in shear flows. Also, maximum energy growth has been found in the

upstream region, where no suction was applied for SSBL. The global modal stability of the flat-plate boundary layer with suction and injection was first investigated by Bhoraniya and Narayanan [15]. They found that suction stabilized the flow, whereas injection destabilized the flow.

The main aim of the present investigation is to study the effect of wall-normal uniform suction and injection on the non-modal stability of boundary layer flow which is not studied to the best of our knowledge. The receptivity analysis is performed via resolvent norm to compute the maximum response of the fluid system corresponding to external perturbations. The effect of different parameters on the maximum energy growth is also investigated.

3 Problem Formulation

A steady, incompressible, 2D boundary layer flow over a horizontal plate surface, as depicted in Fig. 1. The plate surface has discrete holes at some finite distance from the leading edge for mass transpiration. The base flow has only streamwise velocity (U_b), which is the only function of y (i.e. wall-normal direction). The governing equations are non-dimensionalized by free-stream velocity (U_∞) and displacement thickness (δ^*). The 3D linearized governing stability equations are as

$$\frac{\partial \hat{u}_p}{\partial t} + U_b i \alpha \hat{u}_p + \hat{v}_p \frac{dU_b}{dy} = -i \alpha \hat{p}_p + \frac{1}{\text{Re}} (D^2 - k^2) \hat{u}_p + \hat{f}_{u_p} \quad (1a)$$

$$\frac{\partial \hat{v}_p}{\partial t} + U_b i \alpha \hat{v}_p = -D \hat{p}_p + \frac{1}{\text{Re}} (D^2 - k^2) \hat{v}_p + \hat{f}_{v_p} \quad (1b)$$

$$\frac{\partial \hat{w}_p}{\partial t} + U_b i \alpha \hat{w}_p = -i \beta \hat{p}_p + \frac{1}{\text{Re}} (D^2 - k^2) \hat{w}_p + \hat{f}_{w_p} \quad (1c)$$

$$\alpha \hat{u}_p + D \hat{v}_p + i \beta \hat{w}_p = 0 \quad (1d)$$

where, $D = \partial/\partial y$, $D^2 = \partial^2/\partial y^2$, $k^2 = \alpha^2 + \beta^2$

Here, subscript 'b' and 'p' represents the base flow and perturb quantities, respectively. \hat{u}_p , \hat{v}_p , \hat{w}_p , \hat{p}_p represents the velocity and pressure perturbations, \hat{f} is external driving term, α and β be the streamwise and spanwise wavenumber, and $\text{Re} (= \rho U_\infty \delta^* / \mu)$ is the Reynolds number.

Next, we eliminate the pressure term in Eqs. (1) via variable transformation by defining the normal vorticity, $\hat{\eta}_p = \frac{\partial \hat{u}_p}{\partial z} - \frac{\partial \hat{w}_p}{\partial x}$. The governing equations are derived in the form of normal velocity (\hat{v}_p) and vorticity ($\hat{\eta}_p$) as similarly mentioned in [16].

$$(D^2 - k^2) \frac{\partial \hat{v}_p}{\partial t} = i \alpha \frac{d^2 U_b}{dy^2} \hat{v}_p - i \alpha U_b (D^2 - k^2) \hat{v}_p + \frac{1}{\text{Re}} (D^2 - k^2)^2 \hat{v}_p + \hat{g}_{v_p} \quad (2a)$$

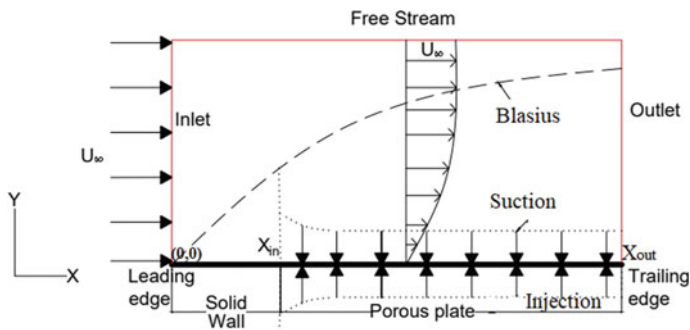


Fig. 1 Schematic diagram of flat-plate boundary layer with uniform suction and injection

$$\frac{\partial \hat{\eta}_p}{\partial t} = -i\beta \frac{dU_b}{dy} \hat{v}_p - i\alpha U_b \hat{\eta}_p + \frac{1}{\text{Re}} (D^2 - k^2) \hat{\eta}_p + \hat{g}_{\eta p} \quad (2b)$$

Boundary conditions: At $y = 0$ (i.e. wall) and $y = \infty$ (i.e. free-stream) as

$$\hat{\eta}_p(x, 0) = 0, \hat{v}_p(x, 0) = \pm v_w, D\hat{v}_p(x, 0) = 0 \quad (3a)$$

$$\hat{\eta}_p(x, \infty) = 0, \hat{v}_p(x, \infty) = 0, D\hat{v}_p(x, \infty) = 0 \quad (3b)$$

where v_w is the suction and injection velocity in terms of % of U_∞ . Here, positive and negative sign is used for injection and suction, respectively.

Equations (2) can be written in the vector form as

$$\frac{\partial}{\partial t} \hat{q} = -iL\hat{q} + B\hat{f} \quad (4)$$

where $\hat{q} = [\hat{v}_p \ \hat{\eta}_p]^{\text{tr}}$, $M = (D^2 - K^2)$, $\hat{f} = [\hat{f}_{u_p}, \hat{f}_{v_p}, \hat{f}_{w_p}]^{\text{tr}}$

$$L = \begin{bmatrix} L_{os} & 0 \\ L_c & L_{sq} \end{bmatrix}, B = \begin{bmatrix} -i\alpha M^{-1} D & -k^2 M^{-1} & -i\beta M^{-1} D \\ i\beta & 0 & -i\alpha \end{bmatrix} \quad (5a)$$

$$L_{os} = M^{-1} \left[\alpha U M - \alpha \frac{d^2 U_b}{dy^2} - \frac{1}{i\text{Re}} M^2 \right] \quad (5b)$$

$$L_{sq} = \alpha U_b - \frac{1}{i\text{Re}} M, L_c = \beta \frac{dU_b}{dy} \quad (5c)$$

Here, L_{os} and L_{sq} represent the O-S and Squire matrices, respectively. In Eq. (4), the O-S and Squire equations are coupled by coupling operator, L_c . For $\beta = 0$,

flow is governed by L_{os} operator (i.e. 2D disturbances), however, for $\beta \neq 0$ (3D disturbances), normal vorticity is driven by normal velocity.

Using time-dependent Fourier Transform equation, ($\hat{q}(y, t) = \tilde{q}(y)e^{-i\omega t}$), after omitting forcing term, \hat{f} Eq. (4) becomes,

$$L\tilde{q} = \omega\tilde{q} \quad (6)$$

where eigenvalue is a complex quantity $\omega = \omega_r + i\omega_i$ (frequency), whose imaginary part represents the growth ($\omega_i > 0$) or decay ($\omega_i < 0$) the perturbations.

The numerical techniques utilizing spectral method for discretization of governing equations using Chebyshev polynomial in wall-normal direction (y). The grid transformation is applied in y-direction for higher resolution within the boundary layer [17].

$$y = \frac{y_i L_y (1 - y_{cheb})}{L_y + y_{cheb} (L_y - 2y_i)} \quad (7)$$

where y_{cheb} be Chebyshev scale range from -1 to 1 , L_y be domain height, y be real scale range from 0 to L_y , and y_i be wall-normal location where half number of points located within range of $0 \leq y \leq y_i$.

The formulated eigenvalue problem (Eq. (6)), which is solved by QZ algorithm with appropriate boundary conditions. The computed eigenmodes and associated eigenfunctions are used for transient growth. For that it is mandatory define energy density and inner product. For an incompressible flow, energy density of a perturbations is a physically meaningful quantity to measure the size of the perturbations [18]. It is derived in similar manner as mentioned by Butler and Farrell [19].

$$E(t) = \frac{1}{8k^2} \int_0^{L_y} \left(k^2 |\tilde{v}_p|^2 + |D\tilde{v}_p|^2 + |\tilde{\eta}_p|^2 \right) dy \quad (8)$$

The inner product and associated norm

$$(\tilde{q}_i, \tilde{q}_j) = \int_0^{L_y} \tilde{q}_i^H M \tilde{q}_j dy, \quad 2E(t) = (\tilde{q}_i, \tilde{q}_j) = \|\tilde{q}\|_E^2 \quad (9)$$

where \tilde{q}_i^H be the Hermitian conjugate of \tilde{q}_i and M be the diagonal matrix whose elements are calculated using Eq. (9) and Chebyshev weight function [18].

The Gain function is defined as,

$$G(t) = \max_{\tilde{q}(0)} \frac{\|\tilde{q}(t)\|_E^2}{\|\tilde{q}(0)\|_E^2} \quad (10)$$

Let us consider the only first K non-orthogonal eigenmodes and associated eigenfunctions for transient growth analysis, then state vector, \tilde{q} can be expressed as

$$\tilde{q} = \sum_{j=1}^{j=K} n_j(t) \tilde{q}_j, n_j(t) = n_j(0) e^{\Lambda t}, \Lambda = -i\omega_j \quad (11)$$

where $n_j(t)$ be the time-dependent vector of expansion coefficient and Λ be the diagonal matrix whose diagonal element contains first K eigenvalues ($-i\omega_j$).

Using Eq. (8), (9), and (11), optimal energy growth at given time (Eq. (10)) becomes

$$G_j(t) = \max_{n_j(0) \neq 0} \frac{\|n_j(t)F\|_E^2}{\|n_j(0)F\|_E^2} = \max_{n_j(0) \neq 0} \|F\Lambda F^{-1}\|_2^2 \quad (12)$$

The Hermitian matrix M in Eq. (9) is decomposed into F^*F , where F^* be the complex conjugate of F .

The L_2 or Euclidean norm of matrix in Eq. (14) has been calculated by singular value decomposition (SVD). The readers are requested to refer Schmid and Henningson [20] for more details about the algebraic energy growth.

3.1 Base Flow Solution

The base flow solution of boundary layer flow with uniform suction and injection has been obtained by an open-source finite volume source code (OpenFOAM). In OpenFOAM software, steady, incompressible, 2D, N-S equation is solved numerically using a simpleFoam solver. The simpleFoam solver's results are also validated with an exact Blasius solution and found in good agreement (not shown for brevity). The following set of boundary conditions are used as

$$\text{At inlet : } U_b(0, y) = U_\infty, V_b(0, y) = 0 \quad (13a)$$

$$\text{At outlet : } \frac{\partial U_b}{\partial x}(L_x, y) = \frac{\partial V_b}{\partial x}(L_x, y) = P_b(L_x, y) = 0 \quad (13b)$$

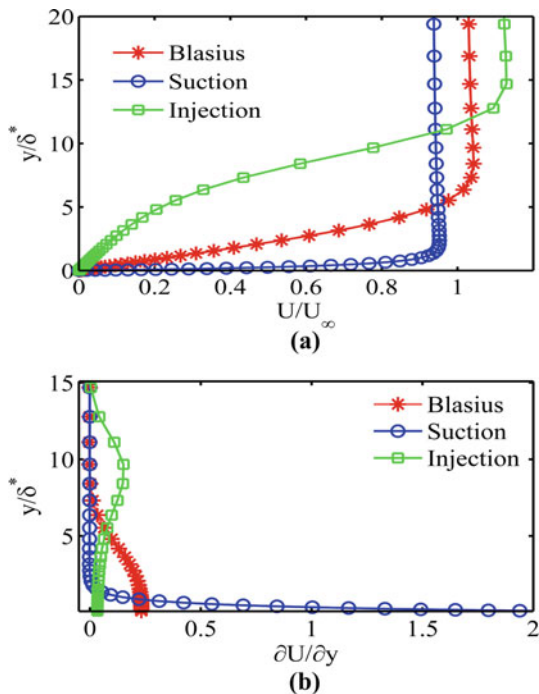
$$\text{At wall : } U_b(0 : x_{in}, 0) = 0, V_b(0 : x_{in}, 0) = 0, \quad (13c)$$

$$\text{At slots : } U_b(x_{in} : x_{out}, 0) = 0, V_b(x_{in} : x_{out}, 0) = \pm v_w \quad (13d)$$

$$\text{At free-stream } \frac{\partial U_b}{\partial y}(L_x, L_y) = \frac{\partial V_b}{\partial y}(L_x, L_y) = 0 \quad (13e)$$

The grid convergence study (GCS) is performed for three different grid size (2001×251 , 1415×177 , 1001×125) with a refinement factor of $\sqrt{2}$ in each direction and compute relative error between two consecutives refined grid size [21]. Here,

Fig. 2 The comparison of **a** U_b and **b** $\partial U_b/\partial y$ of the Blasius profile with uniform suction and injection. The suction and injection intensity = 0.5% of U_∞

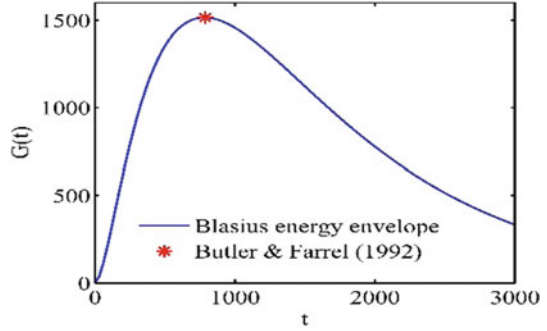


grid size 2001×251 is used for all base flow computation with relative less than 0.1% (GCS table not present for brevity). Fig. 2a presents the comparison of the velocity profile of the Blasius profile with uniform suction and injection. Due to suction, the velocity profile shifts towards the wall and gets a fuller profile. However, the velocity profile moves away from the wall due to injection and gets steeper. The shear stress has been found higher at the wall and decays with y for uniform suction. However, for uniform injection, the point of inflection is observed at a certain y -distance, where shear stress has a maximum value (except at the wall) within the boundary layer, as shown in Fig. 2b.

4 Results and Discussion

The collocation points, $N = 121$, have been considered for energy growth and it was enough for convergence of results. We used the two different nomenclature as adopted by Hanifi et al. [18]. First one, $G_{\max} = \max[G(t \geq 0)]$, present the maximum value of $G(t)$ over the whole time interval and t_{\max} is the time at which the G_{\max} is obtained. Second, $G_{\text{opt}} = G(t = t_{\text{opt}})$ presents the optimal value of $G(t)$ only for short time before exponential or modal growth take place and t_{opt} is the time at which higher non-modal growth is obtained.

Fig. 3 Energy gain curve, $G(t)$ for the Blasius profile with $\alpha = 0$, $\beta = 0.65$, and $Re_{\delta^*} = 1000$



4.1 Validation

For validation of transient growth code, consider an exact solution of boundary layer with parallel flow approximation. The energy growth of 3D perturbations is obtained for $\alpha = 0$ and $\beta \neq 0$. For $Re_{\delta^*} = 1000$, $G_{\max} = 1515$ at $t_{\max} = 778$ corresponding to $\beta = 0.65$. It was an exact match with result of Butler and Farrell [19] as shown in Fig. 3. The eigenfunctions at t_{\max} have a streamwise vortices are observed (not shown for brevity).

4.2 Optimal Perturbations

Figure 5 presents the comparison of the energy curve, $G(t)$ for boundary layer flow with suction and injection with $\alpha = 0.15$, $\beta = 0.96$ and $Re = 580$ (near to critical Re). For suction and Blasius profile, an algebraic growth has been found ($O(10^2)$ and (10^1) , respectively) for short time followed by exponential decay as per least stable eigenmode. All eigenmode lies down on lower stable half plane for a mentioned parameters in Fig. 5 for suction and Blasius profile. However, an energy grows algebraically up to $O(10^3)$ within a short time in case of injection. It reaches the peak level (G_{opt}) and once transient effect subside, unstable eigenmode dominant over a non-modal growth, and followed an exponential (or modal) growth. The comparison of growth in energy predicted by excluding and including the unstable eigenmode as shown in Fig. 6. For a short time, remarkable faster transient growth has been found by including all stable modes and it has higher than the growth predicted by only single unstable mode. Figure 6 also depicted that the including unstable mode, an energy can experience large exponential growth after a non-modal growth.

The spatial structure of optimal perturbations corresponding to optimal transient growth G_{opt} at optimal time $t = t_{\text{opt}}$ are plotted as contour of real part of streamwise u_r and wall-normal v_r components of perturbations in Fig. 7a and b for suction(left) and

Fig. 5 Effect of suction and injection on the transient growth for $Re = 580$, $\alpha = 0.15$, $\beta = 0.96$, and intensity $= 0.5\%$ of U_∞ .

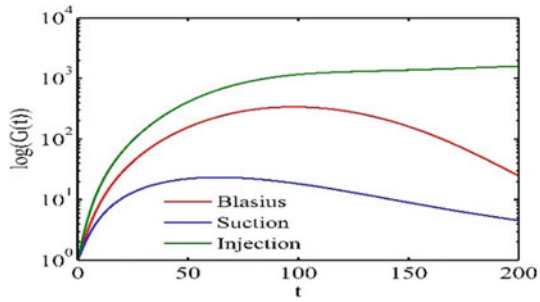
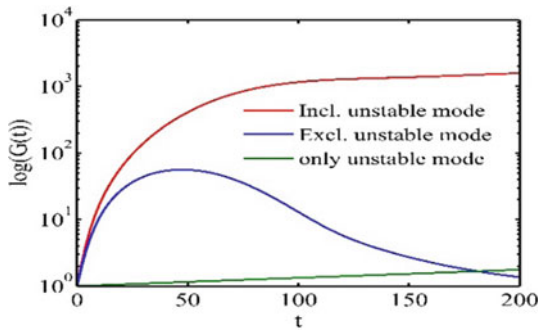


Fig. 6 Effect of different modes on the transient growth of injection for a parameters mentioned in Fig. 5



injection(right), respectively. The structure perturbations are elongated in the stream-wise direction grows robustly in boundary layer flow. For 3D disturbances, perturbations are primarily gains energy due to vortex tilting mechanism ($\alpha = 0, \beta \neq 0$) and obtained an additional energy from 2D Reynolds stress mechanism ($\alpha \neq 0, \beta = 0$) due to favourable initial structure tilted opposite to mean shear direction. The location of maximum growth of tilted structure of perturbations (u_r, v_r) has been found closer to wall for suction. However, it shifts slightly away from the wall for injection.

Next, we considered the 3D disturbances that are not depend on flow direction (i.e. $\alpha = 0$). A significant amount of energy amplification has achieved for suction and injection corresponding $\alpha = 0, \beta = 0.65$, and $Re = 1000$ as shown in Fig. 8. All eigenmodes are stable because of temporal growth rate, $\omega_i < 0$. The flow is modally stable even at higher intensity and Re for $\alpha = 0$. The transient energy growth corresponding to $t = t_{opt}$ for Blasius profile is higher than the suction, but lower than the injection. The real part of streamwise (u_r) and wall-normal (v_r) components of optimal perturbations have streamwise vortices as shown in Fig. 9a and b, respectively, for suction(left) and injection(right). The growth of streamwise vortices or velocity streaks generated due to vortex tilting mechanism is stopped by the viscosity [19]. The location of maximum growth of streamwise vortices of perturbations is found closer to wall for suction than the injection as shown in Fig. 9.

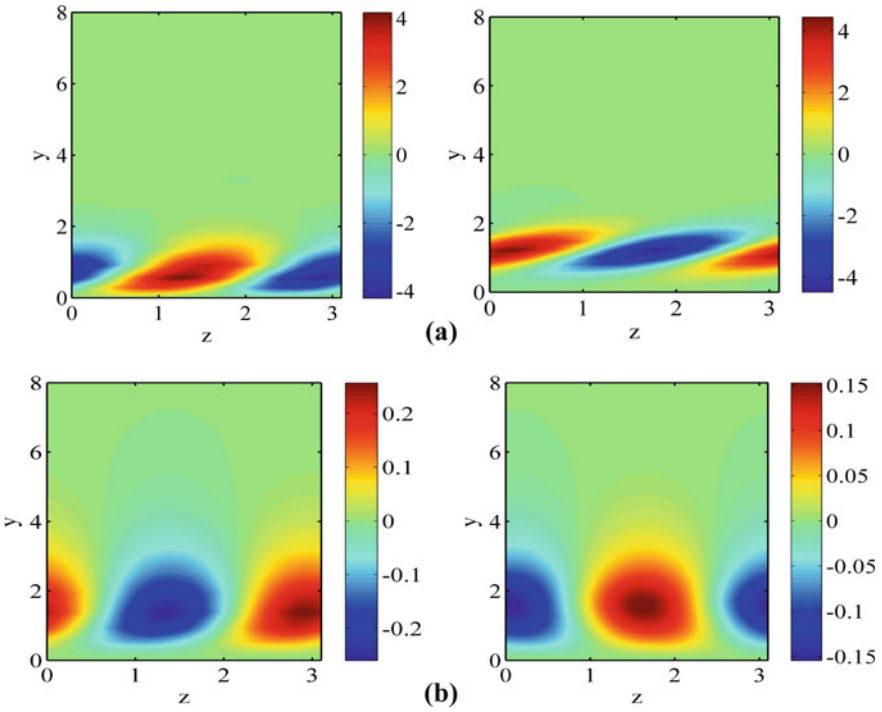
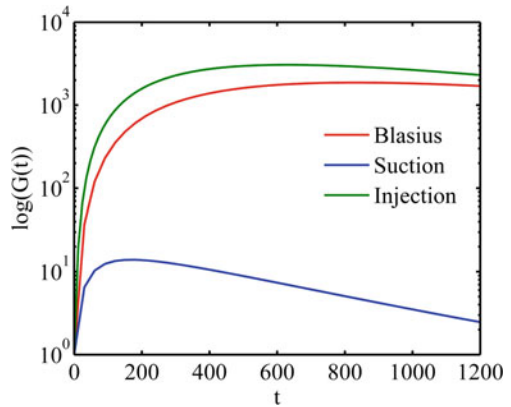


Fig. 7 Optimal contours of **a** streamwise, u_r , and **b** wall-normal, v_r component of perturbations for suction (left side) and injection (right side) corresponds mentioned parameter in Fig. 5

Fig. 8 Effect of suction and injection on transient growth for $Re = 1000$, $\alpha = 0$, $\beta = 0.65$, and intensity = 0.5% of U_∞ .



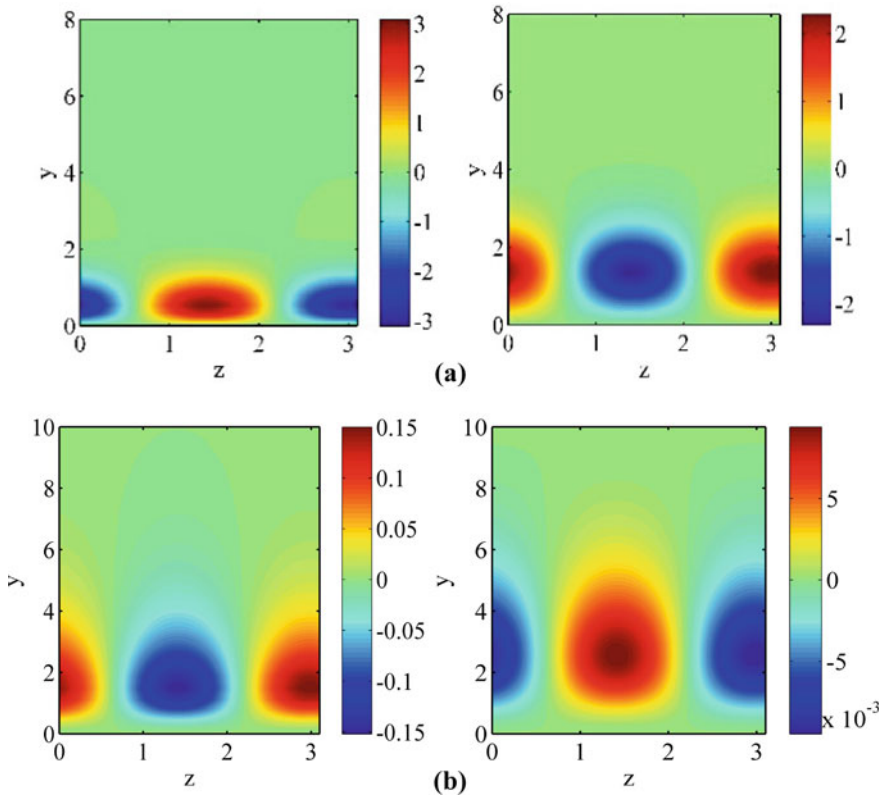
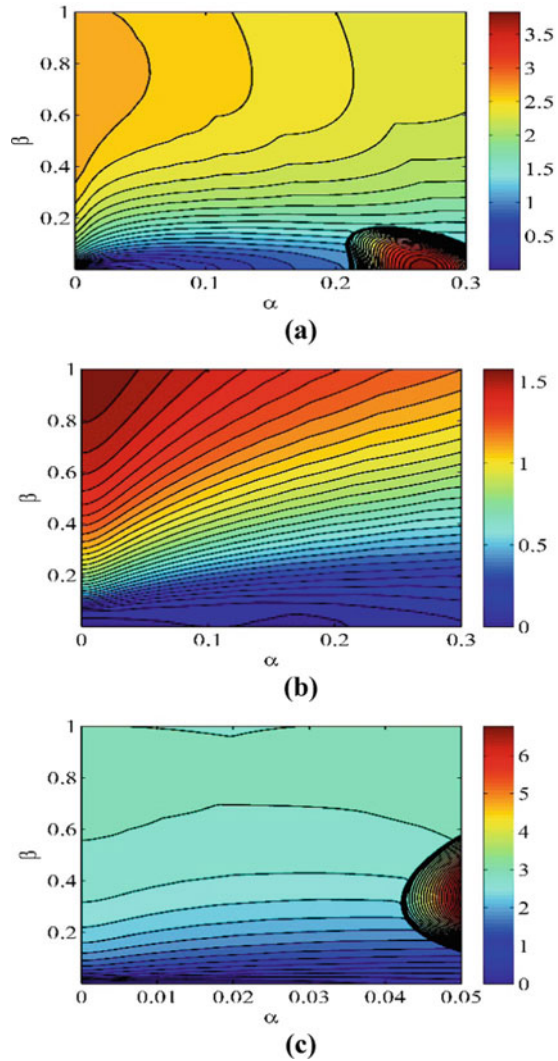


Fig. 9 Optimal contours of **a** streamwise, u_r and **b** wall-normal, v_r component of perturbations for suction (left side) and injection (right side) corresponds mentioned parameters in Fig. 8

4.3 Parametric Study

The governing stability equation contains numerous parameters such as streamwise (α) and spanwise (β) wave numbers, Reynolds number (Re), and time horizon (t) which significantly affect the stability of fluid system. The transient growth depends on these parameters and compute the maximum energy growth by varying the wave numbers for fixed Reynolds numbers. It helpful to identify that which wavenumbers are most favoured for maximum energy amplification. Figure 10 shows the results of maximum transient growth for varying wavenumbers α and β corresponding to $Re = 580$ (near to critical). The area under the thick black line (in Fig. 10a and c) represents the linearly unstable region of the α - β plane. In this region, large infinite energy amplification has been achieved due to modal instability or exponential growth. However, no unstable region is found in α - β plane for suction. In all cases, large transient growth is obtained for $\alpha \approx 0$ with β of order one.

Fig. 10 Contour plot of maximum transient growth for **a** no suction/injection, **b** uniform suction, and **c** injection corresponding to $Re = 580$ and intensity = 0.5% of U_∞ . The G_{\max} is based on \log_{10} scale in the contours



4.4 Receptivity Analysis

The receptivity analysis shows the reaction of the fluid system corresponding to external perturbations. The external perturbations are in the form of FST, surface roughness, acoustic, etc. The receptivity described by resonance term and given by closeness of external frequencies to any eigenvalue of the harmonic driven system. We will return to Eq. (4) and adopt an input–output framework to compute maximum output response ($g = \hat{g} \exp(i\omega t)$) of the fluid system with external harmonic driving frequencies ($f = \hat{f} \exp(i\omega t)$).

$$\hat{g} = C(i\omega I - L)^{-1} B \hat{f} \quad (14)$$

where B and C are input and output quantities.

The maximum response in energy is defined as

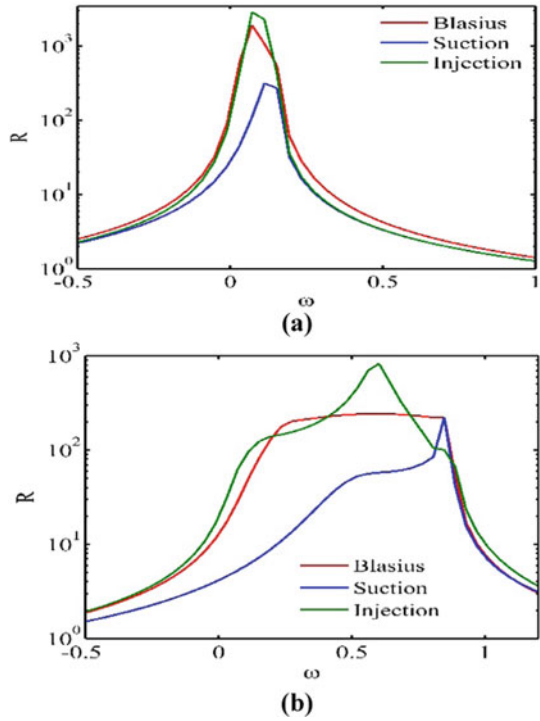
$$R(\omega) = \max_{\hat{f}} \frac{\|\hat{g}\|_E^2}{\|\hat{f}\|_E^2} = \|C(i\omega I - L)^{-1} B\|_E^2 \quad (15)$$

Equation (15) is known as resolvent norm. The readers are requested to refer article [16] for more details about resolvent norm. Figure 11 shows the resolvent norm (R) which is a function of external forcing frequencies (ω). The highest or lowest energy peak is found for boundary layer flow with uniform injection or suction, respectively corresponding to different values α and β . The strong peak values of resolvent norm corresponding to particular frequency (ω) shows the value of ω is nearest to most stable/unstable eigenmode and ω is called resonating frequency. A resonating frequencies (ω) of external forcing term must be avoid for delay the flow transition. For injection, value of resonating frequency, ω , responsible for peak resolvent is 0.07143 and 0.602 corresponding to $\alpha = 0.15$, $\beta = 0.96$, and $\alpha = 0.87$, $\beta = 1.7$, respectively. The same value of ω is detected for peak response of energy in case of BL. However, in a case of suction, strong peak response in energy is found at $\omega = 0.1122$ and 0.8469 for $\alpha = 0.15$, $\beta = 0.96$, and $\alpha = 0.87$, $\beta = 1.7$, respectively.

5 Conclusions

Local non-modal stability analysis of flat-plate boundary with uniform suction and injection is investigated. The velocity profile shift towards and away from the wall with suction and injection, respectively. The largest optimal energy growth has been found for injection and least one for suction corresponding to various parameters. The flow is modally stable in a case of injection with a higher Re for $\alpha = 0$, $\beta \neq 0$. However, it becomes unstable even at lower Re for $\alpha \neq 0$. The streamwise vortices of optimal disturbances has been found at $t = t_{opt}$ corresponding to $\alpha = 0$, $\beta \neq 0$, whereas streamwise elongated tilted structure is found corresponding to $\alpha \neq 0$. The location of maximum magnitudes of optimal perturbations is found closer to wall for suction than the injection. In a case of suction, no unstable region is found in $\alpha - \beta$ plane even at a higher α and β for fixed Re , whereas reverse trend is observed for injection. The receptivity analysis performed via resolvent norm using the input-output framework and supplementary equation. The peak response in energy of harmonically driven fluid system is detected at resonant frequency $\omega = 0.07143$ and 0.602 for injection corresponding to $\alpha = 0.15$, $\beta = 0.96$, and $\alpha = 0.87$, $\beta = 1.7$, respectively. However, resolvent norm found peak at $\omega = 0.1122$ and 0.8469 for suction corresponding to $\alpha = 0.15$, $\beta = 0.96$, and $\alpha = 0.87$, $\beta = 1.7$, respectively.

Fig. 11 Comparison of Resolvent norm $\| (i\omega I - L)^{-1} \|$ of boundary layer flow with different cases for **a** $\alpha = 0.15, \beta = 0.96$ and **b** $\alpha = 0.87, \beta = 1.7$ corresponding $Re = 1000$ and intensity = 0.5% of U_∞



The optimal growth, G_{opt} , is increased with increasing injection intensity, whereas reverse trends are observed for suction.

Acknowledgements Authors would like to thanks Science and Engineering Research Board (SERB), Government of India for financial support to this project.

Nomenclature

- α Streamwise wave number
- β Spanwise wave number
- Re Reynolds number
- ω External frequency [rad/s]

References

1. Schrauf G (2005) Status and perspectives of laminar flow. Aeronaut J 109(1102):639–644

2. Libby PA, Laufman L, Harrington RP (1952) An experimental investigation of the laminar boundary layer on a porous flat plate. *J Aeronaut Sci* 2:127
3. Reynolds GA, Saric WS (1986) Experiments on the stability of the flat-plate boundary layer with suction. *AIAA J* 24:202–207
4. Saric W, Reed L (1986) Effect of suction and weak mass Injection on boundary-layer transition. *J AIAA* 03:383–389
5. Huang Z, Wu X (2016) The effect of local steady suction on the stability and transition of boundary layer on a flat-plate. *AIAA* 1–12
6. Aydin O, Kaya A (2005) Laminar boundary layer flow over a horizontal permeable flat plate. *App Math Comp* 161:229–240
7. Wang S, Lei J, Zhen H, Lee C (2015) Numerical investigation of wall cooling and suction effects on supersonic boundary layer transition using large eddy simulation. *Advan Mech Eng* 1–12
8. Hinvi L, Monwanou V, Orou J (2014) Linear stability analysis of Poiseuille flow in porous medium with small suction and injection. *Fluid Dyn* 12:1–11
9. Sadri S, Babaelahi M (2013) Analysis of a laminar boundary layer flow with injection or suction. *J App Mech Tech Phys* 54(1):59–67
10. Palanichamy P (2017) Heat and mass transfer on flat plate with suction and injection. *Global J Math Sci: Prac* 9(3):367–386
11. Reddy SC, Henningson DS (1993) Energy growth in viscous channel. *J Fluid Mech* 252:209–238
12. Kurian T, Fransso JHM (2011) Transient growth in the asymptotic suction boundary layer. *Exp Fluids* 51:771–784
13. Fransson JHM, Corbett P (2003) Optimal linear growth in the asymptotic suction boundary layer. *Eur J of Fluid Mech* 22:259–270
14. Byström MG, Levin O, Henningson DS (2007) Optimal disturbances in suction boundary layers. *Eur J Fluid Mech* 26:330–343
15. Bhorniya R, Narayanan V (2021) Global stability analysis of spatially developing boundary layer: effect of wall suction and injection. *Springer lecture notes in mechanical engineering*, pp 509–517
16. Schmid PJ, Brandt L (2014) Analysis of fluid systems: stability, receptivity, sensitivity: lecture notes on advanced instability methods for complex flows. *Appl Mech Rev* 66(2):024803
17. Malik MR (1990) Numerical methods for hypersonic boundary layer stability. *J Comp Phys* 86(2):376–412
18. Hanifi A, Schmid PJ, Henningson DS (1996) Transient growth in compressible boundary layer flow. *Phys Fluids* 8(3):826–837
19. Butler KM, Farrell BF (1992) Three-dimensional optimal perturbations in viscous shear flow. *Phys Fluids A* 4(8):1637–1649
20. Schmid PJ, Henningson DS (2001) *Stability and transition in shear flows*. Springer
21. Roache PJ (1994) A method for uniform reporting of grid refinement. *J Fluid Eng* 116(3):405–413

Linear Stability Analysis of Two-Dimensional Mixed Convective Flow Past a Square Cylinder



Rudram Dushe, Basheer A. Khan, and Arun K. Saha

Abstract Linear stability analysis of two-dimensional mixed convective flow past a heated square section cylinder is performed, to determine the flow stability for given flow parameters, and to study the onset of vortex shedding suppression as the Richardson number (Ri) increases. All analyses are performed in the assisted buoyancy regime ($Ri > 0$). The results from the linear stability analysis are also validated against the results from Direct Numerical Simulation (DNS). The Reynolds number (Re) and the Prandtl number (Pr) are fixed at 100 and 0.7, respectively, and the effect of Richardson number on the suppression of vortex shedding phenomena is studied, by varying Ri in the range [0.13, 0.17]. A critical Richardson number of 0.16 corresponding to the onset of suppression of vortex shedding was found through DNS. Through the linear stability analysis, this transition from unsteady to steady flow field was found to occur via a Hopf bifurcation. The behavior of the eigenmodes of the most unstable perturbations was studied. Lastly, a discussion has been made regarding the possible mechanisms that cause the transition in flow stability.

Keywords Mixed convection · Linear stability analysis · DNS · Vortex shedding suppression

1 Introduction

Mixed convective flows past heated bluff bodies are of practical importance in engineering, because of their occurrence and applications in heat exchangers, cooling of machine equipment, etc. By heating the bluff body, the control of vortex shedding from the bluff body can also be achieved. However, this phenomenon of vortex shedding suppression, especially for flow past a square section cylinder, has not been studied in detail and the mechanism causing this transition in the stability of the flow is not clearly understood. Out of the existing few studies present on mixed convective flows past heated bluff bodies, most are based on a circular cylinder. Although flows

R. Dushe (✉) · B. A. Khan · A. K. Saha
Department of Mechanical Engineering, IIT Kanpur, Kanpur 208016, India
e-mail: rudram@iitk.ac.in

© The Author(s), under exclusive license to Springer Nature Singapore Pte Ltd. 2024
K. M. Singh et al. (eds.), *Fluid Mechanics and Fluid Power, Volume 2*, Lecture Notes in Mechanical Engineering, https://doi.org/10.1007/978-981-99-5752-1_7

past a circular and square cylinder resemble each other to quite an extent, the instability mechanisms and the flow characteristics are quite different for these two cases, mostly owing to the presence of fixed flow separation points for a square cylinder as opposed to variable separation points for a circular cylinder.

Sharma and Eswaran [1] numerically investigated the characteristics of mixed convection flow past a square cylinder for $Re = 100$, $Pr = 0.7$, and for a range of Richardson number, $Ri = [-1, 1]$. In the assisted buoyancy regime, they found that the degeneration of Kármán vortex street which leads to the transition of the flow from unsteady periodic to steady occurs at a critical Richardson number of 0.15.

Hasan and Ali [2] numerically investigated the flow past circular and square cylinders at different free stream orientations and Richardson numbers. For a square cylinder at $Re = 100$, $Pr = 0.71$, and free stream angle of 0° , they found the critical Richardson number for suppression of vortex shedding to be 0.129, which was obtained by extrapolation of simulation data using the Landau model.

Considering the overview of the past work done on mixed convective flow past a square cylinder, it can be concluded that none of the studies have focused on the linear stability analysis of these flows, which is important for understanding the bifurcations and mechanisms which lead to flow transition. In the present work, numerical simulations have been performed for two-dimensional mixed convective flow past a heated square section cylinder at a constant temperature, assuming that the buoyancy forces act along the direction of inlet flow velocity (i.e., buoyancy-assisted flow configuration). This resembles the upward flow of fluid past a heated cylinder in vertical configuration so that the buoyant forces caused by gravity as a result of variation in density due to heating act in the upward direction, i.e., along the direction of inlet velocity. Here, a similar case has been simulated, only in a horizontal orientation.

2 Methodology

Considering the values of the flow parameters used in the present study, it can be affirmed from previous knowledge that the flow at these values is of laminar, two-dimensional nature. Thus in the present study, without the loss of generality, the flow around the heated square section cylinder at constant temperature has been simulated assuming a laminar two-dimensional, viscous and unsteady flow. The equations are used in their non-dimensional, conservative form. The non-dimensional flow variables used in the present work are related to the real flow variables as follows:

$$U = \frac{u}{u_\infty}; V = \frac{v}{u_\infty}; \tau = \frac{tu_\infty}{B}; X = \frac{x}{B}; Y = \frac{y}{B};$$

$$\theta = \frac{T - T_\infty}{T_s - T_\infty}; P = \frac{p}{\rho u_\infty^2}$$

where u = streamwise velocity along x ; v = transverse velocity along y ; p = fluid pressure; T = fluid temperature; ρ = fluid density; u_∞ = free stream fluid velocity; B = edge length of the square cylinder; T_∞ = free stream fluid temperature; T_s = constant surface temperature of the square cylinder; t = time.

The dimensionless numbers used are defined as:

$$\text{Re} = \frac{\rho u_\infty B}{\mu} \text{Ri} = \frac{\text{Gr}}{\text{Re}^2} \text{Pr} = \frac{\mu c_p}{k}$$

where Grashof Number $\text{Gr} = \frac{g\beta(T_s - T_\infty)B^3}{\nu^2}$; β = coefficient of volumetric thermal expansion; ν = kinematic viscosity; μ = dynamic viscosity; g = gravitational acceleration; c_p = specific heat of the fluid; k = thermal conductivity of the fluid. The Richardson number (Ri) captures the relative influence of natural convection (effect of buoyancy) compared to forced convection.

The governing equations which form the basis of the present study are:

$$\frac{\partial U}{\partial X} + \frac{\partial V}{\partial Y} = 0 \quad (1)$$

$$\frac{\partial U}{\partial \tau} + \frac{\partial(UU)}{\partial X} + \frac{\partial(VU)}{\partial Y} = -\frac{\partial P}{\partial X} + \frac{1}{\text{Re}} \left(\frac{\partial^2 U}{\partial X^2} + \frac{\partial^2 U}{\partial Y^2} \right) + \text{Ri}\theta \quad (2)$$

$$\frac{\partial V}{\partial \tau} + \frac{\partial(UV)}{\partial X} + \frac{\partial(VV)}{\partial Y} = -\frac{\partial P}{\partial Y} + \frac{1}{\text{Re}} \left(\frac{\partial^2 V}{\partial X^2} + \frac{\partial^2 V}{\partial Y^2} \right) \quad (3)$$

The temperature field is solved via the non-dimensional energy equation, assuming negligible viscous dissipation:

$$\frac{\partial \theta}{\partial \tau} + \frac{\partial(U\theta)}{\partial X} + \frac{\partial(V\theta)}{\partial Y} = \frac{1}{\text{RePr}} \left(\frac{\partial^2 \theta}{\partial X^2} + \frac{\partial^2 \theta}{\partial Y^2} \right) \quad (4)$$

At the inlet, U was set equal to 1, while V was set to 0. No-slip boundary condition was applied on the surface of the square cylinder. The constant non-dimensional temperature was set equal to 1 on the surface of the cylinder, and equal to 0 at the inlet. On the top and bottom artificial boundaries, a free slip condition for U and θ was used, while V was set equal to 0. At the outlet, a convective boundary condition was used: $\partial U/\partial \tau + U_c \partial U/\partial X = 0$, $\partial \theta/\partial \tau + U_c \partial \theta/\partial X = 0$, $\partial V/\partial \tau + U_c \partial V/\partial X = 0$, with the celerity constant $U_c = 0.8$.

For performing DNS, the modified MAC algorithm has been used to solve the above-mentioned equations on a non-uniform staggered Cartesian grid system. The domain was taken to be 43B units along the x -direction and 31B units along the y -direction, with the cylinder's center placed at the origin (Fig. 1). A non-uniform grid of 308×198 cells was used to discretize the domain.

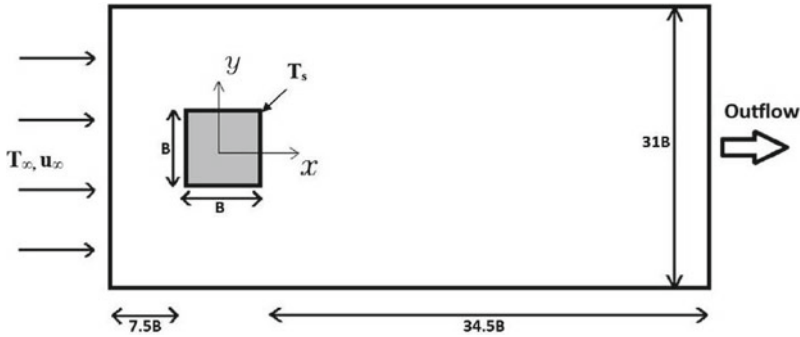


Fig. 1 Computational domain for flow past a heated square cylinder

2.1 Formulation for Linear Stability Analysis

To obtain the governing equations of flow perturbations, the flow variables are decomposed into two components, the steady-symmetric components, and the perturbations. The steady-symmetric components act as the base flow variables on which the flow perturbations are superimposed to obtain the actual non-dimensional flow field variables. Therefore:

$$U = U_b + \tilde{u} \quad (5)$$

$$V = V_b + \tilde{v} \quad (6)$$

$$P = P_b + \tilde{p} \quad (7)$$

$$\theta = \theta_b + \tilde{\theta} \quad (8)$$

where the subscript ‘*b*’ indicates the steady-symmetric components (base flow variables) and \tilde{u} , \tilde{v} , \tilde{p} and $\tilde{\theta}$ are the perturbations in U , V , P , and θ , respectively.

To obtain the base flow, the same DNS code was run only in the bottom half domain while applying symmetric boundary conditions across the center line ($y = 0$). Also, at the outflow boundary, the boundary condition $\partial\phi/\partial x = 0$ was used instead of the convective boundary condition as the base flow variables are time-invariant (ϕ represents the base flow variables U_b , V_b , or θ_b). The rest of the things were kept the same. These base flow variables obtained in the bottom half of the domain were used to obtain the base flow variables in the top half by using the fact that the base flow is symmetric about the center line, i.e., for $y > 0$ (top half domain), $U(y) = U(-y)$, $V(y) = -V(-y)$, $P(y) = P(-y)$ and $\theta(y) = \theta(-y)$. Imposing these conditions drives the solution toward a steady-symmetric kind irrespective of the nature of the

original solution. Thus, the base flow variables satisfy the steady-symmetric part of the Navier–Stokes and the Energy equation.

The perturbations satisfy the time-varying part of the Navier–Stokes equations. On substituting the Eqs. (5)–(8) in Eqs. (1)–(4), and subtracting the steady-symmetric part of the equations (equations for the base flow variables) from them, while neglecting the nonlinear terms in perturbations assuming that perturbations are small in magnitude (hence, the name linear stability analysis), we get the governing equations for the flow perturbations. Also, we assume the following functional form of the perturbations which helps us to determine the behavior of the perturbations as a function of time:

$$\tilde{u}(x, y, t) = \hat{u}(x, y)e^{\lambda t} \quad (9)$$

$$\tilde{v}(x, y, t) = \hat{v}(x, y)e^{\lambda t} \quad (10)$$

$$\tilde{p}(x, y, t) = \hat{p}(x, y)e^{\lambda t} \quad (11)$$

$$\tilde{\theta}(x, y, t) = \hat{\theta}(x, y)e^{\lambda t} \quad (12)$$

This assumption is called the normal mode decomposition. The perturbations are assumed to grow exponentially with time. The idea is to find the values of lambda for which the solutions to the perturbation equations exist. Thus, since we are dealing with linear perturbation equations, the final perturbation field would be represented as the linear combination of all the perturbation modes obtained corresponding to the found values of lambda. If the values of lambda found have a negative real part, the perturbations will decay with time and the flow will tend to go toward steadiness. If the values of lambda have a positive real part, the perturbations will keep growing exponentially with time, and after a while, their magnitude will increase so high that the assumption of neglecting the nonlinear terms in perturbation equations assuming that they have low relative magnitude compared to other terms, becomes questionable. However, this is not a concern of the present study, as the idea is to only know whether the perturbations will grow or decay with time, which tells whether the flow is steady or unsteady. Since the present work only focuses on cases near flow transition between steady and unsteady states, the magnitudes of the perturbations can be expected to be small, which serves as a justification for the linear stability model used in this study.

On substituting Eqs. (9)–(12) in the governing equations for flow perturbations, we get the final form of perturbation equations as:

$$\frac{\partial \hat{u}}{\partial X} + \frac{\partial \hat{v}}{\partial Y} = 0 \quad (13)$$

$$2 \frac{\partial(U\hat{u})}{\partial X} + \frac{\partial(V\hat{u})}{\partial Y} + \frac{\partial(U\hat{v})}{\partial Y} + \frac{\partial\hat{p}}{\partial X} - \text{Ri}\hat{\theta} - \frac{1}{\text{Re}} \left(\frac{\partial^2\hat{u}}{\partial X^2} + \frac{\partial^2\hat{u}}{\partial Y^2} \right) = -\lambda\hat{u} \quad (14)$$

$$\frac{\partial(U\hat{v})}{\partial X} + \frac{\partial(V\hat{u})}{\partial X} + 2 \frac{\partial(V\hat{v})}{\partial Y} + \frac{\partial\hat{p}}{\partial Y} - \frac{1}{\text{Re}} \left(\frac{\partial^2\hat{v}}{\partial X^2} + \frac{\partial^2\hat{v}}{\partial Y^2} \right) = -\lambda\hat{v} \quad (15)$$

$$\frac{\partial(U\hat{\theta})}{\partial X} + \frac{\partial(\theta\hat{u})}{\partial X} + \frac{\partial(V\hat{\theta})}{\partial Y} + \frac{\partial\theta\hat{v}}{\partial Y} - \frac{1}{\text{RePr}} \left(\frac{\partial^2\hat{\theta}}{\partial X^2} + \frac{\partial^2\hat{\theta}}{\partial Y^2} \right) = -\lambda\hat{\theta} \quad (16)$$

Equations (13)–(16) are first discretized using the central differencing scheme and then morphed into the form of a generalized eigenvalue problem. For using the central differencing scheme, the perturbations are defined at the center of the grid cells and the values of the base flow variables are interpolated to obtain their values at the center of grid cells. The eigenvalues of the problem give the possible values of lambda for which the solution to the perturbation equations exists. The eigenvectors of the eigenvalue problem represent the possible perturbation modes (eigenmodes). The final equation for the generalized eigenvalue problem becomes:

$$A\hat{w} = \lambda B\hat{w} \quad (17)$$

where A and B are sparse matrices of size 4×4 mn ($m = \text{no. of cells along } x = 308$, $n = \text{no. of cells along } y = 198$), and \hat{w} is a vector of length 4 mn defined as:

$$\hat{w} = \begin{bmatrix} \hat{u} \\ \hat{v} \\ \hat{p} \\ \hat{\theta} \end{bmatrix}$$

Equation (17) is solved using the ‘eigs()’ function of MATLAB to obtain the eigenvalues with the largest real part (i.e., eigenvalues corresponding to the most unstable perturbations).

2.2 Code Validation and Grid-Independence Test

The validity of the code used for performing DNS in the present work can be verified through the work of Saha et al. [3] and Saha [4] on the fully developed fluid flow through a channel with a built-in square cylinder and normal flat plate respectively, as we have used the same code with the inclusion of buoyancy effect. The addition of buoyancy term in the given code is also previously validated in the work of Saha and Malik [5]. Based on the results of the grid-independence test, we selected the grid to be used for simulations.

3 Results and Discussion

3.1 Direct Numerical Simulation

From the instantaneous streamlines near the cylinder shown in Fig. 2, it can be clearly seen that for $Ri = 0.13$ and $Ri = 0.15$, the vortex shedding process is active, whereas it becomes suppressed for $Ri = 0.16$ and $Ri = 0.17$. This marks the transition from unsteady periodic flow (Kármán vortex street) to steady symmetric (pair of twin vortices). The periodicity of the unsteady flow field for $Ri = 0.15$ can be visualized in Fig. 3, which shows the variation of drag and lift coefficients of the cylinder with non-dimensional time, whereas for $Ri = 0.16$, the amplitude of oscillations dies out and the flow attains steady nature. The transition of the far-wake region from having an unsteady periodic, flapping nature to a steady symmetric one can be demonstrated through the instantaneous vorticity contours (Fig. 4).

The recirculation region is defined as the region of negative mean u -velocities. For the unsteady periodic regime, the length of the recirculation region behind the cylinder is observed to increase as the Richardson number increases (From $Ri = 0.13$ to $Ri = 0.15$), while for the steady-symmetric regime, it is found to decrease with an increase in Richardson number (from $Ri = 0.15$ to $Ri = 0.17$). This can

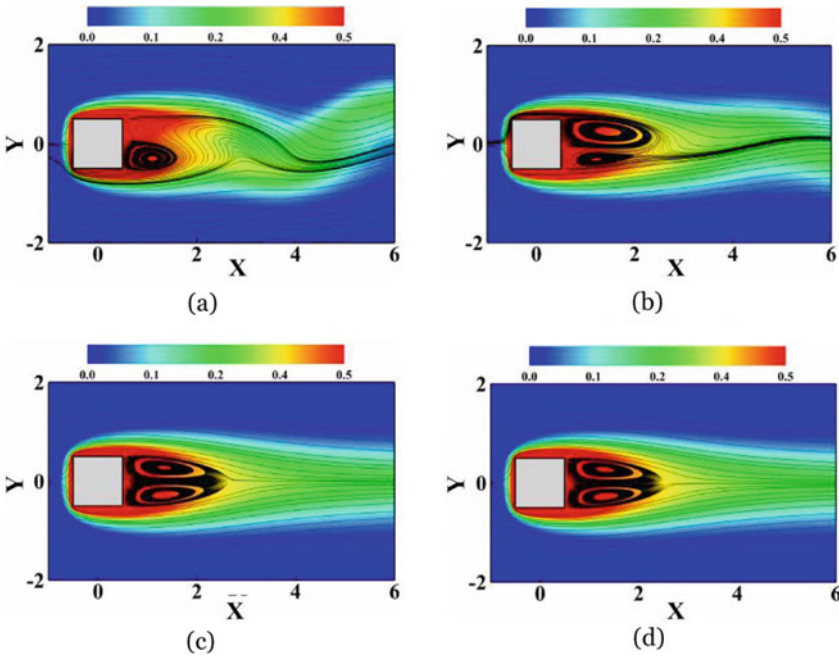


Fig. 2 Instantaneous streamlines and temperature contours for a $Ri = 0.13$ b $Ri = 0.15$ c $Ri = 0.16$ and d $Ri = 0.17$

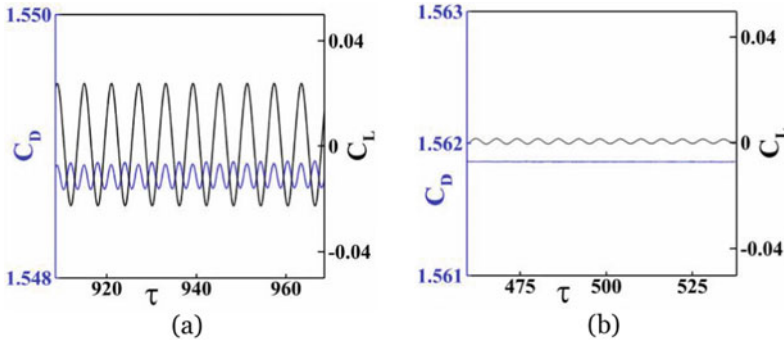


Fig. 3 Variation of drag (C_d) and lift (C_l) coefficients with time for **a** $Ri = 0.15$ and **b** $Ri = 0.16$

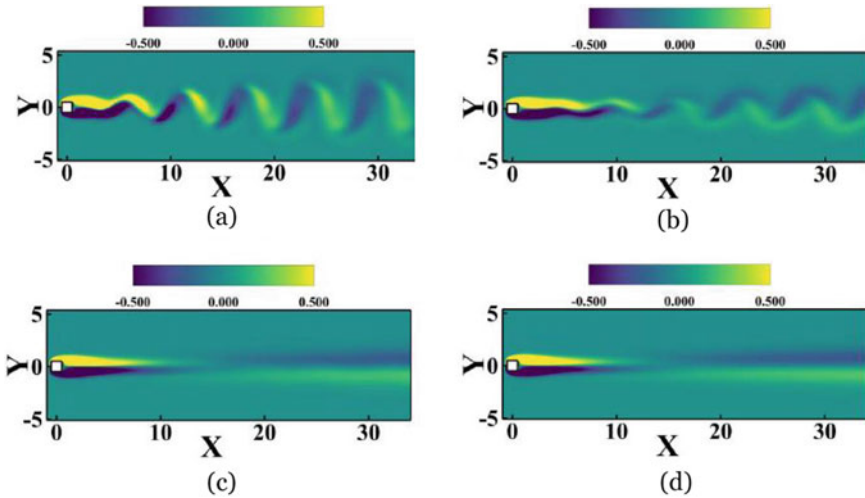


Fig. 4 Instantaneous vorticity contours for **a** $Ri = 0.13$ **b** $Ri = 0.15$ **c** $Ri = 0.16$ and **d** $Ri = 0.17$

be seen from the mean u -velocity profiles along the centerline (Fig. 5). The profiles are plotted starting from the region right behind the cylinder all the way up to the far-wake region. Note that the point of intersection of the mean velocity profile with $y = 0$ indicates the maximum x coordinate of the recirculation region, and hence the distance of this point from the aft surface of the cylinder is a measure of the recirculation region length.

The variation of the time-averaged Nusselt number for the cylinder and the time-averaged Drag coefficient with the Richardson number is given in Table 1. As the majority of the heat transfer from the cylinder to the fluid occurs through the front, top, and bottom faces of the cylinder, a plot showing the variation of the time-averaged Nusselt number corresponding to heat transfer by the front, top, and bottom faces of the cylinder with Ri is shown in Fig. 6. It can be readily observed that the Nusselt

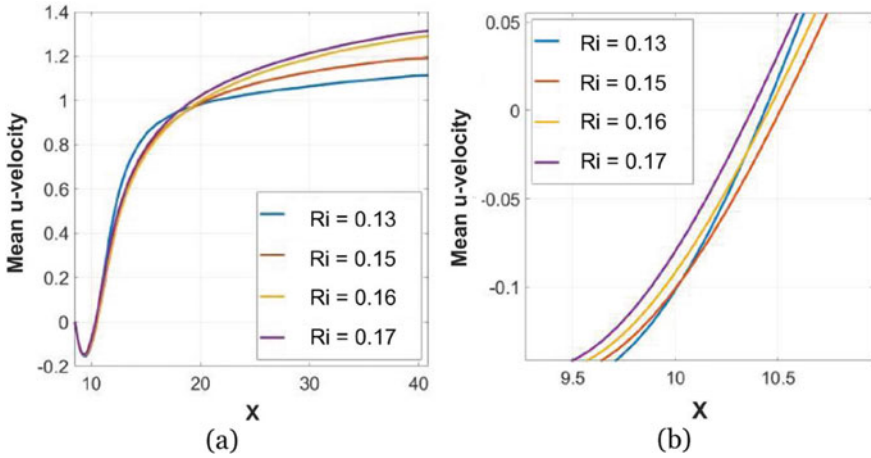


Fig. 5 **a** Time-averaged u -velocity profile along the centerline ($y = 0$). **b** Close-up of the velocity profile shown in **a**. The recirculation length is determined by the point of intersection of the profile with $y = 0$ line

Table 1 Time-averaged Nusselt number for the cylinder, Nu_c , and drag coefficient, Cd at different Richardson numbers

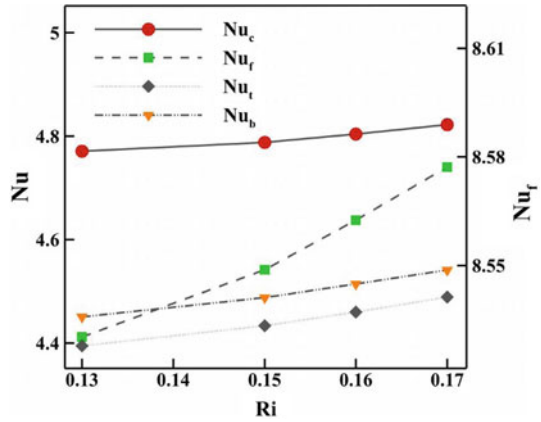
Ri	Nu_c	Cd
0.13	4.77	1.54
0.15	4.79	1.55
0.16	4.80	1.56
0.17	4.82	1.58

number increases monotonically with Ri, implying higher heat transfer with higher Richardson number. This can be attributed to the fact that higher Ri accelerates the shear layer, which leads to higher mean velocities, and thus higher heat transfer through convection. The Drag coefficient is also found to be monotonically increasing with Ri.

3.2 Linear Stability Analysis

Let us first understand how to interpret the results from linear stability analysis. As previously mentioned in section II (A), the perturbations were imposed on the solution of the steady-symmetric part of the Navier–Stokes and the energy equation. If the actual flow is steady, we require perturbations that decay to zero eventually with time (negative real part of λ), so that the base flow solution plus the perturbations will represent the actual flow field. This is because the actual flow variables are modeled as the summation of base flow variables and the perturbations in the stability model.

Fig. 6 Variation of Nusselt number with Ri. Nu_c = Average Nusselt number for the cylinder; Nu_b = Average Nusselt number for the bottom surface; Nu_t = Average Nusselt number for the top surface; Nu_f = Average Nusselt number for the front surface. Note that the Nusselt number corresponding to front surface has been plotted on the right-side y-axis



Also, a negative real part of λ ensures that the time derivative term, which goes as $e^{\lambda t}$, goes toward zero and the equations tend to attain a steady form. The imaginary part of λ represents the frequency of oscillations of the perturbations. Since the base flow is steady without any oscillations, this frequency is also the frequency of oscillations of the actual flow variables. Similarly, it can be said that for unsteady flows, we must obtain some λ as our solution that has a positive real part so that the time derivative term does not go toward zero and we have the unsteady form of the equations. The critical point of transition is represented by that value of Ri at which the found values of λ have a maximum real part of exactly zero.

A Fig. 7 shows the plots of the eigenvalues obtained at different values of Ri. The eigenvalues which have the maximum real part are found to shift leftwards, eventually crossing the imaginary axis and undergoing a change from positive to negative real parts, as the Richardson number was increased. From Fig. 7, it is clear that this crossing over of the imaginary axis occurs at $Ri = 0.15$. Thus, the linear stability model predicts the critical Richardson number = 0.15. It is mentioned in Strogatz [6] that when the equilibrium state (which corresponds to the steady state here) loses stability as a result of the growth of small disturbances, with the resulting motion being a small amplitude, sinusoidal, limit cycle oscillation about the former steady state, it is supercritical Hopf bifurcation. It also mentions the existence of complex conjugate pairs of eigenvalues as a characteristic of this bifurcation. Based on this information, the transition between steady and unsteady states in the present work can be identified as the supercritical Hopf bifurcation. Figures 8 and 9, respectively, show the stream function contours of real and imaginary parts of the most unstable eigenmode at different Ri. A notable feature of these plots is the heart-shaped enclosures, which have also been observed in previous studies involving stability analysis of flows past bluff bodies (Kelkar and Patankar [7], Camarri and Giannetti [8]). It is interesting to note that as Ri is increased, the most dominant perturbations shift to the far-wake region, and the influence of perturbations on the near wake region diminishes. This observation can be linked to the fact that in the regime of active vortex shedding (which happens in the near wake region), high

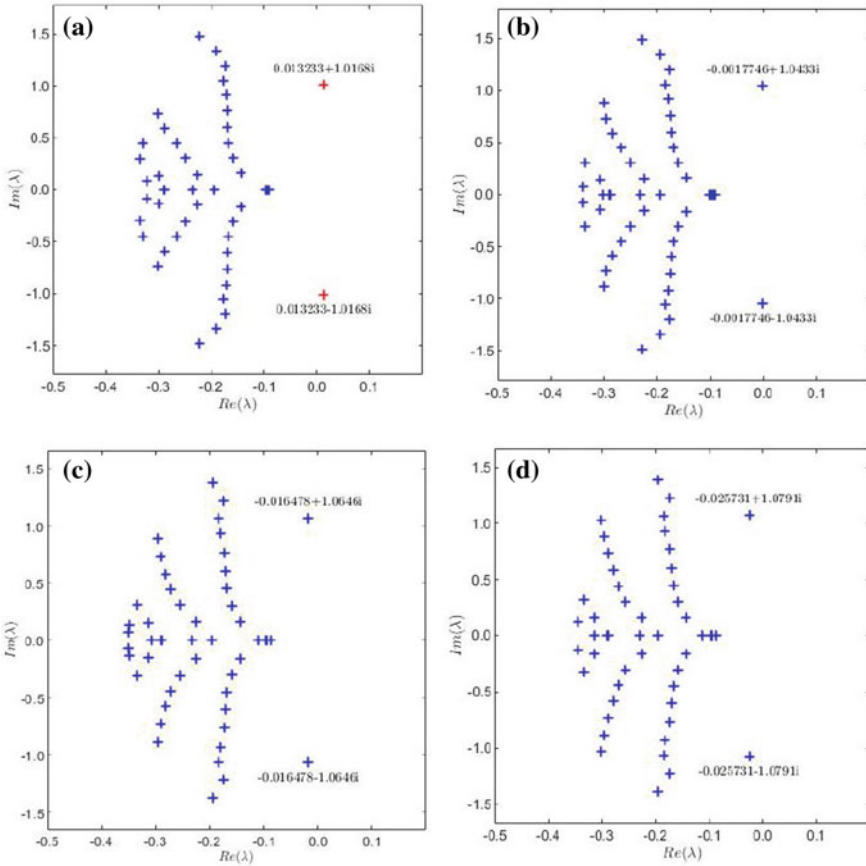


Fig. 7 Plots of eigenvalues for **a** $Ri = 0.13$ **b** $Ri = 0.15$ **c** $Ri = 0.16$ **d** $Ri = 0.17$

magnitude perturbations are expected in the near wake, which causes unsteadiness in the flow. While on the other hand, in the regime of suppressed vortex shedding (steady flow), the magnitudes of perturbations are expected to go down in the near wake region, which leads to a steady flow there.

3.3 Mechanism of Flow Transition

Several previous studies have focused on providing an explanation of the mechanism leading to flow transition in mixed convective flows past bluff bodies. As described in the work of Su and Chung [9], the inverse of Re is a measure of the importance of momentum diffusion while $(RePr)^{-1}$ is a measure of the importance of thermal diffusion. Thus, for $Pr \sim O(1)$, which corresponds to our case of $Pr = 0.7$, the

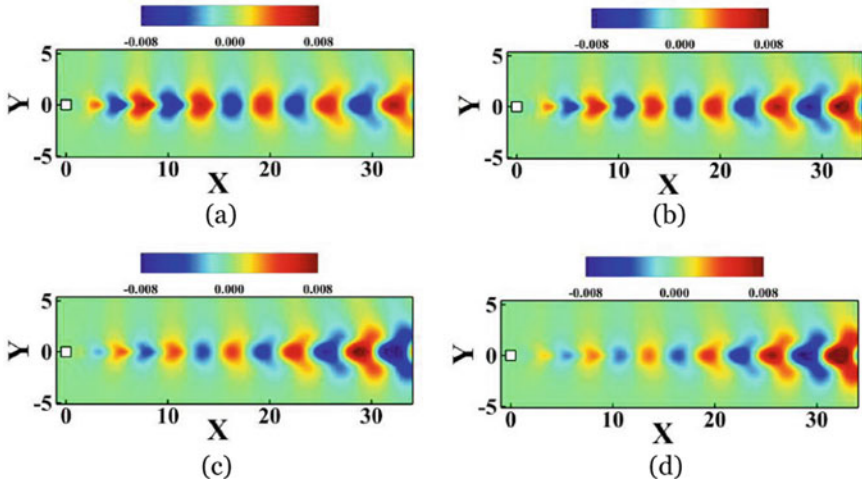


Fig. 8 Stream function contours of the real part of the most unstable eigenmode at **a** $Ri = 0.13$ **b** $Ri = 0.15$ **c** $Ri = 0.16$ **d** $Ri = 0.17$

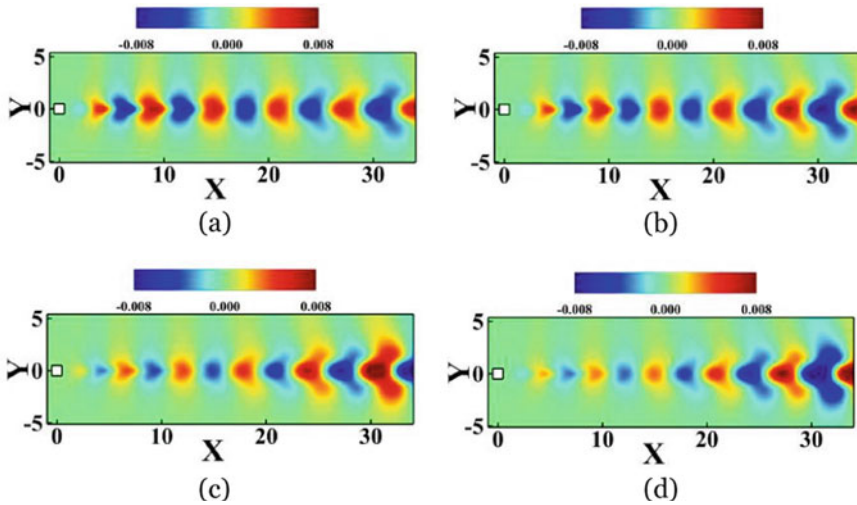


Fig. 9 Stream function contours of the imaginary part of the most unstable eigenmode at **a** $Ri = 0.13$ **b** $Ri = 0.15$ **c** $Ri = 0.16$ **d** $Ri = 0.17$

momentum and thermal diffusion terms are both influential. Therefore, neither the thermal disturbances nor kinetic disturbances have a dominating magnitude over the other. Thus, the overall stability characteristics are determined by the combined effects of thermal and kinetic disturbances in our case. Kakade et al. [10] stated that the first effect of cylinder heating is to increase the velocity of the fluid particles, however, with further increase in Ri , the diffusion of thermal energy in the near wake

of the cylinder creates stabilizing buoyant forces with respect to the ambient fluid just outside the shear layer, which aids the suppression of vortex shedding once Ri is greater than a critical value. For the case with a circular cylinder, Chang and Sa [11] mentioned that with an increase in Grashof's number, the wall boundary layer accelerated and the velocity in the wake region increased, which led to a thinner boundary layer, causing the shedding frequency to increase. However, the weakened roll-up process reduced the entrainment of ambient flow into the wake cavity, until the vortices finally ceased to be shed from the cylinder surface. Michaux and B elorgey [12] mentioned the effect of natural convection (buoyancy effect) was to fill the momentum deficit which arises in the wake of the cylinder due to its drag, which ultimately leads to the suppression of vortex shedding. This filling of the deficit happens due to the existence of a secondary flow and is also responsible for lowering the length of the recirculation region as Ri was increased in the steady flow regime (Fig. 5). Hasan and Ali [2] identified the baroclinic vorticity generation rate as essential for the cause of vortex shedding suppression.

4 Conclusions

In this paper, linear stability analysis of two-dimensional mixed convective flow past a heated square cylinder has been presented. A critical Richardson number of 0.16 was identified through DNS as the critical point at which the flow changes its nature from unsteady to steady. This transition of flow is featured by the suppression of vortex shedding beyond the critical Richardson number. The variation of the Drag coefficient, Nusselt number, and the recirculation length with the Richardson number was discussed, where a monotonically increasing variation of the Drag coefficient and Nusselt number with the Richardson number was found. The results from linear stability analysis give the critical point of transition at $Ri = 0.15$, which agrees well with the results from DNS. The variation could possibly be attributed to the fact that the nonlinear terms in perturbation equations were neglected. The transition to steadiness and the onset of vortex shedding suppression is identified to occur via Hopf bifurcation through the linear stability analysis. Since the Prandtl number $\sim O(1)$, it is identified that the instability in the flow leading to unsteadiness is caused by the combined influence of thermal and kinetic disturbances, with both the disturbances playing an equivalent role. Lastly, some possible mechanisms responsible for this transition, as mentioned in some previous studies, were discussed.

References

1. Sharma A, Eswaran V (2004) Effect of aiding and opposing buoyancy on the heat and fluid flow across a square cylinder at $Re = 100$. *Numer Heat Transf, Part A: Appl* 45(6):601–624

2. Hasan N, Ali R (2013) Vortex-shedding suppression in two-dimensional mixed convective flows past circular and square cylinders. *Phys Fluids* 25(5):88
3. Saha AK, Muralidhar K, Biswas G (2000) Vortex structures and kinetic energy budget in two-dimensional flow past a square cylinder. *Comput Fluids* 29(6):669–694
4. Saha AK (2007) Far-wake characteristics of two-dimensional flow past a normal flat plate. *Phys Fluids* 19(12):128110
5. Saha AK, Malik T (2012) Mixed convective flow and heat transfer through a horizontal channel with surface mounted obstacles. *J Enhanced Heat Transf* 19(4)
6. Strogatz SH (2018) *Nonlinear dynamics and chaos: with applications to physics, biology, chemistry, and engineering*. CRC press
7. Kelkar KM, Patankar SV (1992) Numerical prediction of vortex shedding behind a square cylinder. *Int J Numer Meth Fluids* 14(3):327–341
8. Camarri S, Giannetti F (2007) On the inversion of the von Kármán street in the wake of a confined square cylinder. *J Fluid Mech* 574:169–178
9. Su YC, Chung JN (2000) Linear stability analysis of mixed-convection flow in a vertical pipe. *J Fluid Mech* 422:141–166
10. Kakade AA, Singh SK, Panigrahi PK, Muralidhar K (2010) Schlieren investigation of the square cylinder wake: joint influence of buoyancy and orientation. *Phys Fluids* 22(5):054107
11. Chang KS, Sa JY (1990) The effect of buoyancy on vortex shedding in the near wake of a circular cylinder. *J Fluid Mech* 220:253–266
12. Michaux-Leblond N, Belorgey M (1997) Near-wake behavior of a heated circular cylinder: viscosity-buoyancy duality. *Exp Therm Fluid Sci* 15(2):91–100

Characteristics of Transitional Separation Bubble Formed Over Negatively and Positively Skewed Anisotropic Rough Surface



K. T. Ganesh and K. Anand

Abstract Effect of leading-edge anisotropic erosion (negative skewness) and deposition (positive skewness) on a transitional separation bubble (TSB) is investigated using single-wire hot wire anemometer for a Reynolds number (Re_c) of 2.5×10^5 , based on the model chord and tunnel free stream velocity. Three different models are fabricated for investigation, whose surfaces are smooth (*SS*), sand blasted (*BS*) and sand deposited (*DS*), respectively. The fabricated rough surfaces are three-dimensionally irregular and replicate the anisotropic pattern of an operationally deteriorated turbine blade due to chronic exposure to harsh working environments. Results of positive and negative skewed rough surfaces are compared with that of smooth surface. The bubble is observed to be shortened by about 35% and 10% of that formed over *SS* for *DS* and *BS*, respectively. Premature transition is observed on *DS*, which is 49% earlier than *BS* case. Though the transition point varies, it is interesting to note that the chord length occupied by the transition and turbulent region of the bubble is almost same for all the cases. Presumably, more than the negatively skewed anisotropic rough surface, the positive counterpart tends to influence the boundary layer stability and thereby the transition characteristic of separation bubble.

Keywords Separation bubble · Geometry-induced separation · Anisotropic roughness · Boundary layer measurements

1 Introduction

Transitional separation bubble is characterized by laminar separation and turbulent reattachment, where the laminar-to-turbulent transition (LTT) happens in the separated shear layer [1–4]. TSB occurring at low Re tends to occupy nearly 15–40% of the airfoil surface, which act as a boundary layer trip [5]. The present work is focused on the occurrence of separation bubble in turbomachinery blades and

K. T. Ganesh · K. Anand (✉)

School of Mechanical Engineering, SASTRA Deemed University, Thanjavur 613401, India
e-mail: anand@mech.sastra.edu

its consequences on aerodynamic performances. Especially, LTT due to damaged leading-edge of turbine blades that operate at low Re besides a strong adverse pressure gradient on the oncoming flow for most part of the operational hours, such as, wind turbine blades [6] and a low-pressure turbine in high bypass-ratio engine [7]. Damaged blades tend to degrade the performance [6, 8] and in certain cases, it may lead to component failure [9]. Operational deterioration by any means, viz. erosion [8], contamination, foreign object collision [10] or higher thermal loads [11], etc., is anisotropic in nature. Hence, it is significant to analyze the effect of surface anisotropy upon the LTT characteristics of separation bubble.

2 Literature Review and Objective

The volume of literature relevant to separation bubble is vast. Ever since the profound work on laminar separation bubble [12, 13], investigation of TSB had increased to a considerable extent. Experimental studies [1, 14–16] had reported the basic characteristics such as the mean separation, transition and reattachment, and paved a strong foundation for modeling of separation bubble. Later, experiments on leading-edge separation at low Re [3, 4, 17–19] presented better interpretation of LTT in separated shear layer. The influence of surface roughness on LTT characteristics were also reported [20–24] along with the other works. The effect of roughness on the flow structures was interpreted with the non-dimensional equivalent sand grain roughness, k_s^+ , employed to determine the roughness Reynolds number (ΔU^+). Roughness related investigations were carried out by using regular structures distributed in an order or random configuration over the surface. Although these configurations provide insight of roughness-induced-transition, the characteristics of flow over a rough wall are significantly different for regular and irregular roughness [25–27].

Flow field analyses on irregular roughness are very less in number due to the intricacy in reproduction and characterization of the 3D roughness parameters. The non-dimensional “*Effective Slope (ES)*” was employed [26] to characterize the 3D regular and non-regular rough surface based on the geometric parameters such as spanwise spacing (λ) and height of roughness (h). It was observed that the results of non-regular rough surface exhibited spatial inhomogeneity of turbulent flow when compared with regular rough surface. Later, the turbulent flow characteristics over 3D irregular roughness were found to be insensitive to *ES* [27] and hence the statistical parameters such as skewness and kurtosis were suggested as the better metrics to characterize irregular roughness. The statistical parameters were grouped into amplitude, feature and hybrid parameters [28]. Feature parameters tend to represent the anisotropy of surface deformation. Influence of skewness (positive and negative) on the near-wall turbulent flow was investigated [29] and found that positively skewed roughness produced higher C_f than negatively skewed surface. Recently, the “*Surface Anisotropy Ratio*” (SAR) was employed [30, 31] to characterize 3D irregular rough surface. SAR is the ratio of streamwise and spanwise correlation lengths

of the surface deformation; used to differentiate spanwise ($SAR < 1$) and streamwise ($SAR > 1$) anisotropy.

The significant characteristics of separated flow transition over smooth [1, 15, 18] and rough surface [21, 22] are documented using hot wire anemometer. Beside the characterization of anisotropic roughness, its effect on the turbulent flow structures [27, 30, 32] is also studied. Though, there were literatures available on characterizing a separated flow over a regular 2D and 3D rough surface, it is rare to find a work on the transitional separation bubble over an irregular (anisotropic) rough surface. In the present work, an attempt is made to determine the parameters that define LTT of a TSB formed over irregularly deformed surface.

3 Experiment Setup and Methodology

The experimental setup for velocity measurements using constant temperature anemometer (CTA) is shown in Fig. 1. Experiments are carried out in a low-speed open-return suction type wind tunnel facility available in School of Mechanical Engineering, SASTRA, Thanjavur. The cross section of the tunnel test section measures 300×300 mm and spans for a length of 1500 mm. The model is firmly fastened to the sidewalls of the test section. A suction fan unit at the diffuser exit sets the airflow through the test section. The freestream velocity is set by controlling the fan using a variable frequency drive (VFD). In the present work, single-sensor constant temperature anemometer (CTA) of Dantec Dynamics Inc., Denmark make is employed for velocity measurements. The CTA module is set to operate at a constant overheat ratio (OHR) of 0.8. Thus, the maximum operating temperature of hot-wire sensor is limited to 267°C , beyond which burnout occurs. The analog output of CTA is digitized using NI-cDAQ 9171 of National Instruments, U.S.A. The signal is calibrated and analyzed with Streamware[®] software supplied by the CTA manufacturer. An automated three-dimensional traverse mechanism is designed and built in-house to precisely position the hot-wire probe during data acquisition. The control unit for traverse mechanism constitutes micro-stepping drivers (SE5045), an Arduino[®] board (Uno) and a DC power supply.

The origin for velocity measurements is the *blend-point* [18] of the model (Fig. 2a). The data is probed at 25 stations designated at a gap of 6 mm ($x/c = 0.013$) along the model chord. At each station, the velocity data is acquired at 79 locations in the wall normal direction. The distance between consecutive points within the boundary layer is 0.1 mm, while it varies from 1 to 3 mm in the freestream. Each data is an ensemble of 8000 samples acquired at 5 kHz sampling rate. In the present investigation, the uncertainty of hot-wire in measuring the velocity near-wall is found to be within 1.8%, whereas in the freestream, it is less than 0.7%.

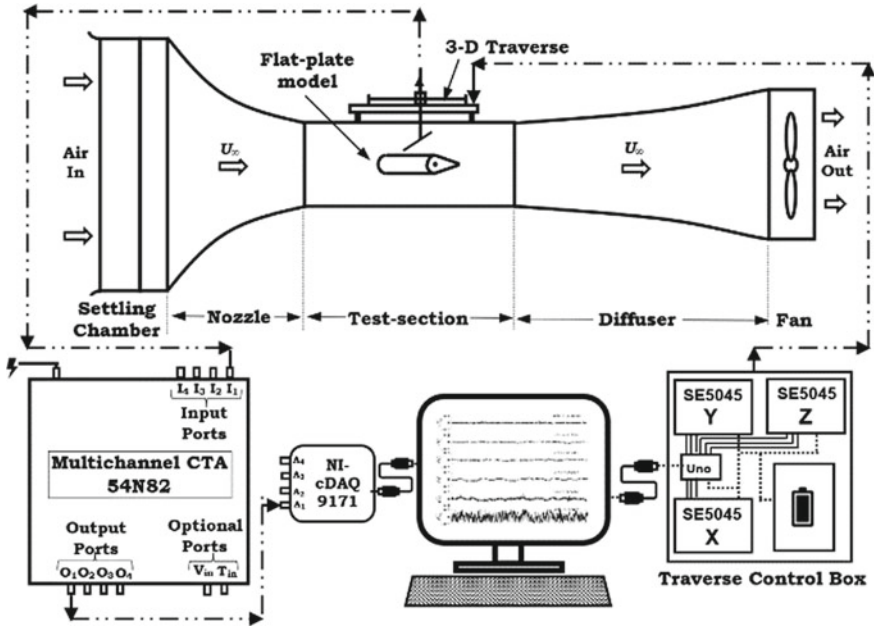


Fig. 1 Schematic of the experimental setup for velocity measurements using CTA

3.1 Negative and Positively Skewed Anisotropic Roughness

Two-dimensional schematic of the semi-circular leading-edge ($D = 69.5$ mm) blunt flat plate model is shown in Fig. 2a, in which the trailing edge of the model constitutes a pitchable flap: used to modify the chord-wise pressure gradient across the model. The design of present model is a modified version of blunt flat plate employed in earlier investigations [14, 18]. Models of smooth and deteriorated surface are fabricated with 5 mm thick acrylic sheets. Photographs of the fabricated models are shown in Fig. 2b, where the magnified portions are shown below the respective model.

One of the models is sand blasted [11] to produce a irregularly worn-out surface that replicates the anisotropic nature of erosion in turbine blades [10]. Since the sand blasted surface is dominated by pits or valleys, it is referred as negatively skewed deformation [8, 29]. On the other hand, sand grains of varying size glued to the surface results in a peak dominated surface: referred as positively skewed rough surface [29]. The latter replicates the actual turbine blade roughness made by deposition [11]. Thus, the individual models made with different surface roughness topology aid to analyze the effect of negative and positive skewed surface on the development of separated shear layer.

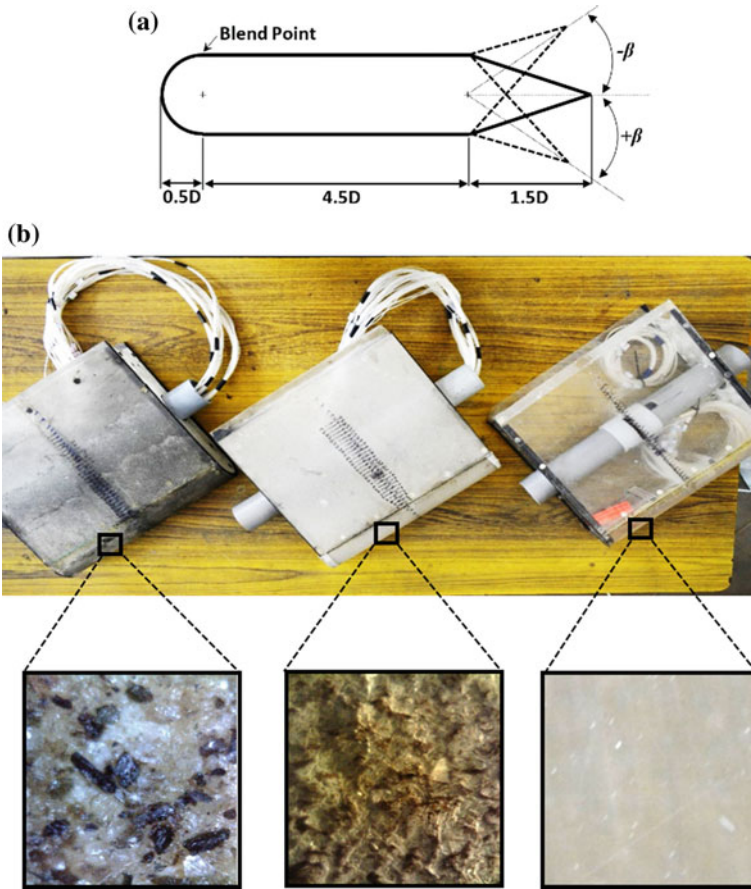


Fig. 2 a Line sketch illustrating the model and b Photographs of the fabricated flat plate models

4 Results and Discussion

The effect of positive and negatively skewed anisotropic roughness on the mean flow characteristics of TSB is elucidated by comparing the results of rough surfaces with that of smooth surface. In the following discussions, the abbreviations *SS*, *BS* and *DS* refer to smooth surface, blasted surface (negatively skewed) and deposited surface (positively skewed) respectively.

4.1 Streamwise Mean Flow Field

To detail out the boundary layer development, the mean (\bar{u}) and fluctuation (u_{rms}) data of streamwise velocity component is given in semi-log plot in Fig. 3. Hence, the near-wall flow field is stretched while the fully inviscid region is suppressed, and the size of separation bubble appears to be exaggerated.

Figure 3a shows the mean velocity distribution in a TSB where, the results of **BS** and **DS** are superimposed over the **SS** case to elucidate the significance of surface topology on the flow characteristics of TSB. The boundary layer separates at the blend-point of the model, $x/c = 0$ in figure, for **SS** and **BS** cases, whereas it is delayed by 2 mm ($x/c = 0.004$) downstream to model origin for the **DS** case. In figure, at $x/c = 0$, the boundary layer of **DS** case is observed to appear close to the wall. This is attributed to the fine-scaled vortices generated by the sand grains resulting in higher turbulent production near-wall [24]. Posterior to separation, the shear layer for **SS** case till $x/c = 0.09$ is observed to be thin, but rapidly thickens within a short distance downstream i.e., $x/c = 0.12$. The rapid increase in thickness is attributed to the sudden breakdown and roll-up of shear layer [15]. Similarly, for **BS** and **DS** cases, the rapid thickening of shear layer is observed to occur earlier by

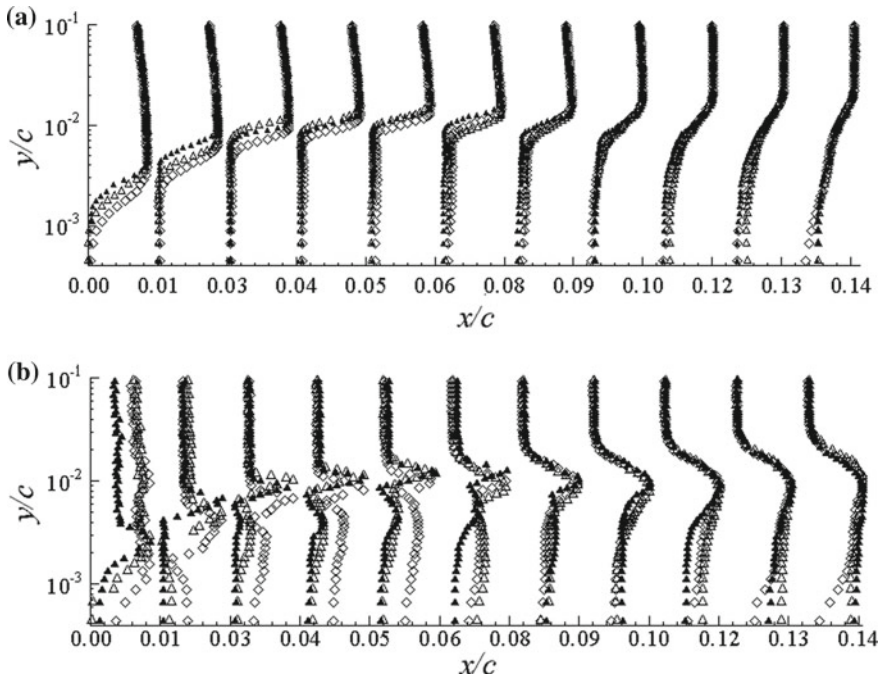


Fig. 3 Effect of positive and negative skewness on mean (\bar{u}/U_e) and fluctuations (u_{rms}/u_{rmsmax}) of streamwise velocity within the separation bubble [Symbols: \blacktriangle —SS; \triangle —BS; \diamond —DS]

$x/c = 0.08$ and $x/c = 0.06$, respectively. It is evident from the figure that the roll-up of shear layer happens at the maximum vertical displacement of the bubble [15].

Since the single-sensor hot-wire tends to be accurate with the magnitude of velocity vector rather than its direction, the reverse flow velocity is measured as a minimal positive velocity. In figure, post $x/c = 0.05$ for all the cases, the forward shift in near-wall velocity corresponds to the influence of recirculation flow formed near reattachment. The near-wall velocity offset increases till the profile resembles that of a developing turbulent boundary layer. Thus, the streamwise station at which the maximum shift in near-wall velocity is observed, it shall be considered as the vicinity of shear layer reattachment.

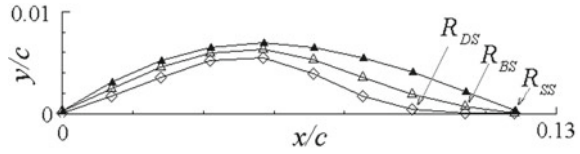
The onset and end of transition can be determined from fluctuation profiles and is discussed in the following section. Figure 3b shows the u_{rms} profiles of **SS**, **BS** and **DS** cases superimposed in the semi-log plot. For all the cases, two peaks of $u_{rms_{max}}$ are observed across each profile between $x/c = 0.03$ and 0.10. In each of the double peak profile, the inner peak beneath the shear layer is an indication of near-wall turbulent activity and the second peak in the outer edge of shear layer is due to the interaction with freestream turbulent flow. This feature is also an indication of transition onset [33]. Accordingly, the first occurrence of minor peak close to the inner edge of shear layer of **SS** and **BS** cases is observed in Fig. 3b at $x/c = 0.03$, whereas for **DS** case, it appears a little earlier at $x/c = 0.01$. The exponential growth rate of disturbances is evident by the gradual growth of inner peak till $x/c = 0.06$; whereas the minor peak rapidly vanishes between $x/c = 0.08$ and 0.10 for all the cases. This trend is not observed in the outer peak since its magnitude is governed by the constant freestream turbulence. Also, the vertical gap between inner and outer peak progressively increases in the streamwise direction. It is likely that the shear layer adjacent to separation bubble at its maximum height tends to entrain both freestream and the recirculation region underneath [13]. In figure, the double peak in u_{rms} profiles of **BS** and **DS** cases keeps its identity till $x/c = 0.06$, whereas the minor peak persists for **SS** case till $x/c = 0.08$. The fusion of double peak into single large peak is attributed to the end of transition or onset of reattachment [33].

4.2 Zero-Velocity Line

The recirculation region cannot be identified from the velocity profiles of Fig. 3a due to the insensitivity of hot wire to negative velocity. In hot-wire measurement, the local minima close to wall is considered as the mean zero-velocity location [2]. These points correspond to the inner edge of shear layer in Fig. 3a. The extracted points of respective cases are plotted in Fig. 4. For better interpretation, the data fit in figure is first-order smoothed and hence a small variation in bubble height is noticed.

In figure, the inner edge of the separated shear layer in the second half of the bubble is observed to move closer to the wall as the skewness changes from negative to positive. This trend is congruent to the above discussion of freestream entrainment

Fig. 4 Locus of zero-velocity in a TSB due to change in surface topology [Symbols: \blacktriangle —SS, \triangle —BS and \diamond —DS]



by the shear layer. Also, this clarifies the increasing gap between inner and outer peak as observed in Fig. 3b. The point of maximum displacement of zero-velocity profile from the wall is approximated as the transition point [19]. The height of reverse flow region does not vary monotonically with change in skewness from negative to positive. Since the external freestream turbulence is constant, the sudden drop in the mean zero profile of *DS* case is likely to be the aftermath of receptivity [17]. The zero-velocity profile of *SS* and *BS* cases is similar except near reattachment.

4.3 LTT Characteristics

Figure 5 illustrates the effect of surface deformation upon the boundary layer characteristics of TSB in terms of integral parameters. The directional insensitivity of hot-wire sensor tends to produce incorrect values of integral parameters but the streamwise trend is unaffected by reverse flow [1]. Hence, the following discussions are focused more on the streamwise variation of integral parameters rather than its magnitude.

In Fig. 5a, the trend in variation of the displacement thickness (δ_1) is same for all the cases. The steep increase in δ_1 is attributed to laminar separation, while the steep downfall indicates the nonlinear breakdown and sudden roll-up of shear layer at its maximum vertical distance from the wall [15, 17]. Thus, the location, where δ_1 exhibits a maximum, is considered as the end of transition (x_T) and it corresponds to the streamwise location of highest level of fluctuations in Fig. 3b of the respective cases [15]. It is observed that the positively skewed roughness promotes transition

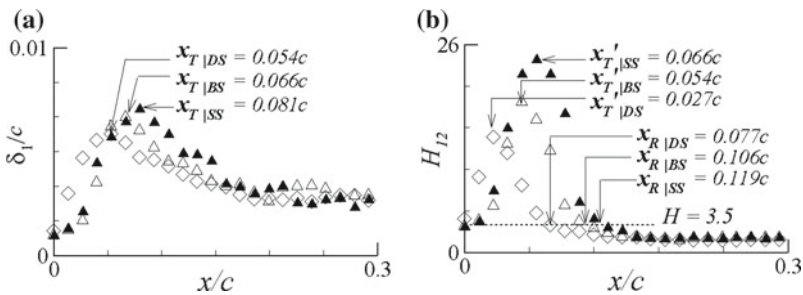


Fig. 5 Streamwise variation of integral parameters. **a** displacement thickness, δ_1 and **b** Shape factor, H_{12} [Symbols: \blacktriangle —SS, \triangle —BS and \diamond —DS]

earlier than its counterpart and *SS* case. Shortly, downstream to x_T , the turbulent shear layer gains enough energy from the external freestream and tend to reattach to the surface. Near reattachment, δ_1 , settle toward a minimum value, which indicates that the boundary layer is attached to the surface. Due to the intrusive effect of hot-wire probe close to the wall, there are small fluctuations in δ_1 and hence the reattachment point cannot be precisely located from figure.

The reattachment points (x_R) are determined from the intercept of universal shape factor value $H_{12} \sim 3.5$ [13] suggested for the reattaching boundary layers. Figure 5b shows the variation of boundary layer shape factor (H_{12}) along the length of the bubble. The respective reattachment locations are indicated in Fig. 5b. Turbulent and non-turbulent portions of TSB can be segregated with H_{12} [34]. In figure, H_{12} increases steeply post the onset of separation till it attains a peak value. Ascending H_{12} usually indicates a fully laminar region, where δ_1 increases and δ_2 (momentum thickness) decrease. The maximum of H_{12} of *DS* case is 40% lesser than that of *SS* and 22% smaller than *BS* case. For all the cases, the onset of transition ($x_{T'}$) is identified by the change in trend after the maximum of respective H_{12} . It is likely that the rapid shrinkage of laminar region due to positive skewness would promote premature transition that could bypass the natural LTT route [17]. Due to a continuous exchange of momentum between the external flow and the transitional shear layer, H_{12} continues to descend with a varying slope. Gradual decrease in H_{12} indicates the onset of primary instability, whereas the steep descend in the trend represents the nonlinear breakdown of shear layer leading to reattachment of turbulent shear layer. Ultimately, the shape factor settles to a minimum value of $H_{12} \sim 1.4$, typical for a developed turbulent boundary layer.

4.4 Bubble Characteristic Parameters

The characteristic parameters of the TSB for the cases investigated in the present work are listed in Table 1. The effect of change in skewness is readily seen in the decrement of mean bubble length (l_b). Following the work of [14], the bubble length is split into three portions, viz. laminar (l_0), transitional (l_1) and turbulent (l_2) region. To get a clear interpretation on the effects of surface topology upon the bubble characteristics, the transitional region is calculated between onset ($x_{T'}$) and end (x_T) of transition. It is inferred from Table 1, that the length of laminar portion (l_0) of the TSB is 56% and 51% of the mean bubble length of *SS* and *BS*, respectively. Whereas, for *DS*, l_0 shrinks up to 0.35 l_b resulting in a very short span for the linear instabilities to develop and mature by itself for the next stage. Shortened laminar portion may result in premature transition, thereby affecting the stability characteristics of entire bubble [35]. It is interesting to note that in *SS* and *BS* cases, l_1 is about half of l_0 ; though l_0 and l_1 are almost equal in *DS* case. Similar trend is observed for l_2 and l_1 . Though the overall bubble length decreases in congruent to the change in surface topology, the length of transitional and turbulent portion of the bubble is almost constant for all the cases. For all the cases investigated, the transition Reynolds number (Re_{l_1}),

Table 1 Variations in the significant mean parameters of TSB corresponding to the surface characteristic

Parameter	<i>SS</i>	<i>BS</i>	<i>DS</i>
l_b	0.119 <i>c</i>	0.107 <i>c</i>	0.074 <i>c</i>
l_0	0.066 <i>c</i>	0.054 <i>c</i>	0.027 <i>c</i>
l_1	0.028 <i>c</i>	0.027 <i>c</i>	0.026 <i>c</i>
l_2	0.025 <i>c</i>	0.026 <i>c</i>	0.024 <i>c</i>
$\tan(\gamma)$	0.086	0.101	0.108
$\tan(\alpha_T)$	0.531	0.466	0.509
$Re_{\delta_{2,s}}$	78.4	77.5	76.2
Re_{l_1}	5875	5650	5523
$\delta_{1_t}/\delta_{2_s}$	23.46	23.45	20.06

based on the length of the transitional region of the bubble, is well-above the critical Re [13, 15] for a separated shear layer to reattach.

The separation angle (γ) is calculated from the mean velocity profiles by adopting the procedure of Ref. [16]. Variation of γ due to different surface topologies follows the relationship of $\tan(\gamma) \propto 1/Re_{\delta_{2,s}}$ [14]. Near separation, the shear layer due to positively skewed rough surface is observed to be closer to the wall in Fig. 3. It is verified by the least value of proximity parameter ($\delta_{1_t}/\delta_{2_s}$) [16].

5 Conclusions

Characteristics of transitional separation bubble past sandblasted (valley dominated) and sand deposited (peak dominated) leading-edge are investigated for a Re_c of 2.5×10^5 . Velocity measurements over smooth, blasted and deposited surfaces are carried out with single-sensor hot-wire anemometer. It is observed that the boundary layer separates at the blend-point for smooth (*SS*) and blasted (*BS*) surfaces, whereas separation is delayed by 2 mm downstream of blend-point ($x/c = 0.004$) for deposited (*DS*) surface. For all the cases, two peaks of $u_{rms,max}$ is observed across each profile between $x/c = 0.03$ and 0.10, which indicates that the boundary layer is inflectional and is likely under the process of laminar-to-turbulent transition. It is observed that the positively skewed roughness promotes transition earlier than its counterpart and *SS* case. The maximum of H_{12} of *DS* case is 40% lesser than that of *SS* and 22% smaller than *BS* case. On a positively skewed surface, laminar portion of the bubble shrinks up to $0.35 l_b$ resulting in a very short span for the linear instabilities to develop and mature by itself for the next stage. Though the overall bubble length decreases in congruent to the change in surface topology, the length of transitional and turbulent portion of the bubble is almost constant for all the cases.

Acknowledgements The present work is part of the research project funded by DST-SERB, New Delhi (File No.: EMR/2016/005834). Also, the resources offered by SASTRA management is sincerely acknowledged.

Nomenclature

c	Chord length of flat plate model [mm]
D	Leading-edge diameter of the flat plate model [mm]
H_{12}	Boundary layer shape factor
Re_c	Reynolds number based on the chord of the flat plate model
$Re_{\delta_{2,s}}$	Reynolds number based on momentum thickness at separation
Re_{l_1}	Transitional Reynolds number (based on transitional length of TSB)
l_b	Mean length of TSB [mm]
l_0	Length of laminar portion of TSB [mm]
l_1	Length of transitional portion of TSB [mm]
l_2	Length of turbulent portion of TSB [mm]
\bar{u}	Streamwise mean velocity [m/s]
U_e	Boundary layer edge velocity [m/s]
u_{rms}	Root-mean-squared fluctuation of streamwise velocity [m/s]
u_{rmsmax}	Maximum of local rms fluctuation of streamwise velocity [m/s]
$x_{T'}$	Streamwise location of onset of transition [mm]
x_T	Streamwise location of end of transition (or) point of transition [mm]
x_R	Streamwise location of reattachment [mm]
γ	Separation angle [°]
δ_1	Displacement thickness of boundary layer [mm]
δ_2	Momentum thickness of boundary layer [mm]
$\delta_{1_t}/\delta_{2_s}$	Proximity parameter (Displacement thickness at transition/Momentum thickness at separation)

References

1. Fitzgerald EJ, Mueller TJ (1990) Measurements in a separation bubble on an airfoil using laser velocimetry. *AIAA J* 28(4):584–592
2. Hatman A, Wang T (1998) Separated-flow transition part 1—experimental methodology and mode classification, paper no. 98-GT-461, international gas turbine and aeroengine congress and exhibition. Stockholm, Sweden
3. Sandham ND (2008) Transitional separation bubbles and unsteady aspects of aerofoil stall. *Aeronaut J* 112(1133):395–404
4. Serna J, Lázaro BJ (2015) On the laminar region and the initial stages of transition in transitional separation bubbles. *Eur J Mech, B/Fluids*. 49(Part A):171–183
5. Mueller TJ, DeLaurier JD (2003) Aerodynamics of small vehicles. *Annu Rev Fluid Mech* 35:89–111
6. Han W, Kim J, Kim B (2018) Effects of contamination and erosion at the leading edge of blade tip airfoils on the annual energy production of wind turbines. *Renew Energy* 115:817–823
7. Bons JP, Taylor RP, McClain ST, Rivir RB (2001) The many faces of turbine surface roughness. *J Turbomach* 123(4):739–748
8. Ravishankara AK, Özdemir H, van der Weide E (2021) Analysis of leading edge erosion effects on turbulent flow over airfoils. *Renew Energy* 172:765–779
9. Bons JP (2010) A review of surface roughness effects in gas turbines. *J Turbomach* 132(2):1–16

10. Laguna-Camacho JR, Villagrán-Villegas LY, Martínez-García H, Juárez-Morales G, Cruz-Orduña MI, Vite-Torres M, Ríos-Velasco L, Hernández-Romero I (2016) A study of the wear damage on gas turbine blades. *Eng Fail Anal* 61:88–99
11. Hamed A, Tabakoff W, Wenglarz R (2006) Erosion and deposition in turbomachinery. *J Propul Power* 22(2):350–360
12. Gaster M (1967) The structure and behaviour of laminar separation bubbles, reports & memoranda no. 3595. Aeronautical research council, pp 1–31
13. Horton HP (1969) A semi-empirical theory for the growth and bursting of laminar separation bubbles, current paper no. 1073. Aeronautical research council, pp 1–44
14. Arena AV, Mueller TJ (1980) Laminar separation, transition, and turbulent reattachment near the leading edge of airfoils. *AIAA J* 18(7):747–753
15. Brendel M, Mueller TJ (1987) Boundary-layer measurements on an airfoil at low Reynolds numbers. *J Aircr* 25(7):612–617
16. O'Meara MM, Mueller TJ (1987) Laminar separation bubble characteristics on an airfoil at low Reynolds numbers. *AIAA J* 25(8):1033–1041
17. Serna J, Lázaro BJ (2014) The final stages of transition and the reattachment region in transitional separation bubbles. *Exp Fluids* 55(9):1–17
18. Anand K, Sarkar S (2017) Features of a laminar separated boundary layer near the leading-edge of a model airfoil for different angles of attack: an experimental study. *J Fluids Eng, Trans ASME* 139(2):1–14
19. Tuna BA, Kurelek JW, Yarusevych S (2019) Surface-pressure-based estimation of the velocity field in a separation bubble. *AIAA J* 57(9):3825–3837
20. Legner HH (1983) A review of roughness-induced nosetip transition. *AIAA J* 21(1):7–22
21. Kerho MF, Bragg MB (1997) Airfoil boundary-layer development and transition with large leading-edge roughness. *AIAA J* 35(1):75–84
22. Downs RS, White EB, Denissen NA (2008) Transient growth and transition induced by random distributed roughness. *AIAA J* 46(2):451–462
23. Simens MP, Gungor AG (2014) The effect of surface roughness on laminar separated boundary layers. *J Turbomach* 136(3):1–8
24. Sengupta A, Vadlamani NR, Tucker P (9–13 Jan 2017) Roughness induced transition in low pressure turbines, paper no. AIAA 2017-0303, AIAA SciTech forum—55th AIAA aerospace sciences meeting. Grapevine, Texas
25. Bons JP, Christensen KT (25–28 June 2007) A comparison of real and simulated surface roughness characterizations, paper no. AIAA 2007-3997, 37th AIAA fluid dynamics conference. Miami, Florida
26. Napoli E, Armenio V, De Marchis M (2008) The effect of the slope of irregularly distributed roughness elements on turbulent wall-bounded flows. *J Fluid Mech* 613:385–394
27. Bhaganagar K, Chau L (2015) Characterizing turbulent flow over 3-D idealized and irregular rough surfaces at low Reynolds number. *Appl Math Model* 39(22):6751–6766
28. Bulaha N, Rudzitis J (2018) Calculation possibilities of 3D parameters for surfaces with irregular roughness. *Latv J Phys Tech Sci* 55(4):70–79
29. Busse A, Thakkar M, Sandham ND (2017) Reynolds-number dependence of the near-wall flow over irregular rough surfaces. *J Fluid Mech* 810:196–224
30. Busse A, Jelly TO (2020) Influence of surface anisotropy on turbulent flow over irregular roughness. *Flow Turbul Combust* 104:331–354
31. Amarloo A, Forooghi P, Abkar M (2022) Secondary flows in statistically unstable turbulent boundary layers with spanwise heterogeneous roughness. *Theor Appl Mech Lett* 12(2):1–7
32. de Marchis M, Napoli E, Armenio V (2010) Turbulence structures over irregular rough surfaces 11(3):1–32
33. Volino RJ, Hultgren LS (2001) Measurements in separated and transitional boundary layers under low-pressure turbine airfoil conditions. *J Turbomach* 123(2):189–197

34. Serna J, Lázaro BJ (2015) On the bursting condition for transitional separation bubbles. *Aerosp Sci Technol* 44:43–50
35. Diwan SS, Ramesh ON (2007) Laminar separation bubbles: dynamics and control. *Sadhana—Acad Proc Eng Sci* 32:103–109

Numerical Study on Effect of Inclination of a Plane on Flow and Heat Transfer by Turbulent Wall Jet



Amiruzzahan Mondal and Animesh Patari

Abstract In this chapter, the heat transfer characteristics of a turbulent wall jet impinging on an isothermal inclined surface has been numerically investigated. Three different angles of inclinations ($\alpha = 3^\circ, 6^\circ$ & 9°) as well as a streamwise orientation of the plane have been considered. All the simulations have been done using Realizable $k-\varepsilon$ Model with Enhanced Wall Treatment assuming zero pressure gradient. The Jet is ejected with Reynold's Number 9600. A localized gain in the local maximum velocity over the jet exit velocity is noticed at the leading edge of inclination which enhances the local heat transfer coefficient. However, the jet self-similarity character remains undisturbed due to inclination. Total heat transfer from the surface as well as the average heat transfer co-efficient decreases slightly with increase in inclination of the plane.

Keywords Turbulent flow · Wall jet · Heat transfer · Numerical simulations · Inclined plane

1 Introduction

A jet is defined as free shear flow with an initial source of momentum (ρu_j). Turbulent wall jet while flowing with very high velocity over a wall, forms a very thin inner layer of thickness (y_m) attached to the wall across which velocity very rapidly changes from zero to maximum value (u_m). At the same time, it exchanges momentum through turbulent shear action due to its fluctuating velocity components with the surrounding fluid medium in another side, where velocity decreases gradually from maximum value and attain a half max-value ($u_m/2$) at a distance $y_{1/2}$ from wall and finally merges to the ambient flow condition. So, wall jet is very motivating topic of research

A. Mondal (✉) · A. Patari

Department of Mechanical Engineering, NIT Durgapur, Durgapur, West Bengal 713209, India
e-mail: amiruzzahan@gmail.com; am.23me1105@phd.nitdgp.ac.in

A. Patari

e-mail: apatari.me@nitdgp.ac.in

in turbulent flow due to these distinct two-scale characteristics. Side by side, wall jet is widely used in engineering industries, such as in thrust generator in rocket and missile, jet engines. It has enormous application in heat transfer engineering like, faster heating and cooling in cement kiln, steel plant, casting furnace industries, defrosting of wind shield, gas turbine blades cooling, so on.

2 Literature Review and Objective

Such wide application of turbulent wall jet in engineering opens the scope for doing lot of research and to explore the complex features of wall jet physics in more details. In the last few decades, lot of experimental [1–7], analytical and a few numerical [8, 9] investigation on wall jet have been done to understand the physics and configuration of turbulent jet on flat and curved surface associated with heat transfer in many cases [3, 5–7]. Launder and Rodi [10] had reviewed in detailed most of the experimental and theoretical research which were done before 1981 and concluded that there was noticeable deviation in the experimental results from one another but the jet growth $\frac{dy_{1/2}}{dx}$ was reported to fall within 0.073 ± 0.002 . To know about heat transfer features Mabuchi and Kumada [7] studied on mass transfer characteristics and proposed a co-relation of Nusselt number from experimental data. Sigalla [2] determined the skin friction co-efficient for wall jet under wide range of Reynold's number and ascertained that it follows Blasius type correlation given for turbulent flow over flat plate but with different coefficient. Wygnanski [4] has done an experiment of incompressible flow of wall jet with exit Reynolds number 3700–19,000. Self-similar stream wise mean velocity was found by them from about 20 times of jet width distance and local maximum velocity was occurred about the distance of $0.15y_{1/2}$ from wall. Eriksson et al. [1] reported that fully turbulent region begins from around 20 slot distance.

There are very few research on turbulent jet on inclined surface. The turbulent features of wall jet on a multiply inclined surface were numerically investigated in the work of Pramanik et al. [11], but no thermal study was performed there in. Among the heat transfer studies on wall jet, worth mentioning is the work of Dakos [5] who experimentally investigated the turbulent structure of heat transfer over a flat and mildly curved surface. He found that wall jet on flat surface spreads slower than curved surface and within the distance from the wall where the local velocity is maximum, 90% of temperature changes happened and the heat transfer is less in curved plane than flat one. Nizou [3] also gave a general skin friction correlation and from his experimental temperature profile it is clear that in $y^+ < 50$ the temperature profiles are ceremonious. AbdulNour et al. [6] found out a function of x/w for isoflux and isothermal boundary conditions and it was identified that the local heat transfer co-efficient gradually decreases from the starting edge of heated surface. Patari [12] had investigated various RANS model to find out the best one of the two equation RANS model which provides more appropriate and close prediction of flow and heat

transfer for wall jet and proposed that the Realizable $k-\epsilon$ model with enhanced wall treatment (EWT) can be the best alternative to DNS or LES.

It is observed after through literature survey that majority of the researches on wall jet are focused on flow and thermal characteristics on either parallel flat surface or mildly curved surface. There are limited number of experimental and numerical investigation on wall jet heat transfer with an inclined surface. Therefore, the main focus of this work is to investigate the effect of inclination of a plane through low angle on flow and heat transfer characteristics of turbulent wall jet compared to flat plate.

3 Problem Statement and Methodology

In this present investigation, a steady incompressible turbulent jet of air is induced through a slot of height $w = 0.01\text{m}$ parallel to an adiabatic horizontal wall of length $12w$ followed by an isothermal inclined wall of temperature 318K . The temperature of the jet and the ambient fluid medium is 295K . Reynolds Number of the jet based on the slot height and the jet velocity $u_j = 15.606\text{m/s}$ is 9600 . Four different angles of inclination ($\alpha = 0^\circ, 3^\circ, 6^\circ$ and 9°) are considered for the investigation.

3.1 Numerical Methodology

A two-dimensional computational domain as shown in Fig. 1, is chosen for the numerical simulation of the fluid flow and heat transfer using Ansys-Fluent 17.1 software. Realizable $k-\epsilon$ model with Enhanced Wall Treatment (EWT) scheme is employed to capture the near wall data quite accurately with pressure gradient effect in near wall region. SIMPLE solution algorithm with second order upwind scheme for momentum, turbulent kinetic energy, turbulent dissipation rate and energy equation have been implemented. Convergence criteria is set as 10^{-9} for energy equation and 10^{-6} for velocity, momentum, turbulent kinetic energy and dissipation. Pressure at the jet inlet, outlet and entrainment boundary is set to zero.

Along with the averaged equations for momentum and energy, the Realizable $k-\epsilon$ model additionally solves the transport equation of turbulent kinetic energy, $k = \frac{1}{2}u'_i u'_i$ as well as dissipation (ϵ) of turbulent kinetic energy, given as

$$\frac{\partial k u_j}{\partial x_j} = \frac{\partial}{\partial x_j} \left\{ \left(v + \frac{v_t}{\sigma_k} \right) \frac{\partial k}{\partial x_j} \right\} + P_k + P_b - \epsilon \tag{1}$$

$$\frac{\partial \epsilon u_j}{\partial x_j} = \frac{\partial}{\partial x_j} \left\{ \left(v + \frac{v_t}{\sigma_\epsilon} \right) \frac{\partial \epsilon}{\partial x_j} \right\} + C_1 S \epsilon - C_2 \frac{\epsilon^2}{k + \sqrt{\nu \epsilon}} + C_{1\epsilon} \frac{\epsilon}{k} C_{3\epsilon} P_b \tag{2}$$

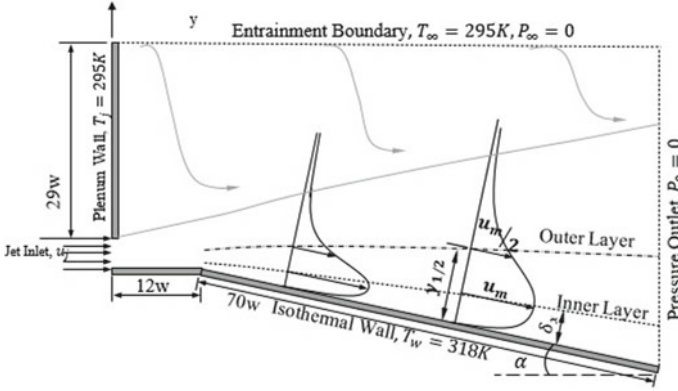


Fig. 1 Schematic diagram of the domain

P_k is the turbulent production of k which equals to $-\overline{u'_j u'_i} \frac{\partial x_i}{\partial u_j}$ and P_b is the production term taking care of the buoyancy [13]. By Boussinesq hypothesis, the Reynolds stress will be expressed as

$$-\overline{\rho u'_i u'_j} = -\frac{2}{3} \left(\rho k + \mu_t \frac{\partial u_k}{\partial x_k} \right) \delta_{ij} + \mu_t \left(\frac{\partial u_i}{\partial x_j} + \frac{\partial u_j}{\partial x_i} \right) \quad (3)$$

The eddy viscosity is given as $\mu_t = \rho C_\mu k^2 / \epsilon$.

3.2 Numerical Grid Convergence Study

Grid density and its distribution over the computational domain play very important role in numerical studies, because the discretization error greatly depends upon the size of the mesh elements. However, one of the well-recognized and globally accepted scientific technique, namely the Grid Convergence Index (GCI), has been adopted to confirm the independency of the computed numerical result for any variables. Out of the four different cases of angular orientation of the plate, $\alpha = 6^\circ$ has been chosen for grid independency test using GCI, following the technique as explained in the literature Celik [14] and Baker [15]. So, three set of mesh have been generated with number of elements N_c , N_m and N_f for coarse, medium and fine grids, respectively through systematic refinement to find the most favorable mesh distribution which affirms that the result is independent of further mesh refinement. Mesh distribution in near wall region (as shown in Fig. 2) has been made very fine ($Y_p^+ \sim 1$) as per the need to implement enhanced wall treatment.

The difference in the values of any variable (say ϕ) between fine and medium grid is $\epsilon_{fm} = \phi_f - \phi_m$ and relative error is $\epsilon_{rfm} = |1 - \phi_m / \phi_f| \times 100\%$. The apparent order, \hat{p} is calculated from the equation below-

Fig. 2 Mesh distribution in near wall region



$$\hat{p} = \frac{1}{\ln r_{fm}} \left| \ln \left| \frac{\epsilon_{mc}}{\epsilon_{fm}} \right| + \ln \left| \frac{r_{fm}^{\hat{p}} - \text{sign} \left(\frac{\epsilon_{mc}}{\epsilon_{fm}} \right)}{r_{mc}^{\hat{p}} - \text{sign} \left(\frac{\epsilon_{mc}}{\epsilon_{fm}} \right)} \right| \right| \quad (4)$$

The extrapolated value and error of variable (ϕ) is calculated by

$$\phi_{ext_{fm}} = \frac{r_{fm}^{\hat{p}} \phi_f - \phi_m}{r_{fm}^{\hat{p}} - 1} \text{ and } \epsilon_{ext_{fm}} = \left| \frac{100(\phi_{ext_{fm}} - \phi_f)}{\phi_{ext_{fm}}} \right| \quad (5)$$

Hence,

$$GCI_{\text{fine}} = 1.25 \frac{\epsilon_{r_{fm}}}{r_{fm}^{\hat{p}} - 1} \quad (6)$$

A sample calculation of the GCI for the wall average heat transfer coefficient is shown in Table 1. The GCI(%) of fine and medium grid are found to be 0.0092 and 0.0367, respectively, and the value of $GCI_{mc}/r_{fm}^{\hat{p}} GCI_{fm}$, stands 1.0343, which is close to 1 and indicates that the results are in well range of convergence. The GCI has been calculated also for temperature at 24 data points along normal to the wall at the location $x/w = 40$. The local order of accuracy \hat{p} ranges between 0.1614 to 7.9724 with an average $\hat{p}_{avg} = 1.7831$. The uncertainty in the computed value of temperature with the fine grid has been plotted in Fig. 3 in the form of error bar along with the temperature data obtained through all three grids. Maximum variation

Table 1 Grid convergence index calculation

Model	Fine grid (f)	Medium grid (m)	Coarse grid (c)
Number of elements, N	224,840	128,622	75,374
$\phi = h_{avg} (W/m^2K)$	47.2022	47.1923	47.2286
Case	$f-m$	$m-c$	$\frac{GCI_{mc}}{r_{fm}^{\hat{p}} GCI_{fm}} = 1.0343$
$r_{fm} = (N_f/N_m)^{1/2}$	1.3221	1.3063	
Apparent order of accuracy, \hat{p}	4.8165		
$h_{ext} (W/m^2K)$	47.2057	47.1785	
$\epsilon_r (\%)$	0.0210	0.0769	
$\epsilon_{ext} (\%)$	0.0074	0.0293	
GCI (%)	0.0092	0.0367	

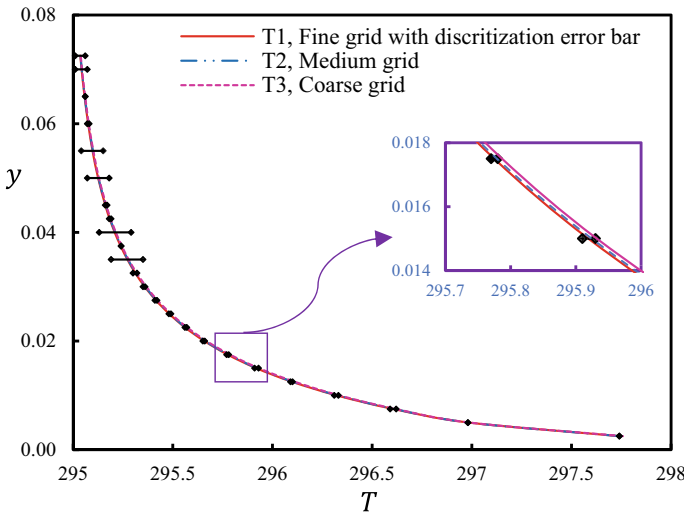


Fig. 3 Temperature variation for fine, medium and coarse grid with error bars of fine grid

of temperature is 0.01%. Utterly, the 224,840 (N_f) number of elements along with respective grid distribution as earlier said, has been finalized for all the numerical simulations.

3.3 Validation of the Numerical Results

Validation of the simulated result with experimental data is a very significant practice in numerical investigation to know the accuracy of numerical result. Here, the numerical data computed for non-dimensional mean velocity profiles are plotted in both

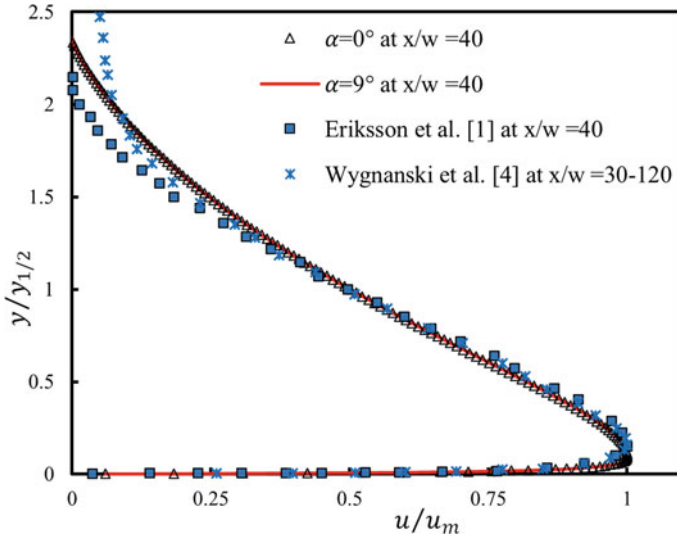


Fig. 4 Mean velocity profile in outer scaling

inner and outer scale for the case of $\alpha = 0^\circ$ and 9° at $x/w = 40$ and compared with experimental data of Eriksson [1] of Reynolds number 9600 as well as Wygnanski [4] having Reynolds number 10,000 (Figs. 4 and 5). An appreciable agreement among the data, particularly in the near wall region is noticed in both the scale. A little deviation of the current result with respect to Eriksson [1] and Wygnanski [4] appears after $1.4y_{1/2}$ which is in evidence in many literature [4, 10]. Here, $y^+ = yu_\tau/\nu$ and $U^+ = u/u_\tau$ where $u_\tau = \sqrt{\tau_w/\rho}$, which is known as friction velocity.

Similarly, the temperature variation θ/θ_m vs y/δ_T along normal to the inclined wall at $x/w = 40$ is presented alongside the data of AbdulNour [6] in Fig. 6. Here, δ_T is the thermal boundary layer thickness based on a value of $\theta = 0.1$, where $\theta = (T - T_j)/(T_w - T_j)$. A little difference (Fig. 4) of the current result with Eriksson [1] and Wygnanski [4] appears after $1.4y_{1/2}$ distance may vary in evidence of [4, 10]. Whatever minor difference appears in the present investigation may be due to the inclination of the surface. From the comparison, it is clear that the present data agreed very well with experimental data which certifies the accuracy of present numerical investigation.

4 Results and Discussion

After the GCI test and validation of the numerical result with several experimental reporting, it is confirmed that the present numerical result is prima facie valid to do the further post processing and analysis. The temperature profile, heat transfer

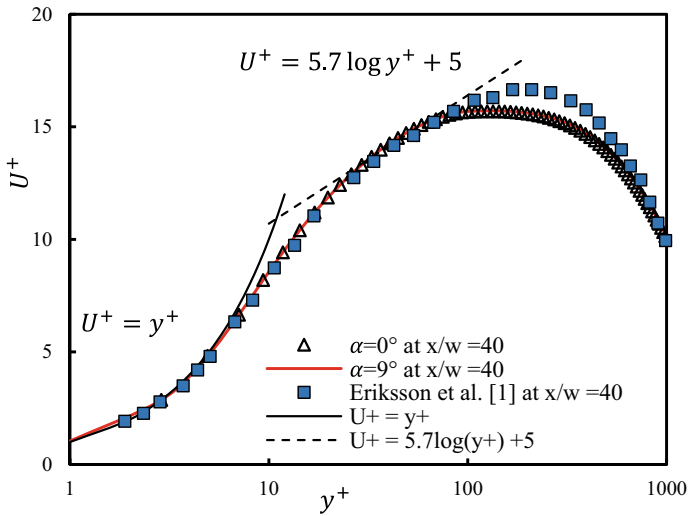


Fig. 5 Mean velocity profile in inner scaling

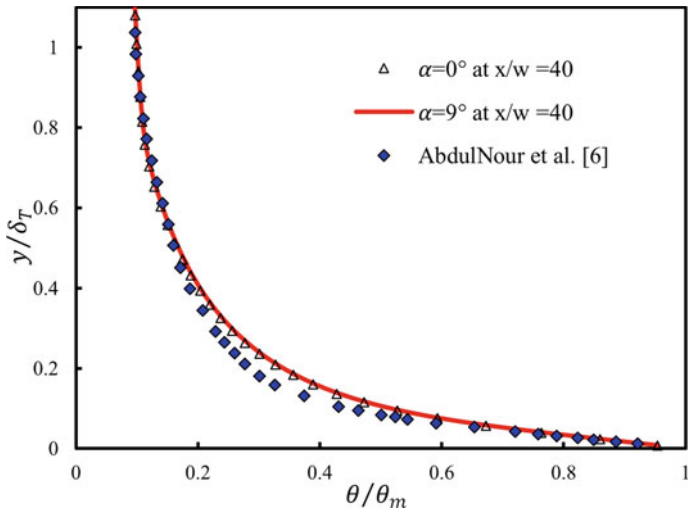


Fig. 6 Non-dimensional temperature variation

characteristics has been studied, analyzed in both the inner and outer scale and proposed along with experimental result wherever available.

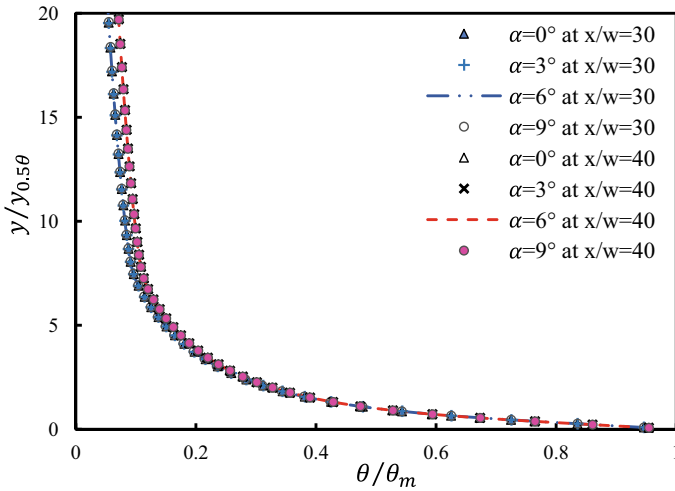


Fig. 7 Self similarity in temperature variation for different inclination angle

4.1 Mean Temperature Profile

Non-dimensional temperature profile has been plotted in Fig. 7 versus dimensionless distance $y/y_{0.5\theta}$ and also in Fig. 8, versus non-dimensional wall coordinate y^+ in the developed zone (at $x/w = 30$ & 40 from jet exit) for different angle α . Experimental temperature data obtained by Nizou [3] has also been shown in inner scale. A representative temperature log-law complying to the numerical temperature data can be obtained as $T^+ = 4.9 \log y^+ + 3.5$ in comparison to the experimental one. Here, $T^+ = (T_w - T)/T_\tau$ with friction temperature $T_\tau = q_w/\rho C_P u_\tau$. No remarkable changes or variation is observed along with changes in α and slot position which confirms its self-similarity.

4.2 Decay of Jet Maximum Velocity

The decay of stream-wise maximum velocity u_m/u_j over the downstream position x/w has been examined with the changes in angle of the plane and compared with the experimental data of Sigalla [2] for a parallel flat plate in Fig. 9. The jet momentum is found to be almost conserved over the initial length of the adiabatic horizontal surface. Near the junction of the horizontal and inclined surface, stream-wise maximum velocity gets accelerated and crosses even the magnitude of jet exit velocity due to creation of localised negative pressure in effect of inclination of the plate. This gain in maximum velocity increases with increase in inclination which helps in enhancing the heat transfer co-efficient in the localized zone.

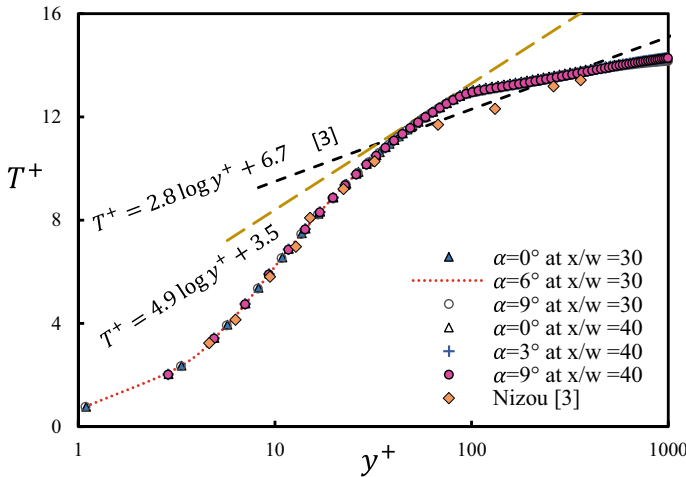


Fig. 8 Mean temperature profile in inner scaling for various inclination angle with ‘log law’

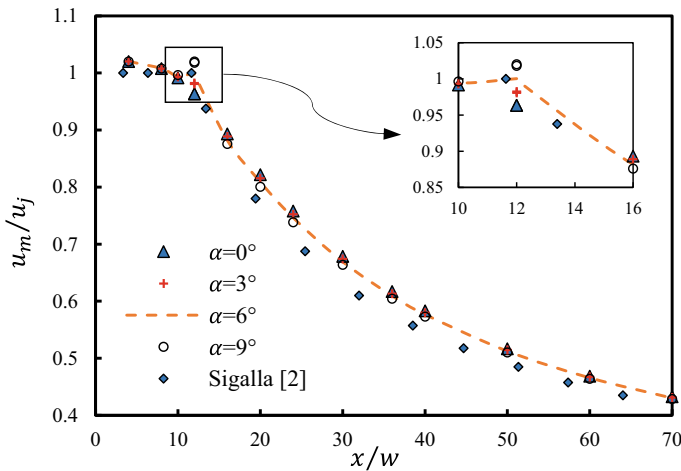


Fig. 9 Jet maximum velocity decay along slot distance

4.3 Growth of Thermal Boundary Layer

For inclination angle $\alpha = 0^\circ, 3^\circ, 6^\circ \& 9^\circ$, the dimensionless thermal boundary layer thickness (δ_T/w) and jet spread ($y_{1/2}/w$) at $x/w = 30$ for inclined plane have been shown in Fig. 10. It is clearly observed that at a particular stream-wise location, $y_{1/2}/w$ increases linearly with a rate $1.27 - 1.42\%$ (in comparison with 0°) for each 3° increase in α . But the changes in thermal boundary layer thickness (δ_T/w) which is found to occur very slowly after 3° inclination is not linear. Overall, more or less

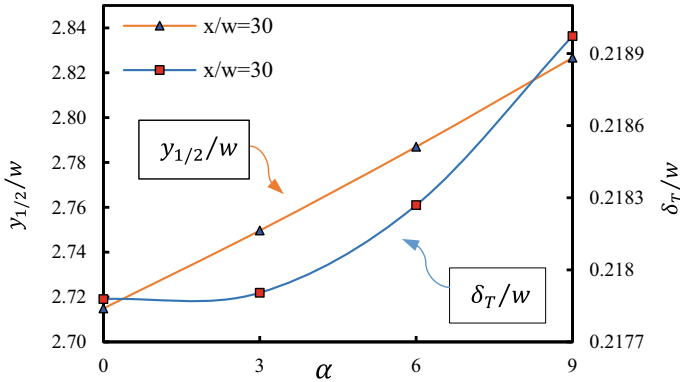


Fig. 10 Changes of non-dimensional thermal boundary layer thickness and jet spread along α for $x/w = 30$

0.5% increase is calculated in thermal boundary layer thickness for changes of 9° inclination angle in comparison to horizontal plate.

4.4 Heat Transfer Characteristics

The local heat transfer co-efficient is plotted in Fig. 11 for the leading length of the inclined wall. An increases of heat transfer co-efficient occurs there locally which goes higher with larger angle of inclination but overall area average heat transfer co-efficient slightly decreases 0.21 – 0.23% for each 3° increases of α .

The variation of local Nusselt number, $Nu_x = hw/k_f$ is plotted against x/w for inclined surface in Fig. 12. in comparison with correlation $Nu_x = 0.102Re_j^{0.8}(\frac{x}{w})^{-0.6}$ introduced by Mabuchi and Kumada [7] in fully developed zone. Numerically simulated data has a very good agreement with Mabuchi and Kumada [7] corelation. As described in previous para, the average Nusselt number slightly decreases along increases of α .

5 Conclusions

The influences of the angle of inclination of a flat isothermal surface on heat transfer characteristics of turbulent wall jet has been numerically investigated for a particular Reynolds number (9600). To capture the near wall features quite accurately, the enhanced wall treatment scheme is coupled with Realizable k-ε model. The exploration and study of numerically simulated data made explicit that for each 3° increases in inclination of plane leads to a velocity gain of 2 – 2.5% of the jet exit velocity (in

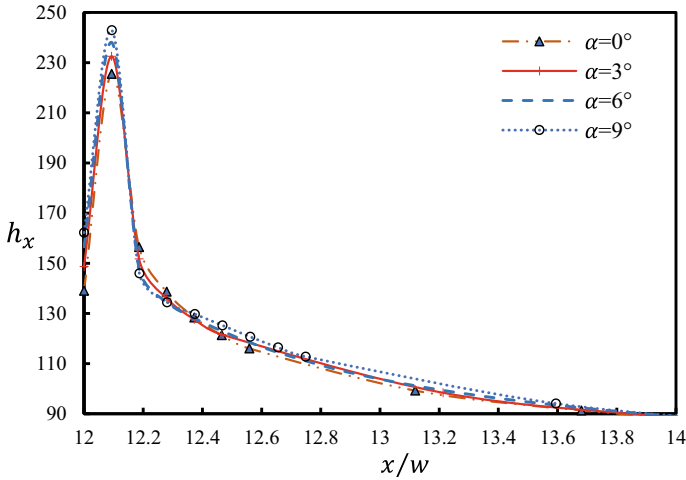


Fig. 11 Local heat transfer co-efficient at the leading edge of the inclined surface

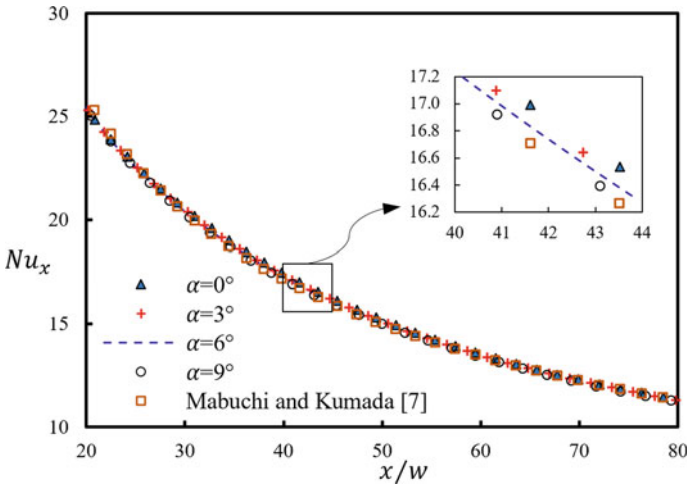
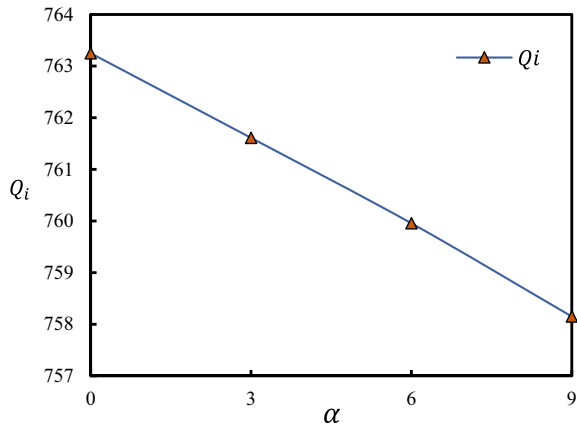


Fig. 12 Local Nusselt number variation

comparison to parallel plane) near the junction of the horizontal and inclined surface. This made a localized gain in heat transfer which increases with α . Very negligible thermal boundary layer thickness (δ_T), less than 0.5% for 9° increase of α , occurs. But the area average heat transfer co-efficient (h_{avg}) or the total heat transfer (Q_i) decreases at a rate 0.21 – 0.23% for each 3° increase in α as shown in Fig. 13.

It may be concluded that turbulent wall jets almost retain its fluid flow and thermal characteristics with small values of inclination of the interacting surface. There is

Fig. 13 Changes of total heat transfer (Q_i) along α



a scope in future to investigate the effect of higher values of inclination of the heat transfer surface with wall jet of higher Reynolds number.

Nomenclature

α	Inclination angle of inclined plate ($^{\circ}$)
C_P	Specific heat capacity of fluid [J/Kg K]
δ_T	Thermal boundary layer thickness [m]
ε	Turbulent dissipation rate [m^2/s^3]
h_{avg}	Area average heat transfer co-efficient [$\text{W}/\text{m}^2\text{K}$]
h_x	Local heat transfer co-efficient [$\text{W}/\text{m}^2\text{K}$]
k_f	Thermal conductivity of fluid [$\text{W}/\text{m K}$]
k	Turbulent kinetic energy [m^2/s^2]
μ	Dynamic viscosity [kg m/s]
Nu_x	Local Nusselt number
q_w	Wall heat flux [W/m^2]
Q_i	Total heat transfer [W]
Re_j	Jet exit Reynolds number
ρ	Fluid density [kg/m^3]
T	Temperature [K]
τ_w	Wall shear stress [Pa]
θ	Non-dimensional temperature
u	Streamwise velocity [m/s]
u_j	Jet exit velocity [m/s]
ν	Kinematic viscosity [m^2/s]
w	Height of Nozzle [m]
x	Distance from jet exit [m]

- $y_{1/2}$ Normal distance from wall where streamwise velocity is half-maximum ($u_m/2$) [m]
 $y_{0.5\theta}$ Normal distance from wall where $\theta = 0.5$ [m]

References

1. Eriksson JG, Karlsson RI, Persson J (1998) An experimental study of a two-dimensional plane turbulent wall jet, Springer. Exp Fluids 25:50–60
2. Sigalla A (1958) Measurements of skin friction in a plane turbulent wall jet. J Royal Aeronaut Soc 62:873–877
3. Nizou PY (Feb 1981) Heat and momentum transfer in a plane turbulent wall jet. ASME J Heat Transf 103:138–140
4. Wygnanski I, Katz Y, Horev E (1992) On the applicability of various scaling laws to the turbulent wall jet. J Fluid Mech 234:669–690
5. Dakos T, Verriopoulos CA, Gibson MM (1984) Turbulent flow with heat transfer in plane and curved wall jets. J Fluid Mech 145:339–360
6. AbdulNour RS, Willenborg K, McGrath JJ, Foss JF, AbdulNour BS (2000) Measurements of the convection heat transfer coefficient for a planar wall jet: uniform temperature and uniform heat flux boundary conditions. Exp Therm Fluid Sci 22(3):123–131
7. Mabuchi I, Kumada M (1972) Studies on heat transfer to turbulent jets with adjacent boundaries. Bull JSME 15(88):1236–1245
8. Naqavi IZ, Tyacke JC, Tucker PG (2018) Direct numerical simulation of a wall jet: flow physics. J Fluid Mech 852:507–542
9. Banyassady R, Piomelli U (2014) Turbulent plane wall jets over smooth and rough surfaces. J Turbul 15(3):186–207
10. Launder BE, Rodi W (1981) The turbulent wall jet. Prog Aerosp Sci 19:81–128
11. Pramanik S, Das MK (2014) Numerical study of turbulent wall jet over multiple-inclined flat surface. Elsevier, Comput Fluids 95:132–158
12. Patari A, Pramanik S, Mondal T (17–20 Dec 2021) Comparison of various RANS models for predicting near wall flow and heat transfer characteristics of a turbulent wall jet, paper no.-IHMTTC2021-713. In: Proceedings of the 26th national and 4th international ISHMT-ASTFE heat and mass transfer conference. IIT Madras, Chennai 600036, Tamil Nadu, India
13. ANSYS Inc, ANSYS fluent theory guide 17.1 (2017)
14. Celik IB, Ghia U, Roache PJ, Freitas CJ, Coleman H, Raad PE (2008) Procedure for estimation and reporting of uncertainty due to discretization in CFD applications. ASME, J Fluids Eng 130:078001
15. Baker N, Kelly G, O’Sullivan PD (2019) A grid convergence index study of mesh style effect on the accuracy of the numerical results for an indoor airflow profile. Int J Vent 19(4):300–314
16. Glauert MB (1956) The wall jet. J Fluid Mech 1(6):625–643

Pattern Formation and Evolution of Viscous and Non-viscous Liquids on a Vertical Vibrating Surface: An Experimental Investigation



Prashant Narayan Panday, Anushka, Prasanta Kumar Das, and Aditya Bandopadhyay

Abstract We experimentally studied the pattern formation of viscous and non-viscous Newtonian liquids on a vertically vibrating finite-size container. Experimental results show that the pattern formation in the case of water at 100 Hz and in the case of silicon oil at 20 Hz and 80 Hz has been verified from the patterns obtained in the literature, which shows excellent agreement. We investigate the physical parameters that significantly impact pattern creation, such as Faraday wave frequency, cross-over wave frequency, Faraday critical acceleration, and decay length. The study found that the Faraday critical acceleration ($a_c = 1.45 \text{ m/s}^2$) is maximum for silicon oil, whereas the decay length ($l_d = 0.1432 \text{ m}$) is maximum for water at a given vibrational frequency. In addition, we also emphasize the well-known Mathieu equation to obtain the value of wavelength as well as wave vector of the generated pattern. Furthermore, the study found that at a given vibrational frequency, the wavelength ($\lambda = 0.016 \text{ m}$) of pattern formation is maximum for water. Additionally, the study is carried out to investigate how driving frequency and Faraday wave frequency affect the physical characteristics of pattern formation.

Keywords Surface waves · Pattern formation · Decay length · Faraday wave frequency

1 Introduction

It is possible to create well-controlled waves in a finite size container by pushing the container in the direction perpendicular to the liquid surface. In both the gravity and capillary limits, these waves—also referred to as Faraday waves—that are subharmonically excited (wave frequency equal to half the driving frequency) have been thoroughly researched. Understanding the physical behaviour of surface standing

P. N. Panday · Anushka · P. K. Das · A. Bandopadhyay (✉)
Department of Mechanical Engineering, IIT Kharagpur, Kharagpur 721302, India
e-mail: adityabandopadhyay@gmail.com

waves, such as capillary or gravity waves, begins with understanding the dispersion relationship, also known as the Kelvin relation for waves on fluid surfaces. Gravitational and capillary forces are combined in this relation, demonstrating that surface tension and gravity dominate waves at the surface of fluids [1–6]. The dispersion relation for finite depth of the container is given by:

$$\omega^2 = \left[\left(gk_w + \left(\frac{\sigma}{\rho} \right) k_w^3 \right) \tanh(k_w h) \right] \quad (1)$$

Equation (1) describes the dispersion relation for the capillary gravity wave for finite depth, considering both gravity and surface tension forces.

The fluid depth can be considered infinite when $\tanh(k_w h)$ is approximately equal to 1. The dispersion relation for capillary and gravity waves for infinite depth is given by Eq. (2)

$$\omega^2 = \left[\left(gk_w + \left(\frac{\sigma}{\rho} \right) k_w^3 \right) \right] \quad (2)$$

To obtain the dispersion relation purely for capillary waves, we have to neglect the first term of the right-hand side of the Eq. (2), and for gravity waves, we have to disregard the second term of the right-hand side of the Eq. (2).

The dispersion relation for the capillary and gravity waves is given by Eq. (3) and Eq. (4), respectively. Dispersion relation for capillary waves:

$$\omega^2 = \left(\frac{\sigma}{\rho} \right) k_w^3 \quad (3)$$

Dispersion relation for gravity waves:

$$\omega^2 = gk_w \quad (4)$$

The waves with a wavelength of a few millimetres and wave vectors of a thousand per meter are known as capillary waves. The amplitude of these waves is very small (approximately 0.1 to 1 μm). In capillary waves, the main dominant force is the surface tension, which brings back the liquid's disturbed surface to the equilibrium position [7–11]. On the other hand, high wavelength and relatively small wave vector waves onto the surface of rivers and oceans are known as gravity waves. Since the propagation of these waves is caused mainly by gravity, they are called gravity waves. As the name implies, gravity is the main restoring force in gravity waves, just like surface tension is in capillary waves [12, 13].

The crossover wave frequency [14] from gravity waves to capillary waves is given by Eq. (5).

$$\omega_{o_i} = \left(\frac{4g^3 \rho}{\sigma} \right)^{1/4} \quad (5)$$

The above equation purely depends on the fluid properties. In their study, Puthenveetil and Hopfinger [14] demonstrated that FC-72 liquid has the highest cross-over wave frequency from gravity to capillary waves, followed by Glycerine–water solution and water. Dense material will result in a smaller surface tension value, thus resulting in a larger cross-over wave frequency. For parametric instability in the capillary, unbounded, and infinite fluid depth limits, the driving threshold acceleration is given by

$$a_c = 8 \left(\frac{\sigma}{\rho} \right)^{1/3} v\omega^{5/3} \tag{6}$$

The Faraday critical acceleration is directly proportional to driving frequency and increases as frequency increases. To obtain the Faraday wave frequency, multiply the driving frequency by a factor of 0.5. Capillary and decay lengths are the two significant parameters that characterize surface waves. The capillary length, also known as the capillary constant, relates gravity to surface tension and is mathematically expressed as the reciprocal of the wave vector at which surface and gravitational potential energies are equal. In finite-size containers, the decay length is essential in producing surface waves. The sidewall effects of the container are felt with decay length. Like capillary length, it also relates gravity to surface tension [15, 16]. If the radius of the container (R) is greater than the decay length, then sidewall boundary effects can be neglected: the system is then considered a 'large system' [16, 17]. The decay length of surface standing waves can be mathematically expressed:

$$l_d = \frac{\sigma}{4v\omega\rho} = \frac{\sigma}{8v\omega_0\rho} \tag{7}$$

The pattern evolution of Faraday waves is complicated above the stability limit. In large systems, Binks et al. [18] demonstrated that the around the instability threshold, theories that suggest three-wave resonant interactions have successfully matched experiments [19, 20]. There is no general theory for pattern evolution in small systems with significant side boundary effects. Ciliberto and Gollub [21] proposed that the evolution of wave patterns can be due to mode competition in small systems. Although the study of pattern formation in the case of water, as well as silicon oil, has been thoroughly studied by many researchers over the past decades. Even though the pattern generation in Newtonian liquids like Kerosene oil and water-glycerine mixture has not been explored in detail. In this chapter, we examined the pattern formation on liquid surfaces in the presence of excited surface waves at different driving frequencies.

2 Methodology

A circular aluminium tray with a diameter of 14 cm and a depth of 6 cm, filled with the test fluid and mounted on a vibrating device, was used as the experimental set-up schematically shown in Fig. 1. In the present case, we used a loudspeaker to meet the requirement of surface vibration. The loudspeaker (8 inches in size) is connected to the amplifier via a frequency generator, which is further connected to the main power supply. The frequency generator was only used to drive the electrical loudspeaker in the vertical direction. The acceleration of the circular bath is given by $a(t) = A\omega^2\sin(\omega t)$, where A is the shaker amplitude. The vibration exciter received a clean sinusoidal signal through electrical isolation from the signal generator and amplifier.

The loudspeaker was mounted on a wooden frame and bolted together to reduce any vibrational effect from the earth's surface. The circular container is placed directly onto the loudspeaker and fixed from the side to prevent its lateral displacement. The working area was illuminated by the two LED light sources mounted directly from the top of the container and inclined at a 45-degree angle. An image of the generated pattern was captured using a Nikon D-750 DSLR camera at 60 frames per second. Image-J software was used for the post-processing of the recorded pattern, and MATLAB was used to plot the data obtained from the image processing.

Adequate precautions were taken to avoid contamination in the fluids. Water, water-glycerine mixture, kerosene oil, and silicon oil were used in the study as the test fluids. The relevant properties of the test fluids are summarized in Table 1. Kerosene and silicone oil has a low surface tension in the air, which makes them

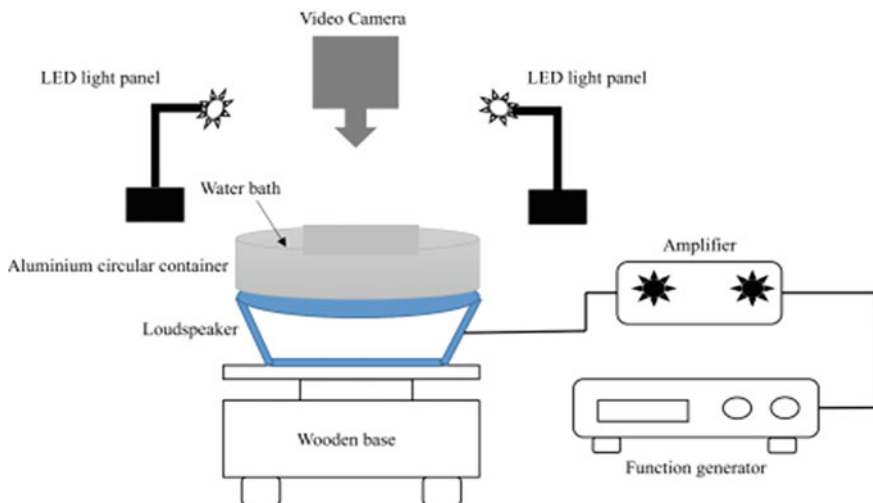


Fig. 1 A schematic illustration of the experimental setup. A container is mounted on the vibrating shaker (loudspeaker), which only vibrates in the vertical direction. The liquid of interest is filled inside the container to observe the pattern at a different frequency. The vibrating shaker is connected to the function generator through an amplifier

Table 1 Physical properties of liquids at 20 °C

Liquids	σ (N/m)	ρ (kg/m ³)	ν (cSt)
Water	0.072	1000	1
Silicon oil	0.040	970	100
Kerosene oil	0.023–0.032	786	1–2
Water + Glyc	0.078	998–1006	1.1295

less susceptible to contamination than water and water-glycerine mixtures. Silicon, as well as kerosene oil, was taken from sealed containers hand handled carefully to avoid contamination. The experiments were conducted over a short duration, and the test fluids were not left exposed to the atmosphere for extended periods. We approximated the system to have an infinite depth for the current configuration because $\tanh(kh) = 1$ for these fluids.

3 Results and Discussion

One of the primary objectives of the present study is to investigate the pattern generation in different liquids inside the circular container over the vertical vibrating surface experimentally. We used water, silicon oil, kerosene oil, and water–glycerine mixture as test fluids. A separate container of equal size is used for viscous and non-viscous liquids. The container contains the desired liquid up to a certain depth placed over the vibrating shaker operated at different frequencies.

First, we explain the pattern formation in water followed by silicon oil, kerosene oil, and water-glycerine mixture.

The pattern formation over the water surface at different frequency are illustrated in Fig. 2. The corresponding physical parameters responsible for pattern generation are tabulated in Table 2. The hollow patterns form onto the water surface at a low value of driving frequency.

Furthermore, these hollow patterns will change into a small benzene-like structure as the value of the driving frequency increases from 20 to 80 Hz. The literature shows that the Faraday critical acceleration, which is one of the prime parameters responsible for pattern generation, is the function of driving frequency that increases as frequency increases. For water, the Faraday critical acceleration (a_c) lies in the range of 0.60 to 6.11 m/s² as the excitation frequency of the container varies in the range of 20 Hz to 80 Hz.

The variation in Faraday critical acceleration with driving frequency is graphically represented in Fig. 6a. The experimental study reveals that at low driving frequency, there is no significant variation encountered in the value of a_c . However, the value of a_c drastically increases as ω increases beyond 200 rad/s. Furthermore, the study is also conducted to obtain the value of the decay length of water, which is also a significant parameter responsible for the pattern generation, lies in the range of

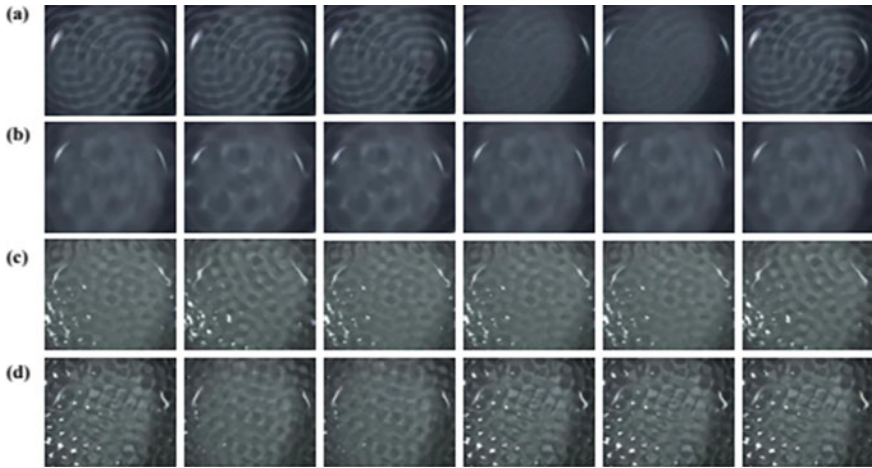


Fig. 2 An image sequence represents the pattern formation on the water surface at a different driving frequency. **a** 20 Hz, **b** 40 Hz, **c** 60 Hz, **d** 80 Hz

Table 2 Represents the value of physical parameters obtained from the experimental observation at different driving frequencies for water

ω (rad/s)	α_c (m/s ²)	l_d (m)	λ (m)	k (m ⁻¹)
125.66	0.60	0.1432	0.016	379.88
251.32	1.92	0.0711	0.010	603.04
376.99	3.78	0.0477	0.0079	790.20
502.65	6.11	0.0358	0.0065	957.26

0.1432 to 0.0358 m for a given frequency range and decreases as the driving frequency increases. The variation in decay length with driving frequency is shown in Fig. 6b.

The study is also conducted to determine the wavelength of the generated pattern in water at different driving frequencies. The wavelength of the water waves decreases from 0.016 to 0.0065 m (shown in Fig. 6c), Whereas the corresponding wave vector, which is inversely related to the wavelength of the waves, increases from 379.88 m⁻¹ to 957.26 m⁻¹ (shown in Fig. 6d) as the driving frequency increases. We further investigate the impact of higher frequency over the pattern formation on water. When the driving frequency increases beyond 80 Hz, we find a circular pattern on the water surface. The formation of Faraday circular waves on the water surface at 100 Hz frequency is shown in Fig. 3.

In the same way, we did before, to explain the pattern formation over the water surface, we will now describe the pattern generation on the silicon oil surface in detail. Here, we examine the pattern formation for the same driving frequency range (20 Hz to 80 Hz). At low driving frequency (up to 125.66 rad/s), a bigger benzene-like structure (shown in the first row of Fig. 4) is formed on the surface of silicon oil,

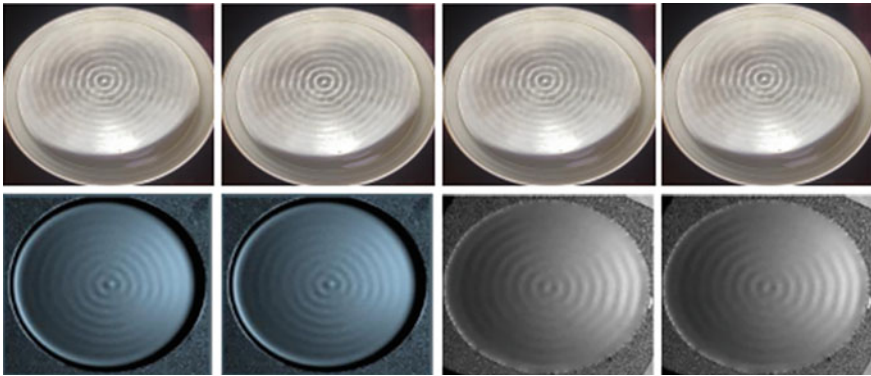


Fig. 3 Faraday circular wave formation over the water surface at 100 Hz frequency. The first row represents our experimental observation and the second row represents the result of Puthenveetil, and Hopfinger [14] from their experiment

whereas these bigger patterns will change into a small size as the driving frequency increases from 125.66 rad/s to 502.65 rad/s.

In this chapter, the pattern formed at 20 Hz and 80 Hz driving frequency is similar to the pattern created by Puthenveetil, and Hopfinger [14] at the same driving frequency. Like in water, in the case of silicon oil, the Faraday critical acceleration increases (from 1.45 to 14.71 m/s²), and the decay length decreases (from 0.041 to 0.010) with increases in the driving frequency. The variation in the physical parameters with driving frequency and effect of Faraday wave frequency on wavelength as

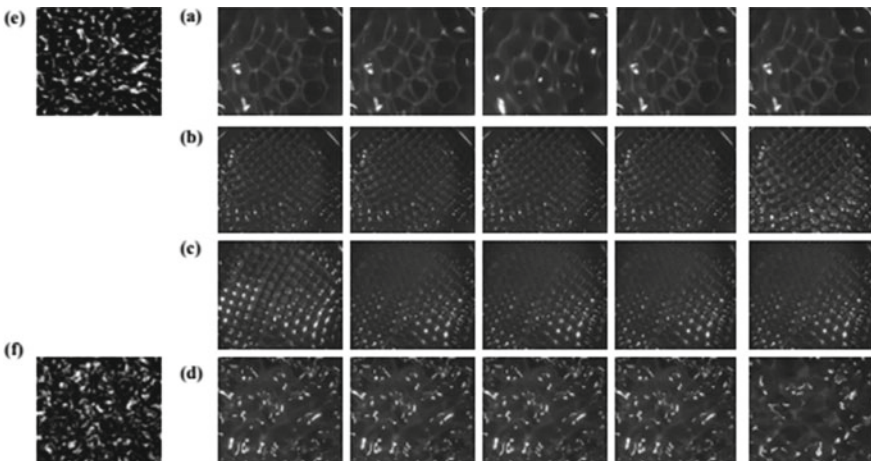


Fig. 4 An image sequence represents the pattern formation in silicon oil at a different frequency. **a** 20 Hz, **b** 40 Hz, **c** 60 Hz, **d** 80 Hz, **e**, and **f** represents the result of Puthenveetil and Hopfinger [14] from their experiment at 20 Hz and 80 Hz, respectively

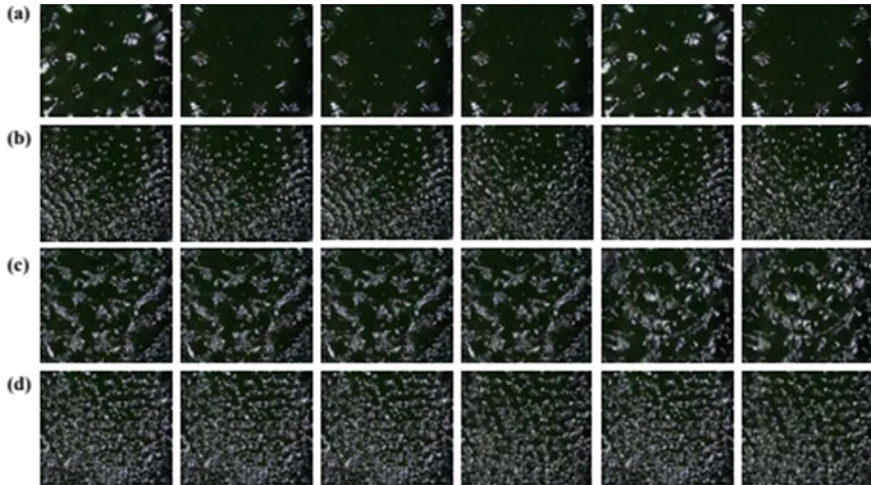


Fig. 5 An image sequence represents the pattern formation on the kerosene oil surface at a different driving frequency. **a** 20 Hz, **b** 40 Hz, **c** 60 Hz, **d** 80 Hz

well as wave vector in cases of silicon oil is shown in Fig. 6. The physical parameters for silicon oil are tabulated in Table 3. Additionally, the variation in the wavelength obtained from experimental and theoretical studies with Faraday wave frequency is shown in Fig. 8b. Furthermore, we also experimentally investigate the pattern formation on the surface of Kerosene oil at the same driving frequency (20 Hz to 80 Hz). The evolution of the pattern formed onto the kerosene oil surface as driving frequency increases is illustrated in Fig. 5. Here, we also found that the Faraday critical acceleration increases and decay length decreases (graphically shown in Fig. 6) as the value of driving frequency increases (refer Table 4).

The parameters responsible for the pattern generation in kerosene oil are tabulated in Table 4. The comparison of experimental and theoretical wavelength variation with ω_0 in the case of kerosene oil is graphically illustrated in Fig. 8c. In the last of this experimental investigation, we also like to examine the pattern generation when the water's viscosity increases by adding a small amount of glycerine (30 mL). The evolution of the pattern generation with an increase in the driving frequency for the water-glycerine mixture is experimentally shown in Fig. 7.

The pattern formed in the case of the water-glycerine mixture is similar to the water. The only difference is that the hallow pattern present in the case of water at low driving frequency is completely eliminated by adding glycerine into the water. At all driving frequencies, we found the benzene like structure over the surface of the water-glycerine mixture. The effect of driving frequency over the a_c and l_d as well as variation of λ and kw with ω_0 are graphically represented in Fig. 6. Furthermore, the variation in experimental as well as theoretical λ and kw with ω_0 is illustrated in Fig. 8d.

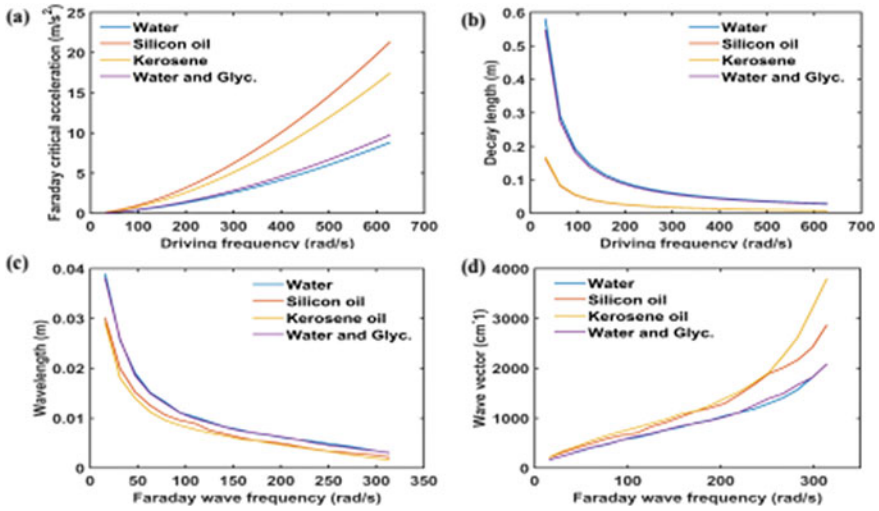


Fig. 6 A graphical representation of the variation of physical parameters with driving frequency and Faraday wave frequency. **a** Faraday critical acceleration versus driving frequency. **b** Decay length versus driving frequency. **c** Wavelength versus Faraday wave frequency. **d** Wave vector versus Faraday wave frequency

Table 3 Represents the value of physical parameters obtained from the experimental observation at different driving frequencies for silicon oil

ω (rad/s)	α_c (m/s ²)	l_d (m)	λ (m)	k (m ⁻¹)
125.66	1.45	0.041	0.013	457.42
251.32	4.63	0.020	0.0086	726.12
376.99	9.11	0.013	0.0066	951.49
502.65	14.71	0.010	0.0054	1152.64

Table 4 Represents the value of physical parameters obtained from the experimental observation at different driving frequencies for kerosene oil

ω (rad/s)	α_c (m/s ²)	l_d (m)	λ (m)	k (m ⁻¹)
125.66	1.16	0.045	0.012	486.16
251.32	3.69	0.022	0.0081	771.74
376.99	7.26	0.015	0.0062	1011.27
502.65	11.73	0.012	0.0051	1225.06

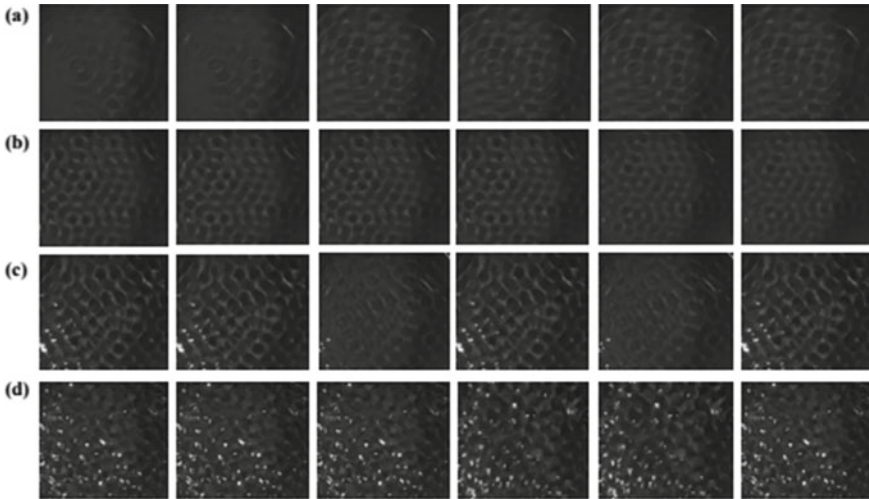


Fig. 7 An image sequence represents the pattern formation in the water-glycerine mixture at a different frequency. **a** 20 Hz, **b** 40 Hz, **c** 60 Hz, **d** 80 Hz

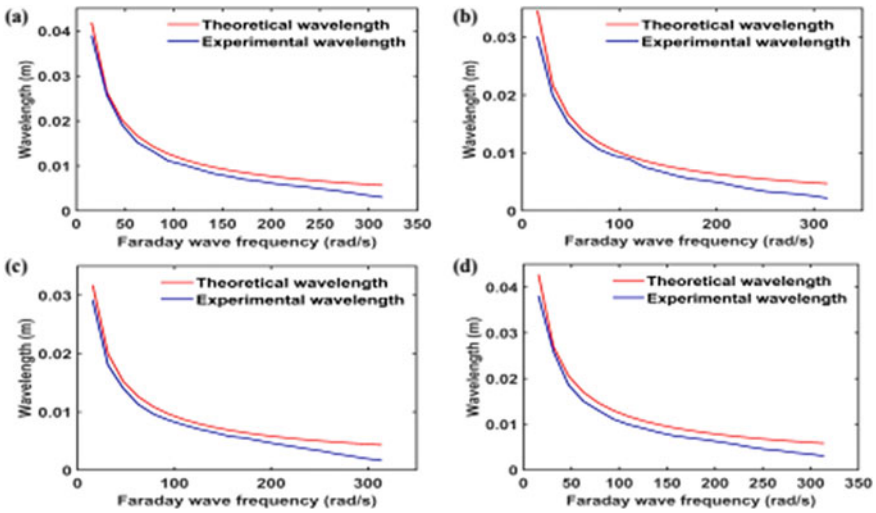


Fig. 8 The variation in experimental and theoretical wavelength for different liquids with Faraday wave frequency (ω_0) is represented graphically. **a** water, **b** silicon oil, **c** kerosene oil, and **d** water-glycerine mixture

4 Conclusions

In this chapter, we presented the simple and cost-effective method of surface vibration to investigate the pattern formation over the surface of viscous (oils) and non-viscous (water) liquids under a wide range of driving frequencies. According to the study, the patterns generated over the water and silicon oil surface for a particular value of the forcing frequency and show excellent agreement with the patterns obtained in the literature. Furthermore, the physical parameters responsible for the pattern generation have also been investigated in detail. The experimental results show that the value of Faraday critical acceleration and decay length of the pattern formation increases and decreases, respectively, as the value of driving frequency increases. For the given driving frequency range, the experimental study found that the Faraday critical acceleration and decay length are maximum for silicon oil and water, respectively. Additionally, the study emphasizes the well-known Mathieu equation to determine the wavelength and wave vector of the generated pattern. The study shows that the wavelength of the generated pattern is maximum in the case of water, whereas minimum in the case of kerosene oil for a given range of frequency. Similarly, the wave vector is found to be maximum in the case of kerosene oil and minimum in the case of water. The pattern obtained over the surface of the water and the water-glycerine mixture is observed to be the same.

Acknowledgements We thank the Ministry of Education, Government of India, for providing a scholarship to carry out the research work. We are also grateful to Saurabh Dhopeswar for his valuable support.

Nomenclature

α_c	Faraday critical acceleration [m/s^2]
f	Linear driving frequency of vibration [Hz]
g	Acceleration due to gravity [m/s^2]
h	Depth of liquid inside the container [m]
k_w	Wave vector [m^{-1}]
l_d	Decay length [m]
λ	Wavelength of the waves [m]
ω	Angular driving frequency of vibration [rad/s]
ω_0	Faraday wave frequency [rad/s]
ω_{0c}	Cross over wave frequency [rad/s]
ρ	Density of the liquid [kg/m^3]
σ	Surface tension of the liquid [N/m]
ν	Kinematic viscosity of the liquid [m^2/s].

References

1. T. B. Benjamin, F. J. Ursell, The stability of the plane free surface of a liquid in vertical periodic motion, *Proceedings of the Royal Society of London. Series A. Mathematical and Physical Sciences* 225 (1163) (1954) 505–515.
2. Miles J, Henderson D (1990) Parametrically forced surface waves. *Annu Rev Fluid Mech* 22(1):143–165
3. Kumar K, Tuckerman LS (1994) Parametric instability of the interface between two fluids. *J Fluid Mech* 279:49–68
4. Besson T, Edwards WS, Tuckerman LS (1996) Two-frequency parametric excitation of surface waves. *Phys Rev E* 54(1):507
5. Melo F, Umbanhowar PB, Swinney HL (1995) Hexagons, kinks, and disorder in oscillated granular layers. *Phys Rev Lett* 75(21):3838
6. J. P. Gollub, Order and disorder in fluid motion., *Proceedings of the National Academy of Sciences* 92 (15) (1995) 6705–6711.
7. Behroozi F, Podolefsky N (2001) Capillary-gravity waves and the navierstokes equation. *Eur J Phys* 22(6):587
8. Behroozi F, Podolefsky N (2001) Dispersion of capillary-gravity waves: a derivation based on conservation of energy. *Eur J Phys* 22(3):225
9. F. Behroozi, Apparatus and method for measurement of fluid viscosity, uS Patent 6,563,588 (May 13 2003)
10. Zhu F, Miao R, Xu C, Cao Z (2007) Measurement of the dispersion relation of capillary waves by laser diffraction. *Am J Phys* 75(10):896–898
11. Miao R, Yang Z, Zhu J, Shen C (2002) Visualization of low-frequency liquid surface acoustic waves by means of optical diffraction. *Appl Phys Lett* 80(17):3033–3035
12. Behroozi F, Perkins A (2006) Direct measurement of the dispersion relation of capillary waves by laser interferometry. *Am J Phys* 74(11):957–961
13. Chowdhury D, Bhunia S, Barik TK (2013) Study the liquid surface capillary wave profile by optical method. *Int. J. Soft Comput. Eng* 2:386
14. Puthenveetil BA, Hopfinger E (2009) Evolution and breaking of parametrically forced capillary waves in a circular cylinder. *J Fluid Mech* 633:355–379
15. Protiere S, Boudaoud A, Couder Y (2006) Particle–wave association on a fluid interface. *J Fluid Mech* 554:85–108
16. Edwards WS, Fauve S (1994) Patterns and quasi-patterns in the faraday experiment. *J Fluid Mech* 278:123–148
17. Bechhoefer J, Ego V, Manneville S, Johnson B (1995) An experimental study of the onset of parametrically pumped surface waves in viscous fluids. *J Fluid Mech* 288:325–350
18. Binks D, Westra M-T, van de Water W (1997) Effect of depth on the pattern formation of faraday waves. *Phys Rev Lett* 79(25):5010
19. Chen P, Vinals J (1999) Amplitude equation and pattern selection in faraday waves. *Phys Rev E* 60(1):559
20. Zhang W, Vinals J (1997) Pattern formation in weakly damped parametric \sim surface waves. *J Fluid Mech* 336:301–330
21. Ciliberto S, Gollub J (1985) Chaotic mode competition in parametrically forced surface waves. *J Fluid Mech* 158:381–398

Activity-Induced Mixing in a Stratified Binary Passive System



Thomas Jacob, Siddhant Mohapatra, and Pallab Sinha Mahapatra

Abstract Active systems have garnered interest from researchers worldwide for their fascinating displays of congregations and the far-reaching scope of biomimetic applications. The current chapter talks about one such application: the use of active particles to induce mixing in a stratified passive system. Simulations using a Langevin model in two dimensions shows the mixing state of the initially stratified system reach a saturation point in finite time. Interestingly, with change in the number of active mixers, only the rate of mixing is found to be affected, while the final mixed state is perceived to be almost similar. Active particles numbering not more than 20% of that of the passive species is found to be enough to induce brisk mixing. An investigation is parallelly carried out into the maximum rotation allowed for each active mixer to maximise the overall mixing effect. The objective of this discourse is to provide a numerical backbone to the feasibility of the use of micro/mini robots for mixing of living/non-living entities, while also discussing the factors affecting the process.

Keywords Active–passive system · Mixing · Gini coefficient · Over-damped Langevin model

1 Introduction

Researchers have always been amused by the pattern formation in schools of fish, swarms of bees, flocks of starlings, armies of ants, etc. The curiosity about the underlying processes leading to such intricate phenomenon have motivated the study and evolution of active matter systems. Such systems continuously consume energy for their activity and hence, are always out of equilibrium. Researchers have been trying to capture and accurately decode the behaviour of such active entities since the last few decades and in the recent years, the advent of high-speed computing facilities has aided the process by allowing large-scale numerical modelling of the active

T. Jacob · S. Mohapatra · P. S. Mahapatra (✉)

Department of Mechanical Engineering, Indian Institute of Technology Madras, Chennai 600036, India

e-mail: pallab@iitm.ac.in

systems with a high temporal and spatial resolution. Some notable mathematical models proposed to mimic these active systems are the Vicsek model [1], the Active Brownian Particle model [2], the Run and Tumble model [3] among others.

The interaction between active (those with the ability to self-propel) and passive (those which cannot self-propel) particles have been a centre of attention for researchers due to intriguing behaviour such as segregation [4], Motility Induced Phase Separation (MIPS) [5], cluster formation [6], etc. The upcoming section discusses several works highlighting the dynamics of such systems with dispersity in motility.

2 Literature Review and Objective

The study of active matter systems was initially pursued from a numerical viewpoint during the 1990s with the advent of various mathematical models [7]. Since then, there has been extensive research in the field using both experimental and computational methods. Even though active matter systems evolved after observing behavioural patterns in living systems, there are reported studies where interactions could also be observed among active (both living & artificial) and passive particles (particles with no activity) in a pool [8, 9]. One of the major limitations with experiments in the field comes from the data collection, where a wide area is often considered for the study. There are also constraints in realising larger systems on a laboratory scale. Such limitations can be overcome by numerical modelling.

Wu and Libchaber [10] carried out experimental investigations on passive beads in an active bacterial (*Escherichia Coli*) bath. They made use of soap film as a substrate upon which both these species are dispersed for interaction. Higher concentration of bacteria resulted in a fluctuated motion of beads where ballistic motion was observed for shorter distances and Brownian motion is detected at long time scales. Experimental investigations by Leptos et al. [11] on the dynamics of passive tracers in both dilute and dense bath of alga *Chlamydomonas Reinhardtii* revealed diffusive movement of the tracer particles. The probability distribution function for the same tracers showed a non-Gaussian (yet similar) form with an exponential tail and broadened base that grows along with swimmer concentration.

Numerical studies in the field have been carried out using both periodic and bounded domains, with most belonging to the former category. Periodic boundaries are usually used to study larger domains where a small unit of the larger domain is analysed. This helps reduce the computational cost and time considerably. Numerical simulations on active-passive particle mixture by Hinz et al. [12] using periodic boundaries demonstrated the emergence of three different phases—a disordered meso-turbulent phase, a polar flocking phase and a vortical phase. The manifestation of the vortical phase is sensitive to the domain size, whereas the other phases are indifferent. It is of particular importance that even a small number of active agents are capable of generating effective dynamics and associated patterns. Phase separation behaviour of an initially disordered mixture of monodisperse active-passive

system is reported in numerical investigations by Stenhammar et al. [5] with periodic boundary conditions. The phenomenon was observed with as low as a 1:6 active–passive particle ratio but at high activity. Their study suggested that by controlling the parameters like activity and active–passive particle ratio, one can transition the system between a homogeneous phase and phase separation. In another study by Dolai et al. [6], interaction between active–passive mixtures of different size ratios and different packing fractions were investigated with comparable volumes of active and passive particles. The results suggested the appearance of three distinct phases for the passive particles—a homogeneous phase, a clustered phase of small and large sizes, and a segregated phase where passive particle segregation is observed. Mixing behaviour of initially segregated binary system constituting only active particles has been investigated by Mahapatra and Mathew [13]. Here, both the particles are initially arranged in two separate boxes connected by a passage. In addition to self-propulsion force and interaction force, alignment and friction forces are also considered in the model. The system exhibits thermal, rotational and oscillatory phases at high packing fraction while exhibiting a predominantly rotational phase at lower packing fractions. The extent of mixing within the system is calculated using a mixing index, i.e., lower the mixing, higher the value of the index. Agrawal and Mahapatra [14] investigated the dynamics of an active–passive particle mixture with and without alignment force in a confined square boundary. Collective milling motion arises as a result of the alignment, whereas the absence of such a force results in a disordered phase. In most of the studies, where active particle systems or active–passive particle systems are investigated, the simulation is carried out in a 2D square domain. The dynamics of a binary mixture of self-propelling active particles and passive particles on a spherical surface is investigated by Ai et al. [15]. The particles are modelled as soft spheres and dynamics is governed by Langevin equations with holonomic constraint. Both rotational diffusion and polar alignment are considered, variation of which causes three distinct phases to occur—two segregated phases and one mixed phase.

From the literature, it is clear that several studies have been carried out to observe the dynamics of active–passive particle mixtures with cases varying from a single passive particle in a pool of active particles to passive particles with volume fractions comparable to active particles. Most of the investigations are in 2D with periodic boundary which not only reduces the complexity but also the computational time. With slight modifications, similar simulations carried out in a 2D surface can be realised over curved surfaces.

It is, however, interesting that there is a paucity of literature, where the active particles have been used to mix two or more different species of passive particles. The current chapter addresses this issue by demonstrating how a small amount of active mixer particles could be used to mix different passive species in a confined domain (which could also be realized under laboratory conditions).

3 Materials and Methods

3.1 Numerical Modelling

In the current work, we consider a monodisperse system of athermal particles arranged inside a 2D circular domain. The particle count is denoted by N_p for passive and N_A for active respectively. All the particles have the same radius (r). The domain radius (R) is chosen as $40r$. The wall of the bounded system constitutes of one layer of circular discs of the same size as that of interior particles. The packing fraction (ϕ) is given by $\phi = Nr^2/R^2$, where N is the number of interior particles.

The dynamics of active particles is governed by the overdamped Langevin equations, consisting of a self-propulsion drive and an inter-particle repulsion drive (see Eqs. 1 and 2) [16].

$$\frac{d\bar{r}_i}{dt} = v\hat{n}_i + \mu \sum_j F_{ij} \quad (1)$$

$$\frac{d\theta_i}{dt} = \eta_i(t) \quad (2)$$

where \bar{r}_i represents the position of the centre of particle i , v represents the self-propulsion speed of the active particles, in direction $\hat{n}_i = (\cos \theta_i, \sin \theta_i)$ μ and k are the mobility and the force constant, respectively. The repulsion force between the particles i and j (the surrounding particles of the particle i) acts when the particles overlap with each other and can be defined as, $F_{ij} = k(2r - d_{ij})\hat{r}_{ij}$, where $d_{ij} = |\bar{r}_i - \bar{r}_j|$ and $\hat{r}_{ij} = (\bar{r}_i - \bar{r}_j)/d_{ij}$. The direction of the self-propulsion velocity depends on an angular Gaussian white noise η where $\langle \eta_i(t)\eta_i(t') \rangle = 2D_r\delta_{ij}\delta(t - t')$. D_r is coefficient of rotational diffusion.

The equation for passive particles differs from that of the active particles due to their inability to self-propel and is formulated in Eq. (3).

$$\frac{d\bar{r}_i}{dt} = \mu \sum_j F_{ij} \quad (3)$$

The parameters μ and k are assumed to have the same values for both active and passive particles. The wall particles are designed to be immobile barriers which confine the interior particles in the domain of interest by way of the repulsion drive. All the particles are assumed to be athermal, that is, the translational diffusion is considered to be negligible compared to the rotational diffusion [16]. To make self-propulsion velocity and time dimensionless, they are scaled by $r\mu k$ and $1/\mu k$ respectively. Scaled speed is represented by v_0 and scaled time is denoted by τ .

The passive particles are segregated into two species. All the particles are initially arranged in a uniform random distribution such that one of the species of passive particles occupy the upper half of the domain and the other species occupy the lower

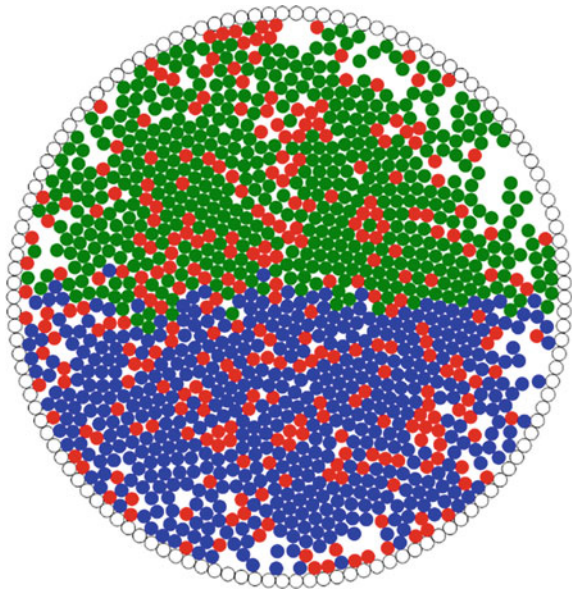
half. The active particles are then distributed in a uniform random sense within the entire circular domain. The initial orientations of the active particles are also uniformly randomized in the range $[0, 2\pi]$.

Passive particle packing fraction $\left(\phi_P = \pi \sum_{i=1}^{N_P} r_i^2 / \pi R^2\right)$, that is, the ratio of the area occupied by the passive particles (numbering N_P) to the total area of the domain is 0.6 and is maintained invariable across all the simulation cases. Simulations are carried out, altering the number of active particles by defining an active–passive particle fraction ($\Psi = N_A/N_P$). The value of Ψ is varied from 0.1 to 0.5 so that the maximum overall packing fraction ($\phi = \phi_A + \phi_P$) is not more than 0.9. Euler–Maruyama scheme is employed for numerical integration of Eqs. 1–3 with a timestep 10^{-2} s.

Figure 1 showcases a representative initial distribution of particles in the domain. The passive species are coloured blue and green, while the active particles are coloured red respectively.

The simulations are carried out till the system reaches a stable state, indicated by the saturation of a mixing parameter defined in the next subsection. The simulations are run using an in-house code written in Python 3.7 along with the JAX functionality for highly parallel GPU computations.

Fig. 1 Distribution of active and passive particles inside the circular domain; ($\Psi = 0.3$)



3.2 *Mixing Parameter*

Mixing index (β) quantifies the degree of mixing of the two passive species on the basis of the current and the initial positions of the particles. The calculation of the mixing index follows the weak sense mixing technique proposed by Doucet et al. [17], employing Principal Component Analysis (PCA) to compute the Eigen values of the position matrix, and used a priori by Mahapatra and Mathew [13]. We define the mixing using a mixing parameter, $\gamma = 1 - \frac{\beta(\tau)}{\beta_0}$, where $\beta(\tau)$ is the current mixing index and β_0 is the mixing index for the initial particle distribution without overlap. Higher values of γ represents a better mix.

3.3 *Validation*

The numerical model used in the current work has been validated against the results reported by Yang et al. [16] on the interactions among mono-dispersed self-propelling athermal disks in a confined square-shaped 2D space. For a range of parameters such as diffusion coefficient, self-propulsion velocity and overall packing fraction, they observed particle aggregation at the walls and quantified it using Gini coefficient (ζ). Gini coefficient is calculated by dividing the domain in to ' n ' concentric squares of equal width and applying the equation $\zeta = \frac{1}{2n^2|\bar{\rho}|} \sum_i \sum_j |\rho_i - \rho_j|$, where ρ is the particle number density in the corresponding strip and $\bar{\rho}$ is the mean density. Higher the value of ζ (beyond 0.50), the system is wall aggregated where as a lower value represents homogeneous state. Using our numerical model with the parameter set and domain properties, the results are found to be in good agreement with those reported by Yang et al. [16] (Fig. 2). Two values of overall packing fraction are considered (0.720 and 0.831); the speed v_0 is varied from 0.01 to 0.10 and the Gini coefficient is computed for each v_0 after the system reaches a steady state. The results displayed are the average of five realisations that have been carried out for each parameter set and the curves seem to be in good agreement. The deviations at higher values of v_0 can be attributed to the stochastic nature of the problem and the slight differences in the model/parameters used.

4 *Results and Discussion*

Preliminary simulations have been carried out to determine the parameter space for inducing mixing in segregated passive systems using active particles. Active particles with a low rotational diffusion coefficient D_r are found to have a tendency to aggregate at the walls instead of promoting mixing (Fig. 3; inset $D_r = 0.001$, $\tau = 2 \times 10^4$). Hence, a study is carried out to determine the optimum values of D_r to obtain maximum degree of mixing. The diffusion coefficient is varied in the

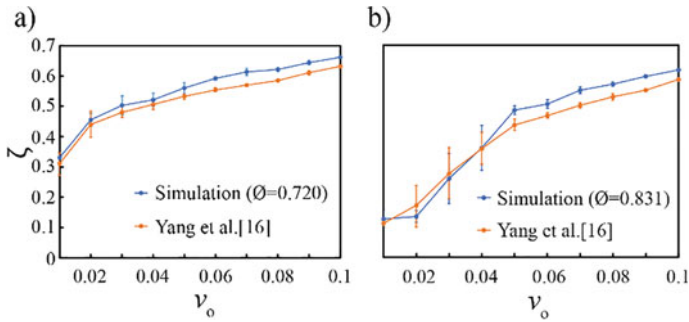
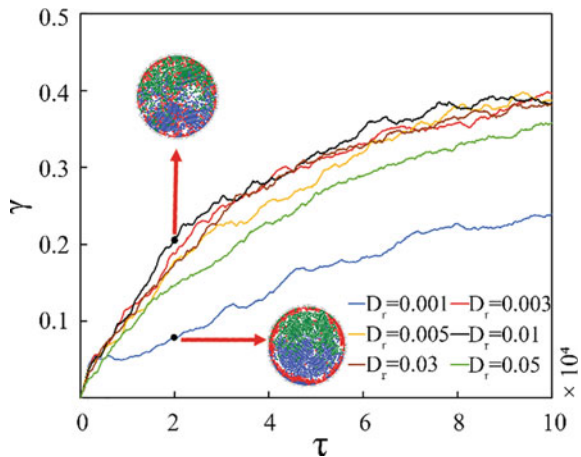


Fig. 2 Comparison of Gini coefficient ζ obtained from our simulation to that of Yang et al. [16] for overall packing fractions: **a** $\phi = 0.720$ and **b** $\phi = 0.830$; ($\mu k = 10 \text{ s}^{-1}$, $r = 1$)

Fig. 3 Variation of mixing parameter γ with time τ for varying D_r ; ($\Psi = 0.3$)

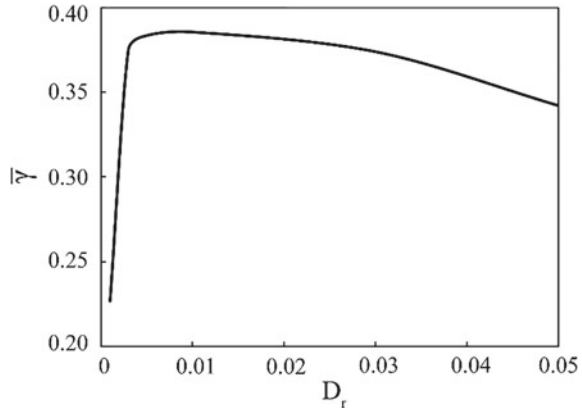


range of 0.001 to 0.05. With higher values of D_r , the active particles are observed to constantly agitate their passive counterparts. The system thus always maintains a dynamic state and the two species of passive particles undergo mixing across the domain. The quantification of this visually detected mixing phenomenon is done with the help of a mixing parameter, as discussed in the next subsection.

4.1 Effect of Rotational Diffusion on Mixing

The system is simulated for different values of D_r keeping the value of Ψ fixed at 0.3. The system is seen to have reached a steady state in around $\tau = 10^5$. The positional data of the passive particles is used to compute the mixing parameter γ throughout the time period of the simulation (see Fig. 3). For any value of D_r , γ is found to increase with the progression of time, as the active mixers keep agitating the

Fig. 4 Variation of time-averaged mixing parameter $\bar{\gamma}$ with rotational diffusion coefficient D_r ; ($\Psi = 0.3$)



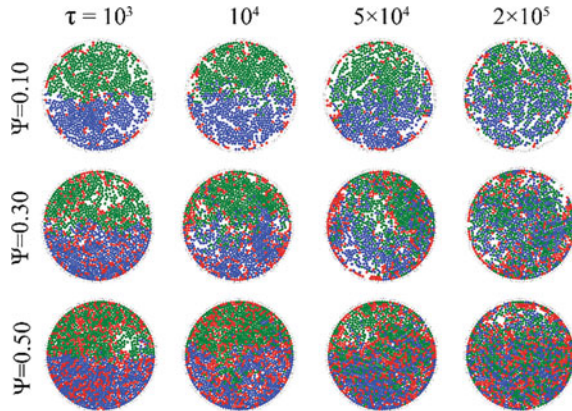
system. However, γ reaches a saturation at a value of around 0.4. There seems to be no further temporal change to the mixing parameter beyond this point. It should be noted, though, that at lower value of D_r (0.001), the value of γ is low in comparison to other cases. As D_r increases to 0.003, there is a sudden increase in γ establishing a better mix within the domain. Increasing the D_r further increases the value of γ albeit at a slower rate. To find out an optimum value of D_r for which γ is maximum, the simulation is further carried with higher values of D_r .

The average of γ in the range $\tau = 8 \times 10^4$ to 10^5 is plotted against D_r (Fig. 4). It can be noted that for lower values of D_r , an increase in the value of D_r increases γ rapidly. This is because the active particles, rather than aggregating at walls, move more vigorously in both rotational and translational manner. However, after reaching a maximum value at $D_r = 0.01$, a further increase in D_r decreases γ but gradually. This could be due to the fact that the active particles tend to undergo more of a local traverse (as they more often take larger turns) than a global one.

4.2 Effect of Active to Passive Particle Ratio on Mixing

The effect of concentration of active particles is studied by varying the active–passive particle fraction (Ψ) from 0.10 to 0.50 in steps of 0.10. For each case, the simulation is carried out until $\tau = 2.5 \times 10^5$. Longer run times ensure the occurrence of a steady state in the system. The rotational diffusion coefficient is set to the optimum value of $D_r = 0.01$. Figure 5 elucidates the occurrence of mixing reported by the mixing parameter γ through snapshots of the particle distribution within the domain at different instances of time. In the figure, four different time instances of the system are showcased corresponding to active–passive particle ratios Ψ : 0.10, 0.30 and 0.50. When Ψ is 0.10, the active particle count is very low to cause sufficient agitation in the system for the mixing to take place. In addition, many of the active particles are concentrated adjacent to the wall. The gradual cross flow of the two passive

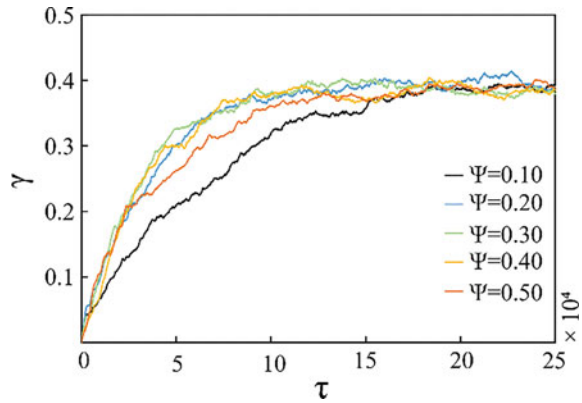
Fig. 5 Snapshots of the system for different active to passive particle ratios ψ at various time instances



species is also elucidated as the time progresses. At $\Psi = 0.30$, the aggregation of active particles near the wall is still evident, albeit to a lower extent. Mixing has improved as there are more active particles dispersed within the domain. Mixing at $\Psi = 0.50$ is comparable to that at 0.30, except the fact that we can see a more uniform distribution of active particles within the domain. In addition, the aggregation of active particles near the wall is less prominent. Ideally, this should further increase the mixing parameter, but a larger number of active particles has created a near-jammed state in the system which leads to local confinement of the active particles and subsequently the inability to move the passive particles.

The manifestation of activity-induced mixing in the domain can be visually confirmed in Fig. 5. To quantify the extent of mixing, the mixing parameter is established (see Sect. 3.2) and computed for the different values of active–passive particle fractions Ψ . The variation in the rate of mixing with the increase in Ψ , delineated in Fig. 6 corroborates the observations from Fig. 5. A striking feature of Fig. 6 is that all the curves (pertaining to different Ψ) tend to attain a similar value of γ (~ 0.40) at steady state. At a very low concentration of active particles ($\Psi = 0.10$), the curve is less steep which implies a longer time for the system to attain a steady mix. By increasing Ψ to 0.20, i.e., by doubling the number of active particles, mixing is achieved at a faster rate and steady state is achieved at a considerably lower time. Increasing the Ψ further to 0.30 helps achieving the same steady state γ at roughly half the time compared to $\Psi = 0.10$. Further increasing Ψ to 0.40 does not cause any significant change in γ or in the time taken to achieve steady-state mixing. Any further hike in the number of active particles proves to be detrimental to mixing as accentuated by the reduction in γ at $\Psi = 0.50$. The analysis of the rate of change of mixing parameter for the different active–passive particle fractions depicts a requirement of the number of active particles not exceeding 20% of the number of passive particles, in order to obtain brisk mixing.

Fig. 6 Change in mixing parameter γ with time τ for varying Ψ ; ($D_r = 0.01$)



5 Conclusions

The behaviour of an initially segregated binary system of passive particles is studied in the presence of a controlled number of active athermal mixers. The system constituting of the two passive species and the active mixers placed in a confined circular domain are modelled using a set of overdamped Langevin equations. At low values of rotational diffusion coefficient, the active mixers are found to aggregate along the wall, leading to little mixing of the passive species. For a certain value of passive packing fraction and active–passive particle fraction, it is found that there exists an optimum value of rotational diffusion coefficient for which mixing occurs most efficiently. The mixing of the two passive species is measured in terms of a mixing parameter based on the Eigen values of the position matrix at any time instant compared to that of the initial positions. In the base case considered ($\phi_p = 0.60$, $\Psi = 0.30$), the optimum value for D_r is obtained as 0.01. It is also observed that the concentration of active particles is a major factor affecting the rate of mixing. However, the extent of mixing in the system on reaching steady state (at large time scales) remains largely unaltered across different active particle concentrations. An important outcome from the current study is the number requirement of the active mixers for obtaining sufficient mixing at comparatively low time scales. It is noted that an active–passive particle fraction not exceeding 0.2 provides ample agitation to cause brisk mixing of the passive species. Due to the confined boundary conditions and the experimentally relatable parameter set, this study could find application in the case of artificial micro-robots to obtain rapid mixing among various living/artificial entities.

Acknowledgements The authors acknowledge the funding received as part of the Institution of Eminence scheme of the Ministry of Education, Government of India [Sanction No: 11/9/2019–U.3(A)].

Nomenclature

r	Particle radius [m]
R	Domain radius [m]
v_0	Non dimensional self-propulsion speed [-]
\vec{r}	Position vector [-]
μ	Mobility [s/kg]
k	Force constant [N/m]
Ψ	Active-passive particle fraction [-]
D_r	Rotational diffusion coefficient [rad^2/s]
γ	Mixing parameter [-]
η	Gaussian white noise [-]
τ	Non dimensional time [-]

References

1. Vicsek T, Czirók A, Ben-Jacob E, Cohen I, Shochet O (1995) Novel type of phase transition in a system of self-driven particles. *Phys Rev Lett* 75(6):1226
2. Marchetti MC, Fily Y, Henkes S, Patch A, Yllanes D (2016) Minimal model of active colloids highlights the role of mechanical interactions in controlling the emergent behavior of active matter. *Curr Opin Colloid Interface Sci* 1(21):34–43
3. Berg HC (ed) (2004) *E. coli* in motion. Springer New York, New York, NY
4. Zhu WJ, Li TC, Zhong WR, Ai BQ (2020) Rectification and separation of mixtures of active and passive particles driven by temperature difference. *J Chem Phys* 152(18):184903
5. Stenhammar J, Wittkowski R, Marenduzzo D, Cates ME (2015) Activity-induced phase separation and self-assembly in mixtures of active and passive particles. *Phys Rev Lett* 114(1):018301
6. Dolai P, Simha A, Mishra S (2018) Phase separation in binary mixtures of active and passive particles. *Soft Matter* 14(29):6137–6145
7. Chaté H (2020) Dry aligning dilute active matter. *Ann Rev Condensed Matter Phys* 10(11):189–212
8. Langlois VJ, Andersen A, Bohr T, Visser AW, Kiørboe T (2009) Significance of swimming and feeding currents for nutrient uptake in osmotrophic and interception-feeding flagellates. *Aquat Microb Ecol* 54(1):35–44
9. Wang X, Baraban L, Misko VR, Nori F, Huang T, Cuniberti G, Fassbender J, Makarov D (2018) Visible light actuated efficient exclusion between plasmonic Ag/AgCl micromotors and passive beads. *Small* 14(44):1802537
10. Wu XL, Libchaber A (2000) Particle diffusion in a quasi-two-dimensional bacterial bath. *Phys Rev Lett* 84(13):3017
11. Leptos KC, Guasto JS, Gollub JP, Pesci AI, Goldstein RE (2009) Dynamics of enhanced tracer diffusion in suspensions of swimming eukaryotic microorganisms. *Phys Rev Lett* 103(19):198103
12. Hinz DF, Panchenko A, Kim TY, Fried E (2014) Motility versus fluctuations in mixtures of self-motile and passive agents. *Soft Matter* 10(45):9082–9089
13. Mahapatra PS, Mathew S (2019) Activity-induced mixing and phase transitions of self-propelled swimmers. *Phys Rev E* 99(1):012609

14. Agrawal NK, Mahapatra PS (2020) Effect of particle fraction on phase transitions in an active-passive particles system. *Phys Rev E* 101(4):042607
15. Ai BQ, Zhou BY, Zhang XM (2020) Binary mixtures of active and passive particles on a sphere. *Soft Matter* 16(20):4710–4717
16. Yang X, Manning ML, Marchetti MC (2014) Aggregation and segregation of confined active particles. *Soft Matter* 10(34):6477–6484
17. Doucet J, Bertrand F, Chaouki J (2008) A measure of mixing from Lagrangian tracking and its application to granular and fluid flow systems. *Chem Eng Res Des* 86(12):1313–1321

Spatio-temporal Stability Analysis of Falling Film Over Heated Inclined Plane



Arnab Choudhury and Arghya Samanta

Abstract Linear stability analysis of a thin liquid film falling down a uniformly heated slippery inclined plane has been performed. The spatial growth rates for thermocapillary P mode and S mode have been estimated by solving a coupled set of boundary value problems employing Chebyshev spectral collocation method. Marangoni number is found to destabilize both the P mode and S mode, and Biot number seems to have a dual influence on the S mode instability. The S mode gets stabilized with the increase in spanwise wavenumber, whereas the P mode gets destabilized. The hydrodynamic shear mode has also been captured analytically for inviscid flow, which indicates a slight stabilizing effect of Marangoni number on it.

Keywords Thin film flow · Hydrodynamic instability · Thermocapillary instability

1 Introduction

Thin film flows are encountered in several engineering and scientific applications such as thermal protection of rocket engines, cooling of semiconductors, heat transfer in condensers and evaporators, etc. Therefore, it is of particular interest to study the instabilities in heated thin film flows as it affects the interfacial heat transfer significantly. The linear stability of a thin film flow down a uniformly heated inclined plane has been studied by Lin [7]. He has analytically predicted the critical Reynolds number as a function of Marangoni number and inclination angle for hydrodynamic surface mode of instability. Lin [6] has also shown the existence of hydrodynamic shear mode in the falling film flow and predicted the critical Reynolds number for it. Goussis and Kelly [3] have examined the influence of Marangoni number on thermocapillary P mode and S mode. Incorporating energy budget analysis, they have also suggested some mechanisms by virtue of which the S mode, P mode, and H mode instability triggers. The influence of Soret number on the temporal and spatial stability of a heated binary film has been studied by Hu et al. [4]. The thermocapillary

A. Choudhury (✉) · A. Samanta
Department of Applied Mechanics, IIT Delhi, Hauz Khas, New Delhi 110016, India
e-mail: arnab.choudhury@am.iitd.ac.in

© The Author(s), under exclusive license to Springer Nature Singapore Pte Ltd. 2024
K. M. Singh et al. (eds.), *Fluid Mechanics and Fluid Power, Volume 2*, Lecture Notes in Mechanical Engineering, https://doi.org/10.1007/978-981-99-5752-1_12

141

P mode has been partially captured for low values of streamwise wavenumber in this study. Samanta [9] has deciphered the effect of electric field on the shear mode instability. He has found a stabilizing effect of applied electric field intensity on shear mode. The effect of different flow parameters on the shear mode at inviscid limits has also been analysed. Pascal and D'Alessio [8] have analysed the linear stability of a heated binary film flow where the density of the liquid film varies with respect to temperature. The influence of Marangoni number at low Reynolds number on surface and S modes of instability have been examined. Bhat and Samanta [1] have carried out a linear stability analysis of a falling film having insoluble surfactant contamination. They have examined the effect of different parameters on the hydrodynamic surface mode and shear mode. They have also performed the inviscid analysis where they have shown a stabilizing influence of slip on shear mode. Choudhury and Samanta [2] have performed the temporal stability of a heated falling film down a slippery incline. The authors have performed a detailed parametric study on four different instability modes i.e., H mode, P mode, S mode, and shear mode.

From these literatures, it can be observed that there exist several studies regarding the temporal stability of all the four modes of instability, that is, H mode, S mode, P mode and shear mode. The studies of spatial stability is also performed for H mode and shear mode only. But there are no studies found regarding the spatial stability of thermocapillary P mode and S mode. Our aim for the present study is to provide these missing links in the present literature.

2 Mathematical Formulation

Consider a viscous liquid thin film falling under the action of gravity down an incline as shown in Fig. 1. The inclined plane is maintained at a uniform temperature T_w which is higher than the ambient temperature T_a and it makes angle θ with the horizon. All the thermophysical properties of the fluid such as viscosity (μ), density (ρ), thermal conductivity (κ) etc. are kept constant for carrying out the linear stability analysis. Although the surface tension (σ) is considered to vary with temperature according to the relation (1) as we are interested to study the thermocapillary modes of instability.

$$\sigma(T) = \sigma_0 - \varepsilon(T - T_a), \quad (1)$$

where, σ_0 denotes the surface tension at ambient conditions and $\varepsilon = -\left.\frac{d\sigma}{dT}\right|_{T=T_a} > 0$. The Cartesian coordinate system is considered to originate from the slippery plane and the orientation of it is shown in Fig. 1. The film thickness corresponding to the base flow is d , and $h(x, z, t)$ denotes the thickness of the perturbed liquid film. Now following the work of Choudhury and Samanta [2] we can formulate the Orr-Sommerfeld type boundary value problem (OS-BVP)

$$(D^2 - k^2)^2 \hat{\phi} = i \text{Re} \left[(k_x \bar{U} - \omega)(D^2 - k^2) + \frac{2k_x}{1 + 2\beta} \right] \hat{\phi}, \quad y \in [0, 1], \quad (2)$$

$$(D^2 - k^2) \hat{\tau} = \text{Pe} \left[i(k_x \bar{U} - \omega) \hat{\tau} - \left(\frac{\text{Bi}}{1 + \text{Bi}} \right) \hat{\phi} \right] = 0, \quad y \in [0, 1], \quad (3)$$

$$\hat{\phi} = 0, \quad \hat{\tau} = 0, \quad D\hat{\phi} - \beta D^2 \hat{\phi} = 0, \quad \text{at } y = 0, \quad (4)$$

$$(D^2 + k^2) \hat{\phi} + 2k^2 \text{Ma} \left[\hat{\tau} - \frac{\text{Bi} \hat{\eta}}{1 + \text{Bi}} \right] + \frac{2ik_x \hat{\eta}}{1 + 2\beta} = 0, \quad \text{at } y = 1, \quad (5)$$

$$\begin{aligned} & [D^2 - i \text{Re}(k_x - \omega) - 3k^2] D\hat{\phi} - 2\hat{\eta} k^2 \\ & \times \left[\frac{\cot \theta}{1 + 2\beta} - k^2 \left(\frac{\text{Ma}}{1 + \text{Bi}} - \text{We} \right) \right] = 0, \quad \text{at } y = 1 \end{aligned} \quad (6)$$

$$D\hat{\tau} - \text{Bi} \left[\frac{\text{Bi} \hat{\eta}}{1 + \text{Bi}} - \hat{\tau} \right] = 0, \quad \text{at } y = 1, \quad (7)$$

$$\hat{\phi} - i(k_x - \omega) \hat{\eta} = 0, \quad \text{at } y = 1, \quad (8)$$

where D stands for the differential operator $\frac{d}{dy}$. In Eqs. (2)–(8), $\hat{\phi}$, $\hat{\tau}$, and $\hat{\eta}$ denotes the amplitude of perturbation velocity, perturbation temperature and perturbation film thickness. The imposed disturbances to the perturbation quantities are considered to be in normal mode form, where $\omega = \omega_r + i\omega_i$ denotes the angular frequency and $k = \sqrt{k_x^2 + k_z^2}$ is the wave number. In this case, k_x and k_z are streamwise and spanwise wavenumbers, respectively. Again the complex spanwise wavenumber can be represented as $k = k_r + ik_i$, where $-k_i$ is the spatial growth rate. The angular frequency ω remains real while calculating the spatial growth rate. The temporal growth rate is denoted by ω_i and the wavenumber k remains real while calculating temporal growth rate. In the OS-BVP (2)–(8), Re, Ma, Bi, Pe, We denotes Reynolds number, Marangoni number, Biot number, Peclet number, and Weber number respectively. Again Peclet number can be written as $\text{Pe} = \text{Re} \text{Pr}$ where Pr denotes Prandtl number. The dimensionless slip length and base flow velocity is denoted by β and $\bar{U} = (2y - y^2 + 2\beta) / (1 + 2\beta)$. To capture the effect of Marangoni number and Biot number on the S mode and P mode instability properly we will use the transformations: $M = \text{Ma}(1 + 2\beta)^{1/3} (2\text{Re})^{2/3}$, $\text{Bi} = \text{B}(2\text{Re})^{1/3} / (1 + 2\beta)^{1/3}$, and $\text{Ka} = \text{We}(1 + 2\beta)^{1/3} (2\text{Re})^{2/3}$. Here Ka denotes the Kapitza number.

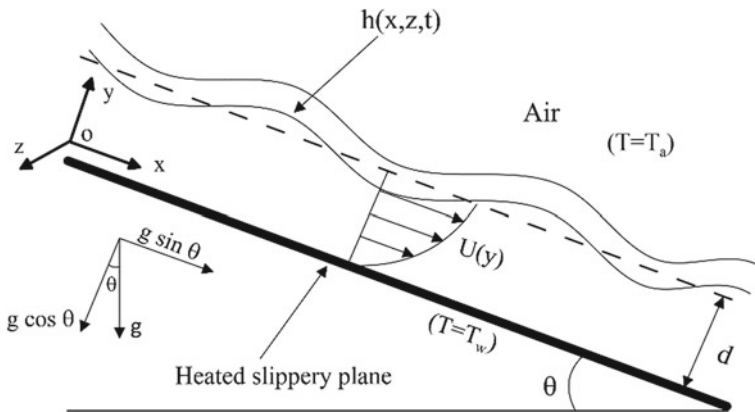


Fig. 1 Schematic of uniformly heated falling film

3 Results and Discussion

3.1 Spatial Stability Analysis

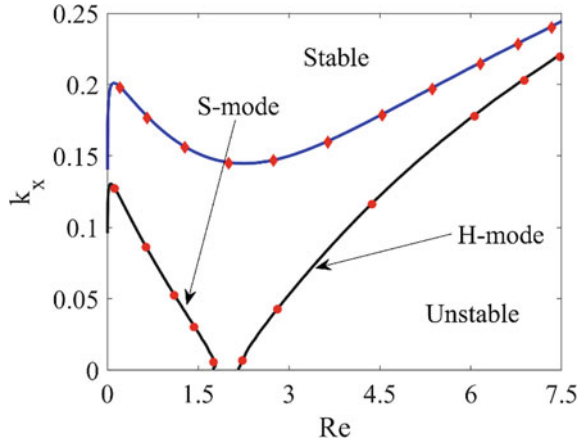
3.1.1 Validation

The Eigen value problem (2)–(8) have been solved numerically incorporating Chebyshev spectral collocation method. To check the consistency of the present numerical code, we have verified the present results with the existing results in literature. In Fig. 2, the neutral stability curve corresponding to H mode and S mode instability has been shown for $M = 15$ and $M = 30$ when $B = 1$, $Ka = 250$, $k_z = 0$, $\beta = 0$, $\theta = 15^\circ$, and $Pr = 7$. It can be clearly observed that present numerical code reproduces the results of Kalliadasis et al. [5] quite accurately. In this case, at lower value of M , we get two separate neutral curves for hydrodynamic H mode and thermocapillary S mode of instability. But as the Marangoni number Ma , or equivalently M increases, both the modes merge and forms a single neutral stability curve.

3.1.2 Influence of Marangoni Number

Here, we shall discuss the independent influence of Marangoni number, or equivalently M on the spatial growth rate of thermocapillary P mode and S mode which have been captured numerically. The modes are distinguished from each other on the basis of their phase speed. Note that from now onwards all the numerical results are produced keeping the parameters $Ka = 240$, $Pr = 6.5$, $\theta = 15^\circ$ and $\beta = 0.03$ fixed. In Fig. 3a, the spatial growth rate for S mode have been plotted in (k_r, k_i) plane for $M = 14$, $M = 10$, and $M = 6$ when $Re = 0.1$, $B = 1$, and $k_z = 0$. The spatial growth rate is found to be increasing with the increase in M for S mode instability. The S

Fig. 2 Evolution of neutral stability curves for $M = 15$ and $M = 30$ when $B = 1$, $Ka = 250$, $k_z = 0$, $\beta = 0$, $\theta = 15^\circ$, and $Pr = 7$. Black and Blue lines represent $M = 15$, and $M = 30$ respectively. The results from Kalliadasis et al. [5] are represented by symbolic points



mode instability triggers at low Reynolds number due to the surface tension gradient imposed by non-uniform temperature distribution at the liquid–air interface. As M increases, the surface tension gradient also increases between crest and trough of the waves at free surface resulting in a destabilizing effect on the flow. It is interesting to note that with the increase in Reynolds number the S mode instability gets stabilized as inertia force takes over the Marangoni force. Now the independent effect of M on the P mode will be analysed. The spatial growth rates related to P mode in (k_r, k_i) plane have been shown in Fig. 3b for $M = 20$, $M = 21$, and $M = 22$ when $Re = 10$, $B = 1$, and $k_z = 0$. Now, from Fig. 3b, it can be clearly observed that as the value of M increases the spatial growth rate also increases significantly. Hence, we may conclude that M or equivalently Ma destabilizes the P mode instability. It can also be observed that the P mode instability is found at the short wave regime unlike the S mode instability, which can only be present at long wave regime.

3.1.3 Influence of Biot Number

Now the influence of Biot number on the spatial growth rate of S mode and P mode will be discussed. Interestingly, we have found a dual effect of Biot number Bi or, equivalently B on the S mode depending upon the range of B . In Fig. 4a the evolution of spatial growth rate $-k_i$ has been plotted against the real part of streamwise wave number k_r , at small values of B ($B \leq 0.75$) when $M = 17$, $Re = 0.1$, and $k_z = 0$. At lower range of B , it can be noticed that B imparts a destabilizing effect on the S mode. On the contrary, at the higher values of B ($B \geq 0.75$) it may be noticed that with the increase in the value of B , the spatial growth rate decreases as shown in Fig. 4b. Therefore we may conclude that B has a stabilizing effect on S mode at higher range of B . This phenomenon can be attributed to the fact that with the increment in B , the relative heat transfer increases, resulting in lower temperature of free surface and hence stabilizing the S mode.

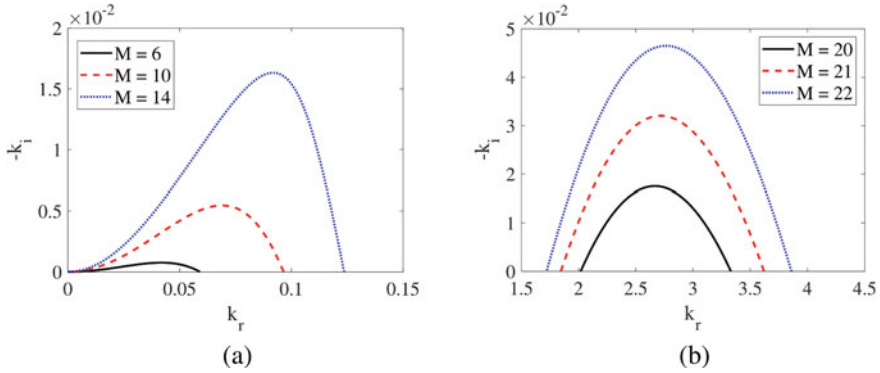


Fig. 3 **a** Evolution of spatial growth rate $-k_i$ for the S mode in (k_r, k_i) plane when $Re = 0.1$. **b** Evolution of spatial growth rate $-k_i$ for the P mode in (k_r, k_i) plane when $Re = 10$. The parameters $B = 1$ and $k_z = 0$ are kept constant

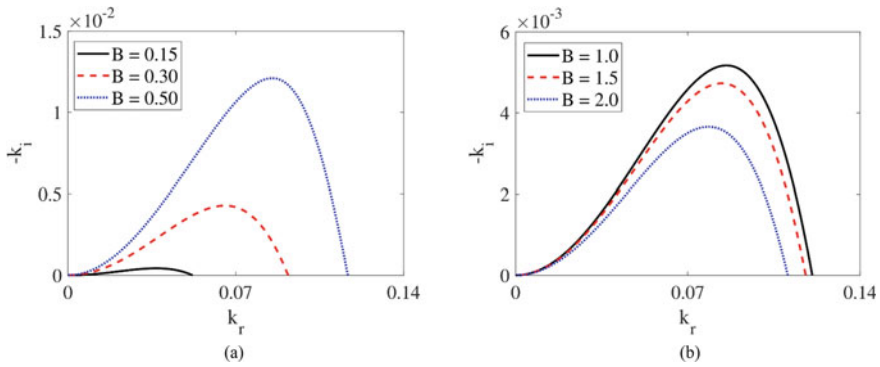
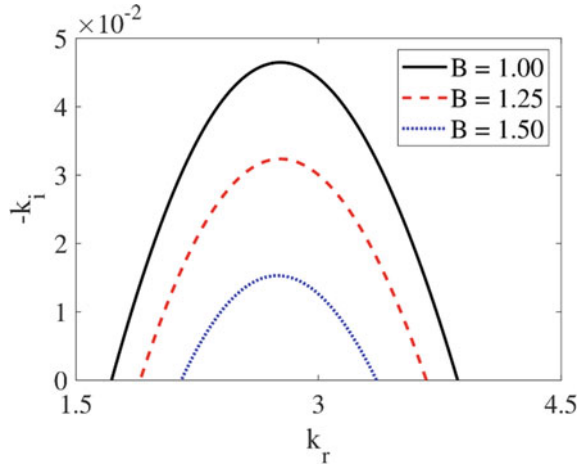


Fig. 4 **a** Evolution of spatial growth rate $-k_i$ for the S mode in (k_r, k_i) plane when $Re = 0.1$. **b** Evolution of spatial growth rate $-k_i$ for the S mode in (k_r, k_i) plane when $Re = 0.4$. The parameters $M = 17$ and $k_z = 0$ are kept constant

Now we will decipher the solo influence of Biot number on the P mode. The P mode instability is basically triggered by the steady convection rolls within the flow which is formed due to the surface tension gradient at the liquid–air interface. The variation of spatial growth rate k_i with respect to real part of streamwise wavenumber has been shown in Fig. 5 for $B = 1, B = 1.25$, and $B = 1.5$, when $Re = 10, M = 21$, and $k_z = 0$. It can be noticed that with the increase in B the spatial growth rate for P mode decreases significantly. Hence we may conclude that Biot number stabilizes the thermocapillary P mode.

Fig. 5 Evolution of spatial growth rate $-k_i$ for the P mode in (k_r, k_i) plane when $Re = 10, M = 21,$ and $k_z = 0$



3.1.4 Influence of Spanwise Wavenumber

In this section the independent effect of spanwise wavenumber on both S mode and P mode instability will be deciphered. In Fig. 6a the spatial growth rates corresponding to S mode have been plotted in (k_r, k_i) plane for $k_z = 0.1, k_z = 0.05,$ and $k_z = 0$ when $Re = 1, M = 25,$ and $B = 1.$ It can be observed that the maximum spatial growth rate for S mode reduces with the increase in $k_z.$ The onset of stability for the S mode also decreases significantly with the increase in $k_z.$ Therefore it may be concluded that spanwise wavenumber has a stabilizing influence on the S mode instability. It is also interesting to note that we have a finite growth rate at $k_r = 0$ at non-zero values of spanwise wave number. Now we will discuss the effect of spanwise wavenumber on the thermocapillary P mode instability. The spatial growth rates corresponding to P mode have been shown in (k_r, k_i) plane for various values of k_z when $Re = 10, M = 20,$ and $B = 1$ in Fig. 6b. It can be noticed that the spatial growth rate increases significantly with the increment in spanwise wavenumber and hence it can be inferred that spanwise wavenumber has a destabilizing influence on the P mode instability. It is also interesting to note that the range of k_r within which the P mode instability occurs, shifts towards lower values of k_r significantly. It indicates that with the increment of spanwise wavenumber the P mode instability shifts towards long wave regime from short wave regime.

3.2 Inviscid Analysis

According to Squire’s theorem, the two dimensional disturbances get unstable at lower values of Reynolds number compared to the three-dimensional ones [2]. Hence,

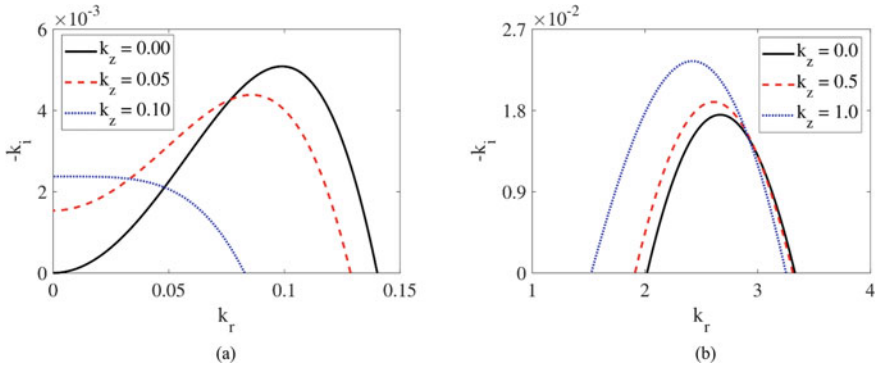


Fig. 6 **a** Evolution of spatial growth rate $-k_i$ for the S mode in (k_r, k_i) plane when $\text{Re} = 1$, and $M = 25$. **b** Evolution of spatial growth rate $-k_i$ for the P mode in (k_r, k_i) plane $\text{Re} = 10$ and $M = 20$. For both the plots $B = 1$

for performing inviscid stability analysis, we will consider two dimensional disturbances only, that is, $k_z = 0$ and $k_x = k$. Now the perturbation velocity is converted to perturbation stream function ψ' as the flow is two-dimensional and it is considered to be in normal mode form

$$\psi' = \hat{v} \exp[ik(x - ct)]. \tag{9}$$

Now we will introduce two new parameters $W = \text{We}/\text{Re}$ and $m = \text{Ma}/\text{Re}$ which will be used equivalently for showing the effect of Weber number and Marangoni number. At inviscid limits, we will consider Reynolds number to be large ($\text{Re} \rightarrow \infty$) and inclination angle to be small ($\theta \rightarrow 0$). Therefore, in this limiting case, the OS-BVP (2)–(8) will take the following form

$$(\bar{U} - c)(D^2 - k^2)\hat{v} + \frac{2\hat{v}}{1 + 2\beta} = 0, \quad y \in [0, 1] \tag{10}$$

$$(\bar{U} - c)\hat{\tau} + \frac{\text{Bi}}{1 + \text{Bi}}\hat{v} = 0, \quad y \in [0, 1], \tag{11}$$

$$\hat{v} = 0, \quad \text{at } y = 0, \tag{12}$$

$$(c - \bar{U})^2 D\hat{v} - 2\left[k^2\left(W - \frac{m}{1 + \text{Bi}}\right) + \frac{2 \cot \theta}{(1 + 2\beta)\text{Re}}\right]\hat{v} = 0, \quad \text{at } y = 0. \tag{13}$$

In Eq. (13) the term $2 \cot \theta / \{(1 + 2\beta)\text{Re}\}$ is not neglected. This is due to the fact that although the value of $1/\text{Re}$ is small, the value of $\cot \theta$ will be large and hence the ratio $\cot \theta / \text{Re}$ will have a finite value. The complex wave speed is denoted by $c = c_r + ic_i$ in Eqs. (10)–(13) where c_r and c_i denotes the real and imaginary part of

c. Now to solve the second-order BVP (10)–(13), we will employ the transformation $\hat{v}(y) = (U - c)\Upsilon(y)$, which will lead to the following set of BVP

$$D[(\bar{U} - c)^2 D\Upsilon] - (\bar{U} - c)^2 k^2 \Upsilon = 0, \tag{14}$$

$$(\bar{U} - c) \left[\hat{\tau} + \frac{\text{Bi}}{1 + \text{Bi}} \Upsilon \right] = 0, \tag{15}$$

$$\Upsilon(0) = 0, \tag{16}$$

$$(\bar{U} - c)^2 D\Upsilon(1) = \left[\frac{2 \cot \theta}{(1 + 2\beta)\text{Re}} + k^2 \left(W - \frac{m}{1 + \text{Bi}} \right) \right] \Upsilon(1) \tag{17}$$

Note that here the Governing energy equation is not considered here as $\hat{\tau}$ can be directly predicted from Eq. (11). In order to solve the set of Eqs. (14)–(17), we will multiply it with Υ^* , the complex conjugate of Υ . After that Eq. (14) is integrated with respect to y when $y \in [0, 1]$ and the boundary conditions (16)–(17) are incorporated to get the following expression.

$$\int_0^1 (\bar{U} - c_r - i c_i)^2 P \, dy = \left[k^2 \left(W - \frac{m}{1 + \text{Bi}} \right) + \frac{2 \cot \theta}{\text{Re}(1 + 2\beta)} \right] |\Upsilon(1)|^2, \tag{18}$$

where $P = (k^2 |\Upsilon(y)|^2 + |D\Upsilon(y)|^2) \geq 0$. Now, to compute the values of c_r and c_i , the real and imaginary parts of Eq. (18) are compared.

$$\int_0^1 [(\bar{U} - c_r)^2 - c_i^2] P \, dy = \left[k^2 \left(W - \frac{m}{1 + \text{Bi}} \right) + \frac{2 \cot \theta}{\text{Re}(1 + 2\beta)} \right] |\Upsilon(1)|^2, \tag{19}$$

$$c_i \int_0^1 (\bar{U} - c_r) P \, dy = 0. \tag{20}$$

Now for the shear mode to become unstable we should have $c_i > 0$. From Eq. (20), it can clearly be observed that for a non-trivial solution the unstable shear mode will not exist if $c_r > 1$. Therefore, for $c_r < 1$, we can have a solution for phase speed of unstable shear mode as

$$c_r = 1 - \left[1 - \frac{\int_0^1 (1 - y)^2 P \, dy}{(1 + 2\beta) \int_0^1 P \, dy} \right]. \tag{21}$$

Now from Eqs. (21) and (19) we get the expression for c_i as follows

$$c_i^2 = \frac{1}{(1 + 2\beta)^2} \left[\frac{\int_0^1 (1-y)^4 P \, dy}{\int_0^1 P \, dy} - \left(\frac{\int_0^1 (1-y)^2 P \, dy}{\int_0^1 P \, dy} \right)^2 \right] - \left[k^2 \left(W - \frac{m}{1 + \text{Bi}} \right) + \frac{2 \cot \theta}{\text{Re}(1 + 2\beta)} \right] \frac{|\Upsilon(1)|^2}{\int_0^1 P \, dy} \quad (22)$$

From the expression of c_i^2 , we can clearly observe that with the increase in m the temporal growth rate related to shear mode increase. Therefore, we may conclude that Marangoni number has a destabilizing effect on the shear mode instability. This result is perfectly consistent with the results of Choudhury and Samanta [2].

4 Conclusion

Linear stability analysis of a liquid incompressible film flowing down an inclined plane has been performed. The inclined plane is considered to be uniformly heated and slippery. The liquid follows the Newton's law of viscosity. At the free surface or, the liquid-air interface the heat transfer is governed by the Newton's law of cooling. To carry out the spatial stability analysis, we have formulated a coupled set of OS-BVP type equations containing perturbation velocity and temperature. In order to estimate the spatial growth rate at arbitrary wave numbers, we have numerically solved the coupled set of equations employing Chebyshev collocation technique. Marangoni number is found to have a destabilizing influence on both the S and P modes. On the contrary, Biot number is found to have dual effect on S mode. At lower range ($B \leq 0.75$) although Biot number has a destabilizing effect on the S mode, at higher range ($B \geq 0.75$), it is found to have a stabilizing effect. Biot number exerts a stabilizing effect on thermocapillary P mode also. It has been observed that with the increase in spanwise wavenumber the spatial growth rate of S mode and P mode attenuates and intensifies respectively. We have also analytically solved the OS-BVP for the limiting case of inviscid flow where $\text{Re} \rightarrow \infty$. In inviscid limit, the temporal growth rate for shear mode been evaluated which indicates a destabilizing effect of Marangoni number on the shear mode.

Nomenclature

Ma	Marangoni number [-]
Re	Reynolds number [-]
Bi	Biot number [-]
Pe	Peclet number [-]
We	Weber number [-]
Pr	Prandtl number [-]

k	Wavenumber [m^{-1}]
k_x	Streamwise wavenumber [m^{-1}]
k_z	Spanwise wavenumber [m^{-1}]
c	Wave speed [m s^{-1}]
ω	Angular speed [rad s^{-1}]
θ	Inclination angel [rad]
σ	Surface tension coefficient [N m^{-1}]
φ	Perturbation velocity amplitude [m s^{-1}]
τ	Perturbation temperature amplitude [K]
η	Perturbation film thickness [m]
Ψ'	Perturbation streamfunction [$\text{m}^2 \text{s}^{-1}$]
β	Dimensionless slip length [-]
T_a	Ambient temperature [K]
T_w	Wall temperature [K]

References

1. Bhat FA, Samanta A (2018) Linear stability of a contaminated fluid flow down a slippery inclined plane. *Phys Rev E* 98(3):033108
2. Choudhury A, Samanta A (2022) Linear stability of a falling film over a heated slippery plane. *Phys Rev E* 105(6):065112
3. Goussis DA, Kelly RE (1990) On the thermocapillary instabilities in a liquid layer heated from below. *Int J Heat Mass Transfer* 33:2237–2245
4. Hu J, Hadid HB, Henry D, Mojtabi A (2008) Linear temporal and spatio-temporal stability analysis of a binary liquid film flowing down an inclined uniformly heated plate. *J Fluid Mech* 599:269–298
5. Kalliadasis S, Ruyer-Quil C, Scheid B, Velarde MG (2012) *Falling liquid films*. Springer
6. Lin SP (1967) Instability of a liquid film flowing down an inclined plane. *Phys Fluids* 10:308–313
7. Lin SP (1975) Stability of liquid flow down a heated inclined plane. *Lett Heat Mass Transfer* 2:361–369
8. Pascal JP, D'Alessio SJD (2016) Thermosolutal Marangoni effects on the inclined flow of a binary liquid with variable density. I. Linear stability analysis. *Phys Rev Fluids* 1(8):083603
9. Samanta A (2013) Shear wave instability for electrified falling films. *Phys Rev E* 88(5):053002

Thermal Gradient-Mediated Instability in a Bilayer Flow Over a Porous Medium



Saurabh Dubey, Vinod B. Vanarse, Prathu Raja Parmar,
Omkar S. Deshmukh, and Dipankar Bandyopadhyay

Abstract In the current work, we explore the noticeable features of thermal gradient-triggered instability of a bilayer placed over a porous media. A comprehensive Orr-Sommerfield (OS) analysis is used to inspect the instability of a bilayer flow narrowed between a Darcy-Brinkman porous medium and a rigid plate. The OS equations are then numerically solved by implying suitable boundary conditions to get the length and time scales of instability aroused in the system. The parametric analysis gives the critical conditions at which the system becomes unstable and causes one of the layers in the bilayer to rupture, leading to the formation of micro-scale shapes. The predicted length scale at which the interface is highly unstable is in good agreement with the existing works. Interestingly, the length scale of the instability after film ruptures is identical to the most catastrophic wavelength of the system and with the available literature.

Keywords Instability · Orr-Sommerfield · Darcy-Brinkman · Bilayer · Micro-scale

Saurabh Dubey and Vinod B. Vanarse: Equal contribution by both the authors.

S. Dubey · D. Bandyopadhyay (✉)
Centre for Nanotechnology, Indian Institute of Technology Guwahati, Guwahati, Assam, India
e-mail: dipban@iitg.ac.in

V. B. Vanarse · P. R. Parmar · O. S. Deshmukh · D. Bandyopadhyay
Department of Chemical Engineering, Indian Institute of Technology Guwahati, Guwahati, Assam, India

D. Bandyopadhyay
Jyoti and Bhupat Mehta School of Health Sciences and Technology, Indian Institute of Technology Guwahati, Guwahati, Assam, India

1 Introduction

Confined bilayer flows of immiscible fluid pairs with one of the heated walls or a heat source along the interface are omnipresent in many industrial and natural situations [1–4]. The presence of a heating arrangement along one of the confined walls or an interface could facilitate the heating in order to transfer the heat to the targeted fluid or due to a chemical reaction [5]. This heat arrangement results in an interplay between heat transfer and hydrodynamics, along with the reactions if the system under consideration is reactive. A few latest studies considered the reactive systems, showing that interplay leads to several hydrodynamic instabilities like solutal or thermal Marangoni, Kelvin–Helmholtz, viscous fingering, and Rayleigh–Taylor instabilities due to property gradients [6–8].

Interestingly, most of the earlier works have not considered the heating parameter in their studies [4–6]. In fact, in many industrial and natural systems, the importance of hydrodynamic flows generated due to imposed temperature gradients cannot be ignored as they walk hand in hand with chemical reactions. A realistic modelling approach to understanding such ubiquitous systems is essential with a genuine model. For instance, to properly mix in a continuous or batch reactor, the shear force is introduced to increase the contact area between the reactants or an axially applied pressure in the case of tubular flow reactors [5]. In one of the studies [9], the authors imposed the thermal gradient across the confinement, considering the linear dependency of the surface tension with the temperature. In another study [10], the stability of stratified Couette flow amid heated plates considering thermocapillary and buoyancy influences has been investigated. But, the parametric analysis was restricted to a few. Recently, a theoretical study has considered these gaps and added the heat sink-source arrangement alongside the interface [11].

An instability arising from the inter-phase thermal gradient between a porous medium and a bilayer flow over it is explored here. The present work is motivated by the recent stand-up problems of micro-particle pollution when the polymer substances come in contact with hot fluids resting on a platform, a porous medium that affects human health in many ways. When heat transfer occurs between two identical or different phases, a well-defined demarcating boundary called an interface triggers instability disintegrating the layer or solid substrates. Thus, the present investigation aims at understanding the stabilizing and destabilizing forces of the system and the interplay between them in order to minimize the system instability.

2 Problem Formulation

The origin is recognized at the porous substrate-Polymer thin layer interface at $z = 0$, as shown in a schematic of the 2D flow system being studied. The Cartesian coordinate system is adopted, and the unit vectors (e_x, e_y, e_z) focussed lengthwise on the coordinate direction (x, y , and z) as presented in Fig. 1. In this problem formulation,

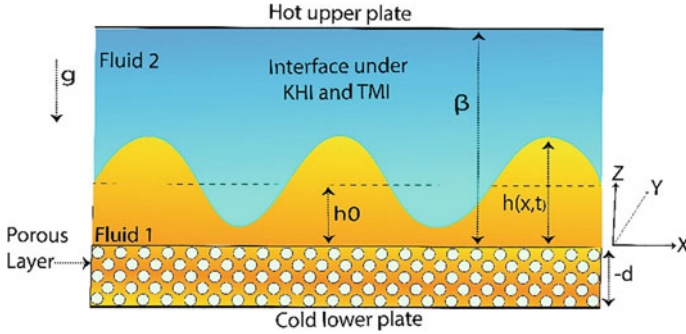


Fig. 1 Schematic representation of the polymer film and a fluid layer placed over the porous medium wherein the top plate is maintained at a higher temperature than the lower plate. The images show the computation domain used in the theoretical formulation where the local thickness of the polymer film is $h(x, t)$, and the top layer is at a distance β from the porous media of thickness $(-d)$

used variables for the thin polymer film and hot water layers are designated by the subscript ‘ i ’ ($i = 1, 2$), and the subscript ‘ m ’ denotes the porous medium.

A bilayer flow of Newtonian, incompressible, and immiscible polymer and water layer with invariant density ρ_i and viscosity μ_i , above a Darcy–Brinkman porous media of porosity δ , permeability k , and depth d is assumed. Here are water and porous medium (ambient) temperatures, respectively.

2.1 Governing Equations

The following scaling scheme is used to reduce the governing equations to their dimensionless forms hiring the lower layer thickness (h_0) as the length scale and $(\rho_1 h_0^2 / \mu_1)$ as the time scale (viscous). The following dimensionless forms are adopted,

$$\begin{aligned}
 (X, Z, D_m, H_1) &= 1/h_0(x, z, d, h_1), \quad T = t \mu_1 (\rho_1 h_0^2)^{-1}, \\
 (U_1, U_2, U_m) &= \rho_1 h_0 \mu_1^{-1} (u_1, u_2, u_m), \quad \rho_r = \rho_2 \rho_1^{-1}, \quad \mu_r = \mu_2 \mu_1^{-1}, \\
 B &= \beta h_0^{-1}, \quad (\Gamma_1, \Gamma_2) = (\rho_1 v_1^2)^{-1} (\gamma_1 h_0, \gamma_2 h_0), \quad P_i = p_i h_0^2 \rho_1 \mu_1^{-2}, \\
 \theta_i &= T_{top} - T_i (T_{top} - T_{lower})^{-1}
 \end{aligned}$$

The dimensionless governing equations, precisely continuity, momentum, and the thermal equations for both fluid layers and porous medium are given by.

$$\nabla \cdot \mathbf{u}_i = 0, \tag{1}$$

$$\rho_i \left[\dot{\mathbf{u}}_i + (\mathbf{u}_i \cdot \nabla) \mathbf{u}_i \right] = -\nabla p_i + \mu_i \nabla^2 \mathbf{u}_i + \rho_i \mathbf{g}, \quad (2)$$

$$\nabla \cdot \mathbf{u}_m = 0, \quad (3)$$

$$\frac{\rho_1}{b} \dot{\mathbf{u}}_m = -\nabla p_m + \mu_e \nabla^2 \mathbf{u}_m - \frac{\mu_1}{\kappa} \mathbf{u}_m + \rho_1 \mathbf{g}, \quad (4)$$

$$(\rho_i C_{spi}) \left(\dot{T}_i + \mathbf{u}_i \cdot \nabla T_i \right) = k_{thi} \nabla^2 T_i. \quad (5)$$

Overhead dots represent the time derivative, and the subscripts separated by a comma from the variable represent partial differentiations concerning the subscripted variable. Here,

$$\nabla = \left(\frac{\partial}{\partial x}, \frac{\partial}{\partial z} \right), \quad \mathbf{u}_i = (u, w).$$

Temperature dependence of surface tension (γ) is used as:

$$\gamma = \gamma_0 - \gamma_T (T - T_0). \quad (6)$$

The appropriate boundary conditions are used to solve the above governing equations.

No-slip and impermeability boundary conditions are implemented at the porous-solid ($z = -d$), and liquid-solid ($z = \beta$) boundaries are given by,

$$u_m = 0, \quad (7)$$

$$u_2 = 0 \quad (8)$$

Continuity of velocity enforced as boundary conditions at the porous-liquid interface $z = 0$,

$$u_1 = u_m. \quad (9)$$

Jump in tangential stress at $z = 0$,

$$\mu_e \mathbf{u}_{mz} - \mu_1 w_{1z} = \frac{\xi}{\sqrt{\kappa}} \mathbf{u}_m. \quad (10)$$

Continuity of normal stress,

$$-p_m + 2\mu_e w_{mz} = -p_1 + 2\mu_1 w_{1z}. \quad (11)$$

At $z = h_1$, the following set of boundary conditions is applied,

$$u_1 = u_2, \quad (12)$$

$$\mathbf{n}_1 \cdot \bar{\boldsymbol{\tau}}_2 \cdot \mathbf{n}_1 - \mathbf{n}_1 \cdot \bar{\boldsymbol{\tau}}_1 \cdot \mathbf{n}_1 = \gamma_1 (\nabla \cdot \mathbf{n}_1), \quad (13)$$

$$\mathbf{t} \cdot \bar{\boldsymbol{\tau}}_2 \cdot \mathbf{n} = \mathbf{t} \cdot \bar{\boldsymbol{\tau}}_1 \cdot \mathbf{n} + \nabla_S \gamma \cdot \mathbf{t}. \quad (14)$$

At the location of the Polymer–Hot water interface $z = h_1$, kinematic boundary conditions are applied,

$$\dot{h}_1 + u_1 h_{1,x} = w_1. \quad (15)$$

The boundary conditions imposed to solve the temperature equation are as at porous solid interface ($z = -d$) is

$$T_m = T_{\text{lower}}. \quad (16)$$

At far within bulk in semi-infinite hot water ($z = \beta$) is,

$$T_2 = T_{\text{top}} \quad (17)$$

At the liquid-porous interface ($z = 0$) boundaries are,

$$T_1 = T_m, \quad (18)$$

$$k_{\text{th1}} T_{1Z} = k_{\text{thm}} T_{mZ}. \quad (19)$$

2.2 Linear Stability Analysis

The variables are divided into base state and perturbed state for the general linear stability analysis (GLSA). To linearize the governing equations, the following linear modes are used,

$$U_j = \bar{U}_j + U'_j, \quad W_j = W_j', \quad P_j = \bar{P}_j + P'_j. \quad (20)$$

Here, over-bar quantities represent the base state, and the prime represents the perturbed term which is then transformed into the stream function.

The following normal modes are used to solve the set of governing equations and boundary conditions to get the equation's final form, which is the disturbance's

growth rate, and k is the wave number.

$$[\psi_i, P_i', H_i', \theta_i](X, Z, T) = [\tilde{\psi}_i(Z), \tilde{P}_j(Z), (1 + \tilde{H}_i(Z)), \tilde{\theta}_j(Z)]e^{(\omega t + ikx)}. \quad (21)$$

The following coupled OS equations for the films and the porous medium are obtained by eliminating the pressure term using the perturbed equation of motion and continuity equation.

$$(D^2 - k^2)^2 \tilde{\psi}_1 = ik[(\bar{U}_1 - C)(D^2 - k^2) - D^2 \bar{U}_1] \tilde{\psi}_1, \quad (22)$$

$$v_r (D^2 - k^2)^2 \tilde{\psi}_2 = ik[(\bar{U}_2 - C)(D^2 - k^2) - D^2 \bar{U}_2] \tilde{\psi}_1, \quad (23)$$

$$(D^2 - k^2)^2 \tilde{\psi}_m = \left(\frac{\delta}{D_a} - ikC \right) (D^2 - k^2) \tilde{\psi}_m. \quad (24)$$

Similarly, all other boundary conditions are perturbed using the normal mode, and for solving the above ODEs, including equations and boundary conditions, we need to transform them into desired domain by using the mapping technique. For this purpose, the computational domain under consideration is mapped into a space $(-1, 1)$ with the help of the proper transformations. These transformations then extended in terms of Chebyshev polynomials $T_n(Z)$. For N Chebyshev polynomials, we obtained the eigenvalues using the $(6N) \times (6N)$ matrix consistent with three fourth-order ODEs and three second-order ODEs along with the eighteen boundary conditions. To check the correctness, the eigenvalues are also corroborated by solving equations using the spectral collocation method with improved precision, as proposed by Weideman and Reddy [12]. We also checked the eigenvalues obtained in the limit from the present work and compared them with the eigenvalues reported by Tilley, Davis and Bankoff [13] for the plane Poiseuille flow (PPF).

3 Results and Discussion

3.1 Validation

The accuracy of the present theoretical formulation is validated alongside the available configuration in the literature. Figure 2 shows the flow rate (Q) functionality with the critical wave number (k) obtained using the spectral collocation method. The plot approves that the present theoretical formulation agrees with the existing work of Tilley et al. [13] in the asymptotic limit, showing the reliability of the present formulation for the bilayer placed over the porous media in the limit when porous media influences are neglected. A former theoretical investigation [14] proposed that a bilayer PPF where density is the same in both layers is unstable either due to

the finite-wave-number shear mode or the long-wave interfacial mode at different viscosity ratio values when compared with the thickness ratio value. The results highlighted in the present work show the significance of the below porous medium or the top plate maintained at a high temperature. We used higher to lesser temperatures and viscosity ratio values to check the system’s stability. To expose the striking features, we used the approximate parameter space shown in Table 1.

Fig. 2 Neutral stability plot showing the flow rate variation (Q) with the critical wave number (k). The symbols (*) are obtained from the results of the spectral collocation technique for the present formulation, whereas the solid colour line is reproduced from Tilley et al. [13] work in an asymptotic limit. Here, the parametric values for $b = 0.01$ and $D_m = 0.01$ are used to validate the present work

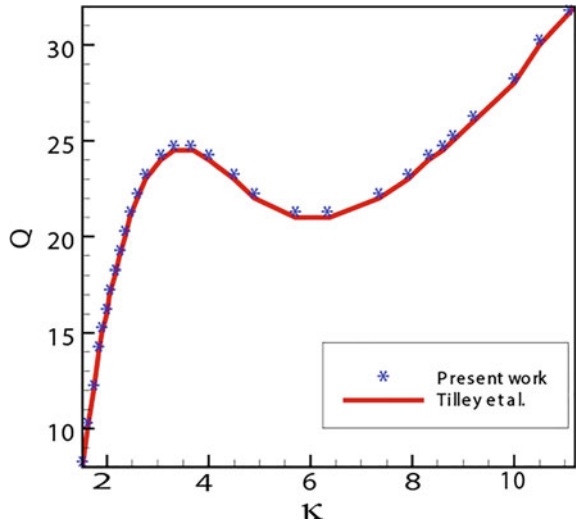


Table 1 Typical parameters used for the calculations

Variables	Values
μ_r	0.8
ρ_r	1.11
α	0
b	0.001
χ	0
D_m	1
D_a	0.0001
k_1	0.150
K_2	0.598
K_m	0.05
C_{sp1}	126.5
C_{sp2}	4184
C_{spm}	200
M	22.5
Q	0.0001

Fig. 3 Dispersion curves plotted for an incremental temperature series wherein the system leads to increased instability. The parametric space used for the plots is given in Table 1

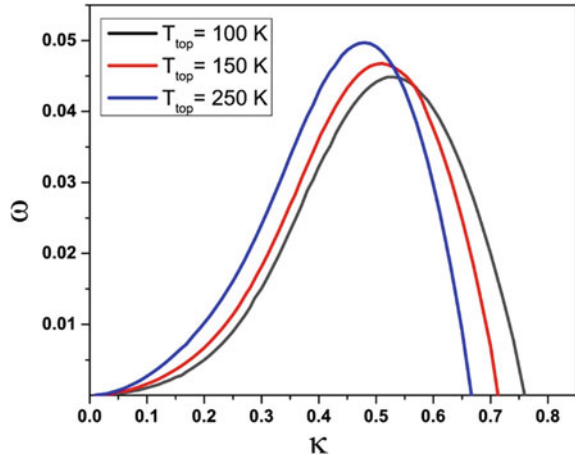
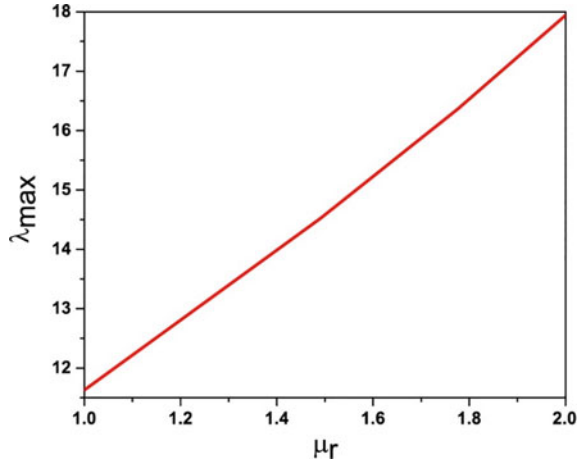


Figure 3 shows the effect of the top plate's temperature variation on the system's stability when the porous medium is maintained at ambient conditions. The bilayer is remarkably sensitive to temperature variations at the top plate showing the thermally unstable behaviour of the system. This unstable system behaviour due to increased top plate temperature is attributed to Kelvin–Helmholtz coupled with thermal Marangoni effects arising from a temperature gradient. The dispersion curve shown in Fig. 3 is the variation of the growth coefficient (ω) with wavenumber (k) at different temperatures. Solid colour lines of the curves show the increasing temperature values resulting in the increase in the growth rate of instability of the system. The dominant wavelength λ_{max} represents the length scale of the system instability. Figure 4 depicts the dependence of the system length scale on the viscosity ratio. As μ_r it increases, that shows an increase in the length scale, indicating that increased viscous resistances try to minimize the destabilizing influences in the system by reducing the speed of propagating unstable waves.

The instability is certainly long-wavelength, as seen in the plot from the trend followed by the wave number (k). As previously mentioned, the upper plate temperature controls the thermal factor's impact on the instability. In fact, not an individual temperature of the top plate or the porous medium at ambient conditions spikes the instability, but the difference between them drives the system towards unstable mode. The changes in top plate temperature mainly cause variations in the system's thermal gradient, which is one of the highlighted parameters playing a crucial role in the system stabilization (destabilization) at lower (higher) values of the upper layer.

This slowed down waves, then die out over the period of time before they progress, further instigating in minimization of a span of larger wave numbers. In other words, the destabilizing forces need to overcome the additional resistance offered by increased μ_r leads to larger time and length scales of instability.

Fig. 4 The variation of dominant wavelength (λ_{\max}) with viscosity ratio (μ_r). The necessary parameters used for the plot are given in Table 1



4 Conclusions

In this chapter, we have presented that the manifestation of the thermal gradient can cause the destabilization in the bilayer flow placed over a porous medium via thermal Marangoni effects as long as a thermal gradient is maintained across the layers. An obligatory condition for thermal Marangoni instability to take place is the thermal gradient in the base state. For the implemented GLSA scheme, we figure out the critical parameters at which the system is most unstable, leading to the film rupture. The obtained length scale of instability for the present work is well matching with the available literature.

In the context of thermal Marangoni instability in a bilayer fluid system, the interface can be stabilized or destabilized depending on the thermal gradient values, disturbing the linear instability mode's nature. This investigation indicates that the thermal Marangoni instability in the case of fluid/s placed over the porous media can play a crucial role in applications such as environmental reformation and healthcare uses [15].

Acknowledgements We are grateful for the support from the Department of Chemical Engineering and Centre for Nanotechnology, IIT Guwahati. V.B.V. and S.D. thank Dr. Siddharth Thakur for their insightful suggestions. S. D. and V.B.V. are grateful to MHRD, the Government of India, for financial support.

Nomenclature

μ_r	Viscosity ratio
ρ_r	Density ratio
k_{th}	Thermal conductivity

ψ	Stream function
ξ	Stress jump coefficient
γ	Surface tension
b	Porosity
κ	Permeability
ω	Growth coefficient
k	Wavenumber
ω_m	Maximum growth coefficient
Pr	Prandtl number for polymer film
Pr _{eff}	Prandtl number for porous layer
D _a	Darcy number
λ_r	Thermal conductivity ratio top to bottom layer

References

1. Bratsun D, De Wit A (2004) On Marangoni convective patterns driven by an exothermic chemical reaction in two-layer systems. *Phys Fluids* 16:1082–1096
2. Gibson I, Rosen DW, Stucker B (2010) Additive manufacturing technologies. Springer
3. Ukrainsky B, Ramon GZ (2018) Temperature measurement of the reaction zone during polyamide film formation by interfacial polymerization. *J Membr Sci* 566:329–335
4. De Wit A (2020) Chemo-hydrodynamic patterns and instabilities. *Annu Rev Fluid Mech* 52:531–555
5. Kumar AP, Goyal H, Banerjee T, Bandyopadhyay D (2013) Instability modes of a two-layer Newtonian plane Couette flow past a porous medium. *Phys Rev E* 87:063003
6. Himanshu Goyal A, Kumar AP, Dipankar Bandyopadhyay R, Usha TB (2013) Instabilities of a confined two-layer flow on a porous medium: an Orr-Sommerfeld analysis. *Chem Eng Sci* 97:109–125
7. Levenspiel O (1999) Chemical reaction engineering. Wiley
8. DeWit A, Eckert K, Kalliadasis S (2012) Introduction to the focus issue: chemo-hydrodynamic patterns and instabilities. *Chaos* 22:037101
9. Eckert K, Acker M, Tadmouri R, Pimienta V (2012) Chemo-Marangoni convection driven by an interfacial reaction: pattern formation and kinetics. *Chaos* 22:037112
10. De Wit A (2016) Chemo-hydrodynamic patterns in porous media. *Phil Trans R Soc A* 374:20150419
11. Wei HH (2006) Shear-flow and thermocapillary interfacial instabilities in a two-layer viscous flow. *Phys Fluids* 18:064109
12. Gumerman RJ, Homsy GM (1974) Convective instabilities in concurrent two phase flow: part I. Linear stability. *AIChE J* 20(5):981–988
13. Patne R, Ramon G, Agnon Y, Oron A (2022) Dynamics of a two-layer flow with an interfacial heat source/sink: viscosity stratification. *J Fluid Mech* 934:A43
14. Weideman JA, Reddy SC (2000) A MATLAB differentiation matrix suite. *ACM Trans Math Softw (TOMS)* 26(4):465–519
15. Tilley BS, Davis SH, Bankoff SG (1994) Linear stability theory of two-layer fluid flow in an inclined channel. *Phys Fluids* 6(12):3906–3922

16. Khaled ARA, Vafai K (2003) The role of porous media in modeling flow and heat transfer in biological tissues. *Int J Heat Mass Transfer* 46:4989
17. Maity S, Bhuyan T, Pattanayak JP, Ghosh SS, Bandyopadhyay D (2021) Real-time transport kinetics of drug encapsulated nanoparticles into apoptotic cancer cells inside microchannels. *Nanotechnology* 32:505704

Compound Matrix Method for Linear Stability Analysis of Flow Over a Flat Plate



Rituparn Somvanshi, Neha Chaturvedi, and Swagata Bhaumik

Abstract Flow transition from laminar to turbulent regime is marked by instability characteristics of the former. The question of transition evolves into how stable the incoming flow is. Linear stability analysis takes in nonlinear governing equations and converts them into the corresponding perturbation equation, that can be studied for solutions seeking the most (un)stable modes and study their propagation. This study uses the Compound Matrix Method (CMM) for solving stability of compressible boundary layer flows. The problem involves flow of air over an adiabatic flat plate. This boundary conditions can be found in surfaces exposed to high-speed flows, such as outer walls of aircraft and spacecrafts. The solution to the problem comes in the form of determining stable and unstable pairs of $(\text{Re}, \omega, \alpha_i)$, with $\alpha_i = 0$ being the neutral curve. The initial and boundary conditions appropriate to the problem are converted appropriately. The use of free stream boundary conditions helps to simplify the system of 6 equations by retaining only 3 decaying modes in the free stream. The region on $\text{Re} - \omega$ with $\alpha_i > 0$ depicts the stable region and $\alpha_i < 0$ depicts unstable. The spatial stability analysis for adiabatic flow over a flat plate at two Mach numbers using CMM to give the critical Reynolds number as 523.7 and 567.7 for $M = 0.1, 0.6$, and results are compared against the incompressible Orr-Sommerfeld equation (OSE).

Keywords Neutral curves · Orr-Sommerfeld equation · Adiabatic boundary layer flow · Compound matrix method

1 Introduction

Physical problems involve fluid flow; either in conjunction with an external geometry, or those involving mixtures of fluids, or both. Fluid flow is governed by a multitude of factors such as convection, diffusion, and body forces. Physically, flow is subject to a wide range of fluctuations that creep in from external sources. Also known as

R. Somvanshi (✉) · N. Chaturvedi · S. Bhaumik
Department of Mechanical Engineering, IIT (ISM) Dhanbad, Dhanbad 826005, India
e-mail: rituparn.19dr0126@mech.iitism.ac.in

© The Author(s), under exclusive license to Springer Nature Singapore Pte Ltd. 2024
K. M. Singh et al. (eds.), *Fluid Mechanics and Fluid Power, Volume 2*, Lecture Notes in Mechanical Engineering, https://doi.org/10.1007/978-981-99-5752-1_14

perturbations, these effects are important in determining the stability characteristics of the downstream flow. The first experimental confirmation came in the form of the vibrating ribbon problem [1, 2]. When considering flow over bluff bodies, the transition point becomes important because the stability characteristics here will determine if the downstream flow remains laminar or turbulent [3]. Some practical problems in this domain include transition prediction for flow over airfoil, heating and cooling off turbine blades, laminar jet flows for gas combustion in IC engines etc. [4].

The process of transition in a boundary layer starts off with a stable flow from the leading edge, followed by unstable laminar flow in two dimensions and subsequently three dimensions. The formation of vortices and eddies is observed at this stage [5]. These are the first instances of fluctuations, known as Tollmien-Schlichting waves that decay back to a laminar flow convert further into turbulence with large vortices [6].

Among other theories [7–10], linear stability analysis (LSA) is the entry point towards understanding the stability characteristics of the flow. The approach assumes that every variable consists of a mean and a fluctuating value. The normal component to the wall is the dependent variable, and the fluctuating component is then broken down into a Fourier series, which consists of all the modes of vibration that the fluctuating variable consists of. These steps convert the governing partial differential equation into the fluctuation equations that will now be studied for stability analysis. Depending on the problem requirements, it is usually desired that the fluctuations decay, as disturbances should be very small, when considering locations far away from the boundary. In the larger context, it is relevant to know the primary conditions that lead to a stable or unstable flow.

There are several approaches developed to perform linear stability analysis [11]. Local and global eigenvalue methods have been developed and are being used for the last few decades [12]. The idea here is to convert the governing equations into a system of linear equations that will be posed as an eigenvalue problem and the eigenvalues determine the critical values at which flow characteristics depend. Further, stability characteristics can be studied in terms of spatially or temporally varying disturbances. They have also been combined into a spatio-temporal framework for a collective analysis of both. The CMM is used for Eigenvalue analysis of stiff ODEs/PDEs. A matrix whose elements are essentially minors of another matrix is a compound matrix [4, 13]. This type of matrix is related to exterior algebras and a compound matrix of minors is also known as the p th exterior product [14]. The advantage offered here is that this approach is capable of dealing with stiff systems of ODEs/PDEs. A compound matrix is a matrix of minors of a given matrix. They are also known as p th exterior power of a matrix. They possess interesting properties that allow them to help express problems as determinantal assignment problems and provide easy route to solving complex singular value decompositions.

In this chapter, we present the methodology to obtain the neutral curves for the flow over a flat plate problem, under adiabatic boundary conditions at a subsonic Mach number. In Sect. 2, LSA is performed over the Navier–Stokes equations, leading to a system of fluctuation equations. The problem statement is described in Sect. 3,

along with its similarity solution in Sect. 4. Thereafter, the compound matrix for the system is derived in Sect. 5. The neutral curves are plotted for $M = 0.1$ in Sect. 6, along with concluding remarks.

2 Linear Stability Analysis

The continuity, momentum, and energy equations for compressible flow, in vector form are given below:

$$\frac{\partial \rho}{\partial t} + \nabla \cdot \rho u = 0 \quad (1)$$

$$\frac{\partial \rho u}{\partial t} + u \cdot \nabla(\rho u) = \nabla \cdot \sigma + \rho f \quad (2)$$

$$\frac{\partial E_t}{\partial t} + \nabla \cdot (E_t u) = \nabla \cdot \sigma u - \nabla \cdot q \quad (3)$$

Here, u refers to the velocity field inside the domain, ρ is the fluid density, σ is the stress tensor, accounting for normal and shear stresses over a fluid element, and q is the total heat energy in the element.

The equations above are non-dimensionalized with respect to certain scaled factors ρ^* , u^* , L^* . The following substitutions are made:

$$\tilde{x} = \frac{x}{L^*}, \quad \tilde{t} = \frac{t}{L^*/u^*}, \quad \tilde{\rho} = \frac{\rho}{\rho^*}, \quad \tilde{u} = \frac{u}{u^*}, \quad \tilde{p} = \frac{p}{\rho^* u^{*2}}, \quad (4)$$

At this stage, certain assumptions are incorporated into the flow for simplification, following similar methodology from [15].

Flow is considered two dimensional (z -components are ignored).

- The mean flow is taken to be in x -direction only, and only fluctuating components are taken to vary in y -direction.
- Terms containing products of fluctuations ($\hat{\phi}_1 \hat{\phi}_2$) are infinitesimally small, and hence ignored
- Body forces are ignored

The first step of LSA requires that each variable (ϕ) be split into its mean ($\underline{\phi}$) and fluctuating component ($\hat{\phi}$).

$$\phi = \underline{\phi} + \hat{\phi} \quad (5)$$

Subsequently, the fluctuation terms are substituted with their Fourier mode decomposition [16], $\hat{\phi} = \phi' e^{i(\alpha x + \beta z - \omega t)}$. Here, α , ω are the wavenumber and frequency respectively. For 2D flows, we consider $\beta = 0$. Note that α and ω are complex quantities. The resulting system of equations is given.

$$i(\alpha U - \omega)\rho' + v' \frac{\partial \rho}{\partial y} + \underline{\rho} \left(i\alpha u' + \frac{\partial v'}{\partial y} \right) = 0 \quad (6)$$

$$\begin{aligned} & \underline{\rho} i(\alpha U - \omega)v' + \frac{1}{\gamma M^2} \frac{dp'}{dy} \\ & = + \frac{1}{\text{Re}} \left[\underline{\mu}' \left(2 \frac{d^2 v'}{dy^2} - \alpha^2 v' + i\alpha \frac{du'}{dy} \right) + \underline{\lambda} \left(\frac{d^2 v'}{dy^2} + i\alpha \frac{du'}{dy} \right) \right] \\ & + \frac{1}{\text{Re}} \left[2c_1 \frac{dv'}{dy} + D_1 \left(\frac{dv'}{dy} + i\alpha u' \right) + i\alpha c_3 T' \right] \end{aligned} \quad (7)$$

$$\begin{aligned} & \underline{\rho} c_{p_{ref}} i(\alpha U - \omega)T' - \frac{\gamma - 1}{\gamma} i(\alpha U - \omega)p' + \left(\underline{\rho} c_{p_{ref}} v' \frac{dT}{dy} \right) \\ & = \frac{1}{\text{Re}} \left[(\gamma - 1)M^2 \left(c_5 T' + 2\underline{\mu} \frac{dU}{dy} \frac{du'}{dy} + 2i\alpha v' \underline{\mu} \frac{dU}{dy} \right) \right] \\ & + \frac{1}{\text{Re Pr}} \left[c_6 T' + 2c_{10} + \frac{dT'}{dy} + \underline{\kappa} \frac{d^2 T'}{dy^2} - \underline{\kappa} \alpha^2 T' \right] \end{aligned} \quad (8)$$

$$\begin{aligned} & \underline{\rho} c_{p_{ref}} i(\alpha U - \omega)T' - \frac{\gamma - 1}{\gamma} i(\alpha U - \omega)p' + \left(\underline{\rho} c_{p_{ref}} v' \frac{dT}{dy} \right) \\ & = \frac{1}{\text{Re}} \left[(\gamma - 1)M^2 \left(c_5 T' + 2\underline{\mu} \frac{dU}{dy} \frac{du'}{dy} + 2i\alpha v' \underline{\mu} \frac{dU}{dy} \right) \right] \\ & + \frac{1}{\text{Re Pr}} \left[c_6 T' + 2c_{10} + \frac{dT'}{dy} + \underline{\kappa} \frac{d^2 T'}{dy^2} - \underline{\kappa} \alpha^2 T' \right] \end{aligned} \quad (9)$$

The constants mentioned in the above equations are:

$$c_1 = \frac{d\underline{\mu}}{dT} \frac{dT}{dy} \quad (10)$$

$$c_2 = \frac{d^2 \underline{\mu}}{dT^2} \frac{dT}{dy} \frac{dU}{dy} + \frac{d\underline{\mu}}{dT} \frac{d^2 U}{dy^2} \quad (11)$$

$$c_3 = \frac{d\underline{\mu}}{dT} \frac{dU}{dy} \quad (12)$$

$$c_4 = \frac{d\underline{\mu}}{dT} \frac{dT}{dy} \frac{dU}{dy} + \underline{\mu} \frac{d^2 U}{dy^2} \quad (13)$$

$$c_5 = \frac{d\mu}{dT} \left(\frac{dU}{dy} \right)^2 \tag{14}$$

$$c_6 = \frac{d^2\kappa}{dT^2} \left(\frac{dT}{dy} \right)^2 + \frac{d\kappa}{dT} \frac{d^2T}{dy^2} \tag{15}$$

$$c_7 = \frac{d\kappa}{dT} \frac{dT}{dy} \tag{16}$$

$$d_1 = \frac{d\lambda}{dT} \frac{dT}{dy} \tag{17}$$

Equations (6)–(9) are the perturbation equations of the governing equations (1)–(3). These can now be converted in to a matrix form by making the substitutions:

$$\begin{bmatrix} X_1 \\ X_2 \\ X_3 \\ X_4 \\ X_5 \\ X_6 \end{bmatrix} = \begin{bmatrix} \alpha u' \\ \alpha u_{y'} \\ v' \\ p' / \gamma M^2 \\ T' \\ T_{y'} \end{bmatrix} \tag{18}$$

resulting system of equations in matrix form:

$$\begin{bmatrix} X_{1'} \\ X_{2'} \\ X_{3'} \\ X_{4'} \\ X_{5'} \\ X_{6'} \end{bmatrix} = \begin{bmatrix} 0 & 1 & 0 & 0 & 0 & 0 \\ A_{21} & A_{22} & A_{23} & A_{24} & A_{25} & A_{26} \\ A_{31} & 0 & A_{33} & A_{34} & A_{35} & 0 \\ A_{41} & A_{42} & A_{43} & A_{44} & A_{45} & A_{46} \\ 0 & 0 & 0 & 0 & 0 & 1 \\ 0 & A_{62} & A_{63} & A_{64} & A_{65} & A_{66} \end{bmatrix} \begin{bmatrix} X_1 \\ X_2 \\ X_3 \\ X_4 \\ X_5 \\ X_6 \end{bmatrix} \tag{19}$$

with the coefficients given in the Appendix.

A. Spatial analysis

A spatial analysis entails that the wavenumber components (α , β) are taken complex, and frequency (ω) is real. Thus, we have $\alpha = \alpha_r + i\alpha_i$ and $\omega = \omega_r$. The Fourier mode decomposition can now be written as,

$$\hat{\phi} = \phi' e^{i(\alpha_r + i\alpha_i)x - \omega t} = \phi' e^{-\alpha_i x} e^{i(\alpha_r x - \omega t)} \tag{20}$$

The above expression gives the spatial amplification rate as $-\alpha_i$, and the stability of the flow depends on how this factor grows (unstable) or decays (stable).

- $i < 0$: unstable wave
- $i = 0$: critically stable wave

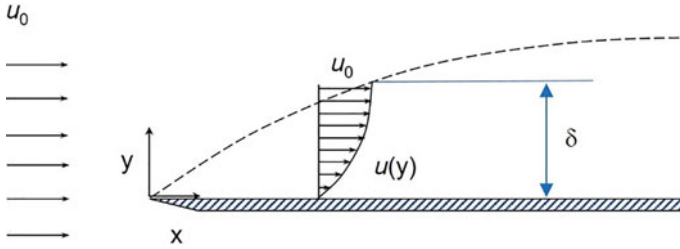


Fig. 1 Boundary layer flow over a flat plate

$i > 0$: stable wave.

Hence, for a spatial analysis problem, the stability of flow depends on the sign of α_i for a given value of Re , ω and Mach number M . The plot for the same at $\alpha_i = 0$ is known as the neutral curve, and shall be presented at the end of the analysis.

3 Problem Formulation

The flow of interest is the adiabatic compressible boundary layer flow over a flat plate. The fluid domain is rectangular, and mean flow is considered to be in the positive x -direction. The domain is divided into rectangular grids and the inlet is taken at the left end. The problem is interpreted in the form of similarity variables (Anderson), and solutions are calculated therewith. Figure 1 shows a schematic of the problem. Thereafter, the compound matrix of the system and its minors are obtained, and solved using RK4.

4 Similarity Profiles

The similarity solution is obtained by coordinate transformation, converting primary variables into transformed independent variables: $f_0 = u/u_e$, $g = h_0/(h_0)_e$. The system of Eqs. (1)–(3) is transformed as

$$\left(\frac{\rho u}{\rho_e u_e} f''\right)' + f f'' = 0 \tag{21}$$

$$\left(\frac{\rho u}{\rho_e u_e} \frac{1}{Pr} g'\right)' + f g' + \frac{u_e^2}{(h_0)_e} \left[\left(1 - \frac{1}{Pr}\right) \frac{\rho u}{\rho_e u_e} f' f''\right]' = 0 \tag{22}$$

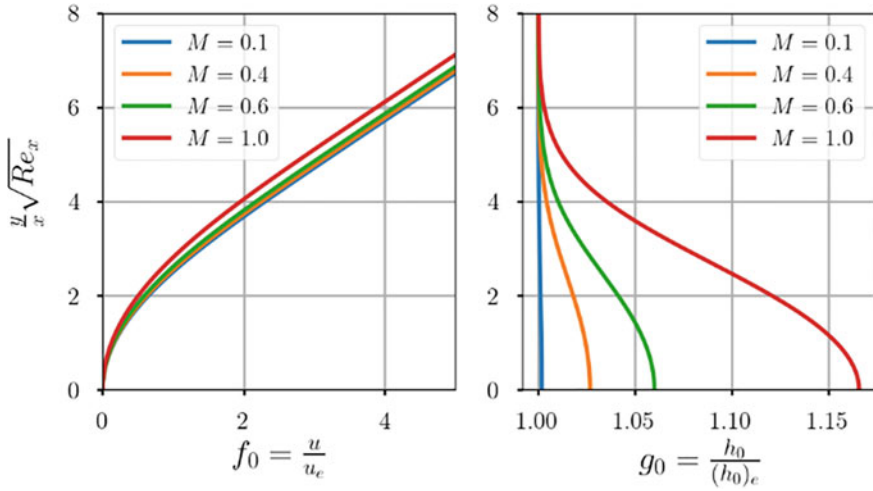


Fig. 2 Similarity profiles for subsonic Mach numbers

with the boundary conditions $f = f' = 0, g' = 0$ at $\eta = 0$ and $f' = 1$ at $\eta \rightarrow \infty$. The terms u_e, ρ_e, μ_e refer to velocity, density and viscosity at the boundary layer edge respectively. The prime quantities here denote differentiation with respect to η , and hence, the velocity profiles plotted are same at any point perpendicular to the wall.

Setting up the simulation requires defining a system of 5 equations of the form $[X]' = A[X]$, where $[X] = [f, f', \alpha f'', g, \alpha g']^T$. The system requires 5 boundary conditions, out of which 3 are known, and 2 are guessed [17]. This is the shooting method where $\alpha f''(0), g(0)$ are guessed such that $f'(\infty) \rightarrow 1, g(\infty) \rightarrow 1$.

Figure 2 shows the profiles for subsonic Mach numbers of $M = 0.1, 0.4, 0.6$.

5 Compound Matrix Method

The system of equations described in Eq. (19) is a sixth order ODE, converted to a system of 6, first order equations. We now create a compound matrix for the equations, using the methodology described below. The objective is to come up with the compound matrix, its minors, and a system of equations with their derivatives (of the minors). For the problem described in Fig. 1, the boundary conditions for the system at the plate are adiabatic:

$$\begin{aligned} X_1(0) = X_2(0) = X_3(0) = X_4(0) = X_6(0) = 0 \\ X_5(0) = T_w \end{aligned} \tag{23}$$

At the free stream, the variables reach their mean values, and derivatives decay to zero:

$$\begin{aligned} X_1(\infty) &= X_3(\infty) = X_5(\infty) = 1 \\ X_2(\infty) &= X_4(\infty) = X_6(\infty) = 0 \end{aligned} \quad (24)$$

Using the polynomial representation as the general solution of the system, we express $X = \sum_{i=1}^6 a_{i,j} X_{i,j}$. Index i represents the 6 equations, and $j = 1, 3, 5$ denotes the three prominent modes.

$$X_i = \sum_{j=1,3,5} a_{i,j} X_{i,j} \quad (25)$$

$$X_{i'} = \sum_{j=1,3,5} A_{ij} X_{ij} \quad (26)$$

$A_{i,j}$ is the compound matrix, of size $(6, 3)$. It has ${}^6C_3 = 20$ minors. They shall be indexed as i, j, k denoting all possible combinations. For instance, the minor for indices 1, 2, 3 would be

$$Y_{1,2,3} = \begin{vmatrix} A_{1,1} & A_{1,3} & A_{1,5} \\ A_{2,1} & A_{2,3} & A_{2,5} \\ A_{3,1} & A_{3,3} & A_{3,5} \end{vmatrix} \quad (27)$$

And ultimately we obtain $Y' = [B]Y$, which is solved using RK4. The matrix $[B]$ is a function of $B(\alpha, \omega, \text{Re}, M)$ and nontrivial solutions exist only for certain combinations of these parameters. This turns the exercise into an eigenvalue problem $\hat{D}(\alpha, \omega, \text{Re}, M) = 0$.

A circular approach is taken to solve the system. We first choose Re, ω , and find pairs of (α_r^*, α_i^*) such that $X_1(0) = 0$. These pairs are the eigenvalues of the system, and only one of them will be the most stable. Once we have a pair of values $(\alpha^*, \omega, \text{Re}, M)$, we now sweep across pairs of Re, ω and calculate α_r, α_i for every such pair. Finally, the curve tracing $\alpha_i = 0$ is the neutral curve for the given Mach number M .

6 Results

The compressible boundary layer flow over an adiabatic flat plate is set up in 2D using CMM, and run for $M = 0.1, 0.6$. The results are compared against the incompressible OSE.

Grid Search Technique: The first step is to perform the grid search, for selected values of Re, ω , looping over ranges defined for α_r, α_i . The simulation also requires guess values of $\alpha f''(0), g(0)$ as described in Sect. 4. The Table 1 lists the values taken in this simulation. The contours in Fig. 3 plot for $Re(y_1(0)), Im(y_1(0))$, and the crossings depict the various modes in the system. The point labelled Mode-1, marked at $(0.28, -0.007)$ among others that are marked similarly. Out of these, only one is the dominant mode and rest are spurious. This is ascertained by refining (α_r, α_i) more.

Polishing: The modes obtained above need to be refined to higher accuracy. It is known that the grid search modes are accurate to an order of magnitude $10^{-2}-10^{-1}$. This needs to be brought down to $10^{-7}-10^{-5}$. Table 2 shows the modes and their respective polished values.

Neutral curve: Once the polished values are established, we get a true set of values for $Re, \omega, \alpha_r^*, \alpha_i^*$. Understanding that the same procedure (grid searching, polishing) can be repeated for other points in proximity to Re, ω , we can sweep throughout the $Re-\omega$ plane, and obtain the curve for which $\alpha_i^* = 0$. This is the neutral curve for the given Mach number and the adiabatic flat plate problem.

Table 1 Grid search parameters for $M = 0.1$

Re	ω	α_r	α_i	$f''(0)$	$g(0)$
1000	0.01	[0, 0.4]	[-0.05, 0.05]	0.33	1

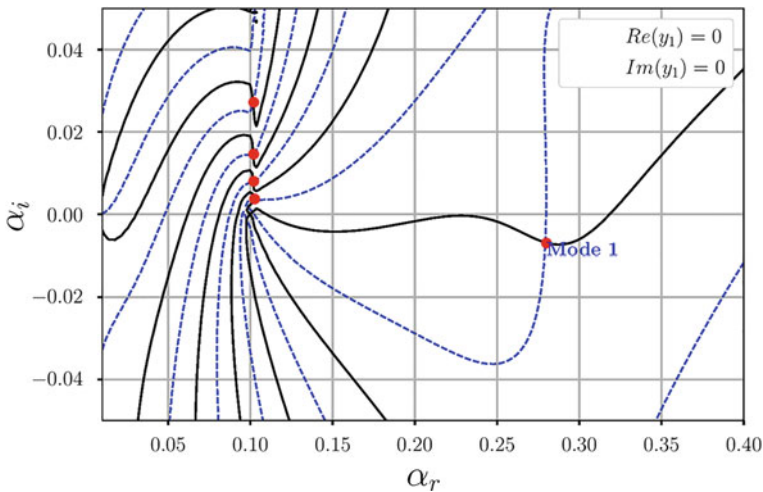


Fig. 3 Contours of $y_1, (0) = 0, y_1, (0) = 0$ for $M = 0.1, Re = 1000, \omega = 0.1$ in (α_r, α_i) plane

Table 2 Polished values for modes obtained from grid search technique $M = 0.1$, $Re = 10^3$, $\omega = 0.1$

	Eigenvalues from Grid search		Polished eigenvalues	
	α_r	α_r	α_r^*	α_r^*
	0.1020	0.0146	0.1386	0.111
	0.1022	0.0272	0.137	0.1077
	0.1023	0.0087	0.133	0.1092
	0.1023	0.0037	–	–
Mode 1	0.2801	–0.0071	0.279	–0.6868E – 02

7 Conclusions

This study explores the problem of 2-dimensional boundary layer flow over a flat plate, with adiabatic boundary conditions, and illustrates the validity of the Compound Matrix Method for the same (Fig. 1).

The system of 3 governing equations is converted into 20 Compound matrix equations. Neutral curves are plotted for $M = 0.1$, 0.6, and the incompressible OSE for validation. The critical Reynolds number is found to be $Re_{cr} = 523.7$, 567.7 for $M = 0.1$, 0.6 respectively.

A neutral curve can be divided into two parts (upper and lower section), separated by the Re_{cr} point. The curves.

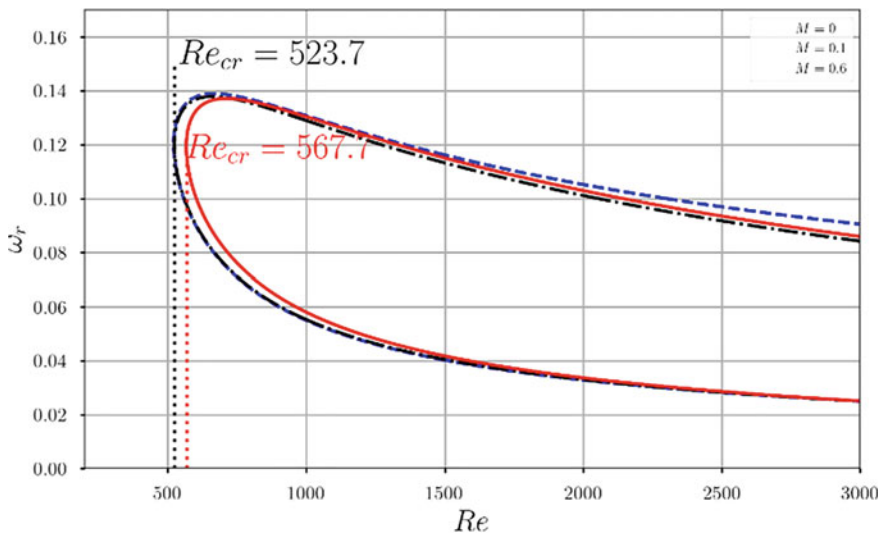


Fig. 4 Neutral curves for $M = 0.1$ (black), $M = 0.6$ (red) compared with incompressible (blue) OSE

- $M = 0.1$ versus $M = 0$ (OSE): the curves are obtained from different sets of equations. The lower section coincides for both, whereas for the upper section, OSE envelopes $M = 0.1$. The deviation is a result of changes in Re and ω , that become significant for large values.
- $M = 0.1$ versus $M = 0.6$: the effects of compressibility start to get more pronounced with increasing Mach numbers. The flow is getting *faster*, and the onset of transition and turbulence are successively delayed. This leads to a slight increase in Re_{cr} , and the curve shifts to the right. Also, the area of unstable region is smaller for $M = 0.6$, and this trend shall continue for further subsonic Mach numbers.

To sum up, this paper provides an outline of CMM and its applicability to simulating compressible linear stability problems. The end result is in the form of neutral curves (Fig. 4) that distinguish a stable and unstable zone for each M . The area of this curve, and Re_{cr} are two important properties that determine the nature of flow and its stability characteristics. Further studies are required to explore the relation between M and Re_{cr} as well as the exact nature of shape of the curve.

Appendix

Coefficients of Eq. (19)

$$A_{21} = \frac{\alpha^2 \mu}{\text{Re}} + i\rho Q \quad (28)$$

$$A_{22} = \frac{-c_1}{\text{Re}} \quad (29)$$

$$A_{23} = \alpha \underline{\rho} U_y - \frac{i\alpha^2 c_1}{\text{Re}} + \frac{i\alpha^2 \left(\frac{\mu + \lambda}{\text{Re}} \right)}{\rho \text{Re}} \underline{\rho}_y \quad (30)$$

$$A_{24} = i\alpha^2 - \frac{\alpha^2 \gamma Q M^2}{\rho T} \left(\frac{\mu + \lambda}{\text{Re}} \right) \quad (31)$$

$$A_{25} = \frac{\alpha^2 Q}{T} \left(\frac{\mu + \lambda}{\text{Re}} \right) - \frac{\alpha c_2}{\text{Re}} \quad (32)$$

$$A_{26} = -\frac{\alpha c_3}{\text{Re}} \quad (33)$$

$$A_{31} = -i \quad (34)$$

$$A_{33} = -\frac{1}{\rho} \underline{\rho}_y \quad (35)$$

$$A_{34} = -\frac{iQ\gamma M^2}{\rho T} \quad (36)$$

$$A_{35} = \frac{iQ}{T} \quad (37)$$

$$A_{41} = \frac{1}{\rho} \frac{2\mu + \lambda}{\text{Re}} \rho_y - \frac{2ic_1}{\text{Re}} \quad (38)$$

$$A_{42} = -i \frac{\mu}{\text{Re}} \quad (39)$$

$$A_{43} = \frac{2\mu + \lambda}{\text{Re}} \left(\left(\frac{\rho_y}{\rho} \right)^2 - \left(\frac{\rho_y}{\rho} \right)_y \right) - \frac{2c_1 + d_1}{\text{Re}} \left(\frac{\rho_y}{\rho} \right) - \frac{\alpha^2 \mu}{\text{Re}} - i\rho Q \quad (40)$$

$$A_{44} = \gamma M^2 \left[\frac{2\mu + \lambda}{\text{Re}} \left(\frac{iQ}{\rho^2} \rho_y + \frac{iQ(\rho T)_y}{(\rho T)^2} - \frac{i\alpha U_y}{\rho T} \right) \right] - \gamma M^2 \left[\frac{2c_1 + d_1}{\text{Re}} \frac{iQ}{\rho T} \right] \quad (41)$$

$$A_{45} = \left[\frac{2\mu + \lambda}{\text{Re}} \left(\frac{i\alpha}{T} U_y - \frac{iQ}{T^2} T_y - \frac{iQ}{\rho T} \rho_y \right) \right] + \left[\frac{2c_1 + d_1}{\text{Re}} \frac{iQ}{T} + \frac{i\alpha C_3}{\text{Re}} \right] \quad (42)$$

$$A_{46} = \frac{2\mu + \lambda}{\text{Re}} \frac{iQ}{T} \quad (43)$$

$$A_{62} = \frac{-(\gamma - 1)M^2 \mu}{\text{Re}} \frac{2}{\alpha} U_y \quad (44)$$

$$A_{63} = \rho c_{p\text{eff}} T_y - 2i(\gamma - 1) \frac{\mu}{\text{Re}} U_y M^2 \quad (45)$$

$$A_{64} = -(\gamma - 1)M^2 iQ \quad (46)$$

$$A_{65} = \rho c_{p\text{eff}} iQ + \frac{\kappa \alpha^2 - c_6}{\text{Re Pr}} - \frac{(\gamma - 1)M^2 c_5}{\text{Re}} \quad (47)$$

$$A_{66} = -\frac{2c_7}{\text{Re Pr}} \quad (48)$$

References

1. Ashpis DE, Reshotko E (1990) The vibrating ribbon problem revisited. *J Fluid Mech* 213:531–547

2. Schubauer GB, Skramstad HK (1947) Laminar boundary-layer oscillations and transition on a flat plate. *J Res Natl Bur Stand* 38:251
3. Cunningham W (1963) The concept of stability. *Am Sci* 51(4):425–436
4. Drazin PG, Reid WH (2004) *Hydrodynamic stability*. Cambridge University Press
5. Mack LM (1984) *Boundary-layer linear stability theory*. California Inst of Tech Pasadena Jet Propulsion Lab
6. Tollmien W (1936) General instability criterion of laminar velocity distributions
7. Köhler M (2011) Development and implementation of a method for solving the laminar boundary layer equations in airfoil flows. Master's Thesis, Technische Universität
8. Gurarslan G, Karahan H, Alkaya D, Sari M, Yasar M (2013) Numerical solution of advection-diffusion equation using a sixth-order compact finite difference method. *Math Probl Eng* 2013
9. Garicano-Mena J, Ferrer E, Sanvido S, Valero E (2018) A stability analysis of the compressible boundary layer flow over indented surfaces. *Comput Fluids* 160:14–25
10. Zhang Y, Oberlack M (2021) Inviscid instability of compressible exponential boundary layer flows. *AIP Adv* 11(10):105308
11. Bertolotti F, Herbert T (1991) Analysis of the linear stability of compressible boundary layers using the PSE. *Theor Comput Fluid Dyn* 3(2):117–124
12. Malik MR (1982) Finite-difference solution of the compressible stability eigenvalue problem. NASA
13. Ng B, Reid W (1985) The compound matrix method for ordinary differential systems. *J Comput Phys* 58(2):209–228
14. Aubry N (1991) On the hidden beauty of the proper orthogonal decomposition. *Theor Comput Fluid Dyn* 2(5):339–352
15. Özgen S, Kırçalı SA (2008) Linear stability analysis in compressible, flat-plate boundary-layers. *Theor Comput Fluid Dyn* 22(1):1–20
16. Tumin A (2010) Flow instabilities and transition. *Encycl Aerosp Eng*, 139–150
17. Anderson JD (1990) *Modern compressible flow: with historical perspective*, vol 12. McGraw-Hill, New York

Wavy Dynamics of Confined and Inclined Falling Liquid Films



Saurabh Dhopeswar, Ujjwal Chetan, Toshan Lal Sahu, Prabir Kumar Kar, Suman Chakraborty, and Rajaram Lakkaraju

Abstract We present direct numerical simulations of thin viscous films falling in inclined channel of constant relative confinement, $\eta = 2$. The two films with the same Kapitza number, $Ka = 509.5$, flow in a passive and quiescent atmosphere of air, in presence of gravity, with a suitable monochromatic perturbation, applied at the liquid-velocity inlets. The study is made for different values of liquid flow Reynolds number, Re as a control parameter defined in terms of Nusselt flat film solution. Any orientation of films other than vertical leads to symmetry breaking causing the waves to grow differently on both interfaces. Variations of film flow characteristics such as wave amplitude (h), streamwise velocity (u), and minimum occlusion distance (d_{\min}) are examined with Re for both films. The oscillatory behavior of films ranging from progressive periodic to solitary waves with flow reversals is observed for different values of Re . These flow variations are subjected to suppression when the films undergo strong confinement. Suitable scaling law is reported for d_{\min} as a function of Re for two different values of channel inclination.

Keywords Reynolds number · Kapitza number · Solitary wave · Hydrodynamic and Rayleigh–Taylor instability

1 Introduction

Liquid film flow in narrow channels has numerous industrial applications. For example, transport operations in microelectronic equipment [1] and distilled columns in structural packing [2] employ liquid films to perform desired functions. In these

S. Dhopeswar (✉) · U. Chetan · S. Chakraborty · R. Lakkaraju
Department of Mechanical Engineering, IIT Kharagpur, Kharagpur 721302, India
e-mail: sadh0206@gmail.com

T. L. Sahu
Advanced Technology Development Centre, IIT Kharagpur, Kharagpur 721302, India

P. K. Kar
School of Energy Science & Engineering, IIT Kharagpur, Kharagpur 721302, India

applications, the wavy interaction between phases becomes important as it governs the efficiency of the concerned technological operation. Films over solid and inclined surfaces undergo an interfacial instability often referred to as hydrodynamic or Kapitza instability [3]. The waves on the liquid–air interface evolve either naturally, or “forced” via the imposition of inlet frequency forcing, which ensures that waves are of constant amplitude on the films within a finite length of the domain [4]. When excited at low frequencies, films exhibit solitary waves, which are large amplitude humps with long tails and steep fronts, along with front running capillary ripples at the interface [5]. The fluctuation of velocity underneath the wave trough and capillary wave region was observed to have much higher values as compared to the other flow regions, due to the large interfacial curvature there [6]. Backflow phenomena or flow reversals in the capillary region due to its short wavelength and curvature are reported for laminar falling liquid films [7, 8]. These reversals are prone to occur due to adverse pressure gradients acting in opposite direction to streamwise gravity. The variations in solitary wave characteristics on inertia-dominated falling films were studied for Reynolds number, plate inclination angle, and other control parameters, and suitable scaling laws were proposed [9]. Films flowing underneath the solid surfaces are also subjected to Rayleigh–Taylor instability apart from the hydrodynamic one [10]. Similar to films flowing over surfaces, these films also show the dependence of wave characteristics on Reynolds number and inclination angle.

Wavy films may experience flooding in the form of wave coalescence or occlusion when three fluid systems flow in a confined environment such as a channel or tube. The trigger of wave occlusion was observed to have a strong dependence on higher values of both Reynolds number and inclination angle [11, 12]. The occlusion scenarios were numerically examined by Dietze et al. [13] in terms of minimum occlusion distance variation with gravity, inertia, and surface tension coefficients. The occlusion was found to get delayed with gravity but precipitated with an increase in inertia and surface tension.

The occlusion scenarios in wavy films flowing in a three-layer system lead to plug formation (or slug flow) that causes enormous stress on the solid walls as well as drastically affects the performance of the desired industrial application [14]. To the best of our knowledge, less attention has been focused on film flows in such geometries. Moreover, a similar study with inclined films motivates us to investigate and compare the wave evolution on films on each channel wall for different orientations and identify the critical parameter(s) that ultimately leads to occlusion scenarios. As far as wave evolution and propagation are concerned, the channel orientation leads to the growth of waves differently on both interfaces. Consequently, it will also affect the flow structures and momentum transport between different fluid phases. In the present work, we study the variation of wave characteristics on two films with time at different Reynolds numbers, such that the channel is oriented at a specific angle. Consequently, we also compare the occlusion distance variation with Re to that of vertically oriented films and deduce a suitable scaling law.

2 Methodology

The solver, interFoam based on FVM framework from OpenFOAM 7.0 toolbox [15, 16] is used to study the present work. It utilizes the volume of fluid (VOF) method [17] particularly to solve multiphase problems of isothermal, incompressible, and immiscible fluids.

2.1 Physical System and Governing Equations

We consider a laminar flow system of two viscous liquid films in a quiescent atmosphere of air and confined between two planar walls of an inclined channel (see Fig. 1). The two films flow under gravity as shown in the figure. The fluid system is initially assumed to have well defined flat liquid–gas interfaces such that by Nusselt’s theory, film thickness and fully developed stream-wise velocity is given by $h_N = (3\nu_l^2 \text{Re}/g \sin \theta)^{1/3}$ and $u_N = g \sin \theta h_N^2 / 3\nu_l$ respectively, where $\nu_l = \mu_l / \rho_l$ is the kinematic viscosity of the liquid films. The two walls of the channel are separated from each other by a constant confinement ratio, $\eta = H/2h_N = 2$ so that $H = 4h_N$. The length, L of the walls is also considered as a function of film thickness, equal to $500h_N$. Such a choice of variable length was found to be sufficient to accommodate the fully developed waves [6]. The Reynolds number for the liquid film is defined as $\text{Re} = u_N h_N / \nu_l$, which compares flow inertia to the viscous effects. The two films are considered to be of the same Kapitza number, $\text{Ka} = 509.5$. The x and y coordinate axes are aligned as shown in the figure such that the channel is symmetrical about the x -axis. The left, right, and top walls of the channel are subjected to no slip and no flux conditions. The two liquid films enter the domain each through an inlet section which is taken the same as the corresponding value of h_N . The inlet velocity of the liquid film is considered as $u_{\text{in}} = 6u_N \left[\left(\frac{Y}{h_N} \right) - \left(\frac{Y}{h_N} \right)^2 \right] \cdot [1 + \varepsilon \sin(2\pi f t)]$, where $Y = \pm(H/2 - y)$ such that the variation in y is valid only in the liquid regions; the positive sign stands for the right film while the negative sign for the left film. The above form of scaled parabolic inlet velocity is coupled with a monochromatic perturbation with amplitude and frequency as $\varepsilon = 0.05$ and $f = 15$ Hz respectively [18].

The fluid flow in the present system is described by Navier–Stokes equations through the VOF method which is based on solving a single set of conservation equations of continuity and momentum for a hypothetical fluid of density ρ and dynamic viscosity μ . These properties of the fluid are calculated as the weighted average of the corresponding properties of individual fluids: $\rho = \alpha\rho_l + (1 - \alpha)\rho_g$ and $\mu = \alpha\mu_l + (1 - \alpha)\mu_g$. The quantity α corresponds to the volume fraction of the reference fluid. Subscripts l and g stand for the liquid and gas phases respectively. The relevant continuity and momentum equations are:

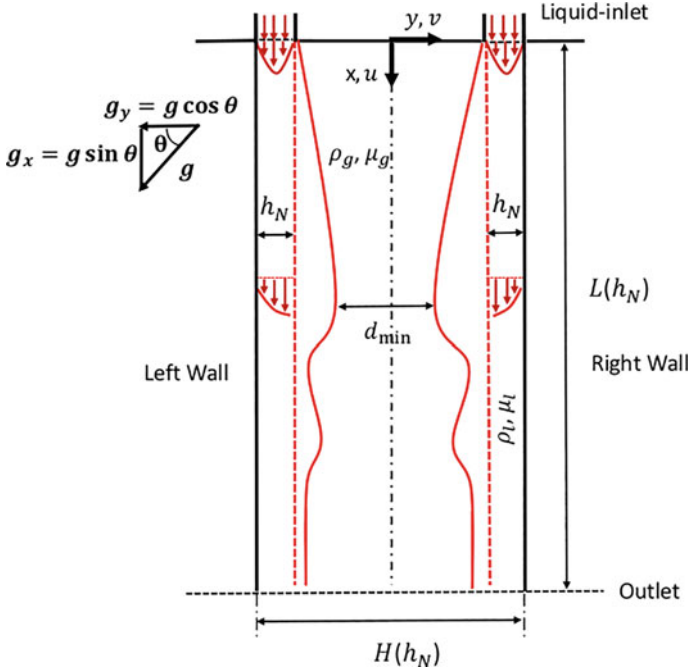


Fig. 1 Schematic diagram of wavy falling films in an inclined channel

$$\nabla \cdot \vec{u} = 0 \quad (1)$$

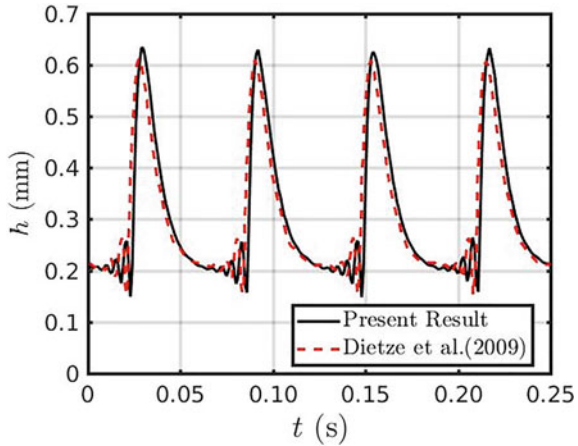
$$\rho \frac{D(\vec{u})}{Dt} = -\nabla p + \mu \nabla \cdot (\nabla \vec{u} + (\nabla \vec{u})^T) + \rho \vec{g} + \vec{F}_s \quad (2)$$

where \vec{u} is the velocity, p is the pressure and \vec{F}_s represents additional forces due to interfacial surface tension which is distributed over a thin interfacial layer. The continuum surface force (CSF) has been employed to model surface tension [19]. With the introduction of weighted average α , the interface between the phases is tracked by solving an additional advection equation 3 of scalar α .

$$\frac{\partial \alpha}{\partial t} + \nabla \cdot (\vec{u} \alpha) = 0 \quad (3)$$

$\alpha = 0.5$ is used for the representation of the liquid–gas interface. In all our simulations, an adaptive time step was used such that the maximum Courant number did not exceed the value of 0.3.

Fig. 2 Validation: Comparison of time variation of dimensional liquid film (in mm) at location $x = 120$ mm from inlet for simulated vertical falling film with $Ka = 509.5$, $Re = 15$, $f = 16$ Hz



2.2 Validation

To assure the validity of the methodology, validation is carried out for the non-linear wave evolution on falling liquid films over plane surfaces (see Fig. 2) with the same flow conditions and transport properties as reported by Dietze et al. [18]. The plots in the figure show good agreement for film height.

3 Results and Discussion

Falling films over flat surfaces are subjected to hydrodynamic instabilities in which the streamwise component of gravity, $g \sin \theta$ assists the waves to grow at the liquid–air interface. The cross-stream component, $g \cos \theta$ acts normal and towards the surface resisting wave growth [3]. On the other hand, films flowing underneath the flat surfaces (hanging films) are subjected to Rayleigh–Taylor instabilities along with the hydrodynamic one [10]. In these cases, $g \cos \theta$ also acts normally but away from the planar surface, thus assisting the wave growth along with that of $g \sin \theta$.

Figure 3 depicts the time variation of liquid film’s heights on both walls at $x/L = 0.75$ and $\theta = 60^\circ$. The heights are normalized with their respective Nusselt thicknesses, h_N . For $Re = 5$ (see Fig. 3a), the waves on the surfaces of the two films vary almost out of phase with each other such that the waves on the right film show higher amplitude as compared to that of the left film. This is because the right film is the hanging one subjected to both hydrodynamic and Rayleigh–Taylor instability. At this Reynolds number, the inertia plays only a perturbative role and the amplitudes of the waves result due to the competition between gravity and viscous forces. These waves are progressive periodic waves resembling the appearance of Stokes waves. At

$Re = 10$, the inertia becomes dominant over both gravity and viscous forces. Consequently, the disturbances over film interfaces also increase showing the formation of large wave humps with small front running capillary ripples. These wave humps are nothing but solitary waves that are of constant amplitudes and occupy the maximum span of the film interfaces. The difference in phases of both films is reduced and the amplitudes with respect to Nusselt thickness are increased. The heights of the films increase further at $Re = 15$ with two additional differences observed as compared to that of $Re = 10$. The first difference is that the number of smaller ripples ahead of the wave hump increase. The second is, the left film responds to the disturbance lately as compared to the right film such that the waves on the left film lag the right one which was the opposite in the case of $Re = 10$. With increase in Re , the difference in wave amplitudes of both films reduce such that at $Re = 17$ (not shown here), the amplitude becomes equal. For $Re \leq 17$, a higher amplitude is found for the right film as compared to the left film. However, at $Re = 20$ (see Fig. 3d) a suppression of instability is observed for the hanging film such that the maximum height of this film decreases as compared to the left one. Instead, the maximum height of the left film was observed to rise with an increase in Re even after $Re \geq 17$ (till the maximum value of Re examined), dominating the spatial region in the cross-stream direction. The growth of disturbance makes both the films come in proximity such that they start interacting in a manner that the one that lags in response to disturbance, dominates the other. At $Re = 20$ the left film lags and hence dominates the hanging film.

Figure 4 shows the time variation of the stream-wise velocity field at location $x/L = 0.75$ measured from the inlet for four different Reynolds numbers. The velocity field is normalized with Nusselt flat film average velocity, u_N . The reason for normalization is that it eases the understanding of the response of the velocity field to the disturbance with respect to the average velocity. Two different location points in the liquid bulk: $\frac{Y}{h_N} = \pm 0.1$ where $Y = \pm(\frac{H}{2} - y)$ are considered for computing the velocities in the liquid domain close to the walls. At $Re = 5$, velocity fields are enslaved to film height evolution with space and time and show similar oscillatory behaviour even though the location of sample points is far from the respective liquid–air interfaces. The velocities vary differently in phases but with the same maximum amplitude. At $Re = 10$ (see Fig. 4b), the fluctuation of velocity fields is almost the same in phase for both films. However, a momentarily negative velocity (in the form of sharp valleys) can be observed that depicts the reverse flow within the liquid film that takes place at a particular instant. The reverse flow is due to the adverse pressure gradient acting in front of the main hump [7]. It is found to be higher in the hanging film as compared to the other one. In the case of $Re = 15$, the velocity fields vary neck to neck for both the films with a slight increment in both peaks and valleys of the right film compared to that of the left film. At $Re = 20$ (see Fig. 4d), a decrement in both maximum and minimum velocities is observed compared to that at $Re = 10$ and 15 for both films. It is important to note that the dimensional velocities would have higher values at this Re as compared to that of lower Re values. At this Reynolds number, the films interact with each other as they come under close confinement leading to the suppression of instability. This too causes a decrement in the growth

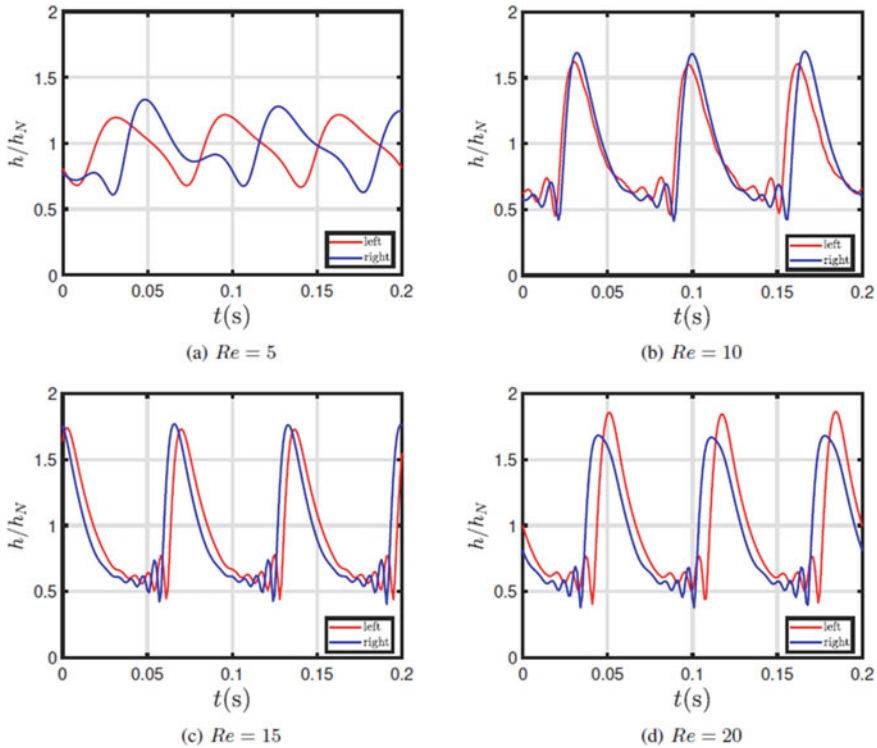


Fig. 3 Variation of normalized film height with time of both the films at $x/L = 0.75, \theta = 60^\circ$ for different Reynolds number

of disturbance on the velocity field, which possibly would not have been observed if the films were largely confined.

Figure 5 depicts the variation of minimum occlusion d_{min} with Re for the two different channel inclination values. d_{min} is calculated by taking the average of all valleys after the waves attained the fully developed state till the final simulation time. For both the angles, d_{min} decreases with an increase in Re with an approximate fit:

$$\delta = d_{min}/H = aRe^2 - bRe + c \tag{4}$$

where a, b, c are constants that depend on the value of θ . The values of fitting parameters are given in Table 1. It is important to note that at every Re value, the magnitude of d_{min} for $\theta = 60^\circ$ is higher as compared to that of $\theta = 90^\circ$. When the channel is vertically oriented, the two films are symmetrical to each other and only the stream-wise component of gravity acts on both films without any presence of a cross-stream component. Therefore, the waves on both films grow and propagate symmetrically with maximum amplitude and phase and minimum occlusion distance is least for vertically oriented falling films. When the channel is oriented at any angle

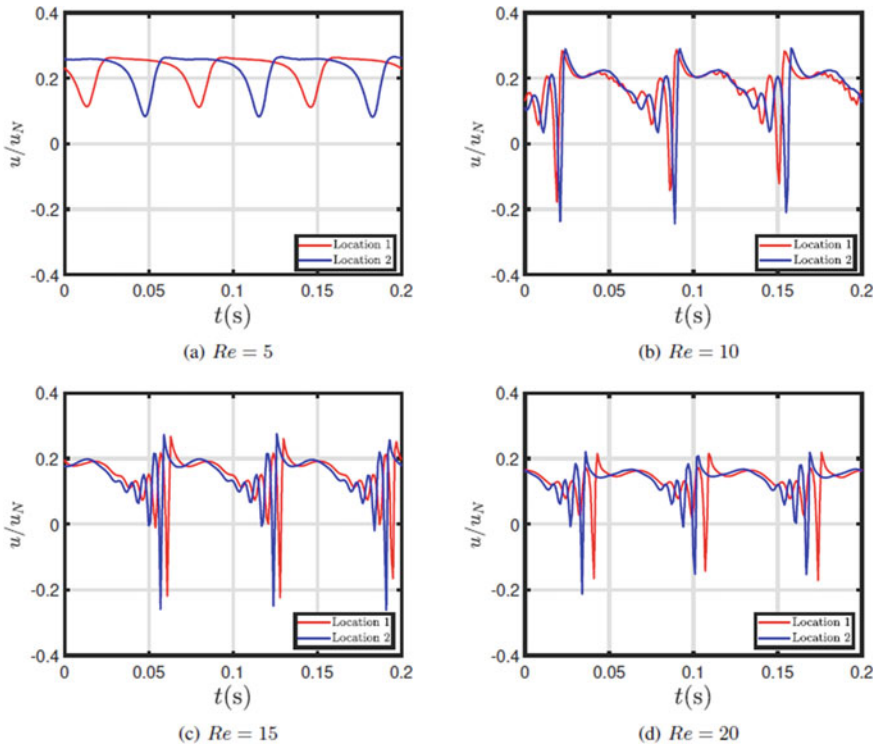


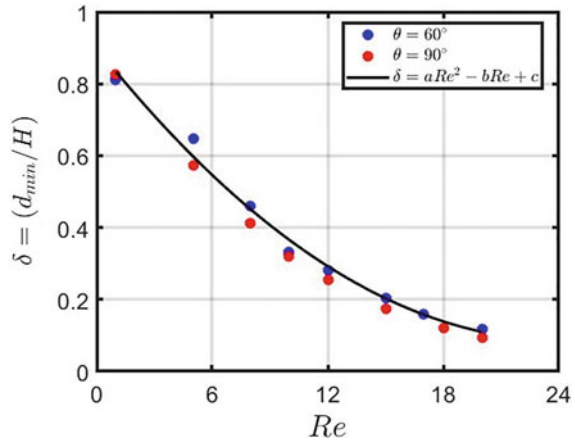
Fig. 4 Variation of normalized streamwise velocity with time in bulk of both the films close to the wall for different Reynolds number. Locations 1, 2: $(x/L, \mp(H/2-y)/h_N) = (0.75, 0.1)$, $\theta = 60^\circ$

other than $\theta = 90^\circ$ ($\theta = 60^\circ$ in the present case), the symmetry breaks due to different actions of the cross-stream component of gravity on both films. The left film now is subjected to only hydrodynamic instability while the right film is subjected to both hydrodynamic and Rayleigh–Taylor instabilities. This leads to a difference in both the growth of wave amplitudes and phases. The peaks now do not lay one over the other as in the case of vertically oriented films, rather their locations are somewhat relatively misaligned. Consequently, the minimum occlusion distance is higher as compared to that of vertical films.

Table 1 The values of the fitting parameters corresponding to the fitting equation in Fig. 5

θ	a	b	c
60°	0.0014	0.067	0.9
90°	0.0017	0.075	0.9

Fig. 5 Variation of minimum occlusion distance with Reynolds number



4 Conclusions

In this chapter, two-dimensional numerical simulations of wavy liquid films in inclined channels are performed using the VOF method. The two films with the same Kapitza number were considered to flow in a quiescent atmosphere between them along with monochromatic forcing applied at their respective inlets. The effects on flow parameters were studied for Reynolds number (Re) as the control parameter. On increasing Re , it was found that the interfacial disturbance grows with space and time on the interface of both the liquid films. Symmetry breaking is observed for films oriented at an angle $\theta = 60^\circ$ due to different actions of the cross-stream component of gravity on both films (which is not applicable for the case of $\theta = 90^\circ$). The hanging film on the right wall showed a higher amplitude than that of the other film at lower Re values. However, at comparatively higher Re values, the waves on films grow and come under proximity to influence each other such that the film that lags in response to disturbance (left film) dominates the other (hanging film). In this case, the stabilizing (left) film occupies the space of destabilizing film suppressing its maximum height. Similar behaviour is reflected in the time variation of the velocity field such that the growth of disturbance on the velocity field suppresses at a higher Reynolds number. Reverse flow is observed at values of $Re \geq 10$. However, the strength of reverse flow decreases when the films come under strong confinement. The minimum occlusion distance is found to vary quadratically with Re for both channel inclinations. The behaviour of the films so observed should be true for all other inclinations and is open for further investigation.

Acknowledgements We sincerely thank National Super Computing Mission-India and Param Shakti for providing the necessary computing resources

Nomenclature

t	Time [s]
g	Gravitational acceleration [m/s^2]
x, y	Streamwise and cross-stream coordinates [mm]
u, v	Streamwise and cross-stream velocities [m/s]
ρ	Density [kg/m^3]
μ	Dynamic viscosity [Pa s]
ν	Kinematic viscosity [m^2/s]
h_N	Nusselt flat film thickness [mm]
u_N	Nusselt flat film average streamwise velocity [m/s]
Re	Reynolds number [–]
Ka	Kapitza number [–]
θ	Channel inclination [–]
L, H	Length and width of channel [mm]
η	Channel confinement ratio [–]
ε	Perturbation amplitude at inlet [–]
f	Perturbation frequency at inlet [Hz]
α	Scalar volume fraction [–]
\vec{F}_s	Interfacial surface tension force [N]

References

1. Kabov OA, Kuznetsov VV, Legros JC (2008) Heat transfer and film dynamic in shear-driven liquid film cooling system of microelectronic equipment. In: The 2nd international conference on microchannels and minichannels
2. Haroun Y, Legendre D, Raynal L (2010) Direct numerical simulation of reactive absorption in gas-liquid flow on structured packing using interface capturing method. *Chem Eng Sci* 65:351–356
3. Kalliadasis S, Ruyer-Quil C, Velarde MG (2011) *Falling liquid film*. Springer
4. Chang H (1994) Wave evolution on a falling film. *Annu Rev Fluid Mech* 26:103–136
5. Nosoko T, Miyara A (2004) The evolution and subsequent dynamics of waves on a vertically falling liquid film. *Phys Fluids* 16:1118
6. Gao D, Morley B, Dhir V (2009) Numerical simulation of wavy falling film flow using VOF method. *J Comput Phys* 192:624–642
7. Dietze GF, Kneer R (2011) Flow separation in falling liquid films. *Front Heat and Mass Transfer* 2:033001
8. Dietze G, Al-Sibai F, Kneer R (2009) Experimental study of flow separation in laminar falling liquid films. *J Fluid Mech* 637:73–104
9. Denner F, Pradas M, Markides CN, van Wachem BGM, Kalliadasis S (2016) Self-similarity of solitary waves on inertia-dominated falling liquid films. *Phys Rev E* 93:033121
10. Rohlfes W, Pischke P (2017) Hydrodynamic waves in films flowing under an inclined plane. *Phy Rev Fluids* 2:044003
11. Drosos E, Paras S, Karabelas A (2005) Counter-current gas-liquid flow in a vertical narrow channel—liquid film characteristics and flooding phenomena. *Int J Multiph Flow* 32:51–81

12. Saenmart K, Cheowuttikul P, Suriyawong A, Wongwiset S (2008) Onset of flooding in a small diameter tube. *Int Commun Heat Mass Transfer* 35:458–465
13. Dietze GF, Lavallo G, Ruyer-Quil C (2020) Falling liquid films in narrow tubes: occlusion scenarios. *J Fluid Mech* 894:A17
14. Romano F, Fujioka H, Muradoglu M, Grotberg JB (2019) Liquid plug formation in an airway closure model. *Phys Rev Fluids* 4:093103
15. <https://openfoam.org/release/7/>
16. <https://www.openfoam.com/documentation/guides/latest/doc/guideapplications-solvers-multiphase-interFoam.html>
17. Hirt CW, Nichols BD (1981) Volume of fluid (VOF) method for the dynamics of free boundaries. *J Comput Phys* 201:201–225
18. Dietze G, Ruyer-Quil C (2013) Wavy liquid films in interaction with a confined laminar gas flow. *J Fluid Mech* 722:348–393
19. Brackbill J, Kothe DB, Zemach C (1992) A continuum method for modeling surface tension. *J Comput Phys* 100:335–354

Co-existence of Multiple Steady States in Bottom Heated Trapezoidal Closed Cavities



Govind Maurya, Alok Kumar, Nadeem Ahmed, and Suneet Singh

Abstract The natural convection in bottom heated symmetric trapezoidal closed cavities filled with air is studied, where inclined side walls were adiabatic. From the simulations, it is observed that multiple stable steady states coexist in obtuse angle trapezoidal cavities (OATZC) beyond critical Rayleigh number (Ra). Out of these, two solutions are mirror image solutions due to the symmetry of OATZC about vertical midplane. Multiple stable steady states in square cavities, having numbers even, have been documented in the literature; however, in the case of the OATZC, odd numbers of coexisting solutions are found, and no such study has been reported previously. The isotherms, velocity profiles, and Nusselt number behaviour have been shown as proof of the same.

Keywords Obtuse angle trapezoidal cavity · Critical Rayleigh number · Steady states · Symmetry

1 Introduction

Natural convection occurring across bottom-heated and top-cooled fluid layers is termed Rayleigh–Benard convection (RBC). RBC in closed square cavities has been investigated a lot and variation of its heat transfer characteristics with respect to various parameters has been presented by many authors [5, 6, 13, 19].

Natural convection in the bottom heated top open cavity has been studied, numerically and experimentally and various characteristics have been presented by [16, 17]. These studies focused on fluid movement inside the cavity and overlooked flow outside the cavity. However, RBC was investigated in top open cavities where fluid was permitted to flow outside the cavities and corner flow at smaller Ra and mirror image stable states has been observed.

The closed cavities can be either rectangular or trapezoidal based on the inclination of the sidewalls. TZC can be of two types depending on the angle of inclination,

G. Maurya · A. Kumar · N. Ahmed · S. Singh (✉)

Department of Energy Science and Engineering, IIT Bombay, Mumbai 400076, India
e-mail: suneet.singh@iitb.ac.in

acute or obtuse. In the same way, as Davis studied side-heated square cavity (de Vahl Davis, 1983) Igor et al. explored side-heated trapezoidal (SHTZ) cavities [12]. Rayleigh–Benard type stability breakdown was seen in AATZC where symmetry was not connected with stability breakdown [11].

Natural convection of air in OATZC was explored with 15° increments for cavity tilt angle from 0 to 90° , and power law behaviour of Nusselt number with Ra was observed over a wide range [8]. Numerical experiments were performed in a tilted non-rectangular enclosure and observed that the heat transfer and fluid motion are strong functions of Ra, Pr, and orientation angle of the cavity [9]. Iyican et al. investigated natural convection in 2D trapezoidal enclosures with adiabatic side walls and parallel cylindrical top and bottom walls using Galerkin's method and presented Nusselt number variation with Ra and sidewall inclination angles [10].

Natural convection in rectangular and trapezoidal cavities has received much attention due to its importance in industry and engineering applications, e.g. for studies of micro-fluids [4, 7], viscoelastic fluids [1], nanofluids [3, 15], nanofluids under external magnetic field [2, 14], magnetic fluids, etc. However, instabilities brought on by bottom heating in trapezoidal cavities are infrequently investigated.

The flow in the TZCs is not zero, even for lesser values of Ra than Ra_c this region is noteworthy. Due to negligible flow, pure conduction zones are found below Ra_c in a closed square cavity and above Ra_c , the flow begins and evolves to anti-symmetric steady states due to thermal-driven buoyant force. However, in the case of OATZC, there is a non-zero initial flow that is always present because of the non-zero component of the temperature gradient perpendicular to gravity. Hence, anti-symmetric steady-state solutions after stability breakdown are not intuitive, unlike closed square cavities, thus steady-state solutions are more interesting in OATZC. Symmetry in cavity leads to the existence of mirror image solutions [16, 18], and, thus even number of stable steady-state solutions coexist at a range of Ra in such cavities. In contrast to that, in 2D OATZC, an odd number of steady-state solutions, 2 anti-symmetric and one symmetric solution, co-exist beyond Ra_c .

2 Methodology

The heat transfer in fluids is regulated by Continuity, Momentum, and Energy equations which represent mass, momentum, and energy conservations in the system, respectively. Since fluid density depends on temperature, Boussinesq approximation, which states that density fluctuations have little impact on any term other than the gravity term, is applied. Conductivity, viscosity, specific heat, and other fluid parameters are considered to remain constant. The Boussinesq approximation holds good in the current investigation since the current work is at a very low Ra. The flow has been modelled by several researchers [7, 13] etc. to be laminar up to $Ra = 10^6$. Furthermore, laminar flow consideration is appropriate since the system is much below the oscillatory regime.

Non-dimensional form of governing equations, that is, continuity, momentum and energy equations are:

$$\partial_X U + \partial_Y U = 0$$

$$\partial_\tau U + \partial_X U^2 + \partial_Y (UV) = -\partial_X P + (\text{Pr}/\text{Ra})^{1/2} \nabla^2 U$$

$$\partial_\tau V + \partial_X (UV) + \partial_Y V^2 = -\partial_Y P + (\text{Pr}/\text{Ra})^{1/2} \nabla^2 V + \Theta$$

$$\partial_\tau \Theta + \partial_X (U\Theta) + \partial_Y (V\Theta) = (1/(\text{Pr} * \text{Ra}))^{1/2} \nabla^2 \Theta$$

$$X = x/H_c, Y = y/H_c, U = u/(g\beta H_c(T_h - T_c)^{1/2}),$$

$$V = v/(g\beta H_c(T_h - T_c)^{1/2}), P = (p - p_\infty)/(g\beta H_c(T_h - T_c)^{1/2}),$$

$$\tau = (g\beta H_c(T_h - T_c)^{1/2})t/H_c, \Theta = (T - T_c)/(T_h - T_c)$$

The velocity components are zero at the walls. The isothermal boundary condition is used at the bottom and top of the cavity while at the side walls, the adiabatic boundary condition is applied.

Isothermal B.C.: $\Theta = 0$

Adiabatic B.C.: $\partial\Theta/\partial n = 0$, where n is the normal direction to the wall.

3 Numerical Approach

ANSYS FLUENT has been used to create a 2-D model of a square cavity and OATZC. Except for density, air characteristic parameters are estimated using a piecewise method. FLUENT's PISO time-dependent scheme is used for the current problem. For the system's solution, the Non-dimensionalized form of continuity, Navier–Stokes, and energy equations are concurrently solved. The momentum and energy solution controls are of the second-order upwind type. 100×100 grid was used for numerical simulation throughout.

The convergence criterion for the continuity and velocity equations is of the order of 10^{-5} and for the energy equation is of the order of 10^{-6} . The ratio of the cavity's bottom length to its vertical height between its top and bottom is known as the aspect ratio. The simulation works have been performed for $A_p = 1$ in both square and trapezoidal cavities. The top and bottom plates are maintained at temperatures of 300 and 320 K, respectively, and Ra is increased by enlarging the cavity size. The remaining parameters are maintained as listed in Table 1. The side adiabatic walls have been subjected to no-slip boundary conditions.

Table 1 Physical property of the air at the mean temperature ($T_m = 310$ K)

g	Gravity (m/s^2)	9.81
β	Thermal expansion coefficient (1/K)	3.37×10^{-3}
ρ	Density (kg/m^3)	1.19
ν	Kinematic viscosity (m^2/s)	1.53×10^{-5}
α	Thermal diffusivity (m^2/s)	2.15×10^{-5}
C_p	Specific heat (J/kg K)	1.0×10^3
κ	Conductivity (w/m K)	0.0258

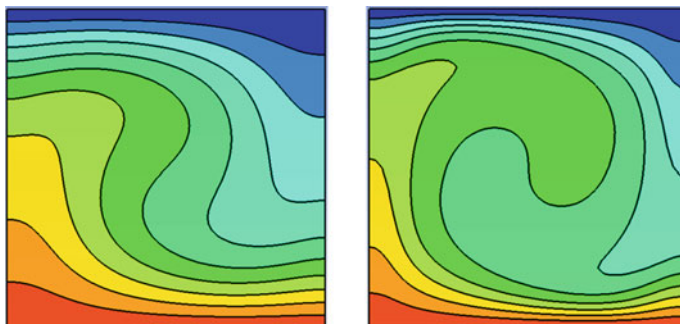


Fig. 1 Isotherms in square cavity for $Ra = 10^4$ and 10^5 respectively

4 Verification with Benchmark

In a closed-bottom heated square cavity, Ouertatani et al. [13] employed the finite volume method and full multigrid acceleration to propose benchmark solutions for isotherms, maximum velocity, and local Nusselt number in the range of Ra , 10^3 – 10^6 (Fig. 1).

The same model was numerically simulated in the ANSYS FLUENT software for validation against the Ouertatani maxima of non-dimensionalized U and V velocities at the vertical and horizontal midplanes of the cavity Table 2 are presented here which match very well with the results of [13]. Although dimensionless U and V velocity profiles and streamlines match well, but not shown here due to constraints. The value of maximum velocities and their positions are well accurate as presented in Table 2.

5 Results and Discussion

In this study, OATZC having cavity angle 95° and aspect ratio 1 has been investigated. The ratio of the cavity's bottom length to the smallest distance between its parallel top and bottom plates is known as the aspect ratio. Simulations are run with at 100×100 mesh size while maintaining the other parameters from Table 1. The simulations

Table 2 Comparison of velocity and position maxima with [13]

Ra	$y(u_{\max})$	u_{\max}	$x(v_{\max})$	v_{\max}
Ouer- 10^4	0.8023	0.25228	0.8263	0.26369
Gov- 10^4	0.7959	0.25119	0.8163	0.26278
%error	0.80	0.43	1.21	0.35
Ouer- 10^5	0.8636	0.34434	0.8973	0.37569
Gov- 10^5	0.8571	0.34342	0.8979	0.37300
%error	0.75	0.27	0.07	0.72

are carried out at 7000 Ra and it is observed that multiple steady-state solutions co-exist together. The isotherms are presented in Fig. 2a–c. Figure 2a and b represents mirror image solutions which are having anti-symmetry about vertical midplane, while Fig. 2c represents a symmetric solution.

Since mirror image solutions have the same streamlines and velocity profiles except for the direction of roll which use to be in the reverse direction. The simulated results of streamlines, velocities U , V , and velocity magnitude have been shown for one anti-symmetric and symmetric type of solution in Fig. 3.

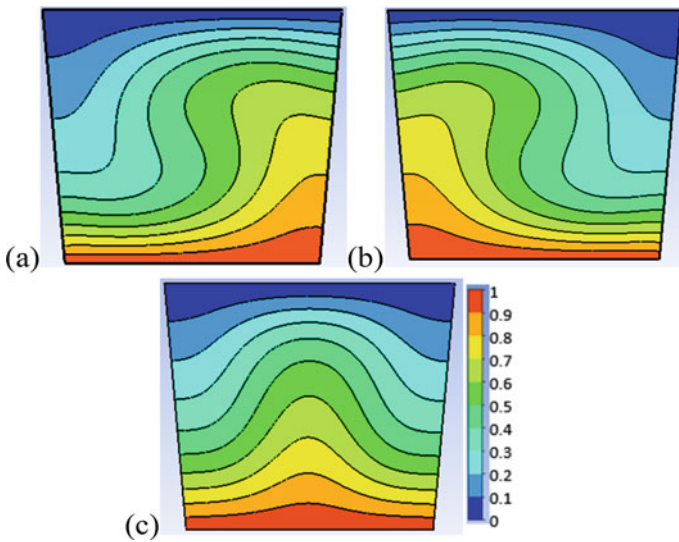
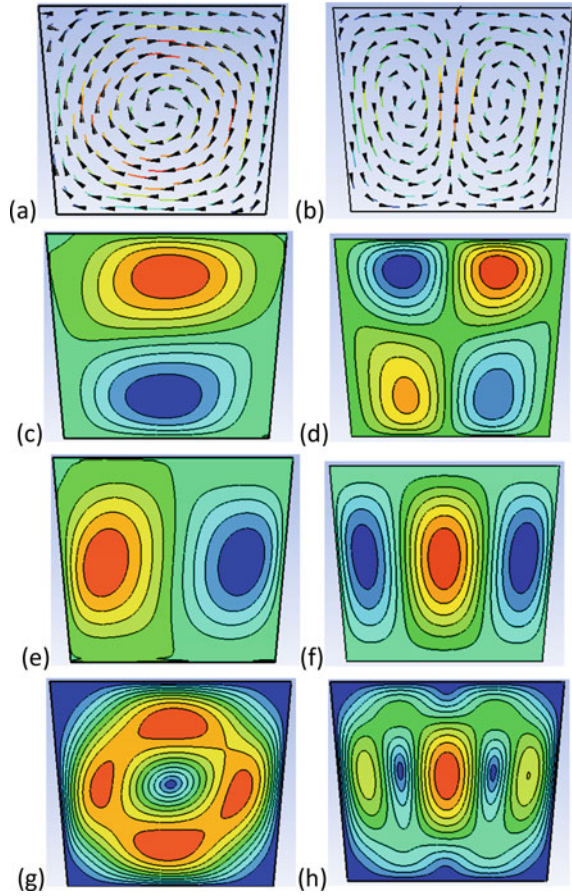


Fig. 2 Isotherms at $Ra = 7000$ for mirror image anti-symmetric and symmetric solutions respectively

Fig. 3 Streamlines, U , V , and velocity magnitude contour in the trapezoidal cavity for $Ra = 7000$ for anti-symmetric and symmetric solutions respectively. Colour bars of velocities are indicative. Real values are obtained by multiplying colour bar values to their maximum values as in Table 3



5.1 Multiple Stable Steady State Solutions

Write [18] studied the stability of steady-state convection within a 2D square cavity using parameter continuation methods by the Galerkin method. They have presented a transition from conduction to conduction state at Ra_c 2585.02 as [6] had reported for this pitchfork bifurcation. This point of transition has been named as branch point (BP1), which is associated with one-roll convection pattern denoted as S_1^\mp . S_1^+ for clockwise roll and S_1^- for anti-clockwise roll. A similar kind of pattern has been obtained in OATZC. The isotherm in Fig. 2a is S_1^+ and its streamlines are as in Fig. 3a. Isotherm Fig. 2b is of S_1^- case of OATZC and the streamlines, in this case, are having an opposite direction to S_1^+ due to mirror image symmetry about vertical midplane.

Venturi et al. [18] used the parameter continuation method and observed another branch point BP2 at $Ra = 6742.31$ with two initially unstable stationary states S_2^\mp

Table 3 Maximum of dimensionless velocities for both symmetric and anti-symmetric solutions for $Ra = 7000$ in OATZC

Solutions	u_{\max}	v_{\max}
Anti-symmetric	0.2535	0.2400
Symmetric	0.1786	0.0946

which become stable beyond $Ra = 11,279$. S_2^\mp are two-roll pattern and symmetric solutions in the range of $Ra = 11,279-22,000$. Thus 4 stable state solutions S_1^\mp and S_2^\mp co-exist together in 2D square cavities. However, OATZC has only 3 stable state solutions beyond stability breakdown. In the current study, two roll convection patterns S_2^- steady state solution is observed and its isotherm is presented in Fig. 2c and streamlines in Fig. 3b. Since OATZC does not have symmetry about the horizontal midplane, other symmetric steady state solution S_2^+ is suppressed.

5.2 Symmetry of Solutions

If we consider the geometry and boundary conditions and the solutions of the above-mentioned steady-state problem are $U(x, y)$, $V(x, y)$ and $\Theta(x, y)$, the discrete symmetry about vertical midplane in OATZC written mathematically as:

$$G[U(x, y), V(x, y), \Theta(x, y)] = [-U(L(y) - x, y), -V(L(y) - x, y), \Theta(L(y) - x, y)]$$

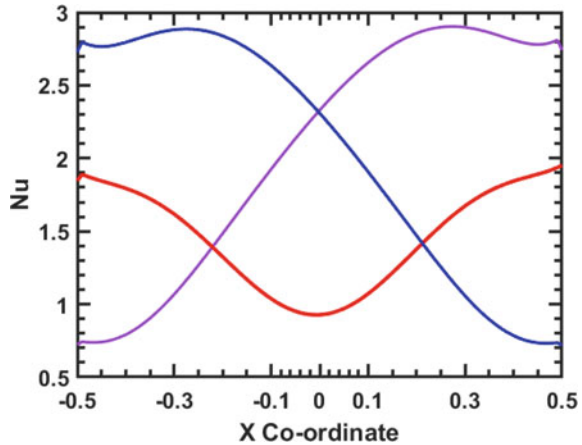
is also a solution. Here $L(y)$ is the width of OATZC which varies from bottom to top and depends on the height y . In current problem, G maps S_1^+ into S_1^- due to symmetry as in square cavity [18]. But there is no symmetry in OATZC about horizontal midplane, two roll convection pattern which is symmetric steady-state solution does not possess map unlike in square cavities. Therefore, in OATZC, only 3 steady-state solutions co-exist out of which two solutions are mirror image anti-symmetric solutions having one roll convection pattern, and one solution is a symmetric solution having two roll convection patterns (Table 3).

5.3 Nusselt Number Variation

Local heat transfer between the bottom the horizontal walls and fluid can be quantified in terms of the local Nusselt number. The local Nusselt number is defined and calculated as:

$$Nu = -(\partial\Theta/\partial y)|_{\text{bottom}}$$

Fig. 4 Variation of Nusselt number at the bottom surface of OATZC. Red curve is for symmetric solution S_2^- and other two curves are for mirror image anti-symmetric solutions S_1^\mp at $Ra = 7000$



Nusselt number for OATZC is calculated from non-dimensionalized temperature gradient at bottom of the cavity and presented in Fig. 4. It shows that Nusselt number at $Ra = 7000$ for symmetric and asymmetric stable state solutions.

6 Conclusions

Natural convection in the bottom heated cavity has been investigated widely in various types of cavities having a variety of fluids. The role of various parameters and symmetry of cavities on the heat transfer characteristics have been explored by many authors in square cavities.

However, in trapezoidal cavities and systems having non-zero initial flow, there are fewer studies. RBC in OATZC filled with air has been simulated in the current study. It is observed that beyond critical Ra , there are three steady-state solutions coexisting together. The isotherms, streamlines, velocity characteristics, and Nusselt number variation at $Ra = 7000$ have been presented for confirmation of the same.

Although the results of the current investigation have certain characteristics similar to square cavity outcomes of [18], there are also important distinctions. In the case of square cavities, there exist discrete symmetries about both horizontal and vertical midplanes. However, in the case of OATZC, only existing symmetry about the vertical midplane leads to mirror image anti-symmetric steady-state solutions of one roll convection pattern. There is no symmetry in OATZC about horizontal midplane and thus only one symmetric steady state solution with two-roll convection patterns S_2^- is observed, unlike in square cavities where 2 such solutions S_2^\pm coexist due to additional symmetry about horizontal midplane.

Acknowledgements The first author would like to acknowledge and thank CSIR HRDG for the fellowship provided during his research work.

Nomenclature

α	Thermal diffusivity (m^2/s)
β	Volumetric coefficient of thermal expansion ($1/\text{K}$)
ΔT	Temperature difference ($T - T_c$)
κ	Conductivity (w/mK)
ν	Kinematic viscosity (m^2/s)
ρ	Fluid density (kg/m^3)
τ	Dimensionless time ($g\beta H_c(T_h - T_c)^{1/2}t/H_c$)
θ	Dimensionless temperature ($(T - T_c)/(T_h - T_c)$)
A_p	Aspect ratio (L_b/H_c)
C_p	Specific heat (J/kgK)
g	Acceleration due to gravity (m/s^2)
h	Convective heat transfer coefficient ($\text{w/m}^2\text{K}$)
H_c	Characteristic height (m)
L_b	Cavity length at bottom (m)
P	Dimensionless pressure ($(p - p_\infty)/\rho\beta g H_c(T_h - T_c)$)
p	Pressure
Pr	Prandtl number (ν/α)
Ra	Rayleigh number ($\beta g H_c^3(T_h - T_c)/\alpha\nu$)
T_c	Cold temperature
T_h	Hot temperature
U, V	Dimensionless velocities ($u/(g\beta H_c(T_h - T_c)^{1/2})$), $v/(g\beta H_c(T_h - T_c)^{1/2})$)
X, Y	Dimensionless Cartesian coordinates ($x/H_c, y/H_c$)
x, y	Cartesian coordinates

Acronyms

RB	Rayleigh-Bénard
RBC	Rayleigh-Bénard Convection
PISO	Pressure Implicit with Splitting of Operator
TOCED	Top Open Cavity with Extended Domain
TZC	Trapezoidal Cavity
AATZC	Acute Angle TZC
OATZC	Obtuse Angle TZC
SHTZC	Side Heated TZC

References

1. Aghighi MS, Ammar A, Masoumi H, Lanjani A (2020) Rayleigh-Bénard convection of a viscoplastic liquid in a trapezoidal enclosure. *Int J Mech Sci* 180:105630. <https://doi.org/10.1016/J.IJMECSCI.2020.105630>
2. Al-Sayegh R (2018) Influence of external magnetic field inclination on three-dimensional buoyancy-driven convection in an open trapezoidal cavity filled with CNT-Water nanofluid. *Int J Mech Sci* 148:756–765. <https://doi.org/10.1016/J.IJMECSCI.2018.09.032>
3. Al-Weheibi SM, Rahman MM, Alam MS, Vajravelu K (2017) Numerical simulation of natural convection heat transfer in a trapezoidal enclosure filled with nanoparticles. *Int J Mech Sci* 131–132:599–612. <https://doi.org/10.1016/J.IJMECSCI.2017.08.005>
4. Basak T, Roy S, Pop I (2009) Heat flow analysis for natural convection within trapezoidal enclosures based on heatline concept. *Int J Heat Mass Transf* 52(11–12):2471–2483. <https://doi.org/10.1016/J.IJHEATMASSTRANSFER.2009.01.020>
5. Calcagni B, Marsili F, Paroncini M (2005) Natural convective heat transfer in square enclosures heated from below. *Appl Therm Eng* 25(16):2522–2531. <https://doi.org/10.1016/J.APPLTHERMALENG.2004.11.032>
6. Gelfgat AY (1999) Different modes of Rayleigh-Bénard instability in two- and three-dimensional rectangular enclosures. *J Comput Phys* 156. <http://www.idealibrary.comon>
7. Nikita G (n.d.) Free convection in a trapezoidal cavity filled with a micropolar fluid. Elsevier Enhanced Reader
8. Iyican L, Witte LC, Bayazitoglu Y (1980) An experimental study of natural convection in trapezoidal enclosures. <http://heattransfer.asmedigitalcollection.asme.org/>
9. Lee TS (1991) Numerical experiments with fluid convection in tilted nonrectangular enclosures. *Numer Heat Transf A Appl* 19(4):487–499. <https://doi.org/10.1080/10407789108944861>
10. Iyican L, Bayazitoglu Y, Witte LC (1980) An analytical study of natural convective heat transfer within a trapezoidal enclosure. <http://heattransfer.asmedigitalcollection.asme.org/>
11. Maurya G, Singh S, Kumar L (n.d.) Stability of Rayleigh-Bénard convection in trapezoidal cavities
12. Miroschnichenko IV, Sheremet MA, Pop I (2017) Natural convection in a trapezoidal cavity filled with a micropolar fluid under the effect of a local heat source. *Int J Mech Sci* 120:182–189. <https://doi.org/10.1016/J.IJMECSCI.2016.11.028>
13. Ouertatani N, ben Cheikh N, ben Beya B, Lili T (2008) Numerical simulation of two-dimensional Rayleigh-Bénard convection in an enclosure. *Comptes Rendus - Mecanique* 336(5):464–470. <https://doi.org/10.1016/j.crme.2008.02.004>
14. Saha SK (2020) Magneto-hydrodynamic buoyancy driven Al₂O₃-water nanofluid flow in a differentially heated trapezoidal enclosure with a cylindrical barrier. *Int Commun Heat Mass Transfer* 114:104593. <https://doi.org/10.1016/J.ICHEATMASSTRANSFER.2020.104593>
15. Saleh H, Roslan R, Hashim I (2011) Natural convection heat transfer in a nanofluid-filled trapezoidal enclosure. *Int J Heat Mass Transf* 54(1–3):194–201. <https://doi.org/10.1016/J.IJHEATMASSTRANSFER.2010.09.053>
16. Saxena A, Kishor V, Singh S, Srivastava A (2018) Experimental and numerical study on the onset of natural convection in a cavity open at the top. *Phys Fluids* 30(5). <https://doi.org/10.1063/1.5025092>
17. Saxena A, Kishor V, Srivastava A, Singh S (2020) Whole field measurements to identify the critical Rayleigh number for the onset of natural convection in top open cavity. *Exp Heat Transfer* 33(2):123–140. <https://doi.org/10.1080/08916152.2019.1586800>
18. Venturi D, Wan X, Karniadakis GE (2010) Stochastic bifurcation analysis of Rayleigh-Bénard convection. *J Fluid Mech* 650:391–413. <https://doi.org/10.1017/S0022112009993685>
19. Xia C, Murthy JY (2002) Buoyancy-driven flow transitions in deep cavities heated from below. *J Heat Transfer* 124(4):650–659. <https://doi.org/10.1115/1.1481356>

Jet Noise Prediction Using Turbulent Scales from LES and RANS



N. P. Shabeeb and Aniruddha Sinha

Abstract This paper studies the modelling of turbulent scales used in an existing steady Reynolds averaged Navier–Stokes solution-based acoustic analogy. The turbulence in the flow has been described as a statistical model of the two-point cross-correlation of the velocity fluctuations, characterized by the turbulent length and time scales. The modelling of the turbulent length and time scales from the $\overline{K}-\overline{\epsilon}$ data used in the steady RANS-based acoustic analogy has been validated with those computed from the cross-correlation of the velocity fluctuations. This was pursued with an LES database comprising an isothermal and a heated ideally-expanded Mach 1.5 round jets. The far-field noise has been computed using the turbulent scales from both the cross-correlation data and the $\overline{K}-\overline{\epsilon}$ data. The two results agree very well, and also display reasonable match with direct predictions from the time-resolved LES data using the Ffowcs Williams-Hawkings method.

Keywords Aeroacoustics · Jet noise prediction · Noise source modelling

1 Introduction

Jet noise is one of the most challenging fluid mechanics problems that researchers have been working on for the last few decades. It is also one of the loudest noises ever produced by mankind. Jet noise consists of turbulent mixing noise, Broadband Shock Associated Noise (BBSAN) and screech tones [1]. The latter two noise components are generated only in supersonic jets when the jet is imperfectly expanded and a shock cell structure is formed in the jet plume. The turbulent mixing noise is the dominant component of the jet noise which is generated by the mixing of the jet with the ambient air. We focus only on the turbulent mixing noise in this paper.

The approach to jet noise prediction has the following elements to it. The designation of a noise source and propagation operator, either calculation or modelling of the noise sources, and solution of the radiated sound. But there is no clear separation

N. P. Shabeeb (✉) · A. Sinha
Department of Aerospace Engineering, IIT Bombay, Mumbai 400076, India
e-mail: 184010008@itb.ac.in

of noise from the rest of the flow and there is no unique designation for the noise source. So there are numerous possible choices for decomposing the flow equations, written compactly here for flow field vector q as $N(q) = 0$, into a noise source S and a propagation operator L as $Lq = S(q)$. This is an exact reformulation, and it is known as an acoustic analogy. The first such theoretical formulation for aerodynamic noise prediction was the work of Lighthill [2]. Lighthill's formulated his analogy by reworking the Navier–Stokes Equation (NSE) itself. He chose the propagator L as the free-space wave operator and the source took on a quadrupolar character. Lilley [3] modified Lighthill's equation by considering the propagation of sound through a locally-parallel medium, as is appropriate for many shear flows, and jets in particular. Later, Ref. [4] proposed a generalized acoustic analogy that was an exact consequence of NSE considering the propagation of sound through an arbitrary medium. These successive developments are geared towards shifting the burden from modelling of the source S to solving the wave operator L .

The direct prediction of the noise generated and radiated by a turbulent flow using Direct Numerical Simulation (DNS) or Large Eddy Simulation (LES) is computationally expensive and time-consuming. Reference [5] proposed a semi-empirical theory to predict the far-field noise from fine-scale turbulence that required minimal information from a CFD database. This model required only the mean flow velocity, density, turbulent kinetic energy and dissipation in the near-field region. The much more economical steady Reynolds averaged Navier–Stokes (RANS) simulation sufficed for this purpose. The turbulent statistics in the source region were modelled using the turbulent length scales, time scales and velocity scales. The authors showed very accurate noise prediction vis-à-vis experimental measurements over a wide range of jet velocities and temperature ratios for single-stream round jets, especially in the sideline and upstream direction where the fine-scale contribution dominates. References [6] and [7] introduced an acoustic analogy based on the linearized Euler equations (LEE) with no assumptions of fine-scale or large-scale noise sources. This approach was also used in Ref. [8] for a Mach 0.9 jet, where comparisons were made with the noise results from the asymptotic solutions given in Refs. [9] and [10]. Miller [11] presented an acoustic analogy that independently predicted the noise from turbulent mixing and shock interactions based on the LEE. Of late, this methodology has been successfully used to predict the noise from chevron jets and axisymmetric dual-stream jets for a wide range of Mach numbers and temperature ratios; it is employed in the present work too.

In all the steady RANS-based acoustic analogies, the local turbulent length and time scales are modelled from local $\overline{K} - \overline{\epsilon}$ data using simple scaling laws and empirical coefficients. In this work, we investigate the accuracy of these models by comparing them with the length and time scales computed directly from the cross-correlation of the velocity fluctuations found in a well-validated LES database [12] comprising of two supersonic round jets—one isothermal and the other heated. In essence, we extract the relevant time-averaged quantities from the LES data, and use only these as input to the RANS-based acoustic analogy model. We find that,

although there are some discrepancies in the modelled scales, the predicted far-field sound from both inputs closely match the sound propagated directly from the time-resolved LES data using the Ffowcs Williams–Hawkings (FW-H) approach.

2 Predicting Jet Noise from RANS

The acoustic analogy presented here is based on the works of Refs. [5–8, 11]. We start from the Euler equations as viscous effects are unimportant for both sound generation and propagation. The equations are

$$\frac{D\pi}{Dt} + \nabla \cdot \mathbf{u} = 0, \quad (1a)$$

$$\frac{D\mathbf{u}}{Dt} + a^2 \nabla \pi = 0. \quad (1b)$$

where $D(\cdot)/Dt$ is the material derivative and $\pi := (1/\gamma) \ln(p/p_\infty)$. These are rewritten by expanding the flow variables as fluctuations on a time-averaged base state and retaining terms on the left hand side (LHS) that are linear in the fluctuations while gathering all remaining terms in the right hand side (RHS). The consequent forced LEE is:

$$\frac{\overline{D}\pi'}{Dt} + \nabla \cdot \mathbf{u}' = -\mathbf{u}' \cdot \nabla \pi' =: f_0, \quad (2a)$$

$$\frac{\overline{D}\mathbf{u}'}{Dt} + \mathbf{u}' \cdot \nabla \bar{\mathbf{u}} + \bar{a}^2 \nabla \pi' = -\mathbf{u}' \cdot \nabla \mathbf{u}' - (a^2)' \nabla \pi' =: \mathbf{f} \quad (2b)$$

where $\overline{D}(\cdot)/\overline{Dt} := \partial(\cdot)/\partial t + \bar{\mathbf{u}} \cdot (\cdot)$. The non-linear terms on the RHS are the noise sources; specifically, f_0 is the unsteady dilatation and \mathbf{f} is the unsteady force per unit mass. For free jets, the mean pressure is generally taken to be the ambient value (i.e., $\bar{p} = p_\infty$). Also, $\pi' \approx \pi = \gamma^{-1} \ln(1 + p'/p_\infty) \approx \gamma^{-1} p'/p_\infty$. The solution to the inhomogeneous equation can be determined by finding its Green's function.

Considering a locally parallel mean flow, we arrive at the following formulation of the forced LEE in cylindrical coordinates $\mathbf{x} := (x, r, \phi)$ in the frequency domain:

$$\overline{D}_\omega \hat{\pi} + \frac{\partial \hat{u}_x}{\partial x} + \frac{1}{r} \frac{\partial (r \hat{u}_r)}{\partial r} + \frac{1}{r} \frac{\partial \hat{u}_\phi}{\partial \phi} = \hat{f}_0, \quad (3a)$$

$$\overline{D}_\omega \hat{u}_x + \frac{d\bar{u}_x}{dr} \hat{u}_r + \bar{a}^2(\mathbf{x}) \frac{\partial \hat{\pi}}{\partial x} = \hat{f}_x, \quad (3b)$$

$$\overline{D}_\omega \hat{u}_r + \bar{a}^2(\mathbf{x}) \frac{\partial \hat{\pi}}{\partial r} = \hat{f}_r, \quad (3c)$$

$$\overline{D}_\omega \hat{u}_\phi + \frac{\overline{a^2}(\mathbf{x})}{r} \frac{\partial \hat{\pi}}{\partial \phi} = \hat{f}_\phi, \tag{3d}$$

where $\overline{D}_\omega := -i\omega + \overline{u}_x \partial / \partial x$.

To make progress, the four periodic vector Green’s functions of the LEE are defined as the solutions of

$$\overline{D}_\omega \hat{\pi}_g^n + \nabla \cdot \hat{u}_g^n = \delta(\mathbf{x} - \mathbf{x}_s) \delta_{0n} \tag{4a}$$

$$\overline{D}_\omega \hat{u}_{g,x}^n + \frac{d\overline{u}_x}{dr} \hat{u}_{g,r}^n + \overline{a^2} \frac{\partial \hat{\pi}_g^n}{\partial x} = \delta(\mathbf{x} - \mathbf{x}_s) \delta_{xn} \tag{4b}$$

$$\overline{D}_\omega \hat{u}_{g,r}^n + \overline{a^2} \frac{\partial \hat{\pi}_g^n}{\partial r} = \delta(\mathbf{x} - \mathbf{x}_s) \delta_{rn} \tag{4c}$$

$$\overline{D}_\omega \hat{u}_{g,\phi}^n + \frac{\overline{a^2}}{r} \frac{\partial \hat{\pi}_g^n}{\partial \phi} = \delta(\mathbf{x} - \mathbf{x}_s) \delta_{\phi n}, \tag{4d}$$

Here, the vector Green’s functions have the common arguments $(\mathbf{x}|\mathbf{x}_s; \omega)$ and are indexed by n , which takes values in $\mathcal{N} := \{0, x, r, \phi\}$. Basically, we are seeking the response at \mathbf{x} due to harmonic forcing at the location \mathbf{x}_s with ω . Moreover, the forcing is of a particular kind—either a volume source or one of the three components of a force source.

The vector LEE operator can be simplified to a third-order scalar operator acting on the most relevant component—viz. $\hat{\pi}_g^n$ —called the Lilley’s operator:

$$\begin{aligned} & \underbrace{\left(\overline{D}_\omega^3 - \overline{a^2} \overline{D}_\omega \nabla^2 - \frac{d\overline{a^2}}{dr} \overline{D}_\omega \frac{\partial}{\partial r} + 2\overline{a^2} \frac{d\overline{u}_x}{dr} \frac{\partial^2}{\partial x \partial r} \right)}_{L_L} \hat{\pi}_g^n \\ &= \overline{D}_\omega^2 (\delta(\mathbf{x} - \mathbf{x}_s)) \delta_{0n} - \overline{D}_\omega \frac{\partial}{\partial x} \delta(\mathbf{x} - \mathbf{x}_s) \delta_{xn} \\ & \quad - \left[\frac{1}{r} \overline{D}_\omega \frac{\partial}{\partial r} (r \delta(\mathbf{x} - \mathbf{x}_s)) - 2 \frac{d\overline{u}_x}{dr} \frac{\partial}{\partial x} \delta(\mathbf{x} - \mathbf{x}_s) \right] \delta_{rn} \\ & \quad - \frac{1}{r} \overline{D}_\omega \frac{\partial}{\partial \phi} \delta(\mathbf{x} - \mathbf{x}_s) \delta_{\phi n} =: \mathcal{S}^n(\mathbf{x} - \mathbf{x}_s; \omega). \end{aligned} \tag{5}$$

Lilley’s operator’s (scalar) Green’s function is such that

$$L_L \hat{g}(\mathbf{x}|\mathbf{x}_s; \omega) = \delta(\mathbf{x} - \mathbf{x}_s). \tag{6}$$

It turns out that it is much simpler to solve the adjoint problem and invoke reciprocity to arrive at \hat{g} [5]. With this in hand, the pressure component of the vector

Green's function of LEE can be written as

$$\hat{\pi}_g^n(\mathbf{x}|\mathbf{x}_s; \omega) = \iiint \hat{g}(\mathbf{x}|\mathbf{x}_t; \omega) S^n(\mathbf{x}_t - \mathbf{x}_s; \omega) d\mathbf{x}_t. \quad (7)$$

The pressure fluctuation is obtained by convolving the four Green's functions' pressure components with the corresponding source terms of the LEE. However, we are interested in (and cannot ask for more than) the spectral density of pressure. This is found as

$$\begin{aligned} \frac{S_p(\mathbf{x}, \omega)}{(\gamma p_\infty)^2} &= \sum_{n, n' \in \mathcal{N}} \int_{\mathbf{x}_s} \hat{\pi}_g^{n*}(\mathbf{x}\mathbf{x}_s; \omega) \int_{\boldsymbol{\eta}} \hat{\pi}_g^{n'}(\mathbf{x}\mathbf{x}_s + \boldsymbol{\eta}; \omega) \\ &\quad \times \int_{\tau} f_n(\mathbf{x}_s, t) f_{n'}(\mathbf{x}_s + \boldsymbol{\eta}, t + \tau) e^{i\omega\tau} d\tau d\boldsymbol{\eta} d\mathbf{x}_s \end{aligned} \quad (8)$$

Thus, the necessary input for our approach is the mean flow field for computing the Green's functions and a model of the two-point–two-time cross-correlation of the nonlinear source terms of the LEE.

Based on extensive round jet databases accumulated over decades, such a model for the spatio-temporal cross-correlations of the source terms has been proposed by many researchers [5, 7, 13], and is of the form

$$f_n(\mathbf{x}_s, t) f_{n'}(\mathbf{x}_s + \boldsymbol{\eta}, t + \tau) = \delta_{nn'} A_n(\mathbf{x}_s) e^{-|\tau|/\tau_s - (\eta_x - \bar{u}_x \tau)^2/\ell_x^2 - \eta_y^2/\ell_y^2 - \eta_z^2/\ell_z^2}, \quad (9a)$$

$$A_0 = B_0^2 \frac{(u_s/a_\infty)^4}{\tau_s^2}, \quad A_n = B_{>0}^2 \frac{(u_s/a_\infty)^2 u_s^4}{\ell_x^2}. \quad (9b)$$

where $n \in \{x, r, \phi\}$. At zero-time lag, this posits a Gaussian decay of the two-point cross-correlation in all directions, albeit with different length scales l_x, l_y, l_z . Moreover, it invokes the frozen field hypothesis and posits an exponential decay of correlation with time having time scale τ_s , if one were to move with the mean flow (assumed negligible in the cross-stream directions for this purpose). Further, the model assumes that the four source terms (for the four equations) are uncorrelated. Finally, the magnitudes of the correlation functions are related by dimensional analysis to the local velocity scale u_s and the length and time scales.

The turbulent length scale is expected to depend on the frequency being considered. Let us denote the frequency-dependent streamwise length scale as $l_x(\mathbf{x}_s, St)$, where $St = \omega D_j / (2\pi U_j)$ is the Strouhal number corresponding to the frequency ω under consideration, D_j is the jet's nozzle-exit diameter, and U_j is its nozzle-exit velocity. Following Ref. [14], all these length scales are modelled as

$$l_i(\mathbf{x}_s, St) = \ell_i(\mathbf{x}_s) \frac{1 - e^{-c_f St}}{c_f St}, \quad \forall i \in \{x, r, \phi\}, \quad (10)$$

where $c_f = 11.25$ was chosen to match the experimental observations.

Assuming that the observer is in the far-field, the vector Green's function of two closely-placed source points differ by only a phase factor:

$$\hat{\pi}_g^n(\mathbf{x}|\mathbf{x}_s + \boldsymbol{\eta}; \omega) \approx \hat{\pi}_g^n(\mathbf{x}|\mathbf{x}_s; \omega)e^{-(i\omega/R/a_\infty)\mathbf{x}\cdot\boldsymbol{\eta}}, \quad (11)$$

where R is the polar radius of the observer (i.e., distance from the jet nozzle exit's centre). Using this simplification, along with the specific model of the spatio-temporal correlation in Eq. (9), allows one to analytically evaluate the integral in Eq. (8) over the spatio-temporal lags (i.e. over $\boldsymbol{\eta}$ and τ) to arrive at

$$\begin{aligned} \frac{S_p(\mathbf{x}, \omega)}{(\gamma p_\infty)^2} &= 2\pi^{3/2} \sum_{n \in \mathcal{N}} \int |\hat{\pi}_g^n(\mathbf{x}|\mathbf{x}_s; \omega)|^2 \sigma_n(\mathbf{x}_s; \omega, \mathbf{x}) d\mathbf{x}_s, \\ \sigma_n &:= A_n l_x l_y l_z \tau_s \frac{e^{-0.25\omega^2(l_x^2 \cos^2 \Theta + l_y^2 \sin^2 \Theta)/a_\infty^2}}{1 + \omega^2 \tau_s^2 (1 - \bar{u}_x \cos \Theta/a_\infty)^2}. \end{aligned} \quad (12)$$

Here, Θ is the polar angle of the observer measured w.r.t. the jet downstream axis, and the local length scales are replaced by their frequency-dependent counterparts.

In the present work, we evaluate the following two alternate approaches to obtaining the necessary inputs to this noise prediction technique, which are the turbulent length and time scales.

2.1 Source Model 1

As mentioned at the outset, we are using an LES database of two supersonic round jets. In this first approach, we start out by calculating the local spatio-temporal cross-correlations of axial velocity fluctuations in the two jets. Then, we obtain the local length scales and time scales of an individual jet by fitting its spatio-temporal cross-correlation with the Gaussian-exponential ansatz of Eq. (9). Specifically, the local time scale $\tau_s(\mathbf{x})$ is determined by fitting with an exponential the peaks of the local two-point two-time cross-correlation data (i.e., $\eta_y = 0$ and $\eta_z = 0$, and η_x assumed to be $\bar{u}_x \tau$). The local axial length scale $\ell_x(\mathbf{x})$ is determined by fitting with a Gaussian the local cross-correlation data at finite streamwise separation and no separation in other coordinates (i.e., $\tau = 0$, $\eta_y = 0$ and $\eta_z = 0$). Following the literature, the cross-stream length scales are assumed to be one-third of the streamwise length scales at all locations:

$$\ell_y(\mathbf{x}) = \ell_z(\mathbf{x}) = \ell_x(\mathbf{x})/3. \quad (13)$$

Finally, the local velocity scale is determined from the local mean turbulent kinetic energy computed from the LES data again:

$$u_s(\mathbf{x}) = c_u \sqrt{2\overline{K}(\mathbf{x})}/3. \quad (14)$$

The free parameters for this model are c_u seen above, c_f appearing in Eq. (10) (and set as mentioned in its discussion), as well as the two amplitude constants B_0 and $B_{>0}$ present in Eq. (9). These last two are determined by best-fitting the noise data across the two jets (see Sect. 3).

2.2 Source Model 2

In the second approach, we start by computing the local time-averaged values of turbulent kinetic energy $\overline{K}(\mathbf{x})$ and dissipation $\overline{\varepsilon}(\mathbf{x})$ from the LES database. Then, the turbulent length and time scales are modeled as [5–8, 11]:

$$\ell_x = c_l \frac{(\overline{K})^{3/2}}{\overline{\varepsilon}}, \quad \tau_s = c_\tau \frac{\overline{K}}{\overline{\varepsilon}}, \quad u_s = c_u \sqrt{2\overline{K}}/3 \quad (15)$$

where c_l , c_τ and c_u are constants. At each point within the jet plume, the cross-stream length scales are estimated from the streamwise one using Eq. (13) as before. Apart from these constants, c_f , B_0 and $B_{>0}$ also have to be set, just as in the first source model described above.

3 Results and Discussion

A steady RANS solution is enough to predict the far-field jet noise using the model explained in the previous section. However, if we want to validate such a model, then we need an independent prediction of the noise, which is impossible with the RANS data. So, instead of using a steady RANS solution, the LES results of Brès et al. [12] are used, and the required input parameters are computed from it as described above for the two source models. The database comprises of an isothermal ideally-expanded round jet (case B118) and a heated ideally-expanded round jet (case B122), summarized in Table 1. The unstructured LES grid had 42 million control volumes; for the current analysis, this data was interpolated to a cylindrical structured grid having about 1.3 million points.

Table 1 Test cases used from LES database of Ref. [12]

LES case	M_{jet}	T_{jet}/T_∞	M_a	Re_{jet}
B118	1.5	1.0	1.5	300,000
B122	1.5	1.74	1.98	155,000

Although the LES used a larger computational domain, for the present work we restricted the streamwise extent to $20D_j$ and the radial extent of $3.5D_j$. The calculation of the Green's function requires the mean streamwise velocity \bar{u}_x and density $\bar{\rho}$. Contours of the former are shown in Fig. 1a for the isothermal B118 jet. Since radial derivatives of this are needed, we fit each radial profile of \bar{u}_x with a truncated Gaussian function of the form proposed originally in Ref. [15], and in turn smooth the Gaussian function's fit parameters with cubic splines [16]. As shown in the same figure, the fitted result matches well the original. Similar smoothing is pursued for the mean density field as well.

Using \bar{u}_x and $\bar{\rho}$ as input, the vector Green's functions of the LEE are computed with a code written in MATLAB following the theory laid out in the preceding section.

Source model 2 needs the mean TKE and dissipation fields; these are shown in Fig. 1b and c for the B118 jet. To avoid spurious artefacts, these are also smoothed, this time using dual Gaussian functions at each axial station. The same figures demonstrate that negligible information is lost in this process.

The length and time scales computed using the first source model (i.e., from the cross-correlation data) are presented in Fig. 2a and c respectively for the heated B122

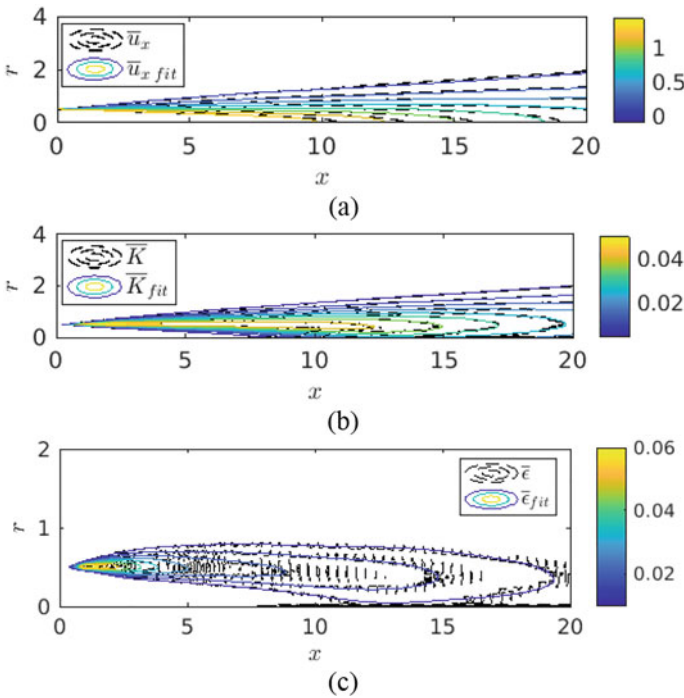


Fig. 1 Comparison of computed and fitted contours of the mean values of **a** streamwise velocity \bar{u}_x , **b** TKE \bar{K} , and **c** dissipation $\bar{\epsilon}$, all for the B118 jet

jet. Equation (9b) shows that the noise source itself vanishes in regions where the velocity scale (and so the TKE) vanishes, which happens outside the shear layer. Thus, the turbulent scales are not computed in these regions; hence, they appear uniformly deep blue in the filled contour plots of Fig. 2. The shear layer starts out being very thin near the nozzle exit and thickens as one moves downstream. Because of this, the turbulent structures are also increasing in size as one progresses downstream, which is in turn reflected in the length scales shown in Fig. 2a. Since larger structures have greater temporal persistence, the time scales also increase as one goes downstream, and especially near the outer edge of the shear layer.

Importantly for the purposes of the present work, a comparison of Fig. 2a and b confirms that the two source models predict qualitatively similar length scales having the same order of magnitude, although there are some subtle differences. Similarly, a

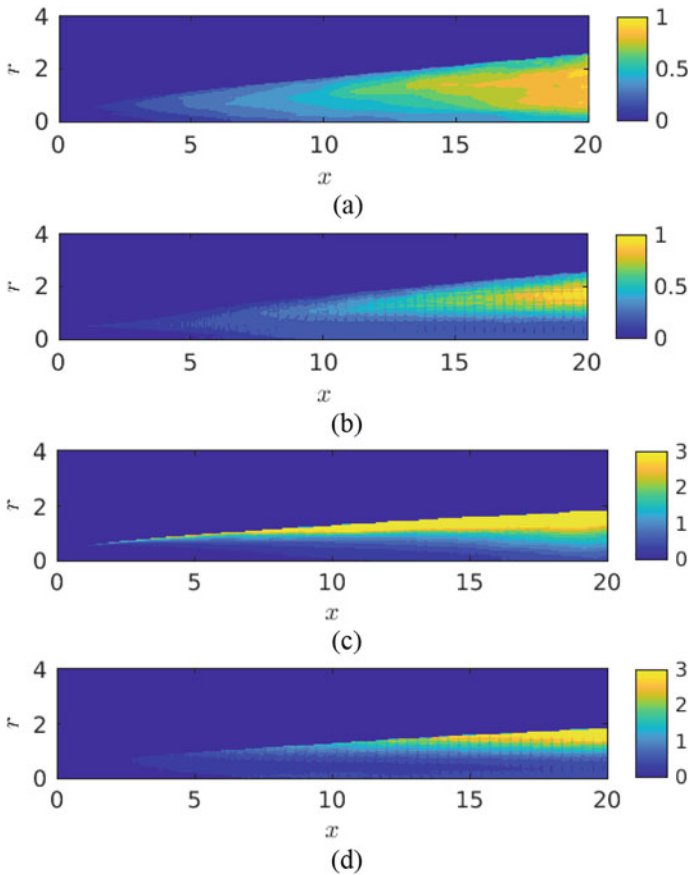


Fig. 2 Comparison of length scales computed for the B122 jet using **a** cross-correlations (i.e., source model 1), and **b** $\overline{K} - \overline{\epsilon}$ (i.e., source model 2). Comparison of time scales computed for the B122 jet using **c** cross-correlations (i.e., source model 1), and **d** $\overline{K} - \overline{\epsilon}$ (i.e., source model 2)

study of Fig. 2c and d confirms that the time scales obtained from the two approaches are also similar. To obtain the length and time scales from source model 2, we need to specify the corresponding coefficients. To obtain the match seen in these figures, these were chosen as

$$c_l = 1.2, \quad c_\tau = 0.18 \quad (16)$$

Note that both these are three times higher than the values used in Ref. [11].

Of course, source model 2 is the only one that is applicable when the input data is a steady RANS solution. Its agreement with the results from the source model 1 shown here, independently validates it using the greater wealth of information available in the present LES database.

The far-field noise is quantified using the sound pressure level (SPL) spectra at various polar angles. The polar radii of these observer positions are chosen to match the location of microphones in the reference experiments of Ref. [17], wherein a rectilinear array was used. The reference noise spectra Figs. 3 and 4 for the two jets are calculated directly from the time-resolved flow field fluctuation data available in the LES solutions of Ref. [12]. For this, the Ffowcs Williams and Hawkings (FW-H) method [18] is used, as was done in Ref. [12]. The authors reported excellent match with the reference spectral data from the experiments of Ref. [17], which validated their LES simulations.

Results from our two different source models are juxtaposed with the reference spectra in Figs. 3 and 4, and they are essentially identical. Moreover, the comparison with the reference spectra is excellent, except at high frequencies. It is evident that our severely approximate models perform very satisfactorily vis-à-vis the much more input-heavy reference approach. To obtain these spectral agreement, we consistently set the remaining parameters that are common to our two models. That is, only one value was used for each parameter across both the jets, and definitely in calculations across all observer locations. These values were

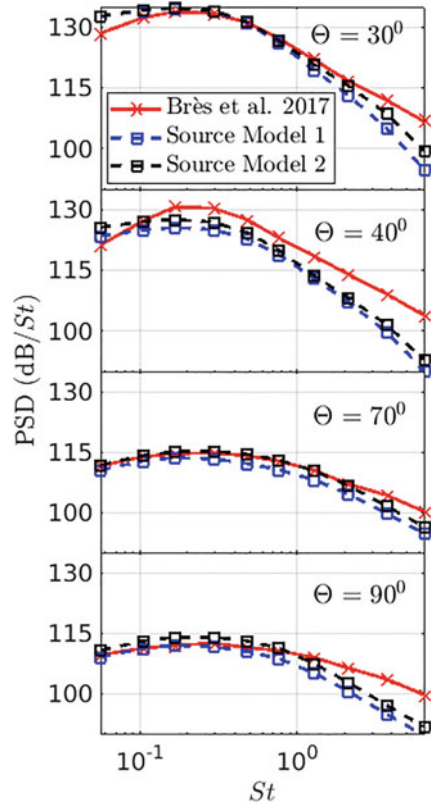
$$B_0 = 0.451, \quad B_{>0} = 4.51, \quad c_u = 1 \quad (17)$$

The first two values are about twice of those reported by Ref. [11]; the last one matches the reference.

4 Conclusions

This chapter explains an existing methodology for the prediction of jet noise based on steady RANS data. The Euler equations are rearranged into a noise propagation operator and noise sources. The propagation operator is simplified to a third-order partial differential equation (PDE) of a single variable—the Lilley’s operator—based on the locally-parallel mean flow assumption. The scalar Green’s function of Lilley’s

Fig. 3 Comparison of the far-field noise predicted with the FW-H results (B118)

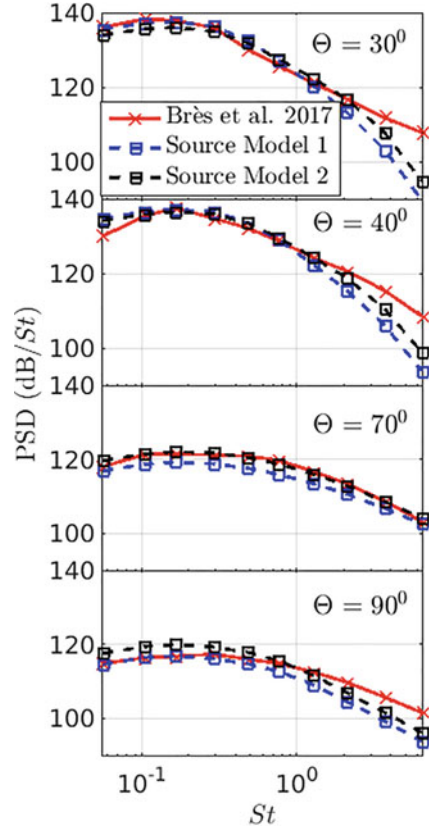


operator is computed numerically using the adjoint approach. Subsequently, the vector Green’s functions of the LEE are recovered from the Lilley’s Green’s function.

On the source side, two noise source models are used in this work. One uses the local values of the mean turbulent kinetic energy \bar{K} and dissipation $\bar{\varepsilon}$; these quantities are readily available from steady $\bar{K}-\bar{\varepsilon}$ RANS simulations. Results from this are compared with another source model that relies on knowledge of the spatio-temporal cross-correlation of the streamwise velocity—information that can only be found from an LES or a DNS database. To enable a comparison of the two models, we used the well-validated LES database of Ref. [12] comprising of an isothermal and a heated Mach 1.5 jets. This work validates the former low-input-burden noise source model against the latter high-input-burden model results using this LES database. Specifically, the turbulent length and time scales computed from the two models demonstrate very similar spatial trends—both qualitatively and quantitatively.

The similarity of the outcomes from the two source models in the near-field region is reflected in the equivalence of their far-field sound predictions also. Moreover, both models show very encouraging agreement with the much more high-input burden FW-H results that required the time-resolved LES solution itself.

Fig. 4 Comparison of the far-field noise predicted with the FW-H results (B122)



Acknowledgements The authors are grateful to Guillaume Brès for sharing the LES solutions for the two supersonic jets, without which this work would not have been possible. Funding from a research grant from Indian Space Research Organization is also gratefully acknowledged.

Nomenclature

- p Pressure
- \mathbf{u} Velocity
- a Local speed of sound
- t Time
- γ Specific heat ratio
- f_0 Unsteady dilatation
- \mathbf{f} Unsteady force vector
- \mathbf{x} Position vector
- ω Radial frequency

δ	Dirac delta function
δ_{ij}	Kronecker delta function
L_L	Lilley's operator
\hat{g}	Green's function of L_L
S_p	Spectral density
τ	Time lag
η	Spatial lag vector
R	Polar radius of the observer
Θ	Polar angle of the observer
B_n	Amplitude constants for various n
St	Strouhal number
D_j	Jet diameter
U_j	Jet exit velocity
τ_s	Turbulent time scale
ℓ_s	Turbulent length scale
u_s	Turbulent velocity scale
K	Turbulent kinetic energy
ε	Dissipation
$\overline{(\cdot)}$	Time-averaged quantity
$(\cdot)'$	Perturbation quantity
$\widehat{(\cdot)}$	Temporal Fourier-transformed
$(\cdot)^*$	Complex conjugate
$(\cdot)_\infty$	Freestream quantity
$(\cdot)_s$	Source quantity
(\cdot)	Ensemble average
$(\cdot)_g^n$	nth component of vector Green's function

References

1. Tam CKW, Chen P (1994) Turbulent mixing noise from supersonic jets. *AIAA J* 32(9):1774–1780
2. Lighthill MJ (1952) On sound generated aerodynamically I. General theory. *Proc R Soc Lond Ser A Math Phys Sci* 211(1107):564–587
3. Lilley GM (1974) On the noise from Jets
4. Goldstein ME (2003) A generalized acoustic analogy. *J Fluid Mech* 488:315–333
5. Tam CKW, Auriault L (1999) Jet mixing noise from fine-scale turbulence. *AIAA J* 37(2):145–153
6. Morris PJ, Farassat F (2002) Acoustic analogy and alternative theories for jet noise prediction. *AIAA J* 40(4):671–680
7. Morris P, Boluriaan S (2004) The prediction of jet noise from CFD data. In: 10th AIAA/CEAS aeroacoustics conference
8. Raizada N, Morris P (2006) Prediction of noise from high speed subsonic jets using an acoustic analogy. In: 12th AIAA/CEAS aeroacoustics conference (27th AIAA aeroacoustics conference)
9. Balsa TF (1976) The far field of high frequency convected singularities in sheared flows, with an application to jet-noise prediction. *J Fluid Mech* 74(2):193–208

10. Goldstein ME (1976) *Aeroacoustics*. New York
11. Miller SAE (2014) Toward a comprehensive model of jet noise using an acoustic analogy. *AIAA J* 52(10):2143–2164
12. Brès GA et al (2017) Unstructured large-eddy simulations of supersonic jets. *AIAA J* 55(4):1164–1184
13. Ribner HS (1964) The generation of sound by turbulent jets. *Adv Appl Mech* 8:103–182
14. Morris PJ, Zaman KBMQ (2010) Velocity measurements in jets with application to noise source modeling. *J Sound Vib* 329(4):394–414
15. Troutt TR, McLaughlin DK (1982) Experiments on the flow and acoustic properties of a moderate-Reynolds-number supersonic jet. *J Fluid Mech* 116:123–156
16. Gudmundsson K (2010) Instability wave models of turbulent jets from round and serrated nozzles. California Institute of Technology
17. Schlinker R et al (2008) Decomposition of high speed jet noise: source characteristics and propagation effects. In 14th AIAA/CEAS aeroacoustics conference (29th AIAA aeroacoustics conference)
18. Ffowcs Williams JE, Hawkings DL (1969) Sound generation by turbulence and surfaces in arbitrary motion. *Philos Trans R Soc Lond Ser A Math Phys Sci* 264(1151):321–342

Reduction in Turbulence-Induced Non-linear Dynamic Vibration Using Tuned Liquid Damper (TLD)



Ananya Majumdar, Biplab Ranjan Adhikary, and Partha Bhattacharya

Abstract In this chapter, an attempt is made to develop a coupled non-linear turbulence-structure-damper model in a Finite Volume-Finite Difference (FV-FD) framework. A Tuned Liquid Damper (TLD) is used as the additional damping system along with inherent structural damping. Real-time simulation of flow-excited bridge box girder or chimney section and the vibration reduction using TLD can be performed using the developed model. The turbulent flow field around a structure is modelled using an OpenFOAM transient PISO solver, and the time-varying drag force is calculated. This force perturbs the structure, causing the sloshing phenomena of the attached TLD, modelled using shallow depth approximation, damping the flow-induced vibration of the structure. The structural motion with and without the attached TLD is modelled involving the FD-based Newmark-Beta method using in-house MATLAB codes. The TLD is tuned with the vortex-shedding frequency of the low-Reynolds number flows, and it is found to be reducing the structural excitation significantly. On the other hand, the high-Reynolds number turbulent flow exhibits a broadband excitation, for which by tuning the TLD with few frequencies obtained through investigations, a good reduction in vibration is observed.

Keywords Turbulence-structure interaction · Tuned liquid damper · Finite difference · OpenFOAM

1 Introduction

Turbulence proves its' prominent presence in our surroundings, which can adversely affect important structures like bridges, high-rise buildings, or chimneys. The excessive flow-induced vibration even leads to collapse. One such iconic example is the Tacoma bridge collapse and a very recent, under-construction bridge collapse in Sultangunj, India on 29th April 2022.

A. Majumdar (✉) · B. R. Adhikary · P. Bhattacharya
Department of Civil Engineering, Jadavpur University, Kolkata 700032, India
e-mail: annatat1397@gmail.com

To reduce the turbulence-excited structural motion it is important to properly model the flow field surrounding the structure. Next, the structural motion is to be estimated with and without a TLD attached to it.

To obtain the desired reduction in the excitation level of the structure, several active and passive damping techniques are used by researchers and engineers. One of the widely used passive damping instruments is TLD, which is essentially tuned to the first fundamental frequency [1, 2] or the first two fundamental frequencies [3] of the vibrating structure for the best damping experience. In the case of harmonic excitation and non-deterministic forcing with a prominent frequency value, the TLD is tuned to the excitation frequency [4]. In the case of turbulent flow, the behaviour of TLD and possible tuning frequency is not studied yet.

2 Literature Review and Objective

Many researchers have investigated the flow past bluff body for different Reynolds numbers (Re) using numerical [5] or experimental techniques [6–8]. The Strouhal number (St) and drag coefficient (C_D) are evaluated and reported. Structural excitation due to any random forcing is estimated using the FD-based non-linear Newmark-Beta method in the time domain [4]. The sloshing behaviour of TLD and resulting structural response reduction is estimated numerically and/or experimentally [1–4] using harmonic or random earthquake ground acceleration.

However, the coupled non-linear model to capture the turbulence-induced structural motion and its reduction using TLD is non-existent.

Therefore, in the present research work, an attempt is made to develop a numerical FV-FD-based non-linear model that will estimate the turbulence forcing, and simultaneously at each time step, it will capture the sloshing-induced base shear produced by the TLD liquid at the TLD-structure junction, eventually producing additional damping to the SDOF system.

3 Methodology

The entire work is subdivided into *two* subsections, each consisting of modelling a part of the full solution technique.

- (a) Modelling the turbulent flow field past a rigid obstacle and estimation of the drag force applied to it.
- (b) Using the time-varying turbulent forcing to estimate the structural response at each time step with and without attached TLD.

3.1 Turbulence Past a Rigid Obstacle

Unsteady or transient simulation for isotropic turbulence is performed using Large Eddy Simulation (LES), which essentially works based on filter operation. Eddies larger than a certain length scale, typically in the order of the grid size, are fully resolved. The smaller eddies are modelled using a sub-grid scale model. As the turbulence is considered to be isotropic, only the size of these smaller eddies becomes important, not the shape. Once the mean velocity field is computed by the RANS model, the fluctuating velocity component (u') can conceptually be estimated by subtracting time-averaged mean velocity \bar{U} , from instantaneous velocity, U . This fluctuating velocity is then used to calculate the turbulent kinetic energy (k) per unit mass, as $k = \frac{1}{2}u'u'$. If all the fluctuating components in three directions are considered, the Reynolds stress tensor can be estimated (per unit density) in symmetric matrix form, and in 3D and 2D domains the resolved kinetic energy becomes

$$k_{\text{res}} = \frac{1}{2} \left[\overline{(u')^2} + \overline{(v')^2} + \overline{(w')^2} \right] \quad (1)$$

$$k_{\text{res}} = \frac{1}{2} \left[\overline{(u')^2} + \overline{(v')^2} \right] \quad (2)$$

The amount of the remaining kinetic energy is termed sub-grid scale kinetic energy, k_{sgs} , and calculated by a sub-grid eddy viscosity model. In the present study, the Smagorinsky–Lilly model is used, where an additional stress term (τ_{sgs}) is applied to break down the eddies larger than the mesh size because molecular viscosity is not sufficiently strong to do so. This stress term can be derived by applying filtering operation on compressible Navier–Stokes equations as follows:

$$\frac{\partial \rho}{\partial t} + \frac{\partial(\rho U_j)}{\partial x_j} = 0 \quad (3)$$

$$\frac{\partial(\rho U_i)}{\partial t} + \frac{\partial(\rho U_i U_j)}{\partial x_j} = -\frac{\partial P}{\partial x_i} + \frac{\partial}{\partial x_j} (\tau_{ij} + \tau_{\text{sgs}}) \quad (4)$$

This sub-grid stress τ_{sgs} is modelled using Eq. (5)

$$\tau_{\text{sgs}} = 2\rho\nu_{\text{sgs}}S_{ij}^* - \frac{2}{3}\rho k_{\text{sgs}}\delta_{ij} \quad (5)$$

$$S_{ij}^* = \frac{1}{2} \left(\frac{\partial U_i}{\partial x_j} + \frac{\partial U_j}{\partial x_i} - \frac{1}{3} \frac{\partial U_k}{\partial x_k} \delta_{ij} \right) \quad (6)$$

Assuming the profile to be linear within the viscous sublayer, and obeying the 1/7th power law in the outside region, the wall function is formulated as described by Germano et al. [9].

$$U^+(y^+) = \begin{cases} y^+ & \text{if } y^+ < 11.8 \\ 8.3(y^+)^{1/7} & \text{if } y^+ > 11.8 \end{cases} \quad (7)$$

where non-dimensionalized velocity (U^+) and wall distance (y^+) are given as

$$U^+ = \frac{U}{U_\tau}, y^+ = \frac{U_\tau y}{\nu} \quad (8)$$

Lilly [10] proposed a value for the Smagorinsky constant C_s as 0.173, considering turbulence to be homogeneous and isotropic, which is true for a shear-free turbulent event far from any wall. However, modern CFD codes typically use different values of C_s for near-wall turbulent events. In the present wall-function approach (SLWF) Smagorinsky-Lilly constant, C_s is considered as 0.1 to determine the sub-grid scale kinematic eddy viscosity.

In the Pressure-Implicit with Splitting of Operators (PISO) algorithm, steady-state flow problems can be solved using the LES model with a pressure corrector.

The coefficient of drag is given by,

$$C_D = \frac{F_D}{\frac{1}{2}\rho U^2 A} \quad (9)$$

F_D Drag Force,

A Projected area.

3.2 Sloshing of Tuned Liquid Damper (TLD)

At any point wave height is h . Assuming shallow wave theory to be valid and no point of time wave is reaching the tank top, partial differential equations for the sloshing motion of liquid can be written as [4],

$$\frac{\partial h}{\partial t} + h \frac{\partial v}{\partial x} + v \frac{\partial h}{\partial x} = 0 - \left(\frac{1}{2\beta} - 1 \right) \ddot{u}_n \quad (10)$$

$$\frac{\partial v}{\partial t} + g \frac{\partial h}{\partial x} + v \frac{\partial v}{\partial x} - g(\theta_{\text{TLD}} - S) + \frac{\partial^2 v}{\partial t^2} = 0 \quad (11)$$

where u is the displacement of the structure at any point of time, thus, displacement of the TLD liquid surface, as it is attached to the structure. θ_{TLD} is the rotational displacement, h is the wave height at location x and time t , v is the particle velocity at location x and time t . The boundary conditions are given by:

$$v(0, t) = v(L, t) = 0 \quad (12)$$

Initial conditions: At the starting of time ($t = 0$) steady state condition is considered,

$$h(x, 0) = h_0; v(x, 0) = 0 \quad (13)$$

Non-dimensional slope of the energy gradient line is written as,

$$S = \frac{\tau_w}{\rho g h} \quad (14)$$

The wall shear stress at the base of the tank, τ_w is given by,

$$\tau_w = \frac{\mu_f v_{\max}}{h}, \quad \text{for } z \leq 0.7 \quad (15)$$

$$\tau_w = \sqrt{\rho \mu_f \omega}, \quad \text{for } z > 0.7 \quad (16)$$

ω is the forcing frequency, $z = \sqrt{\frac{\omega g}{2\mu_f}}$; μ_f is the absolute viscosity of fluid, here water. Sloshing force (F) acting on the walls of the water tank is given by:

$$F = 0.5 \rho g B (h_R^2 - h_L^2) + \int_0^L \rho g B h S dx \quad (17)$$

h_R, h_L Wave height with respect to bottom of the tank at the right and left wall of the tank.

ρ Density of fluid, here water.

The sloshing frequency of the tank liquid is given as,

$$f_w = \frac{1}{2\pi} \sqrt{\frac{\pi g \tanh\left(\frac{\pi h}{L}\right)}{L}} \quad (18)$$

f_w Fundamental natural frequency of liquid sloshing

L Tank length.

3.3 Solving Non-linear Partial Differential Equations

The non-linear partial differential equations used to describe tuned liquid damper system discussed in the previous section are solved in iterative finite difference technique. Any general function f can be written as,

$$f = \alpha f_i + (1 - \alpha) \frac{f_{i+1} + f_{i-1}}{2} \quad (19)$$

The function can be velocity (v), wave height (h), or slope of the energy gradient line (S). In this numerical approach space derivatives are estimated as,

$$\frac{\partial f}{\partial x} = \frac{f_{i+1} - f_{i-1}}{2\Delta x} \quad (20)$$

for a particular time step. Δx is the element dimension. ' i ' is the node number. Time derivatives are estimated as,

$$\frac{\partial f}{\partial t} = \frac{f_i^{k+1} - \left[\alpha f_i + (1 - \alpha) \frac{f_{i+1} + f_{i-1}}{2} \right]}{\Delta t} \quad (21)$$

Δt is the time step size. ' k ' is the time step number. $\alpha = 0.98$.

3.4 Newmark- β Method

In this method, response of a damped or undamped structural system can be evaluated by involving numerical discretization of space and time. The second-order differential equation for a general excited structural system can be written as,

$$M\ddot{u} + C\dot{u} + Ku = F_{\text{turbulence}} \quad (22)$$

Using the extended mean value theorem, the first time-derivative of the motion is expressed as

$$\dot{u}_{n+1} = \dot{u}_n + \Delta t \ddot{u}_\alpha \quad (23)$$

where,

$$\ddot{U}_\alpha = (1 - \alpha)\ddot{U}_n + \alpha\ddot{U}_{n+1}, \quad 0 \leq \alpha \leq 1 \quad (24)$$

This transforms the Eq. 23 into

$$\dot{u}_{n+1} = \dot{u}_n + (1 - \alpha)\Delta t \ddot{u}_n + \alpha \Delta t \ddot{u}_{n+1} \quad (25)$$

As to incorporate the temporal change of the second time derivative of the motion, in the estimation of the displacement, the following formulations are suggested,

$$u_{n+1} = u_n + \Delta t \dot{u}_n + \frac{1}{2} \Delta t^2 \ddot{u}_\beta \quad (26)$$

where,

$$\ddot{u}_\beta = (1 - 2\beta)u_n + 2\beta\ddot{u}_{n+1}, \quad 0 \leq 2\beta \leq 1 \tag{27}$$

Therefore, Eq. 26 becomes

$$u_{n+1} = u_n + \Delta t \dot{u}_n + \frac{1}{2}(1 - 2\beta)\Delta t^2 \ddot{u}_n + \beta \Delta t^2 \ddot{u}_{n+1} \tag{28}$$

The finite difference formulas for the Newmark Beta scheme are

$$\ddot{u}_{n+1} = \frac{1}{\beta \Delta t^2}(u_{n+1} - u_n) - \frac{1}{\beta \Delta t} \dot{u}_n - \left(\frac{1}{2\beta} - 1\right) \ddot{u}_n \tag{29}$$

$$\dot{u}_{n+1} = \frac{1}{\beta \Delta t}(u_{n+1} - u_n) - \left(\frac{\alpha}{\beta} - 1\right) \dot{u}_n - \Delta t \left(\frac{\alpha}{2\beta} - 1\right) \ddot{u}_n \tag{30}$$

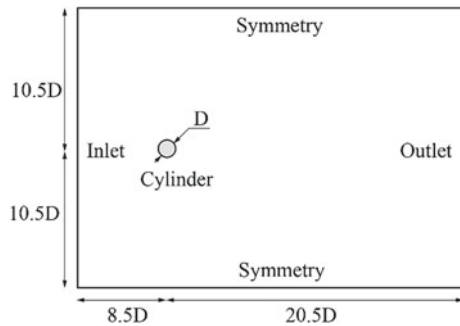
4 Results and Discussion

4.1 Validation 1: Suitability of SLWF Model

A flow domain of $21D$ height is considered for the problem, where D is the diameter of the cylinder. Upstream and downstream boundary distances of the domain are kept at $8.5D$ and $20.5D$ from the centre of the cylinder, respectively. D is taken as 19 mm or 0.019 m. Inlet flow velocity is kept uniform with a magnitude of 69.2 m/s, which leads to a flow Reynolds number of 90,000. An attempt has been made to numerically replicate the experiment performed by Revell et al. [11]. A schematic of the problem is presented in Fig. 1.

At first, transient simulation (LES) is performed to extract globally averaged flow parameters, like wall shear stress, τ_w coefficient of skin friction C_f , etc. at different points on the cylinder wall, using both OpenFOAM (v-2012) and ANSYS-Fluent (V14.5). The mesh refinement is optimized as suggested by Wang et al. [12]. A total

Fig. 1 Schematic of flow past bluff body



of 94,651 quadrilateral cells are used. An unstructured grid with necessary refinement close to the cylinder wall is used in the form of 360 and 80 mesh nodes in the circumferential and radial directions, respectively. Incompressible Navier–Stokes equations are solved at each grid in a PISO solver. To reduce the computation cost, the Non-Iterative Time-Advancement scheme is chosen along with the Fractional Step method (FSM). Spatial discretization is performed using the Bounded Central Difference scheme. Unsteady pressure is interpolated over the entire domain using PRESTRO algorithm. To keep Courant–Friedrichs–Lewy (CFL) number below 1.5, the time step size is chosen to be 1×10^{-6} s. Two different sub-grid eddy viscosity models are used for computation, (a) the Smagorinsky-Lilly model with Wall Function (SLWF) and (b) the Dynamic Smagorinsky-Lilly model (DSL). The comparison results obtained from ANSYS-Fluent is presented in Figs. 2 and 3 in order to select the suitable model between SLWF and DSL.

Between these two models, SLWF tends to behave better for flow past bluff body, that is why, the next problem case of flow past square cylinder for high Re is evaluated with this method.

Fig. 2 Coefficient of pressure at different angle (θ) of the points over the body, measured from the trailing edge. (Experimental results are from Revell et al. [11])

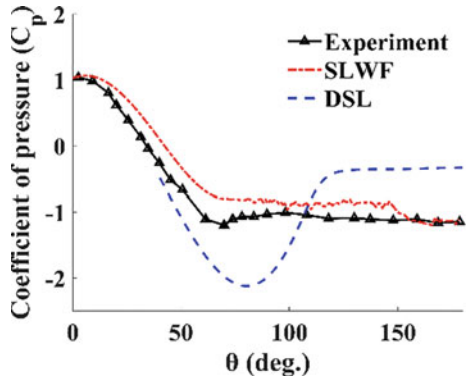
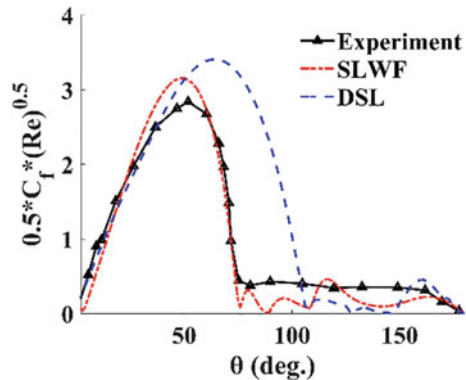


Fig. 3 Scaled skin friction coefficient at different angle (θ) of the points over the body, measured from the trailing edge. (Experimental results from Revell et al. [11])



4.2 Validation 2: Flow Past Square Cylinder

A square cylinder of dimension D , is placed in a fluid domain, with a free stream velocity of U_0 at zero angle of attack. An inlet turbulence of intensity 0% is set at first, which is the laminar approaching flow case [5]. From this case, the mean and root mean square values of coefficient of drag (C_D), have been evaluated and compared with the experimental results [6–8], and presented in Table 1. The schematic of the general problem is shown in Fig. 4, and meshing in Fig. 5. For the present validation purpose, TLD is not considered.

Table 1 Validation for flow past square cylinder

	Re	St	$\overline{C_D}$	C'_D
Experimental (Lee 1975) [6]	1.76×10^5	0.122	2.07	
Experimental (Pocha 1971) [7]	9.1×10^4	0.12	2.06	0.19
Experimental (Noda and Nakayama 2003) [8]	6.89×10^4	0.131	2.16	0.207
Numerical (Li et. al 2018) [5]	10^5	0.129	2.085	0.218
Present study	10^5	0.101	2.025	0.206

Fig. 4 Schematic of the turbulence-structure-TLD system

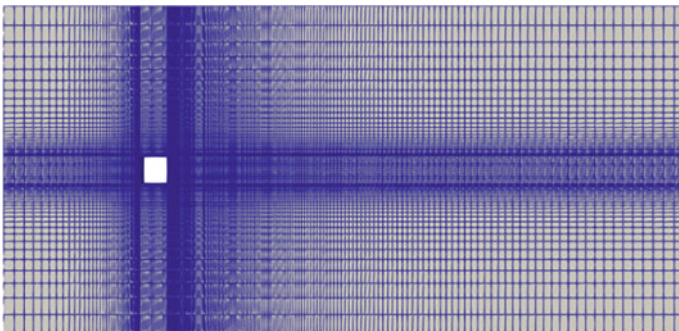
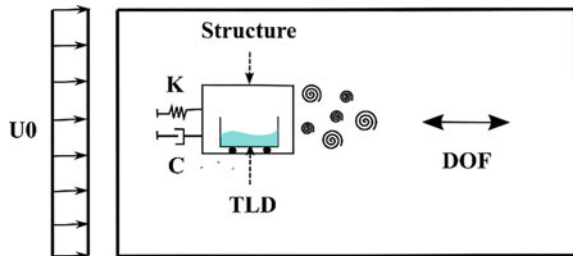
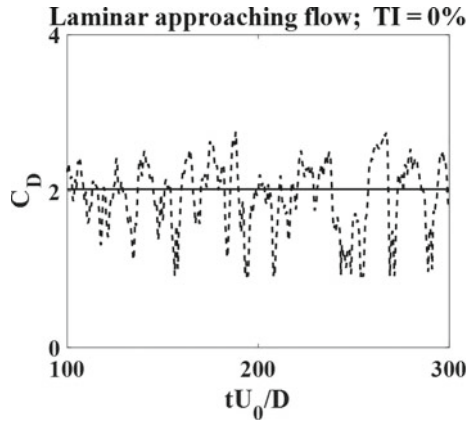


Fig. 5 Meshing in OpenFOAM

Fig. 6 Coefficient of drag over time



As seen in Fig. 6 the turbulent flow is simulated for an initial smaller time duration, which possibly resulted in a lower C_D value. A better prediction is expected for a longer simulation.

4.3 Validation 3: TLD-Structure Interaction

In order to validate the developed TLD-structure interaction model, the shaking table experiment performed by Sun et al. [2] is considered. TLD tank is 59 cm long, and 33.5 cm wide. The water depth is 3 cm. The frequency ratio is the ratio between the natural frequency of the structure to that of the TLD liquid (here water). The structural displacement with and without attached TLD for different frequency ratios is presented in Fig. 7. The frequency ratio vs maximum and minimum wave height is presented in Fig. 8.

Fig. 7 Structural displacement with and without TLD [2]

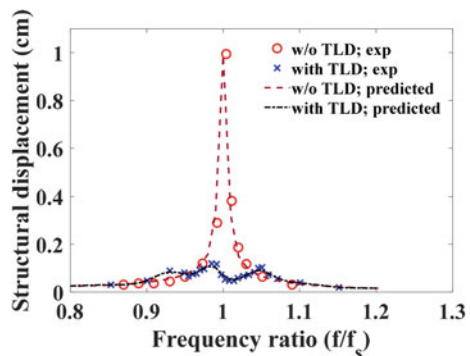
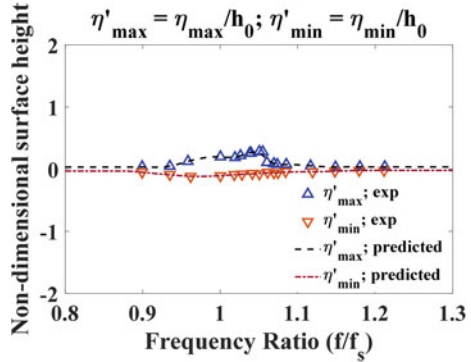


Fig. 8 Maximum and minimum surface height [2]



Once the turbulence modelling around a bluff body and the TLD-structure interaction modelling are validated, next two case studies are performed for laminar ($Re = 250$) and turbulent ($Re = 10^5$) flows. In both the cases time-varying drag force is used as the forcing to the next stage of TLD-structure interaction model. The general problem schematic is presented earlier in Fig. 1. The obstacle is considered as the square cylinder used in the validation 2 problem (Sect. 4.2). The results from the two problems are presented and discussed in Sects. 4.4 and 4.5.

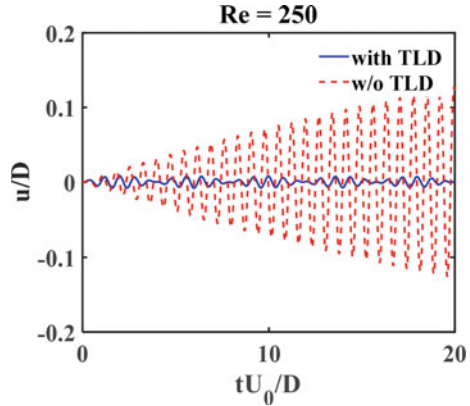
4.4 Turbulence-Structure-TLD Interaction; $Re = 250$

In this segment, a laminar flow ($Re = 250$) is considered. The computed drag coefficient and Strouhal numbers are presented in Table 2. This drag coefficient is subsequently used to estimate the force and the TLD parameters are so chosen that it is tuned to the corresponding natural frequency of 0.538 Hz (for $St = 0.138$). The predicted damped and undamped displacement (non-dimensionalized by the cylinder dimension, D) is presented in Fig. 9. The inherent structural damping is taken as 0.32% [2]. The spring stiffness is calculated accordingly.

Table 2 Drag coefficient for $Re = 250$ flow case

	Re	St	C_D
Numerical (Franke 1990) [13]	250	0.141	1.67
Present study	250	0.138	1.78

Fig. 9 Structural response; natural frequency of 0.538 Hz



4.5 Turbulence-Structure-TLD Interaction; $Re = 10^5$

In this segment, a turbulent flow ($Re = 10^5$) is considered. The computed drag coefficient is already presented in Table 1. This drag coefficient is subsequently used to estimate the force.

As the turbulent flow produces a broadband spectrum it is very difficult to find any particular forcing frequency, and eventually tuning the TLD also becomes challenging. In order to estimate the TLD performance in the reduction of the structural response, an extensive study is carried out in two stages.

- (a) TLD properties are varied to obtain different natural frequencies, replicating a broadband spectrum (using Eq. 18)
- (b) For each frequency the TLD-structure interaction is simulated and the performance is measured in terms of the ratio of the maximum displacement with and without TLD.

The result of the performance study is presented in Fig. 10.

From this study, few frequencies are identified where the TLD can reduce the structural response. In the other frequencies, the effect of attached TLD is found to be adverse though. Next, the structural response with and without TLD at a few identified frequencies are presented in Figs. 11 and 12.

The predicted damped and undamped displacements are non-dimensionalized by the cylinder dimension, D .

Fig. 10 Performance of TLD in a broadband spectrum

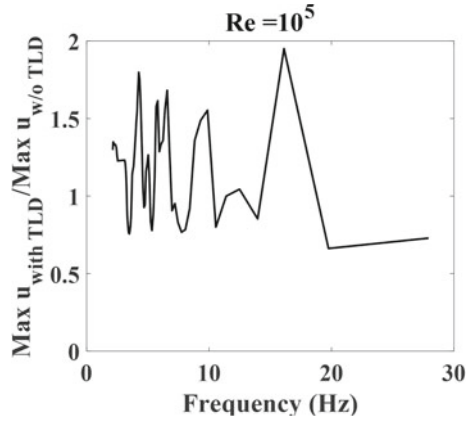


Fig. 11 TLD performance at 19.76 Hz frequency

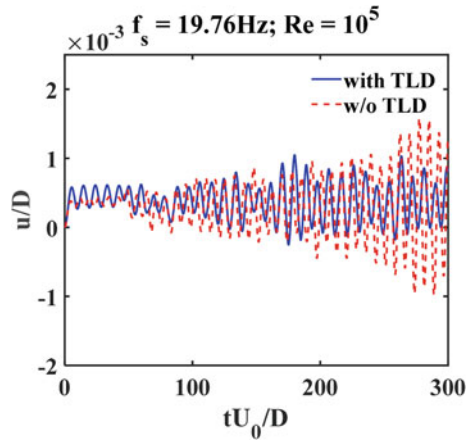
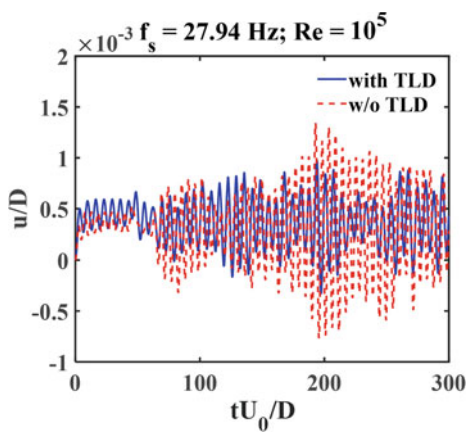


Fig. 12 TLD performance at 27.94 Hz frequency



5 Conclusions

In the present research work, a turbulence-structure TLD model is proposed, developed in FD framework. Open-source flow solver (OpenFOAM) and in-house MATLAB based TLD- structure interaction model is used. The significant conclusions are:

- (a) In case of laminar flow induced structural vibration, the TLD works perfectly when it is tuned with the vortex-shedding frequency.
- (b) In case of turbulence, the broadband force spectrum restricts to select any particular tuning frequency. However, in the present work a detailed study is carried out to identify few possible tuning frequencies that eventually is found to be reducing the structural response for the particular present case.
- (c) There is a requirement of further extensive studies with different turbulent conditions involving two-way FSI model to reach at any practical conclusive decision.

Nomenclature

U	Turbulent velocity [m/s]
u	Structural displacement [m]
\dot{u}	Structural velocity [m/s]
\ddot{u}	Structural acceleration [m/s ²]
v	TLD liquid velocity [m/s]
u'	Fluctuating velocity component [m/s]
\overline{U}	Time-averaged mean velocity [m/s]
k	Turbulent kinetic energy per unit mass [J/kg]
k_{sgs}	Sub-grid scale kinetic energy [J]
τ_{sgs}	Sub-grid stress [N/m ²]
C_D	Drag coefficient [-]
$\overline{C_D}$	Mean drag Coefficient [-]
C_D'	Root mean square drag coefficient [-]
F_D	Drag force [N]
A	Projected area [m ²]
h	Wave height at a particular location x [m]
t	Time [s]
μ_f	Absolute viscosity of water [Pa s]
ρ_f	Density of water [kg/m ³]
L	Tank length [m]
ρ	Density of air [kg/m ³]
F	Sloshing force acting on the walls [N]

References

1. Fujino Y, Sun L, Pacheco B, Chaiseri P (1992) Tuned liquid damper (TLD) for suppressing horizontal motion of structures. *J Eng Mech* 118(10):2017–2030
2. Sun L, Fujino Y, Pacheco B, Chaiseri P (1992) Modelling of tuned liquid damper (TLD). *J Wind Eng Ind Aerodyn* 41–44:1883–1894
3. Hu X, Zhao Z, Weng D, Hu D (2022) Design of a pair of isolated tuned liquid dampers (ITLDs) and application in multi-degrees-of-freedom structures. *Int J Mech Sci* 217
4. Chang Y, Noormohamed A, Mercan O (2018) Analytical and experimental investigations of Modified Tuned Liquid Dampers (MTLDs). *J Sound Vib* 428:179–194
5. Li YC, Chung CY, Fang FM (2018) Effect of turbulent uniform flow past a two-dimensional square cylinder. *J Appl Fluid Mech* 11(5):1185–1192
6. Lee BE (1975) The effect of turbulence on surface pressure field of a square prism. *J Fluid Mech* 69:263–282
7. Pocha JJ (1971) On unsteady flow past cylinders of square cross section. Ph.D. Dissertation, Queen Mary University of London, United Kingdom
8. Noda H, Nakayama A (2003) Free-stream turbulence effects on the instantaneous pressure and forces on cylinders of rectangular cross section. *Exp Fluids* 34:332–344
9. Germano M, Piomelli U, Moin P, Cabot WH (1991) A dynamic subgrid-scale eddy viscosity model. *Phys Fluids A Fluid Dyn* 3
10. Lilly DK (1966) The representation of small-scale turbulence in numerical simulation experiments. National Centre for Atmospheric Research, Boulder, Colorado
11. Revell JD, Prydz RA, Hays AP (1977) Experimental study of airframe vs. drag relationship for circular cylinders. Lockheed Report 28074. Final Report NASA Contract NAS1-14403
12. Wang YP, Chen J, Lee HC, Li KM (2012) Accurate simulations of surface pressure fluctuations and flow-induced noise near bluff body at low Mach numbers. In: *The seventh colloquium on bluff body aerodynamics and applications (BBAA7)*
13. Franke R, Rodi W, Schonung B (1990) Numerical calculation of laminar vortex-shedding flow past cylinders. *J Wind Eng Ind Aerodyn* 35:237–257

Transition of the Boundary Layer Subjected to Freestream Turbulence



Ravi Kumar and S. Sarkar

Abstract Influence of freestream turbulence (fst) on the transition to turbulence of a boundary layer under an adverse pressure gradient (APG) is investigated using a constant temperature hotwire anemometer and electronically scanned pressure (ESP). The experiments are carried out for two fst levels of 1.05 and 3.5% at a constant APG and Reynolds number (Re). A laminar separation bubble (LSB) is observed for a fst of 1.05%, and shear layer undergoes transition via the inviscid instability. The excitation of flow is evident from the beginning for an increased fst of 3.5%, while the LSB is completely suppressed and a change in the mode of flow transition is also observed. The location of onset of transition is highly affected by the variation of fst. Thus, the transition of a boundary layer under an APG is highly sensitive to freestream disturbances.

Keywords Laminar separation bubble · Experiments · Transition · Turbulence · Freestream turbulence

1 Introduction

In the presence of a strong adverse pressure gradient, the laminar boundary detaches from the surface. It then undergoes a transition in the separated region and associated momentum exchange in wall-normal direction leads to flow reattachment. The enclosed fluid region between separation and reattachment location forms a so-called laminar separation bubble (LSB) [1, 2]. The LSBs are witnessed in many low Re engineering applications such as diffusers, low-pressure turbines (LPT), high-lift multi-element airfoil, and unmanned air vehicles (UAVs). The formation of LSB is associated with undesirable effects such as reduction in the usable lift and increased drag. Moreover, some other adverse effects like increased unsteadiness and noise are also caused by the separation of flow.

R. Kumar · S. Sarkar (✉)

Department of Mechanical Engineering, Indian Institute of Technology Kanpur, Kanpur 208016, India

e-mail: subra@iitk.ac.in

The transition of an LSB depends upon many geometrical and flow parameters such as Re , APG, free stream turbulence (fst), surface curvature, etc. The transition associated with the boundary layer in the presence of APG is not unique and can be triggered via different routes. For example, in a low disturbance environment, the Tollmien–Schlichting (TS) waves amplify exponentially (modal growth) and initiate the transition. Later on, the inviscid instability mechanism (Kelvin–Helmholtz instability) sets in due to the inflectional velocity profile in LSB that causes perturbations to grow with even higher rates [3]. In case of a high level of environmental disturbances, the transition is preceded by the transient growth (non-modal) of streamwise disturbances due to ‘lift-up’ mechanism which might result in the formation of strong streamwise streaks [4]. Moreover, there may be situations where disturbances from different routes to transition coexist and interact with each other [5–8].

2 Literature Review and Objective

Such dramatic influence of fst on the transition of boundary layer under streamwise APG has motivated a large number of researchers in the past. Haggmark [9] performed experiments to study the effect of fst on LSB induced by an APG. They reported no evidence of the existence of 2D waves for fst of 1.5%. On the other hand, the appearance of low-frequency streaky structures upstream of separation and in the initial part of the LSB was revealed by the smoke flow visualization. Another preliminary investigation on the effect of fst on the LSB transition includes the work of Wissink and Rodi [10] who performed DNS on a 2D LSB formed on a flat plate under an imposed APG by an upper contoured wall. They observed that the K-H instability was triggered much earlier with an incoming fst level of 1.5% at the leading edge of the plate which led to a significant reduction in bubble length. Using a similar setup as Wissink et al. [11] carried out LES on the LSB under different fst levels ranging from 0 to 2%. They also observed elongated streamwise structures (K-modes) before the separation which results in a faster breakdown of KH vortices. It was also seen that the energy carried by the K-modes increases with increasing fst level leading to a greater reduction in bubble length. McAuliffe and Yaras [4] made a numerical study to understand the transition mechanism associated with LSB at different fst . They reported a change in instability mechanism from amplification due to KH instability to the growth of streamwise streaks at higher fst levels. Brinkerhoff and Yaras [12] performed a numerical study (DNS) of an attached flow subjected to streamwise pressure gradients and high fst levels. A stabilizing effect of longitudinal streaks with increasing fst level was observed in the favorable pressure gradient region. In the APG region, varicose secondary instability of low-speed streak induces transition to turbulence. The numerical simulation of Balzer and Fasel [13] investigated the fst influence on the LSB formed over a flat plate. They showed that the size of LSB is very sensitive to fst level. One important observation was that the KH instability was present even for the high fst case of 2.5% and was not ‘bypassed’, and the transition to turbulence was the consequence of both enhanced 3D disturbances and

primary shear layer instability. Moreover, there are studies where the flow separation is completely suppressed by transitioning the flow upstream of the LSB [8].

The underline flow physics of laminar-to-turbulent transition of the separated boundary layer is very complex where the role of fst remains highly elusive till date. Moreover, a large number of numerical studies have been reported in the literature concerning the influence of fst. On the contrary, only a few experimental studies have been carried out which are concentrated over the boundary layer transition under APG at realistic fst levels. In light of this, the authors think that it is worthwhile to dedicate further efforts in this direction. Thus, the present study is aimed at providing a deeper insight into the mechanism associated with the LSB transition under different levels of environmental disturbances through experiments. Here, the experiments are carried out for two levels of fst at a fixed Re of 2×10^5 where the inlet free stream velocity was kept at 2.74 m/s. The flow physics is explored using instruments like a single-wire hotwire anemometer and pressure scanner (ESP). Note that only preliminarily results are presented here to appreciate the flow features.

3 Experimental Detail

In the present study, the experiments are carried out in suction-type low-speed wind tunnel facility available at the energy conversion laboratory of IIT Kanpur. To ensure uniform and parallel flow, the flow passed through a flow straightener made of honey-combed plastic straws of diameter 25 mm and length of 162.5 mm. The flow straightener is followed by four wire meshes of coarse to fine grade to smoothen the flow. The flow is then passed through a 2D contraction cone of 3:1 area ratio to achieve the required velocity in the test section. The test section consists of an 1140-mm-long and 178-mm-wide acrylic flat plate with 6:1 elliptic leading edge which is firmly held by bolting it to the sidewall. The elliptic leading edge is chosen to avoid leading-edge flow separation that may alter the transition process. A schematic of the test section is presented in Fig. 1. To measure the surface static pressure, the plate is provided with 64 pressure taps at the midspan along the streamwise direction. The upper wall of the test section consists of a converging front part, throat and an adjustable rear part. The rear part has a provision to adjust the opening angle (α) to impose a required APG on the flat plate. The LSB is created on the flat plate by fixing the rear part of the upper wall at an arbitrary opening angle of 9.5° . Further, to avoid flow separation on the upper wall, two trip wires are provided at the end of the throat. The tunnel has a default fst level of 1.05% at the throat ($x/L = 0.263$ and $y/L = 0.0508$) with the flat plate. The tunnel has a provision to insert a replaceable turbulence grid prior to the test section to vary the fst in the flow. Experiments are carried out for two cases of turbulence intensity namely 1.02% (low fst) and 3.1% (high fst). Moreover, a streamwise slot is also provided at the upper wall to insert and move the hotwire probe along the streamwise direction. A diffuser is provided at the end of the test section to reduce the velocity.

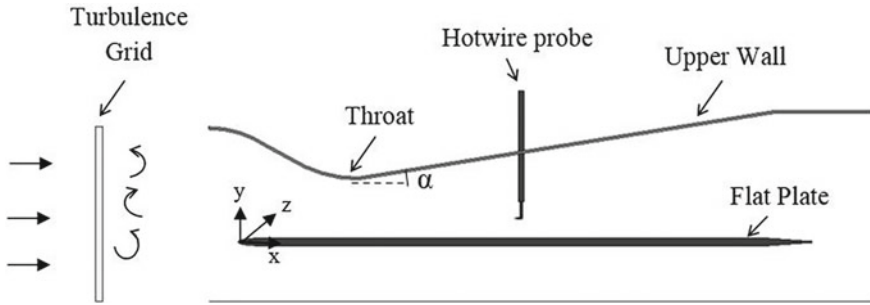


Fig. 1 Schematic diagram of the setup

The pressure measurements are carried out using two electronically scanned pressure (ESP) transducers with a differential pressure range of ± 2.5 kPa. Each ESP is equipped with 32 ports where individual transducers along with two additional reference ports for acquisition and calibration are provided for each port. The ESPs are calibrated against a known pressure and the calibration coefficients are converted from volts to Pascal following Sharma and Poddar [14]. The data are recorded for 10 s at a multiplexing frequency of 20 kHz where the sampling rate was kept at 400 samples/s per port and the uncertainty in measurements was 0.06%.

Dantec Dynamic's boundary layer probe (5- μ m-diameter platinum wire) is employed in constant temperature mode to measure the instantaneous velocity. The data were taken for 2^{15} instances in 6.55 s at a sampling frequency of 5 kHz. The calibration of hotwire was performed against the micro-manometer. An uncertainty analysis is carried out following Yavuzkurt [15], and the uncertainty associated with the velocity measurement was found to be less than 1.1%.

4 Results and Discussion

Figure 2 represents the coefficient of pressure (C_p) distribution over the flat plate for different fst . For low fst , the C_p shows that the pressure decreases gradually in the favorable pressure gradient portion and attains minima at the throat. Further, a pressure plateau followed by a sharp pressure rise is evident in the APG region which depicts the presence of an LSB [16] where the beginning of the pressure plateau marks the separation point. A method proposed by Gerakopoulos [17] is used to precisely mark the separation point (x_S), onset of transition (x_{to}), and reattachment point (x_R) where the intersection of the straight line fitted in constant pressure, pressure recovery, and the APG region downstream gives the separation, onset of transition, and reattachment points. The separation, onset of transition are located at $x/L = 0.367$, and 0.40 , respectively, where the reattachment point is at $x/L = 0.553$. On the other hand, the flow in high fst case does not indicate any constant pressure

portion in the APG region rather it gradually increases confirming an attached flow through the entire plate.

The contours of rms of streamwise velocity fluctuations for the two fst cases are shown in Fig. 3 to appreciate the evolution of the disturbances in the flow. It is observed that the fluctuations begins to grow suddenly at $x/L = 0.40$ due to the onset of transition for low fst and the maximum u_{rms} values are concentrated in a particular region ($x/L = 0.43-0.53$) away from the wall attributing to the formation of LSB. For high fst, the fluctuations increase gradually from the $x/L = 0.34$ indicating that the transition of flow was underway from the beginning. Further, the maximum u_{rms} fluctuations spread over a larger portion of the plate and remain close to the wall, compared to the low fst case.

The evolution of maximum u_{rms} fluctuations along the streamwise directions for different fst are presented in Fig. 4 to illustrate the growth of disturbances. The fluctuations do not exhibit any significant growth up to $x/L = 0.39$ in case low fst. After

Fig. 2 Static pressure coefficient distribution for different free stream turbulence intensities

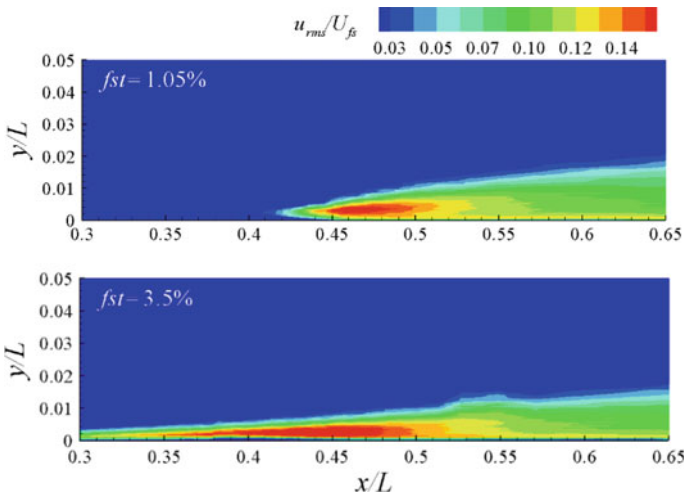
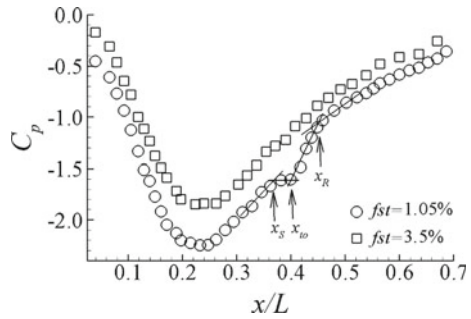
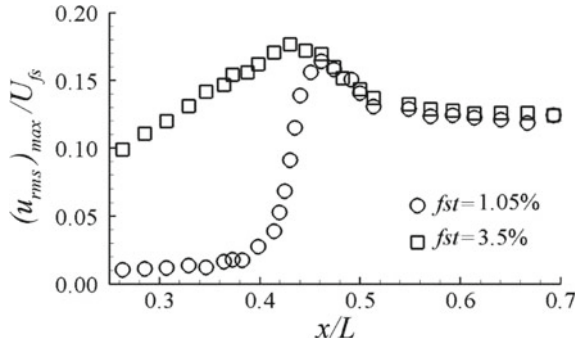


Fig. 3 Contours of u_{rms} fluctuations of streamwise velocity for different free stream turbulence intensities

Fig. 4 Evolution of maximum u_{rms} fluctuations of streamwise velocity for different free stream turbulence intensities



$x/L = 0.39$, a sudden exponential (modal) growth is observed where the fluctuations attain maxima at $x/L = 0.39$ and then undergo saturation at $x/L = 0.513$. This growth of fluctuations may be attributed to the inviscid instability mechanism (KH instability) associated with the transition of LSB [18, 19]. On the contrary, a linear growth (non-modal) of fluctuations is evident from the beginning which becomes maximum at $x/L = 0.429$ and then saturates at $x/L = 0.513$. Such fluctuations growth is most probably associated with bypass transition where the transition occurs due to the receptivity of the background disturbances [20, 21]. Thus, the flow follows a different route to transition depending upon the magnitude of inlet fst . Further, the maximum of u_{rms} can be used to mark the end of transition and it is seen that the flow in the high fst case undergoes transition earlier than in the low fst case.

To appreciate the instability mechanism associated with the transition for the two fst cases, power spectra of streamwise velocity fluctuations at the different streamwise locations are shown in Fig. 5 where the vertical axis is shifted by an arbitrary amount to improve the visualization. For the low fst case, a clear selective amplification is evident for $f = 45$ Hz which corresponds to a normalized frequency (based on the momentum thickness and edge velocity at separation) of 0.0072 that lies in the range of K-H instability [4, 22]. Thus, the shear layer transition in case of low fst is attributed to the K-H instability that arises in the flow due to the inflectional velocity profile in LSB. Further, no such selective amplification is observed in the high fst case rather it shows an evenly distributed band of frequency at all streamwise locations pointing that flow transition might be like a classical bypass transition.

5 Conclusions

The influence of fst on the transition of a boundary layer over a flat plate subjected to an APG is investigated experimentally. The hotwire and ESP results show the presence of an LSB over the flat plate for a low fst of 1.05%. The shear layer undergoes transition via the inviscid instability resulting in an exponential (modal) growth of

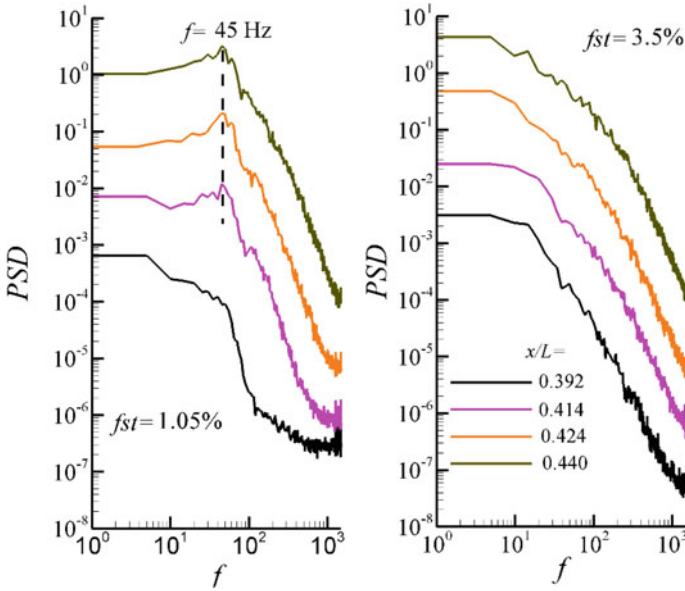


Fig. 5 Power spectra of streamwise velocity fluctuations for different free stream turbulence intensities

streamwise disturbances along the shear layer followed by the saturation of turbulence. When *fst* is increased to 3.5%, the LSB is completely suppressed, and the flow is transitional from the beginning. Further, a linear (non-modal) growth of streamwise fluctuations is observed depicting that the transition occurs due to the receptivity of background disturbances.

Nomenclature

- U_{fs} Local free stream velocity
- f Frequency
- L Length of flat plate
- x, y, z Coordinate axes
- C_p Coefficient of pressure, $C_p = (p - p_{ref})/0.5\rho U_i^2$

Subscript

- to Onset of transition
- te Transition end

S	Separation
R	Reattachment
rms	Root mean square
max	Maximum

References

1. Horton HP (1968) Laminar separation in two and three-dimensional incompressible flow. Ph.D. thesis, University of London
2. Gaster M (1969) The structure and behavior of laminar separation bubbles. ARC Reports and Memoranda 3595, Aeronautical Research Council (ARC)
3. Marxen O (2005) Numerical studies of physical effects related to the controlled transition process in laminar separation bubbles. Ph.D. thesis, Universität Stuttgart
4. Mcauliffe BR, Yaras MI (2010) Transition mechanisms in separation bubbles under low and elevated-freestream turbulence. *Trans ASME J Turbomach* 132(1):011004–011010
5. Kosorygin VS, Polyakov NP (1990) Laminar boundary layers in turbulent flows. In: *Laminar-turbulent transition, Proceedings of the IUTAM symposium*. Springer, pp 573–578
6. Wu X, Durbin PA (2001) Evidence of longitudinal vortices evolved from distorted wakes in a turbine passage. *J Fluid Mech* 446(1):199–228
7. Wu X, Jacobs R, Hunt J, Durbin PA (1999) Simulation of boundary layer transition induced by periodically passing wakes. *J Fluid Mech* 398(1):109–153
8. Zaki TA, Wissink JG, Rodi W, Durbin PA (2010) Direct numerical simulation of transition in a compressor cascade: the influence of free-stream turbulence. *J Fluid Mech* 665(1):57–98
9. Häggmark C (2000) Investigations of disturbances developing in a laminar separation bubble flow. Ph.D. thesis, KTH, Department of Mechanics, Stockholm
10. Wissink JG, Rodi W (2006) Direct numerical simulations of transitional flow in turbomachinery. *Trans ASME J Turbomach* 128(4):668–678
11. Lardeau S, Leschziner M, Zaki T (2012) Large eddy simulation of transitional separated flow over a flat plate and a compressor blade. *Flow Turbul Combust* 88(1):19–44; White FM (2011) *Fluid mechanics*. McGraw-Hills, New York, USA
12. Brinkerhoff JR, Yaras MI (2015) Numerical investigation of transition in a boundary layer subjected to favourable and adverse streamwise pressure gradients and elevated free stream turbulence. *J Fluid Mech* 781(1):52–86
13. Balzer W, Fasel HF (2016) Numerical investigation of the role of free-stream turbulence in boundary-layer separation. *J Fluid Mech* 801(1):289–321
14. Sharma DM, Poddar K (2010) Investigations on quasi-steady characteristics for an airfoil oscillating at low reduced frequencies. *Int J Aerosp Eng*, 940528
15. Yavuzkurt S (1984) A guide to uncertainty analysis of hotwire data. *ASME J Fluids Eng* 106(2):181–186
16. Tani I (1964) Low-speed flows involving bubble separations. *Progress Aerosp Sci* 5:70–103
17. Gerakopolous R, Boutilier MSH, Yarusevych S (2010) Aerodynamic characterisation of a NACA 0018 airfoil at low Reynolds numbers. *AIAA Paper*, pp 2010–4629
18. Jones L, Sandberg R, Sandham N (2008) Direct numerical simulations of forced and unforced separation bubbles on an airfoil at incidence. *J Fluid Mech* 602(1):175–207
19. Yarusevych S, Kawall JG, Sullivan PE (2008) Separated-shear-layer development on an airfoil at low Reynolds numbers. *AIAA J* 46:3060–3069
20. Yang Z (2019) On bypass transition in separation bubbles: a review. *Propulsion Power Res* 8(1):23–24

21. Katiyar S, Sarkar S (2021) Transitional flow and heat transfer on the pressure surface of a C-D compressor blade. In: Proceedings of the ASME 2021 international mechanical engineering congress and exposition, volume 10: fluids engineering. Virtual, Online. 1–5 Nov 2021
22. Samson A, Sarkar S (2016) Effects of free-stream turbulence on transition of a separated boundary layer over the leading-edge of a constant thickness aerofoil. *ASME J Fluids Eng* 138(2):021202

Introduction of Critical Filling Parameter on Faraday Instability and Its Dependencies on Fluid Densities



K. P. Choudhary, S. P. Das, and Shaligram Tiwari

Abstract In the present work, we have studied two immiscible Newtonian fluid systems having different pairs of comparable densities on a rectangular container undergoing vertical oscillation. Inspired by the Floquet analysis of Kumar and Tuckerman (J Fluid Mech 279:49–68, 1994 [1]), stability analysis is carried out to calculate the threshold. A two-fluid system filled with different volumes of fluids is defined by a filling parameter ($\psi = h_1/(h_1 + h_2)$), where h_1 and h_2 are the lower and upper-layer heights, respectively. It has been found that the threshold curve for Faraday instability shows bidirectional behavior with filling parameter (ψ) for a two-fluid system with comparable densities. The point about which the threshold curve shows bidirectional nature has been first time introduced here as a critical filling parameter (ψ_c). An investigation on effect of density difference ($\Delta\rho$) and density ratio (ρ_r) on threshold curve ($f - A_c$ curve) and ψ_c has been performed, in which an increment in ψ_c with $\Delta\rho$ and ρ_r has been observed.

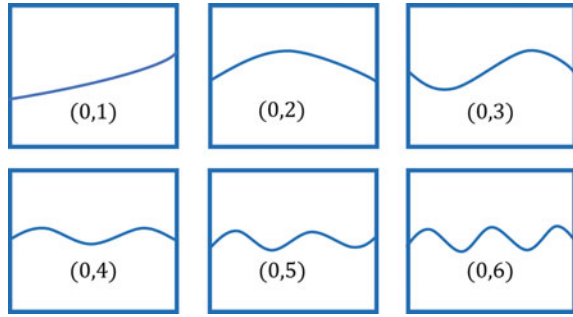
Keywords Faraday instability · Two-fluid system · Floquet analysis · Critical filling parameter · Density ratio

1 Introduction

A container filled with a two-fluid system (one having negligible density) undergoing deterministic or chaotic motion shows the motion of fluids inside the container. This is a very well-known phenomenon and is called liquid sloshing [2]. Similarly, a two-fluid system undergoing vertical sinusoidal oscillation shows the motion of fluids inside the container under certain conditions. Unlike horizontal oscillation, the interface is shows wavy interface and the waves appears at the interface are known as Faraday waves. The response frequencies of waves at the interface may have a subharmonic and harmonic response or sometimes may have periodic tripling.

K. P. Choudhary (✉) · S. P. Das · S. Tiwari
Department of Mechanical Engineering, Indian Institute of Technology Madras, Chennai 600036, India
e-mail: kushalchoudhary432@gmail.com

Fig. 1 Standing wave modes (m, n) $((0, 1)$ to $(0, 6)$) [3] that can be induced at the interface. The zero ($m = 0$) indicated that the waves are two-dimensional and have negligible motion along the width



The wave structures present at the interface, having different modes are shown in Fig. 1. The modes are represented as (m, n) where $m = 0$ indicated that the waves are two-dimensional and the interface remains flat along the width [3]. Two-fluid systems have found many industrial applications in solvent extraction, chemical mixing, pharmaceutical processes, liquid metal batteries etc. However, it is not always the case when both fluids have equal volume. Thus, the present work relates to various volumetric ratios of fluids in a two-fluid system.

2 Literature Review and Objective

Faraday (1831) first observed the Faraday wave once a vibrational source was applied to the fluid system [4]. The first inviscid analysis on Faraday instability is done by Benjamin and Ursell [5]. They formulated the inviscid governing equation into the form of Mathieu equation. Kumar and Tuckerman [1] considered the effect of fluid viscosity in their analysis with infinite (lateral dimension) bilayer Newtonian fluids subjected to vertical vibration. They have used a Fourier–Floquet analysis to get the marginal stability curves of harmonic and subharmonic responses. We have used the theory proposed by them in the present work. Besson et al. [6] extended the linear stability analysis of Kumar and Tuckerman [1] to the two-frequency oscillation. Both theories agree with the experiments and direct numerical simulation [7, 8]. The unstable wave pattern at the interface is independent of container geometry [4]. However, it requires a finite size analysis to get the critical unstable mode [3, 8].

An experimental study by Binks et al. [9] explains the variation of unstable interfacial structures with different depths in a cylindrical container. A numerical simulation done by Ubal et al. [10] neglected the motion of the upper fluid because of its negligible density compared to the lower fluid. They investigated the effect of various filled levels on the threshold curve ($f - A_c$). The two-fluid system also shows variations in its threshold curve ($f - A_c$) with different filling parameters [11]. The threshold curve for a fixed frequency shows a bidirectional behavior in a two-fluid system.

The objective of the present work is to introduce a critical filling parameter ψ_c (ψ , at which $\psi - A_c$ curve changes its increasing or decreasing slope (of having

Table 1 Fluid density pairs considered in the present study; other properties are kept constant

S. No.	ρ_2 (kg/m ³)	ρ_1 (range) (kg/m ³)
1	600	900–2400
2	800	1100–2600
3	1000	1300–2800

zero slope) with the filling parameter, where A_c is threshold amplitude for Faraday instability). The filling parameter is defined as $\psi = h_1/(h_1 + h_2)$, i.e., the percentage volume of lower fluid compared to total volume of the container [11]. We also investigated the possible dependencies of density difference ($\Delta\rho = \rho_1 - \rho_2$) and density ratio ($\rho_r = \rho_1/\rho_2$) on $f-A_c$ curve and ψ_c .

The filling parameter ψ is varied for a system having a fixed forcing frequency and a bilateral behavior is found. It has been observed that the minimum threshold is not at $\psi = 0.5$. This motivates us to find the possible reason for this phenomenon. In the present work, all the analysis has been done on set of fluids with various density pairs while keeping other fluid properties fixed to show the behavior of ψ_c with fluid density. The properties of fluid-1 (kinematic viscosity (ν_1) of 4.26×10^{-7} (m²/s)) and fluid-2 (kinematic viscosity (ν_2) of 9.48×10^{-7} (m²/s)) with interfacial tension 0.00077 N/m considered in this work are shown in Table 1. The fluid densities are an important factor because, at different filling parameters, the dominance effect of fluids (inertia of fluids) changes [10] because of the change in the mass of respective fluids.

3 Methodology

The schematic diagram of the considered domain ($L \times H = 35 \times 29.3$ mm²) is shown in Fig. 2, which is similar to the work by Jajoo [3]. In the linear stability analysis of Kumar and Tuckerman [1], the lateral dimensions (X and Y) are infinite. The finite length ($L = 35$ mm) produces a finite size effect in X -direction. It is noteworthy to say that the periodic boundary at the side wall has a similar effect as putting a finite size domain without having a physical wall, as shown in Fig. 2 [8]. This indicates that the side wall effect is not counted in our study since the Floquet analysis of Kumar and Tuckerman [1] is applicable for infinitely long in lateral directions. The gravitational acceleration value is $g_0 = 9.81$ m/s². The two-fluid system is subjected to a vertical sinusoidal forcing acceleration ($a = A_0\omega^2$), where $A_0 =$ displacement amplitude in (m) and $\omega = 2\pi f$, circular frequency in (rad/s) and f is forcing frequency (Hz). The lower and upper-layer fluids have depths of h_1 and h_2 , respectively.

In the calculation of threshold points for a given system (known fluid properties, filling parameter, and forcing parameter), a Floquet analysis on the full hydrodynamic system (FHS) proposed by Kumar and Tuckerman [1] has been used. The detailed procedure for linear stability analysis is available in Kumar and Tuckerman [1]. The system consists of two immiscible, incompressible Newtonian fluids with a

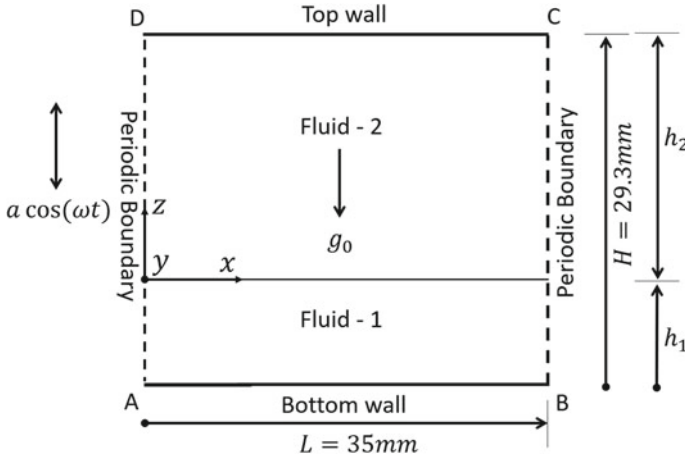


Fig. 2 Schematic diagram of the domain. The dashed lines indicate the periodic boundary, which acts like a finite size domain

gravitationally stable state. The frame of reference is moving with the oscillating two-fluid system; hence, the motion of the container is taken into consideration by temporally modulated gravitational acceleration $G(t) = g_0 - a\cos(\omega t)$.

The governing equations for each layer are linearized about the state of rest as $U_j = 0, P_j(t) = -\rho_j G(t)z$ for the perturbation field u_j, p_j onto the two-fluid system, where U_j and P_j are base flow velocity and pressure fields, and u_j, p_j are perturbation fields. The subscript j indicates 1 and 2 for the lower and upper fluid layers, respectively [1]. The no-slip condition has been imposed on the top and bottom walls. In the perturbed interface ($z = \zeta(x, y, t)$), kinematic surface condition has been linearized at $z = 0$ because of the small perturbed amplitude compared to fluid layer heights. The remaining conditions were derived from the stress tensors. The tangential component of the stress tensors must be continuous for the continuous deformation of the interface [1]. Whereas the curvature of the interface generates discontinuity in the normal component of the stress tensor, which is compensated by surface tension force, this is also known as the pressure jump condition. The perturbed governing equations along with mentioned boundary conditions are known as the full hydrodynamic system (FHS) [1]. The solutions of Floquet form $w_j(z, t) = e^{(\eta+i\alpha)t} \tilde{w}_j(z, t \bmod 2\pi/\omega)$, (the $t \bmod 2\pi/\omega$ is the reminder value of the term $t/(2\pi/\omega)$) has been applied in the FHS on the sinusoidal oscillating container with a time period $2\pi/\omega$ where, w_j is the vertical component of perturbed velocity field, $\eta + i\alpha$ is the Floquet exponent, $e^{(\eta+i\alpha)2\pi/\omega}$ is Floquet multiplier, and \tilde{w}_j is some periodic function which can be expanded in Fourier series [1]. The two cases $\alpha = 0$ and $\alpha = (1/2)\omega$ are known for harmonic and subharmonic responses, respectively. The final stability analysis is done by using the pressure jump condition because, this is the only equation that couples the different Fourier modes. The pressure jump condition can be expressed as [1]

$$\Delta[\rho\{\eta + i(\alpha + n\omega)\} + 3\mu k^2]\partial_z w_n - \Delta\mu\partial_{zzz} w_n + (\Delta\rho g_0 - \sigma k^2)k^2 \zeta_n = \Delta\rho k^2 \left[f(t)\tilde{\zeta}(t) \right]_n \tag{1}$$

where μ is dynamic viscosity and $\left[f(t)\tilde{\zeta}(t) \right]_n$ denotes the n th Fourier component of the product. The entire left-hand side of Eq. (1) can be written as $\frac{1}{2}\Delta\rho k^2 A_n \zeta_n$, having $A_n = A'_n + iA''_n$ complex and ζ_n is n th Fourier coefficient of the perturbed.

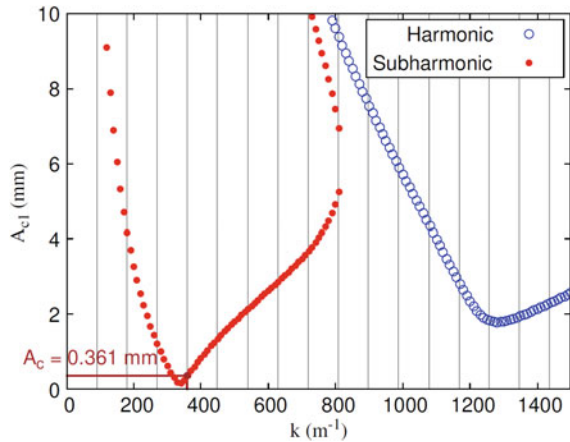
Equation (1) can now be written as:

$$\mathbf{A}_n \zeta_n = a(\zeta_{n+1} + \zeta_{n-1}) \Rightarrow \mathbf{A}\zeta = a\mathbf{B}\zeta \tag{2}$$

where \mathbf{A} is a diagonal complex matrix, and \mathbf{B} is a banded matrix, which depends on the α [1]. The stability analysis is done by fixing the wavenumber k and keeping $\eta = 0$ for both $\alpha = 0$ and $\alpha = (1/2)\omega$. Then, Eq. (2) has been solved for eigenvalues a , and the smallest real positive eigenvalue from a is known as the marginal stability boundary a_{c1} (a_{c1} is the minimum acceleration required for the wavenumber k at the interface) [1].

Figure 3 shows all the possible wavenumber k with the marginal amplitude ($A_{c1} = a_{c1}/\omega^2$) for fluid pair [1500 800] kg/m³. The vertical lines shows the possible wavenumber $k_{possible}$ that can be induced at the interface ($k_{possible} = n\pi/L$ where n is mode number 1, 2, 3, 4 . . .) in the considered finite size domain ($L = 35$ mm). The threshold point of Faraday instability for the finite size domain is obtained from the intersection of the curves with the wave number (vertical lines) at the lowest value of A_{c1} . The shape of the corresponding modes $(0, n)$ at the interface is presented in Fig. 1. The response frequency (f_R) of the unstable interface can be harmonic ($f_R = f$) or subharmonic ($f_R = f/2$). An example of subharmonic response is shown in Fig. 3, for which $A_c = 0.361$ mm and $(0, 4)$ mode will appear once the interface is unstable.

Fig. 3 $k - A_{c1}$ plots from linear stability analysis for $\psi = 0.5$, [1500 800] kg/m³ and having 10 Hz forcing frequency. The vertical lines indicate the possible wavenumber ($k_{possible} = n\pi/L$, where $n =$ mode number 1, 2, 3, 4 . . .) that can be produced in the considered domain of $L = 35$ mm



4 Results and Discussion

In this section, the changes in mode for different density pairs, keeping (a) density difference and (b) density ratio constant have been discussed. Along with this, the critical filling parameters (ψ_c) and its dependencies on $\Delta\rho$ and ρ_r are also discussed. The threshold point A_c has been calculated as discussed in the previous section.

4.1 Effect of Density Ratio and Density Difference on $f - A_c$ Curve for $\psi = 0.5$

The threshold curves from Floquet analysis have been carried out for the range of frequency 8 to 12 Hz. In the present work, this limitation on the simultaneous variation of density difference and ratio has been removed by taking six different density pairs such that, (a) for three density pairs, density differences are constant ($\Delta\rho = 1500 \text{ kg/m}^3$), and (b) for the other three, density ratios are constant ($\rho_r = 2$). The filling parameter ($\psi = h_1/(h_1 + h_2)$) is taken as 0.5, which means fluid-1 and fluid-2 have equal volume ($h_1 = h_2$).

Figure 4 shows the effect of density ratio on the threshold curve. The frequency bandwidth decreases with increasing value of density ratio (ρ_r) [3]. The left shift in the $f - A_c$ curve indicates that the system becomes more unstable with the decrement in the density ratio. Whereas, in Fig. 5, there are no significant differences between $f - A_c$ curves for different density differences. Observation from Figs. 4 and 5 shows that the density ratio has a more substantial effect on $f - A_c$ curve than the density difference provided the other one (density difference or density ratio) is fixed. This phenomenon can be explained by the Mathieu equation derived by Kumar and Tuckerman [1] for ideal fluids. The Mathieu equation from Kumar and Tuckerman [1] is as follows:

$$\ddot{\zeta} + \omega_0^2[1 - \hat{a} \cos(\omega t)]\zeta = 0 \tag{3}$$

where

$$\omega_0^2 = \frac{(\rho_1 - \rho_2)g_0k + \sigma k^3}{\rho_1 \coth(kh_1) + \rho_2 \coth(kh_2)} \tag{4}$$

The above equation can be rearranged by introducing the density ratio $\rho_r = \rho_1/\rho_2$.

$$\omega_0^2 = \frac{(\rho_r - 1)g_0k + (\sigma k^3/\rho_2)}{\rho_r \coth(kh_1) + \coth(kh_2)} \tag{5}$$

In the present study, the second term (right-hand side) of Eq. (5) $\left(\frac{\sigma k^3/\rho_2}{\rho_r \coth(kh_1) + \coth(kh_2)}\right)$ is negligible compared to the first term (right-hand side). Hence,

Fig. 4 Comparison of $f - A_c$ curves for fluid pairs having constant density difference ($\Delta\rho = 1500 \text{ kg/m}^3$) with three different density ratios for $\psi = 0.5$. The mode with the star mark shows the harmonic mode, while other modes are subharmonic

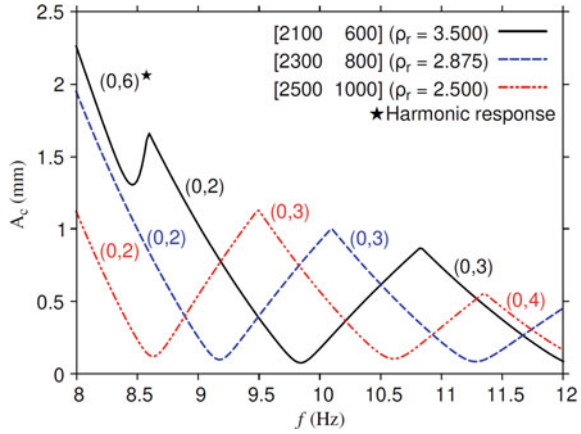
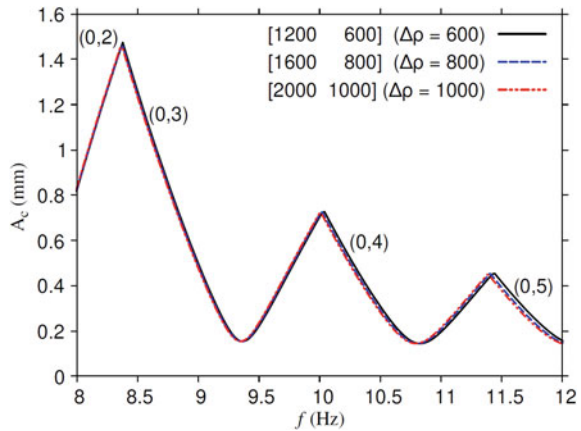


Fig. 5 Comparison of $f - A_c$ curves for fluid pair having constant density ratio ($\rho_r = 2$) with three different density differences for $\psi = 0.5$. All the modes are subharmonic

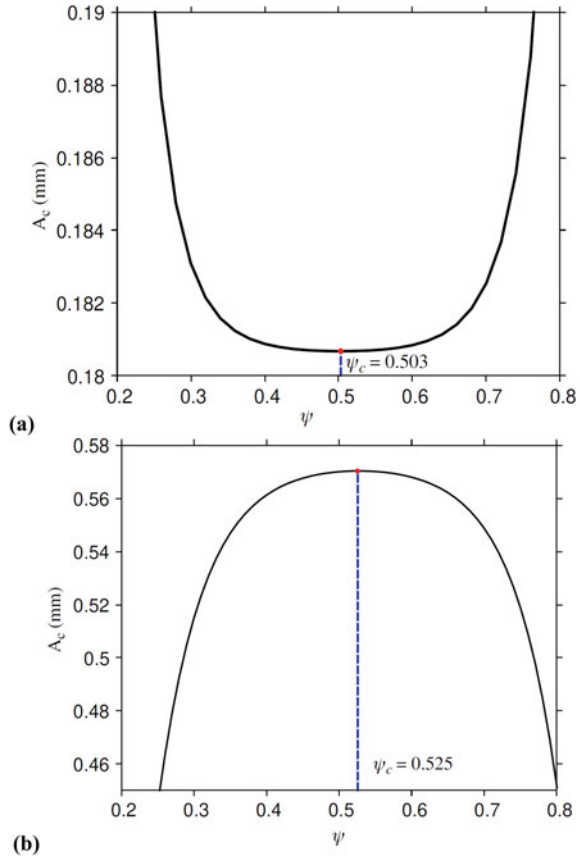


the ω_0^2 will only be the function of the density ratio (ρ_r). In Eq. (5), the natural frequency of the system increases with increment in ρ_r , which can be seen in Fig. 4. The threshold curve for varying density difference ($\Delta\rho$) with a fixed value of density ratio (for example $\rho_r = 2$ in Fig. 5) shows only minor deviation. These minor deviations may arise from the viscous and interfacial tension effects between the fluids.

4.2 Calculation of Critical Filling Parameter (ψ_c)

As defined in Sect. 4.1, the critical filling parameter (ψ_c) is calculated using the linear stability analysis following Kumar and Tuckerman [1]. The filling parameter (ψ) is varied, keeping the fluid properties and forcing parameter fixed. The ψ

Fig. 6 An example of the calculation of the critical filling parameter ψ_c at the forcing frequency of 10 Hz. The plot showing the threshold values with different filling parameters for the fluid properties of having density pair: **a** [1800 1000] kg/m³, **b** [2500 1000] kg/m³ and 10 Hz forcing frequency



has different effect on threshold amplitude for supercritical (right-hand side of the minimum threshold) and subcritical (left-hand side of the minimum threshold) bifurcation within a mode [12]. The $f - A_c$ curve shifts toward the left-hand side for the ψ value having interface lies near the wall. Resulting for ψ varies from 0 to 1 threshold value for supercritical bifurcation first decreases, then increases, and vice-versa for subcritical bifurcation. The ψ value is recorded from where the nature of threshold value is changing and represented as a critical filling parameter (ψ_c) as shown in Fig. 6a for supercritical bifurcation and Fig. 6b subcritical bifurcation.

4.3 Effect of Density Ratio and Density Difference on ψ_c

The critical filling parameters for fluid pairs given in Table 1 have been calculated at 10 Hz and plotted in Figs. 7 and 8 with varying density difference and density ratio, respectively. In Sect. 4.1, we have discussed the Faraday instability modes

and threshold changes due to fluid properties. In our parametric study, although the modes, instability type (supercritical and subcritical bifurcation), and thresholds values of Faraday instability are changing, as shown in Fig. 4, overall, the ψ_c value is increasing with increment in $\Delta\rho$ and ρ_r (refer to Figs. 7 and 8). The possible reason for this, is the increment in ρ_1 with respect ρ_2 showing its dominant effect over fluid-2. There are some local variations in ψ_c as the mode passes through its operating frequency (10 Hz). However, these local variations are negligible. In Figs. 7 and 8, the circled symbols are off the trend from other data because while calculating threshold values for Faraday instability, the $k_{possible}$ is occurring near the nose of the $k-A_{c1}$ curve (refer Fig. 3). In the nose of the $k-A_{c1}$ curves, the curvature effect is dominant, and hence the ψ_c is off the trend.

Keeping density difference ($\rho_2 - \rho_1$) fixed (refer to Fig. 7), one can observe the significant change in ψ_c over the fluid pairs, whereas that is absent for the fixed density ratio (refer to Fig. 8). The increment in ψ_c with density ratio is almost linear,

Fig. 7 Variation of the critical filling parameter (ψ_c) with density difference. The fluid properties are given in Table 1

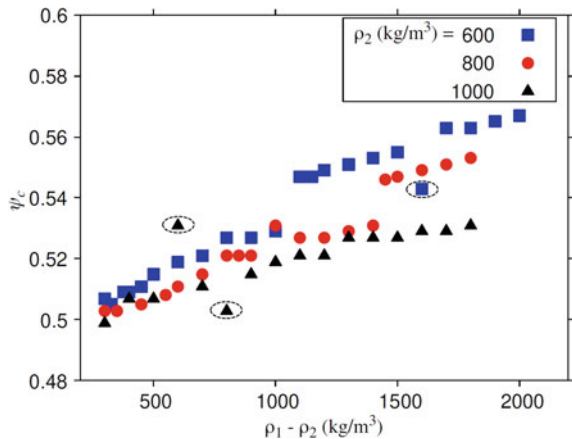
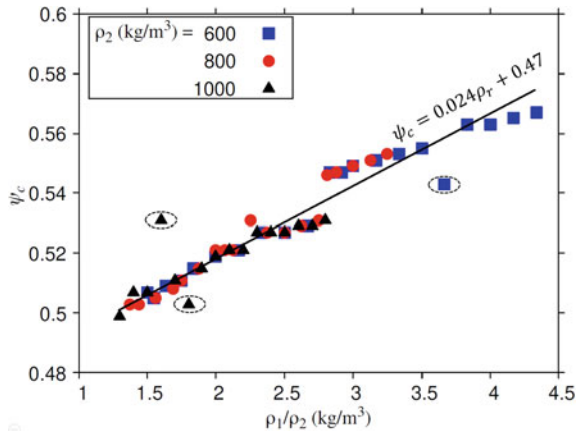


Fig. 8 Variation of the critical filling parameter (ψ_c) with density ratio. The fluid properties are given in Table 1



and a line has been plotted with linear data fit. The circled data have not been added to the data fit. The line equation $\psi_c = 0.024\rho_r + 0.47$ of linear data fit has a coefficient of determination of 0.95, which shows a perfect data fit.

5 Conclusions

Linear stability analysis for two-fluid systems has been performed for various Newtonian fluid pairs undergoing vertical oscillations. The threshold points for these fluid pairs are calculated based on the finite size domain. It has been found that the density ratio (ρ_r) has more substantial effect on the threshold curve than the density difference ($\Delta\rho$), provided the other one ($\Delta\rho$ or ρ_r) is fixed. The critical filling parameters (ψ_c) has been introduced and calculated for all the fluid pairs. In particular, we have found that ψ_c increases with increment in density difference ($\Delta\rho$) and density ratio (ρ_r). A negligible change in ψ_c has been observed for fixed ρ_r . This study shows the dominant effect of fluid-1 over fluid-2 by the increment of density difference or density ratio. The present study is only applicable for two Newtonian fluid pair having same order of density (comparable density).

Nomenclature

ρ_1	Density of fluid-1 [kg/m ³]
ρ_2	Density of fluid-2 [kg/m ³]
ν_1	Kinematic viscosity of fluid-1 [m ² /s]
ν_2	Kinematic viscosity of fluid-2 [m ² /s]
σ	Interfacial tension [N/m]
ρ_r	Density ratio [-]
$\Delta\rho$	Density difference [kg/m ³]
L	Length of the domain [m]
H	Total height of the domain [m]
h_1	Height of fluid-1 [m]
h_2	Height of fluid-2 [m]
ψ	Filling parameter [-]
ψ_c	Critical filling parameter [-]
g_0	Gravitational acceleration of earth = 9.81 m/s ² [m/s ²]
A_0	Forcing amplitude [mm]
A_{c1}	Marginal forcing amplitude [mm]
A_c	Threshold forcing amplitude in finite size domain [mm]
f	Forcing frequency [Hz]
ω	Circular frequency [rad/s]
a	Forcing acceleration [m/s ²]
a_{c1}	Marginal forcing acceleration [m/s ²]

t	Time [s]
m	Mode in y -direction [-]
n	Mode in x -direction [-]
k	Wavenumber [m^{-1}]
f_R	Response frequency [Hz]
k_{possible}	Wavenumber possible in consider domain ($= n\pi/L$) [m^{-1}]
$\tilde{G}(t)$	Modulated gravitational acceleration ($g_0 - a \cos(\omega t)$) [m/s^2]
\mathbf{U}_j, P_j	Base flow velocity and pressure field [m/s]
\mathbf{u}_j, p_j	Perturbed velocity and pressure field [N/m^2]
w_j	The vertical component of the perturbed velocity field [m/s]
$\eta + i\alpha$	Floquet exponent [s^{-1}]
$\tilde{f}(t)$	$= a \cos(\omega t)$ [m/s^2]
$\tilde{\zeta}(t)$	A periodic function appears in the Floquet form of interface fluctuation and can be expanded in the Fourier series [m]

References

1. Kumar K, Tuckerman LS (1994) Parametric instability of the interface between two fluids. *J Fluid Mech* 279:49–68
2. Ibrahim RA, Pilipchuk VN, Ikeda T (2001) Recent advances in liquid sloshing dynamics
3. Jajoo V (2017) Faraday instability in binary fluids (Doctoral dissertation)
4. Faraday M (1831) On the forms and states of fluids on vibrating elastic surfaces. *Philos Roy Soc* 52:319–340
5. Benjamin TB, Ursell FJ (1954) The stability of the plane free surface of a liquid in vertical periodic motion. *Proc R Soc Lond Ser A Math Phys Sci* 225(1163):505–515
6. Besson T, Edwards WS, Tuckerman LS (1996) Two-frequency parametric excitation of surface waves. *Phys Rev E* 54(1):507–513
7. Bechhoefer J, Ego V, Manneville S, Johnson B (1995) An experimental study of the onset of parametrically pumped surface waves in viscous fluids. *J Fluid Mech* 288:325–350
8. Perinet N, Juric D, Tuckerman LS (2009) Numerical simulation of Faraday waves. *J Fluid Mech* 653:1–26
9. Binks D, Westra MT, van de Water W (1997) Effect of depth on the pattern formation of Faraday waves. *Phys Rev Lett* 79(25):5010
10. Ubal S, Giavedoni MD, Saita FA (2003) A numerical analysis of the influence of the liquid depth on two-dimensional Faraday waves. *Phys Fluids* 15(10):3099–3113
11. Tipton CR, Mullin T (2004) An experimental study of Faraday waves formed on the interface between two immiscible liquids. *Phys Fluids* 16(7):2336–2341
12. Das SP, Hopfinger EJ (2008) Parametrically forced gravity waves in a circular cylinder and finite-time singularity. *J Fluid Mech* 599:205–228

Surface Roughness Heterogeneity Effects on Five Turbine Wind Farm Evaluated Using Large Eddy Simulation



Naveen N. Kethavath, Kingshuk Mondal, and Niranjan S. Ghaisas

Abstract The effect of an abrupt transition in the surface roughness from relatively rough conditions to smoother conditions on a five-turbine wind farm is examined using a large eddy simulation (LES). The LES are carried out using a high-order numerical framework with a state-of-the-art subgrid scale model and with the wind turbines modelled as rotating actuator disks. The surface roughness transition in the absence of turbines leads to an increase in the mean wind speed close to the bottom surface and a decrease in the turbulence intensity. The same effects are observed in the presence of wind turbines, and as a result, the evolution of the wakes of the individual turbines and the combined wake of all turbines is affected. The velocity deficit in the wake of each wind turbine grows approximately linearly from one to four diameters downstream of the turbine. This wake growth rate is different for a five-turbine wind farm sited on homogeneously rough surface and that sited on a heterogeneously rough surface. The wind turbine wakes also display an asymmetry between the profiles above and below the rotor hub heights. The presence of a surface roughness heterogeneity is found to reduce this asymmetry. These results have implications for the development of analytical models and ultimately for optimal layout of wind farms on heterogeneously rough surfaces.

Keywords Large eddy simulation · Wake growth rate · Surface heterogeneity · Atmospheric boundary layer · Wind farm wakes

Nomenclature

z_{01} Upstream aerodynamic roughness [m]

N. N. Kethavath (✉) · K. Mondal · N. S. Ghaisas
Department of Mechanical and Aerospace Engineering, Indian Institute of Technology,
Hyderabad, Telangana 502284, India
e-mail: me20resch11010@iit.ac.in

N. S. Ghaisas
Department of Climate Change, Indian Institute of Technology, Hyderabad, Telangana 502284,
India

z_{02}	Downstream aerodynamic roughness [m]
d	Turbine diameter [m]
H_{hub}	Turbine hub height [m]
C_T	Coefficient of thrust [-]
σ_u	Standard deviation of velocity fluctuation [-]
k^*	Wake growth rate [-]

1 Introduction

The lowermost part of the troposphere is influenced heavily by the fluxes of momentum, heat, and moisture imposed by the varying surface characteristics of the earth surface. This leads to the formation of the atmospheric boundary layer (ABL) which inherently influences day-to-day human activities such as weather, pollution, agriculture, and energy extraction from wind. The heterogeneous nature of the earth surface modulates the ABL flow through variations in the scalar fluxes thus making the study of heterogeneity of earth surface a major field in ABL study [1]. Wind energy has gained increased attention due to rise in reliability on renewable energy. ABL flow influences energy extraction by wind turbines and has become a challenge in wind farm design.

Energy extraction from the incoming wind by a wind turbine creates a region of lowered wind speed with increased wind shear and turbulence. This is called wind turbine wake region [2, 3]. Wake losses is the difference between the reduced power generated in a wind farm due to interaction between wakes of multiple turbines and the installed capacity. Wakes are dependent on the turbine as well as the ABL statistics and has become a crucial field of study in wind farm design and operation.

Numerous studies on ABL flow over heterogeneous surface ranging from field observations [4, 5], analytical models [6, 7] to numerical simulations [8, 9] have been carried out in the geophysical regime. These studies focused on an abrupt change in aerodynamic surface roughness (z_0) normal to the mean wind flow direction. None of the previously mentioned studies studied the effect of the heterogeneity in the wind turbine wake evolution.

Wake interactions in a wind farm has been studied using analytical models [10, 11], experiments/field observations [12, 13], and numerical simulations [14]. All the above studies assumed that the wind turbines are sited on a homogeneous surface.

This paper aims to study the effect of a heterogeneous surface with an abrupt change in surface roughness on multiple wind turbines, or small wind farm. The LES methodology and runs studied are described in Sect. 2. Results are presented and discussed in Sect. 3. Brief conclusions are presented in Sect. 4.

2 Numerical Methodology

2.1 LES Methodology

Large eddy simulations (LES) are carried out to solve the incompressible Navier–Stokes (N-S) equations using the concurrent-precursor simulation method [2]. Two domains, viz. precursor and main domain, of dimensions $(L_x \times L_y \times L_z)$ are employed, where x is streamwise, y is spanwise, and z is the vertical direction. The bottom surface of the precursor domain is homogeneous (with aerodynamic roughness z_{01}) without any wind turbine installed. The flow in this domain is driven by a pressure gradient $-u_*^2/L_z$. The main domain contains a heterogeneously rough surface, with the roughness changing from z_{01} to z_{02} abruptly at the location x_s . Multiple wind turbines are included in this domain, at locations $x_{t,i}$. The ‘fringe’ region constitutes the last quarter portion of the main domain and has the same surface roughness as the in the precursor domain and in the region upwind of x_s in the main domain. The flow is nudged toward the same upstream conditions as in the precursor using an additional forcing term in this fringe region. The x and y -directions are considered to be periodic. No-penetration, free-slip conditions are imposed on the top boundary, whereas a wall-modeled slip velocity condition is imposed at the bottom wall.

An in-house Fortran code, PadeOps-igrid [15], is used for the simulations. It uses Fourier-spectral discretization in the streamwise and spanwise directions, 6th-order compact finite-difference scheme in the vertical direction with 3rd-order Runge–Kutta method for time advancement. The subgrid scale model used is the Anisotropic Minimum Dissipation [16] model. The turbine-induced forces are imposed using the rotating actuator-disk model [14]. The viscous sublayer becomes extremely difficult to resolve on moderately sized grids due to the large Reynolds number of the flow (based on the height of the boundary layer) which is in the order of 10^{10} . This difficulty is overcome by dropping the viscous terms from the filtered N-S equations and using a wall model that mimics the effect of the viscous terms, which is important only very close to the wall. We use the wall model proposed by [17] which is suitable for homogeneous as well as heterogeneously rough surfaces.

2.2 Cases Simulated

Three different LES simulations are carried out as shown in Table 1. Run 3 incorporates five wind turbines; one is upstream of $x_s/d = 7.2$ and the other four are downstream of the abrupt change in surface roughness at x_s . This run is compared with Run 1, where turbines are placed at the same locations, but the abrupt change in surface roughness is removed, and Run 2, where the abrupt change in surface roughness is retained at same location, but the turbines are removed. All cases employ $330 \times 60 \times 90$ grid points. The computational domain size is $(L_x, L_y, L_z) =$

Table 1 Summary of LES runs studied

Run	Name	Step change ($x_s = 7.2d$)	Multiple turbines ($x_{t,i}$)
1	Homogeneous with turbine (Homog WT)	No	Yes
2	Heterogeneous with no turbine (Heterog NT)	Yes	No
3	Heterogenous with turbine (Heterog WT)	Yes	Yes

($44d, 4.8d, 5d$), where d is the diameter of the turbine. The five turbines are located at $x_{t,i}/d = 5, 10, 15, 20, 25$. The hub height of each turbine is $H_{\text{hub}} = 0.833d$. We use turbine diameter $d = 0.15\text{m}$ corresponding to the experiments of Chamorro and Porté-Agel [18], and surface roughness values of $z_{01} = 3.75 \times 10^{-3}d$ and $z_{01} = 4.5 \times 10^{-5}d$, as per the experiments of Chamorro and Porté-Agel [5]. Appropriate comparisons have been made with these experimental studies in our previous work. Specifically, we have validated our code for a single turbine sited on a homogeneous surface [19] as well as Run 2 [20]. All simulations are carried out over 180-time units, where one non-dimensional time unit is d/u_{*} , and statistical averaging is performed over the last 100-time units. These are sufficient to allow a statistically stationary state to be set up and for the statistical averaging to converge.

3 Results and Discussion

Contours of the time-averaged streamwise velocity in the vertical ($x - z$) plane at mid-span obtained from LES simulations for the three runs are shown in Fig. 1. In runs 1 and 3, wind turbines are marked by the solid lines. The wind turbine wakes can be identified by the low-speed region behind each wind turbine. In both runs, each downstream turbine is affected by the wakes of the turbines located upstream of it. The wake has not fully recovered even at $(x - x_{t,5})/d = 10$, or, $x/d = 35$, which is the farthest location that is studied here.

The normalized velocity profiles at two different downstream locations for runs 1 and 3 are shown in Fig. 2. The dashed line represents the incoming or upstream wind velocity (labeled ‘ups’). This value is same across all three runs since the surface roughness here is z_{01} for all cases. The symbols represent the velocity at locations downstream of the five wind turbines. The reduced aerodynamic roughness downstream of the step (denoted by the dashed vertical line in Fig. 1) causes the flow to accelerate close to the wall. This is seen qualitatively in the contours in Fig. 1b, c and quantitatively in Fig. 2b.

The streamwise turbulence intensity (TI) is defined as the standard deviation of the streamwise velocity divided by the velocity at the turbine’s hub height (i.e., $TI = \sigma_u/U_{\text{hub}}$), where $\sigma_u = \sqrt{u'u'}$. The vertical profiles of TI are plotted at two

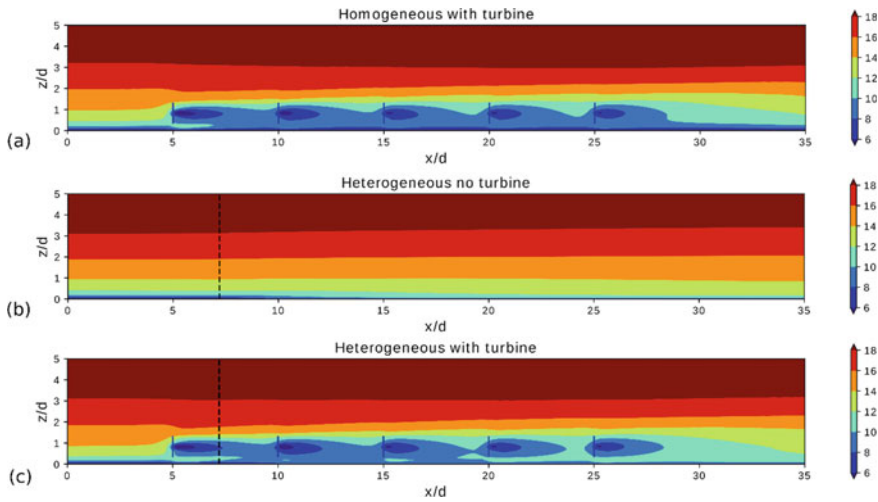


Fig. 1 Contours of the time-averaged streamwise velocity in the mid-span plane, where **a** run 1, **b** run 2, and **c** run 3. Solid blue and dashed black lines represent the rotor disc of the wind turbine and step change, respectively

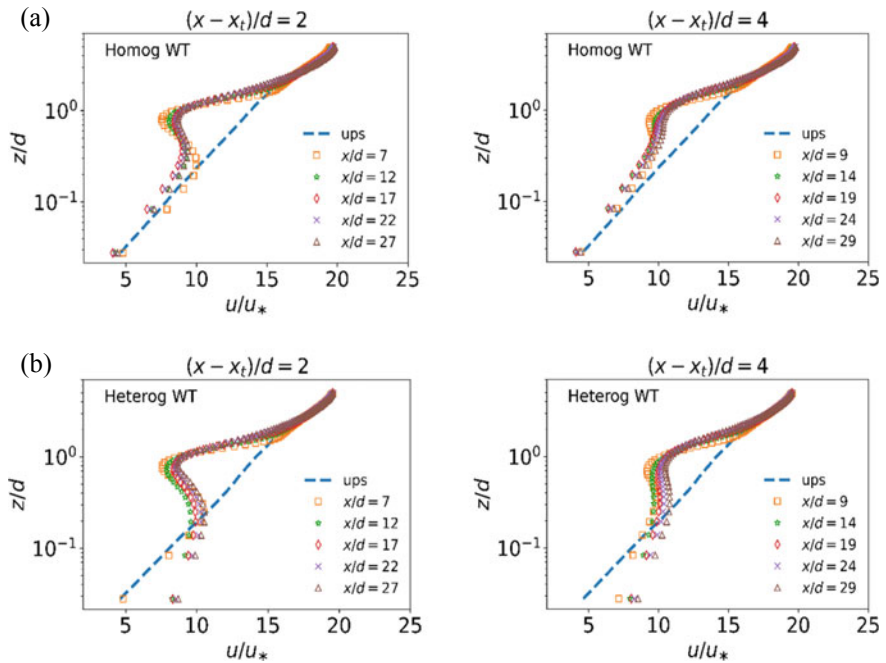


Fig. 2 Vertical profiles of the normalized time-averaged streamwise velocity for two downstream locations relative to the wind turbine. **a** run 1, **b** run 3. Dashed line and symbols represent the upstream location and downstream locations of the wind turbine

different downstream locations of each turbine in Fig. 3 in order to more quantitatively characterize turbine-induced turbulence. A significant increase in the turbulence intensity can be seen downstream of the turbines (placed at $x_{t,i} = 5, 10, 15, 20, 25$) compared to the turbulence in the incoming, upstream wind. The turbulence intensity at the top-tip level, $H_{hub} + d/2$, peaks as expected due to the strong shear at those locations. In both runs, the TI is clearly not zero at the lower grid point due to the slip boundary constraint and the wall model enforced at the lower boundary. Closer to the bottom surface, the TI values at the downstream locations are similar to the upstream values for run 1 (see, Fig. 3a). The heterogeneously rough surface in run 3 leads to a reduction of TI close to the wall at $x/d = 9$ onwards (see, Fig. 3b). These smaller TI values compared to at the upstream location are due to the abrupt reduction in surface roughness at $x_s/d = 7.2$.

The thrust coefficient (C_T) is the axial force imposed by the turbine on the flow non-dimensionalized using free-stream velocity and the rotor disk area. In the present study, C_T is not imposed, but a rate of rotation of the blades is imposed by prescribing a fixed tip-speed ratio equal to 4. The C_T is then calculated from the velocities obtained from the simulations. Figure 4a shows the thrust coefficient of each wind turbine for runs 1 and 3. In both runs, the value of C_T is equal for the first turbine because both operate in the same conditions (same z_{01}). The C_T values are smaller for the downstream turbines which reflects the wake effects. The C_T values obtained for the downstream turbines over homogeneous and heterogeneously rough surfaces

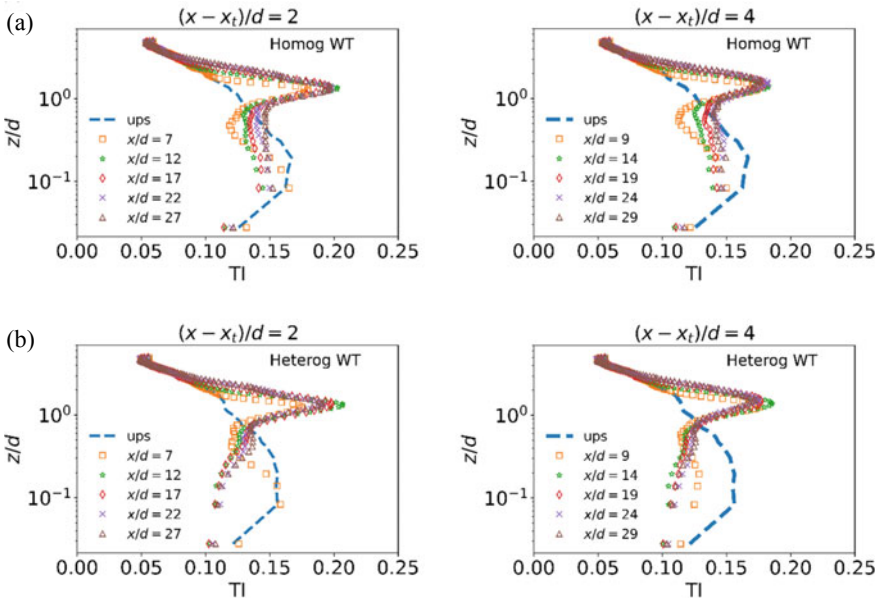


Fig. 3 Vertical profiles of the streamwise turbulence intensity for two downstream locations relative to the wind turbine. **a** run 1, **b** run 3. Dashed line and symbols represent the upstream location and downstream locations of the wind turbine

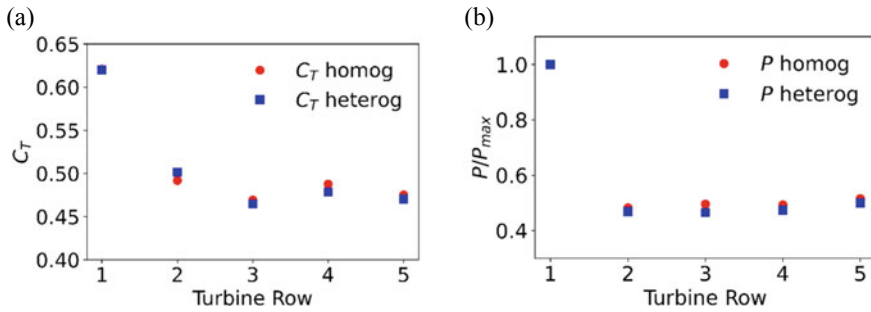


Fig. 4 Comparison of run 1 and 3 as a function of at each row location of a wind turbine. **a** Thrust coefficient, **b** The normalized power output

are slightly different due to the acceleration of the velocity downstream of the surface roughness jump.

The power generated by a turbine is computed as $P_i = -\overline{F_i u_{d,i}}$, where F_i is the instantaneous force exerted by turbine i , $u_{d,i}$ is the instantaneous wind speed at the disk and the overline represents a time-averaging operation. This power is normalized by the power of the first turbine, which generates maximum power, i.e., P_i/P_{max} , and is plotted in Fig. 4b for runs 1 and 3. In both runs, the downstream turbines generate around 50% of the power of the upstream turbine. The power generated slightly increases from row 2 to 5. Small differences are seen between runs 1 and 3, indicating the effect of surface heterogeneity. The maximum difference between the relative powers in runs 1 and 3 is seen for turbine row 3, which suggests that the position of a wind turbine relative to the location of the step change in surface roughness plays a role in determining its performance.

The width of the wake of a turbine n is characterized by σ_n , which is defined as the geometric mean of the wake widths along the spanwise (σ_y) and vertical directions (σ_z), $\sigma_n = \sqrt{\sigma_y \sigma_z}$. The spanwise and vertical velocity deficit profiles are fitted with a Gaussian shape to obtain σ_y and σ_z . The streamwise evolution of σ_n for all five turbines is shown in Fig. 5 for runs 1 and 3. The wake widths are calculated using two different definitions of velocity deficit. The deficit for run 1 is the difference between the upstream wind velocity, at $(x/d = 4)$, and at a downstream location. The deficit for run 3 is defined as the difference between wind velocities at the same location between runs 2 and 3, i.e., between the velocity with a step change in surface roughness but no wind turbines and the velocity with a step change in surface roughness as well as wind turbines [21].

Figure 5 shows that the wake width increases with increasing distance from the turbine. The wakes expand almost linearly in the region $1 < (x - x_t)/d < 4$ behind each turbine, with the slopes k^* . The k^* values are monotonically increasing for run 1, but do not monotonically increase for run 3. This further indicates that the rates of evolution of wind turbine wakes are affected by surface roughness heterogeneity.

The velocity deficit displays an asymmetry between its upper and lower parts (not shown). Here, the portions above and below the hub height are referred to as upper

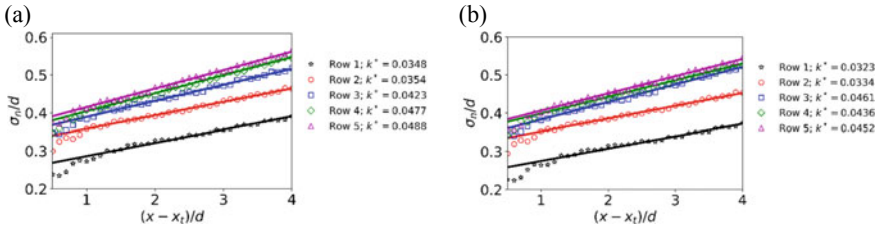


Fig. 5 Normalized standard deviation of the velocity deficit profiles at each row downstream of wind turbine. **a** run 1, **b** run 3. Symbols are LES and solid lines are linear fit $x \in [1, 4]$

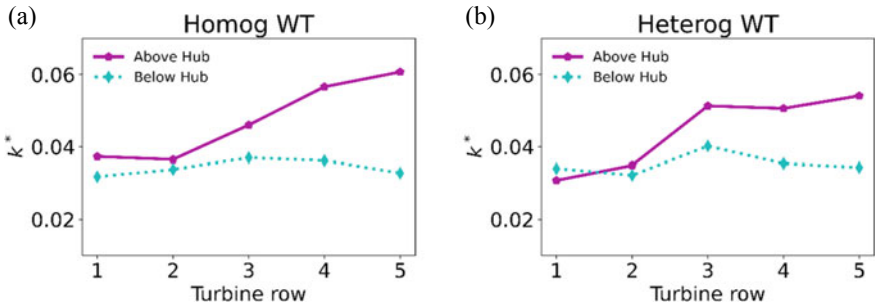


Fig. 6 Comparison of wake growth rate (k^*) of above and below hub height of turbine along Gaussian Shape of velocity deficit. **a** run 1, **b** run 3. Solid line represents the k^* value at above hub height to top-tip region, and dotted line represents the k^* value at below hub height to bottom-tip region

and lower parts, respectively, and are characterized by. The rate of change of the wake widths above and below the hub height are studied in Fig. 6. The values plotted are calculated by considering the Gaussian shape of velocity deficit from hub height to top-tip (i.e., Above Hub), and from the hub height to bottom-tip (i.e., Below Hub) for runs 1 and 3. The difference between the k^* values above and below the hub height is more pronounced for run 1 compared to run 3. This indicates that the velocity deficit profiles are more asymmetric for the homogeneously rough surface while the surface heterogeneity leads to a more symmetric development of the wakes.

4 Conclusions

We have carried out large eddy simulations (LES) of the flow over multiple turbines sited on a heterogeneously rough surface. This is compared to the flow over multiple wind turbine on a homogeneously rough surface on the one hand, and to the flow over a heterogeneous surface without turbines, on the other. The surface heterogeneity is in the form of an abrupt change in aerodynamic roughness from a high value to a smaller

value. The rough-to-smooth surface roughness heterogeneity leads to an acceleration of the mean wind speed and a reduction of the turbulence intensity downstream of it. These changed conditions in turn affect the evolution of wind turbine wakes. The thrust coefficient, relative power, and wake growth rate and asymmetry of the wakes are also affected by the surface roughness jump to differing extents. Continuing work focuses on quantifying the effects of surface roughness heterogeneities on the wind turbine wake evolution and development of analytical models for such conditions.

Acknowledgements NSG thanks the IIT Hyderabad institute seed grant and SERB Startup Research Grant for enabling this work as well as computational resources made available under the National Supercomputing Mission on Param-Brahma at IISER Pune.

References

1. Li B, Avissar R (1994) The impact of spatial variability of land-surface characteristics on land-surface heat fluxes. *J Clim* 7(4):527–537
2. Stevens RJAM, Meneveau C (2017) Flow structure and turbulence in wind farms. *Annu Rev Fluid Mech* 49:311–339
3. Porte-Agel F, Bastankhah M, Shamsoddin S (2020) Wind turbine and wind farm flows: a review. *Boundary-Layer Meteorol* 174:1–59
4. Bradley EF (1968) A micrometeorological study of velocity profiles and surface drag in the region modified by a change in surface roughness. *Q J Royal Meteorol Soc* 94:361–379
5. Chamorro LP, Porte-Agel F (2009) Velocity and surface shear stress distributions behind a rough-to-smooth surface transition: a simple new model. *Boundary-Layer Meteorol* 130:29–41
6. Elliott WP (1958) The growth of the atmospheric internal boundary layer. *Eos Trans AGU* 39:1048–1054
7. Ghaisas NS (2020) A predictive analytical model for surface shear stresses and velocity profiles behind a surface roughness jump. *Bound-Layer Meteorol* 176:349–368
8. K. S. Rao, J. C. Wyngaard, and O. R. Coté. The structure of the two-dimensional internal boundary layer over a sudden change of surface roughness. *J Atmos Sci*, 31:738–746, 1974.
9. Shir CC (1972) A numerical computation of air flow over a sudden change of surface roughness. *J Atmos Sci* 29:304–310
10. Jensen NO (1983) A note on wind generator interaction. *Risø-M-2411 Risø National Laboratory Roskilde*, pp 1–16. ISSN 01676105
11. Bastankhah M, Porte-Agel F (2015) A new analytical model for wind-turbine wakes. *Renew Energy* 70:116–123
12. Bastankhah M, Porte-Agel F (2019) Wind farm power optimization via yaw angle control: a wind tunnel study. *J Renew Sustain Energy* 11(2):023301
13. Smith SE, Travis KN, Djeridi H, Oblgado M, Cal RB (2021) Dynamic effects of inertial particles on the wake recovery of a model wind turbine. *Renew Energy* 164:346–361
14. Wu YT, Porte-Agel F (2011) Large-eddy simulation of wind-turbine wakes: evaluation of turbine parametrisations. *Boundary-layer Meteorol* 138(3):345–366
15. Subramaniam A, Ghate A, Ghaisas NS, Howland MF et al (2021) PadeOps GitHub repository. In: Available: <https://github.com/FPAL-StanfordUniversity/PadOps/tree/igridSGS>. Last Accessed 5 Aug 2021
16. Rozema W, Bae HJ, Moin P, Verstappen R (2015) Minimum-dissipation models for large-eddy simulation. *Phys Fluids* 27:085107
17. Bou-Zeid E, Meneveau C, Parlange MB (2004) Large-eddy simulation of neutral atmospheric boundary-layer flow over heterogeneous surfaces: blending height and effective surface roughness. *Water Resour Res* 40:W02505

18. Chamoro LP, Porte-Agel F (2009) A wind-tunnel investigation of wind-turbine wakes: boundary-layer turbulence effects. *Boundary-layer Meteorol* 132:129–149
19. Ghaisas NS (2020) Effect of vertical domain size on wind turbine large-eddy simulations in a half-channel. In: 1st International conference on advances in computational and experimental mechanics. IIT Kharagpur. Paper ID FM-20–027
20. Kondu A, Naik KN, Mondal K, Ghaisas NS (2021) Sensitivity of atmospheric boundary layer statistics to LES wall shear stress models behind a surface roughness jump. In: 48th national conference on fluid mechanics and fluid power (FMFP). BITS Pilani. Paper ID FMFP2021–01–108, 2021
21. Naik KN, Mondal K, Ghaisas NS (2022) Large eddy simulation study of a wind turbine sited behind an abrupt surface transition. In: 1st International conference in fluid thermal and energy systems, June 9–11, 2022. NIT Calicut, Kerala, India. Paper ID ICFTES2022-ES-152

Resonant Three-Wave Interactions in a Shear Flow with Density Stratification



Lima Biswas and Priyanka Shukla

Abstract This paper examines resonant three-wave interactions between internal gravity waves in a uniform shear flow with stable stratification confined between two oppositely moving horizontal plates. In particular, we present the existence of 1: 2: 3 resonance interactions among internal waves in a uniform shear flow with stable density stratification by varying the Richardson number. Such resonances occur when a fundamental wave (k_m, ω_m) interacts with its second harmonic ($2k_m, 2\omega_m$) and produce the third harmonic ($3k_m, 3\omega_m$), where k_m and ω_m , respectively, denote the wave number and frequency of the fundamental mode. In this study, we develop an algorithm to classify resonating modes and critical Richardson number at which 1:2:3 resonances occur by solving the linearized Boussinesq Navier–Stokes equation. Finally, the existence of 1: 2: 3 resonance and the spatial structures of resonating modes are graphically demonstrated for a particular critical Richardson number.

Keywords Stratified shear flow · Internal gravity waves · Resonance · Higher harmonic resonance

Nomenclature

$\overline{U}, \overline{\rho}, \overline{p}$	Base state velocity, density, pressure profiles
\overline{U}_p	Plate speed
\mathbf{g}	Gravitational acceleration
$\mathbf{u} = (u, w)$	Velocity vector

L. Biswas (✉)

Department of Aerospace Engineering, Indian Institute of Science, Bengaluru 560012, India
e-mail: limabiswas.ju@gmail.com

Department of Mathematics, Gandhi Institute of Technology and Management,
Hyderabad 502329, India

P. Shukla

Department of Mathematics, Indian Institute of Technology Madras, Chennai 600036, India

δ	Error tolerance
ϵ	Expansion parameter
∇, ∇^2	Gradient and Laplacian operators
ω_m	m -th mode frequency
ψ	Streamfunction
ρ_d	Density difference between the plates
ρ_m	Mean density
Ri	Richardson number
c_m	m -th mode phase velocity
$D = d/dz$	Derivative operator
H	Distance between the plates
I_ν, K_ν	Modified Bessel functions of order ν
J	Jacobian determinant
k_m	m -th mode wavenumber
p	Pressure
t	Time
x, z	Horizontal and vertical directions
N	Buoyancy frequency
ω, c, k	Frequency, phase velocity and horizontal wave number

1 Introduction

Internal gravity waves (IGWs) appear inside stably densitystratified ocean due to small-to-large perturbations. These perturbations cause fluid to move up or down resulting in a wave like motion [1]. Oceanic IGWs are usually generated through the flow over topography, imbalance of large-scale circulations, river plumes, etc., and have a significant influence on local and global climates, marine ecosystem, and biological productivity [2], marine engineering and submarine navigation [3], and underwater acoustics [4] through nonlinear interactions and mixing. IGWs contribute in exchanging energy among different ocean layers and transport nutrient through nonlinear interactions. Understanding nonlinear interactions among IGWs is therefore crucial as they (i) eventually lead to small-scale ocean mixing and the dispersal of matter, and (ii) impact ocean structures, ocean acoustics, and ship navigation.

The theory of nonlinear wave interactions has been attracted a lot of attention from scientific community over the past many decades [5–8]. Existence of resonance interactions among IGWs, surface waves, and interfacial waves in different types of density stratified systems are well known. A recent study by Biswas & Shukla [9] has shown the existence of triadic resonance interactions and self-resonances between IGWs in a uniform shear flow with uniform density stratification. However, the energy cascade process among different harmonics of fundamental internal gravity wave mode is poorly understood. To this end, the present work focuses on resonant three-wave interactions among three IGWs—a fundamental and their second and

third harmonics, i.e., their wavenumbers (k_m, k_n, k_r) and frequencies $(\omega_m, \omega_n, \omega_r)$ are in the ratio 1: 2: 3. Such interactions are responsible for a considerable exchange of matter, momentum, and energy among different IGW modes and the underlying deep ocean [1, 10]. Thus, resonant three-wave interactions require special attention, as they have a major impact on the redistribution of energy among various wave modes of different spatial and temporal scales and finally, lead to small-scale ocean mixing [11–14].

Resonance interactions involving a fundamental wave and its higher order harmonics are generally known as higher harmonic resonances, and are widely reported in the context of thermal convection problems, e.g., see Refs. [15–17]. A particular type of higher harmonic resonance is 1 : 2 resonance or self-resonance; under which a primary internal wave mode with frequency ω and wavenumber k interacts with itself and resonantly excites the second harmonic mode with frequency 2ω and wavenumber $2k$. Recently, the existence of such resonance interactions among IGWs in a uniform shear flow with stable density stratification between two oppositely moving horizontal parallel plates has been presented by Biswas & Shukla [9]. Note that, in the uniformly stratified uniform shear flow, self-resonances are the consequence of background shear current [7]. However, in the case of nonuniform stratification, background sheared current is not necessary for self-resonances. The simplest form of shear flow, i.e., uniform shear flow, supports self-resonances even in the uniformly stratified medium. Furthermore, the existence of self-resonances depends on the strength of stratification and shear [9].

The objective of the present paper is to derive an efficient algorithm using the dispersion relation (relation between the wavenumber and frequency of a wave) to determine the parameters for 1: 2: 3 resonances in any type of geophysically or industrially important flow configuration. Specifically, our aim is to provide the existence of 1: 2: 3 resonances among IGWs in a uniform shear flow with stable density stratification using linearized Boussinesq Navier–Stokes equations. Such resonance interactions among IGWs are important to understand the energy dissipation from a fundamental mode to its harmonics, which eventually leads to small-scale ocean mixing. The detailed analysis of the energy transfer mechanism among resonating IGWs using the amplitude evolution equation is beyond the scope of the present paper.

The rest of the paper is arranged as follows. The problem description and the governing equations are discussed in detail in section II. The normal mode analysis to study the linearized system is discussed in Section III. The algorithm to show the existence of 1:2:3 resonances among IGWs in the system is discussed in Section IV. Finally, the paper is concluded in Section V.

2 Problem Formulation

Consider a two-dimensional inviscid, incompressible, Boussinesq uniform shear flow confined between two horizontal parallel plates with infinite horizontal extent separated by a vertical distance H . The plates are moving at the same speed \overline{U}_p but in the opposite direction. The base flow profile consists of a parallel shear flow $\overline{U}(z)$ in a uniformly stratified density field $\overline{\rho}(z)$, which satisfy

$$\overline{U}(z) = \overline{U}_p z/H, \quad \text{and} \quad \overline{\rho}(z) = \rho_m - \frac{1}{2} \rho_d \frac{z}{H} \quad (1)$$

where ρ_m and ρ_d represent a mean density (constant) and the density mismatch between upper ($z = H$) and lower ($z = -H$) plates, respectively. Here x and z are the flow and the vertical directions, respectively, and the gravity is acting in the downward (negative z) direction. Note that, both the shear rate (\overline{U}_p/H) and the vertical gradient of background density ($-\rho_d/H$) are constant. The base state pressure $\overline{p}(z)$ varies in the vertical direction according to the hydrostatic balance, as follows

$$\frac{\partial \overline{p}}{\partial z} = g \overline{\rho}. \quad (2)$$

The incompressible, inviscid, Boussinesq flow is governed by the mass balance, energy conservation, and the momentum balance equations, which take the following form (neglecting the effect of viscosity, diffusivity, and Earth's rotation),

$$\begin{aligned} \nabla \cdot \mathbf{u} &= 0, \\ \frac{\partial \rho}{\partial t} + \mathbf{u} \cdot \nabla \rho &= 0, \\ \rho_m \left(\frac{\partial}{\partial t} + \mathbf{u} \cdot \nabla \right) \mathbf{u} &= -\nabla p + \rho \mathbf{g}, \end{aligned} \quad (3)$$

where $\vec{u} = (u, w)$ is the velocity vector with u and w , respectively, being the horizontal and vertical velocity components. ρ , p , and \mathbf{g} , respectively, represent the density, pressure, and gravity fields. Note that, the Boussinesq approximation assumes that the density variation can be neglected except in the buoyancy force term, which is a useful approximation for oceanic internal gravity waves where the density difference between different layers is very small.

To derive the perturbation equations, we decompose each of the flow variables (u , w , ρ , and p) into two parts, (i) the base state part (denoted by “bar” over the variables), and (ii) the perturbation from the base state solution (denoted by the superscript “prime”). Thus, we have $\rho(x, z, t) = \overline{\rho}(z) + \rho'(x, z, t)$,

$$p(x, z, t) = \overline{P}(z) + p'(x, z, t), \quad (4)$$

$$[u(x, z, t), w(x, z, t)] = [\bar{U}(z) + u', w'].$$

Substituting (4) into (3), subtracting the base flow equations, and omitting the superscript prime over the perturbed variables (to avoid notational complexity), we get

$$\begin{aligned} \frac{\partial u}{\partial x} + \frac{\partial w}{\partial z} &= 0, \\ \left(\frac{\partial}{\partial t} + \bar{U} \frac{\partial}{\partial x}\right) \rho &= -w \frac{\partial \bar{\rho}}{\partial z} - \left(u \frac{\partial \rho}{\partial x} + w \frac{\partial \rho}{\partial z}\right), \\ \left(\frac{\partial}{\partial t} + \bar{U} \frac{\partial}{\partial x}\right) u + \frac{d\bar{U}}{dz} w &= -\frac{1}{\rho_m} \frac{\partial p}{\partial x} - \left(u \frac{\partial u}{\partial x} + w \frac{\partial u}{\partial z}\right), \\ \left(\frac{\partial}{\partial t} + \bar{U} \frac{\partial}{\partial x}\right) w &= -\frac{1}{\rho_m} \frac{\partial p}{\partial z} - \frac{g\rho}{\rho_m} - \left(u \frac{\partial w}{\partial x} + w \frac{\partial w}{\partial z}\right). \end{aligned} \tag{5}$$

At the top and bottom walls $z = \pm H$, both the horizontal and vertical components of perturbation velocity, i.e., u and w are zero and the density perturbation ρ is considered to be zero.

For nondimensionalization, we use the length, velocity, time, and density scales, respectively as $H, U_p, H/U_p,$ and ρ_m . After eliminating the pressure and introducing the perturbation streamfunction ψ defined as $u = \frac{\partial \psi}{\partial z}$ and $w = -\frac{\partial \psi}{\partial x}$, the dimensionless Eqs. (5) read

$$\begin{aligned} \left(\frac{\partial}{\partial t} + \bar{U} \frac{\partial}{\partial x}\right) \nabla^2 \psi - \frac{gH}{U_p^2} \frac{\partial \rho}{\partial x} &= J(\psi, \nabla^2 \psi) \\ \left(\frac{\partial}{\partial t} + \bar{U}(z) \frac{\partial}{\partial x}\right) \rho + N^2 \frac{\partial \psi}{\partial x} &= J(\psi, \rho) \end{aligned} \tag{6}$$

Here, $\bar{U}(z)$ and $N = \frac{H}{g} \sqrt{\frac{g}{\rho_m} \frac{d\bar{\rho}}{dz}}$ is the buoyancy frequency. Note that, the right-hand side terms represent the nonlinear terms quadratic in perturbation variables, where J is the Jacobian determinant, defined as $J(f, g) = (\partial f/\partial x)(\partial g/\partial z) - (\partial f/\partial y)(\partial g/\partial x)$

The ratio between the squared buoyancy frequency (N^2) and the squared flow shear rate (\bar{U}'/gh) is called the Richardson number, which is expressed as $Ri = N^2/(\bar{U}'^2/gh)$. Note that, in the present paper, we consider the background density as uniform and stably stratified, i.e., $d\bar{\rho}/dz$ is a negative constant. Consequently, the Brunt-Vaisälä frequency (N) and Richardson number (Ri) turn out to be positive constants. The perturbation stream function ψ and density perturbation ρ satisfy the Dirichlet boundary conditions at the top and bottom walls, i.e., $\psi = \rho = 0$ at $z = \pm 1$.

3 Analysis of the Linear System

We seek the solutions of (6) satisfying the Dirichlet boundary conditions at the walls using a regular perturbation series expansion in terms of a small dimensionless parameter ϵ of the form

$$(\psi, \rho) = \epsilon(\psi^{(1)}, \rho^{(1)}) + \epsilon^2(\psi^{(2)}, \rho^{(2)}) + \dots, \tag{7}$$

where ϵ measures the relative magnitude of the nonlinear terms of the governing equation for perturbation variables. Substituting the expansion (7) into (6) and collecting the coefficients of $O(\epsilon)$ terms, we obtain the linearized system, which is expressed in the matrix form as follows:

$$\begin{bmatrix} \left(\frac{\partial}{\partial t} + \bar{U}(z)\frac{\partial}{\partial x}\right)\nabla^2 & -\frac{gH}{U_j^2}\frac{\partial}{\partial x} \\ N^2\frac{\partial}{\partial x} & \left(\frac{\partial}{\partial t} + \bar{U}(z)\frac{\partial}{\partial x}\right) \end{bmatrix} \begin{bmatrix} \psi^{(1)} \\ \rho^{(1)} \end{bmatrix} = 0, \tag{8}$$

where $\psi^{(1)}$ and $\rho^{(1)}$ satisfy $\psi^{(1)}(\pm 1) = \rho^{(1)}(\pm 1) = 0$.

The above-linearized system (8) and the boundary conditions do not explicitly depend on x and t ; thus, we can seek a solution in terms of normal mode. The linearized stream function $\psi^{(1)}$ and density function $\rho^{(1)}$ are written as

$$X^{(1)}(x, z, t) = \begin{bmatrix} \psi^{(1)} \\ \rho^{(1)} \end{bmatrix} = \sum_{j=0}^{\infty} X_j^{(1)}(z)e^{ik_j(x-c_jt)} + c.c., \tag{9}$$

where $X_j^{(1)}(z) = [\psi_j^{(1)}(z), \rho_j^{(1)}(z)]$ is the spatial amplitude of the perturbation, k_j and c_j represent the horizontal wavenumber and phase velocity of the j -th mode, respectively, where the index j takes integer values.

Substituting the normal mode solution (9) into the linearized system (8) and equating the coefficients of $e^{ik_j(x-c_jt)}$ on both sides, we get the following matrix eigenvalue problem for the j -th eigenmode

$$L_j \hat{X}_j^{(1)} = c_j M_j \hat{X}_j^{(1)}, \tag{10}$$

where $\mathcal{L}_j = \begin{bmatrix} \bar{U}(z)(D^2 - k_j^2) & -\text{Ri}_0 \\ N^2 & \bar{U}(z) \end{bmatrix}$, $\hat{X}_j^{(1)} = \begin{pmatrix} \hat{\psi}_j^{(1)}(z) \\ \hat{\rho}_j^{(1)}(z) \end{pmatrix}$,

and $M_j = \begin{bmatrix} (D^2 - k_j^2) & 0 \\ 0 & 1 \end{bmatrix}$.

The linear stability analysis of (10) shows that the system is neutrally stable and contains infinitely many discrete neutrally stable eigenvalues c_j (with zero imaginary part) at each wave number k_j for $\text{Ri} > 0.25$ [18]. Furthermore, the system (10) is symmetric, i.e., both (k_j, c_j) and $(k_j, -c_j)$ pairs simultaneously satisfy (10). The

vertical structures of eigenmodes corresponding to (k_j, c_j) and $(k_j, -c_j)$ are of the form $\psi_j^{(1)}(z)$ and $-\psi_j^{(1)}(-z)$, respectively (for more details, see [19]). Furthermore, depending on the phase speed, the discrete eigenmodes present in the system can be classified into two categories: (i) forward propagating modes, which travel faster than the background shear flow $\overline{U}(z)$ ($-1 \leq U(z) \leq 1$), i.e., $c_j > 1$, and (ii) the backward propagating modes traveling slower than the background shear flow, i.e., $c_j < -1$. The relation between k_j and frequency ($\omega_j = k_j c_j$) of the j -th mode can be expressed in the following compact form [20]

$$D(\omega_j, k_j, Ri) = \begin{vmatrix} I_\nu(-k_j - \omega_j) & K_\nu(-k_j - \omega_j) \\ I_\nu(k_j - \omega_j) & K_\nu(k_j - \omega_j) \end{vmatrix} = 0, \tag{11}$$

where I_ν and K_ν represent the modified Bessel functions of complex order $\nu = (0.25 - Ri)^{1/2}$.

This paper considers the resonant interactions among forward propagating neutrally stable internal wave modes. Thus, we consider $Ri > 0.25$ and the phase speed of the interacting modes $c_j > 1$. At each horizontal wavenumber, the system contains various modes with different phase speeds (and vice versa). These modes can be arranged in descending order of their phase speed, and labeled as mode 1, mode 2, mode 3, and so on. The mode with the highest phase speed, or the fastest traveling mode, is mode 1. Here onwards, the suffixes m, n , and r shall be used to denote the mode number of the corresponding mode.

As mentioned earlier, the objective of the present study is to show the existence of 1: 2: 3 resonances among forward propagating internal gravity wave modes by solving the linearized Boussinesq Navier–Stokes equation expressed as the generalized matrix eigenvalue problem (10). We use the Chebyshev spectral collocation method with appropriately selected collocation points [21]. In the next section, we shall graphically illustrate the existence such resonances.

4 Existence of 1:2:3 Resonances

In this section, we will discuss the existence of 1: 2: 3 resonance interactions among IGWs, i.e., resonance interactions among the fundamental mode, and corresponding second and third harmonics. Under such resonances, the horizontal wavenumbers k_m, k_n, k_r and frequencies $\omega_m, \omega_n, \omega_r$ of the fundamental mode and second and third harmonics, simultaneously, satisfy the spatial and temporal conditions $k_m: k_n: k_r = \omega_m: \omega_n: \omega_r = 1: 2: 3$, respectively, where the subscripts m, n , and r denote the mode numbers of the corresponding modes. These conditions can equivalently be written in terms of their phase speeds — defined as $c_m = \omega_m/k_m, c_n = \omega_n/k_n$, and $c_r = \omega_r/k_r$ — of the resonating modes as $c_m = c_n = c_r$, i.e., under 1: 2: 3 resonance the phase speeds of the second and third harmonics must be the same as the phase speed of the fundamental mode.

For illustration purposes, we choose the range for Richardson number (Ri), wave number of the fundamental mode (k_m) and the mode numbers of the interacting modes (m, n and r) as $1 \leq Ri \leq 10$, $1 < k_m < 5$, and $1 < m, n, r < 6$, respectively. Here, we follow the following algorithm to find the wavenumber and frequencies of the resonating modes.

Algorithm 1 To find (Ri, k) values for the 1:2:3 resonances 1: Discretize (Ri, k) plane in to $n_{Ri} \times n_k$ grid points. At each point perform the following steps

2: Compute the following sets at each grid point

$$\Omega_k = \{\omega | D(\omega, k; Ri) = 0\},$$

$$\Omega_{2k} = \{\omega | D(\omega, 2k; Ri) = 0\},$$

$$\Omega_{3k} = \{\omega | D(\omega, 3k; Ri) = 0\}.$$

3: Arrange each set Ω_k, Ω_{2k} , and Ω_{3k} in the descending order and extract first six values ω from each set

4: Denote the extracted elements as $\omega_k^i, \omega_{2k}^i$, and ω_{3k}^i respectively, for $1 \leq i \leq 6$

5: for $i, j = 1$ to 6 do

6: compute $\Delta_{ij}^{(2)} = 2\omega_k^i - \omega_{2k}^j$ and $\Delta_{ij}^{(3)} = 3\omega_k^i - \omega_{3k}^j$

7: end for

8: for $i, j = 1$ to 6 do

9: If $|\Delta_{ij}^{(2)}| = |\Delta_{ij}^{(3)}| = 0$ or $|\Delta_{ij}^{(2)}|, |\Delta_{ij}^{(3)}| < \delta$ then

10: i and ω_k^i correspond to resonance

11: else

12: Go to another index

13: end if

14: end for

The conditions for 1: 2: 3 resonances reduce to

$$|\Delta_{ij}^{(2)}| = |\Delta_{ij}^{(3)}| = 0.$$

In other words, at a given Ri, each of the three pairs $(\omega, k), (2\omega, 2k)$, and $(3\omega, 3k)$ must satisfy the dispersion relation (11) simultaneously. However, due to the numerical calculations, $|\Delta_{ij}^{(2)}| = |\Delta_{ij}^{(3)}| = 0$ cannot be exactly obtained. Thus, we can say that 1: 2: 3 resonances exist if $\Delta_{ij}^{(2)}$ and $\Delta_{ij}^{(3)}$ are zero with a reasonably good approximation specified by an error tolerance δ . In this paper, without any loss of generality, we fix $\delta = 10^{-5}$, and we conclude 1: 2: 3 resonances exist if $|\Delta_{ij}^{(2)}| < \delta$ and $|\Delta_{ij}^{(3)}| < \delta$.

For various Richardson numbers Ri, obtained by varying the base state density gradient (strength of density stratification), a fundamental mode and its second and third harmonics satisfying the conditions for 1:2:3 resonance are identified using the algorithm mentioned above, and the results are summarized in Table 1. Specifically, at various Ri (listed in column 1), column 2 denotes the horizontal wavenumber and frequency pair (k_m, ω_m) of the fundamental mode. Similarly, columns 3 and 4,

respectively, show the wavenumber and frequency pairs for the resonating second and third harmonic wave, i.e., $(2k_m, \omega_r^{2km})$ and $(3k_m, \omega_r^{3km})$. Finally, the last two columns of the table display the quantities $\omega_r^{2km}/2\omega_m$ and $\omega_r^{3km}/3\omega_m$, respectively, which reveal that how accurately $(2\omega_m, 2k_m)$ and $(3\omega_m, 3k_m)$ satisfy the dispersion relation. Note that for each Ri listed in the table, 1: 2: 3 resonance occurs among the waves whose wavenumbers and frequencies are listed in columns 2, 3, and 4. To what follows, using the above-mentioned algorithm for a wider range of Ri and k , one can identify the critical parameters (Ri, k_m, ω_m) for 1:2:3 resonance.

The existence of 1: 2: 3 resonances has been graphically demonstrated in Fig. 1. The blue, red, and magenta vertically aligned circles, respectively, represent the frequencies of different modes, obtained by solving the dispersion relation (11), at wavenumber $k_m, 2k_m$, and $3k_m$, where $k_m, 2k_m$, and $3k_m$ are listed in the second, third, and fourth columns of the shaded row of Table 1. The horizontal reference lines from top to bottom (black, red, and magenta) represents frequencies of the fundamental mode (ω_m), second harmonic ($2\omega_m$), and third harmonic ($3\omega_m$), respectively. The intersection point of a horizontal line and the same color vertically aligned circles are marked using the black ‘+’ symbol. The zoomed portions clearly show that each of the three pairs (k_m, ω_m) , $(2k_m, \omega_r^{2km})$, and $(3k_m, \omega_r^{3km})$ (listed in the shaded row of Table 1) satisfies the dispersion relation (11) with reasonably good accuracy. Thus, the conditions for 1:2:3 resonance are satisfied for the parameters of the shaded row of Table 1. Following the same process, the existence of resonances can be graphically illustrated for other sets of parameters listed in the table.

The spatial structures of the resonating modes, identified using the algorithm explained above, having the horizontal wavenumber and frequency pair $(k_m, \omega_m) = (3.305085, 3.304628)$, $(k_n, \omega_n) = (6.61017, 6.60925)$ and $(k_m, \omega_m) = (9.915255, 9.913893)$ at $Ri = 2.525424$, are presented in Fig. 2a–c, respectively. Note that the mode number of an internal gravity mode depends on the number of zero crossing as well as the number of extremum of the eigenfunction. In other words, if n is the

Table 1 Parameters corresponding to 1:2:3 resonances

Ri	(k_m, ω_m)	$(2k_m, \omega_r^{2km})$	$(3k_m, \omega_r^{3km})$	$\omega_r^{2km}/2\omega_m$	$\omega_r^{3km}/3\omega_m$
1.4211	(2.4211, 2.4209)	(4.8422, 4.8419)	(7.2633, 7.2628)	0.999998	1.00000
2.47368	(5.2631, 5.2631)	(10.5262, 10.52549)	(15.7893, 15.78826)	0.999999	1.00000
2.241379	(1.68965, 1.68943)	(3.3793, 3.378856)	(5.06895, 5.068294)	0.999993	1.0000012
2.551724	(3.48276, 3.48228)	(6.96455, 6.964546)	(10.44683, 10.44684)	0.999999	1,000,000
2.220339	(1.54237, 1.54217)	(3.084746, 3.084332)	(4.627119, 4.626507)	0.99999	0.99999
2.525424	(3.305085, 3.304628)	(6.61017, 6.60925)	(9.915255, 9.913893)	0.99999	1.00000

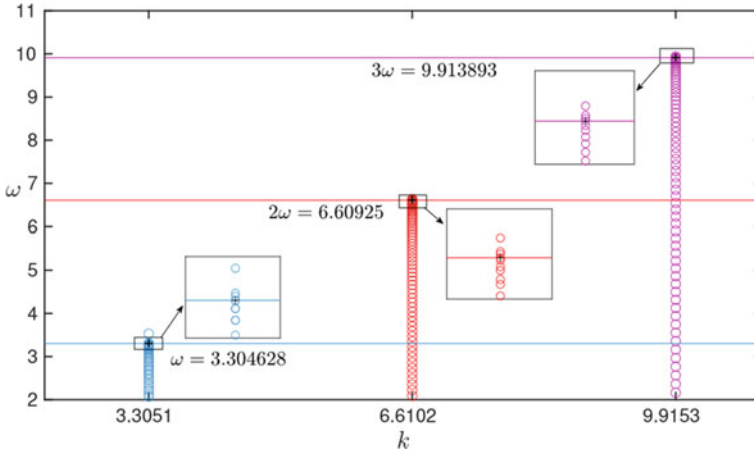


Fig. 1 Variation of ω for three values of k , where the zoomed portion illustrates the evidence of 1: 2: 3 resonance for the parameters corresponding to the shaded row of Table 1

mode number of the internal gravity mode, then the corresponding eigenfunction has $n - 1$ zero and achieves extremum n times inside the domain $z \in (-1, 1)$. Thus, the modes with mode number one, two, three, and four cross the $\hat{\psi} = 0$ line (dotted line) zero, one, two, and three times, respectively, and reach extremities one, two, three, and four times, respectively. As seen in Fig. 2a–c, the mode numbers of the resonating fundamental mode, its second, and third harmonics are 3, 4, and 4, respectively. By observing the interaction pattern for various Ri , we can conclude that the mode numbers of the resonating higher order harmonics are less than the mode number of the fundamental mode. This observation is also in tune with our results for selfresonating case [9].

As seen in Fig. 2a–c, the mode numbers of the resonating fundamental mode, its second, and third harmonics are 3, 4, and 4, respectively. By observing the interaction pattern for various Ri , we can conclude that the mode numbers of the resonating higher order harmonics are less than the mode number of the fundamental mode. This observation is also in tune with our results for the self-resonating case [9].

5 Conclusions

In this paper, we have presented the existence of 1: 2: 3 resonances among internal gravity waves (IGWs) in an inviscid uniform shear flow with stable density stratification by solving the linearized Navier–Stokes equations under the Boussinesq approximation. The existence of such resonances among IGWs significantly influence the energy cascading process that finally leads to ocean turbulence and small-scale ocean mixing. To the best of the authors’ knowledge, this is the first work,

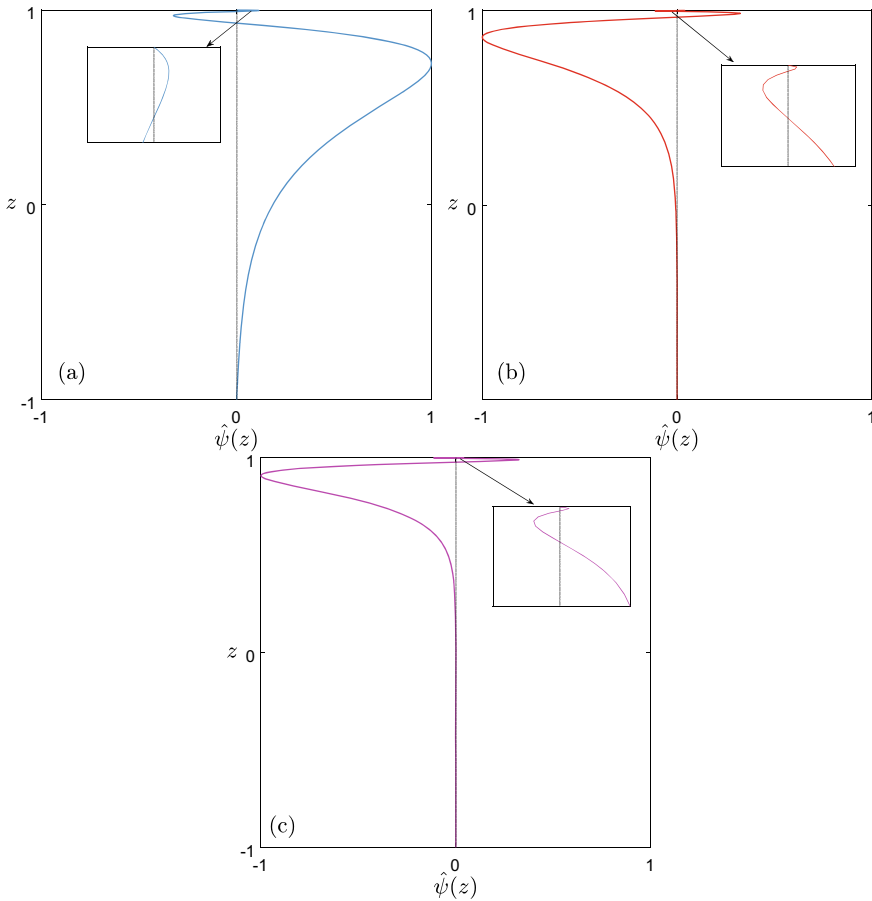


Fig. 2 Spatial structures of the resonating modes at $Ri = 2.525424$. The wave numbers and frequencies of the modes shown in panels (a), (b) and (c) are listed in second, third, and fourth columns of the corresponding row (highlighted row) of Table 1, respectively

which considers the higher harmonic resonances among IGWs in a stably stratified uniform shear flow system. Here, we have provided an algorithm to show the existence of 1: 2: 3 resonances among IGWs, which can be further modified to present the existence of higher harmonic resonances in different flow configurations observed in nature, for instance, (i) ocean-like nonuniform stratified density profiles where the density varies rapidly in the vertical direction in a pycnocline region closer to the free surface, and (ii) estuarine complex velocity profiles, which is a combination of a free shear flow profile at the top and the boundary layer profile at the bottom. Further, the present study shows that the existence of higher harmonic resonances depends on the strength of density stratification and shear rate. Thus, the present study helps us to understand the energy cascade mechanism among IGWs of different wave numbers

in a uniformly stratified uniform shear flow system. Higher harmonic resonances among interfacial and internal waves in three or multi-layered system could be a straightforward extension of this theoretical analysis. Moreover, the present work could serve as an initial step to studying resonant three-wave interaction problems in different types of stratified flow configurations; for instance, stratified flows of viscous fluid and compressible stratified flows, etc.

References

1. Bruce R (2010) Sutherland. Cambridge University Press, Internal Gravity Waves
2. Hung J-J, Wang Y-H, Fu K-H, Lee I-H, Tsai S-S, Lee C-Y, Lu W-T, Shen Y-J, Lin Y-H (2021) Biogeochemical responses to internal-wave impacts in the continental margin off dongsha atoll in the northern south china sea. *Prog Oceanogr* 199:102689
3. Huang X, Chen Z, Zhao W, Zhang Z, Zhou C, Yang Q, Tian J (2016) An extreme internal solitary wave event observed in the northern South China sea. *Sci Rep* 6:30041
4. Kuperman WA, Lynch JF (2004) Shallowwater acoustics. *Phys Today* 57:55–61
5. Phillips OM (1960) On the dynamics of unsteady gravity waves of finite amplitude part 1. The elementary interactions. *J Fluid Mech* 9:193–217
6. Ball FK (1964) Energy transfer between external and internal gravity waves. *J Fluid Mech* 19:465–478
7. Thorpe SA (1966) On wave interactions in a stratified fluid. *J Fluid Mech* 24:737–751
8. Dauxois T, Joubaud S, Odier P, Venaïlle A (2018) Instabilities of internal gravity wave beams. *Annu Rev Fluid Mech* 50:131–156
9. Biswas L, Shukla PF (2022) Resonant triad interactions in a stably stratified uniform shear flow. *Phys Rev Fluids* 7:023904
10. Alex DD (1971) Craik, non-linear resonant instability in boundary layers. *J Fluid Mech* 50:393–413
11. Phillips OM (1981) Wave interactions—the evolution of an idea. *J Fluid Mech* 106:215–227
12. Muller P, Holloway G, Henyey F, Pomphrey N (1986) Nonlinear interactions among internal gravity waves. *Rev Geophys* 24:493–536
13. Hammack JL, Henderson DM (1993) Resonant interactions among surface water waves. *Annu Rev Fluid Mech* 25:55–97
14. Komen GJ, Hasselmann S, Hasselmann K (1984) On the existence of a fully developed wind-sea spectrum. *J Phys Oceanogr* 14:1271–1285
15. Dangelmayr G (1986) Steady-state mode interactions in the presence of 0(2)-symmetry. *Dyn Stab Syst* 1:159–185
16. Proctor MRE, Jones CA (1988) The interaction of two spatially resonant patterns in thermal convection. part 1. exact 1: 2 resonance. *J Fluid Mechanics* 188:301–335
17. Fujimura K (1992) Higher harmonic resonances in free convection between vertical parallel plates. *Philos Trans Royal Soc A* 340:95–130
18. Case KM (1960) Stability of an idealized atmosphere I. Discussion of results. *Phys Fluids* 3:149–154
19. Davey A, Reid WH (1977) On the stability of stratified viscous plane Couette flow. Part 1 Constant buoyancy frequency. *J Fluid Mech* 80:509–525
20. Engevik L (1971) A note on a stability problem in hydrodynamics. *Acta Mech* 12:143–153
21. Canuto C, Hussaini MY, Quarteroni AM Jr, Thomas AZ (1988) Spectral methods in fluid dynamics. Springer, Berlin

The Differences in the Near Wall Turbulent Structure Between a Uniform Flow and a Wall Jet with Co-Flow—A Numerical Study



Prithwisha Nath and Animesh Patari

Abstract The characteristic differences in the near wall turbulent structure and the shear stress pattern between a uniform flow and a wall jet with a co-flow stream over a flat surface have been numerically investigated in the present work. A uniform flow of free stream Reynolds number $Re_\infty = 8.64 \times 10^5$ is considered to be flowing over a flat plate in one case. Separately, a wall jet with nozzle exit Reynolds number $Re_j = 18000$ along with parallel co-flow stream of Reynolds no 8.64×10^5 is assumed for the investigation. Realizable $k-\varepsilon$ model with an enhanced wall treatment scheme has been implemented to capture the near wall features with more details and accuracy. Numerical study reveals that the introduction of turbulent wall jet along with uniform co-flow stream increases the wall shear stress noticeably. The near wall flow structures on introduction of wall jet completely differ from that of the uniform flow. The turbulent fluctuations and the resulting turbulent stress components are found comparatively much higher in case of wall jet.

Keywords Turbulent flow · Wall jet · Eddy Viscosity · Boundary layer · Numerical simulation

Nomenclature

u_∞	Free stream velocity [m/s]
u_j	Jet velocity at nozzle exit [m/s]
ρ	Density of air [kg/m^3]
ν	Fluid kinematic viscosity [m^2/s]
μ	Fluid kinematic viscosity [m^2/s]
w	Nozzle slot thickness [m]

P. Nath (✉) · A. Patari
Department of Mechanical Engineering, NIT Durgapur, Durgapur 713209, India
e-mail: pn.19u10085@btech.nitdgp.ac.in

A. Patari
e-mail: apatari.me@nitdgp.ac.in

τ_{wx}	Wall shear stress at location x [Pa]
$y_{1/2}$	Wall normal distance where the local stream-wise velocity (u) is half the maximum velocity [m]
y_m	Wall normal distance where the local stream-wise velocity (u) is maximum. [m]
δ	Boundary layer thickness for the uniform flow over flat surface.[m]
$Re_j = \frac{u_j L}{\nu}$	Jet exit Reynolds number
$Re_\infty = \frac{u_\infty L}{\nu}$	Free stream Reynolds number based on plate length L
$C_{fx} = \frac{2\tau_{wx}}{\rho u_m^2}$	Local skin friction coefficient

Subscript

∞	Free stream
j	Jet
wx	Position along the wall
m	Maximum value
t	Turbulent

1 Introduction

When a uniform flow is introduced parallel to a smooth flat plate, a boundary layer is formed attached to the plate across which the stream-wise velocity changes from zero at the wall to the free stream value at the edge of boundary layer. But if a turbulent jet is introduced parallel to the plate along with some external parallel co-flow stream, the near wall flow pattern completely differs. In case of wall jet, two distinct shear layers are formed. In the inner layer, attached to the wall the stream-wise velocity same way changes from zero to maximum. But, from this point onward, the velocity gradually starts decreasing and at some point asymptotically merge with the free stream velocity. This region is called outer layer in which a huge momentum exchange takes place due to turbulent fluctuation in the flow similar to a free shear layer. The inner layer may be assumed to be not same but synonymous to a boundary layer over a flat plate.

2 Literature Review and Objective

Wall jets find many important applications in engineering, for example in aero engines and stationary gas turbines, where wall jets are used for cooling of combustion chamber walls and the leading edges of the turbine itself. Wall jets are also used in

drag reduction on air craft wing where the wall jet is ejected tangential to the wing along with the external stream. Such paramount application of wall jet along with its typical physical features attracts many scientists and engineers to do research on wall jet since last few decades. Accordingly, lot of experimental, analytical and numerical investigations were performed for wall jet with variety of configurations of walls, with or without co-flow stream. Launder and Rodi [1] reviewed that the maximum velocity in wall jet occurs at a non-dimensional wall normal distance of the range 0.13–0.17. The mean flow and turbulent structure of wall jet without co-flow stream was experimentally investigated by Eriksson et al. [2] using LDV technique. Sigalla [3] experimentally determined correlation between the skin friction coefficient and the Reynolds number similar to the Blasius correlation applicable for uniform flow over flat plate. One of the most remarkable investigations on wall jet with co-flow stream on a flat and curved surface was the work by Dakos [4] who experimentally determined the turbulent structure of fluid flow and heat transfer quite in detail. He determined that the point of zero shear appears a little closer to the wall than the point of maximum velocity. The turbulent structure of boundary layer particularly in the near wall zone was experimentally investigated by Kline et al. [5]. Gunther et al. [6] measured the mean and fluctuating velocity components along with the turbulent stresses for a turbulent flow through a channel using LDV. Direct numerical simulation of turbulent channel flow was performed by Abe et al. [7] to investigate the detailed turbulent structure and near wall turbulent as well as total shear stress profile.

It can be realized after thorough survey of literature related to wall jet as well as turbulent boundary layer over a flat plate that in the near wall region, there are lot of similarities between the flow structure of turbulent boundary layer on flat plate and wall jet, such as formation of viscous sub layer, buffer layer and log layer, etc. But there are certain differences as well particularly between the boundary layer over a plate and the inner shear layer of wall jet. A few experimental research works on wall jet [1, 4] shade light on such disparities but explain mainly about the relative location of zero shear and maximum velocity, velocity log-law, the skin friction characteristics, etc. Addition of co-flow with wall jet will further influence the inner layer characteristics. Therefore, a comprehensive study can be performed to highlight such disparities in a comparative way between a flat plate turbulent boundary layer and the inner shear layer of wall jet with co-flow stream.

In the present work, a comparative numerical study has been performed with the objective to understand the characteristics difference in the turbulent features as well as the shear characteristics of the near wall region between a uniform flow and a wall jet with co-flow over a flat plate.

3 Numerical Methodology

A steady incompressible turbulent jet of air of Reynolds number 18000 based on the jet exit velocity u_j and the slot height w is supposed to be ejected through the slot tangential to a wall of length $80w$. A two-dimensional rectangular flow domain of height $30w$ above the flat plate is considered for the numerical investigation as shown in Fig. 1. A co-flow stream of Reynolds number 8.64×10^5 based on free stream velocity measuring 60% of the jet exit velocity and the length of the plate is allowed to flow parallel to and over the jet. Two different uniform flow over a flat surface with respective free stream Reynolds number same as that of the co-flow and 1.44×10^6 have been separately investigated under zero pressure gradient. Velocity inlet boundary conditions with zero-gauge pressure are used for the inlet and zero pressure is set at the outlet as well as the top boundary.

All the numerical simulations were performed employing Realizable $k - \varepsilon$ model coupled with enhanced wall treatment scheme using finite volume-based ANSYS-Fluent 17.1 tool. The Reynolds average Navier–Stoke equations which are solved for the mean flow are as follows:

$$\text{Continuity : } \frac{\partial u_j}{\partial x_j} = 0 \tag{1}$$

$$\text{Momentum : } \frac{\partial u_i u_j}{\partial x_j} = \frac{1}{\rho} \frac{\partial}{\partial x_j} [\tau_{ij} - \rho \overline{u'_i u'_j}] + g_i \tag{2}$$

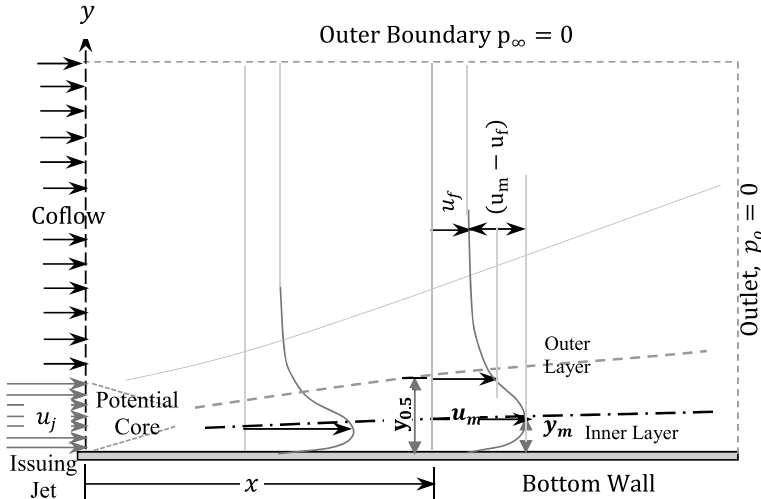


Fig. 1 Schematic diagram of the wall jet domain

In addition to that, in Realizable $k - \varepsilon$ model, the following transport equations for the turbulent kinetic energy (k) and the turbulent dissipation (ε) are solved

$$\frac{\partial k u_j}{\partial x_j} = \frac{\partial}{\partial x_j} \left\{ \left(\nu + \frac{\nu_t}{\sigma_k} \right) \frac{\partial k}{\partial x_j} \right\} + P_k + P_b - \varepsilon \tag{3}$$

$$\frac{\partial \varepsilon u_j}{\partial x_j} = \frac{\partial}{\partial x_j} \left[\left(\nu + \frac{\nu_t}{\sigma_\varepsilon} \right) \frac{\partial \varepsilon}{\partial x_j} \right] + C_1 S \varepsilon + C_{1\varepsilon} \frac{\varepsilon}{k} C_{3\varepsilon} P_b - \frac{C_2 \varepsilon^2}{k + \sqrt{\nu \varepsilon}} \tag{4}$$

Here, the turbulent production of k is $P_k = -\overline{u'_j u'_i \frac{\partial x_i}{\partial u_j}}$ and the term $-\overline{\rho u'_i u'_j}$ is known as turbulent stress and expressed as

$$-\overline{\rho u'_i u'_j} = -\frac{2}{3} \left(\rho k + \mu_t \frac{\partial u_k}{\partial x_k} \right) \delta_{ij} + \mu_t \left(\frac{\partial u_i}{\partial x_j} + \frac{\partial u_j}{\partial x_i} \right) \tag{5}$$

whereas the eddy viscosity is given as $\mu_t = \rho C_\mu k^2 / \varepsilon$. The SIMPLE algorithm is used for the numerical computation employing second-order scheme for pressure and second-order upwind scheme for momentum, turbulent kinetic energy and dissipation. A residual of 10^{-6} has been set for all the variables as the criteria for convergence. Default values are taken for all the model constants.

3.1 Grid Independence Study

In numerical simulation, whatever numerical schemes are used to solve a problem, the accuracy of the computed results is greatly affected by improper shape, size and distribution of the mesh elements over the computational domain. For the present investigation, the 2-D domain is discretized using rectangular non-uniform mesh elements. To apply the enhanced wall treatment approach, the near wall mesh has been resolved to very fine size maintaining the average y^+ value of the wall attached cells less than 1.

A representative near wall mesh structure is shown in Fig. 2. Three sets of mesh, namely coarse, medium and fine mesh are generated through systematic grid refinement whose number of elements as shown in Table 1. These three sets of numerical data for any variable are then analysed for the Grid Convergence Index(GCI) values as explained methodologically in the literature [8–10] to check whether the numerical results require further mesh refinement or not. The GCI values of the fine and medium grids are calculated for any variable ϕ using the formulation as given in the Table 1. Here, the details of the GCI calculation for the average skin friction coefficient, C_f over the length of the wall are shown in Table 1. The apparent order of accuracy is iteratively calculated using the correlation

$$\hat{p} = \frac{1}{\ln r_{12}} \left| \ln \left| \frac{\epsilon_{23}}{\epsilon_{12}} \right| + \ln \left| \frac{r_{12}^{\hat{p}} - \text{sign}\left(\frac{\epsilon_{23}}{\epsilon_{12}}\right)}{r_{23}^{\hat{p}} - \text{sign}\left(\frac{\epsilon_{23}}{\epsilon_{12}}\right)} \right| \right| \quad (6)$$

For the second-order numerical scheme adopted in this investigation, the apparent order of accuracy \hat{p} is calculated to be 1.978. The GCI analysis is also done for the local wall shear stress at 21 data points over the length of the plate. The local order of accuracy \hat{p} varies in the range 0.91–7.58 with an average of $\hat{p}_{av} = 2.84$. The uncertainty in the local values of shear stress are calculated using this \hat{p}_{av} and presented as error band over the fine grid solution in the Fig. 3. The maximum

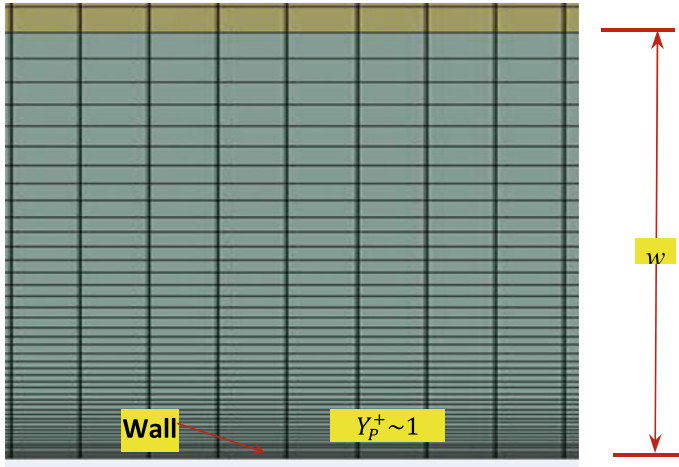


Fig. 2 Representative near wall mesh structure

Table 1 Grid Convergence Index for area average skin friction coefficient

Grid	Fine (1)	Medium (2)	Coarse (3)
Number of elements, N	180,852	105,333	61,542
$\phi = C_f$	0.004039	0.004059	0.004093
Case	1–2	2–3	$\frac{GCI_{23}}{r_{12}^{\hat{p}} GCI_{12}} = \mathbf{0.995}$
Refinement ratio $r_{12} = (N_1/N_2)^{1/2}$	1.3103	1.3092	
Apparent order of accuracy, \hat{p}	1.978		
Extrapolated value $\phi_{ex} = \frac{r_{12}^{\hat{p}}\phi_1 - \phi_2}{r_{12}^{\hat{p}} - 1}$	0.00401	0.00401	
Relative error $\epsilon_{12} = \frac{\phi_1 - \phi_2}{\phi_1} \times 100 \%$	0.49517	0.83764	
Extrapolated error $\epsilon_{ext} = \frac{\phi_{ex} - \phi_1}{\phi_{ex}} \times 100 \%$	0.70547	1.20414	
$GCI_1 = 1.25 \frac{\epsilon_{12}}{r_{12}^{\hat{p}} - 1} (\%)$	0.87567	1.48727	

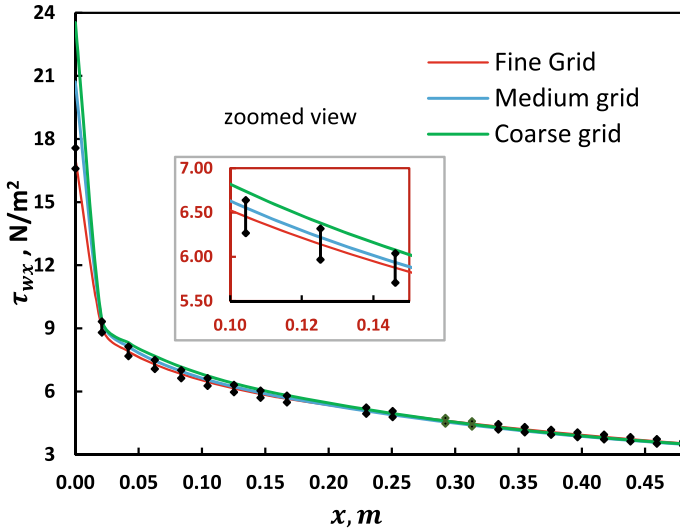


Fig. 3 Wall shear stress in coarse, medium and fine grids solution with discretisation error bar in fine grid

uncertainty is found to be around 3.69%. Therefore, the numerical results obtained by the fine grid solution can be assumed to be grid independent.

3.2 Validation

The results of numerical computation are compared with some well-recognized experimental findings to test the accuracy and acceptability of the result for the purpose of validation. The stream-wise velocity has been chosen as a parameter to test the accuracy of the numerical simulation. Non dimensional velocity u/u_0 has been plotted in Fig. 4 against a non-dimensional wall normal distance at stream-wise location $X = 40$. In case of wall jet $u_0 = u_m - u_\infty$ and wall normal distance $y/y_{1/2}$ is taken, whereas for uniform flow $u_0 = u_\infty$ and wall normal distance is taken as y/δ . The ratio of the ordinates of the two scales is set equal to $\delta/y_{1/2} = 0.60$. The computed velocity profile for the wall jet is compared with the experimental findings of Dakos [4]. The non-dimensional velocities $U^+ = u/u_\tau$ for the wall jet and the uniform flow are also plotted in logarithmic (inner) scale ($y^+ = u_\tau y/\nu$) in Fig. 5 and compared respectively with the experimental velocity profile of Dakos [4] and Kline[5]. Here, $u_\tau = \sqrt{\tau_w/\rho}$ is known as friction velocity. It is very clear from the figures that there is remarkable agreement between the numerical and experimental velocity profiles. Though the ratio $y_m/y_{1/2} = 0.405$ is found a bit higher than the experimental value of 0.354 of Dakos [4].

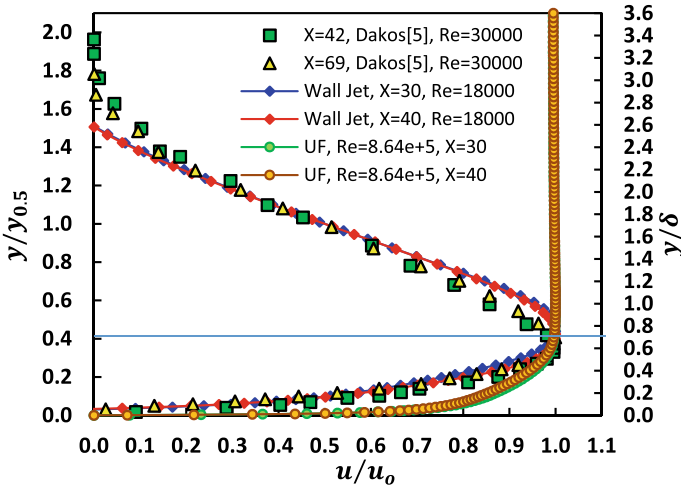


Fig. 4 Stream-wise mean velocity in outer scaling

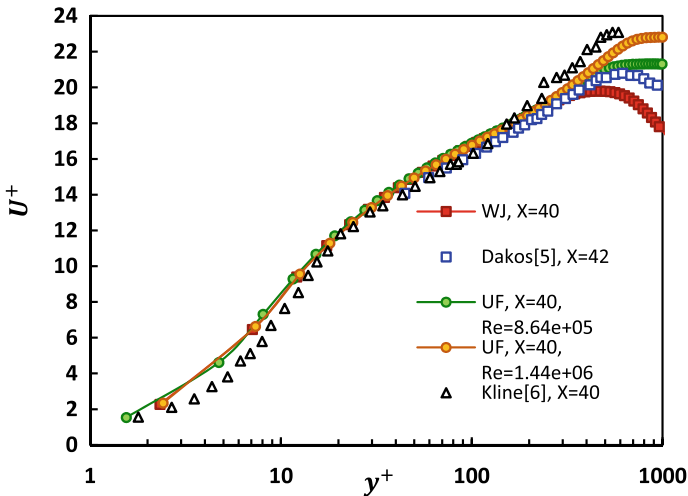


Fig. 5 Stream-wise mean velocity in inner scaling

4 Results and Discussion

The numerical results obtained from simulations of three different cases of the investigation are analysed in detail. The data related to the velocity, shear stress, skin friction coefficient as well as the turbulent stress components are graphically presented in the figures along with some well-recognized experimental data. The outcomes of the analysis are stated in the following segments.

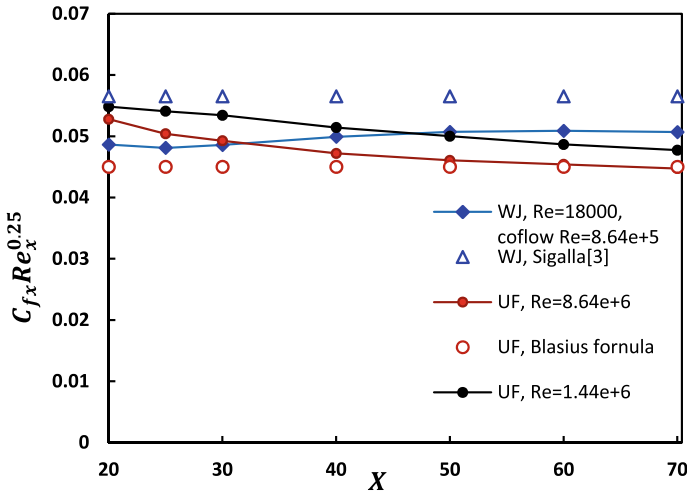


Fig. 6 Local skin friction coefficient in developed zone

4.1 Skin Friction Coefficient

The correlation for the local skin friction coefficient in case of turbulent flow over a smooth flat plate as given by Blasius is $\frac{\tau_{wx}}{1/2\rho u_m^2} = 0.045\left(\frac{u_m \delta}{\nu}\right)^{-0.25}$, which is found to be followed by the numerical skin friction coefficient data very well. Here, the maximum velocity $u_m = u_\infty$ for the boundary layer flow. However, Sigalla [3] proposed a similar correlation applicable for wall jet for downstream location beyond $X = 20$, but the coefficient in the right side of the above equation should be changed to 0.0565. For wall jet as well, the skin friction data of numerical computation is supposed to comply with the correlation with acceptable accuracy (Fig. 6). Analysis of the numerical data for the local shear stress shows that the local shear stress for both the wall jet and the uniform flow with free stream velocity equal to the jet exit velocity is almost same, whereas the shear stress for the uniform flow with free stream velocity equal to the wall jet co-flow velocity (60% of the nozzle exit velocity) is comparatively lower, as shown in the Fig. 7.

4.2 Shear Stress Profile in Wall Layer

The non-dimensional total shear stress τ/τ_{wx} is plotted against non-dimensional wall normal distance y/y_m at a stream-wise position $X = 40$. In both the cases, y_m is the wall normal distance where the stream-wise velocity becomes maximum (i.e., for the uniform flow $y_m = \delta$). The total shear stress consists of two parts—the viscous shear stress which is given by $\tau_{vis} = \mu\left(\frac{\partial u}{\partial y} + \frac{\partial v}{\partial x}\right)$, and the turbulent counterpart given by

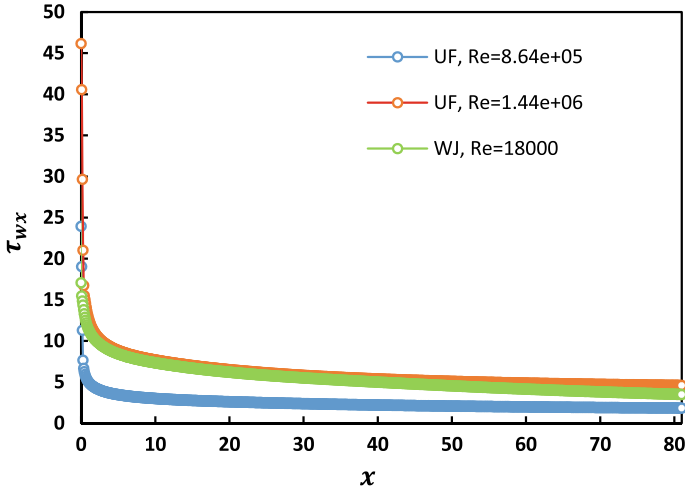


Fig. 7 Relative magnitude of wall shear stress

$\tau_{\text{turb}} = \mu_t \left(\frac{\partial u}{\partial y} + \frac{\partial v}{\partial x} \right)$. The characteristics for the shear stress profile completely differs from that of a uniform flow when a jet is introduced in between the wall and co-flow stream. For turbulent wall jet, the total shear stress is much higher than that of the uniform flow throughout the inner layer. It is also observed from the numerical study that at the stream-wise location $X = 40$, the total shear stress reaches zero value in case of wall jet at around $y = 0.992y_m$ distance normal to the wall, which is a little earlier than the point of maximum velocity. The corresponding experimental value, however, was reported [4] to be around $0.946y_m$, a bit lower at the same stream-wise location, whereas, in the uniform flow over a flat surface, it is the boundary layer thickness δ , at which the velocity reaches 99% of the free stream value and the shear stress theoretically vanishes (Fig. 8).

4.3 Turbulence Characteristics

The turbulent structure in a flow field is described in terms of the turbulent fluctuations of the field variables. The correlations among the fluctuating velocity components represent the turbulent stresses which can be quantitatively expressed with the help of eddy diffusivity hypothesis as explained in the literature [11, 12], using Eq. (5). Accordingly, the two normal stress components for incompressible steady flow can be expressed respectively as follows:

$$\overline{u'u'} = \frac{2}{3}k - 2\nu_t \frac{\partial u}{\partial x} \tag{7}$$

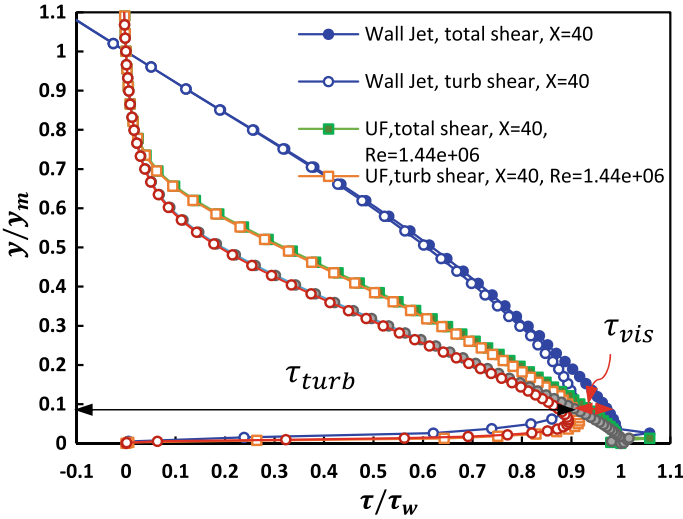


Fig. 8 Viscous and turbulent shear stress in the inner layer

$$\overline{v'v'} = \frac{2}{3}k - 2v_t \frac{\partial v}{\partial y} \tag{8}$$

The turbulent shear stress is represented same way as

$$\overline{u'v'} = \mu_t \left(\frac{\partial u}{\partial y} + \frac{\partial v}{\partial x} \right) \tag{9}$$

The non-dimensional values of these stress components normalized with u_0^2 are presented in the Fig. 9, 10 and 11, respectively, against a non-dimensional wall normal coordinate $Y = y/y_{1/2}$ for the wall jet. The corresponding stress components for the uniform flow of $Re_\infty = u_\infty L/\nu = 8.64 \times 10^5$, same as that of the co-flow in wall jet, are presented in the same figures but with a secondary scale, normalized by u_∞^2 to exaggerate the view of the turbulent stresses. For the cases of uniform flow, the distance from the wall is normalized by the boundary layer thickness δ .

It is evident from the graph that the order of magnitude of the turbulent normal stress components, stream-wise and cross stream both, for the wall jet are much higher than that of the uniform flow in the outer region. For uniform flow, the turbulent fluctuation is limited within the boundary layer, whereas in the inner shear layer of the wall jet, the turbulent normal stress gradually decreases up to the point of maximum velocity and again start increasing in the outer layer to reach another peak approximately near the jet half thickness $y_{1/2}$ and then starts falling again and vanishes asymptotically in the outer region.

The turbulent shear stress in uniform flow is again confined within the boundary layer and it is always negative. But in wall jet, the turbulent shear stress starts

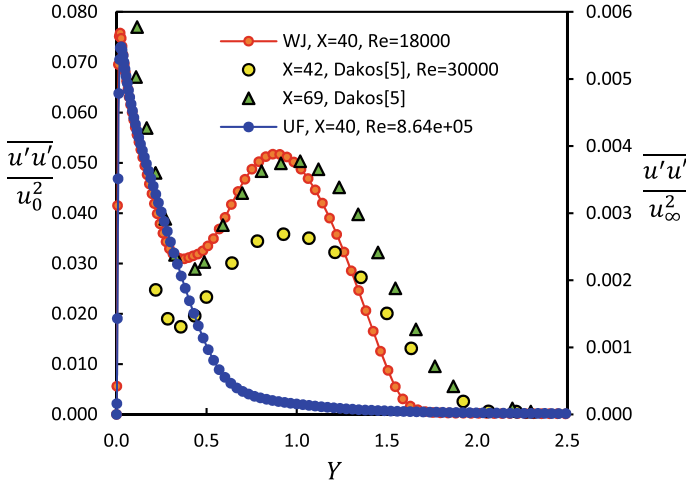


Fig. 9 Stream-wise turbulent normal stress

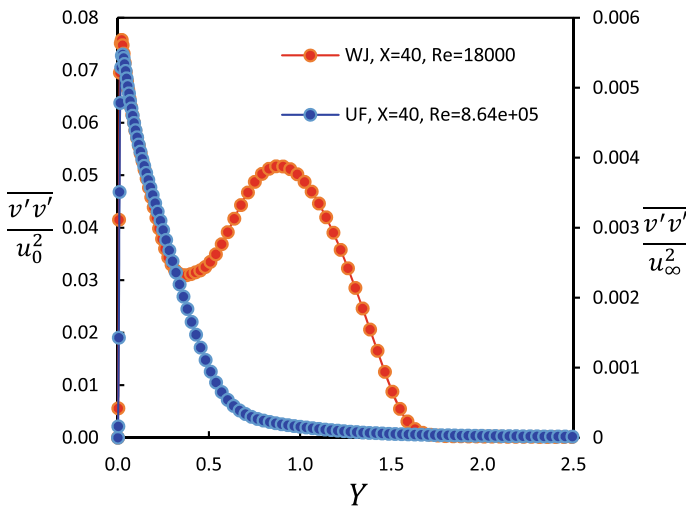


Fig. 10 Turbulent normal stress across stream

decreasing from a maximum value very close to the wall (just outside the viscous sublayer) to zero value just before the point of maximum velocity and further it gains higher magnitude until it reaches to another peak and finally reduces towards zero value in the far away field.

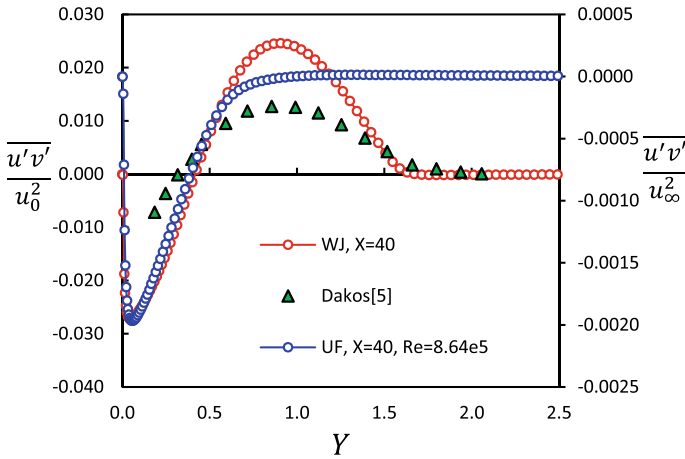


Fig. 11 Variation of turbulent shear stress

5 Conclusions

The notable differences in the turbulent structure and the shear stress variation in the near wall region of a uniform flow and a wall jet with parallel co-flow stream have been reported here through numerical investigation. It is assumed to have equal values of free stream Reynolds number of 8.64×10^5 in both the cases. The free stream velocity is equal to 60% of the jet exit velocity, where the jet Reynold's number is calculated based on the slot thickness of 6 mm to be 18,000. Qualitatively, the near wall turbulence characters are completely unmatched in the two cases considered. Firstly, the wall shear stress in case of wall jet is at least double of that for uniform flow. In wall jet, the maximum velocity is achieved much closure to the wall, at around 35–38% of the boundary layer thickness of the uniform flow in the developed region ($X > 30$). The turbulent fluctuations are noticeable mainly within the boundary layer in case of uniform flow. But the behaviour of the turbulent stresses is completely different in the inner and outer layer of a wall jet. The point of zero shear is noticed in wall jet at a distance around 99% of the point of maximum velocity unlike a uniform flow. Therefore, it is found that the introduction of wall jet in between the wall and the co-flow stream enhances the shear stress quite appreciably.

References

1. Launder BE, Rodi W (1981) The turbulent wall jet. *Prog Aerospace Sci* 19:81–128
2. Eriksson JG, Karlsson RI, Persson J (1998) An experimental study of a two-dimensional plane turbulent wall jet. *Exp Fluids* 25:50–60
3. Sigalla A (1958) Measurements of skin friction in a plane turbulent wall jet. *J Royal Aeronautical Soc* 62:873–877

4. Dakos T, Verriopoulos CA, Gibson MM (1984) Turbulent flow with heat transfer in plane and curved wall jets. *J Fluid Mech* 145:339–360
5. Kline S, Reynolds W, Schraub F, Runstadler P (1967) The structure of turbulent boundary layers. *J Fluid Mech* 30(4):741–773. <https://doi.org/10.1017/S0022112067001740>
6. Günther A, Papavassiliou DV, Warholic MD, Hanratty TJ (1998) Turbulent flow in a channel at a low reynolds number, experiments in fluids 25(5/6):503–511
7. Abe H, Kawamura H, Matsuo Y (2001) Direct numerical simulation of a fully developed turbulent channel flow with respect to the reynolds number dependence. *ASME J Fluids Eng* 123(2):382–393. <https://doi.org/10.1115/1.1366680>
8. Roache PJ (1994) Perspective: a method for uniform reporting of grid refinement studies. *J Fluids Eng* 116(3):405–413. <https://doi.org/10.1115/1.2910291>
9. Celik IB, Ghia U, Roache PJ, Freitas CJ, Coleman H, Rand PE (2008) Procedure for estimation and reporting of uncertainty due to discretization in CFD applications. *J Fluids Eng* 130(7):078001. <https://doi.org/10.1115/1.2960953>
10. Baker N, Kelly G, O’Sullivan PD (2019) A grid convergence index study of mesh style effect on the accuracy of the numerical results for an indoor airflow profile. *Int J Vent* 19(4):300–314. <https://doi.org/10.1080/14733315.2019.1667558>
11. ANSYS Inc, ANSYS Fluent Theory Guide 12.0, 2015.
12. Biswas G, Eswaran V (2002) *Turbulent flows-fundamentals, experiments and modelling*. Alpha Sci Int Ltd, Pangbourne, UK

Linear Stability Analysis of Phase Inversion-Induced Viscous Fingering



Vinod B. Vanarse, Siddharth Thakur, Prathu Raja Parmar, Saurabh Dubey, Tapas Kumar Mandal, and Dipankar Bandyopadhyay

Abstract When the less viscous fluid displaces the high viscosity fluid in a porous medium driven by the pressure gradient, the interface between them is likely to be unstable. In this study, we explore various salient features of such a system leading to viscous finger formation when phase inversion takes place via a linear stability analysis using lubrication approximation which is corroborated by experiments. The theoretical model developed here concerns the onset of instability point that results in morphological changes in the system. The theoretical predictions show system instability to the random perturbations to the interface on reducing the interfacial tension and increasing density difference (ρ_D). Also, higher viscosity ratio ($\mu_r > 1$), drives the system toward stability. This estimate is attributed to the steep concentration gradient near the interface. The formulated model also predicts finger spacing (λ). This theoretical investigation corroborates well with the experimental observations of the viscous finger spacing in the radial geometry.

Keywords Viscous finger · Porous medium · Interface · Stability · Phase inversion

1 Introduction

Mixing two or more liquids is ubiquitous in natural and industrial processes. Mixing often leads to a fascinating morphology at the liquid–liquid interfaces. The dynamics of the process at an interface between a pair of viscous fluids in the restricted geometry

V. B. Vanarse · S. Thakur · P. R. Parmar · T. K. Mandal · D. Bandyopadhyay (✉)
Department of Chemical Engineering, Indian Institute of Technology Guwahati, Assam, India
e-mail: dipban@iitg.ac.in

S. Dubey · T. K. Mandal · D. Bandyopadhyay
Centre for Nanotechnology, Indian Institute of Technology Guwahati, Assam, India

T. K. Mandal · D. Bandyopadhyay
School of Health Sciences and Technology, Indian Institute of Technology Guwahati, Assam, India

have been very well explored from various perspectives for almost five decades [1–6]. The study done in the Hele-Shaw cell geometry is one of the seminal works in the field that highlighted the phenomenon of viscous fingering when a low-viscosity fluid displaces the highly viscous one in a confined space separated by spacers [7]. At different times, engineers quested for secondary crude oil recovery [8], whereas physicists intended to uncover the physics of morphological instability resulting in interfacial pattern formation [9–14].

Owing to the advanced industrial importance of applications related to fluid interaction, this type of mixing has been studied extensively, with many experimental and theoretical works [15–17]. One of the pivotal works by Saffman and Taylor in 1958 [1] opened up many possibilities to study the phenomenon of viscous fingering. The interfacial instability here is known as Saffman–Taylor instability arising from viscosity differences of the two fluids placed side by side or one top over the other. However, the morphological instability at the interfaces due to viscosity contrast in unconfined systems is also widespread in different natural and industrial settings compared to their confined counterparts in the Hele-Shaw cell [18].

In this study, experiments with a simple theoretical model uncover the physics of viscous finger formation, emphasizing the onset of instability point in an unconfined system [19] where water is spilled over the CA–DMSO spin-coated on a glass substrate. An exchange between DMSO and water due to high affinity toward each other gets gelled up, forming a solid-like phase. This transformation from a homogeneous polymer mixture to a solid state in a controlled manner is known to happen because of the phase inversion process. Here, in this process, the initial uniformly mixed polymer solution later due to de-mixing results in the solid phase. An interplay between stabilizing and destabilizing forces is aroused because property contrast decides the morphological changes and the spacing between them at the interface resulting in a beautiful pattern. Finger spacing predicted by the model matches well with the experiments for different CA loadings in DMSO.

2 Materials and Methods

2.1 Experiment Formulation

Cellulose acetate (CA) and dimethyl sulfoxide (DMSO) were purchased from Merck, India, and utilized without further preprocessing. The chemicals were of analytical grade quality. DI water was used for washing as well as experimental purposes. Leica microscope (2300 DM) was hired to capture the optical images chasing the development of viscous finger growth in a porous medium.

Initially, the prepared glass substrates were spin-coated with the polymeric solution at different speeds of rotation in order to maintain the film thickness. The film thickness obtained was lower for different CA loadings at higher rotation speeds. The DI water is spilled over the coated substrate. After some time, DI water starts

interacting with the spin-coated solution due to more affinity toward DMSO than CA in the solution. Initially, a thin layer formed at the top due to the steep concentration gradient at the interface when water started interacting with the polymer solution. Later, the convective cells set in due to a large concentration gradient that leads to interface destabilization. Later this destabilized interface starts expanding uniformly in radial directions forming strikingly regular structures. This morphological evolution of the interface ends up giving finger-like structures called viscous fingers. The inception of pore formation was initially observed when DMSO started leaving the solution. Finally, a set of distinct fingers were seen after the complete interaction of water with the solution coated on the substrate.

2.2 Theoretical Formulation

In order to analytically evaluate the viscous fingering phenomenon, a numerical approach has been undertaken with the primary objective of studying the interfacial variations with time. The linear stability technique has been adopted for analyzing the interface evolution. Following are the equations employed while defining this problem considering porous media where Darcy’s law is used in the porous medium for fluid layer 1. The fluid layer 2 goes with the standard governing equations using Navier–Stokes. The different variables utilized here are u, w (velocity components), x, z (spatial coordinates), h (vertical distance from the interface), t (time), p (pressure), μ (viscosity), κ (permeability), g (gravity), and ρ (density).

The set of governing equations for respective layers where $i = 1,2$ for layers I and II, respectively, precisely contains continuity and momentum balance for x and z directions in the limit of low Re and Darcy’s law as,

$$\nabla \cdot \mathbf{u}_i = 0, (\mathbf{u}_i = u_i, w_i) \tag{1}$$

For layer II (water),

$$-\frac{\partial p_2}{\partial x} + \mu_2 \left(\frac{\partial^2 u_2}{\partial x^2} + \frac{\partial^2 u_2}{\partial \bar{z}^2} \right) = 0, \tag{2}$$

$$-\frac{\partial p_2}{\partial \bar{z}} + \mu_2 \left(\frac{\partial^2 w_2}{\partial x^2} + \frac{\partial^2 w_2}{\partial \bar{z}^2} \right) - \rho_2 g = 0, \tag{3}$$

As we seek an averaged description of the flow in a porous medium formed during water interaction with the coated polymer solution, Darcy’s law provides such a required description. The volume-averaged velocity in a porous medium is determined by Darcy’s law which is given as [20],

For the layer I (porous medium)

$$\mathbf{u}_1 = \frac{-\kappa}{\mu_1} \nabla(p_1 + \rho_1 g z). \quad (4)$$

A pair of superimposed Newtonian fluids has been assumed. The fluid interface is initially fixed at $z = 0$. The spatial resolution followed in the derivation has been fixed such that it is not much larger than the average porous length.

At $z = 0$ (interface), continuity of velocities and normal stress balance conditions [21] can fulfill the purpose of solving the second-order equation obtained after all the algebraic simplifications, which is explained in the next section, and kinematic condition [21] to track the spatiotemporal movement of the interface are employed.

$$u_1 = u_2; w_1 = w_2, \quad (5)$$

$$\mathbf{n} \cdot \boldsymbol{\tau}_2 \cdot \mathbf{n} - \mathbf{n} \cdot \boldsymbol{\tau}_1 \cdot \mathbf{n} = \gamma(\nabla \cdot \mathbf{n}), \quad (6)$$

where, \mathbf{n} , $\boldsymbol{\tau}$, γ are unit outward vectors normal to the interface, Newtonian stress tensor for respective layer, and interfacial tension.

$$\frac{\partial h}{\partial t} = -u \frac{\partial h}{\partial x} + w. \quad (7)$$

2.2.1 Linear Stability Analysis (LSA)

Linearization of all the governing equations and boundary conditions done by implementing the normal modes

$$u = \tilde{u}e^{\omega t + ikx}, w = V + \tilde{w}e^{\omega t + ikx}, p = \bar{p}(z) + \tilde{p}e^{\omega t + ikx}, h = h_0 + \tilde{h}e^{\omega t + ikx} \quad (8)$$

where, ω and k represent the linear growth coefficient and the wavenumber of the disturbance, respectively. In these normal modes, the variables \tilde{u} , \tilde{w} , and \tilde{p} are the infinitesimal amplitudes perturbations to the corresponding variables and are functions of z . The \tilde{h} symbol represents an infinitesimal height perturbation and \bar{p} and h_0 base states of pressure and height.

On solving the above equations of motion with the given set of boundary conditions incorporating normal modes results following fourth-order bi-harmonic equations for respective layers with the general solution given below:

$$\frac{d^4 \tilde{w}_1}{dz^4} - 2k^2 \frac{d^2 \tilde{w}_1}{dz^2} + k^4 \tilde{w}_1 = 0 \quad (9)$$

$$\frac{d^4 \tilde{w}_2}{dz^4} - 2k^2 \frac{d^2 \tilde{w}_2}{dz^2} + k^4 \tilde{w}_2 = 0 \quad (10)$$

The general solution of the fourth-order equation is,

$$\tilde{w}_1 = (A_1 + B_1z)e^{-kz} + (C_1 + D_1z)e^{kz} \tag{11}$$

$$\tilde{w}_2 = (A_2 + B_2z)e^{-kz} + (C_2 + D_2z)e^{kz} \tag{12}$$

We assume here that the disturbance decays far from the interface in $+z$ and $-z$ direction that gives the conditions such as,

$$w_1 \rightarrow 0, \quad z \rightarrow -\infty; \quad w_2 \rightarrow 0, \quad z \rightarrow \infty \tag{13}$$

In this limit, we get rid of two constants each from both Eqs. (10) and (11), which then takes the form

$$\tilde{w}_1 = (C_1 + D_1z)e^{kz} \tag{14}$$

$$\tilde{w}_2 = (A_2 + B_2z)e^{-kz} \tag{15}$$

Finally, using all the equations mentioned above and replacing these expressions of the variables, such as in the boundary conditions, we obtain five homogeneous linear algebraic equations with five unknown constants $A, B, C, D,$ and \tilde{h} . The dispersion relation is attained from the determinant of the coefficient matrix of these algebraic equations. The dispersion relation with an analytical solution of a second-order algebraic equation ω is in the form $\omega = f(k)$.

A necessary and sufficient condition for the instability (stability) of the interface was $\omega > 0$ ($\omega < 0$). An interplay between the stabilizing and destabilizing influences in the system decides the fate of viscous fingering instability. We solved a cumbersome dispersion equation not given here due to its lengthy and complex form. We obtained the groups of terms those then categorized them based on their signs and nature. They are shown in the theoretical results as destabilizing and stabilizing forces in the system. The finger spacing (λ_{avg}), defined as a tip-to-tip distance between two fingers theoretically stated, was attained by evaluating the dominant growth rate (ω_{max}) using the criteria $\omega_{r,k} = 0$, wherein ω_r is the real part of ω ²⁶ and k at the base of the variable represented the differentiation concerning mentioned parameter unless otherwise mentioned. Analytically solving all these cumbersome algebraic equations and boundary conditions is performed using the symbolic commercial package MATHEMATICA™. Later, after identifying the crucial parameters in the system playing a vital role in systems stabilization and destabilizing, we figured out viscosity and density are those parameters and used them as viscosity ratio ($\mu_r = \mu_2/\mu_1$) and density difference ($\rho_D = \rho_2 - \rho_1$) afterward by proper algebraic modification.

3 Results and Discussion

3.1 Experimental Section

The droplet-initiated phase inversion process starts by placing water over the CA in a DMSO bath, as shown in Fig. 1a. Due to the very high affinity of the solvent (DMSO) in water compared to CA, the non-solvent (water) tends to mix with the solvent, leaving the polymer behind, i.e., analogous to the salting-out effect. In the presence of viscosity and density difference, along with the gravitational force acting upon the spilled water, instability is created along the droplet circumference (similar to Saffman–Taylor instability). The changing chemical potential within the system, along with the other fluid property contrast, leads to the growth of the perturbed interface, as shown in Fig. 1b. Initially, small porous structures (sponge pores) are present, indicating the apparent incorporation of non-solvent within the polymer solution. The creation of polymer-lean and polymer-rich regions took place. The presence of pores is attributed to the convection cells as they break the formed thin layer at the beginning of the process. The thin layer breakage allows the invading fluid structures to pass through the previously formed porous medium. However, beyond a certain period, it was observed that many such tiny pores merge to form finger-like structures, as shown in Fig. 1b. This gradient in polymer concentration leads to a rapid increase in the finger pore length. Finally, this drives the fingers to coalesce with one another and travel till equilibrium is attained between the polymer-lean and polymer-rich phases, as shown in Fig. 1c. Multiple perspectives of finger growth are present in the literature based on the different parameters such as geometry and pair of polymer–solvent used [22–24].

The optical micrograph in Fig. 3 depicts the finally formed viscous fingers when water availability for the DMSO vanishes. The remaining part outside the fingers

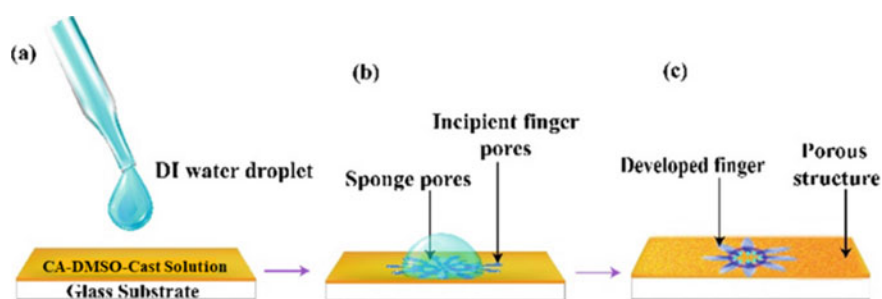


Fig. 1 Schematic diagram of the process steps involved in the viscous finger formation due to the phase inversion process. **a** DI water is spilled over the spin-coated polymeric solution over the substrate. **b** The inception of the pore-like finger formation occurs after some time when water interacts with the coated solution. **c** Distinct finger formation occurs when all the water in contact with the below polymeric solution interacts specifically with DMSO

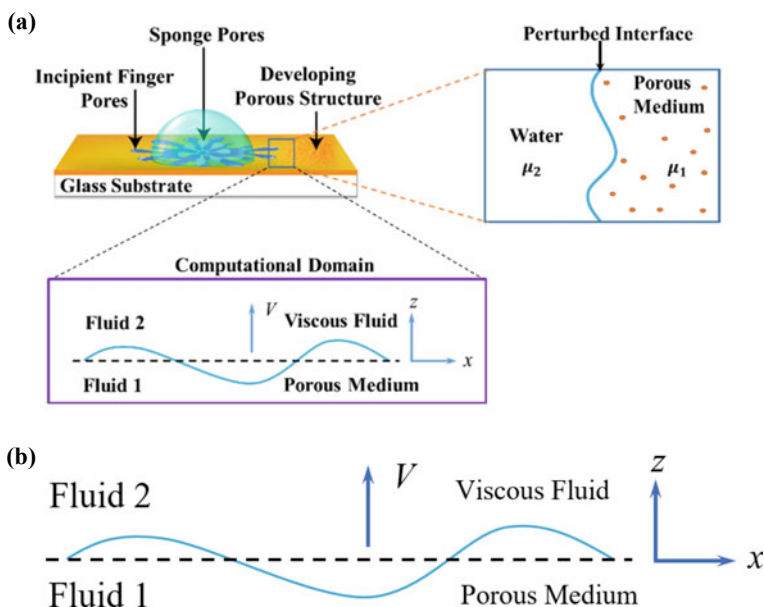


Fig. 2 Schematic representation of water placed over the CA–DMSO-coated solid substrate. **a** The image shows the typical computation domain used in theoretical formulation wherein the total thickness of the layers is d , and fluids are extended in the semi-infinite limit from $z = +h$ to $z = -h$. The right-hand side is the representation in the radial direction. The system is solved in Cartesian coordinates by rotating it through 90° . **b** A simplified theoretical picture for the modeling in which an interface moves with uniform velocity V in the upward direction²⁵

and where water is not reached to mix with DMSO became porous because of the humidity due to exposure to atmospheric conditions.

Fig. 3 Experimental micrograph of the formed fingers in the phase inversion process

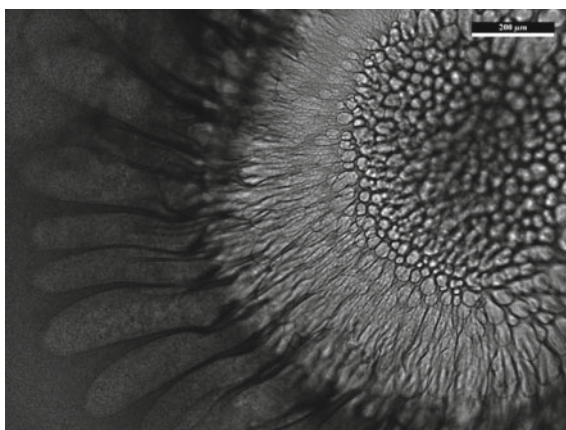
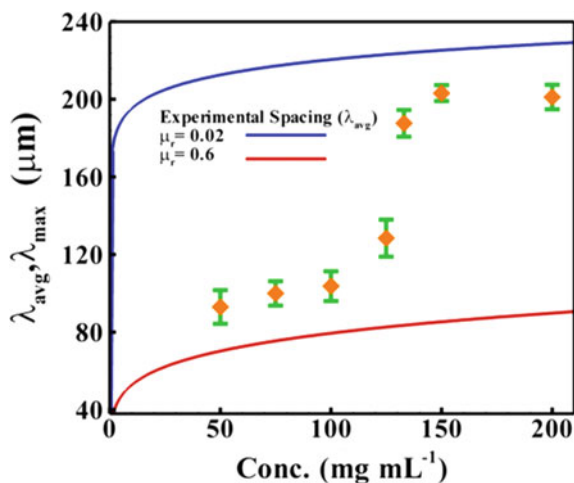


Fig. 4 The variation of the experimentally obtained (λ_{avg}) and theoretically calculated (λ_{max}) finger spacing with the different loadings of CA dissolved in DMSO, where the increased quantities show improvement in the finger spacing when the interface is destabilized



As shown in Fig. 4, the loading quantity of the CA in DMSO is a critical factor that decides finger spacing. The increased CA leads to improved finger spacing over the period. This increment in spacing is attributed to the viscosity increase of the polymeric blend that increases the resistance when the water–DMSO mixture, after sufficient contact, starts to flow. As resistance increases due to the increased viscosity of the blend, the flow speed reduces. When the speed reduces, that offers more time for finger width to develop than the finger length, ultimately slowing down the fingertip speed. As a result, the distance between the fingers increases over the period. At the end of the process, the tip-to-tip distance between fingers becomes constant, as shown in Fig. 4. This increase in distance is attributed to water unavailability for the DMSO to mix and add up in both finger width and spacing, as well as the restricted movement of fingers due to higher resistance offered by elevated viscosity.

3.2 Theoretical Section

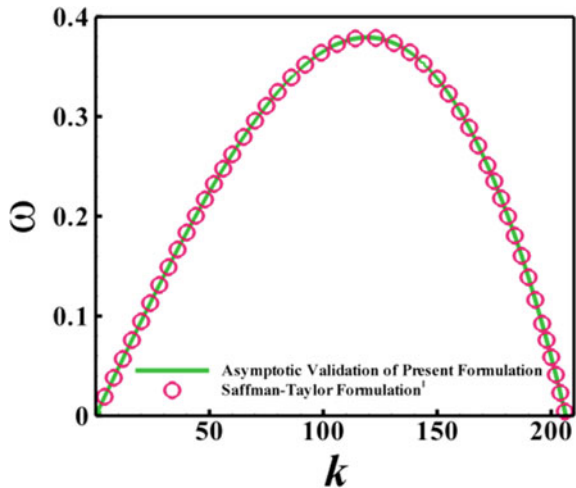
In this section, an attempt is made to unravel the physics of the finger formation with the help of the dispersion relation obtained from the linear stability analysis (LSA), and the dispersion curve is shown in Fig. 5. In order to check the accuracy of the formulation, we validated it with the existing work asymptotically. Figure 5 shows that our formulation matches well with the Saffman–Taylor¹ asymptotically when the terms corresponding to fluid 2 are absent, indicating the formulation's reliability. As discussed below, a few parameters playing an essential role in the system are considered for the theoretical analysis. As mentioned earlier, an increased concentration of CA in polymer solution increases the viscosity offering higher resistance to invading fingers to overcome. The capillary pressure forces in the system support initially set convection cells promoting the viscous fingers. We refer to the

difference in pressure across the interface as capillary pressure, and the expression for this is obtained by solving Eq. (6). Increased viscosity is always in a hurry to set the dominance of viscous forces in the system at every stage of the finger movements. Initiated fingers were initially supported by capillary force and then nurtured by inertial forces in the middle stage of the process, as seen in Fig. 4, where finger spacing started to increase drastically from 100 to 150 mg/mL. Inertial forces help the finger sustain in the middle stage as viscous forces dominate the process. In the last stage, viscous forces entirely owned the dominance by vanishing the effect of the other two forces, resulting in increased finger spacing. Over the period, system reaches the stage where viscous forces completely restrict the fingers, and the system gets saturated completely.

Figure 4 also compares the experimental (λ_{avg}) and theoretical (λ_{max}) finger spacing and their agreement. Here, we enveloped the experimental results between the theoretical findings showing the theory parameters span matching the experimental observations. Of course, this calculation is extraordinarily gross and does not comprise the various parameters set. However, even this gross calculation indicates the first-hand parameters playing a vital role in driving the mechanism.

The increasing density difference ρ_D decreases the maximum growth rate ω_{max} and its corresponding wave number k_{max} , as depicted in Fig. 6a. The plot (a) complements our claim of inertial forces as helping to sustain in the middle stage of the process as their existence destabilizes the interface and strives for continuous movement of fingers even if viscous forces try to dominate over them. In the dispersion relation $\omega = f(k)$ at different viscosity ratios, Fig. 6b shows viscosity as an instability-suppressing parameter in the system upon increasing the viscosity ratio as it offers improved resistance to instability arising from surface movement. Theoretical results also follow the experimental findings discussed earlier in the above section. We

Fig. 5 An asymptotic validation. The Saffman–Taylor formulation represented by solid circles corresponds to the seminal work by Saffman and Taylor¹. The solid line (green) represents asymptotic validation for the present theoretical formulation in the absence of fluid 2 (water)



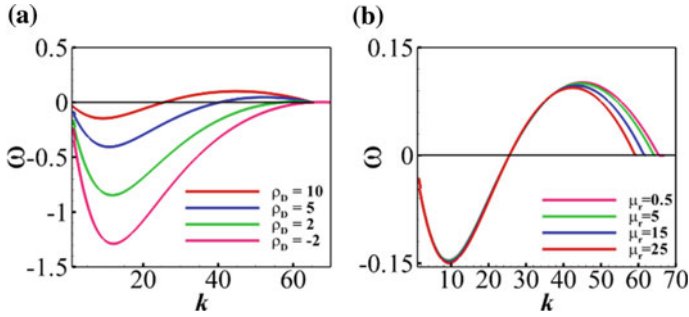


Fig. 6 Dispersion curves obtained analytically show the variation of growth rate ω with wave number k using LSA. Plot **a** shows the dispersion curves at different density difference ρ_D values. Plot **b** shows the wave numbers and instability growth rate for different values μ_r . The parameter space used for the calculation is as $g \rightarrow 9.81$, $\kappa \rightarrow 1 \times 10^{-5}$, $V \rightarrow 1 \times 10^{-6}$, $\gamma \rightarrow 0.005$ follows

theoretically also observed the same system behavior shown at different viscosity ratios in the experiments resulting in increased finger spacing.

4 Conclusions

In this work, we explored viscous finger formation's physics in the CA–DMSO-coated substrate system when water is spilled over it. Experiments revealed that the CA loading in DMSO plays a pivotal role in finger spacing and width. An increase in the viscosity on increasing the loading offers more friction to the water–DMSO to slide over the solution, leading to the reduction in their movement ending with the fingers formed at a distance apart when compared with the low quantity of CA in the polymeric solution. Theoretical predictions also complement experimental conclusions of viscosity ratio and density difference variation. According to theory, as depicted in Fig. 6, an increment in the density difference leads to system destabilization, which is reflected in the increased growth rate of the system instability. But the contribution of viscosity increase, on the other hand, leads to a system of stability as it offers high resistance to invading fingers leading to minimization of destabilizing influences of the system. Therefore, an interplay between the destabilizing influence of density and stabilization by viscosity decides the ultimate fate of finger formation and the spacing between them, which is the tip-to-tip distance between two fingers. With these two influential parameters, the system stability and, ultimately, the interfacial morphology can easily be controlled. The fingering phenomenon in this type of open system is also of great importance in many biological applications [25, 26], where the destabilizing influences need to be minimized in order to analyze their behavior. So, understanding the fingering phenomenon and the control parameters is very important where dendritic structure or fingering needs to be avoided. This type of study, where experiments complement the theoretical front, can significantly help

and need to be profoundly investigated further. Due to the highly complex nature of the system of viscous finger formation in the case considered for the present work, it is tough to claim about the parameter behavior or the system physics strongly. That is the reason why only probable reasons are highlighted. The 3-D non-linear and CFD simulation can significantly help with a prior understanding to set the experiments and other aspects of the phenomena.

Acknowledgements We acknowledge the support from the Department of Chemical Engineering and Centre for Nanotechnology, IIT Guwahati, for the instrumentation facility. Suggestions given by Prof. Omkar S. Deshmukh, IIT Guwahati, in improving the quality of the manuscript are highly appreciated. We also thank MHRD, the Government of India, for financial support.

Nomenclature

ω_{\max}	Maximum growth rate
k_{\max}	Maximum wave number
$\rho_D = \rho_2 - \rho_1$	Density difference
$\mu_r = \mu_2/\mu_1$	Viscosity ratio
\tilde{h}	Perturbed height
κ	Permeability

References

1. Saffman P, Taylor G (1958) Proc R Soc London, Ser A 245:312
2. Homsy G (1987) Annu Rev Fluid Mech 19:271
3. Bensimon D, Kadanoff L, Liang S, Shraiman BI, Tang C (1986) Rev Mod Phys 58:977
4. Couder Y (2000) In: Perspectives in fluid dynamics, Batchelor HMGK, Worster M (eds). Cambridge University Press, Cambridge
5. Tanveer S (2000) J Fluid Mech 409:273
6. Casademunt J, Magdaleno FX (2000) Phys Rep 337:1
7. Hele-Shaw H (1898) Nature (London) 58:33
8. Engelberts WF, Klickeberg LJ (1951) Petr Congr Third World 544
9. Langer JS (1987) In: Souletie J, Vannimenus J, Stora R (eds) Chance and matter, 1986 Les Houches lecture. North-Holland, Amsterdam
10. Kessler DA, Koplik J, Levine H (1988) Adv Phys 35:255
11. Pelcé P (ed) (1988) Dynamics of curved fronts, perspectives in physics. Academic, Boston
12. Brener EA, Mel'nikov VI (1991) Adv Phys 40:53
13. Pomeau Y, Amar MB (1992) In: Godre'che C (ed) Solids far from equilibrium. Cambridge University Press, Cambridge
14. Gollub J, Langer J (1999) Rev Mod Phys 71:S396
15. Zimmerman WB, Homsy GM (1991) Nonlinear viscous fingering in miscible displacement with anisotropic dispersion. Phys Fluids A 3(8):1859–1872
16. Nijjer JS, Hewitt DR, Neufeld JA (2018) The dynamics of miscible viscous fingering from onset to shutdown. J Fluid Mech 837:520–545

17. Chuoke RL, van Meurs P, van der Poel C (1959) The instability of slow, immiscible, viscous liquid-liquid displacements in permeable media. *Trans AIME* 216(01):188–194
18. Ray RJ, Krantz WB, Sani RL (1985) Linear stability theory model for finger formation in asymmetric membranes. *J Membrane Sci* 23:155–182
19. Vanarse V, Thakur S, Ghosh A, Parmar P, Bandyopadhyay D (2023) Coupled instability modes at a solute-non-solvent interface to decorate periodic fingers and cellulose acetate flowers
20. Leal GL (2007) *Advanced transport phenomena*. Cambridge University Press
21. Ravi B, Chakraborty S, Bhattacharjee M, Mitra S, Ghosh A, Gooh Pattader PS, Bandyopadhyay D (2017) *ACS Appl Mater Interfaces* 9:1066–1076
22. Chen CY, Meiburg E (1998) Miscible porous media displacements in the quarter five-spot configuration. Part 1 the homogeneous case. *J Fluid Mech* 371:233–268
23. Hopp-Hirschler M, Safdari Shadloo M, Nieken U (2019) Viscous fingering phenomena in the early stage of polymer membrane formation. *J Fluid Mech* 864:97–140
24. Sharma V, Nand S, Pramanik S, Chen CY, Mishra M (2019) Control of radial miscible viscous fingering. *J Fluid Mech* 884
25. Fridman D (2020) Applications of Bayesian inference for modelling dynamic instability in neuronal dendrite morphogenesis. *Yale Undergraduate Res J* 1(1), Article 12
26. Alert R, Blanch-Mercader C, Casademunt J (2019) Active fingering instability in tissue spreading. *Phys Rev Lett* 122:088104

Stability Characteristics of Linear Unstable Modes in Flow Past Elliptic Cylinders



Deepak Kumar and Bhaskar Kumar

Abstract Linear stability analysis of steady two-dimensional flow past elliptic cylinders with different aspect ratios (Ar) has been conducted for Reynolds number (Re) up to 200. The main characteristics of the steady flow (bubble length, bubble width, drag coefficient, and maximum vorticity on the cylinder surface) have been presented. From the linear stability computations, we find that there are three sets of complex eigenmodes which become unstable with increasing Re . We refer to them as primary wake mode (PWM), secondary wake mode, and tertiary wake mode (TWM), respectively. PWM and SWM have already been reported in the literature for flow past a circular cylinder. In this work, we report a new unstable mode (TWM) along with PWM and SWM in the wake of elliptic cylinders. The structure of TWM shows that it is not so prominent in the near wake but has the longest range of presence and extends all the way up to the downstream boundary. The critical Re for the onset of instability of these modes and the corresponding Strouhal number (St) have been computed. Least-square fit equations for critical Re and St as a function of Ar have also been presented.

Keywords Steady flow · Linear stability analysis · Elliptic cylinders

Nomenclature

a	Semi-major axis [m]
b	Semi-minor axis [m]
Ar	Aspect ratio [–]
H	Computational domain half width [–]
L_B	Bubble length [–]

D. Kumar (✉)

Department of Mechanical Engineering, NIT Durgapur, Durgapur 713209, India
e-mail: dkumar.me@nitdgp.ac.in

B. Kumar

Department of Mechanical Engineering, IIT Guwahati, Guwahati 781039, India

W_B	Bubble width [–]
C_D	Drag coefficient [–]
ω_{max}	Maximum vorticity on the cylinder surface [–]
Re	Reynolds number [–]
St	Strouhal number [–]
λ_r	Growth rate [–]
PWM	Primary wake mode [–]
SWM	Secondary wake mode [–]
TWM	Tertiary wake mode [–]

1 Introduction

Bluff body wakes have been of interest in fluid mechanics since a long time. Flow past an elliptic cylinder is the generalization of flow past a circular cylinder which involves a new variable: the aspect ratio (Ar). In the past, there have been several attempts to investigate this flow [5, 12–14, 20, 24, 26]. The dynamics of the wake of an elliptic cylinder is much more rich compared to the same for a circular cylinder. As we change the aspect ratio of the cylinder, the flow becomes more and more complex. For example, flow past an elliptic cylinder is characterized by the presence of a near wake vortex street (von Kármán vortex street) followed by the diffusion of vortices to form two parallel shear layers. As we go downstream in the wake, the oscillations in the shear layers intensify, finally causing the secondary vortex street to develop [19]. With a decrease in aspect ratio, the extent of the von Kármán vortex street reduces in the wake and the onset location of the secondary vortex street moves close to the cylinder. For low aspect ratios, the shedding pattern is very complex and chaotic with the appearance of vortex pairing and long wavelength wake oscillations [24].

The flow transition between steady to unsteady occurs at Re which depends on Ar of the cylinder. Several researchers [12, 17, 24] in the past have conducted linear stability analysis of steady flow past elliptic cylinders in order to investigate the transition phenomenon. Based on such studies, it is known that the cause and appearance of the Kármán vortex street could be related to the first instability of the wake. The first instability of the wake is related to the growth of the unstable mode, sometimes referred to as the Kármán mode. In the present work, we refer to it as PWM. This is therefore seen as the fundamental cause of unsteadiness in the flow. In the literature, the nature and characteristics of this mode is known for more than forty years. For flow past a circular cylinder, Barkley and Henderson [2] concluded that there is only one mode which becomes unstable leading to the primary wake instability in a two-dimensional flow before the three-dimensionality appears. In contrast, Boppana and Gajjar [3] reported the presence of a second unstable mode before the onset of three-dimensionality. We refer this mode as SWM. According to them, the second unstable mode loses stability somewhere between $Re = 125$ and 150 . In the same year, Verma

and Mittal [25] conducted a linear stability investigation of two-dimensional flow past a circular cylinder. They reported $Re = 110.8$ for the onset of instability of the SWM. They found that structure of SWM is very similar to PWM. However, SWM has a lower growth rate and higher St than PWM.

In this work, we share the discovery of yet another mode which is unstable in flow past elliptic cylinders, apart from the two already known. We refer this new mode as TWM. Knowledge of the nature and characteristics of these modes is of great relevance in understanding the wake flows. The present work examines the characteristics of these modes. We conduct this study for varying Ar of the cylinder and different Re in the range 30–200.

2 Methodology

The governing equations for the fluid flow are the incompressible form of the Navier–Stokes equations. In this work, we use the stabilized finite element formulation to solve the Navier–Stokes equations as well as the eigenvalue problems emanating from the linear stability equations. The stabilized finite element (streamline-upwind/Petrov–Galerkin and pressure-stabilizing/Petrov–Galerkin) method has been developed and used by several researchers in the past [4, 10, 11, 16, 23]. Mittal and Kumar [16] briefly describe the formulation and the numerical method employed here.

Applying the finite element formulation to linear stability equations leads to a generalized matrix eigenvalue problem, and its solution results in the eigenpair. Since the numerical dimension of the problem is usually very large, we look for the few modes which have the largest real part.

Figure 1 illustrates the flow configuration, the computational domain, as well as the boundary conditions. The elliptic cylinder is placed symmetrically in a rectangular domain with its major axis ($2a$) aligned with the flow direction. The cylinder center is considered the origin of the Cartesian coordinate system. Semi-major axis of the ellipse is taken as the length scale for presenting the results. The length of the minor axis is denoted by $2b$, and b/a represents Ar of the cylinder. Nine different Ar values ($= 1, 0.75, 0.5, 0.375, 0.25, 0.125, 0.0625, 0.03, 0.01$) are used in this study. In the present work, the domain boundaries are located far enough so that there is no significant effect on the overall flow field. The distance of the downstream, the upstream, and the cross-stream boundaries are 700, 200, and 100 from the center of the cylinder. The finite element mesh employed in this work contains 249,165 nodes and 247,654 elements in the computational domain. Close to the cylinder surface and in the wake region, the mesh is kept fine enough to capture the separating shear layer, the boundary layer, the wake bubble of the steady flow, and the linear stability modes accurately. In the direction away from the cylinder, the mesh gradually becomes coarser. The details about the finite element mesh can be found in our recent article [15].

The following boundary conditions are used to compute the steady base flow. The velocity at the upstream boundary is given a free-stream value. In the downstream

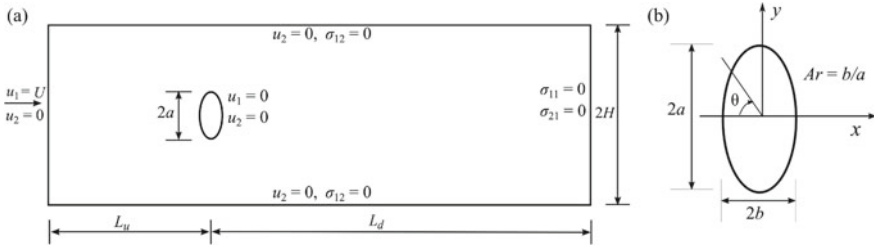


Fig. 1 Problem description: **a** computational domain and boundary conditions, where L_d and L_u represent the downstream and upstream boundaries location, and H denotes the half width of the cross-stream dimension. **b** elliptic cylinder geometry. The cylinder center is used as an origin to measure all the linear distances

boundary, a boundary condition of Neumann type is imposed on the velocity, which corresponds to a zero stress vector. The components of velocity normal to and stress vector along the lower and upper boundaries are assigned zero values. The cylinder surface is a no-slip boundary. Linear stability computations are based on the same boundary conditions except at the inflow border, where the velocity components are set to zero.

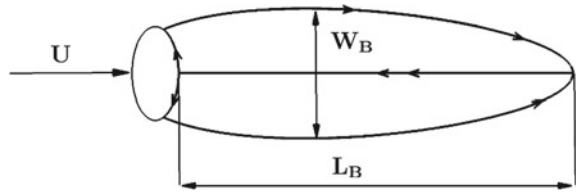
The mesh convergence study is comprehensively discussed in one of our recent publications. Tables I and II of Kumar and Kumar [15] provide a detailed discussion of the mesh convergence study, and based on these results, it can be safely concluded that the mesh considered here is appropriate for performing the present study. Tables III and IV of Kumar and Kumar [15] compare the steady flow characteristics with the published data. The comparison reveals that the present results match very well with the earlier investigations on flow past elliptic cylinders.

3 Results and Discussion

3.1 Steady Flow Results

Here, we display results for steady flow past elliptic cylinders for (nine) different Ar and for Re in the range 30–200. As of now, it is well established that, beyond a particular Re , the flow separates from the cylinder surface [5, 20], which causes the formation of the wake bubble. Figure 2 demonstrates the description of the separation wake bubble. The bubble length (L_B) is characterized as the distance between the rear stagnation point and the wake stagnation point along the wake centerline of the cylinder. The bubble width (W_B) is measured as the maximum distance between the lower and upper separation streamlines.

Fig. 2 Description of the symmetric wake bubble: L_B denotes the bubble length, while W_B represents the bubble width



$$\left. \begin{aligned} L_B &= -0.7155 + 0.1301\text{Re} \\ W_B &= 0.4788 + 0.2444\text{Re}^{0.5} \\ C_D &= 0.2938 + 7.6937\text{Re}^{-0.5} \\ \omega_{\max} &= -2.9870 + 2.3980\text{Re}^{0.35} \end{aligned} \right\} \quad (1)$$

Figure 3 displays the variation of the bubble parameters with Ar and Re . For each Ar , it has been found that L_B grows practically linearly as Re increases. The decrease in Ar causes bubble to substantially grow. A non-linear growth is observed for W_B as Re increases while Ar decreases. The drag coefficient (C_D) shows a monotonic decrease with increase in Re and Ar . The maximum vorticity on the cylinder surface (ω_{\max}) increases with decrease in Ar and increase in Re . The least-square fit of the steady flow data shown in Fig. 3 indicates that for $Ar = 1.0$, L_B , W_B , ω_{\max} , and C_D vary linearly as a function of Re , $Re^{0.5}$, $Re^{0.35}$, and $Re^{-0.5}$, respectively. These results agree with the characteristics of steady flow past a circular cylinder reported by several investigators in the past [6–8, 21, 22]. Theoretical study by Smith [22] showed that L_B grows linearly with Re while W_B increases like $O(Re^{1/2})$. Fornberg [6] calculated the steady flow numerically up to $Re = 600$. He observed that L_B increases linearly with Re , whereas W_B grows as $O(Re^{1/2})$ up to $Re = 300$ and increases linearly after that. Recently, Sen et al. [21] reported the empirical relations for steady flow past $Ar = 1.0$ at low Re in the range 6–40. They found that L_B , C_D , and ω_{\max} vary with Reynolds number as Re , $Re^{-0.5}$, and $Re^{0.5}$, respectively. The variation of ω_{\max} is accurate for low Re . For $Re > 30$, we find $Re^{0.35}$ gives better results.

The empirical equations obtained for the curve fit for $Ar = 1.0$ are given in Eq. 1 for Re in the range 30–200. In general, with the decrease in Ar , it is observed that, the characteristics of the wake bubble vary in the same fashion as for $Ar = 1.0$, except that a higher-order polynomial fit is required. This shows that the non-linearity in the bubble properties increases with decrease in Ar . However, C_D is one exception to this change. It shows linear variation with $Re^{-0.5}$ even for smaller aspect ratios. The maximum percentage error between the actual value and the data obtained from the given equations are 0.88 for L_B , 2.22 for W_B , 0.31 for C_D , and 0.53 for ω_{\max} . The trends represented by the equations therefore are a good representation of the variation of the flow properties.

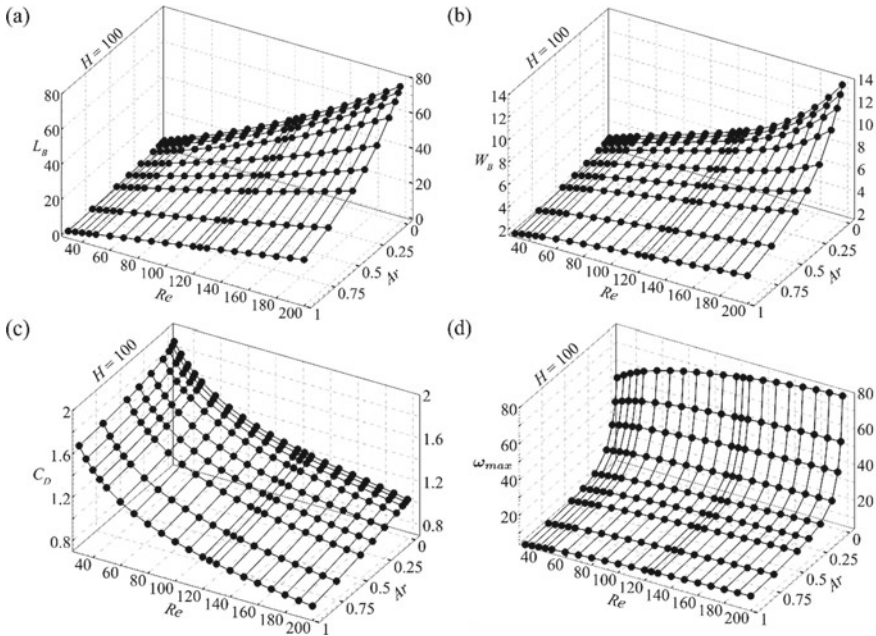


Fig. 3 Steady flow characteristics: effect of Re and Ar on **a** L_B , **b** W_B , **c** C_D , **d** ω_{max} on the cylinder surface

4 Linear Stability Analysis

In the past, linear stability analysis of flow past an elliptic cylinder has been carried out by several researchers [12, 17, 24]. However, the results are very scanty and do not give a comprehensive view of the flow behavior. Here, we provide a detailed analysis of the related flow problem. The linear stability study is carried out for cylinders with different Ar and different flow Re . Our results show the presence of three different kinds of eigenmodes in the flow which become unstable with increase in Reynolds number. We refer to them as PWM, SWM, and TWM. These are identified based on their growth rate and modal structure in the flow field. The growth rate (λ_r) of PWM is the highest. It loses stability at relatively low Re and is responsible for shedding of von Kármán vortices. Upon increasing the Re further, first the SWM and then the TWM loses stability. However, TWM is not observed to become unstable for $Ar = 0.75$ and 1.0 .

The parameters like Ar and Re significantly affect the flow behavior, and hence, their effect is studied in more detail. Figure 4 illustrates the variation of λ_r and St with Re for PWM, SWM, and TWM. For PWM, the λ_r curves for $Ar = 1.0$ and 0.75 show a monotonic increase with Re . For other aspect ratios, it first increases and then passes through a maximum. It is found from these results that flow past a cylinder with low Ar exhibits higher growth rate at lower Re . Consequently, the critical Reynolds

number (Re_c) for the onset of vortex shedding decreases for cylinder with smaller Ar [13, 24]. Similar observations can be made for SWM and TWM. For SWM, the λ_r curve for $Ar = 1.0, 0.75,$ and 0.5 increases monotonically with Re . For other aspect ratios, it shows a non-monotonic increase passing through a maximum. For TWM, the monotonic increase in λ_r is observed for Ar down to 0.25 . Below this, the non-monotonic increase similar to that found with the other modes is observed. For the considered Re range, TWM remains stable for $Ar = 1.0$ and 0.75 . It becomes marginally unstable for $Ar = 0.5$ at $Re = 200$. And for lower Ar , it becomes unstable over a range of Re . Bottom row of Fig. 4 displays the variation of St with Re for the three modes. For PWM, St curves show a non-monotonic variation for higher aspect ratio cylinders ($Ar = 1.0, 0.75, 0.5$). Similar observation has been reported for $Ar = 1.0$ by several researchers in the past [1, 9, 18]. For lower Ar , St of PWM shows a non-monotonic decrease with increase in Re . SWM and TWM exhibit a monotonic decrease in St with increase in Re , for each Ar . There is however one difference in the St curves for TWM. Overall, the slope of the St curves, for TWM, is smaller than the other two modes, and therefore, the minimum which they reach, in the range of Re shown, is higher than that achieved by the other two modes.

We determine the critical parameters (Re_c and St_c) for PWM, SWM, and TWM, corresponding to their zero growth rate.

Figures 5 and 6 show that the value of Re_c and St_c for each eigenmode decreases as we decrease the cylinder aspect ratio. The possible reason for the decrease in Re_c is because the flow past a cylinder with low Ar exhibits higher growth rate at lower Re (see Fig. 4). Our calculations show that TWM does not become unstable for $Ar = 1.0$ and 0.75 below $Re = 200$. Thompson et al. [24] performed linear stability analysis of flow past elliptic cylinders with varying Ar . The critical parameters reported in their work for the onset of instability correspond to the same for PWM in our case. For $Ar = 1.0, 0.75, 0.5,$ and 0.25 , they reported Re_c value as $47.2, 42.6, 38.8,$ and 35.6 , respectively. In the present study, we find Re_c value for $Ar = 1.0, 0.75, 0.5,$ and 0.25 as $46.9, 42.1, 38.3,$ and 35.1 , respectively. Similarly, they reported the corresponding

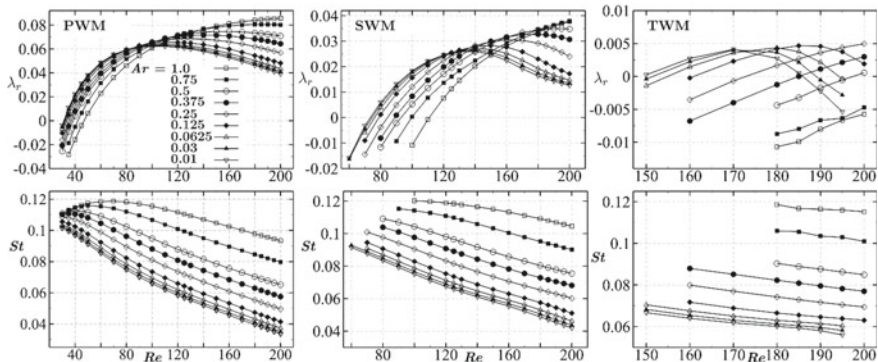


Fig. 4 Variation of λ_r (top) and St (bottom) of PWM (left), SWM (middle), and TWM (right) with increasing Re for different Ar

St_c value for $Ar = 1.0, 0.75, 0.5,$ and 0.25 as $0.1163, 0.1144, 0.1120,$ and $0.1074,$ respectively. We find St_c for the same values of Ar as $0.1167, 0.1150, 0.1126,$ and $0.1082,$ respectively. The comparison shows that the results are in agreement.

The work done by Boppana and Gajjar [3] on flow past a cascade of circular cylinder showed the presence of second unstable pair (SWM in the present nomenclature) which becomes unstable between $Re = 125$ and 150 . The critical value was however not reported. Verma and Mittal [25] were the first to determine Re_c value for the SWM for flow past a circular cylinder. Re_c value reported by them is 110.8 and St_c though not mentioned explicitly is close to 0.12 . The data presented in Fig. 5 depict a close match with these results. The difference in Re_c value with the prediction of Boppana and Gajjar [3] could be attributed to the use of different lateral width of the domain. Table 1 gives the least-square curve fit equations for Re_c and St_c as a function of Ar . The maximum percentage error between the data obtained from the

Fig. 5 Variation of Re_c with Ar for PWM, SWM, and TWM

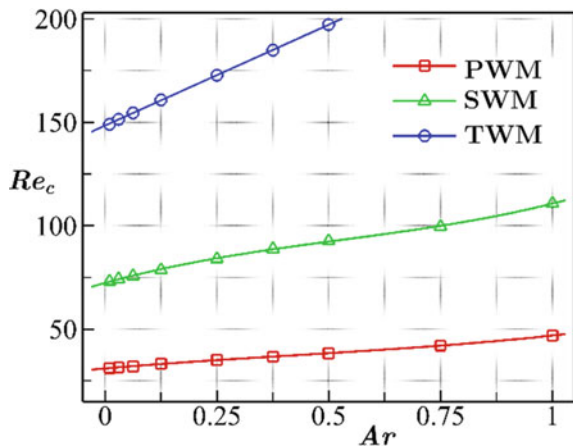
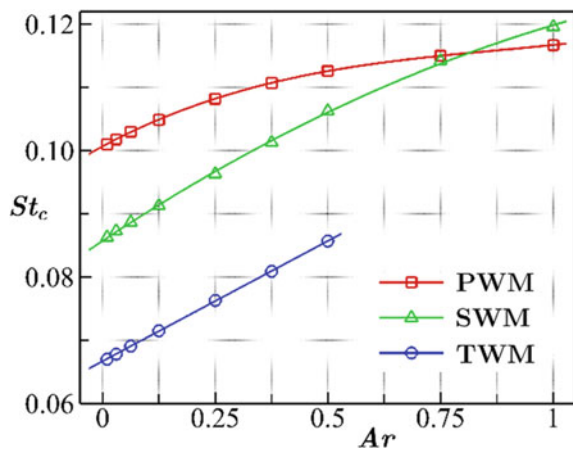


Fig. 6 Variation of St_c with Ar for PWM, SWM, and TWM



given equations of Re_c and the actual value are 0.26 for PWM, 0.47 for SWM, and 0.19 for TWM.

Similarly for St_c , the maximum percentage errors are 0.07 for PWM, 0.41 for SWM, and 0.12 for TWM.

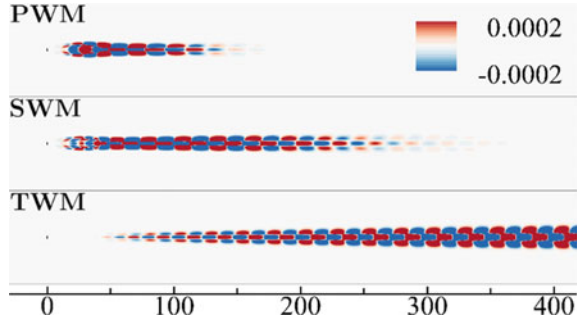
Figure 7 presents the vorticity field for the real parts of PWM, SWM, and TWM for flow past a cylinder with $Ar = 0.25$ at $Re = 180$. The mode structures shown are typical and are observed to have similar features at other Reynolds numbers as well. The vorticity field of these modes is symmetric about the wake centerline. This is opposite to that of the base flow. From the figure, we can see that the strength and extent of the three modes vary in the flow field. Here, it should be noted that the range of the vorticity was kept same for all plots. PWM appears more prominent in the near wake and decays rapidly as we move downstream. Comparatively, SWM extends to a much larger distance away from the cylinder. Its strength seems to increase as we move downstream; however, there is a decrease in strength in the far wake. TWM is not so prominent in the near wake, but has the longest range of presence and extends all the way up to the downstream boundary. In general, it is found that the modes with larger growth rates come close to the cylinder and are shorter in their streamwise length compared to the modes which have lower growth rates. In other words, stronger modes tend to approach the cylinder and also contract, whereas the modes which are weaker tend to recede and elongate. Also, the size of the vortical structure in the modes decreases with increase in their oscillation frequency. These observations are in agreement with the wide range of calculations which we have conducted and can also be seen to agree with the images shown in Fig. 7.

Table 1 Least-square fit equations for Re_c and St_c for PWM, SWM, and TWM, obtained as a function of Ar

	Re_c	St_c
PWM	$10.2144 Ar^3 - 13.0845 Ar^2 + 18.7881 Ar + 31.0082$	$0.0131 Ar^3 - 0.0352 Ar^2 + 0.0381 Ar + 0.1007$
SWM	$37.3984 Ar^3 - 59.4328 Ar^2 + 60.3704 Ar + 72.3436$	$-0.0131 Ar^2 + 0.0472 Ar + 0.0857$
TWM	$97.5631 Ar + 148.410$	$0.0381 Ar + 0.0667$

For PWM and SWM, $0.01 \leq Ar \leq 1.0$ and for TWM, $0.01 \leq Ar \leq 0.5$

Fig. 7 Structure of the eigenmodes: vorticity fields (real parts) of PWM, SWM, and TWM obtained for $Re = 180$ flow past a cylinder with $Ar = 0.25$



5 Conclusion

The linear stability analysis of two-dimensional steady base flow past elliptic cylinders of varying aspect ratios ($0.01 \leq Ar \leq 1.0$) and Reynolds number ($30 \leq Re \leq 200$) has been investigated. The steady flow parameters, like L_B , W_B , ω_{\max} on the cylinder surface, and C_D , have been presented, and their trends are discussed. Linear stability analysis of steady flow past elliptic cylinders yields the presence of three different eigenmodes (PWM, SWM, and TWM). It is observed that these modes show a non-monotonic variation of growth rate with Re for low Ar cylinders. This may also be true for higher Ar cylinders for a larger range of Re . Low Ar cylinders exhibit higher growth rate at lower Re . As a result, Re_c value for the onset of vortex shedding decreases for smaller Ar . For PWM, the variation of St with Re is non-monotonic for higher Ar . For SWM and TWM, St decreases monotonically with Re for all Ar . An interesting correlation exists between the structure of the eigenmodes and their growth rate and St . Modes which have larger growth rate reach close to the cylinder surface and have comparatively shorter length in the wake. Additionally, the size of the vortical structures present in a mode is large if its St is small and vice versa. The difference in the structure of PWM, SWM, and TWM among themselves can be related to the corresponding change in their growth rate and St .

References

1. Barkley D (2006) Linear analysis of the cylinder wake mean flow. *Europhys Lett* 75:750
2. Barkley D, Henderson RD (1996) Three-dimensional floquet stability analysis of the wake of a circular cylinder. *J Fluid Mech* 322:215–241
3. Boppana VBL, Gajjar JSB (2011) Onset of global instability in the flow past a circular cylinder cascade. *J Fluid Mech* 668:304–334
4. Brooks AN, Hughes TJR (1982) Streamline upwind/petrov-galerkin formulations for convection dominated flows with particular emphasis on the incompressible Navier Stokes equations. *Comput Methods Appl Mech Eng* 32:199–259
5. Dennis SCR, Young PJS (2003) Steady flow past an elliptic cylinder inclined to the stream. *J Eng Math* 47:101–120

6. Fornberg B (1985) Steady viscous flow past a circular cylinder up to Reynolds number 600. *J Comput Phys* 61:297–320
7. Fornberg B (1991) Steady incompressible flow past a row of circular cylinders. *J Fluid Mech* 225:655–671
8. Gajjar JSB, Azzam NA (2004) Numerical solution of the Navier-Stokes equations for the flow in a cylinder cascade. *J Fluid Mech* 520:51–82
9. Giannetti F, Luchini P (2007) Structural sensitivity of the first instability of the cylinder wake. *J Fluid Mech* 581:167–197
10. Hughes TJR, Brooks AN (1979) A multidimensional upwind scheme with no crosswind diffusion. In: *Finite element methods for convection dominated flows*, Hughes TJR (ed). ASME, pp 19–35
11. Hughes TJR, Franca LP, Balestra M (1986) A new finite element formulation for computational fluid dynamics: V. circumventing the babuška-brezzi condition: a stable petrov-galerkin formulation of the stokes problem accommodating equal-order interpolations. *Comput Methods Appl Mech Eng* 59:85–99
12. Jackson CP (1987) A finite-element study of the onset of vortex shedding in flow past variously shaped bodies. *J Fluid Mech* 182:23–45
13. Johnson SA, Thompson MC, Hourigan K (2001) Flow past elliptical cylinders at low Reynolds numbers. In: *Proceedings of 14th Australian fluid mechanics conference*. Adelaide, pp 343–346
14. Johnson SA, Thompson MC, Hourigan K (2004) Predicted low frequency structures in the wake of elliptical cylinders. *Eur J Mech (B/Fluids)* 23:229–239
15. Kumar D, Kumar B (2022) Steady flow past elliptic cylinders with blockage effects. *Phys Fluids* 34(5):053606
16. Mittal S, Kumar B (2003) Flow past a rotating cylinder. *J Fluid Mech* 476:303–334
17. Paul I, Prakash KA, Vengadesan S (2014) Onset of laminar separation and vortex shedding in flow past unconfined elliptic cylinders. *Phys Fluids* 26:023601
18. Pier B (2002) On the frequency selection of finite-amplitude vortex shedding in the cylinder wake. *J Fluid Mech* 458:407–417
19. Pulletikurthi V, Paul I, Prakash KA, Prasad B (2019) On the development of low frequency structures in near and far laminar wakes. *Phys Fluids* 31:023604
20. Sen S, Mittal S, Biswas G (2012) Steady separated flow past elliptic cylinders using a stabilized finite-element method. *Comput Model Eng Sci* 86:1–27
21. Sen S, Mittal S, Biswas G (2009) Steady separated flow past a circular cylinder at low Reynolds numbers. *J Fluid Mech* 620:89–119
22. Smith FT (1979) Laminar flow of an incompressible fluid past a bluff body: the separation, reattachment, eddy properties and drag. *J Fluid Mech* 92:171–205
23. Tezduyar TE, Mittal S, Ray SE, Shih R (1992) Incompressible flow computations with stabilized bilinear and linear equal-order interpolation velocity-pressure elements. *Comput Methods Appl Mech Eng* 95:221–242
24. Thompson MC, Radi A, Rao A, Sheridan J, Hourigan K (2014) Low-Reynolds-number wakes of elliptical cylinders: from the circular cylinder to the normal flat plate. *J Fluid Mech* 751:570–600
25. Verma A, Mittal S (2011) A new unstable mode in the wake of a circular cylinder. *Phys Fluids* 23:121701
26. Yoon HS, Yin J, Choi C, Balachandar S, Ha MY (2016) Bifurcation of laminar flow around an elliptic cylinder at incidence for low Reynolds numbers. *Prog Comput Fluid Dyn* 16:163–178

Linear Stability Analysis of Open Cavity Flow Using OpenFOAM®



Ravi Kant, Samarth Acharya, and Ramesh Bhoraniya

Abstract Present paper deals with the modification of existing icoFoam solver (we name it—stabilityFoam) in OpenFOAM® (Open source Field Operation And Manipulation—C++ based toolbox) to solve linearized Navier–Stokes stability equations for a two-dimensional open cavity flow. The objective of this work is to obtain the spatio-temporal perturbation field around the base flow of an open cavity flow. In this view, we construct a new modified solver called “stabilityFoam” by altering the standard incompressible solver i.e. icoFoam and its associated libraries to obtain the disturbance fields around the base flow solution. The numerical simulation is performed for two Reynolds numbers ($Re = 1400$ and 1900). At Reynolds number $= 1400$, the computation showed wake mode instability in the cavity region, whereas, at Reynolds no $= 1900$, it showed shear mode instability near downstream of the flow. At larger times, both the perturbation structure resembles the eigenvalue solution.

Keywords Fluid flow instability · OpenFOAM® · Transitional flows · Open cavity flow

1 Introduction

A collection of CFD tools (including proprietary and open source solvers) are accessible for academic and research purposes. The open-source tools include OpenFOAM® [1], SU 2 [2], NEKTAR++ [3], NEK5000 [4], etc. The advantage of using open-source solvers allow it’s free to access and reproducible [5]. In the present scenario, the fluid flow instability study often relies on computational resources. The

R. Kant (✉)

Mechanical Engineering, Pandit Deendayal Energy University, Gandhinagar 382007, India
e-mail: ravi.kant@sot.pdpu.ac.in

S. Acharya

Mechanical Engineering, BITS Pilani, KK Birla Goa Campus, Goa 403726, India

R. Bhoraniya

Mechanical Engineering, Marwadi University, Rajkot 360 003, India

flow instability generally begins with receptivity followed by turbulent spots and its spatio-temporal evolution, ultimately undergoing a turbulent regime [6]. Jovanovic et al. [7] numerically studied the impulse response of linearized Navier–Stokes equation. We expedite the similar study of spatio-temporal evolution of initial perturbation in open cavity flow. Unlike another open-source packages such as NEK500 and NEK-TAR ++ and in-house codes SIMSON [8], OpenFOAM® does not consist inbuilt solver to solve the linearized Navier–Stokes equation. With this motivation, we have modified the existing icoFoam solver and named it “stabilityFoam”. Linear stability analysis of fluid flows was first investigated by Osborne Reynolds [9], Lord Rayleigh [10], and Hermann Von Helmholtz [11]. Since then, several flow scenarios were examined such as linear stability of plane Poiseuille flow, Couette flow, boundary layer flow, open cavity flow, etc. Open cavity flows are characterized by flow over a square cavity (see Fig. 2). In real practice, these cavities range from small gap/crack in the vehicle, inconsistent roughness in a pipe, cargo bays on an airplane, even large flow circulation in an urban street canyon. There are several pieces of literature on stability of open cavity flow [12–19]. Fundamentally, there are two different modes of cavity instability present on top of the base flow. These modes are stated as shear layer mode and wake mode. In this article, we aim to construct a new modified solver to capture the instability structures such as shear layer and wake modes. We now discuss the flow set-up and governing equation based on theoretical fundamentals.

2 Flow Set-Up

A two-dimensional open cavity flow is set up in a stream-wise direction with length (L) and depth (D) of the cavity as shown in Fig. 1. The inlet flow is set up in a stream-wise direction. The Reynolds number (Re) is defined as $U_{inlet} D/\nu$, where U_{inlet} is the inlet velocity in the domain, D is the depth of the cavity, and ν is the kinematic viscosity of the fluid. The upper boundary is imposed with far-field condition.

Lower walls and cavities are chosen to be the no-slip condition. Also at the exit, the zero-gauge pressure outlet condition is imposed. Moreover, the ratio $L/D = 2$ is chosen for the study. To get the spatio-temporal evolution of disturbances, perturbed incompressible linear Navier–Stokes equation (LNSE) along with the perturbed continuity equation is considered,

$$\nabla \cdot U = 0 \quad (1)$$

$$\frac{\partial U}{\partial t} + (U_B) \cdot \nabla U + U \nabla (U_B) = -\nabla P + \frac{1}{Re} \nabla^2 U \quad (2)$$

where $U = (U_x, U_y)$ is the perturbation velocity field, p is the perturbation field, Re is the Reynolds number based on U_{inlet} , and D defined earlier. U_B is the base flow velocity field that needs to be calculated a priori. After setting up the boundary

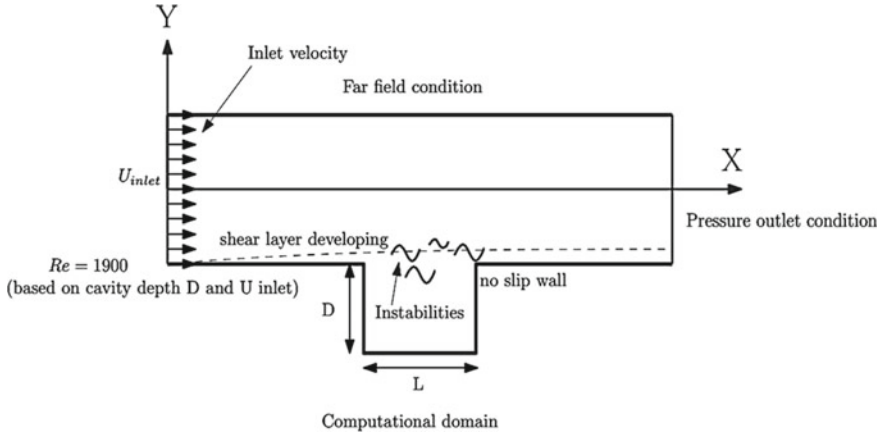


Fig. 1 Computational domain for open cavity flow

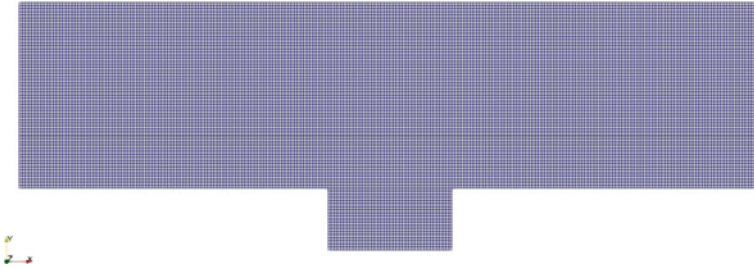


Fig. 2 Mesh visualization of open cavity flow domain using ParaView

conditions of “ U ” and “ P ” in the zeros folder, icoFoam solver is utilized for incompressible base flow computations. The mesh is generated using simple grading with 1000 elements in stream-wise and 100 elements in wall-normal direction as shown in Fig. 2. In OpenFOAM®, we perform the numerical simulation for base flow at two different Reynolds numbers (1400 and 1900). The contours for base flow velocity magnitude are shown in Figs. 3 and 4, respectively. We can observe the shear layer developing in both cases. Once we have the base flow computed results, we can then simulate for perturbation evolution over the base flow solution.

2.1 “Stabilityfoam”—A Modified Icofoam Solver

The LNSE (linearized Navier–Stokes equation) perturbed set of equations are quite similar to the usual Navier–Stokes equation. The standard incompressible icoFoam solver can be easily modified, and the perturbation field solutions can be sought. The



Fig. 3 Open cavity base flow solution at Reynolds no = 1400



Fig. 4 Open cavity base flow solution at Reynolds no = 1900

usual compressible Navier–Stokes equation can be solved using an inbuilt OpenFOAM® solver named “icoFoam”. The new modified solver i.e. “stabilityFoam” is capable of solving the linearized Navier–Stokes equation. They propose “stabilityFoam” solver is obtained by modification a few files and folders. The modified folder structure is depicted as shown in Fig. 5. In the file structure of any OpenFOAM® simulation case, one can find three basic folders, named 0, constant, and system. In the system directory, there are four files, which include the blockMeshDict file, the control diet file, fvSchemes, and fvSolutions, and of these four, the first two is case-specific and the latter two govern the methods employed to iterate towards the solution. Apart from the three basic folders in any OpenFOAM® case files, additionally, we create a new folder named stabilityFoam. This consists of two files (creatFields.H and stability form. C) and a compiler folder. The stabilityFoam.C file is modified in the following manner. The usual icoFoam.C is copied from the opt/solver folder, and inside the script, the momentum predictor (fvVectorMatrixUEqn) is modified and pasted in the stabilityFoam.C file as follows in the enlisting.

U is the perturbation velocity field and UB is the base flow velocity field. phi and phiB are the previous time step perturbed flow velocity field and previous time step base flow velocity fields, respectively. When we modify the standard solver by using

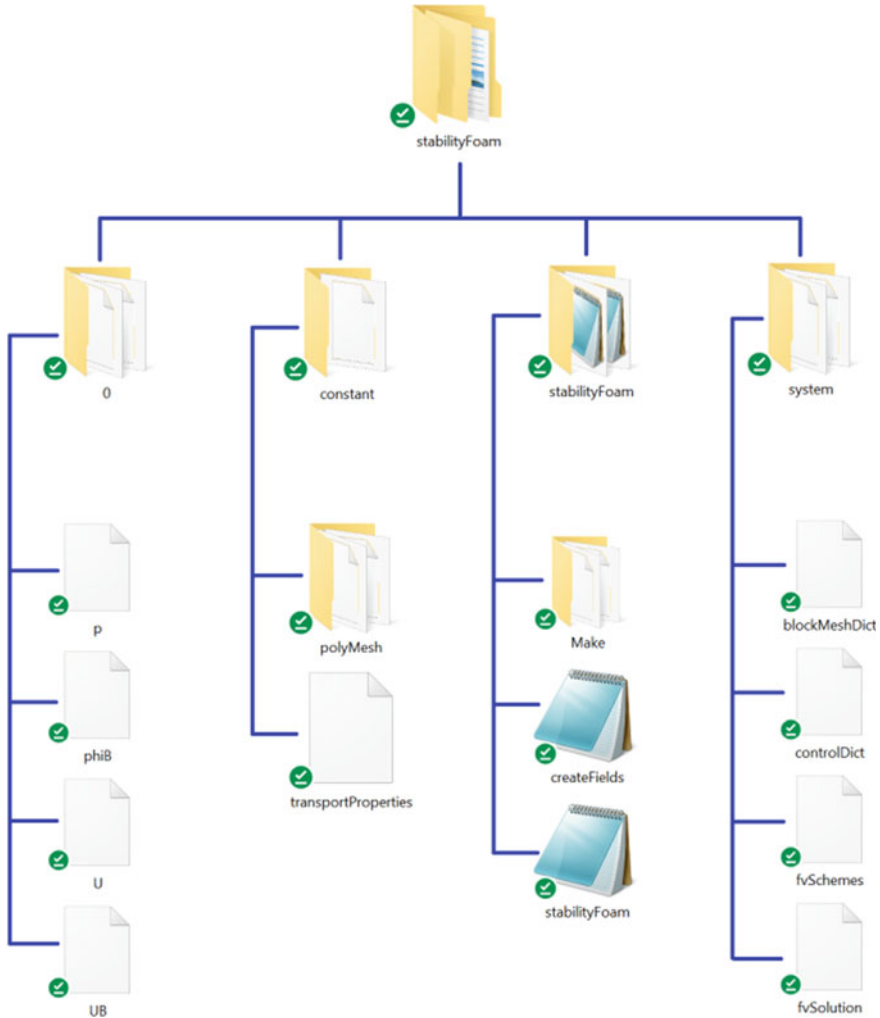


Fig. 5 Folder structure of stabilityFoam solver

terms like UB, phiB, etc., we end up introducing new fields that the solver must read. In the structure of OpenFOAM, each code is accompanied by another file, which is a header file called createFields.H which includes all the associated variables that are to be utilized for the solution. Thus, for this purpose, we must define these quantities in the createFields.H file. These two new fields (UB and phiB) can be thus introduced as follows in enlisting Figs. 6 and 7.

Once stabilityFoam.C and createFields.H are defined and modified, several other files are also modified in similar manner. When adding a new field in the application to be called, it is essential to specify the method of solving for those values in

Fig. 6 Modification of code in stabilityFoam.C file

```

//Momentum predictor
fvVectorMatrix UEqn
(
    fvm::ddt(U)
    + fvm::div(phiB, U)
    + fvc::div(phi, UB)
    - fvm::laplacian(nu, U)
);

```

Fig. 7 Modification of CreatFields.H file

```

Info<< "Reading field UB\n" << endl;
volVectorField UB
( IOobject
    ("UB",
    runTime.timeName(),
    mesh,
    IOobject::MUST_READ,
    IOobject::AUTO_WRITE),
    mesh);
surfaceScalarField phiB
( IOobject
    ("phiB",
    runTime.timeName(),
    mesh,
    IOobject::READ_IF_PRESENT,
    IOobject::AUTO_WRITE),
    fvc::flux(UB));
#include "createPhi.H"

```

these files. In our case, we must make the following modifications in the fvSchemes and fvSolutions files, respectively. The modification in fvSchemes is done incorporating UB and phiB. Similarly, the fvSolutions file is also modified accordingly. The controlDict file is also modified with the application name same as stabilityFoam. Readers can look at the modified version of codes available at <https://github.com/ravikgpiit/Open-Cavity-Flow-Instability>.

The folder and the file structure are ready but not fit for compilation, since we have to source the environment to run the new stabilityFoam solver and also base flow solutions should be available beforehand. Following are intermediate steps to get solution of perturbation velocity field.

1. First, solve the base flow case using a standard icoFoam solver to establish the base flow velocity field solution.
2. After getting the base flow solution, call the field results (U and p) of the final time step of the standard icoFoam solution and initialize the perturbation field. The initialization is done by renaming the “ U ” file as “UB” in the “0” directory of stability Foam and also copying the file “ p ” file as it is.
3. The folder should contain UB as well as U file. Create the new “ U ” file in the “0” directory to initialize the perturbed flow field.
4. After sourcing the environment, run the stabilityFoam solver to get the perturbation fields.
5. The next step is to compile the solver to be able to run the application. But just before this site, the sourcing of the environment is done in the following way. The files in the make folder of the solver folder also need to be modified/renamed to use the command stabilityFoam in the terminal to call the application. Once that is done, the commands “wclear” and “wmake” in succession to compile the code and make it suitable to run it. The compilation is done by typing the previously mentioned commands in the terminal from the directory of the solver. We have put all the files and folders of stabilityFoam solver in the link (<https://github.com/ravikgpiit/Open-Cavity-Flow-Instability>). The stabilityFoam solver is run for 1 s and the time step deltaT is kept to be 0.0001 s. The simulation is done for several grid sizes to ensure the grid convergence up to three decimal places. The final perturbation results are visualized in the associated data viewer ParaView.

3 Results and Discussion

The grid independence study was also performed, and the converged solutions were obtained for three decimal places. The perturbation and base flow variable contours were visualized in associated open-source package ParaView. The stream-wise U_x perturbation contours at different time steps for Reynolds number $Re = 1400$ are shown in Fig. 8. It shows the spatio-temporal evolution of stream-wise U_x perturbation contours at time $t = 0, 0.1, 0.2, 0.3, 0.4, 0.5, 0.6, 0.7, 0.8, 0.9,$ and 1 s. The perturbation structure also matches with the contours depicted in the literature [5]. Figure 9 shows the wall-normal U_y perturbation velocity field contours at time $t =$

0, 0.1, 0.2, 0.3, 0.4, 0.5, 0.6 s at Reynolds number = 1400. At this Reynolds number, the system leads to wake mode instability. The wake mode instability is associated with the internal cavity region of the flow set-up. The perturbation structure at the large time also matches with the eigenvalue solution depicted in the literature [5]. Although the magnitude of perturbations is of the order of $10^{-5} - 10^{-6}$, these small fluctuations may lead the laminar flow into transition. At a higher Reynolds number ($Re = 1900$), the perturbation structure resembles shear mode instability. The shear mode instability is dominant in the downstream region of the flow also depicted in Fig. 10. It shows the stream-wise U_x perturbation velocity field contours at time $t = 0, 0.1, 0.2, 0.3, 0.4, 0.5, 0.6$ s. Figure 11 shows the wall-normal U_y perturbation contours at different time steps (time $t = 0.001, 0.1, 0.2, 0.3, 0.4, 0.5, 0.6, 0.7, 0.8, 0.9$, and 1 s) for Reynolds number $Re = 1900$. At final time steps, we also observe that the perturbation fields resembles the eigenvalue solutions, which is also matches the eigenvalue solutions in the literature [5]. For both the Reynolds numbers, we observe perturbations dominating the base flow, eventually leading to transition. We get both wake mode and shear mode instability for Reynolds numbers 1400 and 1900, respectively. Nevertheless, the disturbances were quite small as compared to the base flow magnitudes, and the dynamics of these disturbances are such that it may lead the laminar flow to undergo transition.

4 Conclusions

In this article, we have constructed a new solver—stabilityFoam in OpenFOAM® to get the disturbance field around the base flow solution of an open cavity flow. This stabilityFoam solver essentially computes the linearized Navier–Stokes equation (LNSE) with prescribed boundary conditions. This stabilityFoam solver allows us to get the spatio-temporal evolution of disturbance fields. The simulations were performed at $Re = 1400$ and 1900, and at both Reynolds numbers, we observe perturbations taking over the base flow undergoing transition process. We get both wake mode and shear mode instability for different Reynolds numbers. Although the disturbances were quite small as compared with the base flow, the dynamics of these disturbances are such that it may lead the laminar flow to undergo into transition to turbulent.

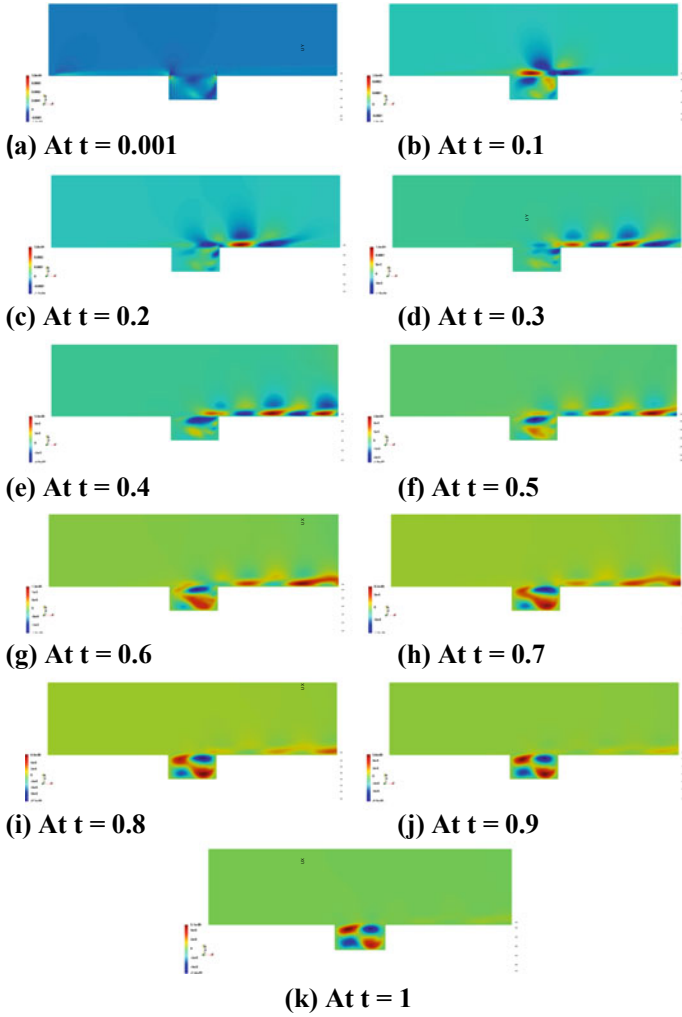


Fig. 8 Stream-wise U_x perturbation contours at different time steps (time $t = 0.001, 0.1, 0.2, 0.3, 0.4, 0.5, 0.6, 0.7, 0.8, 0.9,$ and 1) for Reynolds number $Re = 1400$

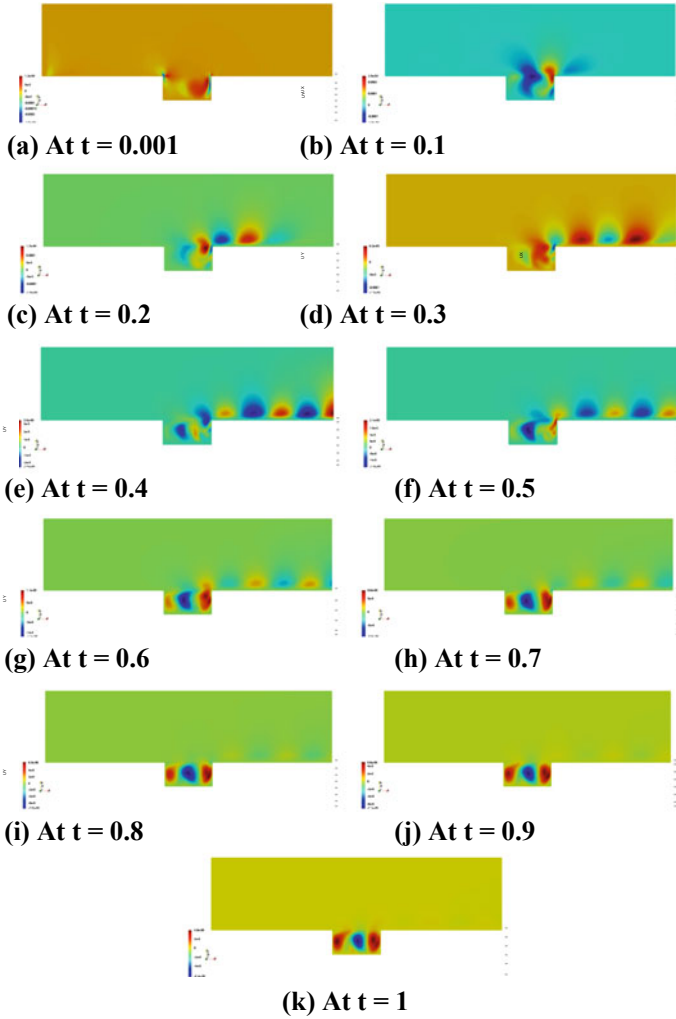


Fig. 9 Wall-normal U_y perturbation contours at different time steps (time $t = 0.001, 0.1, 0.2, 0.3, 0.4, 0.5, 0.6, 0.7, 0.8, 0.9,$ and 1) for Reynolds number $Re = 1400$

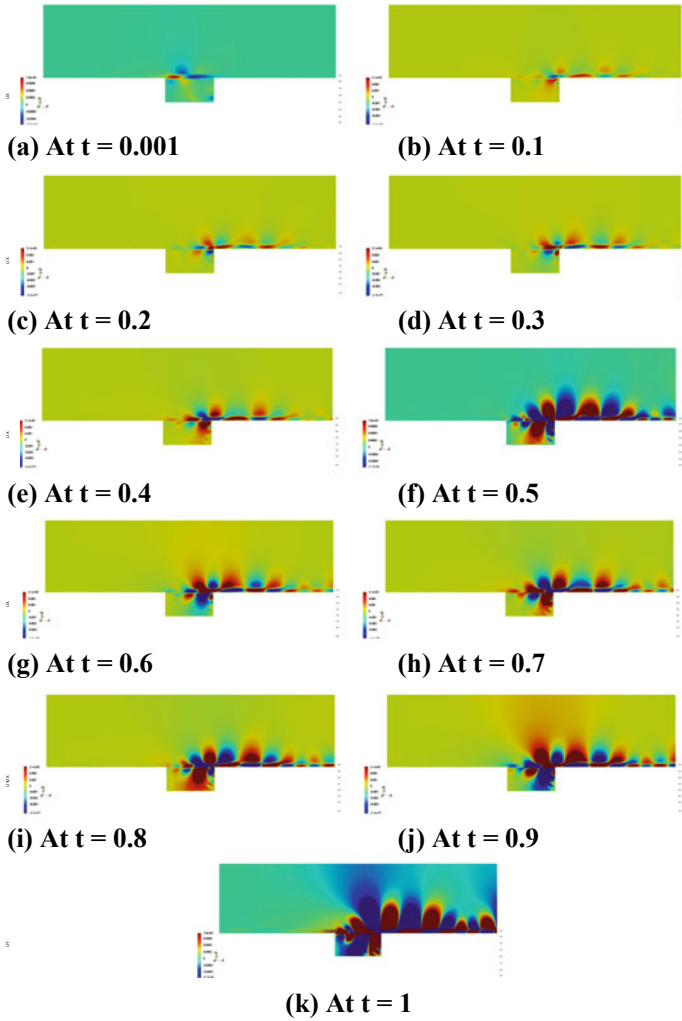


Fig. 10 Stream-wise U_x perturbation contours at different time steps (time $t = 0.001, 0.1, 0.2, 0.3, 0.4, 0.5, 0.6, 0.7, 0.8, 0.9,$ and 1) for Reynolds number $Re = 1900$

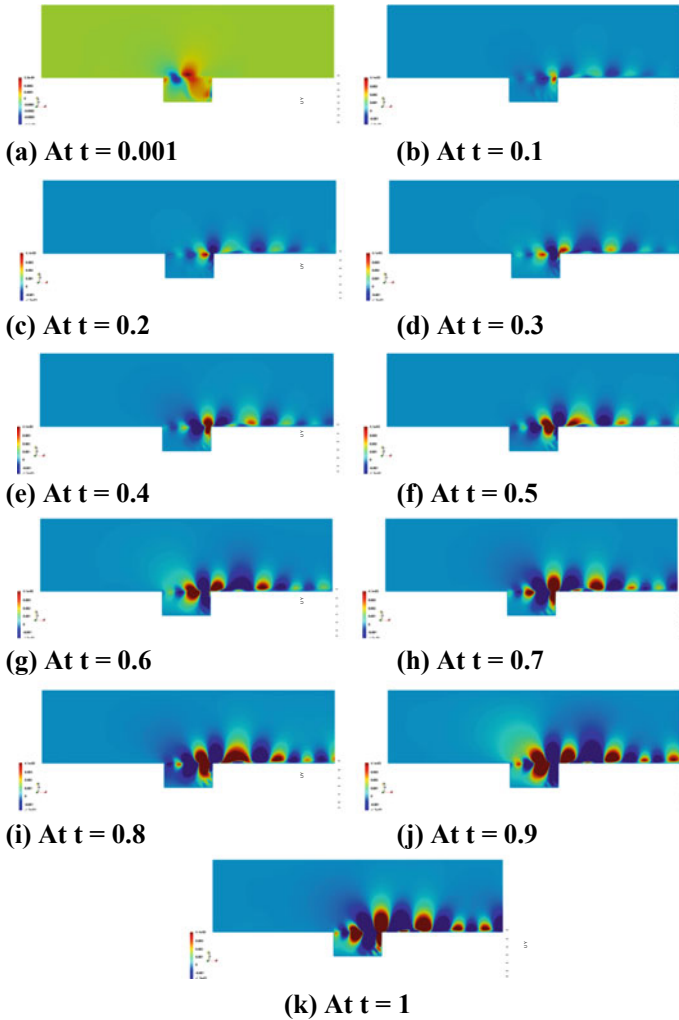


Fig. 11 Wall-normal U_y perturbation contours at different time steps (time $t = 0.001, 0.1, 0.2, 0.3, 0.4, 0.5, 0.6, 0.7, 0.8, 0.9,$ and 1) for Reynolds number $Re = 1900$

Acknowledgements The authors would like to state that the paper has no conflict of interest. Also the OpenFOAM source codes are available at <https://github.com/ravikgpit/Open-Cavity-Flow-Instability>

Nomenclature

L Length of cavity in stream-wise direction m

D	Depth of the cavity m
Re	Reynolds number [-]
U_{inlet}	Inlet velocity in the domain m/s
ν	Kinematic viscosity of the fluid $\text{m}^2 \text{s}^{-1}$
U	Perturbed velocity magnitude field m/s
U_x	Stream-wise perturbation velocity m/s
U_y	Wall-normal perturbation velocity m/s
P	Pressure N/m^2
U_B	Base velocity m/s
Φ	Previous time step perturbed flow velocity field m/s
Φ_B	Previous time step base flow velocity field m/s

References

1. OpenFOAM (2014) OpenFOAM User Guide. The OpenFOAM foundation
2. Economou TD et al (2016) SU2: an open-source suite for multiphysics simulation and design. *Aiaa J* 54(3):828–846
3. Cantwell CD, Moxey D, Comerford A, Bolis A, Rocco G, Mengaldo G, De Grazia D, Yakovlev S, Lombard J-E, Ekelschot D et al (2015) Nektar++: an open-source spectral/hp element framework. *Comput Phys Commun* 192:205–219
4. Paul JWL, Fischer F, Kerkemeier SG (2008) nek5000 Web page. <http://nek5000.mcs.anl.gov>
5. Liu Q, Gomez F, Perez J, Theofilis V (2016) Instability and sensitivity analysis of flows using OpenFOAM. *Chinese J Aeronautics* 29(2):316–325
6. Morkovin MV (1985) Bypass transition to turbulence and research desiderata
7. Jovanovic M, Bamieh B (2001) The Spatio-temporal impulse response of the linearized Navier-stokes equations. In: *Proceedings of the 2001 American control conference*. (Cat. No. 01CH37148), vol 3. IEEE, 1948–1953
8. Chevalier M, Lundbladh A, Henningson DS (2007) Simson—a pseudo-spectral solver for incompressible boundary layer flow
9. Reynolds O (1883) An experimental investigation of the circumstances which determine whether the motion of water shall be direct or sinuous, and of the law of resistance in parallel channels. *Proc R Soc Lond* 35(224–226):84–99
10. Rayleigh L (1879) On the stability, or instability, of certain fluid motions. *Proc London Math Soc* 1(1):57–72
11. Koenigsberger L (1903) Hermann von Helmholtz, Vieweg Braunschweig, vol 2
12. Meseguer-Garrido F, De Vicente J, Valero E, Theofilis V (2014) On linear instability mechanisms in incompressible open cavity flow. *J Fluid Mech* 752:219–2014
13. Colonius T, Basu A, Rowley C (1912) Numerical investigation of the flow past a cavity. In: *5th AIAA/CEAS aeroacoustics conference and exhibit*, 1912
14. Liu Q, Gomez F, Theofilis V (2016) Linear instability analysis of incompressible flow over a long rectangular finite-span open cavity. *J Fluid Mech* 799:2016
15. Murray N, Sällström E, Ukeiley L (2009) Properties of subsonic open cavity flow fields. *Phys Fluids* 21(9):095103
16. Rona A, Brooksbank E (2003) Pod analysis of cavity flow instability. In: *41st aerospace sciences meeting and exhibit*, p 178
17. Theofilis V (2000) Globally unstable basic flows in open cavities. In: *6th aeroacoustics conference and exhibit*, p 1965

18. Yamouni S, Sipp D, Jacquin L (2013) Interaction between feedback aeroacoustic and acoustic resonance mechanisms in a cavity flow: a global stability analysis. *J Fluid Mech* 717:134–165
19. de Vicente J, Basley J, Meseguer-Garrido F, Soria J, Theofilis V (2014) Three-dimensional instabilities over a rectangular open cavity: from linear stability analysis to experimentation. *J Fluid Mech* 748:189–220
20. Schmid PJ, Henningson DS, Jankowski D (2002) Stability and transition in shear flows. *Appl Math Sci* 142,; *Appl Mech Rev* 55(3):B57–B59

Aerodynamics

Impact of Roughness Strip Location on Improving Aerodynamic Characteristics of Circular Cylinder



A. N. S. Prakash Kurakula, Sk Abdul Zakaria, B. Avinash Reddy, and Tamal Jana

Abstract This present study aims to investigate flow over smooth and rough circular cylinders with a full rough surface and locally applied rough patches at different angular locations. The RANS simulation is conducted using commercial software ANSYS Fluent. The numerical investigation is carried out at a Reynolds number of 25,000, and the associated flow (air) velocity is 37 m/s. It is observed that the rough cylinder is very effective in reducing drag when compared with the smooth cylinder. Further, the roughness strips, extended over 15° circumferential locations, are added separately at different angular orientations of 0, 22.5, 37.5, 52.5, 67.5, and 82.5 degrees over the surface of the cylinder. It can be noted that, with the changes in the position of roughness, there is a significant change in the aerodynamic characteristics. When the surface roughness is implemented over the surface, there is a decrease in the coefficient of drag. Particularly, the roughness strip at 37.5° angular orientation shows a superior effect in reducing the drag.

Keywords Bluff body · RANS simulation · Surface roughness · Drag · Lift

Nomenclature

- C_l Coefficient of lift [–]
 C_d Coefficient of drag [–]
 D Diameter of cylinder [m]
 k Roughness height [m]
 θ Circumferential range of the roughness strip ($\theta = 15^\circ$) (°)
 α Angular location central point of the roughness strip with respect to freestream flow (°)

A. N. S. P. Kurakula · S. A. Zakaria · B. A. Reddy · T. Jana (✉)
Department of Aerospace Engineering, JAIN (Deemed-to-Be University), Bangalore, India
e-mail: fortamal@gmail.com

T. Jana
Department of Aerospace Engineering, B.M.S. College of Engineering, Bengaluru, India

1 Introduction

Most of the structures created by humans are bluff bodies. The bluff bodies are of such types of shapes where pressure drag is prominent. It is well known that drag is one of the major reasons for the structural instability and decrease in the time of serviceability. The drag vortex shedding activities exhibited by the fluid medium over the bluff bodies are the primary reason for their less life span or even the structural failure. There is a need to investigate the control mechanism of the drag and vortex shedding activity in order to make the structures more stable and make it last long. There are several investigations conducted on bluff bodies over last few decades on different problems. However, there are many aspects which need further investigation for the proper understanding of the inherent flow physics. The current study aims to investigate the effects of surface roughness on flow over a bluff body. Lots of experiments and wind tunnel experiments are conducted on this topic. One of the earliest research projects was conducted by Baines [1] about flow over a bluff body in a wind tunnel. He tested different models of bluff bodies in wind tunnels. He observed distinct differences in the pressure distribution and streamline distribution for boundary layer type flow in the case of tall buildings, cubes, and walls with different aspect ratios. He stated some general rules for the consideration of wind loads in the case of building design. Baetke and Werner [2] tested the standard $k-\epsilon$ model for flow over a surface-mounted cube. They mentioned the need for improved second-moment closure for the RANS equations to attain accuracy in the numerical prediction of the wind engineering flows.

In the experiment conducted by Achenbach [3], the impact of the surface roughness is investigated for the flow over an axisymmetric cylinder. The study concluded that the subcritical flow region could not be affected by rough surface. Besides, the drag force abruptly decreases to a minimum value with the increase in Reynolds number, which is inside the critical flow region. Further increase in Reynolds number results in an increase in the drag force (supercritical flow regime) attaining a nearly constant value (trans-critical flow regime). Interestingly, in the trans-critical flow regime, the drag force increases with the surface roughness.

Though several studies concentrated on the effect of roughness in drag reduction, applying the roughness value over the whole cylinder may not be the wise option as it will increase skin friction drag. Instead, a small roughness strip can be deployed over the cylinder surface and investigations can be carried out to find the optimum location of the roughness strip. Shruthi et al. (2019) investigated the effect of locally applied roughness height [4]. They found that the aerodynamic characteristics were significantly dependent on the roughness location. Therefore, further investigations are necessary on the roughness effect. Hence, the current study particularly aims to investigate the impact of the location of the roughness strip, extended over 15° circumferential locations, over a circular cylinder in reducing drag.

2 Computational Model and Validation

For the current study, a 2-D geometry of a cylinder of radius 0.01 m is considered. As we need to add roughness to the circumferential surface of cylinder at certain angles, we divided the surface of the cylinder into 24 parts, where each part extends for angle $\theta = 15^\circ$ over the circumference, as shown in Fig. 1. These parts can be called as roughness strips. α is the angle what a roughness strip makes with the incoming flow.

The present numerical investigation is performed using commercial software ANSYS Fluent. Particularly, the computations are carried out using RANS with the SST $k-\omega$ turbulence model in order to determine the effects of surface roughness on the bluff body. Since the SST $k-\omega$ turbulence model is effective in predicting the separated flow region under adverse pressure gradient, as stated by Vu [5] and Pang [6], that particular model is utilized. At first, the investigations are carried out for the smooth cylinder and compared with the results obtained for a fully rough cylinder. Subsequently, the computations are conducted for the rough cylinders where the location of rough patches is provided at different angular orientations separately.

A rectangular domain is created around the cylinder as shown in Fig. 2. From the center of the cylinder, the distances of the inlet and outlet of the numerical domain are 12D and 48D, respectively.

The appropriate meshing of the numerical domain is one of the most important aspects of a numerical simulation, and a good or optimal grid should be capable of capturing all details of the flow throughout the domain. A structured grid is more economical and more accurate than an unstructured grid. In this investigation, the mesh around the geometry is made coarser than that of the other places. The number of nodes used here is 181,700. The mesh generated looks as shown in Fig. 3. The domain is discretized by employing the quadrilateral mesh.

The second-order upwind scheme is used for pressure, momentum, turbulent kinetic energy, and dissipation. The transient formulation is second-order implicit. The velocity of air is calculated to be 36.7 m/s at the inlet. The monitors for drag

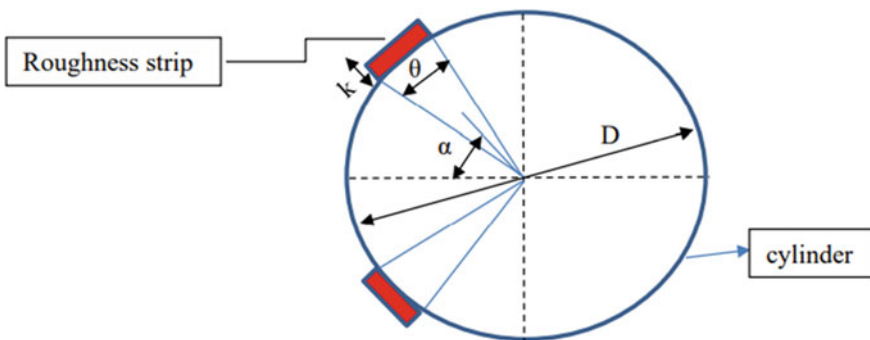


Fig. 1 Model geometry and test configuration

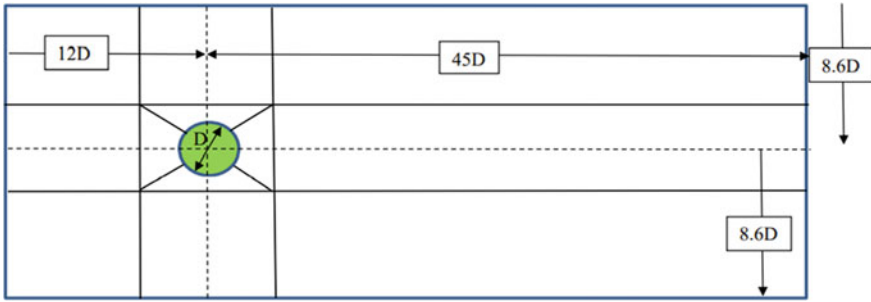


Fig. 2 Numerical domain (dimensions are taken from ref. [4])

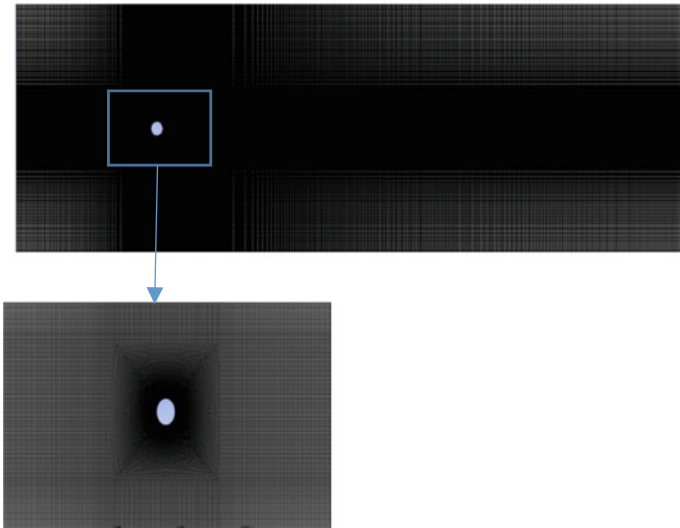


Fig. 3 Mesh modeling

and lift are considered. Flow behavior is taken as transient in order to observe the flow at different time steps. For the smooth cylinder, the total surface of the cylinder is considered to be smooth. Different geometries are modeled with roughness strips positioned at $\alpha = 22.5^\circ, 37.5^\circ, 52.5^\circ, 67.5^\circ,$ and 82.5° . The ratio of roughness height to cylinder diameter (k/D) is taken as 75×10^{-5} . Roughness height is added to each strip separately, and the results are observed and compared. In order to verify the observations, the coefficient of drag calculated from the present investigation is validated with Achenbach [3] and Sruthi [4] with roughness applied over the cylinder (Table 1).

Table 1 Validation result of numerical results with experimental data of C_d for smooth and rough cylinders

Reynolds number	k/D	Achenbach [3]	Shruthi et al. [5]	Present study
25,000	Smooth cylinder	1.48	1.45	1.4
25,000	75×10^{-5}	1.385	1.4	1.31

3 Results and Discussion

The investigations on the aerodynamic structures particularly concentrate on the pressure distributions over the bodies. In the present numerical study, the lift and drag coefficients are compared for the smooth and rough cylinders. Furthermore, the rough patches are distributed at different angular orientations over the circular cylinder to optimize the location of the rough strip in order to reduce the pressure drag. The data obtained from the present numerical simulation of the flow around these structures can be used for better designing and construction of structures with a lesser aerodynamic load.

The velocity contour for the smooth cylinder is shown in Fig. 4. The shed vortices are clearly visible in the velocity contour. It can be observed that the fluid velocity immediately behind the cylinder is very less, which is the wake region.

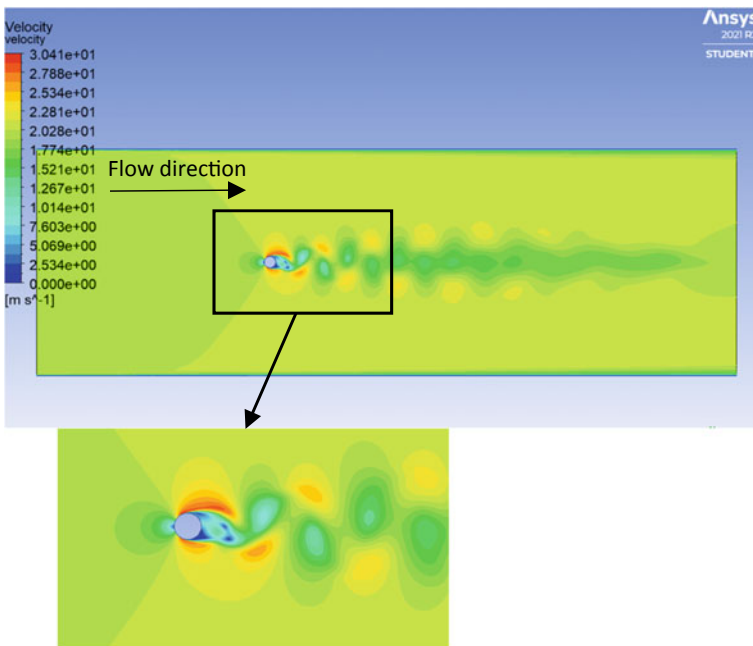


Fig. 4 Velocity contour for a smooth cylinder

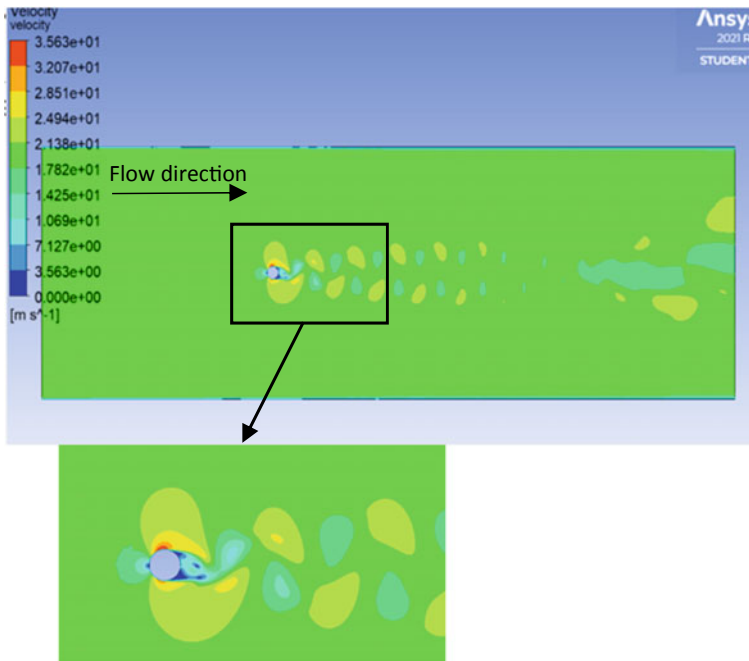


Fig. 5 Velocity contour for a rough cylinder

For a rough cylinder, the velocity contour obtained is shown in Fig. 5. It can be observed that the velocity is very less at the immediate front and back of the cylindrical body. The velocity close to the surface at 90° incidents to the cylindrical body is very high.

The development of vortices, shed from the circular cylinder, is shown in Fig. 6. It is observed that, for a smooth cylinder at $t = 0.01$ s, there is no sign of separation or formation of the wake. However, the variation in velocity over the cylinder surface is visible from the contour plot. At $t = 0.5$ s, the attached separation bubble is visible for the smooth cylinder. It is interesting to note that for rough cylinder, at $t = 0.5$ s, the wake already started detaching. Maybe, due to an increase in surface roughness, the vortex shedding phenomenon accelerated. However, the reason behind the faster separation of wakes needs further investigation. At $t = 1.0$ s, the bubble increases its strength and size for the smooth cylinder. At $t = 1.5$ s, the separation bubble for the smooth cylinder starts oscillating. Consequently, at $t = 2.0$ s, the flow started to detach from the smooth cylinder. Reaching the flow time $t = 2.5$ s, the detachment and formation of wakes are clearly observed for both the smooth and rough cylinders.

When a streamline representation of flows over a smooth and a rough cylinder is observed (Fig. 7), we can see that there is a delay in the separation point of flow near the surface of the body in a rough cylinder compared to a smooth cylinder. This separation occurs due to huge momentum loss near the wall in the boundary layer moving downstream against an adverse pressure gradient. When roughness is

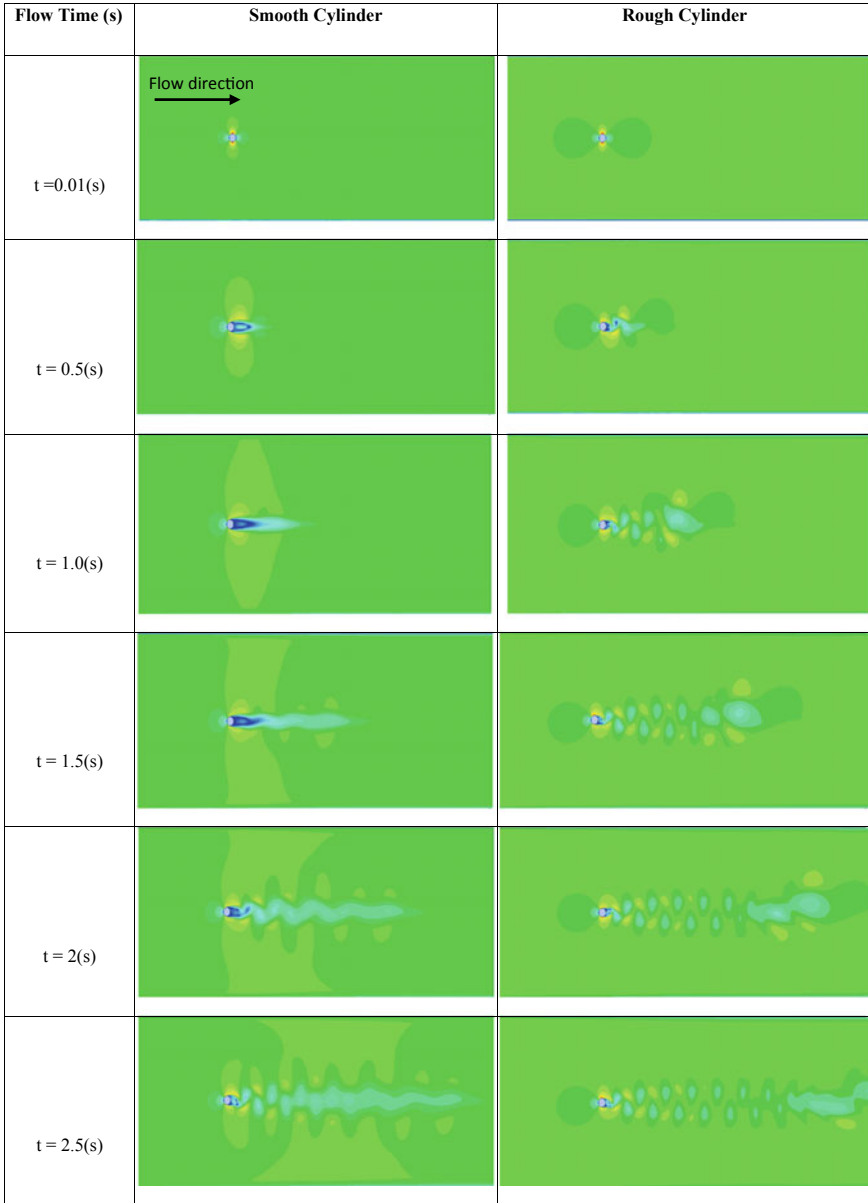
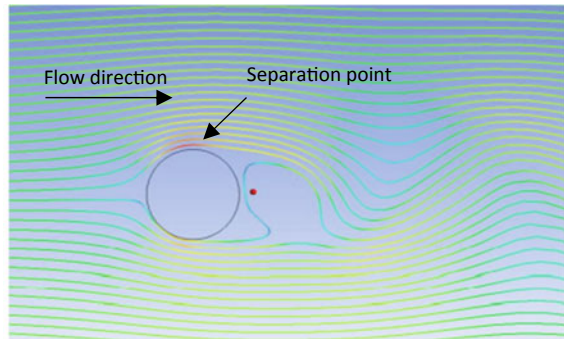


Fig. 6 Time resolved flow field for both smooth and rough cylinders

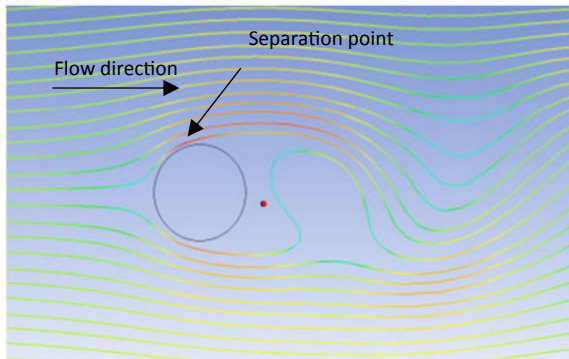
applied, the turbulent intensity increases which lead to rapid interaction between the near wall and freestream fluids. This essentially energizes the fluid particles near the wall. As a result, the resistance against flow separation increases. This leads to a delay in the separation point which thereby reduces the wake region and the pressure drag decreases. Also, it can be observed from Fig. 7 that the separation gets delayed for the rough cylinder when compared to the smooth cylinder. Since the energy added to the boundary layer fluid act as a resistance to flow separation, the separation gets delayed for the rough cylinder.

The results of the coefficient of drag (C_d) are taken for a smooth and a completely rough cylinder and compared with the results of Achenbach and Heinecke [3] and Shruthi et al. [4] as shown in Table 1. The result of the present numerical study is in good agreement with both Achenbach and Heinecke [3] and Shruthi et al. [4]. The coefficient of drag (C_d) decreases when the rough surface is introduced over the cylinder. This essentially indicates that the rough cylinder is very effective in reducing drag. Further, it can be observed that the roughness level significantly influences the coefficient of lift as there is a decrease in coefficient of lift for rough cylinder when compared it with smooth cylinder.

Fig. 7 Streamline representations of the flow field over a rough cylinder **a** smooth cylinder



(a)



(b)

In this investigation, simulations are conducted for cylinders with roughness strip of $k/D = 75 \times 10^{-5}$ at different angular locations (α) on the circumference of the cylinder. A graph is plotted for coefficient of drag (C_d) obtained from the numerical simulations for cylinder with rough strip at different angular locations (α), as shown in Fig. 8.

Besides, a graph is plotted for the coefficient of lift (C_l) obtained from numerical simulations for cylinders with the rough strip at different angular locations (α), as shown in Fig. 9.

Figures 8 and 9 show that the value of C_d and C_l is low when the rough strip is at location $\alpha = 37.5^\circ$ and then increases and reaches its highest value when the position

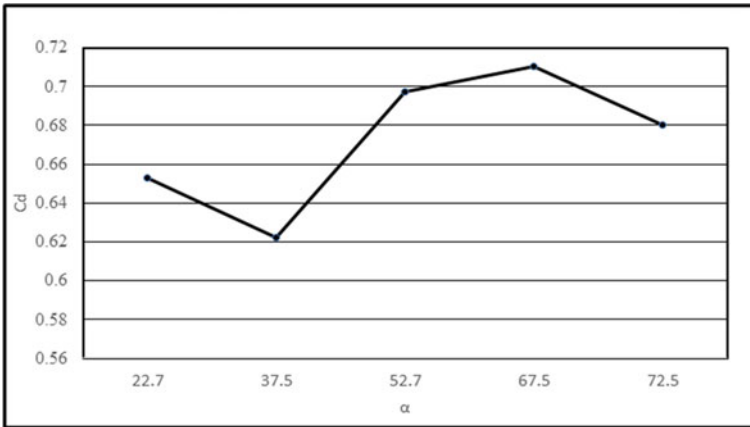


Fig. 8 Coefficient of drag (C_d) versus different angular locations (α) of rough strip

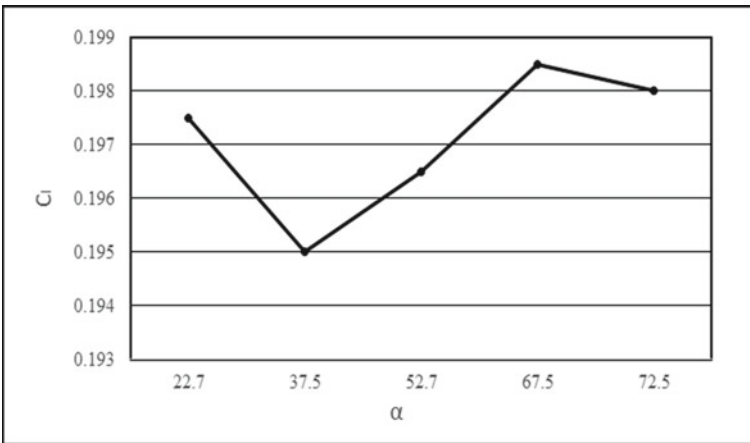


Fig. 9 Coefficient of lift (C_l) versus different angular locations (α) of rough strip

of the strip is at $\alpha = 67.5^\circ$. The plot for values of C_d and C_l falls after the strip angular position of $\alpha = 67.5^\circ$. From this observation, it can be noted that the ideal position of the rough strip is at $\alpha = 37.5^\circ$ as the values of C_d is minimum compared to other angular locations of the rough strip.

4 Conclusions

In this investigation, the flow over the circular cylinder is numerically analyzed using ANSYS Fluent when the cylinder is considered to be smooth, fully rough, and partially rough with a rough strip, added at different angular orientations over the cylinder surface, at a subcritical Reynolds number of 25,000 and velocity of the air at 36.7 m/s. The aerodynamic behavior such as the drag and lift force coefficients is analyzed with respect to the roughness location. From the results of the current investigation, it can be concluded that.

1. The rough cylinder is very effective in reducing drag when compared with the smooth cylinder.
2. There is a delay in the separation point when roughness is induced over the cylinder surface.
3. The time-resolved flow visualizations show the distinct flow development pattern for the smooth and the rough cylinder.
4. The roughness strip (extended for $\theta = 15^\circ$) shows superior effects at $\alpha = 37.5^\circ$ angular orientations since the coefficient of drag is minimum for that case.

References

1. Baines WD (1963) Effects of velocity distribution on wind loads and flow patterns on buildings. In: Proceedings of symposium, No. 16, wind effects on buildings and structures, vol. 1. NPL, UK, pp 197–225
2. Baetke F, Werner H (1990) Numerical simulation of turbulent flow over surface-mounted obstacles with sharp edges and corners. *J Wind Eng Ind Aerodyn* 35:129–214
3. Achenbach E, Heinecke E (1981) On vortex shedding from smooth and rough cylinders in the range of Reynolds numbers 6×10^3 to 5×10^6 . *J Fluid Mech* 109:239–251
4. Sivadas S, Kumar KA, Kumar RA (2019) Effect of selectively applied surface roughness and wake splitter plate on the aerodynamic characteristics of a circular cylinder. In: Saha P, Subbarao P, Sikarwar B (eds) *Advances in fluid and thermal engineering*. Lecture notes in mechanical engineering. Springer, Singapore, pp 697–705. https://doi.org/10.1007/978-981-13-6416-7_65
5. Vu HC, Ahn J, Hwang JH (2016) Numerical investigation of flow around circular cylinder with splitter plate. *KSCE J Civ Eng* 20:2559–2568
6. Pang LJ, Skote M, Lim SY (2016) Modeling high Re flow around a 2D cylindrical bluff body using the k- ϵ (SST) turbulence. *Prog Comput Fluid Dyn* 16:48–57

Chaotic Onset in the Flow Past a Flapping Foil Depends on the Free-Stream Reynolds Number



Sourav Dey, Dipanjan Majumdar, and Sunetra Sarkar

Abstract Dynamical route to chaos and the corresponding transitional onset is very crucial for the efficient design of flapping-based aerial and underwater vehicles. Different size, shape, and flight speed of the wide range of natural flyers/swimmers manifest different Reynolds numbers (Re). The present study investigates the effect of Re on the dynamical behaviour of the flow field past a plunging elliptic foil. Numerical simulations have been carried out using a discrete forcing immersed boundary method-based in-house flow solver. Different non-linear time series tools such as phase portrait and wavelet spectra have been employed to identify the dynamical characteristics of the flow field. Distinct difference is observed for the qualitative dynamics of the flow field at $Re = 100$ and $Re = 300$, though the dynamical plunge velocity (κh) was kept constant.

Keywords Flapping foil · Unsteady wake · Dynamical transition · Chaotic onset

1 Introduction

Natural flyers/swimmers use the flapping motion of their wings/fins to simultaneously generate the necessary lift and thrust to fly in the air or propel through the water. Wing motion consists of a complex combination of three different flapping motions i.e., plunging, pitching, and surging, where plunging is studied simultaneously in the literature. An elementary understanding of the flapping mechanism is not only a crucial research interest but also important for the efficient design of futuristic micro-aerial vehicles (MAV) and automotive underwater vehicles (AUV) [1]. The fluid forces (lift and drag) generated by a flapping foil and the corresponding wake pattern depend on the combined effect of kinematic parameters i.e., flapping frequency

S. Dey (✉) · D. Majumdar · S. Sarkar
Department of Aerospace Engineering, IIT Madras, Chennai 600036, India
e-mail: sourav585398@gmail.com

S. Sarkar
Complex System and Dynamics Group, IIT Madras, Chennai 600036, India

and amplitude, which can be better understood by the combined non-dimensional parameter, the dynamic plunge velocity, κh . Here, κ is the reduced frequency and h is the non-dimensional plunge amplitude. Depending on the parametric range, commonly three typical qualitative dynamical signatures are observed in the flow field of flapping foils.

In the first type, wake structure is periodic and undeflected, with the average wake velocity profile being parallel to a mean horizontal line. This type of wake has been observed at a low value of κh ($\kappa h < 1.0$) [2, 3]. The periodic wake pattern can further be of three subtypes namely, regular Kármán, reverse Kármán, and neutral wake [2, 3]. Depending upon the different combinations of κ and h value, a variety of vortex patterns such as 2P, P + S, 2P + S, and 2P + 2S have also been reported in literature [4], where P and S denote the vortex pair and single vortex, respectively, shed in one plunging cycle. As the κh value increases beyond 1.0, downstream wake deflects about the mean horizontal line but the periodicity of the wake is not affected [2, 3]. Jones et al. [2] reported that the wake behind a plunging airfoil deflects upward and downward for $\kappa h > 1$, showing a loss of symmetry but flow remains periodic. Similar deflected wake patterns for flapping foils are also reported by Godoy Diana et al. [5], Cleaver et al. [6], and Zheng and Wei [7].

Next, there exists a transition regime where the flow field behind a flapping foil gradually loses its periodicity and approaches towards aperiodicity and an irregular wake pattern. In this regime, the flow field becomes quasi-periodic [8–10] or exhibits sporadic chaotic bursts interspersed by windows of quasi-periodicity [11].

In the third category, at significantly high κh , periodic nature of the wake is completely lost and the flow field transitions into chaos. Lewin and Haj-Hariri [12] numerically showed that the vortex patterns and the aerodynamic forces can become aperiodic for a flow past plunging foil at $\kappa h = 1.5$. Similar aperiodic flow patterns behind plunging and pitching foils have been reported extensively in the literature [8–10, 13–17].

Dynamical route to aperiodicity or chaos and corresponding transitional onsets are crucial for the design of man-made flapping devices. Aerodynamic loads may get affected due to chaotic interaction of vortices behind the foil and become unpredictable in the long term. These chaotic loads can influence the motion of the body, which in turn become chaotic, posing difficulties to design suitable flapping devices. Thus, it is very crucial to have thorough knowledge about the transition onsets along the kinematic as well as geometric parameters. Earlier studies that discussed the dynamical route to chaos in the flow field of flapping foil mainly considered κh or Strouhal number (St) as the bifurcation parameter. Notable literature are by Vittori and Blondeaux [18], Blondeaux et al. [15], Ashraf et al. [14], Badrinath et al. [16], Bose and Sarkar [8], Majumdar et al. [9]. A quasi-periodic route to chaos was reported by Ashraf et al. [14], Bose and Sarkar [8], and Majumdar et al. [9]. The primary cause of this aperiodic transition is the aperiodic formation and growth of the primary leading-edge vortex (LEV) and its subsequent interaction with trailing-edge vortices (TEVs) through different vortex interaction mechanisms namely, merging, splitting, collision etc. Bose and Sarkar [8] presented a chaotic flow field at $\kappa h = 2.5$, for $Re = 1000$. Majumdar et al. [9] investigated the flow field dynamics of a plunging elliptic

foil and reported the chaotic onset to be at $kh = 1.9$ for $Re = 300$. An intermittency route to chaos for plunging airfoil was found by Badrinath et al. [16], who presented the chaotic flow field at $kh = 2.4$ for $Re = 1000$. Note that all the above-mentioned studies discussed the dynamical transition route and chaotic onset by varying the kinematic parameters keeping the flow Reynolds number to be fixed. However, the growth of the primary LEV and LEV–TEV interactions can get affected significantly by the free-stream Re , and therefore, the dynamical transition may get altered. It is an open question to test whether the chaotic onset reported earlier is independent of Reynolds number or not. To the best of the authors' knowledge, there is no such study that explores the effect of free-stream Reynolds number on dynamical transitional behaviour. The present study will take up this task in a systematic manner.

2 Methodology

A two-dimensional elliptic foil with thickness to chord ratio of 0.12 is considered here. Sinusoidal plunging motion is taken as the primary actuation for the foil. The kinematic equations, i.e. displacement and velocity of the foil, can be written in non-dimensional form as

$$\bar{y}_c(\bar{t}) = h \sin(\kappa\bar{t}), \quad \dot{\bar{y}}_c(\bar{t}) = \kappa h \cos(\kappa\bar{t}) \quad (1)$$

where, $h = (A/c)$ is non-dimensional plunge amplitude, $\kappa = 2\pi f_e c$ is reduced frequency, and $\bar{t} = tU_\infty/c$ is the non-dimensional time. U_∞ and c are the free-stream velocity and chord length of the foil, respectively. Unsteady flow past the plunging foil is considered as 2D laminar and governed by 2D incompressible Navier–Stokes (NS) equation which can be written in non-dimensional form as

$$\frac{\partial \bar{\mathbf{u}}}{\partial \bar{t}} + \nabla \cdot (\bar{\mathbf{u}}\bar{\mathbf{u}}) = -\nabla \bar{p} + \frac{1}{Re} \nabla^2 \bar{\mathbf{u}}, \quad (2)$$

$$\nabla \cdot (\bar{\mathbf{u}}) = 0 \quad (3)$$

Here, $\bar{\mathbf{u}} = \mathbf{u}/U_\infty$ is the non-dimensional flow velocity, $\bar{p} = p/\rho_f U_\infty^2$ is the non-dimensional pressure, and ρ_f is density of fluid. Re indicates the free-stream Reynolds number and defined as $Re = \rho_f U_\infty c/\mu$, μ being the viscosity of the fluid. Aerodynamic load coefficients are defined as

$$C_D = \frac{D}{\frac{1}{2}\rho_f U_\infty^2 c} \quad \text{and} \quad C_L = \frac{L}{\frac{1}{2}\rho_f U_\infty^2 c} \quad (4)$$

where, D is the drag force (taken positive along positive x -axis) and L is the lift force (taken positive along the y -axis). The flow equation is solved using an in-house solver based on discrete forcing immersed boundary method (IBM). The NS equations are

solved on a background Eulerian mesh taking primary flow variables (u, v, p) on staggered arrangement, whereas the location of the plunging foil is tracked by a finite number of Lagrangian markers. A forcing term called ‘momentum forcing’ is added in momentum conservation equation. This forcing rebuilds the velocity field at all grid point inside the solid domain in such a way that the no-slip/no-penetration boundary condition is satisfied exactly at the solid boundary. Also, a source/sink term is incorporated in the continuity equation to confirm mass conservation across the immersed boundary. A finite volume based semi-implicit fractional step method is applied for time advancement. The convection and diffusion terms are discretized using Adams–Bashforth and Crank–Nicolson techniques, respectively. Further details of the in-house IBM flow solver can be found in our previous study [9]. A schematic diagram of the computational domain and the structured non-uniform Cartesian mesh used in this study are shown in Figs. 1 and 2, respectively. A uniform grid with size $\Delta x \times \Delta y$ is taken in the body movement zone. Grid spacing is increased gradually towards the outer boundaries following a geometric progression. Boundary conditions used in this study are as follows: uniform constant velocity ($u = 1, v = 0$) at inlet, convective flow boundary ($\frac{\partial u}{\partial t} + u_s \frac{\partial u}{\partial x} = 0$) condition at outlet, and slip boundary condition ($\frac{\partial u}{\partial y} = 0, v = 0$) at top and bottom surface. The size of the computational domain has been taken as $[-10c, 25c] \times [-12.5c, 12.5c]$. The grid size in the uniform region is considered as $\Delta x = \Delta y = 0.004$. A time-step size of $\Delta t = 0.0001$ has been taken for all the simulation. Note that these computational domain, mesh, and time-step sizes are selected after performing appropriate convergence tests. Details of these convergence results were already presented in an earlier work [9] by our group, and, therefore, not repeated here only for the sake of brevity. Moreover, a thorough validation of the current IBM solver can be found in [9].

Fig. 1 Computational domain

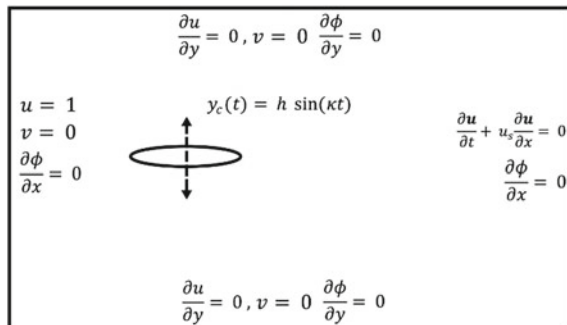
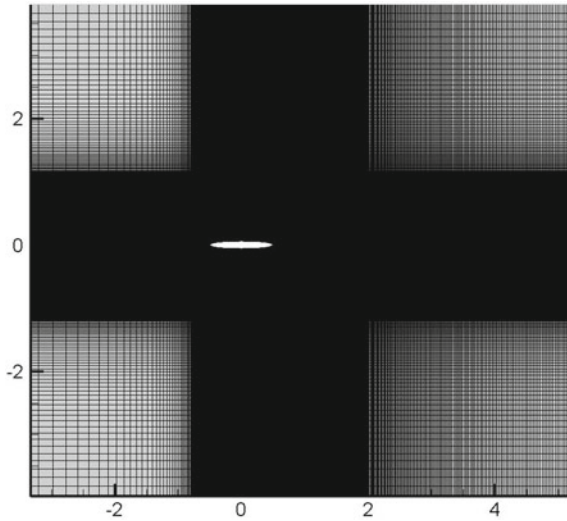


Fig. 2 Zoomed view of mesh near the body



3 Results and Discussion

The unsteady flow around the plunging foil has been simulated at $\kappa h = 1.9$, keeping κ as constant at 4.0. Two different Reynolds numbers, $Re = 100$ and 300, are taken into consideration to study the effects of Re on the chaotic onset, i.e. if the chaotic onset along κh remains the same for different Re . Vorticity contour of the flow field and aerodynamic load coefficients are analysed to investigate the aperiodicity of the wake. To conclusively characterize different dynamical states based on the dynamical systems theory, several non-linear time series analysis tools such as phase portrait [19], fast Fourier transform (FFT), and Morlet wavelet transform [20] are employed. Advantage of these tools over the classical chaos theory-based measures (such as largest Lyapunov exponent, correlation dimension) is that these can identify the nature of dynamics conclusively even with a shorter length of the time history data.

3.1 Chaotic Signature at $Re = 300$

Figure 3 represents the time history of drag coefficient at $\kappa h = 1.9$, and it shows an irregular aperiodic behaviour. C_L-C_D phase portrait shown in Fig. 4 depicts an unorganised phase space trajectory with long-term unpredictability, which confirms the dynamical behaviour as chaos. The FFT of C_D time history shows the presence of a broad banded frequencies spectra of multiple dominant peaks in the signal (Fig. 5), further establishing chaos. Moreover, the Morlet wavelet transform of C_D also shows multiple scattered frequency bands in the time–frequency scalogram plot (Fig. 6),

confirming the existence of chaos. A similar chaotic transition was also presented in an earlier study by our group [9] at $Re = 300$. The authors reported $k\hbar = 1.9$ to be the chaotic onset at $Re = 300$.

The flow field behaviour during this chaotic transition is presented in terms of the phase average vorticity plots [21], along with the quantitative values of the average correlation (ρ) of the vorticity field [9]. ρ is calculated as an average of the correlation values of last 20 flapping cycles. The phase average vorticity contour is obtained using the same number of flapping cycles as well. Figure 7 displays a completely blurry image of the average vorticity contour accompanied by $\rho = 0.11$. This indicates that

Fig. 3 Drag coefficient C_D at $Re = 300$

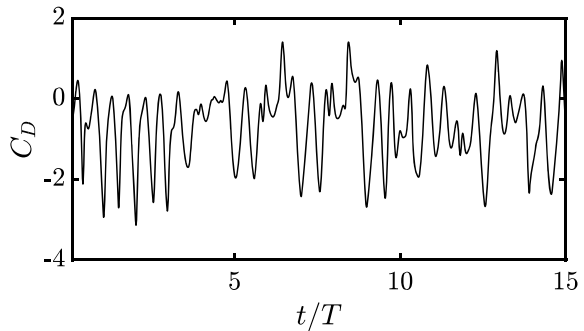


Fig. 4 Phase portrait at $Re = 300$

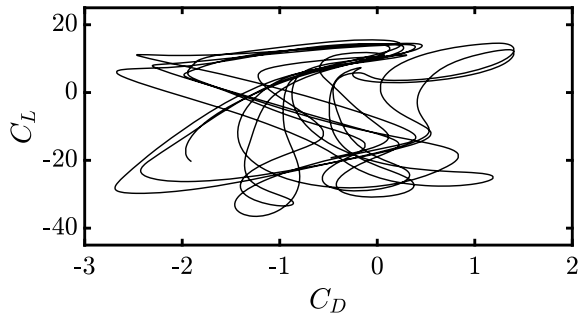


Fig. 5 Fourier spectrum of C_D at $Re = 300$

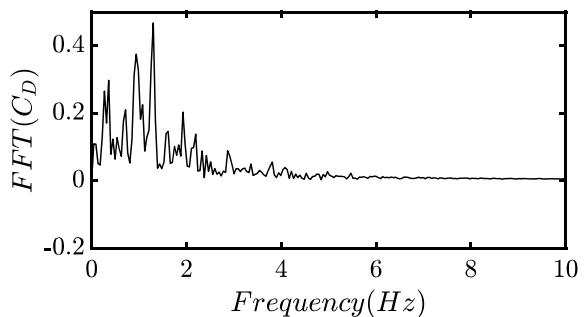


Fig. 6 Morlet wavelet transform of C_D at $Re = 300$

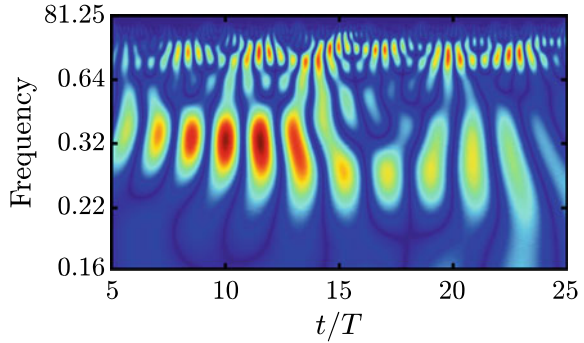
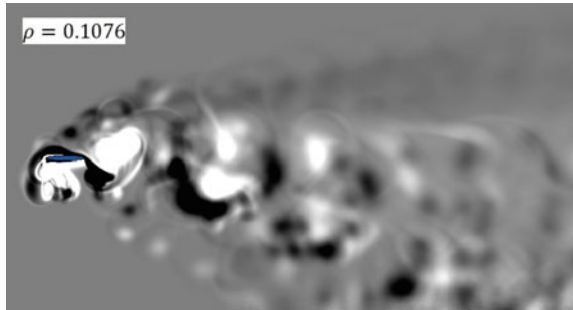


Fig. 7 Phase average vorticity contour at $kh = 1.9$ for $Re = 300$



there is almost no correlation between the flow fields at different cycles during chaos, and the long-term flow behaviour is unpredictable.

3.2 Periodic Flow Field Behaviour at $Re = 100$

Figures 8 and 9 depict the C_D time history and the C_L-C_D phase portrait at $kh = 1.9$ and $Re = 100$, respectively. The time evolution of C_D exhibits a periodic signature, and the C_L-C_D trajectory repeats on a close loop pattern. Fourier spectra of C_D in Fig. 10 also represents a periodic dynamics with a dominant frequency peak at the double of the plunging frequency and the other peaks being the sub- and super-harmonics. Morlet wave transform of C_D also confirms the periodic dynamics (Fig. 11), where the scalogram shows an organised pattern of two narrow frequency bands corresponding to the dominant peaks observed in the FFT plot (Fig. 10). As the flow field during periodicity repeats exactly in consecutive cycles, the phase average vorticity contour gives a prominent and crisp image of the organized downward deflected wake pattern at $Re = 100$ (Fig. 12). The corresponding average correlation of the vorticity field takes a value close to unity ($\rho = 0.98$) which signifies the flow fields in different cycles are correlated with each other and repeats quite closely. So,

it is observed that the dynamical signature of the flow field around a flapping foil can vary with Re , despite the non-dimensional plunge velocity is kept fixed. At $Re = 300$, the trailing wake became chaotic at $kh = 1.9$, but at $Re = 100$, it is still in the periodic regime. This indicates that the chaotic transition onset may have been delayed significantly for $Re = 100$. This can be attributed to the stronger viscous effects at the lower Re where the vortices are more stable and do not undergo complex interaction. As a result, any disturbance in the flow field eventually gets dissipated and the flow becomes regular, thus delaying the chaos. The findings of the current investigation clearly establish the dependence of chaotic transitional onsets on the free-stream Reynolds number.

Fig. 8 Drag coefficient C_D at $Re = 100$

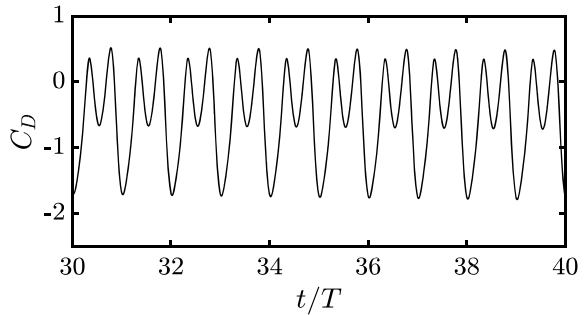


Fig. 9 Phase portrait at $Re = 100$

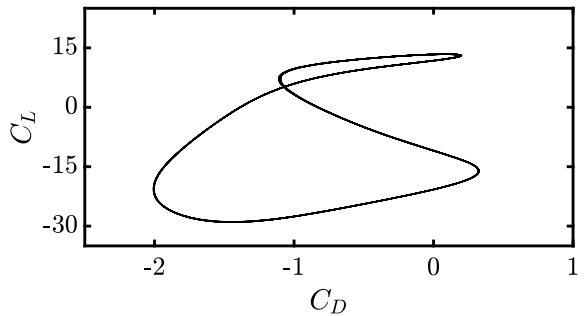


Fig. 10 Fourier spectrum of C_D at $Re = 100$

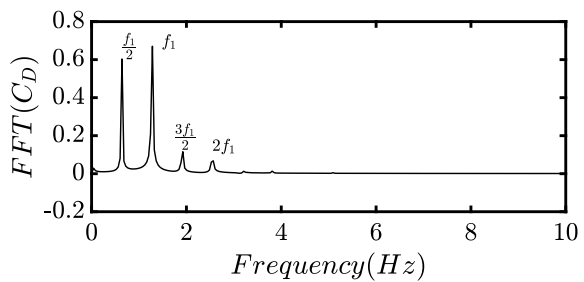


Fig. 11 Morlet wavelet transform of C_D at $Re = 100$

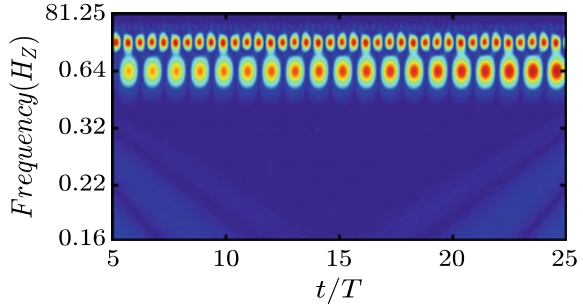
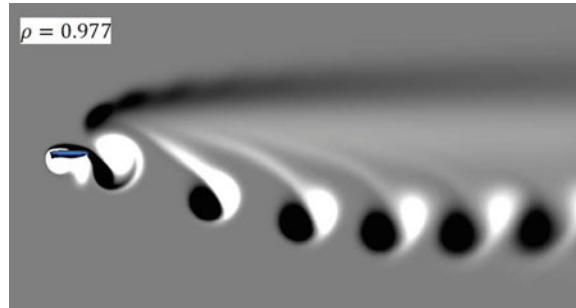


Fig. 12 Phase average vorticity contour at $kh = 1.9$ for $Re = 100$



4 Conclusions

Effect of Reynolds number on dynamical and flow behaviour of a flow past a harmonically plunging elliptic airfoil has been investigated using a discrete forcing immersed boundary method-based in-house flow solver. The dynamical behaviour of the wake changes with Re indicating a definite dependence on Reynolds number. At lower Re value ($Re = 100$), flow field represents a periodic wake pattern resulting in periodic aerodynamic forces even at high ranges of $kh = 1.9$, whereas a clear signature of chaotic wake has been confirmed for $Re = 300$. This clearly signifies that the chaotic transition onset may get delayed substantially for lower Re , and the reason behind it is the consistent dominance of viscous force over inertia at lower Re . Due to strong viscous effects, vortices behind the foil are more stable and unable to do complex vortex interaction (e.g., merging, splitting, and collision), which are otherwise the key mechanism behind triggering chaos and sustaining it [8, 9, 16]. Therefore, in the absence of any significant disturbances, the flow field gradually becomes regular and periodic, thus delaying chaos. The results of current study demonstrate unambiguously the dependence of chaotic transitional onsets on the free-stream Reynolds number.

Acknowledgements We would like to extend our gratitude to the HPCE Team, P.G. Senapathy, Center for Computing Resources of IIT Madras, for providing the computational resources.

References

1. Shyy W, Aono H, Chimakurthi SK, Trizila P, Kang CK, Cesnik CES, Liu H (2010) Recent progress in flapping wing aerodynamics and aeroelasticity. *Prog Aerosp Sci* 46(7):284–327
2. Jones KD, Dohring CM, Platzer MF (1998) Experimental and computational investigation of the knoller-betz effect. *AIAA J* 36(7):1240–1246
3. Lai JCS, Platzer MF (1999) Jet characteristics of a plunging airfoil. *AIAA J* 37(12):1529–1537
4. Schnipper T (2010) Exotic wakes of flapping fins., Ph.D. thesis, Department of Physics, Technical University of Denmark
5. Godoy-Diana R, Aider JL, Wesfreid JE (2008) Transitions in the wake of a flapping foil. *Phys Rev E* 77(1):016308
6. Cleaver DJ, Wang Z, Gursul I (2012) Bifurcating flows of plunging aerofoils at high Strouhal numbers. *J Fluid Mech* 708:349–376
7. Zheng ZC, Wei Z (2012) Study of mechanisms and factors that influence the formation of vortical wake of a heaving airfoil. *Phys Fluids* 24(10):103601
8. Bose C, Sarkar S (2018) Investigating chaotic wake dynamics past a flapping airfoil and the role of vortex interactions behind the chaotic transition. *Phys Fluids* 30(4):047101, 1–27
9. Majumdar D, Bose C, Sarkar S (2020) Capturing the dynamical transitions in the flow-field of a flapping foil using immersed boundary method. *J Fluids Struct* 95(102999):1–33
10. Majumdar D, Bose C, Sarkar S (2022) Transition boundaries and an order-to-chaos map for the flow field past a flapping foil. *J Fluid Mech* 942(A40):1–32
11. Bose C, Gupta S, Sarkar S (2021) Dynamic interlinking between near and far-field wakes behind a pitching heaving airfoil. *J Fluid Mech* 911(A31):1–36
12. Lewin GC, Haj-Hariri H (2003) Modelling thrust generation of a two-dimensional heaving airfoil in a viscous flow. *J Fluid Mech* 492:339–362
13. Lentink D, Muijres FT, Donker-Duyvis FJ, Van Leeuwen JL (2008) Vortex-wake interactions of a flapping foil that models animal swimming and flight. *J Exp Biol* 211(2):267–273
14. Ashraf MA, Young J, Lai JCS (2012) Oscillation frequency and amplitude effects on plunging airfoil propulsion and flow periodicity. *AIAA J* 50(11):2308–2324
15. Blondeaux P, Guglielmini L, Triantafyllou MS (2005) Chaotic flow generated by an oscillating foil. *AIAA J* 43(4):918–921
16. Badrinath S, Bose C, Sarkar S (2017) Identifying the route to chaos in the flow past a flapping airfoil. *Euro J Mech B/Fluids* 66:38–59
17. Khalid MSU, Akhtar I, Dong H, Ahsan N, Jiang X, Wu B (2018) Bifurcations and route to chaos for flow over an oscillating airfoil. *J Fluids Struct* 80:262–274
18. Vittori G, Blondeaux P (1993) Quasiperiodicity and phase locking route to chaos in the 2-d oscillatory flow around a circular cylinder. *Phys Fluids A* 5(8):1866–1868
19. Hilborn RC et al (2000) *Chaos and nonlinear dynamics: an introduction for scientists and engineers*. Oxford University Press, New York, USA
20. Grossmann A, Kronland-Martinet R, Morlet J (1990) *Reading and understanding continuous wavelet transforms*. Springer, Wavelets
21. Lentink D, Van Heijst GF, Muijres FT, Van Leeuwen JL (2010) Vortex interactions with flapping wings and fins can be unpredictable. *Biol Lett* 6(3):394–397

Wake Interactions Around a Pair of Porous Cylinders in a Side-By-Side Arrangement in Channel Flow



Saqib Jamshed and Amit Dhiman

Abstract In this study, we have investigated the flow around two side-by-side porous cylinders in a confined channel. The study reports various flow patterns as well as an absolute suppression of the vortex-shedding process at high permeability levels. An unsteady flow at Reynolds number $Re = 150$ at two different parameters, Darcy number (Da) and gap ratios (s/d) for the ranges of $Da = 10^{-6} - 10^{-2}$ and $s/d = 1.5 - 6$, is found to exhibit asymmetric flip-flop and synchronized anti-phase wake patterns. A jet-like flow in the vicinity of cylinders, mainly on the gap side, controls the wake patterns. A jump in the flow characteristics in the intermediate range of Darcy number is also explained by means of backflow phenomena. The velocity profiles on the freestream sides, the gap side, and the surface pressure distribution curve are discussed to give insight into the formation and suppression of wakes. The effects of gap ratios and Darcy number on the drag coefficient are also examined.

Keywords Darcy number · Porous cylinders · Gap ratio and wake patterns

Nomenclature

d	Diameter of the porous cylinder
d_p	Diameter of the particle constituting the porous body
C_D	Drag coefficient
C_p	Pressure coefficient
C_F	Forchheimer coefficient
Re	Reynolds number
Da	Darcy number
u	X-component velocity

S. Jamshed (✉) · A. Dhiman
Department of Chemical Engineering, IIT Roorkee, Roorkee, Uttarakhand 247667, India
e-mail: sjamshed@ch.iitr.ac.in

A. Dhiman
e-mail: amit.dhiman@ch.iitr.ac.in

v	Y-component velocity
U	Velocity magnitude
ε	Porosity
κ	Permeability
ρ	Density
μ	Dynamic viscosity

1 Introduction

Flow past a single porous cylinder or multiple ones generate various flow patterns, and it is more intriguing to understand the complex physics behind it [1–3]. Permeable cylinders are used to improve the physical interaction between the fluid and solid surfaces and to control the flow behavior by modifying the permeability level [3]. At low permeability, both inertial and viscous resistances work together and generate vorticity due to flow instability [4]. On the contrary, more fluid oozes through the cylinder at higher permeability (κ) and porosity (ε), which in turn suppresses the flow instabilities. Flow control and noise reduction using some passive control techniques, such as flow past permeable bodies, have gained much attention recently. Some experimental investigations [5–9] have been performed to facilitate the investigators with some facts and guidelines to empirically test the theory of porous media in practical applications; however, this area of research demands more manifestation.

Permeable bodies are mainly employed for better interaction of fluid with solid surfaces and to control the flow using some highly porous material considering the fact that a large amount of fluid permeates through the body carrying off the suppression of flow instabilities which is a primary concern in the design of constricted structure such as cooling tower, bridge pilings, electronic cooling system, porous bioreactors, and aeroacoustic noise control devices [1, 10]. There are many investigations dealing with the flow around a single permeable cylinder of various shapes [1, 11–17]. At a low Darcy number ($Da \leq 10^{-6}$), a very less amount of fluid passes through the body, and hence, the cylinder behaves like a solid cylinder [1, 11]. But at a higher Darcy number, fluid follows the tortuous path of the porous cylinder resulting in the reduction of forces and wake length [3, 11]. Bhattacharyya et al. [11] reported that the drag ratio (the ratio of the drag value of the porous cylinder to that of the solid cylinder of the same dimension) was found to be approaching zero from unity as Da is increased from a low to a high value (10^{-6} to 1.5). Although, a jump in the flow characteristics has been reported by Anirudh and Dhinakaran [1], for the intermediate range of Darcy number.

Flow past two cylinders in side-by-side configuration demonstrate rich flow dynamics and complex physics despite basic configuration. The proximity of cylinders affects the flow parameters, force coefficients, noise generation, and vibration. Flow study around a pair of cylinders has been published by many researchers [18–23], but the flow behavior around multiple porous cylinders is still unexplored. The

work of Jamshed and Dhiman [3] is the latest to date in which they studied flow around two side-by-side porous square cylinders. Therefore, in this study, the authors are of the view of obtaining the details of the flow mechanism and the dependency of the design parameters for two side-by-side circular porous cylinders.

2 Problem Statement and Related Equations

In this present study, flow past a pair of porous cylinders in a side-by-side configuration kept within 11.11% transverse wall confinement is shown schematically in Fig. 1. The height of the computational domain is 18 times the diameter of the circular cylinder (d), as per the previous studies [3, 18, 19, 21]. The domain-independent tests are performed, and the optimum upstream and downstream lengths are found to be $15d$ and $50d$, respectively. The optimal grid cell size of $0.01d$ is finalized on each cylinder. The computational domain is divided into the porous zone and the clear fluid non-porous zone. These zones are governed using the Darcy–Brinkman–Forchheimer model and Navier–Stokes equations [1, 3]. Also, the porous zones are supposed to be saturated with the same flowing fluid [1, 3, 16]. The inlet is assumed to be a fully developed laminar flow, and a constant mass flux condition is assumed at the outlet boundary. No-slip boundary condition is imposed on the confined walls existing in the domain. The following sets of 2-D equations are used in the present study:

Momentum equations for the clear fluid domain:

$$\rho \left(\frac{\partial u}{\partial t} + v \frac{\partial u}{\partial Y} + u \frac{\partial u}{\partial X} \right) = -\frac{\partial p}{\partial X} + \mu \left(\frac{\partial^2 u}{\partial Y^2} + \frac{\partial^2 u}{\partial X^2} \right) \quad (1)$$

$$\rho \left(\frac{\partial v}{\partial t} + v \frac{\partial v}{\partial Y} + u \frac{\partial v}{\partial X} \right) = -\frac{\partial p}{\partial Y} + \mu \left(\frac{\partial^2 v}{\partial Y^2} + \frac{\partial^2 v}{\partial X^2} \right) \quad (2)$$

Momentum equations for the porous zone:

$$\begin{aligned} & \frac{\rho}{\varepsilon^2} \left(\varepsilon \frac{\partial u}{\partial t} + v \frac{\partial u}{\partial Y} + u \frac{\partial u}{\partial X} \right) \\ & = -\frac{\partial p}{\partial X} + \frac{\mu}{\varepsilon} \left(\frac{\partial^2 u}{\partial Y^2} + \frac{\partial^2 u}{\partial X^2} \right) - \frac{\mu}{\kappa} u - \frac{\rho C_F}{\sqrt{\kappa}} |\bar{U}| u \end{aligned} \quad (3)$$

$$\begin{aligned} & \frac{\rho}{\varepsilon^2} \left(\varepsilon \frac{\partial v}{\partial t} + v \frac{\partial v}{\partial Y} + u \frac{\partial v}{\partial X} \right) \\ & = -\frac{\partial p}{\partial Y} + \frac{\mu}{\varepsilon} \left(\frac{\partial^2 v}{\partial Y^2} + \frac{\partial^2 v}{\partial X^2} \right) - \frac{\mu}{\kappa} v - \frac{\rho C_F}{\sqrt{\kappa}} |\bar{U}| v \end{aligned} \quad (4)$$

The porosity (ε) and permeability (κ) are related through Kozeny–Carman equation [1, 4]:

$$\kappa = \frac{1}{180} \frac{\varepsilon^3 d_p^2}{(1 - \varepsilon)^2} \tag{5}$$

To maintain uniformity throughout the work, the non-dimensional size of dp/d is kept constant at 0.01 [1, 3].

The mesh was generated in Workbench tool and solved for the above governing equations with the boundary conditions given in [24]. By using QUICK and Green-Gauss node-based scheme, the connective terms of momentum equation and gradient were discretized. Coupling of pressure–velocity was done by employing a SIMPLE scheme, and the unsteadiness during transition is taken care of with a second-order implicit approach.

3 Results and Discussion

The numerical methodology adopted in the present study is thoroughly validated first with a single porous cylinder at $Da = 2.5 \times 10^{-3}$ and compared with the results of Bhattacharya et al. [11] and the results match with a maximum of 1.67% deviation, as reported in our previous study [24]. The values of drag coefficient (C_D) stay well within 1.5% of the values determined by Chaitanya and Dhiman [25], and Kang [23] in their investigation of flow past a pair of side-by-side circular cylinders in an unconfined domain with forced convection (Fig. 1).

The simulation results of all the cases are reported following the initial transient condition being enabled to settle down, and every unsteady case is run for at least $t = 150$ s flow time. It should be noted that the Reynolds number is based on the maximum

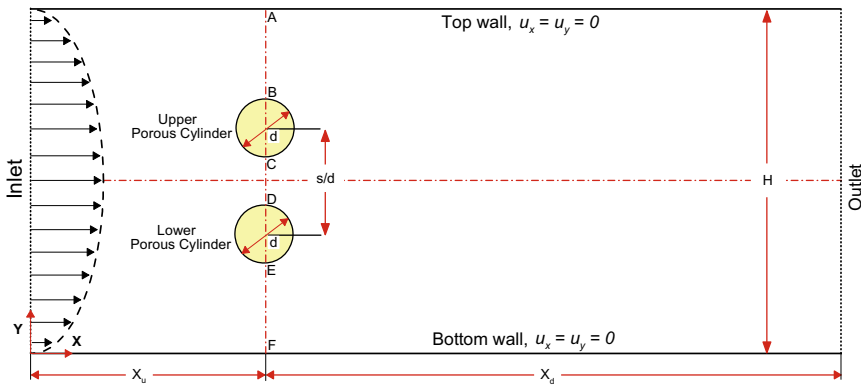


Fig. 1 Schematic of a pair of side-by-side porous cylinders in a confined domain

inlet velocity [3]. The effect of Reynolds number has been investigated in our previous study [24]. Here, the results are reported at $Re = 150$, which sufficiently surpasses the critical Reynolds number (for the transition from steady to the unsteady regime) and is reasonably small to dodge any three-dimensional effects. Flow patterns for $Re = 150$ at various permeability levels for all gap spacing are depicted in Fig. 2. The plots of flow patterns in Fig. 2 show that both asymmetric flip-flops as well as synchronized flow patterns are found. The unsteadiness in the flow appears due to jet-like flow in the gap of cylinders. The shedding process is completely suppressed as permeability is raised up to $Da = 10^{-2}$; however, a special case of $Da = 10^{-3}$ is discussed here because a jump in the flow characteristics can be seen here. Asymmetric pattern with flip-flopping mode is observed for $s/d = 1.5$, and synchronized anti-phase modes are observed for $s/d = 3.5$ and 6. Similar findings of synchronized vortex shedding are recoded in previous investigation [23] that for all $s/d \geq 2.5$, side-by-side circular cylinders exhibit an anti-phase mode. Further increase in $Da > 10^{-3}$ delays the vortex-shedding process and ultimately suppresses at for $Da = 10^{-2}$, and the contours of vorticity are clustered and elongated toward the centerline (Fig. 2c, f, i).

The formation and suppression of the vorticity can also be explained with the help of velocity profile. Figure 3 illustrates the mean x-velocity in the gap side and freestream sides of the cylinder (zoomed view of velocity profile for case of $s/d = 1.5$ is also shown to get a clear picture of the gap velocity). A nonzero velocity, i.e., the slip velocity, exists at the porous surface. This slip velocity is responsible for delaying the flow separation from the surface and ultimately preventing the vortex generation [17]. A jet-type velocity profile is developed in the gap side for $s/d > 1.5$, and subsequently, the mean velocity becomes constant at the center with increasing gap implying the

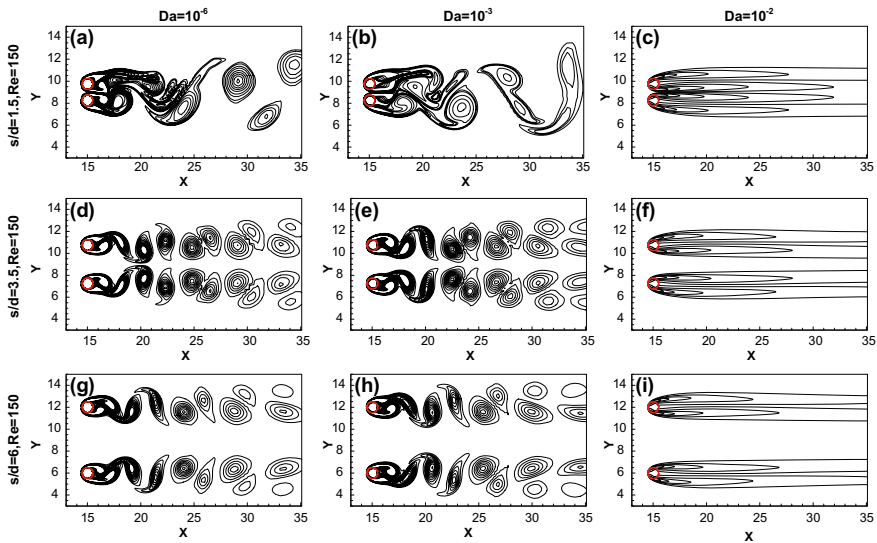


Fig. 2 Contours of instantaneous velocity fields for different Da for all s/d

termination of interplay between the two cylinders. It is also noticeable that the gap side mean velocity predominates the freestream side velocity for both extreme values of Da , signifying a higher shear rate in the gap side, and this anomaly can support the formation of bigger vorticity strands in the gap side at $Da = 10^{-2}$.

Porous cylinders offer flow resistance because of the viscous and inertial forces [1, 3]. By changing the porosity of the body, one can change the drag forces accordingly. At low Darcy number ($Da = 10^{-6}$), the body acts like a solid body and receives high shear stress while obstructing the flow, and the fluid tends to recirculate near the cylinder. At a high Darcy number ($Da = 10^{-2}$), fluid permeates through the cylinder, causing low pressure and low velocity gradient across the cylinders (as discussed earlier for the velocity profile). The variation of C_D with Re is shown in Fig. 4 at different Darcy numbers. The impact of one cylinder on the other can also be seen in the figure. Drag values first increase up to $s/d = 3.5$, then started to decrease for $s/d > 3.5$, and this can further be explained with the aid of pressure coefficient plots. Agarwal et al. [18] suggested that the cylinders kept in proximity experience larger pressure because there exists a repulsive force in the gap between the cylinders. For all gap ratios, there is an increase in drag values on increasing permeability ($Da = 10^{-4}$ - 10^{-3}), and this jump in C_D is attributed to the surface roughness [26] or the backflow inside the rear side of the porous body [27].

The variation of pressure distribution from the front stagnant point to the rear stagnant point along the gap side of the upper cylinder is depicted in Fig. 5. There is an increase in C_p value for all gap ratios and Darcy numbers in between 90° and 180° , due to the formation of recirculating wake behind the cylinder. The oscillatory pattern of C_p flattens as the permeability level is increased from $Da = 10^{-4}$ to $Da = 10^{-2}$. From the figure, it is evident that stagnation pressure at the porous cylinder is less because of the nonzero slip velocity on the porous surface. Also, the local minima in the pressure distribution curves are not observed for high permeability levels which are normally witnessed for solid cylinders.

Strouhal number St is often used to describe the frequency of vortex shedding in unsteady conditions, as shown in Fig. 6. Here, it also witnessed a slight increase in vortex frequency for Darcy number, which should have been reduced. In the flow control techniques, where the primary objective is the minimization of flow fluctuation, this increase in shedding frequency at $Da = 10^{-3}$ is undesirable. To maintain flow stabilization, larger permeability levels ($10^{-3} < Da < 10^{-2}$) were suggested by Anirudh and Dhinakaran [1]. The value of St drops with an increase in transverse spacing because a stronger flow that is present in the gap side causes an increase in shedding frequency, as explained earlier.

4 Conclusions

“The present case study attempts the flow around two identical side-by-side porous cylinders placed in a fully developed laminar flow using the Darcy–Brinkman–Forchheimer extended model. The effects of the control parameters, such as Darcy number

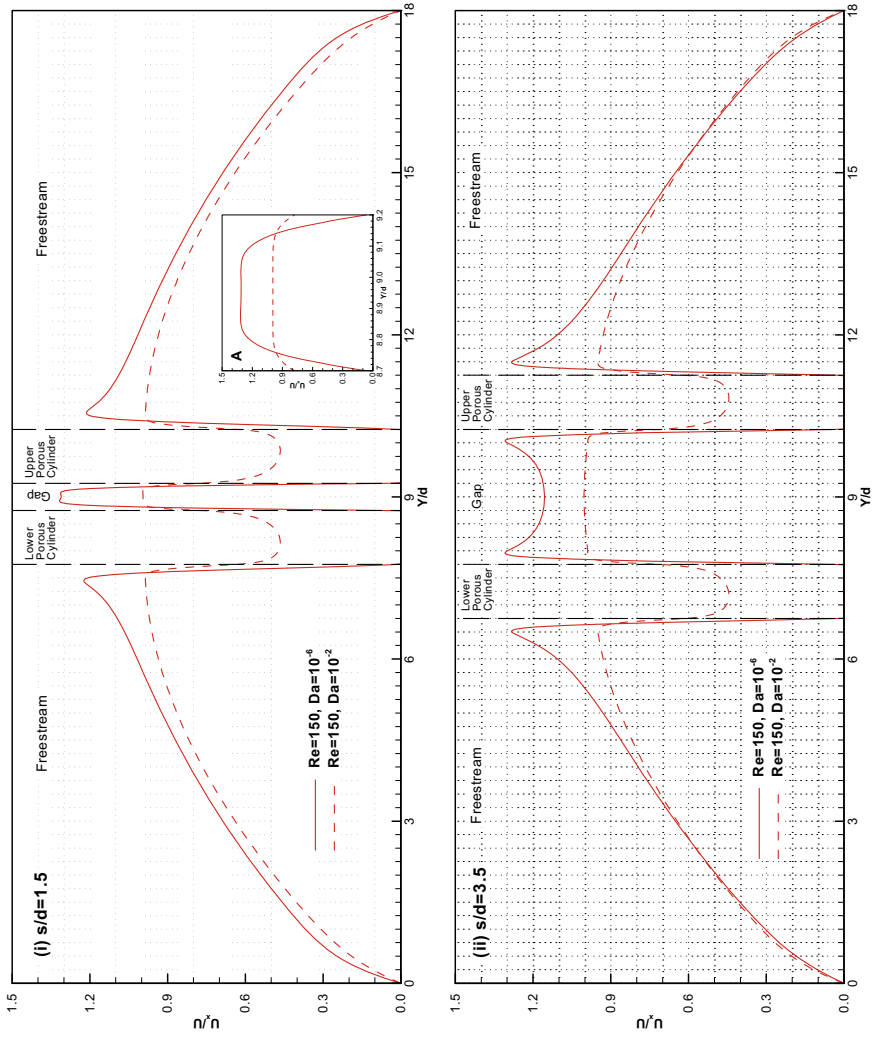
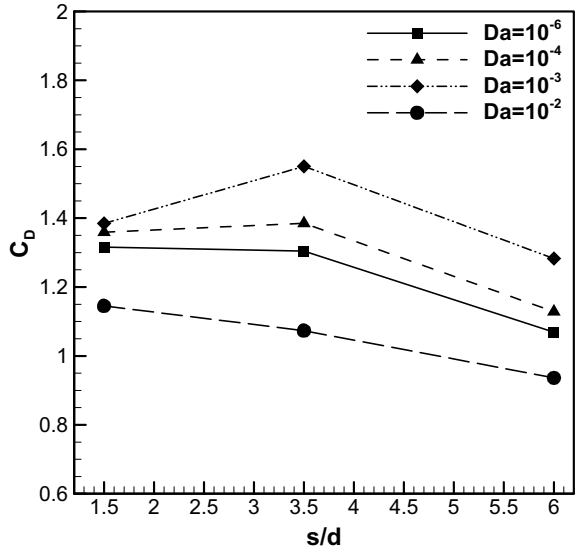


Fig. 3 Mean velocity in the gap and freestream at two extreme values of Da for (i) $s/d = 1.5$ and (ii) $s/d = 3.5$ (with zoom view of gap velocity profile for $s/d = 1.5$)

Fig. 4 Variation in C_D with Da for different s/d



and gap ratios, are studied, and the different flow patterns have been discussed. It was conferred from the mean velocity profile for the gap side and freestream side that there exists a slip velocity at the porous surface; thus, at high permeability, this slip velocity is mainly responsible for the delayed onset of flow separation and vortex formation. A jump in C_D values is observed for the mid-range of Darcy numbers, and this anomaly is conceivably caused by the increase in surface roughness [26] or the backflow in the rear side of the porous cylinder [27]. This property can be practiced where materials of light weight and strength are in demand. From this investigation, it can also be inferred that the porous bodies can be used to regulate the vibration and redundant flow characteristics by manipulating the permeability.”

Fig. 5 Pressure coefficient C_p of upper cylinder for different Da and s/d

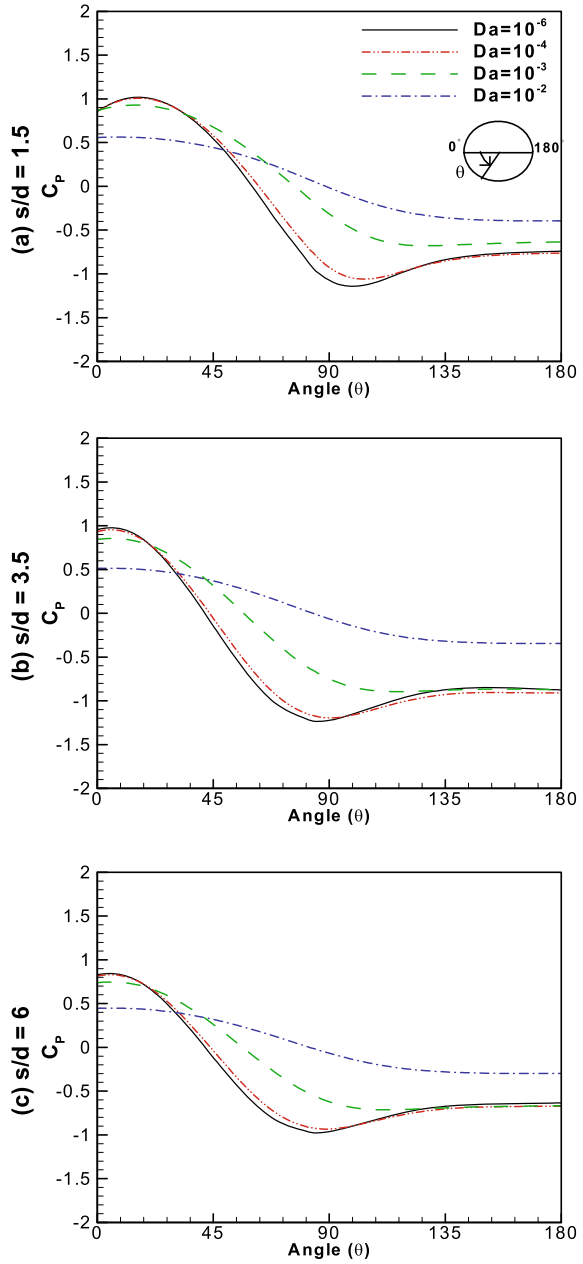
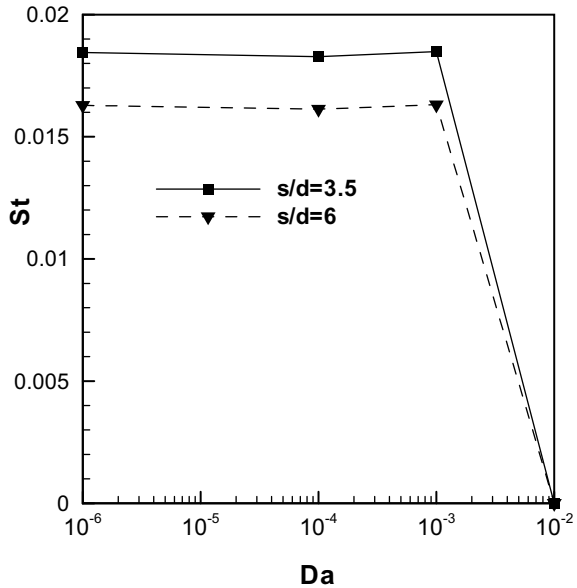


Fig. 6 Strouhal number St at different Da for $s/d = 3.5$ and $s/d = 6$



References

1. K Anirudh S Dhinakaran 2018 On the onset of vortex shedding past a two-dimensional porous square cylinder *J Wind Eng Ind Aerodyn* 179 200 214
2. HW Wu RH Wang 2010 Convective heat transfer over a heated square porous cylinder in a channel *Int J Heat Mass Transf* 53 9–10 1927 1937
3. S Jamshed A Dhiman 2021 Channel-confined wake structure interactions between two permeable side-by-side bars of a square cross-section *J Fluids Eng* 143 9 1 14
4. S Dhinakaran J Ponmozhi 2011 Heat transfer from a permeable square cylinder to a flowing fluid *Energy Convers Manag* 52 5 2170 2182
5. S Camarri BEG Fallenius JHM Fransson 2013 Stability analysis of experimental flow fields behind a porous cylinder for the investigation of the large-scale wake vortices *J Fluid Mech* 715 499 536
6. K Klausmann B Ruck 2017 Drag reduction of circular cylinders by porous coating on the leeward side *J Fluid Mech* 813 382 411
7. T Sueki T Takaishi M Ikeda N Arai 2010 Application of porous material to reduce aerodynamic sound from bluff bodies *Fluid Dyn Res* 42 1 015004
8. PD Noymer LR Glicksman A Devendran 1998 Drag on a permeable cylinder in steady flow at moderate Reynolds numbers *Chem Eng Sci* 53 16 2859 2869
9. Zhao F, Kinoshita T, Bao W, Itakura H (2009) Theoretical and experimental study on a porous cylinder floating in waves. *J Offshore Mech Arct Eng* 4(PART B):1261–1268
10. PG Ledda L Siconolfi F Viola F Gallaire S Camarri 2018 Suppression of von kármán vortex streets past porous rectangular cylinders *Phys. Rev. Fluids* 3 10 103901
11. S Bhattacharyya S Dhinakaran A Khalili 2006 Fluid motion around and through a porous cylinder *Chem Eng Sci* 61 13 4451 4461
12. TC Jue 2004 Numerical analysis of vortex shedding behind a porous square cylinder *Int J Numer Methods Heat Fluid Flow* 14 5 649 663
13. S Rashidi M Bovand I Pop MS Valipour 2014 Numerical simulation of forced convective heat transfer past a square diamond-shaped porous cylinder *Transp Porous Media* 102 2 207 225

14. MS Valipour S Rashidi M Bovand R Masoodi 2014 Numerical modeling of flow around and through a porous cylinder with diamond cross section *Eur J Mech B/Fluids* 46 74 81
15. TR Vijaybabu K Anirudh S Dhinakaran 2018 Lattice Boltzmann simulations of flow and heat transfer from a permeable triangular cylinder under the influence of aiding buoyancy *Int J Heat Mass Transf* 117 799 817
16. P Yu Y Zeng TS Lee HX Bai HT Low 2010 Wake structure for flow past and through a porous square cylinder *Int J Heat Fluid Flow* 31 2 141 153
17. P Yu Y Zeng TS Lee XB Chen HT Low 2011 Steady flow around and through a permeable circular cylinder *Comput Fluids* 42 1 1 12
18. A Agrawal L Djenidi RA Antonia 2006 Investigation of flow around a pair of side-by-side square cylinders using the lattice Boltzmann method *Comput Fluids* 35 10 1093 1107
19. P Burattini A Agrawal 2013 Wake interaction between two side-by-side square cylinders in channel flow *Comput Fluids* 77 134 142
20. A Sanyal A Dhiman 2017 Wake interactions in a fluid flow past a pair of side-by-side square cylinders in presence of mixed convection *Phys Fluids* 29 10 103602
21. AVVS Durga Prasad AK Dhiman 2014 CFD analysis of momentum and heat transfer around a pair of square cylinders in side-by-side arrangement *Heat Transf Eng* 35 4 398 411
22. S Ma CW Kang TBA Lim CH Wu O Tutty 2017 Wake of two side-by-side square cylinders at low Reynolds numbers *Phys Fluids* 29 3 033604
23. S Kang 2003 Characteristics of flow over two circular cylinders in a side-by-side arrangement at low Reynolds numbers *Phys Fluids* 15 9 2486 2498
24. S Jamshed R Kharbanda A Dhiman 2022 Study of flow through and around a pair of porous cylinders covering steady and unsteady regimes *Phys Fluids* 34 103601
25. NSK Chaitanya AK Dhiman 2012 Non-newtonian power-law flow and heat transfer across a pair of side-by-side circular cylinders *Int J Heat Mass Transf* 55 21–22 5941 5958
26. JH Masliyah M Polikar 1980 Terminal velocity of porous spheres *Can J Chem Eng* 58 299 302
27. AK Jain S Basu 2012 Flow past a porous permeable sphere: hydrodynamics and heat-transfer studies *Ind Eng Chem Res* 51 4 2170 2178

A Study on the Aerodynamic Characteristics and the Flow Separation of a Circular Cylinder with Longitudinal Ridges



B. Kailashnath, J. Harisankar, Anirudh Renganathan, E. Karthik Vel, G. Vinayagamurthy, and S. Nadaraja Pillai

Abstract Any bluff body subjected to a flow experiences flow separation. This flow separation occurs due to loss of momentum in the boundary layer as the flow progresses over the body. One main consequence of this flow separation is the retarding aerodynamic force called ‘Drag.’ Drag is the penalty for achieving the optimum aerodynamic performance of any object subjected to airflow; thus, it is of utmost importance to reduce drag, and this can be achieved by delaying the flow separation. Flow separation can be delayed using an active or a passive flow control device. In this experiment, we have used ridges, a passive flow control device, on a circular cylinder subjected to airflow in the subsonic wind tunnel at a wind speed of 30 m/s corresponding to the Reynolds number of 1.015×10^5 . Ridge ratios of 0.12, 0.16, and 0.20 are used in the investigation. The ridges (tubes) were placed symmetrically on the top and bottom hemispheres at varying angular locations starting from 75° to 105° (measured from the stagnation point) in the range of 15° . The pressure distribution over the circular cylinder before and after placing the ridges was obtained from the simultaneous ethernet-based scanivalve pressure scanner. The variation of the coefficient of pressure was plotted for various test cases. The angles of flow separation and the coefficients of drag were obtained for all the cases considered (varying diameters and varying angular locations). It was observed that the maximum drag reduction occurs when the ridge is placed at 105° . It was also observed that the coefficient of drag was least for the 6-mm ridge placed at 105° among all the other modified cases.

Keywords Circular cylinder · Ridge · Flow separation · Coefficient of pressure · Coefficient of drag · Ridge ratio

B. Kailashnath · J. Harisankar · A. Renganathan · E. K. Vel · S. N. Pillai (✉)
Turbulence and Flow Control Lab, School of Mechanical Engineering, SASTRA Deemed to Be University, Thanjavur 613401, India
e-mail: nadarajapillai@mech.sastra.edu

G. Vinayagamurthy
Center for Innovation and Product Development & School of Mechanical Engineering, VIT, Chennai 600127, India

1 Introduction

Cylindrical structures are fundamentally used in various fields and have numerous applications, some of which are pillars of tall buildings, wind turbines, bridges, etc. Although the usage of cylindrical structures is aerodynamically efficient, it still has many drawbacks that affect the structures. The flow separation, drag force, vortex shedding, and vortex-induced vibration [1] influence the damage severity caused and the overall performance of the structure. By delaying the flow separation, we can reduce the drag induced and improve the aerodynamic characteristics of the structure. There are many studies concerning the delay of flow separation, and many methods have been implemented to do the same, some of which are the usage of passive flow control devices with various geometric modifications to attain the optimum result.

At a low Re (Reynolds number), the flow can be considered steady, while with increasing Re , the symmetry between the upstream and downstream pressure disappears as the flow becomes unsteady. From [2], flow separation is characterized by the detachment of streamlines from the cylinder surface usually downstream of the cylinder. The point from which the flow is separated from the surface of the cylinder is the separation point 'S' and the angular position is ' θ_s .' There is also a low C_p point where the resultant flow is perpendicular to the surface of the cylinder and then the flow accelerates and separates from the surface of the cylinder.

The flow over circular cylinders had been subjected to intensive research for a long time. A circular cylinder produces large drag due to the pressure difference between the upstream and downstream directions of the flow. The pressure difference is caused by the periodic separation of flow over the surface of the cylinder. Periodic separation induces fluctuations in the flow and makes the cylinder vibrate. To reduce the amount of drag or the drag coefficient of a cylinder, various active and passive flow control methods have been employed such as cylinder with dimpled surfaces [3], cylinder with longitudinal grooves [4], and cylindrical rings [5]. In this experiment, we are planning to use a circular ridge over the surface of the circular cylinder along the longitudinal axis.

In the study of Raatan et al. [6], circular ridges are placed on the airfoil surface to partially increase the momentum of the flow to overcome the adverse pressure gradient, thereby delaying the flow separation and reducing the drag.

In many of the research works that are mentioned in the literature survey section, no one has proceeded with the use of circular ridges on a circular cylinder to delay the flow separation and drag reduction.

2 Literature Review and Objective

In the study by Yan et al. [3], flow over the circular cylinder with the introduction of dimpled surfaces has been studied both computationally and experimentally. In the simulation, the Reynolds-averaged Navier–Stokes equation (RANS equation) has

been used to study turbulent flows. Experimentally, the PIV technique was adopted and all the necessary flow ratios such as vortex shedding, velocity field, pressure distribution, and force coefficient were analyzed. It was concluded that the introduction of dimples over the smooth cylinder can reduce the drag up to a maximum of 19% within a certain range of Reynolds number values. In the adverse pressure region, the flow velocity recovery was significantly higher for the dimpled cylinder case than for the smooth cylinder case. Due to the dimples, the vortex shedding frequency also dropped as a result of drag reduction. This drag reduction effect was found to reduce to as low as 12.16% when the number of dimples increased. It was also found that beyond a certain critical velocity of flow, yet again this drag reduction effect was found to be less effective. Due to the dimples, the vortex shedding frequency also dropped as a result of drag reduction. In the adverse pressure region, the flow velocity recovery was significantly higher for the dimpled cylinder case than for the smooth cylinder case.

From Cetin Canpolat [7], flow over a circular cylinder with rectangular grooves had been analyzed. Six cases of rectangular groove patterns at varying angular locations on the cylinder starting from 0° (stagnation point) to 150° were tested. The tests were conducted using the PIV technique. Time-averaged data such as vorticity, streamline, and turbulent kinetic energy were collected and analyzed. The angular positions of the grooves significantly affect the symmetry of the flow ratios, and as an effect of the grooves, the Karman vortex shedding frequency was found to reduce on the grooved side of the cylinder, along with other frequencies of varying magnitudes.

The objective of this work is to delay the flow separation by increasing the momentum of the flow by placing circular ridges at various angles along the longitudinal axis of the cylinder and to study its effect on drag. As cylindrical structures are used everywhere, their stability is also important, as it has many aerodynamic drawbacks like drag force, flow separation, vortex shedding, and vortex-induced vibration. To reduce those, we are going with circular ridges on a circular cylinder.

3 Materials and Methods

The materials and devices used in this experiment are the subsonic wind tunnel, circular cylinder, tubes (Ridges) of varying diameters of 6 mm, 8 mm, and 10 mm, double-sided tape, 64-port Scanivalve pressure scanner, and a computing unit.

The experimental procedure involves testing the cylinder model in the subsonic wind tunnel, subjecting it to a constant speed flow of 30 m/s at Re of 1.015×10^5 . Second, the flow characteristics over a plain circular cylinder were studied experimentally by calculating the surface pressure simultaneously (Fig. 1).

The pressure at various locations on the cylinder was measured using the Scanivalve pressure scanner, by connecting the cylinder and the scanner with the 21 probe connectors. The ridges (tubes) of varying diameters of 6 mm, 8 mm, and 10 mm were taped-fixed on the cylinder's surface at varying angular locations of 75° , 90° , and 105° from the stagnation point symmetrically on top and bottom of the cylinder.

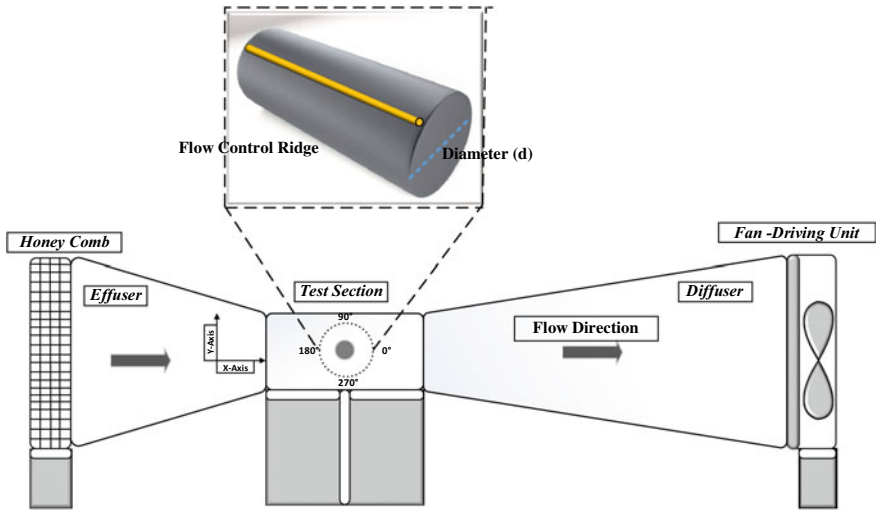


Fig. 1 Schematic representation of the wind tunnel setup

The subsequent pressures were measured with the 64-channel scanivalve pressure scanner for each case, and the C_p values were calculated. Let the diameter of ridges be ‘R’ and the diameter of the cylinder be ‘ R_c .’ Let ‘ R_r ’ be the ridge ratio which is defined as the ratio of the diameter of the cylinder to the ratio of the diameter of the ridge.

$$R_r = \frac{R}{R_c} \tag{1}$$

The C_p distribution graphs were plotted for all of the cases, including the plain cylinder, and the separation points were obtained from these graphs. Finally, the drag coefficients were calculated for the above cases. With all of the obtained plots and calculated aerodynamic characteristic ratios, some key observations and inferences were recorded and a conclusion was drawn. For the calculation of the coefficient of drag (C_D), we take all the horizontal components of the coefficient of the pressure value (C_p), multiply it with the elemental area $d\theta$, and integrate it as stated in [8].

$$C_D = \int_0^\pi C_p \cdot \cos \theta \cdot d\theta \tag{2}$$

With this equation, all the C_D values for all the cases are obtained and results are noted.

However, continuous pressure data cannot be easily gathered over a given area. Instead, pressure probes are used to gather pressure data at given points. To adapt the continuous equation for discrete data points, an integral approximation method such as the trapezoidal rule must be used (Eq. 3), where C_{Di} , is defined by (Eq. 4).

$$C_D \approx \sum_{i=1}^N ((C_{D,i+1} + C_{D,i})(\theta_{i+1} - \theta_i))/2 \tag{3}$$

$$C_{Di} = C_{pi} \cos \theta_i \tag{4}$$

4 Results and Discussion

4.1 C_p Distribution for Various Ridge Ratios

The 6 mm, 8 mm, and 10 mm ridges were placed at 75°, 90°, and 105° on both the top and bottom surfaces of the cylinder. The C_p data obtained for the three cases of the ridges with a diameter of 6 mm are compared with the C_p data obtained for the smooth circular cylinder, and the flow separation angle and the coefficient of drag are calculated (Fig. 2, 3 and 4).

Fig. 2 Comparative C_p distribution for the cylinder with $R_r = 0.12$ and the plain cylinder

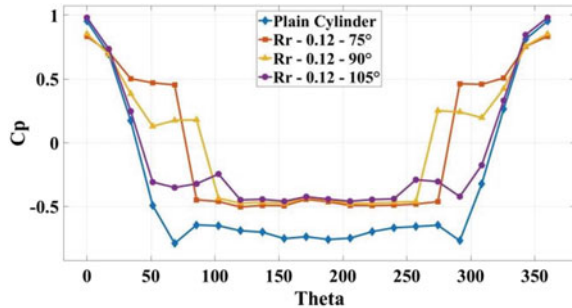


Fig. 3 Comparative C_p distribution for the cylinder with $R_r = 0.16$ and the plain cylinder

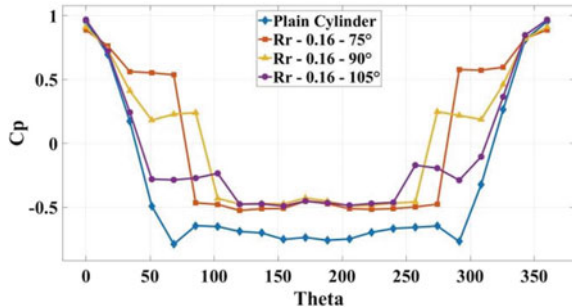
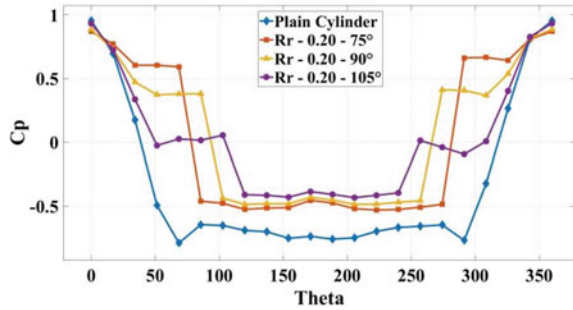


Fig. 4 Comparative C_p distribution for the cylinder with $R_r = 0.20$ and the plain cylinder



4.2 Flow Separation Analysis

The experiments were performed for various ridge ratios and the flow separation angle for each case is tabulated in Table 1.

From Table 2, it is observed that the flow separation is getting delayed with the addition of a ridge when placed at 105°. There is no change in the flow separation angle when the ridge is placed at 90° and the flow separation happens early when the ridge is placed at 75°. From Table 2, we can conclude that the flow separation angle is independent of the ridge ratio (R_r) considered for the investigation performed.

Table 1 Ridge ratio

Ridge diameter (R)	6 mm	8 mm	10 mm
Ridge ratio (R_r)	0.12	0.16	0.20

Table 2 Flow separation angles

Ridge ratio R_r	Ridge placement (θ)	Flow separation angle (θ_S)
Plain cylinder	–	85°, 274°
0.12	75°	68°, 291°
0.12	90°	85°, 274°
0.12	105°	102°, 257°
0.16	75°	68°, 291°
0.16	90°	85°, 274°
0.16	105°	102°, 257°
0.20	75°	68°, 291°
0.20	90°	85°, 274°
0.20	105°	102°, 257°

4.3 Drag Analysis

The bar graph makes it clear that the ridges irrespective of R_r , when placed at 75° and 90° , cause a slight increase in C_D compared to the plain cylinder because the ridge placed is a geometrical modification of the actual cylinder which increases the effective area over which the net pressure difference (fore and aft of the cylinder) acts. This change in pressure difference combined with the early flow separation caused by the ridges directly translates to the net pressure drag acting. On comparison, we see that the maximum reduction in C_D has occurred for R_r of 0.12, placed at 105° . This is primarily because of the delay in flow separation and the change in the effective area caused, compared to the other ridges, which is also smaller. The major inference is that C_D is dependent not only on the angular location of the ridge placed but also on the ridge ratio R_r . From Figs. 5, 6 and 7, we can see that the drag is getting reduced as the ridge placement angle is increased, and from the figures, we get to see that the coefficient of drag is not only depend on the ridge placement but also depend on the ridge ratio (R_r), and the C_D is low for $R_r = 0.12$ and is increased as the ridge ratio is increased.

Fig. 5 C_D versus theta for $R_r=0.12$

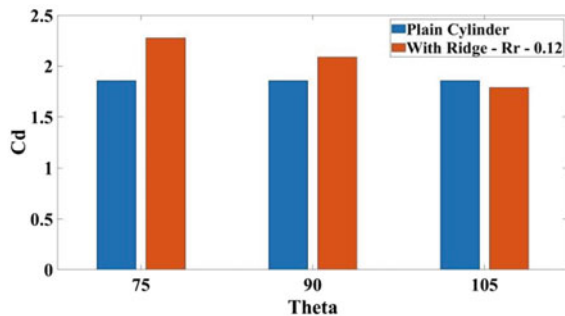


Fig. 6 C_D versus theta for $R_r=0.16$

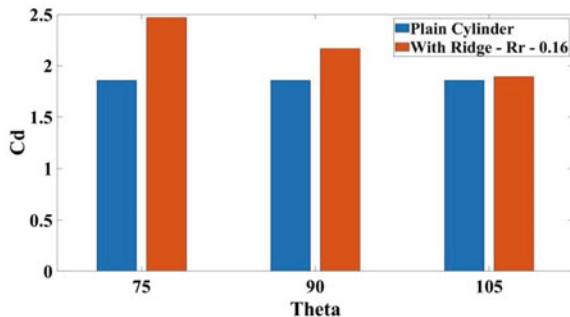
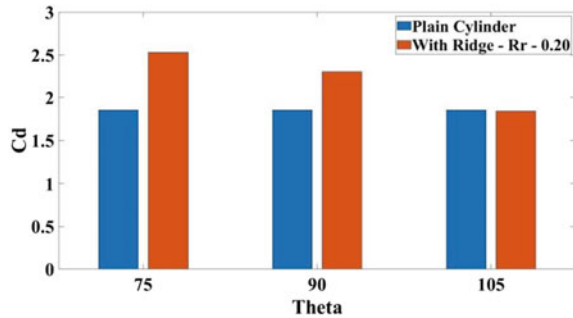


Fig. 7 C_D versus theta for $R_r=0.20$



5 Conclusion

From this experimental study, we can say that the placement of circular ridges along the longitudinal axis of the cylinder had quite a profound effect on the flow separation and drag.

1. The placement of ridges at 75° and 90° yields an early flow separation, but, when the ridges are placed at 105° , we can observe a significant delay in flow separation ($\theta_S = 102.85^\circ$). This delay in the separated flow in turn has an effect on the drag force acting.
2. For the angular locations of 75° and 90° , the increased drag coefficients are commensurate with the early flow separation caused by the ridges. However, the highlighting point would be the reduction of the drag coefficient at 105° degrees, compared to 75° and 90° .
3. It is important to note that the coefficient of drag for $R_r = 0.16$ and $R_r = 0.20$ at 105° is almost the same as that for a plain cylinder but we can observe that C_D is least for $R_r = 0.12$, at 105° .

Thus, we can conclude that when ridges of lower R_r values are placed at 105° , the flow separation is delayed as well as the drag coefficient can be reduced significantly. This delay in flow separation can be attributed to an increase in the upstream flow momentum which is in turn caused by a low-pressure region just downstream of the ridge.

The coefficient of drag is less for an 8 mm ridge placed at 105° because the downstream pressure varies significantly for both cases and we conclude that this may be due to an increase in momentum across the ridges which reduces the wake region by increasing the downstream pressure. The flow separation angle is independent of the diameter in our case and is only dependent on the placement of the ridges.

Further, repeating the same experiment between the angular locations of 90° and 105° , with ridges of even lower R_r values, could provide us with a much more elaborate understanding of the results obtained in this work.

Acknowledgements This work was supported by the Science Engineering Research Board (SERB), Department of Science and Technology (DST), Government of India (File No: CRG/2021/005720).

Nomenclature

Re	Reynolds number [–]
C_P	Pressure coefficient [–]
C_D	Drag coefficient [–]
VIV	Vortex-induced vibration [–]
PIV	Particle image velocimetry [–]
R_r	Ridge ratio [–]
d	Diameter [m]
Θ	Pressure port angle (°)
θ_S	Flow separation angle (°)
S	Flow separation point [–]
R	Ridge diameter [m]

References

1. Bearman PW (2011) Circular cylinder wakes and vortex-induced vibrations. *J Fluids Struct* 27(5–6):648–658. <https://doi.org/10.1016/j.jfluidstructs.2011.03.021>
2. Mudimeli DH (2019) Boundary layer separation from a circular cylinder. <https://doi.org/10.13140/RG.2.2.36111.84642>
3. Yan F, Yang H, Wang L (2021) Study of the drag reduction characteristics of circular cylinder with dimpled surface. *Water (Switzerland)* 13(2). <https://doi.org/10.3390/w13020197>
4. Lim HC, Lee SJ (2002) Flow control of circular cylinders with longitudinal grooved surfaces. *AIAA J* 40(10):2027–2036. <https://doi.org/10.2514/2.1535>
5. Nakamura H (2011) Vortex shedding suppression for a circular cylinder by attaching cylindrical rings (a consideration of the mechanism). *ASME-JSME-KSME 2011 Jt Fluids Eng Conf AJK 2011 1(PARTS A, B, C, D):2863–2873*. <https://doi.org/10.1115/AJK2011-16008>
6. Raatan VS, Ramaswami S, Mano S, Pillai SN (2016) Effect of stall delay characteristics of symmetrical aerofoil using lateral circular ridges. *Wind and Struct – an Int J* 34(4):385–394. <https://doi.org/10.12989/was.2022.34.4.385>
7. Canpolat C (2015) Characteristics of flow past a circular cylinder with a rectangular groove. *Flow Meas Instrum* 45:233–246. <https://doi.org/10.1016/j.flowmeasinst.2015.06.028>
8. Anderson JD (2016) *Fundamentals of aerodynamics* (6th edn)

Effect of Surface Roughness on Boundary Layer Thickness



Saurabh Powar, Neha Chitrakar, Lalit Chacharkar, Prakhar Adarsh, Shankar Karhale, Rohan Patil, and Pramod Kothmire

Abstract Surface roughness effects over a rough flat plate are compared for different surface roughness conditions using CFD techniques. Velocity readings were taken at equal intervals over the flat plate with a free stream velocity of 11.11 m/s. Velocity profiles are plotted at different sections along the boundary layer thickness. The growth of the boundary layer for different conditions gives us a brief idea of flow over the plate surface. Results such as eddy viscosity, turbulent kinetic energy, velocity variations and wall shear variations are presented.

Keywords Flat plate · Boundary layer · Surface roughness · Wall shear · Near wall effects

1 Introduction

During the manufacturing process of fluid devices, the surfaces produced do not have ideal surface roughness due to some manufacturing defects or burr formation. The fluid interacting surfaces which are being used for different applications are analyzed for an ideal surface roughness condition. Hence, the boundary layer thickness obtained is for the ideal condition. For real conditions, surface roughness may vary which impacts on changing the boundary layer thickness, wall shear and transition from laminar to turbulent boundary layer. The current study focuses on varying the surface roughness for different conditions and obtaining results based on that. The geometry used here is of a flat plate with different values of surface roughness.

The model used in this study is the k - ω SST model which captures surface effects. Also, PISO Scheme is taken into use for solving governing equations. For surface roughness, roughness height and roughness constant are provided which determine irregularity of the surface. Inlet velocity is given to be 11.11 m/s over a flat plate. Four different manufacturing processes of plate are used namely as casting,

S. Powar · N. Chitrakar · L. Chacharkar · P. Adarsh · S. Karhale · R. Patil · P. Kothmire (✉)
School of Mechanical Engineering, MIT Academy of Engineering, Alandi, Pune 412105, India
e-mail: ppkothmire@mitaoe.ac.in

forging, shaping and planning having different values of surface roughness and the corresponding results are compared.

During literature review, the major gap identified was that the account of the surface roughness by different manufacturing processes was not taken into consideration. Due to this, the experimental results were not validating with the practical results. So, here four differently manufactured plates having different surface roughness values and compared their boundary layer thickness results. The CFD techniques are used in order to see how the surface roughness increases the overall wall shear and boundary layer thickness. Furthermore, understanding and predicting the effects of drag would help in the development and performance of some other applications whose parameters are changed and affected by surface roughness.

2 Literature Review and Objective

In some papers, experiments were conducted in slow-moving wind tunnel testing with velocity ranges of 10–25 m/s [1]. The wind tunnel is made up of a testing section in the center where its velocity in the air flow is nearly uniform [1]. Wu [2018] studied separating the turbulent boundary layer with LES (large eddies simulation) on a flat plate, which solves filtered equations of conservation of mass and momentum [3]. Usta [2013] used Reynolds Averaged Navier Stokes (RANS) solver for modeling incompressible, viscous, unsteady and turbulent layers. The governing equations were solved by using a realizable k-epsilon turbulence model [4]. Song [2020] used the roughness function in the wall function of CFD boundary conditions to represent surface roughness. The flow was modeled using the Unsteady Reynolds Averaged Navier Stokes (URANS) method, with second order upwind thermal scheme and first order sequential discretization for momentum equations. The SIMPLE algorithm served as the foundation for the overall solution procedure [5]. Akbar Javadi [2020] conducted research on the DH turbine using NACA 0015 aerofoil. The CFD model was used to simulate the turbine in 6 different average roughness heights. The turbulence model was the k-(SST) model [6]. Mohamed M. El-Mayit conducted theoretical and experimental studies on the boundary layer properties across a flat plate. Smooth surface boundary layers were discovered to have denser boundary layers than rough surface boundary layers [7]. Walid varied the magnitude and position of the roughness on the airfoil's aerodynamic properties in order to study the impact of surface roughness. It was discovered that the airfoil model with the roughness at the trailing edge exhibits the least amount of drag and the maximum lift [8]. Vivek Gupta investigated the effects of boundary layer inclination in a low-speed wind tunnel under various roughness conditions [1]. By Schultz, measurements of turbulence for boundary layers on a rough wall are shown and compared to those for a smooth wall. Using velocity-defect scaling, he found out that the mean velocity profiles for the smooth and rough walls reveal remarkable similarities in the outer layer [9]. Mohammadreza's research concludes that the structure of turbulent flow is still not completely understood. This is primarily due to a lack of research studies

on the structural system of turbulent flow, as well as the wide range of roughness that influences flow dynamics in roughness sublayers [10]. The effects of surface roughness on a separating turbulent boundary layer were investigated by Wen Wu. The separated shear layer has increased turbulent kinetic energy in the case of the rough-wall (TKE) [3]. Ibrahim studied the effect of surface roughness on turbulent flow. For various roughness values, CFD analysis is performed to determine how heat transmission and fluid properties change as roughness increases [11]. Mohammad found out that surface roughness has a significant impact on the resistance properties of flat plates [4]. Mohammad's experimental and simulation-based analysis of a Darrieus hydro turbine shows that surface roughness degrades turbine performance and increases turbulence and reduces the active dynamic energy required to rotate it [6]. Joná discovered that the transitional zone gets shorter as the roughness number increases. He investigated the transition of flat plate boundary layers on surfaces near the acceptable roughness limit [12]. By comparing measurements taken over two rough walls to measurements taken from a boundary layer on a smooth wall, the effects of surface roughness on a turbulent boundary layer are examined by Krogstadt. The turbulent energy generation and the turbulent diffusion between the two rough surfaces were found to be considerably different [2]. R. A. Antonia investigated the impact of the surface roughness on the boundary layer and discovered that rough surfaces exhibit different turbulent transport features [2]. The impact of surface roughness on the vane endwall of an axial turbine's heat transmission was studied numerically by Lutum [5].

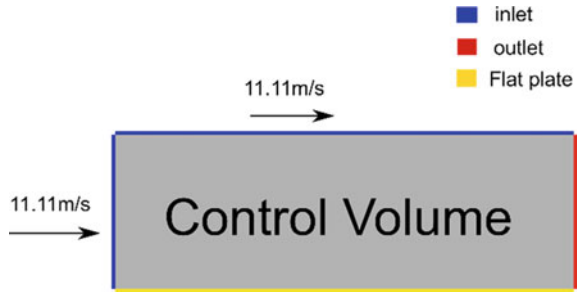
3 Methodology

In this study, CFD simulations were performed in order to simulate flow on a rough flat plate. To represent surface roughness in CFD simulations, roughness special wall functions were applied in boundary conditions. The objective of study was to see transition of flow from laminar to turbulent flow on the flat plate with variations of roughness affecting the transition region. Initial flow velocity and plate length was selected accordingly to render flow from laminar to turbulent region, with the flow velocity of 11.11 m/s and plate length of 2.2 m. Theoretical Reynolds number up to length 0.8 m had a value of 4×10^5 which is in the laminar region and from beyond that point the turbulent region would start.

3.1 Software

ANSYS Fluent 19.2 is a general-purpose computational fluid dynamics (CFD) software that can be used to simulate fluid flow, heat and mass transfer, chemical reactions, as well as other phenomena. Fluent has a modern, user-friendly interface which

Fig. 1 Schematics of flat plate



simplifies the CFD process from pre-processing to post-processing inside a single window workflow.

3.2 Geometry

The geometry used for this study is a rectangular surface geometry with dimensions of 2200 mm length and 80 mm height for 2D flow simulation in which the lower edge is considered as a rough flat plate (Fig. 1).

3.3 Meshing

Mesh size	Edges	3 mm
	Surface	0.8 mm
Mesh element	Quadrilateral	
No. of nodes	86,990	
No. of elements	41,903	

The fine mesh was performed near the plate boundary to properly capture the boundary layer development and its transition from laminar to turbulent.

Meshing was done in ANSYS software with size of face mesh 3 mm and at boundary, mesh size is 0.8 mm as shown in Fig. 2.

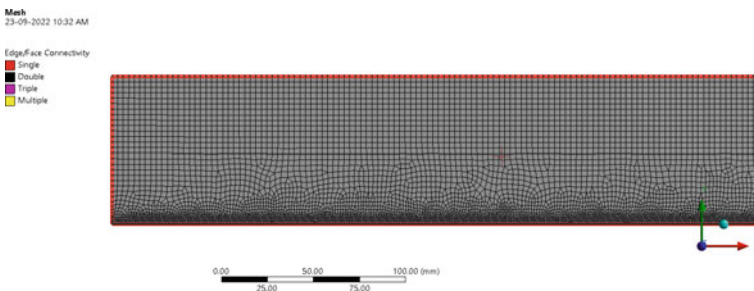


Fig. 2 Meshing of flat plate

Table 1 Surface roughness associated with machining processes

Machining	Roughness (Ra) (μm)
Casting	500
Forging	105
Shaping and planning	25
Surface grinding	6

3.4 Boundary Conditions

The 2D flow simulations were performed with control volume being cut plane in direction of flow.

In boundary conditions, the inlet velocity of 11.11 m/s was given with flat plate treated as wall and roughness was provided with roughness height and roughness constant, latter giving how the roughness is distributed over flat plate.

From the literature review, the surface roughness values for various machining operations were found and are listed in Table 1.

3.5 Governing Equations

$$\frac{\partial(\rho k)}{\partial t} + \frac{\partial(\rho u_j k)}{\partial x_j} = \rho P - \beta^* \rho \omega k + \frac{\partial}{\partial x_j} \left[\left(\mu + \sigma_k \frac{\rho k}{\omega} \right) \frac{\partial k}{\partial x_j} \right], \text{ With } P = \tau_i \frac{\partial(\rho \omega)}{\partial t}$$

$$\frac{\partial(\rho \omega)}{\partial t} + \frac{\partial(\rho u_j \omega)}{\partial x_j} = \frac{\alpha \omega}{k} \rho P - \beta^* \rho \omega^2 + \frac{\partial}{\partial x_j} \left[\left(\mu + \sigma_\omega \frac{\rho k}{\omega} \right) \frac{\partial \omega}{\partial x_j} \right] + \frac{\rho \sigma_d}{\omega} \frac{\partial k}{\partial x_j} \frac{\partial \omega}{\partial x_j}$$

The *k*-omega SST model was selected to simulate the flow; the *k*-omega model is used to capture flow properties near the boundary. It used *k*-omega near the boundary and *k*-epsilon in the free stream. Shear stress transport model is used to model turbulence effects and hence it was included.

To solve the governing equations, the PISO scheme was used, with a second order scheme for gradient, a second order upwind scheme for momentum equations, and a first order upwind scheme for turbulent kinetic energy.

4 Results and Discussion

After simulating flow over flat plate for 4 different surface roughness, comparison was done based on the boundary layer thickness and wall shear for each case.

Initially, the flow is laminar ($Re = 5 \times 10^5$ for flat plate) till $x = 0.55$ (for $Ra = 6 \mu\text{m}$), then after that at $x > 0.55$, the flow becomes turbulent ($Re > 5 \times 10^5$). This pattern was the same for all 4 cases that were studied. The eddy viscosity contour is a proportionality factor that describes the turbulent energy transfer caused by moving eddies. It is seen that after some distance, the eddy viscosity starts increasing indicating the starting of the transition region and then the turbulent region starts.

For every case, the transition region was started around 0.25 m, with only in $Ra 500 \mu\text{m}$ case, the transition was delayed by 10–15 mm (Fig. 3).

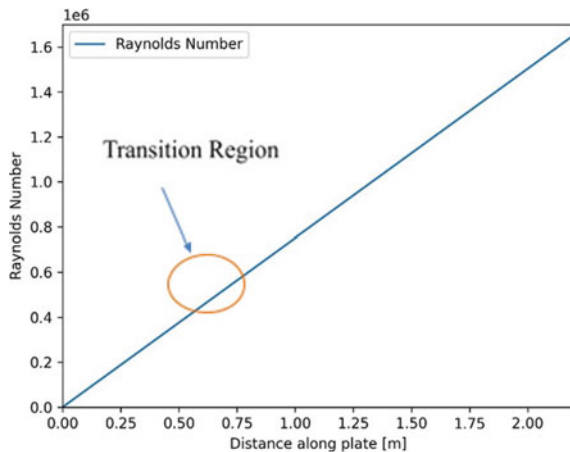
In contour for Turbulence kinetic energy, there is color distribution showing the mean kinetic energy per unit mass, associated with the respective eddy in a turbulent flow. It measures the intensity of turbulence in a flow. As shown in fig at $x = 2.2 \text{ m}$, there is change in turbulence kinetic energy. As shown in Fig. 4c, the velocity contour has changed in velocity at the end of plate.

Figure 4a–c show the contours for Turbulent kinetic energy, Eddy Viscosity Contour, velocity at the inlet wind velocity of 11.11 m/s on a flat plate for surface roughness value of 6 $Ra \mu\text{m}$.

4.1 Velocity Profile Graphs

In the velocity graph for the $Ra 6 \mu\text{m}$ case, velocity distribution profile along boundary layer at various locations of plate is observed. This distribution indicates how the boundary layer has developed over the length of the plate. From the velocity

Fig. 3 Reynolds number at various locations along plate



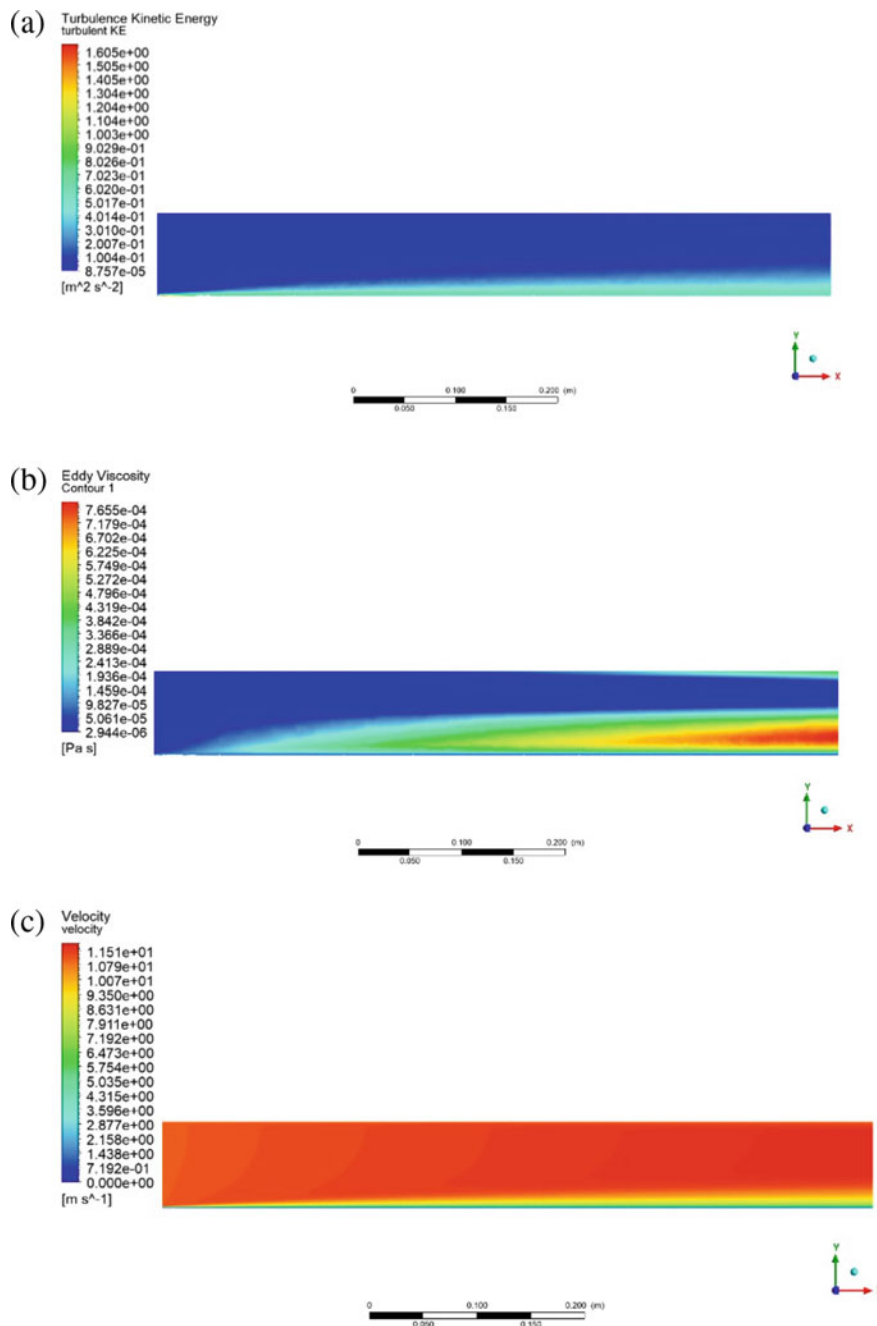
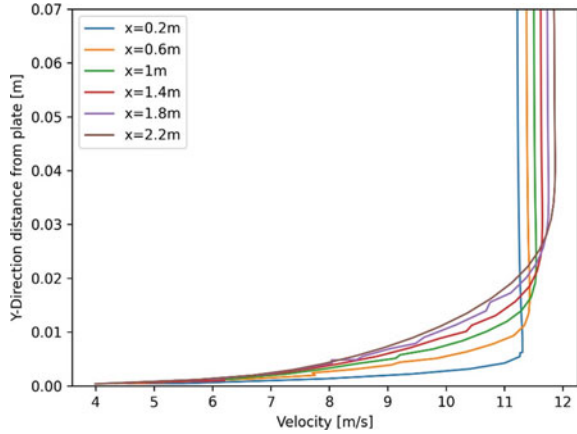


Fig. 4 a Turbulent kinetic energy contour. b Eddy viscosity contour. c Velocity contour

Fig. 5 Velocity profile in Ra 6 μm plate at various locations



profile graph, as the boundary layer converts to turbulent region, the $U_{99\%}$ increases with turbulence (Fig. 5).

4.2 Boundary Layer Thickness

In Fig. 6, the boundary layer thickness variation as the roughness of plate is changed, with BL thickness increasing with surface roughness.

For the Ra 6 μm and Ra 25 μm , the BL thickness is closely matched with little variations, but for the Ra 105 μm and Ra 500 μm case, it can be seen that there is a variation in BL thickness.

Fig. 6 Boundary Layer thickness along plate for different plate roughness

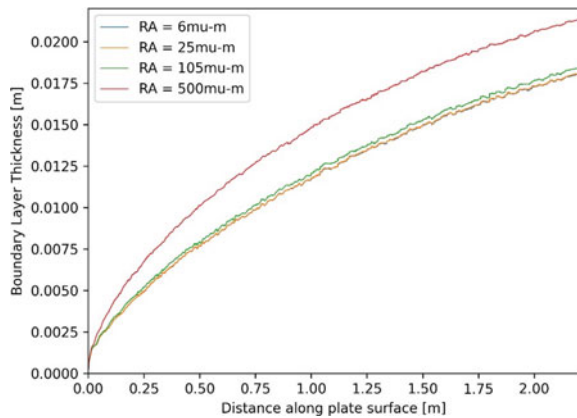


Table 2 Wall shear with roughness of each plate

Surface roughness (Ra) (μm)	Unit wall shear (N/mm^2)
6	0.281691
25	0.282081
105	0.290569
500	0.406072

4.3 Wall Shear

From Table 2, we can see trends similar to BL thickness, for the Ra 6 μm and Ra 25 μm case, the wall shear has changed negligibly but the variation starts to occur with Ra 105 μm and Ra 500 μm case.

5 Conclusions

In this analysis, a 2-D rectangular flat plate is considered & variations of four different surface roughness values were done by which different results like the roughness increases and the disturbance in the boundary layer increases. It was observed that for surface roughness to have significant impact on BL thickness and wall shear minimum deviation should be around 100 μm .

For transition from laminar to turbulent region, there was no significant impact due to surface roughness change, with only difference of Ra 500 μm causing to delay transition by 10–15 mm.

Nomenclature

- Ra Roughness Average [μm]
- Re Reynolds number
- BL Boundary Layer

References

1. Gupta V, Kumar A, Effect of inclination on boundary layer in a low speed wind tunnel on different roughness
2. Krogstadt PÅ, Antonia RA (1999) Surface roughness effects in turbulent boundary layers. Experiments Fluids 27(5):450–460
3. Wu W, Piomelli U (2018) Effects of surface roughness on a separating turbulent boundary layer. J Fluid Mech 841:552–580

4. Usta O, Korkut E (2013) A study for the effect of surface roughness on resistance characteristics of flat plates. Marine Coatings, London, UK
5. Lutum E, et al (2015) A computational investigation of the effect of surface roughness on heat transfer on the stator end wall of an axial turbine. In: Proceedings of the institution of mechanical engineers, Part A. J Power Energy 229(5):454–464
6. Khanjanpour MH, Akbar A (2020) Javadi. Experimental and CFD analysis of impact of surface roughness on hydrodynamic performance of a darrieus hydro (DH) turbine. Energies 13(4):928
7. El-Mayit MM, Alarabi AAB, Alhwinat NDA, Experimental and theoretical study of laminar boundary layer over flat plate
8. Chakroun W, Al-Mesri I, Al-Fahad S (2004) Effect of surface roughness on the aerodynamic characteristics of a symmetrical airfoil. Wind Eng 28(5):547–564
9. Schultz MP, Flack KA (2007) The rough-wall turbulent boundary layer from the hydraulically smooth to the fully rough regime. J Fluid Mech 580:381–405
10. Kadivar M, Tormey D, McGranaghan G (2021) A review on turbulent flow over rough surfaces: fundamentals and theories. Int J Thermofluids 10:100077
11. Ibrahim M, et al (2004) CFD modeling of surface roughness in laminar flow. In: 2nd International energy conversion engineering conference
12. Jonáš P, et al (2011) By-pass transition of flat plate boundary layers on the surfaces near the limit of admissible roughness. J Phys Conf Ser 318(3). IOP Publishing

Effect of Secondary Swirl Strength on the External Aerodynamics of a Gas Turbine Fuel Injector



Vivek Sahu, Devin Chugh, Deepanshu Mittal, and K. P. Shanmugasas

Abstract The present work investigates the effect of the secondary swirler geometry on the gas flow field and the shear layer thickness in a counter-rotating gas turbine swirl injector. The counter-rotating swirl injector geometry consists of a primary swirler and a counter-rotating secondary swirler separated by a pre-filming thin surface. Three counter-rotating swirl injectors having different swirl numbers of the secondary swirler have been used for this study. The primary swirler's swirl number is kept constant and within the strong swirl regime. The gas flow field in the axial and transverse plane is captured using particle image velocimetry (PIV) experiments. The geometry with a high swirl number has the highest axial, radial, and tangential velocities. The secondary swirler's swirl strength affects the recirculation zone that the primary swirler creates at the injector outlet, and radial expansion in the central toroidal recirculation zone (CTRZ) has also been observed.

Keywords Counter-rotating swirlers · Gas turbine fuel injector · Swirl number · Particle image velocimetry

1 Introduction

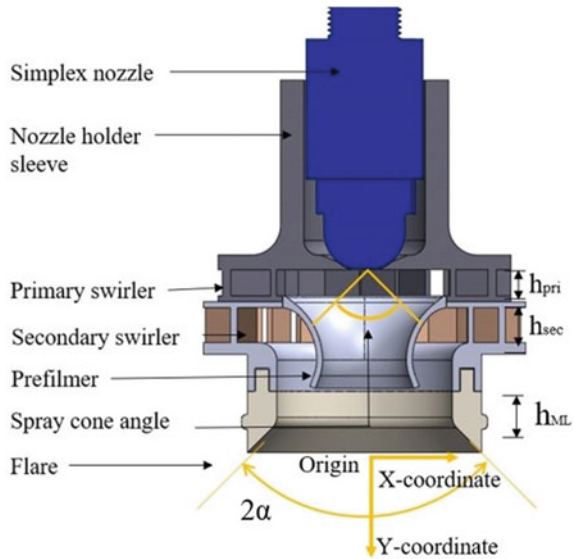
In gas turbine combustors, atomization and mixing of the liquid fuel are achieved by the highly turbulent swirling flows generated by the injector assembly [1]. The efficient performance of the fuel injector is critical to the successful operation of any combustion system [2]. The design and performance of gas turbine engines are greatly influenced by injector aerodynamics [3]. To stabilize the flame, a strong recirculation zone is required at the injector exit, which primarily originated from the primary swirler of the injector. Swirling flow characteristics enhance flame stabilization and air/fuel mixing. The flow field at the injector exit substantially influences the spray's droplet size and spatial homogeneity [4].

V. Sahu · D. Chugh · D. Mittal · K. P. Shanmugasas (✉)

Department of Mechanical Engineering, Indian Institute of Technology, Jammu J&K, 181221, India

e-mail: shanmugasas.kp@iitjammu.ac.in

Fig. 1 Fuel injector arrangement with counter-rotating swirlers



The present paper discusses the flow features of a typical piloted pre-filming airblast injector which is used in rich burn aero-engine gas turbine combustors [5]. The injector schematic is presented in Fig. 1. The main components of the counter-rotating swirl injector assembly include the primary swirler, venturi, secondary swirler, and fuel nozzle. The pilot nozzle generates the primary spray, which is atomized by the primary swirler air. The primary swirler generates a central toroidal recirculation zone which originates from the pilot swirler exit plane and extends to the primary zone of the combustor [6]. The counter-rotating shear layer formed at the venturi exit by the primary and secondary swirlers atomizes the liquid rim formed at the tip, and a fine spray is formed at the injector exit.

2 Design of Counter-Rotating Swirler

The fuel–air mixer characteristics of rich burn gas turbine injectors are investigated in detail by a number of previous investigations [7]. Characteristics of the external spray structure and aerodynamics are captured under atmospheric and high-pressure conditions [8]. Mehta et al. conducted measurements in models to evaluate the effects of swirling directions (counter-swirl or co-swirl) on the generated flow field [9].

The external spray characteristics are dictated by the internal atomization characteristics. The internal flow evolution inside such injectors is also investigated recently [10]. It is observed that the primary air swirl dictates the formation of the CTRZ [11].

Swirler configurations are shown to be effective for control of the flow field, and hence it can control emissions and combustion dynamics, but each has certain

limitations. Even though elaborate investigations are done on a broader range of aspects related to the injector, the effect of secondary air swirl is not investigated much. The thickness of the shear layer and the accumulated liquid rim thickness at the rim decide the external spray characteristics [3]. It is known that the strength of the shear layer influences the atomization process, which depends on the primary and secondary swirl numbers.

The present work aims to investigate the effect of secondary air swirls on the injector aerodynamics. Experimental investigations are conducted by varying the swirl number of the secondary swirler, keeping all other parameters constant.

3 Experimental Setup and Diagnostics

3.1 Geometrical Details of the Counter-Rotating Swirlers ($G1$, $G2$, and $G3$)

Counter-rotating swirler assembly is manufactured using Nylon PA2200 material, with the help of the 3D printing SLS technique. Table 1 contains geometrical information related to the swirler assembly. The swirler's flow inlet areas are kept in such a way so that it allows 40% of air from the primary swirler and 60% from the secondary swirler to pass through.

The primary and secondary swirlers are purely radial in nature. Vanes are arranged circumferentially at a particular angle to deflect incoming air to the desired degree of swirl. The rotation of the airflow causes the axisymmetric swirl to develop [12]. The entering air is rotated clockwise by the primary swirler and counter-clockwise by the secondary swirler in the configuration as shown in Fig. 2.

The flow split and swirl numbers are close to the injector hardware's real values. The flare angle (2α) is kept as 90° . The primary swirler's geometrical swirl number is kept at 1.22, while the secondary swirler's swirl number is varied from 1.33 to

Table 1 Dimensional variation in counter-rotating swirler's secondary swirler geometry

Dimensional parameters	Counter-rotating swirler-1	Counter-rotating swirler-2	Counter-rotating swirler-3
Blade angle ($^\circ$)	76.3	77.3	78.2
Number of blade, n	14	14	14
Inner diameter (mm)	34	34	34
Outer diameter (mm)	50	50	50
Blade height (mm)	8.2	7.7	7.4
Blade thickness (mm)	1	1	1

Fig. 2 Primary (clockwise) and secondary swirler (counter-clockwise) swirling directions

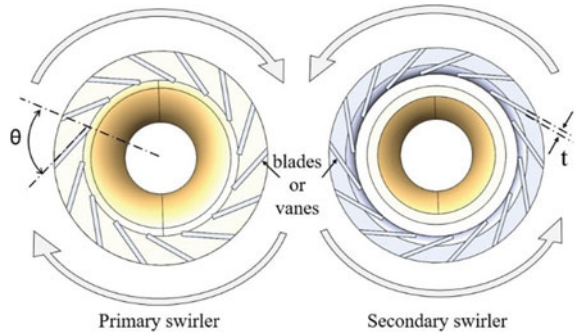


Table 2 Variation of swirl numbers primary and secondary

Cases	Primary swirler’s swirl number	Secondary swirler’s swirl number
G1	1.22	1.33
G2	1.22	1.52
G3	1.22	1.79

1.79 as given in Table 2. The correlations, provided by Sheen et al., are employed for the computation of geometrical swirl numbers [13]. Geometrical swirl number can be written as,

$$S = 0.28 \left(\frac{1}{1 - \varphi} \right) \left(\frac{\tan \theta}{1 + \tan \theta \cdot \tan \frac{\pi}{n}} \right) \tag{1}$$

where, S is the geometrical swirl number; θ is the blade angle; n is the number of blades; φ is the blockage factor.

Blockage factor can be written as,

$$\varphi = \frac{n \cdot t}{(2 \cdot \pi \cdot R_{\text{inner}} \cdot \cos \theta)} \tag{2}$$

where, t is the blade thickness (mm); R_{inner} is swirler inner radius (mm).

3.2 Experimental Arrangements

Experiments are conducted under atmospheric ambient conditions. A brief schematic of the test rig is presented in Fig. 3. The test rig includes two major segments: a liquid flow line (kept isolated while doing these tests) and an airflow line, which also includes an olive oil seeder. Swirler was fixed on a settling chamber such that the

flare is exposed to the atmosphere. Airflow was controlled using Alicat MCR series gas mass flow controller (MFC) of range 0 to 4000 slpm.

Experiments are conducted at scaled-down flow conditions following [3]. A simplex nozzle with a hollow cone spray angle of 90° and a flow rate of 1.15 g/s is selected as the nominal condition to calculate the air flow rate. Test operating conditions are decided by varying the air-to-liquid ratio from 12 to 25, keeping the liquid flow rate constant.

Operating test conditions are listed in Table 3. By adjusting the upstream pressure regulator and MFC, the airflow rate can be changed. For PIV investigations, the airflow is seeded using an olive oil seeder. The main air supply line's seeding density is uniform due to the air supply arrangements and the olive oil droplet size, which is measured to be $\sim 3 \mu\text{m}$.

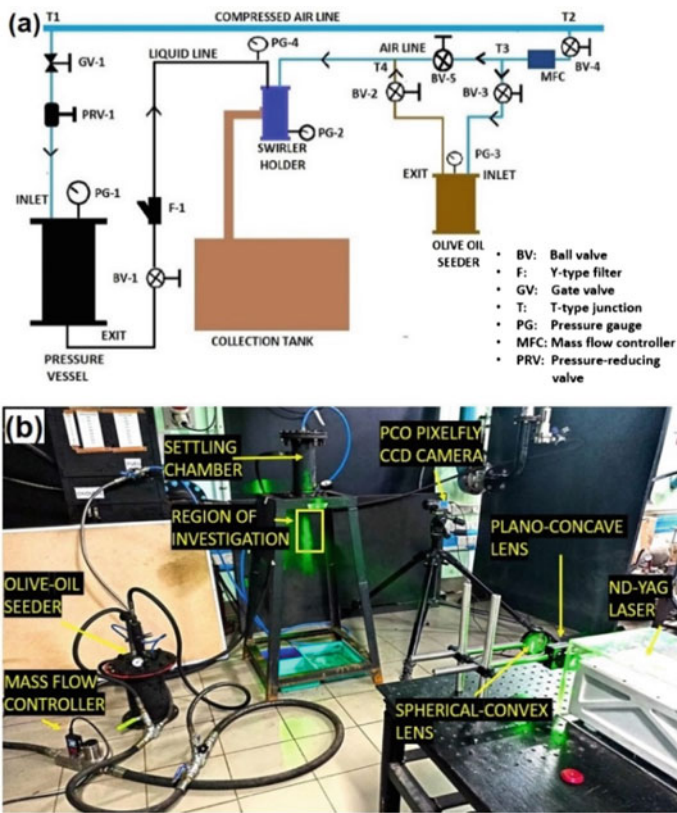


Fig. 3 a Schematic of the test rig b actual test rig

Table 3 Test operating conditions

ALR	Air mass flow rate (g/s)
12	13.6
14	16.1
16	18.4
18	20.7
20	23.0
25	28.8

3.3 Laser Diagnostics

The air velocity field is quantified using different laser diagnostic experiments. Axial plane PIV experiments are conducted to get the axial velocity field and recirculation zone characteristics. PIV experiments are performed using a 10 Hz, Nd: YAG laser (Litron Bernoulli Series). The laser beam is converted to a 1 mm thin light sheet using one cylindrical plano-concave lens of -20 mm focal length and one spherical convex lens of the focal length of 2000 mm. The light sheet is directed axially to obtain the axial velocity. Similar to this, cross-plane PIV experiments are carried out at 3 mm and 10 mm from the flare exit while maintaining the light sheet in such a way that it was cutting the flow field in the transverse plane to acquire the radial, tangential velocity components, and shear layer thickness.

A CCD double shutter camera (PCO Pixel fly) along with a 100 mm zoom lens is used to capture the images. The camera and laser are synchronized using a sequencer that was built in-house. Images are processed using the commercial PIV software DaVis. Axial plane experiments are conducted with Δt of 20 μ s and transverse plane experiments are done at Δt of 6 μ s. A total of 1000 double images are acquired for each flow condition.

4 Results and Discussion

4.1 Analysis of the Air Velocity Flow Field

The air velocity field at the injector exit is measured using axial plane PIV and cross-plane PIV experiments. When the primary air swirl undergoes a vortex breakdown under a strong swirl flow regime, a CTRZ is produced. The creation of the recirculation zone at the injector outlet is seen in the axial velocity field. Figure 4 displays an ensemble-averaged axial velocity field.

The size of the recirculation zone is estimated as the maximum width of the CTRZ bubble, whose boundary is identified by the zero-velocity streamline. Variations in the width of CTRZ with air flow rate for different swirl injectors are shown in Fig. 5.

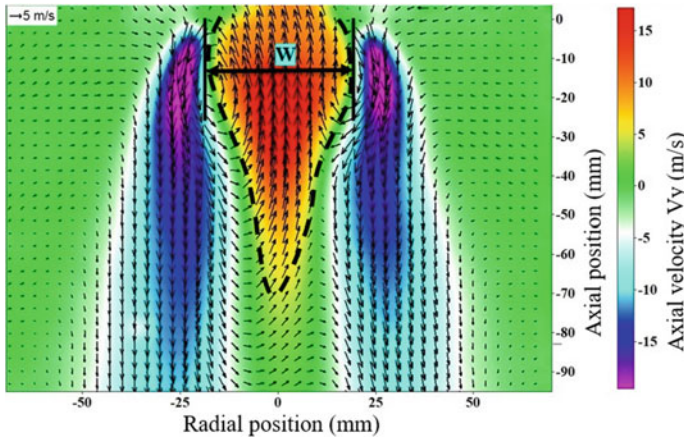
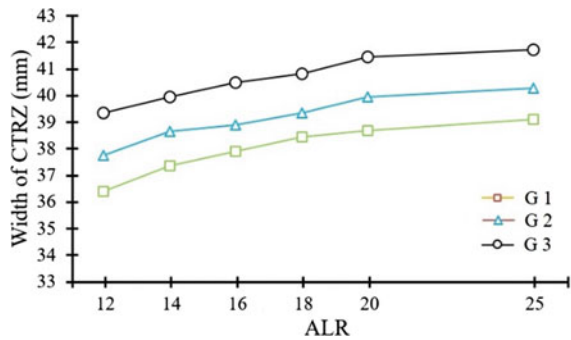


Fig. 4 Average of axial air velocity (V_y) field of swirler-2 (ALR-18) at injector exit marked with CTRZ width (W)

Fig. 5 Variation in the width of CTRZ with air flow rate for different swirl injectors

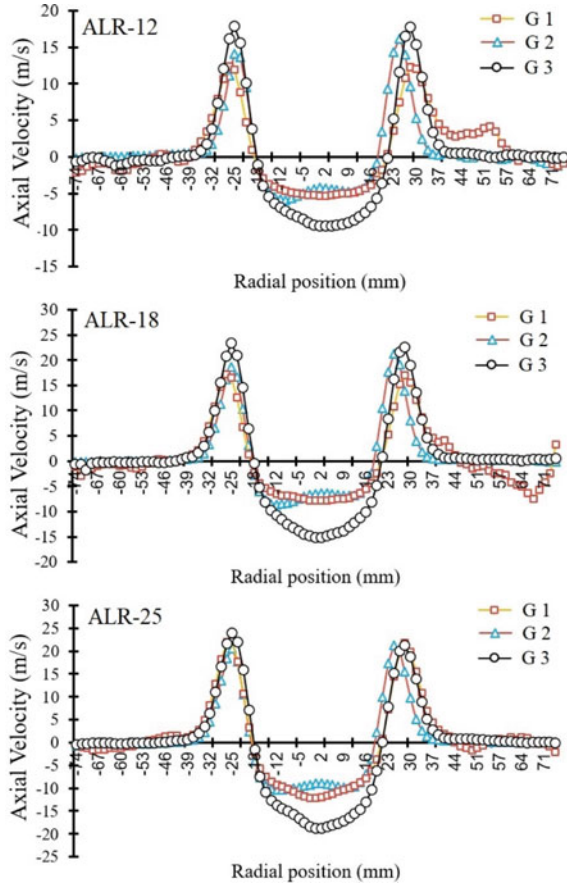


The width of the CTRZ increased with the air flow rate in the case of all injectors. The CTRZ formation is mainly dictated by the primary swirl air. It is observed that the secondary swirl strength affects the formation of CTRZ and the higher radial pressure gradients result in the expansion of the recirculation zone. This is evident as the increase in the width of CTRZ for the injectors: G3 as compared to the G1.

Figure 6 represents the axial velocity variation at 10 mm from the injector exit plane for the three injectors. The G 3 provides a dominant flow pattern with peak negative velocities in the range of 9.46–18.84 m/s in the central region for different ALR conditions. The axial velocity in the shear layer region varies from 18.86 to 24.02 m/s for similar operating conditions.

At the injector exit, the flow is predominantly swirling in the same direction as the secondary air swirl in all three cases. Variations in the radial and tangential velocities are captured using the cross-plane PIV experiments. A sample ensemble-averaged velocity field is shown in Fig. 7. The variation in tangential and radial velocities for all the geometries are presented in Figs. 8 and 9. Radial and tangential velocities

Fig. 6 Axial velocity variation for three swirlers measured at 10 mm from the exit plane for different operating conditions (ALR 12–25)



peak at the shear layer region. Tangential and radial velocities peaks are higher for the G3 injector as compared to other injectors for the different air flow rates.

4.2 Analysis of the Shear Layers

The effect of an increase in the secondary swirl number can be captured by estimating the shear strength of the shear layer. The area of the shear layer is where vorticity and shear strength attain maximum values. The strength of the shear layer is represented by shear strength which is estimated as the eigen values of the matrix,

$$\begin{bmatrix} E_{XX} & E_{XX} \\ E_{YX} & E_{YY} \end{bmatrix}$$

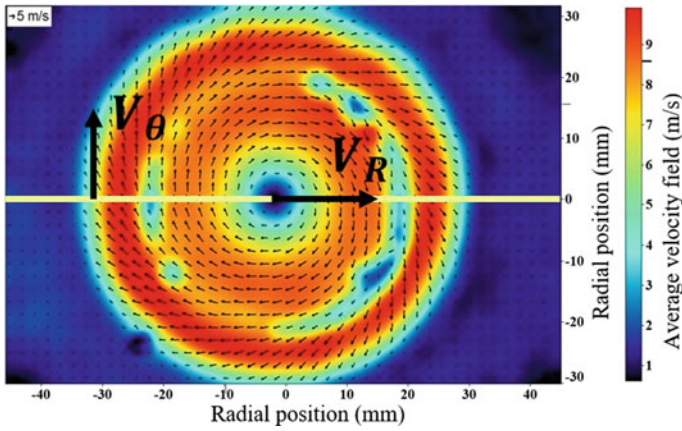


Fig. 7 Cross plane velocity field of swirler-2 (ALR-18) at 10 mm from injector exit, tangential velocity (V_θ), and radial velocity (V_R)

Fig. 8 Tangential velocity variation for three swirler at different test operating conditions (ALR 12–25)

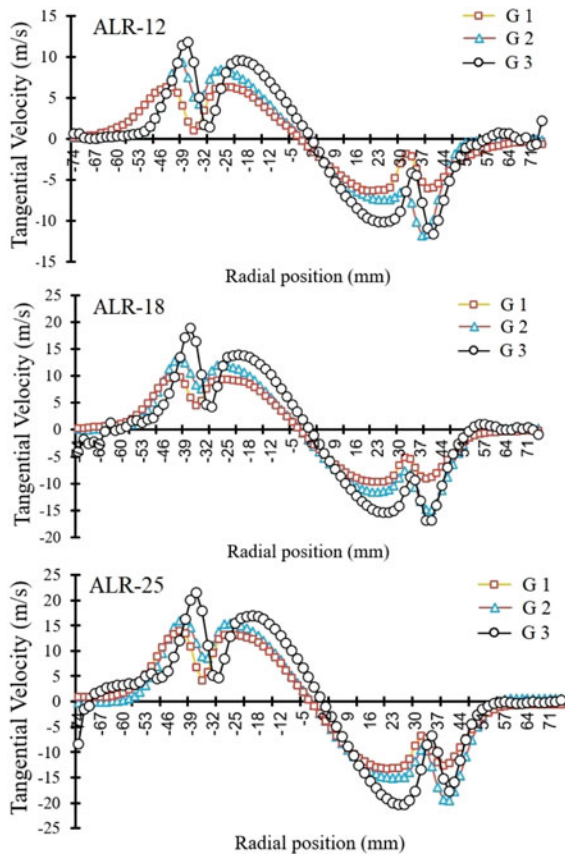
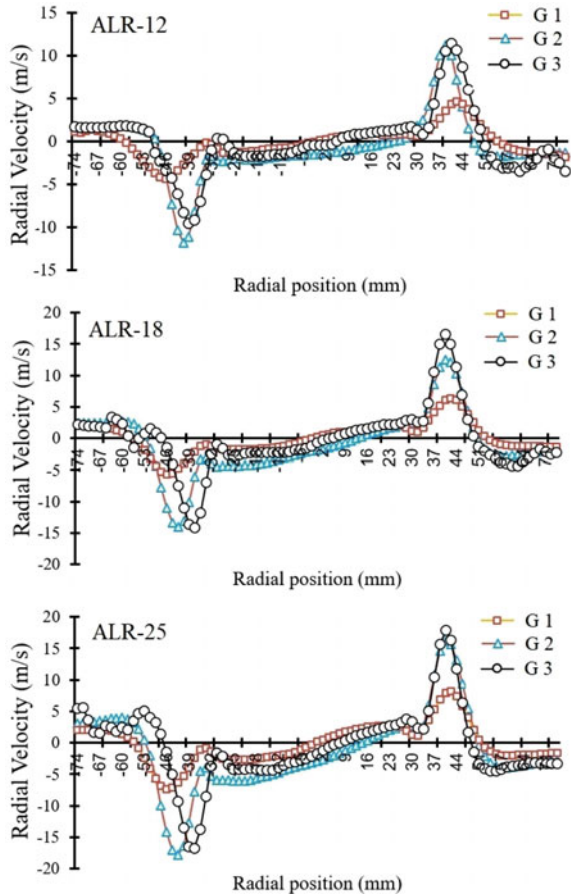


Fig. 9 Radial velocity variation for three swirler at different test operating conditions (ALR 12–25)



in 2-D, it has the form $a \pm \sqrt{b}$ with,

$$b = E_{XY} - (E_{XX} - E_{YY}) + (E_{XX}^2 - E_{YY}^2)/4 \tag{3}$$

when b is positive, it represents the shear strength.

The variation of shear strength is estimated from the cross-plane PIV data and a sample case is presented in Fig. 10.

The shear layer thickness is depicted in Figure at various radial positions. The thickness of the air shear layer when there is a sharp gradient shift in the shear strength is known as the shear layer thickness. Using Davis software, this region was located from the shear strength contour plots and is shown in Fig. 11 as a binarized zone. Eight radial sites are used to assess the shear layer’s thickness, and the mean value is then provided. With an increase in air flow rate, the shear layer thickens as well as the shear strength increases. For three swirl injectors (G1, G2, G3), an increase in shear layer thickness is observed as the swirl number increases, as shown in Fig. 12.

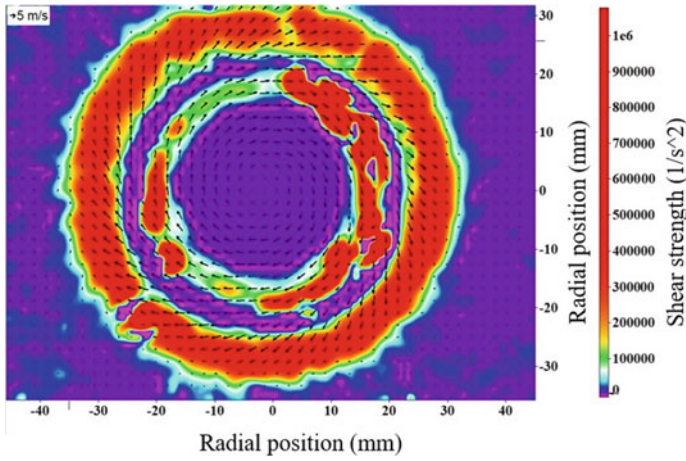


Fig. 10 Variation of shear strength in the transverse plane at 10 mm from flare exit

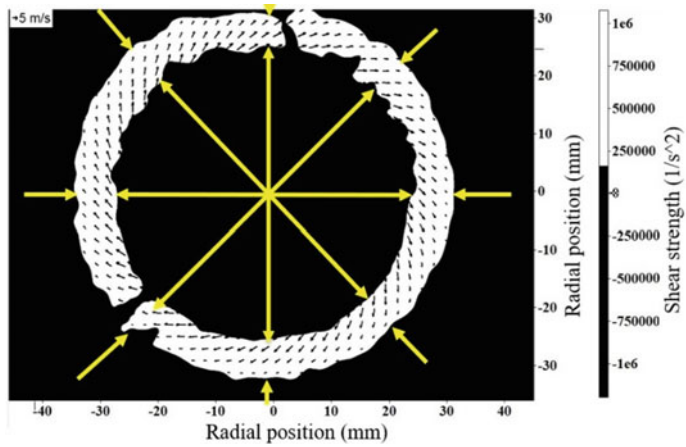
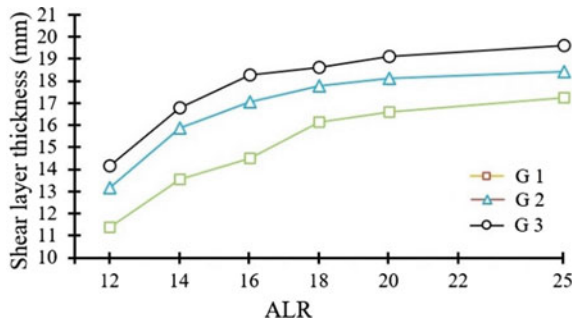


Fig. 11 Shear layer thickness at eight radial locations for airflow field at 10 mm from injector exit

Fig. 12 Variation of shear layer thickness with increasing mass flow rate for different swirl numbers



5 Conclusions

The effect of an increase in the geometric swirl number of the secondary swirler of a rich burn gas turbine fuel injector is investigated experimentally. Three injector geometries are realized using additive manufacturing methods, varying the geometric swirl number of the secondary swirler. Three-component velocity field and the characteristics of CTRZ and shear layers are captured by conducting PIV experiments in the axial and cross planes. The recirculation zone formed at the injector exit by the primary swirler is influenced by the secondary swirl strength. Larger pressure gradients generated by the secondary air swirl resulted in the radial expansion of the CTRZ. Axial, radial, and tangential velocity peaks are maximum in the case of high swirl number geometry. The strength of the shear layer is quantified from PIV data and results showed similar trends.

Further experiments are planned to investigate the effect of shear strength on the atomization characteristics of the injector.

Acknowledgements The experimental works are conducted at the National Centre for Combustion Research and Development (NCCRD), IIT Madras. We thank NCCRD for facilitating diagnostics equipment and Mr. Aravind I B for supporting us while performing experiments.

Nomenclature

ALR	Air to liquid ratio
CTRZ	Central toroidal recirculation zone
h_{pri}	Primary swirler height [mm]
h_{sec}	Secondary swirler height [mm]
θ	Angle of swirler blades [°]
Nd: YAG	Neodymium-doped Yttrium Aluminium garnet
μm	Micro-meter
slpm	Standard liter per minute
CCD	Charged coupled device
μs	Micro-seconds
ML	Mixing length [mm]
E	Shear stress [N/m^2]
X	X-axis in cartesian coordinate
Y	Y-axis in cartesian coordinate
α	Flare angle [°]

References

1. Lefebvre AH, Ballal DR (2010) Gas turbine combustion: alternative fuels and emissions. CRC press
2. Candel S, Durox D, Schuller T, Bourgoquin JF, Moeck JP (2014) Dynamics of swirling flames. *Ann Rev Fluid Mech*
3. KP Shanmugasdas SR Chakravarthy 2017 A canonical geometry to study wall filming and atomization in pre-filming coaxial swirl injectors *Proc Combust Inst* 36 2 2467 2474
4. Rajamanickam K, Pontis A, Kumar KRS, Sivakumar D, Basu S (2019) On the influence of geometrical parameters on the spray characteristics of high shear injectors. *Experimental Thermal Fluid Sci*
5. Mongia HC (2001) A synopsis of gas turbine combustor design methodology evolution of last 25 years. In: *Proceeding of the 15th ISOABE, ISABE—international symposium on air breathing engines, Bangalore, India*
6. Wang S, Yang V, Hsiao G, Hsieh SY, Mongia HC (2007) Large-eddy simulations of gas-turbine swirl injector flow dynamics. *J Fluid Mech* 99–122
7. Giridharan M, Mongia HC, Jeng SM (2003) Swirl cup modeling-part VIII: spray combustion in CFM-56 single-cup flame tube. In: *41st Aerospace sciences meeting and exhibit*, p 319
8. Rajamanickam K, Mukhopadhyay A, Basu S (2018) On primary atomization in propulsive device fuel injectors—a short review. In: *Droplets and sprays*. Springer, pp 117–140
9. Mehta JM, Hyoun SW, Wisler DC (1989) Mean velocity and turbulent flow field characteristics inside an advanced combustor swirl cup, AIAA, Paper No. 89-0215
10. KP Shanmugasdas ES Manuprasad RN Chiranthan SR Chakravarthy 2021 Fuel placement and atomization inside a gas-turbine fuel injector at realistic operating conditions *Proc Combust Inst* 38 2 3261 3268
11. Y Fu J Cai SM Jeng HC Mongia 2005 Confinement effects on the swirling flow of a counter-rotating swirl cup *Turbo Expo Power Land Sea Air* 4725 469 478
12. Gupta AK, Lilley DG, Syred N (1984) *Swirl flows*. Abacus Press. Tunbridge Wells, England
13. Sheen HJ, Chen WJ, Jeng SY, Huang TL (1996) Correlation of swirl number for a radial-type swirl generator, experimental thermal and fluid science, Avenue of the Americas, New York

Effects of Flapping Frequency on the Aerodynamic Performance of the Elliptical Tandem Flapping Wings



Rahul Ranjan, Akashdeep Singh, Jit Sinha, and Sunil Manohar Dash

Abstract The present numerical study investigated the effects of the flapping frequency on the aerodynamic performance of two-dimensional tandem elliptical flapping wings in the presence of incoming flow at a Reynolds number of 5000. We have considered identical front and rear wings, keeping their aspect ratio fixed at 8. The spacing between the wings is fixed as $1c$, where c is the wing chord length. The non-dimensional flapping frequency or Strouhal number, St , is varied from 0.1 to 0.7 to investigate the thrust performance of the tandem flapping wings at various effective angle of attack amplitudes ($\alpha_0 = 10^\circ, 15^\circ, \text{ and } 20^\circ$). It is noticed that upon increasing the St , similar to an isolated wing, the time-averaged thrust coefficient of the front and rear wing increases up to the critical St (St_{cr}), and beyond that, it deteriorates significantly for all the α_0 values. Moreover, the thrust performance of the rear wing is superior to the front wing and isolated wing in $St < St_{cr}$. However, the St_{cr} of the rear wing is found less compared to the front and isolated wing. The combined time-averaged thrust of the tandem flapping wings is always observed to be higher than that of the isolated flapping wing. Additionally, we have thoroughly analyzed the flow physics associated with the aerodynamic performance of the tandem flapping wings.

Keywords Tandem flapping wings · Strouhal number · ANSYS fluent · Dynamic meshing · Shear layer interaction

1 Introduction

Flapping wing-based Micro aerial vehicles (MAVs) and Unmanned underwater vehicles (UUVs) are bio-inspired devices that mimic the locomotive techniques of aquatic and aerial animals. They have primary applications in defense, surveillance, deep sea terrain monitoring, earthquake detections, etc. Moreover, for better maneuverability and stealth capabilities, flapping-based MAVs and AUVs are preferred

R. Ranjan · A. Singh · J. Sinha · S. M. Dash (✉)
Department of Aerospace Engineering, IIT Kharagpur, Kharagpur 718302, India
e-mail: sunilmanohardash@gmail.com

© The Author(s), under exclusive license to Springer Nature Singapore Pte Ltd. 2024
K. M. Singh et al. (eds.), *Fluid Mechanics and Fluid Power, Volume 2*, Lecture Notes in Mechanical Engineering, https://doi.org/10.1007/978-981-99-5752-1_33

over fixed or rotary propeller types. In the realm of insects and aquatic animals, dragonflies and flying fish are classic cases of tandem wing system, where two pairs of wings/fins on either side of the body can flap independently but in a synchronized manner. The tandem wings are advantageous than the single flapping wing in terms of propulsive performance. Furthermore, the flapping frequency (or St) of the natural fliers varies between 0.2 and 0.4, where the rear wing performs better than the single wing. But at higher St , the intense pitching rate of the wing changes the near wake flow pattern significantly, which may alter the propulsive performance. In this study, we focused on a wide range of St for tandem flapping wing's aerodynamic performances.

2 Literature Review

In the past, studies like [1, 2] showed that the dragonflies use their pair of flapping wings on each side of their body to produce twenty times more lift force than their weight of the body. They also can cruise, hover, fly sideways and even backward [3–5]. Reference [6] experimented on two purely pitching hydrofoils and reported almost two times propulsive efficiency of the tandem wing than an isolated wing. This motivated many researchers to focus on the aerodynamic characteristics of tandem wings. There are five principal parameters in tandem wing studies; shape of the foil (shape of the cross-section, aspect ratio, size ratio), the phase angle between heave and pitch, phase difference between front and rear wings, wing spacing, and flapping frequency. The non-dimensional form of flapping frequency or Strouhal number (St) is defined as $= fA/U_\infty$, denoting the oscillating flow mechanisms like number of wing beats per second, where f denotes the oscillation frequency of the airfoil in Hz, i.e., $f = \omega/(2\pi)$, and A is the characteristic width of the wake which is equal to double the heaving amplitude (h_0), i.e., $A = 2 h_0$ [7]. It is also known as maximum excursion of the tip of the wing during a full flapping cycle. Generally, a wing beat comprises of a downstroke for power and lift generation and an upstroke for recovery. In single flapping wing studies, [2, 8–11] analyzed the flapping frequencies of insects, bats, and birds during cruising and reported that they operate within a narrow range of St between 0.2 and 0.4, which gives better thrust performance due to formation of reverse Von—Kármán street.

References [12–14] have analyzed the different near wake characteristics of the tandem foils both following pitching-plunging motions. It is observed that the wake of front wing strongly interacts with rear wing, which corresponds to enhanced aerodynamic forces and propulsive efficiency of the rear wing at some specific phase angles. [15] did a numerical and experimental investigation of the tandem wing by changing the phase angle and wing spacing. They have taken various phase angles ranging from -180° to 180° and four different wing spacing ($1.5c$, $2c$, $3c$, $4c$), where c is the chord length of the front and rear wings. They found that a tandem wing can produce higher thrust than two single isolated wings together, but that depends on where and when the shear layers of the front wing interact with the rear wing. One

of the wing–wake interaction types (constructive vortex interaction) is favorable to thrust generation, in which the shedded shear layer from the front wing crosses the rear wing and takes advantage of the increased effective angle of attack. This advantageous interaction is highly effective during the onset of downstroke. In the other type of wing–wake interaction (destructive vortex interaction), the rear wing stays in front wing’s wake and experiences an increased effective angle of attack. Having said that, the wake-induced velocity sheds the LEV on the rear wing much earlier, consequently thrust performance reduces. The thrust performance of an oscillating airfoil in a tandem configuration is governed by how the vortex shed from the front wing interacts with the rear airfoil. Although previous studies primarily focused on the salient factors responsible for the thrust enhancement of flapping wings in single and tandem wing configurations, the detailed physics of wake interaction in tandem configuration is not fully understood. Hence, examining the flow physics behind the vortex interaction at different St would bridge the research gap and is the aim of the present study.

3 Problem Statement

The downstroke and upstroke of the front and rear wing in a flapping cycle are depicted in Fig. 1. The wings follow a sinusoidal pitching-plunging motion profile as per Eqs. (1)–(4).

$$h_F(t) = h_0 \cos(2\pi ft) \quad (1)$$

$$\theta_F(t) = \theta_0 \cos(2\pi ft + \phi) \quad (2)$$

$$h_R(t) = h_0 \cos(2\pi ft + \varphi) \quad (3)$$

$$\theta_R(t) = \theta_0 \cos(2\pi ft + \phi + \varphi) \quad (4)$$

Here, h_0 is the heaving amplitude ($=0.75C_F$), θ_0 is the pitching amplitude, and f is the flapping frequency. h_F , h_R , θ_F , and θ_R represent the instantaneous heaving locations and geometric pitching angles of the front and rear wings, respectively. The phase difference (denoted by ϕ) between pitching and plunging motion is set as 90° because of higher propulsive efficiency in case of a single flapping wing [16]. The initial phase angle between the front and rear wing (denoted by φ) is selected as 0° degree (in-phase flapping) in this study. The chord length-based Reynolds number (Re) is considered to be 5000 and the corresponding freestream velocity (U_∞) is calculated to be 0.125 m/s considering the fluid medium to water. The spacing between the wings (trailing edge of front wing to leading edge of rear wing, denoted by R) is taken as $1C_F$, which is = 0.04 m. The geometric parameters C_F and C_R are the

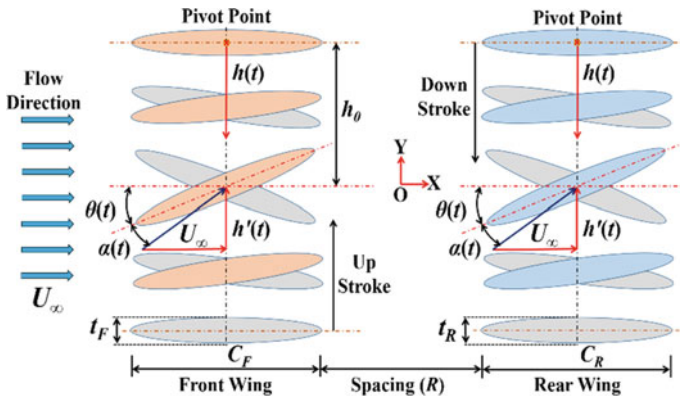


Fig. 1 Schematic diagram showing the downstroke and upstroke of an elliptic airfoil following sinusoidal heaving and pitching motion in tandem orientation

chord length of the front and rear wings, respectively (see Fig. 1). Also, t_F and t_R are the thickness of the front and rear wings, respectively. The aspect ratio (AR) of the front and rear wings, i.e., C_F/t_F and C_R/t_R , is kept constant at 8. The size ratio is defined as $SR = C_F/C_R = 1$. The flapping frequency is varied between 0.1 and 0.7 at an interval of 0.1 for an effective angle of attack amplitudes of $10^\circ, 15^\circ$, and 20° . The pivot location for all the wings is fixed at their geometric center. Note that the pitching amplitude θ_0 for each St is determined following the effective angle of attack expression mentioned in [16].

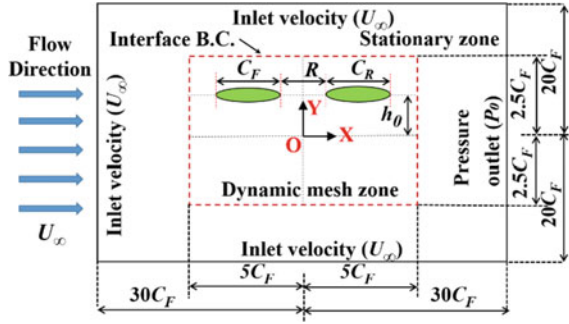
3.1 Numerical Methodology

Numerical simulation of the tandem airfoils was carried out with the help of the Finite Volume Method (FVM)-based CFD solver ANSYS® FLUENT v18.0. The present solver has proven to be highly efficient in solving flapping airfoil applications [17, 18]. In the present study, the conservative integral form of the incompressible governing equation in the Arbitrary Lagrangian–Eulerian (ALE) formulation [19] [see Eq. (5)] is solved in an inertial reference frame.

$$\frac{\partial}{\partial t} \int_{cv} \rho \psi dV + \int_{cs} \rho \mathbf{n} \cdot (\mathbf{v} - \mathbf{v}_g) \psi dS - \int_{cs} \rho \Gamma_\psi \mathbf{n} \cdot \nabla \psi dS = \int_{cv} S_\psi(\psi) dV \quad (5)$$

In Eq. (5), cv and cs correspond to a random control volume and its boundary or control surface. Fluid density, fluid velocity, and mesh velocity are denoted by ρ , \mathbf{v} , and \mathbf{v}_g respectively. Γ_ψ is the diffusion coefficient, S_ψ is the source term of ψ per unit volume, and \mathbf{n} is the normal unit vector to the control surface. Fixing the values of ψ to 1 and \mathbf{v} , the mass and momentum transfer equations can be obtained

Fig. 2 Shows the schematic drawing of the rectangular computational domain



from the general transport equation (i.e., Eq. 5). Similar to the study in [19], we considered the present flow regime turbulent at $Re = 5000$. Here, the one-equation Spalart–Allmaras (SA) turbulent model was used for the unsteady simulation to capture the flow field evolution. To couple the pressure and velocity, a second-order Pressure-Implicit with Splitting Operators [19] (PISO) scheme is utilized. For spatial discretization, a second-order upwind scheme and for time discretization, first-order implicit were used [20, 21]. Double-precision fluent setting is selected to minimize the PC-round-off. For better convergence, the mass and momentum residuals are selected in the order of below $O(10^{-5})$.

The present numerical simulation of the tandem wings is carried out on a rectangular shaped domain of size $60C_F \times 40C_F$, as shown in Fig. 2. The dynamic mesh technique has been utilized to update the mesh around the moving wings inside the dynamic mesh zone. Additionally, mesh deformation and position around the airfoil were controlled by diffusion-based smoothing method setting the diffusion factor as 1. An in-house built user-defined function (UDF) was compiled to get the desired sinusoidal flapping motion of the tandem wings as per Eqs. (1)–(4). Left and right side of the domain is given free stream velocity inlet and zero-gauge pressure outlet boundary conditions, respectively (see Fig. 2). The solution was initialized with the inlet velocity.

3.2 Computational Domain, Mesh Details, and Validation

For the validation of the present CFD solver, an identical tandem flapping wing case in the ref [20] ϕ was considered. Here, the parameters $h_0, \theta_0, f, \phi, U_0, Re, St,$ and $C_F = C_R = R$ are defined as 0.03 m, $30^\circ, 0.667$ Hz, $\pi/2, 0.125$ m/s, 5000, 0.32, and 0.04 m, respectively. Unstructured mesh around the airfoils, along with the inflation layers shown in Fig. 3, was followed in this study. To further check the influence of the mesh resolution on the results, four different meshes (Mesh_1–4) are considered, as shown in Table 1. As shown in Table 1, for Mesh_2, the error percentage of the time-averaged C_T value of the rear wing is below 1%.

Fig. 3 Close-up view of the unstructured mesh and inflation layers around the tandem elliptic airfoils

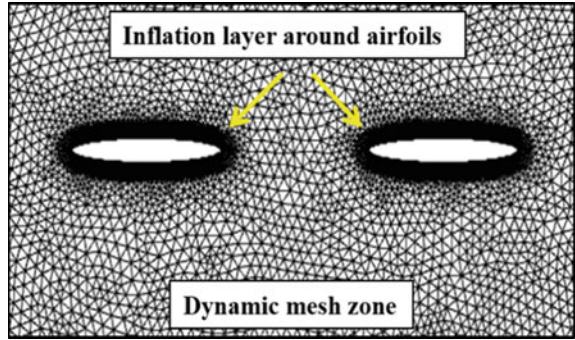
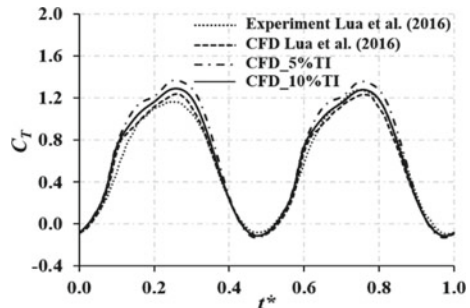


Table 1 Shows the mesh independency study to check the influence of mesh sizes. The error % of the time-averaged C_T of the rear wing is compared for different mesh sizes

Mesh type	Element size	No. of elements	Average C_T	% Error
Mesh_1	0.0005	723,390	0.634042	–
Mesh_2	0.0010	202,972	0.631206	0.449218
Mesh_3	0.0020	652,340	0.628034	0.956643
Mesh_4	0.0040	259,620	0.619299	2.380559

Hence it is selected for the rest of the tandem wing simulations. In addition, we have used Turbulence Intensity (TI) of 5% and 10% for the solver validation. Figure 4 shows the plot of transient thrust (C_T) for the SA model with 10% TI is in good agreement with the experiment results of [1], and it has been used in all our present simulations.

Fig. 4 Comparison of the transient C_T profiles of rear wing, obtained in the present numerical study having 5 and 10% turbulence Intensity (TI) with that of an experimental and numerical study of [1]



4 Results and Discussion

4.1 Time-Averaged Thrust Variation

In the present study, the flapping frequency (St) of the tandem flapping elliptical wings varied from 0.1 to 0.7 at an interval of 0.1 for various effective angles of attack. The plot in Fig. 5 represents the time-averaged C_T as a function of St for single (isolated wing configuration), front, rear, and combination of tandem wings (i.e., an average of the front and rear wing C_T) for $\alpha_0 = 10^\circ, 15^\circ,$ and 20° . It shows that the time-averaged C_T increases with St up to the critical Strouhal number (St_{cr} , vertical dotted lines in Fig. 5); beyond that, it decreases significantly. This trend of the time-averaged C_T variation is observed for the single, front, rear, and combination of tandem wings in the considered parametric space. The front and single wings generate almost the same thrust with minor variations for the entire set of parameters. Whereas, the time-averaged C_T of the rear wing is higher than the single or front wing up to a certain St . At very high St , the rear wing thrust performance deteriorates more than that of the single or front wing. Also, notice in Fig. 5 that St_{cr} for the rear wing appears before the single wing despite generating higher thrust. It is worth noting that the St_{cr} and the peak value of the time-averaged C_T increase with the increase in α_0 . In addition, we have evaluated the time-averaged C_T of the combined front and rear wing, and it follows the same distribution pattern with St as the rear flapping wing.

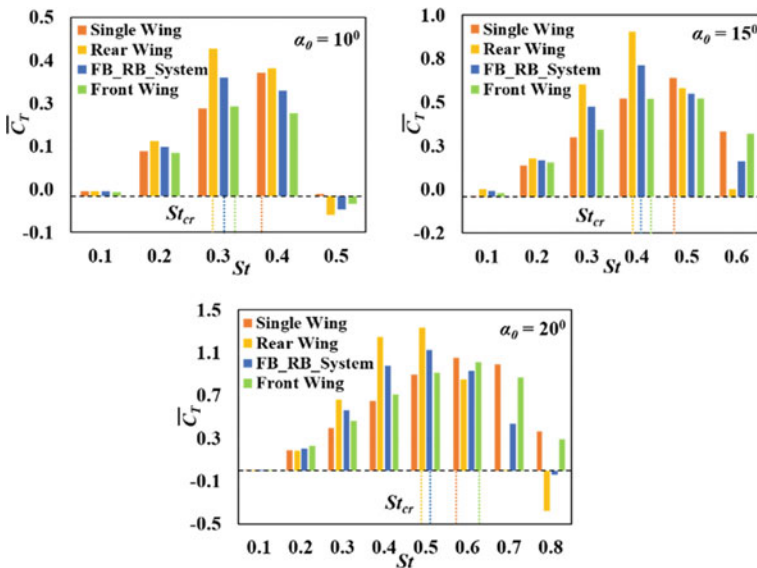


Fig. 5 Plot representing the time-averaged C_T variation of the single, front, rear, and combination of tandem wings with St (0.1 to 0.7) at $\alpha_0 = 10^\circ, 15^\circ,$ and 20° . Dotted vertical lines denote the respective critical St (St_{cr})

Table 2 Categorization of the transient C_T profiles

Transient C_T profile types	Characteristics
Type 1	A parabolic transient C_T profile with a single peak in one flapping stroke
Type 2	A parabolic transient C_T profile with a single peak and flat-edge near the starting of the flapping stroke
Type 2a	A parabolic transient C_T profile with a flat-edge and near the starting of stroke
Type 3	A parabolic transient C_T profile with two valleys in one flapping stroke

We will investigate the transient C_T profiles and associated flow patterns to explain further the time-averaged C_T performance of the tandem flapping elliptic airfoils.

4.2 Transient Thrust Variation

The transient C_T profiles of the front, rear, and single (isolated) wing are primarily categorized into four types, namely Type 1, Type 2, Type 2a, and Type 3. Here, we have considered representative cases to discuss the salient features of different transient C_T profiles (refer to Table 2 and Fig. 6). Type 1 transient C_T profiles can be seen in low St ($< St_{cr}$), where the time-averaged thrust distribution is parabolic with St , which means increases monotonously and then decreases. On the contrary, the Type 2 transient C_T profile is reported at low-medium St ($\leq St_{cr}$). Like Type I, Type II is also similar except a flat edge near the stroke reversal with a higher peak value. Type 2a transient C_T profile mainly occurs at a high-flapping frequency ($St > St_{cr}$) and has one peak and one valley region in one stroke with decreasing trend of time-averaged thrust value. Type 3 transient (C_T) profile is observed at a much higher flapping frequency ($St \gg St_{cr}$) and possesses multiple peaks and in-between valleys in one flapping cycle (upstroke or downstroke). In the upcoming sections, we will try to find out the rear wing's aerodynamic performances compared to the single wing at three different St ($St = 0.2, 0.4, \text{ and } 0.6$) as representative cases.

4.3 Near Wake Flow Pattern at $St = 0.2$

To understand the flow physics at $St = 0.2$, we investigated the pressure and vorticity contours (see Fig. 7) for isolated and tandem wing systems at $\alpha_0 = 15^\circ$ and $t^* = 0.2$. Here, a Type 1 transient C_T profile is observed for the front, rear, and single wing. It is reported that both the front and isolated (single) wings show similar leading edge vortex (LEV) strength toward the leading edge. However, for the front wing, the LEV formation is more delayed than the single wing; that's why the transient

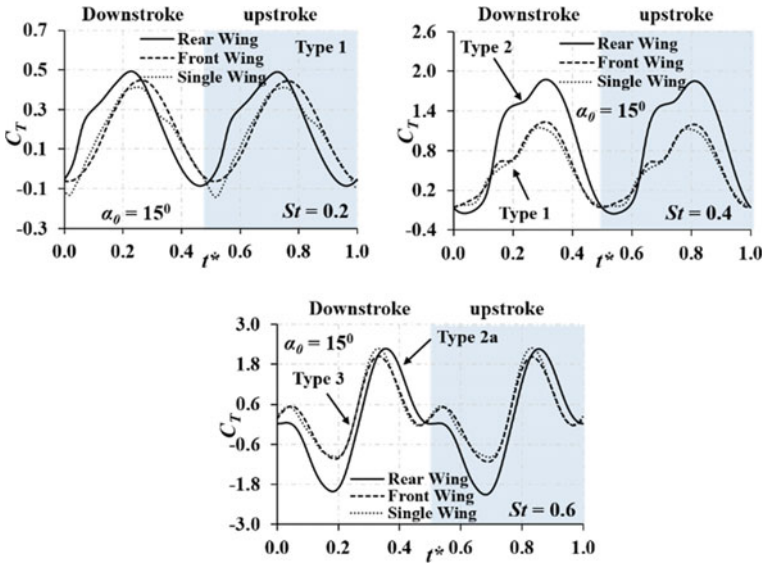


Fig. 6 Different types of transient C_T profiles of the front, rear, and single flapping wing at $\alpha_0 = 15^\circ$ at $St = 0.2, 0.4,$ and 0.6 . $t^* = 0.2$ is the time instance where vorticity and pressure contours are discussed

peak for the front wing attains a higher peak than the single wing. On the other hand, in the presence of the front wing wake, the enhanced LEV on the rear wing creates a higher peak in the transient profile, thus producing a better time-averaged thrust.

At $St = 0.4$, $t^* = 0.2$, similar to $St = 0.2$, the front and single wing exhibits similar LEV strength (refer Fig. 8), which results in the nearly identical transient Type 1 profile. But for rear wing, Type 2 profile is observed. It is important to note that a shear layer shredded from the front wing interacts with the rear wing near the half-chord length, favoring thrust formation (Constructive vortex interaction).

The enhanced LEV on the rear wing and this constructive vortex interaction create a higher transient C_T peak and yield higher time-averaged C_T . For $St = 0.6$, $t^* = 0.2$, the rear wing shows a low-strength LEV on the upper surface and a thrust-reducing suction region on the bottom surface (see Fig. 9). A similar flow regime was observed in [16], where they identified the thrust-reducing suction region formed due to the high pitch rotation rate of the wing at a high-flapping frequency.

In the case of tandem wing arrangement, an intense drag-generating valley region is formed compared to the front or single wing transient profile. As a result, the rear wing aerodynamic performance substantially deteriorates compared to the front and single wing at the high-flapping frequency ($St \gg St_{cr}$). At this high St , for front and single wing, typically Type 3 is observed, but for the rear wing, Type 2a is reported. Details of Type 3 can be referred from [16] and are not discussed here for brevity.

In Fig. 10, we have summarized the observed transient C_T for the front and rear wing with the variation of St and α_0 values considered.

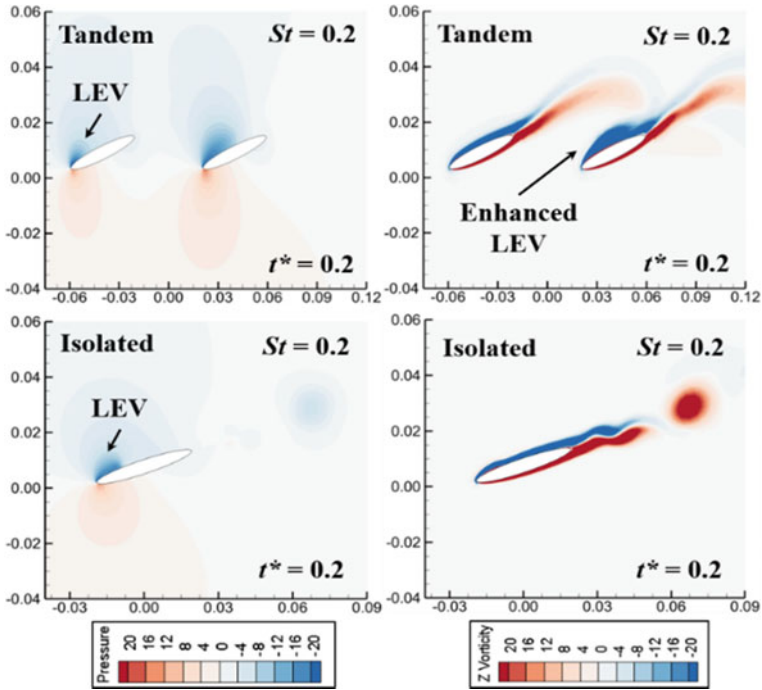


Fig. 7 Pressure and vorticity contours for isolated and tandem wing arrangement at $\alpha_0 = 15^\circ$ at $St = 0.2$, $t^* = 0.2$

In summary, the generation of these transient C_T profiles is mainly due to two factors: around airfoil wake region and pitch velocity. For low-moderate St , the positive impacts of the vertical structures dominate but at $St > St_{cr}$, the diminishing effect of wing pitch velocity becomes prominent, which results in multiple peaks and valleys in the C_T distribution that results in time-averaged thrust reduction. The thrust-reducing valley in the temporal C_T profile augments with increasing St . It is also observed that upon increasing α_0 , the critical Strouhal number (St_{cr}) is also postponed to a greater St (see Fig. 10). This corresponds to higher thrust production even at higher flapping frequency, and that delays the shift of the transient profile from Type 1 to Type 2a and then to Type 3 transient C_T profile.

5 Conclusions

The present study investigates the time-averaged and transient thrust performance of the flapping wings in tandem orientation by varying St in the range of 0.1–0.7, $\alpha_0 = 10^\circ, 15^\circ$, and 20° at $Re = 5000$. It is observed that rear wing’s time-averaged C_T in the tandem flapping arrangement is substantially higher than that of the identical wing in

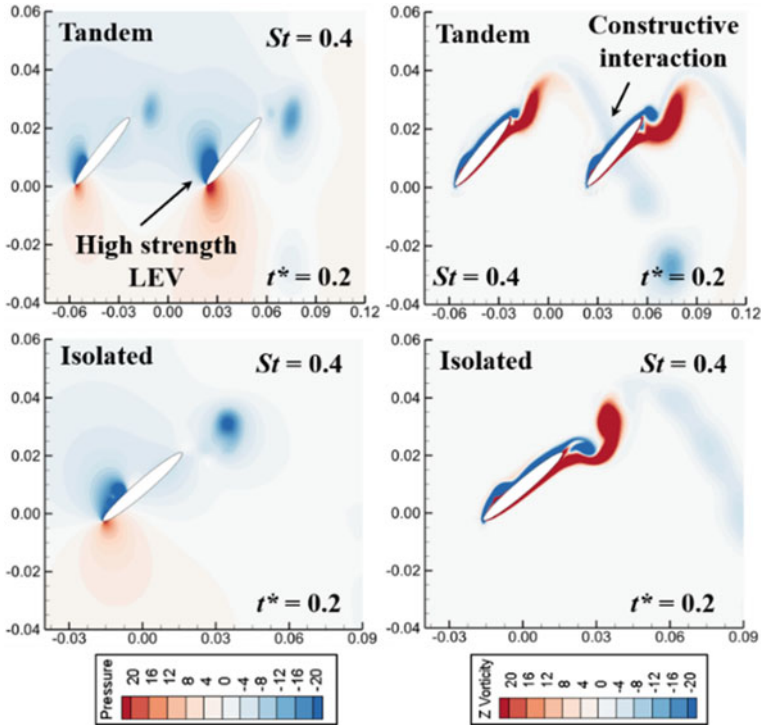


Fig. 8 Pressure and vorticity contours for isolated and tandem wing arrangement at $\alpha_0 = 15^\circ$ at $St = 0.4$, $t^* = 0.2$

a single flapping setup. The increased propulsive performance in the tandem flapping wing is attributed to the constructive relation between shedded shear layer within the front and rear wing and enhanced LEV strength of the rear wing in the presence of the front wing’s wake. These are absent in the single flapping mode. Beyond the critical flapping frequency ($St > St_{cr}$), there is a sharp decrease in the time-averaged C_T of the rear wing compared to the single flapping case due to lower strength LEV which makes the intensified drag-producing valley region in the transient profile. Furthermore, we have classified the transient (C_T) profile into four types based on St and α_0 ; Type 1 corresponds to ($St < St_{cr}$), Type 2 ($St \leq St_{cr}$), Type 2a and Type 3 correspond to ($St > St_{cr}$). Further studies on the characterization of different flow types will be done in future work.

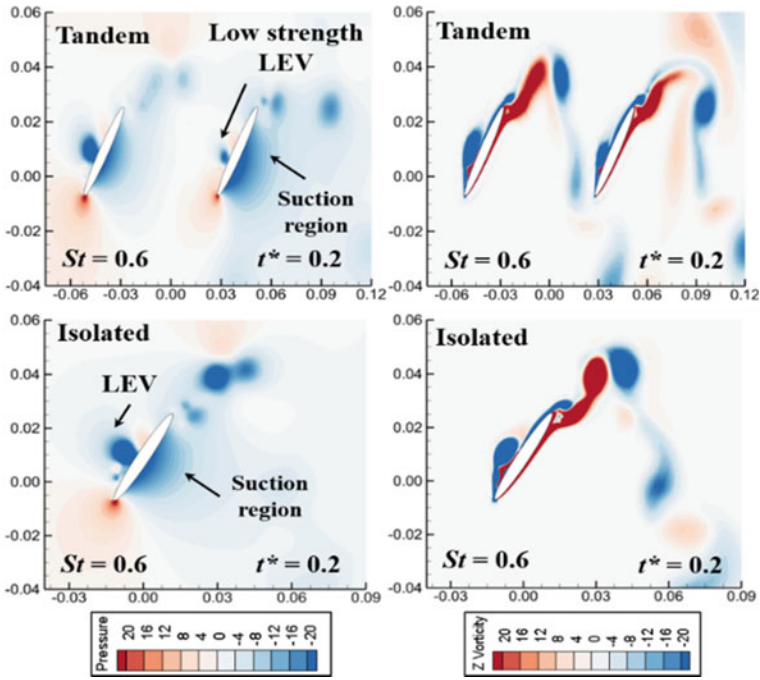


Fig. 9 Pressure and vorticity contours for isolated and tandem wing arrangement at $\alpha_0 = 15^\circ$ at $St = 0.6$, $t^* = 0.2$

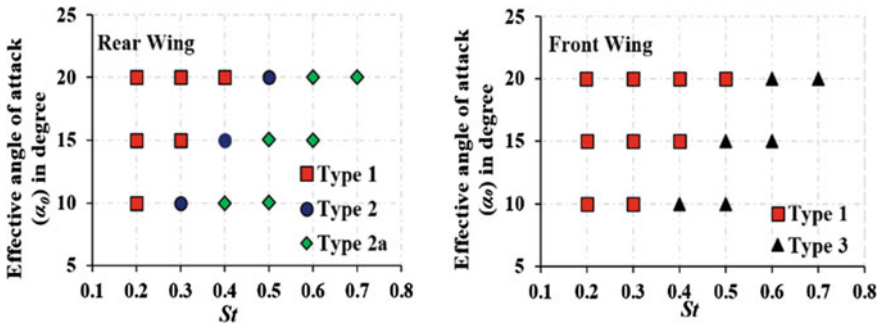


Fig. 10 Characterization of different types of transient C_T profiles of the front and rear wing with the variation of St and α_0

Acknowledgements The authors are indebted to **IIT Kharagpur** for numerical infrastructure, **SERB** (Science and Engineering Research Board), and **ARDB** (Aeronautics Research and Development Board) for providing funding for research.

Nomenclature

A	Width of the wake (m)
c	Chord length (m)
C_T	Thrust co-efficient
f	Flapping frequency (Hz)
h_0	Heaving amplitude
$h_F(t)$	Heaving kinematics of the front wing
L	Span of airfoil v
Re	Reynolds number
St	Strouhal number
t	Physical dimensional time (sec)
T'	Physical flapping cycle time (sec)
U_∞	Free stream velocity (m/s)
ω	Angular flapping frequency (rad/s)
$\theta_F(t)$	Pitching kinematics of the front wing
α_0	Effective angle of attack amplitude ($^\circ$)
θ_0	Pitching amplitude ($^\circ$)
ϕ	Phase angle ($^\circ$)
C_F	Front wing chord length (m)
t_F	Thickness of front wing (m)
R	Spacing of the tandem airfoil (m)
SR	Size ratio

References

1. Lua KB, Lim TT, Yeo KS, Oo GY (2007) Wake-structure formation of a heaving two-dimensional elliptic airfoil. *AIAA J* 45(7):1571–1583
2. Taylor GK, Nudds RL, Thomas ALR (2003) Flying and swimming animals cruise at a Strouhal number tuned for high power efficiency. *Nature* 425(6959):707–711
3. Sinha J, Sreedharan N, Dash SM (2021) Effect of the pivot point locations on the wake dynamics and thrust performance of a flapping elliptic airfoil: a numerical study. In: Prabu T, Viswanathan P, Agrawal A, Banerjee J (eds) *Fluid mechanics and fluid power. Lecture Notes in Mechanical Engineering*. Springer, Singapore. https://doi.org/10.1007/978-981-16-0698-4_21
4. Alexander DE (1984) Unusual phase relationships between the forewings and hindwings in flying dragonflies. *J Exp Biol* 109(1):379–383
5. Thomas ALR, Taylor GK, Srygley RB, Nudds RL, Bompfrey RJ (2004) Dragonfly flight: free-flight and tethered flow visualizations reveal a diverse array of unsteady lift-generating mechanisms, controlled primarily via angle of attack. *J Exp Biol* 207(24):4299–4323
6. Dewey PA, Quinn DB, Boschitsch BM, Smits AJ (2014) Propulsive performance of unsteady tandem hydrofoils in a side-by-side configuration. *Phys Fluids* 26(4):041903. <https://doi.org/10.1063/1.4871024>
7. Triantafyllou MS, Triantafyllou GS, Gopalkrishnan R (1991) Wake mechanics for thrust generation in oscillating foils. *Phys Fluids A Fluid Dyn* 3(12):2835–2837

8. Huang H, Sun M (2007) Dragonfly forewing-hindwing interaction at various flight speeds and wing phasing. *AIAA J* 45(2):508–511
9. Platzer MF, Jones KD, Young J, Lai JCS (2008) Flapping-wing aerodynamics: Progress and challenges. *AIAA J* 46(9):2136–2149
10. Lai JCS, Platzer MF (1999) Jet characteristics of a plunging airfoil. *AIAA J* 37(12):1529–1537
11. Anderson JM, Streitlien K, Barrett DS, Triantafyllou MS (1998) Oscillating foils of high propulsive efficiency. *J Fluid Mech* 360:41–72
12. Sinha J, Dash SM, Lua KB (2023) Effects of the pivot point locations on the propulsive performance of a two-dimensional flapping elliptic airfoil with a pitching angular offset. In: Bhattacharyya S, Benim AC (eds) *Fluid mechanics and fluid power* (Vol. 2). FMFP 2021. *Lecture Notes in Mechanical Engineering*. Springer, Singapore. https://doi.org/10.1007/978-981-19-6970-6_1
13. Birch JM, Dickinson MH (2003) The influence of wing-wake interactions on the production of aerodynamic forces in flapping flight. *J Exp Biol* 206(13):2257–2272
14. Wang ZJ (2005) Dissecting insect flight. *Annu Rev Fluid Mech* 37:183–210
15. Lua KB, Lu H, Zhang XH, Lim TT, Yeo KS (2016) Aerodynamics of two-dimensional flapping wings in tandem configuration. *Phys Fluids* 28(12):121901
16. Sinha J, Lua KB, Dash SM (2021) Influence of the pivot location on the thrust and propulsive efficiency performance of a two-dimensional flapping elliptic airfoil in a forward flight. *Phys Fluids* 33(8):081912. <https://doi.org/10.1063/5.0058923>
17. Ferziger JH, Perić M, Street RL (2002) *Computational methods for fluid dynamics*, vol 3. Springer
18. Dash SM, Nishanth S, Sinha J, Lua KB (2019) Effect of the rear wing size on the thrust performance of the two-dimensional tandem flapping wing. 72nd Annual Meeting of the APS Division of Fluid Dynamics 2019, Abstract: S17.00001
19. De Croon G, De Clercq KME, Ruijsink R, Remes B, De Wagter C (2009) Design, aerodynamics, and vision-based control of the DelFly. *Int J Micro Air Veh* 1(2):71–97
20. Nishanth S, Dash SM, Lua KB (2020) A numerical study on the influence of the rear wing size on the thrust performance of the two dimensional tandem flapping wings. In: 2020 11th International Conference on Mechanical and Aerospace Engineering (ICMAE), Athens, Greece, pp. 77–81. <https://doi.org/10.1109/ICMAE50897.2020.9178898>
21. Sreedharan N, Sinha J, Chavda SD, Dash SM (2023) A numerical study on the effects of wing spacing on the thrust performance of the two-dimensional tandem flapping wings for different rear wing sizes. In: Bhattacharyya S, Benim AC (eds) *Fluid Mechanics and Fluid Power* (Vol. 2). FMFP 2021. *Lecture Notes in Mechanical Engineering*. Springer, Singapore. https://doi.org/10.1007/978-981-19-6970-6_52

Aerodynamic Performance of a Tandem Wing Configuration Inspired from Dragonfly Gliding Flight for MAV Application



Rajosik Adak, Arindam Mandal, and Sandeep Saha

Abstract The design of micro air vehicles (MAVs) involves optimizing aerodynamic performance challenges due to the small size and, consequently, the low Reynolds number ($O(10^4-5)$). MAVs are often inspired by the flight capability of insects and birds; and are mimicked for the design of MAVs. The dragonfly frequently uses a gliding flight mode relative to the other small fliers and operates at a range of $O(10^{2-4})$. The literature suggests that the corrugated profile improves the aerodynamic efficiency around Reynolds number at 10^4 . It allows us to investigate the aerodynamic advantages of tandem corrugated airfoil inspired by the dragonfly wing. In this paper, we perform direct numerical simulations of flow past bio-inspired corrugated wing to understand the impact of the tandem wing configuration. The horizontal distance between the wings is fixed, and the vertical distance varies. The results reveal that the forewing/hindwing interaction increases the lift of the forewing relative to the isolated wing for all the case studies. The combined drag coefficient drops by $\approx 7\%$, and overall efficiency drops by $\approx 13\%$ relative to an isolated wing for a case study with zero vertical spacing between forewing and hindwing at 3° angle of attack, fixed for both wings. With no vertical gap, the aerodynamic efficiency matches close to the isolated wing with the decrease in tandem wing combined drag coefficient compared to an isolated wing.

Keywords Micro aerial vehicle · Dragonfly · Corrugated wing · Tandem configuration

1 Introduction

Micro aerial vehicles (MAVs) are designed to perform a wide range of tasks, such as aerial surveillance, inspection of infrastructure, and search and rescue missions. The MAV provides a valuable asset in gathering real-time data, enabling one to act

R. Adak · A. Mandal · S. Saha (✉)
Department of Aerospace Engineering, IIT Kharagpur, Kharagpur 721302, India
e-mail: ssaha@aero.iitkgp.ac.in

appropriately in hostile situations. An effective MAV is a crucial requirement for the coming generation with its increasing use in defence and disaster management. The key requirement for MAV development is low cost, portability, small size, and ease of operation. MAVs come in different configurations, including fixed-wing, rotary-wing, and flapping wing, each suited for specific requirements. The fixed-wing MAVs are used for long-range missions due to their gliding flight mode limitations. The rotary and flapping wings are primarily designed for low-speed indoor conditions. This paper focuses on fixed-wing MAVs. The MAVs are limited to less than 15 cm and have an operational speed of around 10 m/s [3]. The flow around the fixed-wing MAVs lies in the regime of Re around $O(10^4)$ – $O(10^5)$. The use of conventional aircraft wings degrades its performance at this low Re [20]. Thus, there is a requirement for an optimized airfoil design for the MAV wing. These provide an opportunity to understand the aerodynamics of the natural fliers, which already possess an optimized wing. The regime of operating Re for insect's flier is in $O(10^2)$ – $O(10^4)$, which is close to MAVs operating Re [12]. Among the insects, dragonflies, locusts, and butterflies use a gliding mode of flight more frequently and show better steady-state aerodynamics than other insects [19]. Dragonflies have two sets of wings: Forewings and hindwings can move independently, allowing them to outmaneuver other insects [13]. Also, the dragonfly glides up to forty-chord lengths per flapping cycle, more significantly than any other insect. This low-cost gliding flight allows them to migrate across the Indian sub-continent to eastern Africa [1]. Investigation of the gliding mode of flight in the operational range of MAVs is required for adaptability for MAVs.

The dragonfly wing has distinct corrugated textures due to the network of veins and cuticle membrane [6]. Studies on the corrugated airfoil wing inspired by dragonflies found negative and positive feedback regarding its comparison to profiled airfoil and flat plate in aerodynamic efficiency. Investigation at low $Re \leq 2000$ has produced no significant advantage over a flat plate or profiled airfoil [4, 9, 10, 15, 17]. At low Re , the flow over the airfoil remains attached and does not cause separation. The trapped vortices in the valley increased pressure drag and thus decreased the lift-to-drag ratio for the corrugated airfoil. With the increase of Re , there is an increase in the separation region over all the airfoil. At moderate Re of $O(10^4)$, the corrugated at the leading-edge acts as a turbulent generator, which promotes early transition to turbulence [17]. These vortices trapped in the valley extract energy from the free stream to provide into the boundary layer to discourage separation and exhibit goodstall characteristics. These cause improvement in the performance of corrugated wings [2, 7, 16, 17]. Murphy and Hu [11] conducted an experimental investigation and found better performance at $Re \leq 10^5$. The previous studies suggest exploring the feature of preventing large flow separation of the corrugated wing in the regime of Re in $O(10^4)$ for MAVs.

Studies on the corrugated wing are done on a single lone airfoil. The dragonfly in gliding mode involves the interaction of forewings and hindwings. Previous studies on tandem wings are mostly done to understand the wing's interaction in the flapping mode of flight. The reader can refer to the review paper on the characteristics of tandem and corrugated wings [9]. Zhang and Lu [21] investigated tandem plate configuration for $Re \leq 2000$. They reported that the tandem configuration had

enhanced the lift and reduced drag compared to the isolated wing. It encourages an investigation of the corrugated wing in the tandem configuration at the range of $Re \sim 10^4$. In this paper, we have done a direct numerical solution (DNS) for a corrugated wing inspired by the dragonfly wing in the tandem configuration to analyze the forewing–hindwing interaction and its performance relative to the isolated wing.

2 Methodology

Direct numerical simulations (DNS) are performed with Incompact3d (www.incompact3d.com). Incompact3d is an open source, MPI-based fortran90 code, incompressible flow solver with spatial discretized with a sixth-order finite difference compact scheme and third-order Adams–Bashforth scheme for time discretization, combined with immersed boundary method [8]. The governing equations are the forced incompressible Navier–Stokes equations.

$$\partial u / \partial t = -\nabla p - \frac{1}{2} [\nabla(u \otimes u) + (u \cdot \nabla)u] + \nu \nabla^2 u + f \quad (1)$$

$$\nabla \cdot u = 0 \quad (2)$$

where $p(x, t)$ is the pressure field (for a fluid with a constant density $\rho = 1$) and $u(x, t)$ is the velocity field. In these forced Navier–Stokes equations, the forcing field $f(x, t)$ is used through an immersed boundary method.

2.1 Mesh Design, Boundary Condition, and Simulation Setup

Initially, DNS for an isolated wing inspired by the dragonfly wing was performed. A grid size of $n_x \times n_y \times n_z = 9601 \times 801 \times 6$, equivalent to 46 million nodes, is used for the solution for an isolated dragonfly at low Re . The mesh is uniform on the x -axis and z -axis, and stretched on the y -axis. The domain was $16c \times 20c \times 0.02c$ in the x , y , and z directions, respectively, where c denotes the chord length of the airfoil. A convective boundary condition at the outlet and free-slip condition on the side of the domain with the uniform flow at the inlet is employed. The periodic boundary condition is set for the spanwise direction of the wing. The simulation has produced results for $Re = 1000$, similar to the literature (ref. Figs. 1 and 2). The analysis of an isolated dragonfly wing was done for further analysis and comparison to the tandem configuration at our selected operating Re at 10^4 .

A methodology is adapted for DNS to use the RANS solution as a Dirichlet boundary condition. This methodology has shown excellent results for the low angle of attack and away from the stall [5, 18]. Initially, a RANS solution was performed using SU2 open source code (<https://su2code.github.io/>). The RANS simulation

Fig. 1 Numerical results performed for an isolated corrugated profile: time average lift (C_L) versus α (ref. [4, 7, 14])

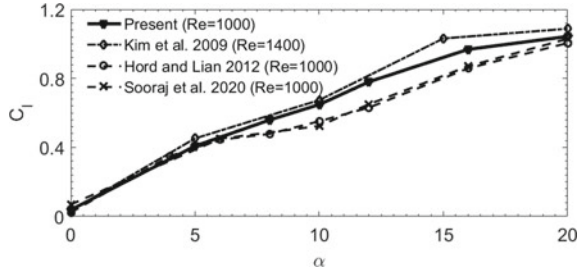
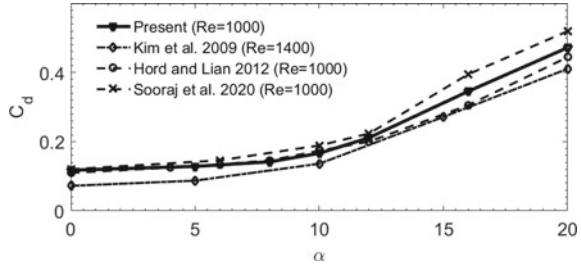


Fig. 2 Numerical results performed for an isolated corrugated profile: time average Lift (C_D) versus α (ref. [4, 7, 14])



involves a large extended domain (refer Fig. 3). This RANS result is used to extract velocity distribution at near-field flow. These data are imposed as Dirichlet boundary conditions for DNS. Results from the DNS with this adapted methodology (DNS_R) and the DNS results (≈ 46 million) from a previous study on an isolated wing are compared, as shown in Fig. 4.

2.2 Problem Definition

The Corrugated profile is obtained from Kesel et al. [6]. RANS for two-dimensional tandem configuration is conducted with 146,979 elements. The maximum y^+ value is 3.4 on the surface of the airfoil. The velocity distribution for boundaries of the DNS domain is interpolated from RANS results. Note that the outlet boundary condition is set with a convective boundary condition. The computational domain for DNS_R is set with $9c \times 4c \times 0.02c$ in the x , y , and z -axis (ref. Fig. 3) with a grid size of $n_x \times n_y \times n_z = 4801 \times 801 \times 6$ (23 million). The finest mesh spacing is $0.001c$ in the center of the domain. In this paper, the DNS for tandem configuration with the horizontal distance between the tandem airfoil is fixed at $G = 1.2c$. The vertical gap varies from $-0.2c$ to $0.1c$. The angle of attack for both of the tandem airfoils is kept the same in each case study, i.e., $\alpha_1 = \alpha_2 = \alpha$.

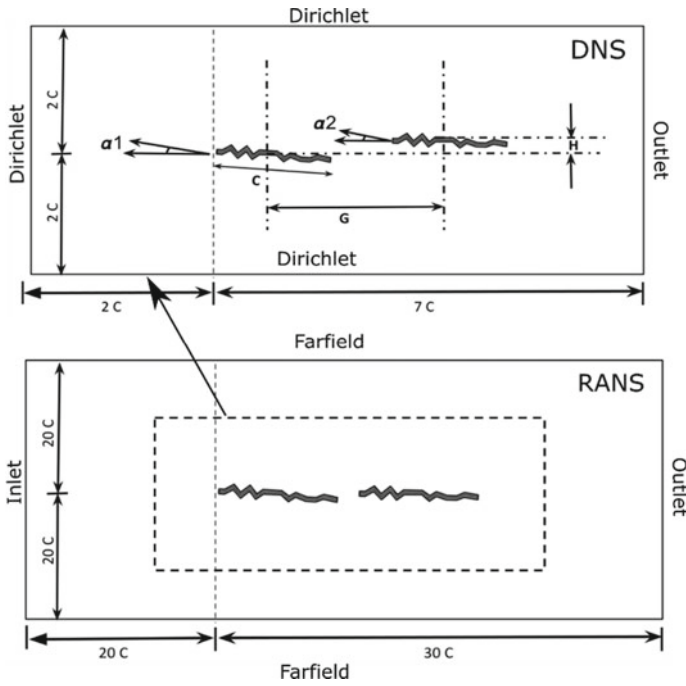


Fig. 3 Problem statement for the flow past a tandem corrugated wing. The schematic diagram for the direct numerical simulation. Down: the computational domain for RANS simulation. Up: the computational domain for the DNS with Dirichlet boundary values interpolated from the RANS solution

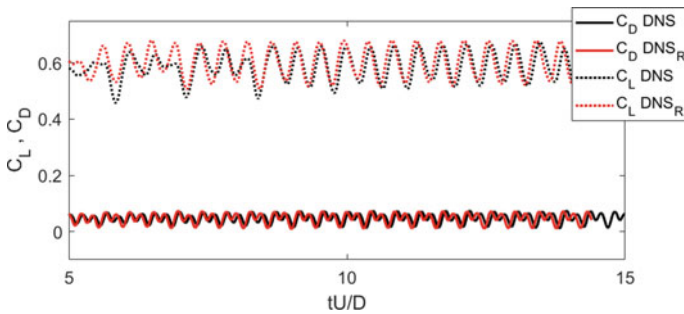


Fig. 4 Comparison of the time history of C_L, C_D in between the DNS- and RANS-assisted Dirichlet boundary value DNS

3 Results and Discussion

The effect of tandem configuration with vertical spacing was investigated. The chord Reynolds number is set at 10^4 . For all the case studies, the horizontal difference between the wing is fixed at $1.2c$. Here, we emphasize understanding the effect of the vertical offset in the tandem configuration at a low angle of attack. The methodology uses the RANs results as Dirichlet boundary conditions for the DNS allowed us to reduce the computational mesh point and thus reduce the computational time. Time average lift and drag coefficient of forewing and hindwing for various values of H , and at $\alpha = 3^\circ, 5^\circ$, are shown in Fig. 5. The simulations have been run for 12.8 chord flow time units. The last ten chord flow units have been considered for calculating the average value.

In Fig. 5, looking into the case study of $\alpha = 5^\circ$, the lift of the forewing has drastically deteriorated with an increase in value of H , while the hindwing shows a negligible change in lift. A similar trend is observed for $\alpha = 3^\circ$. Note that the negative

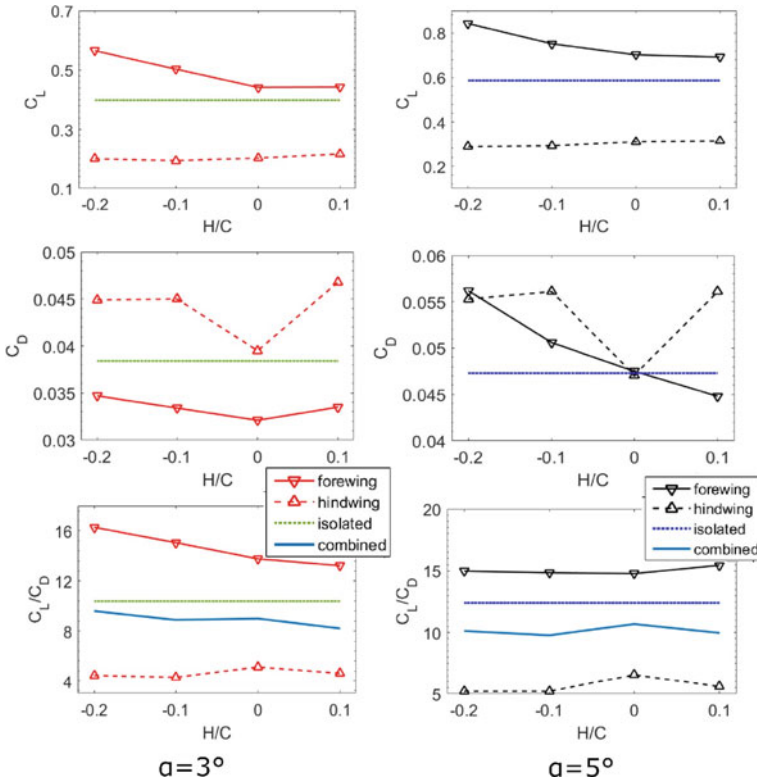


Fig. 5 Time average aerodynamic coefficient ((a) C_L , (b) C_D) and efficiency (C_L/C_D) in tandem configuration in comparison to an isolated wing. The right-hand figures represent the case study for $\alpha_1 = \alpha_2 = 5^\circ$, whereas the left-hand figure represents the case study for $\alpha_1 = \alpha_2 = 3^\circ$

value of H indicates that the hindwing is relative in the lower vertical position with respect to the forewing. The drag characteristic shows the forewing drag successively reducing with the increase in value of H . Except at $H = 0.1c$, in the case study of $\alpha = 3^\circ$ the C_D has increased from its previous value at $H = 0c$. For the hindwing, the drag coefficient dips for $H = 0$, indicating fore/hind wing interaction leading to more chaotic shedding of the vortex. The vortex shedding from the forewing pairs with those shedding from the hindwing, as shown in Fig. 6. In the cases of $H = 0.2c$, the vortex shedding from each of the individual wings remains distinguishable downstream of the flow. Whereas in the case of $H = 0c$, the vortices from the forewing seem to interact with the hindwing, releasing combined vortices.

A comparison has been made to an isolated wing, where the wing area of the isolated wing is considered the same compared to the tandem configuration. The lift generated on the forewing is higher w.r.t the isolated wing in all scenarios. Whereas the hindwing generates lesser lift w.r.t the isolated wing. Also, the forewing experiences less drag w.r.t to the isolated wing for $\alpha = 3^\circ$. In Table 1, a case study has been shown. With tandem configuration, the lift of the forewing increases along with a decrease in drag relative to the isolated wing. With the vertical distance between the wing reduced to zero, the drag characteristics have changed drastically. Interestingly, the drag of the combined tandem wing produced is lesser than that of an isolated wing without compromising much of its efficiency. This observation has pointed out to possible understanding that the tandem arrangement of the wing allows for reducing the drag while possessing enough lift for its weight to glide.

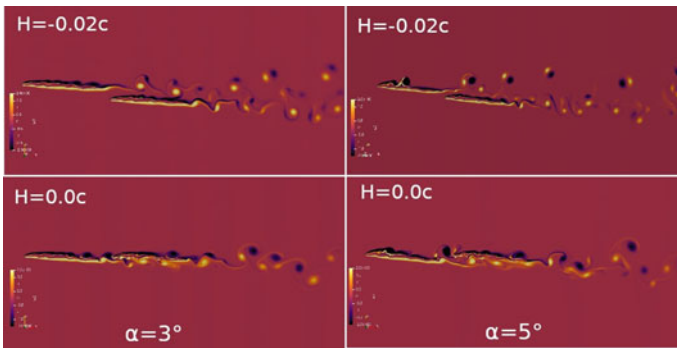


Fig. 6 Vorticity plot of the tandem corrugated wing configuration at two different value of H . (Left) $\alpha = 3^\circ$, (Right) $\alpha = 5^\circ$

Table 1 Comparison of isolated wing to tandem wing at $\alpha = 3^\circ, H = 0.0c$

	C_L	C_D	C_L/C_D
Forewing	0.4420	0.0321	13.7695
Hindwing	0.2024	0.0395	5.1241
Combined wing	0.3222	0.0358	9.00
Isolated wing	0.399	0.0384	10.39

Table 2 Comparison of isolated wing to the combined tandem-wing at $\alpha = 3^\circ$

H	C_L	C_D	C_L/C_D
0c	0.3222	0.0358	9
-0.1c	0.3480	0.0392	8.89
-0.2c	0.3825	0.0398	9.6
0.1c	0.3295	0.0402	8.2
Isolated wing	0.3990	0.0384	10.39

In Table 2, the comparative study of the aerodynamic performance is done on the isolated wing w.r.t the combined wing for $\alpha = 3^\circ$. The averaged value of the combined efficiency drops by $\approx 12\%$ relative to the isolated wing for the non-positive value of H , and the average value of the drag coefficient is similar to the isolated wing. At $H = 0.1c$, the efficiency drops by $\approx 21\%$. These results reflect that the configuration with the hindwing at the lower vertical distance w.r.t the forewing shows better aerodynamics.

4 Conclusions

A Direct numerical simulation is conducted on the tandem corrugated wing inspired by the dragonfly. Understanding the natural selection of gliding as a frequently used flight mode for dragonflies is likely to result in using the tandem configuration for MAVs. A methodology is adapted to use the results of the RANS simulation as a near-boundary velocity field for DNS. The results are verified with the DNS in a large domain. The tandem configuration is compared to the isolated wing to understand its advantages. The paper reported an increase in the lift for the forewing in the presence of the hindwing. Whereas the lift drops for the hindwing relative to the isolated wing. A reduction in the overall drag coefficient w.r.t the isolated wing for zero vertical distance between the forewing and hindwing is reported. The interaction between the forewing/hindwing has increased at a vertical distance close to zero. For the case study, with the hindwing positioned below the forewing at $\alpha = 3^\circ$, the average combined efficiency drops by $\approx 12\%$ relative to an isolated wing. Whereas the combined wing drag remains equivalent to the isolated wing. Exceptionally at zero vertical position, the combined wing drag drops by $\approx 7\%$. Thus, the tandem configuration reduces drag in specific arrangements during the gliding mode of flight, in addition to excellent maneuverability known from the literature.

Acknowledgements We acknowledge the PARAM Shakti at IIT Kharagpur supercomputing facility, part of the National Super Computing Mission, Government of India, for their support in fostering this research.

Nomenclature

C_D	Drag coefficient
C_L	Lift coefficient
H	Vertical Gap between the tandem airfoil (c)
α	Angle of attack ($^\circ$)

References

1. Charles Anderson R (2009) Do dragonflies migrate across the Western Indian Ocean? *J Trop Ecol* 25(4):347–358
2. Barnes CJ, Visbal MR (2013) Numerical exploration of the origin of aerodynamic enhancements in [low-reynolds number] corrugated airfoils. *Phys Fluids* 25(11):115106
3. Hassanalian M, Abdelkefi A (2017) Classifications, applications, and design challenges of drones: a review. *Progr Aero Sci* 91:99–131
4. Hord K, Liang Y (2012) Numerical investigation of the aerodynamic and structural characteristics of a corrugated airfoil. *J Aircraft* 49(3):749–757
5. Hosseini SM, Vinuesa R, Schlatter P, Hanifi A, Henningson DS (2016) Direct numerical simulation of the flow around a wing section at moderate Reynolds number. *Int J Heat Fluid Flow* 61:117–128
6. Kesel AB, Philippi U, Nachtigall W (1998) Biomechanical aspects of the insect wing: an analysis using the finite element method. *Comp Biol Med* 28(4):423–437
7. Kim WK, Ko JH, Park HC, Byun D (2009) Effects of corrugation of the dragonfly wing on gliding performance. *J Theor Biol* 260(4):523–530
8. Laizet S, Lamballais E (2009) High-order compact schemes for incompressible flows: a simple and efficient method with quasi-spectral accuracy. *J Comput Phys* 228(16):5989–6015
9. Lian Y, Broering T, Hord K, Prater R (2014) The characterization of tandem and corrugated wings. *Prog Aerosp Sci* 65:41–69
10. Meng XG, Sun M (2013) Aerodynamic effects of wing corrugation at gliding flight at low Reynolds numbers. *Phys Fluids* 25(7):071905
11. Murphy JT, Hu H (2010) An experimental study of a bio-inspired corrugated airfoil for micro air vehicle applications. *Exper Fluids* 49(2):531–546
12. Nick Pornsin-Sirirak T, Tai YC, Nassef H, Ho CM (2001) Titanium-alloy MEMS wing technology for a micro aerial vehicle application. *Sens Actuators Phys* 89(1–2):95–103
13. Salami E, Ward TA, Montazer E, NikGhazali NN (2019) A review of aerodynamic studies on dragonfly flight, proceedings of the institution of mechanical engineers. Part C *J Mech Eng Sci* 233(18):6519–6537
14. Sooraj P, Sharma A, Agrawal A (2020) Dynamics of co-rotating vortices in a flow around a bio-inspired corrugated airfoil. *Int J Heat Fluid Flow* 84:108603
15. Tamai M, Wang Z, Rajagopalan G, Hu H, He G (2007) Aerodynamic performance of a corrugated dragonfly airfoil compared with smooth airfoils at low Reynolds numbers. In: 45th AIAA aerospace sciences meeting and exhibit, p 483
16. Tang H, Lei Y, Li X, Fu Y (2019) Numerical investigation of the aerodynamic characteristics and attitude stability of a bio-inspired corrugated airfoil for MAV or UAV applications. *Energies* 12(20):4021
17. Vargas A, Mittal R, Dong H (2008) A computational study of the aerodynamic performance of a dragonfly wing section in gliding flight. *Bio-Inspiration and Biomimetics* 3(2):026004

18. Vinuesa R, Hosseini SM, Hanifi A, Hen-Ningson DS, Schlatter P (2015) Direct numerical simulation of the flow around a wing section using high-order parallel spectral methods. In: 9th International symposium on turbulence and shear flow Phenomena, Begel House Inc.
19. Wakeling JM, Ellington C (1997) Dragonfly flight. I. Gliding flight and steady-state aerodynamic forces. *J Experiment Biol* 200(3):543–556
20. Winslow J, Otsuka H, Govindarajan B, Chopra I (2018) Basic understanding of airfoil characteristics at low Reynolds numbers (10^4 – 10^5). *J Aircraft* 55(3):1050–1061
21. Zhang J, Lu XY (2009) Aerodynamic performance due to forewing and hindwing interaction in gliding dragonfly flight. *Phys Rev E* 80(1):017302

Aeroacoustic Characteristics of the Supersonic Free Jet at Mach Number 1.6



K. Manikandan, Jeevitha Jagajeevan, M. Aruna Priyadharshini,
Rajarshi Das, and P. Booma Devi

Abstract The goal of this research is to look at the aeroacoustic properties of optimum and non-optimum expansion characteristics of a Mach 1.6 free jet. The single jet of cold flow has been studied to better understand its aerodynamic and acoustic properties. To demonstrate the various expansion modes of the jet, the nozzle pressure ratios (NPRs) that were considered are 3.25, 4.25, and 5.25. The acoustic oscillations produced by these jets illustrate that the NPR has a substantial impact on the jet's acoustic signature. The shock-cell behavior of the off-design operating jet was evaluated using the centerline Mach number decay and numerical shadowgraph methods. The overexpanded and underexpanded jets' severe Mach number fluctuation virtually starts at $X/De = 4$; the variations travel downstream until the jets are fully expanded. The oscillation ends at $X/De = 9$ for the overexpanded jet, but at $X/De = 13$ for the underexpanded jet. The total shock-cell length of the underexpanded jet is 37% longer than the overexpanded free jet. The observed sound pressure level (SPL) for various microphone locations demonstrates the jet's directivity. The SPL at 45° fluctuates significantly all across the frequency scale. The angles from 15° to 90° exhibit maximum SPL values between 125 and 170 dB. As the angle of the microphone increases from 15° to 90° , the maximum value of the SPL decreases. Also, the nature of variations of the SPL is virtually identical for the microphone locations of 30° , 60° , and 90° , whereas the remaining locations show a different trend along the frequency scale.

Keywords Aeroacoustics · Free jet · Shadowgraph · Sound pressure level

K. Manikandan (✉) · J. Jagajeevan · M. A. Priyadharshini · R. Das
Department of Aerospace Engineering, School of Mechanical Engineering, SASTRA University,
Thanjavur 613401, India
e-mail: manikandan@mech.sastra.edu

P. B. Devi
Department of Aeronautical Engineering, Sathyabama Institute of Science and Technology,
Chennai 600119, India

1 Introduction

The aviation sector has seen tremendous expansion in the past and present, paving the way for the development of high-thrust-to-weight-ratio jet engines for commercial and military use. To achieve the high thrust demand, these engines require proper expansion of the exhaust jet into the still environment. The contact of these high-speed jets with atmospheric air, on the other hand, can cause a large pressure fluctuation, which can result in sound waves. The three primary noise components that dominate the acoustic nature of these free jets are shock-associated noise, turbulent mixing noise, and screech. The ability to fine-tune jet intensity requires a deeper understanding of these noise component properties, and noise reduction can be beneficial to the environment. In recent years, the problem of jet noise prediction has been numerically solved through a wide range of methods.

Barbarino et al. [2] performed the computational aeroacoustics approach (i.e., Stochastic Noise Generation and Radiation), based on CFD Reynolds averaged Navier–Stokes (RANS) solutions to noise prediction and reduction from the subsonic jets. The 3D model was solved using RANS equations with turbulence accounted for through $K-\epsilon$ and $K-\omega$ Shear Stress Transport (SST) models. The results show that the RANS analysis results are in fairly good agreement with experimental data and the Large-Eddy Simulations (LES) results of the free jet. Andersson et al. [3] carried out the analysis on the axisymmetric model by the LES combined with Kirchhoff surface integration. The turbulent kinetic energy prediction close to the nozzle exit using LES is slightly higher than the measured values and one from the RANS, which leads to the prediction of the shorter region of potential flow. Furthermore, the predicted sound pressure levels (SPLs) obtained using the RANS method were shown to be fairly lower than the measured levels of the free jet. Niklas et al. [4] explored the 3D LES of a compressible jet of Mach 0.75 with the Reynolds number 5.0×10^4 . Two conditions were simulated, an isothermal and a higher temperature jet. SPLs in the far-field were evaluated using Kirchhoff surface integration. Predicted SPLs were in excellent agreement with the measured values for both jets using the RANS method. Mankbadi et al. [7] investigated the ability of LES for predicting flow features and noise from a supersonic jet. The 2D axisymmetric model was used to qualitatively evaluate the free jet flow behavior and its acoustic signature. The time-dependent flow structures were recorded to represent the sound source; Lighthill's theory was utilized to calculate the far-field noise, with the sound source obtained from the calculated time-dependent near field. Tide et al. [5] carried out the numerical simulations of 3D round, compressible, turbulent jets of Mach 0.75 using the SST $K-\omega$ model to understand the acoustic benefits of the chevron effect. The three-dimensional calculation is done using a tetrahedral mesh with 0.9 million cells. Two jets, one cold and hot, are simulated; SPLs at far-field observer locations have been calculated using Ffowcs Williams–Hawking's (FWH) acoustic model equation. The Unsteady Reynolds averaged Navier–Stokes (URANS) calculations are not able to predict the absolute values for the overall SPL but predict trends reasonably well. Moreover,

the present simulation shows that the SST $K-\omega$ model can predict mean, turbulence quantities as well as trends in acoustic quantities of the free jet.

Rajarshi Das et al. [6] explored the induced pressure fluctuations by cavities under different thermal conditions at Mach 2.08. Steady and unsteady simulation is done using density-based URANS formulation; the density-based solver is adopted due to the compressible nature of high Mach number flows. The gathering of mesh was done near the wall to give a $y^+ \sim 1$ for the steady solutions. The Power Spectral Density (PSD) was calculated using Fast Fourier Transform (FFT). Chen et al. [8] performed the LES simulation to study the flow field and acoustic characteristics of a rectangular supersonic jet. The focus is to study the high-temperature effects on the jet. The multi-block structured mesh was used, the grid points are amassed in the jet region where large flow gradients are possible, and it is stretched slowly in both the axial and radial directions in the mesh domain. Also, the mesh has a first layer thickness with a $y^+ \sim 1$. Martelli et al. [1] studied the complex turbulent flow separation for sub-scale parabolic nozzles. The analysis of the nozzle flow field is performed by 2D axisymmetric time-accurate perfect gas RANS solver. The subsonic inflow condition is imposed at the nozzle inlet (i.e., total temperature and total pressure), adiabatic wall, assigned pressure, and non-reflecting boundary condition on the upper and on the right side, respectively. Hence, complex phenomena (i.e., free jet aerodynamic and aeroacoustic) can be simulated using the 2D axisymmetric model with sensible accuracy. Indeed, a minimum first cell distance normal to the nozzle wall (i.e., y^+) is preferred for along the nozzle wall to where the viscous and gradient effects are significant.

2 Computational Methodology

The research technique is separated into two parts. The first component involves running steady and unsteady simulations to record mean-flow characteristics and time-series acoustic pressure data. The SPL of an input from all microphones is calculated in the second section using time-series pressure data and the FFT. To reach the design Mach number of 1.6, the nozzle contour was created using the method of characteristics (MOC) for an area ratio of 1.24 (i.e., $A_e / A_t = 1.24$). Using the Area-Mach number relation, the area ratio for the relevant design Mach number has been determined by Eq. (2). Three different Nozzle Pressure Ratios (i.e., NPR) of 3.25, 4.25, and 5.25 are used to simulate the over, ideal, and underexpanded jet. For this investigation, a 2D axisymmetric model is preferred. In addition, to ensure far-field, the computational domain is expanded up to $40D_e$ on the XY plane. Figures 1 and 2 show the entire domain as well as near-wall mesh details. Similarly, Fig. 3 depicts the boundary condition in further detail. Near the wall, a fine mesh is desirable because it allows the solver to realistically capture flow behavior near the wall (i.e., boundary layer growth). Similarly, fine mesh is used to anticipate free jet growth downstream in places such as the core-jet and shear layer (i.e., large pressure gradients). Correspondingly, a smaller first cell distance along the nozzle wall is

desirable [1, 6, 8], and in this study, it was kept below or equal to 5 (i.e., $y^+ \sim 5$). The aspect ratio is the cell's longest length to shortest length and the ideal aspect ratio is 1 [6, 8]. The average aspect ratio of the mesh was maintained at 3 which ensures the quality of the mesh element and the worst cell was found to be only one element with an aspect ratio > 4 . The nozzle inlet was subjected to a pressure inlet condition, and the total pressure was computed using the isentropic relation 1. The nozzle wall has a no-slip adiabatic wall condition, whereas the remaining boundaries get an atmospheric condition. With an ideal gas assumption of a total temperature of 300 K (i.e., Cold flow), the density-based solver is used; Sutherland's law with a three coefficient model for viscosity estimation is enabled throughout the simulation.

The RANS equation, in combination with the SST $K-\omega$ model, can reasonably predict the aerodynamic and acoustic characteristics of a supersonic free jet, as per literature [2–5, 7]. Also, 2D axisymmetric simulations were found to be reliable for analyzing the compressible jets' aeroacoustic characteristics. As a result, over the entire simulation, the RANS equations with turbulence accounted for using the $K-\omega$ SST model are used. Up to a residual of 10^{-6} , all equations are solved. TECHPLOT 360 was used to post-process the solution after it had converged. For all of the nozzle's NPR values, the numerical shadowgraph is used to illustrate the shock pattern, shock-cell length, and shear layer development. For all situations, an unstable RANS simulation is used with a time step of $\Delta t = 1.0 \times 10^{-5}$ s and a total duration

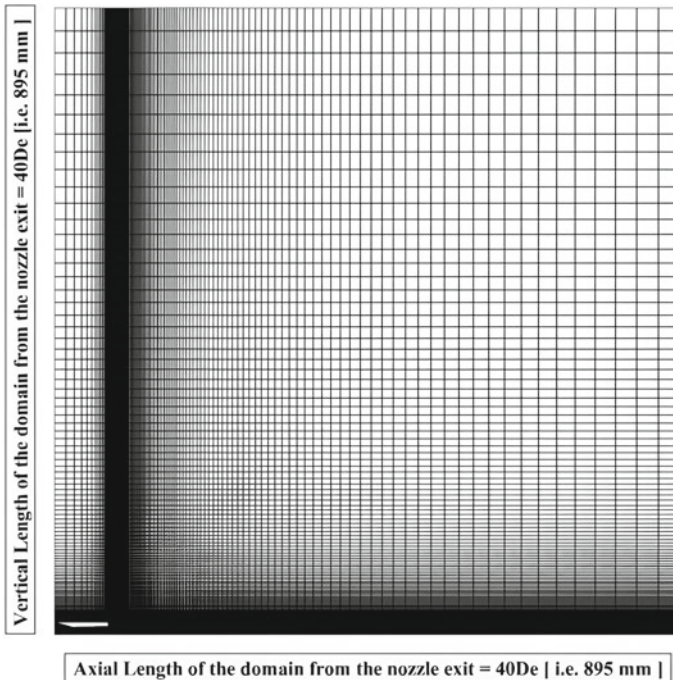


Fig. 1 Domain mesh details

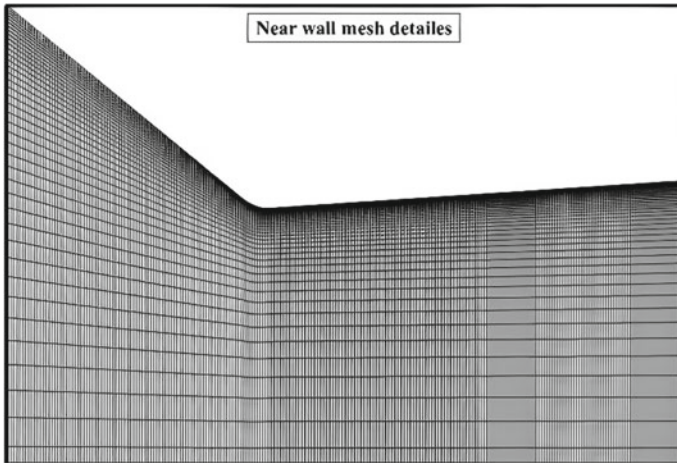


Fig. 2 Near wall mesh details

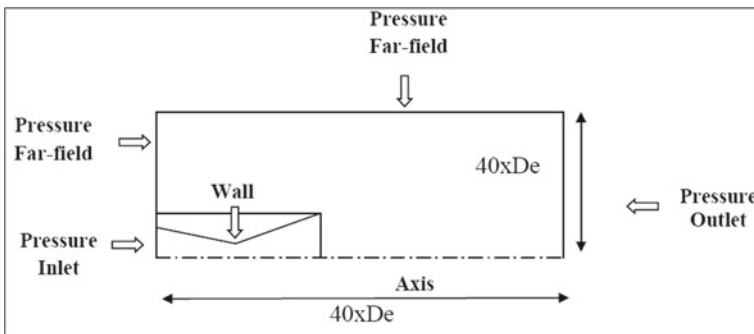
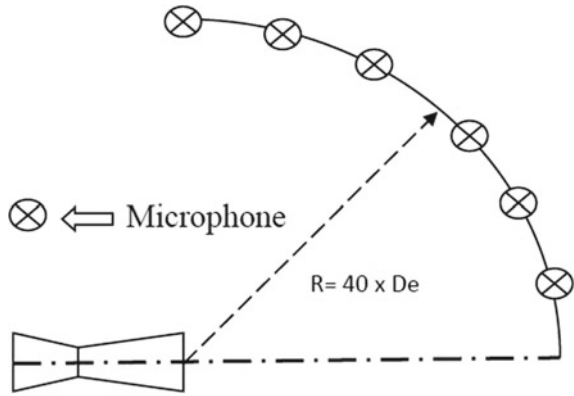


Fig. 3 Boundary conditions

of 0.5 s. According to the literature [2, 3, 5, 8], the microphones should be placed at a specific distance from the acoustic source (i.e., Free jet) to avoid the near field effect (i.e., Nonlinear). To ensure the far-field impact, R/D_e should be adequate (i.e., $30 \geq R/D_e \leq 50$). The acoustic pressure (i.e., dynamic pressure) data is captured on the microphones at $R/D_e = 40$ for each time step. There are six microphones in total, each having a 15° angle of separation. The corresponding microphone arrangements can be seen in 4. Time-series acoustic pressure values were processed in MATLAB using the FFT approach to calculate an Amplitude-frequency spectrum of the acoustic signal, and the corresponding SPL was calculated using the 3. For NPR values of 3.25 (i.e., Overexpansion), 4.25 (i.e., Ideal-expansion), and 5.25 (i.e., Ideal-expansion), the free jet Mach number is plotted along the nozzle axis (i.e., Under expansion). For the relevant NPR, the subsequent events were used to visualize the characteristics of Mach number decay as well as shock-cell formation (Fig. 5).

Fig. 4 Microphone location



$$\frac{P_0}{P_\infty} = \left(1 + \frac{\gamma - 1}{2} M^2\right) \tag{1}$$

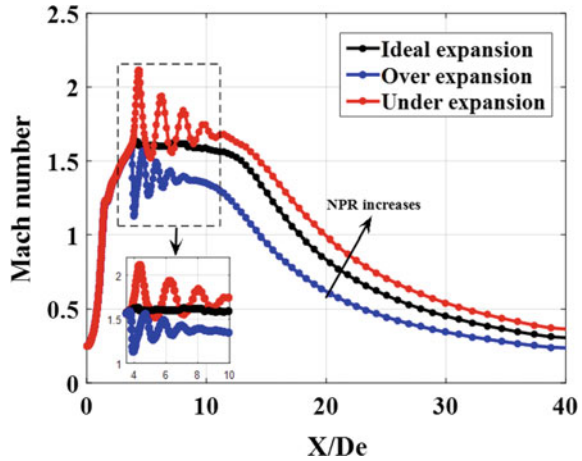
$$\left(\frac{A}{A_*}\right)^2 = \frac{1}{M^2} \left\{ \left| \frac{2}{\gamma + 1} \left(1 + \frac{\gamma - 1}{2} M^2\right) \right| \right\}^{\frac{\gamma + 1}{\gamma - 1}} \tag{2}$$

$$\text{SPL(dB)} = 20 \log_{10} \left[\frac{P_{\text{rms}'}}{P_{\text{ref}}} \right] \tag{3}$$

3 Results and Discussion

Figure 5 represents the centerline Mach number decay of three expansion modes (i.e., ideal, under, and overexpansion) of free jet. At $X/De = 4$, the overexpanded jet's oscillations continue until the pressure at the centerline equals the atmospheric pressure (i.e., backpressure). Whereas, except for a minor change in Mach number at $X/De = 4$, the fluctuations in the optimally expanded jet are essentially non-existent. Also, obtained Mach number at the exit of the nozzle for the ideal case is almost 1.59 which is very close to the ideal design Mach number of 1.60. Hence, the result shows a minimal difference between the isentropic exit Mach number (i.e., ideal) and the computational result. The same can be utilized for validation. Figure 5 also shows the expansion through the nozzle, which allows for an isentropic expansion (zero oscillations in the Mach number curve) within the nozzle. Significant Mach number oscillations are observed in the case of the overexpanded jet for X/De between 4 and 9 (i.e., $4 \geq X/De \leq 9$), after which the jet Mach number drops monotonically downstream. Likewise, Mach number fluctuations were seen for the underexpanded

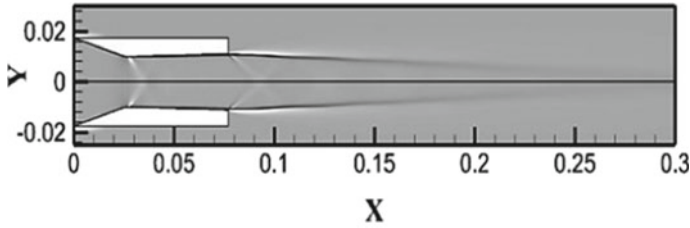
Fig. 5 Mach number variation along the nozzle axis for the ideal, over, and under expansion modes



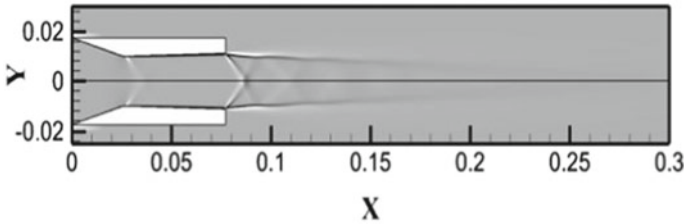
for X/De between 5 and 13 (i.e., $5 \geq X/De \leq 13$). As a result, the overall shock-cell length of the underexpanded jet is 37% longer than that of the overexpanded free jet. When a longer segment of a quasi-periodic shock-cell interacts with jet vortices, a powerful auditory signal (i.e., noise) is released into the atmosphere. An overexpanded jet with a shorter shock-cell length, on the other hand, is projected to produce weaker acoustic waves than an underexpanded jet. Due to the added shock-induced noise component, off-design expanded jets are more likely to generate a higher acoustic signal than ideal jets.

The numerical shadowgraphs for the NPR: 4.25, 3.25, and 5.25 are shown in Fig. 6a, 6b, and 6c, respectively, in order to visualize the nature of shock-cell and potential core formations. Even for the ideal expansion, Fig. 5 shows a marginal wavering in exit Mach number, and a weak expansion fan can be seen at the nozzle exit of Fig. 6a (i.e., Ideal expansion), providing the answer to the minimal Mach number fluctuation of the ideally expanded jet seen in figure 5. Apart from the infinitesimal expansion fan, there was no visible discontinuity in the jet, which is compatible with Mach number degradation of ideal expansion observed in Fig. 5. To match the reduced jet exit pressure (i.e., P_e) with the atmosphere back pressure (i.e., P_∞), a significant oblique shock formation can be seen from the nozzle exit in Fig. 6b. The shadowgraph image of the overexpanded jet (i.e., NPR = 3.25) also revealed multiple follow-on shock-cells. The NPR of 5.25 demonstrates under expansion behavior, as seen in Fig. 6c, with an expansion fan formation at the nozzle outlet and subsequent shock-cell forms. Overall, shadowgraph images make it much easier to examine the mechanism of shock/expansion fan formation as well as the length of the potential core of the jet.

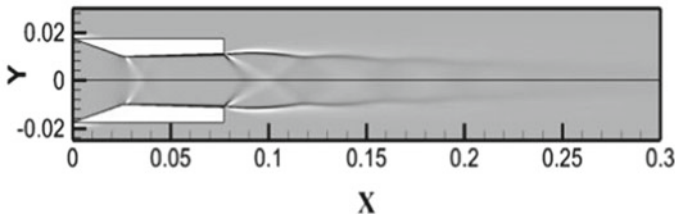
Microphones located at the 15° , 30° , 45° , 60° , 75° , and 90° , concerning the jet axis, are used to record dynamic pressure fluctuations. Figure 7a depicts SPL fluctuations at 15° ; all three expansion types (i.e., ideal, over, and under expansion) display the highest values for lower frequency values, then descend to the minimum as frequency



(a) NPR 4.25



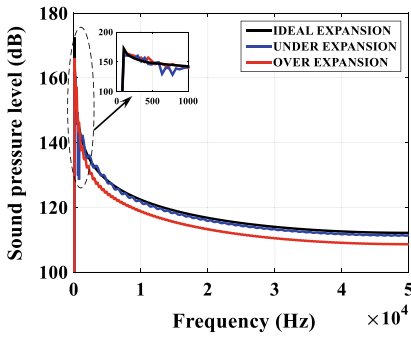
(b) NPR 3.25



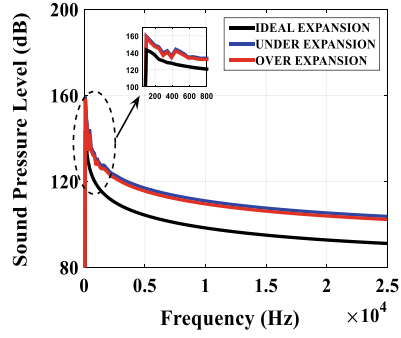
(c) NPR 5.25

Fig. 6 Numerical shadowgraph for the ideal, over, and underexpanded free jet of Mach 1.6

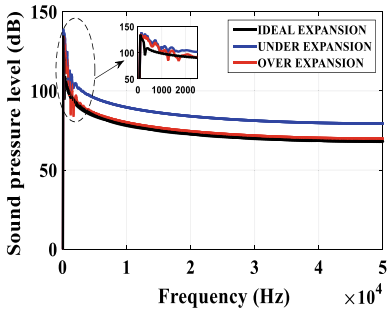
increases. Between 245 and 350 Hz, the SPL value of the under expansion mode drops to 135 dB from 148 dB, indicating a significant fluctuation. Except for the initial peak, the SPL values for a jet in under expansion mode closely match and sometimes exceed the SPL values of an ideal jet up to 5000 Hz, then show the marginal drop values all across the range of frequency. For the initial frequency values, the SPL values of the overexpanded jet nearly match those of the other expansion modes (i.e., ideal and under expansion), but then show a significant drop all along the frequency scale. Figure 7b shows that the SPL values of off-design expanded jets (i.e., under and overexpanded jets) outperform the ideal jet across the entire frequency range. Figure 7 shows that there is a difference of more than 30 dB between the off-design and ideally expanded jets. The formation of shock-cells and their quasi-periodic fluctuations are the primary causes for this substantial SPL difference [1], as shown by the numerical shadowgraphs in Fig. 6b and c (i.e., the development of shock/expansion waves).



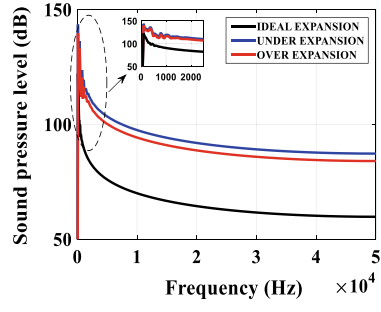
(a) Microphone at 15°



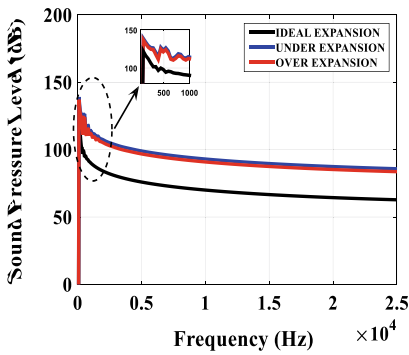
(b) Microphone at 30°



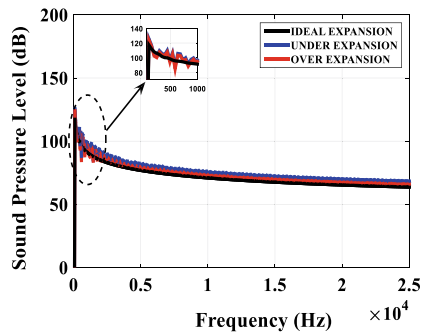
(c) Microphone at 45°



(d) Microphone at 60°



(e) Microphone at 75°



(f) Microphone at 90°

Fig. 7 Acoustic characteristics of an overexpanded jet of Mach 1.6

Figure 7c exhibits the SPL variation for the 45° microphone location. The over and underexpanded jets experience considerable fluctuations up to 2500 Hz, with no such fluctuation from the ideally expanded jet. The SPL characteristics of over and ideally expanded jets are closely matched between the frequencies 2500 and 25,000 Hz. In addition to that, the underexpanded jet experiences a higher value of SPL all along the frequency scale than both the ideal and overexpanded jet. In Fig. 7d, it can be observed that the trend of the SPL curve (i.e., microphone at 60°) for all three jets is almost identical to the microphone location at 30° (i.e., Fig. 7). The SPL variation at 45° is depicted in Fig. 7c. The over and underexpanded jets exhibit significant fluctuations up to 2500 Hz, whereas the ideally expanded jet exhibits no such fluctuation. Between 2500 and 25,000 Hz, the SPL characteristics of over and ideally expanded jets are nearly identical. Furthermore, the underexpanded jet has a higher SPL value all along the frequency scale than both the ideal and the overexpanded jet. Figure 7d shows that the trend of the SPL curve (i.e., microphone at 60°) for all three jets is nearly identical to the microphone location at 30° (i.e., Fig. 7). Similarly, SPL characteristics at 75° show an improved match when compared to SPL at 30°. SPL values for 90° (i.e., Fig. 7f) show different trends than the other microphone locations. Off-design expanded jets are nearly dominating, with the ideally expanded jet having slightly higher SPL values across the frequency spectrum. Overall, the SPL characteristics of off-design expanded jets are almost always higher than the ideal case for all measured microphone locations, except the 15° location. Furthermore, the SPL characteristics differ for each measured angle, ensuring the free jet's directivity.

4 Conclusion

Computational fluid dynamics was used to investigate the aerodynamic and acoustic aspects of a Mach 1.6 free jet. As per the axial Mach number decay plot, the under-expanded jet has a maximum theoretical core length that is roughly 37% longer than the overexpanded jet. Likewise, numerical shadowgraph images make it easier to investigate the nature of shock and expansion fan formation, as well as the jet core length. The observed shock/expansion phenomenon of the NPR from 3.25 to 5.25 demonstrates the reason for the Mach number decay, which can influence the acoustic signature of the jet. At 45°, SPL fluctuates significantly all along the frequency scale. But in case of the remaining angles (30° to 90°), SPL fluctuates minimally. After that, it decays monotonically for the remainder of the frequency scale. The SPL characteristics ensure the directivity of the free jet.

Nomenclature

NPR	Nozzle Pressure Ratio
SPL	Sound Pressure Level [dB]

CFD	Computational Fluid Dynamics
RANS	Reynolds Averaged Navier–Stokes
SST	Shear Stress Transport
LES	Large-Eddy Simulations
M	Mach number
URANS	Unsteady Reynolds Averaged Navier–Stokes
FWH	Ffowcs Williams–Hawking
PSD	Power Spectral Density [W/Hz]
FFT	Fast Fourier Transform
MOC	Method of Characteristics
P_∞	Atmosphere back pressure [Pa]
P_e	Jet exit pressure [Pa]
y^+	First cell distance
$3D$	Three dimension
$2D$	Two dimension
Δt	Time step [s]
X	Axial distance along the nozzle axis [m]
D_e	Nozzle exit diameter [m]
A_e/A_t	Nozzle area ratio
P'_{rms}	Root mean square value of sound pressure [Pa]
P_{ref}	Reference pressure [20 μPa]

References

1. Martelli E, Nasuti F, Onofri M (2010) Numerical calculation of FSS/RSS transition in highly overexpanded rocket nozzle flows. *Shock Waves* 20:139–146
2. Barbarino M, Ilsami M, Tuccillo R, Federico L (2017) Combined cfd-stochastic analysis of an active fluidic injection system for jet noise reduction. *Appl Sci (Switzerland)* 7
3. Andersson N, Eriksson L (2008) Prediction of flowfield and acoustic signature of a coaxial jet using rans-based methods and large-eddy simulation. *Int J Aeroacoust* 7:23–40
4. Andersson N, Eriksson L, Davidson L (2004) A study of Mach 0.75 jets and their radiated sound using large-eddy simulation. In: *Collection of technical papers—10th AIAA/CEAS aeroacoustics conference*, vol 3, 2520–2543
5. Tide P, Babu V (2009) Numerical predictions of noise due to subsonic jets from nozzles with and without chevrons. *Appl Acoust* 70:321–332
6. Das R, Ye A, Setoguchi T, Kim H (2015) Flow oscillations in supersonic cavity-induced combustion. In: *International symposium on turbulence and shear flow phenomena*, vol 9
7. Mankbadi R, Hayer M, Povinelli L (1994) Structure of supersonic jet flow and its radiated sound. *AIAA J* 32:897–906
8. Chen S, Gojon R, Mihaescu M (2018) High-temperature effects on aerodynamic and acoustics characteristics of a rectangular supersonic jet. In: *2018 AIAA/CEAS aeroacoustics conferences*

Aerodynamic and Thermal Optimization of Plate Heat Exchanger Fin Arrangements



Pratyush Padmanabhan, Sanatkumar Samvit Rajagopalan,
and Chennu Ranganayakulu

Abstract Plate-fin heat exchanger systems today are exceedingly prevalent but greatly unoptimized because of the use of off-the-shelf heat exchangers, which considerably affect system efficiency. This study aims to provide a methodology for a plate-fin heat exchanger's aerodynamic and thermal optimization to create a bespoke cooling solution based on given constraints and operating conditions. The authors studied a radiator to cool the EMRAX 208 electric motor to develop the requisite analytical and numerical models. A literature review was undertaken to compare and shortlist the best configurations, optimized through a MATLAB algorithm, and analysed and iterated in Ansys Fluent on a case-by-case basis. The results of the study point towards the superiority of serpentine fins over the other kinds, with approximately 40% higher heat transfer coefficients (at 80kmph) compared to the triangular finned models, which results in an indirect reduction in the frontal area and, subsequently, lower drag and pressure losses. The study concluded with the serpentine finned cylindrical tube heat exchanger as the best cooling solution. The exact dimensions and layout of the heat exchanger, along with the optimal fin distribution, can be obtained with the combination of the created algorithm and CFD analysis.

Keywords Radiator · CFD · Serpentine fins · MATLAB · Forced convection

1 Introduction

Forced convection is a heat transfer mechanism through a fluid in the presence of bulk fluid motion initiated by external means [1]. This is the scientific basis of the functioning of a heat exchanger. A heat exchanger is a device that allows for

P. Padmanabhan and S.S. Rajagopalan contributed equally to this work as first authors.

P. Padmanabhan (✉) · S. S. Rajagopalan · C. Ranganayakulu
Department of Mechanical Engineering, Birla Institute of Technology and Science Pilani, 333031,
Pilani, India
e-mail: f20190380@pilani.bits-pilani.ac.in

heat exchange between two fluids at different temperatures without intermixing. It works on a hybrid convection process in each fluid and conduction through the wall separating them [2]. A heat exchanger utilizes the immense variety of cooling capacities of two fluids, air and oil/water. Because of their compactness, they find numerous applications in the refrigeration industry, cryogenics, and spaceflight.

Today, the most industrially relevant heat exchangers are the plate-fin and tube-fin heat exchangers. These are characterized by densely packed fins winding between plates or cylindrical tubes carrying heated fluid, whose heat is then convected away by incoming air. Their compactness and high-thermal coefficients make them ideal for refrigeration and cryogenic purposes and use in spacecraft and aeroplanes.

Due to its availability and industry presence, this study chose to focus on the automotive radiator as a model to analyse these heat exchangers. Specifically, a radiator was to be modelled to sufficiently cool an EMRAX 208 electric motor in BITS Pilani's Formula Student vehicle. To help determine the most optimal radiator layout, this study chose to start with the geometric constraints and cooling requirements, consider a range of ambient temperatures, and then work backwards to determine the ideal spacing of the radiator's components.

Previous contributors to the topic of FSAE radiators provided either completely analytical output [3] or based their calculations on plate-fin heat exchangers [4]. During this study, the authors found that no analysis allowed one to obtain information about the layout of the fins with a degree of customization. On the occasions that fins were discussed, there was no analytical calculation done—instead, CFD analysis of a CAD model of an existing radiator was carried out [5]. Given the cooling load, a study that optimized the layout of the tubes and fins was needed. There has also been an overwhelming lack of verification of pressure drop across these heat exchangers, which is essential to understanding the aerodynamics of a vehicle.

The objective of the following analysis was to design a plate finned heat exchanger by starting with a given set of weather conditions and geometric constraints and ending up with an optimal arrangement and size of fins through iterative optimization. The authors chose this methodology because most practical applications of a heat exchanger involve using a top-down approach and expect having prior knowledge about the heating and cooling requirements.

2 Methodology

A. Governing Equations

The design criteria representing the constraints of the study are given by the motor characteristics, which include the cooling load required, the motor power (heat) generation, optimal working temperature, coolant (specified as water) and coolant flow rate [6]. These define the cooling required, the resulting temperature, and the outlets for both air and water.

The inlet and outlet temperatures define the Logarithmic mean temperature difference. LMTD is the logarithmic difference between a heat exchanger's hot and cold outlets and is used to quantify the heat transfer rate across a heat exchanger [2]. For a cross-flow heat exchanger (like the radiator), LMTD also requires the inclusion of a geometric correction factor, which quantifies the deviation of the heat exchanger under study from an ideal counter-flow heat exchanger with identical inlet and outlet temperatures. The governing equations to obtain the LMTD are presented below.

$$\dot{Q} = m_a C_{p_a} (T_{c_o} - T_{c_i}) = m_w C_{p_w} (T_{h_o} - T_{h_i}) \quad (1)$$

$$\dot{Q}_o = U * A * (\text{LMTD}) \quad (2)$$

$$\text{LMTD} = \frac{((T_{h_i} - T_{c_o}) - (T_{h_o} - T_{c_i}))}{\ln \left[\frac{T_{h_i} - T_{c_o}}{T_{h_o} - T_{c_i}} \right]} \quad (3)$$

$$\dot{m}_a = \rho_a A_{\text{frontal}} v \quad (4)$$

$$\dot{m}_w = \rho_w \dot{V} \quad (5)$$

Using ram temperature is essential in defining air inlet temperature to accurately incorporate compressibility's effects on air temperature (especially at higher Mach numbers). It can be determined from the following equation [6]:

$$T_{c_i} = T_{\text{ram}} = T_{\text{static}} \left(1 + \frac{\gamma - 1}{2} \text{Ma}^2 \right) \quad (6)$$

To determine the convective surface area, Eq. 7 is first used to find the overall heat transfer coefficient for the radiator. An overall heat transfer coefficient is required since the heat is being convected through two different surfaces, i.e., the cylindrical tubes and the finned surface area. Equation 8 obtains the Nusselt number for the air convecting heat across serpentine fins [7, Eq. 16], and Eqs. 9–11 are employed for the triangular finned case [8, Eqs. 4, 8 and 9]. Equation 12 [9, Eq. 2.3.1], defined as the Dittus-Boelter equation for fully developed flows, is used to calculate the Nusselt number for the interior pipe flow of the coolant. Finally, Eq. 13 [1, Eqs. 6–5] is used to associate the Nusselt number, characteristic dimension and thermal conductivity with the convective heat transfer coefficient.

$$U = \frac{1}{h_i A_i} + \frac{1}{h_o A_o} \quad (7)$$

$$\text{Nu}_{o, \text{serpentine}} = 10.415 \ln[\text{Re}_a - 46.081] \text{Pr}_a^{0.33} \quad (8)$$

$$h_{a,\text{triangular}} = J_a G_a C_{p,a} / \text{Pr}_a^{2/3} \quad (9)$$

$$J_a = 0.174 / \text{Re}_a^{0.383} \quad (10)$$

$$G_a = \mu_a \text{Re}_a / D_x \quad (11)$$

$$\text{Nu}_i = 0.023 \text{Re}_w^{0.8} \text{Pr}_w^{0.3} \quad (12)$$

$$h_x = \frac{\text{Nu}_x \cdot K_x}{D_x} \quad (13)$$

Using Eq. 2, the total heat transfer area can be found. The area ascertained is greater than A_o . This study now constrains the cylindrical tube radius to a fixed quantity to be able to focus on fin optimization. Thus, the radiator's fins contribute to the additional heat transfer area ($A - A_o$). Using an optimization program written in MATLAB that considers weather, geometric, and heating load constraints, successive iterations are carried out to obtain the minimum surface area and the maximum possible U that can be derived. The algorithm also communicates the optimized fin curvature and density using the formula below.

$$\text{fin density} = \frac{\text{Number of fins}}{A_{\text{frontal}} \text{ (in cm}^2\text{)}} \quad (14)$$

This completes the analytical heat transfer solution. The aerodynamic portion is simplistic and is governed by a single equation, i.e., the isentropic Mach relations, which relate the free stream pressure and the local static pressure based on the Mach number of the free stream as given below [7].

$$\Delta P = P_{\text{static}} * \left[\left(1 + \frac{\gamma - 1}{2} \text{Ma}^2 \right)^{\frac{\gamma}{\gamma - 1}} - 1 \right] \quad (15)$$

The usage of the above equation is valid since a free stream flow can be assumed to be isentropic, and the static pressure is generated because of the fluid coming to rest isentropically.

B. Geometry and Approximation

The investigation begins with two 30 cm × 30 cm × 3.2 cm and 30 cm × 21.5 cm × 3.2 cm automotive radiators with three layers of tubes and fins stacked one on top of the other. These dimensions, which corresponded to the dimensions of commonly available radiators on the market, became the ideal starting point. Because this is an optimization problem, all possible fin and tube configurations are taken into account.

Six cases are identified, each with two different fin and three different tube configurations. Flat and cylindrical tube configurations, as well as wavy/triangular, rectangular/vertical, and serpentine fin configurations, are all included.

Based on the results presented in [11], the flat plate geometry is eliminated from the study. Another factor to not research further is the more prevalent supply and manufacturing of cylindrical tubes. However, it is essential to note that the MATLAB code can accommodate the flat tube geometry or any other plate geometry the user finds necessary.

Next, the vertical finned configuration is eliminated due to its lower thermal capability than the triangular fins [12]. Finally, the heat transfer characteristics of serpentine and triangular fins are compared. Equations 9–11 are used to calculate the Nusselt number and heat transfer coefficients, which are then optimized in MATLAB. The triangular fins are impractical because the program specifies a fin angle of 89° , whose manufacturing costs far outweigh the benefits. As a result, the serpentine finned cylindrical tube radiator is the only case considered for the CFD analysis.

The EMRAX 208 motor's specifications sheet and weather charts give information about total and average power generated, water circulation temperature, motor efficiency and volumetric flow rate [6]. Ambient temperature and vehicle speed are assumed. From here, the total heat load required to be taken up by the radiator is determined to be 9640 W. This is a conservative estimate, as upper limits on motor efficiency and operating speeds are considered.

According to Eq. 15, the 30 cm \times 30 cm model has 23 tubes and the 30 cm \times 21.5 cm model has 16 tubes. The tubes themselves are 8 mm in diameter, as specified on the radiator's specifications sheet. For this study, a distance of 5 mm between two adjacent radiator tubes and an ideal fin width of 3 mm are assumed.

$$\text{Radiator width} = 8n + 5(n - 1) \quad (16)$$

The only two unknowns are the total area and the overall heat transfer coefficient, which are iterated by the MATLAB program. Because of the algorithm's flexibility, it can analyse a triangular fin setup to optimize the fin angle. After excluding the triangular fins case, the study only considered the two remaining cases with differences in radiator size and, as a result, fin arrangement.

A CAD model with the desired fin radius and length is created based on the results of the MATLAB optimization program. However, due to computational constraints, only the most optimal geometry is used for the CFD analysis. The analysis design includes only a portion of the original radiator. It is made up of all three layers of tubes (absolute depth), but with a repeating unit that has a smaller frontal area. This is possible because the pressure analysis is performed without using any energy or heat equations. To make use of this smaller cross-section, spatial marching in the x and y directions is used, as the pressure drop across a representative area is representative of the pressure drop and aerodynamics of the airflow across the entire radiator. As described in the following section, the smaller model size allows for the use of much finer elements, resulting in a more accurate mesh.

Table 1 Mesh Statistics for 30 cm × 21.5 cm radiator

	Average values
Element quality	0.885
Aspect ratio	1.98
Orthogonality	0.978
Skewness	0.03135

C. Computational Setup

At this point, it is essential to reiterate that due to computational power limitations and access to a licensed ANSYS workstation, only the two best cases out of the six that are shortlisted can be thoroughly analysed in the allotted time frame for simulations.

To analyse the pressure drop and flow characteristics, the model was imported into Ansys Workbench. Owing to the small size and frequent curvature of the radiator fins, the Cartesian Cutcell assembly meshing method is used to generate the mesh, as seen in Fig. 2. The Cutcell assembly method, as opposed to the conventional meshing strategies, is not limited to complete elements. Instead, individual cells are spliced where the boundary walls cut through them. This also implies that the boundary wall contours are maintained (not skewed due to cell shape), which ensures better near-wall and boundary layer flow accuracy [13]. Further, the addition of inflation layers minimizes any irregularities during the analysis.

A body sizing of 4e-3 m and 10 inflation layers with a first layer height of 2.25e-5 m are employed. These values are obtained after performing a mesh independence study, shown in Fig. 3, which determines that approximately 3.88 million nodes are required to ensure the analysis and results are not influenced by the mesh characteristics.

The quality characteristics for the resulting mesh used for simulation on Fluent is presented in Table 1.

The setup is processed in Fluent with an air density of 1.225 kg/m³ and uses the *k-ε*-realizable viscous model with scalable wall functions and curvature correction enabled [14]. A velocity inlet and an ambient pressure outlet boundary condition are implemented. The inlet velocity is parameterized in order to iterate the Fluent solution. The pressure drop across the enclosure and velocity at the exit is measured in post-processing.

Both models, representing the results from the two tested radiator geometries, are simulated in a high-performance workstation with an AMD Ryzen 5 3600X 6-core processor with an Nvidia RTX 2060 Super with 32 GB of RAM running Ansys 18 Academic.

3 Results and Discussion

It is evident from Fig. 4 that the heat transfer coefficient of the triangular finned radiator lags far behind the serpentine finned radiators. This is enough to omit the triangular fins from the study further, which would require either a much larger surface area or an impractically high-fin angle to obtain the same cooling load. This supports the earlier analytical observation regarding the triangular fins.

Further, it can be observed that the variation for both serpentine finned radiator sizes is largely similar, with the two curves almost overlapping. These two observations give rise to the theory that fin shape, rather than fin density, is the defining factor in heat transfer at similar cross-sectional areas. As shown in Table 2, the 113% rise in fin density for the smaller radiator (30 cm × 21.5 cm) is responsible for the heat transfer coefficient being always maintained to satisfy the cooling requirements of the motor. The corresponding changes bring about higher fin density seen in the fin geometry with the diameter of the curved portion, as seen in Fig. 1, reducing from 0.31 cm to 0.14 cm.

Figure 4 also implies the marginally sharper decline in heat transfer rate for the 30 cm × 30 cm case. This can be hypothesized by a similarly reduced radiator efficiency with a sparser fin layout. However, this will have to be reviewed after further simulations.

The deciding factor for the radiator choice becomes the pressure drops for each case, as explained in Fig. 5.

Post-processing the data obtained numerically for a wide range of air speeds reveals that the pressure drop increases with the velocity as expected. Although it can be observed that the slope for the 30 cm × 30 cm radiator is much higher than the other case, which points to a worsening situation at higher speeds. At the highest tested velocity (90 km/h), the 30 cm × 30 cm heat exchanger had a peak pressure drop of 339.04 Pa. In contrast, the 30 cm × 21.5 cm heat exchanger generated a much smaller peak pressure drop with a value of 298.27 Pa. At lower velocities, the differences gradually reduce until a difference of just 1.5 Pa at 30 km/h.

The proportionality of ΔP to the square of the Mach number of air gives rise to the polynomial characteristic of the curve whose behaviour has the same variation pattern as is obtained numerically (as seen in Fig. 5). However, the deviation in results increases with operating speeds, as evidenced in Table 3, at 30 km/h (approximately the turning speed), the deviation between the numerical and analytical results is within acceptable limits. At 80 km/h (average speed of the car), the CFD results achieve an equivalency of up to 91% to the analytical derivations for the 30 cm × 30 cm case and an 83% equivalency for the 30 cm × 21.5 cm case. Figure 6 confirms

Table 2 30 cm × 21.5 cm and 30 cm × 30 cm optimized results

	A (m ²)	Fin density (fins/cm ²)	Fin dia (cm)
30 cm × 21.5 cm	1.70	16	0.14
30 cm × 30 cm	1.64	7.51	0.31

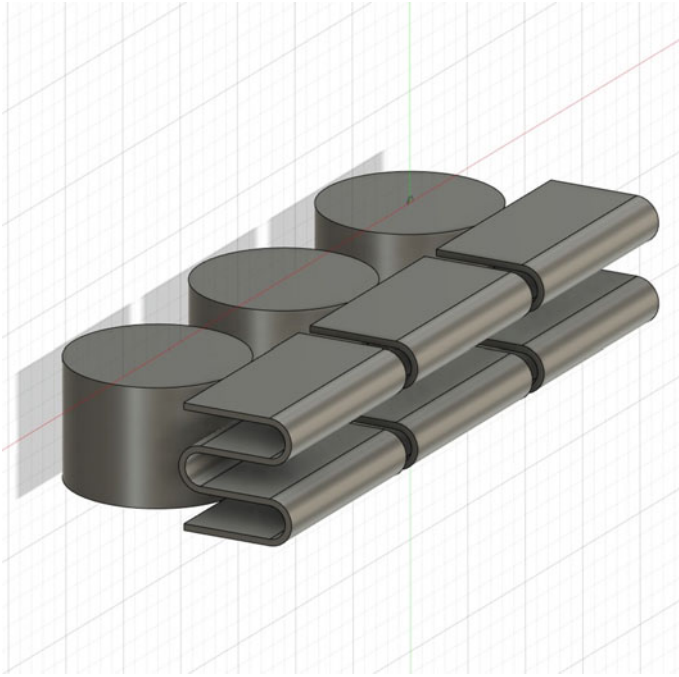


Fig. 1 CAD model created in Fusion 360, with one column of tubes and fins, reduced length-wise elements, and absolute depth

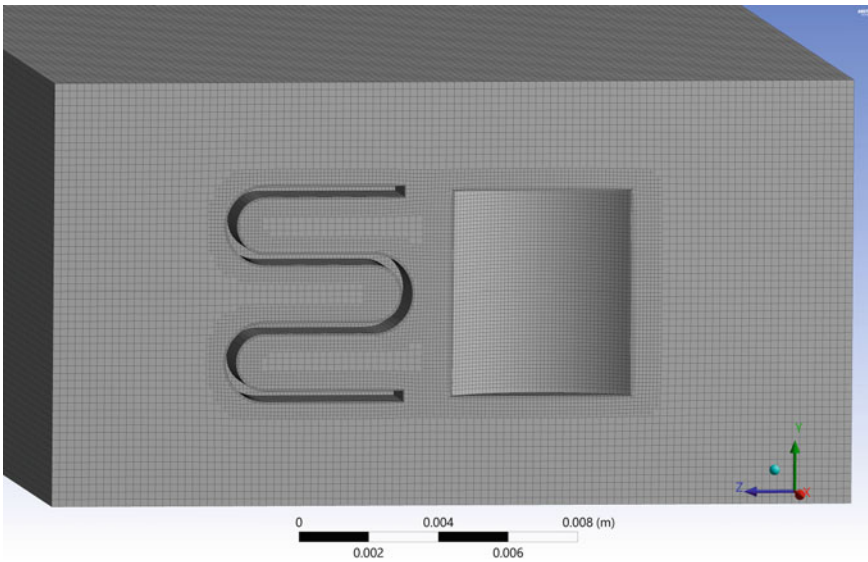


Fig. 2 Sectional view of fluid domain

Fig. 3 Mesh independence study

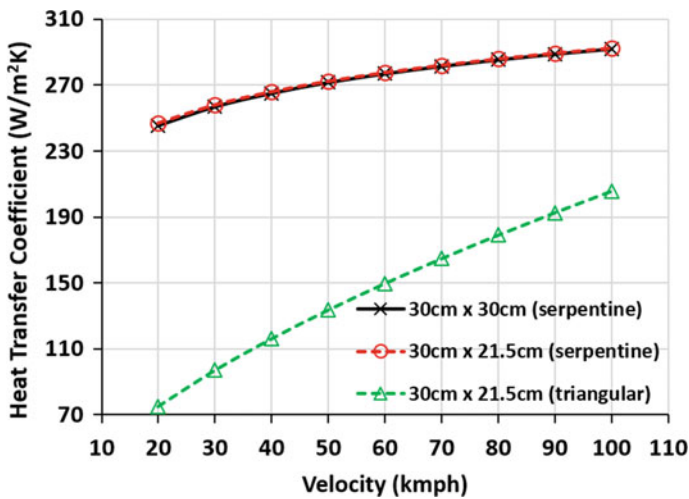
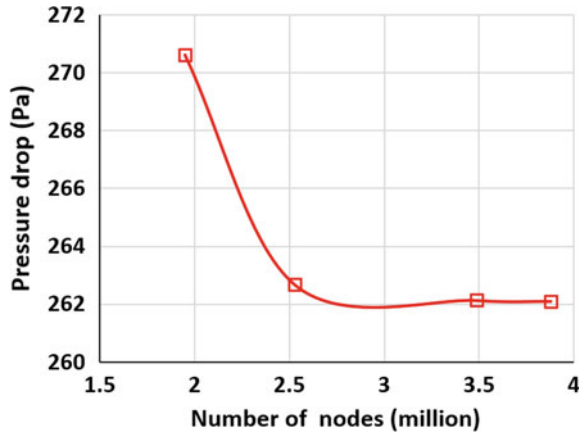


Fig. 4 Variation of heat transfer coefficient with velocity for 30 cm × 30 cm and 30 cm × 21.5 cm serpentine fin models, and the 30 cm × 21.5 cm triangular fin model

the increasing deviation at higher velocities. This slight divergence between the numerical and analytical results exists primarily due to the inherent assumption that air comes to rest isentropically in Eq. (15), which represents the ideal situation.

In reality, a portion of the air flows through the heat exchanger at reduced velocities and interacts with the curvature of the tubes and fins. It then re-joins the free stream behind it, causing the pressure drop across the heat exchanger to be slightly lower than predicted, as visualized in Fig. 7, where the inner convex curvature of the fins causes a higher pressure drop than other points in the local region. A potential reason for this could be that a higher fin density leads to a more streamlined flow through the

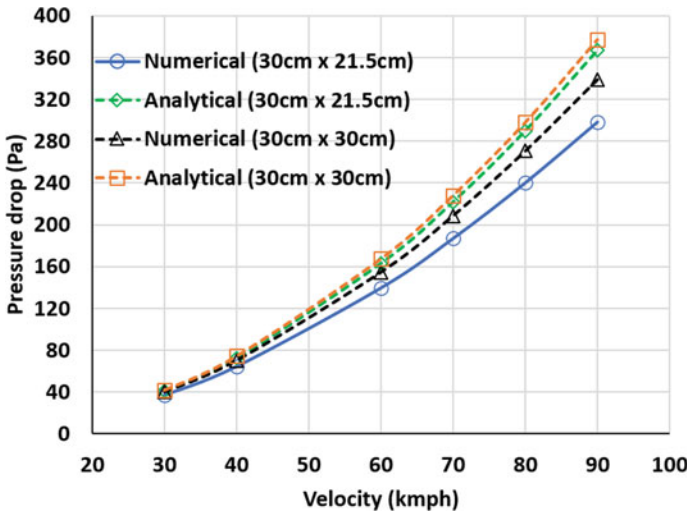


Fig. 5 Comparison of numerical and analytical pressure drop for the 30 cm × 30 cm and the 30 cm × 21.5 cm radiators

Table 3 Pressure drops as per numerical and analytical methods for multiple radiator geometries and air speeds

Velocity (kmph)	ΔP (numerical) (Pa)	ΔP (analytical)	% Difference
		30 cm × 21.5 cm	
30	37.36	40.69 Pa	8.18
80	240.17	289.62 Pa	17.07
		30 cm × 30 cm	
30	39.92	41.87 Pa	4.65
80	270.62	298.03 Pa	9.19

radiator. In comparison, the greater free volume within the 30 cm × 30 cm radiator causes more significant disturbances in the flow.

Further, through the comparison of the variation in area A with the overall heat transfer coefficient U presented in Fig. 8, it can be verified that the optimized values for the selected radiator still conform to the pattern indicated by the analytical heat exchanger relation.

However, this is shown to be an effective validation method even at high speeds since the CFD results follow the same trend as the theoretical ones, and because of maintenance of relatively high-simulation accuracy which can be used to arrive at a preliminary design. Most importantly though, simulations can be undertaken at a tiny fraction of the original computational requirement due to the incorporation of the *spatial marching technique*.

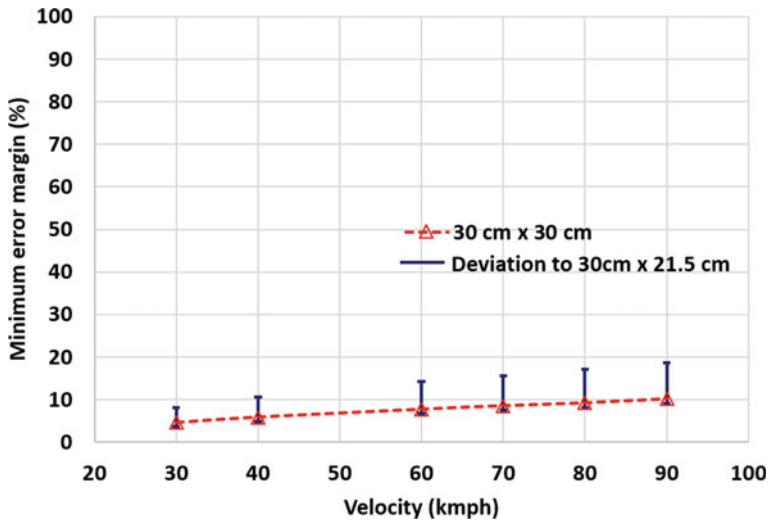


Fig. 6 Analytical and numerical result deviation

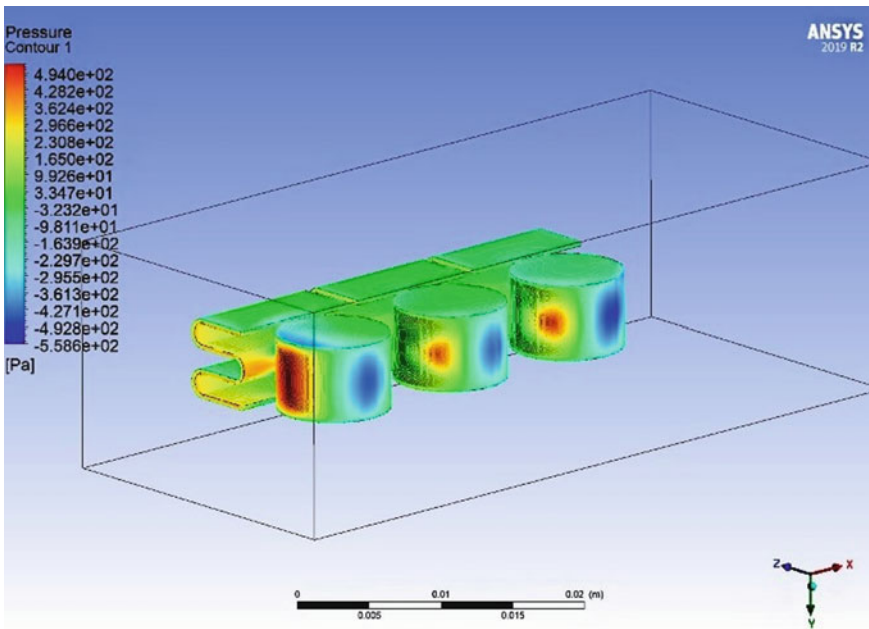


Fig. 7 Pressure contours of tested geometry

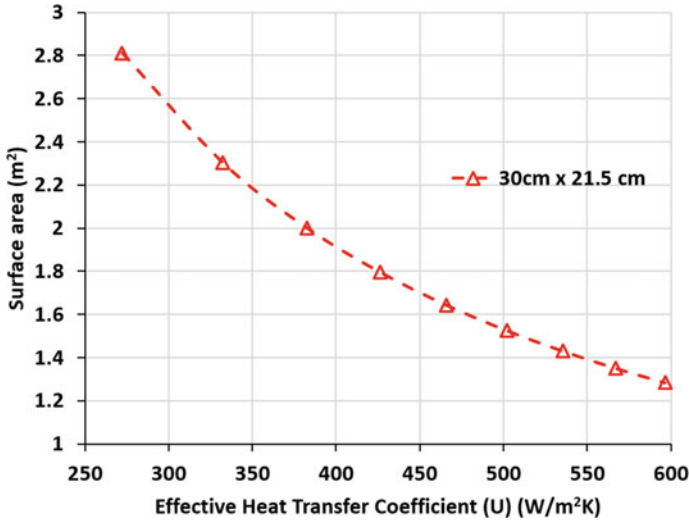


Fig. 8 Variation of optimized heat transfer surface area with effective heat transfer coefficient

4 Conclusions

The study determines the 30 cm × 21.5 cm serpentine finned radiator as the most suitable geometry to cool an EMRAX 208 electric motor. Since the cooling load is being maintained, the deciding factor is the form drag being generated. A 12% decrease in peak pressure drop combined with a 28.33% reduction in the frontal area demonstrates the superiority of the smaller radiator.

Across the two cases, the involved methodology yielded a median equivalency of 87% with the analytical solution, making it a promising fin evaluation technique given the computational constraints.

Although the benefit of increased fin density is obvious, the extent to which it can be increased and whether manufacturing constraints will be a limiting factor have yet to be investigated.

There are two such potential sources of improvement for the obtained results. First is to use a larger simulation model incorporating the energy equation. The computational power for this was unfortunately not available during the project’s time frame, which would greatly improve understanding of the effect of fin shape on turbulence, leading to more accurate results.

The second, more robust option is to increase the number of iterative variables in the MATLAB program. Implementing a more comprehensive ΔP governing equation in the algorithm can aid in achieving minimal deviation. The algorithm’s adaptability ensures that the technique is suitable for most plate-fin heat exchanger applications and allowing for the incorporation of additional design variables such as fin width and tube diameter. Furthermore, the code has the potential to include additional

constraints such as economic, manufacturing and supply chain constraints to create a completely customized heat exchanger solution.

Acknowledgements The authors would like to extend their gratitude to the Mechanical Engineering Department at BITS Pilani for facilitating this research project and to Team Inspired Karters Electric, who provided their EMRAX 208 motor and previous cooling system to analyse for the same. Special thanks also go out to Dr. Ishappa Bandi (Deputy Librarian, BITS Pilani) for providing special access to the requisite computing facilities that were pivotal to the completion of this study.

Nomenclature

Terminologies

A	Frontal Area [m^2]
C_p	Specific Heat Capacity [$\text{J kg}^{-1} \text{K}^{-1}$]
D	Characteristic linear dimension [m]
G	Mass velocity [$\text{kg m}^{-2} \text{s}^{-1}$]
h	Convective heat transfer coefficient [$\text{W m}^{-2} \text{K}^{-1}$]
J	Colburn factor
K	Conductive heat transfer coefficient [K]
k	Turbulent kinetic energy [J kg^{-1}]
kmph	Kilometres per hour [km h^{-1}]
LMTD	Logarithmic mean temperature difference [$^{\circ}\text{C}$]
\dot{m}	Mass flow rate [kg s^{-1}]
Ma	Mach number
n	Number of radiator tubes
Nu	Nusselt number
P	Pressure [Pa]
Pr	Prandtl Number
\dot{Q}	Rate of heat transfer [J s^{-1}]
Re	Reynolds number
T	Temperature [K]
U	Overall heat transfer coefficient [$\text{W m}^{-2} \text{K}^{-1}$]
V	Volumetric flow rate [$\text{m}^3 \text{s}^{-1}$]
v	Velocity [m s^{-1}]

Greek Letters

Γ	Heat capacity ratio
Δ	Difference
ϵ	Turbulent dissipation rate [$\text{J kg}^{-1} \text{s}^{-1}$]

μ	Dynamic viscosity [Pa s]
ρ	Density [kg m^{-3}]

Subscripts

a	Air
w	Water
i	Inlet
o	Outlet
C_o	Cold fluid outlet
C_i	Cold fluid inlet
h_o	Hot fluid outlet
h_i	Hot fluid inlet
frontal	Frontal surface area
ram	Ram property
static	Static (at rest) property
serpentine	Relating to serpentine fins
triangular	Relating to triangular fins
x	Variable

Appendix

Iterative serpentine fin code developed in MATLAB

```

q=9640; f=0.97; l_tube=0.3; t_gap=0.005; do=0.008; di=0.0075; lmtd=13.629;
d_curv=0.001625; %initial curvature dia is 1.625 mm
l_straight = t_gap-(d_curv); l_curv = pi*(d_curv/2);
n_1row = l_tube/d_curv;
a_fins_init=(n_1row-2)*(l_curv+l_straight)*0.01*69*2+ 2*(l_curv+l_straight+d_curv/2)*0.01*69*2;
atubes = 69*pi*do*l_tube; ao = a_fins_init + atubes;
ai = 69*pi*di*l_tube; hi=18361.025; ho=288.659; u=(ho*hi*ao*ai)/(ho*ao+hi*ai);
a=q/(u*f*lmtd);
while (a < ao - 0.0001)||(a > ao + 0.0001) u=(ho*hi*a*ai)/(ho*a+hi*ai); ao=a;
a=q/(u*f*lmtd);

```

end

$u_{\text{final}} = u$

$a_{\text{final}} = a$

$a_{\text{fins}} = a - a_{\text{tubes}}$

$a_{1\text{row}} = a_{\text{fins}} / 69$

$r_{\text{curv_new}} = 1 / (200 * ((a_{1\text{row}} / (0.01 * l_{\text{tube}}) + 1 - \pi)))$

$d_{\text{curv_new}} = r_{\text{curv_new}} * 2$

$n_{\text{serpents_1row}} = \text{floor}(l_{\text{tube}} / d_{\text{curv_new}})$

$n_{\text{serpents_total}} = n_{\text{serpents_1row}} * 69$

References

1. Cengel YA (2003) Heat transfer: A practical approach, 2nd edn. McGraw-Hill, pp 333–336, 441, 667–715
2. Shah RK, Sekulic Dusan P (2003) Fundamentals of heat exchanger design. Wiley
3. LaMarre J (2015) FSAE electric vehicle cooling system design. Williams Honors College, The University of Akron—Honors Research Projects 33
4. Farouk A, Amin A, Ali E, Abdullah A, Mohamed T, ZUFS Team, Gawad AA (2021) Study of the performance of an FSAE cooling radiator. In: Paper No. ICFD14EG-7S05, Fourteenth international conference of fluid dynamics, 04, 2021
5. Indira Priyadarshini C, Ratna Reddy T, Anjani Devi P (2022) Design and performance analysis of automotive radiator using computational fluid dynamics. *Int J Mech Eng* 7(3)
6. EMRAX d.o.o. (2016) EMRAX 208 technical data table (dynamometer test data)
7. Anderson JD (2021) Modern compressible flow with historical perspective. McGraw Hill
8. Vithayasai S, Kiatsiriroat T, Nuntaphan A (2006) Effect of electric field on heat transfer performance of automobile radiator at low frontal air velocity. *Appl Therm Eng* 26(17):2073–2078
9. Sheikhzadeh GA, Hajilou M, Jafarian H (2014) Analysis of thermal performance of a car radiator employing nanofluid. *Int J Mech Eng Appl* 2:47–51
10. Kothandaraman CP, Subramanyan S (2007) Heat and mass transfer data book. New Age International
11. Holik M, Zivić M, Virag Z, Barac A (2018) Comparison of finned tube and plate-finned heat exchangers in waste heat recovery. *Trans FAMENA* 42(Si1):1–12
12. Iyengar M, Bar Cohen A (1998) Least-material optimization of vertical pin-fin, plate-fin, and triangular-fin heat sinks in natural convective heat transfer. In: Sixth intersociety conference on thermal and thermomechanical phenomena in electronic systems (Cat. No. 98CH36208), pp 295–302
13. ANSYS Inc. (2016) ANSYS fluent user's guide, release 15, 2016
14. Raghu Vamsi P, Hemanth SMK, Ranganayakulu C (2021) Numerical analysis of generation of Colburn-j factor for the plain rectangular fins of a compact heat exchanger using CFD approach (fmfp2021-03-273). In: 48th National conference on fluid mechanics and fluid power

Computational Study on Wingtip Fluid Injection for Enhancing Wing Performance



Vishwanath Nagaraj, Darshan Purushan, Ashish Patra, Nimal Prakash, and V. Krishna

Abstract Wingtip vortices arise from the pressure difference between the top and bottom surfaces of the wing, and stimulate downwash of the airflow. This results in additional drag, known as lift-induced drag, which significantly adds to the overall drag on the aircraft. It also results in the reduction of effective lift. Several wingtip devices such as winglets are used to improve wing performance by the mitigation of wingtip vortices. The goal of this study is to analyse a method of increasing the lift to drag ratio of finite wings, at transonic conditions. A non-conventional method of improving performance, wingtip fluid injection is studied. Computational fluid dynamics tools were used to examine the improvement in wing performance, and it was observed that a higher lift to drag ratio was present for wings with fluid injection. This can be translated into better fuel economy, higher range or more payload capacity.

Keywords Wingtip fluid injection · Induced drag · Lift coefficient · Drag coefficient · Wingtip vortices

1 Introduction

A wing is generated from an airfoil profile, whose shape is optimised to produce high lift and low drag. Lift is produced by speeding up the air above the wing, thus reducing pressure relative to the lower part of the wing and producing a net upward force. Drag can be split into two components: pressure drag which is caused due to the overall chordwise pressure on the wing and skin friction caused due to the shearing force of the air neighbouring the airfoil.

In 3-dimensional flow, the pressure difference between the top and bottom surface of the wing has the tendency to try to equalise over the wingtip. In this process of high pressure air “leaking” to the top surface, a trailing vortex is generated, which is linked to downwash. Downwash is the change in the direction of the relative wind,

V. Nagaraj (✉) · D. Purushan · A. Patra · N. Prakash · V. Krishna
Department of Mechanical Engineering, PES University, Bangalore 560085, India
e-mail: vishwanath.nagaraj917@gmail.com

© The Author(s), under exclusive license to Springer Nature Singapore Pte Ltd. 2024
K. M. Singh et al. (eds.), *Fluid Mechanics and Fluid Power, Volume 2*, Lecture Notes in Mechanical Engineering, https://doi.org/10.1007/978-981-99-5752-1_37

447

which causes the lift vector on the wing to tilt backward, thus increasing drag and reducing lift.

Conventional wingtip devices such as winglets are commonly used to prevent this phenomenon but have several limitations; they add to the weight of the wing and aircraft, and thus have a negative effect on the fuel efficiency and also add bending stress on the wing. They also tend to be fixed rigid structures, not optimised to every different flight condition. In this regard, an unconventional approach was considered: wingtip air injection.

Thimmegowda et al. [1] conducted CFD analysis on wingtip vertical fluid injection for the reduction of induced drag. Their findings on the NACA 0012 at subsonic velocities showed that there was an improvement in L/D and a reduction in drag. The aim of this study is to apply the concept of wingtip injection to 3D transonic flow, and examine its viability.

A typical Boeing 737 wing was imitated, with a NACA 2412 airfoil as the profile for the wing whilst the operating conditions were set to mimic that of cruising flight. Various fluid injection velocities were tested at 0 and 2.5 degrees angle of attack and the corresponding lift and drag coefficients were found. This analysis was done for both, a clean wing and a wing with a blended winglet.

2 Literature Review and Objective

2.1 Literature Review

Thimmegowda et al. [1] analysed a fluidic winglet as an alternative for a rigid winglet. In their model, air was injected in the vertical direction, from a slot at the tip of the wing. The effect of fluid injection on the efficiency of a 3D wing at velocities of 10, 20, and 30 m/s was analysed using the numerical approach at angles of attack 6°, 8°, and 10°. It was observed that for these angles of attack, C_L remains relatively constant for every injection velocity. However, the value of C_D reduced with increasing injection velocity, and thus provided a better L/D ratio. This effect was especially noticeable at higher angles of attack.

Zacara et al. [2] studied the effectiveness of a synthetic jet actuation on the wingtip vortices in an unswept, rectangular wing. The wing was investigated experimentally and a synthetic jet was operated at different actuation frequencies and amplitudes. A PIV setup was used to analyse the formation of the wingtip vortices in the near wake at a distance equal to 3 times the length of the chord from the wing trailing edge. The results implied that the actuation of synthetic jets significantly affected the wingtip vorticity distribution, causing an outward diffusion which increased with the frequency of actuation, with a maximum reduction of 46%.

Manni et al. [3] performed CFD analysis on a NACA 0012 airfoil, the k- ω SST model was used as a turbulence model for this study. The Mach numbers of $M = 0.5$ and $M = 0.7$ were evaluated using simulations and the free stream total temperature

was set to 311 K. Calculations were done for an angle of attack $\alpha = 1.55^\circ$. The airfoil profile meshes were created using structured meshes of quadrilateral elements. The resolution of the mesh was kept higher in regions where greater computational accuracy was needed, such as the region near the airfoil.

De Mattos et al. [4] reviewed the current understanding and techniques used in winglet design. Trailing vortices, downwash, and their behaviour with various wingtip devices were assessed and evaluated. Studies on various CFD methods were used and validated with existing experimental research, and it was established that, if designed correctly, wingtip devices irrefutably improve wing performance.

Öztürk et al. [4] reviewed the effects of different types of winglets and wingtip devices on the aerodynamic performance of the aircraft. CFD analysis using various turbulence models and experimental studies were compiled. It was found that the use of winglets and wingtip devices significantly reduces vortex formation which leads to an increase in lift force and a decrease in induced drag which further increases the fuel economy of the aircraft.

Devenport et al. [5] carried out a study on the structure and development of a wingtip vortex produced by a conventional wing. Experimental study of vortex characteristics for a given airfoil, with measurements of flow velocities up to 30 chord lengths behind the wing was conducted. Mathematical models were developed for predicting the flow in the given conditions. The experimental results supported the mathematical models, even with vortex wandering.

2.2 Mathematical Modelling

The equations describing the primary aerodynamic coefficients are given below by (1) and (2). The lift-induced drag varies with the square of the lift coefficient, and the target variables to reduce induced drag are the Oswald efficiency factor (e) and the effective aspect ratio.

$$C_D = \frac{2D}{\rho V^2 S} \quad (1)$$

$$C_L = \frac{2L}{\rho V^2 S} \quad (2)$$

$$C_{D, \text{Total}} = C_{D,0} + \frac{C_L^2}{\pi e AR} \quad (3)$$

2.3 Objectives

The main aim of this study is to apply the concept of wingtip fluid injection to commercial airplane wings, and analyse the performance of the aerodynamic coefficients of these wings. This concept has shown promise as an alternative to winglets for low aspect ratio wings at low subsonic speeds, this work explores the effectiveness of this concept at the transonic conditions of commercial airplane flight.

3 Materials and Methods

3.1 Geometry

The wing geometry was designed by taking the approximate dimensions of the wing of a commercial narrow body jet. The wing was based on the NACA 2412 airfoil, which is suitable for transonic flight and was designed using SHAPR3D. The test section was created around it, and sufficient space was given around the wing. Greater importance was given to the region behind the wing, so as to allow the flow to fully develop and reach convergence easily. Figures 1, 2, 3 and Table 1 give all the geometric details of the wing and test domain.

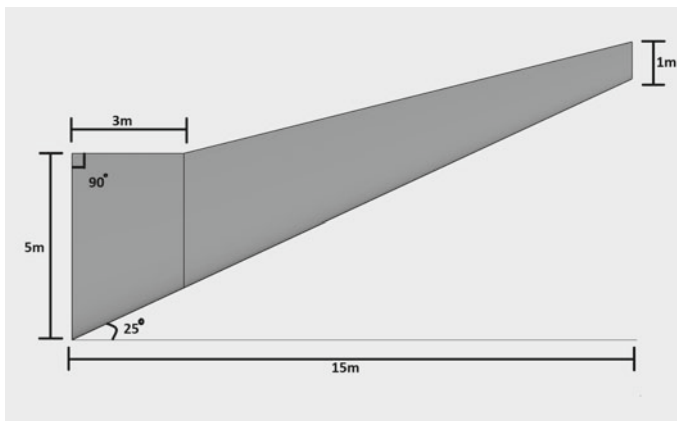


Fig. 1 Dimensions of the clean wing

Fig. 2 Blended winglet dimensions

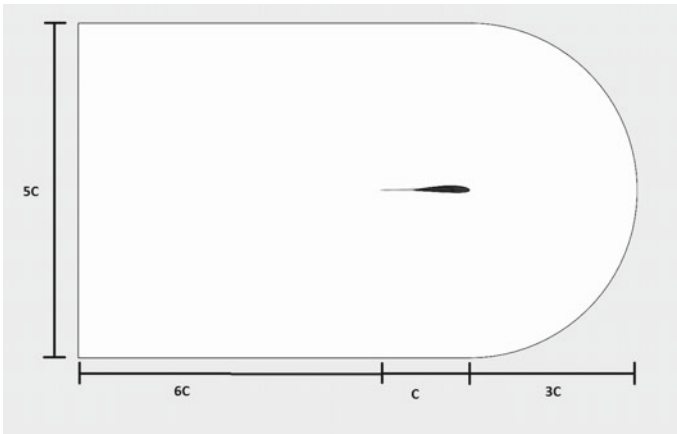
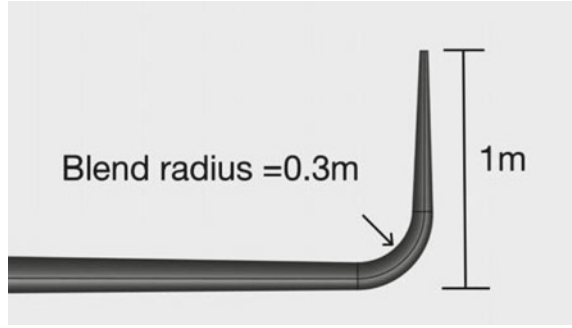


Fig. 3 The test domain

Table 1 Wing details

Wing parameter	Value
Airfoil used for wing generation	NACA 2412
Root chord	5 m
Tip chord	1 m
Sweep angle	25°
Dihedral angle	0°

3.2 Meshing

The model was meshed using ANSYS Workbench meshing software. A polyhedral mesh was created, with inflation layers and face sizing being added to capture the flow on the wing accurately. A polyhedral mesh was chosen over tetrahedral because of its lower sensitivity to cell stretching and improved numerical stability. Significant

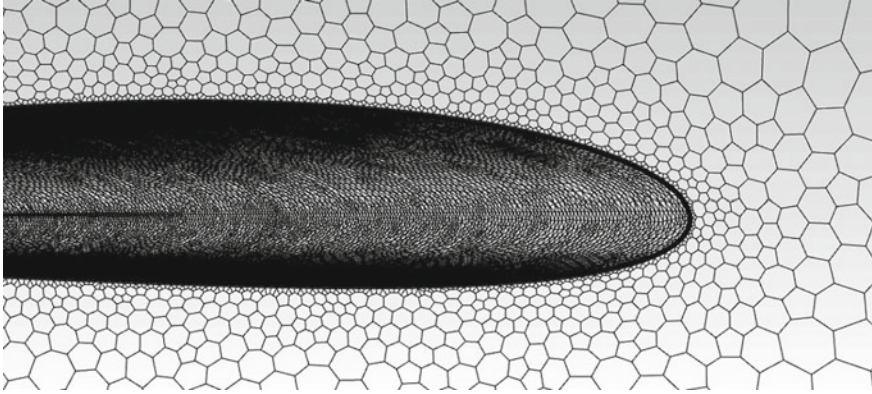


Fig. 4 The polyhedral mesh

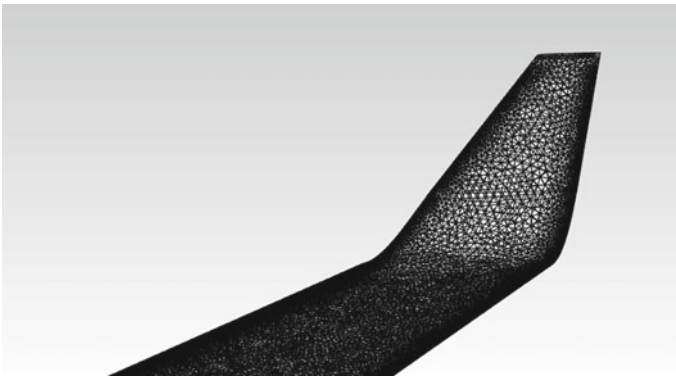


Fig. 5 Mesh on the winglet face

effort was used to obtain a mesh that was accurate and Figs. 4 and 5 show the mesh which was used. Grid independence study found that 2.5 million elements were sufficient to give accurate results.

3.3 Setup

Due to the flow being in the transonic regime, several considerations were needed. The density of air was no longer constant due to compressibility effects, thus the ideal gas model was selected. The Sutherland model of viscosity was also incorporated, to account for viscous heating. ANSYS FLUENT was used to solve the domain.

The density-based solver was chosen, with the Spalart–Allmaras turbulence model, both of which are suitable for this type of flow. Both full multi-grid (FMG)

initialisation and solution steering were employed to maintain stability and reach convergence.

3.3.1 Boundary Conditions

The external surfaces of the fluid domain were taken as far-field pressure, and the wing surface was taken as a wall with zero slip condition. The injection port at the wingtip was taken as a velocity inlet, ejecting air from the wing, into the atmosphere. The operating conditions were similar to a flight in cruising condition at 9000 m. In this regard, the ambient static temperature was chosen as 216 K and the static density as 0.466 kg/m³. The complete boundary conditions are given in Table 2.

Fluid injection in the case of the clean wing was done spanwise, with a backward sweep of 25° to keep consistency with the shape of the wing. In the case of the wing with a winglet, injection was done upwards, with a backward sweep of 25°. Figures 6 and 7 show the direction of injection.

Table 2 Boundary conditions

Name	Boundary condition	Value
Test domain external surfaces	Far-field pressure	230 m/s, 0 Pa gauge pressure
Wingtip injector	Velocity inlet	0, 50, 100, 150 m/s
Wing external surface	No slip wall	Standard wall roughness

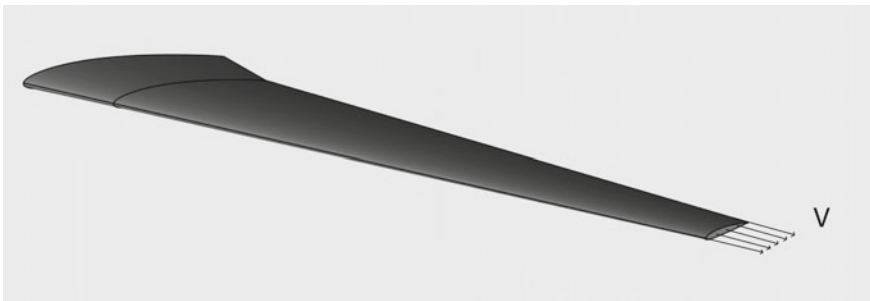


Fig. 6 Visualisation of fluid injection for the clean wing

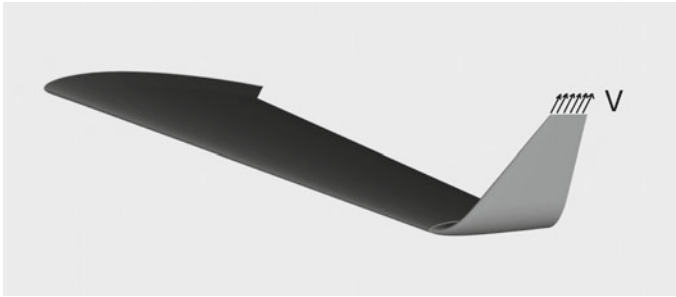


Fig. 7 Visualisation of fluid injection for the wing with winglet

4 Results and Discussion

4.1 Aerodynamic Coefficients Behaviour

The CFD results indicate that fluid injection had tangible improvements in the lift force produced and in the lift to drag ratio. The injected fluid is hypothesised to reduce the loss of low pressure and mitigate downwash, and therefore induced drag. However, it also adds to total drag, and thus must be optimised for ideal performance.

A baseline for comparing ejection velocity was created by finding the lift and drag coefficients for a (i) clean wing, and (ii) wing with a blended winglet, where there was no fluid injection. Fluid ejection was then conducted for 50, 100, and 150 m/s. It can be seen from Fig. 8 that fluid injection consistently helps increase lift as the injection velocity increases, for the clean wing at 0°. At 2.5° AoA, the improvement is negligible after 50 m/s.

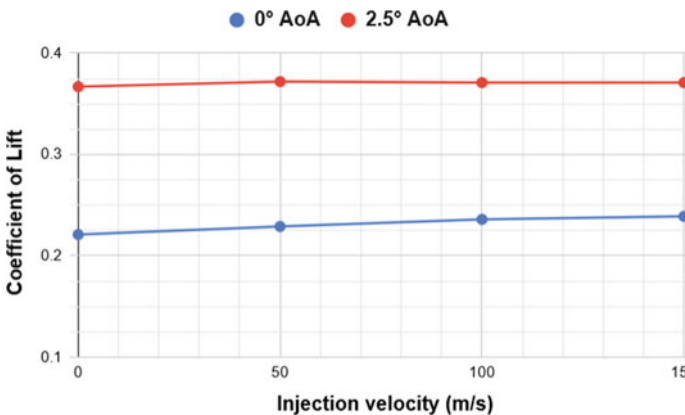


Fig. 8 Coefficient of lift versus injection velocity for clean wing

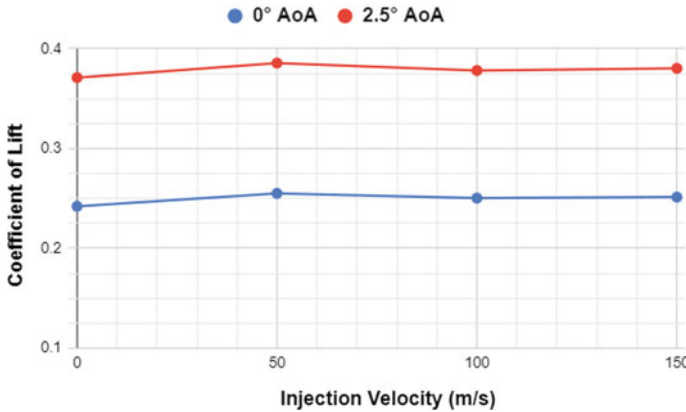


Fig. 9 Coefficient of lift versus injection velocity for wing with winglet

Lift generated by a wing is majorly due to the low pressure on the top surface rather than the high pressure on the bottom surface. The injected fluid acts as a barrier that safeguards the low pressure on the top surface of the wing from being diminished by the vortex. It seems intuitive that as the injection velocity gets higher, the effective barrier would become stronger, but the obtained results indicate that this effect diminishes beyond 50 m/s.

Figure 9 shows the variation for C_L with injection velocities and it can be noted that it reduces beyond 50 m/s. This may be attributed to the distinction that the fluid injection here is vertically upward, creating a reaction force that counteracts the benefit of weakening the wingtip vortex. As the injection velocity increases, the reaction force increases with the square of the velocity, and is the possible reason behind the reduction in lift beyond 50 m/s.

The drag coefficient universally increases with increasing injection velocity as seen in Figs. 10 and 11. There is a significant increase from 50 to 100 m/s for both the clean wing and the wing with a winglet. From these results, it is clear that fluid injection causes excess drag, and could be attributed to form drag or interference drag due to the introduction of the air from the wingtip to the ambient air.

For fluid injection velocity from 50 to 100 m/s, the increase in the drag coefficient is much more significant for the clean wing as compared to the wing with a winglet.

Figure 12 shows the variation of lift to drag ratio with injection velocities for a clean wing, indicating that at 50 m/s injection velocity, the best performance is achieved. For injection velocities higher than this, the L/D ratio falls lower than even the clean wing without any fluid injection.

As seen in Fig. 13, the variation of the lift to drag ratio for a wing with winglet shows similar characteristics to the clean wing, with an increase in lift to drag ratio from 0 to 50 m/s, but a subsequent drop in performance from there on. This pattern is consistent with the behaviour of the variation of the lift coefficient.

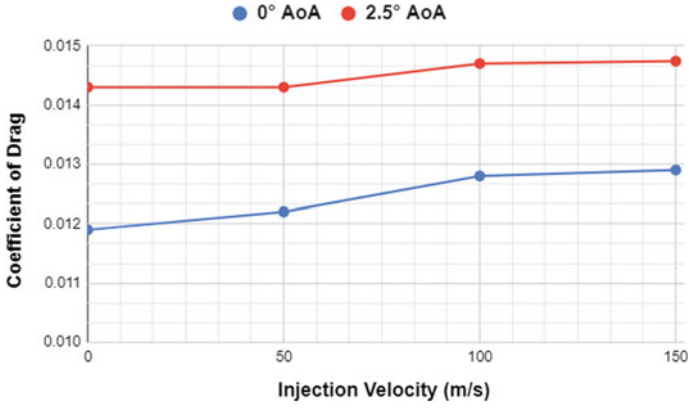


Fig. 10 Coefficient of drag versus injection velocity for clean wing

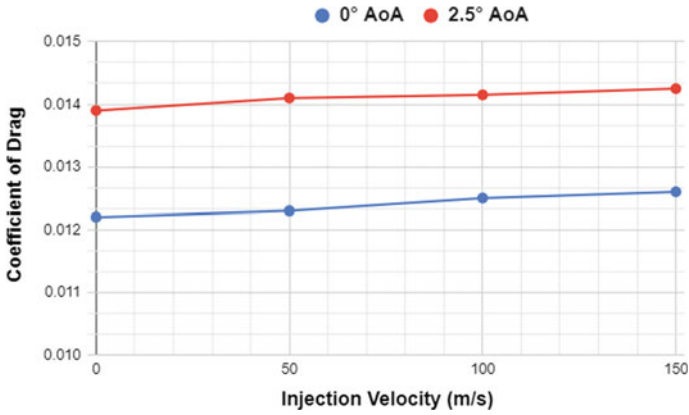


Fig. 11 Coefficient of drag versus injection velocity for wing with winglet

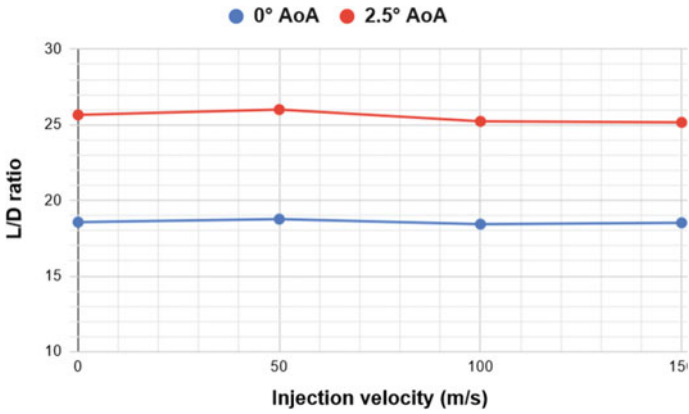


Fig. 12 L/D versus injection velocity for a clean wing

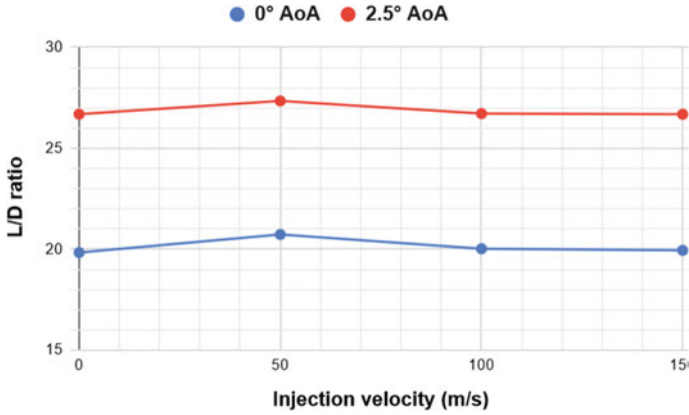


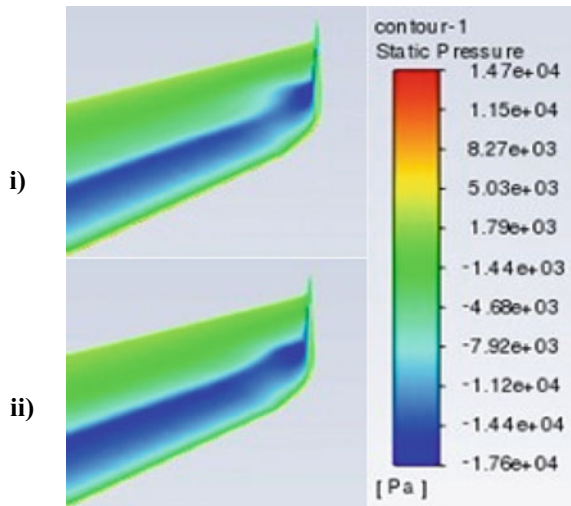
Fig. 13 *L/D* versus injection velocity for wing with winglet

The effect of fluid injection has a significantly larger improvement for the wing with a winglet, than the clean wing. There is a 4.54 and 2.44% increase in *L/D* at 0° and 2.5° angle of attack respectively, for the wing with the winglet. The clean wing only yields a 1 and 1.32% increase for the same angles of attack.

The pressure contours also indicate better lift distribution with the presence of fluid injection, especially close to the wingtip, as seen in Fig. 14. This is likely due to the injected air mitigating the action of relatively high pressure air next to and under the wing, on the top surface of the wingtip. It acts like a fluidic winglet in this regard and mitigates the effect of the wingtip vortex.

Figure 15 shows the complex flow physics involved in fluid injection and external mixing. The formation of the vortex can be clearly seen with this method.

Fig. 14 Contours of Static pressure for (i) wing without fluid injection and (ii) wing with 150 m/s fluid injection



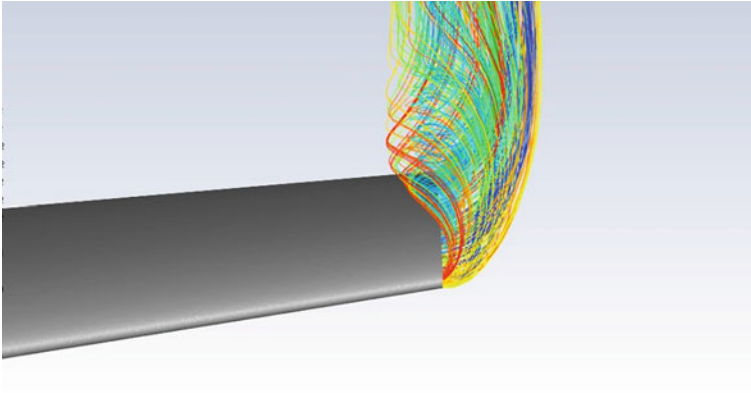


Fig. 15 Path lines of the air injected at 150 m/s for a clean wing at 2.5°

4.2 Cost of Fluid Injection

Since the ideal injection velocity is shown to be 50 m/s, calculations were done to estimate the pumping power required for this method of flow control. The estimation is done by assuming the most energy intensive case, that is, the air is accelerated from 0 to 50 m/s, before being pumped through a tube passing through the span of the wing. The curved section of the winglet contributes to the minor losses. The total power required in this scenario is 10 kW, which is well within the capacity of the aircraft's 50 kW generator.

Thus, fluid injection at 50 m/s appears to be a viable option for enhancing wing performance. Beyond this velocity, the pumping power drastically increases whilst the wing performance also reduces, making it unsuitable for improving wing performance.

Structurally, the wing is a complex component with provisions for storing fuel and housing various mechanisms for the control surfaces. Thus, adding a narrow fluid injection tunnel with the width of the wingtip would not pose a massive design challenge nor would it severely compromise existing functions. Large reservoirs would not be needed to store compressed air or limit the fluid injection, rather a separate intake in the engine could be utilised for the continuous collection of air for the purpose of injection.

5 Conclusions

Fluid injection is shown to be a good alternative and supplement to winglets. At both 0° and 2.5° angle of attack, fluid injection improved the coefficient of lift for all injection velocities. It also increased the L/D ratio when limited to 50 m/s. For both lift and drag coefficient, there is negligible change in the value from 100 to 150 m/s.

It contrasts from a conventional winglet in that it increases total drag on the wing, rather than reducing it at a fixed angle of attack. This implies that the fluid injection concept is a viable option during the landing and take-off phases of flight, where maximising the lift is a priority, even at the cost of increased drag. However, it could still be used by aircraft in cruise flight by using the improved L/D for lower drag at the same lift as in the case of no fluid injection.

Acknowledgements We would like to extend our gratitude firstly to Dr. V. Krishna, our guide for this project. We would also like to thank the faculty and students of PES University for their support and advice. We appreciate the help, resources, and assistance from the students and faculty of the PMR lab, PES University. Lastly, we would like to thank our parents for their constant backing and encouragement.

Nomenclature

e	Oswald efficiency factor
AR	Aspect ratio
C_D	Coefficient of drag
C_L	Coefficient of lift
C_p	Coefficient of pressure
α	Angle of attack ($^\circ$)
ρ	Density of air [kg/m^3]
L/D	Lift to drag ratio

References

1. Thimmegowda H, Krishnan Y, Gisa G (2021) Computational study on wingtip vertical fluid injection for induced drag reduction. In: Proceedings of the 8th international conference on fluid flow, heat and mass transfer
2. Zaccara M, Paolillo G, Greco CS, Astarita T, Cardone G (2021) Flow control of wingtip vortices through synthetic jets. *Exper Therm Fluid Sci*
3. El Maani R, Radi B, El Hami A (2018) CFD analysis of the transonic flow over a NACA 0012 Airfoil, Research gate, 2018. 10.2149
4. de Mattos BS, Macedo AP, da Silva Filho DH (2003) Considerations about winglet design. In: Applied aerodynamics conference on AIAA 2003-3502
5. Öztürk Ş, Örs İ (2020) An overview for effects on aerodynamic performance of using winglets and wingtip devices on aircraft. *Int J Aeron Astron*

6. Devenport WJ, Rife MC, Liapis SI, Follin GJ (1996) The structure and development of a wing-tip vortex. *J Fluid Mech* 312:67–106
7. Yahaya N, Ismail AMM (2015) Investigation of Whitcomb's winglet flow behaviour using PIV and FLUENT. *J Adv Res Fluid Mech Thermal Sci*
8. ANSYS Inc. (2015) ANSYS fluent theory guide 12.0
9. White FM (2011) *Fluid mechanics*. McGraw-Hills, New York, USA
10. Anderson JD (2011) *Introduction to flight*. McGraw-Hills, New York, USA

Numerical Studies of the Influence of Strouhal Number on the Flow Characteristics of Synthetic Jet Impingement



Pawan Sharma, Dnyanesh Mirikar, Jitendra K. Choudhary, Raghuvamsi Bokka, Jay Joshi, Santosh K. Sahu, and Harekrishna Yadav

Abstract In this work, the efficacy of synthetic jet impingement has been investigated for cooling applications. Numerical study is being carried out for two different Strouhal numbers (Sr) = 0.03 (low) and 0.43 (high) at constant $Re = 3215$ for 8 mm orifice diameter. In the present study, the SST $k-\omega$ model is used for the computational study along with the user-defined functions (UDF) to describe the movement of the diaphragm. The results showed that the jet's Sr plays a significant role in the flow behaviour of SJ. At low Strouhal number (i.e., $Sr = 0.03$), the synthetic jet flow field is characterized by primary vortex ring followed by a trailing jet. Each vortex ring impinges on the surface separately due to the large wavelength between the coherent structures. However, high Sr jet flow field is exhibited by the train of primary vortices, which accumulate and even break up into smaller structures before impinging on the surface. At an intermediate surface spacing ($z/d = 6$), jet with high Sr exhibits a 9.9% higher heat transfer rate at the stagnation point than a low Sr jet. The intermittent vortex pairing in high Sr jet causes the breakdown of naturally occurring vortices and promotes a higher heat removal rate.

Keywords Synthetic jet · Frequency · Strouhal number · Flow recirculation · Numerical · Flow morphology

1 Introduction

The ever-increasing demand of compact-sized electronic gadgets has created challenges for the thermal management of such devices. Many technologies have been devised to sort out the problem of their thermal management. Amongst them, cooling by synthetic jets has gained rapid attention from the engineers and developers in recent time. A synthetic jet (SJ) is developed using an actuator which consists of an

P. Sharma (✉) · D. Mirikar · J. K. Choudhary · R. Bokka · J. Joshi · S. K. Sahu · H. Yadav
Department of Mechanical Engineering, Indian Institute of Technology, Indore, India
e-mail: phd1901203008@iiti.ac.in

oscillating mechanism like a piston-cylinder arrangement, speaker, or piezoelectric diaphragm. There are two strokes in the synthetic jet: suction and ejection strokes. The mass of fluid sucked into the cavity during the suction stroke is expelled from the cavity during the ejection stroke. The unique characteristics of synthetic jets i.e., zero-net-mass flux and non-zero momentum flux [3], no external flow requirement, low power consumption, and ease of integration with complex devices make them a viable option in various applications. Recent studies on the flow mechanism of impinging synthetic jets have shed light on the influence of Strouhal number w.r.t flow field characteristics of SJ. This motivates our investigation into the effects of jet's Strouhal number on the flow and heat transfer characteristics of synthetic jet impingement.

2 Literature Review and Objective

The synthetic jet technology has attracted many researchers for cooling of compact-sized electronic devices due to their compact size and high reliability. In many studies, it has been found that excitation frequency and corresponding Strouhal number play a critical role in the thermal characteristics of impinging jets. Pavlova and Amitay [1] studied the excitation frequency ($f = 420$ and 1200 Hz) effect on SJ cooling performance. They argued that at the lower orifice to surface distance ($z/d < 10$), the high-frequency jet ($f = 1200$ Hz) outperformed the low-frequency jet. However, at a higher surface distance ($z/d > 15$), a low-frequency jet ($f = 420$ Hz) dissipates more heat w.r.t to high-frequency jet. According to them, for low-frequency jets, vortex rings impinge on the surface individually due to large wavelengths between coherent structures. In contrast, for high-frequency jets, vortex rings come apart and fuse. Vejrazka et al. [2] explored the effect of excitation frequency corresponding to Strouhal number, $Sr = 0.2-4$ and $Re = 10,000$ at a low surface distance ($z/d = 2$). They explored that low-frequency excitation causes large-sized vortices to form compared to those without excitation.

Tianshu and Sullivan [3] studied the excited impinging jet at a small distance ($z/d \leq 2$). They observed that at a frequency excitation of $Sr = 0.85$ forms bigger and structured vortices which causes a local reduction in heat transfer. However, heat transfer is increased by exciting at $Sr = 1.6$, which induces arbitrary and irregular small-size vortices. Gharib et al. [4] studied the size of vortices formation for different Strouhal numbers. They found that with increasing the Sr , the size of vortex core diameter decreases. They also argued that with a large stroke length, L (low Sr), the SJ flow field comprises of a primary vortex ring trailed by a trailing jet. However, the flow field arises from small L (high Sr) jet showed only a single vortex ring. The transition between these two distinct cases occurs at approximately $Sr = 0.25$ (termed as formation number). The maximum circulation for the vortex ring is also attained at $Sr = 0.25$. Greco et al. [5] analysed the behaviour of a turbulent impinging synthetic jet for different dimensionless stroke lengths and orifice-to-plate distances. At low dimensionless stroke lengths, no trailing jet is present, and the flow field is

characterized by the simultaneous presence of multiple primary vortex rings, which impinge on the plate, separately. At high dimensionless stroke lengths, the synthetic jet flow field consists of two main structures: the trailing jet and the primary vortex ring.

In the literature, there is no study which presents the flow morphology of synthetic jet at different Strouhal numbers for constant input power. So, in the present study, the flow characteristics of the impinging synthetic jets are studied numerically for Strouhal number of 0.03 and 0.43 at a constant Reynolds number of 3215, jet to surface spacing $z/d = 2-16$.

3 Materials and Methods

3.1 Numerical Methodology

In current study, the numerical simulation is carried out based on the exit flow parameters of a loudspeaker-based SJ actuator. The entire study is carried out on a 2-dimensional geometry of the numerical set-up using commercially available software, ANSYS FLUENT. In this study, orifice diameter $d = 8$ mm, orifice thickness $h_o = 2.5$ mm, and surrounding size $= 30d$ (laterally) are chosen as per Jain et al. [6]. The value of axial spacing (z) is varied in a certain range of $z/d = 2-16$ keeping other geometric parameters same. The schematic geometry used for present simulation has been shown in Fig. 1 along with the boundary conditions.

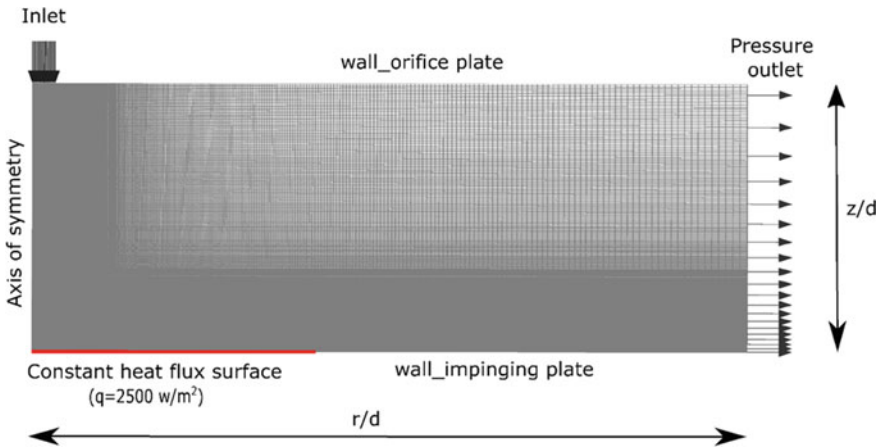


Fig. 1 Schematic diagram of axisymmetric 2D geometry showing the boundary conditions

3.2 Numerical Solver and Procedure

This section describes the procedure and physics used in commercially available ANSYS FLUENT software to study the flow characteristics of the synthetic jet with different strokes lengths. The rapid change in pressure/density due to the oscillatory motion of the diaphragm creates the synthetic jet flow as compressible and turbulent. To account for this, the unsteady Reynolds-averaged Navier–Stokes (RANS) equations are generally used as governing equations. According to a study by Yoo and Lee [7], Menter’s shear stress transport (SST) turbulence $k-\omega$ model accounts for the turbulent characteristics of the synthetic jet flows. Added, a $k-\omega$ model offers a more accurate solution near the wall boundary. So, in the present study, the SST $k-\omega$ model is used for the computational study along with the user-defined functions (UDF) to describe the movement of the diaphragm. The pressure-based, segregated, unsteady solver with axisymmetric geometry is used with a first-order implicit time scheme that is stable with the time step size. The SIMPLE pressure–velocity coupling scheme describes the iterative corrections for pressure and velocity. The Second-order upwind spatial discretization is used for the momentum, turbulent kinetic energy, and turbulent dissipation rate.

3.3 Mesh and Its Independence

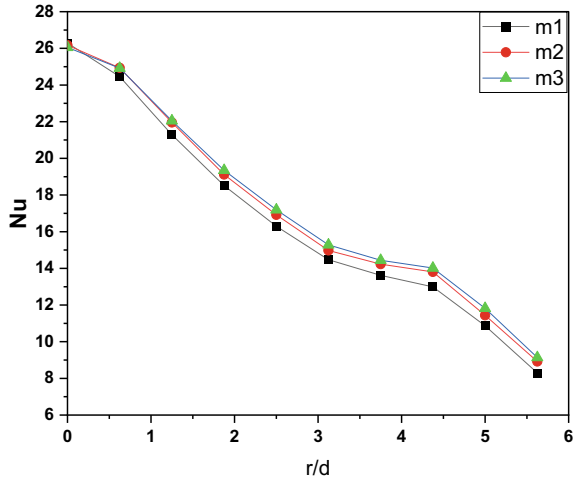
In the present simulations, quadrilateral mesh topology is used as shown in Fig. 1. The grid size is kept such that $y+$ values at the impingement surface are always below one during the simulations and the corresponding first cell height of $2.5e-5$ is chosen for the impingement wall. Three meshes with different number of elements have been tested for mesh independence as shown in Table 1.

To check the effect of grid size on the important parameters, simulation was run on each mesh for 0.5 s, for $Sr = 0.03$; $z/d = 6$. Figure 2 shows the variation Nu on the impinging surface for different mesh sizes. From the Fig. 2, the error between the successive mesh size reduces gradually. For the optimum simulation time and accuracy, the mesh $m2$ with 104,400 elements was selected for further simulations.

Table 1 Different sizes of meshes considered in the mesh independence study

Mesh sizes	Number of elements
$m1$	51,156
$m2$	104,400
$m3$	176,436

Fig. 2 Mesh independence study for three different mesh sizes



3.4 Experimental Methodology

The experimental setup comprises a Synthetic Jet Actuator (SJA) assembly, hot-wire anemometry, an IR thermal imaging setup along with a heated foil. The SJ actuator assembly uses a loudspeaker of 73 mm diaphragm size and an 8 mm diameter orifice plate. A power oscillator (SI-28DR) supplies the input sinusoidal signal to the SJ actuator. The amplitude of the input signal is maintained constant ($= 4V_{rms}$). A constant temperature hot-wire anemometer (Mini CTA 54 T42) with a single wire probe is employed to measure the flow velocity at the orifice exit. A 120 mm × 120 mm size matte finish test foil (SS material, AISI-304) is heated by a direct current power source for a constant heat flux of 2.5 kW/m². The back side of the test surface is painted with flat black paint to achieve uniform emissivity ($\epsilon = 0.95$). The thermal imaging technique with an IR camera (FLIR: A655sc) is used to study the heat transfer characteristics by gauging the temperature of the test surface. The IR camera measures temperatures from 0 to 2000 °C with an uncertainty of 1.5%. A calibration technique elaborated in [8] is employed to obtain the emissivity of 0.95 from the IR camera setup. More details of the experimental procedure and data reduction can be found in our previous study on SJ impingement [8].

3.5 Data Reduction

The mean time-averaged centreline velocity is computed by integrating the instantaneous velocity ($u(t)$) during the ejection phase and averaged over a whole cycle time period (T) [9] and it is labelled as

$$U_0 = \frac{1}{T} \int_0^{T/2} u(t) dt \quad (1)$$

Based on the centreline mean time-averaged velocity at the orifice exit, Reynolds number (Re) is computed as follows [10]

$$\text{Re} = \frac{\rho U_0 d}{\mu} \quad (2)$$

where d is the orifice diameter, and the dynamic viscosity of the working fluid is denoted by μ .

The dimensionless Strouhal number describes the oscillating flow mechanism or the flow fluctuations. As per definition, the Strouhal number is a measure of the ratio of the inertial forces by virtue of the local acceleration (flow unsteadiness) to the inertial forces due to convective acceleration. It is the inverse of dimensionless stroke length

$$\text{Sr} = \frac{f \times d}{U_0} \quad (3)$$

where f is vortex shedding frequency (or Strouhal frequency).

For the heat transfer calculations, the local convective heat transfer coefficient (h_i) and the equivalent Nusselt number (Nu_i) can be computed for i th control volume based on the following equations

$$h_i = \frac{q_{\text{conv},i}}{A_i(T_{s,i} - T_{a,i})} \text{ and } \text{Nu}_i = \frac{h_i d}{k_f} \quad (4)$$

Here, $T_{s,i}$ denotes the surface temperature of the test foil, and $T_{a,i}$ is the temperature of the ambience/surrounding for the i th control volume. More details can be found in our latest article [8].

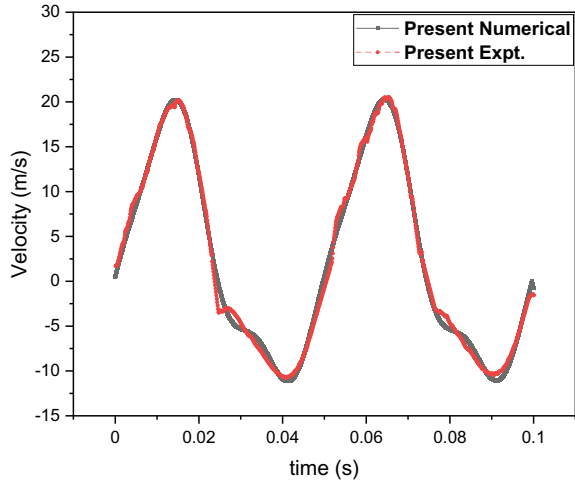
4 Results and Discussion

4.1 Validation Study

As discussed in the literature review, the velocity for the vibrating diaphragm has been modelled using,

$$U = U_0 \sin(2\pi ft) \quad (5)$$

Fig. 3 Experimental and numerical comparison for the flow velocity at the orifice exit



The values obtained numerically are compared to our own experimental data. Experiments are conducted by using an acoustic actuator with constant orifice diameter of 8 mm. Due to paucity, the complete details of experimental procedure and its data reduction can be found in our previous study on SJ impingement [8]. Figure 3 shows the comparative plot for the velocity between the numerical and experimental studies. It is clear from Fig. 3 that the velocity model for the numerical analysis is correct and valid for the inlet condition.

Heat transfer effects on the impinging plate by the SJ have been studied for the different dimensionless stroke lengths. The average Nusselt number (Nu_{avg}) has been monitored with the axial surface spacings and numerical results are being compared to the experimental findings for dimensionless Strouhal number, $Sr = 0.03$ (Fig. 4). The maximum deviation between the numerical and experimental results is found to be $\pm 9.89\%$ at $z/d = 2$.

4.2 Effects of Strouhal Number on Vorticity Magnitude

The effects of Strouhal number (Sr) been studied w.r.t the flow characteristics of SJ impingement Table 2. From Fig. 5, it can be inferred that at low Strouhal number (i.e., $Sr = 0.03$), the synthetic jet flow field is characterized by primary vortex ring followed by a trailing jet [4, 5]. The vortex ring impinges on the surface separately due to the large wavelength between the coherent structures. A trailing jet can further be interpreted by a region of the potential core with low turbulence intensity bounded by a zone of shear layer [38]. Furthermore, the primary vortex rings and their successive Kelvin–Helmholtz vortex rings generate secondary vortex rings along the impinging plate during the sweeping phase [1, 5–11]. However, the flow mechanism in a high Strouhal number ($Sr = 0.43$) jet is entirely different. High Sr jet flow field is illustrated

Fig. 4 Average Nusselt number variation at $z/d = 6$ for $Sr = 0.03$

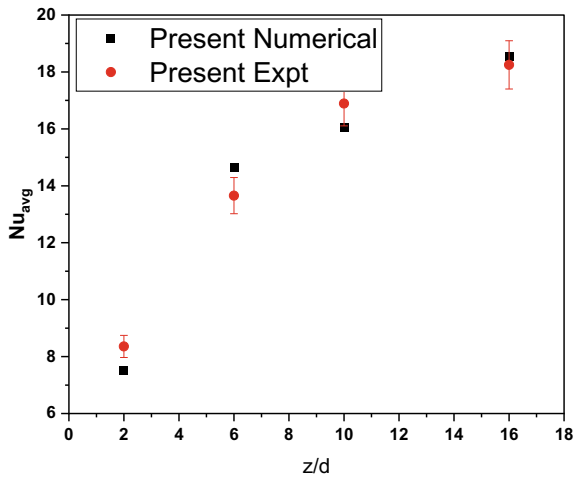


Table 2 Actuating parameters of the input signal for different stroke length

Actuating frequency, f (Hz)	Mean ejection velocity, U (m/s)	Reynolds number (Re)	Strouhal number (Sr)
20	12.18	3215	0.03
330	12.18	3215	0.43

by the train of primary vortices, which accumulate and even break up into smaller structures before impinging on the surface. Here, no trailing jet is found due to very less wavelength between the successive primary vortices.

4.3 Pressure Variation at Different Surface Spacing

The static pressure has been monitored for two different Strouhal no. ($St = 0.03$ and 0.43) at varied orifice to surface spacing. The static pressure variation of two such Sr jet is studied in the near-field and far-field region (i.e., $z/d = 2$ and 10) respectively (Fig. 6). From Fig. 6, it can be inferred that the mean static pressure of high Sr jet is higher than the low Sr jet at the stagnation region for $z/d = 2$. However, at higher surface spacing of $z/d = 10$, low Sr jet ($Sr = 0.03$) exhibits significantly higher static pressure on the impinging plate at $r/d \leq 2$. It is also observed that the pressure distribution is almost identical at a distance far from the stagnation region ($r/d \geq 2$) in both the cases of Sr. Shu Lee et al. [36] observed a similar pressure variation over the impinging plate with the radial positions. The pressure variation along the radial direction also shows the negative pressure for the $Sr = 0.43$. It shows that at low surface spacing, high strength vortices impinge at the surface which causes flow separation [11].

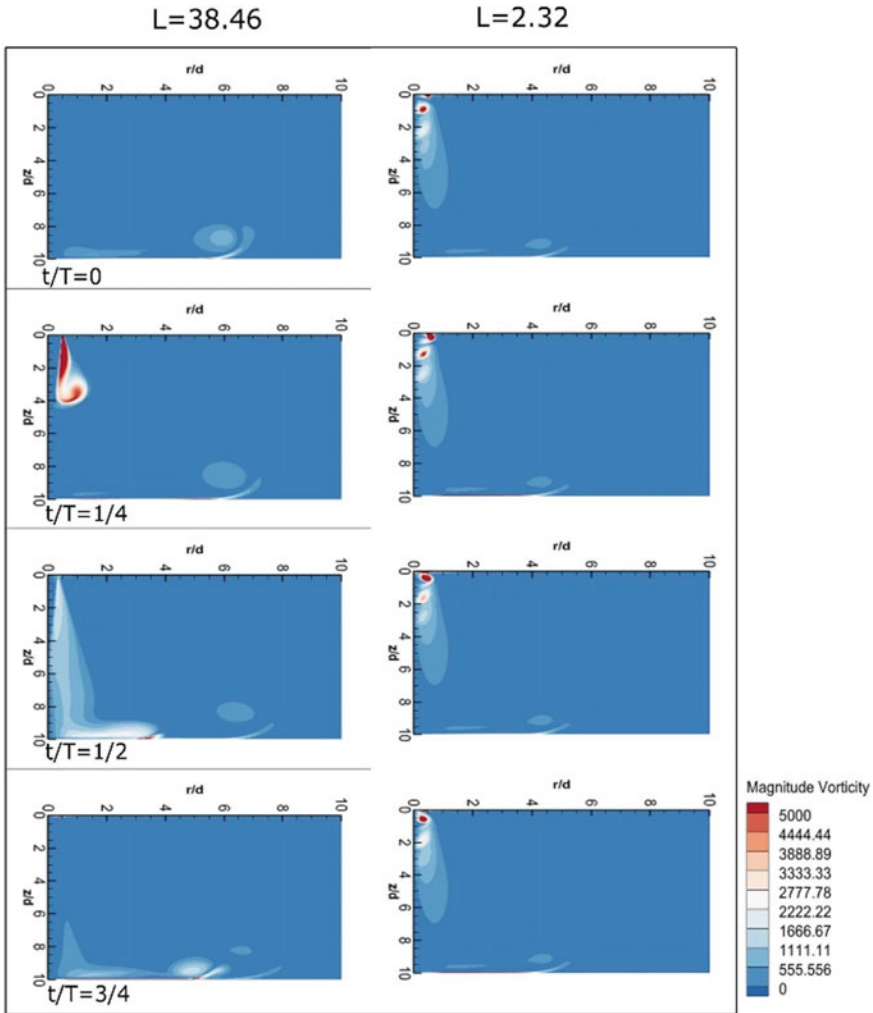
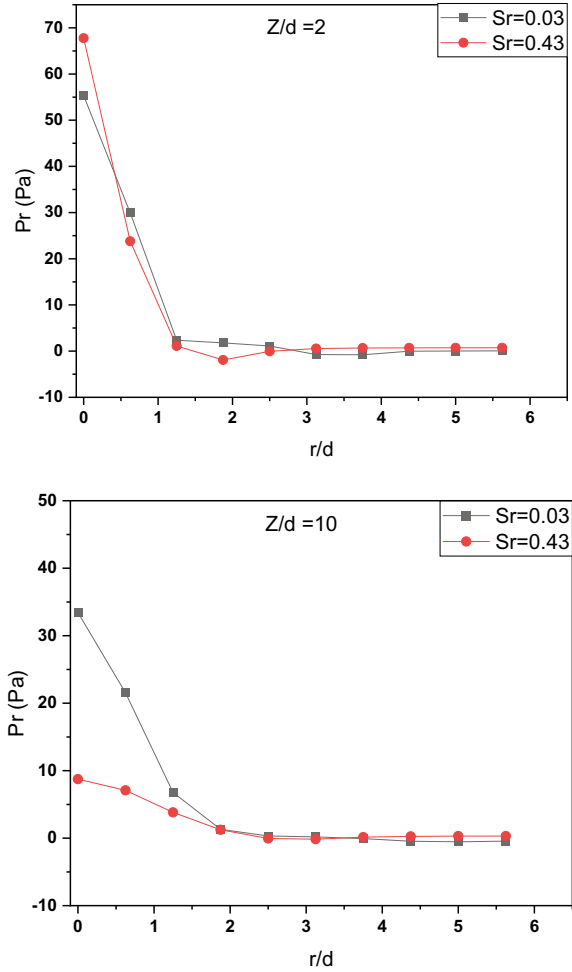


Fig. 5 Instantaneous flow field of an impinging SJ at a) low Sr ($Sr = 0.03$) (left) and b) high Sr ($Sr = 0.43$) (right)

4.4 Average Nusselt Number Variation for Different Strouhal Number

Figure 7 shows the variation of the average Nusselt number (Nu_{avg}) with normalized surface spacings for two different Strouhal numbers ($Sr = 0.03$ and 0.43) jet. In near surface spacing of $z/d = 2$, the heat transfer characteristics of low Sr are obtained to be higher than the high Sr SJ. These result shows the opposite trend as obtained with continuous and pulsatile impinging jets, i.e., for lower surface spacing, a high Sr jet

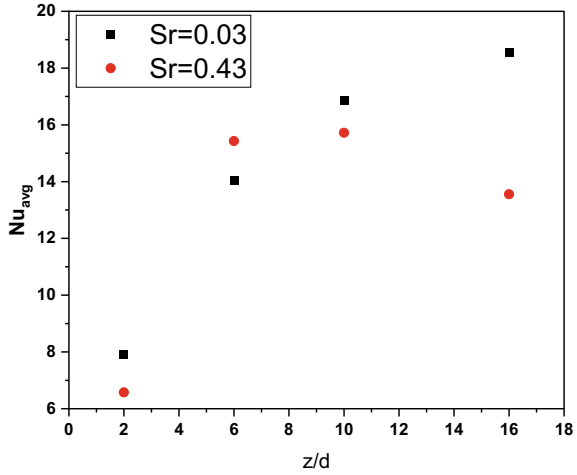
Fig. 6 Static pressure variation of SJ impingement at two different Strouhal number



exhibits better cooling characteristic and vice-versa. The cause for the lower cooling performance of high Sr in near spacing is due to the negative impact of recirculation which occurs majorly with high Sr SJ. At an intermediate surface spacing of $z/d = 6$, the cooling performance of high Strouhal no. ($Sr = 0.43$) jet shows more heat transfer rate than the low Sr jet. At $z/d = 6$, a high Sr jet exhibits 9.9% more average Nu compared to a low Sr jet (Fig. 7). At intermediate surface spacing ($z/d = 6$), the effect of recirculation diminishes as also observed by Yadav et al. [12]. So, with a high Sr jet, the frequency of intermittent vortex formation is close to the natural frequency of jet formation. This adds to the high heat transfer rate of high Sr jet compared to low Sr jet at such spacing.

Further, at high surface spacing, the jet operating at low Sr overcomes the high Sr jet in terms of the cooling effect. Since the frequency of vortex passing reduces

Fig. 7 Variation of average Nusselt number for different z/d at two different Sr jet



with moving in downstream [13]. So, when the jet is excited at low Sr, vortex passing frequency is about the natural frequency of jet formation at such high surface spacing ($z/d \geq 10$) which adds in their high thermal performance. At $z/d = 16$, low Sr jet exhibits 36.7% enhancement in heat transfer rate as compared to high Sr jet.

5 Conclusions

In the present experimental study, heat transfer characteristics of synthetic jets with different Strouhal numbers ($Sr = 0.03$ and 0.43) are studied for an 8 mm orifice at $Re = 3215$. At low Strouhal number ($Sr = 0.03$), the SJ flow field comprises of primary vortex rings followed by a trailing jet. Each vortex ring impinges on the surface separately due to the large wavelength between the coherent structures. However, high Sr jet flow field is illustrated by the train of primary vortices, which accumulate and even break up into smaller structures before impinging on the surface. Here no trailing jet is found due to very less wavelength between the successive primary vortices. w.r.t. heat transfer characteristics, a high Strouhal number ($Sr = 0.43$) jet exhibits 17.5% higher average Nusselt number compared to a low Sr jet. At an intermediate surface spacing of $z/d = 6$. It occurs because the high frequency of intermittent vortex formation in high Sr jet is close to the natural frequency of the vortex formation, which adds to their high heat transfer rate at such surface spacing. Further, at the higher surface spacing of $z/d = 16$, the low Sr ($Sr = 0.03$) jet exhibits 15.3% better heat transfer as compared to the high Sr ($Sr = 0.43$) jet. This occurs because a low Sr jet promotes the stable vortex pairing, and such large-scale vortices excite near to the natural frequency of jet formation at such high spacing and dissipate more heat compared to a high Sr jet.

Acknowledgements The present work is partially supported by the Science and Engineering Research Board, India [grant number: CRG/2021/005458].

Nomenclature

d	Orifice diameter (mm)
Sr	Strouhal number
t	Orifice plate thickness (mm)
Nu_{avg}	Average Nusselt number
Re	Reynolds number
T_s	Surface temperature of test foil ($^{\circ}C$)
T_a	Ambient temperature ($^{\circ}C$)
z/d	Dimensionless orifice to surface distance
SJ	Synthetic jet

References

1. Pavlova A, Amitay M (2006) Electronic cooling using synthetic jet impingement. *J Heat Transfer* 128(9):897–907. <https://doi.org/10.1115/1.2241889>
2. Vejrazka J, Tihon J, Mart P, Sobolík V (2005) Effect of an external excitation on the flow structure in a circular impinging jet. *Phys Fluids* 17(10). <https://doi.org/10.1063/1.2084207>
3. Tianshu L, Sullivan JP (1996) Heat transfer and flow structures in an excited circular impinging jet. *Int J Heat Mass Transf* 39(17):3695–3706. [https://doi.org/10.1016/0017-9310\(96\)00027-0](https://doi.org/10.1016/0017-9310(96)00027-0)
4. Gharib M, Rambod E, Shariff K (1998) A universal time scale for vortex ring formation. *J Fluid Mech* 360:121–140. <https://doi.org/10.1017/S0022112097008410>
5. Greco CS, Paolillo G, Ianiro A, Cardone G, de Luca L (2018) Effects of the stroke length and nozzle-to-plate distance on synthetic jet impingement heat transfer. *Int J Heat Mass Transf* 117:1019–1031. <https://doi.org/10.1016/j.ijheatmasstransfer.2017.09.118>
6. Jain M, Puranik B, Agrawal A (2011) A numerical investigation of effects of cavity and orifice parameters on the characteristics of a synthetic jet flow. *Sens Actuat A* 165(2):351–366. <https://doi.org/10.1016/j.sna.2010.11.001>
7. Yoo I, Lee S (2012) Reynolds-averaged Navier-Stokes computations of synthetic jet flows using deforming Meshes. *AIAA J* 50(9):1943–1955. <https://doi.org/10.2514/1.J051539>
8. Sharma P, Sahu SK, Yadav H (2022) Experimental investigation of flow and thermal characteristics of synthetic jet issuing from sharp-edged orifices. *Experim Heat Transf* 00(00):1–25. <https://doi.org/10.1080/08916152.2022.2105449>
9. Holman R, Utturkar Y, Mittal R, Smith BL, Cattafesta L (2005) Formation criterion for synthetic jets. *AIAA J* 43(10):2110–2116. <https://doi.org/10.2514/1.12033>
10. Smith BL, Glezer A (1998) The formation and evolution of synthetic jets. *Phys Fluids* 10(9):2281–2297. <https://doi.org/10.1063/1.869828>
11. Yadav H, Agrawal A (2018) Effect of vortical structures on velocity and turbulent fields in the near region of an impinging turbulent jet. *Phys Fluids* 30(3):35107. <https://doi.org/10.1063/1.5001161>

12. Yadav H, Joshi A, Chaudhari M, Agrawal A (2019) An experimental study of a multi-orifice synthetic jet with application to cooling of compact devices. *AIP Adv* 9(12):125108. <https://doi.org/10.1063/1.5128776>
13. Han B, Goldstein RJ (2003) Instantaneous energy separation in a free jet. Part I. Flow measurement and visualization. *Int J Heat Mass Transf* 46(21):3975–3981. [https://doi.org/10.1016/S0017-9310\(03\)00245-X](https://doi.org/10.1016/S0017-9310(03)00245-X)

Aerodynamic Analysis of Stretched Trailing Edge Over NACA 0020 Airfoil at Various Turbulence Intensities



E. Livya and S. Nadaraja Pillai

Abstract To understand how the stretched trailing edge customizes the airfoil aerodynamics in an experimental approach, the present work studied the symmetrical NACA 0020 airfoil subjects to the incoming airflow at higher intensities of freestream turbulence (i.e. 12%). The Reynolds number was fixed as $Re = 2.4 \times 10^5$, the airfoil was tested under various turbulence intensities of 0.3, 7 and 12%. The trailing edge of the airfoil has been stretched for the extension (h) of 10%, 20% and 30% of chord (c) and the test carried for the angle of attack varies from 0° to 35° . It has been realized that stretching the airfoil trailing edge can augment the lift with a less significant increment in drag. The stretched trailing edge is simply an add-on thin plate fixed together with the airfoil at the trailing edge without altering the elemental structure of the conventional airfoil benefits to advance the aerodynamic performance. The obtained results direct that revising the airfoil trailing edge revises the flow pattern over the airfoil. The modification in terms of stretching the trailing edge acts as a flow control tool and aids to maintain the performance even operating at higher freestream turbulence.

Keywords Stretched trailing edge · Freestream turbulence intensity · Wind tunnel experiment · Pressure scanner · Stall delay

1 Introduction

Airfoils operating in the region are frequently subjected to an immense range of imminent flow circumstances, notably within the limit of the earth's atmosphere. For instance, aircraft approach to take-off and landing, wind turbine blades employed in the windmill etc. Within the earth's boundary level, the instability taking place in the flow is unpredictable due to the existence of surface roughness, and various landscape and climatic conditions. During certain circumstances, the aerodynamic properties

E. Livya · S. N. Pillai (✉)

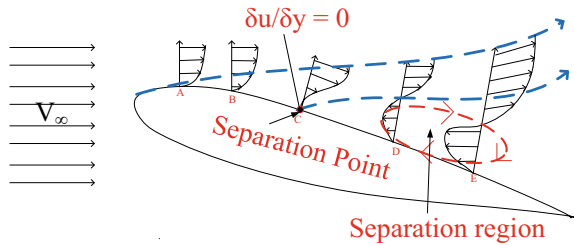
Turbulence and Flow Control Lab, School of Mechanical Engineering, SASTRA Deemed University, Thanjavur 613401, India
e-mail: nadarajapillai@mech.sastra.edu

of the airfoil may undergo possible alterations. The test done by [1] observing the magnitude of the T.I. present in the surrounding environment initially from 50 to 150 m of altitude from the earth's surface measures to be more or less 35%. The measurement was taken in Australia. The aerodynamic properties of the airfoil can surely be affected when operating in the regional zone. F.S.T was generated by [2] inside the wind tunnel by using the fine mesh screen placed 20 cm before the test model. Knowingly, this was the initial study to obtain knowledge on how the aerodynamic properties are affected by the F.S.T. The NACA 0021 (symmetric) airfoil profile was tested, and the results say a rise in the T.I. will improve the lift parameter and even delay the effect of a stall [19]. The lift measures along the straight linear regime stay consistent. The Clark-Y (camber) airfoil exhibits the identical behaviour as mentioned for the symmetrical airfoil, but the lift gradient tends to decrease with an increase in turbulence intensity. In conflict with the symmetric and cambered airfoil, the thin NACA 0006 (thin and symmetric) exhibits independence from turbulence intensity. Research like [3] targets the transition of airflow from laminar to turbulent behaviour in range over the surface boundary layer. The analysis is necessary for the design of subsonic airfoils employed in low-range Reynolds number of the boundary layer remains laminar. Test conducted by the [4] with NACA 0015 airfoil at five distinct turbulent intensities from 0.3 to 12%. They induced the turbulence by using the passive turbulent grid using a set of rods. The lift co-efficient increases till the turbulent intensity reaches 9%, after there exists a minimum rise in the lift factor. Report [5] shows the behaviour of the NACA 0021 airfoil at the various T.I. of 0.5, 4 and 6% at the freestream velocity of 35 m/s. The stall angle gets delayed considerably. However, there exists no important change in the lift factor. A wind turbine test conducted by [6, 7] with the airfoil profiles of DU93-W210 and NREL S809 at different turbulent intensities observed that the lift gets maximized with no stall delay. PIV results in displays at $\alpha = 14^\circ$, the separation point gets delayed to further at greater turbulent intensities. The test with NREL S826 by [8] shows that a lift improvement occurs at the Reynolds number range of 10^4 , when increasing the Reynolds number to 10^5 range, there is no improvement.

Wind turbine airfoil self-developed by [9] tested at maximum turbulence intensity of 13% at the Reynolds number of 2×10^5 . The results display that lift increases at higher angles and the lift gradient is not changed in the narrow region. The flow homogeneity is an important factor. The airfoil model was tested in non-homogeneous conditions [10], they suggest as the measured values are either direct or integrated forms of pressure distribution, hence the aerodynamic parameter are sensitive to flow uniformity. In the case of non-uniform flow, the values will vary along the span. The net results are an integrated form of the entire span. It directly mentions that the properties depend on the level of flow uniformity.

To produce high lift, industries try to design high-lift generating devices attached to the wing. Existing base flaps will produce the heavy drag usually exposed during aircraft approaches to take-off and landing but not matched during cruise flights. Micro-flaps [11–13] are tested at both low speed [14] and high speed [15]. The specially designed flaps will improve the aerodynamic characteristics of aircraft by lift augmentation and delay the flow separation. The flap fitted to the airfoil as an

Fig. 1 Schematic view of airflow over the airfoil



add-on device with a slot undergoes deflection and is mentioned as the flap deflection angle. The flap deflection will also change the aerodynamic properties. An expanded review of trailing edge tools and other existing flow control devices as mentioned in the reference paper [16].

The wing of the owl and merganser has a thin feather extended from a base airfoil, this event represents the structure of the avian wing, and this impresses the thought of STE. The conventional airfoil stays unaltered but it is simply stretched to a certain amplitude at the trailing edge using a thin stainless steel plate. As mentioned in Fig. 2, the structural specification of the conventional airfoil is airfoil chord c and amplitude of STE (h). In the recent working environment, our STE is fixed in line with the base airfoil trailing edge rigidly. STE plates are not deflected and vibrated during measurement. The impact of STE on the airfoil aerodynamics is primarily due to the alteration that takes place in the flow behaviour of the trailing edge. The lift augmentation due to the stretched airfoil is mainly because of the camber effect. Currently, stretching the airfoil at the rear will increase the camber of the airfoil reflected in a larger revision in the flow momentum around the airfoil, changing the value of ΔP (pressure difference) results in rising in the lift [18] and the minor drag penalty is noted for STE. Drag comparison made focused on the base airfoil.

The work initially tested the base airfoil and STE under the mentioned conditions. In addition, for real case operation and to observe the effect of T.I. on the airfoil performance, the measurement is taken for the conventional and STE airfoil in the turbulence level of 0.3, 7 and 12%. The lift augmentation is achieved by STE, the L/D ratio remains mostly similar. The stretched trailing edge airfoil helps to sustain the aerodynamic properties even at a very higher level of turbulence intensity.

2 Experimental Method and Equipment Detail

The aerodynamic properties of the stretched trailing edge airfoil at different freestream turbulence were tested at the subsonic low-speed open type wind tunnel available at Aerodynamics Laboratory, SASTRA Deemed University [17]. The NACA 0020 series airfoil was chosen with a chord measuring 10 cm hooked with the stretched trailing edge exposed to the freestream velocity of 30 m/s related to the

Fig. 2 Illustration of stretched trailing edge airfoil

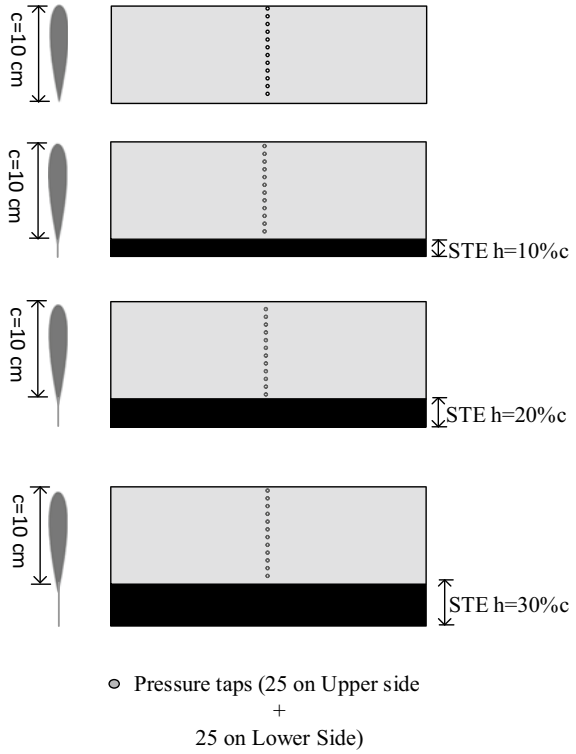
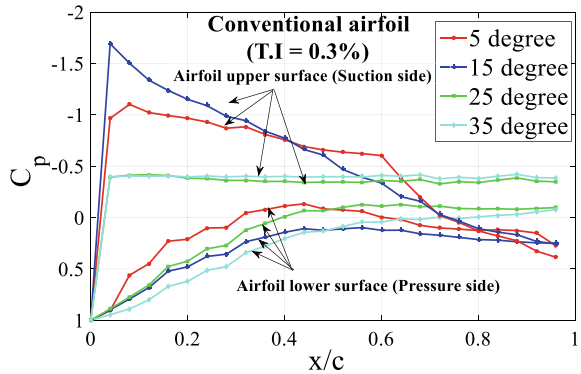


Fig. 3 C_p distribution along dimensionless chord (x/c) for the conventional airfoil at various α



Reynolds number of 2.4×10^5 . The angle of attack was altered from 0° to 35° with $\Delta\alpha$ of 5° at each step.

2.1 Wind Tunnel Facility

The experiment was carried out with the aid of a subsonic wind tunnel [17]. The volume of the test section measures height \times breadth \times length as 30 cm \times 30 cm \times 150 cm. A symmetrical airfoil of NACA 0020 was selected for the study. The honeycomb followed by the narrow segment (contraction cone) filters the dust particle for the air and passes to the test section with increased airstream speed. The available tunnel can attain an airspeed of 60 m/s extremes. The air velocity can be altered by adjusting the motor fan rotating RPM displayed in the control unit. The readings are taken with the decided air speed of 30 m/s in the test section.

2.2 Airfoil and Stretched Trailing Edge Design Detail

A symmetrical airfoil of NACA 0020 was selected for the study. The conventional airfoil measures 10 cm total chord length from the leading edge to the trailing edge where the maximum thickness of 1 cm lies at 15% of the entire chord gauging from the leading edge. Primarily, the airfoil was fixed in the test section precisely at 0° in line with the incoming flow direction with the support of a prolonged aluminium circular hollow rod provided at the two sides of the airfoil. The ϕ 1 mm diameter ports are provided over the airfoil with the Δc of 0.35 cm in the count of 25 ports separately at both airfoil upper and lower sides (Total 50 pressure ports). The provided pressure ports help to collect the air samples passing over the airfoil surface from the respective location.

To examine the stretched trailing edge, the 2 mm thick stainless steel plate was shaped out in form of a rectangle where the breadth matched with infinite airfoil span i.e. 30 cm and the length is stretched to three different amplitudes of 10%*c*, 20%*c* and 30%*c*. The clear specification of adapted STE is mentioned in Fig. 2.

2.3 Turbulence Formation

A square grid frame measuring 30 cm \times 30 cm was designed. The hollow cylindrical PVC pipes of different counts and diameters have gripped in a parallel manner [19]. To induce the required amount of turbulence into the freestream entering the test section. The passive kind of turbulence-generating grid is developed, which requires no additional energy to stimulate the required amount of turbulence. The details of the grid arrangement and achieved turbulence magnitude are discussed in Table 1.

Table 1 Specification of the accuracy of aerodynamic independent variables

No. of the hollow pipes	Diameter of the pipe (cm)	Obtained T.I. in %
–	–	Wind tunnel calibrated turbulence intensity 0.3
5	2	7
4	3	12

2.4 Pressure Scanner

The transient miniature multichannel (64-channel) Scanivalve model piezo-electric pressure scanner [17] is used to sense the magnitude of pressure acting over the airfoil surface acting at the respective ports. The sample air collected from each tap runs to the specially designed flexible transparent tube of 1 mm diameter connected to scanner channels. When the air hits the scanner diaphragm provided at each channel, the diaphragm will expand or contract according to the respective pressure. This mechanical movement will pass an electrical signal. The electrical signal is recorded and sent to the A/D converter. Finally, the digital pressure values are stored for the future estimation of aerodynamic properties.

3 Results and Discussion

The consequence of turbulence present in the freestream over conventional NACA 0020 airfoil and a stretched rear edge measuring the amplitude of $h = 10\%c$, $20\%c$ and $30\%c$ is studied for the fixed Reynolds number of 2.4×10^5 [20], α was changed from 0° to 35° in a step of 5° . The intensity of turbulence varied from 0.3, 7 and 12% to examine the aerodynamic significance of the conventional and stretched trailing edge, airfoil models. The obtained results indicate stretching the trailing edge in the existence of high turbulence level, displays significant alteration in the aerodynamic flow properties.

3.1 Effect of STE Over Pressure Distribution

Figures 3 and 4 sketch the local surface pressure acting over the airfoil at respective ports of conventional and STE and its behaviour at the angle of attack varying from 5° to 35° . For a case of conventional airfoil, rising the angle will have no speakable change in the lower side pressure. The pressure measurement on the upper surface shows a speakable pressure variation concerning α . Figure 3, C_p over the top surface for $\alpha = 15^\circ$, maps the peak negative pressure ($C_p = -1.7$). On behalf of magnified flow acceleration, peak negative pressure indicates the pressure loss, the pressure

loss takes place at $x/c = 0.03$ followed by abrupt pressure recovery towards the trailing edge. It indicates the flow separation and reattachment process as shown in Fig. 1. Nearly at the rear edge, the pressure at the top and bottom surface matches identically. Elevating α further from 25° to 35° , the pressure loss taken place is minimal, very minimal, and the pressure becomes plateau towards the trailing edge. The lift increment from 25° to 35° is due to the higher pressure acting on the bottom surface for 35° than the 25° . Figure 4 reads the pressure distribution data of the STE airfoil, the peak pressure reads at $\alpha = 5^\circ$ itself ($C_p = -1.4$), in contrast to conventional airfoil at 15° , the pressure loss seems very less and becomes plateau towards the trailing edge. This indicates the earlier stall taking place may be around 12° from Fig. 5. However, the C_L value will get augmented due to reduced pressure loss compared to the conventional airfoil. Figure 5 supports the above statement.

Fig. 4 C_p distribution along dimensionless chord (x/c) for the STE airfoil at various α

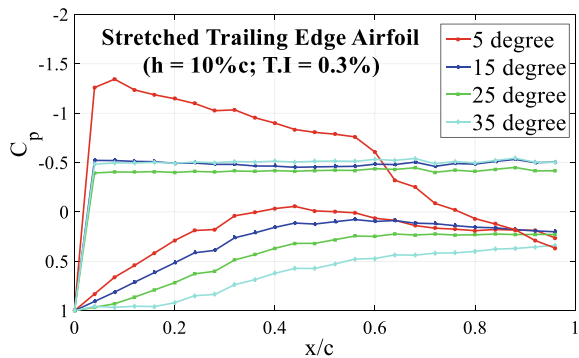
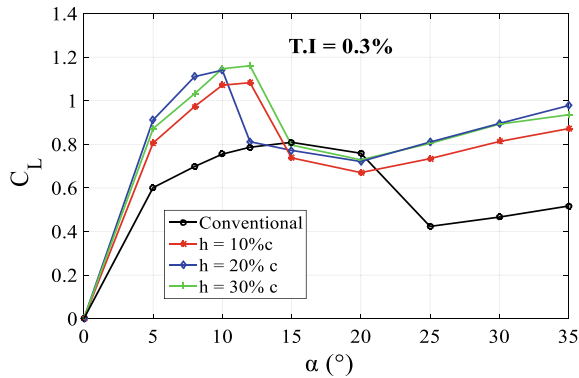


Fig. 5 Relating C_L distribution along α at $T.I. = 0.3\%$ and its effects over STE



3.2 Effect of Turbulence Intensity on Conventional and S.T.E Airfoil

Figures 6 and 7 display the obtained lift coefficient for concerning α at respective T.I. of 0.3, 7 and 12% for the conventional and STE airfoil. The C_L for conventional airfoil reads a maximum of 0.8 at 15° at 0.3%, on measuring the values in presence of turbulence intensity, the value of C_L slightly decreases to 0.78 but shows improved performance in the post-stall region at the moderate T.I. of 7%. At a higher T.I. of 12%, the lift co-efficient got damaged with the advantage of the delayed stall. All the effects are seen in Fig. 7. On stretching the TE to $h = 10\%c$, the C_L value raised to 1.05 for the stretched case at 0.3% T.I. with deep stall action at 12° . On 7% of T.I. The deep stall is turned into a smooth stall phenomenon. On further testing at higher T.I. of 12%, the value of C_L dropped but not more than the conventional airfoil in a similar range of T.I. The stall got delayed.

A similar concept is observed for the stretched airfoil of amplitude $h = 20\% c$ and $h = 30\%c$ as shown in Figs. 8 and 9. The lift has been increased to 1.2 and 1.3 at 12° respectively at moderate T.I. of 7% on increasing to 12% the lift got

Fig. 6 Relating C_L with the corresponding α for the conventional airfoil and its behaviour at various T.I.

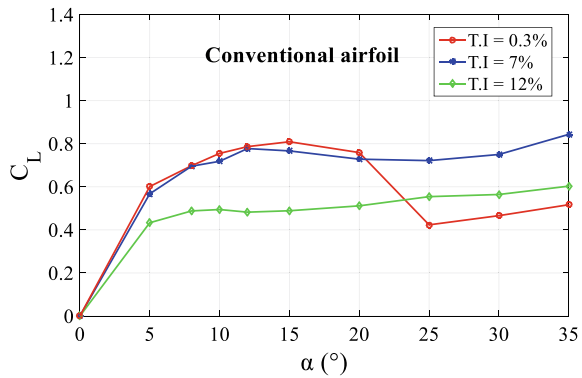


Fig. 7 Relating C_L with the corresponding α for stretched trailing edge airfoil of amplitude $h = 1$ cm at various T.I.

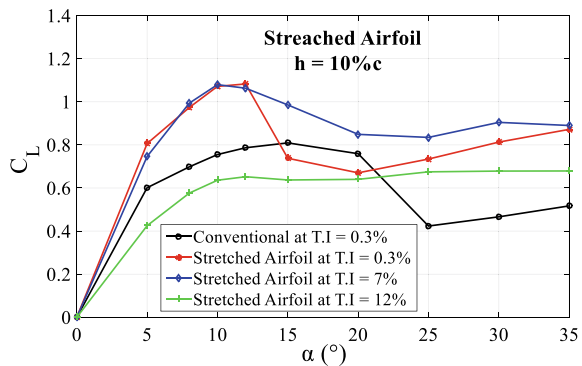


Fig. 8 Relating C_L with the corresponding α for stretched trailing edge airfoil of amplitude $h = 2$ cm at various T.I.

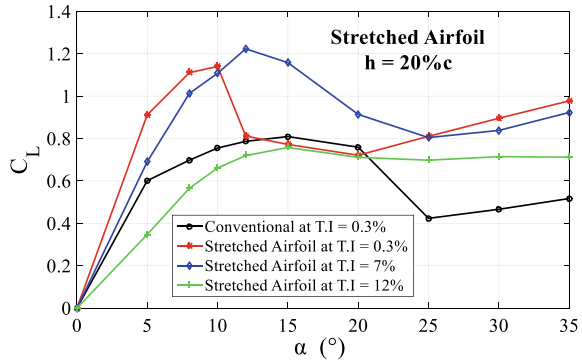
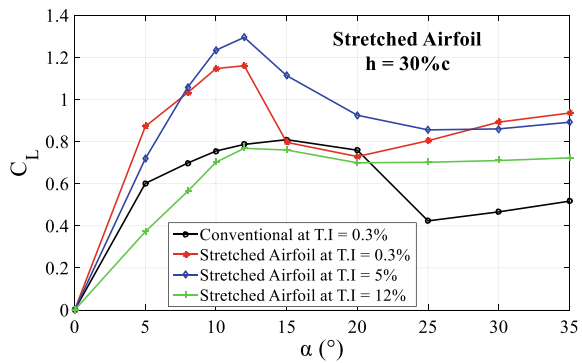


Fig. 9 Relating C_L with the corresponding α for stretched trailing edge airfoil of amplitude $h = 3$ cm at various T.I.



decreased but matches with the conventional airfoil operating at 0.3% T.I. Altogether, the stretched airfoil supports very well in moderate T.I. = 7% and also tries to sustain the aerodynamic properties at a higher T.I. of 12%.

The tendency of the C_D curve for all the cases of stretched T.E remains similar. At the T.I. of 7% and 12%, the slight increment in drag exists behind 20° from Figs. 10, 11, 12, 13 and 14. This is due to the drag polar (induced drag is directly proportional to the square of the C_L) noticed from the C_L graph of the same condition which displays the makeable lift increment.

4 Conclusions

The test is conducted to analyse the consequences of stretching the airfoil trailing edge of the NACA 0020 airfoil. The trailing edge of an airfoil had been stretched to the extension (h) of 10% c , 20% c and 30% c in form of a rectangular thin plate. Time series local pressure around the airfoil surface were gathered for 700 Hz using 64-channel pressure scanner. The readings are utilized to predict the aerodynamic

Fig. 10 Relating C_D with the corresponding α for the conventional airfoil and its behaviour at various T.I.

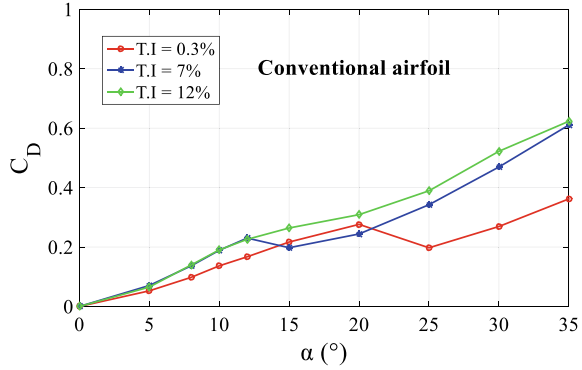


Fig. 11 Relating C_D with the corresponding α at T.I. = 0.3% and its effects over STE

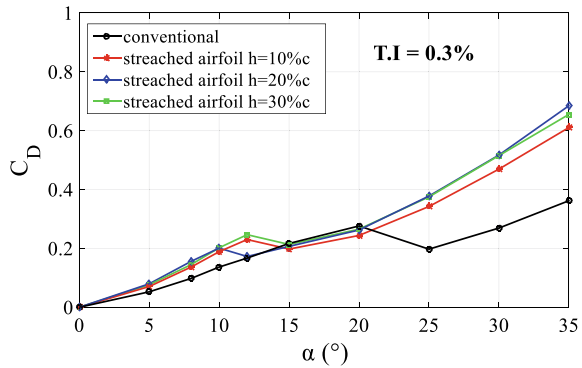
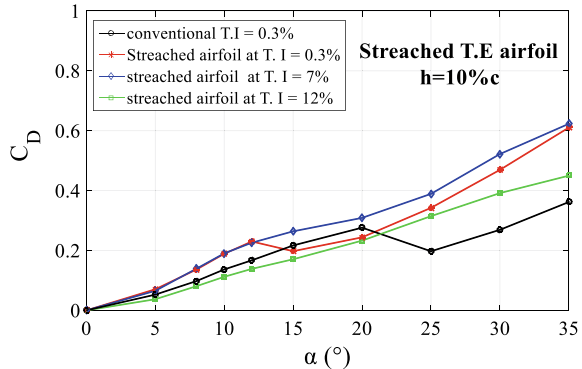


Fig. 12 Relating C_D with the corresponding α for stretched trailing edge airfoil of amplitude $h = 1$ cm at various T.I.



forces for the α ranges from 0° to 35° . The below-listed conclusions are made from the experiment.

- There is a direct rise in the lift coefficient (C_L) by around 28% for the STE airfoil.

Fig. 13 Relating C_D with the corresponding α for stretched trailing edge airfoil of amplitude $h = 2$ cm at various T.I.

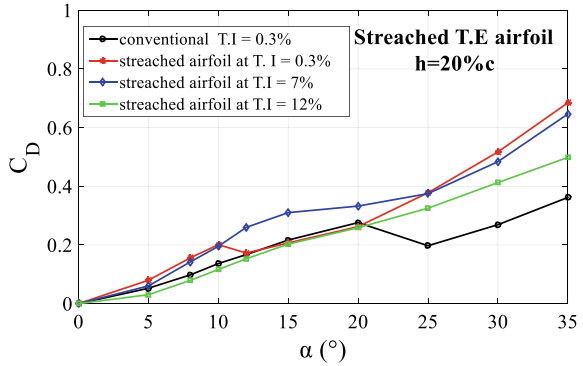
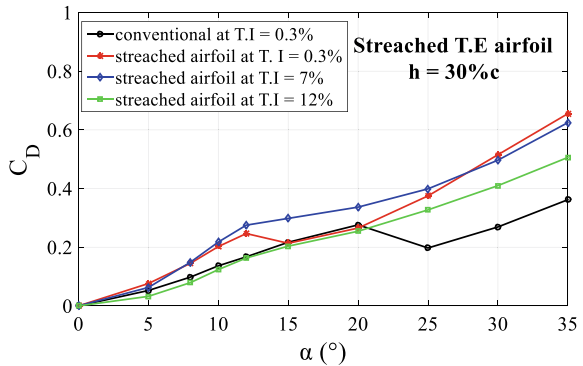


Fig. 14 Relating C_D with the corresponding α for stretched trailing edge airfoil of amplitude $h = 3$ cm at various T.I.



- The stall took place 3° earlier for the STE airfoil compared to the conventional airfoil as compensation for lift increment.
- The abrupt pressure loss taken place for the conventional airfoil had overcome by the STE airfoil.
- In presence of turbulence intensity, the aerodynamic performance of the all-designed STE improved.
- Overall, the stretched trailing edge airfoil performs well even in turbulent regimes.

Acknowledgements This research work was supported by the Science Engineering Research Board (SERB), Department of Science and Technology (DST), Government of India, File No: CRG/2021/005720.

Nomenclature

- T.I. Turbulent Intensity (%)
- TE Trailing edge

STE	Stretched trailing edge
c	Chord (cm)
F.S.T	Free stream turbulence
Re	Reynolds number
L/D	Lift-to-drag ratio
h	Amplitude of stretched trailing edge (cm)
C_p	Pressure coefficient
C_L	Lift coefficient
C_D	Drag coefficient
α	Angle of attack ($^\circ$)

References

- Mucke T, Kleinhans D, Peinke J (2011) Atmospheric turbulence and its influence on the alternating loads on wind turbines. *Wind Energy* 14(2):301–316
- Stack J (1931) Test in the variable density wind tunnel to investigate the effects of scale and turbulence on airfoil characteristics. Tech Rep 364. NACA
- Gaster M (1967) The structure and behaviour of laminar separation bubbles. NPL
- Hoffmann JA (1931) Effects of freestream turbulence on the performance characteristics of an airfoil. *AIAA J* 29(9):1353–1354
- Swalwell KE, Sheridan J, Melbourne WH (2001) The effect of turbulence intensity on stall of the NACA 0021 aerofoil, In: 14th Australasian fluids mechanics conference
- Kamada Y, Maeda T, Murata J, Toki T, Tobuchi A (2011) Effects of turbulence intensity on dynamic characteristics of wind turbine airfoil. *J Fluid Sci Technol* 6(3):333–341
- Maldonado V, Castillo L, Thormann A, Meneveau C (2015) The role of free stream turbulence with large integral scale on the aerodynamic performance of an experimental low Reynolds number S809 wind turbine blade. *J Wind Eng Ind Aerodyn* 142:246–257
- Sarlak H, Mikkelsen R, Sarmast S, Sørensen JN (2014) Aerodynamic behaviour of NREL S826 airfoil at $Re \frac{1}{4} 100,000$. *J Phys Conf Ser* 524:012027
- Li QA, Kamada Y, Maeda T, Murata J, Nishida Y (2016) Effect of turbulent inflows on airfoil performance for a horizontal axis wind turbine at low Reynolds numbers (part I: static pressure measurement). *Energy* 111:701–712
- Isaza J, Salazar R, Warhaft Z (2014) On grid-generated turbulence in the near and far field regions. *J Fluid Mech* 753:402–426
- Storms B, Ross J (1995) Experimental study of lift-enhancement tabs on a two-element airfoil. *J Aircr* 32(5):1072–1078
- Lee HT, Kroo IM, Bieniawski S (2022) Flutter suppression for high aspect ratio flexible wings using micro flaps. *AIAA Paper* 1717:22–25
- Liebeck RH (1978) Design of subsonic airfoils for high lift. *J Aircr* 15(9):547–561
- Storms B, Jang CS (1994) Lift enhancement of an airfoil using a gurney flap and vortex generators. *J Aircr* 31(3):542–547
- Bechert DW, Stanewsky E, Hage W (1999) Wind tunnel measurements on a transonic wing with flow control by various devices. DLR, German Aerospace Research Center Rept. DLR-IB 223-99C05/IB 92517-99/b3-2, June 1999, Stuttgart, Germany.
- Stanewsky E (2001) Adaptive wing and flow control technology. *Prog Aerosp Sci* 37(7):583–667
- Livya E, Nadaraja Pillai S (2021) Effect of trailing-edge modification over aerodynamic characteristics of NACA 0020 airfoil. *Wind Struct* 33(6):463–470

18. Nadaraja Pillai S, Sunderesan A, Gopal R, Priya SBM, Ali Pasha A, Ali Zubar Jameel A, Reddy M, Juhany KA (2021) Estimation of chaotic surface pressure characteristics of ice accreted airfoils—A 0—1 test approach. *IEEE Access* 9:14441–114456.
19. Arunvinthan S, Nadaraja Pillai S, Cao S (2020) Aerodynamic characteristics of variously modified leading-edge protuberanced (LEP) wind turbine blades under various turbulent intensities. *J Wind Eng Indust Aerodyn* 202:104188
20. Suresh V, Premkumar PS, Senthilkumar C (2019) Drag reduction of non-circular cylinder at subcritical Reynolds numbers. *J Appl Fluid Mech* 12:187–194

Control of Flow Separation Using Hemispherical Protuberance on the Leading Edge



Pradeep Singh, Ravi Kumar, and S. Sarkar

Abstract The boundary layer separation control by a hemispherical protuberance near the leading edge has been discussed here. The protuberance is placed on the leading edge of a modelled aerofoil at an angle 60° from the theoretical stagnation point. The experiments are performed at a Reynolds number (Re) of 1.6×10^5 and freestream turbulence (f_{st}) of 1.2%. For the surface without protuberance, the flow separates near the leading edge evolving normal vortex shedding and forming a two-dimensional separation bubble. The application of protuberance significantly modifies the flow field by generating the streamwise vortices that interact with the shear layer downstream. These interactions augment the local turbulence, resulting in a three-dimensional separation bubble where the bubble length is reduced by 31–78%. Further, the separation bubble length, vortex shedding, and turbulence statistics become highly asymmetric in the spanwise direction, whilst the influence of protuberance is felt up to 6 k.

Keywords Laminar separation bubble · Vortex dynamics · Transition · Turbulence · Protuberance

1 Introduction

The laminar boundary layer generally separates near the leading edge of an aerofoil at relatively high angles of attack. The flow separation is also encountered in low-pressure turbine (LPT) blades, sailplanes, and micro air vehicles (MAV) when the developing laminar boundary layer is exposed to the strong positive pressure gradient. The shear layer reattaches to the surface downstream as a turbulent boundary layer after undergoing a rapid transition process, forming a laminar separation bubble (LSB) [1]. Sometimes, the shear layer fails to reattach, known as a bubble bursting. The transition of an LSB is highly susceptible to f_{st} , and thus the shear layer is

P. Singh · R. Kumar · S. Sarkar (✉)
Department of Mechanical Engineering, Indian Institute of Technology Kanpur, Kanpur 208016,
India
e-mail: subra@iitk.ac.in

inherently unstable. Any modification in fst modifies the topology of an LSB that dictates the downstream boundary layer, enhancing the drag and adversely affecting the stall characteristics of an aerofoil [2–4]. Hence, the prevention of boundary layer separation improves the aerodynamic performance, which allows the application of more aerodynamically loaded airfoils. Therefore, the investigation of flow separation control is of prime importance in enhancing the aerodynamic performance of an airfoil.

2 Literature Review and Objective

Several studies have reported that the shear layer is excited by external disturbances in the control of an LSB. The excitation induces the earlier transition and reattachment of the shear layer, resulting in reduced separation extent. By applying 3D forcing, Jones et al. [5] suppress the flow separation over a NACA0012 airfoil and thus improves its aerodynamic performance [5, 6]. It has also been observed that the implication of acoustic forcing enhances the lift-drag ratio of the Eppler 387 airfoil by 70% [7]. DeMauro et al. [8] completely remove the LSB over NACA0009 airfoil by exciting the $K-H$ instability using electro-active polymers. When a two-dimensional impulsive disturbance is introduced on an LSB, a convective amplification of perturbations is observed along the shear layer evolving wave pockets [9]. Introducing the harmonic disturbances, upstream of separation often eliminates the separation bubble if forcing amplitude is high [10]. Singh and Sarkar [11] excite the shear layer by introducing the surface roughness of different heights, where pre-transitional perturbations induce the earlier transition and reattachment of the leading-edge separation bubble.

Moreover, many researchers have employed vortex generators of different shapes and sizes to control the flow separation. The vortex generator re-energizes near-wall flow by injecting the higher momentum fluid from the far wall region [12]. The vortex generator developed cross-stream vortices that suppressed the boundary layer separation and reduced the losses by 50% [13]. Further, Sarkar et al. [14] described an LSB excitation to the periodic passing wakes near the leading edge using LES. During the wake-induced path, the transition involves the formation and convection of coherent vortices, where the viscous effect is substantial.

Furthermore, the boundary layer separation is often controlled by employing an isolated leading-edge protuberance of different shapes and sizes. The protuberance generates the streamwise vortices that interact with downstream flow and positively affect the performance of an aerofoil, mainly in the post-stall regime. Johari et al. [15] experimentally investigated the influence of sinusoidal protuberances at the leading edge. The protuberance enhanced the lift coefficient almost up to 50% in the post-stall region, whereas the drag was almost invariant. Miklosovic and Murray [16] also reported similar observations where the wavy leading-edge aerofoil exhibited improved aerodynamic characteristics in the post-stall region with a maximum increment in C_L and L/D of 54.5% and 67.7%, respectively, with a reduction of C_D by 6.7% [17]. Further, the protuberance with a larger amplitude to wavelength ratio has

better flow separation control [18]. Recently, Singh and Sarkar [19] studied the excitation of leading-edge separation bubble under the wakes of the hemispherical protuberance. The protuberance almost kills the separation along the mid-plane, whereas away from the protuberance, a three-dimensional separation bubble reappears.

The protuberance sheds the streamwise vortices that augment the local turbulence near the leading edge and affect the flow field in streamwise and spanwise directions. A hemispherical protuberance is placed at the leading-edge upstream of separation to investigate the three-dimensionality of flow features and flow separation control. The experiments have been conducted for the surface with and without protuberance using ESP, hotwire and flow visualization with the help of particle image velocimetry (PIV).

3 Experimental Setup

The experiments are conducted in an open-circuit blowing wind tunnel, where the air speed varies in the range of 3–30 m/s in the test section. A diffuser immediately downstream to a blower guides the flow to a flow-conditioning chamber comprising honeycomb and three wire meshes to break up the large-scale eddies. It is then followed by a two-dimensional contraction cone of a 6:1 area ratio and guided to the test section, which has a cross-section of 0.610 m \times 0.230 m and a length of 0.750 m. The surface pressure was measured with the help of an electronically scanned pressure (ESP) transducer. ESP measures the differential pressure at the multiplexing frequency of 20 kHz within a range of ± 2.5 kPa. A NI-PXI interface was used to acquire data at the rate of 400 samples/sec/port for 10 s. The uncertainty of surface pressure measurements was within 0.07%, whereas static error in each port whilst calibration was within $\pm 0.05\%$.

A planar PIV made of Dantec Dynamics was employed to conduct the flow visualizations at the mid-span of the modelled aerofoil. The measuring plane was illuminated by a laser sheet of 532 nm wavelength and about 1 mm thick with a repetition rate of 15 Hz from a set of two Nd:Yag Litron laser cavities. 2048 \times 2048 pixels charged coupled device (CCD) camera with 50 mm Carl Zeiss T* planar lens with a maximum aperture of f1.4 has been used to acquire images. The time delay is estimated considering a particle displacement with the freestream velocity in an image pair equivalent to 10–12% of the interrogation area. The adaptive correlation technique has been adopted to evaluate the instantaneous velocity field over an interrogation area of 32 \times 32 pixels, resulting in uncertainty of 0.368 pixels. It gives an uncertainty of about 4.0% in velocity measurements with PIV. The measuring surface was painted black to reduce the surface reflection.

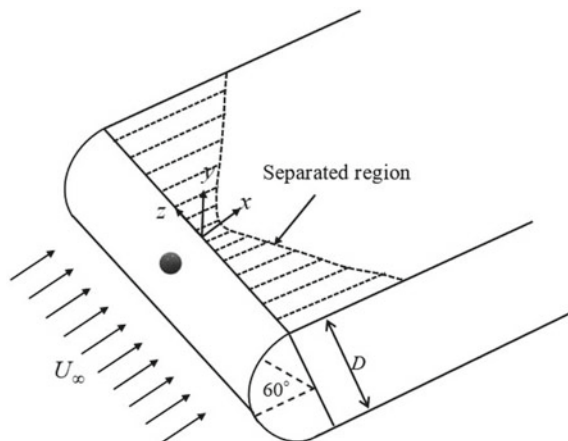
The hotwire boundary layer probe of Dantec Dynamics, consisting of 5 μ m diameter platinum wire, was operated in constant temperature mode to measure the instantaneous velocity. 2¹⁵ instantaneous data were acquired at each measuring location for 6.55 s at a 5 kHz sampling frequency. The calibration of hotwire was performed

against the micro-manometer. In the present study, the uncertainty associated with the velocity measurement was less than 1.3% following Yavuzkurt [20].

4 Results and Discussion

The augmentation of local turbulence originated by applying the hemispherical protuberance near the leading edge and led to the development of an axis-symmetric three-dimensional separation bubble. In appreciation of this, the experiments have been conducted for the surface with and without protuberance. An isolated hemispherical element is placed at the leading edge of a constant thickness model aerofoil upstream of separation. The investigation is carried out on a model aerofoil with a semi-circular leading edge of diameter ($D = 100$ mm) followed by a flat plate and a tail flap downstream of $4D$ and $2D$, respectively. The reason for choosing such an unconventional aerofoil is to develop an LSB of sufficient length and height, which is the prime requisite for the present investigation. The protuberance of diameter (d) 6 mm or height $k = 3$ mm, is placed at the mid-span and 60° from the theoretical stagnation point illustrated in Fig. 1. The origin 30° downstream to an element is the location where the curved portion blends tangentially with the flat plate. The coordinates, x , y and z , represent the streamwise, wall-normal and spanwise directions. Moreover, the shaded region shown in Fig. 1 depicts the three-dimensional separated region, where the onset of separation is almost invariant near the origin. However, the reattachment moves downstream as the flow approaches away from the protuberance in the spanwise direction. Thus, flow features with the application of a protuberance become the function of space and time.

Fig. 1 Schematic of the leading edge with protuberance. The hatched region indicates the axis-symmetric three-dimensional separation

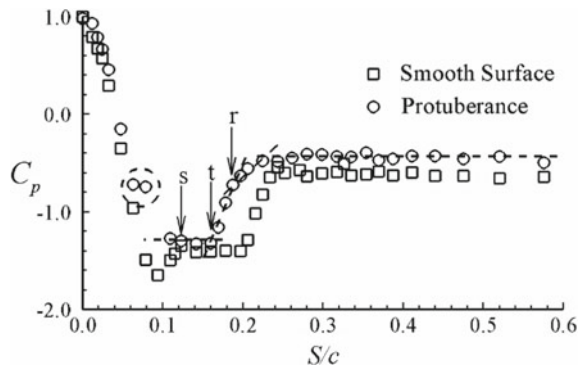


4.1 Pressure Measurement

The normalized pressure (C_p) distribution along the mid-plane ($z/d = 0$) for the surface with and without protuberance is presented in Fig. 2. The C_p is evaluated as $2(p - p_\infty)/(\rho U_\infty^2)$. The point of maximum C_p corresponds to the theoretical stagnation point, from where the flow accelerates along the leading edge and approaches a minimum pressure at $S/c = 0.093$. Thereafter, the C_p starts rising, elucidating that the flow passes the adverse pressure gradient region and a constant pressure plateau downstream. The beginning and end of the plateau indicate the onset of separation and onset of transition, respectively. Also, the region corresponding to the plateau signifies the dead air region where almost no flow velocity exists. At the end of the plateau, pressure again starts rising until it settles down gradually, known as pressure recovery or transition region. After that, a constant pressure region indicates the attached flow. Interestingly, the protuberance kills the adverse pressure gradient before separation. This was also indicated by Singh and Sarkar [11], where the surface roughness removed the adverse pressure gradient before separation.

The onset of separation, transition and reattachment are determined using the intersection of best-fit lines drawn across the pressure data [11, 21]. It is illustrated in Fig. 2, where the lines are indicated for the surface with the protuberance. For the smooth surface, the separation occurs at $S/c = 0.121$ and reattachment at 0.241, which gives the bubble length of about 78 mm. However, the protuberance shortens the bubble length by 47.5%, where the onset of separation appears almost unchanged ($S/c = 0.123$), and reattachment moves upstream to $S/c = 0.186$. Here, S is the surface length measured from the theoretical stagnation point. It is also to be noted that a small separation bubble is detected over the protuberance elucidated by a constant C_p , encircled in Fig. 2.

Fig. 2 Normalized static pressure variation along the chord length for the smooth surface and the surface with protuberance



4.2 Instantaneous Flow Characteristics

The change in instantaneous behaviour of a shear layer when the protuberance is applied at the leading edge is illustrated in Fig. 3, by presenting the streamwise velocity contours superimposed with vectors. The data shown in Fig. 3, along the plane $z/d = 0, 3$ and 5 , are obtained using PIV. For the surface without protuberance, the flow accelerates along the leading edge, attributing to a favourable pressure gradient. It is then encountering an adverse pressure gradient which forces the laminar flow to separate near the origin. The enhanced receptivity of the shear layer attributing to the roll-up of vortices that convects and evolving the normal vortex shedding near the reattachment [11].

For the surface with the protuberance, the flow is highly chaotic from the beginning, illustrating almost the turbulent flow along the plane $z/d = 0$. The protuberance

Fig. 3 Instantaneous contours of streamwise velocity superimposed with vectors

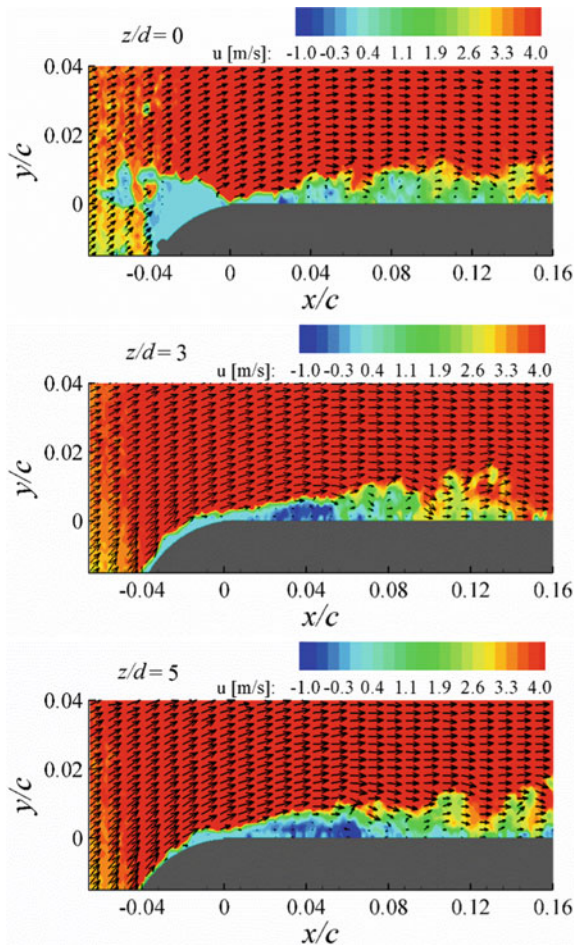


Table 1 Mean onset of separation and reattachment locations at different z/d planes obtained from PIV

Surface	Planes	Separation (x/c)	Reattach. (x/c)	Bubble length (mm)
Smooth	$z/d = 0$	0	0.115	75.14
Protuberance	$z/d = 0$	-0.034	0.002	23.40
	$z/d = 1$	0	0.026	17.09
	$z/d = 3$	0	0.065	42.25
	$z/d = 5$	0	0.080	52.00

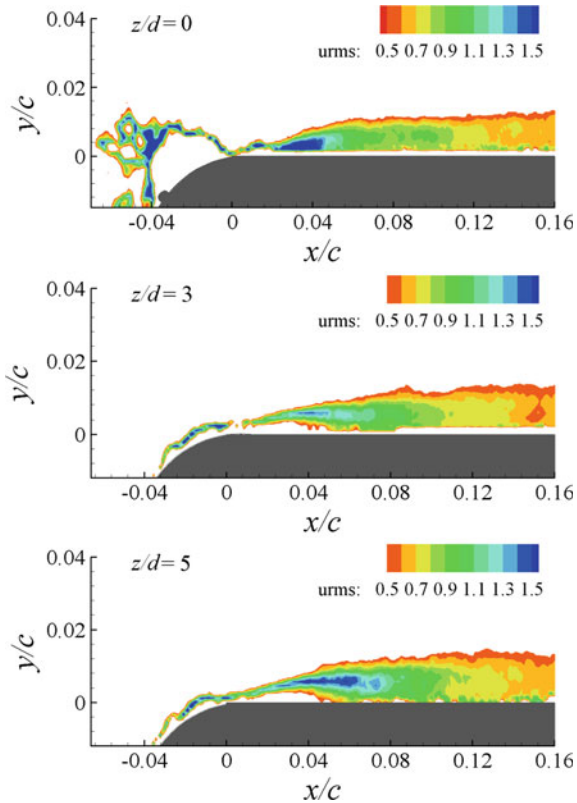
lifts the boundary layer and reattaches immediately near the origin leading to higher vortical activities in the outer layer with abundant small-scale eddies, Fig. 3a. This led to complete suppression of the separation bubble downstream along the plane $z/d = 0$. However, away from the protuberance at $z/d = 3$ and 5, the separation bubble gradually reappears where the irregular vortex shedding is visible in the vicinity of reattachment. The influence of protuberance is felt even at $z/d = 5$. Moreover, the onset of separation and reattachment evaluated from the time-averaged PIV data is given in Table 1. The bubble length becomes the function of spanwise coordinate where its length varies between 0.3 and 0.69 times that of the smooth surface. The onset of separation and reattachment is evaluated using $(\partial \bar{u} / \partial y)_{y=0} \approx 0$, apart from visual inspection of \bar{u} -profiles.

4.3 Excitation of Flow

The u_{rms} contours from PIV data at different z/d -planes for the surface with the protuberance are presented in Fig. 4. For the smooth surface, the growth of u_{rms} occurs along the shear layer attributing to the formation of an LSB that becomes maximum near 70% of l_b followed by saturation of turbulence. With the protuberance, the amplification of u_{rms} is significantly changed. The lift-up and break down of the shear layer in the vicinity of protuberance augment the local turbulence that alters the flow field in streamwise and spanwise directions. At $z/d = 0$, the turbulence level is significantly high from the beginning, suppressing the downstream boundary layer separation. Since the turbulence intensity decreases as the flow progresses in the spanwise direction, the separation bubble gradually reappears. The bubble length starts increasing away from the protuberance but is still less than the smooth surface even at $z/d = 5$. Thus, the flow features become the function of spanwise coordinate where the influence of protuberance is still prevalent at $z/d = 5$.

The \bar{u} and corresponding u_{rms} profiles at different streamwise locations for $z/d = 0$ and 5 with the protuberance obtained from hotwire are projected in Fig. 5. The data for the smooth surface are also superimposed to illustrate the difference. For the smooth surface, the appearance of velocity deficit almost from the origin suggests the flow separation till $x/c = 0.11$, where the deficit recovers and the boundary

Fig. 4 Augmentation of turbulence in the streamwise direction at different spanwise planes



layer reattaches to the surface, forming an LSB of about 72 mm length. u_{rms} grows along the shear layer after the separation due to augmentation of f_{st} and becomes maximum near $x/c = 0.086$. The breakdown occurs attributing to three-dimensional motions with an active outer layer. \bar{u} -profiles with the single protuberance depict the attached flow throughout the chord length for a plane $z/d = 0$. Away from the protuberance, \bar{u} -profiles for $z/d = 5$ tend to blend the profiles of the smooth surface. The high values of u_{rms} near the wall for $z/d = 0$ illustrate augmentation of turbulence immediate downstream to the protuberance. However, in the outer layer, the u_{rms} exhibits lower values than the smooth surface attributing to the attached flow. For the plane $z/d = 5$, the profiles of u_{rms} suggest the formation of a separation bubble, where the peak value and its location of occurrence approach the smooth surface. Thus, flow characteristics vary along the spanwise direction with the appearance of a three-dimensional separation bubble when the protuberance is applied on the leading edge.

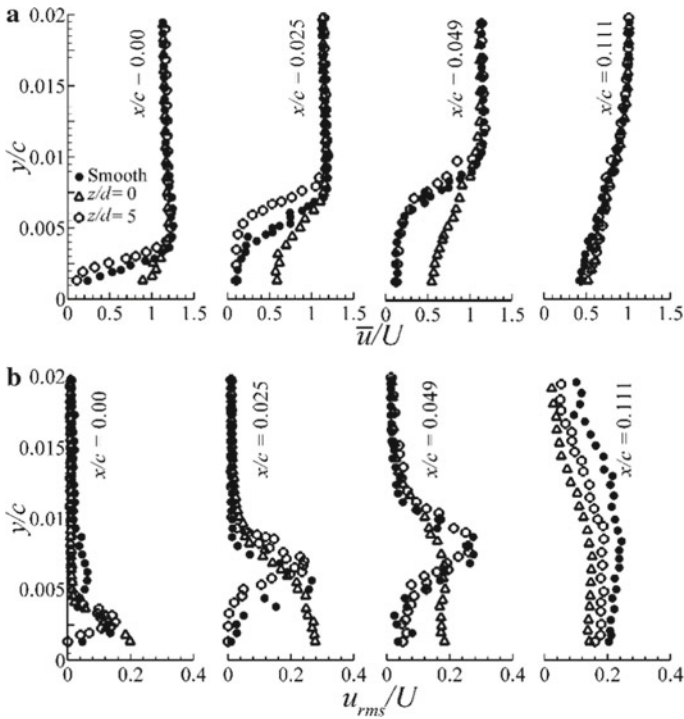


Fig. 5 **a** Streamwise velocity profiles and **b** corresponding u_{rms} -profiles, for the surface with and without protuberance

5 Conclusions

The application of protuberance at the leading edge of a model aerofoil upstream of separation excites the boundary layer and consequently reduces the extent of the separated region. For the smooth surface, the boundary layer separates near the origin, evolving the normal vortex shedding in the vicinity of reattachment, where the three-dimensional motions are evident. However, the immediate augmentation of turbulence due to the protuberance led to the development of a three-dimensional separation bubble near the leading edge. The flow features become the function of space and time, where the bubble length varies between 0.3 and 0.69 times that of the smooth surface.

Nomenclature

- c Chord length [mm]
 d Diameter of protuberance [mm]

D	Leading-edge diameter [mm]
H	Shape factor
k	Protuberance height [mm]
S	Surface length [mm]
\bar{u}	Time-averaged streamwise velocity [m/s]
U	Local free stream velocity [m/s]
C_p	Coefficient of pressure
U_∞	Inlet free stream velocity [m/s]
p	Surface static pressure [Pa]
p_∞	Wind tunnel static pressure [Pa]
Re	Reynolds number, $U_\infty c/\nu$
x, y, z	Cartesian coordinates
δ^*	Displacement thickness [mm]
θ	Momentum thickness [mm]

References

- Gaster M (1969) The structure and behaviour of laminar separation bubbles. Aeronautical Division N.P.L., Ministry of Technology, London, Reports and Memoranda No. 3595
- McAuliffe B, Yaras M (2010) Transition mechanisms in separation bubbles under low and elevated-freestream turbulence. *ASME J Turbomach* 132:011004–011010
- Simoni D, Lengani D, Ubaldi M, Zunino P, Dellacasagrande M (2017) Inspection of the dynamic properties of laminar separation bubbles: free-stream turbulence intensity effects for different Reynolds numbers. *Exp Fluids* 58(66)
- Durović K, De Vincentiis L, Simoni D, Lengani D, Pralits J, Henningson DS, Hanifi A (2021) Free-stream turbulence-induced boundary-layer transition in low-pressure turbines. *ASME J Turbomach* 143(8):081015
- Jones LE, Sandberg RD, Sandham ND (2008) Direct numerical simulations of forced and unforced separation bubbles on an airfoil at incidence. *J Fluid Mech* 602:175–207
- Marxen O, Henningson DS (2011) The effect of small-amplitude convective disturbances on the size and bursting of a laminar separation bubble. *J Fluid Mech* 671:1–33
- Yang SL, Spedding GR (2013) Separation control by external acoustic excitation at low Reynolds numbers. *AIAA J* 51(6):1506–1515
- DeMauro EP, Dell’Orso H, Zaremski S, Leong CM, Amitay M (2015) Control of laminar separation bubble on naca 0009 airfoil using electroactive polymers. *AIAA J* 53(8):2270–2279
- Michelis T, Yarusevych S, Kotsonis M (2017) Response of a laminar separation bubble to impulsive forcing. *J Fluid Mech* 820:633–666
- Yarusevych S, Kotsonis M (2017) Steady and transient response of a laminar separation bubble to controlled disturbances. *J Fluid Mech* 813:955–990
- Singh P, Sarkar S (2021) Excitation of shear layer due to surface roughness near the leading edge: an experiment. *ASME J Fluids Eng* 143(5)
- Gad-ek-Hak M, Bushnell DM (1991) Separation control: review. *ASME J Fluids Eng* 113:5–33
- Lengani D, Simoni D, Ubaldi M, Zunino P, Bertini F (2011) Turbulent boundary layer separation control and loss evaluation of low profile vortex generators. *Exp Thermal Fluid Sci* 35:1505–1513
- Sarkar S, Babu H, Sadique J (2016) Interactions of separation bubble with oncoming wakes by LES. *ASME J Heat Transf* 138(2):021703, 1–12

15. Johari H, Henoch C, Custodio D, Levshin A (2007) Effects of leading-edge protuberances on airfoil performance. *AIAA J* 45(11):2634–2641
16. Miklosovic DS, Murray MM (2007) Experimental evaluation of sinusoidal leading-edges. *J Aircr* 44(4):1404–1407
17. Zhang MM, Wang GF, Xu JZ (2014) Experimental study of flow separation control on a low-re airfoil using leading-edge protuberance method. *Exp Fluids* 55(1710):1–13
18. Wei Z, New TH, Cui YD (2015) An experimental study on flow separation control of hydrofoils with leading-edge tubercles at low Reynolds number. *Ocean Eng* 108:336–349
19. Singh P, Sarkar S (2021) Excitation of a laminar separation bubble by a hemispherical protuberance near the leading edge, Paper No. IMECE2021-73068. In: ASME international mechanical engineering congress and exposition, November 1–5, 2021, Virtual Online
20. Yavuzkurt S (1984) A guide to uncertainty analysis of hotwire data. *ASME J Fluids Eng* 106(2):181–186
21. Gerakopoulous R, Boutilier MSH, Yarusevych S (2010) Aerodynamic characterisation of a NACA 0018 airfoil at low Reynolds numbers. *AIAA Paper No.* 2010-4629

Numerical Investigation to Study the Effects of Wing Flexibility on the Store Trajectory Using MSC CoSim



Varun Palahalli, R. Ganesh Pawar, Nuza Nigar, and T. Praphul

Abstract Traditional flight testing and wind tunnel testing require expensive resources in terms of time and cost. Safety and cost concerns in the testing of store separation necessitates the need for a numerical analysis. This paper studies the effect of wing flexibility on store separation trajectory by coupling the fluid dynamics of the airflow with the elastic structural behavior of the wing. The co-simulation is performed by using the MSC CoSim engine that couples structural behavior simulated in MSC Nastran and fluid dynamics simulated in Cradle CFD. The simulation Mach number for this analysis is 0.95. The Eglin Test Model of a flexible wing is used for analysis at Mach number 0.95. The objective of the paper is to investigate the flexibility effects of the wing on the store trajectory. The solver has been validated using a rigid wing of the Eglin Test Model for store drop and then extended to perform the store drop simulation from a flexible wing. The study focuses on comparing the linear and angular displacements of the store dropping from the rigid wing and the flexible wing. It was observed that the trajectory of the store for the flexible wing case showed deviation from the trajectory of the store for the rigid wing.

Keywords Multiphysics · Eglin test model · Flexible wing · Reynolds averaged Navier stokes equation · Fluid–structure interaction

1 Introduction

The separation of the store from the air vehicle is a critical issue in terms of the missile integration process. Whenever a store separates from the aircraft during flight it is essential that it does not come in contact with the aircraft [1]. Traditionally, flight tests were performed to test the store separation, however, they were very time-consuming and often required years to certify a projectile [2]. In the 1960s, wind tunnel testing was done to perform the store separation tests. However, such testing

V. Palahalli (✉) · R. G. Pawar · N. Nigar · T. Praphul
Hexagon Manufacturing Intelligence, Bangalore 560043, Karnataka, India
e-mail: varun.palahalli@hexagon.com

had long lead times and limited accuracy. The method used in such a wind tunnel test is known as the Captive Trajectory System [3]. Since the CTS system had no accuracy in time, it couldn't account for the inherent unsteadiness encountered by the store during separation. The usage of small-scale models often leads to a reduction in accuracy due to the scaling issues [4]. The development of High Parallel Computing and numerical algorithms have paved the path to numerical simulation for store separation. Such numerical modeling and simulations have reduced the certification cost and increased experimental validity [5]. Trajectories of stores released from internal weapons bays have been shown in recent tests to diverge from predicted paths. Unsteady aerodynamics induced on the store due to wing flexibility results in a change in the trajectory.

2 Eglin Test Model

The EGLIN Test Model [3] is made up of three parts that were created using SOLIDWORKS. The first is a delta wing with a constant NACA 64A010 airfoil section and a 45° sweep, the second is a pylon with ogive-shaped leading and trailing edges. The third is a finned store body with a standard missile profile. The wing's trailing edge has no sweep angle and a taper ratio of 0.133. On the store are four identical fins made of a clipped delta wing of a constant NACA 0008 airfoil section with a 45° sweep. Fins have leading and trailing edges with sweep angles of 60° and 0°, respectively. The pylon and the store body are separated by 35.6 mm.

The length and diameter of the store are 3017.5 and 508.1 mm, respectively, as shown in Fig. 1. The store is ejected with a specified force to begin a safe initial separation. The ejector forces act for a duration of 0.052 s. Also, the store is subjected to aerodynamics and gravity loads [3]. The model orientation is such that the gravity is in the Z direction, the flow is in the negative X direction and the span of the wing is in the Y direction as seen in Figs. 2 and 3.

3 Computational Methodology

The study involved validation of the Eglin Test Model of a rigid wing against the paper "Numerical Simulations of Store Separation Trajectories Using the EGLIN Test", by Sunay et al. [3]. The analysis was then extended to study the effect of the flexibility of the wing on the store trajectory (Fig. 4).

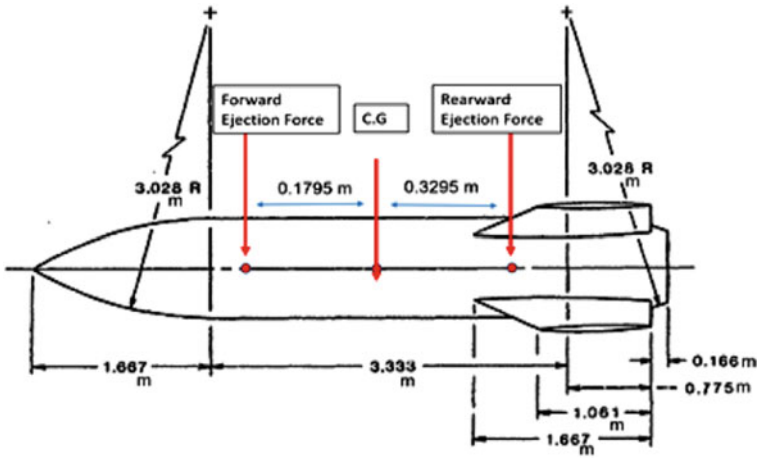


Fig. 1 Dimensions of the store [1]

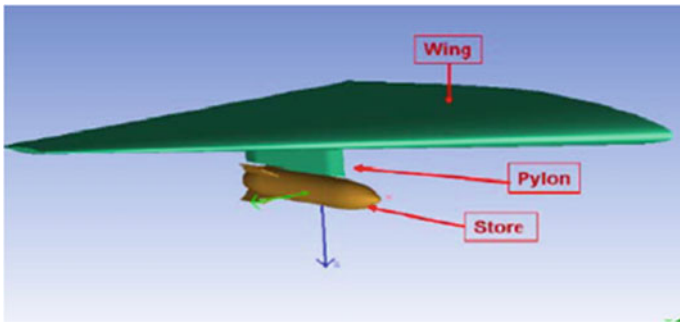


Fig. 2 Geometry of Eglin wing, pylon, and store [1]

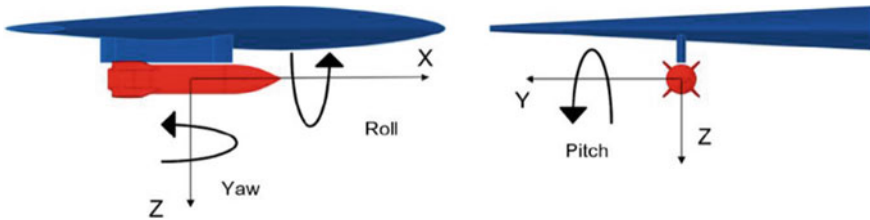


Fig. 3 Angular orientation of the Eglin test [2]

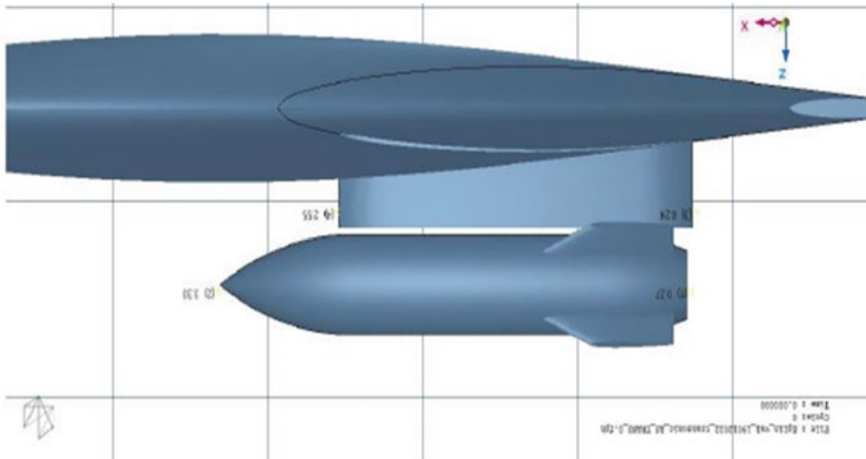


Fig. 4 scFLOW model used in the analysis

3.1 Computational Fluid Dynamics

Unsteady Reynolds Averaged Navier Stokes Equation describes how pressure, temperature, and density are related to a moving fluid. They consist of a set of coupled partial differential equations; one continuity equation for mass conservation, three equations for momentum conservation, and one equation for energy conservation, all of which are time dependent.

To simulate flows around moving objects, scFLOW employs the Arbitrary Lagrangian–Eulerian (ALE) method [6], which handles both the moving coordinate system and the fixed coordinate system at the same time. The effect of mesh movement is added to the equation of the fixed coordinate system in the moving region, and the fixed and moving coordinate systems are calculated simultaneously. Moving condition setting for a moving region as well as the selection and setting of the connection method for both static and moving regions are required in the simultaneous calculation with the ALE method. By applying the moving condition to the volume region containing the object, the moving object is developed. Translation and rotation are examples of settable motions. The static and moving regions can be connected by an overset mesh.

The Eglin Test Model consists of the wing, the pylon, and the store is modeled as shown in Fig. 2, to which an external flow domain is added, known as the computational domain where the external flow over the model will be analyzed. The dimensions of the domain are a length and breadth being 747.6 m each. The depth of the domain is 347.6 m. The size of the computational domain must be large enough so as to not have any far field flow perturbation influence on the store. A subdomain domain of length, breadth, and depth of 5.02, 2.91, and 2.91 m, respectively, are created and centered on the center of gravity of the store which is used to create overset mesh over the domain. The total number of mesh elements is 2201265. The

mesh contains its spatial hexahedral meshing with prism elements at the walls and polyhedral at the transition between hex and prism elements (Figs. 5 and 6).

The wing pylon body and the missile body are modeled as obstacles. The fluid around the obstacles is modeled as compressible air at 20°C, due to which the density-based solver is used. The turbulence model employed for this study is the standard k- ϵ model [7]. The k- ϵ model is a 2-equation closure model which includes two additional transport equations, which are the Turbulence Kinetic Energy k and the Turbulence Dissipation ϵ .

A steady-state analysis is performed for the model without the motion initiation of the store to stabilize the solution. The results of the steady-state simulations are adopted as the initialization for the transient state calculation for the store drop

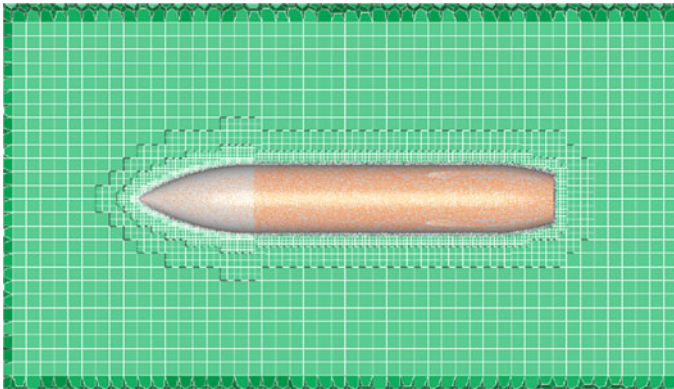


Fig. 5 Mesh of the model in scFLOW

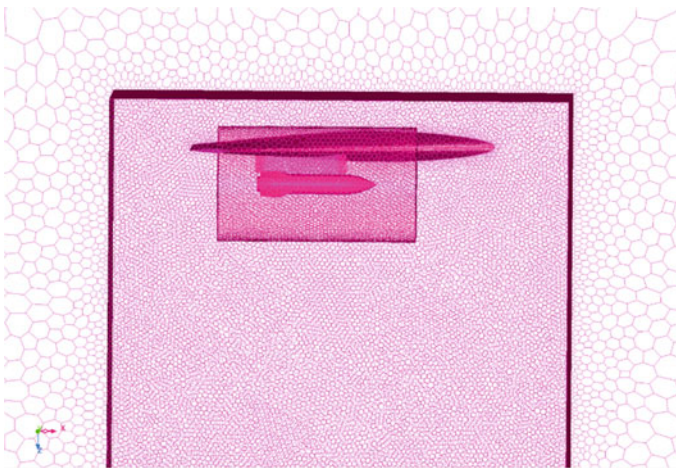


Fig. 6 Polyhedral meshing of the full model in scFLOW

Table 1 Flow parameters used in the study [3]

Parameters	Value
Static temperature (K)	236.7
Reference pressure (Pa)	36,042
Mach no.	0.95
Turbulence model	RANS, k-epsilon
Time-step (s)	1e-04
No. of elements	2.2 million

Table 2 Rigid body dynamic characteristics for the store [3]

Parameters	Value
Mass (kg)	907.185
Center of mass	1417.3 mm (aft of STV nose)
I_{xx} (kg-m ²)	27.1163
I_{yy} (kg-m ²)	488.0944
I_{zz} (kg-m ²)	488.0944
Forward ejector force (N)	10,676.01
Aft ejector force (N)	42,703.0

trajectory analysis using a rigid wing. The same steady-state simulation is also used for the transient state analysis using CoSim for the flexible wing. For this study, the steady-state simulation was run for 2000 cycles. The default temperature is set at 236.7 K. The flow parameters are shown in Table 1.

Second-order accuracy with a limiter is used for the accuracy of the convective terms for the mass, momentum, energy, turbulence, and diffusion equations. First-order accuracy of Time Derivative is used. The Least Square Method is used for Gradient Calculation.

The simulation has been performed in the transonic regime. The Mach number under consideration is 0.95 [3]. The 6 DOF Parameters used are specified in Table 2.

3.2 Computational Structural Mechanics

To simulate the flexible wing FEM Model, MSC Nastran is used. This study uses Implicit Non-Linear Analysis [3]. Mid-surfacing is used to represent the wing and pylon and the equivalent model is meshed using shell elements. CTRIA 6 [8], a Higher-order quadratic element, is an isoparametric triangular shell element, is used for meshing the wing and pylon. The material properties of the Eglin Wing are given in Table 3.

An assumed linear isotropic material is used for the flexible structural model in the analysis. The root of the wing has all the 6 DOF constrained. Nodal points for

Table 3 Material properties of Eglin wing

Parameter	Value
Youngs modulus (MPa)	68.9 E03
Poisson's ratio	0.33
Shear modulus (MPa)	25,902.256
Density (t/mm ³)	2.7 E-09

the reaction forces to act on the wing are created corresponding to the location of the ejector forces applied to the store. The wing surface and the structural shell surface are coupled for data exchange in the CoSim engine. The weight of the store is modeled as loads being supported by the ejectors at the pylon, ejector forces are applied on the store, and corresponding equal and opposite reaction forces are applied on the wing pylon as shown in Figs. 7 and 8. The store itself is modeled as a rigid body in CFD and is not modeled in the flexible wing FEA model.

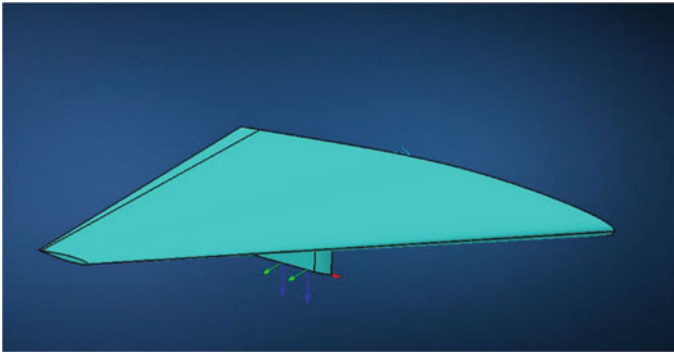


Fig. 7 Structure model developed in MSC apex

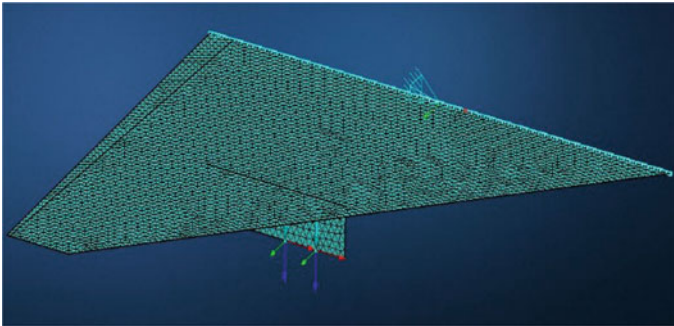


Fig. 8 2D structure meshing on wing and pylon

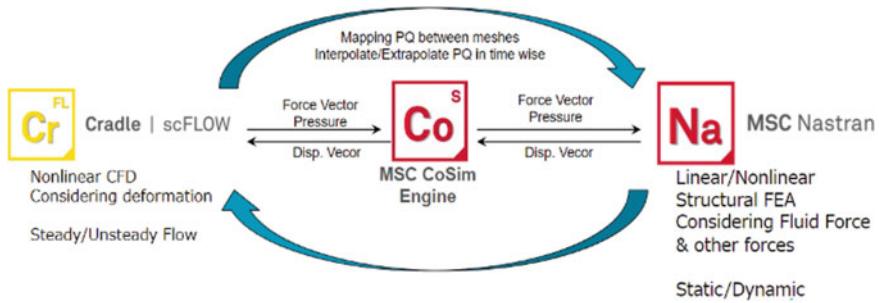


Fig. 9 MSC CoSim data exchange between MSC Nastran and scFLOW

3.3 Multiphysics Co-Simulation Using MSC CoSim

MSC CoSim [4] creates an interface to replace the arbitrary pressure applied in MSC Nastran with the CoSim search parameters. Interpolation functions map the CFD outputs to the structure and structural outputs to CFD to form a strong, two-way coupling in real-time. MSC CoSim is used to establish the co-simulation coupling between CFD Solver and Nastran as shown in Fig. 9. The two-way coupling happens through the surface where the data mapping region is the upper and lower surface of the wing and the sides of the pylon. The pressure and velocity data are transferred from scFLOW to Nastran and the displacement vector is received from Nastran to scFLOW. The method of mesh deformation is selected as Linear Displacement Combination [5] (LDC).

4 Results and Discussion

For the flexible wing, wing oscillations are observed upon ejection of the store. The oscillations are caused by the ejection forces that act on the wing. The elasticity of the wing causes oscillations that affect the surrounding fluid, thus altering the store's trajectory. As a result, the trajectory of the store ejecting from the flexible wing shows a deviation when compared to the trajectory of the store ejected from the rigid wing.

X, Y, and Z displacements of the store are shown in Figs. 10, 11 and 12. A small difference in the X trajectory and Y trajectory was observed.

The X trajectory of the store dropping from the flexible wing of assumed stiffness appears to be a closer match to the experimental case which also has some flexibility than the X trajectory of the store dropping from the rigid wing.

The Y trajectory of the store dropping from the rigid wing appears to be a closer match than the store dropping from the flexible wing.

The effect of the flexibility of the wing on the store's translation in Z is seen to be negligible. The effects of the ejector and gravity forces dominate the effect of the aerodynamic forces in the Z direction [2]. The graph for the store trajectory dropping

Fig. 10 Linear displacement versus time graph in x direction comparing flexible and rigid wing

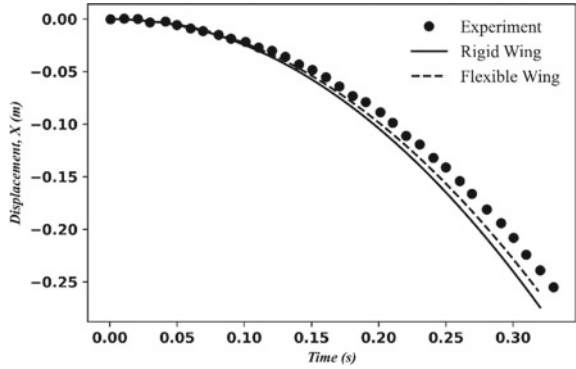


Fig. 11 Linear displacement versus time graph in y direction comparing flexible and rigid wing

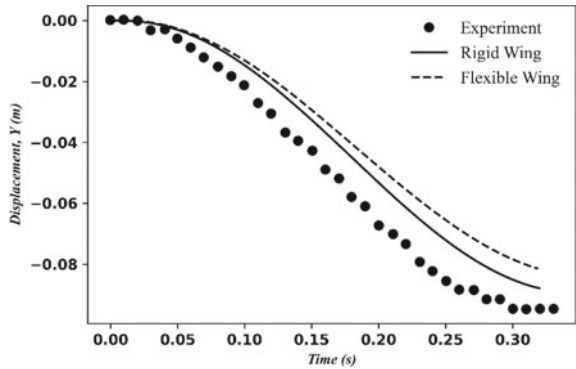
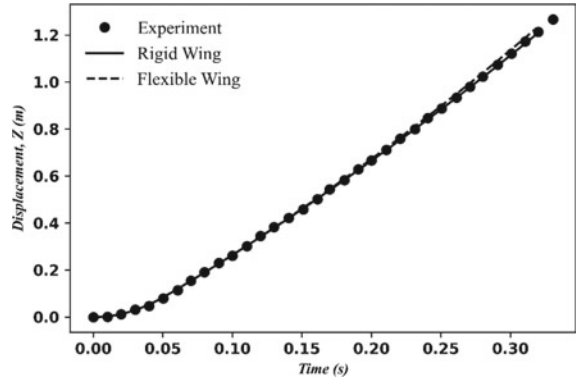
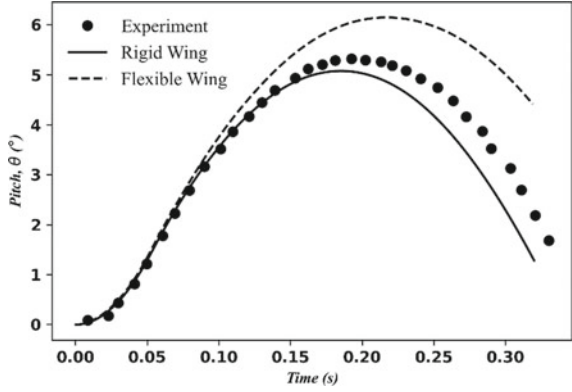


Fig. 12 Linear displacement versus time graph in z direction comparing flexible and rigid wing



from the fixed wing as well as the rigid wing is in good agreement with the graph of the experimental data as depicted in Fig. 12.

Fig. 13 Pitch versus time graph comparing flexible and rigid wing



The store angular orientation is shown in Fig. 3. Figures 13, 14 and 15 compares the store angular orientations with respect to the time of the experimental, rigid, and flexible wing cases.

Fig. 14 Roll versus time graph comparing flexible and rigid wing

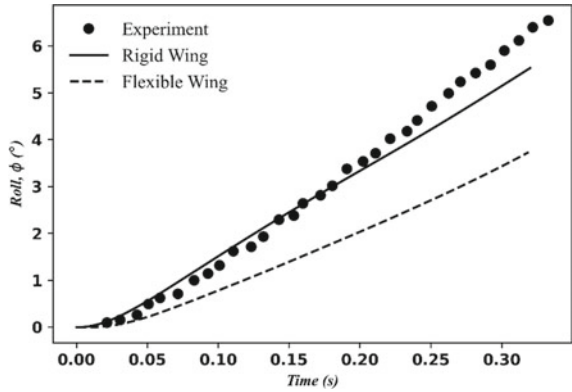
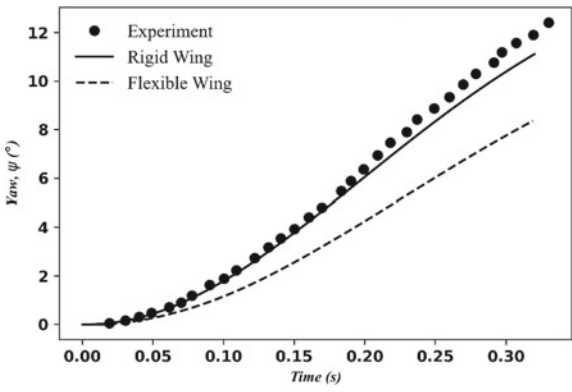


Fig. 15 Yaw versus time graph comparing flexible and rigid wing



The pitch-up motion observed in the angular orientation graph for both rigid and flexible wing cases is due to the action of the ejector force. However, with an increase in time, the pitching trend of the flexible wing case differs from that of the rigid wing case. Approximately after 0.15 s, the store begins to pitch down as shown in Fig. 13. This behavior may be attributed due to the onset of aerodynamic and gravity forces upon store separation.

It is observed from Fig. 13 that the pitching angle of the store's trajectory, ejected from the flexible wing is pronounced from that of the rigid and experimental cases. Additionally, the experimental case's pitching angle curve can be seen to lie between that of the rigid wing's store and the flexible wings. This is inherently due to the experimental wing having flexibility. The marked deviation in the flexible CoSim case's store trajectory is due to the assumed stiffness value owed to the lack of literature stating the exact stiffness or construction of the experimental wing.

The rolling motion of the rigid wing shows much proximity to the experimental results as compared with the flexible wing. The yaw motion for the flexible wing case and rigid wing case shows a similar trend with respect to each other. This is also due to the assumed stiffness of the flexible wing taken. The rigid wing case shows a close match with the experimental case which too has some amount of unknown stiffness. However, if the stiffness of the wing for the flexible case matched the stiffness of the wing of the experimental case, the discrepancy could have been avoided which is also a scope of work in the future.

An aeroelastic test can be performed as a further scope of this study to ascertain the effects of wing stiffness.

5 Conclusions

Numerical analysis using the Eglin Test Model for the flexible and rigid wing cases successfully shows that there is a deviation in the trajectory of the store for the flexible wing case when compared to the trajectory of the store for the rigid wing case. This paper provides scope to perform this Multiphysics simulation with a validated wing stiffness that is obtained either through experimental investigation of a physical model or from additional literature. Additionally, grid-independent studies are ongoing for this analysis and may show changes in the values of the trajectories for the store. Multiphysics computational analyses similar to the one performed in this study help predict real-world flight conditions, ease the testing during weapon integration, reduce costs and time, improve accuracy, and thereby reduce the risk involved in the testing operations.

Acknowledgements We would like to express our token of gratitude to Dr. Karthik Sundarraj, Shripathi V., Sakujiro Hatazawa, and Sachin Pande for their constant support.

A special thanks to Hexagon Manufacturing Intelligence for providing this opportunity to conduct this study.

References

1. Demir HÖ, Selimhocaoglu BT, Demir G, Alemdaroglu N (2018) CFD applications in store separation. NATO OTAN, S&T Organization, pp 5-1-5-30
2. Panagiotopoulos EE, Kyparissis SD (2010) CFD transonic store separation trajectory predictions with comparison to wind tunnel investigations. *Int J Eng (IJE)* 3(6):538-553
3. Sunay EY, Gülay E, Akgül A (2013) Numerical simulations of store separation trajectories using the EGLIN test. *Sci Tech Rev* 63(1):10-16
4. Madasamy S, Thilagapathy G, Arulalagan R (2016) Investigation of store separation and trajectory of weapons in military aircraft. *Int J Sci Eng Res* 7(2):84-88. Retrieved from <http://www.ijser.org>
5. Heim ER (1990) CFD wing/pylon/finned store mutual interference wind tunnel experiment. Arnold Engineering Development Center, AD-B152 669
6. Donea J, Huerta A, Ponthot J-Ph, Rodríguez-Ferran A (2004) Chapter 14: arbitrary Lagrangian-Eulerian methods. In: *Encyclopedia of computational mechanics*, pp 413-437
7. Versteeg HK, Malalasekera W (2007) Conservation laws of fluid motion and boundary conditions. In: *An introduction to computational fluid dynamics: the finite volume method*, vol M, pp 9-38. Retrieved from <http://www.mie.utoronto.ca/labs/mussl/cfd20.pdf>. Accessed on 11 May 2022
8. Hexagon MI documentation center. Retrieved from https://help.hexagonmi.com/bundle/MSC_Nastran_2021.2/page/Nastran_Combined_Book/qrg/bulkc2/TOC.CTRIA6.xhtml. Accessed on 15 Aug 2022

Aerodynamics of Flapping Fin Inspired from Manta Ray



Dharambir Poddar, Nitin Kumar, Javed Mohd., and Debopam Das

Abstract We developed a scaled-down model of a Manta ray in order to obtain a greater understanding of the flow dynamics that govern this large animal's movement so that we could implement it in underwater robots. Flexible foil-based flapping wings mimicking the Manta ray are fabricated using Mylar sheets. This research focuses mostly on modelling the sheet's kinematics, which is determined by trial and error by altering the thickness of the sheet. We compare the qualitative motion of actual Manta rays in order to validate our result. Additionally, PIV was utilised to explore the prominent flow structures present in the flow of flexible foil. Presence of a strong tip vortex has been observed similar to the fish generated pair of moveable vortices that propel them forward (Guo et al. in Hydrodynamic analysis of propulsion process of zebrafish. *Phys Fluids* 34(2):021910, [10]).

Keywords Manta rays · Rays · Biomimicry · Underwater robotics

1 Introduction

Manta rays are one of the ocean's largest creatures, with a maximum length close to eight metres and a weight of approximately 1400 kilogrammes, despite inhabiting all of the world's water temperatures [1]. Marine biologists continue to be unfamiliar with it, and our knowledge of it approaches ignorance. The first reported sighting was in 1798, and since then it has remained a strange animal. Researchers and scientists are investigating the movement of aquatic animals and striving to emulate it in order to develop a propulsion system that utilises the least amount of energy possible. As people become more aware of the need to protect the environment, there has been a substantial surge in interest in the creation of novel underwater vehicles that utilise propulsion technologies inspired by biological processes. According to fish [2], such vehicles have the potential to boost mobility, efficiency, and speed, as well as provide new mission options.

D. Poddar (✉) · N. Kumar · J. Mohd. · D. Das
Department of Aerospace Engineering, IIT Kanpur, Kanpur 208016, India
e-mail: dpoddar@iitk.ac.in

© The Author(s), under exclusive license to Springer Nature Singapore Pte Ltd. 2024
K. M. Singh et al. (eds.), *Fluid Mechanics and Fluid Power, Volume 2*, Lecture Notes in Mechanical Engineering, https://doi.org/10.1007/978-981-99-5752-1_42

513

Earlier study with rigid fin shows (Clark and Smits [3]) that the efficiency and thrust production by oscillatory motions with constant flow velocity is higher compared to flapping motion. However, this study does not replicate the flexible motion of the flapping fin and hence, the exact nature of Manta ray fin kinematics are not modelled. The wide, flat bodies of Manta rays assist them to retain stability while swimming. This permits them to prevent their body and caudal fins from oscillating.

In this study, we aim to study the flow field due to swimming of this marine behemoth which has been optimised by natural selection over the millions of years. We will discuss the details of the experimental model with the particulars of the kinematics and fin design, and subsequently discuss the significance of the design in relation to the Manta ray swimming. In addition, we will qualitatively compare the lab model and real Manta ray model.

2 Experimental Methodology

This section presents the details of the manta ray inspired flexible foil model fabrication.

(A) Design of Transmission Mechanism

With the assistance of the Arduino Uno, a low-friction and easy-to-manage transmission mechanism was developed in order to convert the spinning motion of the servo motor (MG958) into the flapping motion of the fins. The seesaw mechanism was selected as the preferred option. The advantage gained from this mechanism's most notable characteristic is that it makes it possible to exercise exact control over the parameters that establish the amplitude and the rate at which the fins flap. The amplitude and frequency of the flapping may be varied by varying the delay in the Sweep code and the voltage that is given to the Arduino Uno.

The mechanism (Fig. 1) was designed using a CAD software. The housing, linkage, and hinge were then 3D printed. As a fin material, Mylar sheets of four different thicknesses were employed. Housing was designed based on the overall vertical amplitude of link 2. Link 1 and link 2 are connected to the hinge at the opposite ends as shown in Fig. 2. This figure shows a schematic front view of an upstroke in which the fin rises from the mean position to the extreme position (top dead centre). Where length of link 1 is OB and length of the link



Fig. 1 Extreme location of the fins **a** at the end of downstroke **b** at the end of the upstroke

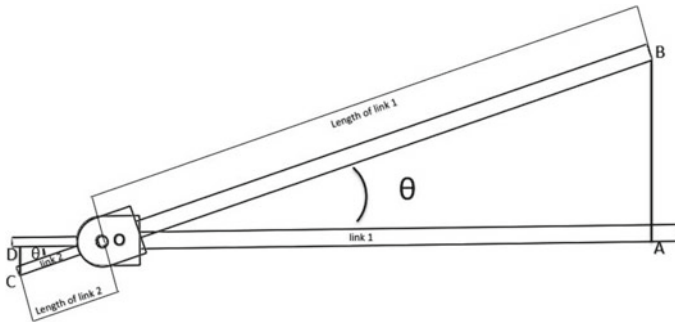


Fig. 2 Geometry of link mechanism for flapping amplitude calculation

2 is OC. If link 1 rotate θ degree anticlockwise then amplitude of link 1 from mean position will be AB.

Now according to the Pythagoras theorem

$$AB = \frac{\sin(\varphi)}{OB}$$

Amplitude of link 2

$$\begin{aligned} (CD) &= \sin(\theta) * OC \\ &= \frac{AB * OC}{OB} \end{aligned}$$

Link 1's total vertical amplitude between its bottom dead centre and top dead centres will be, as shown in Fig. 2.

$$\begin{aligned} &= 2 * AB \\ &= 2 * \frac{\sin(\varphi)}{OB} \end{aligned}$$

Finally, link 2's total vertical amplitude between its bottom dead centre and top dead centres will be

$$\begin{aligned} &= 2 * CD \\ &= 2 * \frac{AB * OC}{OB} \end{aligned}$$

(B) Fin Design

A Manta ray can be recognised by its flat, diamond-shaped body. The shape and size of its two fins, as well as the streamlined shape of its body, are essential for swimming. By flapping its pectoral fins, it produces lift and propulsion. The fins of the project were modelled after the fins of Manta ray. The only variable in this project is the fin thickness, which spans from 0.03 to 0.125 mm; the fin area and aspect ratio are also set. The fins of a Manta ray are seen in a scaled image in Fig. 3. The fin span is twice the body length. Four fins with varying thicknesses and the same area are employed in the current work. Their thicknesses are 0.03, 0.5, 0.8, and 0.125 mm, respectively. Detailed schematics of the four fins are shown in Fig. 4.

(C) Setup

Fig. 3 Manta ray scaled diagram. The two fins' and body's measurements are standardised to the fin span

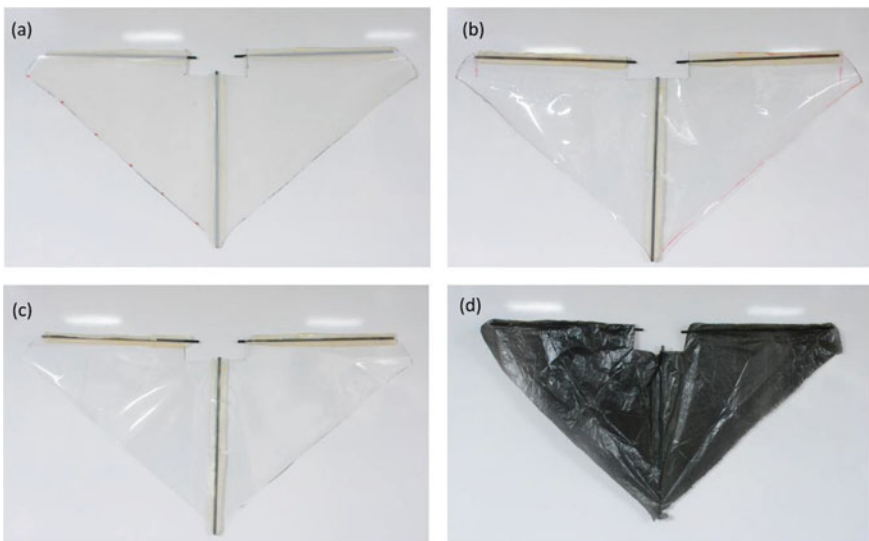
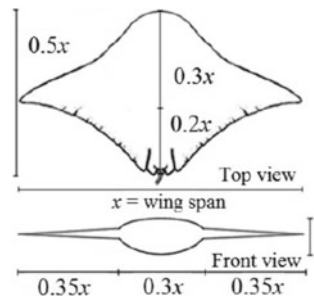


Fig. 4 Fins with different fin thickness **a** 0.125 mm **b** 0.08 mm **c** 0.5 mm **d** 0.03 mm

In the Unsteady Aerodynamics Laboratory of the Aerospace Engineering Department at IIT Kanpur, the experiments were designed and carried out. By analysing the velocity field, flow visualisation, and aerodynamic forces generated during the flapping process, the researchers aimed to gain a greater understanding of the nature of flapping motion. We are utilising PIV to achieve a visualisation of the prominent flow structures. Figure 5 illustrates the experimental setup with PIV measurement arrangement. Examining the chord section of a fin to determine the vortices pertinent to this situation. After the model has been equipped with a load cell and prepared for force measurement, a modification to the model's fins and a change in frequency due to a change in the servo motor delay are necessary. In contrast, PIV measurements are performed using a water tank, with the model placed in the middle of the tank to eliminate the boundary effect. Fifty micrometre-sized seeding particles are utilised to visualise the flow. Using injection, seeding particles are injected into the tank, and settling time is provided as part of the process to eliminate any undesirable velocities that may be introduced during the injection of seeding particles. It is necessary to acquire information through trial and error in order to estimate the quantity of seeding particles that should be placed inside the chamber, and the most successful trial must be repeated multiple times in order to obtain the velocity.

(D) Flow Visualisation

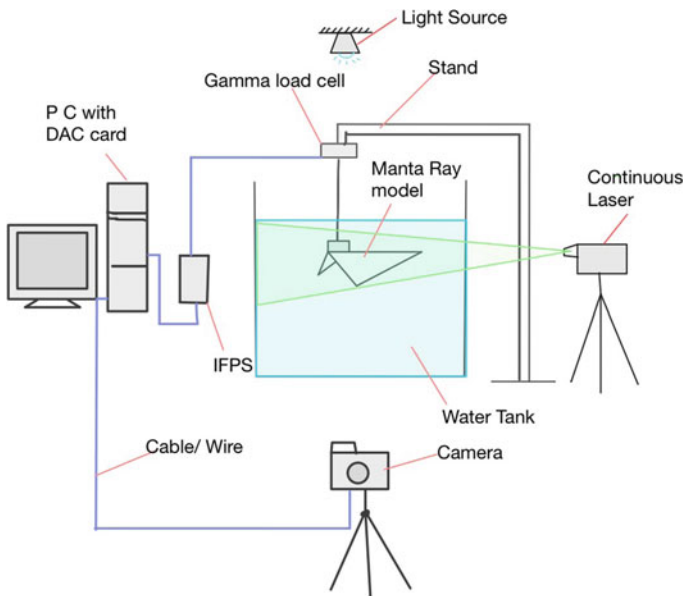


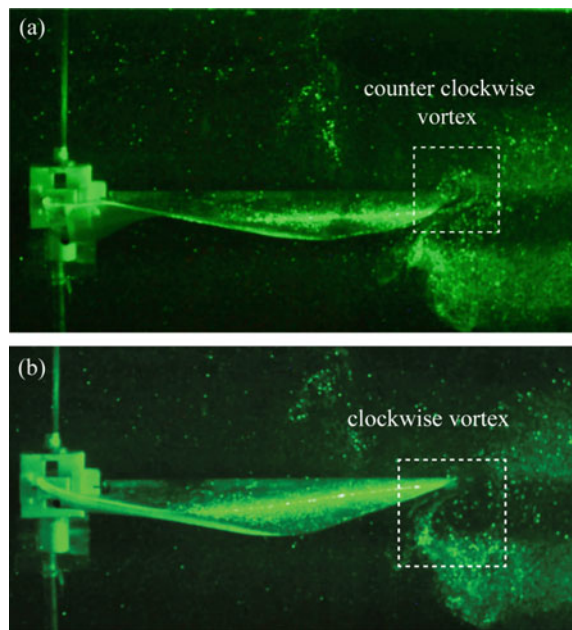
Fig. 5 Experimental setup

Flow is “visualised” by introducing dye, smoke, or pigment into the flow in the area under investigation. The primary advantage of this method is its capacity to explain a model’s flow without requiring extensive data reduction and analysis. For the investigations, we employ the dye visualisation approach with a 150 cm by 50 cm by 75 cm water tank. Using a sodium fluorescent dye, the fluid path was traced. This type of turbulent flow often possesses complex flow characteristics dominated by vortical patterns. By injecting dye at appropriate spots over the fin, researchers have attempted to detect and explain the role of this vortex-dominated flow during flapping flight. In order to produce a suitable visualisation, the injection volume and site are calculated through trial and error. Using a light sheet, a portion of the flow field under observation is lighted. Using a video camera positioned perpendicular to the light sheet, the entire occurrence is recorded in this plane. Figure 6 illustrates the captured image at the trailing edge of model. We also ensure that the model (Manta Ray) is fully submerged during the upstroke and the downstroke Fig. 5.

(E) PIV Measurement

The PIV tests are conducted in a water tank. Measurements are taken in a cross-sectional plane along the chord of the fin at the same spanwise point for each fin. Because the fins are linked to the dc servo motor by linkages, the current and voltage (5 V) supplied to the motor are maintained constant, which also keeps the constant frequency of flapping. Flow field was illuminated using a diode-pumped solid-state continuous laser of wavelength 532 nm and power

Fig. 6 Sodium fluorescent dye visualisation on manta ray



1 W. The Polyamide Seeding Particles (PSP) of 50 μm provided by Dantec Dynamics® are used near the edge of the flapping fins. Please note that all the fluid in the experimental tank was not seeded since at this preliminary stage we are only interested in the flow structure near the fin edge. The PIV images were acquired using the camera (Nikon D5200, 24.1 MP, 60 fps). For velocity data calculation, the open-source PIV tool PIVlab (Thielicke and Sonntag) [4] is utilised. The image is preprocessed with contrast limited adaptive histogram equalisation (CLAHE) with a 20-pixel window size. For image smoothing, a two-dimensional (2D) adaptive noise-removal filter with a window size of 3 pixels was used. Using a fast Fourier transform (FFT) window deformation PIV technique, the cross-correlation was computed. The analysis was conducted using two runs with an interrogation window of 128×128 pixels and 64×64 pixels with a 50% overlap, respectively. A Gaussian function is used to estimate the cross-correlation intensity peak at the subpixel level.

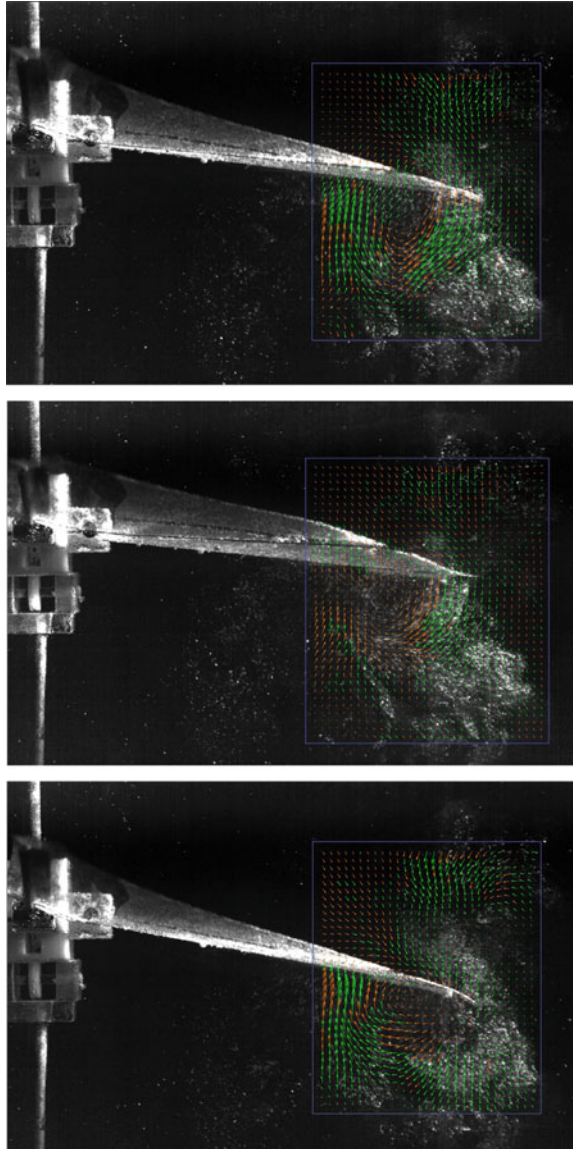
(F) Force Measurement

To obtain quantitative readings of the force created by fin flapping, the model is secured to the ATI Gamma load cell with the necessary attachments and then placed within the tank. This is crucial for ensuring that the actual lift forces are effectively transmitted to the Gamma load cell. Since it requires changing frequency, the servo motor is powered by a direct current source. By altering the delay setting on the servo, we can achieve a range of flapping frequencies. To explore the effect of fin thickness on the formation of lift, various fin thicknesses were tested, however here we provide the data for a single thickness (0.125 mm) fin that most closely resembles kinematics. Figure 7 is a schematic depiction of the experimental environment. On an ATI Gamma load cell, the model was secured. The load cell is connected by cable to the NI card, which is then connected to the system's central processing unit (CPU). On the other hand, fishing wires connect model linkages to the servo motor. By giving a reciprocating motion to the fishing wires, which are attached to the servo motor, this enables the model to have a flapping motion. This pattern of flapping will eventually produce a response force. According to our interests, we have only caught the significant lift and thrust forces. This force data was acquired by the installed load cell and subsequently transformed into the plot depicted in the Fig. 8.

3 Results and Discussion

Prior to the experiment, the movement of the Manta ray is observed in great detail. We attempted to simplify its mechanism without compromising the kinematics of the pectoral fin. The shape and variation in geometry of the pectoral fin of the Manta ray are crucial for imitating its motion [5]. Thus, our study demonstrates that it is possible to reproduce the kinematics of a real Manta ray using a flexible foil or sheet.

Fig. 7 Visualisation of the tip vortex at the fin edge using PIV



The developed model shows a moving wave [6] through the flexible foil fins similar to the one found in the real Manta rays. In the preliminary analysis this has been verified by visual inspection of the real Manta rays swimming videos [1] and comparing it to our model motion. A qualitative comparison of the kinematics of the model and real Manta ray has been presented in Fig. 9.

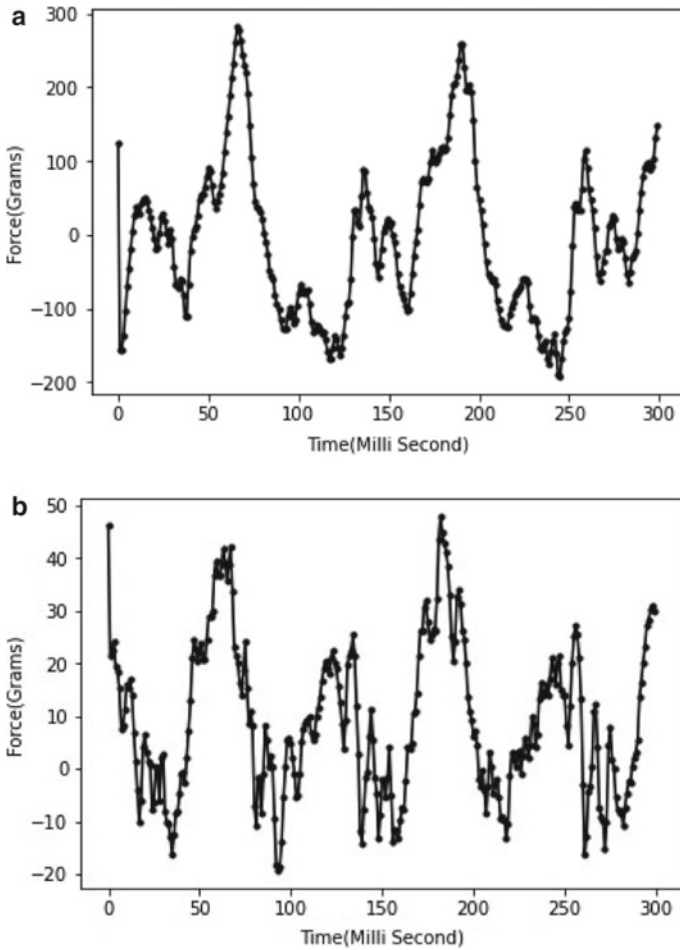


Fig. 8 Load cell force measurement showing the lift and thrust component

Flapping motion of the fish fins is often associated with the generation of alternate vortex pairs [7–9]. Therefore, to get an insight into the main flow features present during the swimming of the Manta ray, we initially performed a flow field visualisation using fluorescent dye as shown in Fig. 6. Where we can see a counter-clockwise vortex at the tip of the fin during its upward motion in top panel and a clockwise vortex at the tip during a downward motion in the bottom panel. Further, to see the flow structures in terms of quantitative velocity field near the tip of the flexible fin, PIV measurements were performed. A continuous laser was used to illuminate the flow. By analysing the particle images we can reconfirm the presence of a counter rotating leading edge tip vortex [10] as seen in Fig. 7 which directly related to fish propulsion [10], however to completely understand the dynamics of flow structures, further experiments need to be performed.

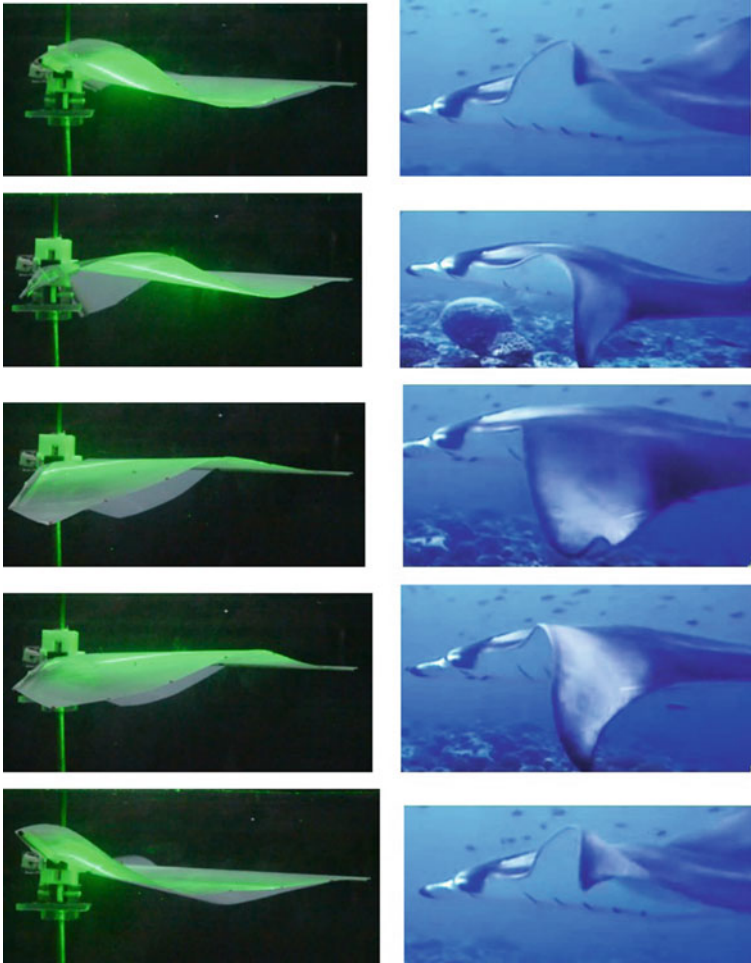


Fig. 9 Kinematic similarity (a wave-like motion on the wings) between Manta ray model (left) and actual Manta ray (right) [1]

After confirming the similarity in the flow field using qualitative and quantitative flow visualisation as discussed above, we performed direct force measurement using a load cell to see the lift and thrust force generated by the model. The load cell data as shown in Fig. 8a demonstrates that the overall net lift force and thrust force Fig. 8b throughout the cycle is positive, and that the net thrust force is generated during flapping, which is directly related to our flow visualisation results.

4 Conclusions

In this study, we fabricated a Manta ray like flexible foil flapping model with simplified transmission mechanism to be used in the development of underwater robots. Due to the spanwise variation in deflection of the flexible foil-body and the smooth trailing edge from which both spanwise and streamwise components of vorticity are shed, the Manta ray geometry generates an unusual wake structure [11], which can be observed quantitatively in our scaled-down model too. A wave-like motion on the wing of the model was observed and qualitatively compared with the real Manta ray swimming pattern. Furthermore, the presence of counter-clockwise and clockwise tip vortex was confirmed using flow visualisation with fluorescent dye and PIV. Finally, the load cell results confirmed that the model produces a net lift and thrust force while swimming with wave-like motion on the wings. Further experiments will be performed in the future to get more insights into the effect of different foil thickness and flapping frequency on the lift and thrust generation.

Acknowledgements We are extremely grateful to our lab technician Mr. Anil K. Pal for his exceptional technical expertise in fabricating the model. We would also want to thank BBC Earth, National Geography, and other individual YouTube content creators for providing free access to high-quality videos.

References

1. New Atlantis WILD Channel. Manta ray, a giant of the ocean
2. Fish FE, Kolpas A, Crossett A, Dudas MA, Moored KW, Bart-Smith H (2018) Kinematics of swimming of the manta ray: three-dimensional analysis of open-water maneuverability. *J Exp Biol* 221(6):jeb166041
3. Clark RP, Smits AJ (2006) Thrust production and wake structure of a batoid-inspired oscillating fin. *J Fluid Mech* 562:415–429
4. Thielicke W, Sonntag R (2021) Particle image velocimetry for MATLAB: accuracy and enhanced algorithms in PIVlab. *J Open Res Softw* 9(1):1–14
5. Zhang Y, Wang S, Wang X, Geng Y (2018) Design and control of bionic manta ray robot with flexible pectoral fin. In: 2018 IEEE 14th international conference on control and automation (ICCA). IEEE, pp 1034–1039
6. Taylor GI (1952) Analysis of the swimming of long and narrow animals. *Proc R Soc Lond A Math Phys Sci* 214(1117):158–183
7. Alben S, Witt C, Baker TV, Anderson E, Lauder GV (2012) Dynamics of freely swimming flexible foils. *Phys Fluids* 24:051901
8. Drucker EG, Lauder GV (2002) Experimental hydrodynamics of fish locomotion: functional insights from wake visualization. *Integr Comp Biol* 42(2):243–257
9. Lauder GV (2015) Fish locomotion: recent advances and new directions. *Annu Rev Mar Sci* 7:521–545
10. Guo C-yu, Kuai Y-fei, Han Y, Xu P, Fan Y-wei, Yu Chang-dong (2022) Hydrodynamic analysis of propulsion process of zebrafish. *Phys Fluids* 34(2):021910
11. Clark R, Smits A (2012) Visualizations of the unsteady wake of manta ray model. In: 44th AIAA aerospace sciences meeting and exhibit, Reno, Nevada (AIAA 2006-352), pp 1–8

Internal and External Aerodynamics of a Lean Burn Gas Turbine Fuel Injector



Preetam Jamod, Ayush Divyansh, Harish Pothukuchi,
and K. P. Shanmugas

Abstract The internal aerodynamics of a lean burn gas turbine fuel injector confined is numerically investigated to understand the recirculation zone characteristics and shear layer interaction. The injector design is based on lean burn fuel injection concepts adopted in aero-engine combustors. Geometry involves a pilot and main mixer assembly which contains co-rotating and counter-rotating swirler arrangements separated by multiple fuel passages. The CFD formulation was based on the standard $k-\epsilon$ model. The model was then numerically resolved using methods of area-mass-flow rate-based techniques with preconditioning and calculated average velocities and turbulence characteristics. The central toroidal recirculation zone (CTRZ) formation by the pilot and main swirlers is captured and the shear layer structure is quantified at different axial locations.

Keywords Lean burn combustor · Swirl injector · Central toroidal recirculation zone · Shear layer · Turbulent kinetic energy

1 Introduction

Recent interests in lean burn combustion concepts (TAPS [Twin Annular Premixing Swirler] [1, 2], LPP [Lean, pre-mixed, pre-vaporized] [3], LDI [Lean Direct Injection] [4] are primarily driven by the growing demand for compact low emission micro gas turbine engines for drones and localized power generation. A typical lean burn combustor employs a complex fuel injector assembly to mix the combustor air and fuel effectively for a wide range of operating conditions. The fuel injector assembly admits 70–80% of the combustor air and it requires elaborate arrangements within the fuel injector to generate the desired primary zone aerodynamics for

P. Jamod · H. Pothukuchi · K. P. Shanmugas (✉)
Department of Mechanical Engineering, IIT Jammu, Jammu 181221, India
e-mail: shanmugas.kp@iitjammu.ac.in

A. Divyansh
Department of Materials Engineering, IIT Jammu, Jammu 181221, India

mixing, atomization, and flame stabilization [2]. Typical injector geometry consists of pilot and main swirler block assemblies and the fuel is injected using a pilot nozzle (simplex or dual orifice type) or using dedicated annular passages [5, 6].

At IIT Jammu, an initiative is launched to develop compact combustor concepts for a 1 KN thrust drone engine. Development of the fuel injector is taken up as the first step, adopting a lean burn fuel injector technology similar to the existing aero-engine injector concepts. The injector is realized using additive manufacturing techniques considering the geometrical complexities and geometrical accuracy required. The design of the injector focuses on two important aspects: (a) design of the swirler assembly to achieve the desired injector aerodynamics that will help for proper flame stabilization and atomization. (b) design of the fuel injector/injection passages that provide proper atomization and mixing at all power levels with appropriate fuel staging.

An injector assembly is realized as shown in Fig. 1. The injector's pilot assembly consists of co-rotating and counter-rotating axial swirlers separated by a curved pre-filming surface. A simplex nozzle of flow number 1.1 is used as the pilot injector to generate a 90° cone spray, which supplies the initial droplets to the pilot mixer. These droplets get atomized by the primary air, and part undergoes wall filming on the prefilmer. A counter-rotating shear layer forms at the prefilmer tip which atomizes the accumulated liquid rim and provides a uniform spray at the exit. The primary air swirl of the primary swirler generates a central toroidal recirculation zone (CTRZ) which extends farther downstream of the injector. The main mixer consists of an axial and radial swirler assembly. A liquid jet ensues from the inner wall of the radial swirler and it mixes with the axial and radial air flows. This forms a jet in swirl cross-flow atomization mechanisms inside the main swirler. The internal flow features are complicated and involve multiple flow phenomena. The primary zone aerodynamics at the injector exit is dictated by the internal flow evolution. The CTRZ and shear layer characteristics of the pilot and main mixers will dictate the atomization and mixing characteristics of the flow. A detailed understanding of the internal flow characteristics is critical for the design of advanced mixer concepts. However, experimental investigation of the internal flow of such injectors is quite challenging considering the geometrical and flow complexities inside. Hence a numerical investigation approach is adopted to understand the internal and external airflow characteristics of the injector. The present work focuses on the CTRZ, streamline pattern, and shear layer characteristics of the pilot and main injector assemblies.

2 Injector Geometry and Flow Conditions

The injector is designed based on the existing lean burn combustor design methodologies in the literature [5]. A turbojet cycle analysis is conducted considering an engine thrust of 1 KN, and the corresponding air and fuel flow rates are estimated. The flow through the injector is split into the pilot and main swirlers based on the

Fig. 1 Cut section view of the injector with four swirler arrangement

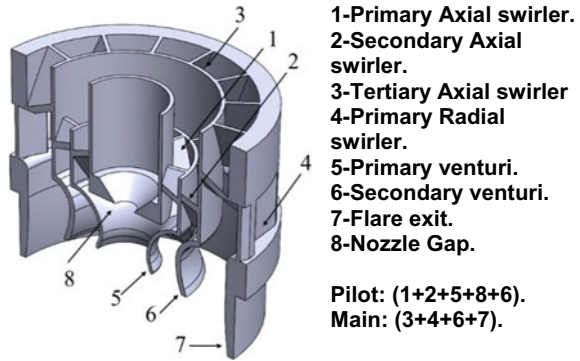


Table 1 Mass flow rate and area ratio of pilot and main

Part	Mass flow rate (kg/s)	Area ratio
Pilot mixer	0.0405	0.32
Main mixer	0.0852	0.68

Table 2 Parameter of swirlers of pilot and main

Part	Geometrical swirl number	Swirler type
Primary pilot	0.44	Axial
Secondary pilot	0.47	Axial
Primary main	0.42	Axial
Secondary main	1.54	Radial

area ratio. Simulations are performed for flow conditions as mentioned in Table 1. The total injector flow rate is 0.125 kg/s.

As shown in Fig. 1, the injector assembly is divided into two parts viz., Pilot and Main. The Pilot consists of primary and secondary axial swirlers, and the Main consists of tertiary axial and primary radial swirlers, as labeled in Fig. 1; Table 2.

3 Numerical Methodology

This section presents the detailed numerical methodology for performing 3D CFD simulations to analyze the internal and external aerodynamics of a lean burn gas turbine fuel injector [7]. Air is considered as the fluid passing through the pilot and main passages. A finite volume-based commercial solver, ANSYS Fluent is used for performing the simulations. The following are the governing equations that represent the conservation of mass and momentum [8].

Continuity equation:

$$\frac{\partial \rho}{\partial t} + \nabla \cdot (\rho \vec{v}) = S_m \quad (1)$$

Momentum equation:

$$\frac{\partial}{\partial t}(\rho \vec{v}) + \nabla \cdot (\rho \vec{v} \vec{v}) = -\nabla p + \nabla \cdot (\overline{\tau}) + \rho \vec{g} + \vec{F} \quad (2)$$

To account for the turbulence, Reynolds Average Navier–Stokes (RANS)-based two-equation model, namely the Standard k - ε model is employed. From the literature [9], it is evident that k - ε model a better solver for the study of complex swirl flows with recirculating zones and shear layers. The transport equations [8] for the standard k - ε model are given as,

$$\begin{aligned} & \frac{\partial}{\partial t}(\rho k) + \frac{\partial}{\partial x_i}(\rho k u_i) \\ &= \frac{\partial}{\partial x_j} \left[\left(\mu + \frac{\mu_t}{\sigma_k} \right) \frac{\partial k}{\partial x_j} \right] + G_k + G_b - \rho \varepsilon - Y_M + S_k \end{aligned} \quad (3)$$

$$\begin{aligned} & \frac{\partial}{\partial t}(\rho \varepsilon) + \frac{\partial}{\partial x_i}(\rho \varepsilon u_i) \\ &= \frac{\partial}{\partial x_j} \left[\left(\mu + \frac{\mu_t}{\sigma_\varepsilon} \right) \frac{\partial \varepsilon}{\partial x_j} \right] \\ &+ C_{1\varepsilon} \frac{\varepsilon}{k} (G_k + C_{3\varepsilon} G_b) - C_{2\varepsilon} \rho \frac{\varepsilon^2}{k} + S_\varepsilon \end{aligned} \quad (4)$$

3.1 Computational Domain for Lean Burn Fuel Injector

The schematic of the 3D computational domain of the injector assembly is presented in Fig. 2. The fuel injector is considered to be enclosed inside a cylinder of 100 mm diameter and 100 mm long. Downstream the exhaust of the injector, a cylindrical domain of 100 mm diameter and 150 mm long is considered to capture the recirculation zone. It is assumed that there is a total variation of 4% (4053 Pa) of atmospheric pressure in the upstream gauge pressure inlet condition and zero-gauge pressure at the exit face [9, 10]. Hybrid meshing is performed for the discretization of the computational domain with a total number of 2.1 million elements. The cut section of the computational mesh is presented in Fig. 3, showing the fine mesh near the Main section for resolving the detailed 3D flow field characteristics. The pressure and velocity coupling are achieved using a SIMPLE algorithm. Second-order numerical schemes are chosen for solving the momentum, turbulent kinetic energy, and turbulent dissipation rate. At the inlet, the mass flow rates are defined (see Table 1), whereas

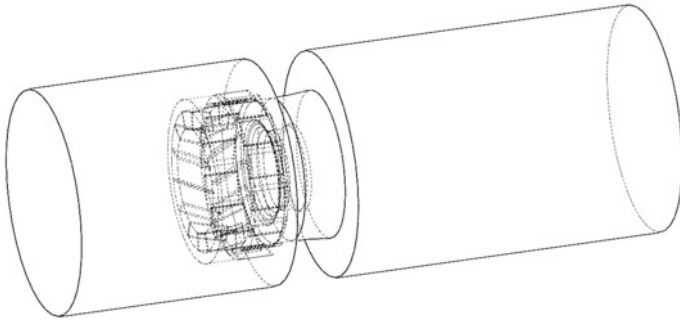


Fig. 2 The schematic of the 3D computational domain of the Lean burn fuel injector

a pressure outlet condition is defined at the outlet. A no-slip boundary condition is imposed on the solid walls (Table 3).

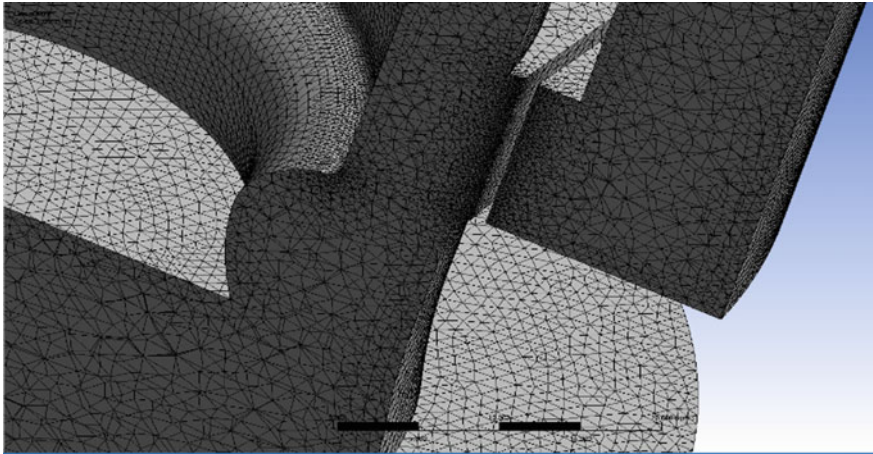


Fig. 3 Hybrid mesh for the lean burn fuel injector

Table 3 Parameters of inlet and outlet domain

Parts	Inlet domain diameter (mm)	Inlet domain height (mm)	Outlet domain diameter (mm)	Outlet domain height (mm)
Total	100	80	200	150
Main	100	100	100	150
Pilot	80	70	100	150

3.2 Grid Independence Study

A systematic grid independence study is performed for different mesh configurations with 1.1, 2.1, and 3.1 million elements as shown in Table 4. The comparison of axial variation of the velocity along the injector is presented in Fig. 4. It can be inferred that there is no significant change in the axial velocity profile for mesh configurations 2 and 3. Hence, mesh 2 is chosen for the rest of the simulations. Considering a fully turbulent flow, the first cell height of 0.5mm is specified for a y^+ of 45 for the near-wall treatment [10].

Table 4 Different mesh configurations and their respective number of elements

S.No	Configurations	Number of elements
1	Mesh 1	1,127,416
2	Mesh 2	2,147,037
3	Mesh 3	3,157,755

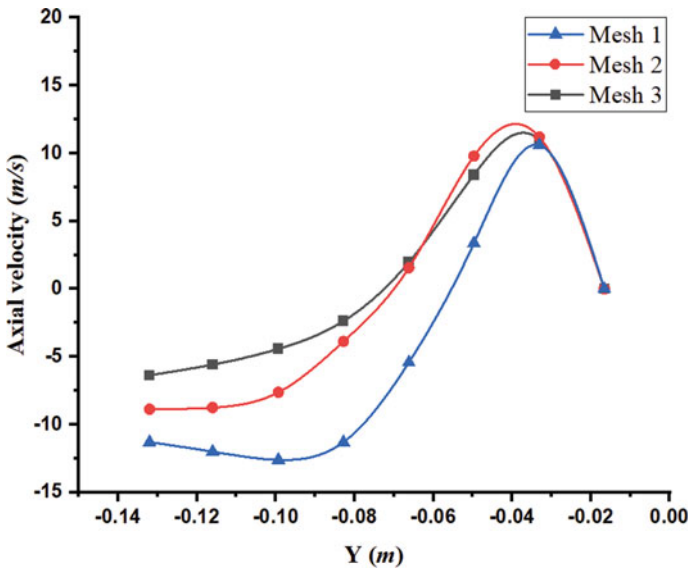


Fig. 4 Comparison of axial velocity with axial distance for different mesh configurations

4 Results and Discussion

The internal aerodynamics of the injector is quite complicated, and it involves the interaction of complex flow structures. The internal airflow is captured systematically considering the geometry in 3 parts: (a) pilot mixer alone, (b) main mixer alone, and (c) fuel injector assembly (pilot + main). The subsequent sections discuss the flow characteristics for the three configurations.

4.1 Pilot Mixer Flow Characteristics

See Figs. 5, 6 and 7.

Figure 5a and b show the velocity contours and streamline pattern through the pilot mixer assembly respectively. Primary and secondary air streams are counter-rotating. Simulation results show that the air enters through the primary and secondary swirlers, and a strong swirl flow is generated at the exit. The primary air flow undergoes vortex breakdown, and a central toroidal recirculation zone is formed at the exit. The size of the recirculation bubble is shown in Fig. 7 as an iso-surface of zero axial velocity. The CTRZ originates 41 mm from the exit plane and extends 28 mm toward the exit of the injector. The flow gets axisymmetric as it accelerates through the venturi region. The wall shear stresses are high in the inner region of the venturi. The primary and secondary air streams interact at the venturi tip and form a thick shear layer. The turbulent kinetic energy is maximum at the venturi tip and decays

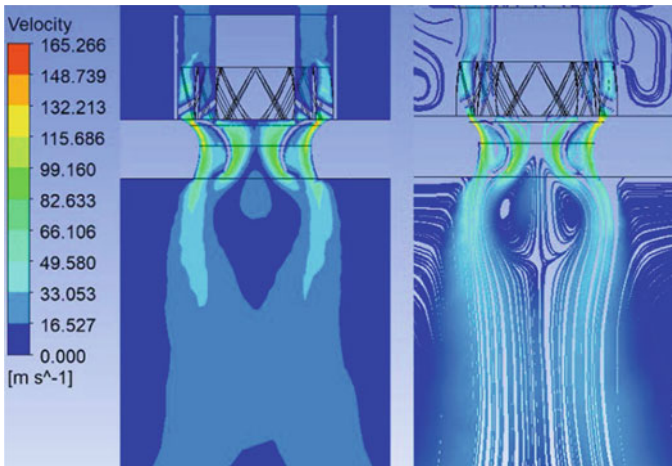


Fig. 5 The velocity field in the pilot injector assembly **a** Contour plot, **b** Streamline pattern ($\dot{m}_p = 0.0405 \text{ kg/s}$)

Fig. 6 TKE variation in the pilot injector assembly ($\dot{m}_p = 0.0405 \text{ kg/s}$)

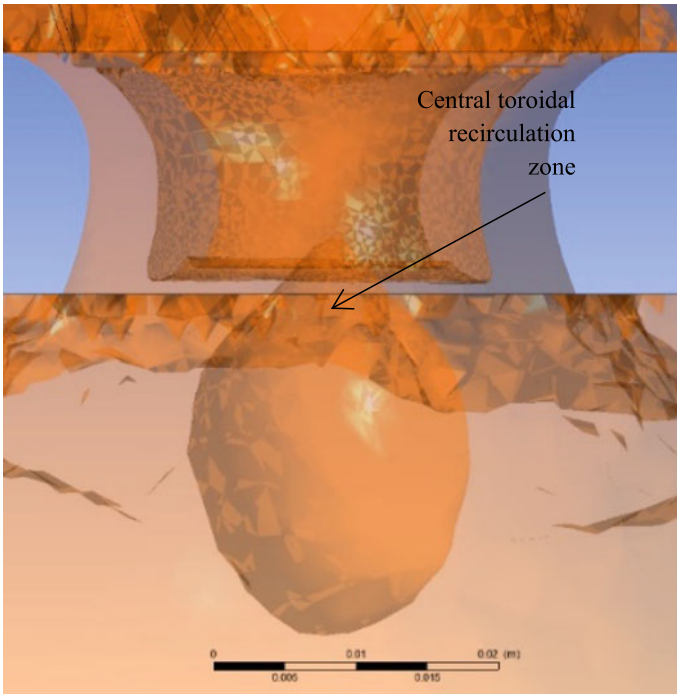
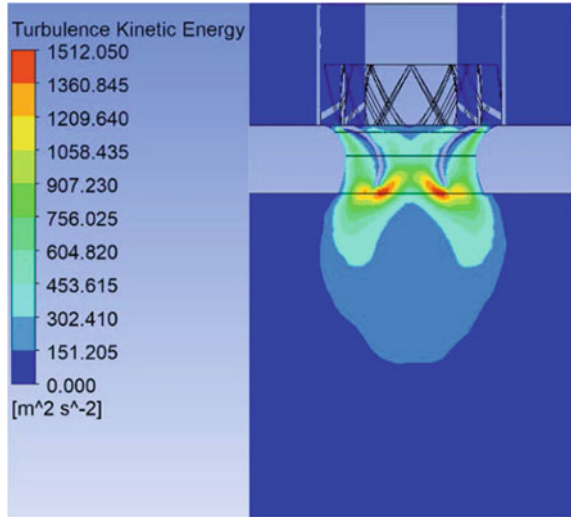


Fig. 7 Iso-surface of zero axial velocity, showing the recirculation bubble

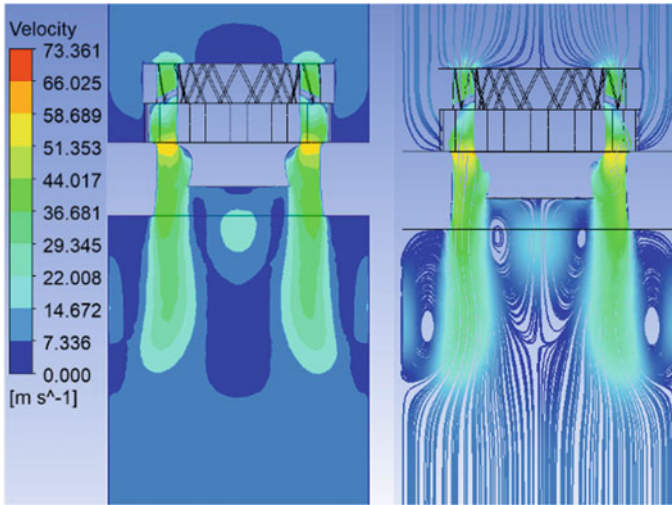


Fig. 8 The velocity field in the pilot injector assembly **a** Contour plot, **b** Streamline pattern ($\dot{m}_m = 0.0852$ kg/s)

as the flow proceeds downstream. Figure 6 shows the TKE variation inside the pilot mixer.

4.2 Main Mixer Flow Characteristics

See Figs. 8 and 9.

The main mixer involves a radial and axial swirler assembly which is counter-rotating. The flow rate through the main mixer is around 0.0852 kg/s and the bulk velocities are observed in the range of 28–40 m/s. The flow through the annulus generates a strong shear layer at the exit, a recirculating flow structure is formed at the exit. However, the recirculation zone is weak and the flow is more axisymmetric toward the downstream region. The TKE variation shows peak regions at the interaction zones of the axial and radial swirl flow, which further leads to the formation of an expanding shear layer in the downstream region. No toroidal recirculation bubble is formed in this case.

4.3 Fuel Injector Flow Characteristics

See Figs. 10, 11, 12 and 13.

The combined airflow field generated by the pilot and main mixer assemblies is simulated using the fuel injector configuration. The velocity contours and streamline

Fig. 9 TKE variation in the main injector assembly ($\dot{m}_m = 0.0852 \text{ kg/s}$)

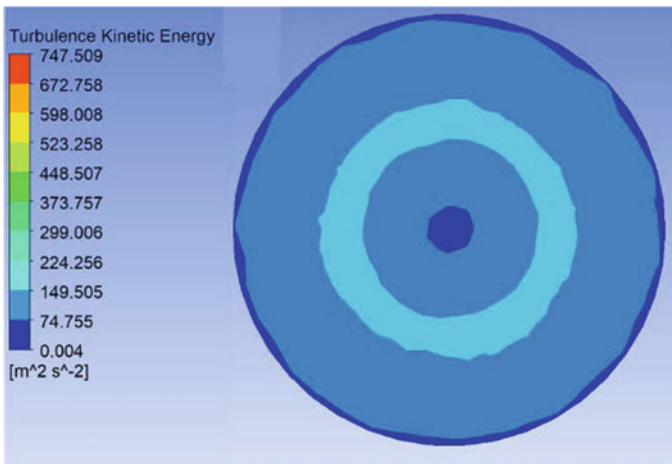
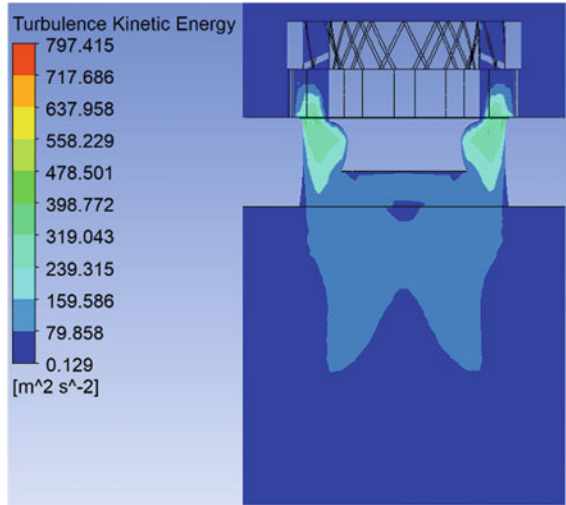


Fig. 10 TKE variation in cross plane at 10 mm from exit plane of the injector assembly ($\dot{m}_t = 0.125 \text{ kg/s}$)

pattern of the injector flow is shown in Fig. 11 a and b, respectively. The flow structures show the dominance of the main mixer flow on the pilot mixer flow field. The CTRZ formed at the pilot mixer exit gets elongated under the influence of the main mixer flow. Peak velocities are observed in both the pilot and main mixer shear layer regions. The TKE and vorticity distribution at 10 mm from the mixer exit plane is presented in Figs. 10 and 12. Both plots show the strong dominance of the main mixer shear layer over the shear layer formed by the pilot mixer.

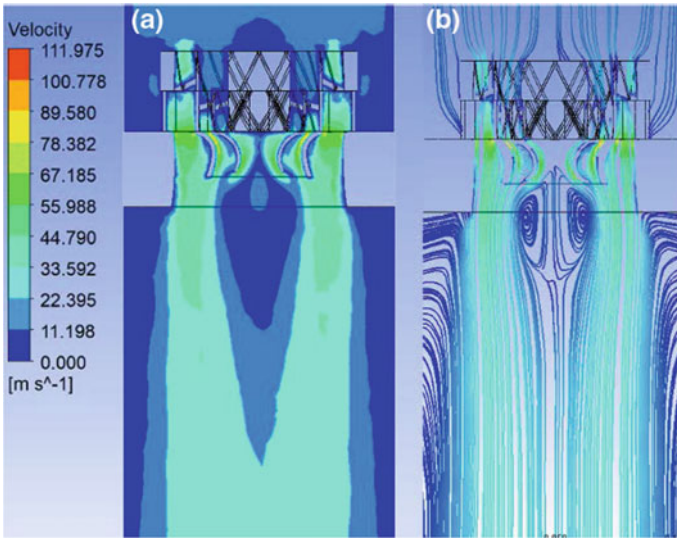


Fig. 11 The velocity field in the pilot injector assembly **a** Contour plot, **b** Streamline pattern ($\dot{m}_t = 0.125 \text{ kg/s}$)

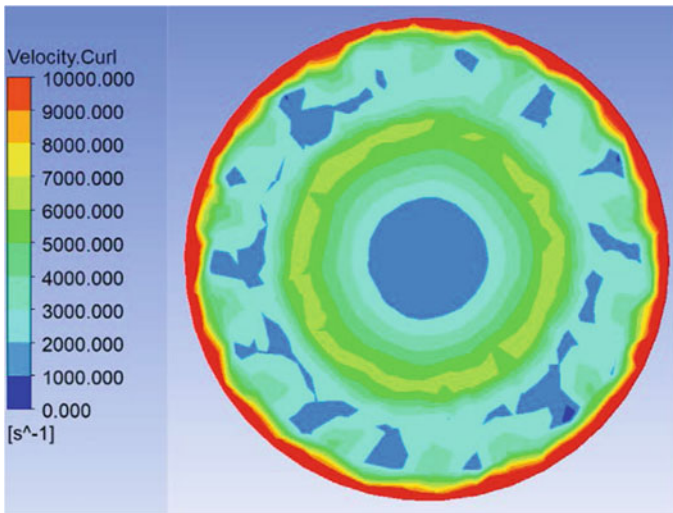
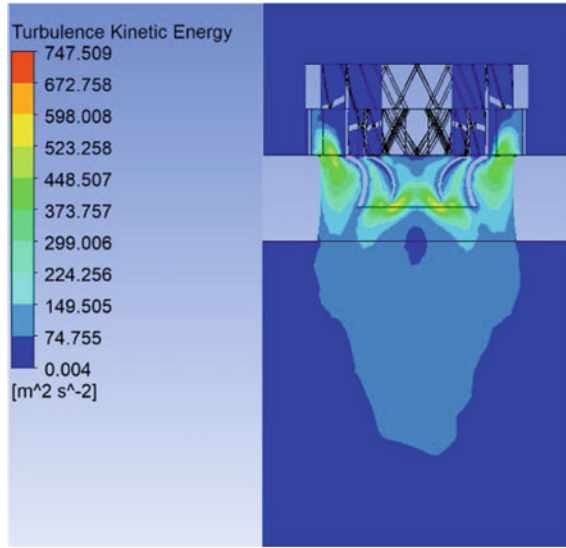


Fig. 12 Vorticity variation in injector assembly ($\dot{m}_t = 0.125 \text{ kg/s}$)

Fig. 13 TKE variation in the injector assembly ($\dot{m}_t = 0.125$ kg/s)



5 Conclusions

The internal and external aerodynamics of a complex lean burn gas turbine fuel injector is investigated numerically. The formation of recirculating flow structures in the pilot and main mixer assembly is captured in the present work. The primary air swirl of the pilot mixer develops a CTRZ and it gets elongated under the influence of the main mixer shear layer. Regions of high TKE are observed near the venturi tip and near the exit region of the main mixer due to the interaction between counter-rotating air swirls. Further works are planned to improve the mesh resolution and also to identify the appropriate turbulence models for better prediction accuracies. Particle image velocimetry experiments are in progress to capture the exit velocity field of the injector and the data will be used to validate the CFD results.

Nomenclature

$C_{1\varepsilon}$	1.44	–
$C_{2\varepsilon}$	1.92	–
C_μ	0.09	–
E_{ij}	Rate of deformation	s^{-1}
F	External body force	N
G_k	Turbulent kinetic energy due to mean velocity gradient	J/kg
G_b	Turbulent kinetic energy due to buoyancy	J/kg
g	Gravitational acceleration	m/s^2
k	Turbulent kinetic energy	J/kg

(continued)

(continued)

\dot{m}_m	Air flow rate through main	kg/s
\dot{m}_p	The air flow rate through pilot air	kg/s
\dot{m}_t	Flow rate through main and pilot	kg/s
p	Static pressure	Pa
S_k	Source term	–
S_m	Mass of vaporized liquid	kg
S_ε	Source term	–
u_i	Velocity component	m/s
v	Velocity	m/s
Y	Axial distance	m
Y_m	Dilatation dissipation	–
ε	Rate of dissipation	m^2/s^3
μ	Dynamic viscosity	Pa-s
μ_t	Eddy viscosity	kg-m/s
ρ	Density of air	kg/m^3
σ_k	1.0	–
σ_ε	1.3	–
$\overline{\tau}$	Stress tensor	Pa

Acknowledgements I would like to thank Mr. Saket Singh, Mr. Prem Bharti, and Mr. Parth Singh for assistance with ANSYS and guidance during the course of the research.

References

1. Foust M, Thomsen D, Stickles R, Cooper C, Dodds W (2012) Development of the GE aviation low emissions TAPS combustor for next generation aircraft engines. In: 50th AIAA aerospace science meeting including the new horizons forum and aerospace exposition, Nashville, Tennessee, AIAA 2012–0936, p 936
2. Mongia HC (2014) TAPS: a fourth generation propulsion combustor technology for low emissions. In: AIAA/ICAS international air and space symposium and exposition: the next 100 years, Dayton, Ohio, USA, AIAA 2003-2657, p 2657
3. Eskin LD, Holton MM, Turner BA, Joklik RG, Klassen MS, Roby RJ (2013) Long-term demonstration of a lean, premixed, prevaporized (LPP) system for gas turbines. In: 2012 20th International Conference on Nuclear Engineering and the ASME 2012 power conference, vol 44984. The American Society of Mechanical Engineers, Paper No: ICONE20-POWER2012-54766, pp 737–745
4. Ren X, Sung C-J, Mongia HC (2018) On lean direct injection research. In: Energy for propulsion. Green energy and technology. Springer, Singapore, pp. 3–26
5. Mongia H, Al-Roub M, Danis A, Elliott-Lewis D, Johnson A, Vise S, Jeng S-M, McDonell V, Samuelsen G (2012) Swirl cup modeling. Part I. In: 37th joint propulsion conference and exhibit, p 3576

6. Mancini AA, Mongia HC (2012) Mixture assembly for gas turbine engine combustor (Patent No.: US 8,171,735 B2)
7. Wang S, Yang V, Hsiao G, Hsieh SY, Mongia HC (2007) Large-eddy simulations of gas-turbine swirl injector flow dynamics. *J Fluid Mech* 583:99–122
8. ANSYS Inc. (2009) ANSYS fluent theory guide 12.0
9. Hsiao G, Mongia HC (2012) Swirl cup modeling. Part 3: grid independent solution with different turbulence models. In: 41th aerospace sciences meeting and exhibit, Reno, Nevada, p 1349
10. Hsiao G, Mongia H (2003) Swirl cup modeling. Part 2: inlet conditions. In: 41st aerospace sciences meeting and exhibit, Reno, Nevada, p 1350

Aero-Thermal Investigation on Commuter Category Turboprop Aircraft Engine Nacelle



C. A. Vinay, G. N. Kumar, S. Venkat Iyengar, and T. Pugazhendhi

Abstract In aircraft industry, the development of composite materials for increased strength and reduced weight is always a priority. The external body of aircraft, i.e. fuselage, nacelle, wings etc., is made of Al alloy and composites. A nacelle of a light turbo-prop tractor-configured aircraft, houses hot components like engine and subsystem. The nacelle is also made of thermally sensitive composite material; hence, it requires specified thermal management study. Thermal ventilation is done by inlet scoops and louvre outlet which keeps the engine and nacelle bay region in lower temperature safe for nacelle surface. Aero-thermal analysis is performed on the engine and nacelle bay ventilation, and the temperature results of the computation fluid dynamics (CFD) analysis is used in assessing the suitable material and its mechanical properties degradation with respect to temperature. For numerical study, a simplified nacelle, engine, and subsystem geometry are considered. ANSYS ICEM CFD™ and CATIA commercial software is used for geometry preparation and tetra meshing. ANSYS Fluent is used as a solver with SST $k - \omega$ viscous model to capture thermal values at the geometry surfaces.

Keywords Aero-thermal · Bay-ventilation · Louvers · Nacelle · Turboprop

1 Introduction

A fast growth is seen in the present days of aircraft manufacturing, and there is a rising demand for lightweight, high strength materials. Figure 1 shows the typical turbo-prop commuter aircraft with tractor propeller configuration which is considered in the present study. It consists of a nacelle and ducts made up of aluminium alloy sheet and composite material. Tensile yield strength (F_{ty}) of this aluminium alloy is

C. A. Vinay (✉) · G. N. Kumar
Department of Mechanical Engineering, National Institute of Technology, Surathkal 575028, India
e-mail: vinay.ca@nal.res.in

S. V. Iyengar · T. Pugazhendhi
CSIR, National Aerospace Laboratories, Bangalore 560017, India



Fig. 1 Turboprop commuter aircraft with tractor propeller configuration

sensitive to temperature. With the temperature raise from 204 to 276 °C, the tensile yield strength of the material drops from 60 to 40% of F_{ty} (100% F_{ty} considered at room temperature). The nacelle is expected to have a material with higher heat resistive capacity, as it houses the engine and its auxiliary components which dissipate heat energy at different temp ranges in conjugated manner and reach at elevated temperature. As the nacelle is made of Al alloy sheet, it cannot withstand high temperature dissipating from the engine. Hence, the bay region presents between engine and nacelle need to be ventilated to circulate the air which enhances the heat transfer and reduces the amount of heat reaching the nacelle.

Through numerical simulation, the heat transfer rate and hence the nacelle surface temperature can be estimated for any flight conditions inside the bay region based on sizing of NACA flush inlet and louvres outlet. The inlet and outlet for the air circulation inside the bay area needs to be placed on the nacelle surface by using appropriate analytical and experience-based method.

2 Literature Review and Objective

Segal (1997) This paper presented of an engine bay idea for a military aircraft demonstrated the engine bay's effective cooling and ventilation both static and in flight [1]. Balland et al. (2008) Airbus and Snecma jointly investigated the nacelle bay area using an aero-thermal technique. In that investigation, they concentrated on radiative and convective heat transport in an aircraft engine's nacelle core compartment. They used real-time engine data to validate the results [2]. Olejnik et al. (2021) In order to accurately model the internal and exterior flow, determine the cooling system's current state, and investigate the effects of modifying the engine cover's baffles, computational fluid dynamics tools were employed in this article. Additionally, two different cover types with various inlet and output cross-sectional areas are put to the test [3]. Buonomo et al. (2013) this article describes a thermo-fluid-dynamic analysis of the flow field surrounding an aircraft nacelle powered by a small pusher turbine engine to determine the thermal field on the nacelle surface [4]. Łapka et al. (2014)

in this research, numerical simulations of fluid flow and heat transfer in the engine compartment of a small aircraft with a tractor configuration were carried out for various air intake circumstances and air inlet and outlet configurations. The simulation results showed that the intake surrounding the spinner mount is advantageous and ensures effective exhaust system cooling. Additionally, they recommend using additional inlets in place of the outlet in the landing gear bay, which is positioned in the rear of the hot compartment above the engine and in the cool part of the nacelle [5]. They further reduced the issue and contrasted the outcomes from one dimension with those from three dimensions. It was determined that the results of these two ways were agreeable, and a subsequent iteration employing a 3D model was conducted. Heat from the engine exhaust gas jet that transfers to the aircraft body was compared between two tractor-configured aircrafts [6].

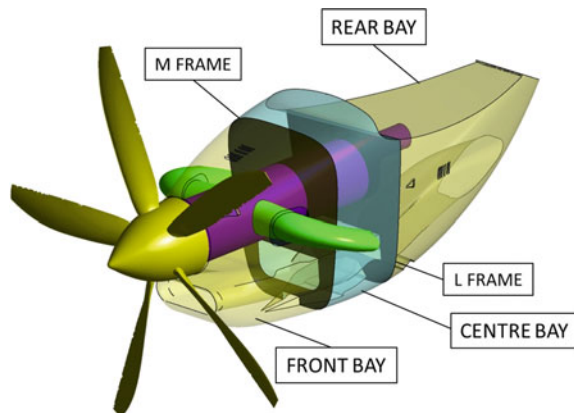
3 Materials and Methods

The engine bay consists of three parts which was separated by a firewall called L- and M-frame. Hot section compartment with engine, front bay and relatively cold section, rear bay is containing other systems; mid part is plenum section, centre bay (compressor region) shown in Fig. 2.

3.1 Geometry Creation

The model for numerical analysis is created using CATIA V5 software. Complex systems like oil cooling ducts, fuel ducts, engine control cables, etc., are not considered in the geometry as they do not significantly contribute as a heat source. The

Fig. 2 Three different zones with firewall



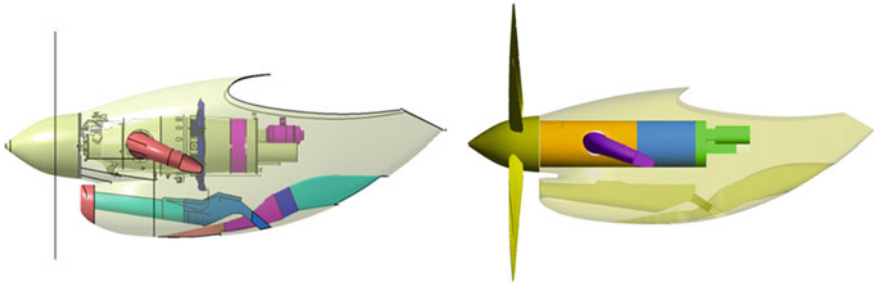


Fig. 3 Simplified geometry from complicated geometry

geometry is simplified to reduce the computational and meshing time shown in Fig. 3.

The region inside the nacelle and the engine surfaces are divided into three zones/bay, viz. front, centre, and rear zone which are separated by L-frame and M adiabatic frames. The front zone consists of exhaust stubs on each side of the nacelle and also reduction gear box, propeller governor, magnetic chip detector is present. In the centre zone, which is a compressor zone, there is no external air circulation/ventilation in this bay region. The rear zone consists of auxiliary gear box, fuel control unit, oil scavenging pump is housed.

3.2 Mesh Generation

The mesh generation was done by using ANSYS ICEM CFD. Grid consists of 13,001,440 control volumes and 26,675,090 faces. To obtain an undisturbed flow, a large cylindrical domain is considered around the engine–nacelle geometry of length 5000 mm upstream and 40,000 mm downstream (larger domain distance downstream is to capture turbulence generated by the propellers downstream), and the domain diameter of 15,000 mm is considered shown in Fig. 4. The domain sizing is finalized by observing turbulent intensity regions in the preliminary study.

3.3 Mathematical Model

The simulations were done for complete aircraft having nacelle and propeller, utilizing ANSYS Fluent software which provides finite volume code. The three-dimensional flow was solved using Reynolds-averaged Navier–Stokes equation, in that $k - \omega$ SST model [7] was selected, and then spatial discretization of the governing equations was solved by second-order upwind method. The pressure–velocity coupling was achieved by SIMPLE scheme, and all other computations

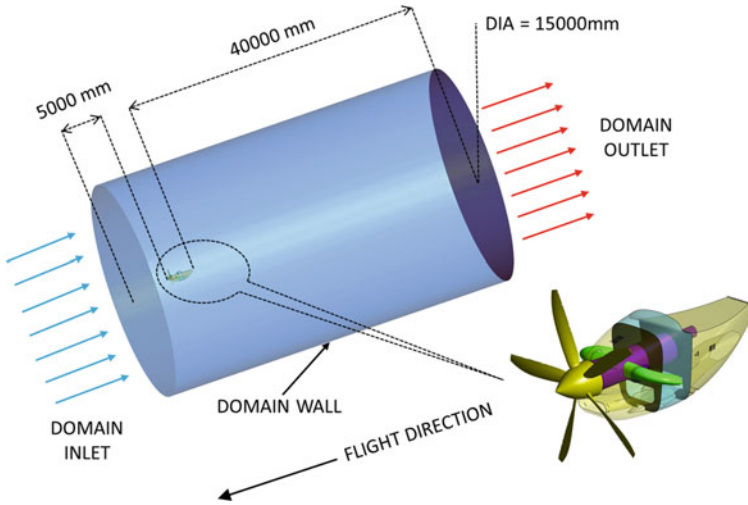


Fig. 4 Domain sizing and simplified nacelle and engine model used for simulation

were generated with double-precision arithmetic scheme. The averaged equations for conservation of mass, momentum, and energy are as follows:

SST $k - \omega$ Equations:

$$\frac{\partial \rho}{\partial t} + \frac{\partial}{\partial x_i}(\rho u_i) = 0 \tag{1}$$

$$\frac{\partial}{\partial t}(\rho u_i) + \frac{\partial}{\partial x_j}(\rho u_j u_i) = -\frac{\partial p}{\partial x_i} + \frac{\partial}{\partial x_j}(t_{ji} + \rho \tau_{ji}) \tag{2}$$

$$\begin{aligned} & \frac{\partial}{\partial t} \left[\rho \left(e + \frac{1}{2} u_i u_i + k \right) \right] + \frac{\partial}{\partial x_j} \left[\rho u_j \left(h + \frac{1}{2} u_i u_i + k \right) \right] \\ &= \frac{\partial}{\partial t} \left[\rho \left(e + \frac{1}{2} u_i u_i + k \right) \right] \\ &= \frac{\partial}{\partial x_j} \left[\begin{array}{l} u_i (t_{ij} + \rho \tau_{ij}) \\ + \left(\frac{\mu}{Pr_L} + \frac{\mu}{Pr_T} \right) \frac{\partial h}{\partial x_j} \\ + \left(\mu + \sigma^* \frac{\rho k}{\omega} \right) \frac{\partial k}{\partial x_j} \end{array} \right] \end{aligned} \tag{3}$$

Turbulent Kinetic Energy:

$$\begin{aligned}
& \frac{\partial}{\partial t}(\rho k) + \frac{\partial}{\partial x_j}(\rho u_j k) \\
& = \rho \tau_{ij} - \beta^* k \omega + \frac{\partial}{\partial x_j} \left[\left(\mu + \sigma^* \frac{\rho k}{\rho \omega} \right) \frac{\partial k}{\partial x_j} \right]
\end{aligned} \tag{4}$$

Specific Dissipation Rate of Kinetic Energy:

$$\begin{aligned}
& \frac{\partial}{\partial t}(\rho \omega) + \frac{\partial}{\partial x_j}(\rho u_j \omega) \\
& = \alpha \frac{\omega}{k} \rho \tau_{ij} \frac{\partial u_i}{\partial x_j} - \beta \rho \omega^2 \\
& \quad + \sigma_d \frac{\rho}{\omega} \frac{\partial k}{\partial x_j} \frac{\partial \omega}{\partial x_j} \\
& \quad + \frac{\partial}{\partial x_j} \left[\left(\mu + \sigma \frac{\rho k}{\omega} \right) \frac{\partial \omega}{\partial x_j} \right]
\end{aligned} \tag{5}$$

Two-equation eddy-viscosity, a mixture of the Wilcox k-omega and k-epsilon models that are utilized in several aerodynamic applications, is a component of the k-SST turbulence model [8]. The Wilcox model close to the wall and the k-epsilon model in the free stream can both be activated using the integration function. To take into consideration the transport implications of the primary turbulent shear stress, it has a modified turbulent viscosity formulation. The k-SST model typically forecasts the size and timing of separation under adverse pressure gradients.

3.4 Simulation Set-Up

The air surrounding the nacelle is assigned as external fluid, which is present in the entire domain, the engine bay, viz. front, centre, and rear are provided with separate working fluid, and to account for propeller suction, a rotating fluid is provided surrounding the propellers, and all the fluid are made as tetra volume mesh. Engine is considered as constant wall temperature with three different temperatures shown in Fig. 5. Nacelle is considered as wall thickness of 0.0012 m to avoid ANSYS Fluent default setting for wall as thermal resistance as shown in Table 1.

4 Results and Discussion

The result contour is plotted after evaluating the proper development of the flow around the nacelle by considering mass balance and energy balance at the domain entry and exit. Figure 6 shows the section location over which the temperature

Fig. 5 Temperature distribution on engine surface

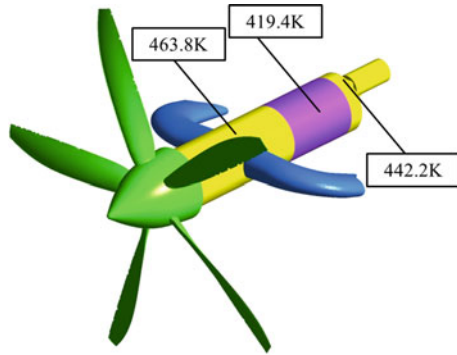


Table 1 Boundary conditions

S. No	Domain	Boundary conditions
1	Domain inlet	Velocity inlet
2	Domain outlet	Pressure outlet
3	Domain	Wall
4	Engine	Constant temperature wall
5	Exhaust annular ring	Interior
6	Exhaust stub	Wall
7	L-frame	Wall
8	Louvres	Interior
9	M-frame	Wall
10	NACA inlets	Interior
11	Nacelle	Wall ($t = 0.0012$ m)
12	Nacelle entry	Interior
13	Propeller blades	Wall
14	Rotating domain	Interior
15	Spinner	Wall

contours will be plotted in the results. The results on these plane show the behaviour of the fluid inside the nacelle.

In this paper, two critical case results were discussed as tabulated in Table 2. Maximum cruise condition, case 3 with maximum speed, i.e. 0.47 Mach and Ground static take-off condition, case 8 with maximum OAT 50 °C. Temperature results observed at all the three zones are tabulated in Table 3.

Y-Z cut plane	Distance (m) from X=0
1	1
2	2.25
X-Z cut plane	Distance (m) from Y=0
3	0.1

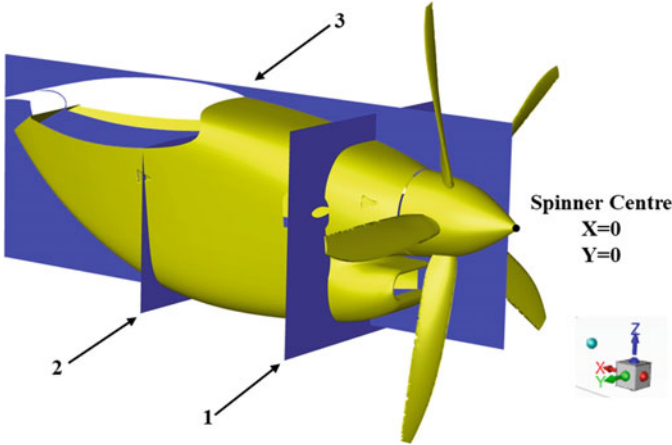


Fig. 6 Cross-section planes where engine surface temperature was taken

4.1 Case 3 (Maximum Cruise)

In this case, the altitude of the aircraft is 25000 feet, and the free stream total pressure and ambient temperature for the corresponding altitude is 43743 Pa and $-34.5\text{ }^{\circ}\text{C}$ (238.65 K), respectively. The speed of the aircraft is 0.47 Mach (159.94 m/s) with propeller speed of 1700 rpm.

Total temperature and static pressure contour on nacelle surface were shown in Figs. 7 and 8, respectively. The engine surface temperature at different plane locations was shown in Fig. 9.

4.2 Case 8 (Ground Static Take-Off)

In this case the altitude of the aircraft is 3000 feet, and the free stream total pressure and ambient temperature for the corresponding altitude is 91709 Pa and $50\text{ }^{\circ}\text{C}$ (323.15 K), respectively. The speed of the aircraft is 0.02 Mach (6.8 m/s) with propeller speed of 1700 rpm.

Table 2 Boundary conditions input values

Flight case	Altitude m (ft.)	Free stream total pressure Pa	OAT °C (K)	Speed m/s (M)	Propeller speed rpm
Case 1 (min. climb)	1371 (4500)	88,578	6.1 (279.25)	71.46 (0.21)	1700
Case 2 (best rate of climb)	3810 (12,500)	66,222	– 9.75 (263.4)	88.47 (0.26)	1700
Case 3 (max. cruise)	7620 (25,000)	43,743	– 34.5 (238.65)	159.94 (0.47)	1700
Case 4 (economy speed cruise)	7620 (25,000)	41,983	– 34.5 (238.65)	136.2 (0.4)	1700
Case 5 (economy speed cruise)	4572 (15,000)	61,661	– 14.5 (258.45)	112.3 (0.33)	1700
Case 6 ground run (take-off condition)	914.4 (3000)	91,709	34 (307.15)	6.8 (0.02)	1700
Case 7 (flight idle condition)	914.4 (3000)	91,709	34 (307.15)	6.8 (0.02)	1020
Case 8 (ground static take-off condition)	914.4 (3000)	91,709	50 (323.15)	6.8 (0.02)	1700

Table 3 Numerical temperature results at different locations

Flight cases	Temperature observations			
	Hot section (front nacelle) °C (K)		Plenum section (centre nacelle) °C (K)	Inlet section (rear nacelle) °C (K)
	Max	Average		
Case 3	85.79 (358.94)	41.92 (315.07)	– 27.61 (245.54)	– 16.36 (256.79)
Case 8	149.9 (423.05)	100 (373.43)	50 (323.1)	50 (323.1)

Total temperature and static pressure contour on nacelle surface were shown in Figs. 10 and 11, respectively. The engine surface temperature at different plane locations was shown in Fig. 12.

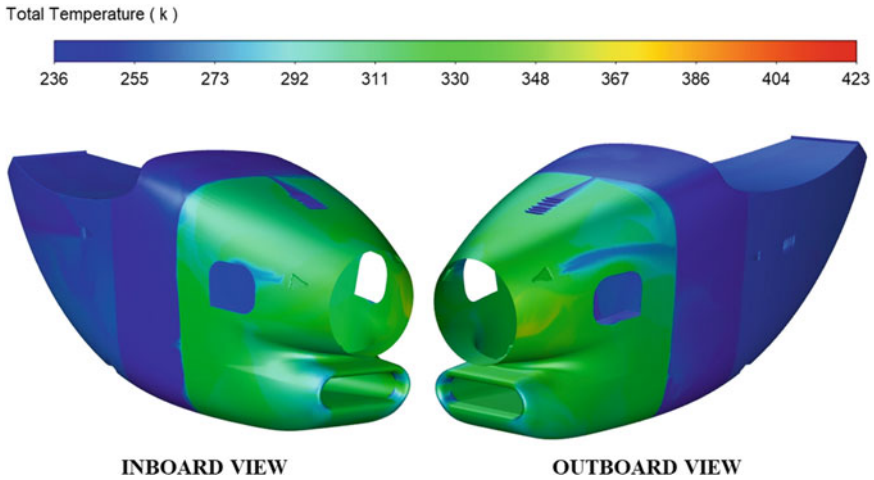


Fig. 7 Total temperature contour on nacelle surface

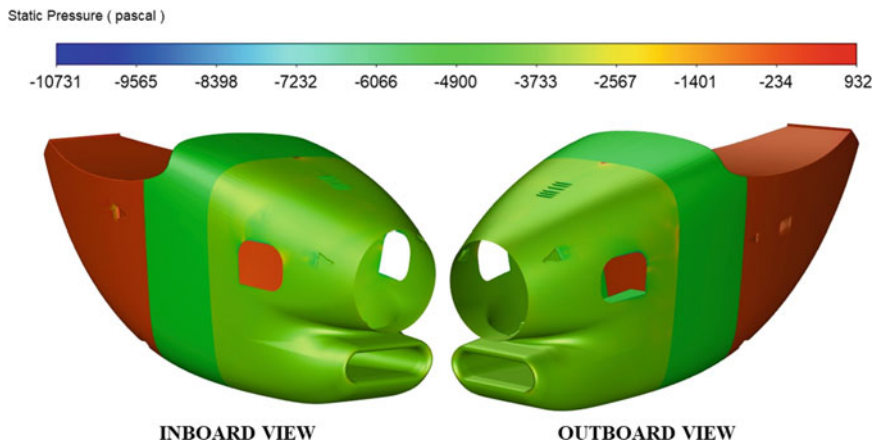


Fig. 8 Static pressure contour on nacelle surface

5 Conclusions

The numerical analysis of the zonal and bay ventilation methodology and its effectiveness over the nacelle surface temperature distribution is carried out in the study. SST $k - \omega$ turbulence model is utilized for the numerical study of internal flow of air through the inlets and outlets over the nacelle surface.

As mentioned earlier nacelle is made of aluminium alloy sheet, and intake ducts made of composite materials. Tensile yield strength (F_{ty}) of this aluminium alloy is sensitive to temperature variations. With the temperature raise from 477 K (204 °C)

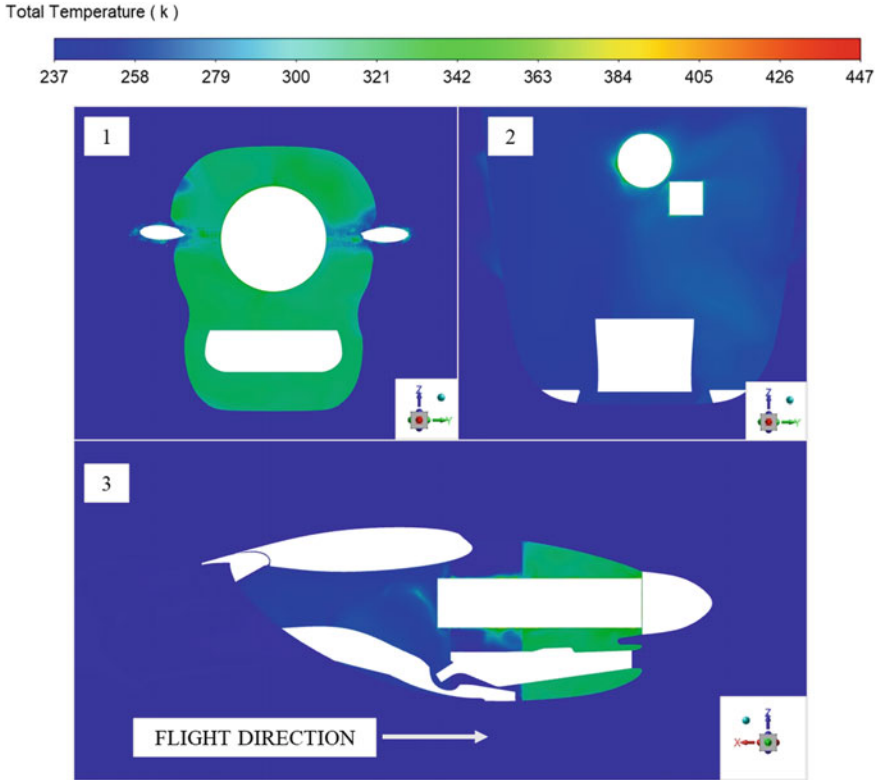


Fig. 9 Total temperature contour on engine surface

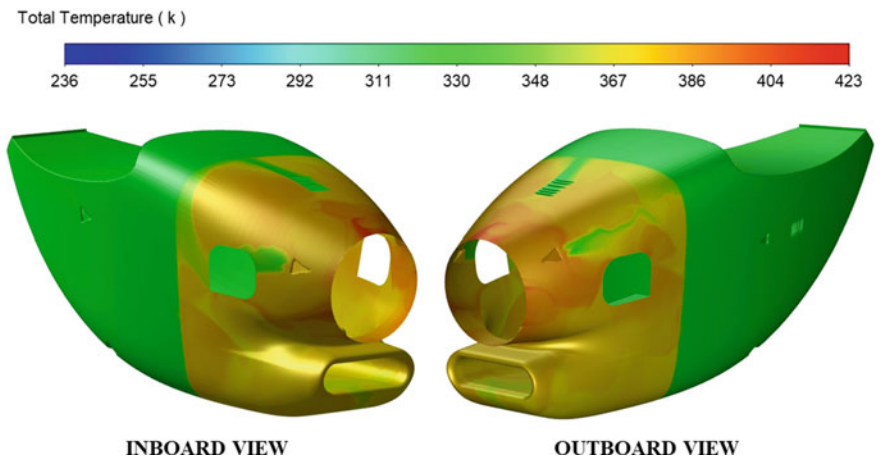


Fig. 10 Total temperature contour on nacelle surface

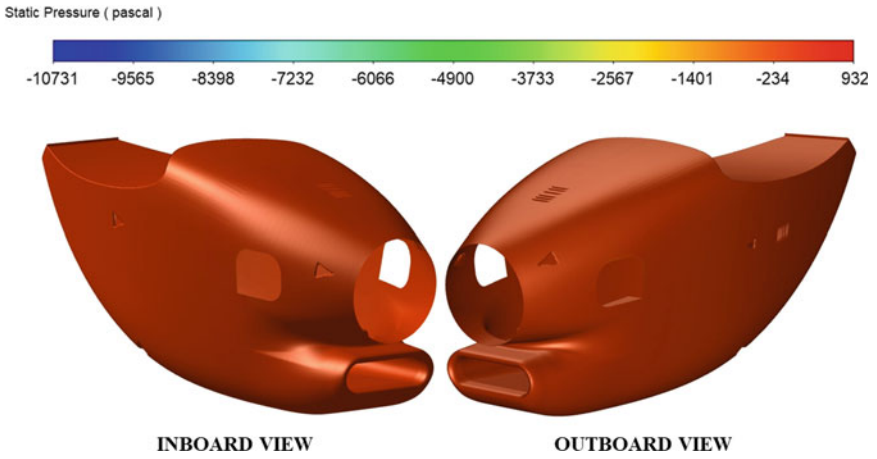


Fig. 11 Static pressure contour on nacelle surface

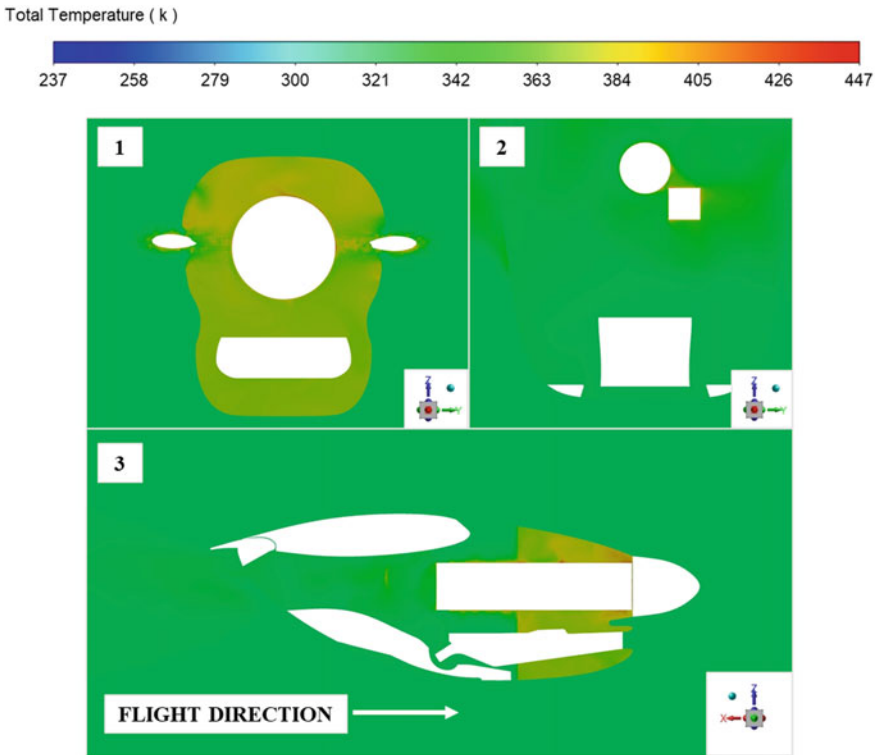


Fig. 12 Total temperature contour on engine surface

to 549K (276 °C), the tensile yield strength of the material drops from 60 to 40% of F_{ty} (100% F_{ty} considered at room temperature).

From the temperature distribution over the nacelle, it can be observed that the peak temperature is not higher than the material yield temperature shown in Table 3. Thus, the bay ventilation design scheme is effective in reducing the heat transferred from engine to the nacelle.

Thus, the overall analysis is quite reliable with the present numerical model and set-up. It is proposed to carry out validation of the numerical model developed by experimentation on the aircraft with appropriate instrumentation. Results obtained from CFD are used as a preliminary design data for selecting the suitable material specification for nacelle and associated subsystems. Hence, the present numerical method can be used for various flight operating conditions like taxi, take-off, and cruise. Further improvement can be made by including the radiation model in the CFD solver.

Nomenclature

F_{ty}	Tensile yield strength	N/m ²
NACA	National advisory committee for aeronautics	
OAT	Outside air temperature	K
RPM	Revolutions per minute	
SST	Shear stress transport	

Acknowledgements The authors wish to thank all partners and associated partners for their contribution to the program and for their permission to publish this paper.

References

1. Segal C (1997) Aircraft engine bay cooling and ventilation: design and modelling. *J Aircr* 34(1):141–144
2. Balland M, Verseux O, Esteve M-J (2008) Aero-thermal computations with experimental comparison applied to aircraft engine nacelle compartment. In: *ASME turbo expo 2005: power for land, sea, and air*, pp 1217–1225. Paper No. GT2005-68995
3. Olejnik A, Dziubiński A, Kiszowski Ł (2021) CFD simulation of engine nacelle cooling on pusher configuration aircraft. *Aircr Eng Aerosp Technol* 93(9):1421–1429
4. Buonomo G et al (2013) Aerothermal analysis of an aircraft nacelle in the framework of a fully coupled approach. In: *Proceedings of the Italian association of aeronautics and astronautics, XXII Conference, Napoli*, pp 1–12
5. Łapka P et al (2014) Simplified thermo-fluid model of an engine cowling in a small airplane. *Aircr Eng Aerosp Technol Int J* 86(3):242–249
6. Łapka P et al (2017) Comparison of 1D and 3D thermal models of the nacelle ventilation system in a small airplane. *Aircr Eng Aerosp Technol* 90(2):114–125

7. Ansys Fluent (2009) 12.0 user's guide. Ansys Inc., Lebanon, NH, USA, pp 4–26
8. Wilcox DC (1993) A two-equation turbulence model for wall-bounded and free-shear flows. Paper No. 93–2905

Design, Analysis and Manufacturing of Twist Morphing Wing for UAV Purpose



Shivang Patni, Kaushal Mahant, Saumya Shah, Anand Makwana, and Jignesh Vala

Abstract The main obstacle in the design of an effective fixed-wing aircraft is the reduction of induced drag, which is a significant factor in the total drag experienced at low speeds. One approach to address this issue is by implementing a twist morphing wing, which aids in minimizing wing tip vortices and eliminating drag caused by gaps and discontinuities between the wing and control surfaces. This research study primarily focuses on examining the aerodynamic properties of a twist morphing wing specifically tailored for unmanned aerial vehicle (UAV) flight characteristics. Numerical analyses are utilized to conduct an analytical comparison between a conventional fixed wing and the morphed wing design. Additionally, a functional prototype of the twist morphing wing, complete with an actuating mechanism, is developed.

Keywords Induced drag · Twist morphing · UAV aerodynamics

1 Introduction

The performance of a typical rigid wing is limited in multi-purpose mission requirements, and traditional hinged control surfaces tend to create flow separation when in use [1]. To address these issues, researchers turned to the twist morphing technology used in the Wright Flyer.

By changing its shape depending on the situation, the morphing wing can achieve high-performance aerodynamics and increase lift-to-drag ratio in all flight conditions [2–4]. This idea was inspired by birds, who efficiently use their wings without using too much energy [4]. Mimicking their approach, morphing technology minimizes the use of thousands of mechanical components, reduces weight, and improves performance [5].

Morphing wing technology has been around since the era of the Wright Brothers, who used the twist morphing type to roll their aircraft with great success [6]. A prime

S. Patni (✉) · K. Mahant · S. Shah · A. Makwana · J. Vala
Department of Aeronautical Engineering, Sardar Vallabhbhai Patel Institute of Technology,
Vasad, Vasad 388306, India
e-mail: shivang.180410101040@gmail.com

example of this technology is the Morphing Flap system made by Flexsys for the Gulf Learjet [6]. In this study, we focus on airfoil profile adjustment type morphing, specifically the span-wise twisting of the trailing edge, to improve aerodynamic performance and prevent drag penalties caused by discontinuities in conventional hinged mechanisms.

We propose a twist morphing concept for a UAV wing using the SD-7037 airfoil, chosen for its characteristics and usage in low Reynolds number UAVs. The wing has a 20 cm chord and a rectangular cross-section with a flexi-rib structure to reduce yield stiffness and provide calibrated trailing edge deflection.

We analyse and visualize the aerodynamic improvements obtained with the morphing configuration in comparison with the hinged configuration, for low Reynolds numbers, as well as to improve manoeuvrability criteria. We examine the wing's performance under different conditions and observe improvements with the morphed configuration in relation to changing requirements.

2 Literature Review

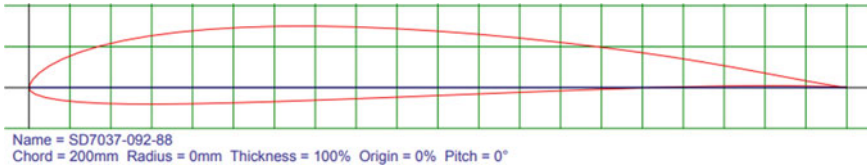
The paper titled “Effectiveness of Wing Twist Morphing in Roll Control” by R. Pecora, F. Amoroso, and L. Lecce from the University of Naples “Federico II”, 80125 Naples, Italy [7], expresses that these findings are highly encouraging and serve as motivation for further exploration of wing twist morphing technology. The focus lies in defining a suitable structural layout for practical implementation. The study emphasizes that the small twist angles required for inducing roll and the potential to design a more flexible and stable wing structure make wing morphing feasible through compliant structures.

In the initial investigation conducted by Benjamin King from Sutton Woods College of Engineering and Michael from Friswell College of Engineering, a concept called Fishbone Active Camber (FishBAC) [8] is introduced. This mechanism allows for continuous and substantial alterations in airfoil camber, requiring minimal energy input through a compliant structure and actuation mechanism inspired by biology. Analytical predictions of the aerodynamic performance demonstrate significant improvements in the lift-to-drag ratio of the FishBAC, compared to a NACA 0012 airfoil with or without a discrete trailing edge flap.

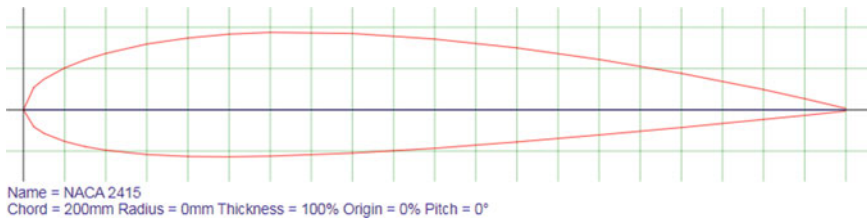
According to the state-of-the-art review titled “Morphing Aircraft Based on Smart Materials and Structures” by Jian Sun, Qinghua Guan, Yanju Liu, and Jinsong Leng, any modification in an aircraft's configuration, particularly its wings, has an impact on its aerodynamic performance [9]. Optimal configurations can be achieved for each flight condition, and morphing technologies offer aerodynamic advantages across a wide range of flight conditions.

3 Airfoil Selection

For the proposed case of low Reynolds number UAV application, two typical airfoils, namely NACA2415 and SD7037, have efficient characteristics.



SD 7037 airfoil



NACA 2415 airfoil

4 Computational Modelling and Analysis

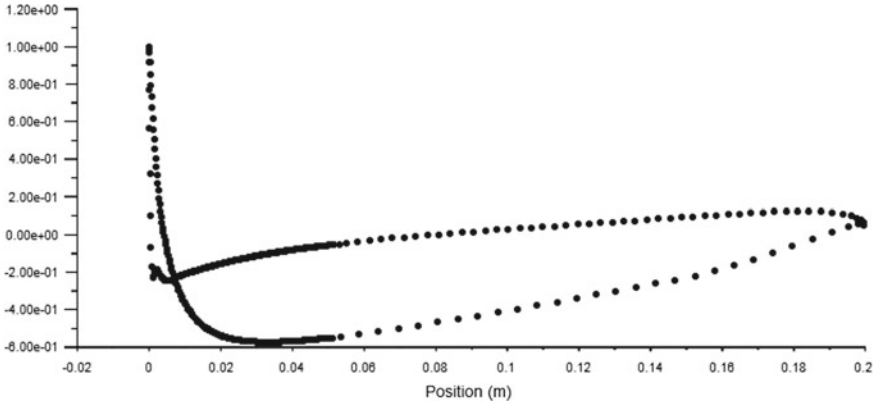
Both airfoils are analysed with the help of computational fluid dynamics.

Value of y^+ was kept below 1 over the airfoil in both cases.

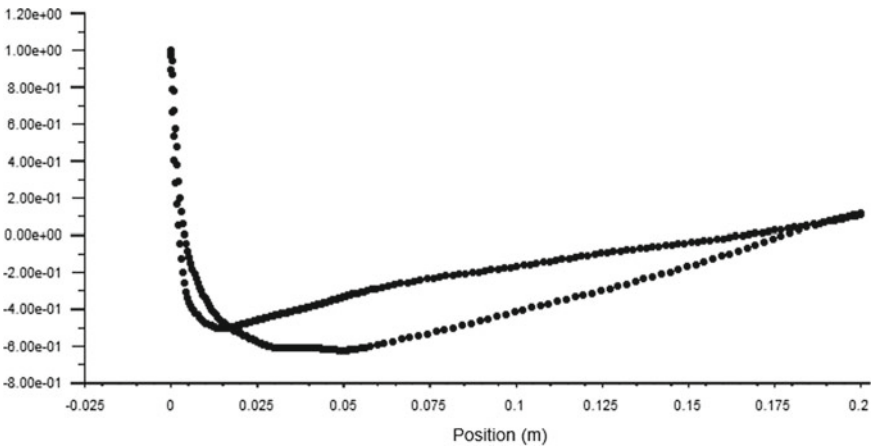
To obtain precise result near the wall, SST KW model is used with convergence criteria of 10^4 .

5 Operating Condition for Both Airfoils

Chord length (m)	0.2
Velocity (m/s)	15
Reynolds number	2,00,000
Operating pressure (atm.)	1



Cp graph of SD7037 airfoil



Cp graph of NACA 2415 airfoil

More lift on upper surface of SD 7037 can be seen in Cp graph as compared to NACA 2415 airfoil. Formation of high pressure on lower surface of SD7037 is also higher as compared to NACA 2415.

6 Results

As per the computational results, SD7037 provides better results for the corresponding Reynolds number.

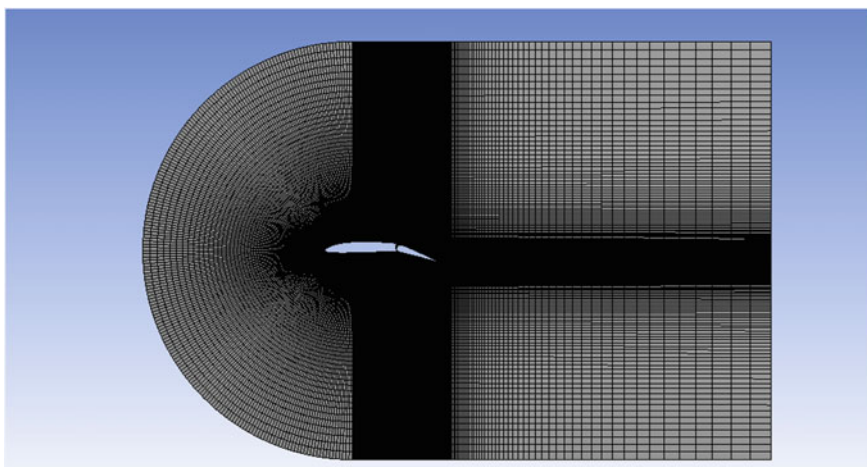
Airfoil name	Cl (AoA = 0)	Cd (AoA = 0)
SD 7037	0.3850	0.00929
NACA 2415	0.2279	0.01085

7 Computational Modelling of Hinged and Morphed Airfoil

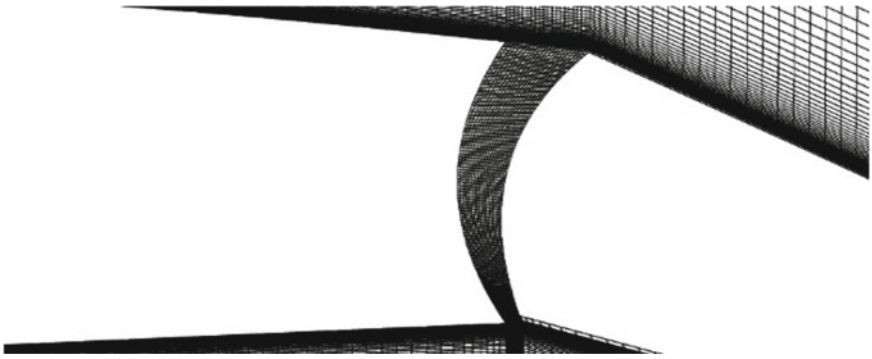
SD 7037 airfoil is selected for this study.

In hinge airfoil hinge is provided at 60% of the chord with 16° in downward direction which gives resultant angle of attack 6.5° . Coordinate of morphed airfoil is extracted from XFLR5 software.

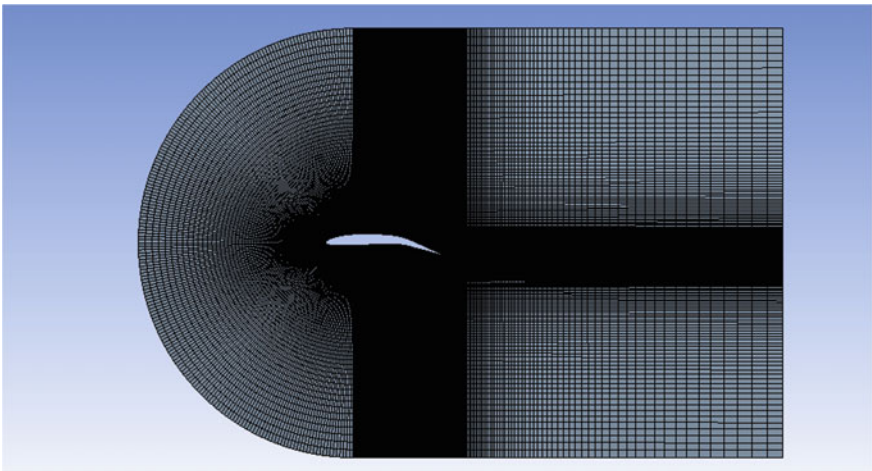
And hinged airfoil is designed in CATIA v5 software.



Meshing of hinged airfoil



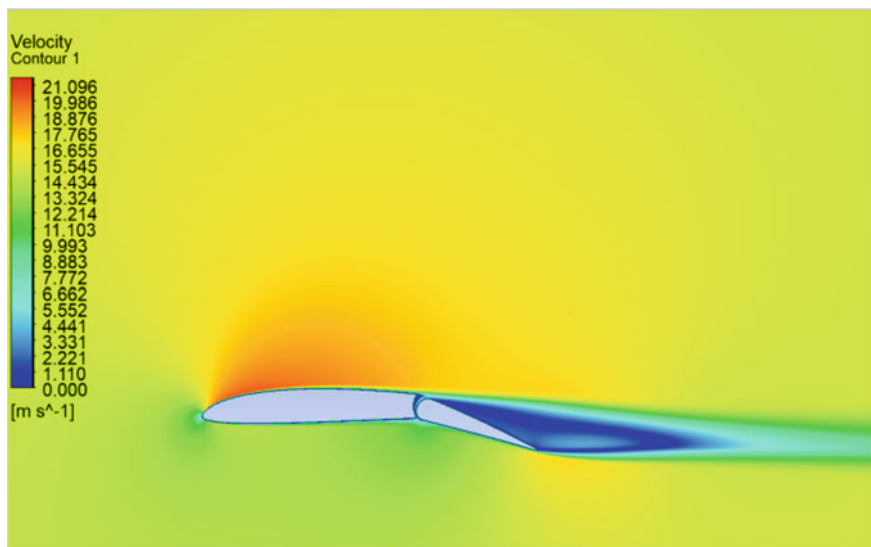
Mesh around hinge of hinge



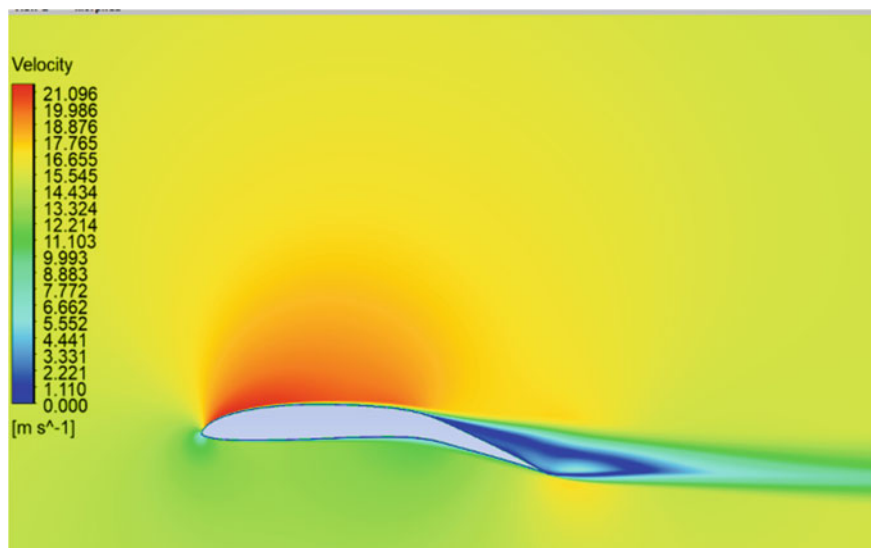
Meshing of morphed airfoil

8 Velocity Contour of Morphed and Hinged Airfoil

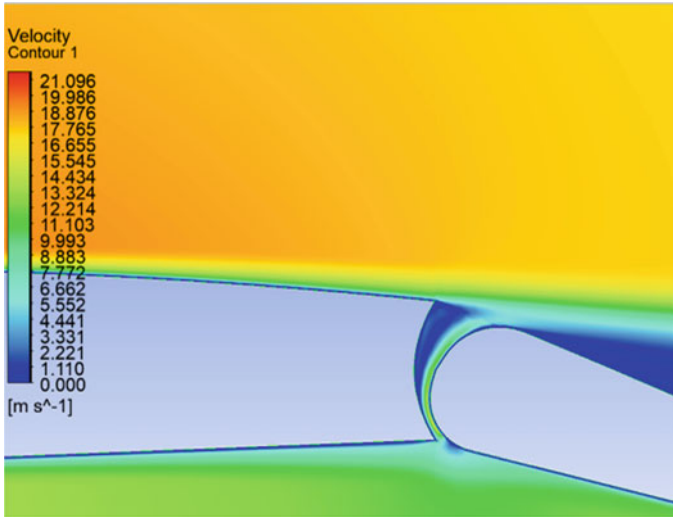
Chord length (m)	0.195
Velocity (m/s)	15
Reynolds number	2,00,000 approx
Operating pressure (atm.)	1
Turbulence model	SSK KW
Convergence criteria	10^4



Velocity contour of hinged airfoil



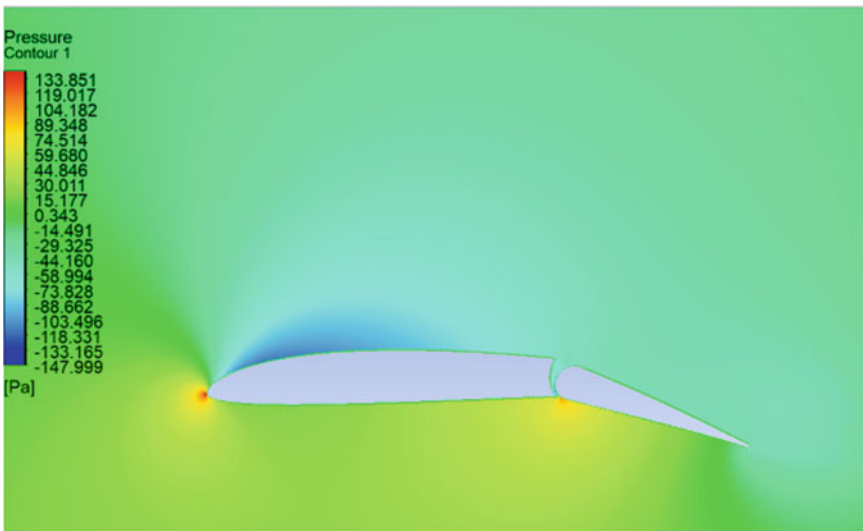
Velocity contour of morphed airfoil



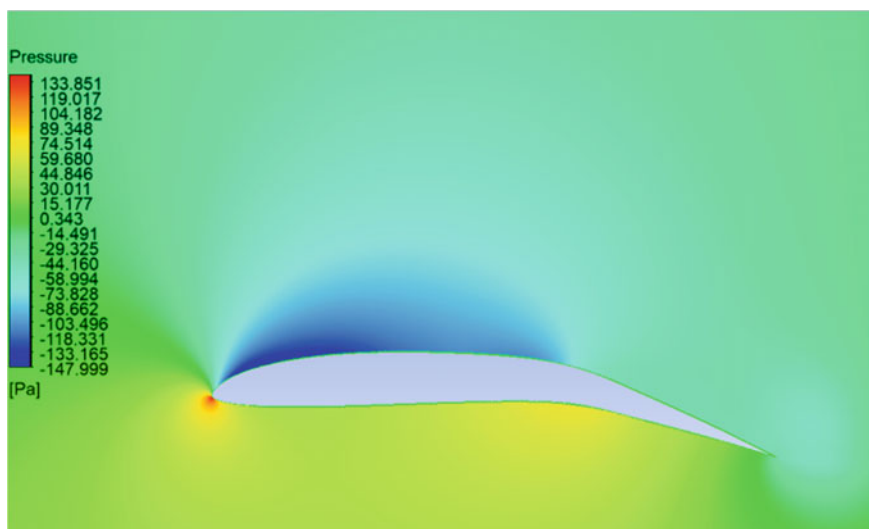
Velocity contour at hinge location

From velocity contour it can be seen that flow separation is high in hinged airfoil and flow also tries to move from lower surface to upper surface from hinge (gap) due to pressure difference which contributes in overall drag.

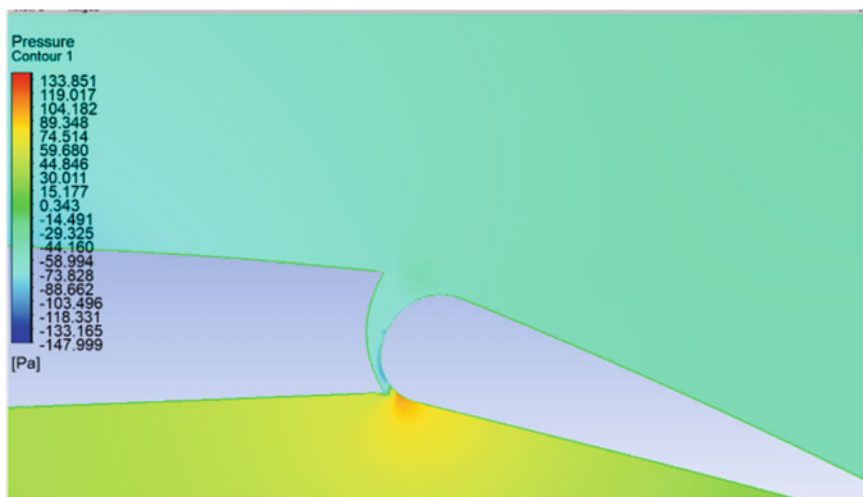
9 Pressure Contour of Hinged and Morphed Airfoil



Pressure contour of hinged airfoil



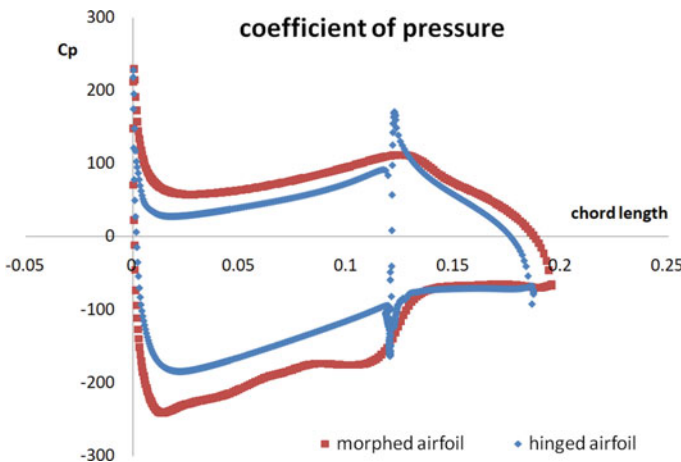
Pressure contour of morphed airfoil



Pressure contour at hinge location

In hinged airfoil pressure contour graph, more than one stagnation point can be observed which causes drag to increase. In morphed airfoil pressure contour graph,

formation of lower pressure on upper surface is on large portion of airfoil as compared to hinge airfoil which leads to more lift production.



Cp graph morphed versus hinged airfoil

Cp graph of both airfoil shows that on upper surface of morphed airfoil pressure is lower as compared to hinged airfoil and also on lower surface pressure is higher as compared to hinged airfoil which shows that lift production in morphed airfoil would be larger as compared to hinged airfoil.

Airfoil	Cl	Cd	Cl/Cd
Hinged airfoil	0.51	0.0771	6.619924
Smooth (morphed)	1.35	0.034	39.62457

10 Wing Design

Wing is designed in such a way that it produces 2 kg of lift with flap condition (A.O.A = 6.5°) at velocity around 9.6 m/s, with aspect ratio of 5. Dimensions are decided trial and error method and using below equations:

$$l = \frac{1}{2} * \rho * v^2 * s * cl$$

$$b^2 = A . R * s$$

where

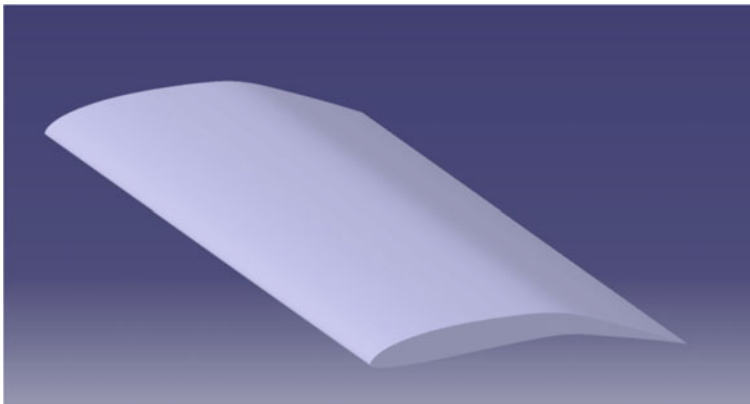
l lift

- ρ density
- v free stream velocity
- s surface area of wing
- cl coefficient of lift
- b span of wing
- $A . R$ aspect ratio

Parameters	Values
Lift (kgs)	2
Chord (cm)	20
Hinge axis from L. E	60% of chord
Deflection (\emptyset)	$\pm 16^\circ$
Wing span (cm)	100
Aspect ratio	5
Half wing plan-form area (cm ²)	1000

11 Parameter of Wing

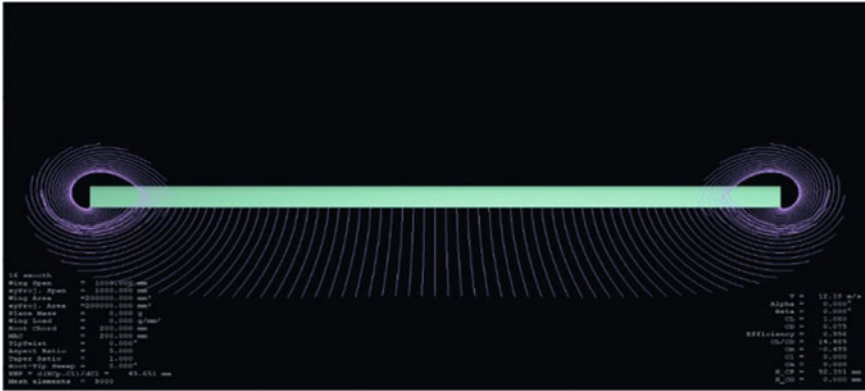
11.1 Wing CAD Model



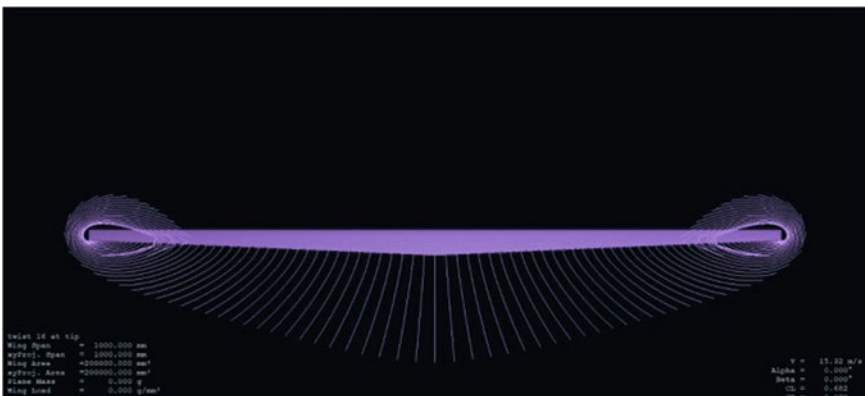
Wing with flap condition

Above model is for half wing span (starboard wing or port wing). After analysing this wing in XFLR5 software and considering that data as initial data, new twist

morphing wing case is designed which is most efficient among other wing for production of 2 kg lift.



Vortices simulation of morphing wing with flap condition



Vortices simulation of new designed twist morphing wing

Angle of attack in twist morphing wing is not same throughout span. Root is at 6.5° A.O.A, and tip is at 0° A.O.A to minimize wing tip vortices causes reduction in induced drag which is major contributor in overall drag at low speed.

Name	CL	CD	Vel.	A.O.A	Drag (N)	Power consumption (W)
Morphed wing with flap	1.736	0.196	9.61	0 (6.5)	1.108	10.64
Span wise twist morphed wing	0.682	0.03	15.32	0 (root-6.5 and tip-0)	0.4312	6.605984

(continued)

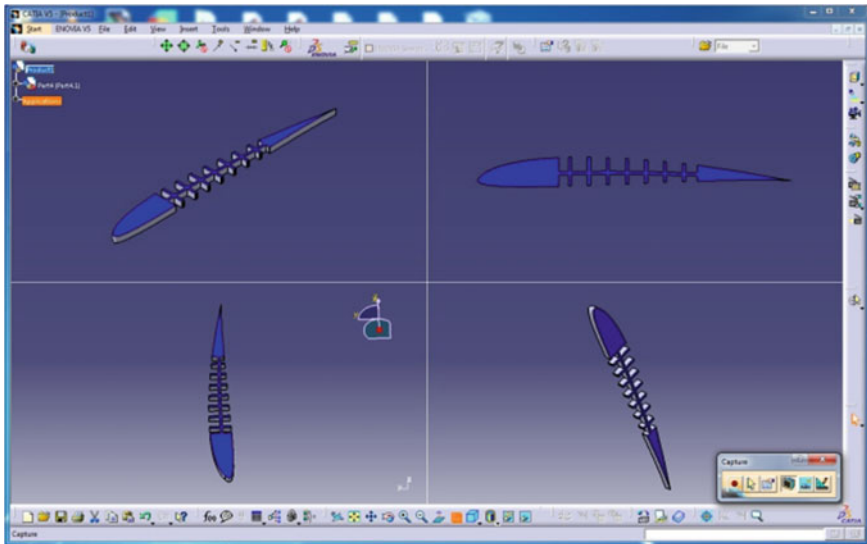
(continued)

Name	CL	CD	Vel.	A.O.A	Drag (N)	Power consumption (W)
------	----	----	------	-------	----------	-----------------------

12 Prototype Mechanism and Manufacturing

12.1 Flexible Rib

The flexi-rib is designed taking reference from fish rib a novel airfoil morphing structure known as the Fishbone Active Camber (FishBAC) [8]. This design employs a biologically inspired compliant structure to create large, continuous changes in airfoil camber and section aerodynamic properties.

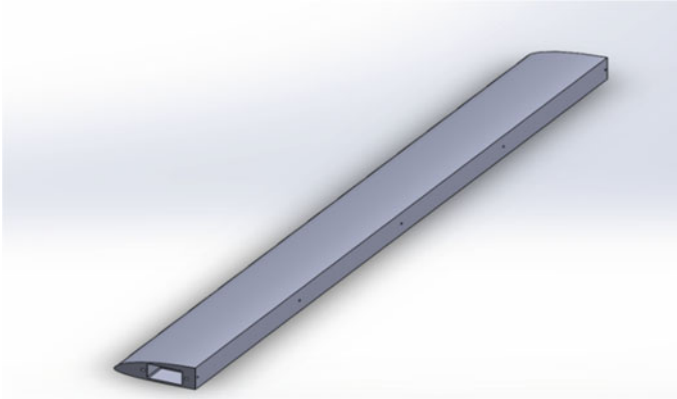


Design of flexible rib

The flexi-rib is developed for high flexibility and the reduce modulus of rigidity. The structure consists of a thin chordwise bending beam spine with stringers branching off to connect it to a pre-tensioned elastomeric skin surface [10].

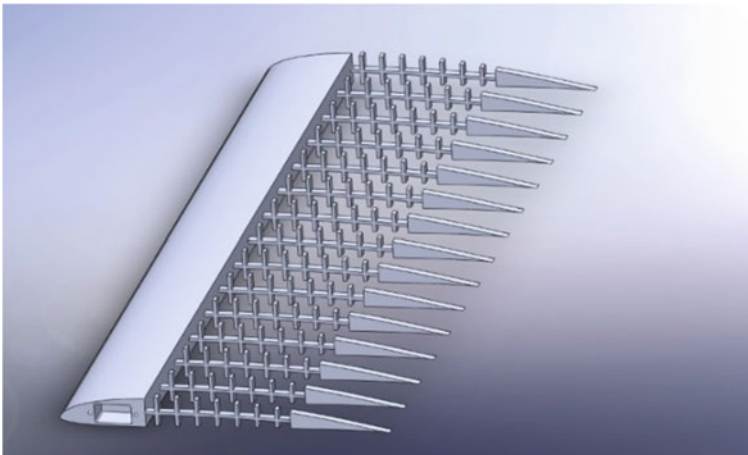
12.2 *Leading Edge Support*

To maintain the parametric shape of airfoil and to provide rigid support to morphing components, the L.E block is designed, which also acts as a support to the actuators.



Design of leading support block

12.3 *Assembled Part*



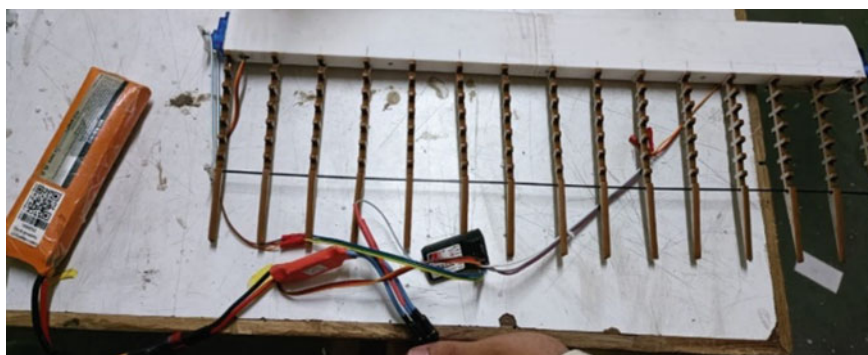
Design of assembled wing in SolidWorks

The components are assembled, and a reference CAD model for prototype manufacturing is developed.

12.4 *Prototype Manufacturing*



Manufactured prototype of flexible rib



Manufactured prototype of wing with mechanism

Two pair of servomotor is used to actuate wing with the help of push rod mechanism.

Leading edge support is prepared by 3D printed material (PLA), ribs are made up of 5 mm PVC sheet, and trailing edge spar is made up of 3 mm carbon fibre rod.

13 Conclusion

Twist morphing wing can eliminate disadvantage associated with rigid wing in small UAV by removing hinge and maintaining continuity throughout surface. Twist morphing wing can be actuated as flap and also as an aileron. Angle of attack at root and tip can be controlled according to requirement which helps to increase aerodynamic efficiency and aircraft performance throughout flight path.

References

1. Fincham JHS, Friswell MI (2015) Aerodynamic optimisation of a camber morphing aerofoil. *Aerosp Sci Technol* 43:245–255
2. Rodrigue H, Cho S, Han M-W, Bhandari B, Shim J-E, Ahn S-H (2016) Effect of twist morphing wing segment on aerodynamic performance of UAV. *J Mech Sci Technol* 30:229–236. <https://doi.org/10.1007/s12206-015-1226-3>
3. Schlup AE, MacLennan T, Barajas C, Talebian B, Thatcher G, Flores R, Perez-Norwood J, Torres C, Kibret K, Guzman E (2021) MataMorph 2: a new experimental UAV with twist-morphing wings and camber- morphing tail stabilizers. In: Proceedings of the AIAA Scitech 2021 forum, Virtual Event. Session: International Student Conference—Team Category, AIAA 2021-0584
4. Secanell M, Suleman A, Gamboa P (2006) Design of a morphing airfoil using aerodynamic shape optimization. *AIAA J* 44(7):1550–1562
5. Nazeer N, Wang X, Groves RM (2021) Sensing, actuation, and control of the SmartX prototype morphing wing in the wind tunnel. *Actuators* 10:107-1–107-20. <https://doi.org/10.3390/act10060107>
6. Hussain SA (2017) Review of morphing wing. Thesis, Emirates, Aviation Industry, Coventry University
7. Pecora R, Amoroso F, Lecce L (2012) Effectiveness of wing twist morphing in roll control. *J Aircr* 49(6):1666–1674. <https://doi.org/10.2514/1.C000328>
8. Woods BKS, Friswell MI (2013) Preliminary investigation of a fishbone active camber concept. In: ASME 2012 conference on smart materials, adaptive structures and intelligent systems, pp 555–536. Paper No: SMASIS2012-8058
9. Sun J, Guan Q, Liu Y, Leng J (2016) Morphing aircraft based on smart materials and structures: a state-of-the-art review. *J Intell Mater Syst Struct* 27(17):2289–2312. <https://doi.org/10.1177/1045389x16629569>
10. Bishay PL, Aguilar C (2021) Parametric study of a composite skin for a twist-morphing wing. *Aerospace* 8(9):259. <https://doi.org/10.3390/aerospace8090259>
11. Abdulrahim M, Lind R (2004) Flight testing and response characteristics of a variable gull-wing morphing aircraft. In: AIAA guidance, navigation, and control conference and exhibit, Providence, Rhode Island. AIAA 2004-5113
12. Rusell MT, Gano SE, Perez VM, Renaud JE, Batill SM (2004) Morphing UAV Pareto curve shift for enhanced performance. In: 45th AIAA/ASME/ASCE/AHS/ASC structures, structural dynamics and materials conference, Palm Springs, California. AIAA 2004-1682

Experimental Validation for Vortex-Induced Vibration of Circular and Square Cylinders of Low and High Mass Damping



Parth Patel, Amit Agrawal, Atul Sharma, and Rajneesh Bhardwaj

Abstract Vortex-induced vibration (VIV), a branch of fluid structure interaction (FSI), is an efficient technique to extract power from rivers/streams at low velocity. The phenomena happens when the submerged body in the flow is elastically mounted. In present study, the response of circular cylinders having low and high mass damping and the square cylinder is analyzed experimentally. The experimental facility uses a water channel with particle image velocimetry (PIV) for flow visualization. In order to record the VIV response of these cross-sections, the experimental setup is developed using air bearings to reduce the damping and springs to simulate the spring-mass system. The high mass damping ratio circular cylinder shows two-branch response (initial and lower branch). While the response of circular cylinder with low mass damping parameter is a three-branch response. A maximum of 1.25D of amplitude is observed in the upper branch. In the initial branch, the amplitude rises quickly, while it is highest in the upper branch, and in the lower branch, it decreases gradually. The response of a square cylinder is similar to galloping. The amplitude of oscillation rises as the reduced flow velocity increases. All the responses are compared with the literature, and they resemble the same trend and characteristics.

Keywords Fluid structure interaction (FSI) · Vortex induced vibration (VIV) · Galloping · Particle image velocimetry (PIV)

1 Introduction

Depleting conventional energy sources has led to non-conventional energy sources of prime importance in today's era. The non-conventional energy sources such as windmills, water turbines, and solar panels are used widely. As the need for energy of humankind is increasing, the decrease in the availability of conventional energy resources has led many researchers to search for new ways to extract energy from

P. Patel · A. Agrawal · A. Sharma · R. Bhardwaj (✉)
Department of Mechanical Engineering, IIT Bombay, Mumbai 400076, India
e-mail: rajneesh.bhardwaj@iitb.ac.in

non-conventional energy resources. Water turbines are an excellent way to extract energy from a flowing fluid. However, the disadvantage is it requires high pressure or the flow velocity of water, thus making it unsuitable to use in small rivers or streams. When the flow occurs around the structure because of the obstruction in the flow path, the fluid exerts a force on the structure. The structure may be rigid or elastically mounted; this phenomenon of coupling between the laws of fluid dynamics and structural mechanics is termed vortex-induced vibration (VIV).

VIV has several branches depending on the behavior and the cross-section of the submerged body. Rostami and Armandei [1] presented a detailed article classifying different branches of FSI. Among this flutter, galloping and vortex-induced vibration (VIV) have the capability of harvesting energy at low flow speeds up to 0.5 m/s. The mass ratio, defined as the ratio of oscillating mass to the displaced fluid mass (m^*), and the damping ratio (ζ) are the critical parameters affecting the system. Earlier the lock-in regime was defined as the match of natural frequency of the system and the body oscillation frequency. Sarpkaya in 2004 [2] redefined the definition as the match in vortex shedding frequency and the frequency of body oscillation as a lock-in regime. Feng in 1968 [3] was the first to carry-out experiments to capture VIV phenomena in the wind tunnel. Feng observed two branches in the synchronization/lock-in regime, and the first is the initial branch and the lower branch. The oscillation amplitude quickly rises in the initial branch and drops gradually in the lower branch. Later Khalak and Williamson [4] prepared a hydro-elastic experimental facility in 1996. The authors used air bearings to minimize the damping of the system. As the water channel is used for experiments, the mass ratio and damping were much lesser than in the experiments conducted by Feng. The response at low mass damping parameter ($m^*\zeta$) indicated three-branch response (i.e., initial, upper, and lower branches). The amplitude of oscillation quickly rises in the initial branch. In the upper branch, the amplitude of oscillation is highest, up to 0.6D of maximum amplitudes are reported. The amplitude decays with the reduced flow velocity in the lower branch. Govardhan and Williamson in 2000 [5], published an extensive analysis of the system at low and high mass damping ($m^*\zeta$) parameter. The high mass damping case has two-branch response. The initial branch has 2S mode of vortex shedding and 2P mode of vortex shedding in the lower branch. Besides the mode of vortex shedding ψ , termed as the phase angle between the vortex shedding and body oscillation. The lower branch has a phase difference of 180° while in the initial branch it is in phase. The low mass damping case exhibits three-branch response. The initial branch shows 2S mode of vortex shedding and 2P mode of vortex shedding is observed in the upper and lower branch. There is a jump of 180° in the phase between vortex and body displacement during the switching of initial to upper branch, while the total phase between the force and body oscillation remains in phase. During the switching of the upper to lower branch, the vortex phase remains the same, but the total phase between the total force and body displacement changes to almost 180° . Decreasing the mass ratio further, there is an increase in oscillation amplitude. This led to the discovery of the critical mass of the cylinder. Govardhan and Williamson in 2002 [6] conducted experiments to find the critical mass of the cylinder. The authors reported beyond an m^* of 0.54 the lower branch of the VIV disappears and the

cylinder experiences VIV forever even at high reduced velocities. The cross-sections other than cylinders have also been investigated by several researchers [7–10]. The square cross-section at a different angle of attack is investigated by Nemes et al. in 2012 [11]. The authors found the cross-section at even zero angle of attack experiences galloping, i.e., the amplitude and the body oscillation frequency increases as the reduced flow velocity is increased. Ding et al. [12] numerically investigated PTC cylinder, Q trapezoid, square, and triangle numerically. The passive turbulence control technique applied to the cylinder is by attaching the roughness strips upstream to the cylinder. This technique is deeply investigated by Chang and Bernitsas [13].

The PTC-treated cylinder experiences galloping, and up to 3.5D of oscillation amplitude is reported. Cyber-physical fluid dynamics (CPFD) facility is developed by Mackowski and Williamson in 2011 [14]. The advantage of the facility is that the experiments with any mass ratio, stiffness, and damping can be conducted by giving the system parameters as input to the LAB view software where control laws are defined. The only physical change required is the cross-section experiencing VIV; this facility gives the flexibility to simulate the nonlinear stiffness and damping behavior.

The present study aims at developing the experimental facility to experimentally study the VIV phenomena. The study also aims at measuring the response of circular cylinders at low and high mass damping ($m^*\zeta$) and that of the square cross-section. The PIV experiments are in progress and will be presented in next research article.

2 Experimental Facility

The non-dimensional parameters used in the study of VIV are as follows:

$$\text{Re} = \frac{U_\infty D}{\nu_f} \quad (1)$$

$$m^* = \frac{m}{\frac{\pi}{4} \rho_f D^2 L} \quad (2)$$

$$\zeta = \frac{c}{4\pi m f_n} \quad (3)$$

$$U^* = \frac{U_\infty}{f_n D} \quad (4)$$

$$f_n = \frac{1}{2\pi} \sqrt{\frac{k}{m}} \quad (5)$$

where D is the hydraulic diameter of the cylinder, U_∞ is the free stream velocity, m is the total mass of oscillating components, ν_f is the kinematic viscosity of the fluid, L is the length of the submerged body, ρ_f is the fluid density, the damping constant

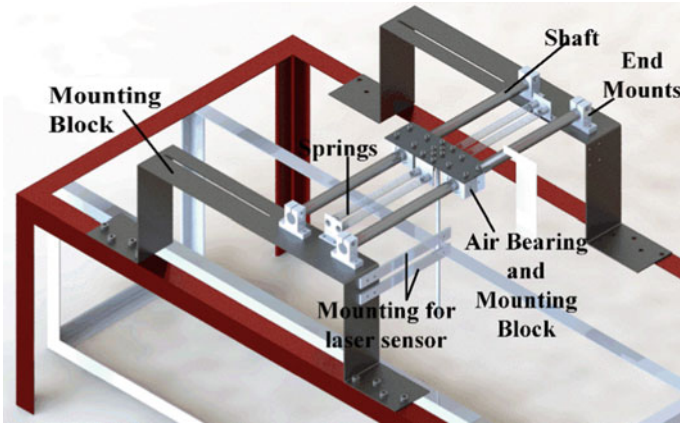
of the system is c , f_n is the natural frequency, and the stiffness of the springs is k . The nondimensional parameters are as follows: Re is the Reynolds number, m^* is the mass ratio, ζ is the damping ratio, and U^* is the reduced flow velocity.

Figure 1 shows the water channel facility used for the experiments to capture VIV phenomena. The water channel has a test section of length of 1500 mm and $400 \times 400 \text{ mm}^2$ cross-sectional area. The water is circulated in a closed circuit. The water is seeded with glass particles of size 8–10 μm for illumination. Nd:YAG double pulse lasers (Beamtech, China; energy: 200 mJ/pulse, wavelength 532 nm, repetition rate: 15 Hz). The images are captured using a CCD camera (PCO Pixelfly, Germany) at a frequency of 5 Hz and image resolution of 1392×1024 pixels. As flow speed varies the time interval between two images is varied from 1.5–40 ms. The displacement of the submerged body experiencing VIV is measured using a non-contact laser sensor (microepsilon, range: 100–600 mm, sampling rate: 4 kHz) with a sampling rate of 4 kHz.

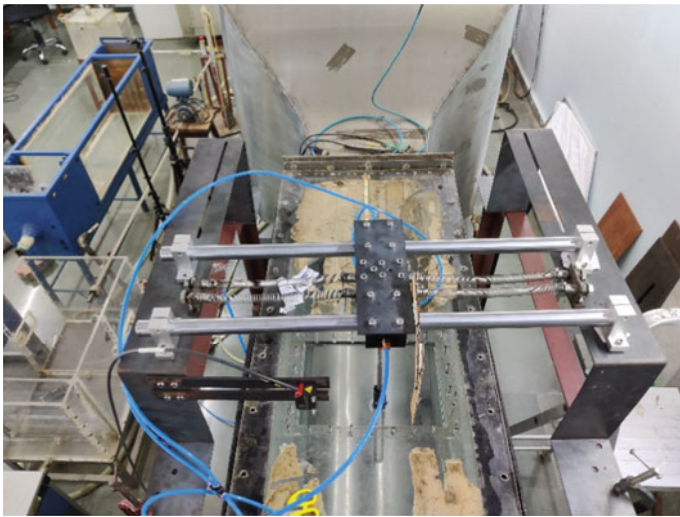
The experimental setup is first modeled using SolidWorks to get a thorough idea of the placement of components and the components required, as shown in Fig. 2a. The experimental setup is assembled in a similar way as modeled in SolidWorks as shown in Fig. 2b. The air bearings are used to minimize the damping of the system; they create a thin film of air between the bore of the bearings and the shaft. The mounting block houses the air bearings and provides mounting attachments to attach the mounting plate. The mounting block is used to house end mounts that support the shaft. The mounting plate houses spring clamps, mounting blocks, and the mount for attaching the submerged body experiencing VIV.



Fig. 1 Water channel facility



(a) CAD modelling of experimental setup



(b) Assembled experimental setup

Fig. 2 Development of experimental setup

3 Results and Discussion

The VIV experiments are carried out for three different cross sections. The first is 25 mm diameter cylinder, second is 70 mm diameter cylinder, and the third is square cylinder having $25 \times 25 \text{ mm}^2$ cross-section. The detailed system parameters are given in Table 1.

The system is initially given a defined amplitude and allowed to oscillate freely to measure the natural frequency and damping ratio of the system in the air. Fast Fourier transform (FFT) will determine the natural frequency of the system, and the curve

Table 1 System parameters

	Cylinder 1	Cylinder 2	Cylinder 3
Hydraulic diameter D (mm)	25	70	25
L/D	14.9	4.3	15.3
Mass ratio (m^*)	10.49	2.07	8.69
Damping ratio (ζ)	4.5×10^{-3}	3.9×10^{-3}	4.9×10^{-3}
$m^*\zeta$	0.048	0.0081	0.042
Natural frequency (f_n)	0.259	0.1983	0.251
Reynolds number (Re)	350–2100	1700–12,500	300–3100

fit of the peak amplitude will determine the damping ratio of the system. Figure 3 shows the response of the cylinder, the cylinder resemblance free-damped response. The red line shows the curve fit to determine the damping ratio.

As the flow velocity is increased in the water channel, the submerged cylinder in the flow becomes susceptible to vortex-induced vibrations. Figure 4 shows the displacement of the system as the flow velocity is increased and the cylinder begins to experience VIV. In Fig. 4a, the lock-in region is not reached, yet oscillations with small varying amplitude and at various frequencies are observed. As the reduced flow velocity is further increased, the amplitude of oscillation gets constant, as shown in Fig. 4b. In the lock-in regime, the system vibrates with constant amplitude and frequency as shown in Fig. 4c.

The response of various cylinders experiencing vortex-induced vibration is shown in Fig. 5. Figure 5a shows the cylinder response having high mass damping ($m^*\zeta = 0.048$). The system response falls in between the experiments conducted by Khalak and Williamson [4] ($m^*\zeta = 0.013$) and Feng [3] ($m^*\zeta = 0.38$). It is important to note that the system response is a two-branch response. The initial

Fig. 3 Free-damped response of circular cylinder (25 mm diameter)

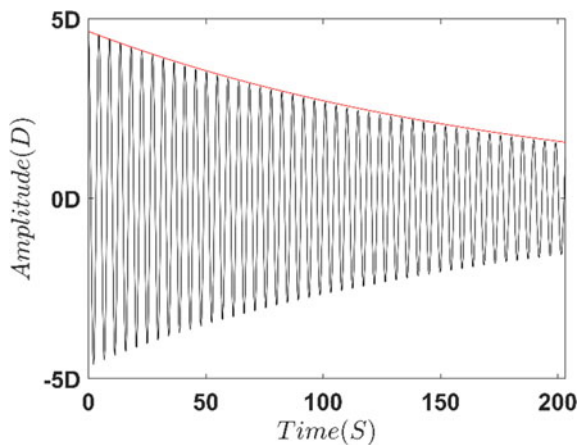
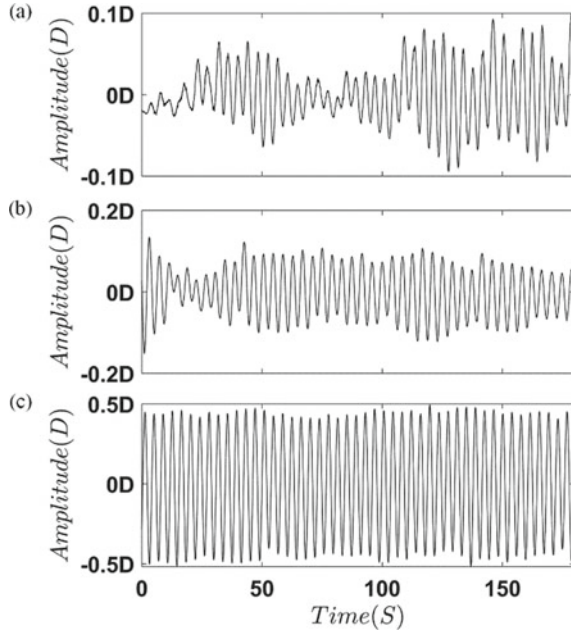


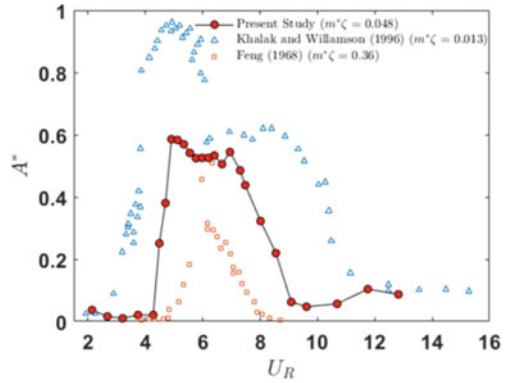
Fig. 4 Amplitude versus time response of circular cylinder (25 mm diameter)
a Unsynchronized regime
b On the onset of lock-in
c Oscillations in lock-in regime



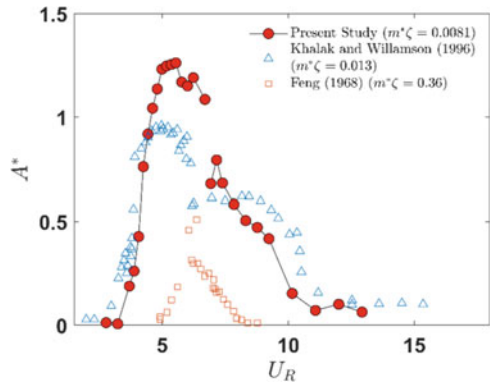
branch where amplitude quickly rises and the lower branch where the amplitude of oscillation falls gradually.

As the diameter of the cylinder is increased from 25 to 70 mm, the displaced fluid mass increases considerably more than the oscillating mass. This decreases the mass ratio considerably from 10.5 to 2.07. With cylinder 2, the mass damping parameter ($m^*\zeta$) decreases in order to obtain three-branch response. The system response for cylinder 2 is shown in Fig. 5b. Three-branch response, i.e., initial, upper, and lower branch, is observed. In the initial branch, the amplitude of oscillations increases rapidly, while in the upper branch, the system experiences maximum amplitude of oscillations. Maximum amplitude of up to 1.25D is observed. As the current system mass damping parameter ($m^*\zeta$) is 0.0081 which is less than the experiments conducted by Khalak and Williamson [4] ($m^*\zeta = 0.013$), the upper branch experiences a higher amplitude of oscillation. The response of cylinder 3 is different from that of cylinder 1 and 2. As the cross-section of cylinder 3 is square, its response should be similar to galloping. Figure 5c shows the response of the square cylinder. The response falls under the experiments conducted by Nemes et al. [11]. As the present system mass damping parameter ($m^*\zeta$) is 0.043 is higher than that of Nemes et al. ($m^*\zeta = 0.0065$), the amplitude response is lesser. It can be noted that the trend followed by Nemes et al. and that of the present study resemble similarity. The amplitude of oscillation increases as the reduced flow velocity is increased. A maximum amplitude of 1.92D is observed at a reduced flow velocity of 25D.

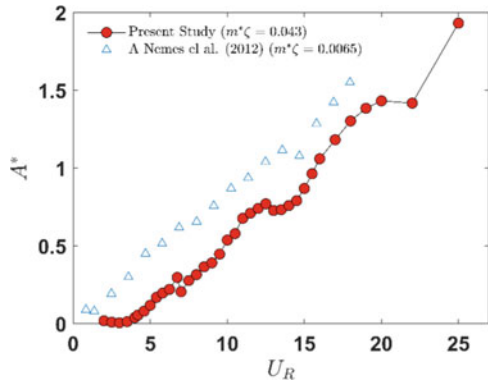
Fig. 5 Response of cylinders experiencing VIV



(a) Response of circular cylinder (25 mm diameter)



(b) Response of circular cylinder (70 mm diameter)



(c) Response of square cylinder (25 mm hydraulic diameter)

4 Conclusions

The present paper compares the response of cylinders with high and low mass damping ($m^*\zeta$) and square cross-sections experiencing vortex-induced vibration (VIV) experimentally. A water channel is used to simulate the flow of water, and to obtain the flow field, particle image velocimetry (PIV) is used. The experimental setup to allow movement of submerged cross-section experiencing VIV at least damping is developed. Air bearings are used to minimize the damping, and springs are used to model a spring-mass system. The response of three cylinders experiencing VIV is analyzed. Cylinder 1 and 2 are circular in cross-section having 25 and 70 mm diameter, respectively. Cylinder 3 is of square cross-section with $25 \times 25 \text{ mm}^2$ cross-sectional area. The first cylinder has a high mass damping parameter ($m^*\zeta = 0.048$), and its response is a two-branch response. In the initial branch, amplitude of oscillation rises quickly, and in the lower branch, it falls gradually. The second cylinder has low mass damping parameter ($m^*\zeta = 0.0081$). Three-branch response is observed in this case. In the initial branch, the amplitude of oscillation increases quickly, while the maximum amplitude of oscillation is observed in the upper branch. A maximum of $1.25D$ amplitude is recorded in the upper branch. In the lower branch, the amplitude of oscillation drops gradually. The response of a square cylinder is similar to galloping. The amplitude of oscillations increases as the reduced flow velocity is increased.

Nomenclature

U_∞	Free stream velocity	(m/s)
D	Hydraulic diameter of cross-section	(m)
m	Mass of oscillating body	(kg)
L	Length of the submerged body	(m/s)
ζ	Damping ratio	–
t	Time	(s)
m^*	Mass ratio	–
U^*	Reduced velocity	–
μ	Kinematic viscosity	(m^2/s)
ρ	Density	(kg/m^3)
D	Hydraulic diameter	(mm)

Acknowledgements The authors hereby acknowledge the financial support given by the PMRF contingency fund for the development of the experimental setup.

References

1. Rostami AB, Armandei M (2017) Renewable energy harvesting by vortex-induced motions: review and benchmarking of technologies. *Renew Sustain Energy Rev* 70:193–214
2. Sarpkaya T (2004) A critical review of the intrinsic nature of vortex-induced vibrations. *J Fluids Struct* 19(4):389–447
3. Feng CC (1968) The measurement of vortex induced effects in flow past stationary and oscillating circular and d-section cylinders. Ph.D. thesis, University of British Columbia
4. Khalak A, Williamson CHK (1996) Dynamics of a hydroelastic cylinder with very low mass and damping. *J Fluids Struct* 10(5):455–472
5. Govardhan R, Williamson CHK (2000) Modes of vortex formation and frequency response of a freely vibrating cylinder. *J Fluid Mech* 420:85–130
6. Govardhan R, Williamson CHK (2002) Resonance forever: existence of a critical mass and an infinite regime of resonance in vortex-induced vibration. *J Fluid Mech* 473:147–166
7. Alonso G, Meseguer J (2006) A parametric study of the galloping stability of two-dimensional triangular cross-section bodies. *J Wind Eng Ind Aerodyn* 94(4):241–253
8. Alonso G, Meseguer J, Perez-Grande I (2005) Galloping instabilities of two-dimensional triangular cross-section bodies. *Exp Fluids* 38(6):789–795
9. Alonso G, Meseguer J, Perez-Grande I (2007) Galloping stability of triangular cross-sectional bodies: a systematic approach. *J Wind Eng Ind Aerodyn* 95(9):928–940
10. Ding L, Zhang L, Chunmei W, Mao X, Jiang D (2015) Flow induced motion and energy harvesting of bluff bodies with different cross sections. *Energy Convers Manage* 91:416–426
11. Nemes A, Zhao J, Lo Jacono D, Sheridan J (2012) The interaction between flow-induced vibration mechanisms of a square cylinder with varying angles of attack. *J Fluid Mech* 710:102–130
12. Ding L, Zhang L, Bernitsas MM, Chang C-C (2016) Numerical simulation and experimental validation for energy harvesting of single-cylinder vivace converter with passive turbulence control. *Renew Energy* 85:1246–1259
13. Chang C-C, Bernitsas MM (2011) Hydrokinetic energy harnessing using the vivace converter with passive turbulence control. *Int Conf Offshore Mech Arct Eng* 44373:899–908
14. Mackowski AW, Williamson CHK (2011) Developing a cyber-physical fluid dynamics facility for fluid–structure interaction studies. *J Fluids Struct* 27(5–6):748–757

Experimental Investigation of Vortex-Induced Vibration of a Circular Cylinder Mounted on a Cantilever Beam



Deepak Kumar Rathour and Atul Kumar Soti

Abstract Experimental investigation of vortex-induced vibration of a bluff body usually requires the use of air bearings that allow motion with negligible friction. The use of air bearings allows us to conduct experiment at very low mass damping. However, air bearing systems are costly and require continuous supply of pressurized air. The pressurized air is supplied through a tube that can act as a source of external damping as the tube vibrates with the system. In this work, we present an alternate and cheap method of conducting vortex-induced vibration experiments while keeping very low mass damping. We use a cantilever beam for the elastic support of the bluff body. The cantilever beam provides restoring force and frictionless motion for the system. In our experiments, we tested one long cantilever beam made of mild steel and one short cantilever beam made of stainless steel. We compared the vibration response of the circular cylinder with the existing literature. For sufficiently long cantilever beams, the vibration response is found to be comparable to that of an air bearing mounted cylinder free to vibrate transverse to the flow. In case of MS cantilever beam, three response branches, initial, upper, and lower branches, are observed. The maximum amplitude of vibration occurs at $U^* = 4.92$, and it is $A_{\max}^* = 0.79D$. For SS cantilever beam, only two response branches, initial and lower, are observed, and the peak amplitude of vibration $A_{\max}^* = 0.70D$ occurs in the lower branch at $U^* = 5.26$. It is observed that on reducing the length of the cantilever beam, the peak of the amplitude reduces.

Keywords Vortex induced vibration · Flow induced vibration · Width of synchronization region · Bluff body

D. K. Rathour (✉) · A. K. Soti
Department of Mechanical Engineering, IIT Guwahati, Guwahati 781039, India
e-mail: r.deepak@iitg.ac.in

A. K. Soti
e-mail: atulsoti@iitg.ac.in

1 Introduction and Literature Review

When a bluff body is placed across the fluid flow, the vortex formation will occur due to the pressure difference between the fore and aft of the cylinder. Vortices are shed from the rear end of the bluff body. Due to the formation of vortices, the bluff body experiences fluctuating lift and drag, which causes the vibration of bluff body. The vibration of elastically mounted bluff bodies caused by the flowing fluid is called the flow-induced motion. In this case, if the cylinder is free to vibrate, then the cylinder will start oscillating vortex-induced vibration is a resonance type of flow-induced vibration in which vortex shedding frequency becomes equal to the natural frequency of oscillation of the oscillatory structure. The first experimental study on vortex-induced vibration was carried out by Feng [1]. CC Feng conducted the experiments in the wind tunnel for a cylinder with a high mass ratio ($m^* = 248$). Feng [1] studied the VIV response of circular and D-shaped cylinder by employing the electromagnetic eddy-current-based damper. He observed only two response branches, initial and lower, in VIV response. In his experiments, there was no discontinuity observed between the initial and lower branch. Khalak and Williamson [2] conducted the experiments for low mass ratio ($m^* = 2.4$), and they observed three response branches: (1) Initial branch corresponding to pseudo periodic amplitude of vibration (2) Upper branch corresponding to the aperiodic amplitude of vibration (3) Lower branch corresponds to the periodic amplitude of vibration. The maximum amplitude of vibration was observed in upper branch, and it was one cylinder diameter [3]. The transition from one response branch to other is associated with the vortex shedding mode and the phase angle. The transition from initial branch to upper branch is due to change in the vortex shedding mode from $2S$ (two single vortices per cycle) to $2P$ (two pairs of vortices form in each cycle of body motion). The transition from upper branch to lower branch is due to the change in total phase angle from 0° to 180° in the phase of lift force. For the detailed analysis of the branching behavior, numerical simulation has been done by Leontini et al. [4] and Willden and Graham [5] for a $Re = 200$ and 50 to 400 , respectively. Luxor and Zhao have done numerical studies for a $Re = 3000$ and 1000 , respectively. The transition of VIV response from three branches to two branches was shown by Klamo et al. by conducting experiments for increasing damping [6]. They observed that the three response branches occurred at low mass-damping and high Reynolds numbers. Klamo, in 2009, suggested using the eddy-current-damping to study the VIV of circular cylinder [7]. Soti et al. [8] conducted experimental studies on the single degree of freedom vortex-induced motion of an elastically mounted single cylinder for different damping ratios. They observed that the amplitude of vibration starts decreasing with an increasing damping ratio. Experiments on 2 DOF VIV of a circular cylinder by using a pendulum arrangement had been done by Jauvtis and Williamson [9]. They observed that the maximum amplitude of vibration for mass ratio 6 or greater was close to the single degree of freedom cylinder. However, a super upper branch was observed for a mass ratio of less than 6, and the maximum amplitude of vibration was $1.5D$, where D is the diameter of the circular cylinder. The cylinder mounted with a cantilever beam acts as a 2 DOF

nonlinear system. For this system, $2T$ type of vortices were observed in the super upper branch by Li and Ishihara [10]. Due to the $2T$ type of vortices, the peak of the maximum amplitude of vibration increases.

2 Experimental Methodology

2.1 Experimental Apparatus

The experiments presented here were conducted in the open surface recirculating water tunnel of the Fluid Mechanics lab at IIT Guwahati. Water tunnels are preferred over wind tunnels for flow measurements because, compared to air, the kinematic viscosity of water is smaller by a factor of about 15, yielding a higher Reynolds number at lower flow velocities. Simultaneously, the time scales of flow structures are increased, thus leading to an improved determination of transient effects with more ease and accuracy [11, 12]. The use of water as a fluid medium allows us to achieve a lower mass ratio. The water tunnel was designed and developed at IIT Guwahati. The flow velocity in water tunnel can be varied from $U = 0.08$ to 0.50 m/s. The flow speed in the water tunnel was varied by changing the rotational speed of the centrifugal pump with the help of a variable frequency drive. The water tunnel has four main components: Inlet plenum: It acts as a water reservoir and housing space for the flow conditioning system. The flow conditioning system consists of one honeycomb and three screens. The cell size of the honeycomb is 6.4 mm, and its thickness is 60 mm. Since the design of the inlet plenum is crucial for the flow quality in the test section of water tunnel, we have simulated the flow to check its uniformity using Ansys Fluent. Contraction section: The contraction section was designed by the 5th-degree polynomial mentioned by Bell and Mehta [13] for making the smooth and non-separating flow of water in test section. A 2.5-dimensional contraction was used to make a contraction ratio of 6. The contraction ratio along width is 3, and in the depth direction, it is 2; hence, the overall contraction ratio is 6. Test section: The test section is the section where the experimental observation has been done. The test section of the water tunnel is 700 mm long, 200 mm wide, and 250 mm in depth. The depth of water in the tunnel is 200 mm. Outlet plenum: The outlet plenum acts as a suction reservoir for the pumping system. The design of the outlet plenum affects the flow in the test section. To overcome the effect on the test section flow, we used two holes in the outlet plenum. The location of the two holes was found by performing the simulations in Ansys Fluent. The top and side views of schematic of the setup used for studying transverse VIV of a circular cylinder are shown in Fig. 1. This figure defines the key parameters used in describing the VIV motion. The VIV experiment presented here consists of a cantilever beam, fixing arrangements for the cantilever beam, cylinder holding arrangements, and the aluminum cylinder. An aluminum cylinder attached to the cantilever is placed across the flow due to the fluid flow, as the vortex shedding frequency synchronizes with the natural frequency of the

cylinder mounted with a cantilevered beam, the aluminum cylinder starts vibrating in the transverse direction. The cantilever beam is fixed into a vice, and the vice is fixed to the test section. The circular cylinder had a diameter of $D = 11 \pm 0.1$ mm. The length of the test cylinder is 300 mm, and its depth of immersion is $H = 195$ mm. Aspect ratio of the cylinder is $H/D = 17.73$. The cantilever beam-mounted cylinder is free to oscillate in both transverse and inline direction, and it can also have a torsional motion.

We have kept its torsional frequency high enough so that it never synchronizes with the vortex shedding frequency, and thereby the torsional motion is suppressed. When the vibrational amplitude of cylinder (A) is much smaller than the length of cantilever beam (L), i.e., $(\frac{A}{L} \ll 1)$, then the cantilever beam can be approximated by a linear spring of stiffness k . Therefore, the equation of motion for the transverse vortex-induced vibration of cantilever beam-mounted cylinder can be presented by Eq. (1).

$$m\ddot{y} + c\dot{y} + ky = F_y \tag{1}$$

where m represents the total oscillating mass, c is the structural damping, k is the equivalent stiffness ($\frac{3EI}{L^3}$) of a cantilever beam, y is the transverse displacement, and F_y is the lift force. Where E is the modulus of elasticity, and I is the area moment

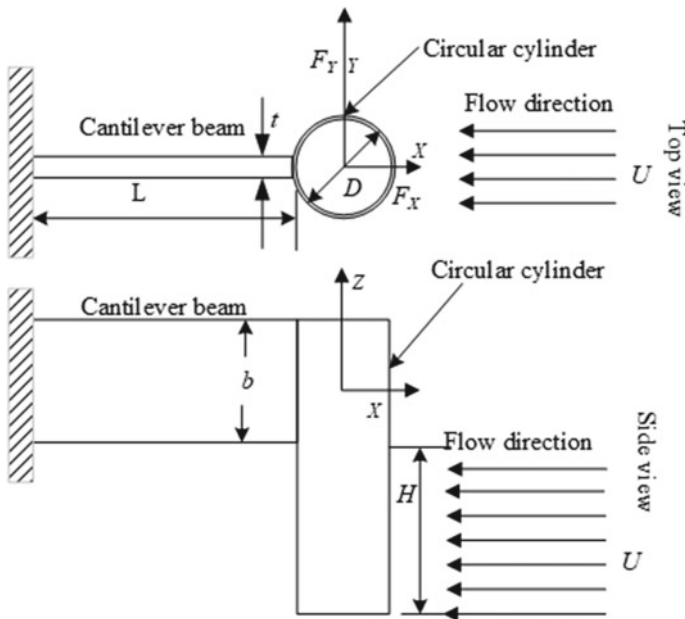


Fig. 1 Definition sketch for transverse vortex-induced vibration of a circular cylinder mounted on cantilever beam

of inertia. The mass of the displaced fluid is calculated as $m_f = \rho\pi D^2 H / 4 = 0.0185$ kg. The total oscillating mass of the cantilever beam-mounted cylinder is calculated by the formula given by Gürgöze [14].

$$m = m_s + \frac{33}{140}ML \tag{2}$$

where m_s is the mass of the cylinder assembly, M is the mass per unit length of the cantilever beam, and L is the oscillating length of the cantilever beam. Two different mild steel and stainless steel cantilevers were used in the experiments. For the mild steel cantilever beam, the length and the total oscillating mass are 54 cm and 117 gms, respectively. For the SS cantilever beam, the length and total oscillating mass were 15 cm and 220 gms, respectively. The natural frequency of the cantilever beam-mounted cylinder was measured using free decaying test. Analytically the natural frequency (f_N) of the cantilever beam can be calculated using the following Eq. (3):

$$f_N = \frac{1}{2\pi} \sqrt{\frac{k}{m_s + \frac{33}{140}ML}} \tag{3}$$

The natural frequency of both the cantilever is given in Table 1. A non-contact laser sensor (Micro-epsilon Opto NCDT 1420) measures the transverse displacement. The nondimensional form of Eq. (1) can be written in the following form

$$\ddot{Y} + \frac{4\pi\zeta}{U^*} \dot{Y} + \frac{4\pi^2}{U^{*2}} Y = \frac{2}{\pi} \frac{C_L}{m^*} \tag{4}$$

where C_L is the lift coefficient. U^* is reduced velocity given by $U / f_N D$, m^* is the mass ratio given by m / m_f , and Y is y / d . For every U^* , the amplitude response was recorded using a laser displacement sensor at a sampling frequency of 2 kHz. Transient displacement was recorded for 30 s. Hence, the number of data points is 60000, which is sufficient for amplitude measurements. Two sets of experiments were conducted for the vortex-induced vibration of a single cylinder mounted on two different cantilever beams made of mild steel and stainless steel, respectively.

Table 1 Parameters used in the two sets of experiments conducted in water tunnel

Cantilever	f_N (Hz)	m^*	ζ	Re
Mild steel	2.73	6.32	0.0032	841–4204
Stainless steel	4.40	12.63	0.0017	1905–3903

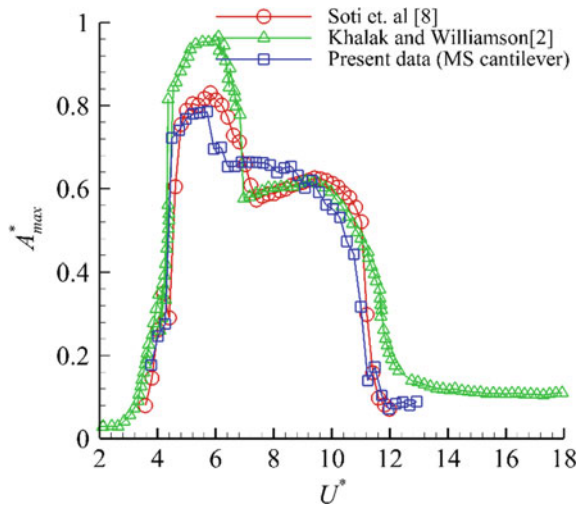
2.2 Experimental Validation

The experimental setup validation was done by comparing the circular cylinder’s amplitude response at low damping with Khalak and Williamson [2] as shown in Fig. 2. The mass ratio and damping ratio for the experiments presented here for mild steel cantilever beam-mounted cylinder are $m^* = 6.32$ and $\zeta = 0.0032$. In the amplitude response for a mild steel cantilever mounted cylinder of mass ratio of $m^* = 6.32$ and damping ratio $\zeta = 0.0032$, three amplitude response branches are obtained, which are similar to the Khalak and Williamson experimental results for a spring-mounted circular cylinder [2]. The experimental results presented here are conducted for $Re = 1245\text{--}4204$. The amplitude response branches for present experiments are much similar to the experimental results of Soti et al. [8]. From Fig. 2, it can be seen that the present results are much similar to the experimental results of Soti et al. [8] for $Re = 2220\text{--}6661$. The present experimental results are similar to Soti et al. [8] as the Re range is not so far. The shift in U^* corresponding to peak amplitude for the present experiment and Soti et al. experiment is due to the use of different medium natural frequencies. In Soti et al. [8] experiments, the used natural frequency was in the water, while in the present experiments, it is in the air.

3 Results and Discussion

In this section, it will be discussed how low-cost cantilevers can replace springs and air bearings. Transient displacement at $U^* = 4.93$ for both directions along and across the flow is shown in Fig. 3. The maximum displacement of the cylinder along

Fig. 2 Comparison of A_{max} of present work for mass ratio $m^* = 6.32$ and $\zeta = 0.0032$ for aluminum cylinder mounted with cantilever beam with Khalak and Williamson $m^* = 2.4$, and Soti et.al [8] for a Reynolds number 2220 to 6661



the flow direction at $U^* = 4.93$ is limited to $0.04D$. Since the peak of maximum amplitude in the transverse direction is $0.79D$, hence we can assume that the major amplitude of vibration is in the transverse direction.

3.1 VIV Response with Mild Steel Cantilever Beam

In set 1 Table 1, the experiments were performed for VIV response of the aluminum cylinder mounted with a mild steel cantilever beam of size length = 540 mm, thickness = 1.6 mm, and width = 30 mm. The cylinder was kept across the flow. The mass ratio ($m^* = 6.32$), diameter of cylinder ($D = 11$ mm), and the natural frequency of system ($f_N = 2.73$) was kept constant. The reduced velocity was varied by varying the free stream flow velocity (U) and keeping the natural frequency constant. In the present experiment, the reduced velocity was varied from $U^* = 3.2$ to 11.2. The vortex shedding frequency of the cylinder mounted with MS cantilever beam is $f_V = 2.79$ Hz. The amplitude response obtained for different reduced velocities is shown in Fig. 5.

Similar transient displacement is recorded in case of stainless steel cantilever, and it is shown in Fig. 4. The maximum displacement of the cylinder along the flow direction at $U^* = 5.26$ is limited to $0.03D$. Since the peak of the maximum amplitude in transverse direction is $0.70D$, we can assume that major amplitude of vibration is in the transverse direction. From both the Figs. 3 and 4, it is clear that we can approximate the cantilever beam with a linear spring of stiffness k . In experimental set 1, the mild steel cantilever was used. The free length of the cantilever beam was 54 cm. The natural frequency of the setup was found by the free decay test in the air.

From amplitude versus reduced velocity Fig. 5, it can be seen that this plot is similar to the vibrational response obtained by Khalak and Williamson (1997) [2]. Three

Fig. 3 Transient transverse and inline displacement for mild steel cantilever in the direction of flow at $U^* = 4.93$

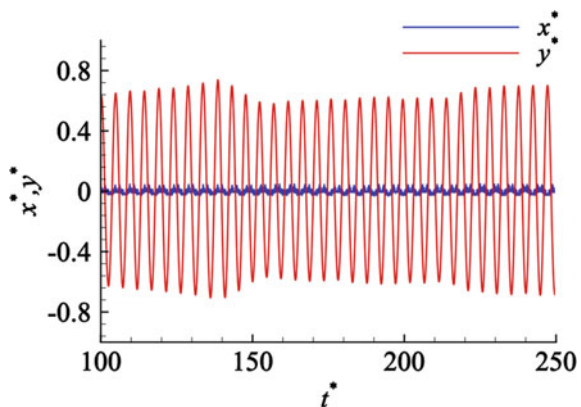
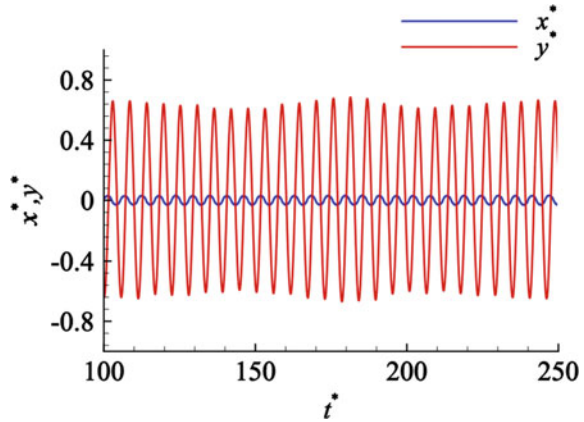


Fig. 4 Transient displacement for stainless steel cantilever in the direction of flow at $U^* = 5.26$



branches were observed. Initial response branch was obtained for the $U^* = 3.2$ to 3.67. The transient amplitude response corresponding to the initial branch at $U^* = 3.47$ is shown in Fig. 5. It can be seen from Fig. 6 that the nature of amplitude is quasi-periodic. The transient amplitude response is similar to that of the spring-mounted circular cylinder [8]. There is a jump in amplitude response observed at $U^* = 3.89$ as shown in Fig. 5. At $U^* = 3.89$, the vortex shedding frequency locks onto the natural frequency of the cylinder; hence, the amplitude of vibration increases significantly. The upper branch is observed from $U^* = 3.89$ to 5.14. The transient response corresponding to the upper branch at $U^* = 4.30$ is shown in Fig. 7. In the upper branch, the vibrational amplitude varies from one cycle to another, i.e., the vibrations are not fully periodic. The peak of the amplitude occurs at $U^* = 4.93$ in the upper branch, and it is $A^* = 0.79D$. At $U^* = 5.55$, a drop in amplitude response is observed. Hence, it can be said that the amplitude response is shifted from the upper amplitude response branch to the lower amplitude response branch, as shown in Fig. 5. The transient amplitude response for the lower amplitude branch is shown in Fig. 8. From Fig. 8, it can be seen that in lower branch, the amplitude response is fully periodic. In lower branch, on further increasing the U^* , the frequency of vibration f synchronizes with the frequency of shedding vortices from the stationary cylinder; hence, the vibration of the cylinder stops.

3.2 VIV Response with Stainless Steel Cantilever Beam

The experiments were performed for the VIV response of stainless steel cantilever mentioned in Table 1. The length, width, and thickness of cantilever beam are 150, 30, and 0.8 mm. The cylinder was kept across the flow in test section of water tunnel. The reduced velocity was varied by varying the free stream flow velocity U while keeping the natural frequency constant. In the present experiment, the reduced

Fig. 5 Maximum amplitude A^* versus U^* for mild steel and stainless steel cantilever beam-mounted cylinder as mentioned in Table 1

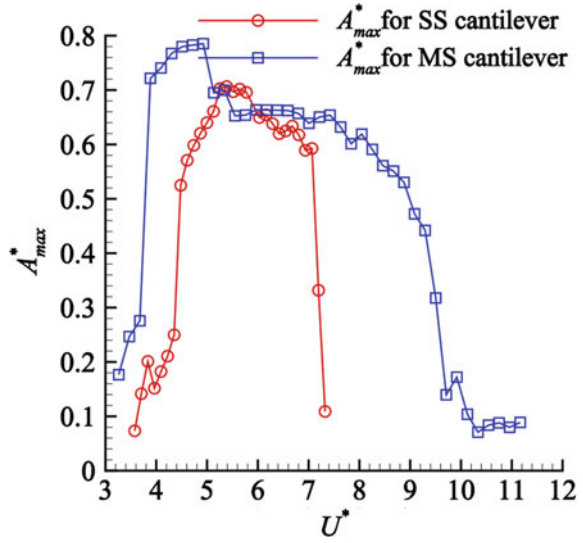


Fig. 6 Transient displacement A^* for mild steel cantilever mounted cylinder at $U^* = 3.47$, ($m^* = 6.32$, $\zeta = 0.0032$)

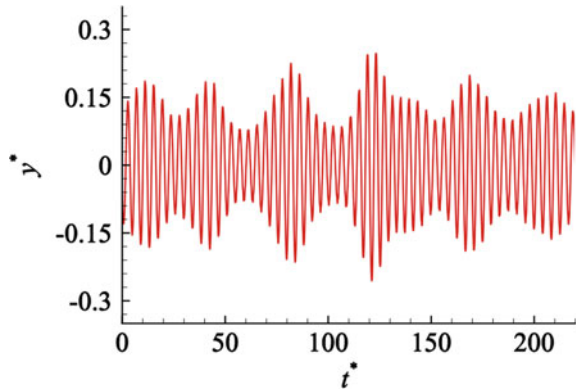


Fig. 7 Transient displacement A^* for mild steel cantilever mounted cylinder at $U^* = 4.30$, ($m^* = 6.32$, $\zeta = 0.0032$)

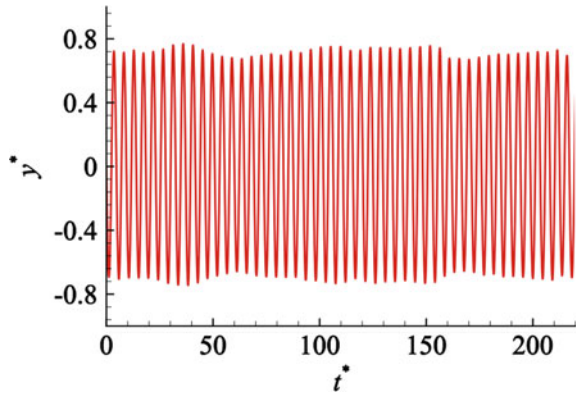
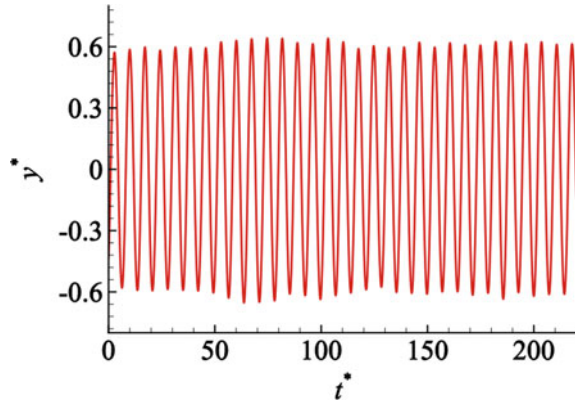


Fig. 8 Transient displacement A^* for mild steel cantilever mounted cylinder at $U^* = 7.22$, ($m^* = 6.32$, $\zeta = 0.0032$)



velocity was varied from $U^* = 3.58$ to 7.33 . The vortex shedding frequency of the cylinder mounted with SS cantilever beam is $f_V = 4.23$ Hz. The amplitude response obtained for SS cantilever is shown in Fig. 5. From the amplitude versus reduced velocity plot 5 for SS cantilever, it can be seen that only two response branches, initial and lower, are found. Initial amplitude response branch was obtained for $U^* = 3.58$ to 4.35 . The transient displacement corresponding to the initial branch at $U^* = 3.84$ is shown in Fig. 9. In initial amplitude response branch, the vibrational amplitude is quasi-periodic. The transient amplitude response is similar to that of the spring-mounted circular cylinder. There is a jump in amplitude response observed at $U^* = 4.48$ as shown in Fig. 5. The jump in amplitude response is due to lock-in of the vortex shedding frequency with the natural frequency of the oscillating structure. Due to lock-in the amplitude of vibration increases suddenly. The transient amplitude response corresponding to lower branch at $U^* = 6.3$ is shown in Fig. 10. The peak of maximum amplitude occurs at $U^* = 5.26$, and the peak amplitude is $A^* = 0.70D$. The transient amplitude response corresponding to lower branch at $U^* = 6.3$ is shown in Fig. 10. The peak of maximum amplitude occurs at $U^* = 5.26$, and the peak amplitude is $A^* = 0.70D$. On further increasing U^* , the vibration amplitude response starts decreasing, and at $U^* = 7.33$ the vibrational frequency locks-in with the frequency of the shedding vortices from the stationary circular cylinder.

Fig. 9 Transient displacement A^* for stainless steel cantilever cylinder $U^* = 3.83, (m^* = 12.63, \zeta = 0.0017)$

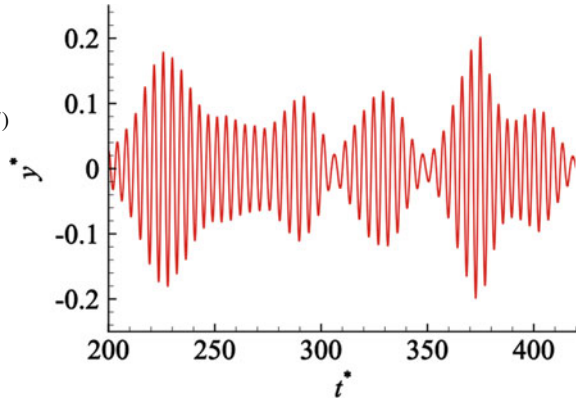
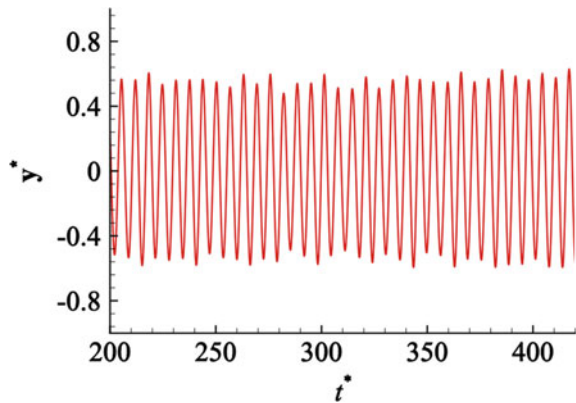


Fig. 10 Transient displacement A^* obtained for stainless steel cantilever mounted cylinder $U^* = 6.3, (m^* = 12.63, \zeta = 0.0017)$



4 Conclusion

The vortex-induced vibration characteristics of a circular cylinder mounted with MS cantilever beam and SS cantilever beam are studied experimentally for $Re = 841-4204$ and $Re = 1905-3903$, respectively. The mass ratio, natural frequency, and damping ratio of 54 cm long, 30 mm wide, and 1.6 mm thick mild steel cantilever beam are $m^* = 6.32, f_N = 2.73$ Hz, and $\zeta = 0.0032$, respectively. Three response branches, initial, upper, and lower, are observed in the amplitude response of vortex-induced vibration of an aluminum cylinder mounted with MS cantilever beam, and at $U^* = 4.30$ the peak of the maximum amplitude is $A^*_{max} = 0.79D$. The response branches and the peak of maximum amplitude of aluminum cylinder mounted with MS cantilever beam are much similar to Soti et al. [8]. The mass ratio, natural frequency, and damping ratio of 15 cm long, 30 mm wide, and 0.8 mm thick stainless steel cantilever beam are $m^* = 12.63, f_N = 4.40$ Hz, and $\zeta = 0.0032$, respectively. In the amplitude response of SS cantilever beam-mounted cylinder, only two response branches, initial and lower, are obtained. In this case at $U^* = 5.26$,

the peak amplitude of vibration $A_{\max}^* = 0.70D$ is 11% less than MS cantilever. The decrease in the peak amplitude may be due to the decrease in the cantilever beam length. The width of the synchronization region decreases as the mass ratio increases. From the above discussion, it is clear that low-cost cantilever beams can replace springs and air bearings. Hence, the effective cost of production of VIV setup can be reduced. Also, the complicated setup can be replaced by the simple VIV setup.

Acknowledgements The authors would like to acknowledge the financial support from Grant No. SRG/2020/001082, provided by Science and Engineering Research Board (SERB), India, and IITG startup grant. The authors are grateful to the Mechanical Engineering Department IIT Guwahati for funding the fabrication of water tunnel in fluid mechanics at IIT Guwahati. Further we are also grateful to the technicians of IIT Guwahati central workshop as they have helped in the preparation of water tunnel and experimental setup.

Nomenclature

A	Amplitude of vibration mm
A^*	Non-dimensional amplitude $\frac{A}{D}$
m_s	Mass of cylinder assembly gm
m	Total oscillating mass gm
m_f	Mass of displaced fluid gm
m^*	Mass ratio $\frac{m}{m_f}$
f_N	Natural frequency of system in air
F_Y	Lift force
t^*	Non-dimensional time $\frac{tU}{D}$

References

1. Feng C (1968) The measurement of vortex induced effects in flow past stationary and oscillating circular and D-section cylinders. PhD thesis, University of British Columbia
2. Khalak A, Williamson CHK (1997) Fluid forces and dynamics of a hydroelastic structure with very low mass and damping. *J Fluids Struct* 11(8):973–982
3. Williamson CHK, Roshko A (1988) Vortex formation in the wake of an oscillating cylinder. *J Fluids Struct* 2(4):355–381
4. Leontini JS, Thompson MC, Hourigan K (2006) The beginning of branching behaviour of vortex-induced vibration during two-dimensional flow. *J Fluids Struct* 22(6–7):857–864
5. Willden RHJ, Graham JMR (2006) Three distinct response regimes for the transverse vortex-induced vibrations of circular cylinders at Low Reynolds Numbers. *J Fluids Struct* 22(6–7):885–895
6. Klamo JT, Leonard A, Roshko A (2006) The effects of damping on the amplitude and frequency response of a freely vibrating cylinder in cross-flow. *J Fluids Struct* 22(6–7):845–856
7. Klamo JT (2009) The application of controlled variable magnetic eddy current damping to the study of vortex-induced vibrations. *Exp Fluids* 47(2):357–367

8. Soti AK, Zhao J, Thompson MC, Sheridan J, Bhardwaj R (2018) Damping effects on vortex-induced vibration of a circular cylinder and implications for power extraction. *J Fluids Struct* 81:289–308
9. Jauvtis N, Williamson CHK (2004) The effect of two degrees of freedom on vortex-induced vibration at low mass and damping. *J Fluid Mech* 509:23–62
10. Li T, Ishihara T (2021) Numerical study on vortex-induced vibration of circular cylinder with two-degree-of-freedom and geometrical non-linear system. *J Fluids Struct* 107:103415
11. Greenblatt D, Mueller-Vahl H, Strangfeld C, Medina A, Ol MV, Granlund KO (2016) High advance-ratio airfoil streamwise oscillations: wind tunnel vs. water tunnel. In: 54th AIAA aerospace sciences meeting, p 1356
12. Schmidt H-J, Woszidlo R, Nayeri CN, Paschereit CO (2017) Separation control with fluidic oscillators in water. *Exp Fluids* 58(8):1–17
13. Bell JH, Mehta RD (1988) Contraction design for small low-speed wind tunnels. NASA contractor report 177488
14. Gürgöze M (2005) On the representation of a cantilevered beam carrying a tip mass by an equivalent spring–mass system. *J Sound Vib* 282(1–2):538–542

Effect of Crosswind on Vehicle Dynamics



P. M. Vamsi Krishna and B. Ravindra

Abstract Crosswinds often play a substantial role in traffic accidents on highways, bridges, and slopes. Accidents occur when the vehicle yaws and the driver loses control. This paper analyzes the passive crosswind response of various automobiles in static situations by neglecting the steering and driver inputs. First, this paper will explore the yawing of vehicles on a straight road using wind data from the Hudhud cyclone (that occurred in 2014), including wind direction, speed, density, and pressure. Second, this study will determine how a vehicle will react to a crosswind when driving on a grade, such as a hill or a mountain, using wind data with varying altitude. The impact of aerodynamic loads on vehicle dynamics is studied in this context. In a crosswind, a car's suitable rearward center of pressure (C.P.) placement is needed to reduce lane deviations. However, changes in the vehicle's axle loads result in a shift in the C.P. location, which turns the automobile. Hence, the yawing of cars moving on a straight road with different axle loads needs to be analyzed. Wind density variation is vital when a car/truck is moving on a road. The change in wind density (caused by pressure changes as elevation increases) will impact the vehicle's response to crosswinds. This paper also examines how wind density variation changes the vehicle dynamics while driving on a hill.

Keywords Crosswind response · Center of pressure · Aerodynamic wind angle · Side force · Neutral steer point

1 Introduction

Crosswinds are the winds moving perpendicularly to the direction of the vehicle's motion. These winds exert a side force on a car's body (equivalent to the dynamic air pressure times the appropriate area of a vehicle), which causes the automobile to yaw and alter its path, causing an accident. The term 'crosswind sensitivity' typically refers to a vehicle's lateral and yawing response to transversal wind disturbances,

P. M. V. Krishna (✉) · B. Ravindra
Department of Mechanical Engineering, IIT Jodhpur, Jodhpur 342037, India
e-mail: krishna.9@iitj.ac.in

© The Author(s), under exclusive license to Springer Nature Singapore Pte Ltd. 2024
K. M. Singh et al. (eds.), *Fluid Mechanics and Fluid Power, Volume 2*, Lecture Notes in Mechanical Engineering, https://doi.org/10.1007/978-981-99-5752-1_48

593

which impair the driver's ability to maintain control of the car and keep it on course. The center of pressure (C.P.) placement and distance from the vehicle's neutral steer point are the most common aerodynamic characteristics that affect crosswind sensitivity. The CP is where the vehicle's lateral force and yaw moment reactions combine to produce an action. The neutral steer point is the spot on the vehicle where a lateral force results in equal sideslip angles at the front and rear axles (NSP). In this paper, the following six categories of vehicles will be used for the analysis: sports car, truck, SUV, EV hatchback, hatchback, and sedan. The wind data of hills of the Araku Valley (Visakhapatnam, Andhra Pradesh), Simhachalam (Visakhapatnam, Andhra Pradesh), and Lambasingi (Alluri Seeta Rama Raju district, Andhra Pradesh) is used for this analysis. Crosswinds can occur even when a heavy vehicle is moving next to another at high speed and tries to overtake it. In this scenario, a significant amount of side force acts on the car's body. This force pushes the car away, causing it to change lanes and get struck by another vehicle behind it unintentionally.

In October 2014, Hudhud, a powerful tropical storm devastated eastern India and Nepal and claimed many lives. Traveling in such an atmosphere, especially in a car, is too dangerous since gusty crosswinds are high. These winds can flip or turn a vehicle on highways and bridges, leading to an accident. This paper analyses how winds with a speed of 180 km/h (Hudhud cyclone's wind data) will affect the selected vehicles.

The aerodynamic loads on a vehicle have huge impact on fuel economy and performance. On a straight road, the wind's drag force significantly impacts the longitudinal dynamics of the car and increases fuel consumption. Similarly, the air density around the vehicle is also significant. Additionally, since driving uphill is against gravity, it uses more fuel. Further, if the wind density varies, it will greatly impact the car's aerodynamics. Usually, when an automobile is moving uphill, the load on the rear axle often increases, shifting the center of gravity. This paper analyses how this variation impacts the automobile's crosswind response. This novelty of this study lies in the analysis of how an upward-moving car responds to changes in aerodynamic loads, wind density, and axle loads.

Prior research mainly focused on how crosswinds affected a vehicle's handling stability. In recent years, several researchers have used numerical simulations and experiments to study the handling stability of vehicles in crosswinds. In 1989, C.C. Macadam has carried out the static turning analysis of vehicles subject to externally applied forces, in which he derived an expression for the yaw rate. By ignoring the suspension and driver inputs, C.C. Macadam et al. have developed a relation for yaw rate in terms of aerodynamic forces and moment arm in their 1990 study. These works formed the basis of further investigations to analyze the influence of crosswinds on various types of automobiles running on plain roads and grades.

The impact of crosswind sensitivity studies for disaster management scenarios has not been explored so far in great detail. This study aids in warning citizens during cyclones. Additionally, it helps in the design of a control system that compensates for vehicle yawing. This research will be helpful in initiating further research for tractor-trailers as well because their aerodynamics differ significantly from that of a

car, and there is a high probability that a heavily loaded tractor-trailer may roll when operating in these types of crosswinds.

2 Literature Review

Driving a vehicle in a safe mode is the most crucial part when crosswinds are present. Many researchers have focused on simulating vehicle's behavior to a crosswind using commercial software packages such as Adams, CarSim, and TruckSim. Extensive wind tunnel testing provides the necessary experimental data to validate these simulations.

In 1989, C.C. Macadam developed a relationship between the yaw rate and inertial forces from first principles [1]. MacAdam et al. in 1990 [2] derived a relation for yaw rate in terms of aerodynamic forces and moment arm. They developed a link between yaw rate and aerodynamic side force. They noticed that the roll compliance increased during the test. Their study concluded that differences in fore-aft weight distribution had an equal impact on subjective and objective assessments of vehicle crosswind sensitivity at vehicle speeds between 90 and 100 mph [2, 3]. In 1982, David H. Weir et al. have studied the impact of aerodynamics on the lateral-directional stability and crosswind response of passenger car/utility trailer combinations [4]. These were determined using a wind tunnel study and computer simulation findings. They concluded that adding aerodynamic elements to the equations of motion reduces trailer yaw damping by a few percent and that minor changes in tow car aerodynamics have minimal impact on trailer yaw stability. In 2015, Vančura and Slavik [5] have studied the crosswind sensitivity of road vehicles. A single-track replica of the vehicle was examined. They created a mechanism that can accurately assess crosswinds road cars' sensitivity. They used laboratory and on-road test experimental procedures in their experimental setting. They concluded that the most significant parameters are speed and wind direction, aerodynamic yaw moment, and the vehicle's frontal area. Essential are also the overall weight, position of the car's center of gravity, and gradient of tire lateral coefficient [5]. Detailed investigation of crosswind response using a simplified car model has been carried out by Guilmineau et al. [6]; Guilmineau and Chometon [7]. These authors have considered transient crosswind gusts on automobiles for moderated yaw angles using computational fluid dynamic solvers.

3 Weather Data, Vehicle Data, and Models

The wind data needed in this work has been taken from Wikipedia [8]. The significant assumptions taken in the calculations were that the wind velocity (50 m/s), angle (20°), and direction (North-Northeast) are equal and constant on the three hills considered. Table 1 shows the wind data. The selected vehicle's data, including mass

(M), the distance between the front axle and center of gravity (a), frontal area (A), wheelbase (L), and C.G. height (h), are shown in Table 2. This data is used for further studies in this paper.

Figure 1 shows a typical free body diagram of a vehicle with lateral forces and having a longitudinal velocity U and turning moment r . These lateral forces are obtained from the dynamic pressure data of Hudhud cyclone. The expression for the relation between the yaw rate and other properties is obtained as follows:

From Fig. 1, using equations of equilibrium $\Sigma F = 0$, and $\Sigma M_{CM} = 0$, we get

$$F_{yf} + F_{yr} + F_c - mUr = 0 \tag{1}$$

$$F_c d + F_{yf} a - F_{yr} b = 0 \tag{2}$$

Table 1 Wind data

Hill	Simhachalam	Lambasingi	Araku valley
Prop's			
Location (State)	Andhra Pradesh	Andhra Pradesh	Andhra Pradesh
Elevation (m)	377	1000	910
Grade (°)	6.719	11.309	3.366
Cyclone	Hudhud	Hudhud	Hudhud
Wind density (kg/m ³)	1.168	1.129	1.155
Dynamic wind pressure (Pa)	1460.00	1411.25	1443.75
Wind direction	N-NE	N-NE	N-NE
Aerodynamic wind angle (°)	20	20	20
Wind velocity (m/s)	50	50	50

Table 2 Basic parameters of selected vehicles

Prop's Vehicle	A (m ²)	M (kg)	a (m)	L (m)	h (mm)
Sports car	2.142	1972	1.750	2.711	480.568
Truck	6.608	17,750	2.585	4.500	1083.351
SUV	2.746	1680	1.500	2.741	520.369
EV hatchback	2.292	1674	1.560	2.649	502.770
Hatchback	1.826	1230	1.420	2.430	293.640
Sedan	2.154	1438	1.400	2.600	572.957

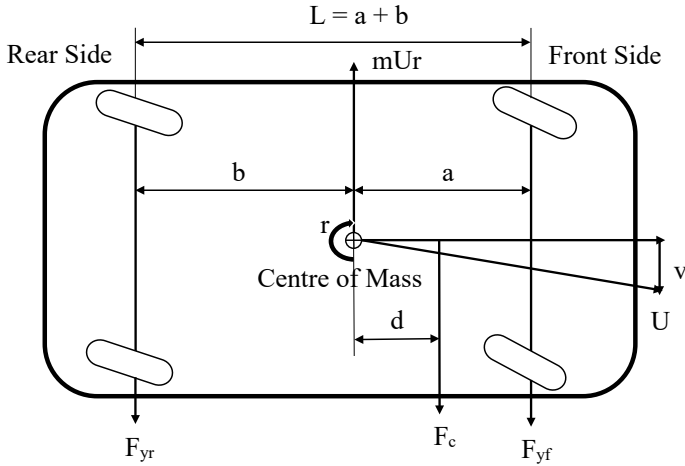


Fig. 1 Forces acting on a vehicle

Also,

$$F_y = -C_{af} \left[\frac{(v + ar)}{(U - \delta_f)} \right], \tag{3}$$

and

$$F_{yr} = -C_{ar} \left[\frac{(v - br)}{(U - \delta_r)} \right].$$

The tire cornering coefficients are C_{af} and C_{ar} . By substituting F_{yf} and F_{yr} into the Eqs. (1) and (2), we get

$$\begin{aligned} & F_c + C_{af}\delta_f + C_{ar}\delta_r \\ &= \left[\frac{(aC_{af} - bC_{ar})}{U} \right] v + \left[\frac{(aC_{af} - bC_{ar})}{U} + mU \right] r \\ & F_c d + aC_{af}\delta_f - bC_{ar}\delta_r \\ &= \left[\frac{(aC_{af} - bC_{ar})}{U} \right] v + \left[\frac{a^2C_{af} + b^2C_{ar}}{U} \right] r \end{aligned}$$

Since, $(F_c + C_{af}\delta_f + C_{ar}\delta_r) = F_T$, i.e., the total force, and this force acts at a distance, $e = \left[\frac{(d \cdot F_c + aC_{af} \cdot \delta_f - b \cdot C_{ar} \cdot \delta_r)}{(F_c + C_{af} \cdot \delta_f + C_{ar} \cdot \delta_r)} \right]$ as shown in Fig. 2.

By dividing F_T by r , we get

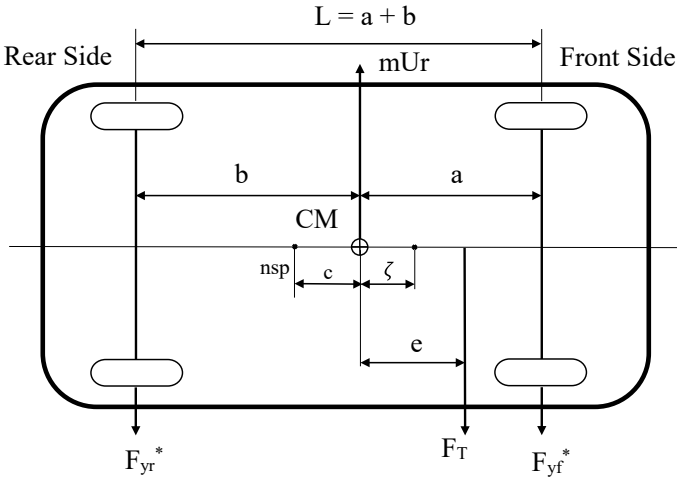


Fig. 2 Inertial forces acting on the center of mass

$$\frac{r}{F_T} = \frac{[(b \cdot C_{ar} - a \cdot C_{af}) + e(C_{af} + C_{ar})]}{\left[\left(\frac{(a+b)^2 \cdot C_{af} \cdot C_{ar}}{U} \right) - (a \cdot C_{af} - b \cdot C_{ar})mU \right]}$$

By rewriting the following equation in its simplest form,

$$\frac{r}{F_T} = \frac{1}{mU} \frac{(d_{ns} + e)}{(d_{ns} + \zeta)} \tag{4}$$

where

$$\zeta = \frac{L^2(C_{af}C_{ar})}{mU^2(C_{af} + C_{ar})}$$

and

$$e = b - \frac{L}{2} + L \left(\frac{C_{mz}}{C_s} \right)$$

The distance ζ is equal to the resistive moment normalized by the inertial force mUr , and ‘ a ’, ‘ b ’ are the distances measured from center of mass to the front and rear axles, respectively. As the vehicle travels on a slope, the distance ‘ a ’ decreases, and ‘ b ’ increases. Distance from the neutral steer point to the center of gravity is denoted by d_{ns} following Gillespie [3].

By expanding the terms of F_T and e , the relation yields [2]:

$$\frac{r}{\alpha} = \frac{qC_s A d_{ns} + \left[a - \frac{L}{2} + L \frac{C_{mz}}{C_s} \right]}{mU (d_{ns} + \zeta)} \tag{5}$$

The aerodynamic wind angle, denoted by α in Eq. (5), is very important since it indicates the direction from which the wind will strike. In this paper, α is 20° by default in each case.

In Eq. (5), $d_{ns} = (bC_{ar} - aC_{af}) / (C_{af} + C_{ar})$. It includes front and rear tire cornering stiffness. An extension of Eq. (5) to include the grade (θ) results in the following the Eq. (6):

$$\frac{r}{\alpha} = \frac{qC_s A \left(\frac{d_{ns} + L \left(\frac{W_r}{W} + \frac{C_{mz}}{C_s} - \frac{1}{2} \right) - h\theta}{(c + \zeta)} \right)}{mU} \tag{6}$$

In this case, the $h\theta$ factor has a sizable effect on the yaw rate. The term $qC_s A$ refers to the side force. It consists of two forces: acting on the front side, F_{yf} , and the rear side, F_{yr} . The values of C_{mz} and C_s depend on the vehicle type and the aerodynamic wind angle [3]. C_s is the tire cornering stiffness, the slope between lateral force and slip angle [3]. The cornering stiffness of the front and rear tires are the lateral force and slip angle ratios.

4 Results and Discussion

Any wind that blows against the direction or line of motion is known as a crosswind. A rigid body will rotate about its yaw axis when a strong wind hits it to point in a different direction, either to the left or right of its motion, known as a yaw rotation or yaw rate. This yawing affects the vehicle’s aerodynamics. Crosswinds cause vehicles’ paths to veer to the side and can be dangerous. Table 3 shows the lateral coefficients, C obtained from Gillespie [3] and force’s F computed from Eq. (3) for different vehicles running on a straight road with constant wind density.

Table 3 Mass and force properties of the vehicles

Prop’s Vehicle	C_s	C_{mz}	F_y (N)	F_{yf} (N)	F_{yr} (N)
Sports car	0.9	0.210	2674.34	1650.82	1023.51
Truck	1.0	0.250	9166.94	5021.45	4145.49
SUV	0.9	0.200	3426.59	1875.52	1551.06
EV hatchback	0.8	0.225	2541.35	1496.48	1044.86
Hatchback	0.8	0.225	2025.03	1183.350	841.68
Sedan	0.7	0.240	2090.11	1064.32	1025.79

A tire with a higher cornering stiffness will result in a stronger lateral acceleration for a given slip angle, which is a crucial performance indicator of any tire. In this paper, C_{af} and C_{ar} are obtained from F_{yf} and F_{yr} .

The yaw rate results computed using Eq. (5) when the car travels at 25 km/h on a straight road are shown in Table 4.

The SUV has the highest yaw rate in this table of vehicles traveling on a flat surface.

Table 4 shows the wind characteristics on the three hills and dynamic pressure corresponding to the Hudhud cyclone.

Properties such as C_{mz} and C_s do not depend on wind or road variations; hence, they are constant for the vehicles considered throughout this paper. Table 5 shows the values of axle loads and side forces on the Simhachalam hill.

Since the C.G. shifts to the rear side as the vehicle climbs the gradient, the weight on the rear axle increases; hence, in Eq. (6), the rear axle weight is considered. The density of wind on this hill is 1.168 kg/m², which will affect the yaw rate since, according to Eq. (6), the yaw rate will fluctuate along with the density. The data for the side forces and axle loads on Lambasingi hill is listed in Table 6.

The Lambasingi hill has a larger grade, and so does the axle load variation. The wind density on this hill is 1.129 kg/m². The values for Araku Valley hill's axle loads and side forces are listed in Tables 7, 8, 9 and 10.

Table 4 Inertial properties and yaw rate of the vehicles

Prop's Vehicle	d_{ns} (m)	C_{af} (lbs./°)	C_{ar} (lbs./°)	ζ (/°·s ²)	r (°/s)
Sports car	0.713	46.68	28.93	0.002663	2.63
Truck	0.550	3080.41	2543.06	0.063569	1.35
SUV	0.162	85.01	81.05	0.007423	8.68
EV hatchback	0.322	95.84	84.07	0.007510	4.81
Hatchback	0.886	317.70	258.87	0.027392	2.56
Sedan	0.15	81.08	74.36	0.007294	8.18

Table 5 Mass and force properties of the vehicles on Simhachalm Hill with a grade of 6.719°

Prop's Vehicle	W_r (N)	W_f (N)	F_{yf} (N)	F_{yr} (N)
Sports car	12,889.66	6155.64	1608.33	1206.25
Truck	104,967.92	68,670.35	5037.95	4609.72
SUV	9385.95	7094.84	2405.92	1202.96
EV hatchback	10,036.41	6385.53	1715.74	960.81
Hatchback	7222.07	4844.22	1502.06	630.867
Sedan	7960.50	6146.27	1572.36	628.94

Table 6 Mass and force properties of the vehicles on Lambasingi Hill with a grade of 11.309°

Prop's Vehicle	W_r (N)	W_f (N)	F_{yf} (N)	F_{yr} (N)
Sports car	13,164.62	6180.56	1554.63	1165.97
Truck	108,334.92	65,300.48	4869.73	4455.80
SUV	9636.60	6844.19	2325.59	1162.79
EV hatchback	10,286.10	6135.84	1658.45	928.73
Hatchback	7338.88	4727.41	1451.91	609.80
Sedan	8209.54	5897.23	1519.86	607.94

Table 7 Mass and force properties of the vehicles on Araku Valley Hill with a grade of 3.366°

Prop's Vehicle	W_r (N)	W_f (N)	F_{yf} (N)	F_{yr} (N)
Sports car	12,689.21	6656.10	1590.45	1192.82
Truck	102,524.09	71,111.98	4981.88	4558.42
SUV	9202.85	7277.94	2379.14	1189.57
EV hatchback	9854.01	6567.93	1696.64	950.12
Hatchback	7136.74	4929.55	1485.34	623.84
Sedan	7778.58	6328.19	1554.86	621.94

Table 8 Inertial properties and yaw rate of the vehicles on Simhachalm Hill with a grade of 6.719°

Prop's Vehicle	d_{ns} (m)	C_{af} (lbs./°)	C_{ar} (lbs./°)	ζ (/°·s ²)	r (°/s)
Sports car	0.512	71.23	32.78	0.000239	4.32
Truck	0.684	2040.0	1500.0	0.003549	1.83
SUV	0.339	42.28	31.04	0.000288	6.48
EV hatchback	0.388	41.15	32.64	0.000275	5.59
Hatchback	0.636	80.38	38.27	0.000448	4.23
Sedan	0.500	71.23	37.71	0.000417	14.56

Table 9 Inertial properties and yaw rate of the vehicles on Lambasingi Hill with a grade of 11.309°

Prop's Vehicle	d_{ns} (m)	C_{af} (lbs./°)	C_{ar} (lbs./°)	ζ (/°·s ²)	r (°/s)
Sports car	0.51	38.65	32.56	0.000237	4.17
Truck	0.89	2208.66	1331.30	0.056845	1.53
SUV	0.23	47.41	40.87	0.000353	8.53
EV hatchback	0.24	43.03	42.26	0.000322	7.81
Hatchback	0.31	49.33	41.44	0.000389	6.36
Sedan	0.12	43.03	41.31	0.000357	14.15

Table 10 Inertial properties and yaw rate of the vehicles on Araku Valley Hill with a grade of 3.366°

Prop's Vehicle	d_{ns} (m)	C_{af} (lbs./°)	C_{ar} (lbs./°)	ζ (/°·s ²)	r (°/s)
Sports car	0.517	40.53	33.77	0.000247	4.23
Truck	0.748	2090.19	1449.78	0.003514	1.73
SUV	0.235	40.42	34.64	0.000300	8.60
EV hatchback	0.293	38.43	35.21	0.000277	6.90
Hatchback	0.295	37.852	32.61	0.000303	6.80
Sedan	0.142	42.266	39.624	0.000346	12.91

The Araku hill has a minor grade among the three, and the density of wind on this hill is 1.155 kg/m². The values for the yaw rate of the automotive on these hills as computed from Eq. (6) are tabulated as follows.

The data computed for various hills indicates that some vehicles are more prone to crosswind than others while moving up a hill.

5 Conclusions

Vehicle dynamics studies due to crosswinds on plain roads and grades are important for the safety of passengers. It is important to predict how the crosswind and its forces affect the yaw rate of an automobile. Wind data from the Hudhud cyclone (2014), including constant wind direction, speed, density, and pressure, is used in this article.

This study shows that the SUV has a higher yaw rate when running on a straight road than other models. The truck exhibits the least yaw rate when subjected to crosswind. The situation with the cars running on hills, however, is different. According to this study, the sedan yaws more when driven on a slope. For the three hills, it virtually always responds with the same yaw. The crosswind sensitivity starts increasing gradually in the sports car as the grade increases. Its yaw rate rose approximately twice when traveling on a gradient as opposed to a flat surface. EV hatchback's response to crosswind is increasing linearly. Further aerodynamic investigations are needed to understand the effect of crosswind on vehicles. The vehicle data used in this study is obtained from the open source data such as the manufacturers and other Web sites. It is used solely for the purpose of obtaining a preliminary understanding of the crosswind sensitivity to cyclones. Authentic data from the manufacturers needs to be obtained for further rigorous studies.

Nomenclature

A	Frontal area of the vehicle	m^2
C_s	Side force coefficient	–
C_{mz}	Yawing moment coefficient	–
α	Aerodynamic wind angle	$^\circ$
ρ	Density of air	kg/m^3
M	Mass of the vehicle	kg
a	Distance from front axle to centre of mass	m
L	Wheelbase	m
h	C.G. height	mm
W_r	Load on rear axle	N
W_f	Load on front axle	N
F_v	Total side force	N
F_{vt}	Side force on front axle	N
F_{vr}	Side force on rear axle	N
C_{af}	Tire cornering stiffness of the front axle	$kg/^\circ$
C_{ar}	Tire cornering stiffness of the rear axle	$kg/^\circ$
d_{ns}	Distance from centre of mass to neutral steer point	m
r	Yaw rate	$^\circ/s$
ζ	Moment arm proportional to the tire force yaw damping moment	$/^\circ s^2$
V	Velocity of the wind	m/s
q	Dynamic pressure of the wind	Pa
v	Forward velocity of the vehicle	m/s
F_T	Total lateral control force	N

References

1. MacAdam CC (1989) Static turning analysis of vehicles subject to externally applied forces—a moment arm ratio formulation. *Veh Syst Dyn* 18(6):345–357
2. MacAdam CC, Sayers MW, Pointer JD, Gleason M (1990) Crosswind sensitivity of passenger cars and the influence of chassis and aerodynamic properties on driver preferences. *Veh Syst Dyn* 19(4):201–236
3. Gillespie TD (1992) *Fundamentals of vehicle dynamics*. Premier Series Books, Warrendale, SAE International, PA 15096–0001, pp 101–109, 198–199
4. Weir DH, Klein RH, Zellner JW (1982) Crosswind response and stability of car plus utility trailer combinations. SAE International, vol 91, sect 1: 820003–820283, pp 570–583
5. Vančura J, Slavík J (2015) Crosswind sensitivity of road vehicles. In: 10th FKFS-conference progress in vehicle aerodynamics and thermal management
6. Guilmineau E, Chikhaoui O, Deng GB, Visonneau M (2013) Cross wind effects on a simplified car model by a DES approach. *Comput Fluids* 78:29–40
7. Guilmineau E, Chometon F (2009) Effect of side wind on a simplified car model: experimental and numerical analysis. *J Fluids Eng* 131(2):021104

8. Retrieved from https://en.wikipedia.org/wiki/Cyclone_Hudhud#:~:text=Extremely%20Severe%20Cyclonic%20Storm%20Hudhud%20%5Bnb%201%5D%20was,circulation%20in%20the%20Andaman%20Sea%20on%20October%206. Accessed on 9th Aug 2022
9. Retrieved from <https://www.windfinder.com/#10/17.9807/83.5304>. Accessed on 10th Aug 2022

Proposal of a Mutual Inertia Force Coupling on the Wake Oscillator Model for Vortex-Induced Vibrations



Adithya Krishna Menon and V. Vinod

Abstract A set of low-order models, used for determining vortex-induced vibrations of a rigid cylinder with elastic support in a uniform flow, were proposed and analysed. A Van der Pol equation is used for modelling wake dynamics which describe the dynamic behaviour of vortex shedding. The wake oscillator links with a one degree of freedom structural oscillator. The coupling terms which model this fluid–structure interaction are considered. The model dynamics are probed analytically and compared to experimental results. Multiple models are proposed involving mutual interaction of couplings and time delay functions. The most appropriate model is determined. The results are to be compared to experimental results and prior linear structural oscillator results. In order to achieve this, the original coupling with linear structural oscillator is recreated, and multiple new approaches to develop it are attempted.

Keywords Structure-wake oscillator · VIV model · Mutual coupling · Time delay · Lock-in region

1 Introduction

Vortex-induced vibration (VIV) is a phenomenon where either a body interacting with an external fluid flow experiences some induced motions or the motion of the body produces periodic irregularities on the fluid flow. It is created by vortex shedding at the back of bluff bodies and could degrade structural performance causing failure. Vortex shedding is an oscillating flow formed when a fluid flows past a body at specific velocities which depends on the geometry. The fluid flow generates low-pressure vortices downstream of the object, which tends to move towards this low-pressure zone. It is an important consideration for offshore structures including pipes, mooring lines, and other equipment and must be accounted for designs.

A. K. Menon · V. Vinod (✉)

Department of Mechanical Engineering, Mar Baselios College of Engineering and Technology, Trivandrum 695015, India
e-mail: vinodv@mbcet.ac.in

The prediction of dynamic behaviour in structures with VIV involves several methods [1]. One method involves resolving Navier–Stokes equations for the fluid engulfing the cylinder by direct numerical simulation and find hydrodynamic loads. This approach is cumbersome due to the determination issues of Reynold’s number associated with many industrial use cases [2]. An alternative is to use phenomenological models based on wake oscillators which could reveal the basic physics of VIV. This enables the dynamics of wake oscillators for 2-D VIV to be developed. There is a requirement for critical analysis based on the primary behaviour associated with the most basic configurations of the model. This is to be attempted in the present work by using various lower order models.

2 Literature Review and Objective

The transverse vortex-induced vibration of a rigid cylinder with elastic support in a fluid flow was studied [2] by Govardhan and Williamson. The experiment was conducted with help of a hydro-elastic facility having provision for a vertical cylinder in the free stream fluid to move transversely. The cylinders used were of a specific diameter and length to diameter ratio with a variable mass ratio. Various transducers were used to measure lift, drag, and displacement. The experiment sought to answer multiple questions regarding such a conceptually plain case of a rigid cylinder with elastic support including modes of response and corresponding wake dynamics, phase-jump phenomenon, and effects of mass ratio.

Concurrent force, displacement, and wake vorticity measurements are used for the first time ever in free vibrations. Two definite types of response are seen depending on the value of a combined mass damping parameter. In case of a high combined parameter, the initial as well as lower branches flank a discontinuous mode transition jump in amplitude and phase is observed. However, for lower combined parameter values, a higher amplitude upper response branch is observed, and thus, two mode transitions are observed. For extremely low mass ratio, vibration frequency amidst synchronization was noted to have increased substantially.

Another study aims to overcome shortcomings in wake oscillator models present in other literature, by modifying them and using a new method to determine empirical parameters used in the wake oscillator model [3]. These parameters are taken from experimental data, which are based on a forced wake oscillator with a fixed structure which has vortex shedding behind it. These results are compared with the experimental data and results from model described in Facchinetti et al. [1].

The Van der Pol equation-based equation was originally developed by Skop and Balasubramanian [4]. It is the governing equation for one component of the varying lift force on the cylinder. The fresh model preserves the modal scaling principle for structural response. This was predicted by the previous models and also verified experimentally. It also provides asymptotic, self-limiting structural response at zero structural damping due to a stall term, which was not found with previous models.

The vortex-induced dynamics of a uniform cylinder pivoted in uniform and shear flow are experimentally investigated [5]. It was based on the Van der Pol oscillator model. Comparisons between experimental and numerically predicted behaviour are made.

This paper details experiments conducted regarding transverse oscillations of a rigid cylinder with elastic support at extremely low mass and damping [6]. It finds that two distinct responses exist which depend on the value of a combined mass damping parameter. For low values, three modes of response are observed, while at higher values only two branches are obtained.

A cylinder in a cross flow is modelled in a simple manner to capture all the essential features. This is due to the issues connected with a full theoretical analysis using Navier–Stokes equation. A double oscillator model involving direct energy transfer is explored [7].

This work analyses existent structure–wake oscillator models modelling VIV in a rigid cylinder with elastic support in a uniform fluid flow [8]. The parameters used in numerical simulations are from experimental studies. Nonlinearity was introduced in the structural oscillator, to probe the possibility of improved results compared to existing models. Three coupling models were explored: displacement, velocity, and acceleration. The inclusion of nonlinear cubic term in the equation of structure was found to be inconsequential for a better result. Additionally, it could not describe the major issue of the acceleration model in previous literature with numerical simulations, which was the inability to replicate experimentally observed amplitude response.

By introducing these new coupling models, the objectives are to seek any changes in lock-in domains, characterize the effects on wake oscillator behaviour as well as the coupled system, and compare the results to those obtained by experimental study in Govardhan and Williamson [2].

3 Methodology

Numerical simulations were conducted using MATLAB. Three main solvers were employed: ode45, ode23s, and dde23 solvers.

3.1 Model 1: Structure–Wake Oscillator Model

A set of low-order structure–wake oscillator models for transverse VIV of elastically supported rigid cylindrical structures in stationary and uniform flow is investigated [1]. The wake region, which can be described as a creation due to the varying nature of vortex shedding, was modelled using Van der Pol equation. Meanwhile, a single degree of freedom oscillator was used for describing the cylindrical structure. Nonlinear coupling terms for the fluid–structure links were ignored. The constant

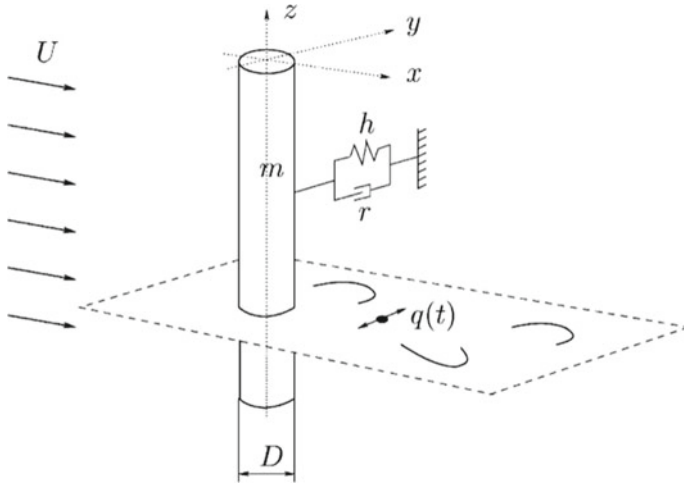


Fig. 1 Model of coupled linear structure and wake oscillators for 2-D VIV [1]

values of model parameters are initially taken from experimental data involving a forced wake oscillator, modelling the vortex shedding beyond a fixed structure.

The two oscillators considered are a structure oscillator and a wake oscillator. The structure is a single degree of freedom rigid cylinder with elastic support and diameter D . It is controlled to oscillate transversely to a uniform stationary flow having free stream velocity U . The wake oscillator is considered as a nonlinear oscillator using Van der Pol equation, which has been widely used for this flow since it is similar to self-sustained oscillation. The structure–wake oscillator model can be portrayed as in Fig. 1.

The structure oscillator in the form of a rigid cylinder is represented by:

$$m\ddot{Y} + c\dot{Y} + kY = S \tag{1}$$

To the Eq. (1), the following parametric terms are substituted: γ , Ω_2 , Ω_1 , ξ and μ ; to obtain the equation:

$$\ddot{Y} + \left(2\xi\Omega_2 + \frac{\gamma\Omega_1}{\mu}\right)\dot{Y} + \Omega_2^2 Y = \frac{S}{m} \tag{2}$$

Equation (2) is further reduced to:

$$\ddot{Y} + n\dot{Y} + \Omega_2^2 Y = \frac{S}{m} \tag{3}$$

where

$$n = \left(2\xi\Omega_2 + \frac{\gamma\Omega_1}{\mu} \right)$$

The typical wake oscillator model uses a single degree of freedom to showcase wake beyond a rigid cylinder. Wake oscillation is modelled as a function of time, say $q(t)$, which uses a wake equation of motion. This is typically a nonlinear, second order, ordinary differential equation. The main aim behind this wake oscillator paradigm is to model the fluctuating lift force. The wake oscillator is represented by Van der Pol’s equation:

$$\ddot{q} + \varepsilon(q^2 - 1)\dot{q} + \Omega_1^2 q = F \tag{4}$$

where

$$\varepsilon = E\Omega_1$$

The equations are converted into dimensionless form by using dimensionless time coordinate $t = T\Omega_f$ and space coordinate $y = Y/D$ leading to the following equations:

$$\ddot{y} + n\dot{y} + \delta^2 y = s = Bq \tag{5}$$

$$\ddot{q} + \varepsilon(q^2 - 1)\dot{q} + q = f \tag{6}$$

where

$$\delta = \frac{\Omega_s}{\Omega_f} = \frac{1}{S_t * U_r}$$

The Strouhal number provides a relation between shedding frequency and flow velocity and an inherent dimension of the body. It is defined as

$$S_t = f_{st} * \frac{D}{U}$$

Here, f_{st} is vortex shedding frequency, also called Strouhal frequency for a resting body. The Strouhal number for a cylinder is around 0.2 over a prominent range of flow velocity values. This allows us to overcome the issue of inaccuracy of Reynold’s number for practical applications.

Dimensionless variables are used to describe the oscillator systems so that the number of variables can be lowered. This reduces experimental data requirements and ignores unit systems.

Dynamical behaviour of the coupled model has been described by exploring the lock-in domain of various couplings. The phenomenon of lock-in, also termed as

frequency synchronization, happens when vortex shedding frequency is comparable to fundamental natural vibration frequency of a structure. This may result in huge, damaging vibrations in the structure. Lock-in domain is represented as a graph between amplitude and reduced velocity. Lock-in domain represented as a graph between amplitude y_0 and reduced velocity U_r .

This was done by using experimental values from various literatures. It must be noted that to keep the model fundamentally simple, fluid–structure coupling terms on the right side of equations are limited to linear functions of q and y . Thus, the only nonlinear term is that of Van der Pol wake oscillator.

Three low-order coupling models are examined and compared for their description of 2-D VIV phenomena. These are as follows:

- Displacement coupling $f = Ay$
- Velocity coupling $f = A\dot{y}$
- Acceleration coupling $f = A\ddot{y}$.

3.2 Model 2: Mutual Interaction in the Coupling Term

In the structure–wake oscillator model by Facchinetti et al. [1] as described in Sect. 3.1, it was specified that the fluid–structure coupling terms on the right side of the equations were limited to linear functions of q and y . This meant that the interaction between wake oscillator model created due to the fluid flow and that of the elastically mounted rigid cylindrical structure oscillator was limited to the left-hand side of the equations. This model has limitations in trying to obtain results obtained experimentally by literature such as Govardhan and Williamson [2].

The proposed model provides a stronger mutual interaction, intending to mimic practical experimental results by numerically simulating the structure–wake interaction in a more realistic manner. In order to facilitate this, the right-hand side of the wake oscillator equation which contains the Van der Pol term on the left-hand side would incorporate an acceleration coupling term based on the wake oscillator variable q . The proposed equations would thus be:

$$\ddot{y} + n\dot{y} + \Omega_2^2 y = s = Bq \quad (7)$$

$$\ddot{q} + E(q^2 - 1)\dot{q} + \Omega_1^2 q = f = A(\ddot{y} - \ddot{q}) \quad (8)$$

This mutual inertia force coupling interaction is validated with existing models and studies.

3.3 Model 3: Introducing Time Delay in the Coupling Term

The mutual interaction model described earlier presumes that the structure–wake interaction occurs instantaneously. Due to this, variations in the parameter of time were not given any role in the proposed numerical model.

In practical systems, this may not be the case. Delays may be experienced due to the time taken for physical interactions to occur. To incorporate these factors into the numerical representation of the proposed model, delay differential equations are used. A delay differential equation can be described as a differential equation, where the derivatives at a particular instant of time is given by values at a certain previous time instant. The extent of this delay is subject to change depending on the history of the equations. These time delays may also be constant, time dependent or state dependent.

In the proposed time delay for mutual interaction coupling term, constant time delay was used. The time delay was represented by a time lag τ .

Multiple variations of the time delay incorporated equations were explored. Initially only the structure variable in right-hand side of wake oscillator equation was given a time delay as follows:

$$\ddot{y} + n\dot{y} + \Omega_2^2 y = Bq \tag{9}$$

$$\ddot{q} + E(q^2 - 1)\dot{q} + \Omega_1^2 q = A(YT - \ddot{q}) \tag{10}$$

where

$$YT = \ddot{y}(t - \tau).$$

The next variation incorporated time delay in both variables in right-hand side of wake oscillator equation:

$$\ddot{y} + n\dot{y} + \Omega_2^2 y = Bq \tag{11}$$

$$\ddot{q} + E(q^2 - 1)\dot{q} + \Omega_1^2 q = A(YT - QT) \tag{12}$$

where

$$QT = \ddot{q}(t - \tau).$$

Another variation explored involved time delay in right-hand side of the structure oscillator equation, in addition to that in right-hand side of wake oscillator equation:

$$\ddot{y} + n\dot{y} + \Omega_2^2 y = Bq(t - \tau) \tag{13}$$

$$\ddot{q} + E(q^2 - 1)\dot{q} + \Omega_1^2 q = A(YT - QT) \quad (14)$$

Various initial input values are to be provided for the variables associated with the equations used. Many of the constant variables used are listed below:

- $A = 12$, forcing term parameter
- $\xi = 0.8$, structure reduced damping
- $\Omega_1 = 1$, vortex shedding angular frequency
- $\varepsilon = 0.3$, damping coefficient
- $S_t = 0.21$, Strouhal's number
- $\gamma = 0.8$, stall parameter.

Various other initial input values are variables which depend on specific conditions and user inputs.

4 Results and Discussion

These lower order models will capture VIV dynamics based on the following two parameters: mass ratio m^* and reduced flow velocity U_r .

Mass ratio is directly dependent on mass number M while reduced velocity U_r is primarily dependent on Ω_s , which is the structural angular frequency. These two parameters will be varied across various ranges and compared to determine various characteristics.

The main experimental literature [2] had observed two different types of response depending on mass ratio m^* and damping ξ . This is represented as a combined mass damping parameter $m^*\xi$. The main contributor to change in this parameter $m^*\xi$ is mass ratio. The two distinct responses were observed at high and low mass ratio values. The following sections will provide details on the numerical analysis results obtained for each mass ratio regime.

4.1 Synchronization Between Structure and Wake Oscillators at Low Mass Ratio

Oscillation amplitude response at low mass ratio is determined by taking value of forcing term B in the right-hand side of structure oscillator, which is dependent on mass ratio, which in this case is a low, $m^* = 0.52$. Damping coefficient ξ is taken as 0.0052. Using these and previously mentioned parameters, oscillation amplitude response plot is drawn with reduced velocity U_r in the x-axis and y_0 in y-axis. Existing low-order model is by Facchinetti et al. [1] is initially compared to experimental results as shown in Fig. 2. It is evident that while the existing model qualitatively

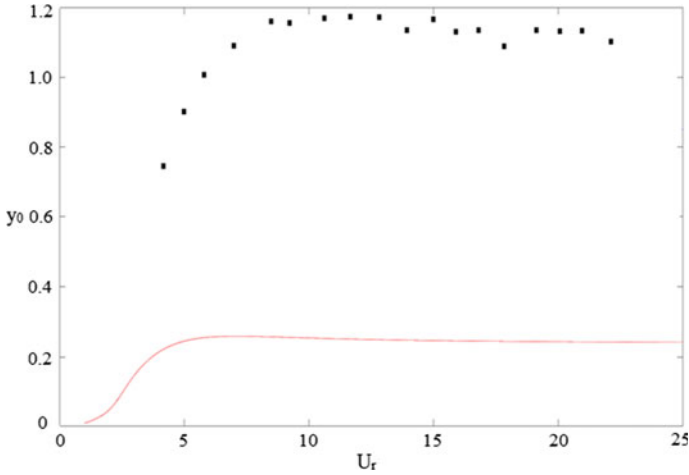


Fig. 2 y_0 versus U_r for experimental results (represented by black dots) and existing low-order model (red)

shows the synchronization of oscillators, it is incapable of quantitatively portraying experimental results obtained by Govardhan and Williamson [2].

However, when the proposed model with mutual interaction as described in Sect. 3.2 was considered and plotted in a similar fashion, it was found that the model showed robustness in matching experimental results and capturing VIV dynamics. As seen in Fig. 3, it can be seen that the proposed mutual interaction model not only maintained the qualitative conformity of Facchinetti et al. to the experimental results by Govardhan and Williamson [2], but was also able to quantitatively outperform the existing model substantially.

This is a significant result as existing literature had been unable to obtain such a quantitative improvement and robustness in matching VIV dynamics obtained experimentally.

Next, to analyse the lock-in domain as a function of mass ratio in lower mass ratio regime, m^* and U_r were varied while damping coefficient $\xi = 0.0052$. This is to check influence of m^* in proposed model. Mass ratio m^* is represented along x-axis and reduced velocity U_r along y-axis.

It can be seen from Fig. 4 that the proposed low-order mutual interaction model was able to fully capture experimental values at low mass ratios. This is an improvement over existing model by Facchinetti et al. [1] which was unable to fully capture experimental values although it was able to qualitatively portray the synchronization of oscillators.

The proposed model showed robustness in matching experimental results and capturing VIV dynamics. However, the range of m^* obtained was substantially larger than experimental values, specifically the upper bound values which could not be included in Fig. 4. The lower bound values completely conform to experimental values at low mass ratio.

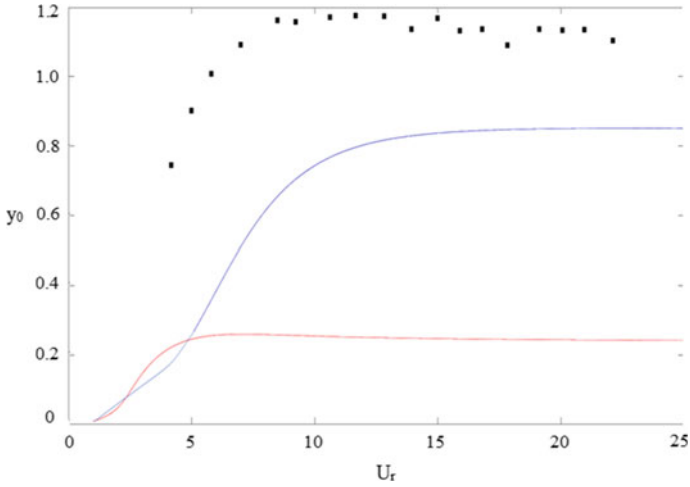


Fig. 3 y_0 versus U_r for experimental results (represented by black dots) and existing low-order model (red) in comparison with proposed mutual interaction model (blue)

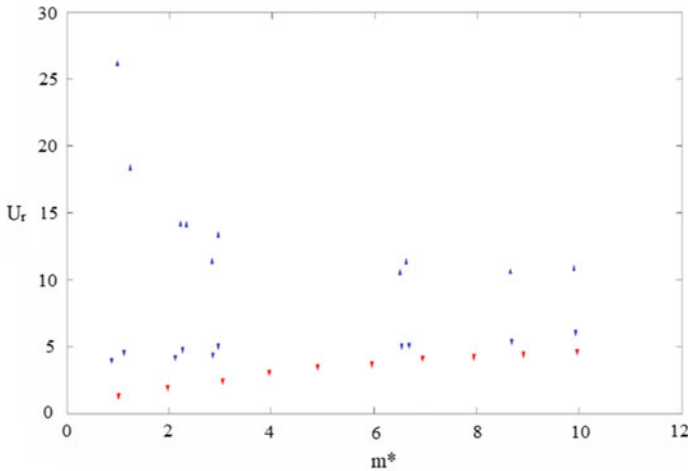


Fig. 4 U_r range for experimental results (blue) and proposed low-order model (red) based on mass ratio

4.2 Synchronization Between Structure and Wake Oscillators at High Mass Ratio

Validation of proposed model, described in detail in Sect. 3.2, with existing model was conducted. This was done by comparing amplitudes of structure oscillator y_0 and wake oscillator q_0 with reduced velocity U_r .

This value of forcing term B in the right-hand side of structure oscillator is dependent on mass ratio m^* . The value of B is taken as 0.0002 and is derived from a high mass ratio $m^* = 250$. Damping coefficient ξ is taken as 0.0031 from experimental literature Govardhan and Williamson [2]. The following plots show that the proposed model is equally as good as the existing model in demonstrating amplitudes albeit at different reduced velocity ranges.

4.3 Incorporation of a Constant Time Delay Function to Improve Synchronization Characteristics

The proposed model has shown robustness in capturing VIV dynamics. However, it has also shown the necessity of exploring certain dynamics further. This includes the large upper bound U_r values at low mass ratio (Fig. 4), indicating the need to narrow down the U_r range as well as the shift in lock-in domain (Figs. 5 and 6).

The use of a time delay function, as described in Sect. 3.3, was attempted to overcome existing limitations of validation and to optimize the improvements noticed in the proposed model, further matching it with experimental results.

It was found that for most relevant time lag τ applicable to the equations, the results were at no point better than that of proposed model without time delay. This was the case in all three types of time delay equations described in equation sets (9,10), (11,12), and (13,14). Hence, the incorporation of constant time delay functions can be considered to have failed.

5 Conclusions

In this work, we try to study three distinct types of low-order models for vortex-induced vibrations. The model comprises two governing equations; the first one is of the structure onto which the VIV are developed; the second one refers to the self-sustained oscillations of the vortex street modelled as wake oscillator by Van der Pol term. The models proposed here are the mutual interaction model, mutual interaction model with constant time delay, and fractional order model. In the initial phase of the work, truncated equations of amplitude and phase were obtained using method of averaging, and existing results in model by Facchinetti et al. [1] were reviewed. Oscillation amplitude response plot is drawn with reduced velocity U_r in the x-axis and y_0 in y-axis for low mass ratio $m^* = 0.52$. It showed notable quantitative robustness in capturing VIV dynamics, matching experimental results in Govardhan and Williamson [2] substantially more than previous models. The proposed model also showcased its ability to encapsulate the entire experimental regime as seen in Fig. 4, with lower bound values closely matching experimental values. However, there is a need to further optimize the upper bound values and narrow the U_r range.

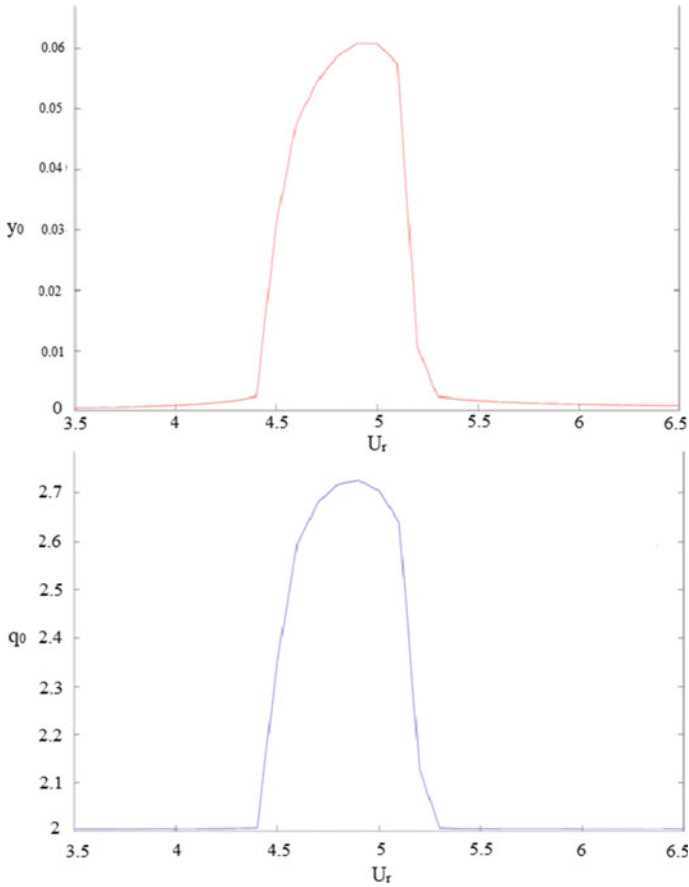


Fig. 5 y_0 versus U_r graph of structure (top) and wake (below) oscillators of existing model in Facchinetti et al. [1]

In an attempt to further optimize the obtained results and increase conformity with experimental results, a constant time delay function was incorporated on the right-hand side of the oscillator models. At higher mass ratio $m^* = 250$, the proposed model was able to demonstrate its ability to capture amplitudes albeit at different reduced velocity range.

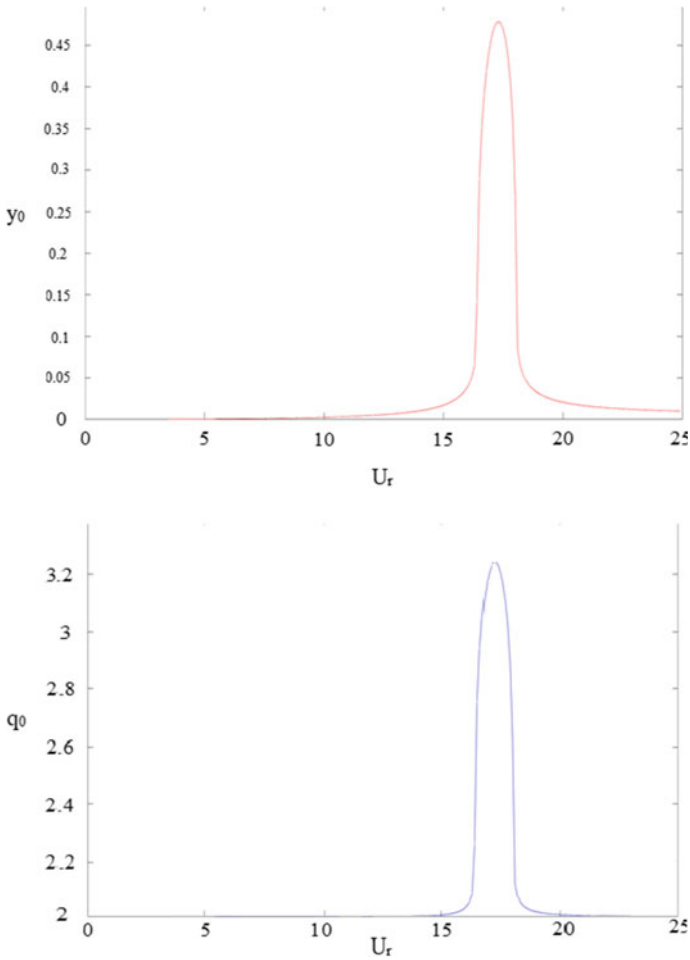


Fig. 6 y_0 versus U_r graph of structure (top) and wake (below) oscillators of proposed model

6 Future Work

All the models described in this work involved models numerically described as differential equations with integer orders. However, in order to obtain numerical simulation results with greater conformity to experimentally obtained results, fractional order coupling in structure–wake oscillator can be attempted. These equations contain derivatives of non-integer order and can include fractional values.

Nomenclature

Ω_1	Vortex shedding angular frequency
Ω_2	Structural angular frequency
δ	Structure reduced angular frequency
ξ	Structure reduced damping
ε	Damping ratio
γ	Stall parameter
St	Strouhal's number
f, s	Forcing terms
μ	Dimensionless mass ratio
M	Mass number
C_L	Vortex lift coefficient
U_r	Reduced velocity
Ω	Common angular frequency
A, B	Forcing term parameters
q_0, y_0	Amplitudes

References

1. Facchinetti ML, de Langre E, Biolley F (2004) Coupling of structure and wake oscillators in vortex-induced vibrations. *J Fluids Struct* 19(2):123–140
2. Govardhan R, Williamson C (2000) Modes of vortex formation and frequency response of a freely vibrating cylinder. *J Fluid Mech* 420:85–130
3. Xu W-h, Wu Y-x, Zeng X-h, Zhong X-f, Yu J-X (2010) A new wake oscillator model for predicting vortex induced vibration of a circular cylinder. *J Hydrodyn Ser B* 22(3):381–386
4. Skop RA, Balasubramanian S (1997) A new twist on an old model for vortex-excited vibrations. *J Fluids Struct* 11(4):395–412
5. Balasubramanian S, Skop RA, Haan Jr FL, Szweczyk AA (2000) Vortex-excited vibrations of uniform pivoted cylinders in uniform and shear flow. *J Fluids Struct* 14(1):65–85
6. Khalak A, Williamson CHK (1999) Motion, forces, and mode transitions in vortex-induced vibrations at low mass damping. *J Fluids Struct* 13(7–8):813–851
7. Krenk S, Nielsen SRK (1999) Energy balanced double oscillator model for vortex induced vibrations. *J Eng Mech* 125(3):263–271
8. Vigneshvar V, Viswanth SR, Venkateshwaran S, Balam B (2019) A comparative study of wake oscillator models for flow induced vibrations. *AIP Conf Proc* 2134:080006

Kinematics of a Low Aspect Ratio Pitching Flexible Panel—A New Insight



Kakulamrri S. N. Abhinav Kumar, Parag J. Deshpande, Ravi Dodamani, and Geetanjali N. Alle

Abstract Experimental work was carried out to understand the kinematics of a low aspect ratio pitching flexible panel. Force measurements and high-speed imaging technique was used in the present study. We observed that due to elastic deformation, the trailing edge of the flexible panel was found to trace a figure-of-eight trajectory during the pitching cycle. The extent of the figure-of-eight loop indicates the phase lag between the leading and trailing edge of the flexible panel, which was also found to increase and reduce with an increase in the pitching frequency and incoming flow, respectively. There is a distinct difference between the time and phase evolution of the instantaneous thrust production for the rigid and flexible panel is observed.

Keywords Pitching motion · High-speed imaging · Thrust generation · Phase lag

1 Introduction

Biomimetics research has been helping the miniaturization of unmanned aerial vehicles (UAVs) and autonomous underwater vehicles (AUVs). This led to the development of micro-air vehicles (MAVs) and handheld AUVs. In the present research, we focus mainly on the fish-like propulsive mechanism. Fish generates the required thrust for their motion by the undulating movement of their tails. It has been reported by Triantafyllou et al. [1] that a rigid panel moving in a simple harmonic motion produces thrust. This thrust is produced because of reverse Karman vortex street generation in the wake. Heathcote and Gursul [2] reported the effect of flexibility on the propulsive efficiency of the 2D and 3D foils.

The undulating flexible panel in water broadly represents the locomotion of sea animals like fish, eel, etc. Generous literature [1–5] is available on hydrodynamics

K. S. N. Abhinav Kumar (✉) · P. J. Deshpande · R. Dodamani · G. N. Alle
UAV Division, CSIR, Bangalore, NAL 560017, India
e-mail: abhinav.nal22j@acsir.res.in

K. S. N. Abhinav Kumar · P. J. Deshpande
Academy of Scientific and Innovative Research (AcSIR), Ghaziabad 201002, India

of oscillating foils and/or panels having varied flexibility characteristics. However, while discussing the role of foil/panel flexibility, most of the pertinent literature focused only the time-averaged quantities like hydrodynamic thrust and torque data, power consumption integrated over a cycle, etc. Until last year Deshpande and Vishwasrao [6] elaborated on the mechanism of instantaneous force generation in a flexible pitching panel for the first time. They showed that the inception of the trailing vortex formation, the panel's elastic deformation (bending), and force generation occur simultaneously in a pitching cycle. Deshpande and Modani [7] showed the time-averaged thrust data variation as a function of flapping frequency for various wing configurations in a bird-like flapping wing. It was shown that for most of the flexible wing configurations, there is an increase in the mean thrust with an increase in the flapping frequency up to a specific frequency, and the thrust generation was found to saturate beyond that frequency. Whereas for rigid wings, the thrust increased approximately with a square flapping frequency. As per our knowledge, no information is available stating the effect of frequency/amplitude and incoming flow on the dynamic deformation characteristics of the panel.

The present study is an extension of the work reported in Deshpande and Vishwasrao [6], where we would like to understand the elastic deformation characteristics of the flexible panel under the different pitching frequencies and flow conditions (without and with the incoming flow). This work will help optimize the panel's hydrodynamic performance as a bio-inspired propulsor. Also, the kinematic and dynamic data from the present study will assist in the application of active deformation while designing a bio-inspired propulsor.

2 Methodology

The present study was carried out in a newly designed re-circulation type water tunnel at CSIR-NAL, Bangalore, the schematic of which is shown in Fig. 1. The tunnel has a rectangular section having 0.3 m in width and 0.4 m in height. The test section has a 1 m length. An acrylic window having a matching size with the test section length and width is used as a top lid, and the tunnel was filled with water till the bottom surface of this lid to avoid wiggle formation in the test section in running condition. The tunnel is driven by a 5 HP AC motor coupled to a centrifugal pump. The rate of discharge of the pump is about 750 LPM giving an average velocity inside the test section of about 80 mm/s. A solid stainless steel (SS) shaft assembly having 8 mm diameter and 500 mm length was immersed vertically in the tunnel, and its top end was connected to the high-speed brush-less digital servo (HiTech HS7954SH), and the bottom end was free-kept 150 mm above the tunnel floor. A cylindrical hollow sleeve was used to connect two parts of the shaft with the help of screws (Fig. 1). Dismantling the longer part of the shaft (immersed in water) and changing the panel configuration became easy due to the provisioning of the sleeve. The present study considers two panel configurations with different thicknesses (h). Both the panels had the same aspect ratio of 0.625, with a chord length of 72 mm and a width of

45 mm. The flexible and rigid panels had 0.5 and 2 mm thicknesses, respectively. A rectangular sleeve screwed to the shaft from the bottom was used to fix the panel, like a sandwich between two rectangular SS plates. A streamlined shape was given to the panel fixture sleeve to have less disturbance in the flow before it interacts with the pitching panels. Sinusoidal pitching motion ($\theta_{LE} = \theta_m \cos(2\pi ft + \pi)$) was given to the shaft. Since there is only a marginal gap between the shaft axis and the leading edge of the panel, it can be assumed that the leading edge has no translational motion.

The servo used to pitch the panel has an in-built encoder which gives feedback information regarding the instantaneous position of the servo to the servo's internal electronics. This feedback information is in the form of voltage and is tapped to collect the instantaneous positional data. Since this data is in the form of voltage, it is calibrated to get the positional data in degrees.

The experiments were performed with and without incoming flow for these two panel configurations. The pitching frequency was changed from 1 to 3 Hz at a step of 0.25 to 2 Hz, and then with a step size of 0.5 Hz, measurements were performed for the remaining frequencies of 2.5 and 3 Hz. Four different pitching amplitudes of $\pm 10^\circ$, 15° , 20° , and 25° were considered for the measurements.

Hydrodynamic forces and torques were measured using a six-component ATI mini 40 F/T sensor which was mounted above the servo on the 8 mm thick SS plate, and the forces and torques experienced by the panel were transferred to the sensor using four MS studs fixed to the horizontal acrylic plate (Fig. 1). The whole assembly of the set-up was mounted on the Linos rails to have the freedom to move and adjust the shaft position in all three directions.

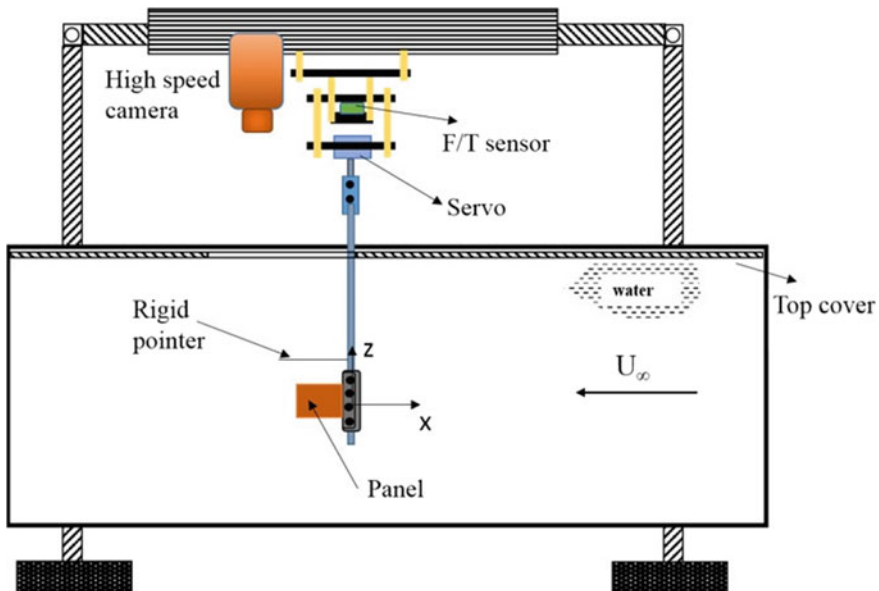


Fig. 1 Schematic of the experimental set-up

A high-speed camera (Phantom 4 M, 430 series) was mounted upside down on the Linos rail above the shaft. Two SS rods having 1.5 mm diameter and 100 mm length were inserted and fixed into the two radially drilled holes 90° to each other, as shown in Fig. 1. These two rods were used as a pointer or moving axes to understand and quantify the deformation characteristics of the flexible panel.

The data from the ATI mini 40 and the positional data from the servo encoder were acquired simultaneously using a NI-USB-6210 DAQ card, and the data were recorded in excel format using LabVIEW. For force measurements, the data were acquired at a sampling rate of 4800 samples per second, and with a moving average of 20 samples, the effective sampling rate became 240 Hz. After the force data is tared, the sample acquisition was commenced, then the pitching motion of the panel was started, and after 15 s, the pitching motion was stopped before stopping the sample acquisition. Because of this data acquisition scheme, we could monitor the force data before and after the pitching of the panel.

The high-speed imaging was performed at 480 FPS speed at a maximum resolution of the 4 MPs. The camera was focused at the midsection along the width of the panel. Using the freeware PCC image processing tool, the instantaneous position of the trailing edge, its trajectory, and its velocity were determined in a cycle. The high-speed imaging was performed only for two frequencies of 1.75 and 3 Hz pitching at an amplitude of $\pm 20^\circ$ for both the panel configurations, with and without incoming flow.

3 Results and Discussion

(A) Time-Averaged Force Data

Figure 2a and 2b shows the variation in mean thrust for the flexible and rigid panel as a function of pitching frequency for quiescent fluid and moving fluid conditions, respectively. For the flexible panel, a general trend shows an increase in the thrust generation with an increase in amplitude and frequency (Fig. 2a). There is a threshold frequency of around 2.5 Hz, beyond which thrust generation is found to get saturated. For the lowest amplitude of $\pm 10^\circ$, the frequency threshold has been reduced to 2 Hz, as depicted in Fig. 2a.

The rigid panel having $\pm 20^\circ$ pitching amplitude shows a monotonic increase in the mean thrust with an increase in the pitching frequency. It can be seen that the mean thrust is found to exceed the mean thrust generated by the flexible panel at 3 Hz frequency for the same amplitude $\pm 20^\circ$. For the incoming flow condition, we computed C_T ($C_T = T / 0.5\rho(U_\infty)^2cb$) for both the panels and plotted C_T as a function of reduced frequency ($k = 2\pi fc / U_\infty$) as depicted in Fig. 2b.

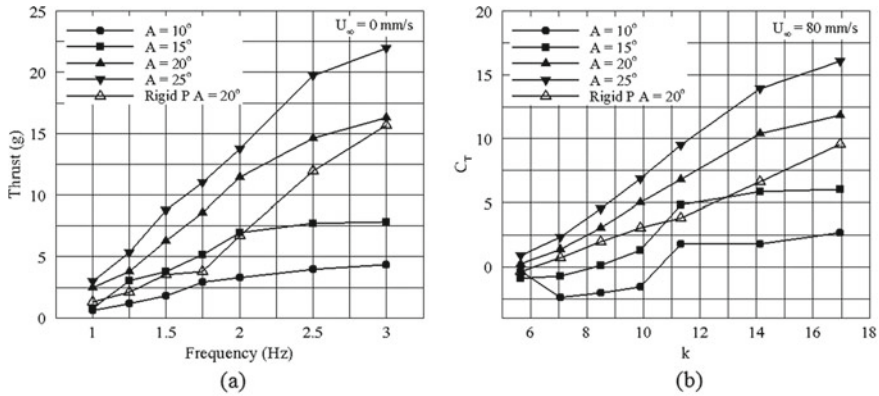


Fig. 2 Time-averaged force data of **a** quiescent flow and **b** with free-stream velocity of 80 mm/s

The interaction of incoming flow with the pitching panel causes the generation of drag. Thus, the F/T sensor records net thrust, i.e. subtraction of absolute thrust and the drag of the panel, and that has been considered while calculating C_T . As expected, there is a reduction in the net thrust for both panels. However, the drop in the thrust for rigid with the flow is substantial compared to the flexible panel (Fig. 2b). Unlike saturation of thrust for a flexible panel in a quiescent condition, we observed that with the flow, particularly at higher amplitudes, the C_T shows a monotonic increase with an increase in k . Due to flexibility, the panel can absorb some amount of the drag, which is reflected in the higher net thrust (higher C_T) even after k is more than 14.

(B) High-Speed Imaging

The pitching of the flexible panel is essentially leading to the passive elastic deformation of its trailing edge. Thus to understand the elastic deformation, the high-speed imaging technique is employed. We obtained the images from the freeware PCC image processing software at an interval of 2.08 ms. Moreover, the locus and velocity data of the trailing edge in a pitching cycle is obtained for rigid and flexible panels at two frequencies of 1.75 and 3 Hz for quiescent fluid and incoming flow conditions.

Figure 3a shows the locus traced by the trailing edge of the rigid panel pitching at two different frequencies in a quiescent fluid condition. At lower frequencies, the trailing edge is found to rotate about the pitching axis tracing a single circular arc, which shows that the leading and trailing edge motions are perfectly in sync with each other due to the absence of elastic deformation of the trailing edge. At 3 Hz, however, the circular arc has transformed into two tiny elliptical loops at both extremes of the stroke (Fig. 3a). These loops show that when the panel’s trailing edge is approaching the end of the stroke, there is an inception of the marginal phase lag between the leading and trailing edge of the panel. This lag is attributed to the elastic bending of the panel due to the

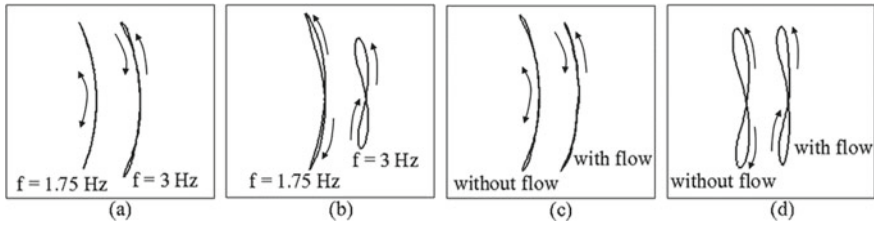


Fig. 3 Trailing edge locus for **a** Rigid panel in quiescent fluid, **b** Flexible panel in quiescent fluid, **c** Rigid panel pitching at 3 Hz, and **d** Flexible panel pitching at 3 Hz

generation of the high hydrodynamic torque acting at the panel's trailing edge. The increase in mean thrust with an increase in frequency (shown in Fig. 2a) is merely attributed to the increase in momentum imparted to the fluid due to the faster pitching of the rigid panel.

Figure 3b shows the locus of the trailing edge of the flexible panel pitching at 1.75 and 3 Hz frequency, respectively. Clearly, it can be seen that the trajectory of the trailing edge is no longer a circular arc, but in the form of a figure of eight. The figure-of-eight trajectory is found in all-natural flyers and swimmers utilizing undulating motion for their locomotion. Due to flexibility, the panel's trailing edge gets elastically bent during the rotation, causing phase lag between leading and trailing edge motion profiles. With an increased rotation speed, the panel gets bent even more; consequently, the phase lag also increases. Apparently, the locus for 3 Hz speed is broader when compared with the locus for 1.75 Hz speed, as depicted in Fig. 3b.

Figure 3c compares the trajectory of the trailing edge with and without flow for rigid panel pitching at 3 Hz. It can be seen that when there is an incoming flow, the tiny loop disappears, and the panel becomes straight, tracing a perfectly circular arc, indicating there is no lag between the leading and trailing edge of the panel. Similarly, in the case of the flexible panel, the size of the loop has shrunk with the flow (Fig. 3d). It means the incoming flow causes a reduction in the extent of the elastic bending of the panel. Referring to Fig. 2, we observed that the reduction in the thrust for rigid panel due to incoming flow at 3 Hz is more distinct when compared with the flexible panel thrust data. As discussed in the previous section, the part of the drag due to the flow might get utilized to reduce the elastic deformation of the panel, and hence, the actual drop in the net thrust is higher for the rigid panel.

Figure 4 shows the trailing edge velocity profiles for flexible and rigid panels against the normalized cycle time obtained from the image processing. The numbering given in Fig. 4 denotes the key locations of the panel during pitching, and the corresponding snapshot of the panel's dynamic position at these locations is depicted in Fig. 5. We also have calculated the velocity profile based on the sine function imposed on the pitching shaft. In the absence of elastic deformation, the velocity profile of the trailing edge of the rigid panel

was precisely following the theoretical velocity profile for both the pitching frequencies (results not shown here).

Figure 4a and b shows the trailing edge velocity profile for flexible panel pitching at 1.75 and 3 Hz frequencies in quiescent fluid, respectively. The phase lag between the theoretical and trailing edge velocity profiles as a consequence of the panel flexibility is visible in the plot. At the beginning of the new stroke (location 1), the leading begins to rotate clockwise, whereas the trailing edge of the panel is rotating anticlockwise with a significant speed ($V \sim 0.5$ m/s). At the inflection location, the panel becomes straight and continues moving towards the stroke’s left extreme (location 2). At location 3, the panel is brought to rest

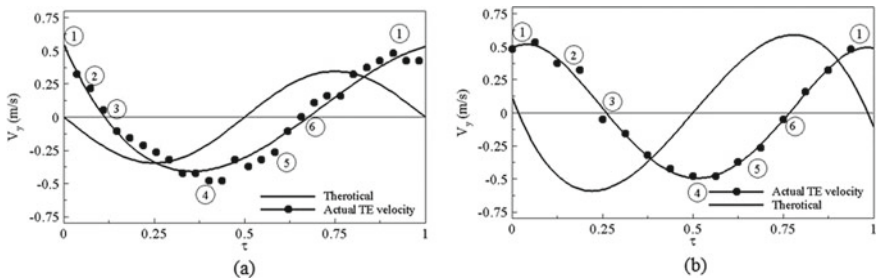


Fig. 4 Trailing edge velocity profiles of flexible and rigid panels at a 1.75 Hz and b 3 Hz

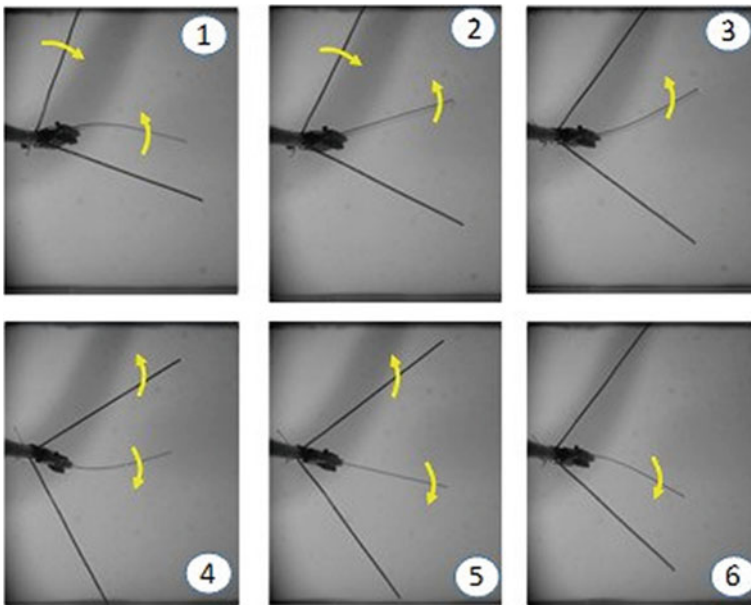


Fig. 5 Snapshots of the high-speed imaging of flexible panel moving at 3 Hz

and begins to rotate clockwise. Subsequently, it regains the speed, after the maximum speed of $V \sim -0.4$ m/s, it starts to decelerate in the second half of the cycle (location 4), and the cycle repeats. One noteworthy observation from the velocity profiles is that the maximum velocity of the trailing edge found exceeds the max theoretical velocity attributed to the effect of flexibility. Due to the no-slip condition, the fluid in the vicinity of the panel surface (especially the trailing edge) will also have the same velocity as that of the panel trailing edge.

The higher the tangential velocity higher is the strength of the trailing edge vortex. It can be linked directly to the instantaneous thrust generation. This might be why the flexible panel pitching at 1.75 Hz frequency has a higher mean thrust than the rigid panel pitching at the same frequency. Whereas, with further increase in the frequency, the flexible panel was found to have much higher elastic deformation resulting in saturation in the mean thrust generation. On the other hand, in the case of a rigid panel, in the absence of deformation (nominal bending), the mean thrust was nearly equivalent (marginally smaller) to the flexible panel pitching at 3 Hz frequency.

Figure 6 shows the time evolution of thrust production for rigid and flexible panels, with and without flow at 3 Hz and 20° pitching amplitude. The results show that the thrust evolution in the rigid panel case goes negative for a period of time. This means when the rigid panel is pitching, it creates a drag force temporarily. When compared to the flexible panel, where we can see that there is minimal thrust in the negative direction. This shows that the flexibility of the panel is helping the panel to generate the thrust without any losses caused due to the thrust going in the negative direction. From Fig. 6, we can also see that the time at which maximum thrust is produced almost matches the time when the trailing edge tip velocity is zero, as observed in Fig. 4. This tells us that the maximum thrust production matches the point where the tip velocity is zero.

In Fig. 3c, it is seen that the rigid panel has elastic deformation in without-flow condition, but it is absent in the with-flow condition. This lack of elastic deformation caused the panel to have no lag between the leading edge and the trailing edge. So, the maximum thrust production has to be at the start of the cycle, as seen in Fig. 6a.

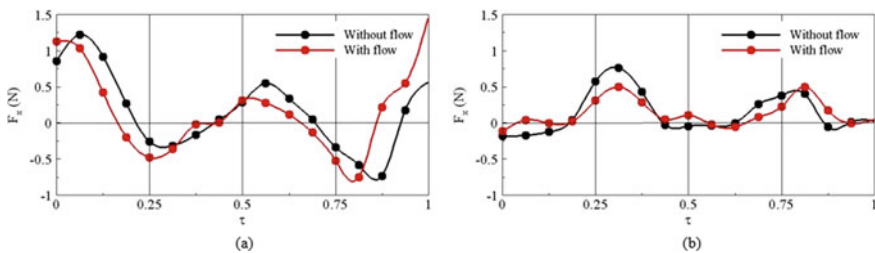


Fig. 6 Time evolution of thrust in **a** Rigid and **b** Flexible panels moving at 3 Hz with an amplitude of $\pm 20^\circ$

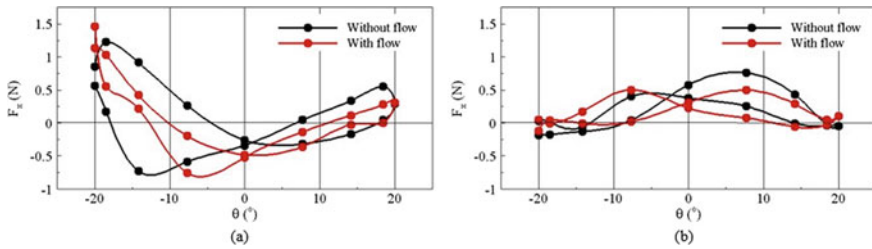


Fig. 7 Phase evolution of thrust in **a** Rigid and **b** Flexible panels moving at 3 Hz with an amplitude of $\pm 20^\circ$

For the flexible panel, when the time evolution of thrust is compared between with-flow and without-flow conditions (Fig. 6b), it is observed that the phase lag is minimal, and there is only a reduction in the peak thrust production for with-flow condition.

In Fig. 7, the data presented in Fig. 6 are shown with phase evolution between $\pm 20^\circ$ of pitching amplitude. This data indicate that the area inside the curves has reduced for the with-flow condition, which corresponds to the reduction in thrust for with-flow condition when compared to without-flow condition.

4 Conclusions

In this study, we investigated and compared the hydrodynamics of the low aspect ratio flexible panel against the rigid panel with pitching motion in quiescent and moving water conditions. Force measurements and high-speed imaging were performed for the range of pitching frequencies and amplitudes. The following are noteworthy observations from these measurements.

- There is an increase in the mean thrust with an increase in the amplitude and frequency of the pitching motion.
- The mean thrust for the flexible panel was found to be significantly higher than the rigid panel for the same amplitude to 2.5 Hz pitching frequency. At 3 Hz, however, the difference in mean thrust generated from the flexible and rigid panels was found to be nearly the same.
- The trailing edge of the flexible panel was found to trace the figure-of-eight trajectory due to the elastic deformation of the panel. Whereas TE of the rigid panel was found to trace perfect circular arc trajectory.
- At higher pitching frequency for the rigid panel, however, trajectory in the form of small elliptical lobes at the end of the pitching strokes suggests that the panel has some elastic bending towards the end of the strokes, which was not noticed in the earlier studies by Deshpande and Vishwasrao (2021).

- The velocity of the trailing edge is found to be higher than the theoretical velocity for the flexible panel, which indicates that the flexibility characteristics of the panel completely dominate the acceleration/deceleration of the trailing edge.
- The effect of incoming flow on the flexible panel's hydrodynamics showed a reduction in the net thrust production for both panels. The shrunk in figure-of-eight loop due to incoming flow indicates a reduction in the elastic deformation and, thus, the phase lag between the leading and trailing edges of the panel.
- There is a distinct difference between the time and phase evolution of the instantaneous thrust for rigid and flexible panels observed. For the rigid panel, the instantaneous thrust varied between positive and negative peaks resulting in a small positive mean thrust despite of very high absolute value of instantaneous thrust. Whereas for the flexible panel, the negative instantaneous peak thrust was found to be absent, and even though positive instantaneous peaks were smaller than the rigid panel, the overall mean positive thrust was higher than the rigid panel. The peak positive thrust production in both the rigid and flexible panels coincides with the trailing edge tip velocity going to zero or when the tip has maximum deflection. Also, maximum negative thrust production in rigid panel occurs when the trailing edge tip velocity is maximum. But in the flexible panel, when the trailing edge tip velocity is maximum, the thrust is maintained at almost zero rather than going negative. This effect of no negative thrust in the flexible panel might be due to the flexibility of the panel.
- The effect of elastic bending of the rigid panel, which is observed in 3 Hz without-flow condition, is absent in the with-flow condition. This effect can be seen in the transient thrust graph, where the peak positive thrust is also shifted accordingly.

Nomenclature

b	Span of the panel	m
c	Chord length of the panel	m
f	Frequency of pitching	Hz
k	Reduced frequency	–
C_T	Coefficient of thrust	–
T	Time averaged thrust	N
U_∞	Free-stream velocity	m/s
V_y	Trailing edge velocity	m/s
θ_{LE}	Leading edge pitching angle	°
θ_m	Maximum pitching angle	°
τ	Non-dimensional time	–

Acknowledgements The authors are grateful to the Director, CSIR-NAL, and the Head of the UAV Design and Integration Division for providing constant support and encouragement. This work is funded by the Department of Science and Technology (DST) under a Core Research Grant (CRG/2019/001445), Government of India.

References

1. Triantafyllou GS, Triantafyllou MS, Grosenbaugh MA (1993) Optimal thrust development in oscillating foils with application to fish propulsion. *J Fluids Struct* 7(2):205–224
2. Heathcote S, Gursul I (2007) Flexible flapping airfoil propulsion at low Reynolds numbers. *AIAA J* 45(5):1066–1079
3. Shinde S, Arakeri J (2014) Flexibility in flapping foil suppresses meandering of induced jet in absence of free stream. *J Fluid Mech* 757:231–250
4. Buchholz J, Smits A (2008) The wake structure and thrust performance of a rigid low-aspect-ratio pitching panel. *J Fluid Mech* 603:331–365
5. David M, Govardhan R, Arakeri J (2017) Thrust generation from pitching foils with flexible trailing edge flaps. *J Fluid Mech* 828:70–103
6. Deshpande P, Vishwasrao A (2021) Kinematics and dynamics of pitching flexible panels in a quiescent fluid. *J Fluid Mech* 922:A13
7. Deshpande P, Modani A (2019) Experimental investigation of fluid–structure interaction in a bird-like flapping wing. *J Fluids Struct* 91:102712

The Effect of Riblet Shapes on Flow Characteristics



Ishita Jain, Issam Wajih, and S. Sarkar

Abstract The effect of riblets with different cross-sectional shapes (i.e. semi-circular (RS), triangular (RT), and square (RSq)) on the spatially developing shear layer in the transitional regime is studied using large eddy simulations (LES). The imposed flow condition at the inlet is given by the value of Re_θ as 360, where Re_θ is defined as Reynolds number based on momentum thickness (θ). Further, the riblets are arranged in a series across the flow field, resulting them to be two-dimensional and homogeneous in a spanwise direction. The assumed values for the riblets' height and wavelength are $k = \delta^*$ and $\lambda = 3k$, respectively. The introduction of surface modifications has influenced the flow characteristics, which are being compared for the three simulated cases with the help of spanwise and time-averaged statistics. An early transition is observed in the presence of wall roughness, which is being supported with the contours of shear stress and *rms* profiles. The rough surface with triangular riblets experiences maximum growth of disturbance and hence early transition when compared to semi-circular and square riblets. Further, the stable recirculation region within the riblets is observed in all the three cases, which allowed the flow to skim over the roughness. Moreover, the time-averaged skin friction coefficient ($\overline{C_f}$) is evaluated above the roughness crest, and the maximum and minimum values of $\overline{C_f}$ are observed for the RT and RS, respectively.

Keywords Transition · Turbulence · Riblet shapes · Mean quantities

1 Introduction

Transition from laminar to turbulent is one of the prime concerns in aerospace industry and turbo machines. Transition is characterized with increase in viscous drag and energy consumption. Degradation of blade surface, due to operational and environmental factors over the years of service, induces roughness over the surface. Therefore, studies regarding roughness-induced transition are of particular interest.

I. Jain · I. Wajih · S. Sarkar (✉)

Department of Mechanical Engineering, IIT Kanpur, Kanpur 208016, India
e-mail: subra@iitk.ac.in

© The Author(s), under exclusive license to Springer Nature Singapore Pte Ltd. 2024
K. M. Singh et al. (eds.), *Fluid Mechanics and Fluid Power, Volume 2*, Lecture Notes in Mechanical Engineering, https://doi.org/10.1007/978-981-99-5752-1_51

631

Attempts have been made to understand roughness-induced transition and associated flow features. It is well established that roughness results in early transition and shortens the transition length. Thus, flow over the rough surface has been one of the areas attracting researchers over the years. Laminar and turbulent flow over different kinds of roughness has been extensively studied. However, transitional regime in these flows has been a less explored field due to the associated complexities.

2 Literature Review and Objective

Classification of roughness is often proposed following the associated flow field. One such classification is done by Perry et al. [1] considering the ratio of pitch (λ) to height (k) as governing parameter. For λ/k less than 4, roughness is referred to as d -type while for λ/k greater than 4 it is denoted as k -type. The d -type roughness is mainly characterized by stable recirculation zones between ribs, which skim the flow over the ribs resulting in drag reduction and no reattachment. In a k -type roughness, only a portion of the wall is covered by the recirculation zones formed, allowing reattachment. Djenidi [2] reported fluid outflow from the cavity for $\lambda = k$, which was computationally corroborated by Leonardi et al. [3].

Several studies can be enumerated regarding turbulent flow characteristics over roughened wall. Jimenez found that these characteristics can be controlled by varying roughness Reynolds number and blockage ratio (ratio of boundary layer thickness and rib height) [4]. Lee and Sung [5] simulated flow over transverse k -type square roughness and found self-similarity in mean profiles in the latter half of the domain. They took into account the form drag and found the mean flow field variables values to approach a constant value. Tachie and Adane [6] conducted experiments to study the effect of transverse ribs of semi-circular, circular, and square cross sections in a shallow turbulent open channel flow. They revealed that viscous drag in k -type roughness is greater than d -type. Mean flow characteristics for d -type roughness were nearly independent of rib geometry. Reshotko [7] proposed that transition of the boundary layer by destabilization of mean flow by the growth of disturbances is associated with small roughness levels. However, larger roughness levels distort flow locally inducing transition. Vadlamani et al. [8] found out transition onset was due to formation of alternating high and low speed streaks near the rough wall, destabilizing the shear layer.

Numerous studies have been conducted to gain insight into governing physics for flow transition and associated characteristics for different kinds of rib geometry. Biomimetic attempts in drag reduction and transition delay are inspired by nature, where evolutionally transformed fish and bird surfaces are mimicked. Notably, Muthukumar et al. [9] have studied the fish scales on laminar to turbulent transition. In their study, transition onset was delayed by 55% downstream, and 27% drag reduction was achieved. Transition delay was found to be associated with attenuation of T-S waves by fish scales and generation of streamwise streaks. Furthermore, they found that streak spacing and amplitude can be controlled by adjusting the spacing

between scale arrays and increasing the number of scales. Walsh [10] also got around 8% drag reduction for a symmetric V-groove, when rib height and spacing based on wall units were 10 and 15, respectively. Bhushan and Dean [11] fabricated and replicated shark skin riblets which impeded advancement of streamwise vortices, reducing vortex ejection into the outer boundary layer and a 10% reduction in viscous drag. Chen et al. [12, 13] conducted experimental investigation on herringbone (Plane 3D and spatial 3D ribs) inspired by bird morphology and calculated around 17–20% reduction in drag. Plane 3D ribs resulted in a maximum drag reduction of 17% with herringbone angle of 60°, while spatial 3D resulted in about 21% drag reduction. Benschop [14] carried out DNS of turbulent channel flow incorporating herringbone ribs for different orientations of ribs along with spatial variation of heights to study the drag and mean flow characteristics. Bechert [15] conducted experiments in oil channel with blade, scalloped, and triangular roughness profiles, at different spacing and height, oriented at different angles to the incoming flow. Drag reduction was found to be maximum for ribs aligned in flow direction due to damping of spanwise velocity component.

The literature was found to be relatively scarce for studies pertaining to the effect of geometry or shape on onset of transition, thus making it a viable research area. LES with dynamic subgrid modelling is used to study the effect of spanwise ribs of three distinct geometrical shapes, i.e. semi-circular, triangle, and square, on the flow field. Spanwise and time-averaged flow characteristics give us a picture of the way the flow transitions to turbulence and modification in drag.

3 Materials and Methods

In-house solver has been utilized to simulate the present problem using large eddy simulation. The filtered non-dimensional equations which are solved on a staggered grid are

$$\partial_i \bar{u}_i = 0 \tag{1}$$

$$\partial_t \bar{u}_i + \partial_j (\bar{u}_i \bar{u}_j) = -\partial_i \bar{p} / \rho + 2\partial_j (v \bar{S}_{ij}) - \partial_j \tau_{ij} + \bar{f}_i \tag{2}$$

where $\bar{S}_{ij} = 1/2(\partial_j \bar{u}_i + \partial_i \bar{u}_j)$ and $\tau_{ij} = \overline{u_i u_j} - \bar{u}_i \bar{u}_j$.

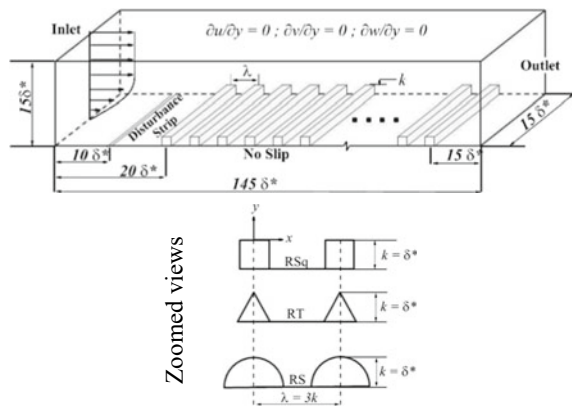
Here \bar{u}_i is filtered velocity field, \bar{S}_{ij} is the filtered strain rate, residual stress tensor is denoted by τ_{ij} , and \bar{f}_i represents the forcing term incorporating the effect of immersed boundary. Normalization of velocity and length scale has been done using inlet free-stream velocity U_∞ and inlet displacement thickness δ^* . Residual stress tensor is modelled for closure of equations. Model coefficient, C_s , is solved dynamically following the Germano–Lilly proposition [16, 17] to achieve better accuracy in results compared to constant value association.

Further, the unsteady, incompressible, and filtered three-dimensional Navier–Stokes equations are solved by employing finite volume technique. Second-order symmetry preserving central difference scheme is used to discretize the spatial terms in mass and momentum equations. The second-order scheme is widely used in LES pertaining to its non-dissipative characteristics. Temporal marching is explicit using second-order Adams–Bashforth scheme, except for pressure term. Pressure term is solved by standard projection method. Immersed boundary method is used for identifying the boundary conditions for geometries that are non-conformal to grids. The velocity field near the boundary of the body is modified at each time step to satisfy no-slip at the boundary [18]. The quadratic unidirectional interpolation is used to find the velocity at points just adjacent to the boundary. The in-house solver implemented in the present study has been proved competent for a varied transitional and turbulent flows [19, 21].

Figure 1 represents the schematic of the computational domain along with the associated boundary conditions implemented for the present analysis. The x , y , and z coordinates shown here are in the streamwise, wall-normal, and spanwise directions, respectively. Velocity components along the corresponding directions are u , v , and w respectively. The simulations here are performed to study the flow characteristics over a series of successive spanwise aligned riblets with three different geometrical shapes, as detailed in zoomed view in Fig. 1. At inlet, the value of imposed Re_θ is around 360. The computational length extends for $L_x = 145$, $L_y = 15$, and $L_z = 15$ in the respective directions. The origin is located at $(20, 1)$ downstream of inlet, which corresponds to the centre of the first riblet. The height and wavelength of the successively placed riblets are given by $k = \delta^*$ and $\lambda = 3k$, respectively. Here, the instantaneous velocity component can be decomposed as $u_i = \bar{u}_i + u'_i$, where \bar{u}_i is the time-averaged, and u'_i is the true stochastic turbulence fluctuation.

Blasius profile is specified at the inlet for the streamwise velocity component. The no-slip condition is applied on the wall and ribbed surfaces. The periodic boundary condition is applied in a spanwise direction, and convective boundary condition is imposed at the exit of the domain. The normal velocity fluctuations having the

Fig. 1 Computational domain along with boundary conditions. Zoomed view explains the riblet shapes, i.e. square (RSq), triangular (RT), and semi-circular (RS)



Gaussian distribution are introduced at the wall at $x = -10$ and $y = 0$ to initiate the transition of the shear layer, following Alam and Sandham [22]. The simulation is carried out with a time step of 0.001, which ensures that the Courant number is always less than 1.0. The number of grids used in the LES simulation is considered as $680 \times 160 \times 64$. Uniform grid spacing is used in the streamwise and spanwise direction, while grids are uniform up to 1.5 times roughness height and then slowly stretched with a stretching factor of 2.2% in the wall-normal direction. The mesh resolution is of $\Delta x^+ = 4.5 - 17$, $\Delta y^+ = 0.8 - 2$, and $\Delta z^+ = 7.4 - 26$ for the whole domain, which appears good for an LES [23].

4 Results and Discussion

The validation for the present study is carried out by simulating the flow over an array of transverse square riblets, following the work of Tirandazi et al. [24]. The height and wavelength of riblet are considered as δ_0^* and $\lambda = 3k$, respectively. The simulation is performed for a characteristics Reynolds number (Re_L) of 10^4 , based on length of the plate and free-stream velocity. The time-averaged streamwise velocity profiles are compared at three streamwise stations (i.e. $x = 16.7, 52.4$, and 91.7% of the cavity length), Fig. 2. Here, the cavity length is defined as the gap present between consecutive riblets. The present simulation results are found to be in good agreement with the results of Tirandazi et al. [24].

Figure 1 explains the three geometries (i.e. semi-circular ribs (RS), square ribs (RSq), and triangular ribs (RT)) that are being used in the present analysis to investigate the flow characteristics with the imposed Re_θ of 360 at inlet. The integral boundary layer parameters such as displacement thickness (δ^*) and momentum thickness (θ) are important to characterize the shear layer over riblets. The following has been reflected in local Re_θ , as shown in Fig. 3. It has been evaluated above the crest of roughness strips, hence neglecting the recirculation region between the consecutive riblets. An increase in Re_θ is observed along streamwise direction for the three simulated cases. However, the rough surface with triangular riblets (RT) has a steeper rise than the other two cases (i.e. RS and RSq), reaching a maximum value of 700.

Fig. 2 Mean velocity profiles at different locations within the cavity. solid lines represent the current simulations and symbols the Tirandazi et al. [24]. The symbol η is defined as $y/x\sqrt{Re_x}$

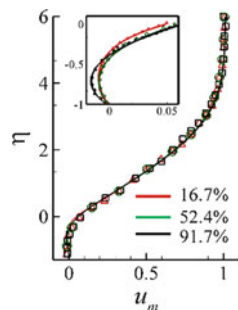
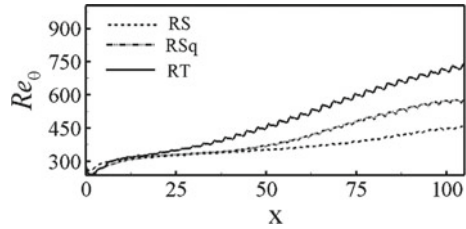


Fig. 3 Comparison of Reynolds number based on momentum thickness (Re_θ) for the three riblet shapes



Similarly, when compared to semi-circular riblets (RS), an increase in Re_θ for square riblets (RSq) is more, attaining maximum values of 565 and 450, respectively. Therefore, the flow appears turbulent in the case of triangular and square-shaped roughened surfaces, whereas the flow is likely to remain in the transitional regime for the surface, RS.

The profiles of mean velocity are plotted at the centre of the space between consecutive riblets and are being compared for different riblet shapes, as shown in Fig. 4. The insets provided depict a zoomed view of the velocity profiles within the riblets. The level at the riblets crest is denoted by a dotted line in the figure. The velocity profiles shown in a zoomed view represent the recirculation region formed between the riblets. The reversal flow which is attributed to negative \bar{u} is observed to be negligible at the streamwise location $x = 10.4$ for the rough surfaces RS, RSq, and RT. A significant change in recirculation region for the RSq and RT surfaces is observed at the locations $x = 70.4$ and 40.4 , respectively. Whereas near to negligible increase in negative velocity is seen for semi-circular riblets. Thus, the reversal strength enhances downstream, while the recirculation size decreases along the streamwise direction.

The influence of riblet shapes on the growth of disturbances is investigated from the *rms* profiles of streamwise velocity fluctuations, which are plotted at the centre of consecutive riblets, as presented in Fig. 5. It has been observed that the surface RT reveals maximum rms values which initiate far upstream at $x = 10$ and progressively increase over the whole domain, when compared with RS and RSq. Whereas the RS

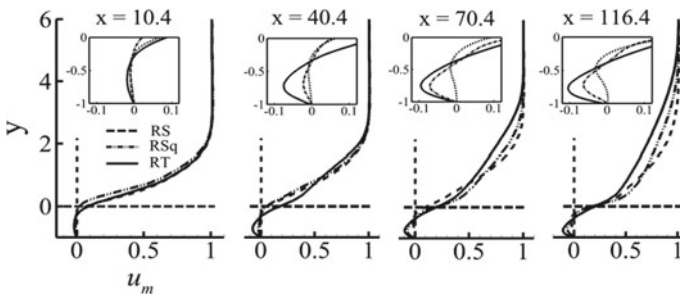


Fig. 4 Profiles of mean streamwise velocity at different streamwise locations. Insets are zoomed views for the profiles within the riblet gaps

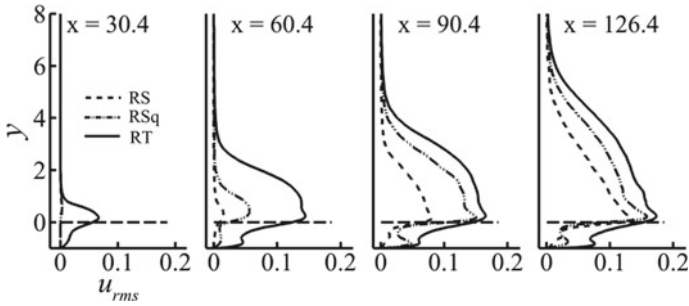


Fig. 5 Profiles of *rms* streamwise velocity fluctuation at different streamwise locations for three riblet shapes

exhibits delayed increase in fluctuations at a location $x = 69$. Further, a prominent double peak feature is observed in *rms* profiles for RSq and RT, where the outer peak explains the effect of riblets on the overlying shear layer and the inner peak reasons about the reversal region present between the riblets. The shifting in outer and inner peaks is observed along x -direction for each case, where the outer peak experiences a faster increase than the inner one, indicating a more stable nature of flow within the riblets.

The previous argument is further supported by the contours of Reynolds shear stress, as depicted in figure. The critical value of the shear stress to locate onset of transition in shear layer is 0.001, as proposed by Ol et al. [25]. Thus, the onset of transition occurs at $x = 10, 43.5$ and 69.5 for the rough surfaces RT, RSq, and RS, respectively. Thus, the onset transition has been shifted upstream in an order of RS, RSq, and RT.

The time-averaged skin friction coefficient, \bar{C}_f , as given by $\bar{C}_f = \tau_w / 0.5\rho U_\infty^2$, is evaluated at the crest of roughness and depicted in Figs. 6 and 7. Here, τ_w and U_∞ are explained as wall shear stress and local free-stream velocity. The value of $\bar{C}_f \bar{C}_f$ for the surface RT is observed to be maximum at every location downstream in the x -direction. Further, it justifies the previous claims about the onset of transition. The flow field for RT remains quasi-transitional in first half of the domain and becomes turbulent in the later half, as illustrated by the nearly constant values of \bar{C}_f . Further, the onset and end of transition for RSq are being denoted by minimum and maximum values of \bar{C}_f , and thus, the flow becomes turbulence towards the end of the domain. Whereas for RS, flow remains laminar for majority length of the domain, while being transitional towards the end of domain.

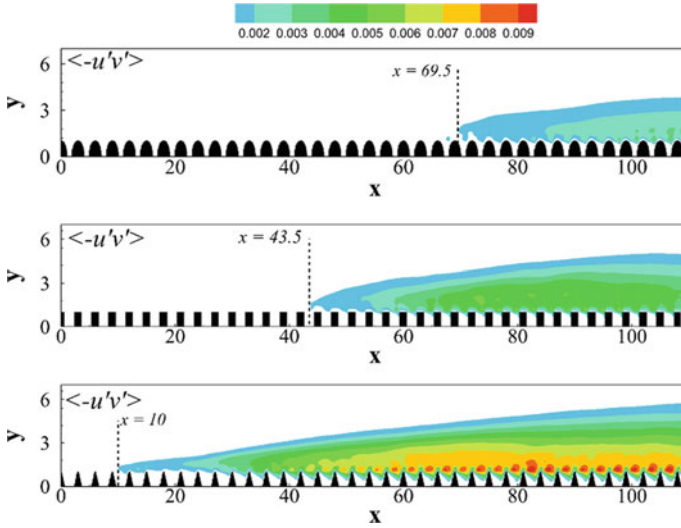
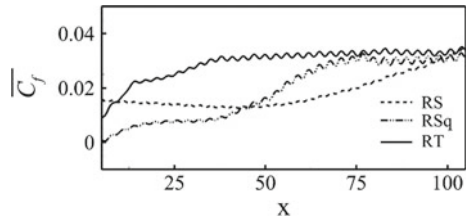


Fig. 6 Contours of normalized Reynolds shear stress for riblet shapes **a** RS **b** RSq **c** RT

Fig. 7 Comparison of mean skin friction coefficient for three different riblet shapes



5 Conclusions

The flow past a series of riblets aligned across the flow field is carried out for three cross-sectional shapes, which are taken as semi-circular, triangular, and square. The important results of the present study are summarized below:

1. The maximum value of Re_θ towards the end of the domain is noted to be 700, 565, and 450 for the rough surfaces RT, RSq and RS, respectively, for an imposed Re_θ of 360 at inlet. Therefore, the flow appears turbulent in the case of triangular and square-shaped roughened surfaces, whereas the flow is likely to remain in the transitional regime for the surface, RS.
2. It has been observed from \bar{u} profiles that the reversal strength enhances downstream, while the recirculation size decreases along the streamwise direction.
3. The growth of streamwise fluctuation quantity is observed to be maximum for RT, whereas being delayed for RS surface. Further a prominent double peak feature is observed in rms profiles for the cases RT and RSq.

4. The onset of transition as depicted from contours of Reynolds shear stress is located at $x = 10, 43.5, \text{ and } 69.5$ for the rough surfaces RT, RSq, RS, respectively.
5. The plot of \overline{C}_f provides good insight about the onset and the length of transition. Thus, the flow field for RT is observed to be quasi-transitional in first half of the domain and turbulent in the later half, as illustrated by the nearly constant trend of \overline{C}_f . Moreover, the onset of transition for RSq is defined when \overline{C}_f reaches its minimum value and further completes transition when \overline{C}_f attains its maximum, leading the flow to be turbulent towards the end of the domain. Whereas for RS, the flow remains laminar for majority length of the domain, while being transitional towards the end of the domain.

Acknowledgements The authors wish to acknowledge the support and the resources provided by PARAM SANGANAK under the National Supercomputing Mission, Government of India at the Indian Institute of Technology, Kanpur.

Abbreviations

C_{fm}	Skin friction coefficient
δ^*	Displacement thickness
θ	Momentum thickness
k	Roughness height
λ	Roughness wavelength
Re_θ	Reynolds number based on θ
U_∞	Free-stream velocity
rms	Root mean square
RS	Semi-circular roughness
RT	Triangular roughness
RSq	Square roughness

References

1. Perry AE, Schofield WH, Joubert PN (1969) Rough wall turbulent boundary layers. *J Fluid Mech* 37(2):383–413. <https://doi.org/10.1017/S0022112069000619>
2. Djenidi L, Elavarasan R, Antonia RA (1998) Turbulent boundary layer over transverse square cavities. In: Proceedings of the 1998 Thirteen Australas Fluid Mechanics Conference, Vol 2, 395, Melbourne, Australia, 13–18 December 1998, pp 837–840
3. Leonardi S, Orlandi P, Smalley RJ, Djenidi L, Antonia RA (2003) Direct numerical simulations of turbulent channel flow with transverse square bars on one wall. *J Fluid Mech* 491:229–238. <https://doi.org/10.1017/S0022112003005500>
4. Jiménez J (2004) Turbulent flows over rough walls. *Annu Rev Fluid Mech* 36(1991):173–196. <https://doi.org/10.1146/annurev.fluid.36.050802.122103>

5. Lee SH, Sung HJ (2007) Direct numerical simulation of the turbulent boundary layer over a rod-roughened wall. *J Fluid Mech* 584:125–146. <https://doi.org/10.1017/S0022112007006465>
6. Tachie MF, Adane KK (2007) PIV study of shallow open channel flow over d- And k-type transverse ribs. *J Fluids Eng Trans ASME* 129(8):1058–1072. <https://doi.org/10.1115/1.2746910>
7. Reshotko E (1994) AIAA m-0001 transition and control 32nd aerospace sciences meeting and exhibit. Control
8. Vadlamani NR, Tucker PG, Durbin P (2018) Distributed roughness effects on transitional and turbulent boundary layers. *Flow Turbul Combust* 100(3):627–649. <https://doi.org/10.1007/s10494-017-9864-4>
9. Muthuramalingam M, Puckert DK, Rist U, Bruecker C (2020) Transition delay using biomimetic fish scale arrays. *Sci Rep* 10(1):1–13. <https://doi.org/10.1038/s41598-020-71434-8>
10. Walsh MJ (1983) Riblets as a viscous drag reduction technique. *AIAA J* 21(4):485–486. <https://doi.org/10.2514/3.60126>
11. Dean B, Bhushan B (2010) Shark-skin surfaces for fluid-drag reduction in turbulent flow: a review. *Philos Trans R Soc A Math Phys Eng Sci* 368(1929):4775–4806. <https://doi.org/10.1098/rsta.2010.0201>
12. Chen H, Rao F, Shang X, Zhang D, Hagiwara I (2014) Flow over bio-inspired 3D herringbone wall riblets. *Exp. Fluids* 55(3). <https://doi.org/10.1007/s00348-014-1698-4>
13. Chen HW, Rao FG, Zhang DY, Shang XP (2014) Drag reduction study about bird feather herringbone riblets. *Appl Mech Mater* 461:201–205. <https://doi.org/10.4028/www.scientific.net/AMM.461.201>
14. Benschop HOG, Breugem WP (2017) Drag reduction by herringbone riblet texture in direct numerical simulations of turbulent channel flow. *J Turbul* 18(8):717–759. <https://doi.org/10.1080/14685248.2017.1319951>
15. Bechert DW, Bruse M, Hage W, Van Der Hoeven JGT, Hoppe G (1997) Experiments on drag-reducing surfaces and their optimization with an adjustable geometry. *J Fluid Mech* 338:59–87. <https://doi.org/10.1017/S0022112096004673>
16. Lilly DK (1992) A proposed modification of the Germano subgrid-scale closure method. *Phys Fluids A* 4(3):633–635. <https://doi.org/10.1063/1.858280>
17. Germano M, Piomelli U, Moin P, Cabot WH (1991) A dynamic subgrid-scale eddy viscosity model. *Phys Fluids A* 3(7):1760–1765. <https://doi.org/10.1063/1.857955>
18. Mittal R, Iaccarino G (2005) Immersed boundary methods. *Annu Rev Fluid Mech* 37:239–261. <https://doi.org/10.1146/annurev.fluid.37.061903.175743>
19. Sarkar S, Sarkar S (2009) Large-eddy simulation of wake and boundary layer interactions behind a circular cylinder. *J Fluids Eng Trans ASME* 131(9):0912011–09120113. <https://doi.org/10.1115/1.3176982>
20. Sarkar S, Sarkar S (2010) Vortex dynamics of a cylinder wake in proximity to a wall. *J Fluids Struct* 26(1):19–40. <https://doi.org/10.1016/j.jfluidstructs.2009.08.003>
21. Sarkar S, Babu H (2015) Large eddy simulation on the interactions of wake and film-cooling near a leading edge. *J Turbomach* 137(1):1–11. <https://doi.org/10.1115/1.4028219>
22. Alam M, Sandham ND (2000) Direct numerical simulation of ‘short’ laminar separation bubbles with turbulent reattachment. *J Fluid Mech* 403:223–250. <https://doi.org/10.1017/S0022112099007119>
23. Ovchinnikov V, Piomelli U, Choudhari MM (2006) Numerical simulations of boundary-layer transition induced by a cylinder wake. *J Fluid Mech* 547:413–441. <https://doi.org/10.1017/S0022112005007342>
24. Tirandazi P, Hidrovo CH (2020) Study of drag reduction using periodic spanwise grooves on incompressible viscous laminar flows. *Phys Rev Fluids* 5(6):64102. <https://doi.org/10.1103/PhysRevFluids.5.064102>
25. McAuliffe BR, Hanff ES (2005) Comparison of laminar separation bubble measurements on a low Reynolds number airfoil in three facilities, May 2014. <https://doi.org/10.2514/6.2005-5149>

Development of New Technology and Design Framework for Supersonic Transport Aircraft



Aravind Seeni 

Abstract Supersonic transport aircrafts are thought to revolutionize air travel in the forthcoming century. New design concepts at early design stages of supersonic transport aircraft design are currently analyzed using low-fidelity tools. In this paper, it is proposed that CFD could be successfully utilized at the conceptual design phase to perform rapid design analyses of a multitude of designs and design trade-off. Such a task can be accomplished with the advancement of technology such as automated meshing and high-performance supercomputing. CFD merged with high-performance computing technology can enable obtaining high-fidelity solutions at a reasonable cost early in the conceptual design phases. This idea is demonstrated through analysis of a technological concept called aerospikes. Aerospike is a new technology being proposed for supersonic transport aircraft design in this paper. Aerospikes when integrated on the nose cone of a supersonic aircraft is hypothesized to reduce shock wave loads and protect the sensitive electronics in the nose cone. However, the analyses performed through CFD on five different models proved otherwise. The generation of oblique shocks in front of the aerospike causes stronger shocks produced at the rear near the nose. The result is significant since the proposed design framework was able to capture the effects of aerospikes and inform the designer accurately. The designer can now look for alternate designs. The results thus demonstrate the effectiveness of the design framework proposed for utilization in the conceptual design phase of an aircraft.

Keywords Supersonic transport aircraft · Aerospike design · Computational fluid dynamics · Conceptual design phase · High-fidelity results

A. Seeni (✉)

Department of Aeronautical Engineering, Rajalakshmi Engineering College, Thandalam, Chennai, Tamil Nadu 602105, India

e-mail: aravindseeni.s@rajalakshmi.edu.in

1 Introduction

This research aims to develop new technology and new design framework to realize more robust approaches to supersonic jet design early in the conceptual design stages through the utilization of CFD. The idea is to develop highly efficient design concepts with the introduction of new, advanced geometries. There is potential to investigate low drag, low heat transfer solutions using aerospike design. The presence of an aerospike in supersonic business jets reduces the aerodynamic and heat loads on the nose cone thereby reduces the chance of damage to the electronics in the nose cone. The geometry of spike can be altered such that more efficient designs can be introduced.

2 Problem Statement

The nose of a supersonic transport aircraft is designed to carry sensitive avionics equipment. However, the nose structure is prone to oblique and Mach wave shocks. Modern technological advancements in the sphere of supersonic aircraft design such as supersonic transport business jets are designed with a sharp coned nose to withstand shock induced aerodynamic and to an extent thermal loads (due to excessive heating). Also, the aerodynamic drag at high speeds is also required to be kept to a minimum.

An example of a supersonic transport aircraft with a sharp nose cone is shown in Fig. 1a. The sensitive avionics protected by the nose cone structure is shown in Fig. 1b.

The conceptual design study of supersonic business jets, so far has been largely performed using low-fidelity computational tools. Examples of such tools have been reported in previous studies by other researchers [1]. The problem with existing tools is that they provide only low-fidelity results.

3 Proposed Aerospike Concept

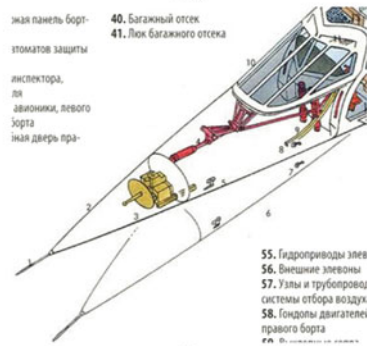
In this paper, the aerospike concept is proposed as a solution to effectively tackle the problem of shocks. Inclusion of aerospike in the nose of modern aircraft development as in supersonic transport aircrafts, reduces shock induced loads to aircraft at supersonic speeds thereby protecting the sensitive electronics in the nose cone from damage.

An aerospike is usually a thin cylindrical rod attached to the nose. The introduction of aerospike can cause significant modification to the flow-field by artificially creating shocks. It replaces the weak oblique shocks generated at the nose tips. A weaker shock is formed in front of the aerospike which creates a stronger shock at the back resulting

Fig. 1 a Supersonic transport aircraft *Concorde* with a sharp pointed nose, and **b** its avionics equipment in nose cone



(a)



(b)

in high temperatures at the back. The designer may utilize this concept to reduce the strength of shocks generated at the tip of the nose cone.

3.1 Hypotheses and Research Questions

The presence of spike generates an oblique shock that increases the temperature at the nose but reduces the velocity along the nose cone. It also increases the pressure and density. The shock strength at the nose is reduced due to the oblique shock at the spike.

The effect of different aerospike geometries on the resulting shock structure from the 2D wedged nose is still unknown. Furthermore, the behavior of the effect of aerospikes at higher supersonic speeds is still unresolved. Hence a detailed investigation on the effect of different spikes by varying the spike angle will be performed. The effect of higher Mach numbers on the flow properties across shocks and the shock structure will also be investigated.

4 Proposed Design Framework for Conceptual Design of Supersonic Transport Aircrafts

A novel design framework proposed in this paper is the use of Computational Fluid Dynamics (CFD) with capabilities such as automated meshing, multicore high-performance computing early in the design phases to provide more robust approach to conceptual design. Such a framework can be successfully realized through the utilization of advancement in technology such as artificial machine intelligence, increased computational resource and speeds.

4.1 Automated Meshing

Automated meshing refers to meshing using machine intelligence and without too much human intervention. The user level inputs provided only are minimum element size requirements and type (hexagonal, polygonal, tetrahedron, etc.). In the traditional method, meshing is performed through a process called block meshing. Here expert level intervention is required particularly for 3D geometries such as a full-scale aircraft and is a time-consuming process. On the contrary, automated meshing allows completion of the process in a fraction of the time through utilization of machine intelligence. Machine intelligence is required for selection of elements and allocate grid density in selected areas of the domain without any form of user inputs. Such a technology helps reduction in work around time when analyzing many different design concepts of aircrafts, components, airfoils, etc. The task of analyzing many different concepts and performing parametric trade-off of a multitude of designs is a typical work requirement at the conceptual design stages for a designer/engineer.

There is dedicated software available that are developed for academic and industrial research as well as commercial purposes for performing automated meshing. Examples are Pointwise and ANSYS's Meshtool. Pointwise is a meshing tool that provides complete automated meshing solutions. User-defined scripting is also included. This allows tailoring the capabilities of software to specific geometries like airfoil or complete aircraft.

While automated meshing can be enabled for simple geometries such as an airfoil, a complete automated meshing solution may not be feasible for complex geometries such as an aircraft. In such cases, semi-automated meshing is feasible. Semi-automated meshing falls in between the work load considered in traditional block meshing and script-based meshing. While automated meshing technology is the need of the hour, semi-automated meshing helps in developing correct meshes with expert monitoring which helps in improved accuracy of the solution.

In addition, the mesh quality from the computed outputs can be further improved using features like adaptive meshing. This helps refining the mesh in areas of specific interest. Dynamic meshing allows adapting the mesh to specific conditions. For

instance, it allows change the mesh around an airfoil with change in angle of attack in order to better resolve the flow properties near the boundary layer.

4.2 Increased Computational Resource and Speeds

The advancement of semi-conductor technology has enabled development of high-speed supercomputing capabilities suited to aircraft design tasks. Enabling CFD at conceptual design stages requires high-speed computing capabilities to provide rapid design analyses of a multitude of designs and trade-off. The problem lies in solving the governing equations of flow in one of the available methods—Reynolds Averaged Navier Stokes (RANS), Large Eddy Simulation (LES), and Direct Numerical Simulation (DNS). Each of these methods provide the designer with different solution accuracy at a specific computational cost.

To explain, it is important to understand turbulence in flows. The flow around an airfoil or an aircraft wing is characterized by different levels of turbulence. Resolving the turbulence to the level required allows to choose one of the above three methods. RANS can only resolve large-scale eddies associated with turbulence. For the purpose of resolving small-scale eddies, the use of LES or DNS is required. The use of higher order meshes of grid size 1011 and above is required in cases of LES and DNS along with high computational resource requirements. Increased computational requirements affects hardware requirements and human effort. However, it can be said as a first step of characterizing only large-scale turbulent eddies, the use of RANS could be adopted instead of LES or DNS at the conceptual design phases. The results can be used to direct future research in the characterization of small-scale eddies or turbulence.

4.3 Geometry Considerations

In this paper, the flow past 2D wedge is considered as the baseline model. The wedge shape is considered due to the reason that it resembles the shape of a supersonic aircraft nose in two dimensions. The baseline model will be used for validating the CFD solver and modeling strategies. After validating the solution for 2D wedge case, the aerospike concept will be studied. The aerospike geometry studied in this work is provided in Fig. 2. The various models along with geometrical parameters are further listed in Table 1.

Fig. 2 Types of aerospike models

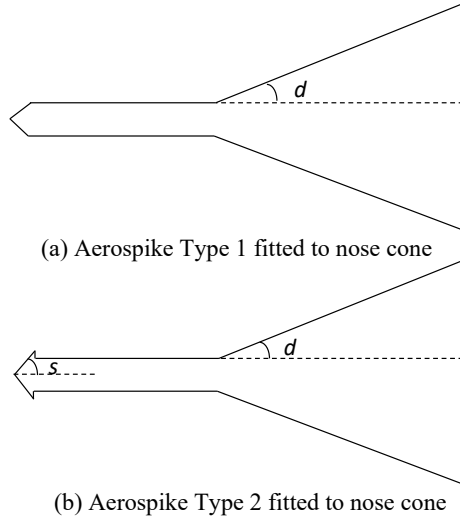


Table 1 Aerospike models considered for the present work

		s (°)	d (°)	Spike stem length (m)
Aerospike type 1 (refer Fig. 2a)	Model 1	–	15	0.5
Aerospike type 2 (refer Fig. 2b)	Model 2	16	15	0.5
	Model 3	18	15	0.5
	Model 4	20	15	0.5
	Model 5	20.5	15	0.5

5 Baseline Model Validation

The flow problem considered for validating the CFD model is the flow past a 2D wedge geometry. The reason for selecting a wedge is that a wedge is widely investigated by researchers and documented. Furthermore, the geometry of a wedge bears close resemblance to that of an aerospike.

5.1 Verification and Validation

A half-wedge geometry with a wedge angle of 15° is assumed. The wedge structure is assumed to be rigid and stationary and the flow is assumed to be steady. A two-dimensional analysis is performed. The Mach number assumed for the validation case is 2.

A grid independence study is conducted to determine the optimum mesh size. Two grids of increasing mesh resolution are assumed. The grid consisting of 10,900 elements and 11,100 nodes is selected based on the results obtained (Figs. 3, 4, and 5). The obtained results are compared with analytical calculations available in tables and charts of NACA report 1135 [2]. The obtained wedge results are found to be in agreement. The verification and validation of results show that the models are correctly solved and the modeling procedure followed is correct. Furthermore, it can be stated that the solver can predict the flow properties around wedge with reasonable accuracy.

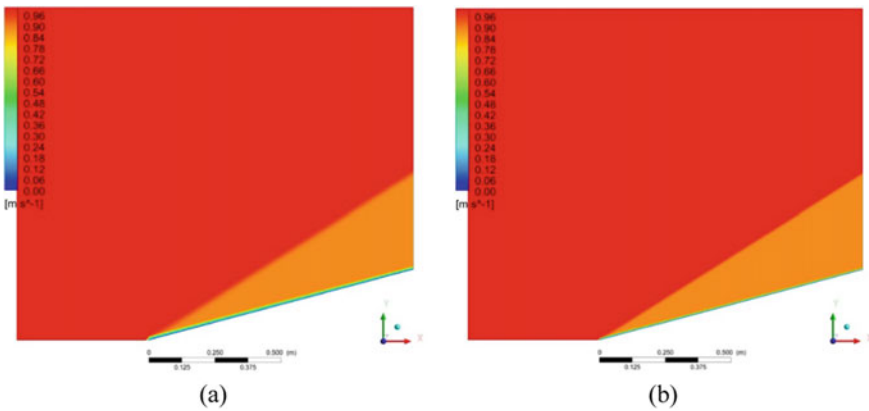


Fig. 3 Grid independence result of Mach number ratio a Mesh 1, b Mesh 2

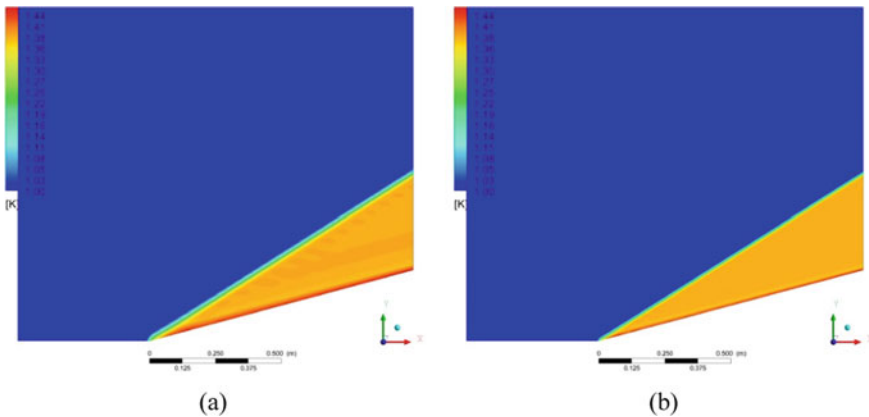


Fig. 4 Grid independence result of static temperature ratio a Mesh 1, b Mesh 2

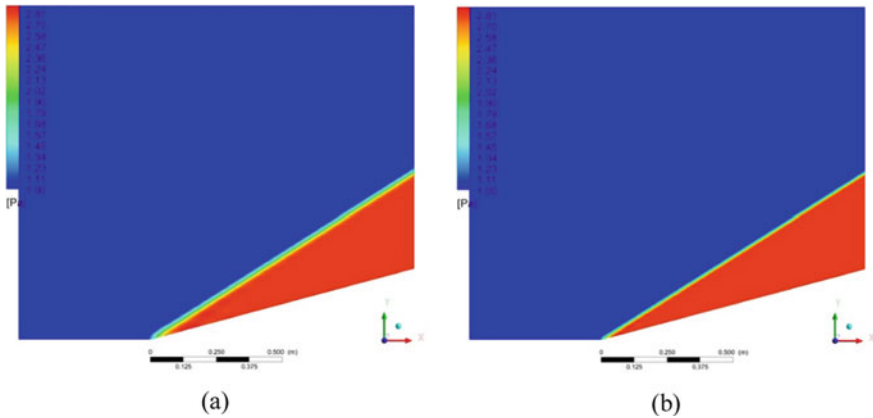


Fig. 5 Grid independence result of static pressure ratio **a** Mesh 1, **b** Mesh 2

6 Aerothermodynamic Analysis of Compressible Flow Over Aerospikes

In this section, the results from the analyses of aerospike models listed in Table 1 are presented and discussed. The geometry of the wedge (nose cone) to which the aerospike is attached has similar dimensions assumed for the baseline case discussed in Sect. 5. The aerospike structure is assumed to be rigid and stationary. A similar flow simulation under steady condition is performed. The Mach number of flow assumed is 2.

The contour plot of pressure ratio in the presence of aerospike for five models namely, Model 1, Model 2, Model 3, Model 4, and Model 5 are provided in Fig. 6a–e.

The contours show that an oblique shock is created in front of the aerospike. The shock produced by the aerospike is expected to alter the fluid properties of Mach number, temperature, pressure, and density above the nose.

Figure 7 compares the Mach number ratio of five aerospike models with those of non-spiked model. The result indicates that the Mach number above the 2D nose is reduced in the presence of aerospike. The highest reduction is observed for Model 5 whereas the lowest reduction is obtained for Model 1.

Similarly, the $\frac{T_2}{T_1}$ and $\frac{p_2}{p_1}$ ratios of aerospike models are compared with those of non-spiked model in Fig. 8 and Fig. 9, respectively. The result indicates that the temperature is increased along the spike length which is an adverse effect. The temperature above the nose is also marginally increased. The highest increase for the most part of the spike length is observed for Model 5 whereas the lowest increase is obtained for Model 1.

The result also indicates that the static pressure is increased along the spike length as well as the nose. The highest increase for the most part of the aerospike length is observed for Model 5 whereas the lowest increase is obtained for Model 1.

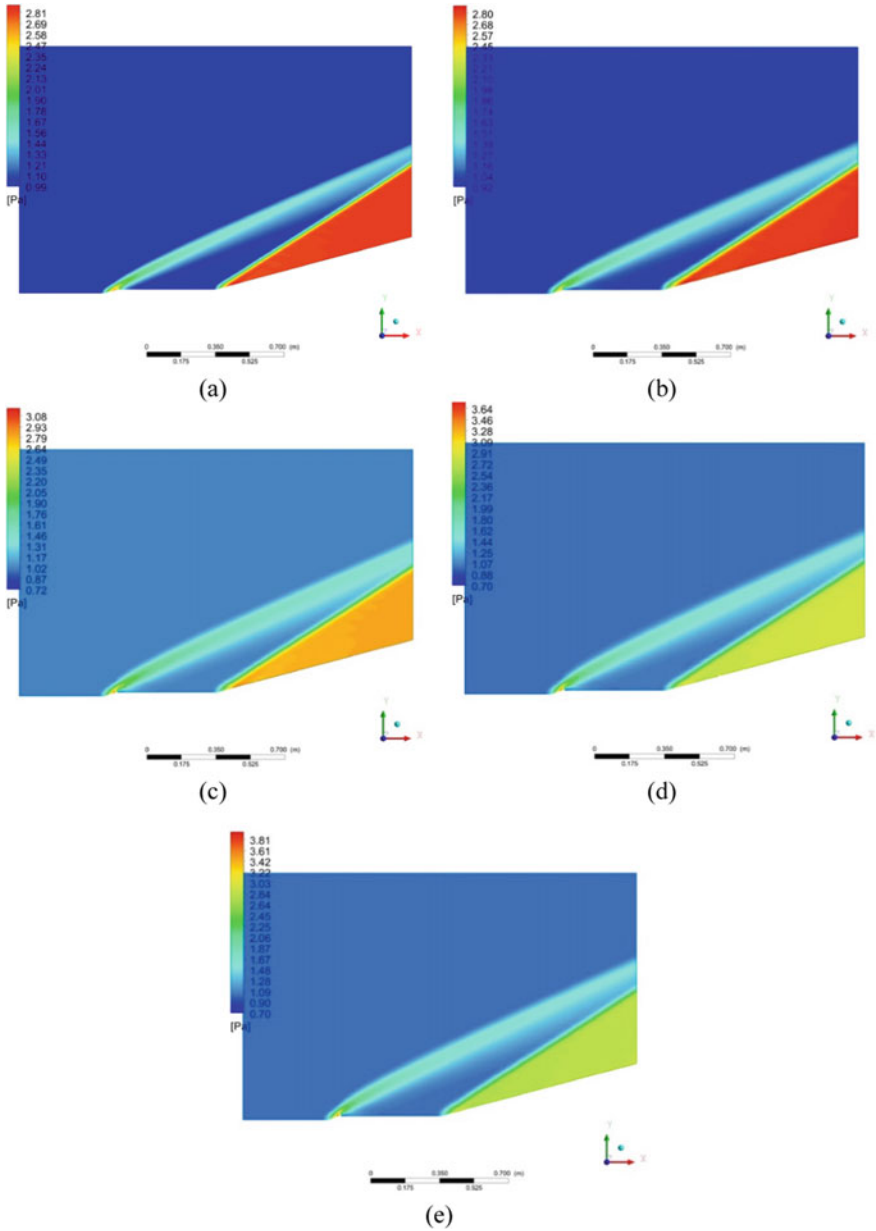


Fig. 6 Contours of pressure ratio for aerospoke—**a** Model 1, **b** Model 2, **c** Model 3, **d** Model 4, and **e** Model 5

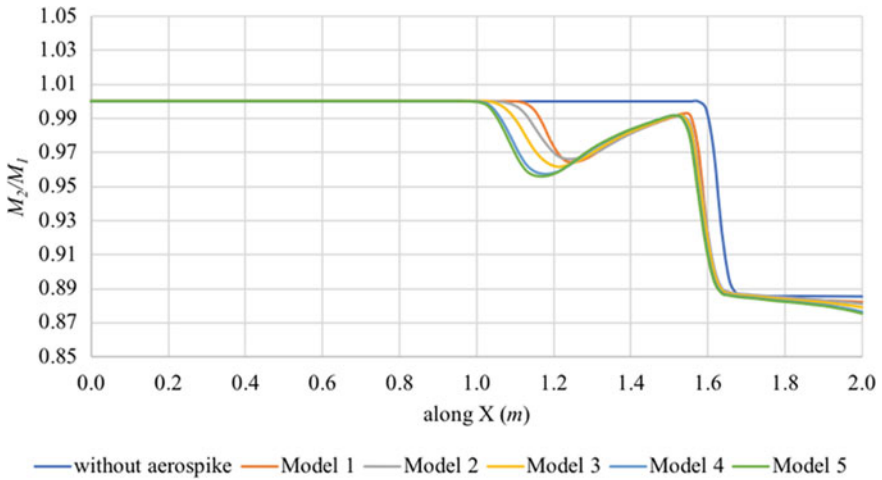


Fig. 7 Mach number ratio of aerospike design compared to baseline model

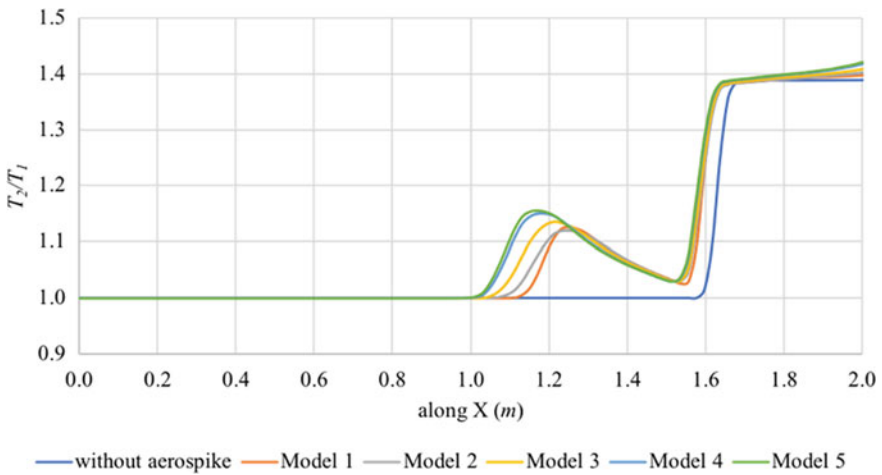


Fig. 8 Temperature ratio of aerospike design compared to baseline model

From the above discussed results, it can be concluded that the presence of aerospike has created an oblique shock in front of the aerospike. The properties of flow when analyzed behind the shock reveals the increase in both pressure and temperature. This change is observed under steady flow assumption. All the five models produced results which detrimentally affect the performance of the nose structure.

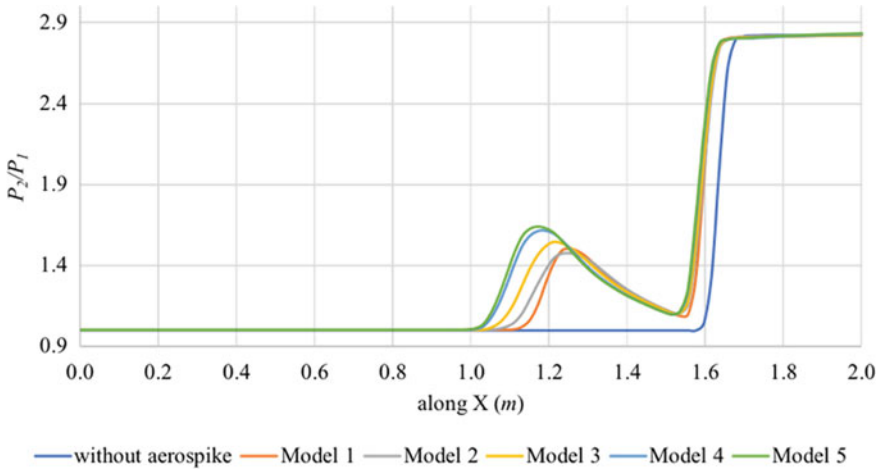


Fig. 9 Static pressure ratio of aerospike design compared to baseline model

7 Implications for Supersonic Aircraft Design

Although the aerospike was originally conceptualized to provide better aerothermodynamic performance, analyses using the proposed design framework utilizing CFD revealed that aerospike will detrimentally affect the performance of a nose. The presence of aerospike produces an oblique shock in front which causes stronger shocks produced at the back in the wedged nose region. This has led to inferior flow properties. The aerospike is thus found to be an infeasible design for this particular application. It can be added that the aerospike concept may not suit for aerodynamic design improvements but could find an interesting alternate application. The analysis of $\frac{P_2}{P_1}$ ratio (Fig. 10) reveals its significance and may find useful application in supersonic engine air intake. Aerospikes design could be employed in front of an aircraft engine intake by fitting in the fore region of the inlet. The increase in density of fluid at high supersonic speeds could contribute to better combustion properties.

8 Conclusions

A novel design framework that utilizes CFD to provide more robust approaches to supersonic aircraft design at the conceptual design phases is proposed. The method was successfully demonstrated through the analyses of different designs of aerospikes, a concept and technology proposed to improve flow properties. The results from the analyses showed the aerospike is not a feasible solution. Nevertheless, the results demonstrated the effectiveness of the proposed design framework

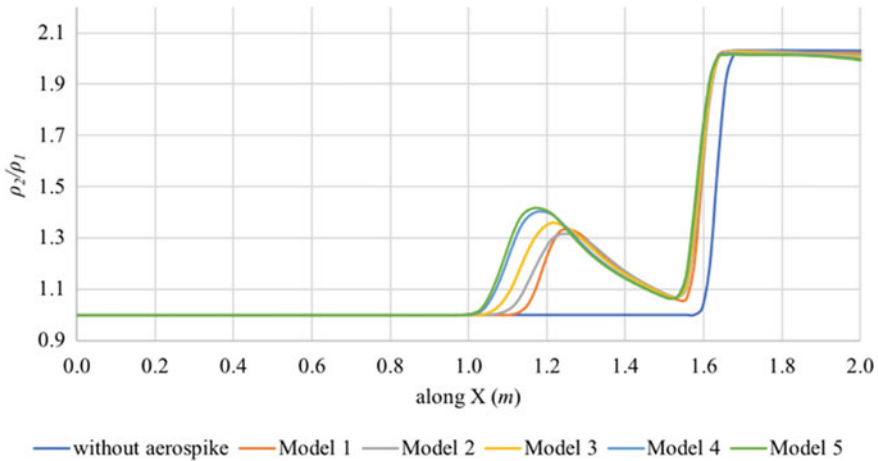


Fig. 10 Density ratio of aerospike design compared to baseline model

in providing accurate results and the possibility to test a multitude of designs, as necessary.

The limitations of this research can now be listed. First, the aerodynamic drag of aerospikes is not measured as this is also an important parameter from aerodynamic design point of view. Second, the 3D effects are not included and only a theoretical 2D wedge design was analyzed. In real world applications, the nose of a supersonic transport aircraft resembles a cone. The flow properties across a cone are different to that of a wedge. In the case of a cone, the streamlines are not deflected parallel to the wedge surface and the deflection angle is much lesser compared to that of a 2D wedge. Hence, this work provides suitable grounds for extending the above work to study cones. Third, unsteady flows around aerospikes still needs to be further investigated.

The total computational expense of simulation is less than a minute for each model on an Intel Core i5 2.5 GHz workstation. While simple geometries such as aerospike integrated to nose with about 11,000 cells can be analyzed for supersonic flows at such low computational cost, it should be a feasible task to perform high-fidelity simulations on a complete aircraft model with more than 100 million nodes at reasonable computational cost. It can be safely stated that design tasks at conceptual level involving multiple designs can be analyzed in no time with the availability of supercomputing facility.

Nomenclature

- s Spike angle ($^{\circ}$)
 d Wedge angle ($^{\circ}$)

$\frac{M_2}{M_1}$	Mach number ratio
$\frac{T_2}{T_1}$	Temperature ratio
$\frac{P_2}{P_1}$	Pressure ratio
$\frac{\rho_2}{\rho_1}$	Density ratio

References

1. Govindarajan N, Jayaswal A, Gaurav K, Seeni A (2022) Higher-fidelity CFD tools for conceptual design of supersonic business jets. ECS Trans 107(1):515. <https://doi.org/10.1149/10701.0515ecst>
2. Ames Research Staff (1947) (NACA 1135) Equations, tables, and charts for compressible flow

Numerical Study of Impulsive Motion Past a Rotating Cylinder for Newtonian and Non-newtonian Fluid



Sibasish Panda, Pratyush Kumar Mohanty, Prateek Gupta, and Chinu Routa

Abstract The flow phenomena for a rotating cylinder with the application of an impulsive translational motion is studied using ANSYS FLUENT 19R3. The study is carried out for power-law index $n = 1$ and 2 at a fixed Reynolds number ($Re = 40$) for different non-dimensional rotation rates ($\alpha = 0.5, 1, 2$). After the initial flow field reaches a steady state, the impulsive motion is applied by implementing a User defined function (UDF) which assigns a zero-inlet velocity. The time evolution of vorticity contours provides insights into the developing flow field after the impulsive motion. For both the power indices, it has been found that a higher rotational rate leads to faster flow stabilization and can be used for flow control. The flow phenomena is studied quantitatively in terms of aerodynamic coefficients. The Drag coefficient value decreases by 36.47% as value of α increases from 0.5 to 2 for $n = 1$. The sudden variation in force coefficients and their subsequent variation is used to interpret the effect of rotation rate on the disturbed flow field due to impulsive motion.

Keywords Rotating cylinder · Impulsive motion · Vortex shedding · Drag coefficient · Lift coefficient

1 Introduction

The study of fluid flow characteristics around a circular cylinder is a classical bluff body problem in fluid mechanics, with studies dating back to the fifteenth century. Flow over a cylinder can be classified as both an external and internal flow. Flow

S. Panda (✉) · P. K. Mohanty · P. Gupta · C. Routa
Department of Chemical Engineering, NIT Rourkela, Rourkela 769008, India
e-mail: S.Panda-2@student.tudelft.nl

S. Panda
Department of Mechanical, Materials, and Maritime Engineering, Technische Universiteit Delft, Delft, Netherlands

P. Gupta
Davidson School of Chemical Engineering, Purdue University, Lafayette, USA

over a cylinder in an unconfined domain can be categorized as an external flow, whereas flow over a cylinder in a confined domain can be categorized as an internal flow. Despite having a simple geometry, flow past a circular cylinder is a baseline example of more complicated flows having significant real-life applications. These applications often involve fluids flowing over complex geometries, like missiles, bridge pillars, jets, wings, submarines, and turbines. Moreover, research pertaining to flow around cylinders serves as a foundation for understanding various industrially significant applications such as heat exchangers, cooling towers, nuclear reactors, chimney stacks, and other offshore structures. Over the years, several studies have employed a wide range of Reynolds numbers to investigate laminar to turbulent transition in the wake, boundary layer transition, unsteady vortex shedding, and turbulent separation. As a fundamental method for flow control, rotating cylinders have gained significant traction over stationary cylinders. Cylinder motion can be classified into two types—forced (externally applied force) or free motion (movement due to fluid flow forces). An impulsive motion, which can be categorized as a forced motion, significantly enhances flow control by altering the flow field drastically. This work aims to develop an understanding and compare fluid flow characteristics over an impulsively rotating circular cylinder for Newtonian and for non-Newtonian fluid using the Carreau Model.

2 Literature Review and Objective

In recent decades of fluid dynamics research, the study of flow phenomena around static and rotating circular cylinders has attracted many researchers. Similarly, studies of impulsive cylinder motion have gained attention due to its application in many real-life scenarios. However, there has been no work on flow past impulsively moving rotating cylinder to the best knowledge of authors. This section aims to provide a brief overview of relevant past studies and their significant findings. Streeter [1], in his book, described several experimental and numerical investigations of the flow dynamics that have been described using hydrodynamic parameters such as drag and lift coefficients, vortex shedding, wake generation. One of the first comprehensive review studies of flow past a steady circular cylinder highlighted vital flow kinematics such as the range of Reynolds number for flow separation, the increase of wake Length, and flow transition with Reynolds number [2, 3]. Chew et al. [4] numerically investigated the shedding of vortices and the formation of wakes in a two-dimensional viscous incompressible flow generated by an impulsively rotating circular cylinder by a hybrid vortex scheme. The results indicated a critical value of $\alpha = 2$ when a closed streamline began to circulate around the cylinder. Prasad et al. [5] investigated the effect of rotation on flow across a cylinder for different blockage ratios ($\beta = 0$ –50%), non-dimensional rotational velocity ($\alpha = 0$ –2), and Reynolds number ($Re = 35$ –170). They concluded that under counter clockwise rotation, a downward lift force was generated, which increased with increasing blockage ratio. Panda et al. [6] explored power-law fluid flow over a rotating cylinder for $0.1 \leq Re \leq 40$ and

non-dimensional rotational velocity $0 \leq \alpha \leq 6$. They found that at low Reynolds numbers, the power-law index has a much stronger influence on drag and lift than at high Reynolds numbers. Thakur et al. [7] explored the steady two-dimensional flow of incompressible Bingham plastic fluids past a rotating circular cylinder for $0.1 \leq Re \leq 40$ and non-dimensional rotational velocity $0 \leq \alpha \leq 5$. They found an increase in the Bingham number with a decrease in the rotational velocity.

Hourigan et al. [8] studied the vortex dynamics of the flow past a suddenly arrested translating circular cylinder. They found that the Kármán wake vortices roll up on each side of the cylinder to form two larger structures over a long distance. Ta Phuoc Loc [9] numerically investigated the mechanism of creating secondary vortices behind an impulsively started circular cylinder with greater precision numerical technique at $Re = 300, 550$ and 1000 . He studied the properties of the creation and the development of the primary and secondary vortices and verified it with the available experimental data. Koumoutsakos et al. [10] investigated the impulsively started Newtonian flow around a circular cylinder via high-fidelity computations. They showed that the interaction of primary and secondary vorticity is the underlying mechanism for drag reduction and increase. Collins et al. [11] studied the initial flow in a viscous fluid in the direction normal to an infinite circular cylinder that is started impulsively from rest with uniform velocity. They found that the friction and pressure drag are equal for all Reynold numbers at the start of the motion. Pantokratoras [12] has numerically investigated the flow of Carreau fluid over a cylinder using drag and lift coefficient and reported the increase in drag coefficient for shear-thickening fluids and a decrease for shear-thinning fluid on increasing the Carreau number (Cu). Ohta et al. [13] studied numerical simulations of Carreau model fluid flows past a circular cylinder. They found the effective Reynolds number advocated in this study allows one to fully describe the flow state of Carreau model fluids past a circular cylinder on par with Newtonian fluid flows.

Based on the literature survey on the flow around a circular cylinder, it is observed that a majority of the work describes the effects of rotation and impulsive motion separately. Furthermore, little is known about the impulsive motion and rotation effects on aerodynamic parameters like drag and lift coefficients. The present work aims to study and compare the flow phenomenon on an impulsively moving rotating circular cylinder for different power-law indices and explain the behaviour of the aerodynamic parameters. As the shear-thickening fluid for power-law index $n = 2$ was modelled, the Carreau model was chosen over the power-law model.

3 Mathematical Modelling

3.1 Governing Equations

The flow is assumed to be 2-D incompressible with a uniform inlet velocity before the impulse. The continuity and momentum equation for the flow can be written as

Continuity equation

$$\frac{\partial u_x}{\partial x} + \frac{\partial u_y}{\partial y} = 0. \quad (1)$$

Momentum equation

$$\rho \left(\frac{\partial u_x}{\partial t} + \frac{\partial(u_x u_x)}{\partial x} + \frac{\partial(u_x u_y)}{\partial y} \right) = -\frac{\partial p}{\partial x} + \left(\frac{\partial \tau_{xx}}{\partial x} + \frac{\partial \tau_{yx}}{\partial y} \right) \quad (2)$$

$$\rho \left(\frac{\partial u_y}{\partial t} + \frac{\partial(u_x u_y)}{\partial x} + \frac{\partial(u_y u_y)}{\partial y} \right) = -\frac{\partial p}{\partial y} + \left(\frac{\partial \tau_{xy}}{\partial x} + \frac{\partial \tau_{yy}}{\partial y} \right) \quad (3)$$

Equation of Carreau model

$$\mu = \mu_1 + (\mu_0 - \mu_1) [1 + (\lambda \dot{\gamma})^2]^{\frac{n-1}{2}} \quad (4)$$

3.2 Boundary Conditions

At the domain boundaries and cylinder wall, the boundary conditions for the present problem are written as follows:

- At the inlet, before the introduction of impulse, a constant uniform flow profile in the x-direction and zero velocity in the y-direction can be written mathematically as

$$u_x = u_\infty \text{ and } u_y = 0 \quad (5)$$

After the introduction of impulse, zero velocity is assigned to both x and y velocity components

$$u_x = 0 \text{ and } u_y = 0 \quad (6)$$

- On cylinder surface: No-Slip boundary condition is applied throughout. It can be written as

$$u_x = u_y = 0 \quad (7)$$

- At upper and lower wall: Symmetry boundary condition in the x direction is applied. It can be written as

$$\frac{\partial u_x}{\partial y} = 0 \text{ and } u_y = 0 \quad (8)$$

- At the outlet: The outflow boundary condition is used throughout. The outflow condition corresponds to zero diffusion fluxes in the direction normal to the outlet planes. It is used for all the dependent variables.

$$\frac{\partial u_x}{\partial x} = 0; \frac{\partial u_y}{\partial x} = 0 \quad (9)$$

3.3 Numerical Methodology

Finite-volume method (FVM)-based commercial software ANSYS FLUENT 19R3 is used to for the current study. Figure 1 shows the computational domain used for the study. Full pressure–velocity coupling is achieved using a pressure-based coupled solver, resulting in faster convergence. The convective term in the flow equation is discretized using Linear Upwind Differencing (LUD) which uses a three-point stencil to give second-order accuracy, whereas the approximation for the diffusion term is automatically second-order accurate. Discretization with respect to time is first-order implicit, magnifying the stability envelope several-fold. A convergence criterion of 10^{-6} is set for the residuals of velocity and continuity terms. The accuracy of our results has been ensured by performing the grid, domain, and time independence tests.

A zoomed-in view of multi-block structured mesh as shown in Fig. 2 is used due to the accuracy and stability of solution provided by the structured mesh over the unstructured mesh.

3.4 Grid Independence Test

A square domain of varying dimensions is considered for the grid independence test. The independence test is performed at Reynolds number $Re = 40$ and dimensionless rotational speed $\alpha = 0.5$ for a Newtonian fluid. Based on the increasing accuracy of aerodynamic parameters shown in Table 1, an optimum grid G2 is finalized for the current study.

Fig. 1 Schematic of the computational domain for initial conditions

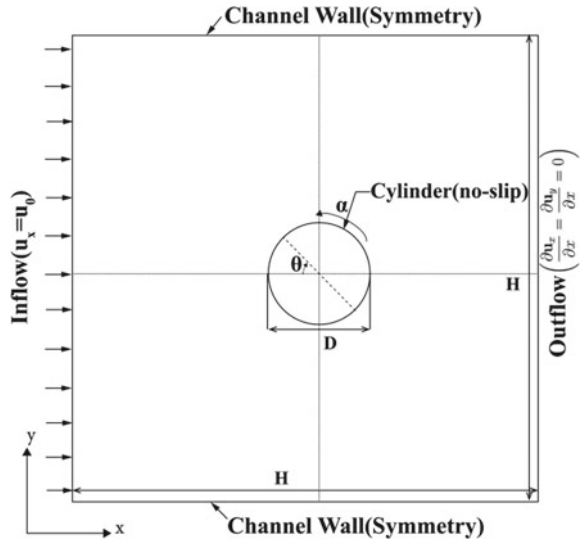


Fig. 2 Multi-block structured mesh used for the study

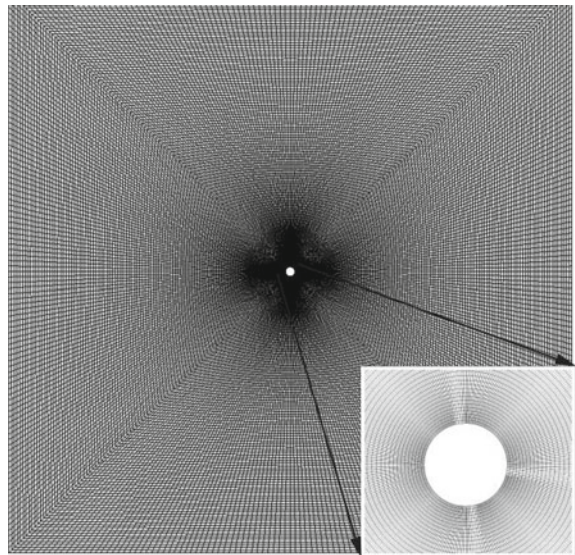


Table 1 Grid independence test

Grid (no. of nodes)	Drag coefficient (C_D)	Lift coefficient (C_L)
G1 (18,800)	0.906	-5.60
G2 (55,200)	0.889	-5.629
G3 (109,200)	0.865	-5.635

Table 2 Comparison of present results with literature

Re	α	n	Present values		Literature values	
			C_D	L_w	C_D	L_w
40	2	1	0.84	–	0.83 [6]	–
40	0	1	1.53	2.24	1.50 [12]	2.15
40	0	2	4.52	0.27	4.33 [12]	0.29

4 Results and Discussion

4.1 Validation

Relevant validity studies have been performed to establish the suitability of chosen numerical methodology. Validation cases Pantokratoras [12] have been used to verify the suitably chosen methodology for fluid flow over stationary cylinder, whereas cases from Panda and Chhabra [6] have been used to validate the same methodology for rotational effects. Table 2 is presented to compare the obtained force coefficient values with literature values. The obtained result shows excellent agreement with the result presented in the literature with a maximum of 4.38% deviation.

4.2 Vortex Shedding Characteristics

Vorticity contours for both the power-law indices have been presented in Fig. 3 to give a qualitative understanding of the flow phenomena. Positive (Counter-Clockwise) vortices are shown by solid lines and Negative (Clockwise) vortices are shown by dashed lines in the vorticity contours. The flow fields are contrasted at different values of α to understand its significance. In this study we have denoted the developed flow field with $t = 0$, at which the flow fully develops with the initial inlet condition. Subsequently, we demonstrate the development of flow field at different instances of time after the impulse.

4.2.1 Power-Law Index $n = 1$

We notice the primary (P) vortices surrounding the cylinder at all values of α . These primary vortices are formed due to boundary layer separation and the formation of a recirculation zone behind the cylinder. As expected, at $\alpha = 2$, the cylinder tries to wrap the nearby vorticity around itself due to extremely high rotational inertia. We observe this dynamic steady state pattern up until $t = 2.5$. At $t = 2.5$, with the implementation of the User Defined Function (UDF) the flow velocity drops to zero instantaneously. In fact, this sudden drop in velocity can be characterized as

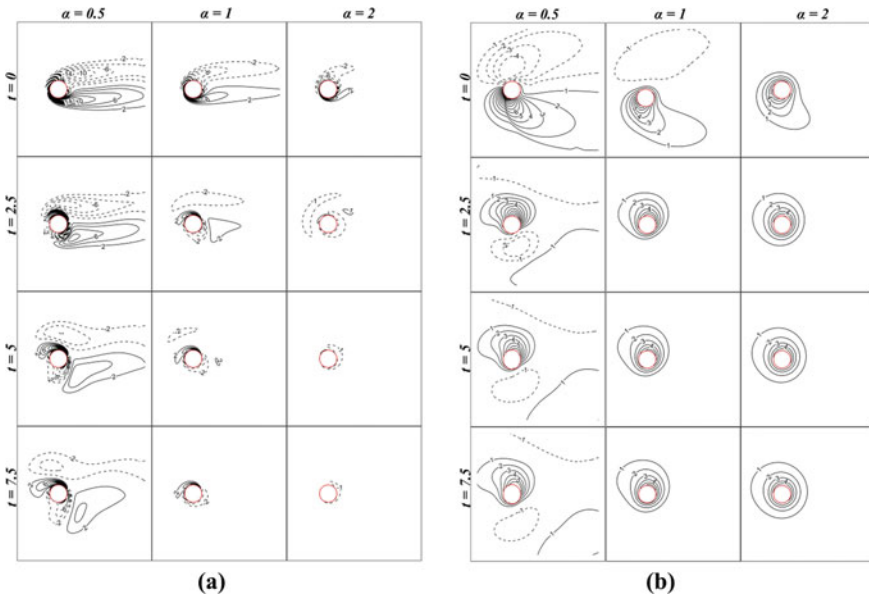


Fig. 3 Comparison of time evolution of vorticity for different rotational rates for **a** $n = 1$ **b** $n = 2$

impulsive. We notice that the primary (P) vortices have detached from the cylinder surface, and the void is filled in by the secondary (S) vortices. Due to the cylinder's continued rotation, these secondary vortices also start to wrap around the surface. As we move from $\alpha = 0.5$ to $\alpha = 2$, the amount of negative vorticity engulfing the cylinder increases. Moreover, as α increases, the diffusion of the primary vortices accelerates. As we move to the subsequent time-instants ($t = 5$ and $t = 7.5$), we notice that for $\alpha = 0.5$, the negative/clockwise secondary vortex starts to spill. Whereas it remains highly compact for $\alpha = 2$. Again, this can be attributed to the increased rotational inertia of the flow. Furthermore, at $t = 5$ and 7.5 , the cylinder space is completely devoid of any hint of primary vortex for $\alpha = 2$. In addition, the cylinder is only surrounded by negative vorticity at $\alpha = 2$ for the time instant $t = 7.5$. Thus, it can be summarized that higher α values can lead to accelerated diffusion of the vortices.

4.2.2 Power-Law Index $n = 2$

Similar to the Newtonian case, we observe primary vortices surrounding the cylinder at $t = 0$. However, one striking feature to note is the magnitude of the vorticity contours and the extent to which they are spread out. Higher inertia of the shear-thickening fluid leads to the development of enveloping vortex for $\alpha = 2$ even before the application of impulse. Implementation of UDF at $t = 2.5$ leads to detachment of primary vortices (P) and development of secondary vortices (S) for $\alpha = 0.5$ whereas

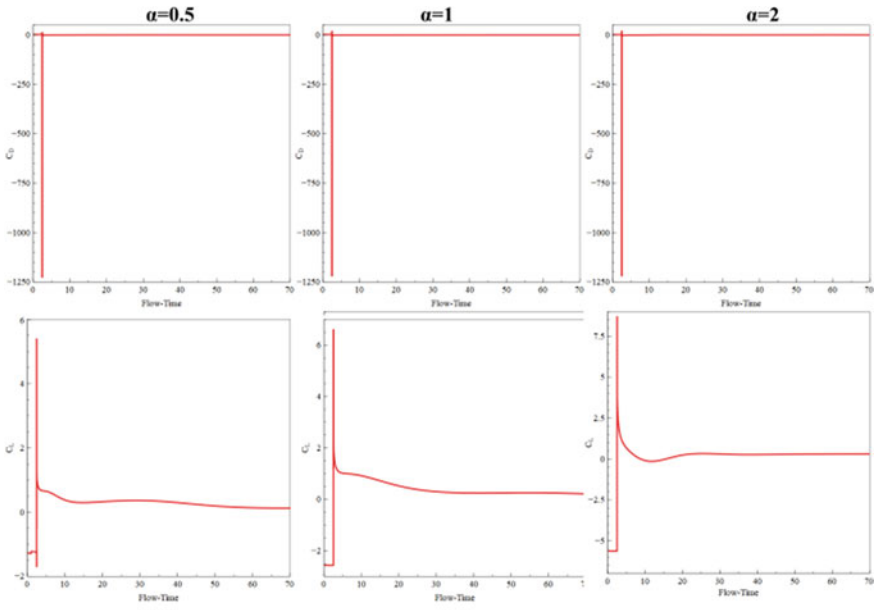
for $\alpha = 1$ and $\alpha = 2$ no visible detachment is observed. The existing counter clockwise (CCW) vortices however change their orientation. The vortices take longer time to decay in comparison to their Newtonian counterparts for all the rotational rates. This behaviour of the flow field can be attributed to shear-thickening nature of the working fluid.

4.3 Variation of Force Coefficients with Time and Rotation Speed

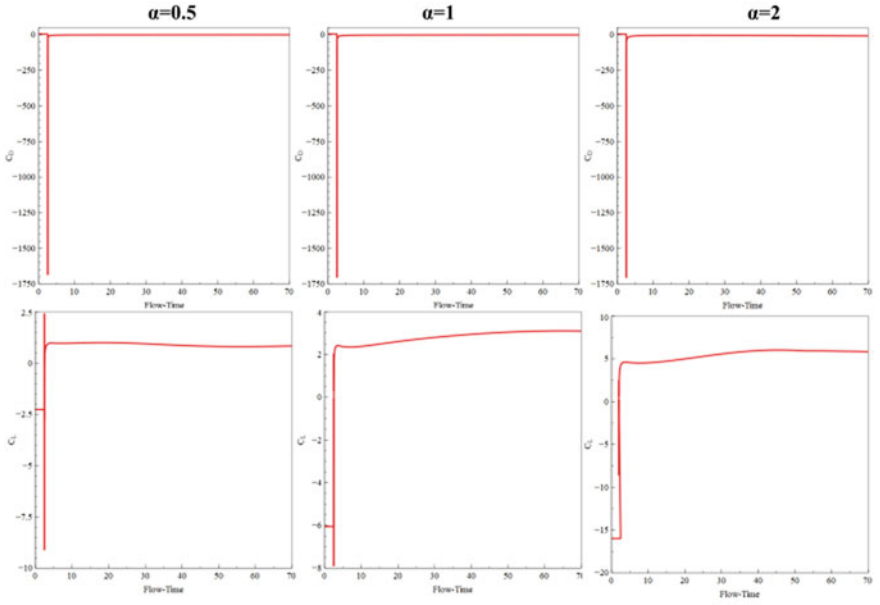
In this section, the variation of force coefficients, for both power-law indices, through the impulsive motion is discussed with the help of Fig. 4. Both the drag and lift coefficients are studied once the flow with the initial inlet condition is fully developed, i.e., at $t = 0$. The sudden spike observed for both drag and lift coefficients can be attributed to the impulsive motion introduced at $t = 2.5$. The dip for drag coefficient can be attributed to a change in flow inertia with the introduction of impulse that leads to an instant detachment of the Primary vortices (P) and subsequent development of Secondary vortices (S). For $n = 1$, the magnitude of dip in drag coefficient is less in comparison to the dip for $n = 2$. The spike in lift coefficient for the Newtonian fluid, can be attributed to detachment and subsequent development of oppositely signed vortices over time. However, for the non-Newtonian case there is no spike for $\alpha = 1$ and $\alpha = 2$ due to non-detachment of vortices. This observation can be attributed to increased inertial properties of the shear-thickening fluid. The variation in coefficients has been studied till they reach a steady state after the introduction of the impulse. An important observation is concluded from observation of time taken, through variation of force coefficients, for the flow to reach steady state after the impulsive motion. For $n = 1$, the time taken by $\alpha = 2$ is less than the amount of time taken by $\alpha = 0.5$. This can be attributed to a faster dissipation rate at $\alpha = 2$ leading to faster stabilization of flow.

5 Conclusions

In this paper application of impulsive translational motion on a rotating cylinder at different rotation rates ($\alpha = 0.5, 1, 2$) for a Newtonian fluid and shear-thickening fluid having power-law index $n = 2$ is studied. The Reynolds number based on cylinder diameter is kept constant. The non-dimensional rotation rate is varied so as to study the effect of rotation on disturbed flow field due to impulsive motion. In order to interpret the results both qualitatively and quantitatively, vorticity contours and force coefficients have been studied respectively. A comparison of the time evolution of vorticity contours for different rotational rates shows the enhanced dissipation rate at a higher rotational rate. In a quantitative sense, the sudden change in sign of



(a)



(b)

Fig. 4 Variation of force coefficients through the impulsive motion for $a n = 1$ $b n = 2$

force coefficients explain the formation of oppositely signed vorticity contours with the application of impulsive motion for the Newtonian fluid and the change in the orientation of enveloping vortices for higher rotational rate for non-Newtonian fluid. Moreover, a significant amount of time is taken, which is monitored here by variation of force coefficients, for $\alpha = 0.5$ in comparison to $\alpha = 2$ establishes the fact that a higher rotation rate leads to better flow control. This study can be further extended to investigate the effect of multiple impulses and their effect on higher rotational rates.

Abbreviations

Nomenclature

C_D	Drag Coefficient
C_L	Lift Coefficient
D	Diameter of Cylinder (m)
H	Height of the computational domain (m)
L_W	Wake length (m)
u_∞	Free stream velocity (m/s)
u_x	x-Component of velocity (m/s)
u_y	y-Component of velocity (m/s)
p	Pressure (Pa)
τ_{ij}	Extra stress tensor (Pa)
n	Power-law index
μ_0	Zero shear viscosity (Pa s)
μ_1	Infinity-shear viscosity (Pa s)

Greek Symbols

α	Non-dimensional rotational velocity [= $D \omega / 2 u_\infty$]
ρ	Density of working fluid
ω	Angular velocity

References

1. Streeter VL (1961) Handbook of fluid dynamics. McGraw-Hill, New York
2. Zdravkovich MM (1997) Flow around circular cylinders, 1 fundamentals. Oxford University Press, New York

3. Zdravkovich MM (2003) Flow around circular cylinders, 2 applications. Oxford University Press, New York
4. Chew YT, Cheng M, Luo SC (1995) A numerical study of flow past a rotating circular cylinder using a hybrid vortex scheme. *J Fluid Mech* 299:35–71
5. Prasad K, Paramane SB, Agrawal A, Sharma A (2011) Effect of channel-confinement and rotation on the two-dimensional laminar flow and heat transfer across a cylinder. *Num Heat Trans Part A Appl* 60(8):699–726
6. Panda SK, Chhabra RP (2010) Laminar flow of power-law fluids past a rotating cylinder. *J Nonnewton Fluid Mech* 165(21–22):1442–1461
7. Thakur P, Mittal S, Tiwari N, Chhabra RP (2016) The motion of a rotating circular cylinder in a stream of Bingham plastic fluid. *J Nonnewton Fluid Mech* 235:29–46
8. Sheard GJ, Leweke T, Thompson MC, Hourigan K (2007) Flow around an impulsively arrested circular cylinder. *Phys Fluids* 19(8):083601
9. Loc TP (1980) Numerical analysis of unsteady secondary vortices generated by an impulsively started circular cylinder. *J Fluid Mech* 100(1):111–128
10. Koumoutsakos P, Leonard A (1995) High-resolution simulations of the flow around an impulsively started cylinder using vortex methods. *J Fluid Mech* 296:1–38
11. Collins WM, Dennis SCR (1973) The initial flow past an impulsively started circular cylinder. *Quart J Mech Appl Math* 26(1):53–75
12. Pantokratoras A (2016) Steady flow of a non-Newtonian Carreau fluid across an unconfined circular cylinder. *Meccanica* 51(4):1007–1016
13. Ohta M, Toyooka T, Matsukuma Y (2020) Numerical simulations of Carreau-model fluid flows past a circular cylinder. *Asia-Pac J Chem Eng* 15(6):e2527

Dynamic Response of a Cantilevered Flexible Vertical Plate in a Uniform Inflow at $Re = 100$



Avinash Kumar Pandey, Gaurav Sharma, and Rajneesh Bhardwaj

Abstract We numerically study the dynamic flow-induced vibration (FIV) response of a flexible vertical plate cantilevered at its bottom in a two-dimensional flow at Reynolds number, $Re = 100$. The incompressible Navier–Stokes and continuity equations are solved for fluid flow, and the Saint Venant–Kirchhoff material model is used for the structure. Plate dynamics is studied concerning reduced velocity, which represents the ratio of solid to fluid dynamic time scales. A parametric study is performed by sweeping through its bending stiffness (or the non-dimensional elasticity) at a constant mass ratio of 10. The dynamic characteristics are studied in terms of amplitude and frequency variation of plate oscillations against the reduced velocity. The oscillation frequencies of the plate are compared with its first and second-mode natural frequencies to understand the lock-in behavior. The modal frequencies are calculated by approximating the plate as an Euler–Bernoulli beam. The observed response is broadly categorized into four regimes: (i) lock-in with the first mode, (ii) de-synchronization, (iii) lock-in with the second mode, and (iv) de-synchronization. Overall, the plate locks in and de-synchronizes with its natural modes as the reduced velocity changes. This behavior is similar to Vortex-Induced Vibrations (VIV) of an elastically mounted rigid cylinder.

Keywords Fluid–structure interaction · Flow-induced vibration · Flexible plate · Lock-in · Energy harvesting

1 Introduction

Flow-induced deformation of flexible plates is ubiquitous. There are plenty of natural and artificial examples of such systems: from aquatic vegetation to flexible blades. These systems inspire many engineering applications such as drag reduction by flow-induced reconfiguration, wind energy harvesting from flow over flexible blades. Many researchers have attempted to model and simulate these problems from both

A. K. Pandey · G. Sharma · R. Bhardwaj (✉)
Department of Mechanical Engineering, IIT Bombay, Mumbai 400076, India
e-mail: rajneesh.bhardwaj@iitb.ac.in

© The Author(s), under exclusive license to Springer Nature Singapore Pte Ltd. 2024
K. M. Singh et al. (eds.), *Fluid Mechanics and Fluid Power, Volume 2*, Lecture Notes in Mechanical Engineering, https://doi.org/10.1007/978-981-99-5752-1_54

static and dynamic perspectives. For instance, [1] and [2] studied the drag variation as a function of the fluid flow velocity. For bluff bodies, the drag and square of velocity ratio scales as the zeroth velocity power, i.e., $D/U^2 \propto U^0$, where D is the drag force, and U is flow velocity. They suggested that this relation gets modified for flexible bodies as $D/U^2 \propto U^e$, where e is an exponent that can be treated as a measure of reconfiguration. They collected numerous data on plants, such as potted pines, and concluded that $e = -1.13$ for speeds above 6 m/s. Luhar and Nepf [3] worked in the same field by using a combination of experiments and theoretical models. They developed an Euler–Bernoulli beam model for static analysis of flexible plants. A balance between drag force, buoyancy, and beam inertia results in a second-order ordinary differential equation that can be solved to find the relation between drag force and flow velocity. Later, [4] modified the same model by adding the role of skin friction. Leclercq and de Langre [5] developed an analytical model to quantify the drag reduction for flexible cantilever beams. They predicted the value of the Vogel exponent that quantifies the drag reduction in such configurations.

The dynamic characteristics of these systems have also been explored vastly. Py et al. [6] studied the dynamic interaction between the waves and crop. They developed a lock-in mechanism model and compared its output with experimental results. De Langre [7] presented a review on the flow–structure interaction between plants and wind, where he examined the dynamics of plants when they are strongly coupled to the wind. He performed this analysis by modifying the elementary oscillator model using wind load to understand the modal response of plants. Luhar and Nepf [8] performed a combination of experimental and numerical studies to describe the motion of flexible blades that imitate the dynamic behavior of aquatic vegetation. They considered two main parameters in their study: (i) Cauchy number (Ca), and (ii) the blade length to wave travel ratio. The studies were performed for $Ca \ll 1$ and $Ca \gg 1$. Zhang et al. [9] investigated the dynamic behavior of wall-mounted 2D flexible filaments (single and double). They demonstrated the frequency lock-in with different structural modes and explained the physical driving mechanisms.

With the understanding gained from these studies, there have been many attempts to develop energy harvesting models to utilize wave energy by applying these systems. Yu et al. [10] presented a review on the energy extraction from flag vibrations. They studied the vibration and vortex dynamics of the proposed system to understand their feasible practical applications. They assert that flag vibrations are a good energy solution to provide power in various industrial applications. Shoele and Mittal [11] developed a numerical model of an inverted piezoelectric flag. They examined the dynamic response of the inverted flag and investigated its energy harvesting performance.

In most studies, the plate is analyzed in a wall-mounted configuration [5–7, 9]. We propose a fixed bottom of the plate, but not mounted to the wall as shown in Fig. 1. This arrangement allows the flow at both top and bottom of the plate, and the flow energy consumption in boundary layer formation near wall is eliminated. It results in a lower critical Re for the onset of flow-induced plate vibrations [9]. As a result, maximum flow energy is utilized in plate vibrations. Such arrangement is useful where intensive plate vibrations are required at low Re such as energy harvesting.

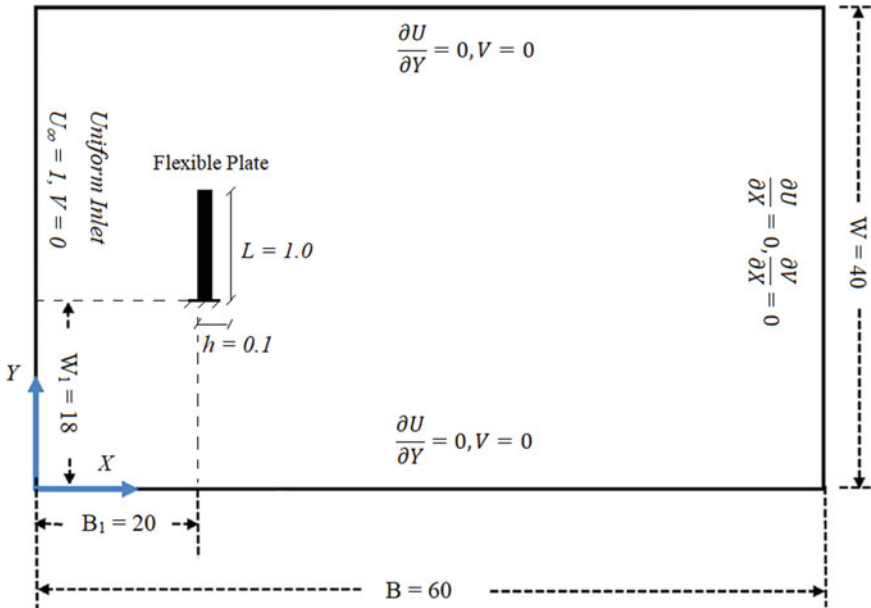


Fig. 1 Schematic of the computational domain with respective dimensions and boundary conditions

2 Computational Model

We use an in-house, partition approach-based fluid–structure interaction (FSI) solver with a two-way coupling between the fluid and solid domains. Fluid is solved over an Eulerian mesh while the structure solver uses the Lagrangian framework. Details of the fluid and structural solver used are as follows.

2.1 Fluid Dynamics

The 2D unsteady, incompressible Navier–Stokes equations are solved along with the continuity equation (Eqs. 1 and 2) using a sharp interface immersed boundary (IB) method-based flow solver developed by [12]. This IB method is based on the ghost cell methodology and uses a Cartesian grid for computations. Discretization in space is done on a cell-centered collocated grid using the finite difference method, and the fractional step method is used for time marching. The flow solver is implemented in two steps: (i) solving the advection–diffusion equation using the Crank-Nicolson scheme, and (ii) solving the pressure Poisson equation using the geometric multigrid method with divergence-free velocity constraint. The method is verified and tested for second-order accuracy [12].

$$\frac{\partial u_i}{\partial t} + u_j \frac{\partial u_i}{\partial x_j} = -\frac{\partial p}{\partial x_i} + \frac{1}{\text{Re}} \frac{\partial^2 u_i}{\partial x_j \partial x_j} \quad (1)$$

$$\frac{\partial u_i}{\partial x_i} = 0 \quad (2)$$

where $\text{Re} = \frac{\rho_r U_\infty L}{\mu}$.

2.2 Solid Dynamics

The structural solver is an open-source finite element solver [13] that was developed at Sandia National Labs, CA. Using it, we solve 2D Navier's equations of motion (Eq. 3) for plane strain condition. We use the Saint Venant-Kirchoff material model to simulate large solid deformations accurately. In this model, the solid is treated as a (i) geometrically nonlinear, (ii) linear elastic material. The constitutive relation and the Second Piola-Kirchoff stress expressed as a function of Cauchy stress is shown in Eq. 4. The Green-Lagrangian strain tensor is written as a function of the deformation gradient as shown in Eq. 5.

$$\rho_s \frac{D^2 d_i}{Dt^2} = \frac{\partial \sigma_{ij}}{\partial x_j} + \rho_s f_i \quad (3)$$

$$S = \lambda \text{tr}(E)I + 2\mu E \quad ; \quad S = JF^{-1}\sigma F^{-T} \quad (4)$$

$$E = \frac{1}{2}(F^T F - I) \quad (5)$$

2.3 Coupling of the Flow and Structural Solvers

The fluid and structural solvers are coupled using an implicit strong coupling (see details in Ref. [14–16]). The FSI field is solved numerically using a partitioned approach where fluid and solid domains are solved alternately with interface boundary conditions. For the flow field, a one-time step is marched to obtain the updated pressure and velocity field with the current deformed shape of the solid. The updated flow field is used to solve the structural dynamics then. At the interface, the continuity of velocity and traction is maintained as given by Eqs. 6 and 7, respectively. These interface conditions are forced as boundary conditions while marching in time for fluid and solid.

$$u_{i, \text{fluid}} = \dot{d}_{i, \text{solid}} \quad (6)$$

$$\sigma_{ij, \text{fluid}} n_j = \sigma_{ij, \text{solid}} n_j \tag{7}$$

2.4 Key Parameters

The geometry and material properties of the plate primarily govern its dynamic response. We consider two such parameters viz. (i) bending stiffness (Eq. 8), and (ii) mass ratio (Eq. 9). We perform the simulations at different values of bending stiffness. These values are obtained by varying the non-dimensional Elasticity (E) and keeping all other parameters constant. We study this dynamic problem concerning reduced velocity, U_R (see Eq. 10). It's a dimensionless parameter representing the ratio of solid to fluid dynamics time scales. The chosen time scale for fluid is the convective time scale. For the solid, the dynamic time scale is the inverse of its natural frequency. Natural frequencies of the plate in vacuum are calculated by treating it as an Euler–Bernoulli beam (Eq. 11). We focus on the first and second modes and ignore the higher modes for the present work. It should be noted that the consideration of natural frequencies in vacuum is an approximation since the plate natural frequencies are modulated by various effects due to the presence of a surrounding fluid: (i) added mass effect, (ii) flow-induced damping effect, (iii) added stiffness due plate curvature in its mean position, and (iv) nonlinear effect due to large amplitude oscillations. Zhang et al. [9] argued that the added mass and flow-induced damping tend to decrease the plate natural frequency while added stiffness effect increases the same. Both cancel each other's effect to some extent, however, implications of nonlinear effects are hard to analyze theoretically. As a result, the natural frequencies in vacuum are approximate plate natural frequency values that are used in this study to compare with the plate's oscillation frequency and analyze its response.

$$K_b = \frac{E}{\rho_f U_\infty^2} \frac{h^3}{12L^3} \tag{8}$$

$$M = \frac{\rho_s h}{\rho_f L} \tag{9}$$

$$U_R = \sqrt{\frac{M}{K_b}} \left(\sim \frac{fn_{\text{fluid}}}{fn_{\text{solid}}} \sim \frac{T_{\text{solid}}}{T_{\text{fluid}}} \right) \tag{10}$$

$$f_{ni} = \frac{k_i^2}{2\pi L} \sqrt{\frac{K_b}{M}} \tag{11}$$

For post-processing of the obtained data, we define an angle θ concerning the probe point (x, y) and reference coordinates of the beam (x_0, y_0) as shown in Fig. 2. This transformation is similar to the θ definition presented by [9] in their study of

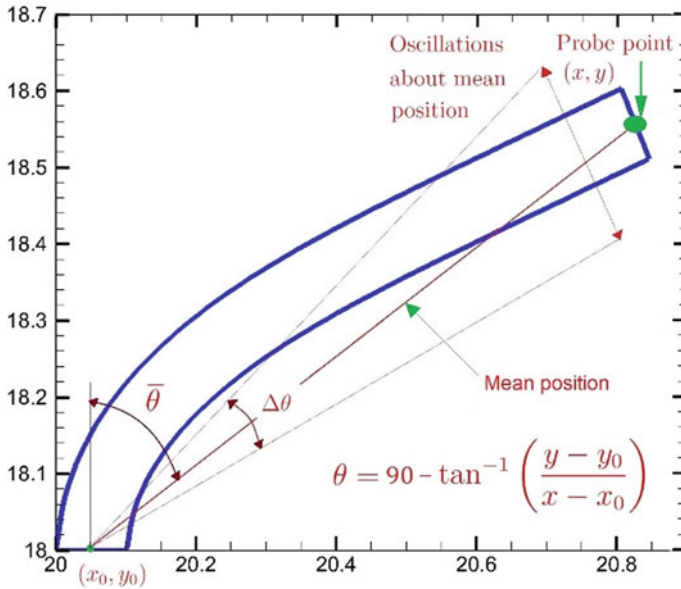


Fig. 2 Location of the probe point, and moving from XY space to θ space for the plate oscillation frequency (f_p) and amplitude (A_θ) calculation

wall-mounted flexible plates. However, they defined θ from the X-axis while we take θ as the angular deformation from its initial vertical position. The probe is installed at the tip of the plate with coordinates $(x, y) = (20.05, 19.00)$ at time $t = 0$. As the solid deforms, the global coordinates of this point change, but it remains fixed locally to the solid. We use this transformation to move from XY space to the θ space for calculating the plate frequency, f_p and amplitude of vibrations, A_θ . The amplitude is now defined as $A_\theta (= \Delta\theta/2)$ instead of ΔX and ΔY separately, and it's calculated as the peak to peak amplitude. Since θ depends on both X and Y-coordinates of the probe point, it results in an advantage of accounting both X and Y parameters into one.

3 Validation and Testing

3.1 Grid and Domain Size Independence Test

The grid and domain independence tests are performed at $Re = 100$. The chosen parameters for the solid are: (i) modulus of Elasticity, $E = 400$, (ii) Poisson's ratio, $\nu = 0.4$, (iii) Mass ratio, $M = 1$. The test cases are compared using the root means square (RMS) displacements (both X and Y) of the probe point (see Fig. 2). First, a

Table 1 Domain independence test for minimum grid size 0.02. % Error is computed with respect to the benchmark case

Domain size	<i>rms dx</i>	% Error	<i>rms dx</i>	% Error
75 × 50	0.844	0.0	0.52	0.0
65 × 40	0.842	0.23	0.524	0.73
60 × 50	0.841	0.29	0.525	0.94
60 × 40	0.8415	0.25	0.5245	0.81

Table 2 Grid independence test for domain size 60x40. % Error is computed with respect to the benchmark case

Grid size (min $\Delta x = \Delta y$)	<i>rms dx</i>	% Error	<i>rms dx</i>	% Error
0.01	0.844	0.0	0.52	0.0
0.02	0.842	0.25	0.525	0.81
0.025	0.841	0.31	0.525	0.98

benchmark case is simulated with a domain size of 75 × 50, a minimum grid size of 0.01 ($\Delta x = \Delta y$) close to the plate, and a time step size of 0.005. During both tests, it serves as the reference solution for computing the relative errors.

For the domain independence test, all the domains consist of a minimum grid size of 0.02 ($\Delta x = \Delta y$) and a time step size of 0.01. The domain sizes are varied in both *x* and *y* directions, as shown in Table 1. For all simulations, the CFL number is retained well below 1 to ensure numerical stability. The chosen domain size for further simulations is 60 × 40 with an error below 1%.

The grid independence test is performed over a domain size 60 × 40 and a time step size of 0.01. Three different grid sizes are chosen, and errors are compared with the benchmark case as shown in Table 2. The selected grid size for further simulations is min. $\Delta x = \Delta y = 0.02$.

3.2 Code Validation

We use a FORTRAN code that is based on the sharp interface immersed boundary method developed by [12]: see Sect. 2.1 for details of the method. The code has been validated extensively in previous literature. The flow solver has been validated by [12] using a combination of 2D and 3D problems, to name a few, flow past: (i) circular cylinder, (ii) sphere, (iii) suddenly accelerated normal plate, etc. The solver has been further extended for flexible body deformation (see Sect. 2.2 for details) by [14]. Bhardwaj and Mittal [14] and Kundu [15] validated the same using the benchmark problem ‘flow over splitter plate attached to a cylinder’ proposed by Turek and Hron [17]. They demonstrated that the structural solver is capable of accurately simulating large-scale deformation problems.

4 Results and Discussion

We perform simulations by varying the plate's modulus of Elasticity, E in a range of $[2 \times 10^5, 365]$ keeping all other parameters constant. It results in a variation of plate bending stiffness (K_b) and reduced velocity (U_R). As these parameters change, the dynamic response of the plate changes. We track the coordinates of the probe point (see Fig. 2) and use this data to compute the oscillation frequency and amplitude of vibrations as explained in Sect. 2.4.

4.1 Frequency and Lock-In Characteristics

Flow over the plate results in vortex shedding from its top and bottom, as shown in Fig. 3. The vortices are shed in a C(2S) pattern at low values of U_R where coalesced vortices of similar signs are shed that are arranged in two distinct rows. At large values of U_R , the plate becomes very soft and is streamlined to the flow. As a result, the vortex shedding modifies to a 2S pattern in which two single vortices are shed in an opposite sense of rotation per cycle. The alternately shedding vortices are a result of the competing inertia and viscous forces that impose a periodic forcing on the plate. Due to this phenomenon, the plate bends at a certain angle and starts to oscillate about a curved mean position as shown in Fig. 2. The mean position of plate, θ depends on the chosen modulus of Elasticity (E): softer the plate (represents a low value of E), larger its mean position.

The dynamic response of the plate is captured by the peak to peak amplitude (A_θ) and frequency (f_p) of its vibrations as shown in Figs. 4 and 5, respectively. Figure 4 demonstrates the variation in plate amplitude (A_θ) with U_R . On the other hand, in Fig. 5, we plot the amplitude spectral density (ASD) of the displacement signal (θ) without any normalization. The contours represent the spectrum of plate oscillation frequency (f_p) with varying reduced velocity (U_R). Histogram distribution is used on a uniform frequency scale ($\Delta f = 0.025$) for interpolating the frequencies. The cut off lowest frequency shown on the plot is 1% of the maximum oscillation frequency. A logarithmic scale is used for plotting the color map, and its normalized with the maximum frequency. Darker contour areas represent a dominant output frequency and vice-versa, at any value of U_R . In addition to this, we compute the first and second-mode natural frequencies of the plate (f_{n1} and f_{n2} , respectively) using Euler–Bernoulli beam theory (see Eq. 11) and plot them as solid red and blue lines, respectively, on the same plot. The resulting plot demonstrates the lock-in/de-synchronization behavior of the system with first/second natural modes as U_R changes. Both plots (i.e., Figs. 4 and 5) are shown on the same scale of the U_R to demonstrate the variations in plate amplitude as the frequencies lock-in or de-synchronize. We qualitatively identify four regions as follows:

Region 1: Lock-in with first mode: It's a small reduced velocity, U_R , region where the plate's modulus of Elasticity, E is high (order of 10^4). Lock-in with the first mode

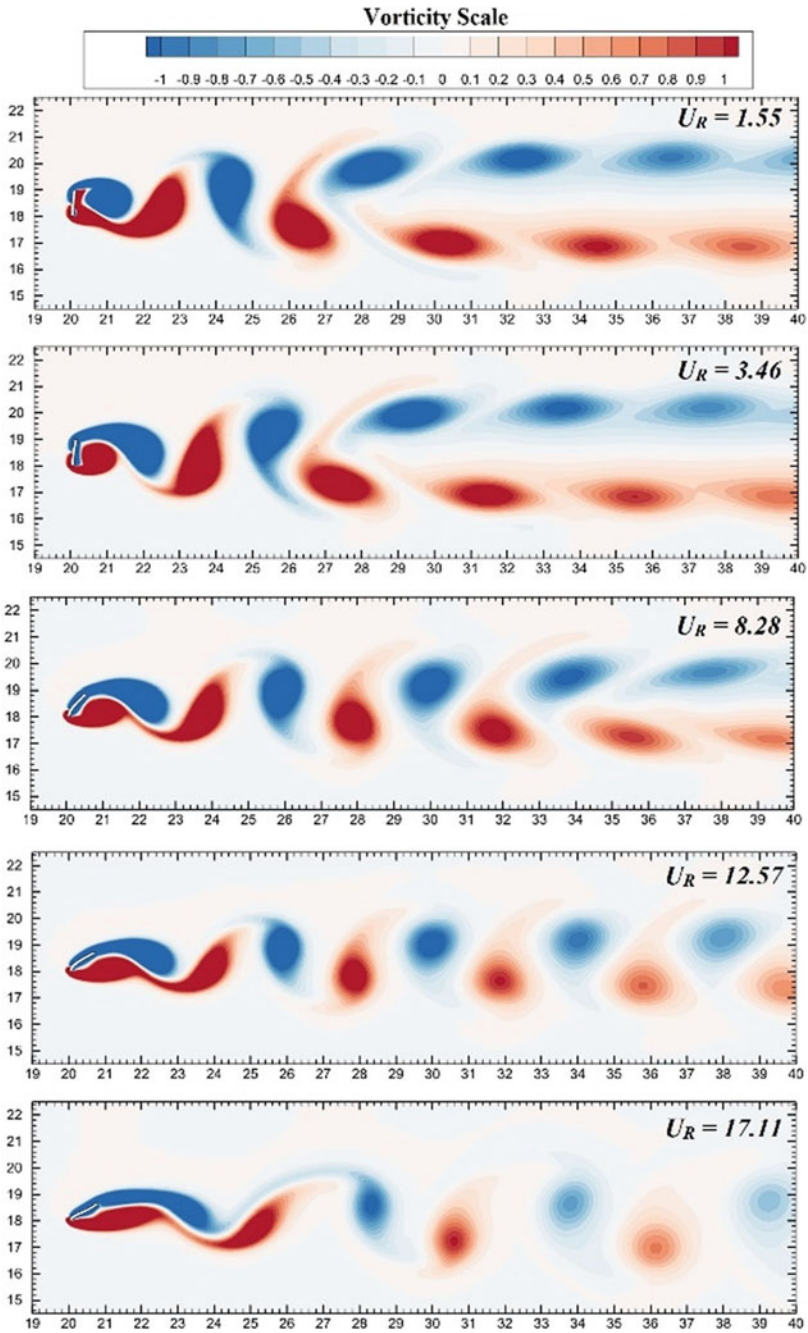


Fig. 3 Vorticity contours along with instantaneous plate deformation at selected values of reduced velocity, U_R for a fully developed flow

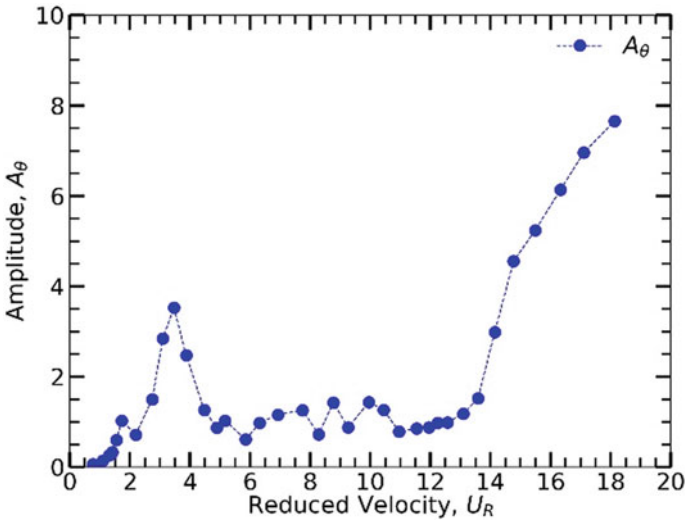


Fig. 4 Variation in amplitude of the plate vibrations A_θ with respect to reduced velocity, U_R

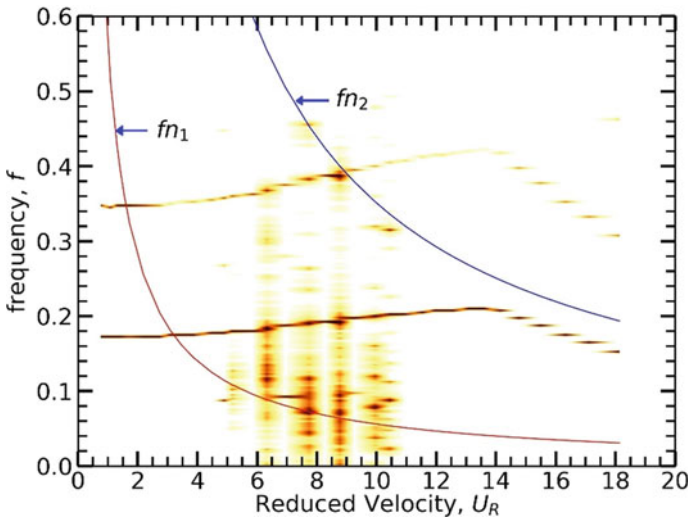


Fig. 5 Contour plot for plate’s frequency response with U_R . The first and second mode plate natural frequency lines (f_{n1} and f_{n2}) are drawn in red and blue, respectively

occurs for a range $U_R \approx (2.0, 4.9)$. In this range, the amplitude starts to increase from a value of 0.7° . At $U_R \approx 3.5$, the observed plate amplitude is maximum, i.e., 3.52° .

Region 2: De-synchronization: As we further reduce E (order of 10^3), the plate becomes softer and it de-synchronizes with its first mode. The amplitude drops back to around 1° . This starts to occur at $U_R \approx 4.9$. The plate keeps oscillating for a large range of U_R where it does not lock-in with any other mode. The observed range of this de-synchronized plate vibrations is $U_R \approx (4.9, 13.0)$. We also observe secondary dominant frequencies in the range $U_R \approx (5.0, 10.5)$. The physics behind the presence of these secondary dominant frequencies in this U_R range is yet to be explored.

Region 3: Lock-in with second mode: With a further reduction in E (order of 10^2), the plate becomes very soft and starts to show large deformations. At $U_R \approx 13.6$ the plate response frequency reaches closer to its second-mode natural frequency and lock-in with second mode is observed. As a result of this lock-in, amplitude of vibrations again starts to increase with U_R . At $U_R \approx 18.13$ plate completely locks in with its second mode and a peak amplitude of 7.54° is noted. This amplitude is almost three times the amplitude in first-mode lock-in. This is understandable by the fact that the plate is softer in the second-mode lock-in as compared to the first-mode lock-in, and is expected to show larger deformations.

Region 4: De-synchronization: The plate remains locked in with its second mode for a larger range of $U_R \approx (14.8 - 20)$. Above $U_R = 20$ the plate becomes extremely soft ($E \approx 150$) and very large deformations occur. Due to a very low mass ratio (M) and modulus of Elasticity (E), the simulations become hard to be handled by our solver at very high U_R . Due to this, for now, we limit our simulations to $U_R = 20$ for maintaining accuracy. However, we are investigating other parametric combinations to achieve high U_R simulation cases as a part of our future plans. It is expected that the plate should de-synchronize with the second mode at a high value of U_R .

5 Conclusions

In this study, we investigated the flow-induced vibrations of a flexible plate in a 2D incompressible flow field. The vortex shedding patterns were examined to understand the onset of plate vibrations. The amplitude and frequency response of these vibrations were plotted, and insights were given into the plate dynamics concerning its first and second-mode natural frequencies with reduced velocity. We found that the plate response is similar to the vortex-induced vibrations (VIV) of elastically mounted rigid cylinder. Similar to the VIV, plate response is divided into various regions. In these regions, the plate locks in and de-synchronizes with its first and second-mode natural frequencies as the reduced velocity changes. Overall, the plate exhibits rich dynamics that later has been further investigated [18] for potential practical applications such as energy harvesting and drag/lift optimization.

Acknowledgements We gratefully acknowledge financial support by a grant (Grant No. MTR/2019/000696) from the Science and Engineering Research Board (SERB), Department of Science

and Technology (DST), New Delhi, India. A.K.P. thanks the support of Prime Minister's Research Fellowship (PMRF) from the Ministry of Education, Government of India.

Nomenclature

A_θ	Plate amplitude (peak to peak)
C_D	Coefficient of drag
C_L	Coefficient of lift
d	Displacement
d_x	Probe point displacement in X
d_y	Probe point displacement in Y
E	Modulus of Elasticity
f_i	Body force
f_{ni}	Plate natural frequency; $i = 1, 2, 3...$
f_p	Plate oscillation frequency
F	Deformation gradient
h	Plate thickness
J	Jacobian
K_b	Bending stiffness
L	Plate length
B	Width of computational domain
W	Height of computational domain
M	Mass ratio
p	Pressure
Re	Reynolds number
S	Second Piola-Kirchoff Stress
St	Strouhal number
t	Time
u	Velocity
U	Free stream velocity
U_R	Reduced velocity
x	Space variable
ρ_s	Plate density
ρ_f	Fluid density
μ	Fluid dynamic viscosity
$\Delta\theta$	Angular displacement of plate
ν	Poisson's ratio
σ	Cauchy Stress

References

1. Vogel S (1984) Drag and flexibility in sessile organisms. *Am Zool* 24(1):37–44
2. Vogel S (2020) *Life in moving fluids: the physical biology of flow* revised and expanded second edition. Princeton University Press
3. Luhar M, Nepf HM (2017) Flow-induced reconfiguration of buoyant and flexible aquatic vegetation. *Limnol Oceanography* 56(6):2003–2017
4. Bhati A, Sawanni R, Kulkarni K, Bhardwaj R (2018) Role of skin friction drag during flow-induced reconfiguration of a flexible thin plate. *J Fluids Struct* 77:134–150
5. Leclercq T, de Langre E (2016) Drag reduction by elastic reconfiguration of non-uniform beams in non-uniform flows. *J Fluids Struct* 60:114–129
6. Py C, De Langre E, Moullia B (2006) A frequency lock-in mechanism in the interaction between wind and crop canopies. *J Fluid Mech* 568:425–449
7. De Langre E (2008) Effects of wind on plants. *Annu Rev Fluid Mech* 40:141–168
8. Luhar M, Nepf HM (2016) Wave-induced dynamics of flexible blades. *J Fluids Struct* 61:20–41
9. Zhang X, He G, Zhang X (2020) Fluid–structure interactions of single and dual wall-mounted 2d flexible filaments in a laminar boundary layer. *J Fluids Struct* 92:102787
10. Yu Y, Liu Y, Amandolese X (2019) A review on fluid-induced flag vibrations. *Appl Mech Rev* 71(1)
11. Shoele K, Mittal R (2016) Energy harvesting by flow-induced flutter in a simple model of an inverted piezoelectric flag. *J Fluid Mech* 790:582–606
12. Mittal R, Dong H, Bozkurtas M, Najjar FM, Vargas A, Von Loebbecke A (2008) A versatile sharp interface immersed boundary method for incompressible flows with complex boundaries. *J Comput Phys* 227(10):4825–4852
13. Tahoe, Tahoe is an open source C++ finite element solver, which was developed at Sandia National Labs, CA. <http://sourceforge.net/projects/tahoe/>
14. Bhardwaj R, Mittal R (2012) Benchmarking a coupled immersed-boundary-finite-element solver for large-scale flow-induced deformation. *AIAA J* 50(7):1638–1642
15. Kundu A, Soti AK, Garg H, Bhardwaj R, Thompson MC (2020) Computational modeling and analysis of flow-induced vibration of an elastic splitter plate using a sharp-interface immersed boundary method. *SN Appl Sci* 2(6):1–23
16. Manjunathan SA, Bhardwaj R (2020) Thrust generation by pitching and heaving of an elastic plate at low Reynolds number. *Phys Fluids* 32(7):073601
17. Turek S, Hron J (2006) Proposal for numerical benchmarking of fluid-structure interaction between an elastic object and laminar incompressible flow. Springer, Fluid-structure interaction, pp 371–385
18. Pandey AK, Sharma G, Bhardwaj R (2023) Flow-induced reconfiguration and cross-flow vibrations of an elastic plate and implications to energy harvesting *Journal of Fluids and Structures* 122:103977. <https://doi.org/10.1016/j.jfluidstructs.2023.103977>

Numerical Investigations of Forced Oscillating Circular Cylinder in Uniform Flow



Ravikant Roy and Simon Peter

Abstract A two-dimensional forced vibration numerical simulation is carried out for a transversely and streamwise oscillating circular cylinder in uniform flow separately. The governing equations for an incompressible flow in a non-inertial frame of reference is solved by the Finite Volume Method (FVM). A Ghost cell immersed boundary method (GCIBM) is applied to the non-body conformal Cartesian grid. The Reynolds number and normalized amplitude of oscillation were kept at constant at 150 and 0.3, respectively. The frequency ratio f_r for transversely and the streamwise oscillating circular cylinder is varied as $0.7 \leq f_r \leq 1.2$ and $0.5 \leq f_r \leq 2.7$, respectively. The lock-in zone for transversely and the longitudinally oscillating circular cylinder were found to be in the frequency ratio of $0.75 \leq f_r \leq 1.05$ and $1.15 \leq f_r \leq 1.9$, respectively. The wake patterns closely match the reported results. The average force coefficients are plotted against f_r and showed the same trend as that of the reported results. In streamwise there are two types of lock-in zone found, harmonic and sub-harmonic region are being observed. Coefficient of energy is increased from 0 to 0.6 in transverse and in streamwise. The value of coefficient of energy is decreased from 0 to -3 .

Keywords Forced vibration · Transversely oscillating cylinder · Lock-in region · FVM · GCIBM

1 Introduction

Every engineering structure, such as a building, chimney, bridge, electric power pole riser tube, or offshore platform, must be able to endure fluid stresses. Failures of these structures can be destructive if fluid forces are ignored throughout design

R. Roy (✉) · S. Peter
Department of Mechanical Engineering, NIT Calicut, Kozhikode 67301, India
e-mail: royravikant4@gmail.com

S. Peter
e-mail: simon@nitc.ac.in

considerations. For example, on November 7, 1940, the Tacoma Narrows bridge in the United States state of Washington was destroyed as a result of VIV [1]. On January 14, 2002, one of the 265-foot-tall towers of the thriller ride, VertiGo in the U.S. state of Ohio collapsed due to VIV [2]. VIV was also caused for the burst of a thermowell within a sodium coolant line in Japan's Monju nuclear reactor on December 8, 1995, which resulted in a severe fire [2]. The current study enhances design engineers in improving the stability, durability, and dependability of a structure.

Mainly there are two popular forms of bluff bodies in which we are taking cylinder to exhibit all physical phenomena. The number and coefficient of forces are expressed below for the structure having uniform velocity (U), characteristics length (D), kinematic viscosity, and density denoted by ν and ρ , respectively. From these respective expressions for the Reynolds number, Coefficients of forces and Strouhal number is given as

$$\text{Re} = \frac{UD}{\nu}, C_i = \frac{F_i}{\frac{1}{2}\rho U^2 A_i}, St = \frac{fD}{U} \quad (1)$$

In oscillating circular cylinder preliminary studies is carried out. Photographs of the wake's flow patterns were taken at the beginning and conclusion of oscillation cycles. This recurrence suggests that the flow and cylinder motion have the same frequency. The state of the wake was known as "lock-in" when the period or frequency of the flow synchronized with that of cylinder oscillation [3].

In the majority of investigations, the wake modes seen in forced vibration analysis are comparable to those of free vibration. The same phenomena, including harmonic oscillation of structures, synchronization, shift in time of vortex shedding, and phase leap, have been seen in both free and forced vibration experiments [4].

Vortex shedding from a circular cylinder occurs across a large range of Reynolds numbers; however, at certain Reynolds numbers, vortex generation ceases, and other modifications in flow patterns occur.

2 Literature Review and Objective

Transverse oscillations are frequently observed in environment flows near around chimneys, transmission lines, suspension bridges, cables and high-rise buildings. It has resulted in a large number of experimental and numerical studies of circular cylinders subjected to forced transverse oscillations. Lock-in generally occurs to unity which means f_e is approximately equals to f_s ; later various experimental studies carried out in streamwise oscillations. It has not that much significant as compared to transverse oscillations due to weaker forces on the structure which is one tenth of the transverse oscillating forces F_x [5]. Lock-in generally observed nearly twice of the vortex shedding frequency f_s and there are two types of locked region found namely harmonic and sub-harmonic in case of streamwise oscillations.

Placzek et al. [6] worked on an explicit staggered algorithm, 2D Navier stokes equation solved by FVM for Re 100. He demonstrated all aerodynamic coefficients including the Strouhal number and found locked in and unlocked in configuration for amplitude 0.25 getting a lower limit as 0.75 and upper limit of frequency ratio as 1.25.

Leontini et al. [7] demonstrated that energy transfer is reliant on frequency, but as amplitude grows, the dependency changes from + ve to -ve, he demonstrated no notable change in wake structure.

Peter and De [8] emphasized the benefits of employing GCIBM in a non-inertial frame of reference. They worked on fluid flow equations and it is solved by using the finite volume method with a collocated arrangement of variables on a non-uniform Cartesian grid. The suggested approach exhibits fair agreement with the results for flow past a stationary sphere, rotating cylinder, and circular cylinder oscillating transversely.

Kim et al. [9] executed flow over a circular cylinder oscillating streamwise at various driving amplitudes and frequencies. When the driving amplitude was increased, the sub-harmonic lock-in zone was discovered in a lower frequency range. Baranyi et al. [10] investigated mechanical energy transfer E between a fluid and a cylinder that is oscillating transversely is the main focus of the study. The fluid minimizes the oscillation of the cylinder when E is negative. When E is positive, the fluid works on the cylinder and can cause vortex-induced vibration (VIV) in circumstances of free vibration.

The present work categorizes into two problems: (1) Transverse forced oscillation of circular cylinder in uniform fluid flow at Reynolds number 150, $A = 0.3D$ and (2) Streamwise forced oscillation of circular cylinder in uniform fluid flow at zone the relation between driving frequencies (f_e) and vortex shedding frequencies (f_s).

3 Materials and Methods

The governing equations, frame of reference and numerical methods for 2D Finite Volume Method (FVM) is explained in the following sections.

3.1 Governing Equations

The continuity and momentum equations in the inertial frame of reference for an incompressible flow in coordinate free form is given by

$$\frac{\partial U_i}{\partial x_i} = 0 \quad (2)$$

Table 1 Normalized variables

Variable	Scale	Normalized variable
Length (x'_i)	L	$x_i^* = \frac{x'_i}{L}$
Velocity (u'_i)	U	$u_i^* = \frac{u'_i}{U}$
Time (t')	L/U	$t^* = \frac{t'}{L/U}$
Pressure (p')	ρU^2	$p^* = \frac{p'}{\rho U^2}$

$$\frac{\partial U_i}{\partial t} + \frac{\partial U_i U_j}{\partial x_j} = -\frac{1}{\rho} \frac{\partial P}{\partial x_i} + \nu \frac{\partial^2 U_i}{\partial x_j \partial x_j} \tag{3}$$

where ρ is the density, ν is the kinematic viscosity of the fluid which are considered as constants and u_i is the i th component of velocity ($i = x, y$), P is the pressure and 't' is time. After that equation is transformed into non-inertial frame with coordinate transformation further it is normalized and the equation is formed in non-dimensional form. Here Table 1 showing all the normalized variables used for present study.

Discretization is done by FVM and CNLM of normalized governing equations and the second-order implicit unsteady solver approach was selected with [11] which is second-order accurate in time.

Two-dimensional numerical simulations were performed on a non-uniform Cartesian grid of 500×450 in both the transverse (y) and streamwise (x) directions, respectively. The computational domain is divided into 9 regions. A square domain of size $283 * 283$ having a side of 1.8 is taken and encloses in cylinder, so a uniform mesh is generated around the cylinder with a grid resolution of $\Delta x = \Delta y = 0.007$. Aspect ratio for x and y is 68.97 and 18.87, respectively. It is ratio of longest edge length to shortest edge length. Skewness, a measure of mesh quality, was less than 0.8 as highly skewed faces are not acceptable. Orthogonality involves the angle formed by the vector that connects two mesh nodes and the normal vector for each integration point surface associated with that edge, it is near to 1 which shows good quality of mesh.

Six meshes were developed for mesh independence analysis and the precise time steps on the solution was investigated. It was found that a time-step independent solution was attained at $\Delta t = 0.0025$. it shows insignificant variation with respect to mesh5 and mesh 6 an also stationary vortex shedding frequency is nearly same for both the meshes, so for better visualization and less computational time and cost-effective mesh 5 is selected for the project study as shown in Table 2. It provides comparison of Strouhal number and mean drag coefficient of the six meshes.

The comparison with good reported results shown in Table 3.

Table 2 Mesh independence study

Mesh size	% Change	$\langle C_D \rangle$	St_o
Mesh 1 (300 × 281)	–	1.3014	0.1929
Mesh 2 (350 × 301)	24.97	1.2899	0.1901
Mesh 3 (400 × 351)	33.27	1.2917	0.1900
Mesh 4 (450 × 401)	28.52	1.2917	0.1894
Mesh 5 (500 × 451)	24.96	1.2915	0.1909
Mesh 6 (550 × 501)	22.19	1.2915	0.1908

Table 3 Comparison of global flow parameter with stationary cylinder

Author	$\langle C_D \rangle$	rms C_L	max C_L	St_o
Lu et al. (2011)	1.330	–	0.530	0.184
Baranyi et al. (2006)	1.330		0.510	–
Present	1.291	0.397	0.560	0.189

4 Results and Discussion

The motion of a circular cylinder caused by forced oscillation in both the transverse and longitudinal directions is depicted below in Fig. 1.

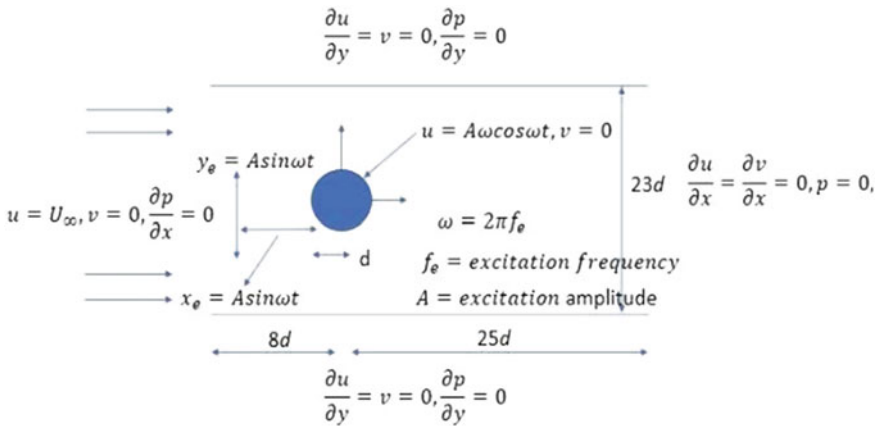


Fig. 1 Schematic diagram of forced oscillation of a circular cylinder in y and x-direction, respectively

4.1 Transverse Direction

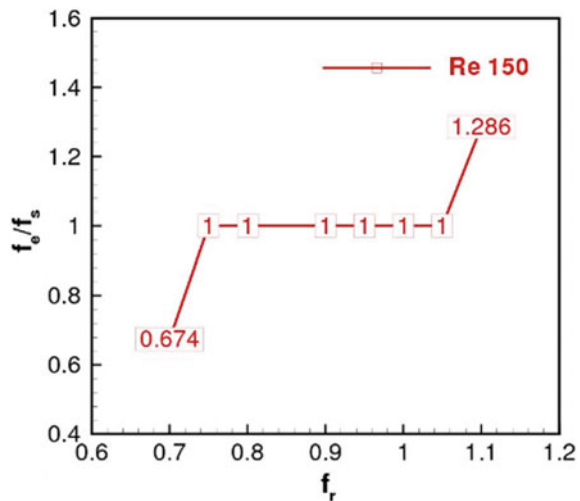
In that the cylinder is given driving or excitation frequency f_e and amplitude which is displacement of cylinder $A = 0.3D$. The wake oscillation or vortex shedding frequency f_s is obtained by carrying out through FFT of the C_L signals of the given frequency ratio. By varying frequency ratio from 0.7 to 1.2, in that we found synchronization or lock-in state in which excitation frequency is equal to vortex shedding frequency, and in non-lock-in range, where f_e and f_s is not unity as it exists linearly with stationary cylinder frequencies. The frequency ratio f_r for the lock-in range is found to be 0.75–1.05 and it is shown in Fig. 2.

The phase portraits of the system talked about to analyze the response by taking lift coefficient signals for the study. Spectra of lift coefficient is showed to highlight the sinusoidal response and it shown that the main frequency which is vortex shedding frequency and excitation frequency is nearly 1 in transverse oscillating case. This shows that aerodynamic forces are governed by excitation frequency instead of stationary vortex shedding cylinder frequency. Figures 3 and 4 shows the phase portraits of lower frequency unlock region at $f_r = 0.7$. Figure 5 shows the phase portraits of lower frequency lock-in region at $f_r = 0.75$. The lobes of phase portraits are aperiodic at $f_r = 0.7$ confirm the non-synchronized state whereas at $f_r = 0.75$ they show one-lobe closed orbits indicate a periodic synchronized state.

The power spectrum of $f_r = 0.7$ in Fig. 4 indicate multiple peak which confirms that the system is in the unsynchronized state whereas the power spectrum of $f_r = 1$ in Fig. 6 indicate the peak at the Strouhal frequency of the stationary circular cylinder and its harmonic peak which confirms that the system reached the synchronized state.

It is observed that the phase portraits of higher frequency unlock- in region at $f_r = 1.1$. Within the synchronization region the coefficient of energy changes its sign

Fig. 2 Lock-in range for transverse forced oscillations at $A = 0.3D$



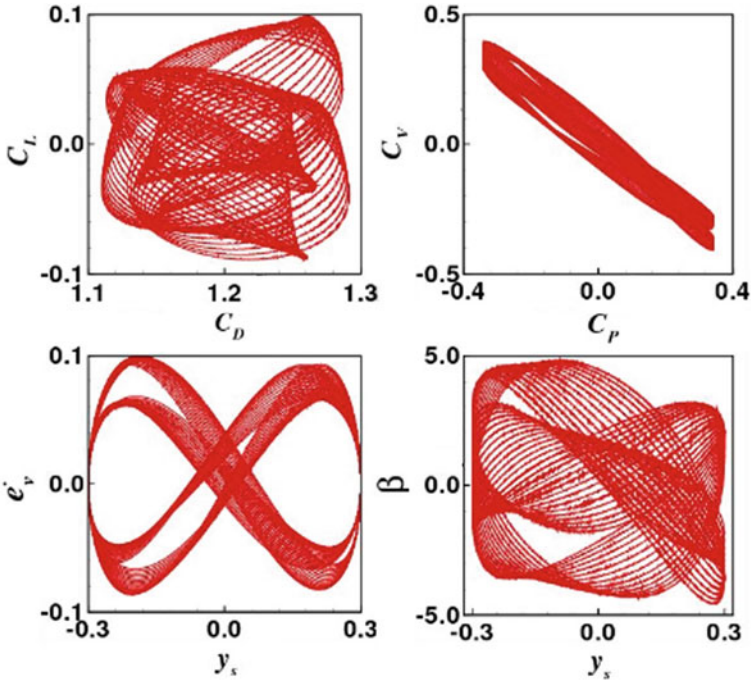
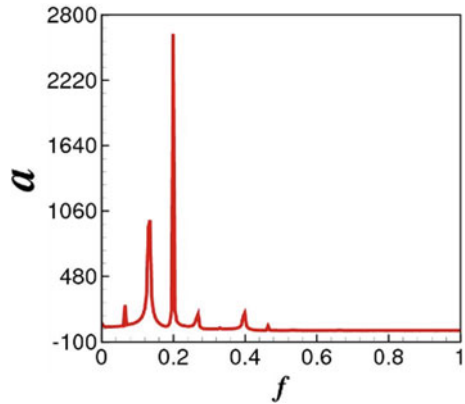


Fig. 3 Phase portraits of lower frequency non-lock-in zone $f_r = 0.7$

Fig. 4 Power spectrum of $f_r = 0.7$



but there is no change in the mode of wake structure. The lobes of phase portraits are aperiodic at $f_r = 1.1$ confirm the unsynchronized state.

The time traces of one oscillation cycle for $f_r = 1.05$ and $f_r = 0.7$ are discussed. The eight distinct dots are present in the time traces at various cylinder positions. These dots show the immediate positions of the circular cylinder in each case as

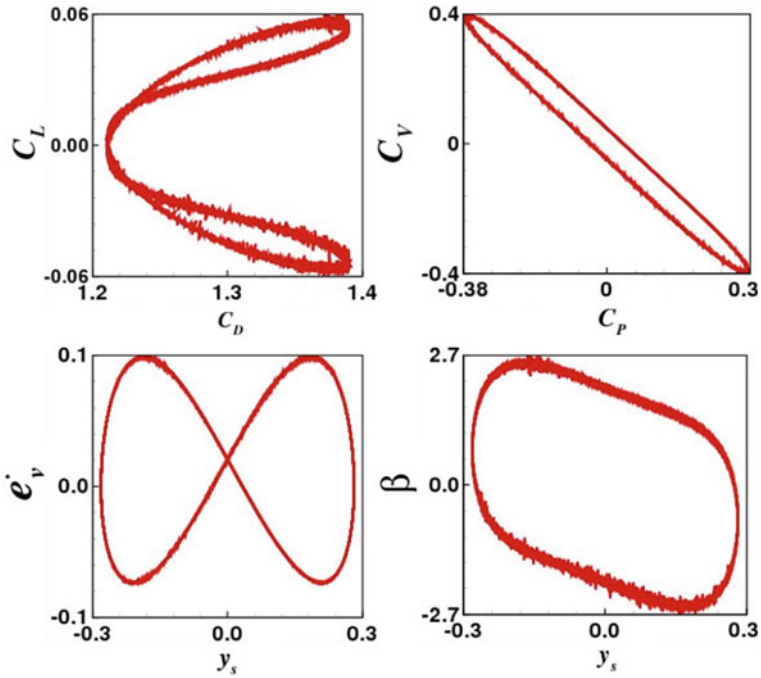
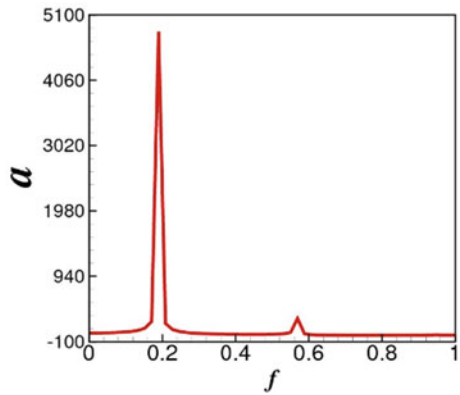


Fig. 5 Phase portraits of lower frequency lock-in zone $f_r = 0.75$

Fig. 6 Power spectrum of $f_r = 1$



well as the variation in the global flow parameter over time. If the system is in the synchronized state, then the first and the last dot of the time traces are on the same horizontal level whereas in case of the non-synchronized state the first and the last dot of the time traces are on the different horizontal level. Time traces of the $f_r = 1.05$ in Fig. 7a confirm that the system is on synchronized state whereas the time traces of the $f_r = 0.7$ confirmed that system is in non-synchronized state.

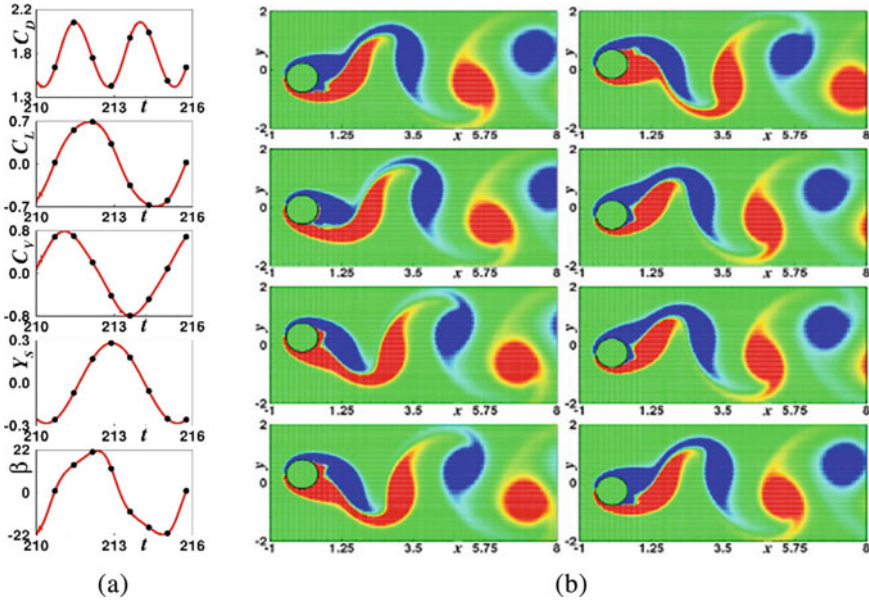


Fig. 7 Time traces and instantaneous vorticity contour of $f_r = 1.05$

Instantaneous vorticity contour of one cycle oscillation of the circular cylinder for $f_r = 1.05$ is shown in Fig. 7b It represent the shedding of the vortices from the cylinder surface in one cycle of the oscillation of the circular cylinder. The lock-in state is also explained in the other manner that when the circular cylinder completes its one cycle of the oscillation at the same time the vortices also complete its one cycle of detachment which means that the one vortex is detached from the top and other is detached from the bottom of the cylinder. Eight different snaps are taken during the oscillation of the cylinder. If the first and eighth snap of the vortices are exactly same then this confirm that the system is in synchronized state otherwise it is in unsynchronized state.

The global parameters like C_D avg, C_L rms were plotted by varying frequency ratio and amplitude. The average value of C_D .

is 1.291 for fixed cylinder whereas the value reaches to 1.735 for $f_r = 1.05$. The maximum value of lift coefficient is 0.560 for stationary cylinder whereas for $f_r = 0.7$ its value decreases to 0.111 and then further increases to 2.011 at $f_r = 1.2$ is shown in Fig. 8.

Mechanical energy transfer is defined as work done by fluid to the cylinder which is represented as positive energy flow and if work done by cylinder to the fluid, then it is represented as negative energy flow. It is measured by energy transfer coefficient and the expression is shown below [4, 10]

$$C_E = \frac{1}{T} \int_0^T C_L(t) y_s'(t) dt \tag{4}$$

Fig. 8 Global flow parameters by varying frequency ratio at $A = 0.3D$

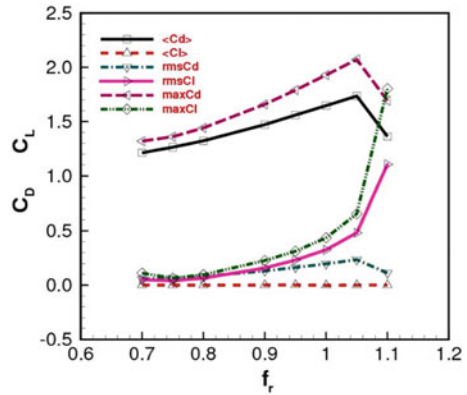
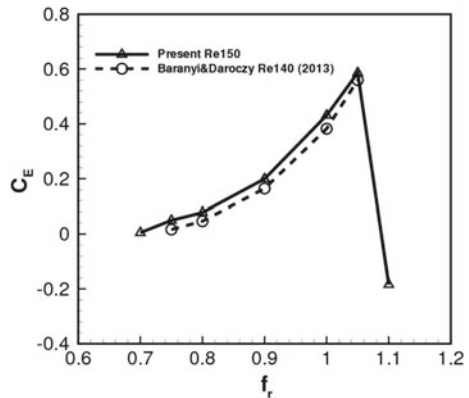


Fig. 9 Mechanical Energy transfer against different frequency ratios for $A = 0.3D$



where T is time interval of the integration, $C_L(t)$ is lift coefficient and y' is velocity of cylinder. it can be observed that at low amplitude by varying frequency ratio coefficient of energy is raised up to 0.6 at $f_r = 1.05$ and then further declined which is shown in Fig. 9. The present study value gives good agreement with reported results.

4.2 Streamwise Direction

Earlier said that there is change in prescribed motion of the cylinder that is inline direction so to validate our in-house code the study is done on Reynolds Number 200. From that at various frequency ratio keeping amplitude 0.1, it is observed that lift and drag coefficients value are getting higher in higher frequency ratio which means the synchronization occurs in that range or it is close to 2. The global flow

parameters of present study are approximately nearer to which means it get good agreement with reported results which is shown in Fig. 10.

In that we found synchronization or lock-in state in which excitation frequency is equal to twice of the vortex shedding frequency, and in non-lock-in range where f_e and f_s is different as it exists linearly with stationary cylinder frequencies. The frequency ratio f_r for the lock-in range is found to be 1.15–1.9 which represented as horizontal line and it is shown in Fig. 11. The lock-in range graph is following same pattern [12].

In streamwise oscillation it is seen that there are two lock-in zone one is harmonic and another is sub-harmonic, from the above it can be observed that frequency ratio from 1.15 to 1.9 is coming sub-harmonic lock-in range and $f_r = 0.9$ is coming harmonic lock-in range. The expression for harmonic lock-in and sub-harmonic lock-in is given [9] by where $n = 0, 1, 2, 3, \dots, \infty$. Here f_s is vortex shedding frequency and f_e is driving frequency harmonic lock-in expression is written below.

Fig. 10 Mean drag coefficients versus frequency ratio

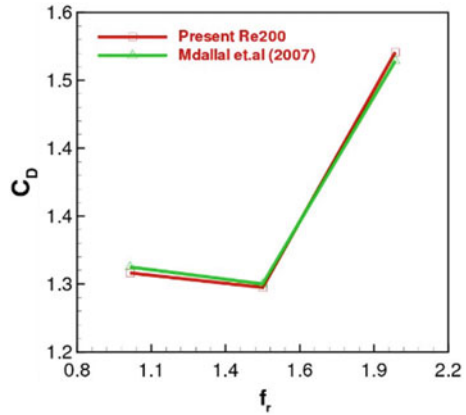
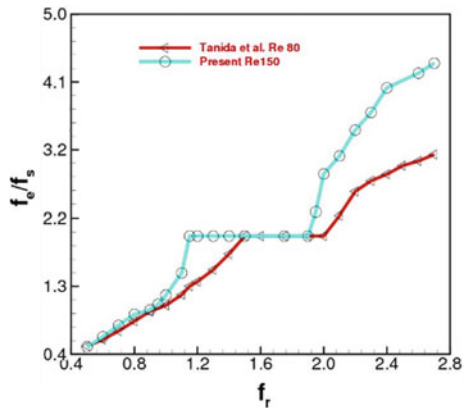


Fig. 11 Lock-in range for inline forced oscillations at $A = 0.3D$ of Re 150 (present study) and Re 80



$$\frac{f_s}{f_e} = 1 + n \tag{5}$$

Sub-harmonic lock-in is expression is written below

$$\frac{f_s}{f_e} = \frac{1}{2} + n \tag{6}$$

In Figs. 12 and 13 showing harmonic and sub-harmonic lock-in case and it is found that approximately same pattern of phase portraits and power spectrum density with [9] which shows good reported results. As it is not seen in the transverse oscillating cylinder case.

The global parameters like C_D avg, C_L max were plotted by varying frequency ratio and amplitude. Figure 14 shows the increment in average C_D by Increasing frequency ratio, it is seen that sudden shoot up to $f_r = 1.9$ and then decrement in C_D avg value. At the end of synchronization avg C_D value drops and max C_L value also drastically decreases. This is due to the shift of stagnation pressure region toward the back of the cylinder. The average value of C_D is 1.291 for fixed cylinder whereas the value reaches to 2.24 for $f_r = 1.9$.

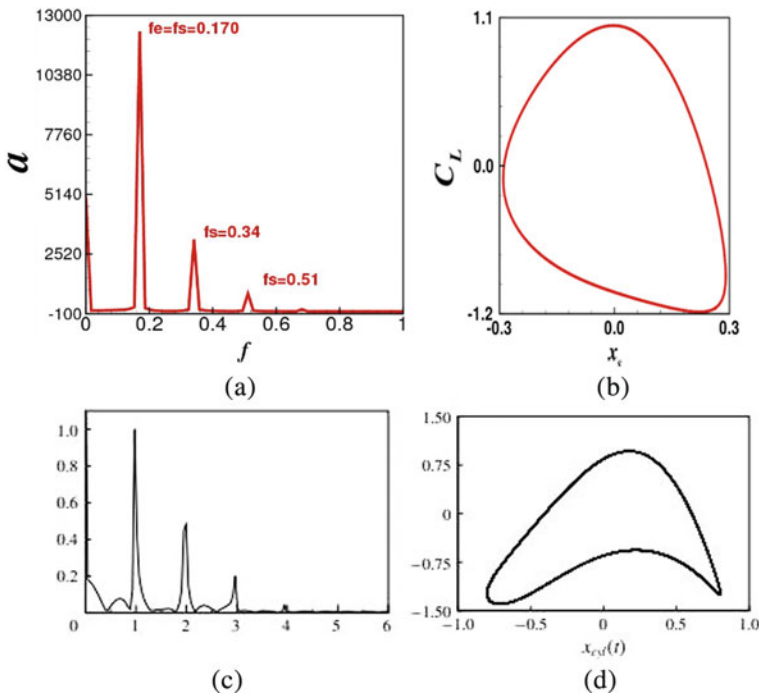


Fig. 12 Harmonic lock-in case of $Re\ 150$ at $A = 0.3D, f_r = 0.9$ **a** power spectrum **b** phase portraits and $Re\ 100$ at $A = 0.8D, f_r = 0.8$ **c** power spectrum **d** phase portraits [9]

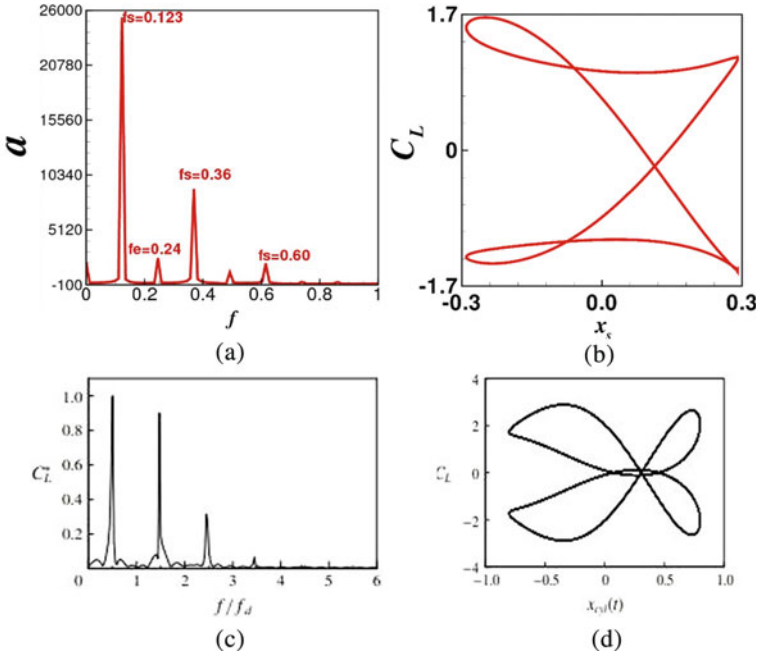
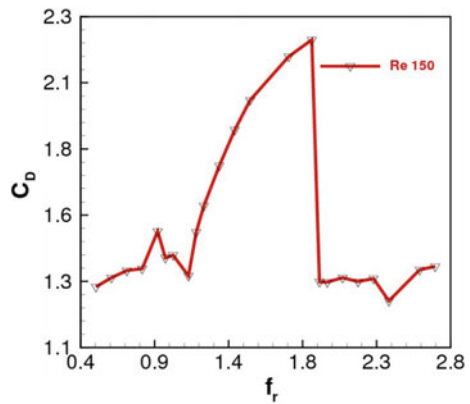


Fig. 13 Sub-harmonic lock-in case of $Re\ 150$ at $A = 0.3D f_r = 1.3$ **a** power spectrum **b** phase portraits and $Re\ 100$ at $A = 0.8D f_r = 1.2$ **c** power spectrum **d** phase portraits [9]

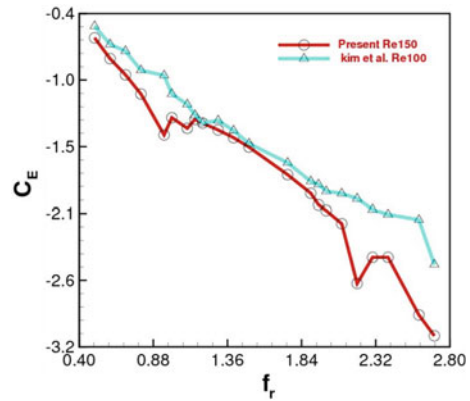
Fig. 14 Global flow parameter C_D avg at $A = 0.3D$ with different frequency ratio



Mechanical energy transfer expression for streamwise is

$$C_E = \frac{1}{T} \int_0^T C_D(t) x_s'(t) dt \tag{7}$$

Fig. 15 Mechanical energy transfer against different frequency ratios for $A = 0.3D$



where T is time interval of the integration, $C_D(t)$ is drag coefficient and x_s' is velocity of cylinder. The relative velocity to the free stream increases as the streamwise pushed oscillating cylinder advances at a negative velocity, increasing the drag force. On the other hand, traveling downstream causes the relative speed to the free stream to slow down, which lowers the drag force which means negative drag fluctuations. As a result, for a streamwise pushed oscillating cylinder, the drag and velocity are typically out of phase, which results in E being negative [9]. The present study value gives good agreement with reported results (Fig. 15).

5 Conclusions

The numerical investigation is carried out at $Re = 150$ with a circular cylinder oscillation amplitude of $0.3D$ in transverse and streamwise oscillation of the circular cylinder. lock-in range is found between $f_r = 0.75-1.05$ in transverse while in streamwise the lock-in range is found from $f_r = 1.15-1.9$ (Sub-Harmonic Lock-in) and harmonic lock-in found at $f_r = 0.9$. Coefficient of energy is increased from 0 to 0.6 and then further decreases by increasing frequency ratio but in case of streamwise coefficient of energy is increased from 0 to -3 by increasing frequency ratio.

Acknowledgements The project work was supported by NIT Calicut, Department of Mechanical Engineering. I would like to express my sincere and utmost gratitude to my guide whose constant support, valuable suggestions, encouragement and mentorship throughout the project is the key factor for the completion of this project.

References

1. Billah KY, Scanlan RH (1991) Resonance, Tacoma narrows bridge failure, and undergraduate physics textbooks. *Am J Phys* 59(2):118–124
2. Khan NB, Ibrahim Z, Khan MI, Hayat T, Javed MF (2018) VIV study of an elastically mounted cylinder having low mass-damping ratio using RANS model. *Int J Heat Mass Transf* 121:309–314
3. Koopmann GH (1967) The vortex wakes of vibrating cylinders at low Reynolds numbers. *J Fluid Mech* 28(3):501–512
4. Blackburn HM, Henderson RD (1999) A study of two-dimensional flow past an oscillating cylinder. *J Fluid Mech* 385:255–286
5. Bishop RED, Hassan AY (1964) The lift and drag forces on a circular cylinder oscillating in a flowing fluid. In: *Proceedings of the royal society of London. Series A. Mathematical and physical sciences*, vol 277, no 1368, pp 51–75
6. Placzek A, Sigrist J-F, Hamdouni A (2009) Numerical simulation of an oscillating cylinder in a cross-flow at low Reynolds number: forced and free oscillations. *Comput Fluids* 38(1):80–100
7. Leontini JS, Stewart BE, Thompson MC, Hourigan K (2006) Wake state and energy transitions of an oscillating cylinder at low Reynolds number. *Phys Fluids* 18(6):067101
8. Peter S, De AK (2016) A parallel implementation of the ghost-cell immersed boundary method with application to stationary and moving boundary problems. *Sādhanā* 41(4):441–450
9. Kim K-H, Choi J-I (2019) Lock-in regions of laminar flows over a streamwise oscillating circular cylinder. *J Fluid Mech* 858:315–351
10. Baranyi L, Daróczy L (2013) Mechanical energy transfer and flow parameter effects for a cylinder in transverse oscillation. *Int J Heat Fluid Flow* 43:251–258
11. De Kumar A, Dalal A (2006) Numerical simulation of unconfined flow past a triangular cylinder. *Int J Numer Methods Fluids* 52(7):801–821
12. Tanida Y, Okajima A, Watanabe Y (1973) Stability of a circular cylinder oscillating in uniform flow or in a wake. *J Fluid Mech* 61(4):769–784

Wake Dynamics of a Longitudinally Oscillating Cylinder at Low Reynolds Number



N. David

Abstract A longitudinally oscillating cylinder in a steady fluid stream has been shown to exhibit some interesting wake dynamics. The wake dynamics of a circular cylinder of diameter, d in a steady air stream at a velocity, U_∞ oscillating longitudinally in the streamwise direction with an amplitude, a and forced excitation frequency, f_e is considered in the current studies at a low Reynolds number, $Re = 500$. The non-dimensional parameters governing the flow dynamics are amplitude ratio, a/d , frequency ratio, f_e/f_s , and Reynolds number, $Re = U_\infty d/\nu$, where f_s is the frequency of the shed vortices, when the cylinder is stationary ($A = 0$) and ν is kinematic viscosity of air. Our simulations have been carried out at $Re = 500$, and we identify various wake geometry such as, A-I mode, harmonic synchronous A-I mode, A-IV mode, and SA mode at several combinations of amplitude and frequency ratios. The observed wake geometry has an effect on the unsteady drag and lift forces and their associated frequency of fluctuations. The results are relevant to physical systems where vortex-induced vibrations (VIV) are important.

Keywords Vortex · Forced oscillation · Cylinder · Reynolds number · Amplitude and frequency ratios · Vortex induced vibrations (VIV)

1 Introduction

Flow features behind a longitudinally oscillating cylinder was observed using Laser Induced Fluorescence (LIF) at several frequency ratio, amplitude ratio combinations and the wake geometry were identified on the frequency ratio amplitude ratio plane [1]. They also observed the vorticity field behind an oscillating cylinder from the particle imaging velocimetry (PIV) measurements. From the particle imaging velocimetry measurements of a cylinder that was free to oscillate in the streamwise direction, A-II, S-I, SA, and A-IV wake geometry were observed at several

N. David (✉)

Department of Aerospace Engineering, Hindustan Institute of Technology and Science, Chennai 603 103, India

e-mail: davidnresearch@gmail.com

amplitude and frequency ratio combinations [2, 3]. Using Finite time Lyapunov exponent (FTLE), they also identified “vortex cells” in the wake region, where new vortices were formed. Numerical simulations of the forced oscillations of a circular cylinder were performed on a moving mesh in OPENFOAM and the unsteady non-dimensional forces were obtained over time and frequency component of the fluctuations was obtained for several wake geometries [4]. At $Re = 900$, PIV measurement of the wake region of a streamwise oscillating cylinder has been performed at frequency ratios, $f_e/f_s \sim 0.04\text{--}0.2$ and unsteady vortex pattern behind a circular cylinder were observed [5]. Synchronized modes were identified in the wake of a streamwise oscillating cylinder over a narrow frequency ratio range at $Re = 200$, for amplitude ratio, $a/d = 0.1$ and 0.3 , $f_e/f_s = 0.2$ [6] from computations; the frequency of the shed vortices and the oscillating cylinder frequency get synchronized in harmonic synchronous regions.

Their results on the harmonic synchronous region has been identified from the simulations on a streamwise oscillating cylinder [7]. From the time series of the lift coefficient, $c_l = L/(0.5 \rho U_\infty^2 A)$ the synchronizing modes of the streamwise oscillating cylinder have been identified on the amplitude ratio, frequency ratio plane [8], where L is the lift force and A is the area of the circular cylinder. Several wake states have been identified in the computations of a streamwise oscillating cylinder at several Reynolds number, amplitude ratio combinations at one frequency ratio, $f_e/f_s = 1.0$ [9]. A streamwise oscillating cylinder at $Re = 300$, $f_e/f_s = 1.8$, $a/d = 0.5$ has been shown to have the same time averaged drag and lift forces, however the root mean square value of the drag force was larger for the oscillating cylinder than that of a stationary cylinder by two-dimensional direct numerical simulations (DNS) [10]. At an excitation frequency twice that of the Strouhal frequency, and $Re \sim \mathcal{O}(10^4)$, the drag forces were observed to reach a value twice of the value, without any cylinder oscillations [11]. In the present work, we carry out two-dimensional simulations of the flow past an oscillating cylinder at $Re = 500$, $f_e/f_s = 0.5\text{--}4.0$, $a/d = 0.05\text{--}2.0$ and identify various geometries of vortices and identify their effect on the force coefficients.

2 Numerical Methodology

The governing equations for fluid dynamics problems involving moving meshes use Arbitrary Euler–Lagrange (ALE) representation in OPENFOAM. The governing equations are given by 1, 2, and 3, where \vec{u} is the fluid velocity, p is the pressure, ν is the molecular viscosity and ρ is the density of the fluid and the grid velocity, U_g . Laplacian equation for cell center displacement, cd is given by $\nabla \cdot (v_1 \nabla cd)$, where v_1 is inversely proportional to the distance from the boundary in motion. The point displacement, p_d is then obtained from the cd field at that instance of time.

The free-stream velocity in the present simulations is $U_\infty = 2.5$ m/s, $d = 2.5$ m, $\nu = 0.01$ m²/s, which corresponds to a Reynolds number, $Re = 500$. The flow is two-dimensional as there is only one cell in the direction normal to the plane of fluid

flow. The wall boundary of the cylinder is set to a simple harmonic motion, given by, $x(t) = A \sin \omega t$, where A is the amplitude of the cylinder oscillations, $\omega = 2\pi f_e$ is the angular frequency, f_e is the excitation frequency in Hertz and t is time in second. The computational domain is such that the inlet is positioned at a distance of $20d$ ahead of the cylinder center, outlet is positioned $30d$ behind the cylinder center and the symmetric faces at the top and bottom are positioned $20d$ away from the cylinder center as in Fig. 1. The moving mesh used in the present simulation was made using blockMesh utility. The boundaries of the mesh were defined using vertices and then the edges of the blocks were constructed in blockMeshDict dictionary. Simplegrading meshing method was utilized for concentric dense packing of cells around the boundary layer region of the circular cylinder in the two-dimensional domain with the first cell size being 0.1 mm and the total number of cells in the mesh were 8800. The boundary conditions at the inlet were a constant inlet velocity condition and a zero gradient in pressure were specified. A uniform pressure value of zero was specified at the outlet and a zero gradient in velocity was specified for pressure. The symmetric walls specified as slip walls, and the front and back faces were specified with an empty boundary condition.

The pimpleFoam solver was used for the moving mesh method, achieving pressure velocity coupling through PISO algorithm. A fourth-order cubic scheme was used to discretize the divergence terms in the momentum equation. The time derivative terms were discretized using a second-order backward difference method. Our computational approach was validated by verifying drag and the frequency component of the lift force at $Re = 500$ for a stationary cylinder for which $A = 0$. The time

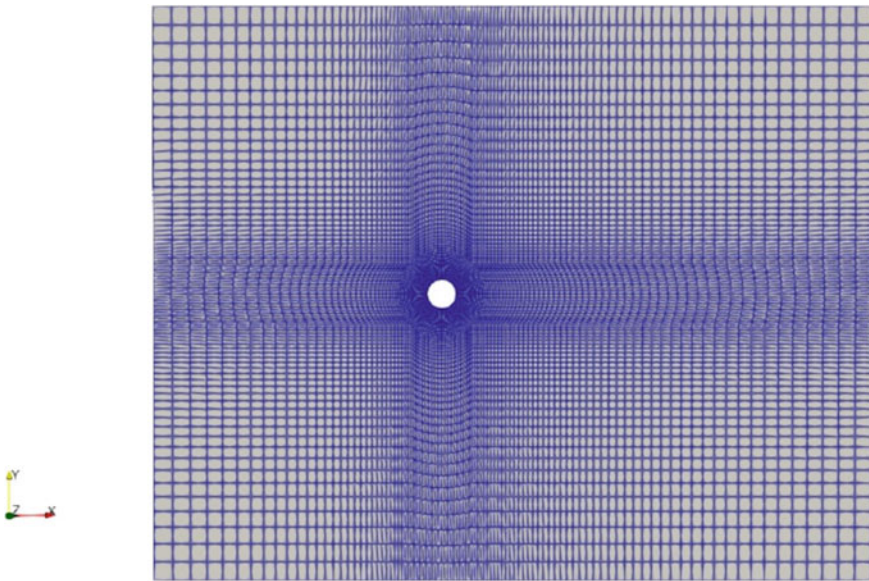


Fig. 1 The moving mesh used in the present simulations

step in the simulations was 0.001 s, maximum courant number in the simulations was limited to 1.0 and the maximum value for the run time modifiable time step was set to 0.1 s.

$$\frac{\partial}{\partial t} \int \rho dV + \oint \rho \vec{n} \cdot (\vec{U} - \vec{U}_g) ds = 0 \quad (1)$$

$$\frac{\partial}{\partial t} \int \rho \vec{U} dV + \oint \rho \vec{n} \cdot (\vec{U} - \vec{U}_g) \vec{U} ds - \oint \rho \nu \vec{n} \cdot \nabla \vec{U} ds + \oint p \vec{n} ds = 0 \quad (2)$$

$$\frac{\partial}{\partial t} dV - \oint \vec{n} \cdot \vec{U}_g dS = 0 \quad (3)$$

3 Results and Discussion

Based on the observed wake geometry, frequency of the vortex shedding, we observe the following wake modes such as, A-I mode, harmonic synchronous A-I mode, A-IV mode, and SA mode at various amplitude ratios, $ald = 0.02, 0.05, 0.1, 0.15$ and 0.2 , and frequency ratios, $f_e/f_s = 0.5, 1, 1.5, 2, 2.5, 3, 3.5$ and 4 at $Re = 500$. Vorticity colormap is plotted to observe the vortices that are shed behind the oscillating cylinder and the arrows of the velocity vectors indicate the direction of the fluid flow at a point and the magnitude of the fluid velocity is represented by the length of the velocity vector arrow in Fig. 2, the color bar indicates the magnitude of vorticity. A symmetric, alternate shedding of vortices is observed about either side of the centerline of the oscillating circular cylinder, similar to a von-Karman vortex street behind a stationary circular cylinder as shown in Fig. 2 at $ald = 0.02, f_e/f_s = 1.0$ and it is called as AI-mode [3]. At very low amplitude ratio and frequency ratio of, $ald = 0.02, f_e/f_s = 1.5$, a pair of vortices are shed alternatively about the centerline of the circular cylinder as observed in Fig. 3 that shows the colormap of vorticity, shown together with the velocity vectors at two instances of time. At one instance in time, the vortex dipole appears above the centerline of the oscillating cylinder, while at another following instance in time, the vortex dipole appears below the centerline of the oscillating cylinder. Such alternate shedding of a vortex dipoles about the either side of the centerline of the oscillating circular cylinder has been termed as A-IV mode [3]. At $ald = 0.1-0.2, f_e/f_s = 4.0$, an asymmetric alternate shedding of vortices is observed about the centerline of the circular cylinder as in Fig. 4 and it is the characteristic of SA wake mode [2]. In Fig. 4, at one instance of time, asymmetric vortices are shed from above the centerline of the oscillating circular cylinder, while at another instance of time, asymmetric vortices are shed from below the centerline of the oscillating cylinder alternatively for SA wake mode.

The periodicity in the lift coefficient time series was identified by performing fast Fourier transform (FFT) and the frequency at which the vortices were shed, f was termed to be the peak maximum value in the frequency spectrum. The time series

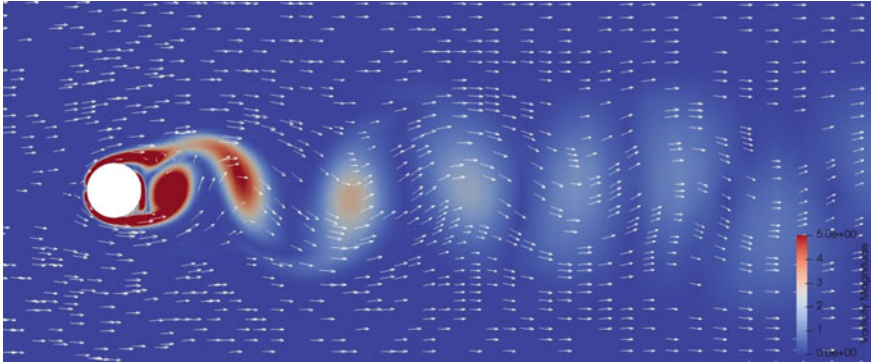


Fig. 2 A-I mode: **a, b** vorticity contours together with the velocity vectors, showing symmetric, alternate shedding on either sides about the centerline of the circular cylinder, $a/d = 0.02$, $f_e/f_s = 1.0$

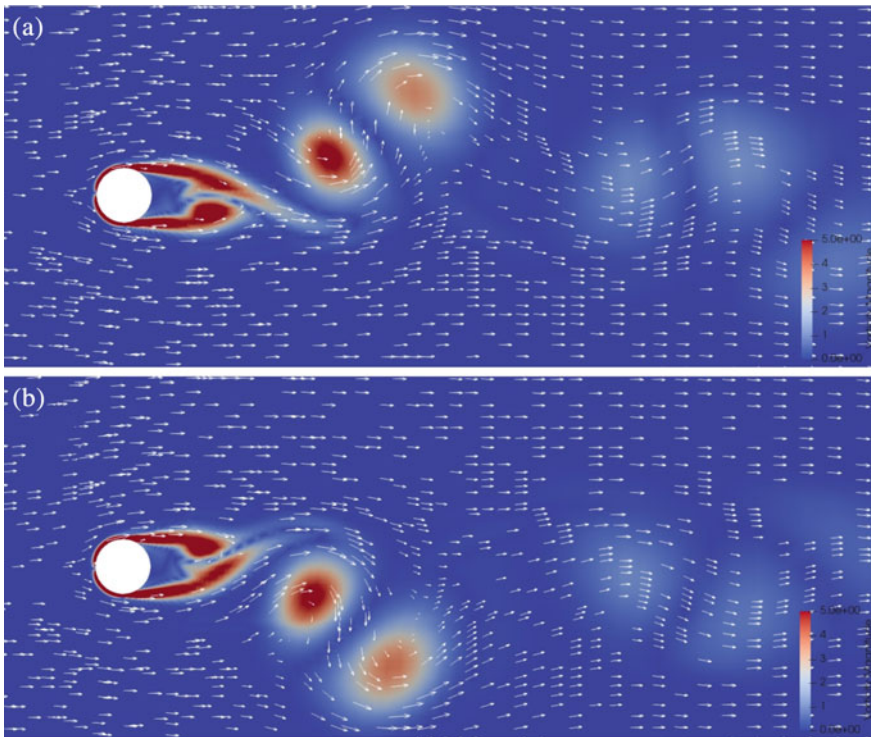


Fig. 3 A-IV mode: **a, b** vorticity contours together with the velocity vectors, showing asymmetric, alternate shedding on either sides about the centerline of the circular cylinder, $a/d = 0.02$, $f_e/f_s = 0.5$

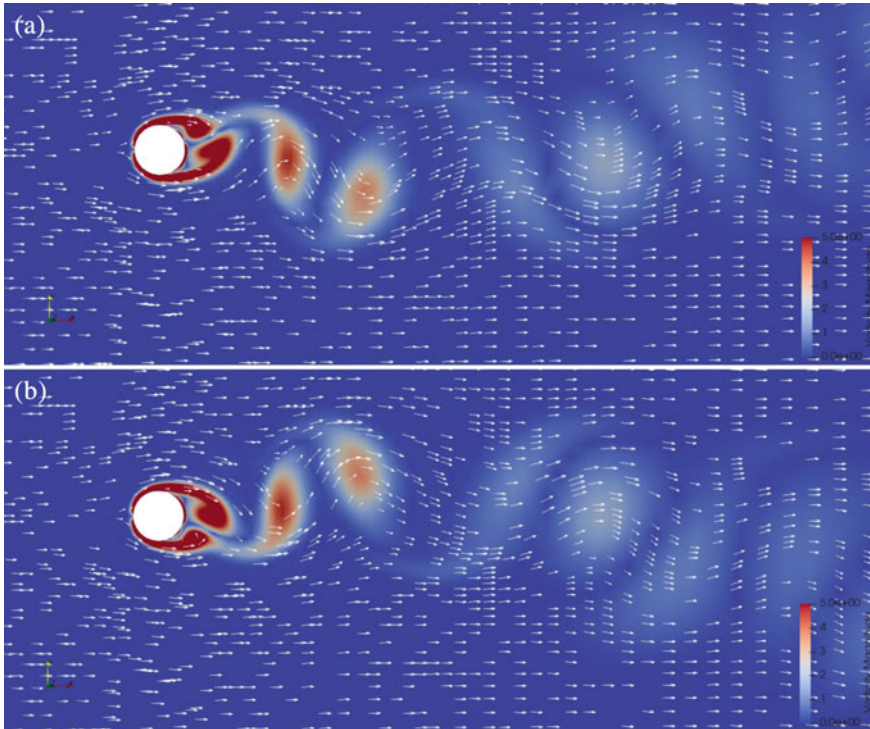


Fig. 4 SA mode: **a, b** vorticity contours together with the velocity vectors, showing asymmetric, alternate shedding on either sides about the centerline of the circular cylinder, $a/d = 0.1, f_e/f_s = 4.0$

of the drag coefficient, c_d and lift coefficient together with the frequency spectrum for $a/d = 0.1, f_e/f_s = 0.5$, corresponding to AI mode and for $a/d = 0.02, f_e/f_s = 1.0$, corresponding to AI harmonic synchronous mode are shown in Fig. 5a and b, respectively, where $c_d = D/(0.5 \rho U_\infty^2 A)$ and D is the drag force. The time series of the drag and lift coefficients together with the frequency spectrum for $a/d = 0.02, f_e/f_s = 1.5$, corresponding to A-IV mode and for $a/d = 0.15, f_e/f_s = 4.0$, corresponding to SA mode are shown in Fig. 6a and b, respectively. In Fig. 5a, corresponding to A-I mode, the drag and lift coefficient time series are periodic in time and a discrete frequency is observed in the frequency spectrum of the lift coefficient. Thus vortex shedding in A-I mode is periodic at a discrete frequency as observed in Fig. 5a frequency power spectrum. In Fig. 5b, corresponding to A-I mode, the drag and lift coefficient time series are periodic in time and the vortices that are shed are harmonically synchronized with the oscillating cylinder motion. Thus vortex shedding in A-I harmonic synchronous mode is periodic and several integral multiples of the peak frequency are observed as in Fig. 5b frequency power spectrum. In Fig. 6a the drag and lift coefficient time series are shown together with the frequency power spectrum for A-IV mode of the vortex shedding, where there is

an alternate shedding of vortex dipoles about the centerline of the circular cylinder. Thus in Fig. 6a, there are two peaks in the frequency power spectrum corresponding to two temporal periodicities. In Fig. 6b the drag and lift coefficient time series are shown together with the frequency power spectrum for SA mode of the vortex shedding, where there is an asymmetric alternate shedding of vortices about the centerline of the circular cylinder. Thus in Fig. 6b, for the asymmetric alternate vortex shedding SA mode, the vortex peak in the frequency power spectrum does not have a large amplitude. Based on the peak frequency in the power spectrum of the time series in the lift coefficient, non-dimensional vortex shedding frequency was defined as, Strouhal number, $St = fd/U_\infty$. The variation of St with f_e/f_s at various a/d values are shown in Fig. 7. It is to be noted that the frequency of the shed vortices decrease with the increase in the frequency ratio, f_e/f_s at all a/d values. However at $a/d = 0.02$, $f_e/f_s = 1.0$, corresponding to harmonic synchronous mode, there is a marked decrease in the value of the peak frequency at which the vortices are shed as in Fig. 7 as a magenta circle marker. Similarly, at $a/d = 0.02$, $f_e/f_s = 1.5$, corresponding to alternate dipole vortex shedding A-IV mode, there is a marked decrease in the value of the peak frequency at which the vortices are shed as seen as a red circle marker in Fig. 7.

4 Conclusions

In this numerical study on the effect of the amplitude ratio, a/d and frequency ratio, f_e/f_s on the wake geometry behind a streamwise oscillating cylinder at $Re = 500$. We identify various wake modes such as A-I mode, harmonic synchronous A-I mode, A-IV mode, and SA mode. The characteristics of the wake modes have been identified through vorticity contours and frequency spectrum analysis. The frequency at which the vortices are shed are observed to decrease with the increase in the frequency ratio at all the amplitude ratios in general at $Re = 500$. The effect of Reynolds number on the wake geometry at these amplitude and frequency ratios could be examined in detail.

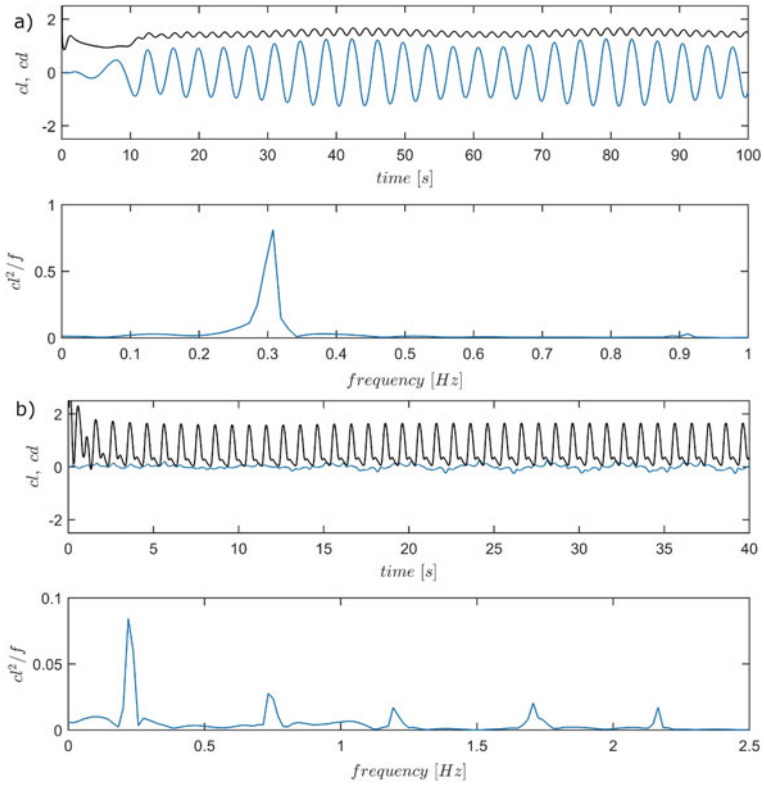


Fig. 5 Time series of drag, lift coefficient and frequency spectrum: **a** A-I mode: $a/d = 0.02, f_e/f_s = 0.5$ **b** A-I harmonic synchronous mode: $a/d = 0.02, f_e/f_s = 1.0$

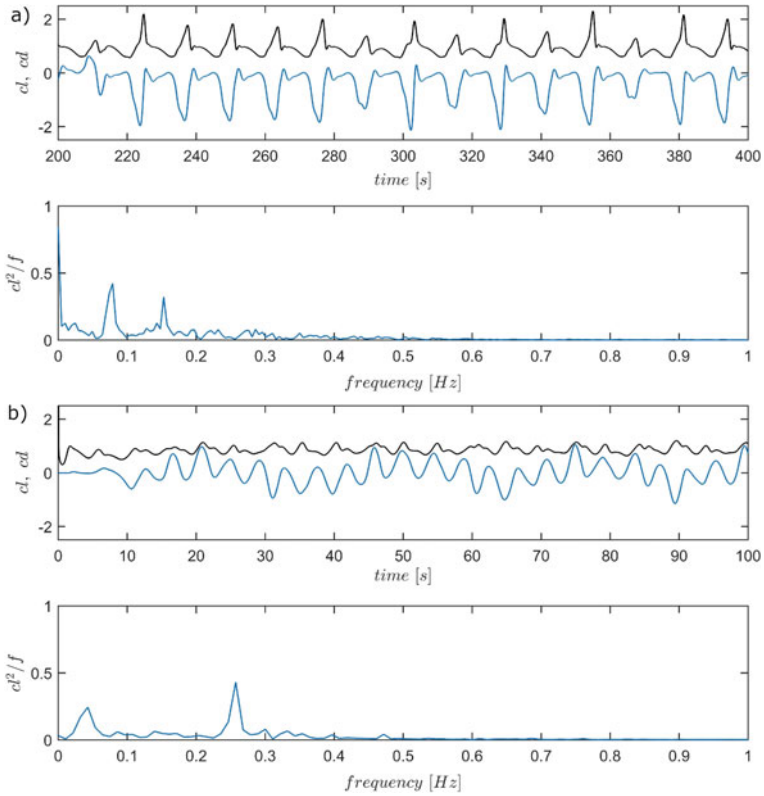
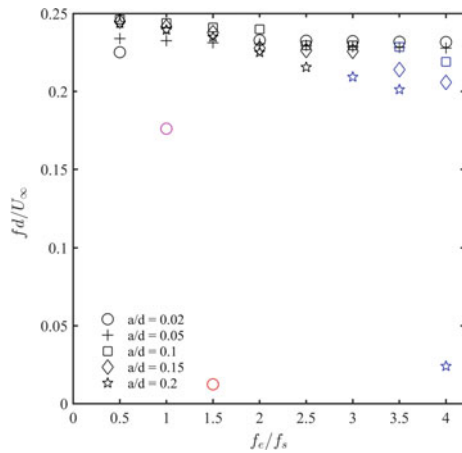


Fig. 6 Time series of drag, lift coefficient and frequency spectrum: **a** A-IV mode: $a/d = 0.02, f_c/f_s = 1.5$ **b** SA mode: $a/d = 0.15, f_c/f_s = 4.0$

Fig. 7 Strouhal number, f_d/U_∞ is shown against frequency ratio, f_c/f_s at various amplitude ratio, a/d . The magenta marker corresponds to harmonic synchronous AI mode, red marker corresponds to A-IV mode, dark marker corresponds to A-I mode, blue marker corresponds to SA mode



Nomenclature

U_∞ [m/s]	Free-stream velocity
Re	Reynolds number
d [m]	Diameter of the circular cylinder
a [m]	Amplitude of the circular cylinder
f [Hz]	Vortex shedding frequency
f_e [Hz]	Excitation frequency
f_s [Hz]	Stationary cylinder shedding frequency
ν [m ² /s]	Kinematic viscosity of the fluid

References

1. Xu SJ, Zhou Y, Wang MH (2006) A symmetric binary-vortex street behind a longitudinally oscillating cylinder. *J Fluid Mech* 556:27–43
2. Cagney N, Balabani S (2013) Wake modes of a cylinder undergoing free streamwise vortex-induced vibrations. *J Fluids Struct* 38:127–145
3. Ongoren A, Rockwell D (1988) Flow structure from an oscillating cylinder part 2: mode competition in the near wake. *J Fluid Mech* 191:225–245
4. Alletto M (2022) Comparison of overset mesh with morphing mesh: flow over a forced oscillating and freely oscillating 2d cylinder. *OpenFOAM® J* 2:13–30
5. Shamaï M, Dawson STM, Mezić I, McKeon BJ (2021) Unsteady dynamics in the streamwise-oscillating cylinder wake for forcing frequencies below lock-on. *Phys Rev Fluids* 6(7):074702
6. Al-Mdallal QM, Lawrence KP, Kocabyik S (2007) Forced streamwise oscillations of a circular cylinder: locked-on modes and resulting fluid forces. *J Fluids Struct* 23(5):681–701
7. Kim K-H, Choi J-I (2019) Lock-in regions of laminar flows over a streamwise oscillating circular cylinder. *J Fluid Mech* 858:315–351
8. Tang G, Cheng L, Tong F, Lu L, Zhao M (2017) Modes of synchronisation in the wake of a streamwise oscillatory cylinder. *J Fluid Mech* 832:146–169
9. Leontini JS, Jacono DL, Thompson MC (2013) Wake states and frequency selection of a streamwise oscillating cylinder. *J Fluid Mech* 730:162–192
10. Alam M, Fu S, Zhou Y et al (2007) Generation of vortices by a streamwise oscillating cylinder. *J Visual* 10(1):65–73
11. Nishihara T, Kaneko S, Watanabe T (2005) Characteristics of fluid dynamic forces acting on a circular cylinder oscillated in the streamwise direction and its wake patterns. *J Fluids Struct* 20(4):505–518

Effect of Wind Gust on Flow Past Pitching Seagull Wing



Jay Rana and Shaligram Tiwari

Abstract In the present study, a three-dimensional seagull wing is pitched about the quarter chord axis in a sinusoidal way. To mimic gust-like realistic conditions, a time-varying velocity is imposed at the inlet. The Reynolds number (Re) based on root chord length is equal to 5000 with specified pitching amplitude and frequency. Unsteady numerical simulations are performed using Open Source Field Operation and Manipulation (OpenFOAM-8). The pitching motion is achieved using dynamic mesh utility *interpolatingSolidBody* motion solver, where the mesh near the wing does not morph but moves rigidly with respect to the wing, and deformation of mesh occurs away from the wing. The effects of gust parameters, i.e. IF and f_g^* has been studied on flow structure and force coefficients. To visualize highly unsteady and 3-D flow features across the wing, streamline topology has been shown. The effect on aerodynamic features like lift and drag is also considered. The nature of flow and the behaviour of coherent structures is predicted using marginal spectral distribution.

Keywords Seagull wing · Fluid–structure interaction · Pitching wing · Marginal spectrum distribution · Aerodynamic loads

1 Introduction

In the modern era of science and technology, advancements in the field of MAVs are emerging, because these vehicles are used for surveillance, and stealth operations in the military as well as these are used at sites where humans cannot reach, e.g. radioactive regions, and exo-planets. During the early stages of aircraft development, humans tried to fly using wings by mimicking the bird's flying motion. But it was found out later that weight is the main reason why humans cannot fly using wings like birds. A MAV is defined as a flying vehicle having dimensions and weight of less than 15 cm and 50 g. In nature, birds have similar weights and sizes. The range of Re in which birds fly is 10^3 to 10^5 . The key parameters of MAVs include efficiency,

J. Rana (✉) · S. Tiwari

Department of Mechanical Engineering, IIT Madras, Chennai 600036, India
e-mail: jayranacool@gmail.com

© The Author(s), under exclusive license to Springer Nature Singapore Pte Ltd. 2024
K. M. Singh et al. (eds.), *Fluid Mechanics and Fluid Power, Volume 2*, Lecture Notes in Mechanical Engineering, https://doi.org/10.1007/978-981-99-5752-1_57

707

manoeuvrability, stability, and low flight noise. These all factors lead researchers to learn and adapt different mechanisms involved in the flying of birds which can be implemented in the development of MAVs.

2 Literature Review and Objective

Early experimental work done by Withers [1] found that bird wings have low aerodynamic efficiency as compared to conventional airfoils. Ennos et al. [2] studied geometric features of pigeon wing and their effect on aerodynamic characteristics. A comparison between 2-D sections of the bionic wing with Selig S1223 and Clark Y airfoils was made by Carruthers et al. [3]. The effect on aerodynamic loads due to leading-edge serrations on a heaving NACA wing was investigated by Liu et al. [4]. For the bionic wing, changes in geometry have a great effect on the aerodynamic characteristics as reported by Soni et al. [5], where flows past actual bird wings, such as owl, seagull, teal, and bat were considered. Kim et al. [6] studied the effect of reduced frequency for pitching NACA0012 airfoil at a low values of Re . The objective of the present study is to understand the complex flow features on the wing by considering the parameters such as IF and f_g^* and their effect on the aerodynamic loadings.

3 Problem Definition and Grid

The present model consists of a seagull wing enclosed in a domain of size $L_1 = 25c$, $L_2 = 10c$, and $L_3 = 7.64c$ in x , y , and z directions respectively, as shown in Fig. 1. The wing geometry is generated using the equations given in reference Liu [7], where the geometry extraction is done by a 3-D laser scanner and the equations for wing surfaces of different birds such as Seagull, Merganser, Teal, and Owl are given. As shown in the figure, the wing is at a distance of $L_4 = 5c$ from the inlet. The values of root chord and wing span are 0.227 m and 0.6 m, respectively. The pitching frequency and gust frequency are normalized with the help of (u_{mean}/c) , and the non-dimensional forms are f_p^* and f_g^* . A structured mesh is generated using ANSYS ICEM CFD 20.1, as shown in Fig. 1. The grid independence study is carried out considering grids G_1 , G_2 , and G_3 as coarse to fine, and the optimal grid is chosen based on the St . In this investigation, the effect of gust parameters IF and f_g^* is obtained keeping other parameters at their mean values. The mean values of IF and f_g^* are 40% and 0.5, whereas the pitching frequency and amplitude are chosen as 1.5507 Hz and 5° , respectively.

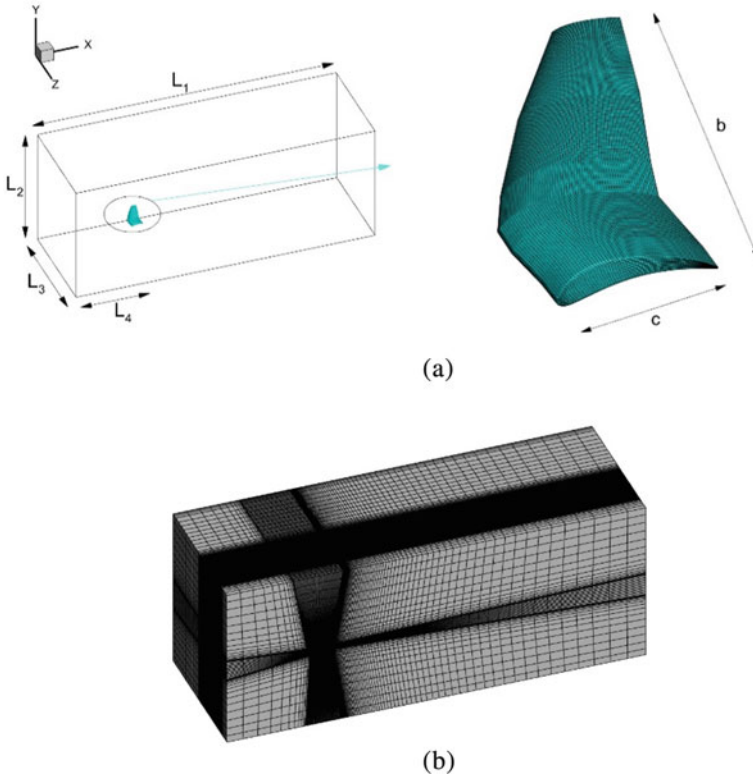


Fig. 1 Schematics of **a** schematic of the computational domain and **b** the grid

4 Numerical Methodology

In the current study, flow is considered as 3-D incompressible and laminar. The coupled governing equations are solved using *pimpleFoam* which adopts a merged PISO-SIMPLE algorithm. The time step for unsteady simulations is taken as 5×10^{-5} s which ensures that the CFL number is always less than 1. The discretization of the transient term is done using the first-order implicit scheme, whereas for the convective term second-order accurate upwind scheme is used. The gradients are calculated using the Gauss-linear method.

The pulsatile velocity inlet is given by Eq. (1),

$$u(t) = u_{\text{mean}} + \text{IF } u_{\text{mean}} \sin \left[\frac{2\pi f_g^* u_{\text{mean}} t}{c} \right] \tag{1}$$

The pitching motion imparted to the wing is governed by Eq. (2),

$$\alpha(t) = \alpha_0 \sin \left[\frac{2\pi f_p^* u_{\text{mean}} t}{c} \right] \quad (2)$$

The chord-based Reynolds number is defined by Eq. (3),

$$\text{Re} = \frac{\rho u_{\text{mean}} c}{\mu} \quad (3)$$

5 Boundary Conditions

5.1 Inlet

The Dirichlet boundary condition is used for the velocity, i.e. $u(t)$ is prescribed.

For pressure, the Neumann boundary condition is derived by applying the momentum equation at the inlet, as shown in Eq. (4),

$$\frac{dp}{dx} = -\rho = - \frac{2\pi\rho f_g^* u_{\text{mean}}^2 \text{IF}}{c} \cos \left[\frac{2\pi f_g^* u_{\text{mean}} t}{c} \right] \quad (4)$$

5.2 Outlet

At the outlet, zero-gradient is specified for velocity, and zero gauge pressure is considered.

5.3 Plane of Symmetry

The plane adjacent to the wing root is referred to as a symmetry plane and a symmetry boundary condition is imposed on that plane.

5.4 Far Field

At the far-field part of the boundary, the slip boundary condition is applied for velocity, and the pressure gradient is considered zero.

5.5 Wing Surface

On the wing surface, a no-slip boundary condition is applied for the velocity, and the pressure gradient is considered zero.

6 Grid Independence and Validation

The grid independence study is carried out by the increasing number of elements on the wing surface. In total three grids are considered G_1 , G_2 , and G_3 . The optimum grid is considered based on the Strouhal number as shown in Table 1. It is clear that the change in St is insignificant after refinement is done from G_2 – G_3 . Therefore all further computations are performed using grid G_2 .

Due to the unavailability of literature to the author’s best knowledge for flow past seagull wing, the numerical schemes are validated for flow past 2-D seagull airfoil. Table 2 shows the comparison of $C_{l_{mean}}$ values obtained from the present study with those reported by Kondo [8]. It is observed that the values of $C_{l_{mean}}$ are in good agreement with those reported by Kondo [8].

Table 1 Grid independence study

Grid	Number of elements	No. of cells		St
		m	n	
G_1	14,12,840	120	50	1.2630
G_2	17,70,888	144	60	1.2927
G_3	22,61,616	174	72	1.3086

Table 2 Validation of computations

α	$C_{l_{mean}}$	
	Kondo (2014)	Present study
0 °	0.5394	0.5472
2 °	1.0939	1.2808
4 °	1.3133	1.3643
6 °	1.4541	1.3929

7 Results

7.1 Streamlines

The geometry of the wing is such that the camber and thickness are varying along the wing span. At the wing root, a highly thick and cambered profile is present. Due to the presence of fluctuating inlet velocity mimicking gust, the flow field is found to be highly dependent on the gust parameters, i.e. IF and f_g^* . This generates different flow structures such as circulation bubbles, leading-edge vortex, and trailing-edge vortex. These vortex tubes create a local region of low pressure which absorbs the energy from mean flow by creating suction which attracts the surrounding fluid, mostly their place of generation affects the aerodynamic characteristics of the wing. For understanding the flow features, the flow separation and reattachment lines are coloured red and green on the wing surface. For every case two figures are shown, one for the upper and another for the lower surface. The flow is visualized by generating streamlines at different sections along the span of the wing and since the flow features of IF value of 20 and 30 are similar streamlines for IF value of 30 is not shown. The three dimensionality in the flow comes due to the end effects, i.e. due to wing tip and root region and also due to the chambered profile of the wing surface. The end effects try to create net downwash in the wake region. The chambered profile will help in flow separation and will generate vortex tubes whose axis is along the span. These vortex tubes aids strong cross flow. The flow near the mid-span can remain 2-D unless the instability due to end effects do not reach the mid-span region. At the end of the pitch-down motion, on the upper wing surface, the flow separation line seems to move towards the leading edge (LE) as shown in Fig. 2. For IF equal to 60, the flow separation region is about 80% on the upper surface as the separation line is very near to LE, as depicted in Fig. 2d. On the lower surface, for all values of IF, the flow separates at the LE and an LEV is seen which extends from approximately mid-span to the wing tip. The flow seems to attach quickly after that for cases IF equal to 20 and 30, for the rest of the cases, the attachment line seems to move towards TE as shown in Fig. 2b–d. For IF values of more than 30 the circulation bubble is seen, this circulation bubble is formed due to the highly negative cambered region and it extends from the wing root region to three fourth of the wing span. This depicts that with increase in IF on lower wing surface the strength of vortex structures increase. At the end of the pitch-up motion, the flow remains attached to the upper surface for IF values of 20–40, but for IF equal to 50 and 60 small regions of flow separation are present, as shown in Fig. 3a–d. For IF equal to 60 on the upper wing surface, a circulation bubble is seen near the wing root region and this can be due to the cambered profile of the wing. On the lower wing surface, major flow attachment and detachment lines move towards TE as IF changes from 20 to 50. The flow on the lower wing surface gets attached after initial separation for all IF values except for 60. As shown in Fig. 3d near the TE there is no clear line of attachment. In addition a large circulation bubble and an LEV are found near the wing root region which shows the nature of flow to be highly three-dimensional.

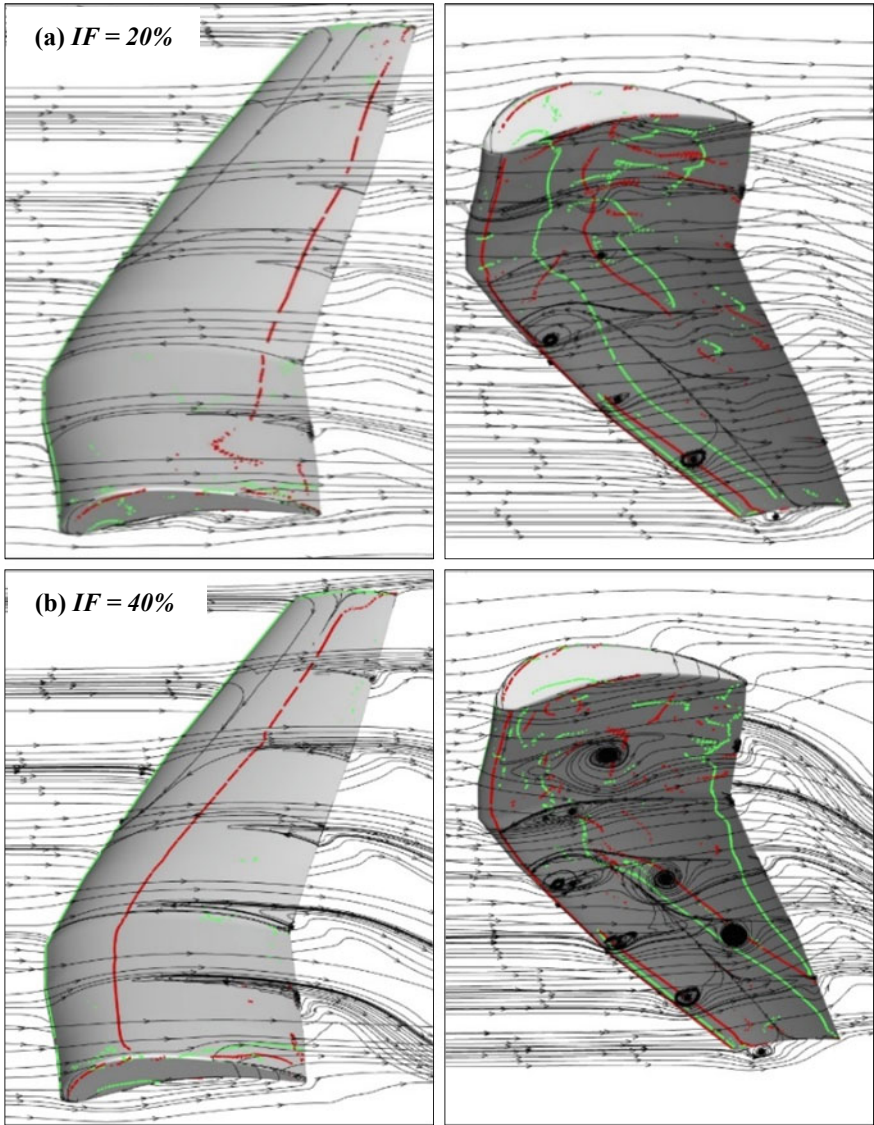


Fig. 2 Flow structures on the wing surface at $\alpha = -5^\circ$ for different values of IF

7.2 Force Coefficients

The net resultant force due to pressure and viscous forces acting on the wing surface is divided into vertical and horizontal forces, known as ‘lift’ and ‘drag’. These forces are normalized which reduces their dependency on different parameters. The variations in force coefficients computed on the wing surface are shown as function of α . The

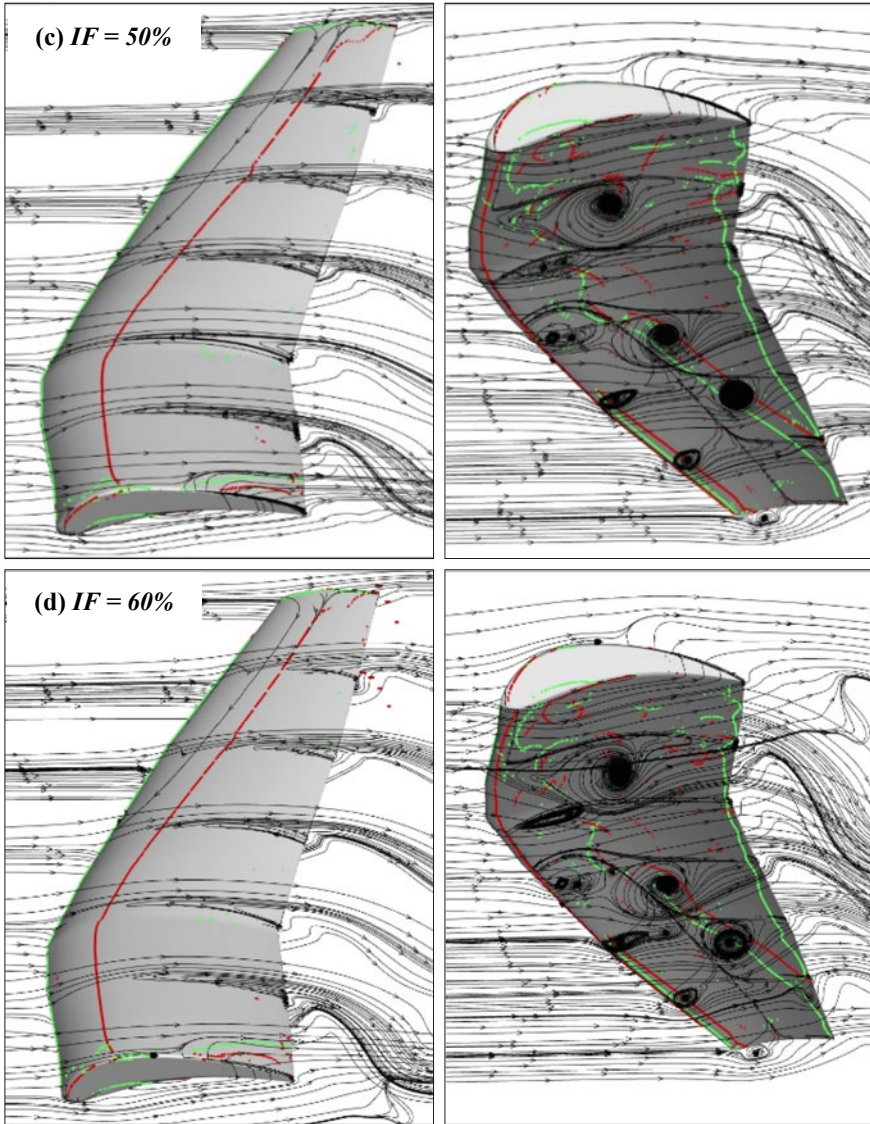


Fig. 2 (continued)

arrows marked in Figs. 4 and 5 represent the direction in which C_L and C_D change with respect to α . The positive angle denotes pitch-up motion while the negative denotes pitch-down motion. The periodic nature of force coefficients is found to be dependent on f_g^* . For all values of IF, two loops of C_L and C_D are present for one pitching cycle which shows the phase difference in wing motion and force coefficients. The height of the hysteresis loop for C_D is getting taller with the increase

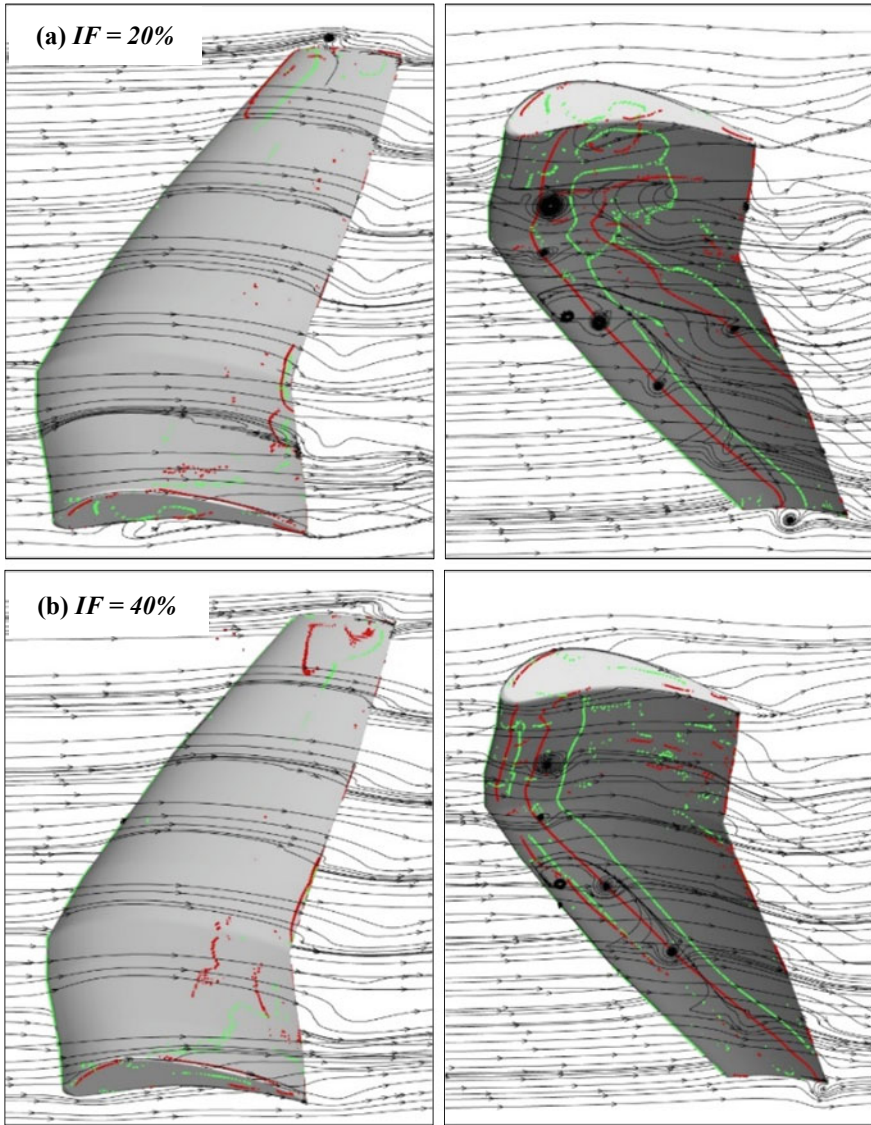


Fig. 3 Flow structures on the wing surface at $\alpha = 5^\circ$ for different values of IF

in IF as shown in Fig. 4b. The larger height of the hysteresis loop means stronger load fluctuations which are detrimental to stability and structural endurance. Figure 5 shows the hysteresis loop of force coefficients for different values of f_g^* . For f_g^* equal to 1, a single loop of C_L and C_D is obtained that is pitching motion of the wing and force coefficients are in phase. The phase difference increases with decrease in value of f_g^* which is evident in Fig. 5. The general trend of C_L and C_D is to increase during

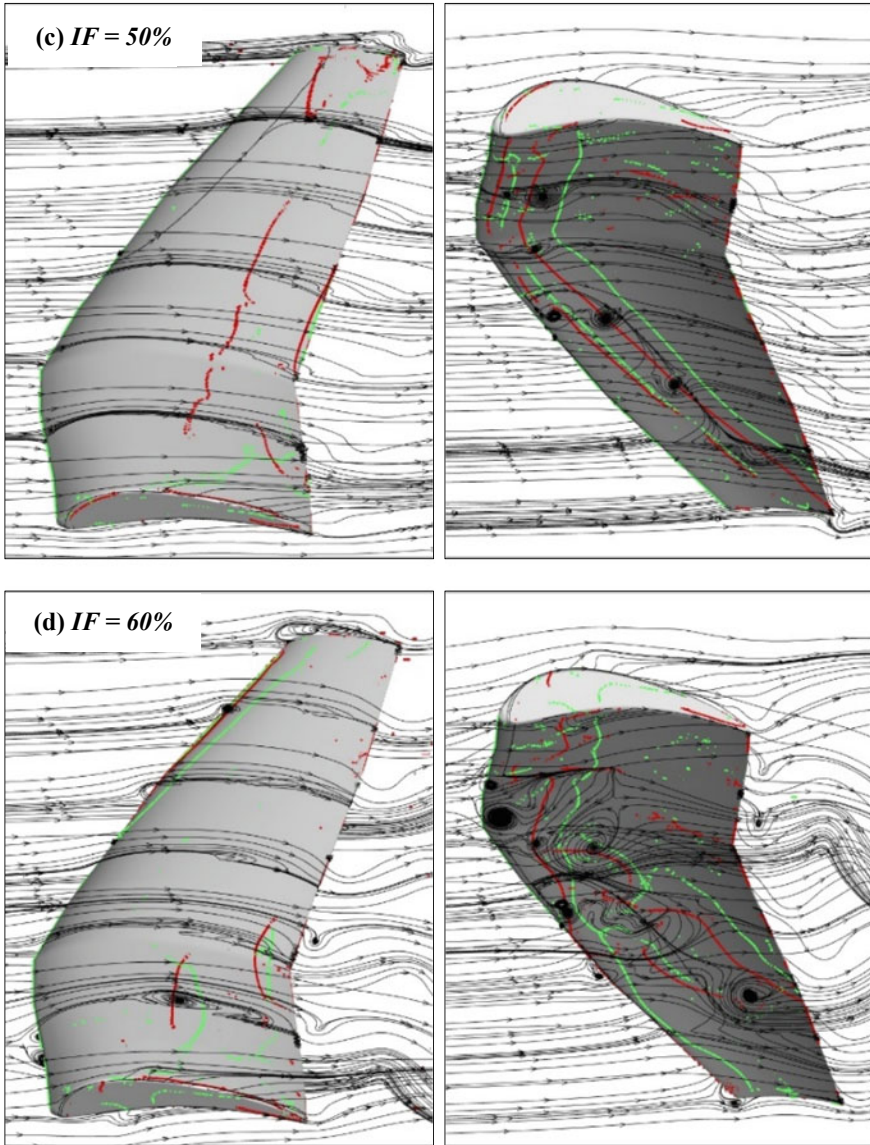


Fig. 3 (continued)

pitch-up motion and vice-versa, but due to influence of gust frequency it is following the reverse trend as shown in Figs. 4 and 5.

To understand the effect of IF and f_g^* over a pitching cycle, RMS of lift and drag coefficients are plotted in Fig. 6. For different values of IF and f_g^* , the direct proportionality is seen with respect to force coefficients, except for some values it is

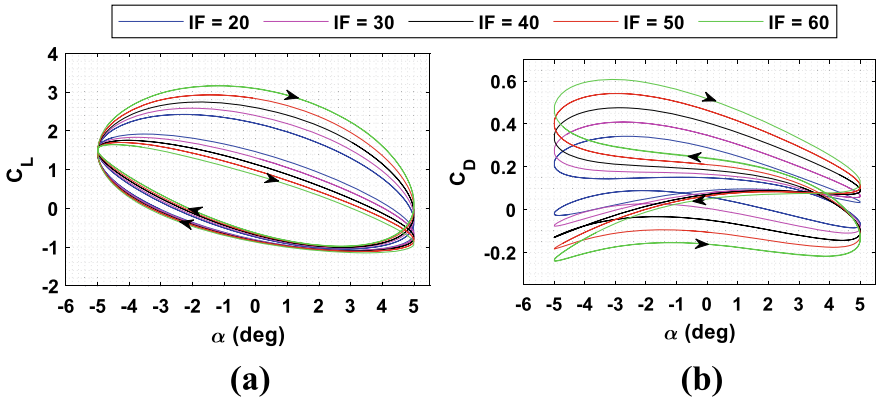


Fig. 4 Comparison of aerodynamic coefficients for different values of IF

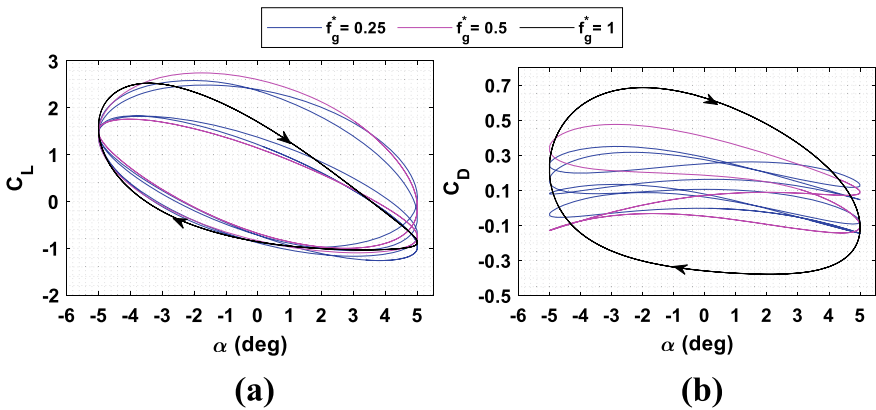


Fig. 5 Comparison of aerodynamic coefficients for different values of f_g^*

off-trend. The high value of gust frequency is found to be detrimental because the maximum increase in lift is about 10% whereas drag is found to increase by 126%. For the increase in IF values, the increment in drag is not severe which is about 50% and the lift increment is about 15%. This signifies flow field dependence on gust frequency.

7.3 Spectral Analysis

The Fourier analysis is the most widely used spectral method which represents a time signal in terms of the linear combination of pure harmonic functions. However, the Fourier transform is restricted to stationary and linear signals. In contrast to the

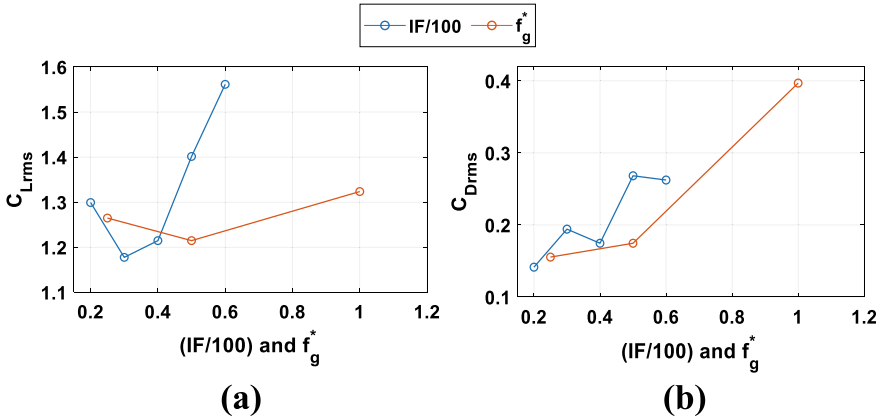


Fig. 6 Variation of RMS lift and drag coefficients for different values of IF and f_g^*

Fourier transform, the Hilbert Huang transform (HHT) can handle non-stationary and non-linear signals without any loss of information. HHT breaks a signal into different basic functions termed as intrinsic mode functions (IMF) which are directly extracted from the actual time signal using an algorithm, viz. ‘Empirical Mode Decomposition’ (EMD) given by Huang [9]. In the current study the marginal spectral analysis is done using transverse velocity signal $v(t)$ taken at different locations in the wake region of the wing. The probes are located at mid-span ($z = b/2$) from the wing root and x denotes the stream-wise distance from the trailing edge of the wing. Figure 7a and b show the comparison of spectra for different values of IF and f_g^* , respectively.

The dominant frequency for IF more than 30 is almost equal to gust frequency; for the IF values of 20 and 30 the frequency peak is not distinct but a spread is found in the range of 1.5–2 Hz. The pitching frequency is also present in this range. For the cases with IF greater than 30, peak frequency is nearly equal to gust frequency which illustrates dependence of the flow on the gust frequency. As the location of the probe is changed from $x = 0.5c-2c$, the frequency spread seen at location $x = 0.5c$ vanishes and the peak frequency is found to be concentrated near f_g^* , except for the case with IF value of 20. The peak frequency denotes the presence of vortical structures which impart periodicity to the flow. At $x = 2c$, for IF values of 50 and 60 the frequency peaks are found to be present, as shown in Fig. 7a. However, for the remaining cases, there is a frequency spread in the range of 0–2 Hz, and this shows the breakdown of vortex structures into smaller eddies, which shed over a wider frequency band. For f_g^* values of 0.25 and 0.5, distinct frequency peaks are present but it is absent for a value of 1 where the frequency spread is seen. At locations $x = 1c$ and $2c$, multiple dominant frequencies are present for both 0.25 and 0.5 values of f_g^* . At a distance $2c$ away from the wing tip, high amplitude frequency peaks are seen alone for the case $f_g^* = 0.25$. This is due to the frequency of pulsating flow being small (i.e. $f_g^* = 0.25$) thereby preserving the vortex structures far away in the wake. Consequently,

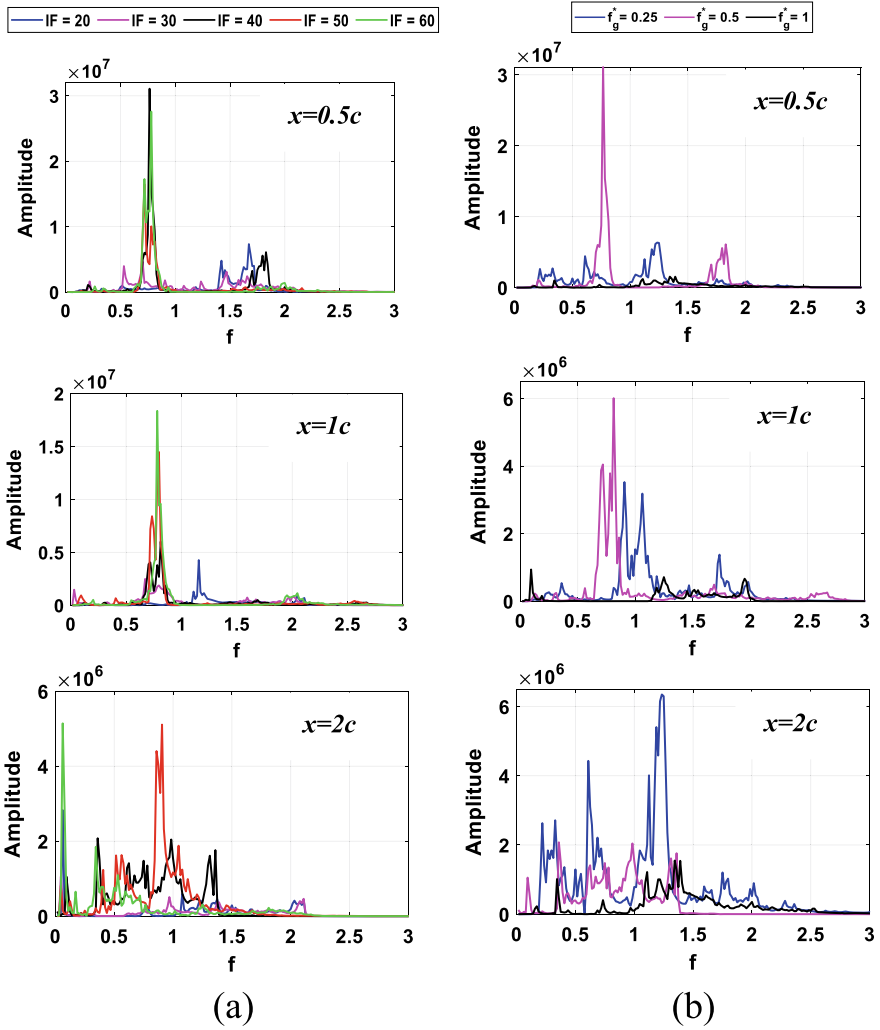


Fig. 7 Marginal spectral distribution of $v(t)$ signal for different values of **a** IF and **b** f_g^*

with rise in f_g^* the growth of vortices gets obstructed which results in formation of weak and smaller vortex structures.

8 Conclusion

In the present study, unsteady numerical simulation of flow past pitching seagull wing is carried out at low Re. To understand the effect of gust parameters on the flow field and on aerodynamic loads different techniques are used. The 3-D nature of the flow is attributed to variable camber, wing thickness along the span and end effects. The 3-D streamlines on wing surface show the presence of vortical structures and their formation, which is due to high cambered profile of the wing and it changes the effective flow direction largely. It is observed that with increase in IF the strength of vortices grows and the flow separated region broadens on the wing surface. The hysteresis curve shows decrease in C_L and C_D during pitch-up motion due to the effect of gust frequency which influences their periodic nature. The force coefficients are found to be proportional to the gust parameters, but for IF values of 30 and 40, off-trend behaviour is also seen. The force coefficients are in-phase with the gust period. The spectral analysis confirms dependence of the flow field on gust frequency. The gust intensity energizes the vortex structures which is evident from the dominant frequency peaks at $x = 2c$ for IF values of 50 and 60. The large value of gust frequency can affect the size of vortices because vortices do not get enough time to grow and shed in the form of small eddies. This has been inferred from the nature of marginal spectral distribution.

Acknowledgements This work was performed using AQUA super cluster and the authors acknowledge the support of high performance computing facility of Indian Institute of Technology Madras, Chennai, 600036, India.

Nomenclature

α	Pitch amplitude [rad]
α_o	Maximum pitch amplitude [rad]
t	Time [s]
u_{mean}	Mean velocity [m/s]
P	Density [kg/m^3]
C	Root chord length [m]
P	Pressure [kg/ms^2]
Re	Reynolds number
St	Strouhal number
CFL	Courant–Friedrichs–Lewy Number
IF	Gust intensity factor
f_g^*	Non-dimensional gust frequency
f_p^*	Non-dimensional pitch frequency
$C_{L\text{mean}}$	Mean lift coefficient
$C_{D\text{mean}}$	Mean drag coefficient
$C_{D\text{rms}}$	RMS of drag coefficient

C_{Lrms}	RMS of lift coefficient
C_D	Drag coefficient
C_L	Lift coefficient
LEV	Leading-edge vortex
TEV	Trailing-edge vortex
TE	Trailing edge
LE	Leading edge
M	Number of elements along the wing span
n	Number of elements along the chord-wise direction
RMS	Root mean square

References

1. Withers PC (1980) An aerodynamic analysis of bird wings as fixed aerofoils. *J Exp Biol* 90(1):143–162
2. Ennos A, Hickson J, Roberts A (1995) Functional morphology of the vanes of the flight feathers of the Pigeon *Columba livia*. *J Exp Biol* 198(5):1219–1228
3. Carruthers A, Walker S, Thomas A, Taylor G (2009) Aerodynamics of aerofoil sections measured on a free-flying bird. In: Proceedings of the institution of mechanical engineers part G journal of aerospace engineering, pp 855–864
4. Liu K, Song B, Xue D, Wenqing Y, Chen A, Wang Z (2022) Numerical study of the aerodynamic effects of bio-inspired leading-edge serrations on a heaving wing at a low Reynolds number. *Aerospace Sci Technol*
5. Soni A, Tiwari S (2019) Three-dimensional numerical study on aerodynamics of non-flapping bird flight. *S Dhan* 44:31
6. Kim D, Jo-Won C, Myong HS (2017) Unsteady aerodynamic characteristics depending on reduced frequency for a pitching NACA0012 airfoil at $Re_c = 2.3 \times 10^4$. *Int J Aeronaut Space Sci* 18(1):8–16
7. Liu T, Kuykendoll K, Rhew R, Jones S (2006) Avian wing geometry and kinematics. *AIAA J* 44:954–963
8. Kondo K (2014) Computational comparative study for design of low Reynolds number airfoil. In 29th Congress of the international council of the aeronautical sciences, St. Petersburg, Russia
9. Huang NE, Shen Z, Long SR, Wu MC, Shih HH, Zheng Q, Yen NC, Tung CC, Liu HH (1998) The empirical mode decomposition and the Hilbert spectrum for nonlinear and non-stationary time series analysis. *Proc R Soc London A* 454:903–995

Aerodynamic Characteristics of Finite Rectangular Wings in Formation Flight with Ground Effect



Ravindra A. Shirsath and Rinku Mukherjee

Abstract The concept of formation flight is not new and so is the ground effect as both are done to reduce the drag and improve an aerodynamic efficiency, but the important thing to investigate is what really happens while wings fly in formation when ground effect is present, an important application of which is a flying train. The present work is an attempt towards understanding this complex flow field when the two wings fly in a lead-trail formation within the ground effect using commercial CFD package ANSYS-Workbench (2020 R1). The aerodynamic performance of finite rectangular wings comprising of NACA 2412 airfoil with $AR \approx 6.66$ for both the leading and trailing wings is analysed in the present work. The lift and drag coefficients for a fixed chord-wise separation between them as $x/c = 4$ and for various ground clearances ranging from $z/c = 0.2$ to $z/c = 0.8$ increasing by $z/c = 0.2$ and $z/c = 6.0$ considered to be the wings formation out of ground effect are reported. Angles of attack ranging from $\alpha = 0^\circ$ to 21° are considered so as to explore both pre-stall and post-stall angles. The performance of both wings through C_L , C_D , and aerodynamic efficiency, i.e. C_L/C_D is investigated.

Keywords CFD · Formation flight · Lead-trail · Wing-in-ground (WIG) effect · Aerodynamic efficiency

1 Introduction

The ground effect machine (GEM) has generated a lot of interest as a huge over-water transport vehicle since it is a potential transport option. In order to compete with existing transport vehicles, a ground effect machine would need to move at faster speeds, necessitating an aerodynamic shape, as proposed by earlier researchers. Another way to concentrate on drag reduction and improved aerodynamic efficiency obviously is through formation flight wherein either fuel can be saved for given range or the range can be improved for given fuel, if the drag can be considerably

R. A. Shirsath (✉) · R. Mukherjee
Department of Applied Mechanics, IIT Madras, Chennai 600036, India
e-mail: aero.ravi22@gmail.com

© The Author(s), under exclusive license to Springer Nature Singapore Pte Ltd. 2024
K. M. Singh et al. (eds.), *Fluid Mechanics and Fluid Power, Volume 2*, Lecture Notes in Mechanical Engineering, https://doi.org/10.1007/978-981-99-5752-1_58

723

reduced. Consequently, the goal of current work is to explore the combined effect of formation flight and ground effect and its influence on the aerodynamics of such an arrangement.

The chord dominated ground effect (2D) has been extensively researched in the past as Ahmed et al. [1] investigated the flow properties over a symmetrical airfoil NACA 0015 and revealed higher lift coefficient when the airfoil was near the ground. Owing to the convergent-divergent passage formed between the ground plate and an airfoil, which causes a suction effect on the bottom surface, the lift decreased for smaller angles of attack and specific ground clearances. Ahmed et al. [2] evaluated the flow parameters over a NACA 4412 airfoil in a wind tunnel equipped with moving ground. Drag and lift forces were determined and wake region was investigated. While the lift increased at larger angles of attack because of significant pressure on the lower surface, it decreased at angles upto 4° due to reduced ground clearance. At all angles, the drag was greater near the ground, mostly as a result of the altered pressure distribution on lower surface. According to Ghadimi et al. [3], aerodynamic characteristics and boundary layer properties were functions of the following parameters as Reynolds number, angle of attack, flight altitude, and airfoil thickness. They also examined the effects of flight altitude in addition to the airfoil thickness moving close to ground. Thorough investigations by Li et al. [4] of the RAE 2822 airfoil's aerodynamic properties at multiple ground clearances along with angles of attack led them to draw the following conclusions: realizable $k - \varepsilon$ model had good ability to predict the flow characteristics, possibility of better lift and improved lift to drag ratio exists only in medium range of angles of attack. Additionally, a static ground state would encourage the boundary layer to separate over the ground and make a difference on the aerodynamic characteristics when it was close to ground.

Additionally, for WIG effect, Liang et al. [5] examined unsteady aerodynamics involving heaving airfoils utilizing a potential-flow-based vortex technique, on a rigid surface together with that on a progressive water waves. Apart from taking the wake roll-up of the shed vortices into account, various types of oscillations as forced harmonic oscillations and self-excited oscillations were examined. A series of tests were carried out to look into the ground effect encountered by propulsive flapping foils close to a solid boundary by Mivehchi et al. [6], and noticed that both the time and phase averaged mean and periodic lift and thrust forces produced by the foil while it was towed and oscillated in heave and pitch had a considerable influence due to the distance from a wall.

Djvarehshkian et al. [7] evaluated the aerodynamic properties of a smart two-dimensional flap in the ground proximity using a numerical simulations and reported smoother pressure coefficient distribution, higher L/D ratio compared to the traditional flap, improved L/D was experienced at $\alpha = 2.5^\circ$ and the minimum ground clearance. Through numerical simulations Qu et al. [8] simulated the NACA 4412 airfoil on the landing approach to explore the dynamic ground effect (DGE) and proposed that DGE can be classified into different regions as large, medium, and small height regions depending on the aerodynamics and flow physics influenced by the ride height above the ground, incidence effect induced by the sinking movement, static ground effect (SGE) along with the compression work respectively.

For investigating span dominated ground effect (3D), a greater contribution of the main wing in resultant aerodynamic coefficients was reported by Dakhrabadi et al. [9] under extreme ground effect with subsequent reduction in performance away from ground while investigating the static height stability and aerodynamic performance of a compound WIG effect through a mathematical model requiring lesser computational time. An empirical estimate was proposed by Abramowski [10] for quantitative evaluation of chord dominated ground effect while numerically investigating the airflow on the craft's wing influenced by ground effect as it approached the ground or sea surface. Wu et al. [11] employed the immersed boundary-lattice Boltzmann method to investigate the ground effect experienced by a flapping wing. High frequency and small clearances resulting in generation of thrust force and large lift force was reported from varying the parameters such as the oscillating frequency and distance between the ground and foil. With decreasing h/c , no change of sign but increased magnitude of lift coefficient measured directly from load cell as well as surface pressure integration for a wing having a NACA 0015 cross-section from wind tunnel experiments was reported by Luo et al. [12]. However, as a result of the convergent-divergent channel effect when h/c reduced from about 0.3 to 0.15 the lift coefficient was observed to fall briefly for $0^\circ < \alpha < 6^\circ$. Thick, cambered wings having different aspect ratios were tested in a wind tunnel by Fink et al. [13] to investigate the effect of ground proximity and reported increased lift-curve slope as the ground was approached with reduced induced drag that ultimately resulted in large increase in L/D ratio. Configurations of rectangular and delta wings along with ailerons and end-plates were considered for numerical simulations by Jia et al. [14] to investigate the aerodynamics of banked wing with ground effect, advantages in terms adverse yaw moment and smaller righting moment were reported for delta wing in banked turning.

Research and development activities of WIG effect technology were surveyed in detail by Rozhdestvensky [15] starting from the definitions of the phenomenon, the background and outlook of technology, the crafts that benefits from ground effect (GE), particular vehicles and projects and possible fields of application were covered.

Gunasekaran et al. [16] examined aerodynamic properties of lead-trail formation under pre and post-stall flow circumstances using a numerical post-stall predictive tool based on 'decambering' technique. In order to investigate the potential for fuel savings, greater range, delayed flow separation, and effective wing location with respect to one another, two basic lead-trail formations of two wings along with extended formation of five wings were explored. It was observed that having more wings in configuration was advantageous. When compared to the second wing in a two wing configuration, the rearmost wing in a five wing configuration faced nearly 39% less aerodynamic load. It mostly had least amount of induced drag, and under some circumstances it was even reported that it had nearly no induced drag. Gunasekaran et al. [17] also examined the impact of wing twist on the induced drag of different lifting surfaces in configuration flight, including at post-stall angles of attack, by utilizing an unique 'decambering' technique based on a vortex lattice method. The influence of both aerodynamic and geometric twist was investigated. It

was discovered that adding only a little geometric twist might significantly alter the induced drag particularly at higher angles of attack.

It is believed that through both the full size prototypes and model experiments the technical viability of WIG effect vehicles has been demonstrated. The key technical issues pertaining to the creation of WIG effect vehicles are well conceived, have been resolved, or are in the process of being resolved. Various aerodynamic designs have been devised and studied, each of which has benefits and drawbacks from the perspective of certain uses. Early GE technology was predominantly used for naval purposes, but today new opportunities are opening up for a significant commercialization of this rapid maritime transit option.

As can be summarized from literature that the two concepts of formation flight and WIG effect are independently studied by many researchers. However the combined effect of formation flight with WIG effect is rarely investigated and an interesting and innovative application of this can be flying train. Additionally when an aeroplane with conventional wing-tail configuration is on the take-off roll or landing approach, it also resembles to a lead-trail formation flight with ground effect. The aerodynamic characteristics of trailing wing as influenced by both, the leading wing and ground proximity needs to be investigated carefully as it has direct connection with the stability of an aeroplane. Hence the present work is an attempt towards answering some of the issues that will prop up for this kind of concept of flying train or formation flight with ground effect.

2 Methodology

A steady-state CFD research is conducted, and the specifics are as follows. First a single wing out of ground effect is investigated followed by wings in lead-trail formation without and with ground effect.

2.1 Geometry and Mesh

Finite wing considered in the present work has $AR \approx 6.66$ and is composed of NACA 2412 (cambered) airfoil section. The vertical distance between ground and trailing edge of the wing is defined to be the ground clearance, z/c . Considering the range of Reynolds number for the vehicles operating in the ground proximity $2 \times 10^5 < Re < 3 \times 10^5$, all computations are performed at $Re \approx 2.4 \times 10^5$.

The computational domain with the corresponding dimensions along the three axes is shown in Fig. 1 with the leading wing placed at the origin and trailing wing at $4c$ aft of the leading wing. The grid used for present work is generated using ANSYS workbench meshing as represented in Fig. 2 which is unstructured hybrid grid. Predetermined first layer thickness to ensure $y^+ < 1$ is used to specify inflation

layers over the ground and wing surface to accurately explore the boundary layer, while rest of the computational domain is covered by unstructured mesh.

Reynolds Averaged Navier Stokes Eqs. (1) and (2), as given in [18] are used to perform the simulations. Absolute velocity formulation is employed while setting up the numerical solver in 3D steady-state condition. Pressure–velocity coupling is dealt with SIMPLE algorithm, the algorithm is primarily a guess and correct procedure for the estimation of pressure on the staggered grid arrangement. Discretized momentum equations are solved using the guessed pressure field to yield the velocity components which do not satisfy the continuity equation. Thus corrections are defined for pressure as well as velocity components and this process is iterated until convergence to get

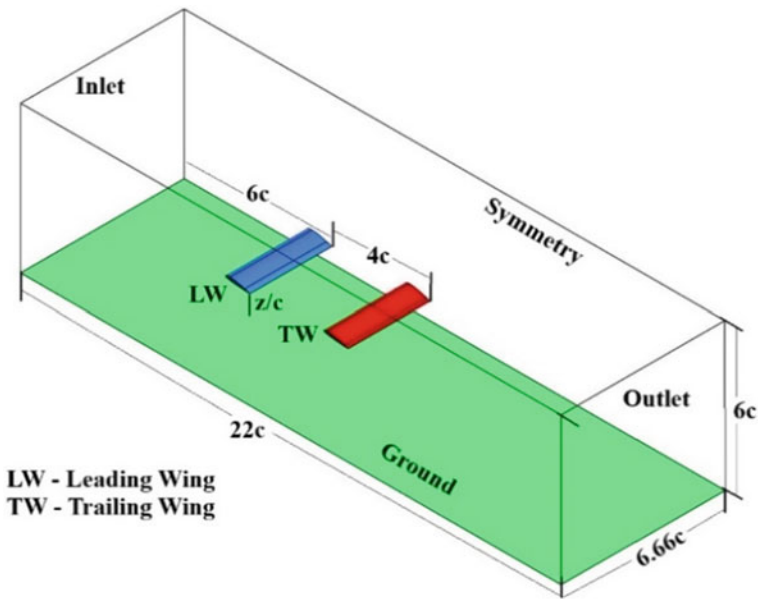


Fig. 1 Computational domain

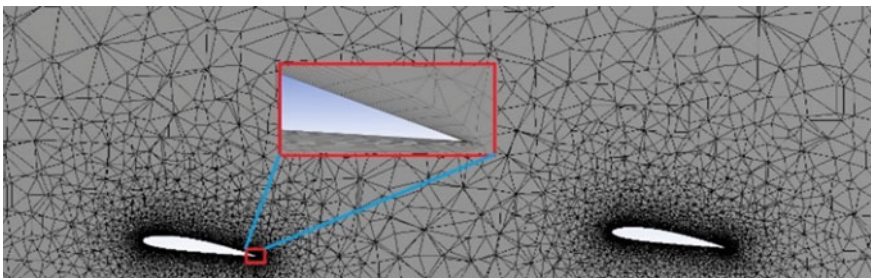


Fig. 2 Unstructured mesh on the wing cross-section

the correct velocity and pressure fields, detailed description of the same can be found in [19]. Gradients are estimated by least squares cell-based method and momentum as well as turbulent kinetic energy and specific dissipation rate are discretized with second-order upwind scheme.

$$\frac{\partial u_i}{\partial x_i} = 0 \quad (1)$$

$$\frac{\partial}{\partial x_j} (\overline{\rho u_i u_j}) = -\frac{\partial \bar{p}}{\partial x_i} + \frac{\partial}{\partial x_j} (\overline{\tau_{ij}} - \overline{\rho u_i' u_j'}) \quad (2)$$

The residuals of flow parameters must meet a convergence requirement as specified to be 10^{-5} . Additionally, the simulations are continued until the force coefficients C_L and C_D become constant.

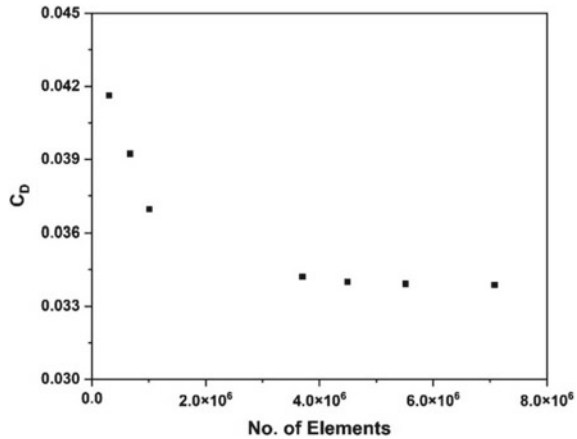
2.2 Boundary Conditions

The boundary conditions as shown in Fig. 1 are as follows: As the simulations are performed for only half of the wing, the right side of the domain is provided with symmetry to optimize the simulation time. Uniform velocity of 3.5 m/s is specified at the inlet in a positive flow direction. Whereas outflow condition is imposed at the outlet boundary. The gauge pressure is set to zero. The side and top of the domain are set to walls. The entire wing surfaces are modelled as solid walls. In addition to the no slip condition, the ground is imposed with a moving wall condition with the same velocity as the free stream velocity. As reported by Watkins et al. [20] the turbulence experienced by moving vehicles at highway speeds is 2.5–10%, thus initial turbulence level in the domain is prescribed through turbulence intensity as 5% and turbulent viscosity ratio of 10 is used. The turbulence closure is achieved with Shear Stress Transport (SST) $k - \omega$.

2.3 Mesh Independence Study

For mesh independence study, the wing at $\alpha = 6^\circ$ is considered in out of ground effect. Multiple grids are generated by progressively increasing the number of elements by varying the respective refinements on the wing surface. An examination of grid convergence is shown in Fig. 3 for C_D of a single wing at $\alpha = 6^\circ$. It is observed that C_D remains almost unchanged for number of elements greater than 3.5×10^6 , eventually the grid with $\approx 7 \times 10^6$ elements is used for the remaining simulations.

Fig. 3 Mesh independence study, $\alpha = 6^\circ$



2.4 Validation

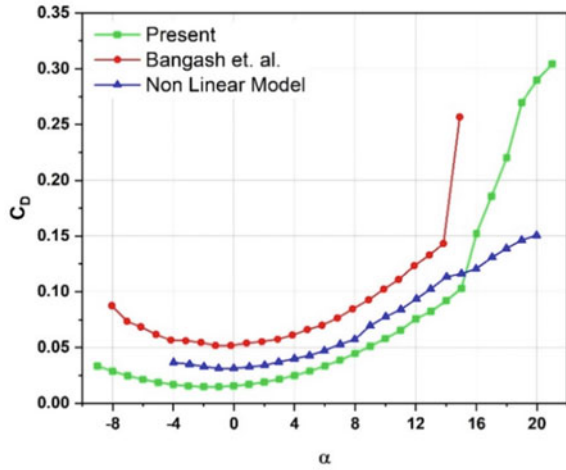
The present computational results are compared with the experimental results of Bangash et al. [21] and Selig’s Cessna 172 nonlinear model [22] for the baseline case, i.e. a single wing out of ground effect as shown in Fig. 4.

Further the results for $C_{L_{TW}} - \alpha$ in lead-trail formation flight are compared with Bangash et al. [21] and Gunasekaran et al. [16] as shown in Fig. 5. In either cases the present results are seen to fairly agree with the results from the existing literature and hence the work is further extended for effect of ground proximity on the formation flight.

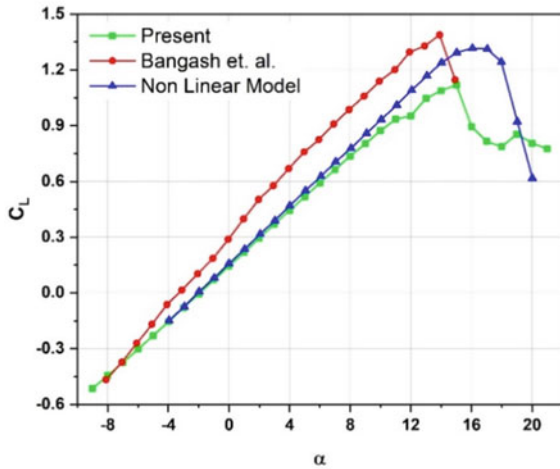
3 Results and Discussion

The results are presented for one particular formation with ground effect where $\alpha_{LW} = 8^\circ$ and is maintained constant throughout while that of the trailing wing is varied, $0^\circ \leq \alpha_{TW} \leq 21^\circ$, the horizontal offset between the two wings, $4c$, same as Bangash et al. [21]. The investigated aerodynamic coefficients of trailing wing for different ground clearances along with WOG are shown in Fig. 6. As seen from Fig. 6a, the $C_{D_{WIG}}$ is less than $C_{D_{WOG}}$ in the range of $0^\circ \leq \alpha_{TW} \leq 12^\circ$ for all ground clearances, while for $\alpha > 12^\circ$ the $C_{D_{WIG}}$ overtakes the $C_{D_{WOG}}$ with lowest ground clearance showing highest increment in C_D . The highest reduction in $C_{D_{WIG}}$ in this range of angles of attack is observed for lowest ground clearance and it decreases gradually and approaches $C_{D_{WOG}}$ with increasing ground clearance. For example, at $\alpha = 9^\circ$ and $z/c = 0.2$, $C_{D_{WIG}}$ is $\approx 30\%$ lesser than corresponding $C_{D_{WOG}}$ while at $\alpha = 21^\circ$ it is $\approx 30\%$ greater and that for $z/c = 0.8$ is $\approx 15\%$ lesser than corresponding $C_{D_{WOG}}$ while at $\alpha = 21^\circ$ it is $\approx 7\%$ greater. Interestingly, the lowest

Fig. 4 Aerodynamic characteristics of single wing from present work and literature



(a) Drag coefficient, C_D

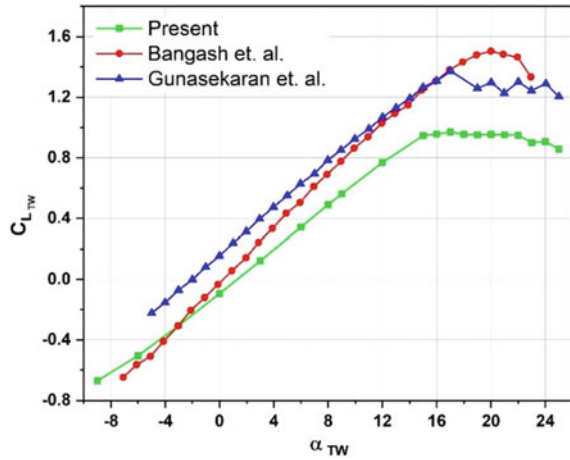


(b) Lift coefficient, C_L

ground clearance, i.e. $z/c = 0.2$ shows highest drag reduction in the pre-stall region and highest drag increment in the post-stall region when compared to WOG.

Corresponding $C_L - \alpha$ is shown in Fig. 6b, it is observed that in spite of being a cambered wing, at $\alpha = 0^\circ$, the C_{LWOG} of the trailing wing is negative (≈ -0.1) which clearly indicates the influence of downwash from the leading wing. However when ground is approached, this effect of downwash is seen to be vanishing and at $\alpha = 0^\circ$, the C_{LWIG} for $z/c = 0.8$ is ≈ 0 while for lower ground clearances, i.e. $z/c = 0.2$, $C_{LWIG} \approx 0.04$ at the same angle of attack. Thus, at $\alpha = 0^\circ$ when compared to C_{LWOG} , the C_{LWIG} is seen to increase by $\approx 88\%$ for $z/c = 0.8$ to $\approx 137\%$ for $z/c = 0.2$. With decreasing z/c , the C_{LWIG} of trailing wing is seen to increase considerably in the range $0^\circ \leq \alpha_{TW} \leq 12^\circ$ with lower z/c experiencing

Fig. 5 Aerodynamic characteristics of trailing wing in formation from present work and literature



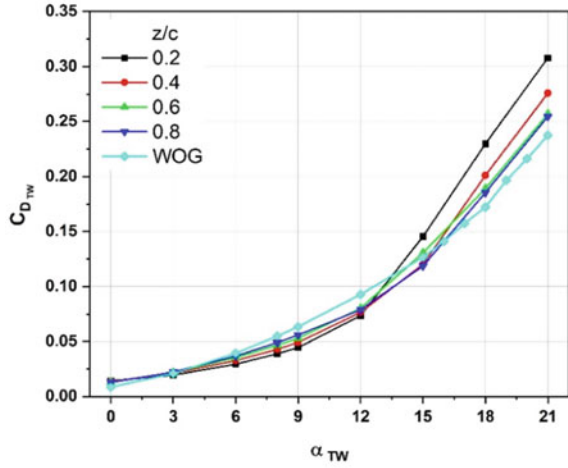
higher increments in C_L . The highest increment of $\approx 191\%$ in $C_{L_{WIG}}$ compared to $C_{L_{WOG}}$ is observed at $\alpha = 3^\circ$ for $z/c = 0.2$.

While highest increment of $\approx 191\%$ in $C_{L_{WIG}}$ compared to $C_{L_{WOG}}$ occurs at $\alpha = 3^\circ$ for $z/c = 0.2$, the lowest happens to be $\approx 86\%$ for $z/c = 0.8$ for the same angle of attack. This effect is seen to be decreasing with increasing angle of attack as the corresponding values are $\approx 80\%$ and $\approx 34\%$ for $\alpha = 6^\circ$ and further decreases to $\approx 46\%$ and $\approx 20\%$ for $\alpha = 9^\circ$. For $\alpha = 15^\circ$, this variation is $< 1\%$ for all the ground clearances except $z/c = 0.6$ for which it is $\approx -6.5\%$. At $\alpha = 21^\circ$, $C_{L_{WIG}} - \alpha$ curve for $z/c = 0.2$ meets with $C_{L_{WOG}} - \alpha$ while $C_{L_{WIG}} - \alpha$ curves for other ground clearances meet at a common point and the difference between them is $\approx 7\%$.

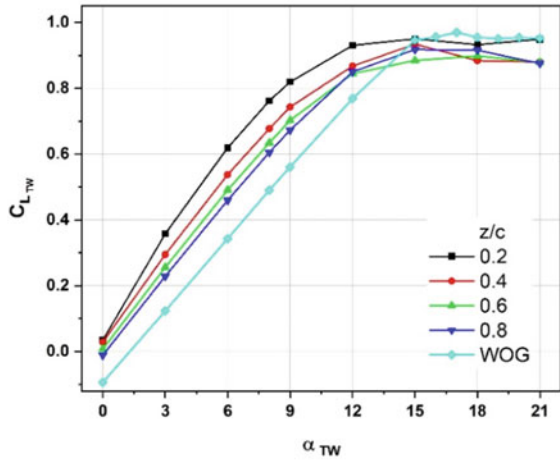
The effect of reduced $C_{D_{WIG}}$ and increased $C_{L_{WIG}}$ as discussed in the pre-stall region is evident on the aerodynamic efficiency as seen from Fig. 7a. The highest $C_L/C_D \approx 21$ is observed at $\alpha = 6^\circ$ for $z/c = 0.2$ while the corresponding value for WOG is ≈ 9 resulting in nearly $\approx 140\%$ increment in aerodynamic efficiency. Highest increment in aerodynamic efficiency in terms of percentage however occurs at $\alpha = 3^\circ$ as seen from Fig. 7b and corresponding value is $\approx 212\%$ at $z/c = 0.2$. Beyond $\alpha = 3^\circ$, the percentage gain in aerodynamic efficiency decreases with increasing angle of attack as well as decreasing ground clearance. For $\alpha \geq 15^\circ$, lowest ground clearance has highest reduction in aerodynamic efficiency of $\approx 25\%$ due to higher C_D as seen from Fig. 6a, while this is seen to decrease with increasing ground clearance.

Thus while operating the two wings in lead-trail formation with ground effect, the trailing wing is seen to gain considerable aerodynamic advantages in terms of reduced C_D , increased C_L and better aerodynamic efficiency, C_L/C_D .

Fig. 6 Aerodynamic characteristics of trailing wing in formation with ground effect



(a) Drag coefficient, C_D



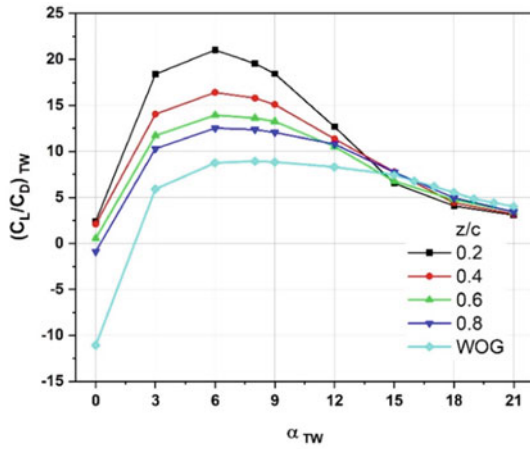
(b) Lift coefficient, C_L

4 Conclusions

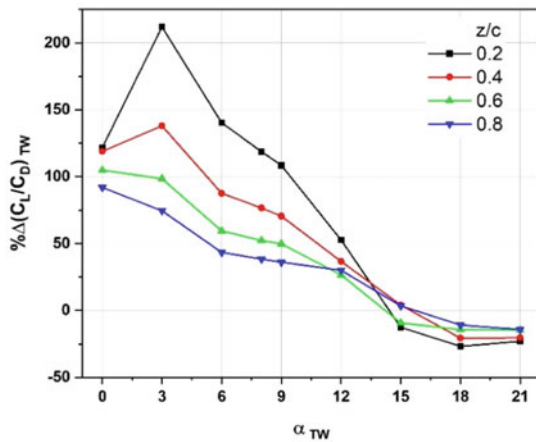
In the present work, the aerodynamic characteristics of a single finite rectangular wing with cambered airfoil section followed by the same for two identical wings in lead-trail formation are reported. Additionally the effect of ground proximity on lead-trail formation is investigated which is distinct in itself and rarely available in the literature.

Present computational results are seen to be in fair agreement with the existing literature in terms of $C_L - \alpha$ and $C_D - \alpha$.

Fig. 7 Aerodynamic efficiency of trailing wing in formation with ground effect



(a) Aerodynamic efficiency, C_L/C_D



(b) Percentage change in aerodynamic efficiency

The aerodynamic properties investigated computationally through CFD are seen to predict $C_L - \alpha$ close to the one predicted by earlier researchers through experiments and Vortex Lattice Method.

Considerable reduction in C_D of the trailing wing in ground effect is observed in the pre-stall region with maximum being $\approx 30\%$ at $\alpha = 9^\circ$ with lowest ground clearance of $z/c = 0.2$ while in the post-stall region it increases with a maximum of $\approx 33\%$ at $\alpha = 18^\circ$ for the same ground clearance.

Lift coefficient C_L of the trailing wing is also observed to be higher for the corresponding conditions with a maximum increment of $\approx 191\%$ at $\alpha = 3^\circ$ and $z/c = 0.2$.

Most importantly, at $\alpha = 3^\circ$, the minimum increment in aerodynamic efficiency of $\approx 75\%$ at $z/c = 0.8$ to a maximum increment of $\approx 212\%$ at $z/c = 0.2$ is observed which can directly result in equivalent fuel savings.

Thus, overall the finite rectangular wings in lead-trail formation flight with ground proximity are seen to be better placed in terms of all the aerodynamic characteristics as C_D , C_L , and C_L/C_D which if implemented accurately can result in a considerable fuel savings and reduced flying cost.

Nomenclature

α	Angle of attack ($^\circ$)
AR	Aspect ratio
CFD	Computational Fluid Dynamics
C_D	Drag coefficient
C_L	Lift coefficient
C_L/C_D	Aerodynamic efficiency
LW	Leading wing
NACA	National Advisory Committee for Aeronautics
Re	Reynolds number
SIMPLE	Semi Implicit Method for Pressure Linked Equations
TW	Trailing wing
x/c	Chord-wise location
z/c	Ground clearance
WIG	Wing-In-Ground
WOG	Wing-Out-of-Ground

References

1. Ahmed MR, Sharma SD (2005) An investigation on the aerodynamics of a symmetrical airfoil in ground effect. *Exp Thermal Fluid Sci* 29(6):633–647
2. Ahmed MR, Takasaki T (2007) Aerodynamics of a NACA 4412 airfoil in ground effect. *AIAA J* 45(1):37–47
3. Ghadimi P, Rostami AB, Jafarkazemi F (2012) Aerodynamic analysis of the boundary layer region of symmetric airfoils at ground proximity. *Aerosp Sci Technol* 17(1):07–20
4. Li S, Zhou D, Zhang Y, Qu Q (2015) Aerodynamic investigation of RAE 2822 airfoil in ground effect. *Procedia Engineering* 126:174–178
5. Liang H, Wang X, Zou L, Zong Z (2014) Numerical study of two dimensional heaving airfoils in ground effect. *J Fluids Struct* 48:188–202
6. Mivechi A, Dahl J, Licht S (2016) Heaving and pitching oscillating foil propulsion in ground effect. *J Fluids Struct* 63:174–187
7. Djavarehshkian MH, Esmaeli A, Parsani A (2011) Aerodynamics of smart flap under ground effect. *Aerosp Sci Technol* 15(8):642–652

8. Qu Q, Jia X, Liu P, Agarwal RK (2014) Numerical study of the aerodynamics of a NACA 4412 airfoil in dynamic ground effect. *Aerosp Sci Technol* 38:56–63
9. Dakhrabadi MT, Seif MS (2016) Influence of main and outer wings on aerodynamic characteristics of compound wing-in-ground effect. *Aerosp Sci Technol* 55:177–188
10. Abramowski T (2007) Numerical investigation of airfoil in ground proximity. *J Theor Appl Mech* 45(2):425–436
11. Wu J, Zhao N (2013) Ground effect on flapping wing. In: *Procedia engineering 7th Asian-Pacific conference on aerospace technology and science*, vol 67, pp 295–302
12. Luo SC, Chen YS (2012) Ground effect on flow past a wing with a NACA 0015 cross-section. *Exp Thermal Fluid Sci* 40:18–28
13. Fink MP, Lastinger JL (1961) Aerodynamic characteristics of low aspect ratio wings in close proximity to the ground. NASA Technical Note, National Aeronautics and Space Administration, United States
14. Jia Q, Yang W, Yang Z (2016) Numerical study on aerodynamics of banked wing in ground effect. *Int J Naval Arch Ocean Engineering* 8(2):209–217
15. Rozhdestvensky K (2006) Wing-in-ground effect vehicles. *Prog Aerosp Sci* 42:211–283
16. Gunasekaran M, Mukherjee R (2020) Aerodynamic analysis of basic and extended lead-trail formation using numerical technique. *Europ J Mech B/Fluids* 79:480–491
17. Gunasekaran M, Mukherjee R (2017) Behaviour of trailing wing(s) in Echelon formation due to wing twist and aspect ratio. *Aerosp Sci Technol* 63:294–303
18. Tennekes H, Lumley JL (1989) *A first course in turbulence*. Butterworth
19. Patankar SV (1980) *Numerical heat transfer and fluid flow*. Hemisphere Publishing Corporation, Electro Skills Series
20. Watkins S, Saunders JW, Hoffmann PH (1995) Turbulence experienced by moving vehicles, Part I, introduction and turbulence intensity. *J Wing Eng Indust Aerodynam* 57(1):01–17
21. Bangash ZA, Sanchez RP, Ahmed A, Khan MJ (2006) Aerodynamics of formation flight. *J Aircr* 43(4):907–912
22. Roskam J (1995) *Airplane flight dynamics and automatic flight controls*. DAR Corporation, Lawrence

Compressible Flow

Experiments on Compressible Vortex Ring Interaction with a Cone Mounted on a Flat Plate



Praveen K. Nuvvula, Amar Yadav, Pawan Kumar Karn, Rijin Rajan, Mohd Javed, and Debopam Das

Abstract When it comes to compressible flows, the formation and development of the vortex ring are of paramount importance, such as starting the rocket nozzles, volcanic outbursts, etc. In this paper, the shadowgraphy flow visualization method has been adapted to find out the behaviour of the flow coming out of an open shock tube interacting with a cone mounted on the flat plate. The impingement of compressible vortex ring with cone and plate validates some new flow features and structures, like formation of tent shock and, instability in jet due to interaction of reflected shock observed in simulations.

Keywords Tent shock · Embedded shock · Compressible vortex ring

1 Introduction

Toroidal vortical structure having rotational core and irrotational outer region in a fluid is called a vortex ring. Vortex rings have been observed in starting flow from a rocket nozzle, gun firing, missiles, etc. Depending on various parameters such as driver section length, driver to driven pressure ratio, Mach number (M_s) and flow conditions at exit, compressible vortex ring shows some compelling flow features during its formation, evolution and propagation [5]. Many researchers have studied and marked such vortex ring [3, 4, 6]. A lot of variations are observed in the compressible vortex ring core flow properties. Baird [1] distinguished in his experiments an embedded shock for some Mach numbers in the vortex ring. An opposite circulation counter-rotating vortex ring in comparison with primary was first noticed by Brouillette and Hebert [2].

P. K. Nuvvula · A. Yadav (✉) · R. Rajan · M. Javed · D. Das
Department of Aerospace Engineering, Indian Institute of Technology Kanpur, Kanpur 208016, India
e-mail: amary20@iitk.ac.in

P. K. Karn
Department of Sustainable Energy Engineering, Indian Institute of Technology Kanpur, Kanpur 208016, India

In a preliminary investigation, the isolated compressible vortex ring had been created by the Murugan [8], and its wall interplay had been detected at a certain x/D location. Using flow visualization, he compared the vortex ring's impingement on the wall and subsequent lift-off for $M_s = 1.31$ and 1.55. In [9], a comprehensive investigation was carried out for initial vortex ring interacting with solid plate and this vortex's engraining with a counter-rotating vortex ring (CRVR). In case of under and over-expanded supersonic jets impinging on an axisymmetric deflector, different flow phenomena both numerically and experimentally were studied by Mehta and Prasad [7].

Compressible vortex ring and its following jet interacting with wall-mounted cone was not the subject of any studies that we could uncover. So, for this particular issue, we went ahead and conducted numerical simulations and experiments. In this paper, we are presenting some initial experimental results to validate the simulation results.

2 Methodology and Experiments

Many experiments have been done using shock tube with the size described in (Fig. 1). The current experimental setup contains driver length of 285 mm and driven length of 1200 mm. In both sections, dry air has been employed as a test gas. The inner diameter is having 64 mm and outer diameter is having 100 mm for the shock tube. Mylar sheet has been used as a diaphragm in the shock tube to withstand pressure up to 150 psi to divide driver and driven regions. A Pneumatically operated plunger has been used to bust the diaphragm to get the required Mach number. Unsteady pressure sensors (PCB) were mounted to monitor the shock movement at various specified positions. All sensor data were fed into DAQ system (National Instruments) which was further utilized to calculate the required parameters using MATLAB. The pressure sensor situated near the edge of shock tube was also fed to delay generator (BNC pulse delay generator) where a specified delay time was provided. A trigger was released from the delay generator to the camera to capture the flow features at specified delay.

To capture the shock and the vortices emerging from the shock tube, shadowgraph method was used. It had a 2500 mm focal length and a 120 mm diameter spherical mirror as its main component. A single LED was utilized as a light source with a slit opening of 3 mm. The light source was placed at the centre of curvature of the spherical mirror. The reflected light was passed through the area of interest. The light ray further converged to a point and the camera was placed after this point to capture the images (Fig. 2).

The moving shock phenomena were initially recorded at 10300 fps with an exposure length of 1 microsecond using a high frame rate camera (9 MP IDT camera). However, the resolution of the acquired pictures was insufficient to discern between the various events. Further, a high-resolution camera (29 MP IMPEREX camera) was utilized to capture a single frame with exposure time of 10 microseconds and the experiments were repeated the required number of times to capture the phenomenon by varying the delay time.

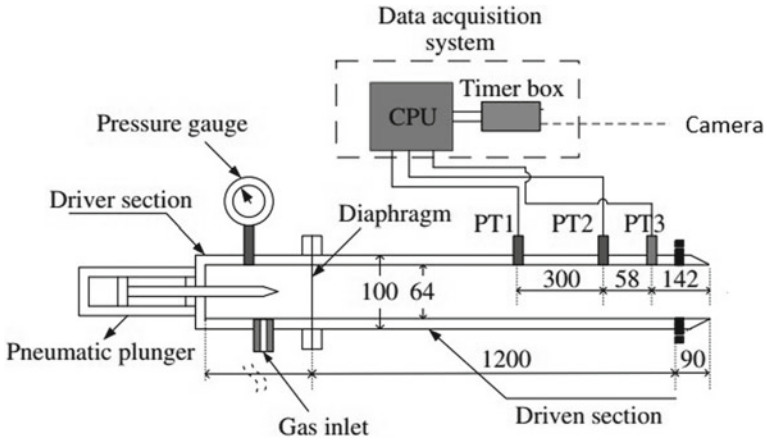


Fig. 1 Schematic of shock tube and other instruments [5]

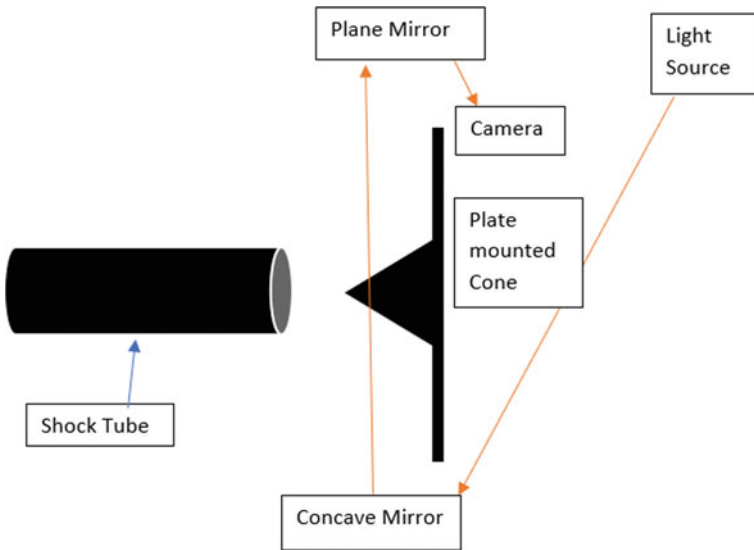


Fig. 2 Schematic of shadowgraph experimental setup

3 Results and Discussion

Compression and expansion waves are formed as the diaphragm is burst using a plunger. In high and low-pressure zones, expansion and compression waves have been moving, respectively. These compression waves have combined and generated a shock wave after being apart from the diaphragm. Upstream of the incidence shock, the flow has divided at the outlet and rolled up to form a vortex ring (Fig. 3) when it

leaves the shock tube. The shear layer has been continually supplying the vorticity into the vortex, and the velocity of the flow above and below the shear layer determines how much vorticity is entering the vortex.

After the primary shock has exited the shock tube, for shock Mach numbers less than 2.07, the flow is a subsonic upstream of the shock. As the expansion waves moved towards the centre line from the corner, the Mach number increases with time which indicates accelerating flow upstream. With time, the flow has become sonic at the exit due to these expansion waves.

The Prandtl Mayer expansion fan forming at the nozzle lip causes the sonic flow to further accelerate. Thus, the accelerated flow has created a locally supersonic flow. Thus, a secondary shock originated inside the vortex ring, decelerating the flow to obtain the conditions behind the primary shock (Fig. 4). As the flow establishes with time, this secondary shock sticks out towards the jet axis and forms embedded shock (Fig. 4). The flow is retarded to match the conditions of the vortex ring's wake due to the development of a re-compression shock or vortex-generated shock (Fig. 4). The expansion waves in the trailing jet created at the nozzle lip reflect off the jet boundary and create an intercepting shock (barrel shock or oblique shock) (Fig. 4). A Mach disc is produced when the intercepting shock has interacted with the embedded shock.

As the primary shock has moved towards the cone, it impinges on the apex of the cone. The primary shock has first gone through regular reflection (RR) at the cone surface and moved along the cone surface (Fig. 4). A weak reflected shock wave is formed encircling the cone apex and moved towards the shock tube. The RR is a two-shock structure because it comprises two shocks: incident shock and reflected shock wave. These two-shock waves interact on the reflecting surface near the point of reflection. There is a change from RR to Mach reflection (MR) when the incident shock travels over the surface. Because the MR wave consists of three shocks—the

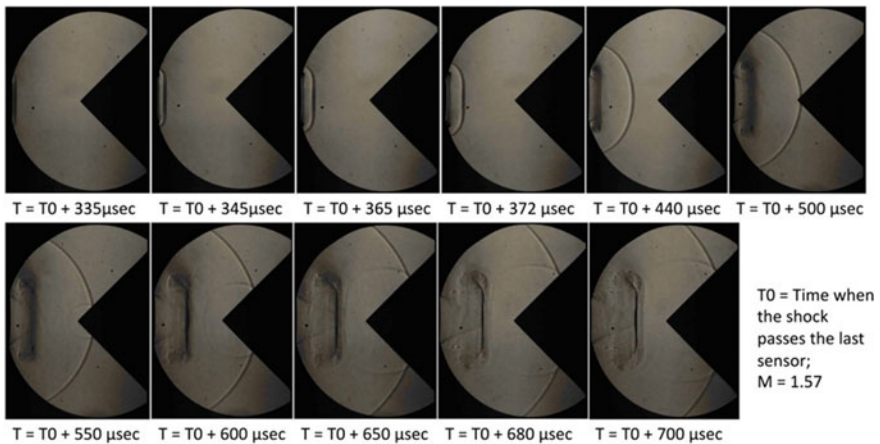


Fig. 3 Shadowgraph image sequence at different times for Mach number 1.57

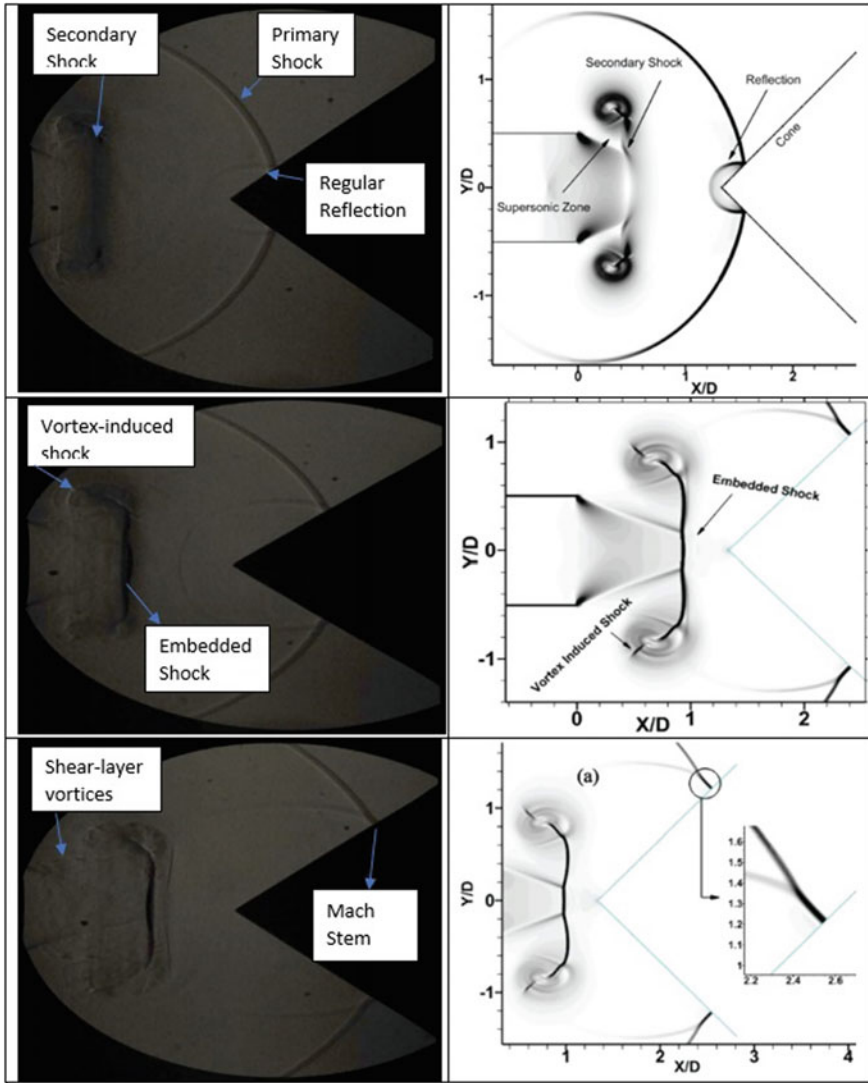


Fig. 4 Different flow features obtained in the experiment for Mach number 1.57 [10, 11]

initial shock, a reflected shock wave, and a Mach stem with slipstream meeting at triple point—it is known as a three-shock structure (Fig. 4).

As the primary shock has moved upstream, Mach stem has undergone through second reflection at the cone corner and the plate. The second reflected shock has moved towards the primary vortex ring (PVR). It is intensified and has formed a second embedded shock with the PVR. The initial Embedded shock and intensified second embedded shock all together have formed a tent-shaped shock structure sitting

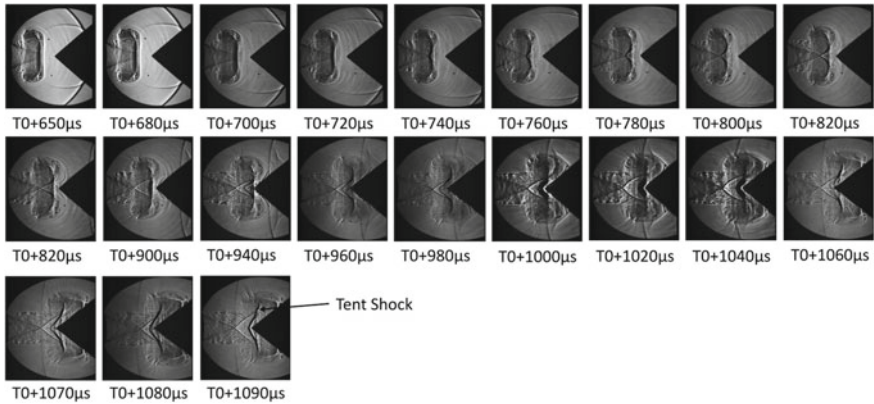


Fig. 5 Continuous shadowgraph image sequence captured for Mach number 1.57

on the cone's apex, which we call Tent shock (TS). More experiments are needed using high-resolution camera with more view area to capture all parts of Tent shock (Fig. 5).

4 Conclusions

The interaction of shock and vortex with anybody provides exciting flow phenomena. In the present experiment, we have carried out the interaction of a compressible vortex ring with a cone mounted on a flat plate. Earlier numerical simulations [10, 11] demonstrate the complicated flow characteristics in the aspects of shock-shock and shock-vortex interaction. A tent shock formation is one of the essential new observations. The present experiment has corroborated experimental observations and established the creation of transient tent shock as a result. In experiments analogous to simulations, additional phenomena, such as the interplay between incident and reflected shock and its transition from RR to MR, are observed.

References

1. Baird JP (1987) Supersonic vortex rings. *Proceed Royal Soc of London. A. Math Phys Sci* 409(1836):59–65
2. Brouillette M, Hebert C (1997) Propagation and interaction of shock-generated vortices. *Fluid Dynam Res* 21(3):159
3. Das D, Bansal M, Manghnani A (2017) Generation and characteristics of vortex rings free of piston vortex and stopping vortex effects. *J Fluid Mech* 811:138–167
4. Didden N (1979) On the formation of vortex rings: rolling-up and production of circulation. *Zeitschrift für angewandte Mathematik und Physik ZAMP* 30(1):101–116

5. Dora CL, Murugan T, De S, Das D (2014) Role of slipstream instability in formation of counter-rotating vortex rings ahead of a compressible vortex ring. *J Fluid Mech* 753:29–48
6. Elder FK Jr, De Haas N (1952) Experimental study of the formation of a vortex ring at the open end of a cylindrical shock tube. *J Appl Phys* 23(10):1065–1069
7. Mehta RC, Prasad JK (1997) Flow structure of a supersonic jet impinging on an axisymmetric deflector
8. Murugan T (2008) *Flow and acoustic characteristics of high mach number vortex rings during evolution and wall-interaction: an experimental investigation*. Indian Institute of Technology, Kanpur, India
9. Murugan T, Das D (2012) Experimental study on a compressible vortex ring in collision with a wall. *J Visualization* 15(4):321–332
10. Nuvvula PK (2022) Compressible vortex ring interaction with a cone mounted on a flat plate. Indian Institute of Technology, Kanpur, India
11. Nuvvula PK, Javed M, Murugan T, Das D (2021) Video: story of shock-vortex interaction during compressible vortex ring and trailing jet impingement on a cone

Numerical and Experimental Studies on Supersonic Free Jet with Various Cross-Sectional Tab Configuration



Srinivasa Rao Lavala, Partha Mondal, and Sudip Das

Abstract Supersonic free jet studies were made with tabbed nozzle configurations having different cross-sections. Experimental and numerical simulations were adopted to obtain the basic flow field features. Pitot tube measurements and Schlieren flow visualization were carried out in experiments, whereas an in-house build, 3D-Euler flow solver was used to obtain the results. The results obtained from the investigation show the basic flows indicating shock distortion, Mach disk location, reduction in core length of the jet, and other features for tabbed configuration.

Keywords Supersonic · Free jet · Blockage ratio · Tab · Shock cell · Nozzle pressure ratio

1 Introduction

Compressible jet applications are commonly used in many aerospace industry problems. The jet configuration mainly depends on the differential pressure, which is defined as the ratio of pressure of exit fluid to ambient fluid. The isolated jet configuration also has a major issue with noise characteristics. The noise emanating from such jets is termed as aeroacoustic problems which are being influenced by its way of generation, the source type, and also the location of such sources. Over the years researchers studied isolated jet configurations and flow structures. The compressible jets flow structure has a periodic quasi-shock cell structure, shock wave interactions, shear layers, wave instabilities, and mode shapes like axisymmetric (toroidal), lateral (flapping), and helical. The interactions of shockwaves, shear layers, and instability waves generate the acoustic waves. These acoustic waves propagate upstream and downstream of the jet and could be detrimental to structures housing them.

Eliminating and reducing such acoustic waves are of prime importance. In past years, researchers have been using two types of control which are active or passive techniques. For active control, there is a need of energy, and passive control does

S. R. Lavala (✉) · P. Mondal · S. Das
Department of Space Engineering and Rocketry, BIT Mesra, Ranchi 835215, India
e-mail: srinuaero116@gmail.com

© The Author(s), under exclusive license to Springer Nature Singapore Pte Ltd. 2024
K. M. Singh et al. (eds.), *Fluid Mechanics and Fluid Power, Volume 2*, Lecture Notes in Mechanical Engineering, https://doi.org/10.1007/978-981-99-5752-1_61

747

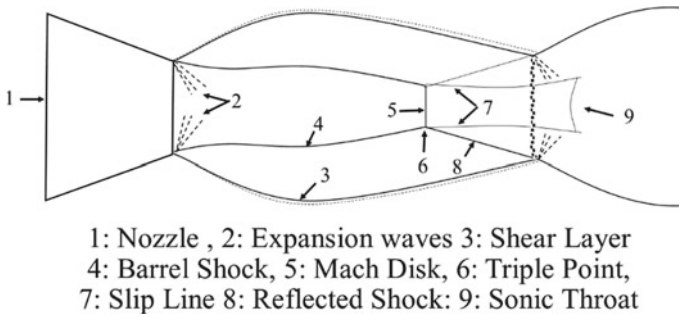


Fig. 1 Isolated jet flow features

not require any force of energy. Present investigation attempts to adopt the passive techniques by using tab configuration shapes like triangular, square, or cylinder. The tabs were inserted at the exit of the jet to face the flow, which produces a pair of vortices, which traverses in the downstream direction along with the jet. The basic features of the jet are the shear layer, barrel shock, Mach disk, reflecting shock, triple point, slip line... etc. as illustrated in Fig. 1. In the present investigation, three rows of elongated tabs were placed circumferentially at 120° apart, so as to block the entire jet exit by a blockage percentage of 11%. The tests were made at a nozzle pressure ratio of 6.0.

2 Literature Review and Objective

Theoretical and mathematical calculations of formation of shock cell and estimation of first shock cell length, with variation of pressure ratios, were reported by Pack [1]. Studies of sonic and supersonic jets experiment results and theoretical predictions were reported by Love et al. [2].

The screeching sound was first investigated by Powell [3], who suggested the emission of feedback mechanism, and the acoustic waves traveling upstream and downstream direction of the jet. The generation of screech tone by a moving source was investigated by Umeda and Ishii [4], and the jet has four stages of modes, which are axisymmetric (A1, A2), lateral (B), helical (C), and lateral (D). The major source dominant helical mode generates the screech tone.

The axisymmetric nozzles tab configurations were first introduced by Bradbury and Khadem [5], who investigated parameters, like boundary layer thickness, flow angle, turbulence level, and tabs. The tab configuration influenced the centreline of the core jet. Various tab configurations were studied by Zaman, et al. [6], and they reported the elimination of screech and mixing enhancement. Axisymmetric heated and unheated jets were investigated by Ahuja and Brown [7], where it has been reported about effective mixing enhancement and screech tone elimination by adopting, three, four-tab configurations at the exit of the jet.

Impinging jets were investigated by Krothapalli [8], who observed two types of discrete tones, one was a screeching tone that was emitted from the third shock cell, and the second one was an impinging tone that was emitted from the impinging region on the rigid plate. Axisymmetric jets were investigated by Singh and Rathakrishnan [9] and reported to weaken shock cells and enhance mixing. Shock cell distortion and core extent reduction were observed using a configuration of Crosswire and tabs investigated by Lovaraju et al. [10]. Axisymmetric convergent-divergent nozzles were investigated by Rathakrishnan [11] and reported that cross wire and tab configurations induce core length reduction, enhance mixing, and reduction/elimination of screech.

Intrusive and non-intrusive methods were investigated by Nagel et al. [12], where they studied on screech elimination, and shock cell distortion using intrusive technique. Investigations to obtain details of the flow field of the first shock cell of the fluid structure interactions were made by Hortensius et al. [13], using PSP, PIV, Schlieren, and oil flow imagery. Axisymmetric jets were investigated by Mitchell et al. [14], using PIV measurements. Imagery analysis of the flow physics of the mode operation of the jet especially the helical mode source from second to fourth shock cell and its generation mechanism was made using proper orthogonal decomposition.

3 Experimental Setup and Methods

Experiments were conducted in a jet flow facility at the Aerodynamic laboratory of Birla Institute of Technology, Mesra, Ranchi. The facility has a settling chamber size with a diameter of 254 mm (10 in.), and a length of 914 mm (36 in.), as illustrated in Fig. 2. Dry air is supplied to the air balloon by 2 Ingersoll Rand compressors in the range of 100–150 psi. For the present investigation, Mach 2.0 nozzles were designed and fabricated (BN) having an exit diameter of 20 mm. The tabs were introduced having cross-sectional shapes as triangle (TT), square (ST), and circular (CT), as shown in Fig. 3. Blockage ratio (BR) is defined as the projected tab area to the exit area of the jet, which for the present investigation is considered as 11%. All the tests which are presented here correspond to a nozzle pressure ratio (NPR) of 6.0.

In-house-built Pitot tubes having OD of 1.8 mm were adopted to measure the jet center line characteristics of the jet. The Pitot probe was mounted on a 2D-traverse unit to investigate the streamwise jet characteristics with a resolution of 1.25 μm . The sensor was connected to the Pitot tube to measure the pressure values. The high-speed data acquisition card is used to acquire the data which is connected to the sensor with a Pitot tube.

The standard 6-Inch Z-type schlieren setup was used to visualize the flow. The images were captured using a BASLER camera (ACA-1300-60gc), having a resolution of 1280×1024 , and using a NI-vision frame grabber.

Numerical computations were made using an in-house built 3D-Euler code for the purpose and were used to corroborate the experimental and computational results. The grid generations and computational domain are depicted in the Fig. 4.

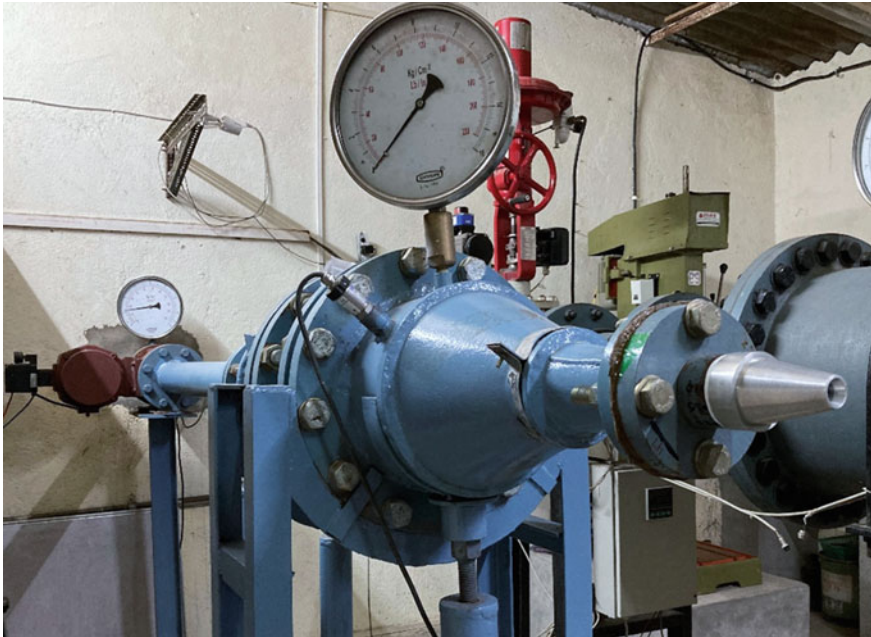


Fig. 2 Free jet facility

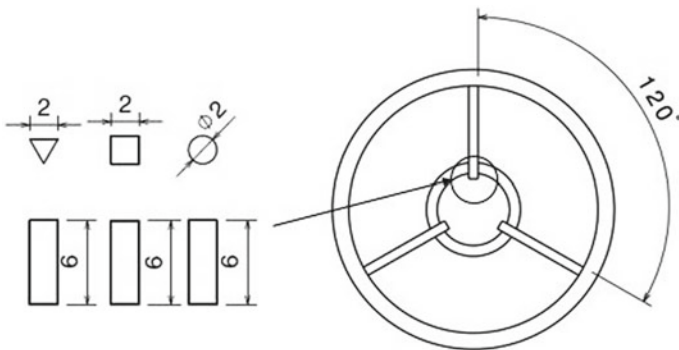


Fig. 3 Tab configuration details and the orientation at the exit of the nozzle

4 Results and Discussion

In the present investigation, tabbed nozzle exit configurations were tested at Mach number of 2.0 with nozzle pressure ratio of 6. The cross-sectional feature of tabs was emphasized here and the shapes with Triangle (TT), Square (ST), and Cylinder (CT) were used. The arrangement of tabs was made such that the blockage ratio at the exit of the nozzle was 11%. The circumferential placement of tabs were 120° apart.

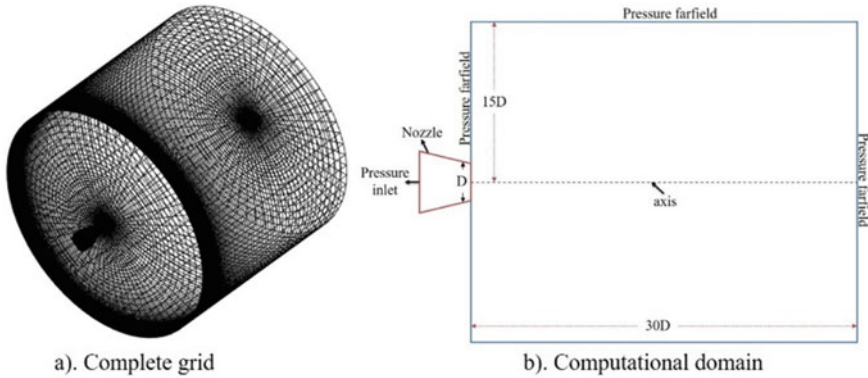


Fig. 4 Grid topology

Figure 5 shows the time averaged schlieren flow visualization photographs of the base and nozzles with the tabbed configurations. The nozzle without tabbed configuration (BN) shows clearly the flow field features and the shock cells. The Mach disk, compression and expansion regions, shock-shock interactions, triple point, shear layers, etc. are having a distinguished representation in the figure. There is a clear difference in jet flow field structure for all tabbed configurations showing distorted shock cells, bulk flow, bisecting and diverting to azimuthal direction, early diffusion, etc. Among all tabbed configurations, the cylindrical tab nozzle shows many patterned features compared to others. The square and triangular tabs indicate almost similar behavior.

The pitot pressure measured along the centreline of jet axis for base nozzle and with various configurations of tabs used in the experiment is shown in Fig. 6. The Pitot tube measurements indicate the pressure oscillation, core jet length, and shock cell details of the jet plume. The rise and fall of total pressures indicate the shock cell formation and compression or expansion waves in the jet. The jet from the base nozzle without tab (BN) configuration clearly indicates the pressure oscillation in the core location of the jet, and diffusing after some extent to the downstream, showing the mixing and entrainment behavior. Adopting of all the tabbed configurations indicate reduction in core length of the jet and shock cells. However, the circular tab shows a comparatively shorter core length among all tabbed configurations.

Figure 7 shows the pitot pressure measurement made in the transverse direction at nine locations downstream of the jet spread. Here also, as indicated by Schlieren and centreline pitot survey, the base nozzle shows a longer and wider jet spread. All the tabbed configurations shows a minimal jet spread in longitudinal as well as lateral directions. The lateral spread for all configurations die down by $X/D = 4$, whereas for base nozzle the influence is seen even at $X/D = 14$. Among the tabs, the cylindrical tab shows the most minimum influence of the jet spread. The lateral pattern of distribution of pitot pressures show distinguished difference between the base nozzle and all tabbed configurations.

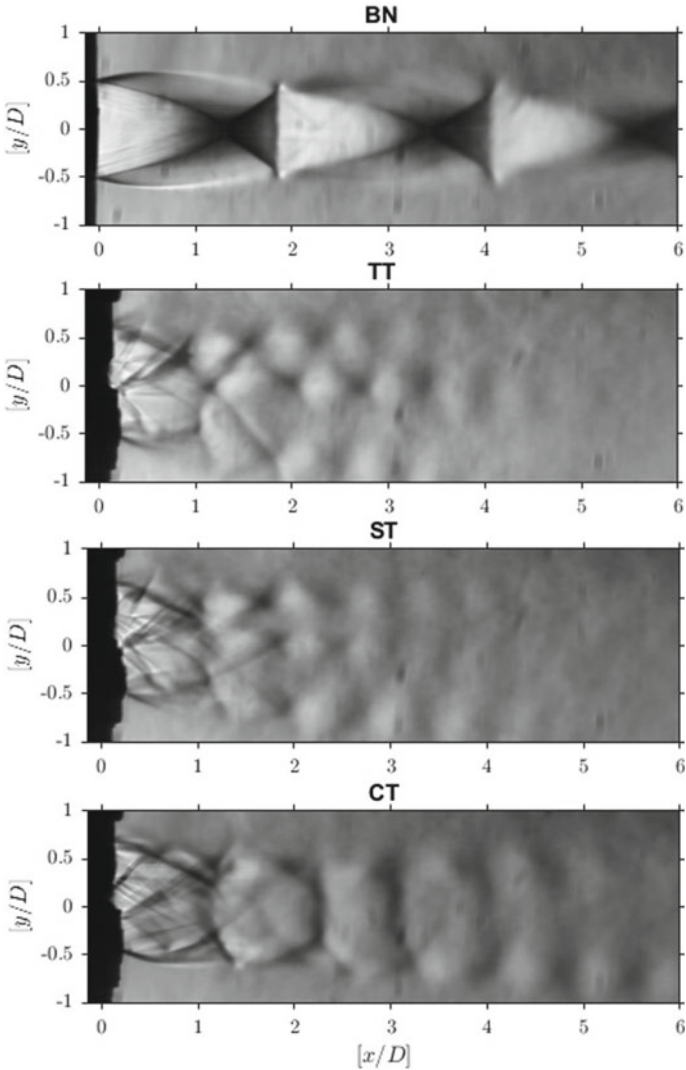


Fig. 5 Schlieren flow visualization of base nozzle and various configurations of tabbed nozzles at NPR = 6.0 and BR = 11%

Table 1 shows the measured first shock cell distance, Mach disk locations, and percentage reduction in core length based on schlieren and pitot measurements for all the configurations tested. The square and triangle tabs show partial disappearance of the shock cells and its distance and Mach disk locations, and the core length reduction was observed for cylinder tabs more than for square and triangular tabs.

Figure 8 shows the comparison of the computed lateral direction static pressure distribution of baseline (BN) and tabbed configuration at a location of $X/D = 4$ from

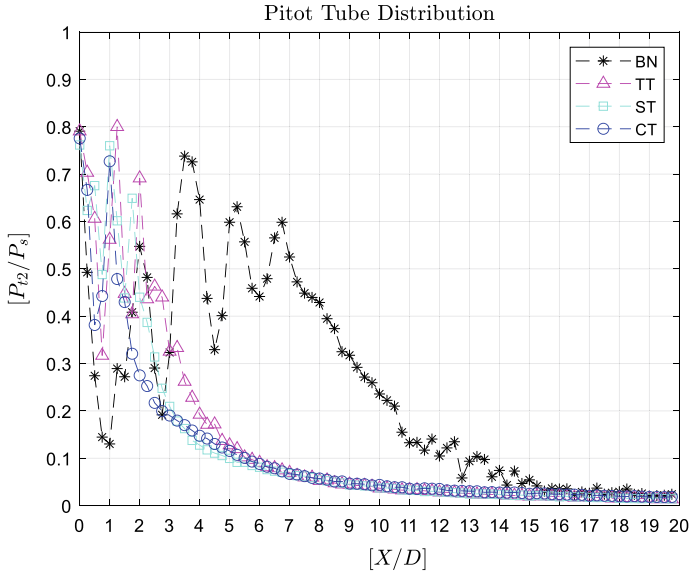


Fig. 6 Measured Pitot tube distribution for base nozzle and nozzle with tabbed configurations at NPR = 6.0 and BR = 11%

the jet exit, which clearly shows jet spread to be more in longitudinal and lateral direction for baseline nozzle than tabbed configuration. This result corroborates the experimental pitot survey measurements.

Figure 9 shows the comparison of the Mach contours with and without tab configurations, downstream of the cross-plane for five X/D locations. The clear disparity pronounced here shows three directional tadpole shapes aligning the tab axis. These shapes vary with different tab configurations. A clear indication of planar flow variation with tabs compared to base nozzle case is observed through the series of figures.

5 Conclusions

Axisymmetric supersonic jet with various tabbed configuration shapes with asymmetric orientation arrangement has been studied in the present investigation. The qualitative and quantitative measurements have been carried out. Core extent was significantly reduced by using tabbed configurations. The shock cell distortion, shock cell, and Mach disk locations disappeared in the triangular and square tabbed configurations. The core length reduction was observed more for cylindrical tab configuration. The computational Mach contours gave tab insight mechanism in the downstream axis of the jet.

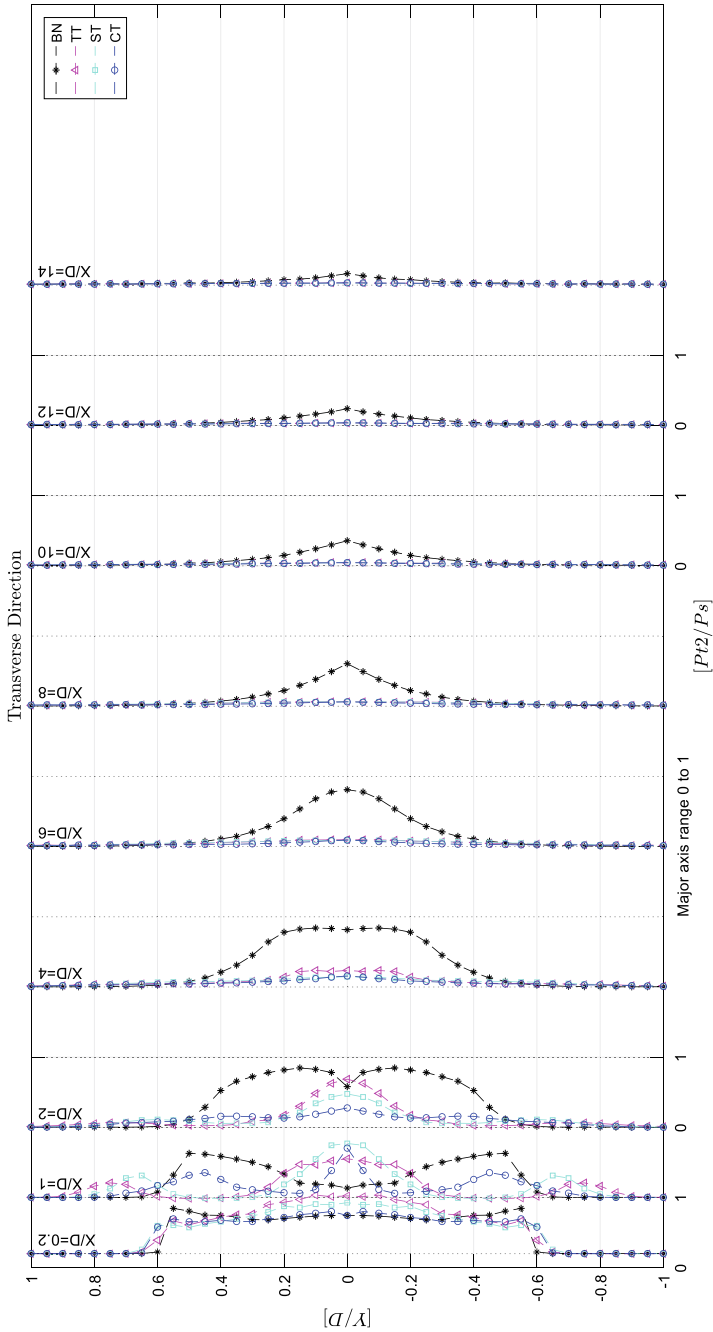


Fig. 7 Measured Pitot tube distribution across the jet (transverse direction) for base nozzle and nozzles with tabbed configuration at NPR = 6.0 and BR = 11%

Table 1 Estimated shock cell distance, Mach disk location, and core length reduction from schlieren flow and Pitot tube measurements of baseline and tabbed configuration at NPR = 6.0 and BR = 11%

	First shock cell distance	Mach disk location	% reduction of core length
BN	1.89	1.30	—
TT	Disappear	Disappear	77
ST	Disappear	Disappear	88
CT	1.39	1.16	93

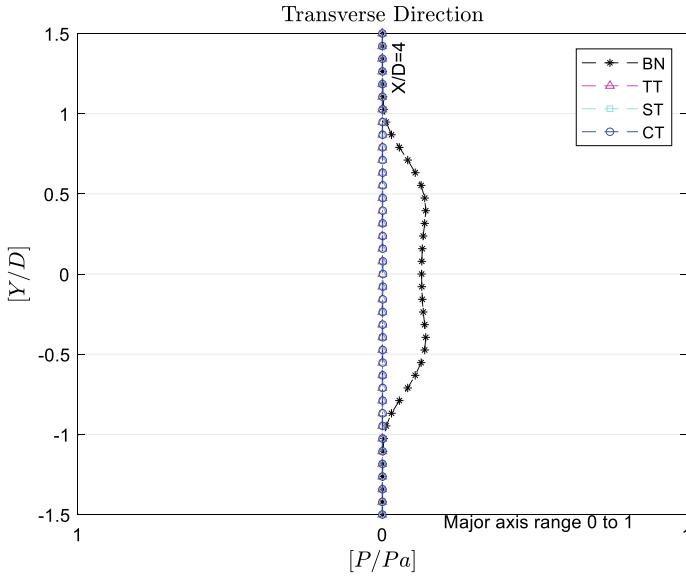


Fig. 8 Computed lateral pressure distribution for all configurations at $X/D = 4.0$

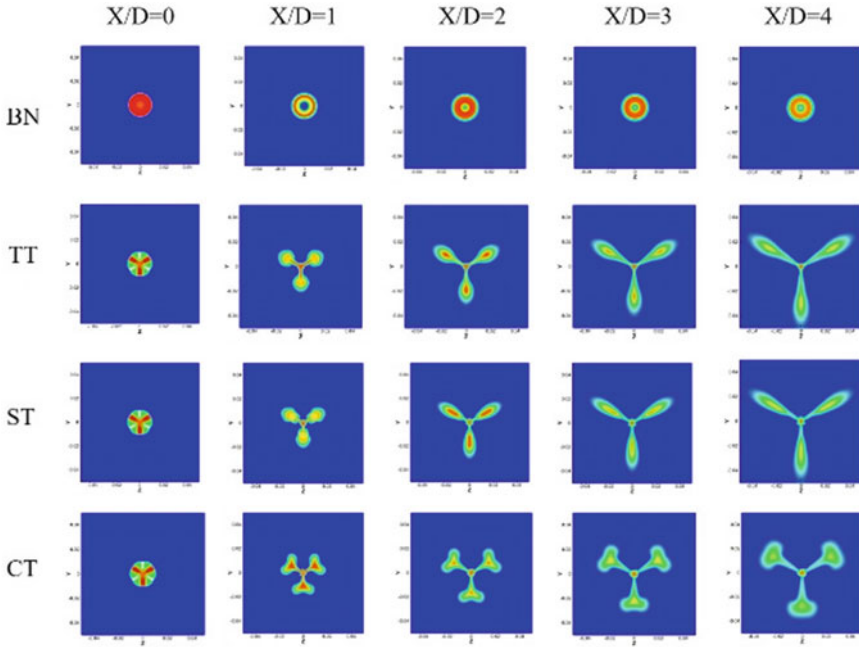


Fig. 9 Mach contours of downstream cross planes at various X/D locations for base nozzle and different tabbed nozzle configurations

Nomenclature

- P Static pressure (N/m^2)
- P_e Exit pressure (N/m^2)
- P_a Ambient pressure (N/m^2)
- P_{t2} Pitot total pressure (N/m^2)
- P_s Settling chamber pressure (N/m^2)
- X Longitudinal axis of the jet (mm)
- Y Transverse axis of the jet (mm)
- D Diameter of the nozzle (mm)
- BR Blockage ratio (-)
- NPR Nozzle pressure ratio (-)

References

1. Pack DC (1948) On the formation of shock-waves in supersonic gas jets: two-dimensional flow. *Quart J Mech Appl Math* 1(1):1-17

2. Love ES, Grigsby E, Lee LP, Woodling MJ (1959) Experimental and theoretical studies of axisymmetric free jets. NASA TR R-6
3. Powell A (1953) On the mechanism of choked jet noise. Proc Phys Soc Sect B 66:1039–1056. <https://doi.org/10.1088/0370-1301/66/12/306>
4. Umeda Y, Ishii R (2001) On the sound sources of screech tones radiated from choked circular jets. J Acoust Soc Am 110:1845–1858. <https://doi.org/10.1121/1.1402620>
5. Bradbury LJS, Khadem AH (1975) The distortion of a jet by tabs. J Fluid Mech 70:801. <https://doi.org/10.1017/S0022112075002352>
6. Zaman KBMQ, Reeder MF, Samimy M (1994) Control of an axisymmetric jet using vortex generators. Phys Fluids 6:778–793. <https://doi.org/10.1063/1.868316>
7. Ahuja K, Brown W (1989) Shear flow control by mechanical tabs. In: 2nd Shear Flow Conference, American Institute of Aeronautics and Astronautics, Reston, Virginia. <https://doi.org/10.2514/6.1989-994>
8. Krothapalli A (1983) On discrete tones generated by an impinging underexpanded rectangular jet 23:1910–1916. <https://doi.org/10.2514/6.1983-729>
9. Singh NK, Rathakrishnan E (2002) Sonic jet control with tabs. Int J Turbo Jet Engines 19:107–118. <https://doi.org/10.1515/TJJ.2002.19.1-2.107>
10. Lovaraju P, Clement S, Rathakrishnan E (2007) Effect of cross-wire and tabs on sonic jet structure. Shock Waves 17:71–83. <https://doi.org/10.1007/s00193-007-0092-z>
11. Rathakrishnan E (2009) Experimental studies on the limiting tab. AIAA J 47:2475–2485. <https://doi.org/10.2514/1.43790>
12. Nagel RT, Denham JW, Papathanasiou AG (1983) Supersonic jet screech tone cancellation. AIAA J 21:1541–1545. <https://doi.org/10.2514/3.60153>
13. Hortensius R, Dutton JC, Elliott GS (2017) Near field of an axisymmetric underexpanded jet and an adjacent parallel surface. AIAA J 55:2489–2502. <https://doi.org/10.2514/1.J055515>
14. Edgington-Mitchell D, Oberleithner K, Honnery DR, Soria J (2014) Coherent structure and sound production in the helical mode of a screeching axisymmetric jet. J Fluid Mech 748. <https://doi.org/10.1017/jfm.2014.173>

Effect of Viscosity on Air Entrapment and Spreading of Molten Droplet in Thermal Spray Coating Deposition



Surendra Kumar, Rajesh Kumar Shukla, and Sayan Sadhu

Abstract When high-velocity molten liquid droplet impacts over a solid substrate, air present in between the droplet and substrate gets trapped inside the droplet and leads to the formation of a pore inside the splat after solidification in thermal spray coating deposition, earlier many researchers have done works in the fields of droplet impact, spreading, and solidification. Despite various experimental and numerical studies, less attention has been focused on the effect of droplet viscosity on the behavior of drop spreading and air entrapment. The current study focused on a numerical study of spreading and entrapped air behavior at low to high viscosity of droplets in the thermal spray coating deposition process. Numerical analysis is carried out by considering heat distribution, solidification, and fluid flow. The result shows that splashing of the droplet in case of high viscosity is more compared to low-viscosity droplet. It has also been observed that at high viscosity, more air entrapment occurs. Splat thickness at the periphery is more in case of high-viscosity droplets.

Keywords Thermal spray · Air-bubble · CFD simulation · Solidification · Viscosity

1 Introduction

Thermal spraying is a generic family of coating processes (Fig. 1) in which the coating material (metallic or nonmetallic) in a fine powder form is injected into a high-temperature and high-velocity gaseous jet, where it is heated and melted and forms a molten droplet. These molten droplets, after impacts over a solid substrate, spread and solidify on the substrate and form a coating deposit (splat). During impingement of high-velocity and high-temperature molten metal droplet on a solid substrate, air present between the droplet and the substrate cannot escape out due to high pressure and gets entrapped between droplet and substrate, which eventually leads

S. Kumar · R. K. Shukla (✉) · S. Sadhu
Department of Mechanical Engineering, Thapar Institute of Engineering and Technology,
Patiala 147007, India
e-mail: rajesh_kumar@thapar.edu

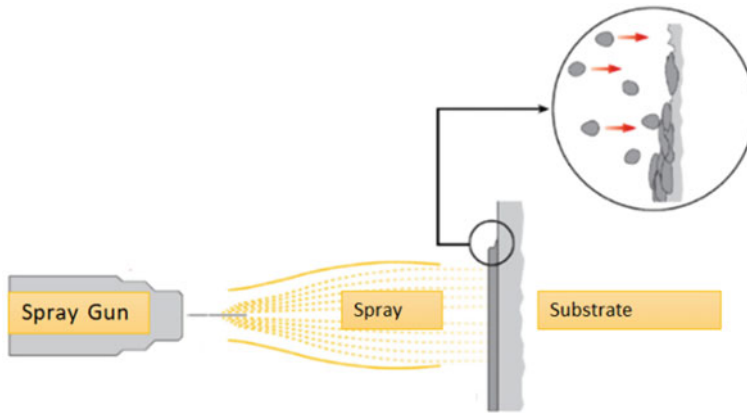


Fig. 1 Thermal-spray coating process

to the formation of pore inside the solidified splat. These formed pores directly affect the quality of coating in the thermal spray deposition process. The viscosity of the droplet has a great impact on the results of the droplet impingement viscosity plays an important role in the entrapment of air and hence the quality of the coating.

2 Literature Review and Objective

Lee et al. [1] measured the air layer thickness and its behavior during the droplet impact using the ultrafast X-ray phase-contrast imaging. It is observed that evolution of air bubble proceeds through a complicated process. It is suggested that bubble can be eliminated from the substrate using low value of contact angle. Tabbara and Gu [2] observed the impact of a tin droplet onto the steel. It has been reported that at high droplet velocity, air is entrapped inside the droplet by penetration of the vortex at the outside surface. It is also highlighted that by increasing the velocity, larger pores can be created. Shukla et al. [3] reported the air entrapment dynamics during actual condition of thermal spray deposition. Influence of air and wettability of the substrate are analyzed using the two-dimensional CFD Model. Dashu et al. [4] observed that air entrapment takes place at the moving front of a droplet approaching the substrate and explained the mechanism of air entrapment through the distribution of pressure and velocity. They also observed that the pressure difference is the main reason for the entrapment of air in the molten droplet. Without taking into account heat transfer between the droplet and the substrate, Mehdi-Nejad et al. [5] investigated the impingement of molten nickel droplets over a solid substrate. They observed that the formation of air bubble take place at the center of the droplet and observed different behavior at different contact angle. Since transparent droplets without phase change were taken into account in the earlier investigations [4–11], it was possible to see the

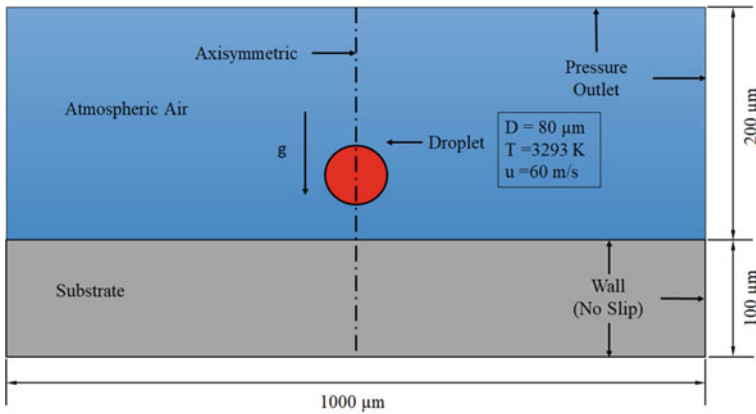


Fig. 2 Geometry of computational domain

trapped air inside the droplet. On the other hand, it was impossible to see the trapped air within the impact of a droplet of opaque molten liquid. This inspired simulations and numerical modeling of the present study to look at the issue. In the literature, less attention has been given to the effect of viscosity on the spreading and air entrapment behavior of molten droplets under the condition of the thermal spray process. The current study focused on a numerical study of spreading and entrapped air behavior at low to high viscosity of droplets in the thermal spray coating deposition process.

2.1 Computational Domain and Mathematical Model

To investigate the present problem, the 2-D axisymmetry domain has been considered as the droplet is spherical in shape, which is shown in Fig. 2. In this problem, at an initial temperature of 3293 K, a molybdenum droplet with a diameter of 80 m strikes a flat aluminum substrate at a speed of 60 m/s. A starting temperature of 300 K is maintained for the aluminum substrate. The thermos-physical property information used in the simulations is shown in Table 1. Droplet is initially placed at a distance of 10 microns from the substrate surface. All the simulations have been performed in Ansys-Fluent.

2.2 Boundary Conditions

The boundary conditions and model considered for the present simulations are listed in the following Table 2.

Table 1 Thermo-physical property data

Contact angle	90°, 30°
Density (air)	1.225 kgm ⁻³
Density (Al)	2390 kgm ⁻³
Density (Mo)	9350 kgm ⁻³
Droplet initial temperature	3293 K
Droplet surface tension	1.5 Nm ⁻¹
Gas phase (droplet surrounding medium)	Air
Impinging droplet	Molybdenum (Mo)
Latent heat of fusion (Al)	3.97 × 10 ⁵ J kg ⁻¹
Latent heat of fusion (Al)	3.97 × 10 ⁵ J kg ⁻¹
Latent heat of fusion (Mo)	3.71 × 10 ⁵ J kg ⁻¹
Liquidous temperature (Mo)	2885 K
Liquidous temperature (Al)	935 K
Solidious temperature (Mo)	2883 K
Solidus temperature (Al)	933 K
Specific heat capacity (air)	1006.43 J kg ⁻¹ K ⁻¹
Specific heat capacity (air)	1006.43 J kg ⁻¹ K ⁻¹
Specific heat capacity (liquid Mo)	570 J kg ⁻¹ K ⁻¹
Specific heat capacity (solid and liquid Al)	1080 J kg ⁻¹ K ⁻¹
Specific heat capacity (solid and liquid Al)	1080 J kg ⁻¹ K ⁻¹
Specific heat capacity (solid Mo)	339 J kg ⁻¹ K ⁻¹
Substrate initial temperature	300 K
Substrate material	Aluminum (Al)
Thermal conductivity (air)	0.0242 Wm ⁻¹ K ⁻¹
Thermal conductivity (liquid Al)	105 Wm ⁻¹ K ⁻¹
Thermal conductivity (liquid Mo)	46 Wm ⁻¹ K ⁻¹
Thermal conductivity (solid Al)	210 Wm ⁻¹ K ⁻¹
Thermal conductivity (solid Mo)	84 Wm ⁻¹ K ⁻¹
Viscosity (air)	1.7894 × 10 ⁻⁵ kgm ⁻¹ s ⁻¹
Viscosity (Al)	0.0013 kgm ⁻¹ s ⁻¹
Viscosity (Mo)	0.005 kgm ⁻¹ s ⁻¹

2.3 Governing Equation

2.3.1 Free Surface Modeling

Air and liquid droplets are immiscible fluids to each other, and the surface interface of air-droplet has been tracked by solving a momentum equation in each computational

Table 2 Boundary conditions

Model	Transient
Gravity	-y direction
Viscous model	k-epsilon model
Fluid	Molten Molybdenum
Velocity	140 m/s
Pressure outlet	Atmospheric, i.e., 1 atm
Solution method	SIMPLE
Momentum	Second order upwind scheme
Turbulent kinetic energy	First order upwind
Solution initialization	Hybrid initialization

cell which basically tracks the volume fraction of air and molten droplets in a cell. The volume fraction (F) of the droplet ranges from zero to unity. If a cell is full of droplets, then the value of $F = 1$, and if a cell is empty of liquid or if a cell is full of air, then the value of $F = 0$.

$F = 0$ cell is full of air or no droplet present.

$F = 1$ cell is full of droplets.

$0 < F < 1$ cell contains air and liquid both (mushy zone).

Volume of fraction F is governed by the following equation

$$\frac{\partial}{\partial t} F + \nabla(uF) = 0$$

2.3.2 Continuity Equation

$$\frac{\partial(\rho u_i)}{\partial x_i} = 0 \tag{1}$$

2.3.3 Momentum Conservation Equation

Momentum conservation is represented by Navier–Stokes

$$\rho u_i \frac{\partial u_j}{\partial x_i} = -\frac{\partial p}{\partial x_j} - \frac{\partial \tau_{ij}}{\partial x_i} \tag{2}$$

where for Newtonian fluid:

$$\tau_{ij} = -\mu_i \left(\frac{\partial u_i}{\partial x_j} + \frac{\partial u_j}{\partial x_i} \right) + \frac{2}{3} \delta_{ij} k \tag{3}$$

2.3.4 Continuum Relations

During the process of solidification, molten droplets in a control volume may contain both solid and liquid phases (mushy state). As a result, the phases share the fields for all properties and variables, which indicate the volume fraction-averaged values. The material characteristics connected to the VOF function are defined as follows for all control volumes. A computational cell can contain solid and liquid i.e., mushy state, during the process of solidification. The property of the material in a computational cell is calculated. The interface evolutions over time are described by a phase function F and the material advection equation.

$$\rho = F\rho_d + (1 - F)\rho_{\text{air}} \quad (4)$$

$$k_{\text{eff}} = Fk_d + (1 - F)k_{\text{air}} \quad (5)$$

$$c_{\text{eff}} = Fc_d + (1 - F)c_{\text{air}} \quad (6)$$

$$\mu_{\text{eff}} = F\mu_d + (1 - F)\mu_{\text{air}} \quad (7)$$

2.3.5 Continuity Equation

$$\nabla \cdot \vec{u} = 0 \quad (8)$$

2.3.6 Momentum Conservation Equation

A single equation for the momentum equation has been considered in both phase air and molten liquid phases. For a 2-phase flow, momentum conservation is represented by Navier–Stokes equations, and this is written as

$$\frac{\partial}{\partial t}(\rho \vec{u}) + \nabla \cdot (\rho \vec{u} \vec{u}) = -\nabla p + \nabla \cdot [\mu_{\text{eff}}(\nabla \vec{u} + \nabla \vec{u}^T)] + \rho \vec{g} + F_{\text{vol}} - S \vec{u} \quad (9)$$

Laminar incompressible flow, constant surface tension, and non-miscible with heat transfer assumption are considered in the simulation.

Source term arising in the momentum conservation equation accounts for the Darcy effect and is governed by

$$S \vec{u} = \begin{cases} \left[C \frac{(1 - f_{1,d})^2}{f_{1,d}^3 + \epsilon} \right] \vec{u} & F = 1 \\ 0 & F < 1 \end{cases} \tag{10}$$

Solidification phase morphology, $C = 150,000 \text{ kg/m}^3/\text{s}$.

Source term arises in those cells only which are full of the droplet and it vanishes in cells having air or cell at the free surface.

F_{vol} represents surface tension force at the interface of droplets and air. The Continuum Surface Force model (CSF) is used to calculate F_{vol} .

It is written as follows

$$F_{\text{vol}} = \sigma \kappa \frac{\rho \nabla F}{\frac{1}{2}(\rho_d + \rho_{\text{air}})} \tag{11}$$

where

ρ_d Density of droplets

ρ_{air} Density of air

F Volume fraction of the droplet

σ Surface tension coefficient between gas and liquid droplet

κ Mean curvature of the free surface

$$\kappa = -(\nabla \cdot \hat{n}) \tag{12}$$

Local surface normal unit vector [5]

$$\hat{n} = \frac{\nabla F}{|\nabla F|} \tag{13}$$

2.3.7 Energy Conservation Equation

The energy equation is expressed as

$$\frac{\partial}{\partial t} (\rho c_{\text{eff}} T) + \nabla \cdot (\rho \vec{u} c_{\text{eff}} T) = \nabla \cdot (k_{\text{eff}} \nabla T) + S_h \tag{14}$$

When liquid droplet phase change takes place to the solid state. During this phase change process, there is some evolution of latent heat takes place, and it is represented by S_h

$$S_h = \begin{cases} -L_d \left[\frac{\partial}{\partial t} (\rho f_{1,d}) \right] & F = 1 \\ 0 & F < 1 \end{cases} \quad (15)$$

L_d Latent heat of fusion for the droplet material

$\rho f_{1,d}$ Density of liquid droplet

The liquid droplet volume fraction is calculated by

$$f_{1,d} = \begin{pmatrix} 0 & \text{if } T \leq T_{\text{solidus},d} \\ 1 & \text{if } T \geq T_{\text{liquidus},d} \\ \frac{T - T_{\text{solidus},d}}{T - T_{\text{liquidus},d}} & \text{if } T_{\text{solidus},d} < T < T_{\text{liquidus},d} \end{pmatrix} \quad (16)$$

2.3.8 Heat Transfer in Substrate Domain

In the substrate, heat transfer is solved by using the following conduction equation:

$$\frac{\partial}{\partial t} (\rho_{\text{subs}} c_{\text{subs}} T) = \nabla \cdot (k_{\text{subs}} \nabla T) \quad (17)$$

3 Results and Discussion

3.1 Effect of Viscosity on Air Entrapment Dynamics

To understand the effect of viscosity on droplet spreading and air entrapment, two cases have been considered, one for high-viscosity droplet impact and another for low-viscosity droplet impact.

3.1.1 Evolution of Spreading and Air Entrapment at Low-Viscosity (0.01 kg/m/s) Droplet Impact

As the droplet impacts the substrate, it starts spreading in a radial direction which can be seen in Fig. 3.

At $t = 0.00629 \mu\text{s}$, initial contact of the molten droplet to the substrate occurred, and air entrapment took place as a layer of a thin film. At $t = 0.1452 \mu\text{s}$, a thin film of air retracts to minimize its surface energy. At $t = 0.2823 \mu\text{s}$, the entrapped air bubble rises up in the molten droplet. At $t = 0.305 \mu\text{s}$, a tiny air bubble gets fused

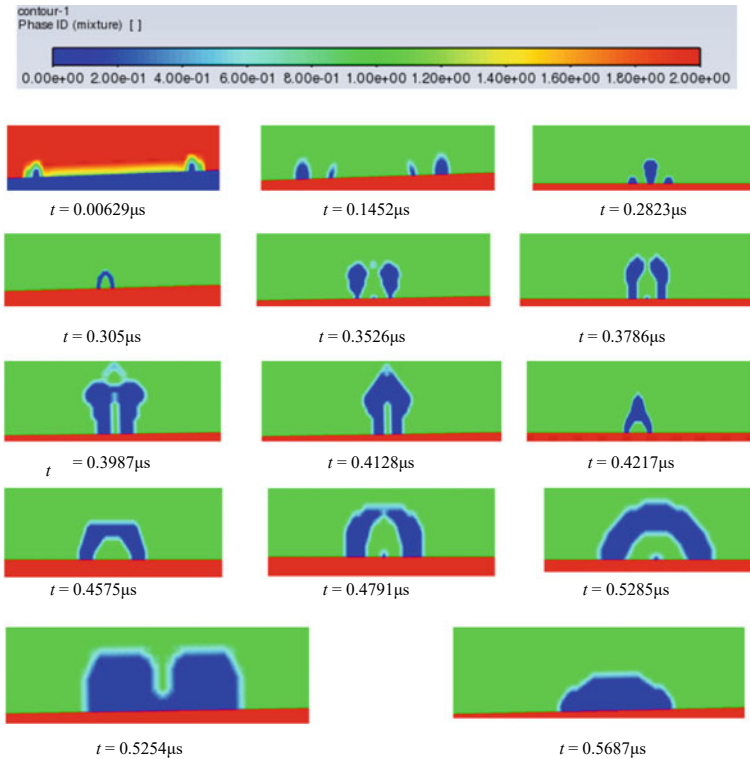


Fig. 3 Air-entrainment dynamics at low viscosity (0.01 kg/m/s) at different time

together. But again, at $t = 0.3526 \mu\text{s}$, they get separated and rise up in the molten droplet. At $t = 0.3786 \mu\text{s}$, the daughter air bubble starts combining from the top, and at $t = 0.3987 \mu\text{s}$, the tip of air bubble fuses together and a cone-type ring of air bubble also gets formed at the top of the bubble.

At $t = 0.3786 \mu\text{s}$, the daughter air bubble starts combining from the top, and at $t = 0.3987 \mu\text{s}$, the tip of the air bubble fuses together, and a cone-type ring of air bubble also forms at the top of the bubble. After that, at $t = 0.4791 \mu\text{s}$ air bubble retracts and starts evolving into a ring shape, and some of the molten liquid droplets also get entrapped inside the ring-shaped air bubble. At $t = 0.5687 \mu\text{s}$, it has been seen that the entrapped molten liquid droplet inside the air bubble gets out from the air bubble, and only a ring-shaped air bubble remains around the central axis of the domain. The diameter of the entrapped is more at the low viscosity, and the thickness of the splat is less.

3.1.2 Evolution of Spreading and Air Entrapment at High Viscosity (0.1 kg/m/s) Droplet Impact

It can be seen from Fig. 4, that as we increase the viscosity of the liquid to 0.1 kg/m/s, some air gets entrapped around the symmetric axis in a ring-shaped ($t = 0.0305 \mu\text{s}$). At $t = 0.0532 \mu\text{s}$, it can be seen that some splashing occurs at the periphery of the spreading droplet. At $t = 0.083 \mu\text{s}$, it can be seen that there is some air entrapment is also seen at the periphery due to high viscosity. At $t = 0.1111 \mu\text{s}$, it can be seen that retraction of entrapped air bubbles takes, and it start to come closer to each other. At $t = 0.2965 \mu\text{s}$, entrapped air bubble comes closer and initiates fusion with each other, and at $t = 0.892 \mu\text{s}$, it fuse inside each other. During this fusion, it can be seen that some droplet also gets entrapped inside the entrapped ring-shaped air bubble. At $t = 4.6793 \mu\text{s}$, it can be seen that the periphery of the splat is thicker than that of the rest part of the splat.

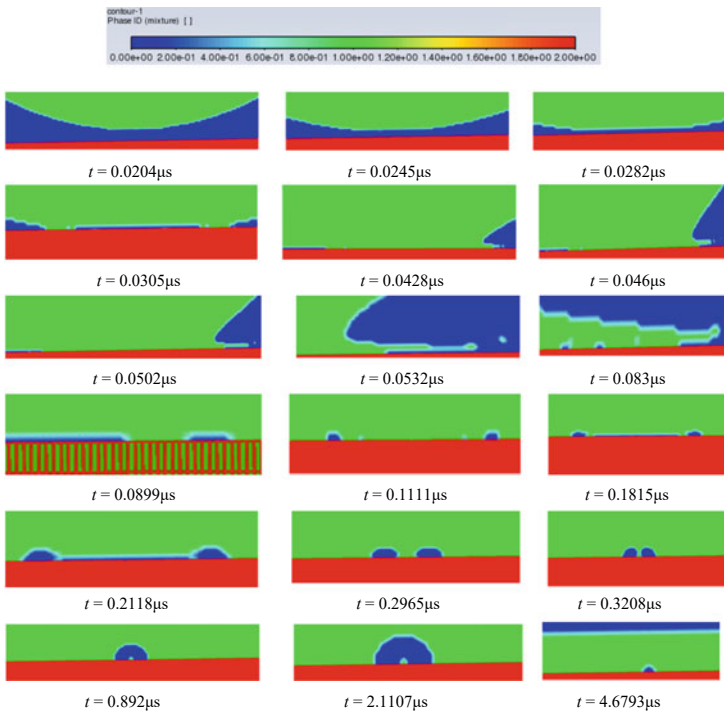


Fig. 4 Air-entrapment dynamics at high viscosity (0.1 kg/m/s)

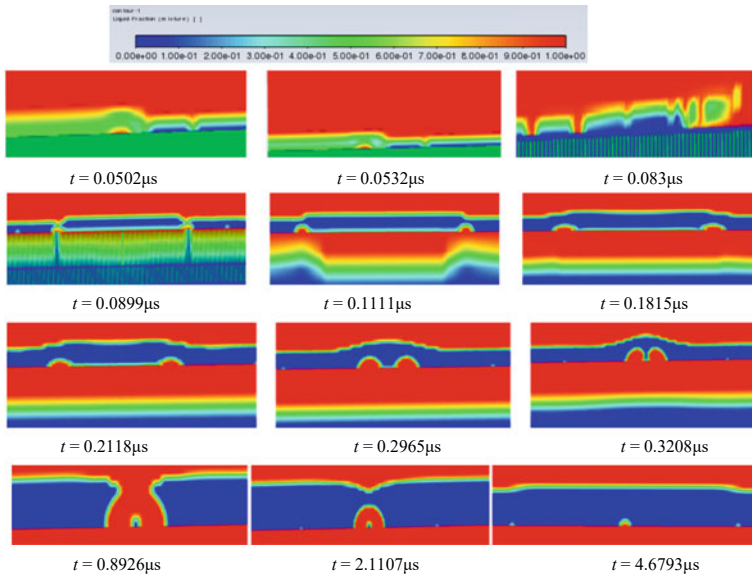


Fig. 5 Contour of liquid fraction at center and periphery portion for viscosity 0.1 kg/m/s

3.1.3 Evolution of Liquid Fraction at the Center and at the Periphery with Viscosity (0.1 kg/m/s)

From the above Fig. 5, it can be seen that as viscosity increases, the air entrapment phenomenon takes place at the periphery of the impacting molten droplet as well as around the central axis. During this process, some of the liquid also gets entrapped inside the entrapped air bubble. It can be seen that at $t = 0.0502 \mu\text{s}$, air also gets entrapped at the periphery of the splat.

At $t = 0.083 \mu\text{s}$, it has been observed that the break-up of radially spreading molten liquid droplets takes place at the periphery. Subsequently, the air entrapped at the center retracts and gets fused together at $t = 0.3208 \mu\text{s}$. The entrapped air bubble at $t = 0.8926 \mu\text{s}$ starts evolving into a ring shape. At $t = 2.1107 \mu\text{s}$, the entrapped air bubble completely transformed into a spherical shape. Further, it can be seen in Fig. 5 that at high viscosity, the breakup of the splat is more at the periphery.

4 Conclusions

In this work, a computational study on molten droplets spreading and air entrapment with high and low viscosity has been studied using the commercial software Ansys-Fluent. The 2-D axisymmetric model has been developed to study the free surface evolution of droplets, solidification, and air entrapment.

It is found that splashing of the droplet in case of high viscosity is more compared to low viscosity. In a high-viscous droplet case, air entrapment, as well as the break-up of splat, occurs at the periphery, which is very less in the case of low-viscosity droplets. Additionally, splat thickness at the periphery is more compared to low-viscosity droplets.

Nomenclature

d	Droplet
sub	Substrate
air	Air
s	Solid
l	Liquid
t	Time [s]
θ_w	Contact angle [°]
T	Temperature [K]
ρ	Density [kg m^{-3}]
σ	Surface tension [N m^{-1}]

References

1. Lee JS, Weon BM, Je JH, Fezzaa K (2012) How does an air films evolve into a bubble during drop impact? *Phys Rev Lett* 109:204501–204505
2. Tabbara H, Gu S (2012) Modelling of impingement phenomena for molten metallic droplets with low to high velocities. *Int J Heat Mass Transf* 55:2081–2086
3. Shukla RK, Kumar A, Kumar R, Singh D, Kumar A (2019) Numerical study of pore formation in thermal spray coating process by investigating dynamics of air entrapment. *Surf Coat Tech* 378:1–16
4. Li D, Zhang D, Zheng Z (2017) Xiaoshuai Tian Numerical analysis on air entrapment during a droplet impacts on a dry flat surface. *Int J Heat Mass Transf* 115:186–193
5. Mehdi-Nejad V, Mostaghimi J, Chandra S (2003) Air bubble entrapment under an impacting droplet. *Phys Fluids* 15:173–183
6. Thoroddsen ST, Etoh TG, Takehara K, Ootsuka N, Hatsuki Y (2005) The air bubble entrapped under a drop impacting on a solid surface. *J Fluid Mech* 545:203–212
7. van Dam DB, Le Clerc C (2004) Experimental study of the impact of an ink-jet printed droplet on a solid substrate. *Phys Fluids* 16:3403–3414
8. Josserand C, Thoroddsen ST (2016) Drop impact on a solid surface. *Annu Rev Fluid Mech* 48:365–391
9. Hicks PD, Purvis R (2010) Air cushioning and bubble entrapment in three-dimensional droplet impacts. *J Fluid Mech* 649:135–163
10. Langley KR, Li EQ, Vakarelski IU, Thoroddsen ST (2018) The air entrapment under a drop impacting on a nano-rough surface. *Soft Matt* 14:7586–7596
11. Pasandideh-Fard M, Qiao YM, Chandra S, Mostaghimi J (1996) Capillary effects during droplet impact on a solid surface. *Phys Fluids* 8:650–659

Effects of Operating Conditions and Geometry in Augmentation of Initial Transients and Hysteresis in Supersonic Vacuum Ejector



Darshan Gohel and M. Deepu

Abstract The vacuum ejector-diffuser system is widely used in high-altitude test (HAT) facilities to generate desired vacuum conditions. The persistence of initial transients has always been a challenge while operating HAT facilities. Hence, a numerical study is conducted to investigate the nature of short-duration initial transients that persist during vacuum ejector start-up. The time scale of these transients is in order of milliseconds. The dynamics of important features of this transient flow like unsteady oscillations, recirculation bubbles, shock structure transitions, and flow hysteresis have been explored. A detailed parametric study is conducted to analyze the effect of chamber conditions and geometric configurations on the evolution of flow features. The unsteady oscillations are observed in flow quantities like mass flow rate and pressure. These unsteady oscillations are found to be closely related to the dynamics of recirculation bubble and primary jet characteristics. It was observed that oscillations die down quickly with an increase in primary chamber stagnation pressure and a decrease in stagnation temperature. It is also seen that decreasing lateral chamber exit height results in rapid ceasing of oscillations. The behavior of static pressure during pressure ramping cycles confirms the presence of flow hysteresis. The study of hysteresis in shock transitions revealed that the geometric configuration has a profound effect on the evolution of shock transitions. The transition of Mach reflection to regular reflection and its reverse transition was observed for one geometric configuration, but the latter transition was not observed for another geometric configuration.

Keywords Vacuum ejector · Parametric numerical study · Starting transients · Hysteresis

D. Gohel · M. Deepu

Department of Aerospace Engineering, Indian Institute of Space Science and Technology, Thiruvananthapuram 695547, India

D. Gohel (✉)

Experimental Mechanics Division, Vikram Sarabhai Space Center, Indian Space Research Organisation, Thiruvananthapuram 695022, India

e-mail: darshan@vssc.gov.in

1 Introduction

Ejectors are simple mechanical systems capable of performing multiple fluid related functions, like vacuum generation, mixing, pumping, condensing, and heat exchanging. Although they have lower efficiency, features like negligible operation and maintenance cost, self-priming, safety, absence of moving parts, versatility, and easy installation, make ejectors an indispensable part of numerous industries. A typical ejector (Fig. 1) consists of the main converging nozzle, lateral chamber, mixing chamber, and downstream diffuser. The ejector in which the lateral chamber is closed is called a vacuum ejector; in such systems, there will be a finite amount of mass supply from the lateral chamber, and hence the lateral chamber pressure will eventually reach a steady value. Vacuum ejectors are primarily used to generate desired vacuum conditions; for example, in the test section of high altitude test (HAT) facility [1]. The working principle is simple: high momentum primary jet will create low-pressure conditions in the mixing chamber, dragging fluid out of the lateral chamber by shearing action [2], creating a vacuum there. In a typical un-started mode of the ejector, the expanded primary jet does not interact with the diffuser wall. Whereas, in a typical started mode operation, the expanding primary jet impinges on the diffuser wall.

Most of the past work on vacuum ejector focus mainly on level of vacuum generated in lateral chamber and performance optimization [3–6]. These works mainly focus on steady-state characteristics, ignoring starting transients of ejector systems. Starting transients are studied in more recent works [7–13]. It is reported that after starting transients, the flow appears to reach the steady state, where there is no more mass entrainment from the lateral chamber. However, the shear layer still persists through the presence of recirculation bubbles in the lateral chamber [8, 14]. Mittal et al. [7] conducted a numerical study and reported damped oscillations of mass flow rate and pressure in the lateral chamber. The dynamic motion of the recirculation bubble was held responsible for such oscillations. Kumar et al. [10–13] conducted experimental and numerical studies to understand physics of flow transients and vacuum generation process in vacuum ejector. They also studied the effect of geometric parameters on the starting transient. Their study revealed that the secondary stream entrainment process evolves non-uniformly as primary jet pressure is ramped up during start-up. These different stages of vacuum generation

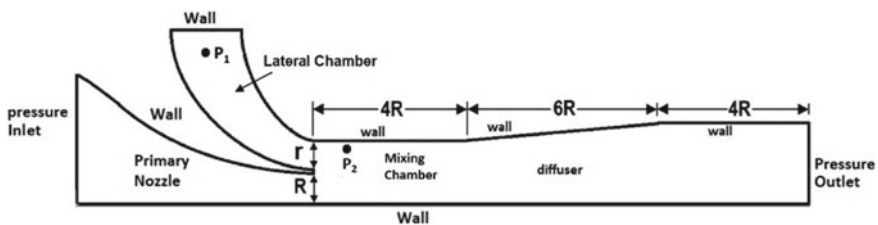


Fig. 1 Computation domain and boundary conditions

are governed by the dynamics of recirculation bubbles in secondary flow stream. They also experimentally revealed the presence of pressure-induced hysteresis in the vacuum ejector system.

The fundamental objective of the present work is to study the effect of geometry and chamber conditions in augmenting the initial transients and associated hysteresis effect. Mittal et al. [7] carried out unsteady simulations based on an initial steady solution. Such a solution may deviate from the actual flow field scenario where the flow evolves directly with unsteady transients. In all works done by Arun Kumar and Rajesh [10–13], they have modeled starting transients in time scales of seconds. However, when the rocket nozzle fires in HAT facilities, the transients may be in the order of milliseconds if the lateral chamber is not shielded from primary flow initially. These kinds of short transients have never been studied elsewhere. Moreover, it is important to know how the flow features like shock structures, recirculation bubbles, unsteady oscillations, and flow hysteresis evolve during such small time scales. It is expected that this knowledge will give more insight into starting transient problems of HAT facilities and will help in improving the design of vacuum ejectors for such facilities. Hence, in the current 2-Dimensional numerical study of vacuum ejector, a direct unsteady transient flow field is simulated, and the lateral chamber is not shielded from the primary flow. The geometry of the vacuum ejector-diffuser system is adapted from experimental work done by Lijo et al. [8], and the starting transients which are in order of milliseconds are analyzed. The unsteady pressure and mass flow rate oscillations arising from the dynamics of the recirculation bubble are studied. A detailed parametric study is carried out to analyze the effect of flow parameters like stagnation pressure and temperature on unsteady oscillations. The effect of geometric variations on such oscillations is also studied. The presence of hysteresis in the flow field is also investigated. The evolution of shock structures and their transitions during pressure ramping cycles are extensively studied with the help of time-resolved numerical schlieren technique. The effect of geometric variations on shock structure evolution is also explored.

Figure 2 shows flow features of the transient flow field inside the vacuum ejector. The under-expanded primary jet will expand through the expansion wave at the exit of the primary nozzle. The consecutive reflection of the expansion wave at the bottom wall and jet boundary will initiate the shock train system, bounded by shear layer on top. Dynamic recirculation bubbles will be formed in the secondary stream above the shear layer, which will govern the flow field in the mixing chamber and diffuser section.

2 Methodology

As the model of the vacuum ejector is rectangular (planar) in shape, there will be a minimal expansion of the primary jet in the Z-direction. Due to the sufficiently large aspect ratio of the model, the side wall effects on the flow field will be negligible. Owing to the above two reasons, the flow field in the rectangular ejector can be

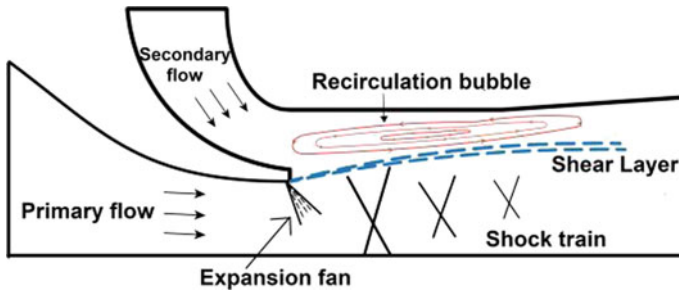


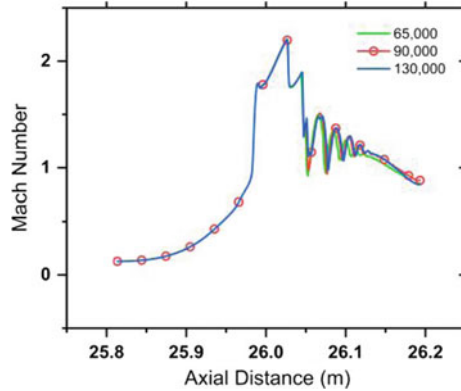
Fig. 2 Flow features of the transient flow field inside the vacuum ejector

modeled as 2-dimensional without inducing any significant errors. The solution of two-dimensional, turbulent, supersonic, compressible flow inside the vacuum ejector system has been obtained by numerically solving the Navier–Stokes equations. For a rectangular model, the jet cannot expand in the Z-direction and the aspect ratio of the model is sufficiently large such that the side wall effects will not influence the flow field. Owing to these two reasons, the flow field in the rectangular ejector can be considered to be predominantly two-dimensional (2-D). Commercial meshing software pointwise is used for grid generation, and ANSYS fluent is used for solving governing equations numerically. The transient formulation is used for the present study. A fully implicit density based solver which uses advection upstream splitting method (AUSM) for flux vector splitting is used for the present study. The AUSM scheme splits fluxes into a convective flux and a pressure flux. Features like good resolution near shocks and the absence of explicit artificial dissipation make the AUSM scheme a suitable choice for modeling the flow field inside the vacuum ejector system, which involves shock train and compressible shear layers. The second order upwind scheme is used for spatial discretization and implicit second order scheme is used for temporal discretization. The SST $k-\omega$ model is used for turbulence modeling in the present study. The working fluid is Air, which is modeled as ideal gas. The dynamic viscosity coefficient is found using Sutherland’s law. The domain is initialized with ambient conditions (1 bar pressure and 298 K temperature). While generating the grid, it is ensured that y^+ at the nearest-to-the-wall grid point remains less than 5.0 so that the near-wall viscous boundary layer is resolved properly.

2.1 Computational Domain and Boundary Conditions

The computational domain of the present problem and its boundary conditions are shown in Fig. 1. The boundary condition at the inlet is specified as a pressure inlet condition. The total pressure and temperature at the inlet are varied in accordance with the parametric studies. The inlet of the lateral chamber is assigned as a wall to simulate the transient effects of a finite chamber. The boundary condition at the

Fig. 3 Axial variation of Mach number in steady-state conditions for three different grid sizes



ejector exit is the pressure outlet with a total pressure of 1 bar and a total temperature of 300 K. However, if the flow becomes locally supersonic, the assigned value of the pressure will not be used; instead, the outflow (zero-gradient) condition will be used. Non-reflecting boundary condition is given at the pressure outlet to circumvent the reflection of pressure waves in a nonphysical manner at the exit. All walls are adiabatic with the no-slip condition.

2.2 Grid and Time Independence Studies

For grid independence studies, three structured grids were generated (for geometry $r = 11.25$ mm, $R = 15$ mm) with 65,000 quadrilateral cells, 90,000 quadrilateral cells, and 135,000 quadrilateral cells. Figure 3 shows the comparison of axial Mach number for three different grids generated. The graph was plotted after the flow has reached the steady state. Since the grid with 135,000 cells does not provide any distinct results from the grid with 90,000 cells, the latter is selected for further analysis. Time independence studies are performed on grid with 90,000 cells using three different time steps: 5×10^{-7} s, 1×10^{-7} s, and 5×10^{-8} s. Figure 4 compares the time history of mass flow rate admitted by the lateral chamber for the three time steps selected. It can be seen that results for time steps 1×10^{-7} s and 5×10^{-8} s are almost overlapping; hence the time step of 1×10^{-7} s is chosen for the analysis.

2.3 Solver Validation

The experimental data recorded by Arun et al. [10] is used for validating the present solution procedure. A two-dimensional (2-D) computational model with the same geometry used in the experiment is created. Static pressure data at a specified location

Fig. 4 Mass flow rate history through the lateral chamber

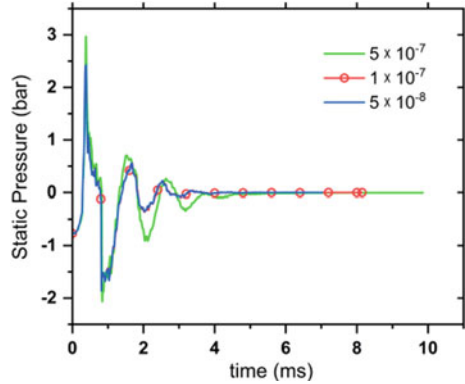
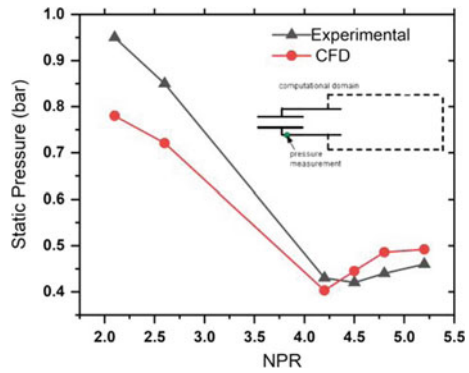


Fig. 5 Comparison of CFD vs experimental pressure, the green dot shows location of pressure measurement



is computed and compared with the experimental data obtained, as shown in Fig. 5. At low inlet stagnation pressure, a relatively high deviation of computed data from experimental data can be attributed to 3-D effects, which are not accounted for in the 2-D domain. Overall, there is good agreement between numerically computed and experimental data.

3 Results and Discussion

3.1 Transient Flow Field and Unsteady Oscillation

Figure 6 shows the Mach contours and streamlines for $r/R = 0.75$ configuration in unstarted mode ($t = 4$ ms). The under-expanded flow coming out of the primary nozzle expands through expansion waves, followed by consecutive reflection and interaction of shock waves, forming a shock train system. Two recirculation bubbles separated by expanding primary jet can be clearly seen in Fig. 6. The first recirculation bubble

is at the exit of the lateral chamber and the second one is in the diffuser section. Figure 7b presents numerical schlieren showing shock structure, for $r/R = 0.75$ configuration in started mode ($t = 7$ ms). It can be seen that regular shock reflection takes place in the mixing chamber which bumps up the boundary layer, which in turn immediately reflects the lower branch of regular reflection. The two reflected shocks then consecutively reflect from the top and bottom walls.

Figure 8a, b show mass flow rate and pressure (measured at point $P1$ shown in Fig. 1) history through lateral chamber during the starting transient of the vacuum ejector. Point ‘a’ marks the start of the transient flow and point ‘h’ marks the end of it. It can be seen that both pressure and mass flow rate oscillations die down at the same time, which is 4.5 ms. At this time, we can say that the steady state is achieved; however, the flow is still dynamic in nature due to the presence of the recirculation bubble at the exit of the lateral chamber [8]. It is also observed that the oscillations die down as soon as the primary jet attaches to the top wall of the diffuser section (started mode), cutting the supply of reverse flow from downstream of the diffuser section. The mass flow rate and pressure oscillations are closely related to movement of the recirculation bubble, as observed by Ankith et al. [7].

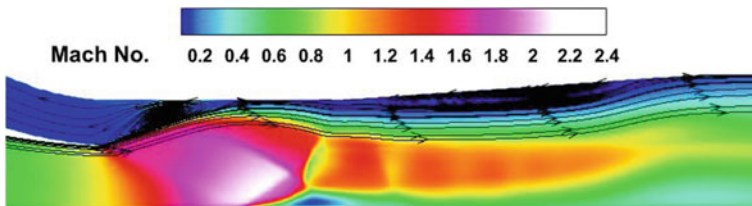


Fig. 6 Mach contours and streamlines for transient flow

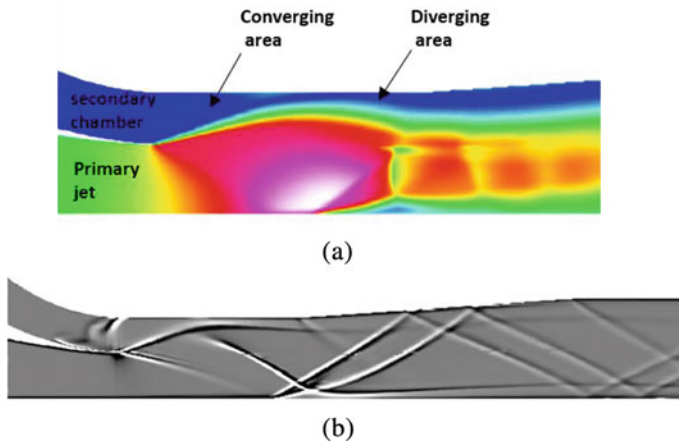
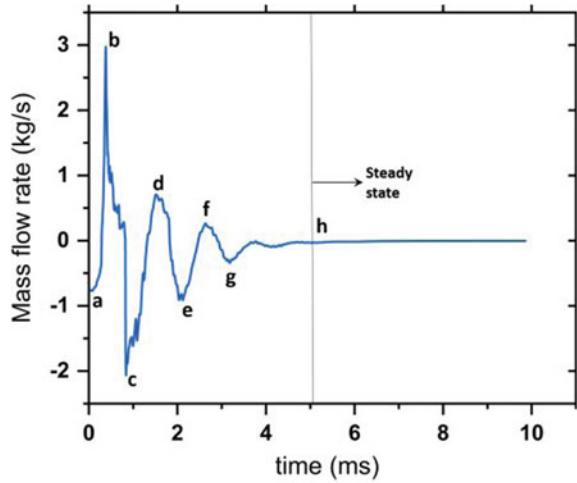
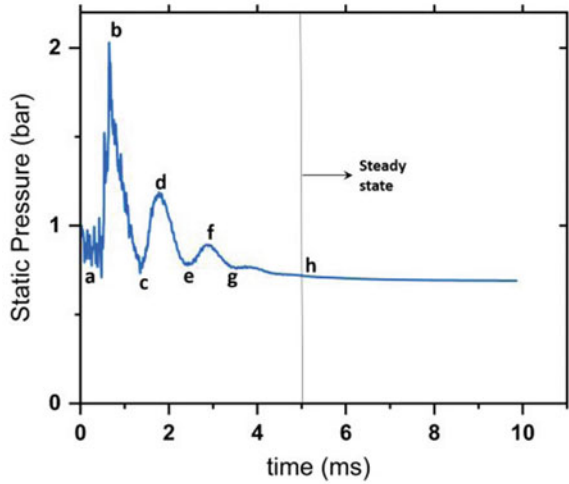


Fig. 7 a Hypothetical converging diverging area in flow b numerical Schlieren showing shock structures

Fig. 8 a Mass flow rate oscillations b pressure oscillations



(a)



(b)

The transient oscillations can be attributed to the inertia effect, as explained below. Initially, the flow is stagnant everywhere. After the flow starts, a high-speed jet will come out of the primary nozzle, reducing pressure in the mixing chamber. The sudden expansion of the primary jet into the mixing chamber leads to flow separation in the shear layer between the primary and laterally induced flows. This effect leads to the formation of a recirculation bubble in mixing chamber and diffuser section. Due to reduced pressure in the mixing chamber, mass will be entrained from the lateral chamber. The induced subsonic fluid stream from the lateral chamber will accelerate as it passes through the hypothetical convergent area (Fig. 7a) formed by expanding

primary jet in the mixing chamber. Due to mass evacuation in the lateral chamber, the pressure there will rapidly fall, and the rate of its decrease will be more than the rate of decrease of pressure in the mixing chamber. Hence in due course, pressure in the lateral chamber will surpass that of in the lateral chamber. Eventually, the pressure difference will overcome the momentum flux rate so that the mass flow rate will be reversed (toward the lateral chamber). As the mass flux enters the lateral chamber, the pressure there will continuously increase; it will surpass the pressure in the mixing chamber, reversing the direction of mass flux again. This process of flow reversals will continue until the ejector attains started mode and the flow attains the dynamic equilibrium.

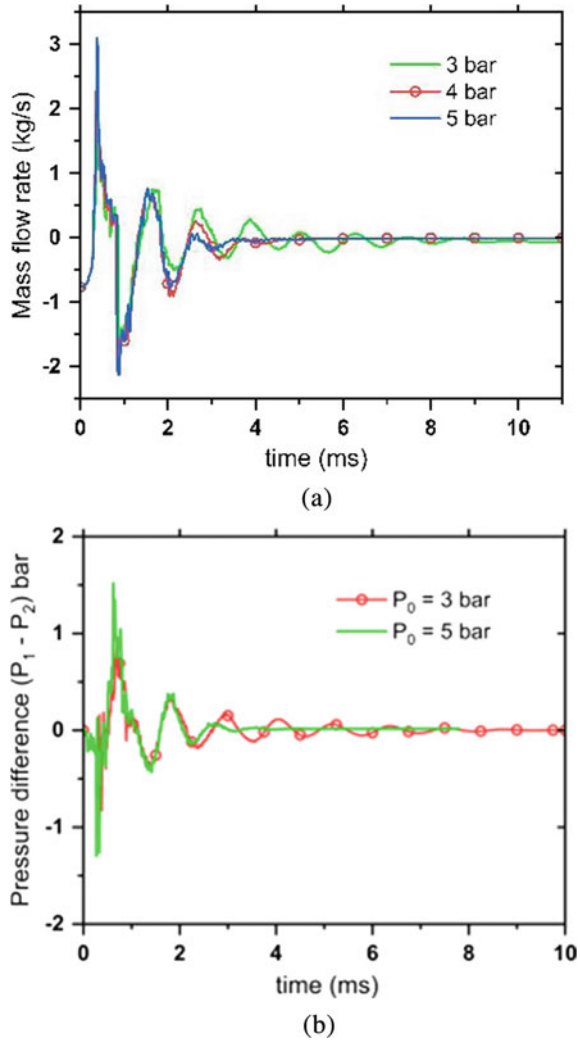
3.2 Effect of Primary Nozzle Stagnation Pressure

Figure 9a shows time histories of mass flow rate through the lateral chamber for various primary chamber stagnation pressure (the ambient pressure is the same for all three cases). It can be noticed that both amplitude of oscillations and time to reach steady state decrease as the P_0 increases. At higher P_0 , the primary jet will have stronger under-expansion (wider plume); hence the ejector attains the started mode (primary jet reaches the diffuser wall) early as compared to cases with lower P_0 . Figure 9b shows that for higher P_0 , the magnitude of pressure difference ($P_1 - P_2$) is always less than that of the case with lower P_0 . With a smaller pressure difference, the momentum flux will take less time to overcome it. Hence the flow will be reversed with less amount of mass flow in the lateral chamber. Due to that, the oscillations in the mass flow rate will be reduced. Hence, we can say that if the jet pressure ratio increases, then the inertial effect will decrease.

3.3 Effect of Primary Nozzle Stagnation Temperature

Figure 10a shows time histories of mass flow rate through the lateral chamber for various primary chamber stagnation temperatures. It can be seen that with an increase in T_0 , both amplitude of oscillations and time to reach steady state increase. When T_0 is increased, keeping P_0 constant, the total enthalpy of flow will increase. With more enthalpy available, the primary nozzle will be able to produce more kinetic energy, and hence the exit velocity of the primary flow will be higher. As a result of high exit velocity, the exit pressure will be lower. Hence flow will be weakly under-expanded for higher T_0 . As we have seen in the previous section, the weakly under-expanded flow will result in higher inertial effects, and hence the higher will be the amplitude of oscillations and time to reach the steady state.

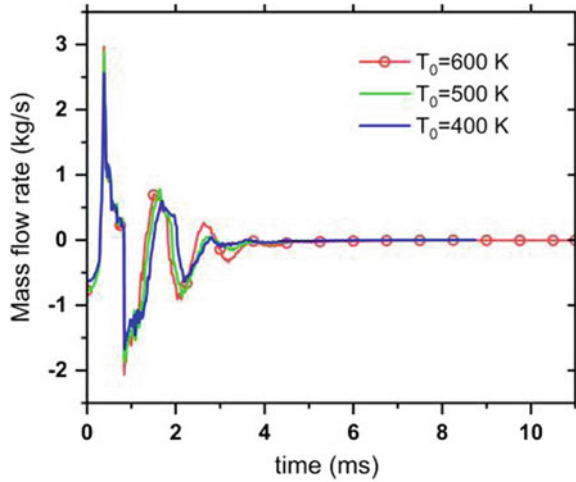
Fig. 9 **a** Effect of P_0 in mass flow rate oscillations
b pressure difference $P_1 - P_2$ for $P_0 = 3$ and 5 bar



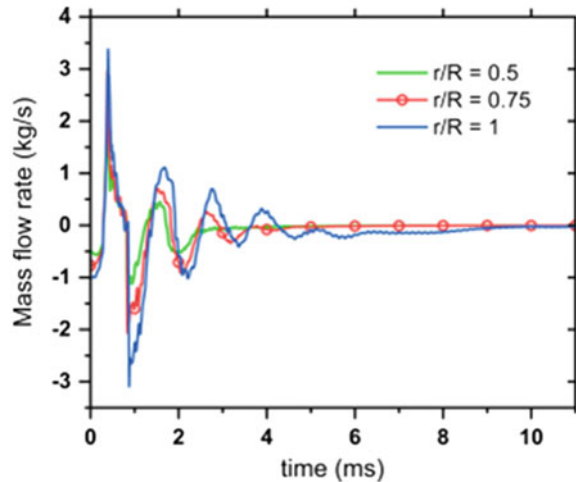
3.4 Effect of Confinement Geometry Variation

Figure 10b shows time histories of mass flow rate through the lateral chamber for three different geometric configurations, classified based on r/R ratio (Fig. 1). While varying r/R ratio, only r is changed, while $R = 15$ mm is kept constant. As the r/R ratio decreases, both amplitude of oscillations and time to reach steady state decreases. With the decrease in r , the primary jet will reach the diffuser wall more quickly, ceasing the unsteady oscillations early as compared to geometry with higher r . Hence, the ejector will attain started mode of operation early in geometry with a smaller r/R ratio.

Fig. 10 **a** Effect of T_0 on mass flow rate oscillations
b effect of r/R ratio on mass flow oscillations



(a)



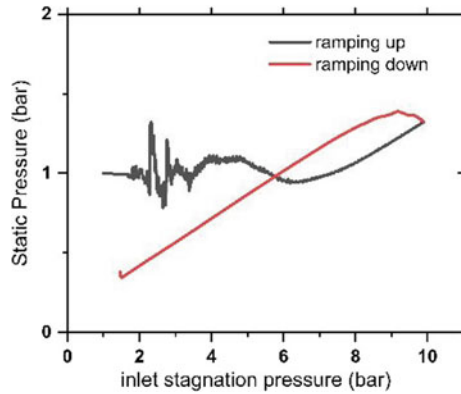
(b)

3.5 Pressure-Induced Hysteresis in the Flow Field and Effect of Geometric Variations on Allied Shock Structures

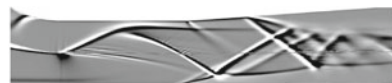
During the start-up and shut-down process of the vacuum ejector system, there will be inherent variation in the primary inlet stagnation pressure (P_0). Under such conditions, the existence of pressure-induced hysteresis (flow hysteresis observed during pressure ramping process) in the flow field is highly likely. Hence in the present study, pressure-induced hysteresis is studied by increasing the P_0 linearly from 1 to 10 bar, and then decreasing it down from 10 to 1 bar. Figure 11 shows the variation in static

pressure at point $P1$ in the lateral chamber corresponding to one pressure ramping cycle. The black line shows the pressure variation during the ramping up process, and the red line shows the pressure variation during the ramping down process. The system follows an entirely different path during reverse operation, confirming the presence of hysteresis. The evolution of shock structures during pressure ramping cycles and the effect of confinement geometry (r/R ratio) on such evolution is studied with the help of time-resolved numerical schlieren images. It is observed that geometry significantly affects the shock transitions during pressure ramping cycles, as illustrated in Figs. 12 and 13. From Figs. 12a, b and 13a, b, we can observe that during ramping up stage, there is shock transition from Mach Reflection (MR) to regular reflection (RR) in both configurations. However, as shown by Figs. 12c, d and 13c, d, during ramping down stage, there is RR to MR transition in case of $r/R = 1$, but no such transition is observed in case of $r/R = 0.5$ configuration. The hysteresis behavior is attributed to the effect of pressure ramping as other parameters are invariant during the analysis; hence the name pressure-induced hysteresis is well suited. The transient flow field inside the vacuum ejector exhibits shock structures, recirculation bubbles, and high-speed shear layer. All these flow features are highly non-linear, which contribute to momentum loss and creation of irreversibilities in the flow field. Such kind of flow conditions favor hysteresis in the flow process.

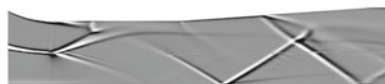
Fig. 11 Pressure-induced hysteresis



(a) $P_0 = 3.6$ bar (ramping up), MR observed



(b) $P_0 = 8$ bar (ramping up), RR observed



(c) $P_0 = 2.8$ bar (ramping down), RR observed



(d) $P_0 = 2$ bar (ramping down), MR observed

Fig. 12 Changes in shock structures during pressure ramping cycle for $r/R = 1$ configuration

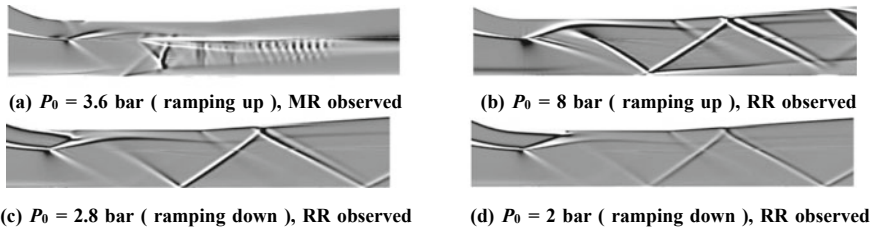


Fig. 13 Changes in shock structures during pressure ramping cycle for $r/R = 0.5$ configuration

4 Conclusion

A numerical study has been conducted to investigate the short transients that persist during vacuum ejector start-up. Unlike previous studies where time scales of transients are in order of seconds, the current study focuses on initial short transients, which are in order of milliseconds. The unsteady fluctuations in mass entrainment rate and pressure in the lateral chamber are observed. These fluctuations are attributed to the inertial effects which arise due to dynamic motion of the recirculatory region in the secondary stream jet. These oscillations cease when the primary jet expands to the top diffuser wall. The effect of flow parameters and geometric variations on these unsteady oscillations is also studied. It was found that both amplitude of oscillations and time to reach decreases if stagnation pressure (P_0) is increased, stagnation temperature (T_0) is decreased, or if the r/R ratio is decreased. If inertial effects are increased due to some change in parameters, then oscillations will be increased and vice-versa. When P_0 is increased, the inertial effect will be reduced due to smaller pressure difference between the lateral and mixing chamber. The increase in T_0 results in higher inertial effects due to weak under-expansion of the primary jet. With the decrease in r/R ratio, the primary jet will reach top diffuser wall early, and hence oscillations will cease early.

It was also observed that the static pressure in the lateral chamber follows different paths during pressure ramping up and down phase, confirming the presence of pressure-induced hysteresis in starting transients. The study on shock transitions during pressure ramping cycle also showed hysteresis behavior in shock structures and revealed that geometric configuration has a profound effect on shock transitions. MR to RR transition was observed during pressure ramping up phase, and its reverse (RR to MR) transition during pressure ramping down phase for $r/R = 1$ configuration. However, no such reverse transition was observed in $r/R = 0.5$ configuration. It is believed that the current study will fill the gaps in existing knowledge on starting transients of vacuum ejectors and contribute to its performance improvement.

References

1. Chen FC, Hsu CT (1987) Experimental study of zero-flow ejectors using gaseous nitrogen. *Energy Res* 11:289–300
2. Farland BLM, Nelson RE, Mandell B, Patmor GO (1964) Scale model testing of 90 deg supersonic turn ejector systems for altitude simulation. *J Spacecraft Rockets* 1:108–111
3. Jones WL, Price HG, Lorenzo CF (1960) Scale model testing of 90 deg supersonic turn ejector systems for altitude simulation. NASA Technical Note, D-230
4. Bauer RC, German RC (1961) The effect of second throat geometry on the performance of ejectors without induced flow. Technical Report, AEDC-AEDC-TN-61-133
5. Wojciechowski CJ, Anderson PG (1981) Parametric analysis of diffuser requirements for high expansion ratio space engine. NASA Technical Note, LMSC-11REC TR D784489
6. German RC, Bauer RC (1961) Effects of diffuser length on the performance of ejectors without induced flow. Technical Report, AEDC-AEDC-TN-61-89
7. Mittal A, Lijo V, Rajesh G, Kim HD (2014) Starting transients in vacuum ejector-diffuser system. *J Prop Pow* 30:1213–1223
8. Lijo V, Kim HD, Rajesh G, Setoguchi T (1994) Numerical simulation of transient flows in a vacuum ejector-diffuser system. *J Aerospace Eng* 224:777–786
9. Lee JH, Park BH, Yoon W (2008) Studies on the starting transient of a straight cylindrical supersonic exhaust diffuser: Effects of diffuser length and pre-evacuation state. *Int J Heat Fluid Flow* 29:1369–1379
10. Kumar RA, Rajesh G (2016) Flow transients in un-started and started modes of vacuum ejector operation. *Phys Fluid* 28:056105
11. Kumar RA, Rajesh G (2018) Physics of vacuum generation in zero-secondary flow ejectors. *Phys Fluid* 30:066102
12. Kumar RA, Rajesh G (2019) A study on the effect of geometric configurations on the starting transients in vacuum ejector. *AIAA J* 57:2905–2922
13. Kumar RA, Rajesh G (2017) Shock transformation and hysteresis in underexpanded confined jets. *J Fluid Mech* 823:538–561
14. Kim HD, Lee JS (2010) An experimental study of supersonic ejector for a vacuum pump. In: *Proceedings of the Korean Society of Mechanical Engineers, Annual Fall Meeting, Vol. B, Korean Society of Mechanical Engineering, Seoul, Republic of Korea*, pp 520–525

The Effects of Shock Waves on OFHC Copper



M. K. Singh and R. K. Anand

Abstract In this paper, the structure of shock waves in solid OFHC (oxygen free high conductive copper) copper has been addressed together with the impact of the material's viscosity. Here, the shock front thickness is measured using thermodynamic parameters including temperature, pressure, change-in-entropy, and particle velocity. The non-dimensional form of thermodynamic variables is used to derive the analytical solutions to the Navier–Stokes equations. In this study, we have observed the shock front thickness of the order of micrometer. On the basis of published articles, we have taken the temperature and density-independent viscosity of the material to be 60 Pa sec and 55 Pa sec, respectively. These findings show that this model may be used in advanced research on the thickness of the shock front in various solid materials.

Keywords Shock wave · Shock front thickness · Mie-Gruneisen equation of state

1 Introduction

A shock wave is regarded as a powerful nonlinear pulse that travels at an incredibly fast rate. A running piston or a momentary explosive is an example of continuous and impulsive energy sources, by which continuous and short pulse of shock waves are generated, respectively. A wide range of substances, including gas, liquid, solid, and plasma, support shock waves [1–4]. Theoretically, the large gradient at the boundary of shock waves, traveling at supersonic speed through the medium can be represented as a discontinuity. A shock wave is continuously generated by a moving piston for the study of condensed matter under extreme thermodynamic conditions. Experimentally, it has been challenging to reconcile the results of static compression and shock at high pressures (100 GPa and greater) [5, 6]. The fundamental equations of state in research and associated advancements have addressed the key distinction

M. K. Singh (✉) · R. K. Anand
Department of Physics (UGC Centre of Advanced Studies), University of Allahabad,
Prayagraj 211002, India
e-mail: mithilesh44144@rediffmail.com

between shock-compressed and statically compressed states as the temperature rises [7–10]. Nowadays, solid materials after being subjected to extremely high pressures and temperatures are described by the Mie-Gruneisen equation of state. The internal energy and material pressure are related by the Mie-Gruneisen equation of state [11, 12]. In this report, we have considered the viscosity of the material to be temperature independent and have demonstrated how the shock strength and its viscosity affect the shock front thickness in the OFHC copper. The copper alloy shock front thickness has been numerically calculated and the results demonstrate how it fluctuates with respect to pressure, temperature, particle velocity, and change-in-entropy.

The graphs presented in this article show the variations of the pressure, temperature, particle velocity, and change-in-entropy with the position.

Here, for the first time, the Navier–Stokes equations for a solid material are solved by using the Mie-Gruneisen equation of state for the study of the structure of shock wave of OFHC Copper. The copper alloy is well known to be widely utilized in the infrastructure and in electronic appliances. As a result, copper has been used in this study to symbolize a substantial contribution to the science of fluid mechanics under high temperature and pressure.

2 Literature Review and Objective

The Navier–Stokes equation is used to depict the shock front structure in OFHC copper. Although substantial research has been done on the shock wave in a solid medium and some published studies have characterized the shock structure in a gaseous medium [13]. Work on the structure of the shock wave in a non-ideal gas with temperature and density dependent viscosity was reported [14]. The articles [15, 16] describe work on the transformation of the copper’s body structure and the coupling of the shock wave and the condensed material. The published articles suggest that its interesting point is shock structure in a solid medium. So, these results contribute to the clear understanding of shock flow in solids. Therefore, it is the addition of the shock structure in various media, such as copper alloy.

The value of required constant parameters of the material OFHC copper has been taken from the published research articles [17, 18] and has been summarized in Table 1.

Table 1 Values of constant parameters of OFHC copper

Material	ρ_0 kg/m ³	a_0 m/s	Γ_0	p_0 Mbar
OFHC copper	8930	3940	2.02	4.590

3 Governing Equation

The governing equations of one-dimension material flow i.e., the conservation of mass, momentum, and energy are expressed as [17, 19, 20]

$$\frac{\partial \rho}{\partial t} + \frac{\partial(\rho u)}{\partial x} + \alpha \frac{\rho u}{x} = 0 \quad (1)$$

$$\frac{\partial(\rho u)}{\partial t} + \frac{\partial\{\rho u^2 + (p - \sigma')\}}{\partial x} = 0 \quad (2)$$

$$\frac{\partial\left(\rho e + \frac{\rho u^2}{2}\right)}{\partial t} + \frac{\partial\left\{\rho u\left(e + \frac{u^2}{2}\right) + (p - \sigma')u\right\}}{\partial x} = 0 \quad (3)$$

The parameters $u(r, t)$, $p(r, t)$, $\rho(r, t)$, $e(r, t)$ and $\sigma'(r, t)$ in the above set of equations respectively indicate the particle velocity, pressure, density internal energy, and viscous-stress tensor per unit mass. The position vector r with regard to the shock front normal measured along is the time coordinate.

The viscous-stress tensor is

$$\sigma' = \frac{4}{3} \mu \frac{\partial u}{\partial x} \quad (4)$$

The Mie-Gruneisen equation of state for solid materials is:

$$e = \frac{p}{\rho \Gamma} \quad (5)$$

where,

$$\Gamma(G) = \frac{3}{2} + \left(\Gamma_0 - \frac{2}{3}\right) \left(\frac{G_m^2 + 1}{G_m^2 + G^2}\right) G \quad (6)$$

and G varies from 0.51 to 0.79 [17].

The shock front remains constant over a short period of time. This shock front is stationary with regard to the coordinate system. Since the term δt may be ignored, these equations reduce to perfect differential equation. For the cylindrical wave front the value of $\alpha = 1$, for spherical $\alpha = 2$ and $\alpha = 0$ for our taking wave front i.e., plane wave front.

$$\frac{d}{dx}(\rho u) = 0 \quad (7)$$

$$\frac{d}{dx}\{\rho u^2 + (p - \sigma')\} = 0 \quad (8)$$

$$\frac{d}{dx} \left\{ \rho u \left(E + \frac{u^2}{2} \right) + (p - \sigma')u \right\} = 0 \tag{9}$$

For the purpose of resolving Eqs. (7–10), it is assumed that the gradient of density, pressure, and particle velocity must vanish at $+\infty$ and $-\infty$ respectively, before and behind the shock front. The end flow variables without script are p , ρ and u the beginning flow variables are denoted by subscripts i.e., ρ_0 , p_0 , u_0 . If U is the shock front speed in a fixed coordinate system with the shock front, then u_0 will be the initial particle velocity.

$$u_0 = U \tag{10}$$

3.1 Exact Solutions for the Flow Variables

$$\rho u = \rho_0 U \tag{11}$$

$$p = \rho_0 U^2 + p_0 + \frac{4}{3} \mu \frac{\partial u}{\partial x} - \rho u^2 \tag{12}$$

$$\frac{p}{\rho} \left(\frac{\Gamma' + 1}{\Gamma'} \right) - \frac{4}{3 \rho_0 U} \mu u \frac{\partial u}{\partial x} = \frac{1}{2} (U^2 - u^2) + \frac{p_0}{\rho_0} \left(\frac{\Gamma'_0 + 1}{\Gamma'_0} \right) \tag{13}$$

The non-dimensional analytical solutions of the above Eqs. (7–9) using boundary conditions are

$$\frac{T}{T_0} = \left(\frac{\Gamma_0 + 1}{\Gamma + 1} \right) \left\{ 1 + M^2 \Gamma_0 \left(\left(a - \frac{1}{2} \right) \eta^2 + b \eta + c + \frac{1}{2} \right) \right\} \tag{14}$$

$$\frac{p}{p_0} = \left(\frac{\Gamma}{\Gamma_0} \right) \left[\left(\frac{\Gamma_0 + 1}{\Gamma + 1} \right) \left\{ 1 + M^2 \Gamma_0 \left(\left(a - \frac{1}{2} \right) \eta^2 + b \eta + c + \frac{1}{2} \right) \right\} \right] \tag{15}$$

$$\frac{\Delta s}{C_v} = \ln \left\{ \left(\frac{\Gamma}{\Gamma_0} \right) \left[\left(\frac{\Gamma_0 + 1}{\Gamma + 1} \right) \left\{ 1 + M^2 \Gamma_0 \left(\left(a - \frac{1}{2} \right) \eta^2 + b \eta + c + \frac{1}{2} \right) \right\} \right] \right\} + (\Gamma + 1) \ln(\eta) \tag{16}$$

$$\begin{aligned} & \left\{ \left(\frac{a\eta^2 + b\eta + c}{a\eta^2 + b\eta' + c} \right) \left\{ \left(\frac{(\eta' - \eta_1)(\eta - \eta_2)}{(\eta' - \eta_2)(\eta - \eta_1)} \right)^q \right\} \right\} \\ & = \exp \left\{ \frac{3}{4\mu} (\Gamma + 2) M \sqrt{(\Gamma_0 + 1) p_0 \rho_0} x \right\} \end{aligned} \tag{17}$$

Here, $q = \frac{b}{\sqrt{b^2 - 4ac}}$

Let us choose the origin at the point of inflection of the velocity profile (the physical center of the thickness of the shock front). The inflection point is obtained by substituting $\frac{d^2\eta}{dx^2} = 0$, which comes out.

$$\eta' = \sqrt{c/a}$$

4 Results and Discussion

A precise solution has been found in this case for the shock flow in the solid materials. The analytical formulation and flow of the variables within the shock transition zone are typically resolved by Eqs. (14–16). These analytical results were derived under the presumption that the shock wave’s reflection is negligible, which means no disturbance is present in the material.

Table 2 displays the relationship between shock front thickness and shock strength as measured by Mach number (M). In this article, the shock wave flow is mediated by the solid material. The shock front thickness reduces as the medium viscosity increases because molten solids are denser than the gas as well as normal liquid. A shock wave will move across the medium, agitating the particles and generating disturbance [21]. The layer of shock front continuously falls as the shock wave’s power grows. It provides extremely clear numerical examples of it and concurs with the shock wave in Table 2.

Thus, these results provided obvious information about the role of viscosity of the materials and the strength of the shock wave along with shock front thickness. This model developed in this article is of interest to physicists, fluid dynamics, and scientists working on the shock wave in fluids. These findings add to the investigation of the effects of the shock strength and how its pressure varies with detachment.

Table 2 Thickness of shock front in OFHC copper

Coefficient of viscosity (Pa sec)	Mach number (M)	Position (r ₁) (μm)	Position (r ₂) (μm)	Difference (r ₂ -r ₁) (μm)
60	2.1	-4.9132	1.9416	6.8548
	2.2	-4.7373	1.8493	6.5866
	2.3	-4.2012	2.0612	6.2624
	2.4	-3.6169	1.6797	5.2966
	2.5	-3.4872	1.4245	4.9117
	2.6	-2.8978	1.5407	4.4385
55	2.1	-4.8722	2.3494	7.2216
	2.2	-4.6743	1.9147	6.5890
	2.3	-4.5876	1.7618	6.3484
	2.4	-3.9940	1.7298	5.7238
	2.5	-3.6920	1.5802	5.2722
	2.6	-3.4476	1.4562	4.9038

Figures 2 and 1 show the thickness of shock front with Mach number at constant Mie-Gruneisen parameter with the dimensionless parameters. These plots display the qualitative and quantitative results of the variation in shock front thickness.

The interaction of a shock wave with the substance is seen in Figs. 1 and 2. At the interaction site, shock waves produce a significant gradient, which is depicted in the figure at the origin point. These diagrams accurately depict the shock wave properties. Following is an explanation in the transition area.

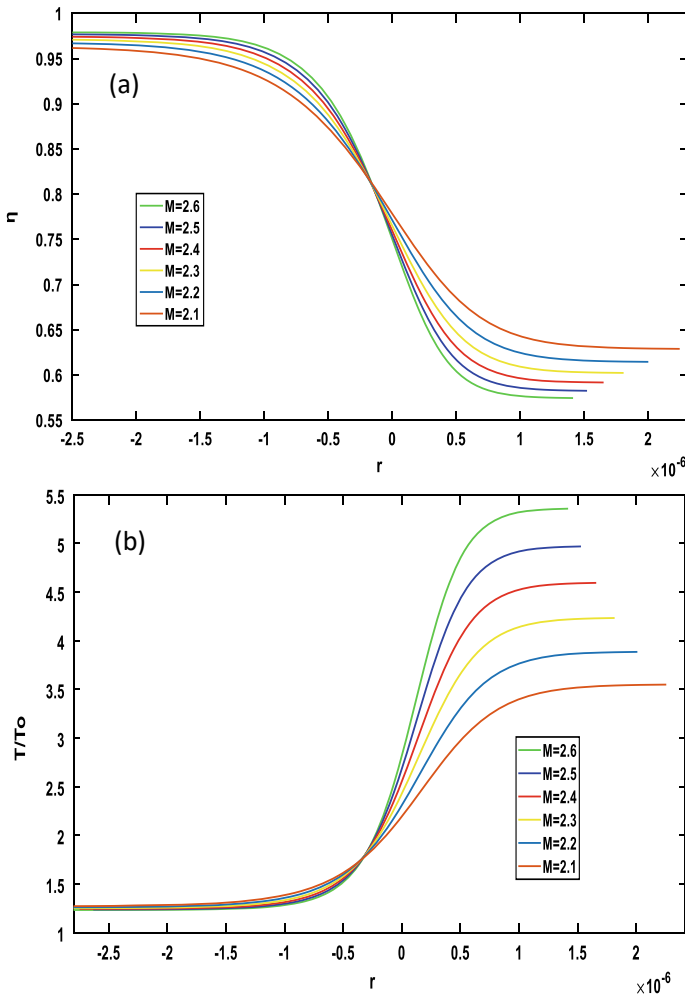


Fig. 1 Flow variables **a** Particle velocity, **b** Temperature, **c** Change-in-entropy, and **d** Pressure within the shock transition zone with the position(r) for different Mach number of $M = 2.6, 2.5, 2.4, 2.3, 2.2, 2.1$ at $\mu = 60$ Pa sec, $\Gamma_0 = 2.02$, $\rho_0 = 8930$, and $p_0 = 5.34$ Mbar

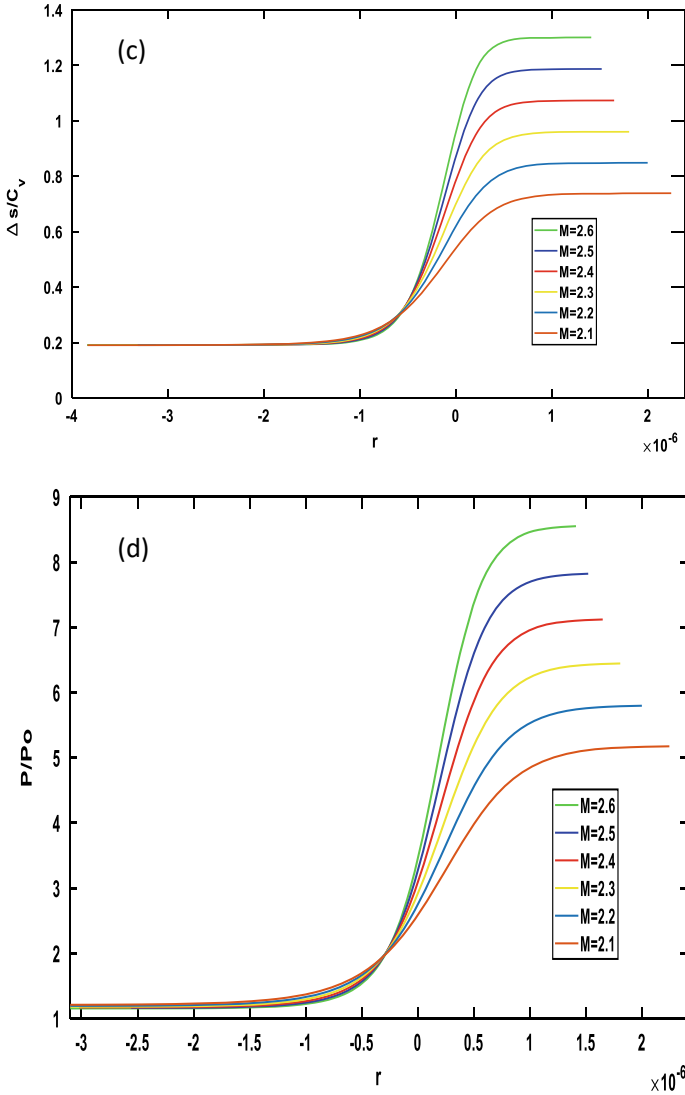


Fig. 1 (continued)

These plots show the effect of a shock wave in solid material in terms of thermodynamic variables. Shock waves contact with a substance the quantities quickly increase and instantaneously reach their saturation point.

1. The variation of particle velocity with position is shown in this plot, and the shock front thickness in terms of particle velocity is measured and presented in Table 2. We can analyze the qualitative and quantitative aspects of the material using Figs. 1a and 2a. Table 2 helps us with the quantitative analysis of the shock front

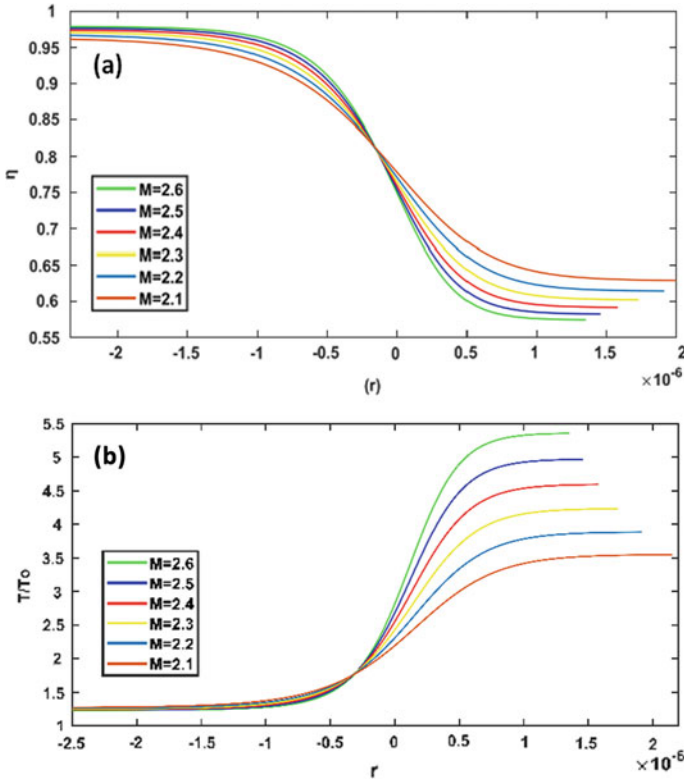


Fig. 2 Flow variables **a** Particle velocity, **b** Temperature, **c** Change-in-entropy, and **d** Pressure within the shock transition zone with position(r) for different Mach number of $M = 2.6, 2.5, 2.4, 2.3, 2.2, 2.1$ at $\mu = 55$ Pa sec, $\Gamma_0 = 2.02$, $\rho_0 = 8930$, and $p_0 = 5.34$ Mbar

thickness with various shock strengths and viscosities of the material. Figures 1a and 2a show the variation in shock front thickness at different Mach numbers. The shock front thickness decreases as the material viscosity and Mach number increase, as shown in Figs. 1a and 2a.

2. These graphics 1(b) and 2(b) display the variation of thermodynamic variables with regard to position. Moving away from the inflection point causes the temperature ratio of the material beneath the transition zone to swiftly increase; it is visible as a steep gradient. At various Mach numbers, the temperature ratio in OFHC copper is used to calculate the shock front thickness. This image is pretty much evidence of the variations in shock front thickness. Figures 1b and 2b help us understand the role of material resistance during adiabatic cooling and heating.
3. One of the most fundamental quantity in the collection of thermodynamic parameters is entropy. This graphic illustrates how change-in-entropy varies with regard to position at various Mach values. The shock effect on the OFHC copper material is clearly shown in this plot. This plot indicates that the material was affected

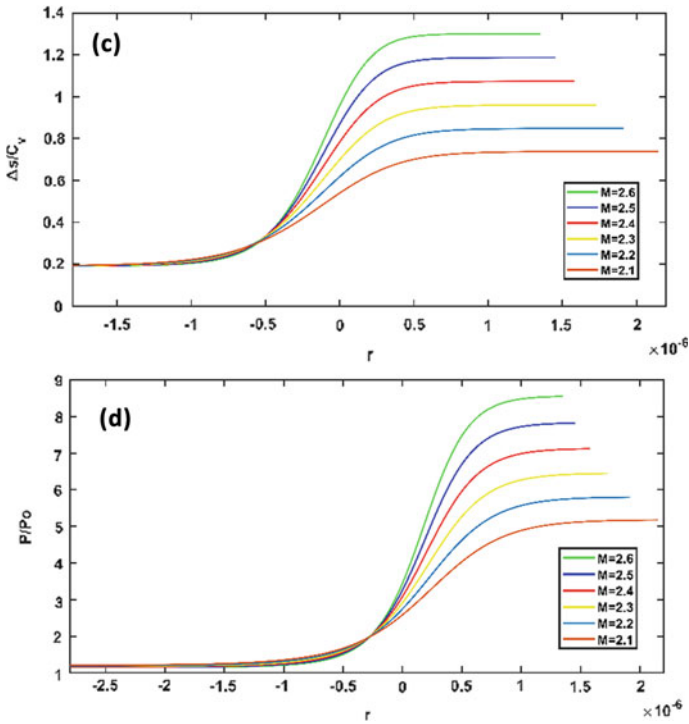


Fig. 2 (continued)

by a shock wave in a bit of time, which is depicted in Figs. 1c and 2c, and it illustrates the variation of shock front thickness.

4. The internal energy of the material is closely correlated with its pressure and density. Because of this, the present work shows the fluctuation of the most crucial factors, such as pressure with regard to position at various Mach values and the viscosity of the material. In this diagram, we can observe how the material's pressure is rising and how the shock front is departing from the inflection point. As a result, as the shock wave travels through the material, it is compressed. Here, the large gradient demonstrates how much compression is experienced by the material in a relatively short time. It's employed to comprehend the compression of shock waves in Figs. 1d and 2d and to depict the variation in shock thickness. After simultaneously analyzing these plots, we can understand the role of material viscosity in shock compression and expansion.

5 Conclusions

The present study has been conducted to better understand the shock front's structure in OFHC copper. The outcomes demonstrate that the shock front structure is significantly influenced by the viscosity of OFHC copper.

Following are the concluding remarks of the current study:

1. The thickness of the shock front is influenced by viscosity of OFHC copper and the thickness of shock front decreases with increase in viscosity.
2. The shock front thickness varies with shock strength and as the Mach number increases the shock front thickness decreases.

The results demonstrate that the shock front thickness in solid media is narrower than the gaseous media as the viscosity of material is higher than that of the gases.

Acknowledgements The author gratefully acknowledges the University Grant Commission New Delhi India for financial support.

Nomenclature

a	Constant
b	Constant
c	Constant
C_v	Specific heat at constant volume [J/Kg]
d	Constant
E	Internal energy of the material [Joule]
G	Shock compression ratio
P	Pressure behind the shock front [Pa]
P_o	Pressure ahead the shock front [Pa]
T	Temperature behind the shock front [K]
T_o	Temperature ahead the shock front [K]
Δs	Change-in-entropy
σ'	Viscus stress tensor
μ	Coefficient of viscosity [PaS]
ρ	Density of the material [Kg/m ³]
M	Mach number
Γ	Mie-Gruneisen parameter [Kg/m ³]
η	Particle velocity

References

1. Zel'Dovich YB, Raizer YP (2002) Physics of shock waves and high-temperature hydrodynamic phenomena. Courier corporation
2. Forbes JW (2012) Shock wave compression of condensed matter, A Primer. Springer
3. Gurnett DA (2005) Introduction to plasma physics: with space and laboratory applications. Cambridge University Press
4. Liepmann HW, Roshko A (2001) Elements of gasdynamics. Published online, Mineola
5. Nellis WJ, Moriarty JA, Mitchell AC et al (1988) Metals physics at ultrahigh pressure: aluminum, copper, and lead as prototypes. *Phys Rev Lett* 60(14):1414
6. Mao HK, Bell PM, Shaner JW, Steinberg DJ (1978) Specific volume measurements of Cu, Mo, Pd, and Ag and calibration of the ruby R 1 fluorescence pressure gauge from 0.06 to 1 Mbar. *J Appl Phys* 49(6):3276–3283
7. Sharma SM, Turneure SJ, Winey JM (2019) Structural transformation and melting in gold shock compressed to 355 GPa. *Phys Rev Lett* 123(4):45702
8. Mandal A, Jensen BJ, Hudspeth MC, Root S, Crum RS, Akin MC (2020) Direct observations of shock-induced melting in a porous solid using time-resolved x-ray diffraction. *Phys Rev Mater* 4(6):63604
9. Kalita P, Specht P, Root S et al (2017) Direct observations of a dynamically driven phase transition with in situ X-ray diffraction in a simple ionic crystal. *Phys Rev Lett* 119(25):255701
10. Kalantar DH, Belak JF, Collins GW et al (2005) Direct observation of the α - ϵ transition in shock-compressed iron via nanosecond X-ray diffraction. *Phys Rev Lett* 95(7):75502
11. Ramsey SD, Schmidt EM, Boyd ZM, Lilieholm JF, Baty RS (2018) Converging shock flows for a Mie-Grüneisen equation of state. *Phys Fluids* 30(4):2018
12. Heuzé O (2012) General form of the Mie-Grüneisen equation of state. *Comptes Rendus Mec* 340(10):679–687
13. Anand RK, Yadav HC (2016) The effects of viscosity on the structure of shock waves in a non-ideal gas. *Acta Physica Polonica A* 129
14. Singh M, Patel A (2019) Shock wave structure in a non-ideal gas under temperature and density-dependent viscosity and heat conduction. *Theor Comput Fluid Dyn*
15. Gupta YM, Stefan JT (2020) Transformation of shock-compressed copper to the body-centred-cubic structure at 180 GPa, *Phys Rev B* 102
16. Gupta YM (2002) The coupling between shock waves and condensed matter, shock compression in condensed matter, AIP, pp 7354–0068
17. Anand RK (2020) On the shock dynamics of weak converging shock waves in solid materials, *Ric di Mat*
18. Walsh JM, Rice MH, McQueen RG, Yarger FL (1957) Shock wave compressions of twenty-seven metals. equations of state of metals. *Phys Rev* 108(2):196–216
19. Laborstory CA, Vfark N (1968) Technical report cal-9S-Pu Sä relaxation in gas-particle flow. Published online
20. Batchelor GK (1987) Fluid mechanics. By L.D Landau and EM LIFSHITZ, 2nd English edn, vol 539. Pergamon Press, pp 593–594
21. Li Y, Liu F, Ma X, Zhang M (2016) Research on viscosity of metal at high pressure. *Shock Waves* 26(6):759–770

Supersonic Flow Field Characteristics of a Sharp Spiked Blunt Body Having Various Nose Cone Fairings



MD. G. Sarwar, P. Kumar, and S. Das

Abstract Experimental and computational investigations were conducted to examine the flow characteristics of a blunt body with a sharp spike attached to different nose cone fairings. This study was performed at the Mach number of 2 with Reynolds number of 3.5×10^6 based on the body's base diameter ($D = 15$ mm). The axial forces acting on the body were measured both without the spike and with the spike, spike tip fixed at a specific fixed location with using of one-component strain gage balance. Additionally, the Schlieren flow visualization technique, which relies on density gradient, was utilized to capture Schlieren photos and analyze the flow field around the model for both configurations (with and without the spike) with varying L/D (length-to-diameter) ratios. Furthermore, a detailed discussion on the computed density gradient for the flow was undertaken. The results indicated that the shear layer angle (α) remained constant across all tested models. However, the body shock angle (Θ) exhibited significant changes due to the shape of the blunt body. The impact of the nose cone fairing on the spike's flow (FTSS) arrangement appeared to be negligible. Overall, the drag experienced by the model remained relatively consistent regardless of the length or presence of body fairings.

Keywords Blunt body · Spike · Nose cone · Nose fairing · Drag

1 Introduction

Due to their large volumetric efficiency, the blunt bodies have a large selection of forebody nose applications in the category of high-speed vehicles, such as rockets, missiles, and re-entry vehicles. Conical, ogival, power series, and hemispherical are the most prevalent forms for forebodies. These forms are typically utilized on supersonic or hypersonic missiles and are chosen based on aerodynamic, guidance, and structural concerns. A hemispherical nose has a lot of drag in terms of aerodynamic

MD. G. Sarwar (✉) · P. Kumar · S. Das
Department of Space Engineering and Rocketry, BIT Mesra, Ranchi 835215, India
e-mail: sarwar251219@gmail.com

drag and performance. However, it is excellent in terms of structural integrity, resistance to aerodynamic heating, and compatibility with some methods of guiding, such as infrared guidance. Because the pressure or wave drag at supersonic speeds can be caused by friction, careful selection of the nose shape is required to ensure that the whole system performs satisfactorily. In missiles that employ infrared (IR) seekers as its homing head, the hemispherical forebody form of nose is more extensively used. At supersonic speeds, these configurations generate a separate strong bow shock wave ahead of them, which raises temperature and pressure and causes significant aerodynamic drag and heating. The vehicle's performance is harmed by excessive aerodynamic drag, while high aerodynamic heating causes material damage. Researchers have been focusing on reducing forebody drag in high-speed space rockets, missiles, and re-entry vehicles for the last four decades.

The nose shape of a high-speed vehicle holds significant practical importance in the fields of drag aerodynamics, heating, and flow characteristics surrounding the body. It plays a crucial role in determining the vehicle's overall aerodynamic performance and its ability to withstand high-speed environments.

Various active and passive techniques are introduced to lower the drag coefficient and reduce the heat load. Huang [1] John and Kulkarni [2], and other authors listed and reported a number of active and passive methods. Among them, spike is a simple and effective method to reduce drag and heat load on the forebodies.

The drag reduction mechanism with spike could be visualized through Fig. 1. At high speed, spikes transform a strong shock into a weak oblique shock and generates a recirculation region. This recirculation region takes the form of a dead region and could replace structures.

Since the 1940s, high-speed flow over a spiked blunt body has been the subject of extensive research. In order to lessen drag on blunt bodies at supersonic speeds, Alexander [3] first proposed the use of spikes for high-speed flow in 1947. A thorough review of studies on spiked bodies was provided by Karimi and Oboodi [4], which provided a detailed account of recent developments in the field of aerothermodynamics of spiked hypersonic vehicles. Numerous researchers have looked into how spike length affects drag reduction. Crawford [5] conducted a thorough experimental investigation of drag and aerodynamic heating on a cylindrical model with spiked hemispheres at Mach number of 6.8. Experimental and numerical research has been done to examine the impact of spike tip and aerodisk design [6, 7]. Milicev et al. [8] conducted experimental study on the effects of various spike shapes mounted on a hemispherical nose. According to Gerdroodbary and Hosseinalipour [9], the best spikes for reducing heat fluxes are those with hemispherical tips, and an L/D ratio of 1 (L/D = length of the spike to diameter of the blunt body) is the best option for reducing both heat and drag. Menezes et al. [10] conducted tests with various spike tips fixed over a blunt cone and discovered that the aerospike is the most efficient at reducing drag. Due to the spike, there is some unsteadiness recorded in the forebody portion of the spiked body. So, several experimental and computational studies have been performed by many researchers. The unstable flow phenomenon on spiked blunt body was initially observed by Mair [11]. He made experimental study on different blunt bodies (hemispheres, flat cylinders, and a two-dimensional

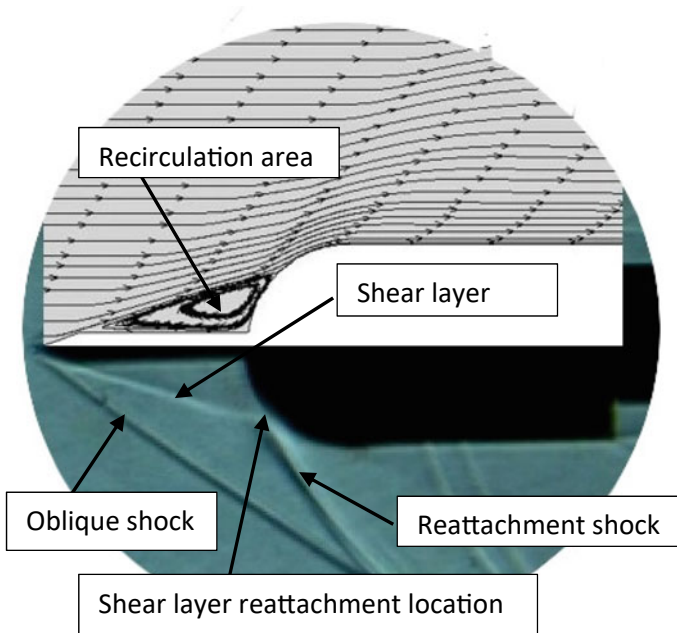


Fig. 1 Characteristics flow over a spiked blunt body captured through experiments and computations

equivalent model) at Mach number of 1.96. He noticed a considerable reduction in the level of flow unsteadiness by converting the flat-face forebody to a hemispherical form. A computational technique was utilized by Kariovskii et al. [12] and Mikhail [13] to understand the flow unsteadiness around the spiked body. Feszty et al. [14] offered a thorough analysis of the mode of oscillation and pulsation of unsteady events.

One of the major limitations of blunt bodies is the generation of a large bow shock wave in front of the forebody, leading to high drag and increased convective heat transfer on the body's surface. To mitigate these issues, exploring new shape variations for blunt bodies has emerged as a reliable approach to reduce drag.

To the best of the authors' knowledge, prior research has mainly concentrated on examining the function of spikes in hemispherical body configurations, which limited the use of spikes with other nose configurations. More research is therefore needed to better understand the flow field characteristics using a variety of different spike lengths and nose cone fairing bodies. In light of this, the current research was conducted to comprehend the flow behaviors around model with various spike lengths and nose cone fairings at supersonic flows. Keeping the spike tip at a fixed location, the body nose fairings were altered.

2 Geometry and Research Methodology

2.1 Geometry

Figure 2 shows the model description with coordinate system. Figure 3 shows the photographs of fabricated models of the adopted model configuration with a fixed tip sharp spike (FTSS) arrangement. A generic spiked supersonic vehicle's forebody has a main body and a spike. The main body which varies has a fixed base diameter $D = 15\text{ mm}$. The spike is a cylindrical rod with a variable spike length to accommodate the fixed tip and a fixed diameter of $0.13D$ with a semi-apex angle of 20° . The interchangeable spikes were fitted at the stagnation point.

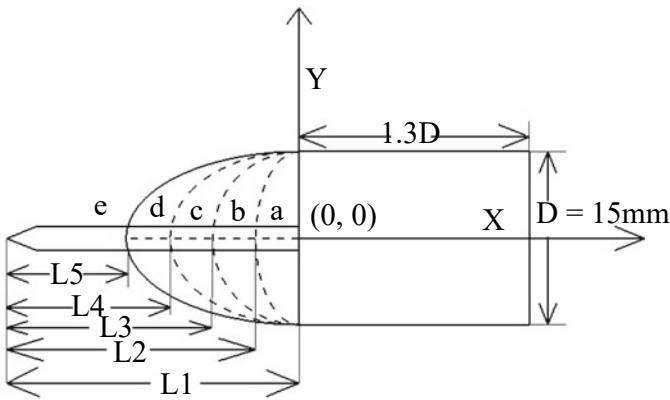


Fig. 2 Adopted model definition with coordinate system of forebody configuration

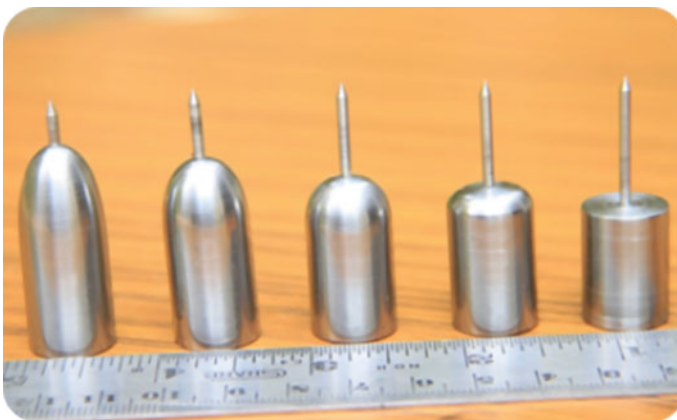


Fig. 3 Photographs of the fabricated model

The term BX.XX-FTSS is used to identify any configuration. B signifies a blunt nose fore body, X.XX gives the value of Sm/D . Here, Sm/D is defined as the ratio of semi-major axis to the base diameter (semi-major axis is the distance from body nose tip to the body shoulder). Sm/D have been chosen with the step increment of 0.25 and the configuration becomes B0.00, B0.25, B0.50, B0.75, and B1.00.

FTSS represents fixed tip location sharp spike.

2.2 Computation

Axisymmetric computation has been performed to compute flow field in and around the body with different nose cone fairings without and with spike configurations. A structured mesh is generated using quadrilateral cells in computations for all configurations, and appropriate boundary conditions have been adopted. For the spike and forebody, the adiabatic no-slip wall condition was applied. The numerical simulations were carried out with the commercially available Fluent flow solver. This solution uses a cell-centered finite volume technique to solve Navier–Stokes equations. A double-precision turbulent k- ω SST model density-based solver is employed in this study.

2.3 Experiment

All the tests were done at Mach 2.0 with a Reynolds number of 3.5×10^5 based on the body base diameter ($D = 15$ mm). The supersonic wind tunnel (WT0204) is used for all the experiments. This facility is located at Birla Institute of Technology Mesra Ranchi in the Aerodynamics Lab of Space Engineering and Rocketry department. This tunnel gives a 50 mm \times 100 mm test section size for the tested model. The wind-tunnel system consists of a two axial rotating compressors with Compressed Air-refrigerated Dryer system (Model number = D108IN-A), a pressure reservoir cylinder, a contoured nozzle for the flow at the desired Mach number, and a high-pressure air supply (settling chamber pressure of about 3.2×10^5 N/m²) via a pneumatic control valve to the test section. The facility has a NI-DAQ instrumentation system as well as the necessary sensors to actuate the designed Mach number at the test section.

One-component strain-gauge balance was used to quantify axial force on the tested model. It has axial specifications of 2 kg, the force balance was calibrated, and slope coefficient was determined prior to experiments.

The flow field and shock wave investigation around the models were examined using the Schlieren flow imaging technique, both with and without spikes. The current 6-inch Z-type Schlieren setup was used for this flow visualization study. The flow visualization images were captured using a Basler camera [ACA-1300-60 gc] with

a resolution of 1280×1024 pixels and a maximum frame rate of 60 frames per second. The pictures were post-processed using MATLAB.

3 Validation and Grid Sensitivity

To ensure the accuracy and reliability of the computations on the chosen geometry, a grid validation test was conducted. The purpose of this test was to optimize the number of grids used and select a suitable turbulence model for the computations. The validation process involved two key aspects: the grid sensitivity test and the comparison between the measured Schlieren photograph and the computed density gradient. The geometry and flow boundary conditions for the computations were selected based on the experimental findings reported by Kalimuthu et al. [15] at a Mach number of 6.0. These experimental results served as a reference for validating the computational approach. In the grid sensitivity test, different grid resolutions were employed to assess their impact on the computed results.

In the current study, a hemispherical-shaped nose body, referred to as B0.50, was employed for validation purposes. To validate the simulations, a hemispherical tip aerospike with an L/D ratio of 1.5 was utilized. Grid sensitivity was investigated using three different grid resolutions to ensure accurate results. The $k-\omega$ turbulence model was chosen for the computational simulations. The grids used for the grid independence test consisted of a coarse grid, a medium grid, and a fine grid. The objective was to determine the level of grid resolution necessary for reliable results.

Figure 4 illustrates the sensitivity test results and provides a comparison between the measured values and the computed values obtained in the present study. The comparison reveals good agreement, particularly for the medium grid, which was deemed suitable for the subsequent simulations. Based on the satisfactory agreement between the measured values and the computations obtained using the medium grid, it was selected as the input grid for the present simulations.

In order to validate the computational simulations, a comparison was also made between the density gradient contours obtained from the computations and the Schlieren photograph. From Fig. 5, it can be observed that there is a favorable agreement between the computational results and the Schlieren photograph. The density gradient contours and the Schlieren photograph visually capture the density gradients and shock wave patterns in the flow. The good agreement between the computed density gradient contours and the Schlieren photograph signifies the reliability of the computational simulations.

Fig. 4 Comparison of the pressure distribution on the hemispherical body with spike of $L/D = 1.50$

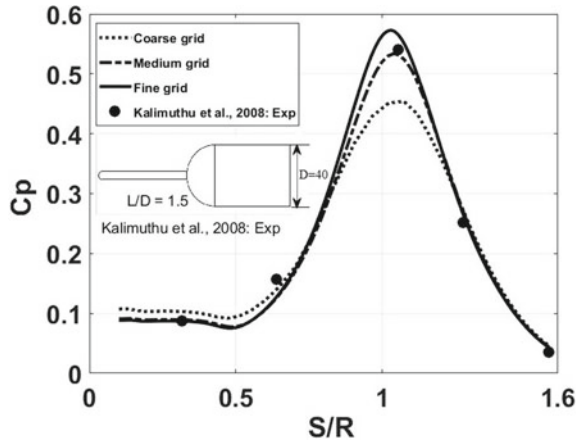
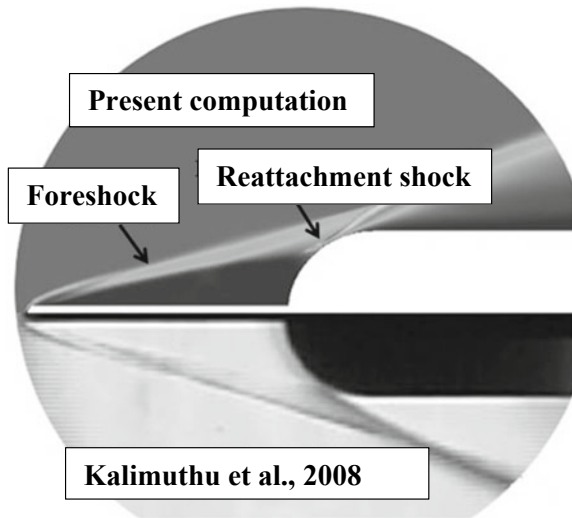


Fig. 5 Computed density gradient compared to measured Schlieren photo [15]



4 Results and Discussion

For each of the geometries studied, appropriate grids were generated to discretize the computational domain. The grid resolution and structure were carefully chosen to ensure accurate representation of the flow features and minimize computational errors. The grid quality and refinement were validated through comparison with experimental data to establish their reliability.

Figure 6 depicts the comparison between computed density gradient contours and Schlieren photographs for different nose cone bodies equipped with the fixed tip location sharp spike (FTSS) arrangement. The computed density gradients and Schlieren

photographs effectively capture the shape and strength of shocks observed in the flow field. Both the computational density gradients and the Schlieren photographs accurately represent the formation of oblique shocks, shear layers, recirculation regions, and reattachment shocks across all model configurations. The computations successfully capture these flow features, matching the observations made in the experimental Schlieren photographs. Furthermore, the reduction in the size of the recirculation region, resulting from variations in body configurations, is well-captured by both the computed density gradients and the measured Schlieren photographs. This demonstrates the ability of the simulations to accurately capture and reproduce the physical phenomena associated with the flow. The agreement between the computed density gradients and the experimental Schlieren photographs supports the reliability and validity of the computational approach in capturing the complex flow characteristics observed in the experiments (Fig. 7).

The flow characteristics observed over the spiked blunt body can be effectively categorized using three key angles: the oblique shock angle (β), the shear layer angle (α), and the body shock angle (Θ). These angles provide valuable insights into the flow structure and help analyze the aerodynamic behavior of the configuration. The oblique shock angle, denoted as β , refers to the angle formed between the leading-edge oblique shock wave and the body axis. The shear layer angle (α) is characterized as the angle between the shear layer and the axis of the body's base. The body shock angle, denoted as Θ , is the angle formed between the body shock wave at a specific location, which intersects the body shoulder, and the body axis. A

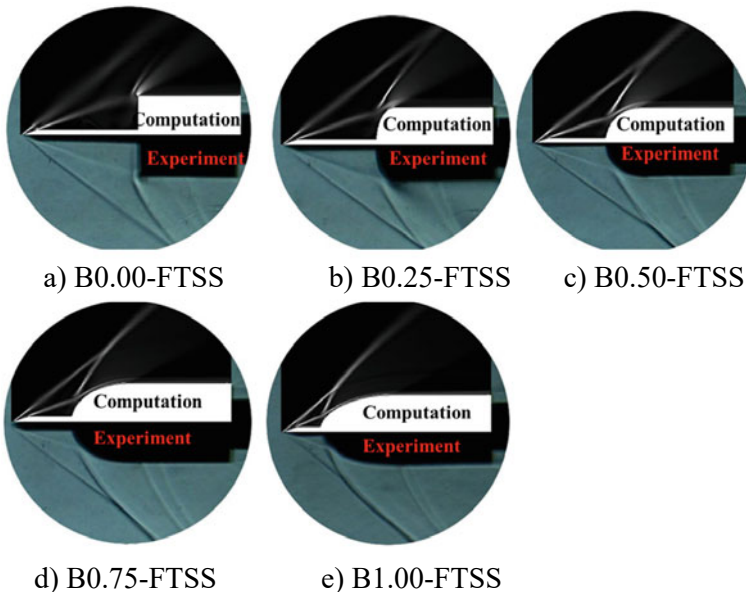
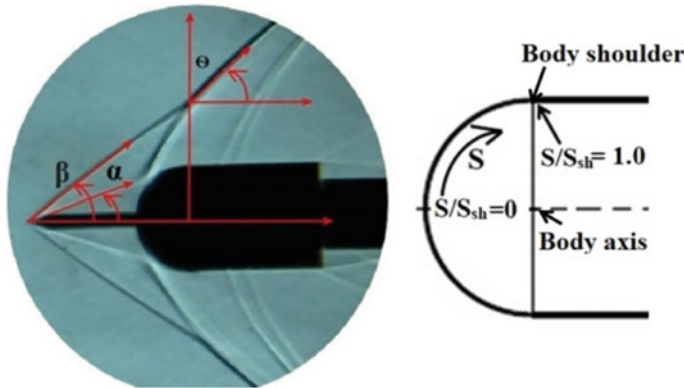


Fig. 6 Comparison of computed density gradient contour and Schlieren for all the shapes tested



S/S_{sh} = Shear layer reattachment point
 β = Oblique shock angle
 α = Shear layer angle
 Θ = Bod y shock ang

Fig. 7 Flow characteristics of measured Schlieren photo

thorough examination and analysis of these three angles provide a holistic insight into the flow patterns around the different nose cone fairing bodies with spike of different L/D ratio, the effects of shockwaves and shear layers on the object, and the resultant aerodynamic attributes. These angles serve as essential parameters for quantifying and interpreting the flow features over the spiked blunt body configuration.

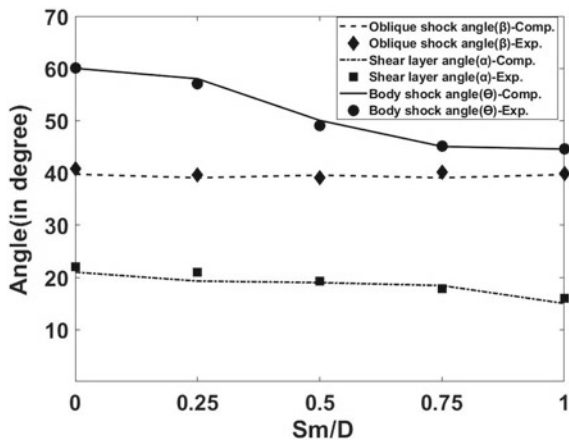
Table 1 provides the measured and computed values of the angles and impingement points for all the model configurations, obtained from both experimental observations and computational simulations. These values are further visualized in Fig. 8, where a plot illustrates the trends and relationships between these parameters. As the S_m/D (semi-major axis is the distance from body nose tip to the body shoulder) ratio increases, a notable trend is observed: the shock impingement point gradually moves closer to the body’s nose tip. This shift in the impingement point effectively reduces the shear layer angle in relation to the body shock angle.

Figure 9 illustrates the pressure distribution along the surface of different configurations. The distribution of static pressure (P) on the body surface is normalized by the freestream pressure (P_∞). The parameter S/S_{sh} , where S is the distance along the body surface and S_{sh} is the reference length, is used to indicate the location along the body. The plot begins at the nose tip, where $S/S_{sh} = 0$, and as we move along the body, this parameter progressively increases. The pressure distribution is depicted by the variation of normalized static pressure along the body surface. The pressure distribution plot provides valuable insights into the aerodynamic characteristics of the body and helps to identify regions of high and low pressure along the surface. It aids in understanding the pressure variations experienced by the body, which play

Table 1 Computed and measured oblique shock, shear layer, and body shock angle for fixed tip location sharp spike

Model config	Computed angles (in degree)			Measured angles (in degree)			S/S_{sh} (comp.)
	β	α	Θ	β	α	Θ	
B0.00-FTSS	39.6	21	60	40.76	22	60	0.973
B0.25-FTSS	39	19.2	58	39.6	21	57	0.734
B0.50-FTSS	39.5	19	50	39	19.25	49.06	0.499
B0.75-FTSS	39	18.4	45	40	17.8	45	0.386
B1.00-FTSS	39.6	15	45	39.8	16	44.5	0.233

Fig. 8 Variation in shear layer angle and body shock angle with fixed tip location sharp spike of different L/D s



a crucial role in determining the forces and aerodynamic behavior of the configurations under consideration. The presented figure truncates the S/S_{sh} parameter until 1.5, as beyond that point, no significant differences in the pressure distribution are observed. This truncation enables a more focused analysis of the relevant regions.

For all model configurations, the maximum pressure on the body surface at the shear layer reattachment point. This location corresponds to the formation of a strong bow shock at the body shoulder. The peak pressure is significantly affected by the changes in the model configuration, demonstrating a decrease as the configuration is altered. The peak pressure on the surface of the blunt body reflects the influence of shock strength. As the shock strength diminishes, the pressure decreases. Notably, the shock strength decreases with an increase in the Sm/D ratio, resulting in a reduction in the peak pressure observed on the surface. These observations highlight the relationship between the model configuration, shock strength, and the resultant pressure distribution along the body surface. The changes in peak pressure provide insights into the aerodynamic behavior and the impact of the different model configurations on the pressure distribution, aiding in the optimization of design and performance considerations.

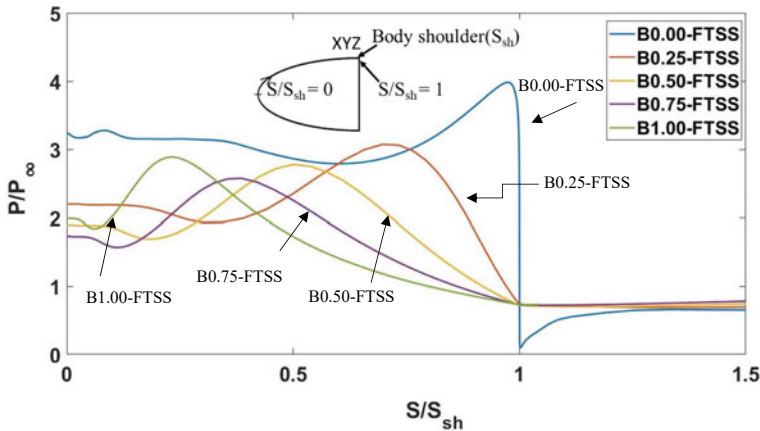


Fig. 9 Computed pressure distribution for fixed tip location sharp spike of different nose cone bodies

The streamline could be employed at supersonic speeds to analyze the flow field around the spiked body. The streamline over the fore body with varying nose cone fairings is shown in Fig. 10. Figure 10 depicts a zone of counter rotating flow in front of the forebody that varies with bodies and is separated by all spikes. Figure 10 depicts the primary structure of the flow field surrounding the spiked body and depicts the streamline of flow. In the case of B0.00, one vortex forms which is large in size in the recirculation zone and this vortex has a major interaction with the forebody. As the nose fairing increases, the recirculation area reduces which is represented by calculating the recirculation volume. In the recirculation area, only one vortex emerges in all cases, but all have intense contact with the forebody; however, the size of the vortex is larger in B0.00 than all model configurations, forming a large separation bubble on the face of the forebodies. As a result, B0.00 has a more significant rate of drag reduction than any other configuration.

Figure 11 represents the chart of recirculation volume and percentage of drag reduction for the spiked body with different nose cone fairings. The recirculation volume is normalized with the recirculation volume of flat model configuration. From the figure, it is observed that maximum percentage of drag reduction 64.6% is obtained for $Sm/D = 0.0$, which is having the maximum volume of recirculation regions. As the Sm/D ratio increases, the volume of recirculation regions starts to decrease in size which also corresponds to similar drop in drag. Hence, a relation could be developed between the drag reduction rate and the volume of the recirculation region.

The drag force is measured using a one-component force balance and computed using axisymmetric computation for every model configuration.

The results of the computed value and measured value of drag force for all model configurations are shown in Fig. 12. The figure shows that the drag coefficient decreases steadily without a spike as the Sm/D ratio rises, which is consistent in both

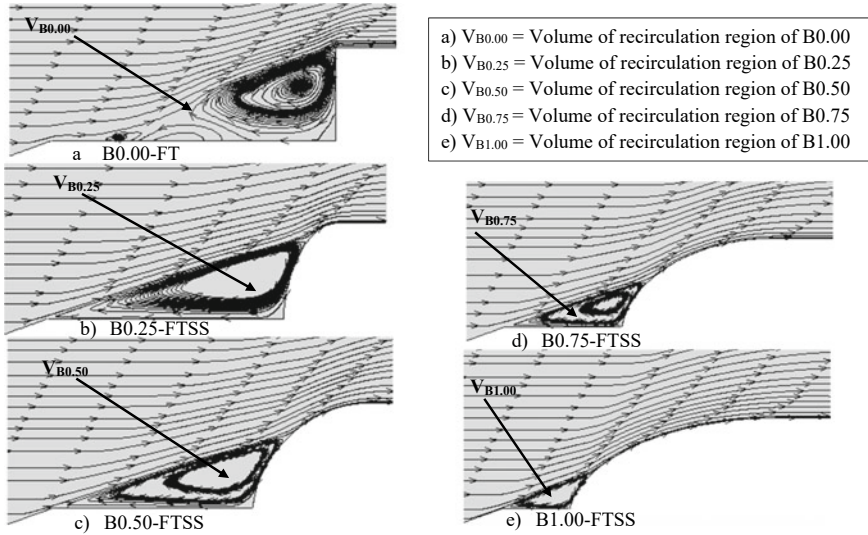
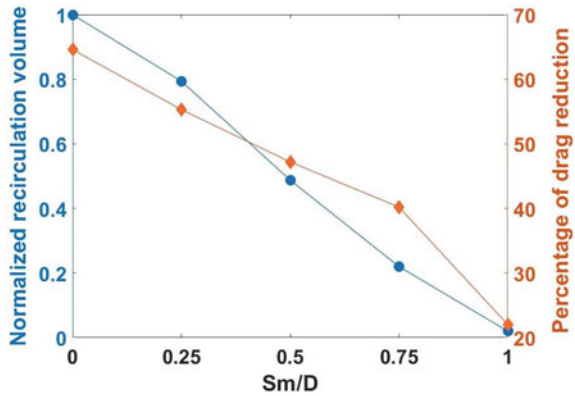


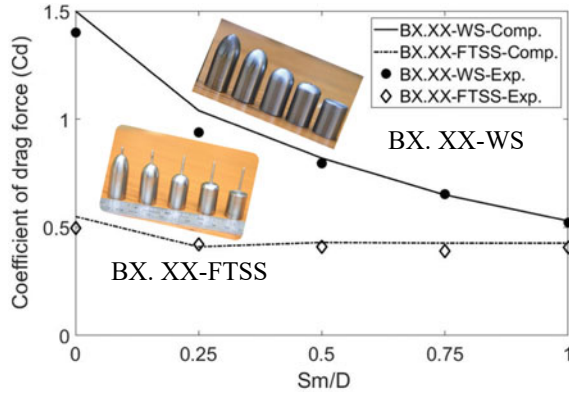
Fig. 10 Streamline along the different bodies of fixed tip location sharp spike

Fig. 11 Variation in volume of recirculation region and percentage of drag reduction with fixed tip location sharp spiked body



experimental and computational methods. The addition of spikes further reduces the drag force. For the body configuration of B0.00, the fixed tip location sharp spike achieves almost similar values for all the bodies under consideration. This shows that the presence of recirculation dead air region/volume and the alternate body presence contributes to the same reduction in absolute value of drag.

Fig. 12 Comparisons of computed C_d and measured C_d for the fixed tip location sharp spike



5 Conclusions

Experiments and computations were made at Mach number of 2.0 for various nose fairings of blunt bodies with a sharp spike having its tip fixed at a location. As the Sm/D (semi-major axis is the distance from body nose tip to the body shoulder) ratio increases, a notable trend is observed: the shock impingement point gradually moves closer to the body’s nose tip. This shift in the impingement point effectively reduces the shear layer angle in relation to the body shock angle. The tests revealed that the absolute drag does not vary for all the configurations.

Acknowledgements Without my supervisor’s extraordinary help, it would not have been possible to complete the research for this paper. His zeal, expertise, and meticulous attention to detail have motivated me and kept my work on schedule. My friends, D. Sahoo, Zeba, Neha K, Pawan Kumar, and Lavala, all contributed thoughtful remarks, for which I am also grateful.

Nomenclature

- P Static pressure (N/m^2)
- P_∞ Freestream pressure
- B Nose cone fairing (mm)
- S Distance along the surface from hemispherical body tip (mm)
- Sm Projected distance of nose tip from body shoulder (mm)
- $D_{X.XX}$ Body base diameter, Value of Sm/D (mm)
- C_D Drag coefficient

References

1. Huang W (2015) A survey of drag and heat reduction in supersonic flows by a counterflowing jet and its combinations. *J Zhejiang Univ-Sci A* 16(7):551–561. <https://doi.org/10.1631/jzus.A1500021>
2. John B, Kulkarni V (2015) Review of drag reduction techniques for hypersonic flows. *Int J Appl Eng Res* 10(18):39488–39495
3. Sidney R (1947) Alexander, results of tests of determine the effect of a conical windshield on the drag of a bluff body at supersonic speeds. National Aeronautics and Space Administration Hampton Va Langley Research Center, RM-No-L6K08a.
4. Karimi MS, Oboodi MJ (2019) Investigation and recent developments in aerodynamic heating and drag reduction for hypersonic flows. *Heat Mass Transf* 55(2):547–569. <https://doi.org/10.1007/s00231-018-2416-1>
5. Crawford DH (1959) Investigation of the flow over a spiked-nose hemisphere-cylinder at a Mach number of 6.8. National Aeronautics and Space Administration, TN-D-118. <https://dp.la/item/e1de7b2f860151cea4f64f4ee1a6ef4d>
6. Sarwar MDG, Kumar P, Das S (2022) Supersonic flow investigation of a drag reducing conical spike on a hemispherically blunted nose body. *Proceedings of the Institution of Mechanical Engineers, Part G: J Aerospace Eng.* <https://doi.org/10.1177/09544100221140942>
7. Sarwar MDG, Kumar P, Das S (2022) Insight into the mechanism of drag reduction for a spiked blunt body. *Aerospace and Associated Technology: Proceedings of the Joint Conference of ICTACEM 2021, APCATS 2021, AJSAE 2021 and AeSI 2021.* Kharagpur: Taylor & Francis: Indian Institute of Technology, p. 71. <https://doi.org/10.1201/9781003324539-13>
8. Milicev SS, Pavlovic MD (2002) Influence of spike shape at supersonic flow past blunt-nosed bodies: experimental study. *AIAA J* 40(5):1018–1020. <https://doi.org/10.2514/2.1745>
9. Gerdroodbary MB, Hosseinalipour SM (2010) Numerical simulation of hypersonic flow over highly blunted cones with spike. *Acta Astronautica* 67(1–2):180–193. <https://doi.org/10.1016/j.actaastro.2010.01.026>
10. Menezes V, Saravanan S, Jagadeesh G, Reddy KPJ (2003) Experimental investigations of hypersonic flow over highly blunted cones with aerospikes. *AIAA J* 41(10):1955–1966. <https://doi.org/10.2514/2.1885>
11. Mair WA (1952) LXVIII Experiments on separation of boundary layers on probes in front of blunt-nosed bodies in a supersonic air stream. *The London, Edinburgh, and Dublin Philosophical Magazine and Journal of Science* 43(342):695–716. <https://doi.org/10.1080/14786440708520987>
12. Kariovskii VN, Levin VA, Sakharov VI (1987) Flow past blunt bodies with nose spikes and surface injection. *Fluid Dyn* 22(4):601–606. <https://doi.org/10.1007/BF01051427>
13. Mikhail AG (1991) Spike-nosed projectiles-computations and dual flow modes in supersonic flight. *J Spacecr Rocket* 28(4):418–424. <https://doi.org/10.2514/3.26261>
14. Feszty D, Badcock KJ, Richards BE (2004) Driving mechanisms of high-speed unsteady spiked body flows, part I: pulsation mode. *AIAA J* 42(1):95–106. <https://doi.org/10.2514/1.9034>
15. Kalimuthu R, Mehta RC, Rathakrishnan E (2008) Experimental investigation on spiked body in hypersonic flow. *Aeronautical J* 112(1136):593–598. <https://doi.org/10.1017/S000192400002554>

Pressure Drop Prediction Using CFD for a Launch Vehicle Payload Fairing Separation Ground Test



Ankur Nagpal and G. Vidya

Abstract Payload fairing (PLF) separation during launch vehicle ascent is necessitated after atmospheric effects cease to exist. Performance evaluation of separation system design requires a full-scale functional ground test, where pressure drop occurring due to sudden movement plays an important role in prediction of fairing trajectory. Unsteady Euler CFD simulations are carried out in ANSYS Fluent to understand pressure drop occurring inside PLF. Factors affecting the pressure drop such as presence of satellite, peak velocity, initial gap, nose opening rate and simulation of actual joint are studied and their effects are brought out.

Keywords PLF separation · Pressure drop · CFD

Nomenclature

L	Height of PLF
D	Diameter of PLF
P_{PLF}	Pressure inside PLF
P_{AMB}	Ambient pressure
P_D	Pressure drop
V	Velocity of PLF
T	Time

A. Nagpal (✉) · G. Vidya
ACMD, Vikram Sarabhai Space Centre, Trivandrum, India
e-mail: ankur.aero@gmail.com

1 Introduction

A launch vehicle payload fairing (PLF) safeguards the payload from aerodynamic and aerothermal effects during the ascent flight. The separation of fairing is necessitated by mission requirements when the atmospheric effects cease to exist. Clean and collision-free separation of fairing halves is essential for the mission success of a launch vehicle. Separation mechanisms in PLF halves may consist of pre-compressed springs or pyrotechnic zip chords depending upon the system configuration. The development of a new launcher requires a successful demonstration of the PLF separation system.

The separation tests may be conducted in a large vacuum chamber with a full-scale PLF model [1], thereby requiring the availability of an appropriate facility and considerable expenditure. In contrast, the Indian launcher's PLF separation tests are performed in air [2–4] by taking into account the aerodynamic effects. Pressure drop resulting from sudden relative movement between the two PLF halves can alter the separation dynamics predictions significantly. The accurate prediction of pressure drop, during PLF separation test in air, is essential for separation dynamics prediction [5] and hence is ensuring a successful functional ground test. Internal pressure measurement during the ground test in air providing the pressure drop inside PLF and aerodynamic force acting on moving body are important parameters for prediction of fairing trajectory [6].

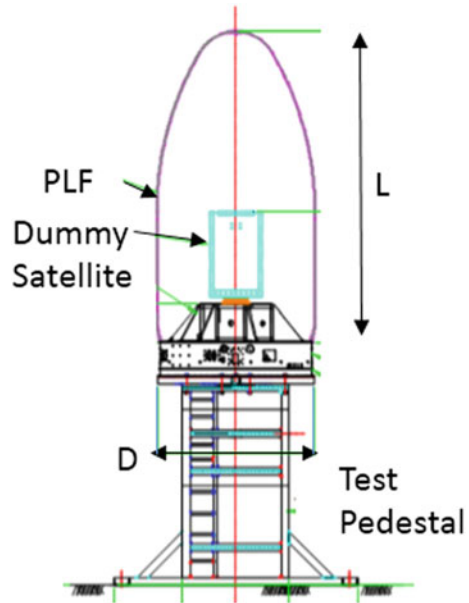
Figure 1 shows the schematic of test setup. L/D for the PLF under study is ~ 2 . The present study shows CFD computations employing overset meshing approach in *ANSYS Fluent* for simulation of moving halves. Pressure drop is predicted considering a typical lateral velocity and nose opening rate profile. Further understanding is developed by simulating the conditions affecting the pressure drop predictions like presence of internals, peak velocity, initial gap, nose opening rate and movement of two halves without developing a gap for initial movement. The last condition simulates the actual joint between two halves and will be discussed in later sections. All the conditions simulated have helped in better understanding the correlation between predicted and measured pressure drops.

2 Computational Approach

2.1 Computational Mesh

Overset meshing approach has been used to simulate relative motion between two bodies. Symmetric half of the domain is simulated with one half of PLF moving with respect to stationary parts like dummy satellite and other internals. Unstructured meshing with prism layers has been carried out using ANSYS workbench meshing. Moving body, i.e. PLF is in the foreground mesh as shown in Fig. 2a having 9.2 million cells. The coordinate system along with origin is shown in Fig. 2a. The test

Fig. 1 Schematic of test setup for PLF testing at ground



bay size is $10D \times 10D \times 15.75D$ as shown in Fig. 2b, which is the domain size for background mesh having 21.3 million cells, and the zoomed view also shows the internal elements like dummy satellite, etc. Figure 2c shows the mesh after overset operation. An initial gap of $0.0055D$ is considered between symmetry plane and one half of PLF. This was initially thought to be necessary while using overset meshing. The choice of initial gap was also based on relevant hardware dimensions. The effect of this gap on pressure drop prediction is discussed in later part of this paper.

2.2 Solver

Unsteady Euler equations are solved on overset meshes in ANSYS Fluent software by employing dual-time stepping approach. The PLF is given a predefined velocity profile for movement, and time-accurate solution is obtained. The simulation duration is 100 ms (milliseconds) as per the time of interest for intended phenomenon to be studied. Time step has been chosen as 0.1 ms with 20 inner loop iterations based on timestep convergence study carried out. Figure 3 shows the inner loop iteration fall for the simulation carried out, and it is seen that more than five orders of magnitude fall take place in each time step. Figure 4 shows the magnitude of X-Force acting on one half of PLF for a typical velocity profile for time step 0.05 ms and 0.1 ms. Though this paper discusses pressure drop occurring inside the PLF, for timestep convergence force data is shown as this is also very important for the separation dynamic study.

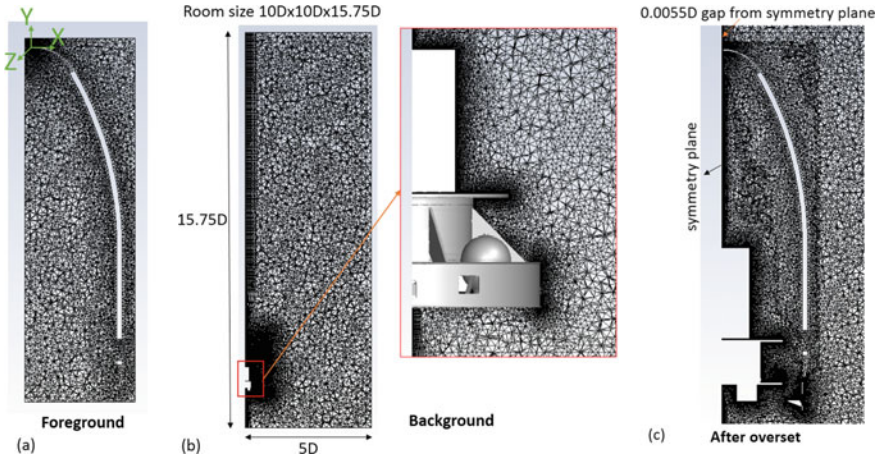
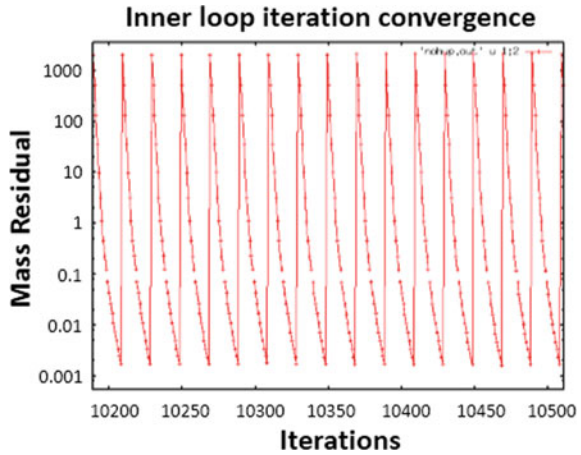


Fig. 2 Domain and computational mesh **a** foreground mesh **b** background mesh **c** after overset operation

Fig. 3 Inner loop iteration convergence



2.3 Velocity Profile

Velocity profile is an output of separation dynamics analysis [5] after a few iterations while also using pressure drop predictions from CFD. In the first iteration, velocity profile is computed in separation dynamics analysis without considering any pressure drop. With the first iteration velocity profile, CFD analysis is carried out to predict pressure drop. This procedure is repeated till a converged velocity profile is achieved.

Figure 5 shows a typical first iteration velocity profile without pressure drop and a converged velocity profile with pressure drop. Converged velocity profile with pressure drop is used for CFD analysis presented in this paper. Peak velocity V_{max}

Fig. 4 Timestep convergence for force in x-direction on PLF half

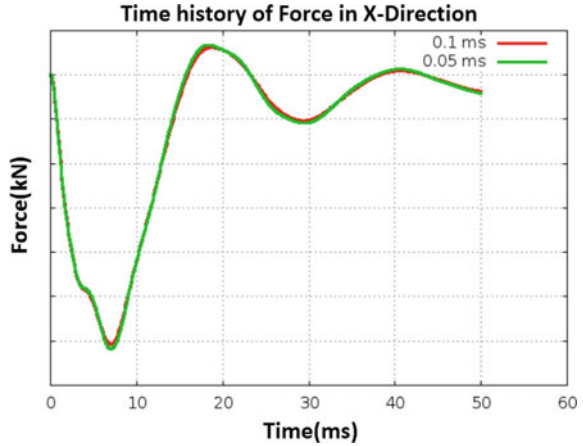
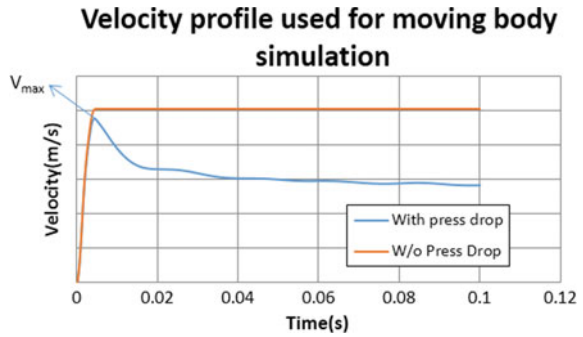


Fig. 5 Velocity profile of PLF



occurs at ~5 ms after separation. It is to be noted that acceleration is sudden due to the impulse provided by the separation system. The velocity drops after V_{max} due to aerodynamic effects, which are governed by transient phenomena due to sudden depressurization. After 40 ms, the velocity is nearly constant due to negligible aerodynamic forces acting on the PLF.

3 Results and Discussion

The pressure drop occurring due to sudden depressurization will be discussed in this section. For the baseline case corresponding to 0.0055D initial gap and velocity profile shown in Fig. 5, the results are discussed in the baseline subsection. In subsequent subsections, the pressure drop for effect of presence of internals, peak velocity, initial gap, nose opening rate and actual joint simulation.

3.1 Baseline Case

Pressure on the inner wall of PLF is monitored on a generator along the height. For better understanding, pressure drop, i.e. after adjusting ambient pressure $[-(P_{PLF}-P_{amb})]$, is analysed. Along the height, the peak pressure drop occurs at $Y = -0.91D$ and the time history of pressure drop at that location is plotted in Fig. 6. The peak pressure drop P_{D1} occurs at 7 ms and pressure is recovered soon hence overshooting to $(-ve)P_{D2}$ at 20 ms. Sudden depressurization leads to a pressure drop $P1$ in this case. However, as the gap between two halves increases due to relative movement, the communication with ambient is stronger. Also, as the pressure difference is large between ambient and inside, PLF gets filled, showing as pressure increase beyond 7 ms up to 20 ms. Pressure contour of $(P_{PLF}-P_{amb})$ at 7 ms is plotted in Fig. 7. The whole process can also be understood in terms of compression and expansion waves. In Fig. 7, we can see the compression wave travelling outwards. It is to be noted that the differential pressure across the PLF is the cause of aerodynamic forces acting. At 7 ms, as shown in Fig. 7, the force in X- direction is going to be negative hence opposing the movement of PLF. Similarly, at 20 ms, the force is positive and hence aiding the movement. The accurate prediction of instant 2 also has an important role in further separation analysis.

Figures 8 and 9 show the pressure drop axial profile evolution with time. $Y/D = 0$ corresponds to nose of the PLF. It is observed that peak pressure drop for the baseline case occurs at 7 ms, which is after the peak velocity instant. The location of peak pressure drop is at $0.91D$ from nose. The axial profile looks flat up to 3–4 ms, beyond which a distinct maxima is visible in pressure drop. The axial location of pressure drop maxima seems to shift away from nose for time 5 ms to 9 ms.

This shows that the depressurization is stronger in the nose region. This could be possibly due to lower volume in the nose region as compared to cylindrical region.

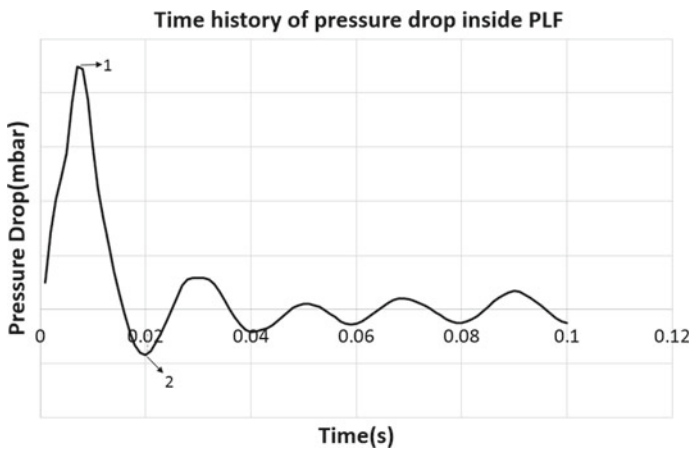


Fig. 6 Time history of pressure drop at $y = -0.91D$

Fig. 7 Pressure contour at peak pressure drop instant

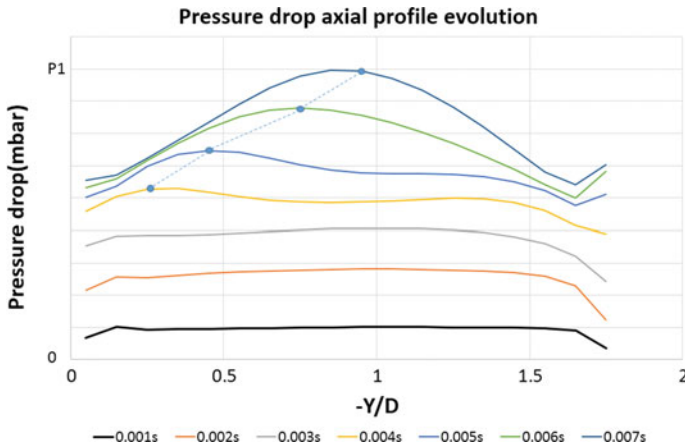
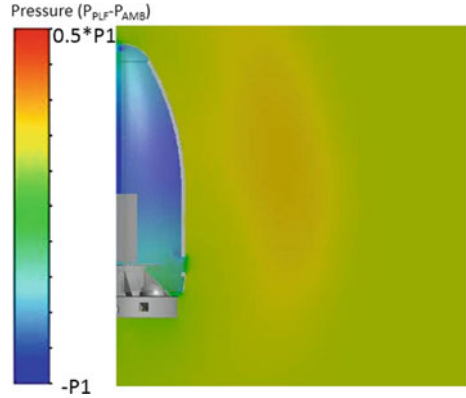


Fig. 8 Pressure drop axial profile evolution up to 7 ms

The depressurization due to sudden movement and filling due to gap creation are simultaneous countering processes. However, it is observed that filling effect dominates at later instants, as the gap between two halves develops along with pressure drop. Also, in the baseline case, the bottom of PLF is partially blocked by internal elements, hence offering blockage for the filling process. For time > 9 ms, it is observed that filling process in the cylindrical region of PLF dominates and hence leads to lowest pressure drop in the cylindrical portion up to 12 ms. Higher filling in cylindrical portion is attributed to larger gap area owing to large circumference.

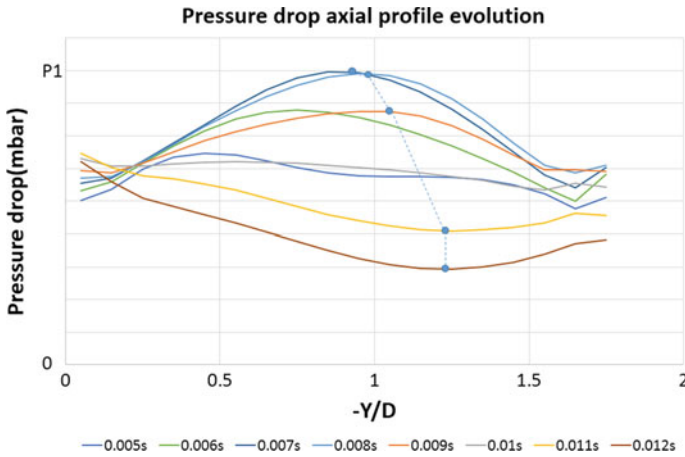


Fig. 9 Pressure drop axial profile evolution from 5 to 12 ms

3.2 Effect of Internal Elements

The effect of internal elements such as satellite modelling on the predictions is studied on the pressure and force acting in X direction. Figure 10 shows the pressure contour at peak pressure drop instant for PLF alone. In this case, the initial internal volume is more than baseline case which would lead to lower pressure drop. However, the bottom portion is fully communicating to ambient unlike the baseline case, and hence, the filling effect would be different. Pressure data for this particular simulation was not saved like other cases, so comparison of X-force is shown in Fig. 11. The peak force at instant 1 is lower by ~5% than baseline case corroborating with lower pressure drop. However, at instant 2, there are changes in the profile as well as the magnitude of force. The filling process happens much faster in this case due to larger opening area. The magnitude of force aiding the separation is higher in this case. This analysis shows that PLF-alone simulations give a lower suction force and higher aiding force, which would not be a conservative scenario for separation studies. Hence, modelling of internal elements is essential for carrying out this type of study.

3.3 Effect of Peak Velocity Increase

The velocity profile shown in Fig. 5 is scaled up in Y-axis by factors 1.1 and 1.2 for 10% and 20% increase in peak velocity, respectively. The results of simulations in terms of pressure drop are shown in Fig. 12. For factor 1.1, 8.6% increase in peak pressure drop is observed, and for factor 1.2, 17% increase is observed. The pressure drop linearly increases with peak velocity magnitude for a given velocity profile.

Fig. 10 Pressure contour at peak pressure drop instant for PLF alone

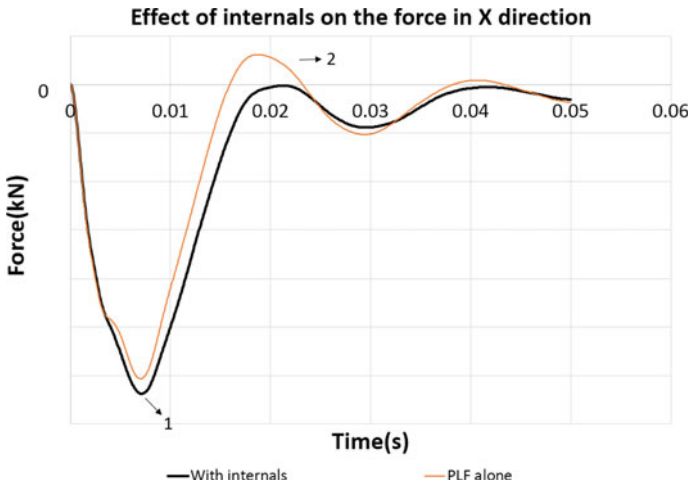
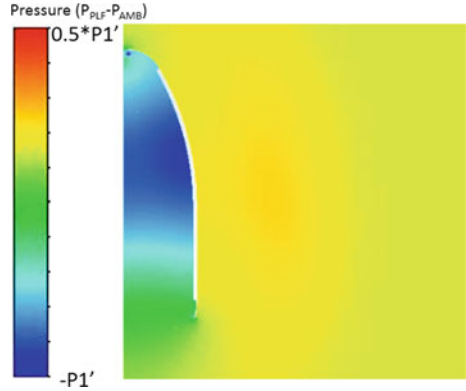


Fig. 11 Effect of internal on force acting on PLF half

3.4 Effect of Nose Opening Rate

Baseline case discussed in Sect. 3.1 brings out pressure drop for parallel separation. Along with separation velocity, nose opening rotation rate is also used as an input. The opening rate is peaking at $\sim 90^\circ/s$ at peak velocity instant. The effect of including nose opening rate in simulations is shown in Fig. 13. Six % increase in peak pressure drop is observed by including the opening rate.

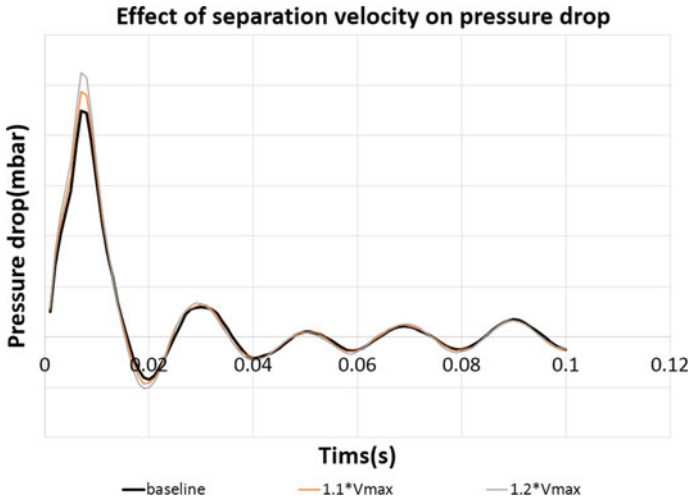


Fig. 12 Effect of peak velocity increase on pressure drop

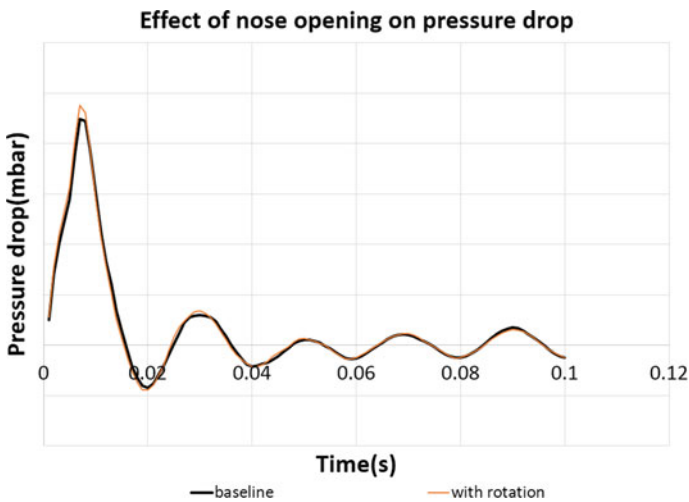


Fig. 13 Effect of nose opening rate on pressure drop

3.5 Effect of Initial Gap

Initial gap, i.e. gap at $T = 0$ between two halves, also influences pressure drop prediction. In the baseline case, the gap is $0.0055D$, which is further halved to $0.00275D$ in order to study the sensitivity. Figure 14 shows the pressure drop for the cases studied. With a reduced initial gap, 2.75% increase in pressure drop is observed.

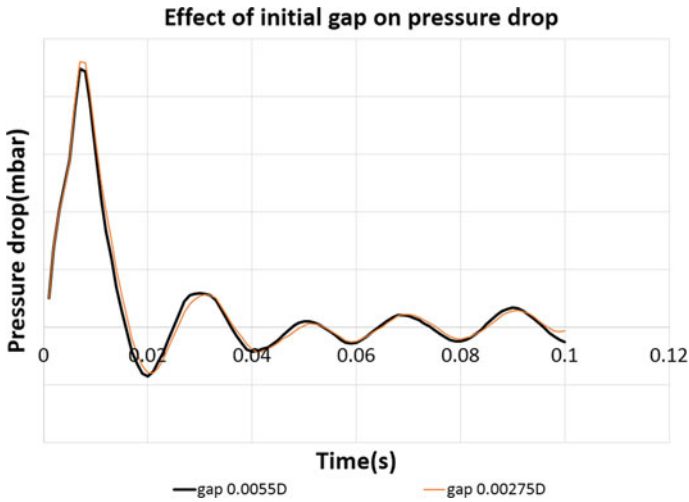


Fig. 14 Effect of initial gap on pressure drop

3.6 Effect of Actual Joint Simulation

Two halves of PLF are connected like a tongue and groove joint running through the length of PLF. After initiation of separation, for the initial movement of around 0.01D for one half, there is no physical gap between two halves. This means that sudden depressurization is taking place without development of a physical gap. This is simulated by suitably modifying the grid so as to capture the physical phenomena. Figure 15 shows the effect of actual joint simulation on pressure drop. About 19.2% increase in pressure drop is observed as compared to a case with initial gap. Also, the time instant of peak pressure drop is delayed, which could be due to delayed filling initiation.

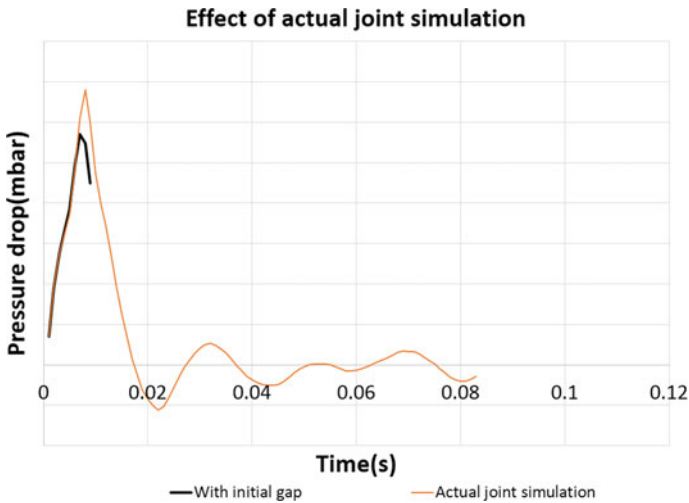


Fig. 15 Effect of actual joint simulation on pressure drop

4 Conclusion

Pressure drop prediction for PLF separation test at ground is carried out by unsteady Euler CFD simulations using ANSYS Fluent. For the baseline case, time history of pressure is analysed for peak pressure drop and recovery which leads to aerodynamic forces affecting the movement of PLF. The physical phenomena of sudden depressurization and filling are explained for the pressure drop temporal profile observed. The axial pressure drop profile evolution indicates depressurization effect being more dominant in the nose region and filling effect more dominant in the cylindrical region. Further, sensitivity to parameters like presence of internals, peak velocity increase, nose opening rate, initial gap and actual joint simulation is brought out. Presence of internal elements increases the peak force magnitude by $\sim 5\%$. Peak velocity increase of 10% leads to 8.6% increase in pressure drop and increase of 20% velocity leads to 17% increase in pressure drop. Inclusion of nose opening rate results in 6% higher pressure drop prediction. Reduction of gap from 0.0055D to 0.00275D leads to 2.5% higher pressure drop. Simulation of actual gap results in 19.2% higher pressure drop. Velocity and actual joint simulation have strong dependence on pressure drop predictions.

Acknowledgements We express our sincere gratitude to Dr. Patil M M, Group Director, ADSG, and Dr. Ashok V, Deputy Director, Aeronautics Entity for constant guidance and support during the work.

We acknowledge the continuous interaction with Shri. Jathaveda M, ACMD, and Shri Kunal Garg, AMCD, which helped in understanding the problem and influencing parameters. Iterative analysis for separation dynamics study was carried out with Smt Sivasakthi R, SDPED, and Smt. Radha N, SDPED, hence providing relevant velocity input file. The earlier efforts in solving this problem with another approach [4] provided a very good starting point for this study.

References

1. Robbins MJ (1991) Ground test program for new Atlas payload fairings. In: General dynamics/space systems division. Sand Diego, CA
2. Lochan R, Adimurthy V, Kumar K (1997) Separation dynamics of heat shield fairings. In: Proceedings of Institution of Mechanical Engineers, Vol 211 Part G, IMechE
3. Chakraborty D, Vasantha S (1991) Aerodynamic simulation of heat shield separation test on ground. The Royal Aeronautical Society, The Aeronautical J
4. Babu C, Das D, Ashok V (2013) Numerical simulation of 3D moving bodies using Cartesian cut cell method. In: 15th Annual CFD Symposium, August 9–10, Bangalore
5. Sivasakthi R, Babu C, Jalan SK, Radha N, Ravikumar C, Das D, Neetha R, Kumar A, V Ashok (2015) Dynamics of a large full scale CFRP payload fairing separation test on ground using time march approach. In: Symposium on Applied Aerodynamics and Design of Aerospace Vehicle (SAROD 2015), December 3–5, Thiruvananthapuram
6. Yasunaga Y, Fukushima Y, Nakamura T, Fujita T (1990) Separation jettison test of Japanese H-II Rocket Satellite Fairing. In: 28th AIAA Aerospace Sciences Meeting, January 8–11, Reno, Nevada

Effect of Upstream Energy Deposition Rate on Flow Characteristics of a Scramjet Engine



Amrita Pathak, Pranjal Khare, Ali Jraisheh, and Vinayak Kulkarni

Abstract The concept of energy deposition method to reduce flow spillage at intake and as a means of deflecting upstream flow into a high compression intake of a Scramjet vehicle at off-design Mach numbers of 5 and 4.5 was explored using Computational Fluid Dynamics (CFD). An in-house developed two-dimensional inviscid CFD solver was used to conduct the studies. The Immersed Boundary Method for boundary reconstruction has been incorporated in the Finite Volume method, which makes the process of generating grids for complex geometries easier. The studies have been carried out based on two different locations for depositing the energy and two different energy strengths of 10 and 30 MW/m³. The performance was assessed in terms of intake mass flow ratio and pressure recovery factor.

Keywords Scramjet intake · Energy deposition · Unstart phenomena · AUSM · Immersed boundary method

1 Introduction

To achieve sustained hypersonic flight, the significance of the Scramjet engine is realized worldwide. In a Scramjet, the function of the intake is to compress the upstream incoming air and supply adequate mass of air to the combustor at a supersonic Mach number. Thus, the design of the air intake becomes crucial for a successful operation of the entire engine.

The ideal geometric condition for the Scramjet intake is shock-on-lip (SOL). This allows for the oblique shocks generated by the ramps to converge at the cowl lip and reflect the single converged shock into the isolator, but the SOL condition is not satisfied for Mach numbers greater or lower than the designed value, as shock angles

A. Pathak (✉) · P. Khare · A. Jraisheh · V. Kulkarni
Department of Mechanical Engineering, IIT Guwahati, Guwahati, Assam 781039, India
e-mail: amrita.pathak@iitg.ac.in

A. Jraisheh
Department of Mechanical Engineering, Damascus University, Damascus, Syria

depend on the flight Mach number. Mostly, intakes are designed for the highest anticipated Mach number in a hypersonic air breathing flight, so for Mach number less than the designed value, flow spillage occurs and air mass capture reduces along with the total pressure recovery at the isolator exit. Moreover, in worst-case scenarios, these losses could lead to an unfavorable phenomenon, i.e., ‘unstart’ [1–3], which refers to the expulsion of the flow from the inlet, which in extreme cases, can even stall the engine.

To control these losses, there have been various studies on variable geometry intakes like rotating the cowl or ramp [1], transitional cowl systems [4] which work by changing the contraction ratio and extending the operational Mach number range. There has been some study regarding implementing a variable geometry cowl sidewall control technique [5] which can be employed to enhance the performance characteristics of the Scramjet at off-design flow conditions. However, the variable mechanical geometric systems would be heavier and will also add complexity in manufacturing them and controlling at hypersonic speed.

In recent years, method of energy addition has come up as a widely used technique to reduce drag in supersonic vehicles [6, 7]. It is also adopted as an alternative approach which can optimize Scramjet inlets by modifying flow field around inlets through energy deposition [8]. The work by Macharet et al. [8] has given the optimal place for energy addition that is near the intersection of the ramp shock with the forward prolongation of the cowl line, but all these works are done on lower compression ratio inlets with only external compression. Therefore, in this article, we have studied the effect of energy deposition for different energy strengths and locations on mixed compression geometry with high compression ratio. Details on the numerical methodology are provided in the following section.

2 Methodology

A. Governing Equations

Governing conservation laws for the current study are the compressible form of two-dimensional Navier–Stokes equations, which can be written collectively in the following format:

$$\frac{\partial \mathbf{U}}{\partial t} + \frac{\partial \mathbf{F}_I}{\partial x} + \frac{\partial \mathbf{G}_I}{\partial y} + \frac{\partial \mathbf{F}_V}{\partial x} + \frac{\partial \mathbf{G}_V}{\partial y} = 0 \quad (1)$$

$$\text{where } \mathbf{U} = \begin{bmatrix} \rho \\ \rho u \\ \rho v \\ \rho E \end{bmatrix}; \mathbf{F}_I = \begin{bmatrix} \rho u \\ \rho u^2 + p \\ \rho uv \\ \rho u \left(E + \frac{p}{\rho} \right) \end{bmatrix}; \mathbf{G}_I = \begin{bmatrix} \rho v \\ \rho uv \\ \rho v^2 + p \\ \rho v \left(E + \frac{p}{\rho} \right) \end{bmatrix}$$

In the above equations, the conserved variables (mass, momentum and energy) is given by the vector, \mathbf{U} ; the inviscid fluxes are represented by \mathbf{F}_I and \mathbf{G}_I in the x and y directions, respectively. By assuming the fluid to behave like a perfect gas, the equation of state is taken into account, and thus, this closes the system of equations. The equation of state is given by,

$p = \rho RT$, where the symbols p , ρ , and T refer to pressure, density, and temperature, respectively, whereas R refers to gas constant.

B. Finite Volume Method

The semi-discrete form of the governing conservation laws can be written as,

$$\frac{d\bar{\mathbf{U}}_i}{dt} = -\frac{1}{\Omega_i} \sum_{J \in i} \mathbf{H}_{\perp J} \Delta S_J - \alpha \bar{\mathbf{S}}_i = R(\bar{\mathbf{U}}_i) \quad (2)$$

Here, summation is over all faces of the cell i and term $R(\bar{\mathbf{U}}_i)$ is referred to as the residual term. Here, \mathbf{H}_{\perp} collectively shows the normal components of the convective fluxes ($\mathbf{F}_I, \mathbf{G}_I$) at the cell faces. The convective fluxes have been evaluated by using the AUSM scheme [9]. As part of convective flux scheme, a second-order accurate reconstruction of flow properties has also been implemented along with Venkatkrishnan limiter [10]. Temporal discretization is achieved using a five-stage Runge–Kutta scheme.

C. Immersed Boundary Method

The Immersed Boundary Method (IBM) presented in this article is based on the concept of using a computational domain in the form of a background mesh, over which the body of the solid is superimposed. Contrary to traditional CFD solvers, this approach leads to a non-conformal mesh, i.e., the mesh not conforming to the solid body's shape. Particular challenge in this method is the method of transmitting the wall boundary conditions onto the background mesh. The IBM approach presented here is similar to the method of Ghias et al. [11]. In this approach, solid, fluid, and ghost cells are classified by their cell centers, where solid cells have their centers inside solid boundaries and fluid cells have their centers outside solid boundaries. It is then determined that ghost cells are the solid cells that lie in a Finite Volume stencil of a fluid cell. Afterward, the ghost cells' image points are found by reflecting the ghost cell centers around the solid boundary. Then, a bilinear interpolation is adopted to interpolate the values at the image points. Finally, the ghost cell values are evaluated from the image point by enforcing the boundary condition at the body intercept along the line from image point to ghost cell center. Implementing this method enables to superimpose a solid boundary over an existing domain, making it particularly useful when dealing with complex geometries.

3 Computational Details

A. Computational Domain

The Scramjet intake geometry is based on the experimental setup used by Devaraj et al. [2] with a design Mach number of 6. The mixed compression intake consists of two external ramps inclined at 10.7° and at 25.6° from horizontal followed by an expansion ramp which is followed by a constant area isolator having height of 6.2 mm and also an internal compression cowl inclined from horizontal at 11.4° . The detailed geometry is provided in Fig. 1, and relevant dimensions are provided in Table 1. All the simulations are carried out at Mach 6, with a freestream total pressure and a freestream total temperature of 7.55 bar and 423.80 K, respectively, and an angle of attack of 0° . To analyze the effect of adding energy hot spots at the upstream of the intake, two locations, viz. location 1 and location 2, were considered. Location 1 is situated at a distance of 15 mm upstream horizontally and vertically at same level as that of the cowl tip as shown by a yellow circle in Fig. 1, whereas location 2 is situated at a distance of 15 mm upstream and vertically 2 mm above of location 1, as shown by a red circle in Fig. 1.

B. Implementation of Boundary Conditions

The implemented boundary conditions are discussed as follows:

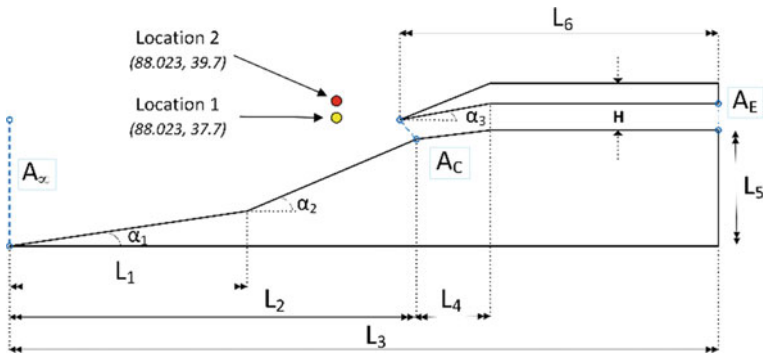
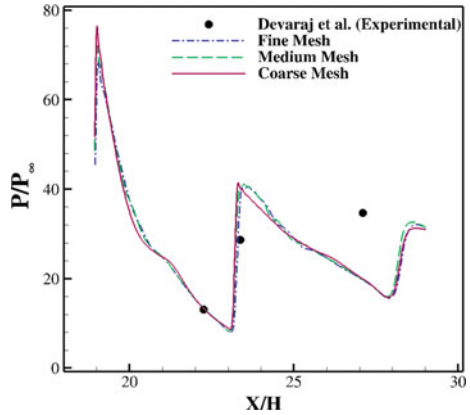


Fig. 1 Schematic of the Scramjet inlet model displaying the locations of energy hot spots

Table 1 Geometric parameters of Scramjet model

L_1	L_2	L_3	L_4	L_5
68.3 mm	106.7 mm	180 mm	10.7 mm	34.4 mm
L_6	H	α_1	α_2	α_3
76.97 mm	6.2 mm	14.9	10.7°	11.4°

Fig. 2 Computed normalized cowl surface pressures on different grids with experimental results of Devaraj et al. [2]



- (1) Supersonic inlet and outlet: The primitive variables are fixed to their freestream values for supersonic inlet, while all variables are extrapolated from the interior cells adjacent to the boundary faces for supersonic outlet.
- (2) No-slip walls: The no-slip boundary condition is imposed by setting the normal and tangential velocities at the surface to zero. A constant temperature is used for isothermal walls, while a zero gradient is used for adiabatic walls.
- (3) Inviscid wall or symmetry boundary: To achieve impermeable wall boundary condition, the normal component of velocity is set to zero.

C. Grid Independence Test and Solver Validation

In order to study the effect of grid resolution on the computed results and to ensure the independence of the generated results with respect to the number of grid cells, a grid independent test was carried out for three grids with different resolutions, i.e., (coarse, medium, and fine), having 86,531, 108,869, and 142,229 number of cells, respectively. The cowl side surface pressures are plotted for the different grids as shown in Fig. 2. It can be noted that the results do not vary as grid is refined from medium to fine. Hence, the medium size grid is selected for all the computations as shown in Fig. 3. For validation of the in-house solver, the numerical results of the surface pressures at cowl side are compared with the experimental results of Devaraj et al. [2] as shown in Fig. 2, which are found to be in good agreement.

4 Results and Discussion

This section illustrates the flow characteristics at the intake, classifying it into two categories, i.e., with and without the addition of energy hot spots' upstream of the intake at different Mach numbers. The freestream conditions are mentioned in Table 2.

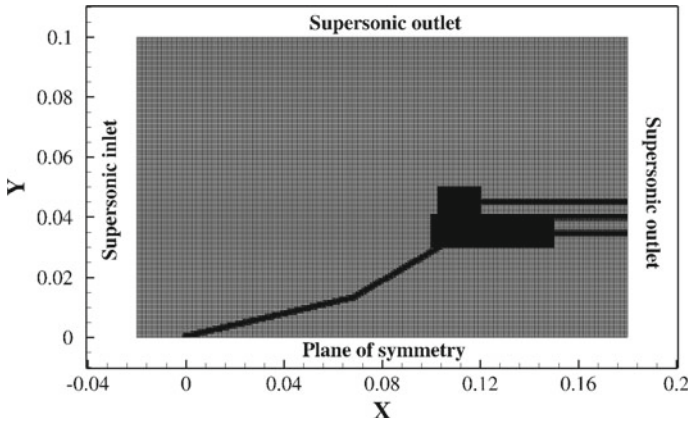


Fig. 3 Grid for computational domain with boundary conditions

Table 2 Freestream parameters used in simulations

M_∞	4.5	5
$P_{0\infty}$	7.55 bar	7.55 bar
$T_{0\infty}$	423.8 K	423.8 K

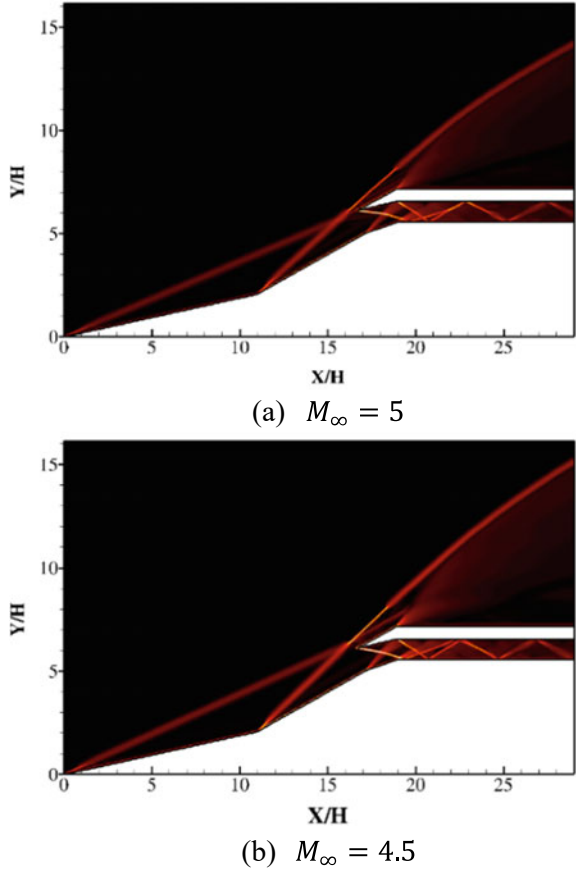
The flow is compared for the two conditions, i.e., with and without energy addition by using two performance parameters, namely, mass capture ratio and pressure recovery factor, as displayed in Eq. 3. Here, mass capture ratio (ϕ_m) is defined as the ratio of actual amount of mass entering the Scramjet intake to the mass that ideally should enter inside Scramjet inlet which is coming from far field. The pressure recovery factor (π_p) is defined as the ratio of the pressure at isolator exit to the freestream pressure.

$$\phi_m = \frac{\dot{m}_c}{\dot{m}_\infty}; \pi_p = \frac{P_{iso}}{P_\infty} \tag{3}$$

A. Without Energy Addition

The flow fields at Mach numbers 5 and 4.5 are shown in Fig. 4 in the form of density Schlieren images and the corresponding pressure contours are displayed in Fig. 7. It can be observed that in both Mach 5 and Mach 4.5, the external ramp shocks are slightly away from the cowl tip, i.e., not satisfying shock-on-lip (SOL) condition which leads to mass spillage from the intake and also causes less pressure recovery at the isolator exit. Here, at $M_\infty = 5$, (ϕ_m) = 0.874 and (π_p) = 0.536, whereas at $M_\infty = 4.5$, (ϕ_m) = 0.781 and (π_p) = 0.629. Thus, it can be said that with decrease in free stream Mach number, mass spillage is seen to increase as the shock moves away from the cowl tip; however, the pressure recovery is also seen to increase. Mach

Fig. 4 Numerical Schlieren images of flow field without energy deposition at different Mach numbers



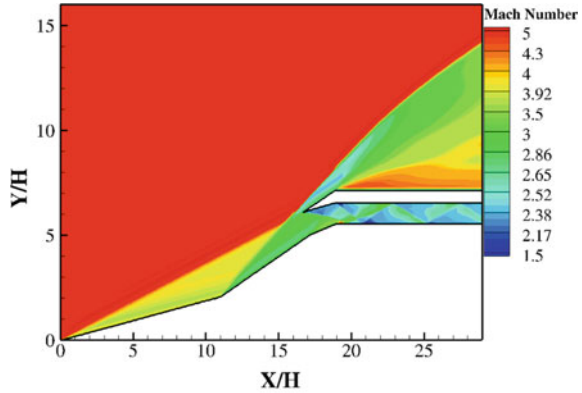
number and temperature contours of the flow fields are presented in Fig. 5 and Fig. 6, respectively (Fig. 7).

B. With Energy Addition

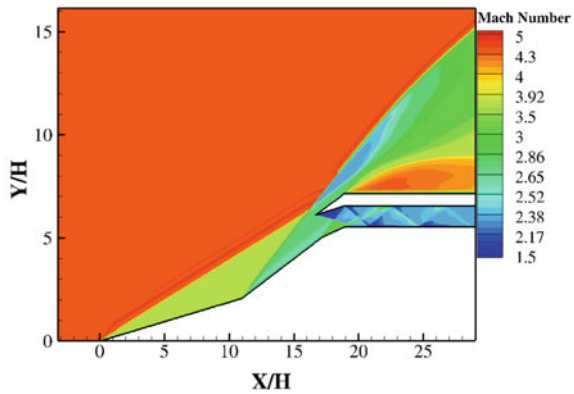
With the introduction of energy upstream of the intake entrance, it can be observed that a parabolic shock is formed that deflects the upstream flow into the inlet. As a result, it is expected that greater air mass flow and less spillage can be achieved, especially at off design Mach numbers where the shock-on-lip (SOL) condition is not satisfied.

- 1 Effect of energy strength: To understand the effect of energy strengths on the flow field, two different amounts of energies (10 and 30 MW/m³) were added over a spherical zone of radius 1mm at location 1 for $M_\infty = 5$, as shown in Fig. 8 in the form of density Schlieren images. In both the cases, formation of a parabolic shock is clearly visible, and as a result of its interaction with the ramp compression shock, more flow deflection inside the Scramjet inlet as compared

Fig. 5 Mach number contours of flow field without energy deposition



(a) $M_\infty = 5$

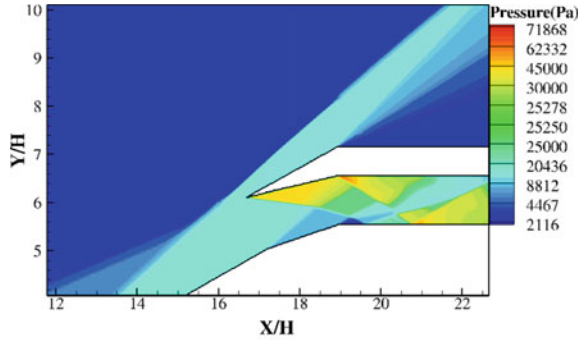


(b) $M_\infty = 4.5$

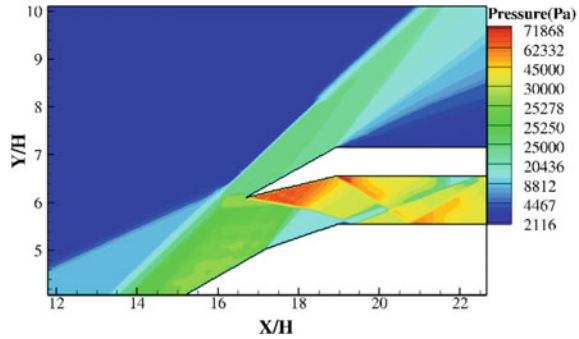
to Fig. 4a. can be clearly seen. From the pressure contours in Fig. 9, it can be deduced that the strength of shock due to energy addition in $10\text{MW}/\text{m}^3$ is less than that of $30\text{MW}/\text{m}^3$; as a consequence, more flow is diverted toward the intake. This can be concluded by the mass capture ratio as well, at $10\text{MW}/\text{m}^3$, $(\phi_m) = 0.896$, and $(\pi_p) = 0.549$, whereas at $30\text{MW}/\text{m}^3$, $(\phi_m) = 0.917$, and $(\pi_p) = 0.531$. However, the pressure recovery factor reduces. This is because air expands due to high energy deposition that affects the stagnation pressure at the throat. Also, the function of inlet is to provide compressed air to combustor; therefore, the expansion is an adverse factor. Moreover, as seen in temperature contour (Fig. 10), higher energy deposition results in higher temperatures near the cowl, which can result in wearing out of the cowl. Therefore, in the following section, we will study the effect of energy deposition at a location above the cowl.

- 2 Effect of energy deposition location: To study the effect of energy location, $30\text{MW}/\text{m}^3$ of energy was deposited at both the locations (1 and 2) for $M_\infty = 4.5$. Density Schlieren images of the resultant flow field can be seen in Fig. 11 and

Fig. 6 Temperature contours of flow field without energy deposition



(a) $M_\infty = 5$

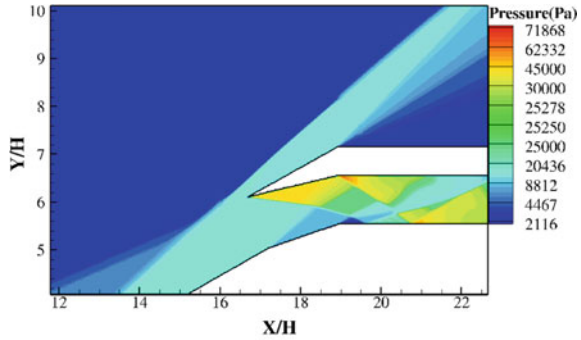


(b) $M_\infty = 4.5$

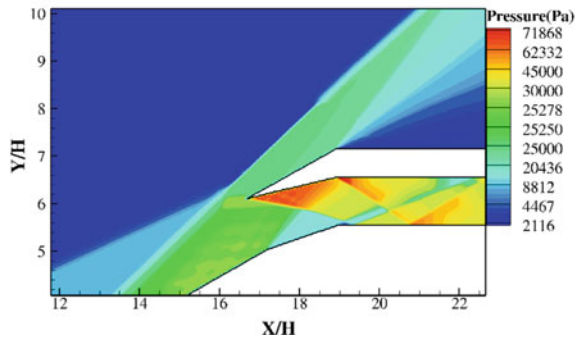
the corresponding pressure contours are shown in Fig. 12. The distinct difference in shock interaction pattern near the ramp shoulder is noticeable for the different energy deposition locations. The shock formed by the energy hot spot at location 2 interacts with external shocks almost at the cowl tip level and thus deflects more mass of air inside the isolator than the case when energy is added at location 1, in which the shock interaction zone is below the cowl level. Here, at location 1, $\phi_m = 0.814$ and $\pi_p = 0.637$, whereas, at location 2, $\phi_m = 0.825$ and $\pi_p = 0.668$. Thus, it can be said that with shifting the energy deposition location vertically upward, mass capture is seen to increase. Also, the adverse effect of high strength energy on pressure recovery factor is controlled and it is seen to increase.

Thus, taking the above points in consideration, the location for energy deposition is preferred to be above the cowl level, so that heated expanded air would miss the inlet, allowing cold and compressed to deflect into the inlet. This will also help in protection of the cowl from wearing out.

Fig. 7 Pressure contours of flow field without energy deposition at different Mach numbers



(a) $M_\infty = 5$



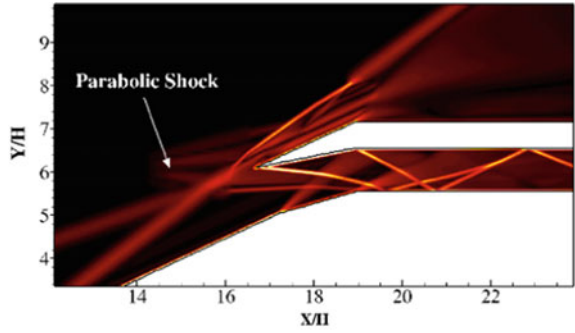
(b) $M_\infty = 4.5$

5 Conclusions

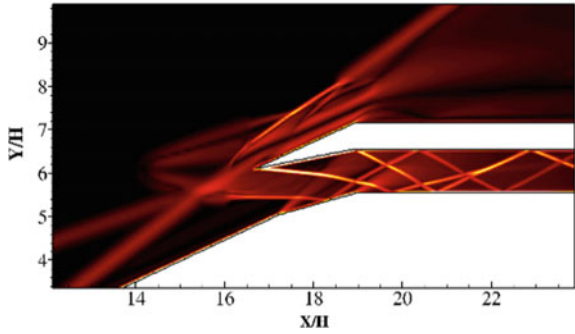
This paper brings forward energy addition as an active flow control method for high compression hypersonic inlets at off-design conditions. The effects of the amount of energy deposited at two different locations were investigated based on two performance parameters. The results of the studies show that depositing energy always led to increase in mass capture ratio; however, the same cannot be said for pressure recovery factor.

At $M_\infty = 5$, introducing energy deposition, a maximum increment of ϕ_m and π_p was achieved by 4.86% and 2.26%, respectively. Also, at $M_\infty = 4.5$, the maximum change in the values of ϕ_m and π_p was found to be 5.82% and 6.05%, respectively, as compared to without energy addition. It is also noted that the addition of energy above the cowl tip level showed better mass flow ratio than that at the cowl tip level.

Fig. 8 Numerical Schlieren images at $M_\infty = 5$ with different energy deposition strengths at location 1

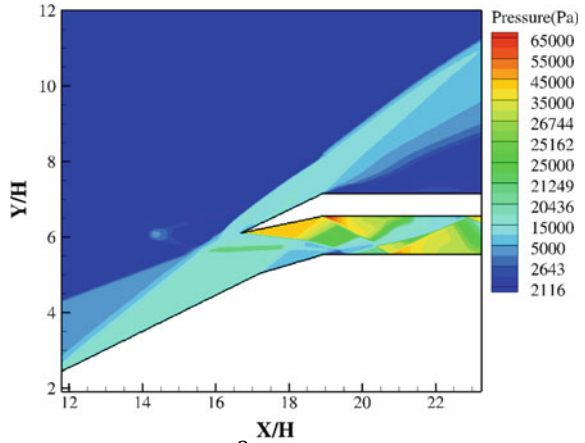


(a) 10 MW/m^3 energy deposition

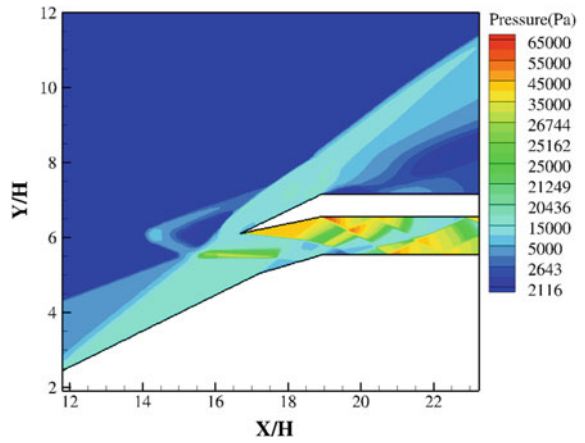


(b) 30 MW/m^3 energy deposition

Fig. 9 Pressure contours at $M_\infty = 5$ with different energy deposition strengths at location 1

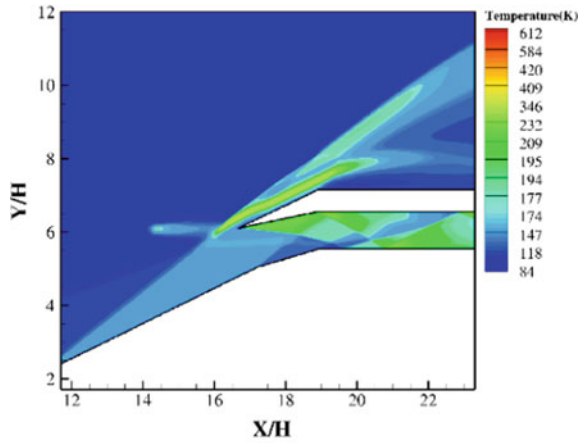


(a) 10 MW/m^3 energy deposition

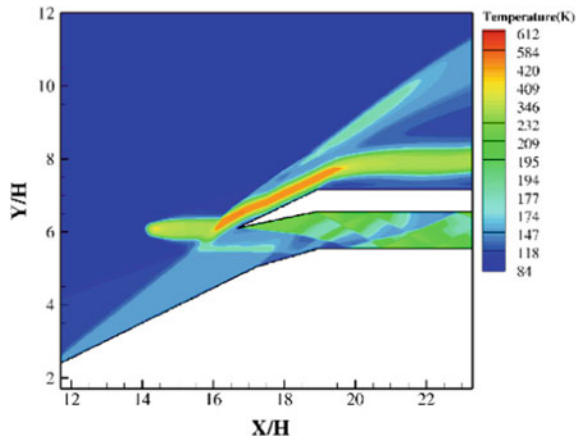


(b) 30 MW/m^3 energy deposition

Fig. 10 Temperature contours at $M_\infty = 5$ with different energy deposition strengths at location 1

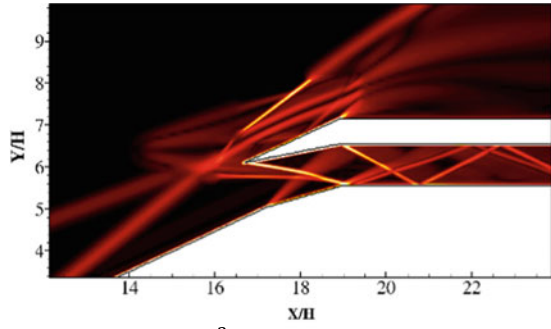


(a) 10 MW/m^3 energy deposition

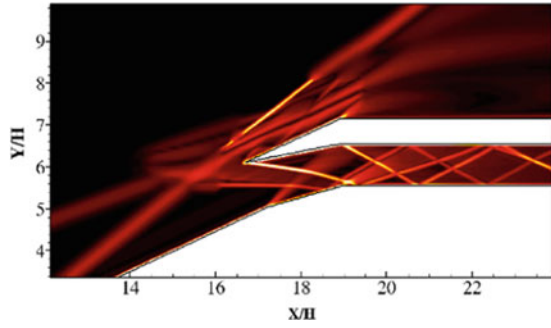


(b) 30 MW/m^3 energy deposition

Fig. 11 Numerical Schlieren images at $M_\infty = 4.5$, With 30 MW/m^3 energy deposition at different locations

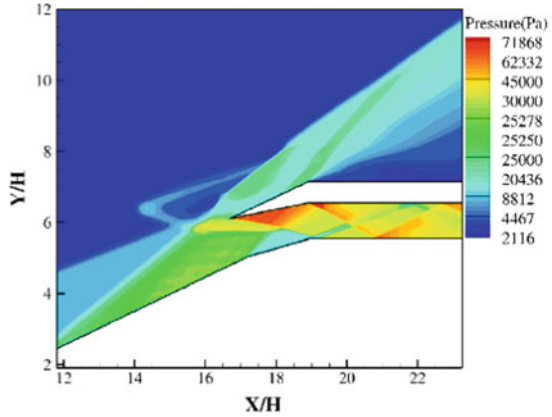


(a) 30 MW/m^3 energy deposition at location 2

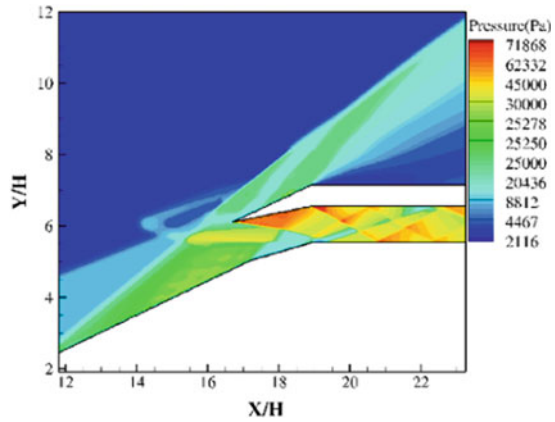


(b) 30 MW/m^3 energy deposition at location 1

Fig. 12 Pressure contours at $M_\infty = 4.5$, With 30 MW/m^3 energy deposition at different locations



(a) 30 MW/m^3 energy deposition at location 2



(b) 30 MW/m^3 energy deposition at location 1

Nomenclature

- A_∞ Area at far field [mm^2]
- A_c Area at Scramjet inlet [mm^2]
- A_e Area at isolator exit [mm^2]
- α Angle ($^\circ$)
- L Length [mm]
- H Isolator height [mm]
- u Velocity in x direction [m/s]
- v Velocity in y direction [m/s]
- E Energy [J]
- M Mach number
- ∞ Free stream conditions

References

1. Chang J, Li N, Xu K, Bao W, Yu D (2017) Recent research progress on unstart mechanism, detection and control of hypersonic inlet. *Prog Aerosp Sci* 89:1–22
2. Devaraj MKK, Jutur P, Rao SM, Jagadeesh G, Anavardham GT (2021) Investigation of local unstart in a hypersonic scramjet intake at a mach number of 6. *Aerosp Sci Technol* 115:106789
3. Wagner JL, Yuceil KB, Valdivia A, Clemens NT, Dolling DS (2009) Experimental investigation of unstart in an inlet/isolator model in mach 5 flow. *AIAA J* 47(6):1528–1542
4. Falempin F, Wendling E, Goldfeld M, Starov A (2006) Experimental investigation of starting process for a variable geometry air inlet operating from Mach 2 to Mach 8. In: 42nd AIAA/ASME/SAE/ASEE Joint Propulsion Conference & Exhibit, p 4513
5. Teng J, Yuan H (2015) Variable geometry cowl sidewall for improving rectangular hypersonic inlet performance. *Aerosp Sci Technol* 42:128–135
6. Gutierrez DR, Poggie J (2018) Effects of power deposition on the aerodynamic forces on a slender body. *AIAA J* 56(7):2911–2917
7. Riggins D, Nelson HF, Johnson E (1999) Blunt-body wave drag reduction using focused energy deposition. *AIAA J* 37(4):460–467
8. Macheret SO, Shneider MN, Miles RB (2004) Scramjet inlet control by off-body energy addition: a virtual cowl. *AIAA J* 42(11):2294–2302
9. Liou MS, Steffen CJ Jr (1993) A new flux splitting scheme. *J Comput Phys* 107(1):23–39
10. Blazek J (2015) *Computational fluid dynamics: principles and applications*. Butterworth-Heinemann
11. Ghias R, Mittal R, Dong H (2007) A sharp interface immersed boundary method for compressible viscous flows. *J Comput Phys* 225(1):528–553

Effect of Geometric Parameters on Steady-State Supersonic Film Cooling of the Basic Conical Rocket Nozzle



V. M. Rahul and N. Gnanasekaran

Abstract The current study proposes simulation results of supersonic film cooling of rocket nozzle by varying the geometric parameters. The study reveals that as the width of the injector opening for coolant injection was altered, the temperature variation trend near the walls differed based on the extent to which the width was increased or decreased. The results captured are shown in upcoming sections of this work. The second parameter varied was the angle of injection, where the variation of the cooling temperature after the injection point and the turbulence variation as a function of axial length were mainly focused. The temperature, turbulence, pressure, and density variation are also shown by varying the above parameters as a function of the axial length of the nozzle. The fluid used for primary and secondary flows was the air with different inlet and outlet pressures and temperatures as boundary conditions.

Keywords Supersonic film cooling · Injector · Rocket nozzle · Primary and secondary flows · Boundary conditions

1 Introduction

The high-temperature mainstream (primary) flow in the diverging region of the nozzle at supersonic speed can be effectively cooled by a secondary flow called the film cooling injected through the injectors. The primary flow (mainstream) at a very high temperature can interact with the nozzle material, and these high temperatures can damage them. Hence, it is necessary to cool down the flow near the solid–fluid interface in the nozzle and mainstream. Cooling methods for rocket nozzles can be achieved by various means, such as ablative cooling, regenerative cooling,

V. M. Rahul (✉) · N. Gnanasekaran
Department of Mechanical Engineering, National Institute of Technology Karnataka Surathkal,
Mangalore 575025, India
e-mail: rahulvm.191me163@nitk.edu.in

N. Gnanasekaran
e-mail: gnanasekaran@nitk.edu.in

© The Author(s), under exclusive license to Springer Nature Singapore Pte Ltd. 2024
K. M. Singh et al. (eds.), *Fluid Mechanics and Fluid Power, Volume 2*, Lecture Notes in
Mechanical Engineering, https://doi.org/10.1007/978-981-99-5752-1_68

841

radiative cooling, film cooling. But this study focuses on supersonic film cooling. Other parameters, along with temperature, are also analyzed in this work, such as turbulence, density, and pressure variations near the fluid–solid interface region of the nozzle. Since the main focus is on cooling, the temperature is the parameter that will look upon, and the cooling efficiency, also called the “Effectiveness” of film cooling, will be calculated and compared to validate the variation trend of the plots. The film cooling effectiveness expression is given below, where

$$\text{Effectiveness} = \frac{T_{\text{with film cooling}} - T_{\text{coolant}}}{T_{\text{without film cooling}} - T_{\text{coolant}}}$$

The expression takes the ratio of the difference in temperature between hot and cold fluids with coolant and without coolant.

2 Literature Review and Objective

Based on the studies by Vijayakumar et al. [1], a study was done on a scaled model of the rocket nozzle, and numerical simulations and experimentation were carried out to validate the results. Sun et al. [2] study to analyze the effect of mixing fluids for supersonic film cooling in the flow field caused by shock waves using different coolant fluids for secondary flows. Ludescher and Olivier [3] studied the film cooling of rocket nozzles and developed models to calculate cooling efficiency from experimental data. Narayana and Reddy [4] did a CFD analysis of a convergent-divergent rocket nozzle by varying the mesh quality and obtaining results for various parameters. The simulations in this work were carried out in ANSYS 2022 [5]. The nozzle theory is referred to the Yunus and Cengel [6]. All the researches carried out in liquid rocket engine film cooling since 1950 are brought together in work done by Shine and Nidhi [7]. Sullivan and Geoffrey [8] focused on the film and transpiration cooling used on bell nozzle geometries and determined their effectiveness on aerospoke nozzle geometries. Kumar et al. [9] proposed Supercritical N₂O as an active coolant for cooling aerospoke nozzles. Shahin and Attar [10] analyzed the transient flow characteristics representing the normal shock wave propagation during the rocket startup process.

The purpose of this study is to first analyze the parameters by varying them, such as injection opening width and the injection angle, and observe the variation in resulting parameters, such as temperature, turbulence, density, and pressure. Based on the simulation data, develop a mathematical model to find the temperature and its effectiveness for a given geometry of the rocket nozzle. This work mainly focuses on the initial part, which consists of the observations made on various output parameters (temperature, turbulence, etc.) upon varying the geometric parameters.

3 Materials and Methods

The current study used some boundary conditions from Vijayakumar et al. [1], which had an experimental setup and numerical simulation. The model used in this study was the turbulent model: k-epsilon 2 equation model (Realizable) with standard wall functions for the near-wall treatment. The fluid used for both primary and secondary flows was air, assumed to be an ideal gas with constant specific heat and thermal conductivity.

The viscosity model used is per Sutherland’s equation, which is based on the kinetic theory of gases. The domain geometry from Narayana and Reddy [4] has been modified for adding injectors after the throat area.

The Nozzle is a basic conical-shaped one with dimensions, as shown in Fig. 1, and has been scaled up by a factor of 20. The secondary injector is present after the throat area with its cross-section width as D , and the angle made by the injector with the x-axis is considered as θ (Fig. 2).

3.1 Parameters Analyzed

Variations of the parameters such as the injection opening width D , injection angle θ , in the range 0.42–0.66 mm for D , and -10° to $+30^\circ$ for θ gave good results for observing variation in the trends of the plots of the resulting parameters for different widths and angles. These results were obtained with the boundary conditions

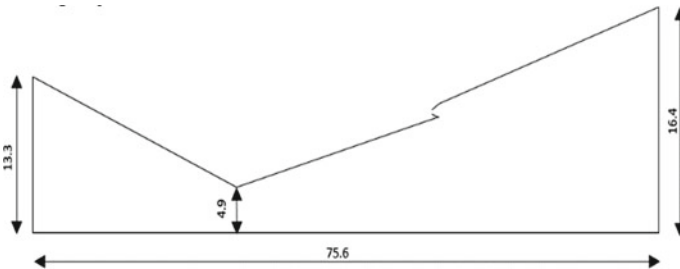
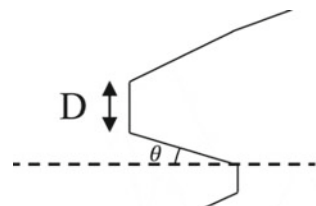


Fig. 1 Dimensions of the domain (in mm)

Fig. 2 Dimensions of the injector



(modified from Vijayakumar et al. [1]) having 10^6 Pa, 1258 K at the inlet and 1.03×10^5 Pa, and 303 K at the secondary inlet. And, the outlet is kept at a vacuum (gauge pressure) and 300 K.

3.2 *Grid Independent Study*

The meshing of the 2D model was carried out by fine-tuning the region in the throat area and the secondary injection region of the nozzle. Upon varying the number of elements, a grid-independent study was carried out to check the convergence of the solution obtained. Since the solution converged at a very large number of elements, which slowed down the computation time, adaptive sizing was implemented after refining the throat and the injection area. This method reduced the number of elements and gave the results very close to the results converging upon using many elements. This improvement reduced the computation time and made it easy to carry out numerous iterations of simulation of varying widths and angles. The convergence test was carried out by implementing this adaptive sizing in meshing, due to which the resulting mesh was more organized.

The images shown in Figs. 3 and 4 have their domain meshing without adaptive sizing. The computation time taken was even lesser upon adaptive sizing since the number of elements was reduced.

The images shown in Figs. 5 and 6 are the ones with adaptive sizing for the same meshing conditions. After varying the elements' size, the lowest temperature after the secondary injection was plotted (Fig. 7) for the convergence test.

Fig. 3 Domain mesh without adaptive sizing

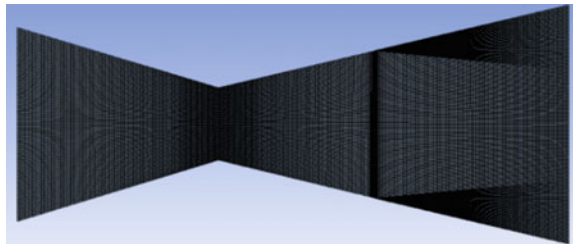


Fig. 4 Injector domain mesh without adaptive sizing

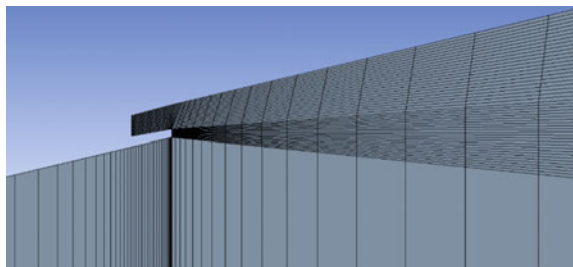


Fig. 5 Domain mesh with adaptive sizing

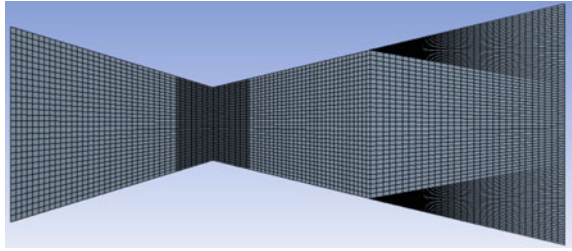


Fig. 6 Injector domain mesh with adaptive sizing

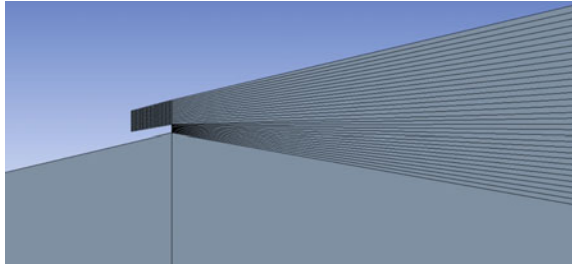
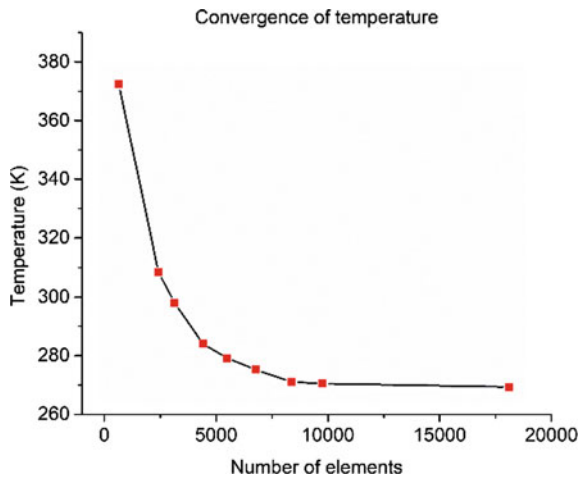


Fig. 7 Temperature convergence test



The solution converged within (~15,000) elements. Meshing was done for (~10,800) elements to improve the computation speed without much loss of accuracy. The convergence graph for the increasing number of elements is shown in Fig. 7.

3.3 Model Validation

The domain geometry was taken from the study done by Narayana and Reddy [4] to validate the current simulation results. Their study describes steps to simulate a rocket nozzle in ANSYS by varying the mesh and plotting graphs of various parameters. As per their study, the meshing condition (Mesh-1) is simulated. The resulting static pressure and Mach number values are shown in Table 1. The results closely matched the values given, and the study was carried out further by making modifications to introduce the secondary injector as described in Sect. 3. The film cooling *effectiveness* plot shown in Fig. 8 had a similar trend to the study conducted by Ludescher and Olivier [3] (with similar contour plot for Mach number as shown in Fig. 9).

Table 1 Comparison of data for validation

Parameter	Validation values	Simulation values
Mach number	2.79	2.80
Pressure (KPa)	292.78	291.56

Fig. 8 Film cooling effectiveness for varying widths

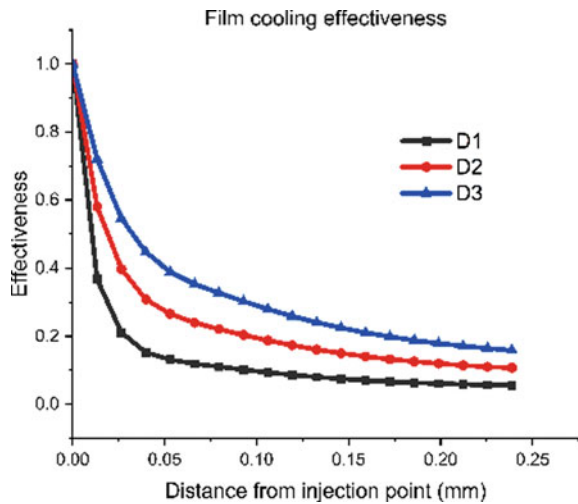
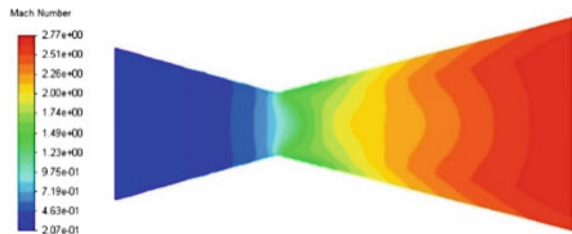


Fig. 9 Mach number contour for validation



4 Results and Discussion

The analysis was carried out by varying the widths D and the angles θ . The contour plots for resulting parameters such as temperature, pressure, and density for D (0.6 mm) and A (13.46°) are shown in Figs. 10, 11, and 12.

The injection temperature cooled down the nozzle’s surface by forming a layer or a film, and its effectiveness was observed up to a certain distance from the injection point (Fig. 13).

4.1 Effect of Varying Widths (D)

The width D was varied in the range (0.42–0.66 mm), and the temperature plot variation is shown in Fig. 14. The increase in the width cooled the nozzle to a much lower temperature, and the temperature rise after cooling was also more gradual than the iterations with comparatively smaller values of D . As a general observation,

Fig. 10 Temperature contour

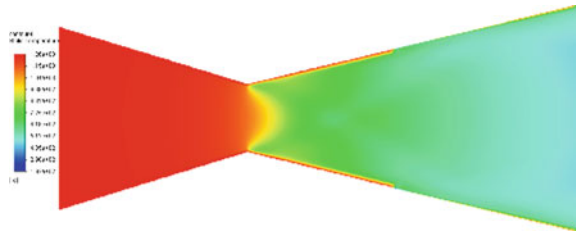


Fig. 11 Pressure contour

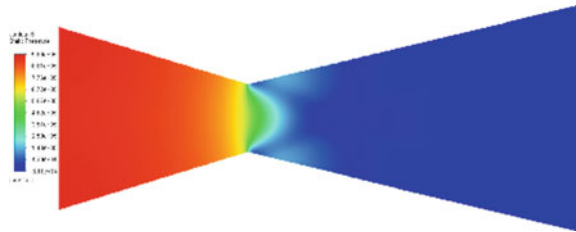


Fig. 12 Density contour

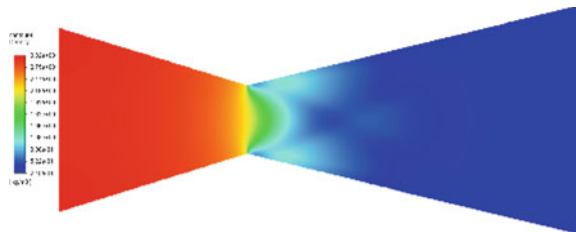


Fig. 13 Temperature contour at the secondary injection

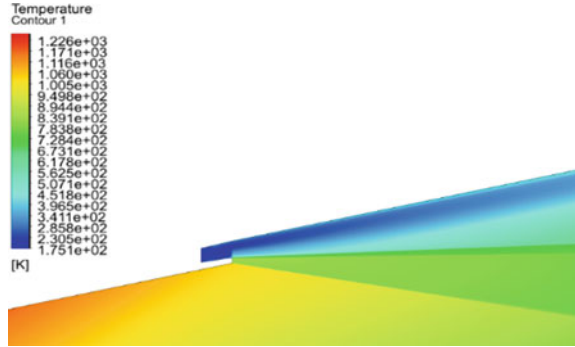
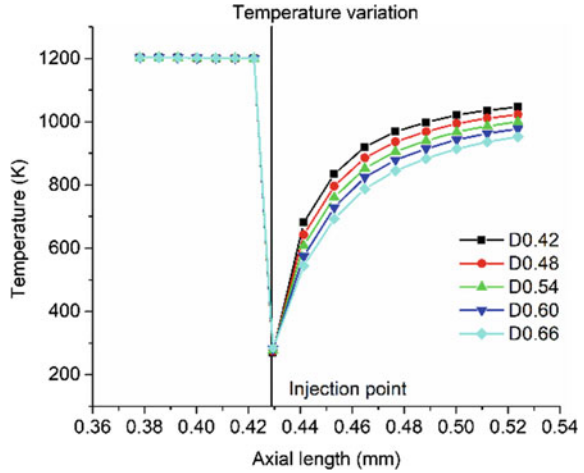


Fig. 14 Temperature versus axial length (varying D)



the larger the secondary injection area, the higher the cooling efficiency. But as the width got smaller, the rate of rise in temperature after the secondary coolant injection point increased. Variations of other parameters are also plotted for varying widths (Figs. 15, 16 and 17).

Since the outlet pressure was kept vacuum, the pressure near the nozzle walls goes below zero, ensuring that the mainstream fluid is spread throughout the diverging section of the nozzle, preventing flow separation from the nozzle walls.

4.2 Effect of Varying Angles (θ)

Variation of parameters as a function of injection angle was plotted where they all reached a peak value when the injection angle aligned to 13.46° , opposite to the nozzle semi-cone angle of the similar magnitude (-13.46°) (Figs. 18 and 19).

Fig. 15 Turbulent kinetic energy versus axial length (varying D)

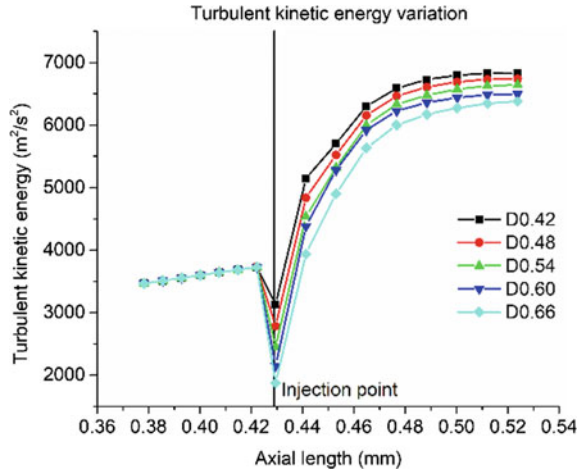
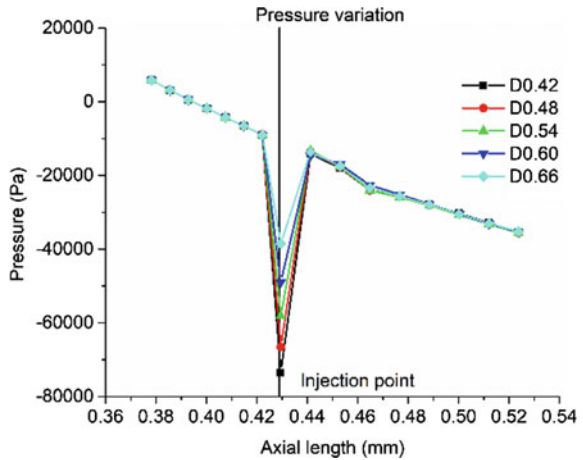


Fig. 16 Pressure versus axial length (varying D)



The effect of varying the injection angle on temperature was not very significant compared to the variation of width D , yet the lowest peak was present at 13.46° .

The turbulence increases when the injection angle aligns opposite to the nozzle's semi-cone angle (13.46°) (Figs. 20 and 21).

5 Conclusions

The film cooling method for the rocket nozzle can significantly cool down the nozzle wall from mainstream temperatures, provided that the angle and the width of the injector opening are appropriate enough. Without which too low D values can increase

Fig. 17 Density versus axial length (varying D)

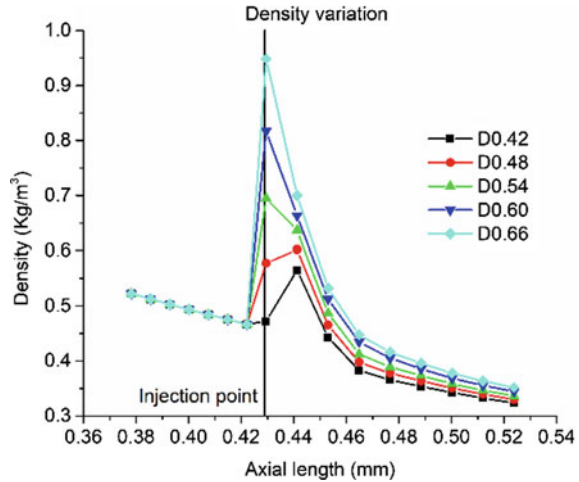
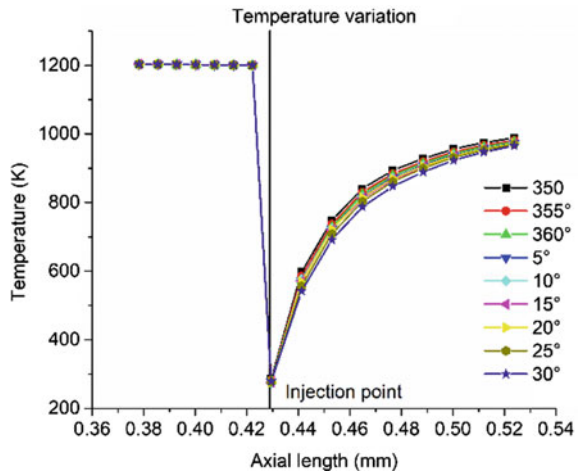


Fig. 18 Temperature versus axial length (varying θ)



the rate of temperature rise after injection compared to cases of larger width. Similarly, the injection angle was effective when it was oriented opposite to the nozzle wall's inclination (nozzle semi-cone angle of 13.46°). The apparent variations that could be concluded from the plots of output parameters at the injection point as a function of increasing width D (Figs. 14, 15, 16 and 17) and aligning the injection angle opposite to the Nozzle's semi-cone angle (as a result of variations observed in the Figs. 18, 19, 20, 21, 22, 23, 24 and 25) are given in Tables 2 and 3.

Further, these data values are being used to develop a mathematical model in further studies for temperature prediction as a function of the axial length of the nozzle and width D as the input values for the chosen geometry and boundary conditions.

Fig. 19 Lowest temperature versus injection angle (θ)

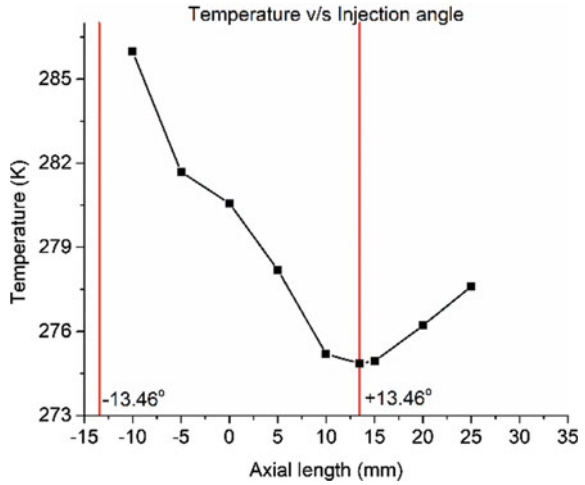
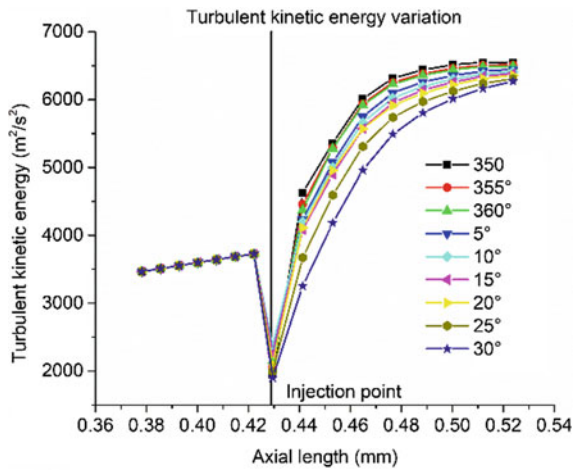


Fig. 20 Turbulent kinetic energy versus axial length (varying θ)



These models will assist in finding out the temperature values, thereby reducing the computation time and effort.

Fig. 25 Density versus injection angle (θ)

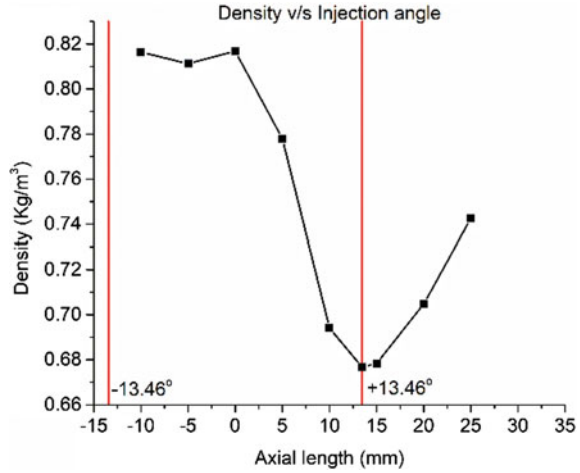


Table 2 Effect on parameters with increasing injection width (D)

Parameters (near injection point)	Variation
Temperature	Decrease
Turbulent kinetic energy	Decrease
Pressure	Increase
Density	Increase

Table 3 Effect on parameters with aligning injection angle opposite to nozzle semi-cone angle

Parameters (near injection point)	Variation
Temperature	Decrease
Turbulent kinetic energy	Increase
Pressure	Decrease
Density	Decrease

Acknowledgements The author would like to thank the supervisor, Dr. Gnanasekaran N., for supporting and guiding me throughout this work. The author and Dr. Gnanasekaran N. would like to thank the 9th International and 49th National Conference on Fluid Mechanics and Fluid Power (FMFP)-2022 for allowing us to present this work.

Nomenclature

- D Injection width (mm)
- θ Injection angle (degree)

References

1. Vijayakumar V, Pisharady J, Balachandran P (2015) Computational and experimental study on supersonic film cooling for liquid rocket nozzle applications. *Therm Sci* 19(1):49–58. <https://doi.org/10.2298/TSCI120908077P>
2. Sun X, Ni H, Peng W, Jiang P, Zhu Y (2021) Influence of shock wave impinging region on supersonic film cooling. *Chin J Aeronaut* 34(5):452–465. <https://doi.org/10.1016/j.cja.2020.12.012>
3. Ludescher S, Olivier H (2021) Film cooling in rocket nozzles, pp 65–78. https://doi.org/10.1007/978-3-030-53847-7_4
4. Narayana KPSS, Reddy KS (2016) Simulation of convergent divergent rocket nozzle using CFD analysis. *IOSR J Mech Civil Eng* 13(04):58–65. <https://doi.org/10.9790/1684-1304015865>
5. ANSYS Inc. (2022) ANSYS fluent theory guide
6. Yunus JMC, Cengel A (2017) Fluid mechanics: fundamentals and applications, vol 4
7. Shine SR, Nidhi SS (2018) Review on film cooling of liquid rocket engines. *Prop Power Res* 7(1):1–18. <https://doi.org/10.1016/j.jppr.2018.01.004>
8. Sullivan, Geoffrey (2022) CFD and heat transfer analysis of rocket cooling techniques on an aerospike nozzle
9. Kumar A, Saini V, Usurumarti PR, Dondapati RS (2017) Feasibility studies on the cooling of hybrid rocket nozzles using supercritical nitrous oxide. *Energy Proc* 109:338–345. <https://doi.org/10.1016/j.egypro.2017.03.080>
10. Shahin A, El Attar A (2017) Numerical simulation of a rocket propulsion nozzle during the startup condition

Effect of Nozzle Internal Shape on Near-Field Characteristics of Transverse Liquid Jet in a Supersonic Crossflow



Chandrasekhar Medipati, S. Deivandren, and R. N. Govardhan

Abstract We experimentally investigated the effect of orifice geometry on the characteristics of a transversely injected liquid jet into a supersonic crossflow. The focus was to highlight the role of orifice inlet shape on the liquid jet penetration and associated bow shock dynamics. It was found that for a given momentum flux ratio, the liquid jet from a sharp-edged nozzle exhibits higher jet penetration and bow shock strength compared to that from a tapered inlet nozzle. High-speed shadowgraphy images show that the observed variation in the jet penetration and bow shock position is due to strong shock wave–boundary layer interaction in the flow. Quantitative measurements of the jet penetration height and shock fluctuations are obtained for both nozzles. The fluctuations of liquid jet injected through the tapered inlet nozzle have significantly higher in the spatial extent compared to that of the sharp-edged nozzle.

Keywords Liquid jet · Bow shock · Shock wave–boundary layer interaction · High-speed shadowgraphy · Momentum flux ratio

1 Introduction

Transverse injection of liquid jet into supersonic crossflow finds its application in Scramjet combustors. In these combustors, the residence of incoming supersonic air in the combustor is extremely limited, and hence, the efficient atomization and mixing of the liquid fuel with the air are very crucial.

C. Medipati (✉)

Interdisciplinary Centre for Energy Research, Indian Institute of Science, Bangalore, India
e-mail: mchandrashek@iisc.ac.in

S. Deivandren

Department of Aerospace Engineering, Indian Institute of Science, Bangalore, India

R. N. Govardhan

Department of Mechanical Engineering, Indian Institute of Science, Bangalore, India

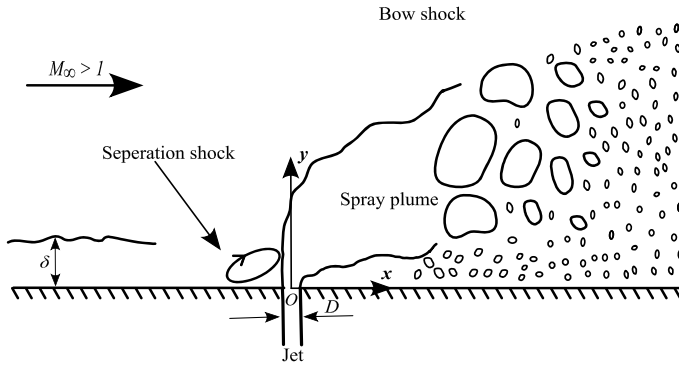


Fig. 1 Schematic of liquid jet into supersonic crossflow

As shown in Fig. 1, the injection of transverse liquid jet into supersonic crossflow results in the formation of 3D bow shock and separation shock, and the interaction between these shocks and the incoming turbulent boundary layer leads to significant shock wave boundary layer interaction. Also, due to the strong exchange of momentum between the crossflow and the jet resulting in atomization of the jet into very fine drops.

2 Literature Review and Objective

The injection of liquid jets in subsonic crossflow has been studied extensively in the recent past. Measurement of penetration of liquid jet into crossflow is an important information for the design of the combustors; hence, large body of literature is focussed on formulation of empirical correlations of spray trajectory. The penetration height and drop size depend strongly on the momentum flux ratio (J) [1] defined as the ratio of momentum flux of the liquid injected to that of the crossflow, exit condition of the liquid jet [2, 3], and the internal shape of the orifice [4]. There have been several initial studies in the supersonic crossflow where the attention is mainly focussed on measurement of penetration heights using shadowgraphy [5, 6] and PDPA [7]. Also, spray characteristics like drop size and its velocity variations are measured using PDPA [7]. Not much attention is given on the effect of the inlet geometry of the orifice on the jet penetration and the shock structures which is very important for the design of efficient supersonic combustors. Our objective of the present study is to experimentally investigate the effect of internal shape (round and sharp edged) of the circular orifice on jet penetration and shock location characteristics, and their unsteadiness when injected into supersonic crossflow keeping the injection location (incoming turbulent boundary layer) and momentum flux ratio between the orifice shapes are same for the entire study.

3 Methodology

All the experiments in the current study are done using the open-circuit blow down wind tunnel at the department of ICER, Indian Institute of science. The tunnel test section cross-section is 15 cm × 15 cm and a length of 1 m. In the entire study, free stream Mach number is kept at 2.5 by maintaining the settling chamber pressure of about 2.8 bar which corresponds to a mass flow rate of 8 kg/s. Both side and top walls of the test section are transparent to provide optical access. Using PIV, the free stream velocity and the turbulence level in the test section were measured and found to be 585 m/s and 1.5% of the free stream velocity, respectively [8].

A high-pressure liquid injection system line is used to deliver liquid into supersonic crossflow. It comprises a liquid chamber, pressure regulator, mass flow metre, flow control valve, pressure gauge, and solenoid valve as shown in Fig. 2. Water is used as the injectant liquid in the entire study. Experiments were conducted with two different nozzle geometries, namely tapered inlet and sharp-edged inlet nozzles, with exit diameters $D = 1$ and 1.2 mm, respectively. In both the cases, the value of L/D is 2. The schematic view of these nozzles is shown in Fig. 3. In the entire study, x , y , and z directions represent streamwise, cross-streamwise, and spanwise directions, respectively.

Both the nozzles were placed at the same streamwise location to ensure that the crossflow turbulent boundary layer thickness approaching the jet would be the same for each ($\delta = 8.85$ mm).

A. High-Speed Shadowgraphy

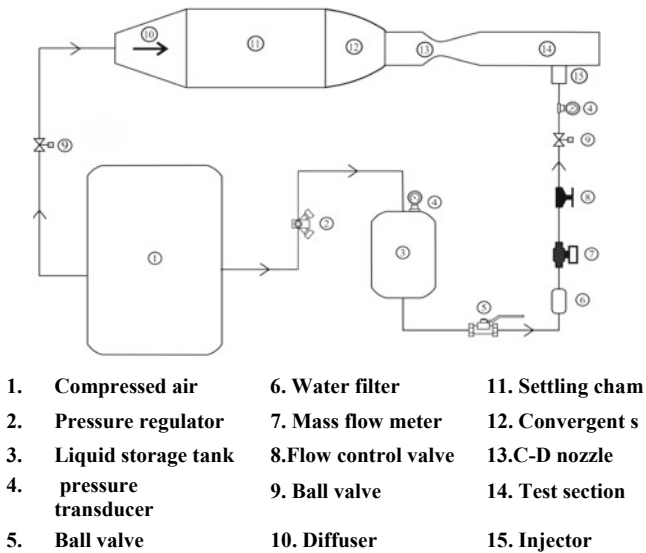


Fig. 2 Schematic of supersonic wind tunnel

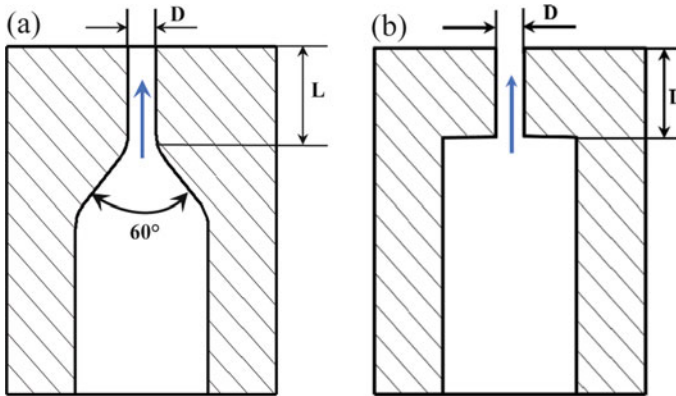


Fig. 3 Schematic of **a** tapered inlet nozzle **b** sharp-edged inlet nozzle

High-speed shadowgraphy is employed for the simultaneous visualization of both shock and the windward edge of the jet. It comprises a 150 W halogen lamp (as light source), condenser lens, a spherical concave mirror, and a high speed Photron camera with 105 mm lens as shown in Fig. 4. A collimated light beam is transmitted through the side window (from back) and the density gradients in the flow were captured with a microsecond exposure at 10,000 fps using the high-speed camera through the other side window (front). The narrow field of view of 10 mm × 15 mm close to the injector exit with a pixel resolution of 0.04 mm/pixel is used in the current study. Choosing a narrow field of view along with the high-speed imaging is extremely helpful to understand the near-field characteristics of shock, windward edge, and their interaction and quantify their unsteadiness.

B. Experimental Details

In the present work, we experimentally study the effect of nozzle internal shape on the interaction between the shock and the windward edge. The important flow parameters used are given in Table 1.

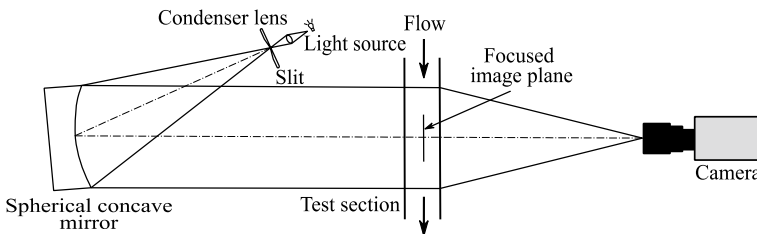


Fig. 4 Schematic of high-speed shadowgraphy

Table 1 Experimental parameters

Parameter	Value
Mach number, $M_\infty = \frac{U_\infty}{\sqrt{\gamma RT_\infty}}$	2.5
Momentum flux ratio, $J = \frac{\rho_j U_j^2}{\rho_\infty U_\infty^2}$	7
Weber number, $We_\infty = \frac{\rho_\infty U_\infty^2 D}{\sigma}$	2403 (1 mm) 2884 (1.2 mm)
Ohnesorge number, $Oh_j = \frac{\mu_j}{\sqrt{\rho_j D \sigma}}$	0.001

4 Results and Discussion

4.1 Instantaneous Images

Figures 5 and 6 represent the instantaneous side view temporally correlated images of liquid jet from the tapered nozzle and sharp-edged nozzle, respectively, for $J = 7$. It is evident from these images that the formation of shock structures and the windward edge (mixing layer) as the jet traverses into the crossflow are completely different.

In the present study, the liquid jet injected from the sharp-edged inlet nozzle has the stronger intact liquid column length for about $y/D = 5$ (from the average) with almost no perturbations unlike the tapered case where the liquid jet is coming out with fluctuations. Due to the presence of stronger intact liquid column at the nozzle exit in the sharp-edged nozzle case helps in increasing the penetration of liquid jet into the crossflow. The liquid structures formed in the windward side are almost ten times larger in the sharp-edged case compared to tapered nozzle. Apart from increasing the

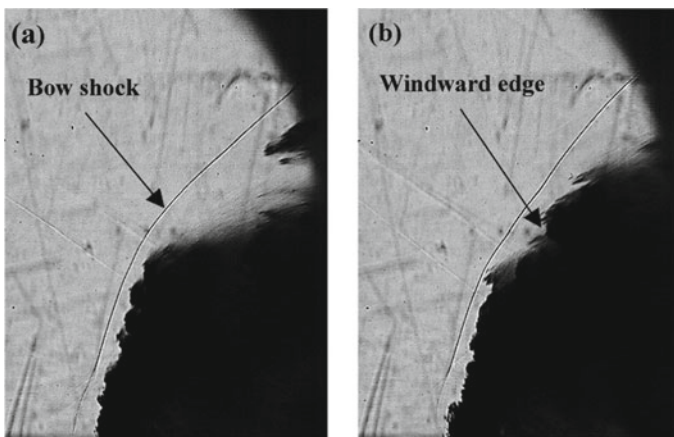


Fig. 5 Instantaneous side view images of tapered inlet nozzle case

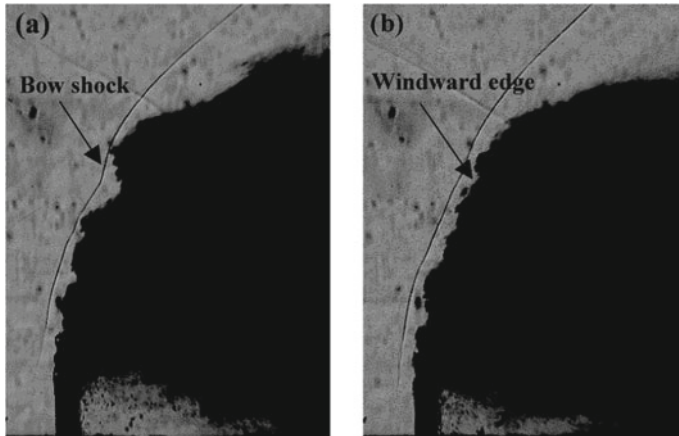


Fig. 6 Instantaneous side view images of sharp-edged inlet nozzle case

penetration, it also leads to increasing the shock strength (due to increase in shock angle).

Increasing the shock strength leads two things: One it helps in increasing the residence time of air in the combustor, and two it also leads to decrease in total pressure. Both are very important factors for the design of combustors.

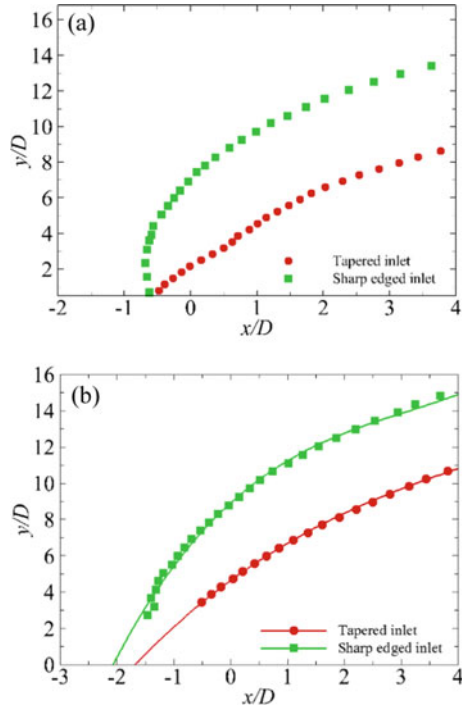
It was also observed that due to the formation of dense irregular liquid structures in sharp-edged case which leads to the formation of ‘bumpy shock’ (Fig. 6b), hence the liquid structure near to that will be subjected to complex velocity field unlike the tapered case where the velocity increase in the downstream of the shock is monotonic because of the formation of conventional bow shock (Fig. 6a).

4.2 Ensemble Averaged Results

Using the in-house algorithm developed in MATLAB, both the shock and windward edge locations were traced for each instantaneous image. About 500 instantaneous temporally correlated images were used for quantifying the mean shock and windward edge locations.

Figure 7a and b represent the variation of mean jet penetration height and mean shock location both in the streamwise and cross-streamwise directions. As evidenced in both the figures when the liquid jet is injected through tapered nozzle, there is a significant amount of reduction in mean penetration height and mean cross-streamwise shock location of about 55% and 36%, respectively, for $x/D = 4$ and $J = 7$. It is evident from the instantaneous images (Fig. 6) and the mean locations (Fig. 7) that the nature of the shock structures and windward edge are completely different for both the nozzles studied. Hence, it is important to understand how these are varying about mean with time.

Fig. 7 **a** Mean penetration height **b** mean shock location



4.3 Unsteady Shock and Jet Motion

Figures 8 and 9 show the variation of the windward edge and shock trajectories between the instants along with their mean locations (shown with thick black line). It is evident from these figures that there is significant amount of fluctuations in shock and jet motion for both the nozzles studied. These fluctuations are due to the presence of significant shock wave boundary layer interactions which is a natural phenomenon that occurs in the high-speed applications [9].

To understand the extent of fluctuations spatially, detailed analysis is being done by choosing a cross-streamwise location (y/D) and tracing the streamwise location of both shock (X_s/D) and windward edge (X_j/D) with time. For presenting, $y/D = 7$ was chosen and the results are shown below.

Figures 10a and b show the spatial extent of fluctuations of streamwise locations of shock and windward edge about their means (indicated with dashed line). It was observed that the spatial extent of fluctuations for both shock and windward edge in the case of tapered and sharp-edged nozzles is $1.7D, 4D$ and $0.9D, 1D$, respectively. There is a significant amount of drop in fluctuations in the case of sharp-edged nozzle due to fact that the jet coming out from the sharp-edged nozzle is relatively stronger as stated earlier.

Fig. 8 Instantaneous **a** windward edge **b** shock locations along with their mean for tapered nozzle case

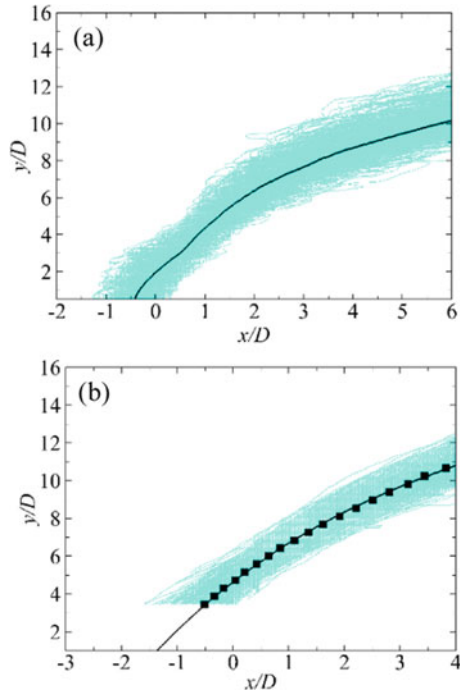


Fig. 9 Instantaneous **a** windward edge **b** shock locations along with their mean for sharp nozzle case

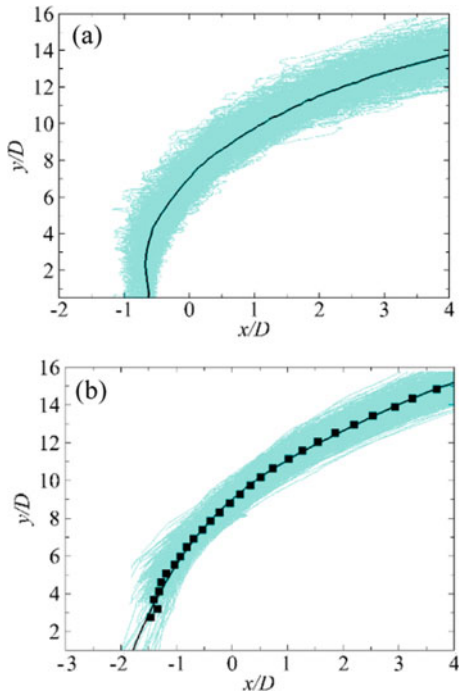
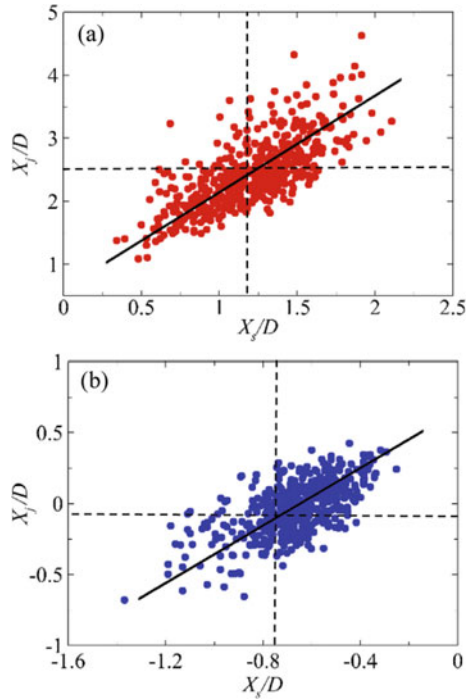


Fig. 10 Scatter plot between instantaneous streamwise locations of shock (X_s/D) and windward edge (X_j/D) for **a** tapered nozzle **b** sharp-edged nozzle



Also, it is important note that in both the cases, the correlation analysis between the shock and jet motion was done at the same y/D . It was found that the correlation coefficient is about 0.73 and 0.63 for tapered and sharp-edged nozzles, respectively, which tells that they are strongly correlated. This clearly indicates that when the jet is more upstream (penetration is more), the shock is pushed to more upstream location and vice-versa. This phenomenon can be easily understood by following the thick black (inclined) line as indicated in Figs. 10a and b. Similar analyses were done at different cross-streamwise locations and yielded the similar results.

5 Conclusions

In the present work, we experimentally studied the effect of injector internal shape on liquid jet penetration and bow shock location when injected transversely into supersonic crossflow with a free stream Mach number of $M_\infty = 2.5$. It was observed that the mean penetration height and bow shock locations are higher in the case of sharp-edged nozzle case compared to tapered nozzle for the same J . It was observed that, due to the presence of strong intact liquid column near the jet exit in the case of sharp-edged nozzle is helping it to penetrate more into the crossflow. Also, there is a significant amount of unsteadiness in shock and liquid jet motion is present in both

the cases. It was found that the fluctuations of shock and liquid jet are spreaded more spatially in the case of tapered injector, since the jet coming out from it is relatively weaker compared to the sharp-edged injector jets. Also, correlation coefficient is quantified between the shock and liquid jet motion and found that they are strongly coupled for the injectors used.

Nomenclature

ρ	Density of the fluid [kg/m ³]
j	Jet
∞	Free stream
s	Shock (°)
U	Velocity [m/s ²]
μ	Dynamic viscosity [N-s/m]
σ	Surface tension [N/m]
D	Orifice diameter [m]
L	Orifice length [m]
γ	Specific heat ratio
R	Gas constant [J/kg-K]
x, y, z	Streamwise, cross-streamwise, and spanwise coordinates [m]

References

1. Wu PK, Kirkendall KA, Fuller RP, Nejad AS (1996) Breakup processes of liquid jets in subsonic crossflows. In: 32nd Joint Propulsion Conference and Exhibit, 13, 1–14
2. Prakash RS, Sinha A, Tomar G, Ravikrishna RV (2018) Liquid jet in crossflow—effect of liquid entry conditions. *Experimental Thermal Fluid Sci* 93:45–56
3. Sallam KA, Aalburg C, Faeth GM (2004) Breakup of round liquid jets in gaseous crossflows. *AIAA J* 42(12):2529–2540
4. Broumand M, Birouk M (2017) Effect of nozzle-exit conditions on the nearfield characteristics of a transverse liquid jet in a subsonic uniform cross airflow. *Phys Fluids* 29:113303
5. Sherman A, Schetz J (1971) Breakup of liquidsheets and jets in a supersonic gas stream. *AIAA J* 9:666–673
6. Ghenai C, Sapmaz H, Lin CX (2009) Penetration height correlations for non-aerated and aerated transverse liquid jets in supersonic cross flow. *Exp Fluids* 46(2009):121–129
7. Lin KC, Kennedy PJ, Jackson TA (2004) Structures of water jets in a Mach 1.94 supersonic crossflow. *AIAA Paper*, 12096–12115
8. Munuswamy N (2017) Jet Injection into supersonic crossflow : flowfield and mixing studies, PhD thesis, Department of Mechanical Engineering, IISc Bangalore, India
9. Clemens NT, Narayanaswamy V (2014) Low-frequency unsteadiness of shock wave/turbulent boundary layer interactions. *Annu Rev Fluid Mech* 46:469–492

Effect of Reduced Mass on Two-Dimensional Compressible Flow Past Circular Cylinder



Sawant Omkar Deepak, Chandan Kumar Bhardwaj, Saurav Sharma, and Swagata Bhaumik

Abstract There are numerous experimental and numerical studies available on the Vortex-Induced Vibration (VIV) for 2D and 3D incompressible flow past bluff bodies (Sen et al in *J Fluid Mech* 620:89–119, 2009 [1]; Sharma et al in *Phys Fluids*, 2022 [2]). However, similar analysis is lacking for the case of high-speed compressible flows past bluff bodies. Here, we assess the effect of reduced mass on the unsteady two-dimensional (2D) VIV of the undamped elastically suspended circular cylinder constrained to move in the vertical y -direction only. We perform Direct Numerical Simulation (DNS) by solving the governing Navier–Stokes equation (NSE) by using high-accurate schemes for spatial discretization and time integration. The computational study has been performed for Reynolds number (based on the diameter of the circular cylinder) of 150 and free-stream Mach number of 0.5 for three cases of reduced mass $m_* = 2m/\rho_\infty D^2 = 1.0, 5.0, \text{ and } 10$, where m and ρ_∞ are the mass of cylinder per unit length and free-stream density of the fluid, respectively. We analyze time-dependent variations in coefficient of lift (C_l), coefficient of drag (C_d), displacement y_{CM} of the cylinder, and variation of (C_l) with (C_d) for a wide range of the reduced velocity ($U_* = U_\infty/f_N D$), to determine its response. Here, k_y and $f_N = 1/2\pi \sqrt{k_y/m}$ are the spring constant and the natural frequency of the vibration of the cylinder, respectively. Based on the results plotted, we have noted interesting patterns in the time history of C_l , C_d , and y_{CM} . For lesser values of the reduced velocity (U_*), presence of multiple modes in the response is noted, while at a higher value of U_* , presence of super-harmonics are noted. The maximum amplitude of the response is noted for some intermediate value of the reduced velocity U_* . We also plot pressure and vorticity contours for the computed cases for visualization of the vorticity patterns and propagation of resulting acoustic waves due to the influence of compressibility whose details will be explained in the presented article.

Keywords Compressible flow · Flow past cylinder · Vortex-induced vibration · Fluid–structure interaction

S. O. Deepak (✉) · C. K. Bhardwaj · S. Sharma · S. Bhaumik
Department of Mechanical Engineering, IIT(ISM)-Dhanbad, Dhanbad 826004, India
e-mail: omkars30.20dr0128@mech.iitism.ac.in

1 Introduction

There are many real-life situations where we come across examples of bluff bodies experiencing Vortex-Induced Vibration subjected to unsteady viscous flows. Some of the applications are oceanic structures like bridges, platforms subjected to waves, flow over airfoil, etc. Unsteady viscous flow past bluff bodies lead to formation of alternating vortices behind the bluff bodies. The vortices are formed because of the unsteady flow separation of shear layers from top and bottom surfaces of the body. As a result, von Kármán vortex street is formed in the wake when the flow Reynolds number is more than critical Reynolds number (Re_{cr}) [3]. This results in unsteady aerodynamic forces on the body causing vibration or oscillation (known as Vortex-Induced Vibration or VIV) of the body, when it is flexible. The detailed insights of physics about VIV of circular cylinder subjected to incompressible steady uniform flow can be found in review studies done by Sarpkaya [4] and Bearman [5]. Ample amount of research has been done to understand VIV flow past circular cylinder when subjected to the incompressible flows which are accounted in [1, 2, 6–9]. However, there are very less attempt made to understand VIV flow past circular cylinder subjected to compressible flow. Present study aims to investigate effect of mass ratio on VIV flow past circular cylinder subjected to compressible flow.

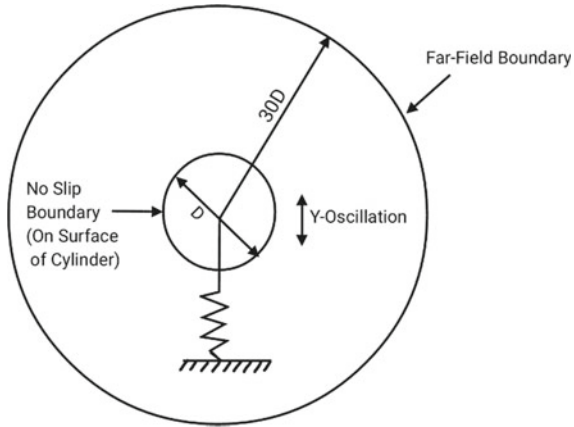
2 Research Methodology

In the present study, we have performed DNS for 2D unsteady Navier–Stokes equation. The computational details are given in consequent sections.

2.1 Geometry and Boundary Conditions

In Fig. 1, we show the geometry of the problem and the applied boundary conditions. We use structured O-grid topology for the computation. The diameter of the cylinder is used to non-dimensionalize all the length scales. The far-field boundary is taken at a radial distance of $30D$ from the cylinder surface. No-slip condition is imposed on the walls, while far-field boundary conditions are imposed based on the 1D isentropic flow based on the normal component of the velocity. The cylinder surface is assumed to be adiabatic. We consider air as the working fluid having free-stream temperature, dynamic viscosity, and density to be $T_\infty = 303$ K, $\mu_\infty = 1.872 \times 10^{-5}$ Pa s, and $\rho_\infty = 1.164 \frac{\text{kg}}{\text{m}^3}$, respectively. The free-stream Mach number is taken to be 0.5, while Prandtl number is assumed to have a constant value of 0.72. Stokes hypothesis is used to correlate the first and the second coefficients of the dynamic viscosities.

Fig. 1 Schematic of the problem showing the geometry and the boundary conditions imposed



2.2 Governing Equations

The governing non-dimensional Navier–Stokes equation for compressible flows, written in strong conservation form in the physical plane, can be written as [10]

$$\frac{\partial \hat{Q}}{\partial \tau} + \frac{\partial \hat{E}}{\partial \xi} + \frac{\partial \hat{F}}{\partial \eta} = \frac{1}{Re} \left(\frac{\partial \hat{E}_v}{\partial \eta} + \frac{\partial \hat{F}_v}{\partial \eta} \right), \tag{1}$$

where ξ and η are the curvilinear coordinate system along azimuthal and radial directions, respectively, while τ represents generalized time capturing the motion of the grid corresponding to its vibration. In Eq. (1), $Q, E, F, E_v,$ and F_v represent the non-dimensional conserved variables, convective and diffusive fluxes, respectively. The detailed expression for these variables may be found in [10]. As noted, here we consider only undamped vibration of the circular cylinder along the vertical y -direction only as shown in Fig. 1. We consider the cylinder to be connected to a linear spring (with spring constant k_y). The non-dimensional equation governing the y -motion of the cylinder is given as

$$y'' + \left(\frac{2\pi}{U_*} \right)^2 y = \frac{C_l}{m_*}, \tag{2}$$

where $m_* = 2m/\rho_\infty D^2, C_l$ and $(U_* = U_\infty/f_N D)$ denote reduced mass, coefficient of lift and velocity, respectively. For the present study, we consider three cases with $m_* = 1.0, 5.0,$ and 10 . Very large values of U_* denote the stiffness of the spring to be very small, while very small values of U_* the spring to be very stiff. The non-dimensional parameter m_* denotes the ratio of the mass of the cylinder to the mass of the displaced fluid. Therefore, $m_* = 1.0$ denotes the case for a very light cylinder,

while $m_* = 10.0$ represents the case when the cylinder material density is roughly ten times to that of the surrounding fluid.

2.3 Grid Generation

Curvilinear-Structured O-Type Grid [11] has been used for the numerical computation. Total 1001 equispaced points are used along the azimuthal direction, while 361 points are used along the radial direction. Grid clustering along the radial direction is achieved using tangent hyperbolic function to minimize aliasing error. Minimum grid spacing of $\Delta r_1 = 1.24 \times 10^{-2}$ is achieved near the cylinder surface, while a maximum grid spacing of $\Delta r_2 = 0.173$ is obtained at the far field of $30D$.

2.4 Numerical Schemes

The convective derivatives appearing in Eq. (1) are discretized using Optimal Upwind Compact Scheme (*OUCS3*) [12], while the viscous derivative is discretized using second-order central differencing schemes (*CD2*). We have used a parallel solver where the parallelization is performed along the azimuthal ξ -direction using MPI techniques. Time integration is performed using 4th-order Runge–Kutta method (*RK4*). Computations have been carried out with a time step of $\Delta t = 5.0 \times 10^{-4}$. Scalar-based JST [13] switch is used for adding numerical diffusion to remove the unphysical high-wavenumber oscillations in the solution.

3 Results and Discussion

We analyze the oscillation by varying the reduced velocity from very small value of 2 to a high value of 7. As stated before, three different values of the reduced mass, i.e., $m_* = 1.0, 5.0,$ and 10.0 are considered here. We consider Reynolds number of $Re = \rho_\infty U_\infty D / \mu_\infty = 150$. For this Reynolds number, a time-periodic flow is noted to occur. In Fig. 2, we plot the amplitude of the oscillation of the cylinder as a function of U_* , for $m_* = 1.0, 5.0,$ and 10.0 . One notes that maximum amplitude to occur at $U_* = 4.8$ for $m_* = 1.0$, at $U_* = 5.2$ for $m_* = 5.0$, while for $m_* = 10.0$, the maximum amplitude is noted at a slightly higher value of $U_* = 5.25$. Therefore, a reduction in the reduced mass leads to the reduction in the value of the U_* corresponding to the maximum amplitude. Another feature is readily noticeable from Fig. 2, and for the lower reduced mass case, the response amplitude is much flatter with respect to U_* as compared to the higher reduced mass case. However, the maximum amplitude of oscillation (which is approximately $0.8D$) is almost identical for the lower and the higher reduced mass cases. While the variation of oscillation

amplitude as a function of U_* for the higher reduced mass case is similar to what was reported in [14] for the incompressible case, the lower reduced mass case is not reported anywhere to the best of our knowledge. In Fig. 3, we plot the variation of Cl_{\max} as a function of U_* , for $m_* = 1.0$, $m_* = 5.0$, and $m_* = 10.0$ cases. The horizontal line depicts the Cl_{\max} corresponding to the stationary cylinder case for all cases of reduced mass. One notes the Cl_{\max} to increase and subsequently drop below the value corresponding to the stationary cylinder case. The variation during this drop in the value of Cl_{\max} is sharper for the higher reduced mass case. In Fig. 4, we plot the variation of Cd_{\max} as a function of U_* for $m_* = 1.0$, $m_* = 5.0$, and $m_* = 10.0$ cases. The horizontal line depicts the Cd_{\max} corresponding to the stationary cylinder case for $Re = 150$. One notes that increase in amplitude is associated with the increase in C_d for all the cases. The drop in the value for C_d is sharper for the higher reduced mass case, similar to the variation corresponding to C_l . For $m_* = 5.0$ case, one can observe interesting wave packet feature in the time variation of C_l , C_d and the displacement of the cylinder as shown in Fig. 5 close to the points where maximum amplitude is noted to occur (U_* ranging between 4.0 and 5.0). One such case is shown plotted for $U_* = 4.0$ in Fig. 5b, c, where the time variation of C_l and C_d is displayed. From the corresponding Fast Fourier Transform (FFT) of the C_l and C_d plot shown in Fig. 5d, e, we noted the presence of multiple modes around the dominant peak. In Fig. 7a, we plot C_l as a function of C_d for this particular case. Multiple limit cycles are noted for this particular case. This is a hallmark for the cases where multiple neighboring modes appear. We noted similar packet-like feature for higher reduced mass case of $m_* = 10.0$. In Fig. 6, we have shown the time variation and its corresponding FFT of C_l and C_d along with displacement of cylinder. For $m_* = 10.0$ case, we observe packet-like feature at values of U_* ranging from 4.5 to 5.0 which lies close to maximum response. Like in case of $m_* = 5.0$ multiple modes can be observed for $m_* = 10.0$ case which is evident from the FFT plots of C_l and C_d as shown in Fig. 6d, e and in variation of C_l as a function of C_d in Fig. 7b. However, such packet-like feature in the time variation of C_l or C_d is not noted in lower reduced mass case of $m_* = 1.0$. For all three reduced mass cases, when U_* is above roughly 5.2, dominant third super-harmonic is noted to occur in the time variation of C_l but not in C_d . The time variation of C_d on the contrary shows time-harmonic behavior. These are shown in Figs. 8, 9 and 10 in terms of time variation of C_l and C_d . The variation of C_l with respect to C_d for all three cases $m_* = 1.0$, $m_* = 5.0$, and $m_* = 10.0$ at $U_* = 5.5$ is shown in Fig. 11a–c, respectively.

In Fig. 12, we plot contours of pressure at six different time instants within a particular segment of the packet in the time variation of C_l for $m_* = 5.0$ and $U_* = 4.0$. It has been noted that the intensity of acoustic wave radiation in the predominant upstream direction is intermittently increased for such cases.

While such vibrations is not seen to affect the directivity of the sound radiation, but the intensity is modified based on the slow variation in the amplitude of the oscillation of the cylinder. Corresponding vorticity contours are shown in Fig. 13, which shows the variation in the intensity of vortex formation on the cylinder surface

Fig. 2 Amplitude of the oscillation of the cylinder plotted as a function of U_* for $m_* = 1.0, 5.0,$ and 10.0

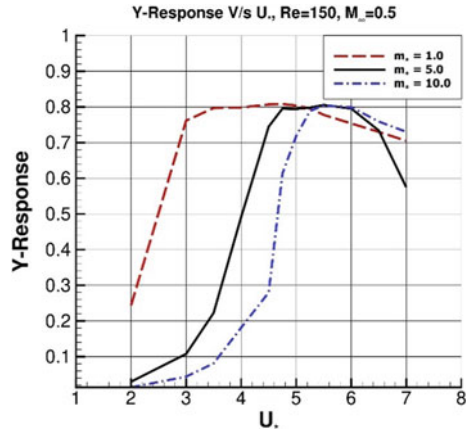


Fig. 3 $C_{l_{max}}$ plotted as a function of U_* for $m_* = 1.0, 5.0,$ and 10.0

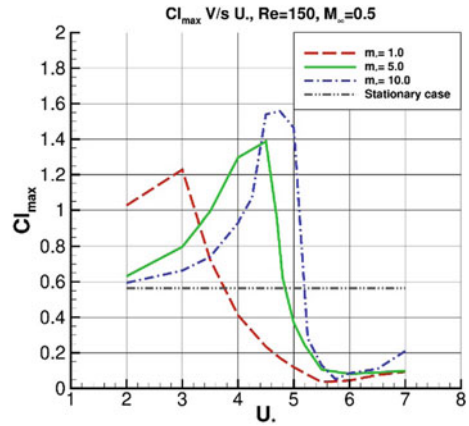
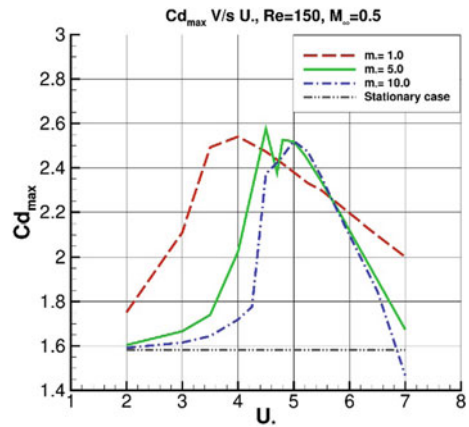


Fig. 4 $C_{d_{max}}$ plotted as a function of U_* for $m_* = 1.0, 5.0,$ and 10.0



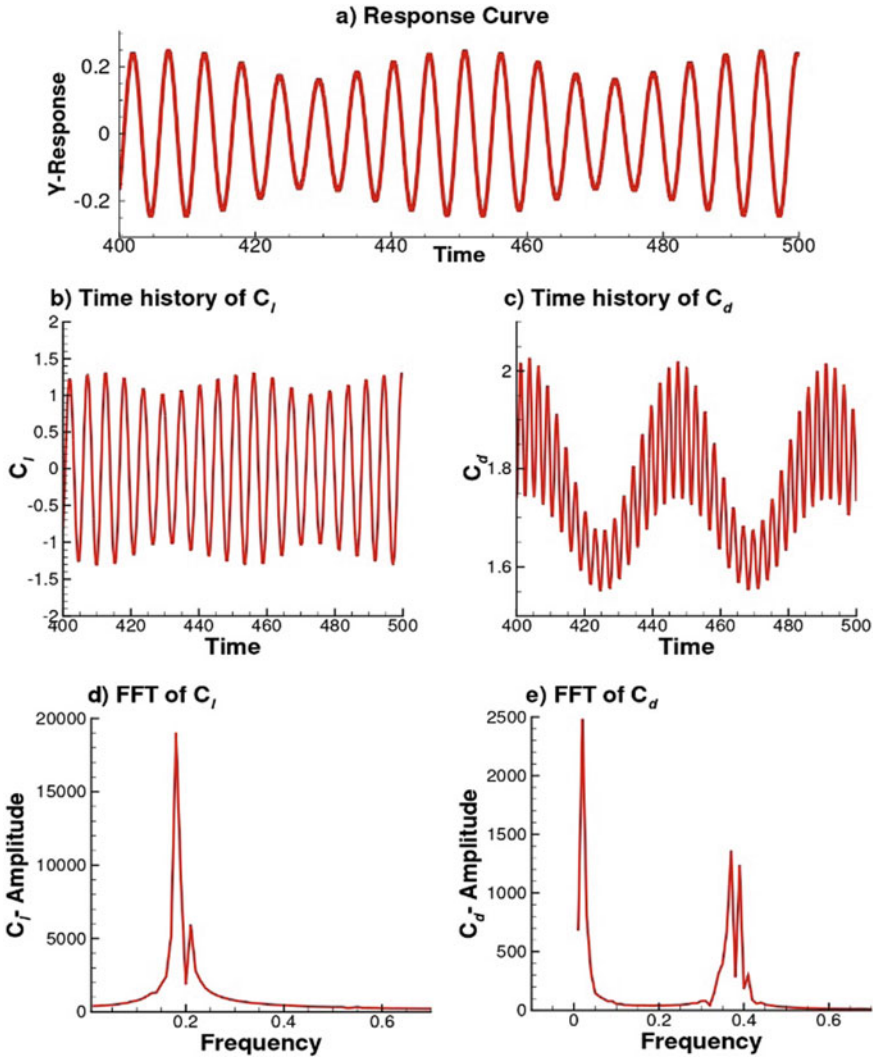


Fig. 5 Time variation and FFT of C_l , C_d for case: $Re = 150$ and $m_* = 5.0$ at $U_* = 4.0$

and its subsequent shedding from it. The details are more clear in the animation and would be discussed in details during the presentation.

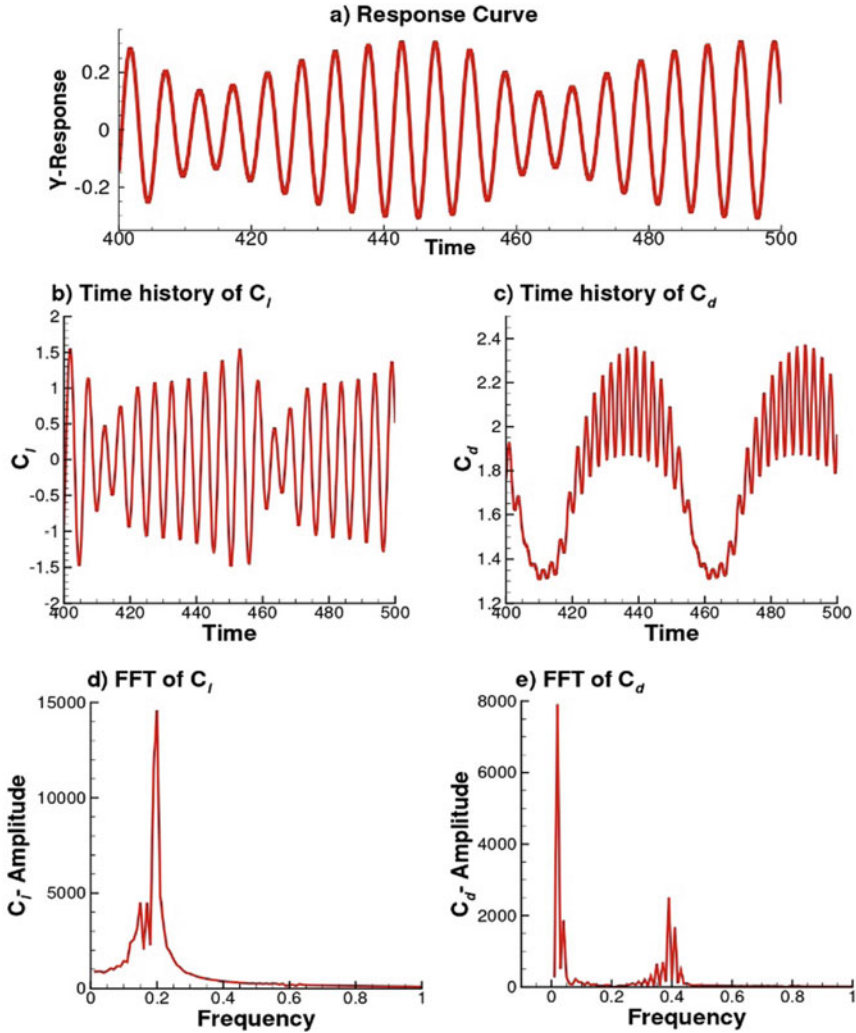


Fig. 6 Time variation and FFT of C_l , C_d for case: $Re = 150$ and $m_* = 10.0$ at $U_* = 4.5$

4 Conclusions

Based on the comparative studies between three cases of reduced mass, we can infer the following points.

- Based on response curve, we note that the peak of the response is achieved at $U_* = 4.8$ for $m_* = 1.0$, $U_* = 5.2$ for $m_* = 5.0$, and at $U_* = 5.25$ for $m_* = 10.0$.
- As we decrease reduced mass from higher value $m_* = 10.0$ to lower value $m_* = 1.0$, curve becomes more flatter.

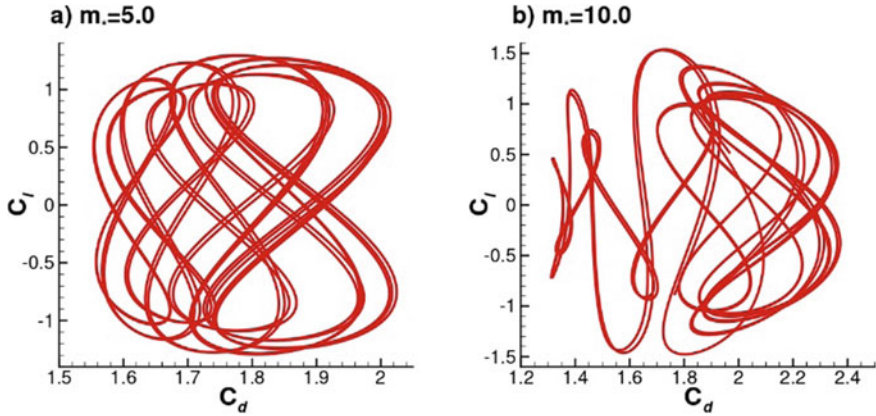


Fig. 7 C_l is plotted as a function of C_d at $Re = 150$ for $m_* = 5.0$ at $U_* = 4.0$ and for $m_* = 10.0$ at $U_* = 4.5$ cases. The time range is chosen to be between $400 \leq t \leq 500$

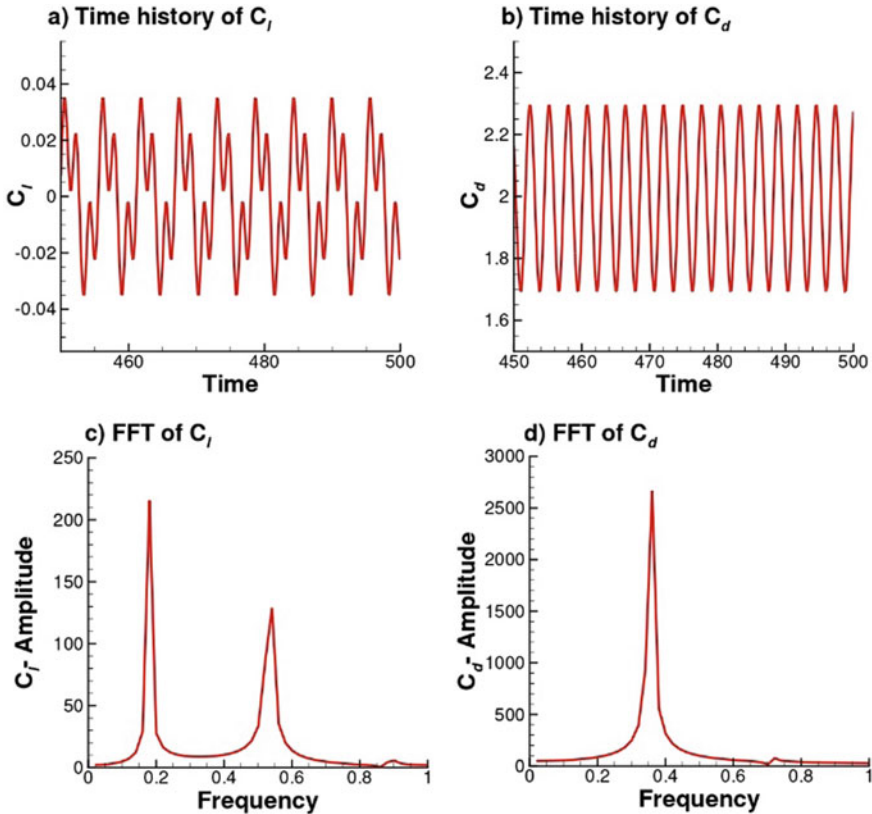


Fig. 8 Time variation and FFT of C_l, C_d . for case: $Re = 150$ and $m_* = 1.0$ at $U_* = 5.5$

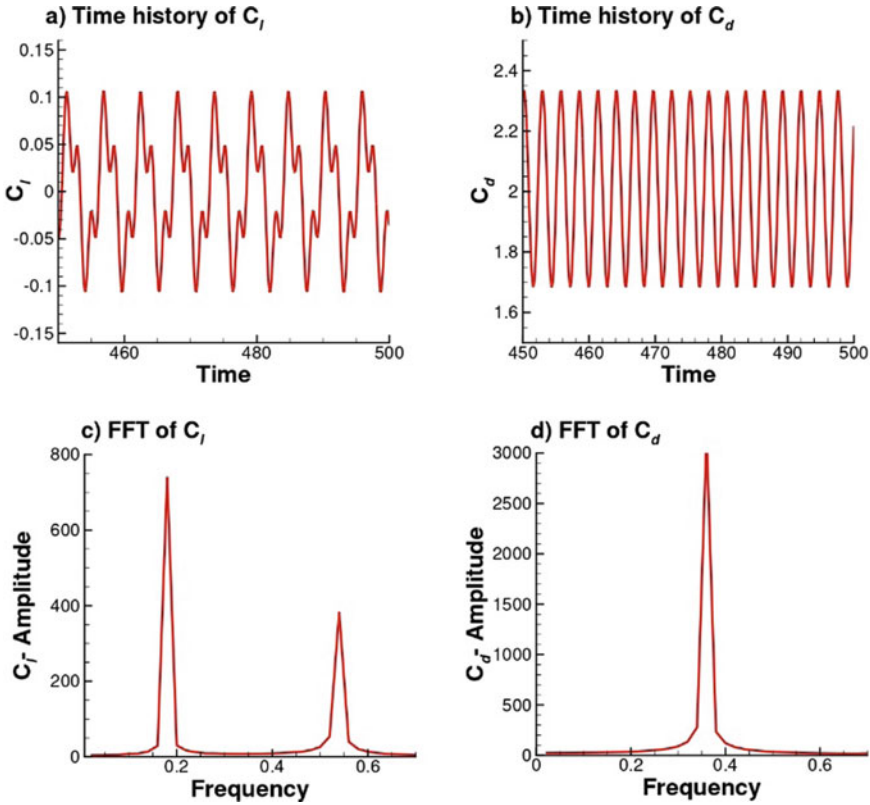


Fig. 9 Time variation and FFT of C_l and C_d for case: $Re = 150$ and $m_* = 5.0$ at $U_* = 5.5$

- Maximum value of the C_l and C_d occurs at less reduced velocity for the lower reduced mass case $m_* = 1.0$ than for the higher reduced mass cases $m_* = 5.0$ and $m_* = 10.0$.
- Wave packet-like feature in the time variation of C_l is noted at higher reduced mass cases ($m_* = 5.0$ and $m_* = 10.0$) around the maximum vibration amplitude points, while the packet-like feature in the time variation in C_l is not noted for the lower reduced mass case ($m_* = 1.0$).
- An increase in the reduced velocity causes the third super-harmonic to appear in the time variation of C_l in all three reduced mass cases, whereas C_d remains time harmonic.
- Intermittent intensity in acoustic radiation is noted for the higher reduced mass case around the maximum amplitude points.

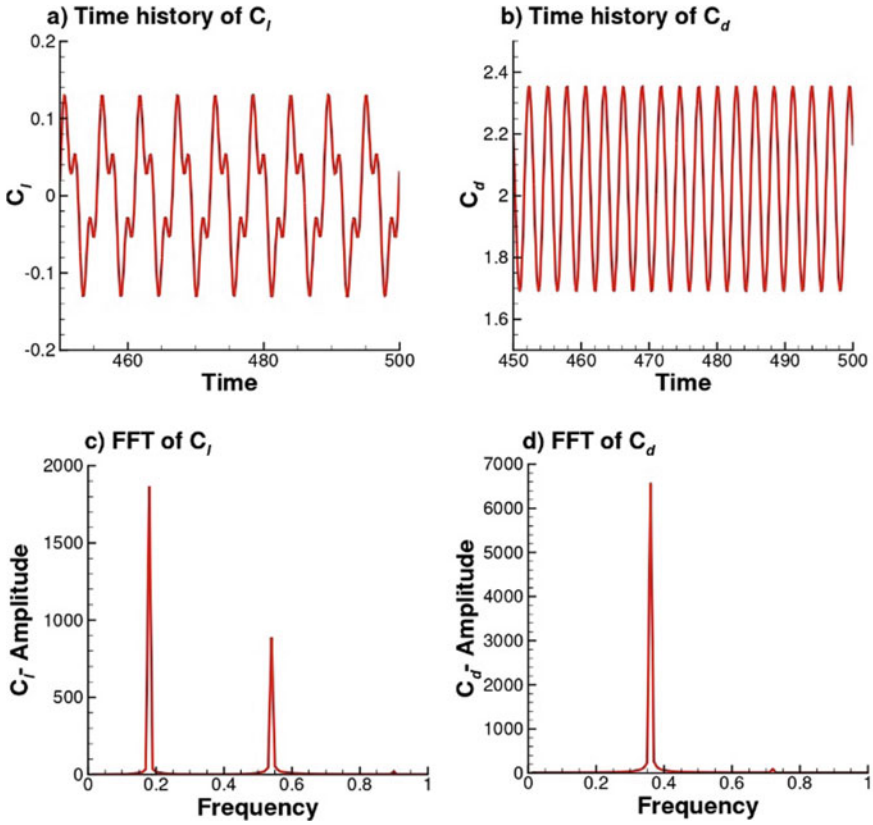


Fig. 10 Time variation and FFT of C_l, C_d for case: $Re = 150$ and $m_* = 10.0$ at $U_* = 5.5$

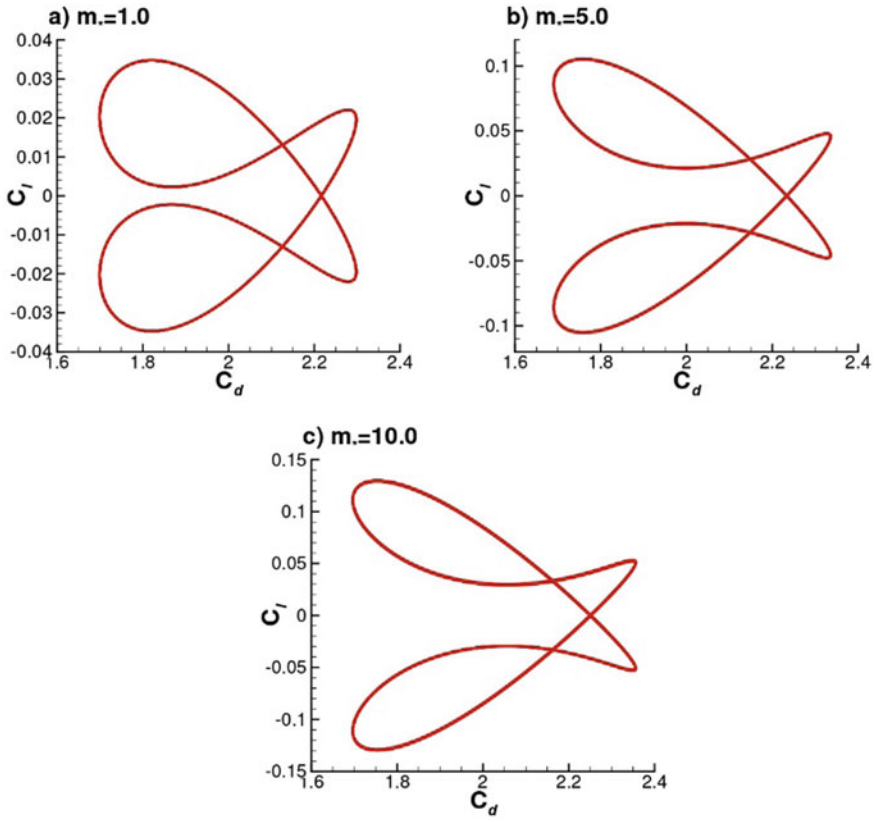


Fig. 11 C_l is plotted as a function of C_d for $Re = 150$, for $m_* = 1.0$, $m_* = 5.0$ and $m_* = 10.0$ at $U_* = 5.5$. The time range is chosen to be between $450 \leq t \leq 500$

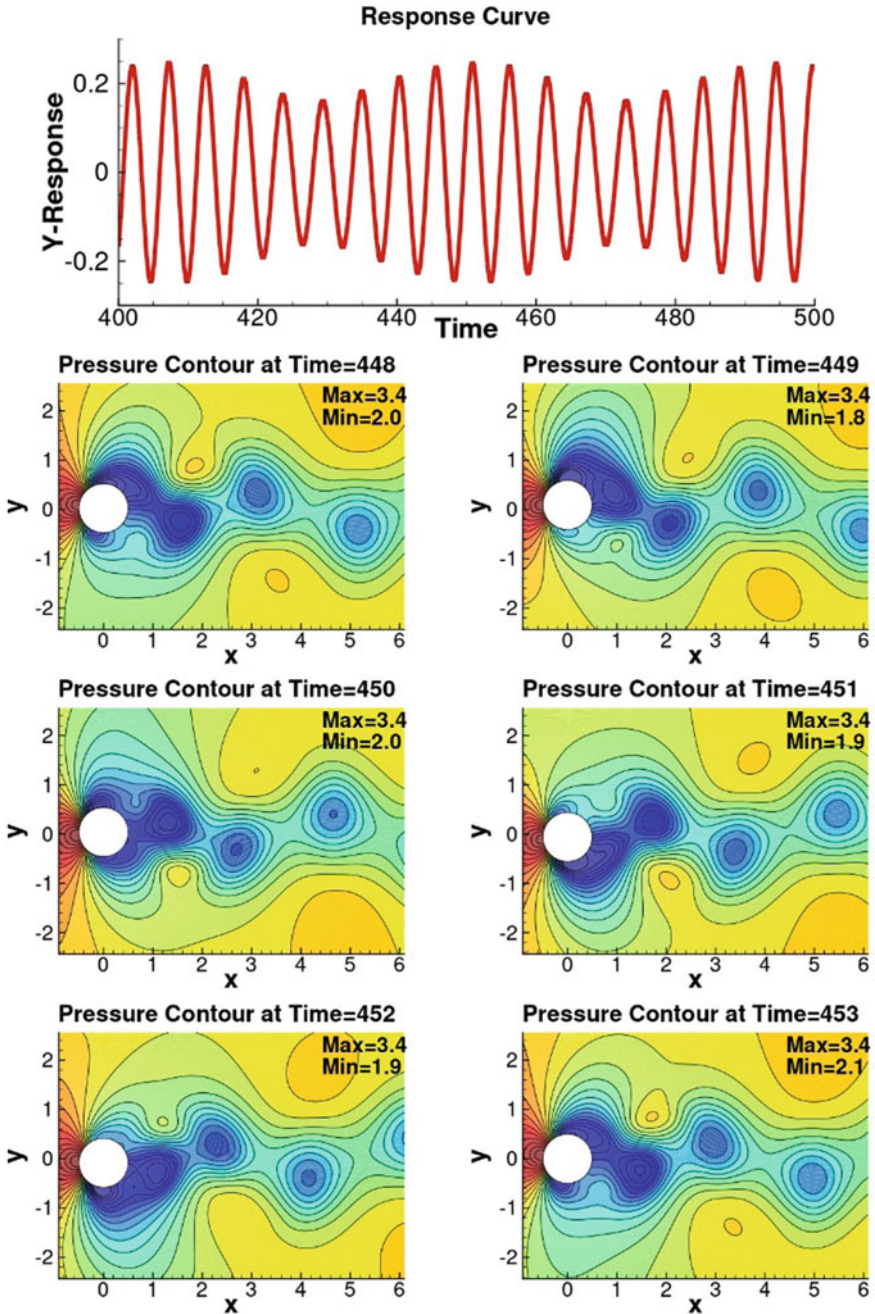


Fig. 12 Pressure contours at wave packet region for case $Re = 150$, $M_\infty = 0.5$, $m_* = 5.0$ at $U_* = 4.0$

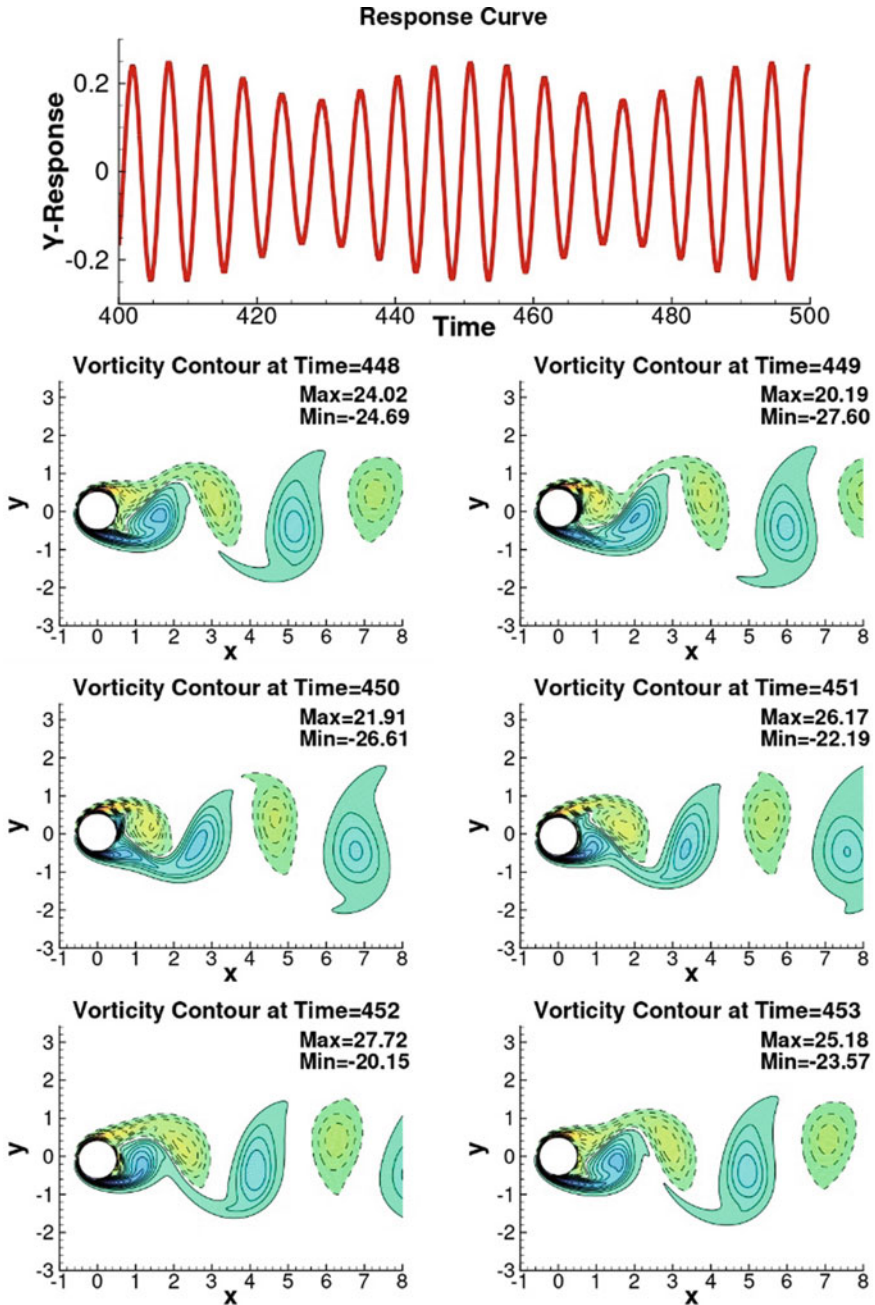


Fig. 13 Vorticity contours at wave packet region for case $Re = 150$, $M_\infty = 0.5$, $m_* = 5.0$ at $U_* = 4.0$

Acknowledgements The simulations were run on the High-Performance Computer facility (Aryabhata) at Indian Institute of Technology (Indian School of Mines), Dhanbad. We acknowledge the HPC facility support given by IIT(ISM)—Dhanbad. Also acknowledge the financial assistance provided by Prime Minister Research Fellowship (PMRF) for encouraging research.

References

1. Sen S, Mittal S, Biswas G (2009) Steady separated flow past a circular cylinder at low Reynolds numbers. *J Fluid Mech* 620:89–119
2. Sharma G, Pandey AK, Bhardwaj R (2022) Effect of shape of frontbody and afterbody on flow past a stationary cylinder at $Re=100$. *Phys Fluids*
3. Kumar B, Mittal S (2006) Prediction of the critical Reynolds number for flow past a circular cylinder. *Comput Methods Appl Mech Eng* 195(44–47):6046–6058
4. Sarpkaya T (2004) A critical review of the intrinsic nature of vortex-induced vibrations. *J Fluids Struct* 19(4):389–447
5. Bearman PW (1984) Vortex shedding from oscillating bluff bodies. *Annu Rev Fluid Mech* 16(1):195–222
6. Prasanth TK, Mittal S (2008) Vortex-induced vibrations of a circular cylinder at low Reynolds numbers. *J Fluid Mech* 594:463–491
7. Singh SP, Mittal S (2005) Vortex-induced oscillations at low Reynolds numbers: hysteresis and vortex-shedding modes. *J Fluids Struct* 20(8):1085–1104
8. Varaprasad Patnaik BS, Aswatha Narayana PA, Seetharamu KN (1999) Numerical simulation of vortex shedding past a circular cylinder under the influence of buoyancy. *Int J Heat Mass Transf* 42(18):3495–3507
9. Singh SP, Chatterjee D (2014) Impact of transverse shear on vortex induced vibrations of a circular cylinder at low Reynolds numbers. *Comput Fluids* 93:61–73
10. Hoffmann KA, Chiang ST (2000) Computational fluid dynamics volume I. In: Engineering education system
11. Chung TJ et al (2002) Computational fluid dynamics. Cambridge University Press
12. Sengupta T (2013) High accuracy computing methods: fluid flows and wave phenomena. Cambridge University Press
13. Jameson A (2017) Origins and further development of the Jameson–Schmidt–Tukel scheme. *AIAA J* 55(5):1487–1510
14. Dorogi D, Baranyi L (2020) Identification of upper branch for vortex-induced vibration of a circular cylinder at $Re=300$. *J Fluids Struct* 98:103135

Effect of Overtaking Disturbances on the Motion of Strong Cylindrical MHD Shock Waves in a Self-Gravitating Van Der Waals Gas



Sewa Singh and R. K. Anand

Abstract In the present manuscript, the analytical solution for one-dimensional adiabatic flow behind the strong shock waves propagating in a non-ideal gas following Van der Waals equation of state is obtained using the modified CCW method. The analytical expressions for the shock velocity, shock strength, pressure, density, and particle velocity are obtained in the presence of an axial and azimuthal magnetic field. The effects of overtaking disturbances on the freely propagating shocks are studied with the variation of the propagation distance r and the non-idealness parameter $b\rho_0$ of the gases. Further, a comparison between the findings of the present study and the previous study has been done in graphical and tabular form. The findings confirm that the shock strength as well as the flow variables gets strengthened with the overtaking disturbances, and also the shock strength increases with the increasing non-idealness parameter of the gases. Finally, the observations confirm that the perturbed shock moves more rapidly than the incident shock and are found in good agreement with the existing results.

Keywords Hydromagnetic shock waves propagation · Axial and azimuthal magnetic field · Self-gravitating Van der Waals gas · Overtaking disturbances · Modified CCW method

1 Introduction

Shock waves are surface of discontinuity which occurs naturally when fluids approach each other with velocity greater than that of sound. Shock waves are disturbances or sudden change in the normal condition of the flow variables, i.e., pressure, density, shock velocity, particle velocity, and shock strength. Such disturbances occur when large energy is deposited in a very small volume over a short interval of time such as in steady transonic or during generation of high energy explosions, spark

S. Singh (✉) · R. K. Anand
Department of Physics, University of Allahabad, Prayagraj 211002, India
e-mail: sewasingh705@gmail.com

discharges in air, earthquakes, hydraulic jumps, and lightning strokes which also occur particularly with phenomenon related with aerospace engineering and supersonic flight. The importance of shock waves has increased in the last few decades because of its application in medical field to treat kidney stone diseases using shock wave lithotripsy and also because of its practical application in nuclear fusion reaction and motion of satellites in the interstellar medium. The shock waves while propagating in a variable cross-section channel gets perturbed because the pressure at higher temperature overtakes the pressure at lower temperature and also due to the contact surfaces and thus the reflected and re-reflected disturbances are generated. Many authors across the world have observed these disturbances in the flow and also investigated on it. Some of them are Chester [1], Chisnell [2], and Whitham [3] who obtained the relation between the shock strength (M) and cross-sectional area (A) in a tube using their different methods which is together known as the modified CCW method. Chester showed that the strength of the shock wave after passing through a cross-sectional area differs by small amount from the incident shock wave. Later, Chisnell integrated Chester's result and formed an expression for the area and Mach number. Since Chester has neglected all the disturbances, so Chisnell descriptions were also for freely propagating shock. Whitham obtained the same expression using the characteristics method. Later, their methods together were known by the CCW method.

2 Literature Review and Objective

Many authors across the world observed phenomena of the overtaking disturbances and studied regarding it assuming various kinds of shock, i.e., plane shocks and spherical shock for perfect gases. Some of them are Yousaf [4, 5] who presented an exact formulation of the effect of the overtaking disturbances on the strength of the shock waves. Milton [6] studied the strong shock and gave a useful relation between the shock strength and the area. Singh [7] studied the effect of overtaking disturbances for cylindrical hydro-magnetic shocks in self-gravitating perfect gases using the CCW method in the presence of magnetic field and obtained the relation for different flow variables. Yadav and Tripathi [8] studied the propagation of shock wave in non-uniform region using the CCW method and also the dependence of shock strength on gravitational force for ideal gases. Kumar and Mishra [9] investigated the propagation of shock using CCW method for perfect gases and found that the shock gets strengthened under the overtaking disturbances and also compared the results with freely propagating gases. All these studies on the propagation of shock wave in ideal gas have established very well its importance in astrophysics. However, according to the author's best knowledge, there is still a lack of attention on the study of effect of overtaking disturbances on the propagation of shock wave in the presence of magnetic field for non-ideal gas following Van der Waals equation of state and this motivated us for the present study.

The aim of the present work is to study and explain the effect of overtaking disturbances behind the flow of the motion of cylindrical hydro-magnetic shock waves through a self-gravitating gas in the presence of axial and azimuthal magnetic field for strong shocks using CCW method. However, the effect of gravitational field is seldom mentioned in the present work. This manuscript contains the expressions of the flow variables such as, (i) shock velocity, (ii) shock strength, (iii) pressure, (iv) density, and (v) particle velocity under certain approximations stated as: (i) the gaseous flow is considered being unsteady and one-dimensional, (ii) the initial density distribution is assumed to be $\rho_0 = \rho' r^{-\omega}$, where ρ' is the density at the axis of symmetry and w a constant, (iii) the magnetic field is assumed to be constant axial and variable azimuthal. The expressions of the flow variables are derived separately for the case when the overtaking disturbances are neglected, i.e., free propagation and when the effect of overtaking disturbances is included. Later, their behaviors are studied and compared through graphical and tabular form results. Finally, the observed results explain that how the shock strength and other flow variables in the shock transition regions are affected by the magnetic field and the non-idealness parameter of the gases.

3 Methods and Mathematical operations

3.1 Basic Equations of Motion and Boundary Conditions

The basic conservation equations for one-dimensional unsteady cylindrical flow of a Van der Waals gas which depends on position (r) and time (t) under the influence of self-gravitation and magnetic field in equilibrium condition have been given as:

$$\begin{aligned} \frac{\partial u}{\partial t} + u \frac{\partial u}{\partial r} + \frac{1}{\rho} \frac{\partial p}{\partial r} + \frac{\mu}{2\rho} \frac{\partial}{\partial r} (H_\theta^2 + H_Z^2) + \frac{\mu}{\rho} \frac{H_\theta^2}{r} + \frac{Gm}{r^2} &= 0 \\ \frac{\partial \rho}{\partial t} + u \frac{\partial \rho}{\partial r} + \rho \frac{\partial u}{\partial r} + \rho \frac{u}{r} &= 0 \\ \frac{\partial p}{\partial t} + u \frac{\partial p}{\partial r} + \gamma p \frac{\partial u}{\partial r} + \gamma p \frac{u}{r} &= 0 \\ \frac{\partial H_\theta}{\partial t} + u \frac{\partial H_\theta}{\partial r} + H_\theta \frac{\partial u}{\partial r} &= 0 \\ \frac{\partial H_Z}{\partial t} + u \frac{\partial H_Z}{\partial r} + H_Z \frac{\partial u}{\partial r} + H_Z \frac{u}{r} &= 0 \\ \frac{\partial m}{\partial r} - 2\pi\rho r &= 0, \end{aligned} \tag{1}$$

where r is the radial co-ordinate, and $u, \rho, p, H_z, H_\theta, \mu,$ and m are respectively the particle velocity, the density, the pressure, axial and azimuthal components of magnetic field, permeability of gas, and mass inside cylinder of unit cross-section and unit length and radius r .

The isentropic velocity of sound (a_o) and Alfven speed (b_o) in Van der Waals gas is given as:

$$a_o^2 = \frac{\gamma p_o}{\rho_o(1 - b\rho_o)} \quad \text{and} \quad b_o^2 = \frac{\mu H_o^2}{\rho_o}, \tag{2}$$

where γ denotes the adiabatic index of the gas and $b\rho_o$ is the non-idealness parameter of the gas.

Boundary Conditions for Strong Shock

The magneto-hydrodynamic condition can be written in terms of single parameter $\xi = \frac{\rho}{\rho_o}$.

In the limiting case of a strong shock, p/p_o is large. In magnetic case, this can be achieved in two ways.

Case I. The purely non-magnetic way when $\xi - \frac{(\xi+1)}{(\xi-1)}$ is very small.

Case II. When the ambient magnetic pressure is large compared with the ambient field pressure the boundary conditions become.

$$\rho = \rho_o \xi, \quad H = H_o \xi, \quad u = \frac{\xi - 1}{\xi} U$$

$$U^2 = \frac{2(1 - b\rho_o)\xi a_o^2}{(\gamma + 1) - (\gamma - 1 + 2b\rho_o)\xi} [1 + \gamma + \xi(2 - \gamma) - b\rho_o(\xi + 1)\xi] \tag{3}$$

$$\frac{p}{p_o} = \chi(\xi) \left(\frac{U^2}{a_o^2} \right) + L, \quad u = \frac{(\xi - 1)}{\xi} U,$$

where

$$L = \frac{[(\gamma + 1) - 2b\rho_o]\xi - (\gamma - 1)}{[(\gamma + 1) - (\gamma - 1 + 2b\rho_o)\xi]} \tag{4}$$

and

$$\chi(\xi) = \frac{\gamma(\gamma - 1)(\xi - 1)^3}{2\xi [\{ 2 - \gamma - b\rho_o(\xi + 1) \} \xi + \gamma]}$$

The Van der Waals equation of motion is given as:

$$p = \frac{\rho RT}{1 - b\rho_o} \tag{5}$$

The internal energy per unit mass of Van der Waals gas is given as:

$$e = \left(\frac{1 - b\rho_o}{\gamma - 1} \right), \tag{6}$$

where the subscript ‘o’ stands for the state immediately ahead of the shock front, and U is the shock velocity.

Characteristic Equations: For diverging shocks, the characteristics’ form of the equation can be easily obtained by forming a linear combination of first and third equations of the system of Eq. (1) in (r, t) plane.

Assuming the total pressure including the magnetic pressure to be $p_t = p + \frac{\mu}{2}(H_\theta^2 + H_z^2) + \int \mu H_\theta^2 \frac{\partial r}{r}$ and simplifying using the first and third equations of the system of Eq. (1), we get,

$$\rho \frac{\partial u}{\partial t} + \rho u \frac{\partial u}{\partial r} + \frac{\partial p_t}{\partial r} + \rho \frac{Gm}{r^2} = 0 \tag{7}$$

$$\frac{\partial p_t}{\partial t} + u \frac{\partial p_t}{\partial r} + \rho c^2 \frac{\partial u}{\partial r} + \rho c^2 \frac{u}{r} = 0, \tag{8}$$

where

$$c^2 = \left(\frac{\gamma p_o}{\rho_o(1 - b\rho_o)} \right) + \frac{\mu H_o^2}{\rho_o} \tag{9}$$

Linear combination of Eqs. (7) and (8) using the condition of derivative to be in one direction only, i.e., $\frac{dr}{dt} = u \pm c$ the characteristics equation have been obtained and given below. The characteristics curve represents the motion of possible disturbances whose velocity differs from particle velocity u , by the value of $\pm c$ (local sound speed), respectively, for diverging and converging shocks.

The total derivative of characteristics equation for diverging shock is given as:

$$dp + \mu H_\theta dH_\theta + \mu H_z dH_z + \rho c du + \frac{\mu H_\theta^2 \partial r}{r} + \rho c^2 \frac{u}{(u + c)} \frac{\partial r}{r} + \rho c \frac{Gm}{(u + c)} \frac{\partial r}{r^2} = 0. \tag{10}$$

Equation (10) represents the characteristics form of equation for diverging shocks, and by replacing the $+c$ in above equation by $-c$, we get the characteristics’ equation for converging shocks given as:

$$dp + \mu H_\theta dH_\theta + \mu H_z dH_z - \rho c du + \mu H_\theta^2 \frac{dr}{r}$$

$$+ \rho c^2 \frac{u}{(u - c)} \frac{dr}{r} - \rho c \frac{Gm}{(u - c)} \frac{dr}{r^2} = 0. \tag{11}$$

Analytical Relations for Flow Variables

The final step is to substitute the boundary conditions given in Eq. (3) into the characteristics' equation for both the diverging and converging shocks.

The equilibrium condition is specified by the conditions:

$$\frac{\partial}{\partial t} = 0 = u \quad \text{and} \quad H_{Z_0} = \text{constant} \quad \text{and} \quad H_{\theta_0} = r^{1/2} H_{Z_0}. \tag{12}$$

The initial distribution of density in unperturbed state is assumed to be of the form,

$$\rho_o = \rho' r^{-\omega}, \tag{13}$$

where ρ' is the density at the plane of symmetry and w is a constant. Using Eq. (12) and first and sixth equations of system of Eq. (1), the variation in pressure with distance r can be written as:

$$\frac{p_o}{p'} = K_1^* r^{1-2\omega} \gamma - \frac{3}{2} \gamma \beta_1^2 r + K', \tag{14}$$

where,

$$\begin{aligned} K^* &= \frac{K_1}{D}, \quad K_1 = \frac{2\pi}{(2\omega - 1)(2 - \omega)}, \quad K' = \frac{K_o}{p'}, \\ D &= \frac{a^2}{G\rho'}, \quad \beta_1^2 = \frac{\mu H_{Z_0}^2}{\gamma p'}, \quad m = \frac{2\pi \rho' r^{2-\omega}}{(2 - \omega)}. \end{aligned} \tag{15}$$

K' is a constant of integration, and G is the universal gravitational constant.

Strong Shock (SS): Substituting the boundary condition (3) into the diverging shock Eq. (10) and using Eq. (14), we get

$$\frac{\partial U^2}{\partial r} + B \frac{U^2}{r} - \frac{3}{2} C_1 a^2 \beta_1^2 r^\omega - \frac{C_2 a^2 2\pi r^{-\omega}}{(2 - \omega)D} = 0, \tag{16}$$

where $A = \frac{\chi(\xi)}{\gamma} + \sqrt{\frac{\chi(\xi)}{\xi}} \frac{\xi - 1}{2\sqrt{(1 - b\rho_0)(1 - b\rho_0\xi)}} = 0,$

$$B' = \left[\frac{\chi(\xi)}{\sqrt{(1 - b\rho_0\xi)}} \left\{ 1 - \frac{\sqrt{\xi \chi(\xi)}}{\xi - 1} \sqrt{\frac{(1 - b\rho_0)}{(1 - b\rho_0\xi)}} \right\} - \frac{\chi(\xi)}{\gamma} \left(\frac{1 - 2b\rho_0}{1 - b\rho_0} \right) \omega \right], \tag{17}$$

$$C'_2 = \left[\frac{L}{(1 - b\rho_0)} - \frac{\xi \sqrt{\xi \chi(\xi)}}{(\xi - 1)\sqrt{(1 - b\rho_0)(1 - b\rho_0\xi)}} \left\{ 1 - \frac{\sqrt{\xi \chi(\xi)}}{\xi - 1} \sqrt{\frac{(1 - b\rho_0)}{(1 - b\rho_0\xi)}} \right\} \right],$$

$$C'_1 = (L - \xi^2)B = \frac{B'}{A}, \quad C_1 = \frac{C'_1}{A}, \quad C_2 = \frac{C'_2}{A}.$$

Integrating Eq. (16), we get the equation of free propagation.

$$U^2 = K_s r^{-B} + \frac{3 C_1 a'^2 \beta_1^2 r^{\omega+1}}{2(\omega + B + 1)} + \frac{C'_2 a'^2 2\pi r^{-\omega}}{(2 - \omega)(1 - \omega + B)D}, \tag{18}$$

where K_s is constant of integration.

Now, for C_- disturbances generated by the shock, the fluid velocity increment are given as:

$$du_- = -\left(\frac{\xi - 1}{\xi}\right)dU$$

Substituting the value of dU from Eq. (18), we get:

$$du_- = -\left(\frac{\xi - 1}{\xi}\right)\left[-\frac{U}{2r}B + \frac{1}{2U}\left\{C_1 a'^2 \beta_1^2 r^\omega + \frac{C_2 a'^2 2\pi r^{-\omega}}{(2 - \omega)D}\right\}\right]dr. \tag{19}$$

Similarly, substituting the boundary condition (3) into the converging shock Eq. (11) and using (14), we get:

$$A' \frac{\partial U^2}{\partial r} + B_2'' \frac{U^2}{r} - \frac{3}{2} C'_3 a'^2 \beta_1^2 r^\omega - \frac{2\pi C'_4 a'^2 r^{-\omega}}{(2 - \omega)D} = 0, \tag{20}$$

where $A = \frac{\chi(\xi)}{\gamma} - \sqrt{\frac{\chi(\xi)}{\xi} \frac{\xi - 1}{2\sqrt{(1 - b\rho_0)(1 - b\rho_0\xi)}}$,

$$B'_2 = \left[\frac{\chi(\xi - 1)}{(1 - b\rho_0\xi)\left((\xi - 1) - \sqrt{\chi(\xi)\xi\sqrt{\frac{1 - b\rho_0}{1 - b\rho_0\xi}}}\right)} - \frac{\chi(\xi)}{\gamma} \left(\frac{1 - 2b\rho_0}{1 - b\rho_0}\right)\omega \right],$$

$$C'_4 = \left[\frac{L}{(1 - b\rho_0)} + \frac{\xi}{\sqrt{(1 - b\rho_0)(1 - b\rho_0\xi)}} \frac{\sqrt{\xi \chi(\xi)}}{\left((\xi - 1) - \sqrt{\xi \chi(\xi)\sqrt{\frac{1 - b\rho_0}{1 - b\rho_0\xi}}}\right)} \right],$$

$$C'_3 = (L - \xi^2),$$

$$\frac{\partial U^2}{\partial r} + B_2 \frac{U^2}{r} - \frac{3}{2} C_3 a'^2 \beta_1^2 r^\omega - \frac{C_4 a'^2 2\pi r^{-\omega}}{(2 - \omega)D} = 0, \tag{21}$$

$$B_2 = \frac{B'_2}{A}, \quad C_3 = \frac{C'_3}{A}, \quad C_4 = \frac{C'_4}{A}.$$

For the C_+ disturbances generated by the shock, the fluid velocity increment using (21) into boundary conditions (3) will be expressed as:

$$du_+ = \left(\frac{\xi - 1}{\xi}\right) \left[-\frac{U}{2r} B_2 + \frac{1}{2U} \left\{ \frac{3}{2} C_3 a'^2 \beta_1^2 r^\omega + \frac{C_4 a'^2 2\pi r^{-\omega}}{(2 - \omega)D} \right\} \right] dr. \tag{22}$$

Now in presence of both the C_- and C_+ disturbances, the fluid increment behind the shock is related as:

$$du_- + du_+ = \left(\frac{\xi - 1}{\xi}\right) dU. \tag{23}$$

Substituting the values from Eqs. (19) and (22) and solving, we get:

$$\frac{\partial U^2}{\partial r} + B^* \frac{U^2}{r} - C_5^* a'^2 \beta_1^2 r^\omega - \frac{C_6^* a'^2 2\pi r^{-\omega}}{(2 - \omega)D} = 0. \tag{24}$$

Integrating above equation, we get:

$$U^2 = K_p r^{-B^*} + \frac{C_5 a'^2 \beta_1^2 r^{\omega+1}}{(\omega + B^* + 1)} + \frac{C_6 a'^2 2\pi r^{1-\omega}}{(2 - \omega)(B^* - \omega + 1)D}, \tag{25}$$

where K_p is a constant of integration, $B^* = B + B_2$, $C_5 = C_1 + C_3$, $C_6 = C_2 + C_4$.

Using Eqs. (18) and (25) into the strong shock boundary conditions (3), the expressions for both the free propagation (FP) and the effect of overtaking disturbances (EOD) have been obtained, respectively, and are given as:

Free Propagation (FP)

$$\frac{U}{a_o} = \left(\frac{K_s}{a'} r^{-B} + \frac{3}{2} \frac{C_1 a'^2 \beta_1^2 r^{\omega+1}}{(\omega + B + 1)} + \frac{C'_2 a'^2 2\pi r^{-\omega}}{(2 - \omega)(1 - \omega + B)D} \right)^{1/2} \left(K_1^* r^{1-\omega} \gamma - \frac{3}{2} \gamma \beta_1^2 r^{1+\omega} r + K r^\omega \right)^{-1/2}, \tag{26}$$

$$\frac{U}{a'} = \left(K_s r^{-B} + \frac{3}{2} \frac{C_1 a'^2 \beta_1^2 r^{\omega+1}}{(\omega + B + 1)} + \frac{C'_2 a'^2 2\pi r^{-\omega}}{(2 - \omega)(1 - \omega + B)D} \right)^{1/2}, \tag{27}$$

$$\frac{u}{a'} = \left(\frac{\xi - 1}{\xi}\right) \left(K_s r^{-B} + \frac{3}{2} \frac{C_1 a'^2 \beta_1^2 r^{\omega+1}}{(\omega + B + 1)} + \frac{C'_2 a'^2 2\pi r^{-\omega}}{(2 - \omega)(1 - \omega + B)D} \right)^{1/2}, \tag{28}$$

$$\frac{p}{p'} = \left[\chi(\xi) \left(\frac{U}{a_o} \right)^2 + L \right] \left(K_1^* r^{1-2\omega} \gamma - \frac{3}{2} \gamma \beta_1^2 r + K' \right), \tag{29}$$

$$\frac{\rho}{\rho'} = r^{-w} \xi. \tag{30}$$

Effect of Overtaking Disturbances (EODs)

$$\frac{U}{a_o} = \left(\frac{K_p^*}{a'} r^{-B^*} + \frac{3}{2} \frac{C_5 \beta_1^2 r^w}{(\omega + B^* + 1)} + \frac{C_6 2\pi r^{1-\omega}}{(2-\omega)(1-\omega + B^*)D} \right)^{1/2} \left(K_1^* r^{1-\omega} \gamma - \frac{3}{2} \gamma \beta_1^2 r^{1+w} r + K r^w \right)^{-1/2}, \tag{31}$$

$$\frac{U}{a'} = \left(\frac{K_p^*}{a'} r^{-B^*} + \frac{3}{2} \frac{C_5 \beta_1^2 r^w}{(\omega + B^* + 1)} + \frac{C_6 2\pi r^{1-\omega}}{(2-\omega)(1-\omega + B^*)D} \right)^{1/2}, \tag{32}$$

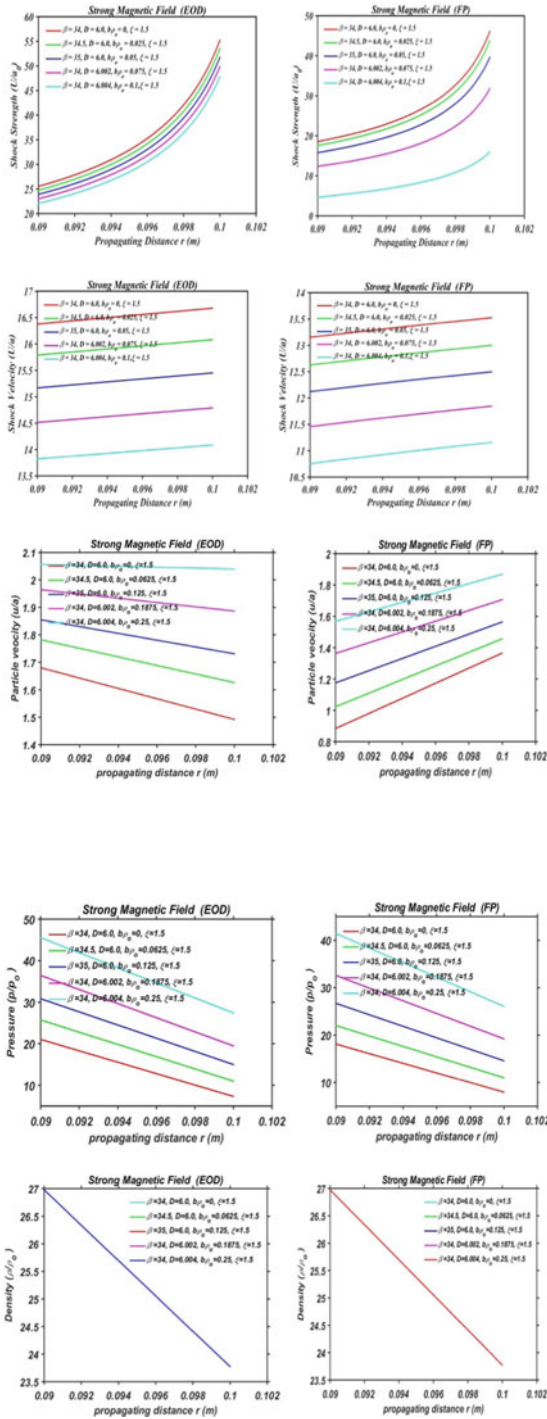
$$\frac{u}{a'} = \left(\frac{\xi - 1}{\xi} \right) \left(\frac{K_p^*}{a'} r^{-B^*} + \frac{3}{2} \frac{C_5 \beta_1^2 r^w}{(\omega + B^* + 1)} + \frac{C_6 2\pi r^{1-\omega}}{(2-\omega)(1-\omega + B^*)D} \right)^{1/2}, \tag{33}$$

$$\frac{p}{p'} = \left[\chi(\xi) \left(\frac{U}{a_o} \right)^2 + L \right] \left(K_1^* r^{1-2\omega} \gamma - \frac{3}{2} \gamma \beta_1^2 r + K' \right), \tag{34}$$

$$\frac{\rho}{\rho'} = r^{-w} \xi. \tag{35}$$

4 Results and Discussion

The behavior of the shock strength, shock velocity, particle velocity, pressure, and density at various values of non-idealness parameter and gravitational constant has been shown in the figures mentioned below.



From above figures, it has been obtained that the shock strength increases with the increasing non-idealness parameter ($b\rho_o$) of the gases as an increase in $b\rho_o$ gives rise to the collisions of gas particles frequently. The shock velocity also increases with $b\rho_o$ for both the motion of free propagation and effect of overtaking disturbances subsequently, but in the case of particle velocity, it increases in the freely propagating case whereas decreases with the inclusion of the overtaking disturbances well. The pressure as well as the density decreases with the increasing value of $b\rho_o$ and G . It can be seen from the density graph that all the plots overlap each other and only a single line is seen because the density only depends on the propagation distance r and a constant w . It is to be noted that the range difference of flow variables for both the FP and EOD case does not vary a lot and the accuracy for all these flow parameters is shown in Tables 1 and 2, respectively. The obtained results of the present problem following Van der Waals equation of state and CCW method are compared with that to the work of Mishra and Kumar [9] following an ideal gas equation of state and the CCW method for plane shocks.

Table 1 Comparison of flow variables with and without disturbances

r	U/a_0 (shock strength)			U/a' (shock velocity)		
	FP	EOD	CP	FP	EOD	CP
0.090	11.484	12.156	0.672	6.829	7.152	0.323
0.092	12.765	13.821	1.056	6.963	7.621	0.658
0.094	14.466	15.123	1.257	7.090	8.105	1.065
0.096	16.916	18.506	1.590	7.211	8.752	1.541
0.098	20.959	21.597	1.738	7.327	9.103	1.776
0.100	29.948	30.876	1.928	7.438	9.875	2.437

Table 2 Comparison of flow variables with and without disturbances

r	u/a' (particle velocity)			p/p' (pressure)		
	FP	EOD	CP	FP	EOD	CP
0.090	1.568	2.056	0.488	41.48	45.535	4.089
0.092	1.636	2.052	0.416	38.134	41.571	3.437
0.094	1.699	2.049	0.350	34.948	37.798	2.793
0.096	1.759	2.046	0.287	31.875	34.180	2.302
0.098	1.815	2.092	0.227	28.915	30.705	1.807
0.100	1.868	2.039	0.171	26.061	27.416	1.355

5 Conclusions

In the present paper, the effect of overtaking disturbances on the motion of strong hydro-magnetic shock is shown and compared with the freely propagating case, i.e., when these disturbances are neglected. The comparison of both the cases is done through tabular and graphical form as mentioned above. It is important to note that the shock gets strengthened when the effect of overtaking disturbances are considered and also with increasing the non-idealness parameter of the gases. The shock strength with the inclusion of the overtaking disturbances increases more rapidly with propagation distance than that predicted for the freely propagating shocks. This implies that the present method is convenient to explain more accurately the abrupt increase in shock strength in the interstellar medium and space. The shock velocity, particle velocity, and pressure as well increase more speedily under the EOD than predicted for the FP.

The density shows the constant behavior because its distribution initially is assumed to be constant and the behavior of pressure as well as density both decrease with increasing non-idealness parameter of the gases.

Acknowledgements The author Sewa Singh is thankful to the UGC New Delhi, India, for the financial support.

Nomenclature

$b\rho_o$	Non-idealness parameter of gas
<i>FP</i>	Freely propagating
<i>EOD</i>	Effect of overtaking disturbances
ρ/ρ'	Density variation
p/p'	Pressure variation
U/a_o	Shock strength
u/a'	Particle velocity
U/a'	Shock velocity

References

1. Chester W (1954) *Phil Mag*, Taylor & Francis 45(7):1293
2. Chisnell RF (1955) The normal motion of shock wave through a non-uniform one-dimensional medium. *Proc Roy Soc (London) A* 232:350
3. Whitham GB (1958) The propagation of shock waves through regions of non-uniform area or flow. *J Fluid Mech* 4:337
4. Yousaf M (1974) The effect of overtaking disturbances on the motion of converging shock waves. *J Fluid Mech* 66(3):577–591

5. Yousaf M (1982) Effect of overtaking disturbances on the motion of a shock wave due to an intense explosion. *AIP Phys Fluids* 25(1):523–533
6. Milton BE (1975) Mach reflection using ray-shock theory. University of New South Wales
7. Singh CV (2003) Effect of overtaking disturbances on the motion of cylindrical hydro-magnetic shock waves in a self-gravitating gas. *Mat Sci Res India* 1(2):83–90
8. Yadav RP, Tripathi S (1995) Effect of overtaking disturbances on the propagation of spherical shock wave. *Astrophys Space Sci* 225:67–80
9. Mishra N, Kumar S (2018) Effects of overtaking disturbances on the motion of plane hydro-magnetic shock waves in a self-gravitating gas. (*JETIR*) *J Emerg Technol Innovative Res* 5(10):2349–5162

An Investigation on the Effect of Changing Bump Geometry on a 2D Supersonic Inlet



Pranav Joshi, Om Kolhatkar, and Prithviraj Ghule

Abstract The present study investigates the utilization of a bump on a 2D supersonic inlet design operating at Mach 2.2. The primary objective is to analyze the flow characteristics on the second ramp of the intake. Different bump sizes, specifically 2 mm, 4 mm, and 6 mm, were computationally examined to assess the disparity in static pressures and efficiencies of a supersonic inlet considering a cowl angle of 1° . The observations were that the 2 mm and 4 mm sized bump resulted in minimal supersonic spillage, whereas the 6 mm exhibited highest spillage. Consequently, it is derived that an increase in the bump size beyond a certain tolerance leads to a greater occurrence of normal shock waves. Furthermore, the adoption of a 2 mm-sized bump resulted in improved total pressure recovery, with visual aids facilitating the understanding of the downstream occurrence of normal shock waves. The analysis of total pressure recovery within the flow field, utilizing the aforementioned bump of 2 mm, provides valuable data for further investigations into the development of supersonic inlets. This research parameter can play a crucial role in determining the efficiencies of inlets in similar operating environments.

Keywords Intake · Back pressure · Bump · Total pressure recovery · Performance

Nomenclature

X	Distance measured from ramp tip [mm]
Y	Distance along the height of inlet [mm]
L	Total length of inlet [mm]
ρ	Density of air [kg/m^3]
M	Mach number [–]
P	Static pressure [Pa]
P_0	Total pressure [pa]

P. Joshi (✉) · O. Kolhatkar · P. Ghule
Department of Aerospace Engineering, MIT Pune, Pune 412201, India
e-mail: joshipranav221@gmail.com

1 Introduction

An aircraft will require one or more intakes to capture the atmospheric air at free-stream Mach number. Moreover, the intake must achieve all these with minimum disturbance to the external flow around the aircraft and thus minimum external drag. It is situated before the compressor and is in the frontal portion of the fuselage, to permit an efficient supply of air under various flight regimes. An inlet is a duct that is required to ensure smooth airflow into the engine despite air approaching the inlet from directions other than straight ahead. This occurs on the ground from crosswinds and in flight with aircraft pitch and yaw motions. Survey on implementation of bump in inlets results in good pressure recoveries compared to ideal inlets. Resulting geometry ensures smooth flow of air in the engine by reducing the total pressure losses taking place due to formation of shockwaves. The following research work is carried out to analyze the inlet performance by adopting a bump of variable diameter and size. Designing supersonic inlets is more difficult than subsonic as the factor of study in determination of the performance including total pressure.

The inlet lip is sharpened to minimize the performance losses from shock waves that occur during supersonic flight. For a supersonic aircraft, the inlet must slow the flow down to subsonic speeds before the air reaches the compressor. Some supersonic inlets use a central cone to shock the flow down to subsonic speeds. Other inlets use flat-hinged plates to generate the compression shocks, with the resulting inlet geometry having a rectangular cross-section. Das [1] studied the computations and experimentations with distinct flow field features inside the inlet with the adoption of a 3D bump. Similar studies of a 3D bump placed on the second ramp of an external compression inlet are studied and investigated by Kim and Song [2] operating at Mach 2. Corresponding application of a 3D bump has also been analyzed experimentally and computationally by Kim and Song [3]. This paper briefly elaborates a study made on a 2D supersonic inlet with the adoption of a bump of variable sizes placed on the second ramp of a mixed-compression inlet operating at free-stream Mach 2.2. Computations are investigated and scrutinized to further validate the bump induced in a distinct flow field. The effect of cowl angle deflection without back pressure has been studied by Das et al. [4] and reported that deflection in cowl angle tends to improve the performance. Chopra et al [1] demonstrated the flow characteristics in an inlet with adoption of a 3D bump and stated that change in shock reflection pattern directly affects the total pressure at the exit of the inlet. Shock train govern the flow requirements inside the inlet. Using a mixed-compression supersonic air inlet for Mach 2.2, the aim of this paper is to study the flow field inside the 2D cavity of a 2D inlet by applying a bump. Computations were done to determine the inlet's performance overall.

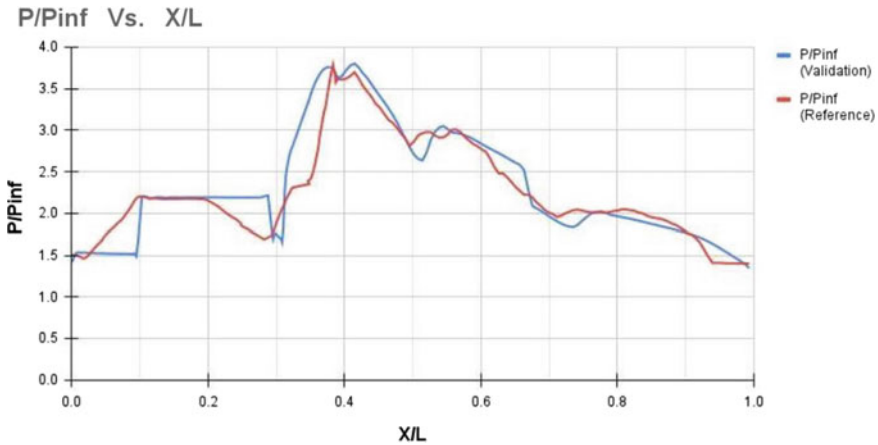


Fig. 1 Surface pressure comparison graph

2 Validation Test

A computational analysis has been carried out and reported in conjunction with Das [1] for a mixed-compression inlet at 1 degree cowl deflection angle operating at Mach 2.2. Similar flow field features have been studied, simulated, and validated with the necessary referenced computation. The blue line represents validation data that has been in alignment with the reference data Das [1] indicated in red. The graphical data signifies similar results simulated on the second ramp shown in Fig. 1, in comparison to the statistics on the validating reference study of Das [1].

3 Computational Methodology

Computation is performed using a two-dimensional, density-based, steady-state model. Work is carried out using commercial software Ansys Fluent.

A. Geometry

The basic bump geometry investigated for this study includes two ramps having angle 7° and 14° , respectively. The cowl deflection angle adopted for this particular study is 1° , respectively.

This specific investigation for this geometry studies implementation of bumps of sizes 2 mm, 4 mm, 6 mm, respectively, placed on the second ramp of the intake. To study the behavior of oblique shocks and further determine the leading total pressure recoveries in further estimating the overall compressor efficiency (Fig. 2).

The structured grid mesh for the validation study was prepared for Coarse (170,550 cells) having y-direction spacing of 0.01. Similar structured grids for the 2 mm bump

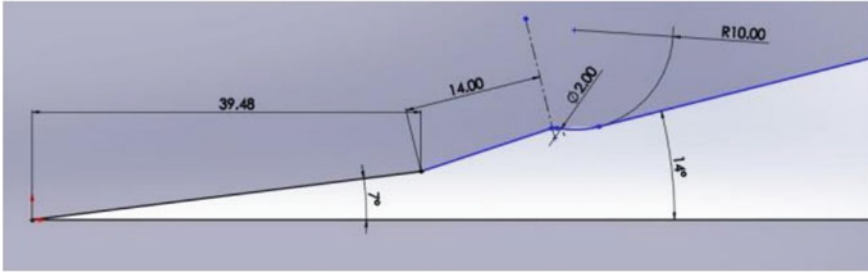


Fig. 2 Schematic of the inlet bump

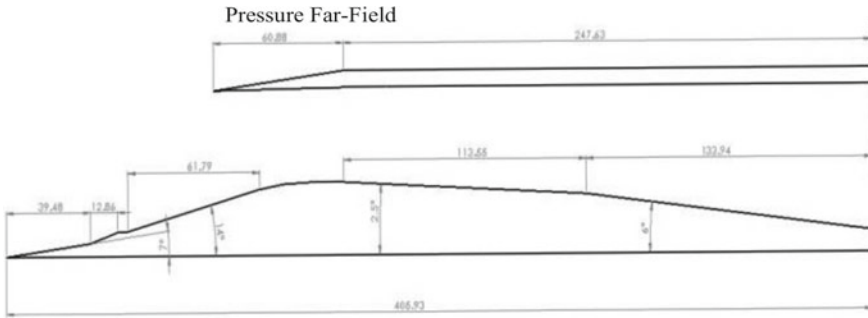


Fig. 3 Geometry of two-dimensional bump intake

were decided for further computation having a cell count of Coarse (238,210 cells) with a y-direction spacing of 0.001. For the 4 mm bump, the prepared structured grid selected was Coarse (249,910 cells) with a similar y-direction spacing of 0.001. Six mm bump computations were carried out using Coarse (254,870 cells) with the same y-direction spacing of 0.001 (Fig. 3).

3.1 Computational Setup and Methods

The entire computational model for the determination of flow field inside the intake has been prepared using a standard K- ω turbulent model. An Explicit coupled solver, Gradient least squares cell based, flow-second order upwind, turbulent kinetic energy-second order upwind, specific dissipation rate-second order upwind, along with energy and transport equations were implemented. Consideration of fluid as air with a density-based solver setup using ideal gas law (Figs. 4 and 5).

Computations are further obtained for the supersonic flow intake with boundary conditions at the inlet to be pressure far field, operating at Mach 2.2 with similar pressure far field conditions at the exit and Reynolds number 2.6×10^7 at the exit.

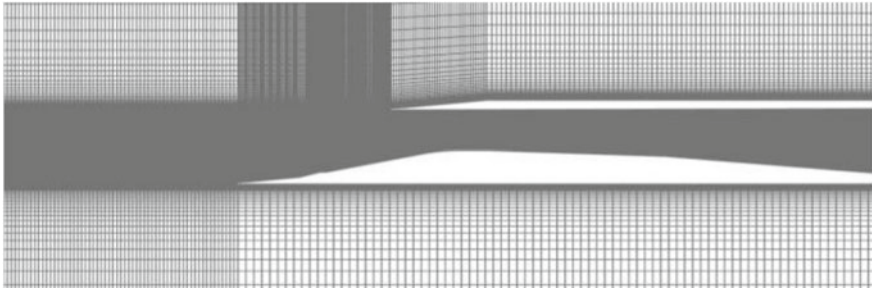


Fig. 4 Domain for the bump geometry

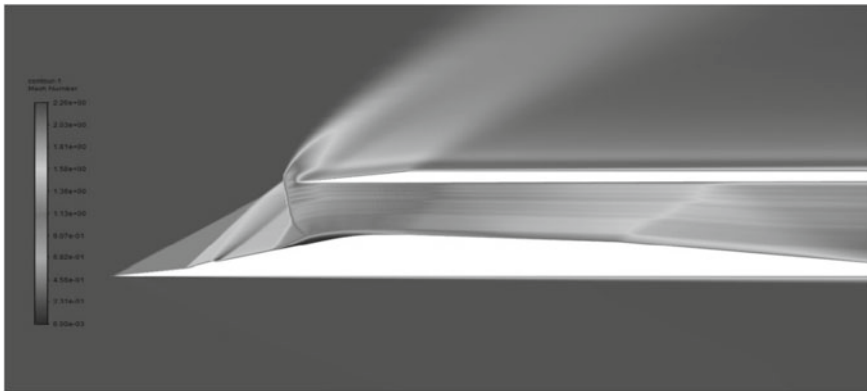


Fig. 5 Black and white contour image

The aligning values from the validation study distinctively indicated the suitability of the turbulent models adopted as well as the boundary conditions used. A similar approach has been uniformly followed while performing computations for all three bumps of 2 mm, 4 mm, and 6 mm, respectively.

The B&W image exhibits flow patterns taking place in a pressurized free-stream condition inside a supersonic flow regime. The formation of oblique shocks at the bump arbitrary angle and similarly a normal shock is seen forming at the entry of the inlet. Inside the inlet, the aftermath of the normal shock waves is seen to have a streamline flow along the centerline of the intake.

4 Results and Discussion

The computations were performed on a mixed-compression supersonic inlet operating at Mach 2.2. The extracted data is further used for determination of two important parameters around which this entire research study involves, ‘Total Pressure

Recovery’ and ‘Efficiency’. The latter is directly proportional to the amount of air supply received and similarly on the quality of air entering the engine. The adoption of a bump of sizes 2 mm, 4 mm, and 6 mm is compared and investigated with the statistical data from Das [5]. The computational study showcased over here compares static and Mach computations obtained for bumps of all three sizes which are thus compared (Figs. 6, 7, 8, 9 and 10).

Computations are further obtained for the supersonic flow intake with boundary conditions at the inlet to be pressure far field, operating at Mach 2.2 with similar pressure far field conditions at the exit and Reynolds number.

The static pressure contours for 2 mm, 4 mm, and 6 mm bumps are shown in Fig. 11 (6 mm), Fig. 9 (4 mm), Fig. 7 (2 mm). Pressure distribution inside the flow field of the inlet indicates the formation of shocks with the application of bumps of variable sizes.

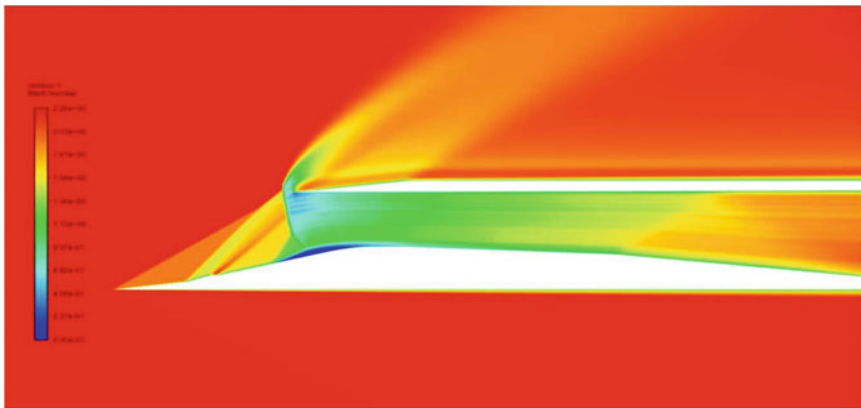


Fig. 6 Mach number contour for 2 mm bump

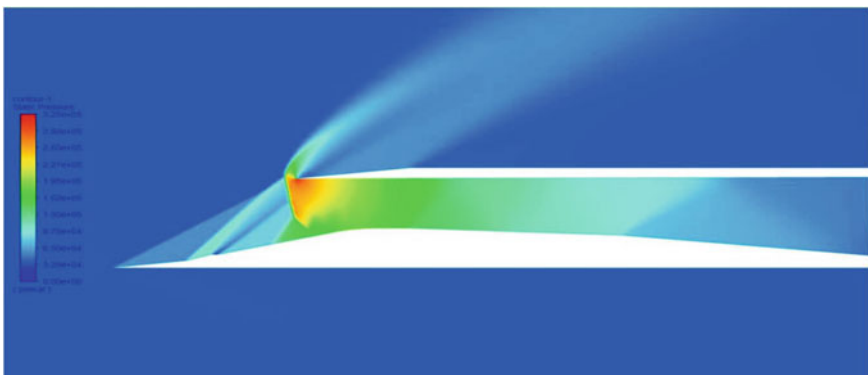


Fig. 7 Static pressure contour for 2 mm bump

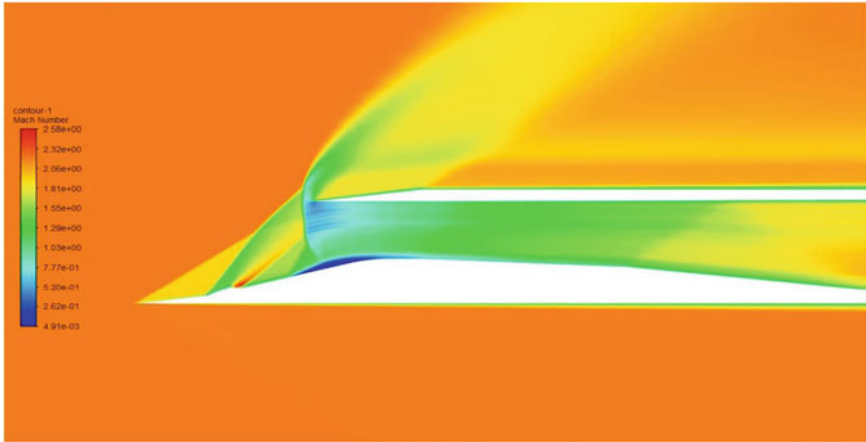


Fig. 8 Mach number contour for 4 mm bump

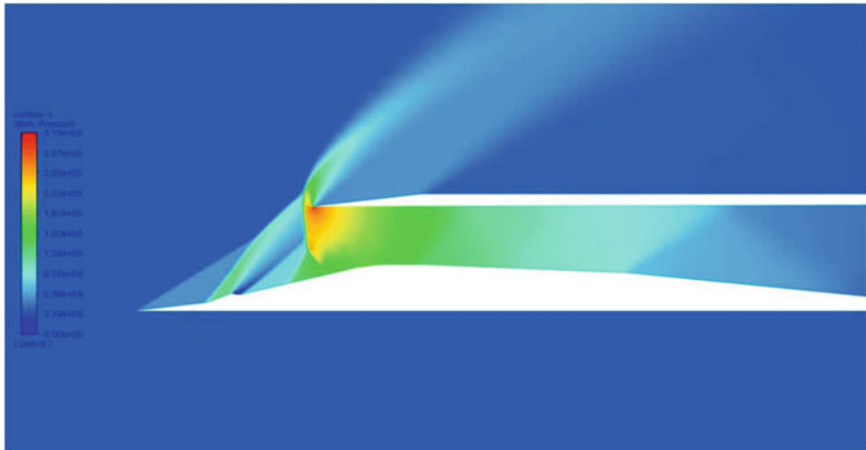


Fig. 9 Static pressure contour for 4 mm bump

A consensus is reached between validation tests and experiments with respect to boundary conditions, meshing parameters as well as flow patterns with the difference in location of normal shocks for all the aforementioned cases.

The above comparison graph shows the result of computation for bump sizes 2 mm, 4 mm, and 6 mm, respectively. The nature of the graph at the second ramp, i.e., at the bump location, a sudden rise in the pressure ratio is observed. Figure 12 shows that from the distance $X/L = 0$ to 0.2 , the 6 mm bump shows greater rise in pressure ratio than the bumps of 2 and 4 mm, thereby concluding that 6 mm bump experiences greater supersonic spillage affecting the total pressure recovery which further influences the engine efficiency. At distance $X/L = 0.2-0.6$, there is a steep

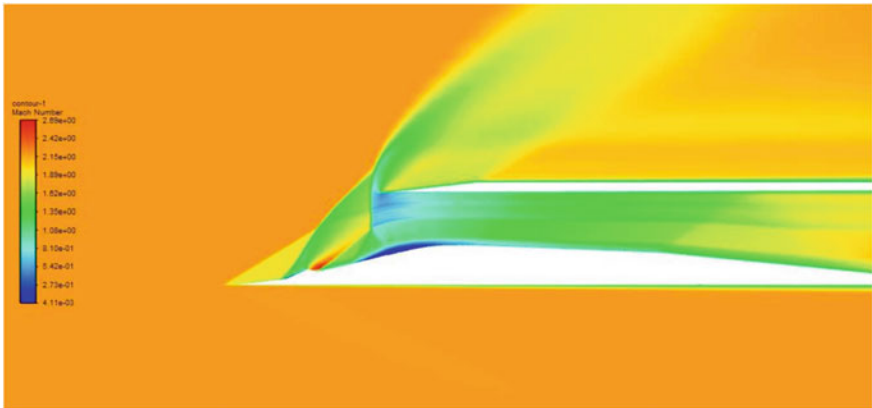


Fig. 10 Mach number contour for 6 mm bump

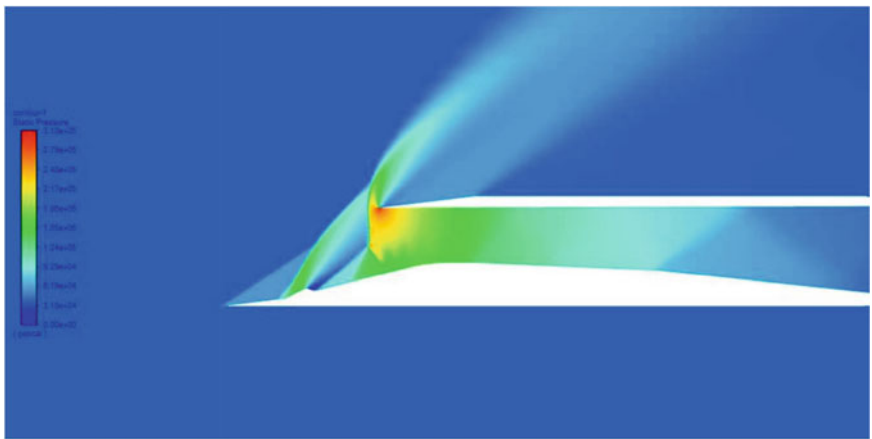


Fig. 11 Static pressure contour for 6 mm bump

rise in the graph. Small size of the bumps of 2 and 4 mm leads to improvement in performance due to flow separation in the larger area of the intake. It is also thereby concluded from the 6 mm statistical data that bumping with an increased size leads to decrease in performance (Table 1).

The total pressure calculated from the data extracted from the computations is 0.8743 for without bump geometry, 0.9372 for geometry with 2 mm bump, 0.9149 for geometry with 4 mm bump, and 0.8848 for geometry with 6 mm bump. The total pressure recovery is observed to be more for 2 mm and 4 mm bump geometry, in comparison with 6 mm bump geometry. A conclusion can be drafted that the total pressure recovery is greater in the intake with a bump.

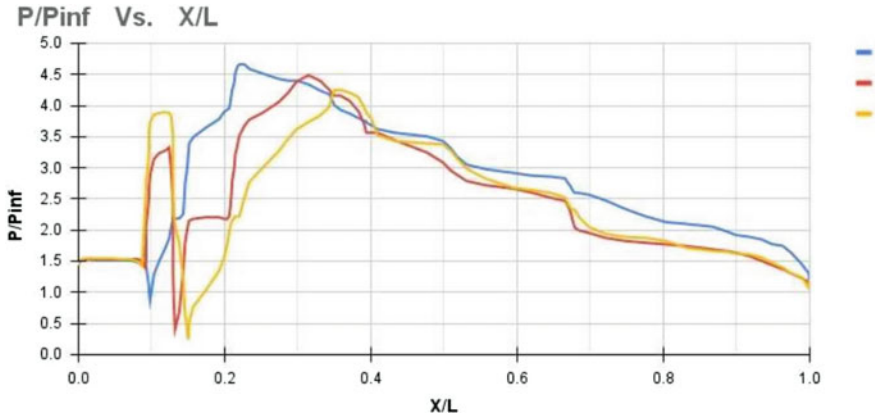


Fig. 12 Comparison graph for P/P_{∞} versus X/L for 2, 4, 6 mm bumps

Table 1 Total pressure recovery and efficiencies

S. no.	Total pressure recovery and efficiency		
	Intake configuration	Total pressure recovery	Efficiency (%)
1	Intake without bump	0.8743	92.3
2	Intake with 2 mm bump	0.9372	96.26
3	Intake with 4 mm bump	0.9149	94.89
4	Intake with 6 mm bump	0.8848	93.01

5 Conclusions

Computations and data have been studied for the inlet bump geometry to study flow field features via implementation of a bump on the second ramp of variable sizes viz. 2 mm, 4 mm, and 6 mm, respectively. Pressure distribution inside the intake indicates variable change in the formation of shock reflection patterns with the adoption of variable bump geometries. Viable parameters including total pressure recovery and efficiencies are calculated. Efficiencies for geometry with 2 mm bump are 96.26%, for geometry 4 mm bump are 94.89%, and for bump geometry 6 mm are found to be 93.01%. Total pressure improvement is observed for the 2 mm bump downstream of the normal shock. The improvement in back pressures is observed as the radius of bump is increased (owing to its semi-conical shape). However, it is noticed that beyond a certain designated radius, it diminishes and drastically decreases given the flow patterns and occurrence of normal shock majorly on the outer surface of the lip substantiating for spillage at the frontal portion leading to lower pressure recoveries and thereby affecting the efficiency. Shape, location as well the number of bumps could be a strong parameter for further research study.

Acknowledgements We would like to thank the Department of Aerospace Engineering MIT Art, Design & Technology University, and our colleagues who have worked tirelessly on the project and for all the constant help and support throughout our research study.

References

1. Chopra G, Das S, Kumar P, Prasad JK (2013) Investigation of flow field inside a supersonic air-intake with a 3-D bump. In: Proceedings of the fortieth national conference on fluid mechanics and fluid power, 12–14 Dec 2013, NIT Hamirpur, Himachal Pradesh, India FMFP2013: Paper 75.
2. Kim SD (2009) Aerodynamic design of a supersonic inlet with a parametric bump. *J Aircr* 46(1)
3. Kim SD, Song DJ (2008) Numerical study on performance of supersonic inlets with various three dimensional bumps. *J Mech Sci Technol* 22:1640–1647
4. Das S, Prasad JK (2009) Cowl deflection angle in a supersonic air intake. *Defense Sci J* 59(2):99–105. Ó 2009, DESIDOC
5. Das S, Prasad JK (2010) Starting characteristics of a rectangular supersonic air intake with cowl deflection. *Aeronaut J* 115(1153)
6. Kim SD, Song DJ, Lim S (2007) A numerical analysis on three-dimensional flow field in a supersonic bump inlet. In: 45th AIAA aerospace sciences meeting and exhibit AIAA 2007-0689 Reno, NV, 08–11 Jan 2007
7. Slater JW, Design and Analysis tool for external compression supersonic inlets. NASA John HGlenn Research Center, Cleveland Ohio 44135.
8. Saunders JD, Keith TG Jr, Result from computational Analysis of a mixed compression supersonic inlet. NASA-Lewis Research Center. Cleveland, Ohio, The Ohio Aerospace Institute Brook Park, Ohio

Laminar Shear Layer Growth in Supersonic Underexpanded Flows



Ali Jraisheh, Jubajyoti Chutia, Amrita Pathak, and Vinayak Kulkarni

Abstract This paper offers an insight on the growth of laminar shear layer in supersonic jets and the extent of the compressible flow region (also known as inviscid core) that is bounded by the barrel shock and shear layer. Numerical simulations are performed on four nozzle shapes, obtained by different optimization methodologies, to probe the near-field area downstream of the nozzle exit. The results are linked to the trend of boundary layer growth within the nozzle and the nozzle wall shape. The viscous and inviscid areas in the near field are closely investigated to understand the factors that trigger the thickness of laminar shear layer and the boundaries of the inviscid core.

Keywords Supersonic jet · Laminar shear layer · CFD · Optimisation

1 Introduction

In the second half of the last century, the interest in shear layer has increased, initially due to near wake problem in turbines, and later on because of its important role in supersonic combustion [1]. There have been extensive studies [2] to explore the transition from laminar to turbulent shear layer that separates two supersonic streams, and the laminar free-of-periodic-oscillation shear layers. The spread rate of shear layer was found to be slower in supersonic jet than it in incompressible shear layer [3]. This difference is found to be partially related to the density ratio between both sides of the shear layer, especially when the supersonic jet is spreading in a quiescent medium. But, the main reason for the slower spread is the different formation processes for shear layer, as it widely depends on its instability in the case of supersonic jet. That is, the supersonic shear layer contains large coherent

A. Jraisheh (✉) · J. Chutia · A. Pathak · V. Kulkarni
Department of Mechanical Engineering, IIT Guwahati, Guwahati 781039, India
e-mail: jraisheh@iitg.ac.in

A. Jraisheh
Department of Mechanical Engineering, Damascus University, Damascus, Syria

structures formed at the earlier stages of instability. Further, the experimental results of Dimotakis [4] show that the dynamics of compressible shear layer do not only depend on the density and velocity ratio, rather they are related to the earlier growth and initial conditions of the boundary layer. In this context, the experiment of Batt [5] revealed that turbulent boundary layer results in a shear layer with more growth rate of thickness and entrainment compared to the undisturbed boundary layer.

In mixing shear layer, Papamoschou et al. [1] coined the concept of convective Mach number, which is the “intrinsic” Mach number when it comes to the effects on shear layer transition. In the case of jet propagating in still gas, convective Mach number is proven to be the same Mach number of the jet.

Fourguette et al. [6] have experimentally probed the evolution of shear layer of an axisymmetric supersonic jet, while matching the exit pressure with back pressure using laser-based Rayleigh scattering techniques. Their findings suggest that the structures in compressible shear layer move in three-dimensional manner, and this aspect gives more three dimensionalities to compressible shear layer compared to the incompressible shear layer.

Rossmann et al. [7] have examined the supersonic shear layer with different compressibilities and convective Mach numbers, numerically and experimentally. It was found that a higher compressibility rate would hamper the growth rate, and it would produce larger structures, while these structures hardly appear in a shear layer of moderate compressibility.

The work of Ma et al. [8] studied the geometrical effect on a growth trend of a confined subsonic–supersonic shear layer. The influencing factors are found to be the combustion chamber height, the splitter plate thickness, and the supersonic nozzle exit diameter. The interaction between the shock train within the supersonic jet and the shear layer is seen to increase its thickness locally.

Another work of Ma et al. [9] has investigated the growth of shear layer between subsonic and supersonic streams in a wind tunnel. It shows that the pressure difference between the streams induces the shear layer to deflect towards the low-pressure stream and hence triggers the shear layer transition.

Davis and Kumar [10] have observed that free jet shear layer is characterised by abrupt growth near the nozzle exit, after which it maintains a linear growth for certain region. In this region, the growth rate is seen to decrease.

The above literature shows a significant interest in shear layers, both between supersonic streams and between a supersonic stream and a stagnant gas. Most of the results are driven by the turbulent model of shear layer and focus on the instabilities induced by the difference in pressure and velocity. Therefore, this study is inclined towards the growth of laminar shear layers between a supersonic jet and a still gas, and the understanding of factors affecting the supersonic gas expansion. The main phenomena are observed in the near-field area, and the thickness of shear layer and the extent of inviscid core are linked to the nozzle geometry and boundary conditions. Such studies are highly desirable for free jet-based testing facilities, astrophysical studies, combustion understanding, and many other applications [11–19].

Section 2 describes the optimization method and the mathematical formulation of the CFD solver, Sect. 3 contains the simulation results and discussion, and Sect. 4 concludes the findings.

2 Methodology

2.1 Optimisation Method

In addition to the well-known conical nozzle, three different approaches are followed to generate the supersonic nozzle wall geometries with correspondent flow at the nozzle exit. For the optimization procedure, gradient steepest descent technique is employed to achieve the minimum overall radial velocity at the nozzle exit using simple one-dimensional code based on gas dynamic relations [20]. The resulting nozzles are as follows:

- Right conical nozzle.
- Nozzle (N1): The wall is mathematically represented by third-order Bezier curve, α in the optimization process is fixed at a value of 0.0001, and the initial angle of divergence is restricted to 15° .
- Nozzle (N2): The wall is mathematically represented by fourth-order Bezier curve, α is calculated using 1D search method, and the initial angle of divergence is not restricted.
- Nozzle (N3): The wall is mathematically represented by fourth-order Bezier curve, α is calculated using 1D search method, and the initial angle of divergence is restricted to 10° .

For each resulting geometry, a grid is prepared, the lines are clustered towards the wall and refined in the near field to capture all the phenomena, and the results are ensured to be independent of the mesh resolution. The mesh is then fed to the CFD solver to obtain the numerical results.

2.2 Computational Domain

To ensure the smoothness of the solution, the domain is extended to 150 throat diameters in axial direction and 50 throat diameters in transverse direction [21]. The domain starts with the nozzle throat as a sonic inlet, considering only the diverging part of the nozzle due to the importance of this region compared to the subsonic part. The unity Mach number, sonic pressure, and temperature are set at the inlet boundary, while the back pressure is set at the outlet boundary. To complete the flow field at the outlet, the temperature is extrapolated from the last cell adjacent to the boundary, and the density is calculated using equation of state. This boundary condition is known

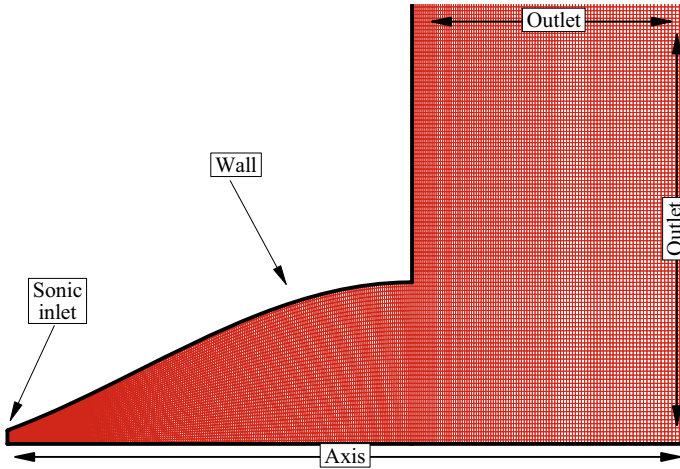


Fig. 1 Computational domain and boundary conditions

as strong pressure averaging, and it is useful in the cases where one is not certain whether the flow is subsonic or supersonic at the exit. Figure 1 illustrates the mesh (enlarged to view the near-field area) and the boundary conditions.

2.3 Governing Equations

In the present work, the numerical procedure involves an in-house CFD programme to solve axisymmetric laminar Navier–Stokes equations, coupled with the equation of state and the energy equation to close the system. Viscosity is treated with Sutherland’s approximation and perfect gas assumption is considered. This solver has already been validated [12].

The axisymmetric Navier–Stokes equations read:

$$\frac{\partial \mathbf{U}}{\partial t} + \frac{\partial \mathbf{F}_I}{\partial x} + \frac{\partial \mathbf{G}_I}{\partial y} + \frac{\partial \mathbf{F}_V}{\partial x} + \frac{\partial \mathbf{G}_V}{\partial y} + \alpha(\mathbf{S}_I - \mathbf{S}_V) = 0,$$

where

$$\mathbf{U} = \begin{bmatrix} \rho \\ \rho u \\ \rho v \\ \rho E \end{bmatrix}; \quad \mathbf{F}_I = \begin{bmatrix} \rho u \\ \rho u^2 + p \\ \rho uv \\ \rho u \left(E + \frac{p}{\rho} \right) \end{bmatrix}; \quad \mathbf{G}_I = \begin{bmatrix} \rho u \\ \rho uv \\ \rho v^2 + p \\ \rho v \left(E + \frac{p}{\rho} \right) \end{bmatrix};$$

$$\mathbf{F}_V = \begin{bmatrix} 0 \\ \tau_{xx} \\ \tau_{xy} \\ u\tau_{xx} + v\tau_{xy} - q_x \end{bmatrix}; \quad \mathbf{G}_V = \begin{bmatrix} 0 \\ \tau_{xy} \\ \tau_{yy} \\ u\tau_{xy} + v\tau_{yy} - q_y \end{bmatrix}.$$

The vectors \mathbf{S}_I and \mathbf{S}_V are inviscid and viscous source terms, respectively, and are relevant only for axisymmetric flows. These may be expressed as,

$$\mathbf{S}_I = \frac{1}{y} \begin{bmatrix} \rho v \\ \rho uv \\ \rho v^2 \\ \rho v \left(E + \frac{p}{\rho} \right) \end{bmatrix};$$

$$\mathbf{S}_V = \frac{1}{y} \begin{bmatrix} 0 \\ \tau_{xy} - \frac{2}{3}y \frac{\partial}{\partial x}(\mu v/y) \\ \tau_{yy} - \tau_{\theta\theta} - \frac{2v}{3y}\mu - \frac{2}{3}y \frac{\partial}{\partial y}(\mu v/y) \\ u\tau_{xy} + v\tau_{yy} - q_y - \frac{2\mu v^2}{3y} - \frac{2y}{3} \frac{\partial}{\partial y} \left(\frac{\mu v^2}{y} \right) \\ -\frac{2y}{3} \frac{\partial}{\partial x}(\mu uv/y) \end{bmatrix},$$

where

$$q_x = -k \frac{\partial T}{\partial x}; \quad q_y = -k \frac{\partial T}{\partial y},$$

$$\tau_{xx} = \mu \left(\frac{4}{3} \frac{\partial u}{\partial x} - \frac{2}{3} \frac{\partial v}{\partial y} \right); \quad \tau_{yy} = \mu \left(\frac{4}{3} \frac{\partial v}{\partial y} - \frac{2}{3} \frac{\partial u}{\partial x} \right),$$

$$\tau_{xy} = \mu \left(\frac{\partial u}{\partial y} - \frac{\partial v}{\partial x} \right); \quad \tau_{\theta\theta} = \mu \left(-\frac{2}{3} \left(\frac{\partial u}{\partial x} + \frac{\partial v}{\partial y} \right) + \frac{4v}{3y} \right).$$

3 Results and Discussion

The nozzle wall shapes for the above-mentioned four nozzles are generated considering throat diameter of 2 mm, exit diameter of 24 mm, and a nozzle length of 30 mm. The flowing gas is argon with a total temperature of 1300 K and a nozzle pressure ratio of 2200. The resulting shapes are used to generate the desired computational domains and then fed to the in-house CFD code. The output of CFD simulations depicts the contours of gas properties in the near-field area. Further, the transverse profiles of these properties are extracted at the nozzle exit plane in addition to four different axial locations, viz., 5 mm, 10 mm, 15 mm, and 20 mm downstream of

the nozzle exit plane, and these locations correspond to 2.5D, 5D, 7.5D, and 10D downstream of the nozzle exit, respectively.

To visualise the thickness of the inviscid core and shear layer at these different locations, density profiles for the conical nozzle, *N1*, *N2*, and *N3* are plotted in Figs. 2, 3, 4, and 5, respectively. The radial coordinate *Y* is normalised to the nozzle throat diameter. For comparison, a dashed line of reference is drawn at a radial location where the inviscid core of conical nozzle ends at an axial location of 20 mm. One can notice that the inviscid core of nozzle *N1* extends farther above the line, indicating more radial extent for the locations downstream of nozzle exit, whereas the flow seems less uniform at the nozzle exit.

Moreover, the flow emitting from nozzle *N2* attains a uniform profile at the nozzle exit and then shear layer starts to take over the inviscid area. At a location of 30 mm downstream the nozzle exit, the flow loses its uniformity, and it appears that inviscid core has been terminated at a location between 15 and 20 mm downstream the nozzle exit. Looking at the radial profile of nozzle *N3* jet, the flow behaves uniformly across the axial and radial directions and the uniform area extends father above the reference line.

Further, the plots show that shear layer of nozzle *N1* is comparable in thickness with that of conical nozzle, whereas nozzles *N2* and *N3* show higher thickness in shear layer. The density in all the nozzles decreases in the downstream direction and it obtains the minimum at a location of 20 mm downstream. However, the same

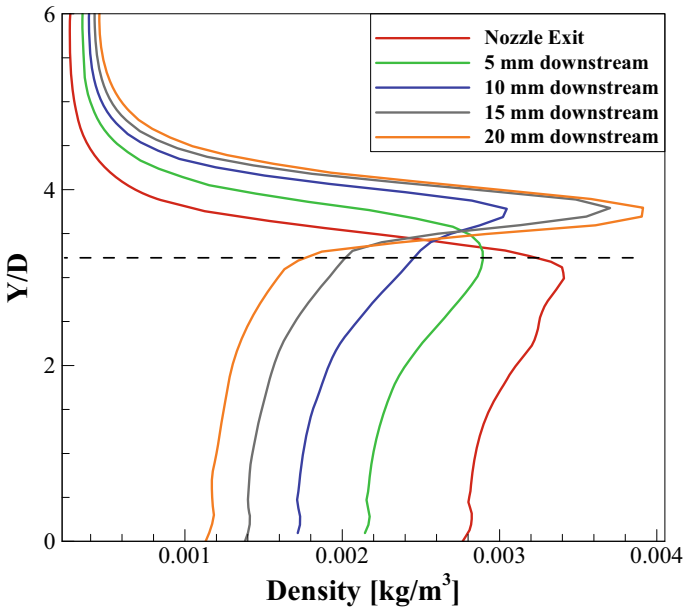


Fig. 2 Radial density profile at the exit and four axial locations downstream the exit of conical nozzle

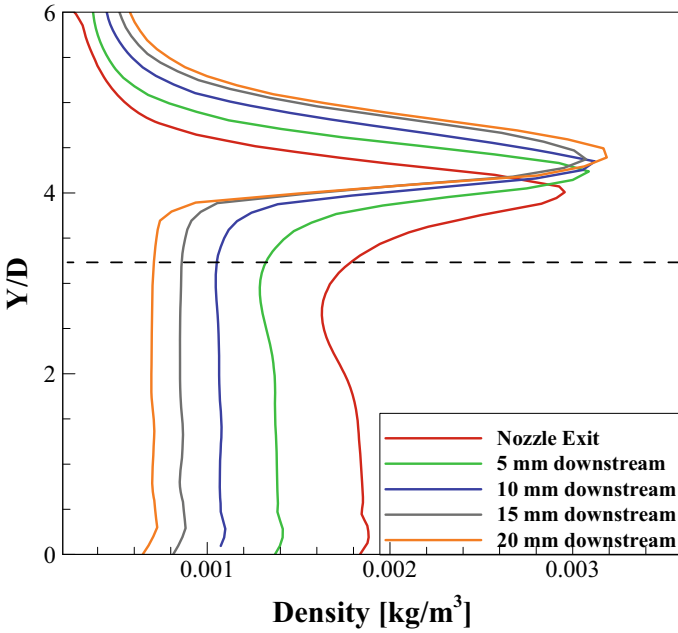


Fig. 3 Radial density profile at the exit and four axial locations downstream the exit of nozzle N1

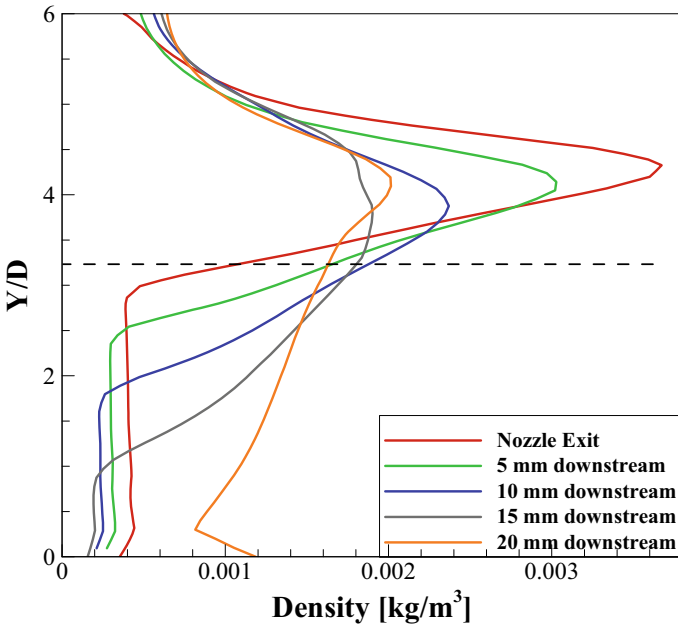


Fig. 4 Radial density profile at the exit and four axial locations downstream the exit of nozzle N2

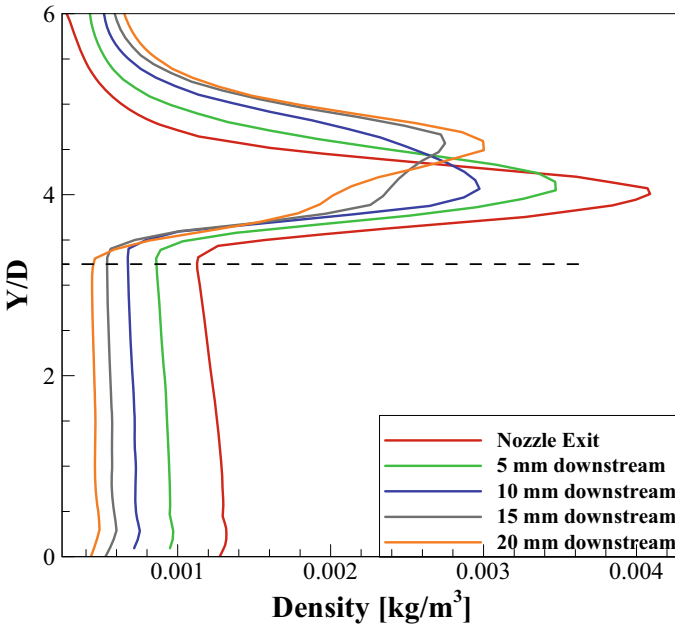


Fig. 5 Radial density profile at the exit and four axial locations downstream the exit of nozzle *N3*

axial location in nozzle *N2* shows higher density, which implies a compression wave upstream of this location, i.e. between 15 and 20 mm downstream.

To investigate the flow field further, Figs. 6 and 7 illustrate isodensity lines for the four nozzles. In these figures, one can discriminate the incident shock (barrel shock) and shear layer (resulting from boundary layer within the nozzle). It is found that there is a weak disturbance within the conical nozzle and nozzle *N1*, which propagates up to the nozzle exit and then diffuses downstream. This disturbance justifies the distorted radial profile at the exit of these two nozzles (Figs. 2 and 3). However, nozzles *N2* and *N3* do not show similar trend and hence the uniform profile at the exit.

Furthermore, the unrestricted divergence downstream the throat of nozzle *N2* allows the jet to expand freely and rapidly within the nozzle, which causes the jet pressure to drop drastically and decreases the degree of underexpansion, and therefore terminates the inviscid core at an earlier axial location. Also, from the isodensity lines of nozzles *N2* and *N3*, there seems to be larger gap between the barrel shock and shear layer than the cases of the conical nozzle and nozzle *N1*. This effect explains the observed thickness of shear layer in Figs. 4 and 5.

To take a closer look at how the flow is propagating, the axial pressure distribution within the four nozzles and in the near-field area is plotted in Fig. 8. In this figure, the axial distance is normalised to the throat diameter, and the jet pressure is normalised to the back pressure.

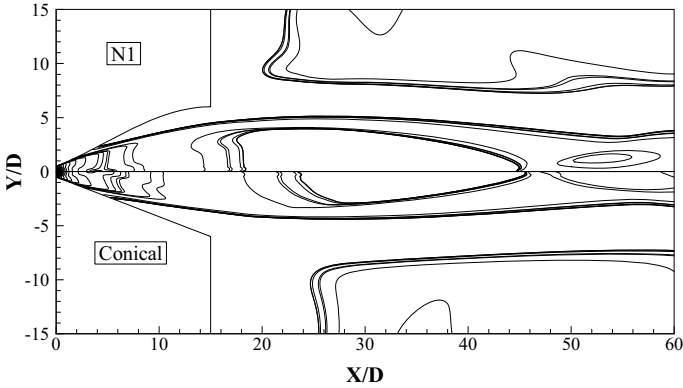


Fig. 6 Isodensity lines for the conical nozzle (bottom) and nozzle *N1* (top)

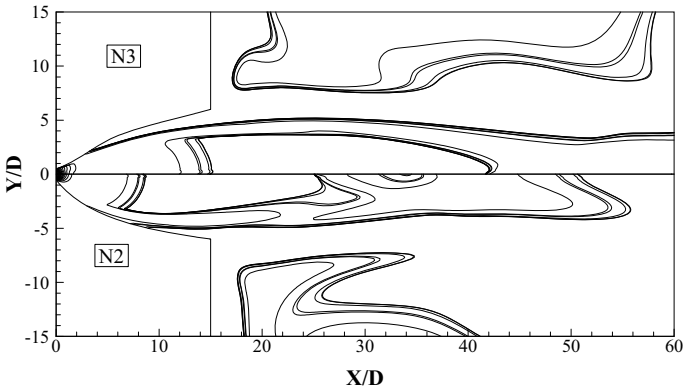


Fig. 7 Isodensity lines for nozzle *N2* (bottom) and nozzle *N3* (top)

It is clear from Fig. 8 that jet expansion is terminated at an earlier location $22X/D$ in the case of nozzle *N2* due to the free expansion. The inviscid core is extended up to $40X/D$, $44X/D$, and $46X/D$ for nozzles *N3*, *N1*, and the conical nozzle. It is further seen that the conical nozzle forms stronger internal shock immediately downstream the throat, whereas this disturbance is weaker for nozzle *N1* and it is not present in nozzles *N2* and *N3*.

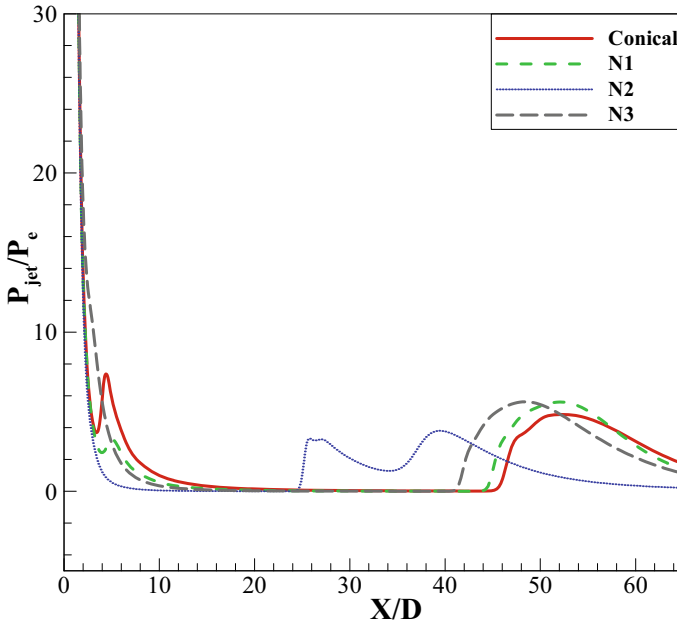


Fig. 8 Axial pressure distribution in the near-field area for the four nozzles

4 Conclusion

This paper describes the near-field area of an underexpanded supersonic jet produced from different nozzles into a still gas, using laminar flow assumption. One-dimensional optimisation code is employed to form the nozzle wall shape using different techniques, and the numerical simulations are performed using an in-house CFD solver. The shear layer contains the compressible flow region, and it draws the jet boundaries. It is found that restricted expansion in the nozzle leads to thin shear layer, due to controlled growth within the nozzle, whereas free expansion within the nozzle increases the thickness of shear layer and enlarges the gap between the barrel shock and shear layer. Further, it is noticed that when the angle of divergence is constrained, the inviscid core extends further downstream due to higher level of underexpansion.

Nomenclature

- D* Orifice diameter (m)
- M* Mach number
- P* Pressure (N/m²)

P_{jet}/P_b	Jet pressure ratio
ρ	Density (kg/m^3)
T	Temperature (K)
τ_{xx} & τ_{yy}	Normal stress (N/m^2)
τ_{xy} & τ_{yx}	Shear stress (N/m^2)
u	X Component of velocity (m/s)
v	Y Component of velocity (m/s)

References

- Papamoschou D, Roshko A (1988) Observations of supersonic free shear layers. *Sadhana* 12(1):1–14
- Demetriades A, Brower TL (1982) Experimental study of transition in a compressible free shear layer. Technology report Montana State University Bozeman Supersonic Wind Tunnel Lab
- Brown GL, Roshko A (1974) On density effects and large structure in turbulent mixing layers. *J Fluid Mech* 64(4):775–816
- Dimotakis PE (1986) Two-dimensional shear-layer entrainment, *AIAA journal* 24(11):1791–1796
- Batt RG (1975) Layer some measurements on the effect of tripping the two-dimensional shear. *AIAA J* 13(2):245–247
- Fourchette DC, Mungal MG, Dibble RW (1991) Time evolution of the shear layer of a supersonic axisymmetric jet. *AIAA J* 29(7):1123–1130
- Rossmann T, Mungal M, Hanson R (2000) An experimental investigation of high compressibility non-reacting mixing layers. In: 38th aerospace sciences meeting and exhibit, p 663
- Ma K, Li J, Li Q, Liu Y, Ao W, Liu P (2020) Numerical and experimental investigation of the geometrical scale effect on a confined subsonic supersonic shear layer. *Acta Astronaut* 173:212–220
- Ma K, Li J, Li Q, Liu Y (2020) Experimental study on evolution characteristics of plane subsonic-supersonic shear layer. *Aerosp Sci Technol* 100:105791
- Davis TB, Kumar R (2015) Shear layer characteristics of supersonic free and impinging jets. *Shock Waves* 25(5):507–520
- Dingilian KK, Lippe M, Kubecka J, Krohn J, Li C, Halonen R, Keshavarz F, Reischl B, Kurten T, Vehkamäki H et al (2021) New particle formation from the vapor phase: From barrier-controlled nucleation to the collisional limit. *J Phys Chem Lett* 12:4593–4599
- Tanimura S, Park Y, Amaya A, Modak V, Wyslouzil BE (2015) Following heterogeneous nucleation of CO_2 on H_2O ice nanoparticles with microsecond resolution. *RSC Adv* 5(128):105537–105550
- Bonnamy A, Georges R, Benidar A, Boissoles J, Canosa A, Rowe BR (2003) Infrared spectroscopy of $(\text{CO}_2)_N$ nanoparticles ($30 < N < 14500$) flowing in a uniform supersonic expansion. *J Chem Phys* 118(8):3612–3621
- Kudryavtsev Y, Ferrer R, Huyse M, Van den Bergh P, Van Duppen P (2013) The in-gas-jet laser ion source: resonance ionization spectroscopy of radioactive atoms in supersonic gas jets. *Nucl Instrum Methods Phys Res Sect B: Beam Interact Mater Atoms* 297:7–22
- Dudas E, Suas-David N, Brahmachary S, Kulkarni V, Benidar A, Kassi S, Charles C, Georges R (2020) High-temperature hypersonic Laval nozzle for non-LTE cavity ringdown spectroscopy. *J Chem Phys* 152(13):134201

16. Potapov A, Canosa A, Jiménez E, Rowe B (2017) Uniform supersonic chemical reactors: 30 years of astrochemical history and future challenges. *Angewandte Chemie Int Ed* 56(30):8618–8640
17. West NA, Millar TJ, Van de Sande M, Rutter E, Blitz MA, Decin L, Heard DE (2019) Measurements of low temperature rate coefficients for the reaction of CH with CH₂O and application to dark cloud and agb stellar wind models. *Astrophys J* 885(2):134
18. Suas-David N, Thawoos S, Suits AG (2019) A uniform flow–cavity ring-down spectrometer (uf-crds): a new setup for spectroscopy and kinetics at low temperature. *J Chem Phys* 151(24):244202
19. Canosa A, Ocana AJ, Antinolo M, Ballesteros B, Jimenez E, Albaladejo J (2016) Design and testing of temperature tunable de Laval nozzles for applications in gas-phase reaction kinetics. *Exp Fluids* 57(9):1–14
20. Anderson JD (1990) *Modern compressible flow: with historical perspective*, vol 12. McGraw-Hill New York
21. Otobe Y, Kashimura H, Matsuo S, Setoguchi T, Kim HD (2008) Influence of nozzle geometry on the near-field structure of a highly underexpanded sonic jet. *J Fluids Struct* 24(2):281–293
22. Jraisheh A, Chutia J, Kulkarni V (2021) Alteration in structure of underexpanded freejet through gas-dynamic perspective. *AIAA J* 59(10):3937–3945

Numerical Investigation on Shock-Wave and Boundary-Layer Interactions Inside the Axisymmetric and Planar Scramjet Intakes with Different Cowl Orientations



S. Sharath and Tamal Jana

Abstract The computational investigations of planar and axisymmetric scramjet intakes with different cowl configurations have been carried out to study the shock-wave/boundary-layer interaction (SWBLI) at Mach 4.03. The 2D numerical simulation has been conducted using the finite volume solver Ansys Fluent. The velocity contour for both the planar and the axisymmetric intakes with straight and bent cowls is analyzed to find the superior intake geometry which can be efficient in suppressing the separation bubble, formed due to SWBLI. It is observed that the axisymmetric intake is very effective in suppressing the separation bubbles. Interestingly, for both the planar and the axisymmetric intakes, the separation bubble is washed away from the bent cowl. Besides, the wall static pressure distribution for both planar and axisymmetric intakes with straight and bent cowl reveals that wall static pressure is less for axisymmetric intake when compared to planar intake. For both the axisymmetric and planar intakes, the shock strength is lesser for the bent cowl, which is evident from the wall pressure plot. In addition, the study has been extended specifically to make a direct comparison between the planar and the axisymmetric intakes. The total pressure at the isolator exit is higher for axisymmetric intake which conveys that the axisymmetric intake is very effective in conserving the total pressure of the incoming flow. The temperature plot over the ramp surface shows that the temperature is higher for planar intake; however, the temperature fluctuations over the ramp surface are more for axisymmetric intake.

Keywords Shock wave · Boundary layer · Straight cowl · Bent cowl · Separation bubble · Planar intake · Axisymmetric intake

S. Sharath · T. Jana (✉)

Department of Aerospace Engineering, Faculty of Engineering and Technology, JAIN (Deemed-to-Be University), Bangalore, India
e-mail: tfortamal@gmail.com

T. Jana

Department of Aerospace Engineering, B.M.S. College of Engineering, Bengaluru, India

1 Introduction

The high-speed flow such as transonic, supersonic, and hypersonic flows is always associated with the generation of shock. Thus, the interaction of shock waves with the boundary layer formed over the inner/outer surface of high-speed aircraft is unavoidable. The repercussions due to shock-wave/boundary-layer interaction (SWBLI) are massive recirculation zone, enormous total pressure loss, fluctuating pressure, thermal load, etc. Therefore, the correct understanding of the SWBLI phenomenon is very essential to alleviate the consequences. Basic aspects of supersonic flow over different geometries and the shock structures are described by Anderson [1]. Besides, the fundamental flow physics of the shock boundary-layer interaction is presented by Babinsky [2]. It can be noted that several investigations have been conducted to study the SWBLI characteristics over flat surfaces or curved planes [3, 4]. Moreover, quite a lot of studies have been done to investigate the control characteristics of SBLIs inside supersonic/hypersonic intake. Extensive experimental work on SWBLI is carried out by Emami et al. [5] at several intake isolator geometries [5]. The investigations provide a thorough insight into the SWBLI structures and their comparison inside different supersonic intakes. Moreover, there are different control mechanisms, such as porous cavities, and MVGs to control the SWBLI inside the intake [6, 7]. The recent review of Jana et al. [8] beautifully documented the repercussions of SBLI over different geometries and the effective control methods to manipulate the interactions [8]. In addition to the numerical study, several numerical simulations are conducted to study detailed flow physics. Janarthanam and Babu [9] computationally investigated the flow structure for different cowl lengths and angles at Mach 4.03 flow [9]. Senthilkumar et al. [10] studied the effect of cowl angle on the performance of the scramjet engine and the effects of cowl angle on the static pressure rise, total pressure recovery, and flow distortion [10]. This study also focuses on the variation in cowl angle and the flow distortion that leads to inlet unsteadiness and loss in total pressure. Later, John and Senthilkumar [11] numerically studied the performance enhancement of the supersonic planar air intake model by implementing the blunted leading edge to the cowl lip section of the model at Mach 3 [11]. However, the aforementioned studies are describing SWBLI over planar intakes. Note that, the flow phenomenon will not be similar due to the three-dimensional relieving effect caused by the axisymmetric geometry. Therefore, there is a need to investigate the impact of axisymmetric geometry over planar geometry in manipulating the SWBLI phenomenon. Since the intake is the most important part of a ramjet/scramjet engine, the present study computationally investigates the impact of axisymmetric intake over the planar one at Mach 4.03.

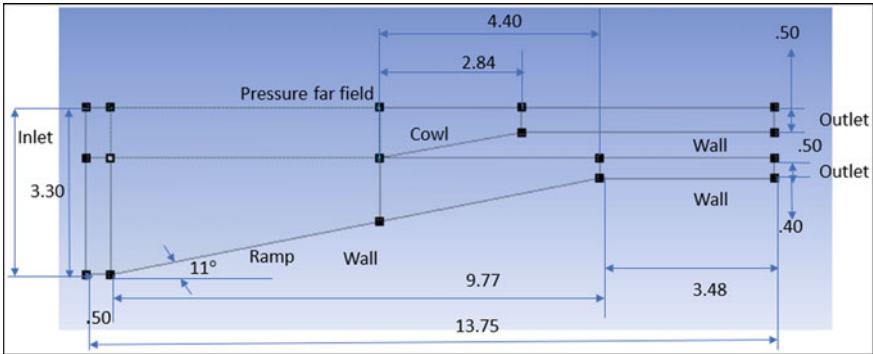


Fig. 1 Two-dimensional geometry of SCRAMJET intake (all dimensions are in “inches”) [5]

2 Numerical Modeling and Methodology

2.1 Numerical Domain and Meshing

The numerical analysis has been carried out using Ansys Fluent. The geometry of the SCRAMJET engine was incorporated from the work of Emami et al. [5], as shown in Fig. 1 [8]. The ramp of the intake is inclined at an angle of 11° with respect to freestream flow (X-direction). The length of the ramp along the X-direction is 9.77 inches. The length and height of the isolator section are 3.48 inches and 0.4 inches, along the X-axis and the Y-axis, respectively. The cowl length is 4.4 inches. The horizontal (length) and vertical (height) dimensions of the computational domain are 13.75 inches and 3.3 inches, respectively. The structured mesh is used throughout the entire domain, as shown in Fig. 2. A total of 2,38,921 nodes are used for the present study.

2.2 Numerical Methodology

The Reynolds-average Navier–Stokes (RANS) equations are solved in the current work utilizing the two equations SST K- ω . The SST k-turbulence model is recommended for issues involving compressible flow and shock-wave–boundary-layer interactions because it adequately captures boundary-layer separation under adverse pressure gradients [9]. An ideal gas is assumed to be the working fluid. The Sutherland three-coefficient approach is used to calculate viscosity. The free stream static pressure is 8724 Pa, the stagnation pressure is 1.31 MPa, and the Mach number is considered as 4.03. The wall surface was selected as an adiabatic and non-slip wall. The inlet and the top and bottom layers of the numerical domain are considered as supersonic inlet using the pressure far-field boundary condition. The outlet of the

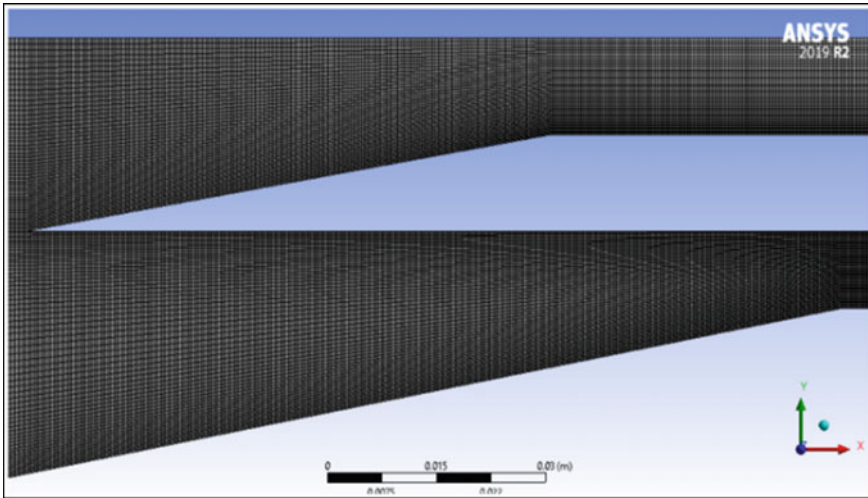


Fig. 2 Mesh structure

numerical domain is taken as pressure outlet. The stagnation temperature at the pressure outlet is taken to be 288 K, while the free stream temperature at the pressure far field is taken to be 69.15 K. The second-order upwind flow type is used with the implicit Advection Upstream Splitting Method (AUSM) scheme as supersonic flow demands more accurate findings. It is important to note that after a sufficient number of iterations, the residuals are fluctuating between 10^{-3} and 10^{-4} . Therefore, the net mass outflux rate is considered as the convergence criteria which is below 0.04 kg/s. Tech Plot is used to assess the results once the solution has converged.

2.3 *Grid Independency Test and Validation Study*

After the grid-independent study, the total number of elements is considered for the present investigation as 236,700. In order to authenticate the numerical investigation, the wall pressure is plotted over the ramp surface and validated with the experimental paper of Emami et al. [5], which can be seen in Fig. 3. The figure plots non-dimensionalized distance x/H_t along X-axis and non-dimensionalized pressure along Y-axis, where H_t is the throat height of the intake, and P and P_∞ are the wall static pressure and freestream pressure, respectively. Near the first shock impingement point around $x/H_t = 17$, there is a slight variation in pressure rise between the experimental and the numerical value, as can be seen in Fig. 3. There is a slight delay in the abrupt pressure rise for the numerical value. This might be due to slight variations in the freestream conditions between the numerical and experimental values.

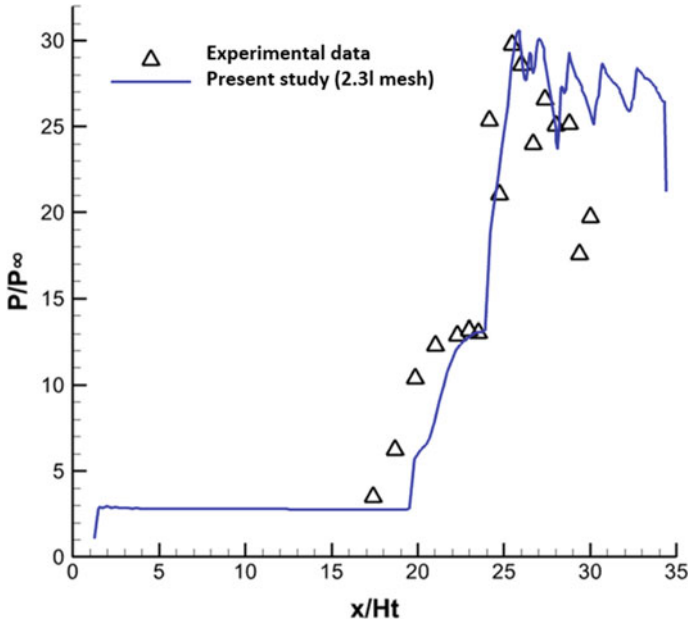


Fig. 3 Validation study

3 Results and Discussion

The numerical investigation is conducted in order to study the shock-wave–boundary-layer interaction characteristics for the straight and axisymmetric intakes. At first, the velocity contour has been plotted for the planar intake for both straight and bent cowls, as shown in Fig. 4. Similar manner, the velocity contour is shown for axisymmetric intake in Fig. 5 for both straight and bent cowls. The formation of the separation bubble along with the separation and the re-attachment shock can be seen in the figures. Besides, shock cell structures are prominent inside the isolator section. It can be easily observed that the size of the separation bubble is bigger for the planar intake. Interestingly, there is no separation bubble over the bent cowls for the planar and the axisymmetric intake. The bent cowl for both the planar and the bent intake is effective in eliminating the separation bubble over the cowl surface. Note that, the separation bubbles are suppressed up to a large extent for axisymmetric intake when compared with planar intake. Besides, the bent cowl for both planar and axisymmetric intakes exhibits better performance in suppressing the separation bubbles.

Figure 6 shows the wall static pressure comparison over the ramp surface of planar intakes with both straight and bent cowls. The wall static pressure (P) is non-dimensionalized with freestream static pressure (P_{∞}) along Y-axis and distance (x) is non-dimensionalized with the intake throat height (H_t) along X-axis. Lesser pressure can be obtained for the bent cowl when compared to the straight cowl. Essentially, the

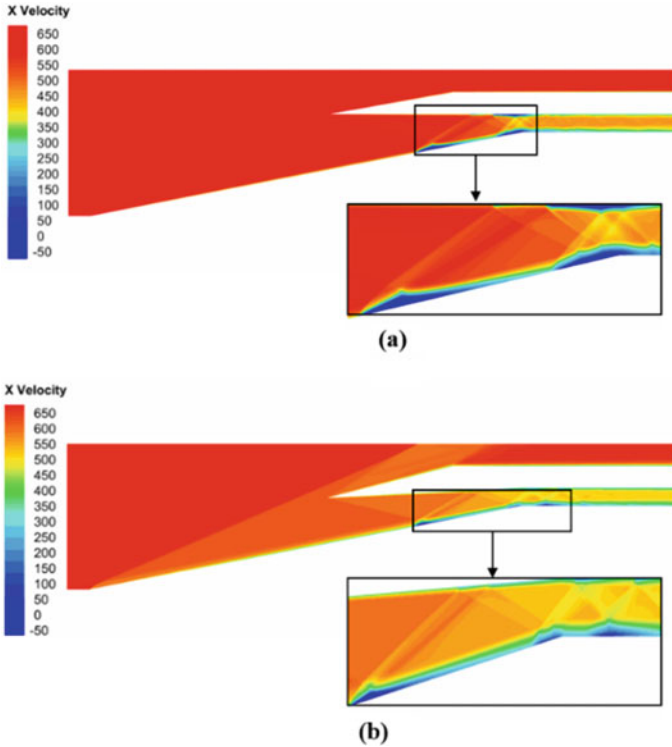


Fig. 4 Velocity contour of separation bubble a straight and b bent cowls inside the planar intake

bent cowl is responsible for the lower cowl convergence angle which thereby reduces the shock strength. The shock of lesser strength results in lower wall static pressure for the bent cowl. The wall pressures over the ramp surface for the axisymmetric intakes with both straight and bent cowls are shown in Fig. 7. Similarly, the wall static pressure is lesser for the bent cowl, as can be seen in the figure. Note that, the wall static pressure is lesser for axisymmetric intake than that for planar intake which is due to the 3D-relieving effect due to axisymmetric geometry.

It is evident from the above observation that the axisymmetric intake is better than the planar intake in effectively suppressing the separation bubble. Therefore, further analysis is carried out specifically to compare total pressure and temperature distributions for axisymmetric and the planar intake with straight cowl to have a direct comparison of the effect of axisymmetric surface.

Since the total pressure of the incoming flow before the combustion chamber is an important consideration for a well-designed intake, the average total pressure across the isolator exit is calculated and shown using the bar plot (Fig. 8). The normalized total pressure at the isolator exits for planar and axisymmetric intakes is around 95 and 110, respectively. This indicates that the axisymmetric intake is far better in conserving the flow energy of incoming flow when compared to the planar intake.

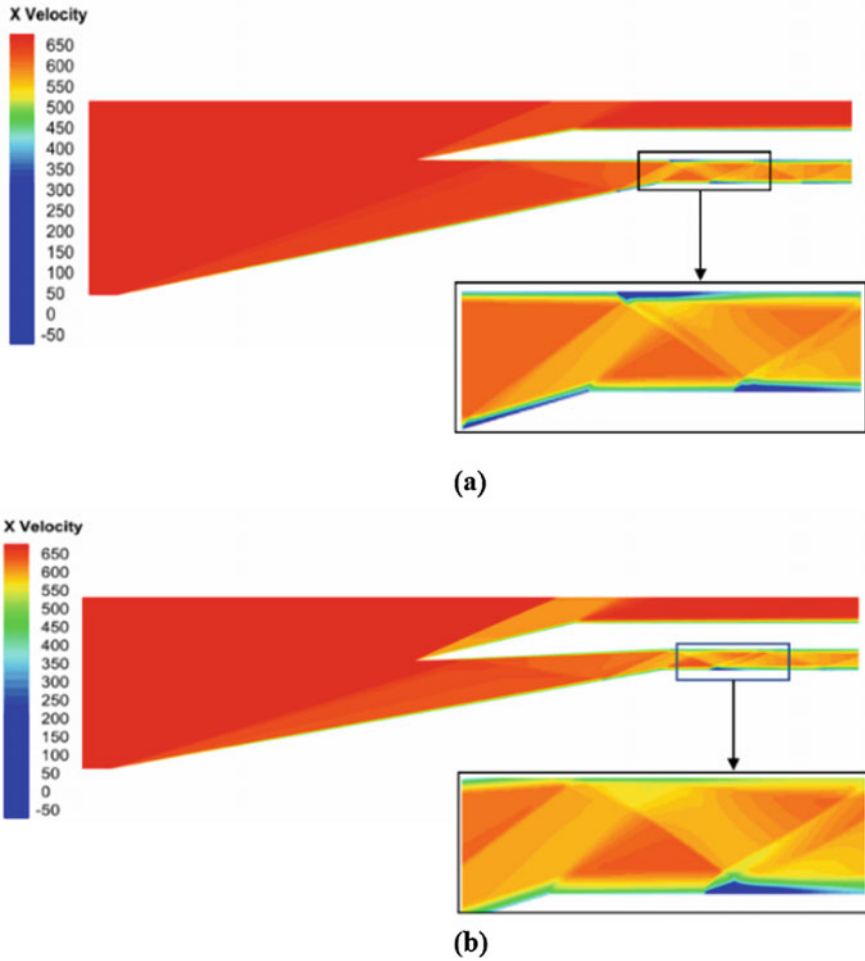


Fig. 5 Velocity contour of separation bubble **a** straight and **b** bent cowls inside the axisymmetric intake

The temperature distributions for the planar and axisymmetric intakes along the ramp surface are shown in Fig. 9. In this plot, the surface temperature is taken along Y-axis, and the distance (x), which is non-dimensionalized with throat height (H_t), is taken along the X-axis. The first rise, followed by a slow decrease in temperature, can be seen at the location of $x/H_t = 1$ and $x/H_t = 4$ for planar and axisymmetric intakes, respectively. The second rise in temperatures can be seen in the location of $x/H_t = 19$ for planar intake and $x/H_t = 24$ for axisymmetric intake. The peak temperatures for planar and axisymmetric intakes are 290 K and 278 K, respectively. Note that the temperature is higher for planar intake; however, the temperature fluctuations over the ramp surface are more for axisymmetric intake. Essentially, due to the

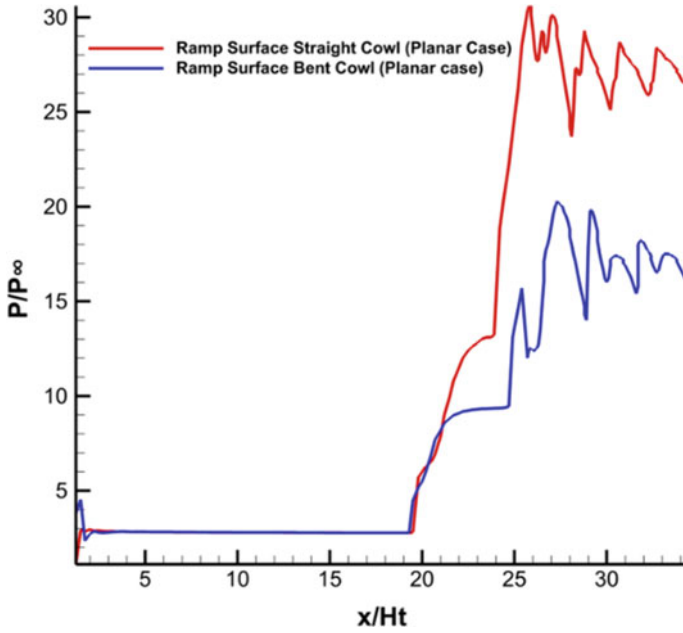


Fig. 6 Static pressure distribution on the ramp surface for both straight and bent cowls (planar case)

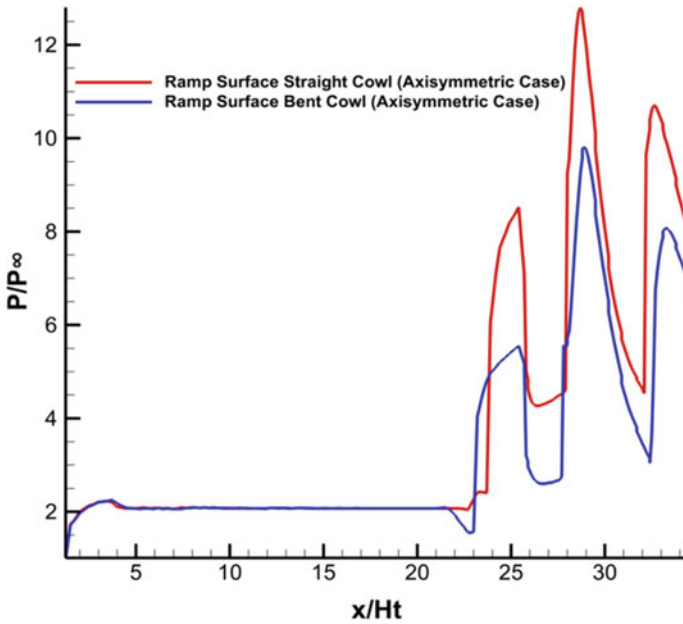


Fig. 7 Static pressure distribution on the ramp surface for both straight and bent cowls (axisymmetric case)

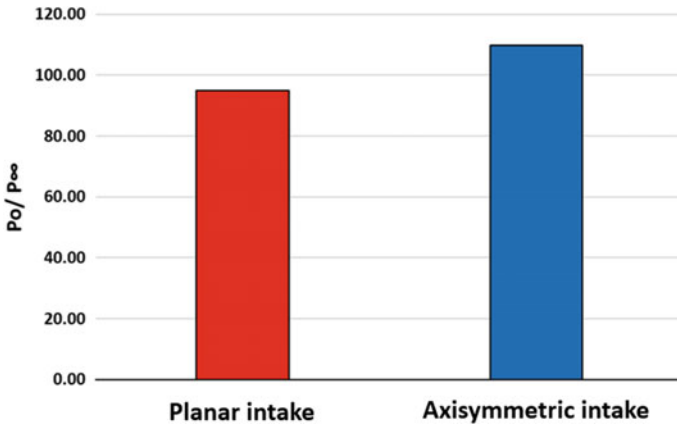


Fig. 8 Total pressure (average) variations at the isolator exit for planar and axisymmetric intakes with straight cowl

lower shock angle for the axisymmetric intake resulting from the 3D-relieving effect, the impinging shock point inside the intake isolator section is shifted toward the downstream side. This might be the reason for the higher fluctuations over the ramp surface in the downstream region of the intake isolator section.

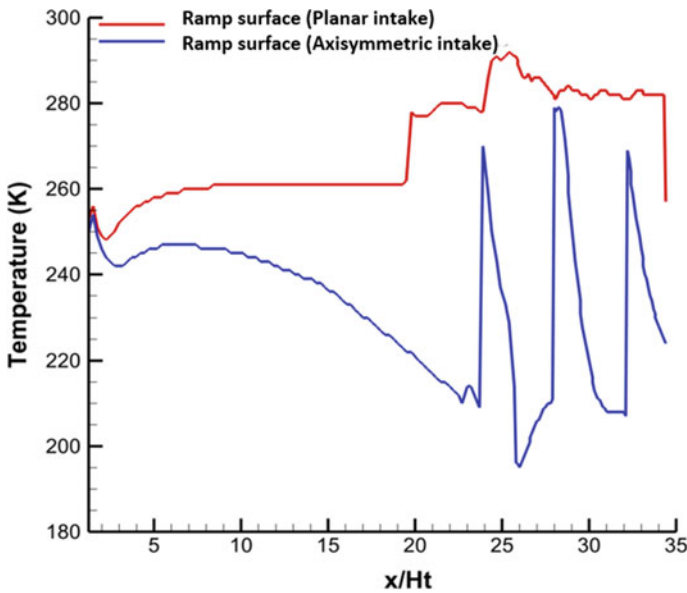


Fig. 9 Temperature distributions along the ramp surface for planar and axisymmetric intakes with straight cowl

4 Conclusions

The shock-wave/boundary-layer interaction (SWBLI) at Mach 4.03 has been studied computationally using planar and axisymmetric scramjet intakes with straight and bent cowl. It has been found that the axisymmetric intake has a significant impact on the suppression of separation bubbles. It is interesting to see that the separation bubble is completely eliminated from the bent cowl for both the planar and the axisymmetric intake. Additionally, the wall static pressure distribution for axisymmetric and planar intake with straight and bent cowl shows that axisymmetric intake has lower wall static pressure than planar intake which is due to the 3D-relieving effect due to axisymmetric geometry. Moreover, the bent cowl has a lower shock strength in comparison with the straight cowl for both axisymmetric and planar intakes. Note that, the axisymmetric intake results in higher total pressure at the isolator exit, indicating that the axisymmetric intake is particularly good in preserving the total pressure of the incoming flow. The temperature over the ramp surface is higher for planar intake; however, the temperature fluctuations over the ramp surface are more for axisymmetric intake. Essentially, the lower shock angle shifted the impinging shock point toward the downstream side, which might cause higher fluctuations over the ramp surface in the downstream side of the intake isolator section.

Acknowledgements The authors acknowledge Dr. Rajasekher K, JAIN (Deemed-to-be University), for his insightful suggestions in conducting the numerical work.

Nomenclature

H_t	Height of the intake throat
K	Turbulent kinetic energy
P	Wall static pressure
P_∞	Static pressure of the freestream flow
<i>RANS</i>	Reynolds-average Navier–Stokes
<i>SST</i>	Shear stress transport
ω	Specific dissipation
x	Distance along X-direction

References

1. Anderson Jr JD (2010) Fundamentals of aerodynamics fifth edition, oblique shocks and expansion waves. McGraw Hill Education (India), ISBN (978-0-070012-3), pp 560–612
2. Babinsky H, Harvey JK (2011) Shock wave-boundary-layer interactions. Cambridge University Press, Cambridge

3. Green JE (1970) Interactions between shock waves turbulent boundary layers. *Prog Aerosp Sci* 11:235–260
4. Viswanath PR (1988) Shock-wave-turbulent-boundary-layer interaction and its control: a survey of recent developments. *Sadhana* 12:45–104
5. Emami S, Trexler CA, Auslender AH, Weidner JP (1995) Experimental investigation of inlet combustor isolators for a dual-mode scramjet at a Mach number of 4, NASA Technical Paper 3502
6. Jana T, Thillaikumar T, Kaushik M (2020) Assessment of cavity covered with porous surface in controlling shock/boundary-layer interactions in hypersonic intake. *Int J Aeronaut Space Sci* 21:924–941
7. Jana T, Thillaikumar T, Kaushik M (2021) Micro-vortex generator controlled shock/boundary-layer interactions in hypersonic intake. *J Aerosp Eng* 34(2):04020120
8. Jana T, Kaushik M (2022) Survey of control techniques to alleviate repercussions of shock-wave and boundary layer interactions. *Adv Aerodyn* 4(27)
9. Janarthanam S, Babu V (2012) Numerical simulations of the flow through the inlet and isolator of a Mach 4 dual mode scramjet. *Aeronaut J* 116(1182):833–846
10. Senthilkumar P, Chandran MS, Sadasivan S, Govindha RN (2017) Effect of cowl angle in the performance of scramjet air intakes. *Int J Mech Eng Technol (IJMET)* 8(11):899–909
11. John B, Senthilkumar P (2018) Alterations of cowl lip for the improvement of supersonic-intake performance. *J Appl Fluid Mech* 11(1):31–41

Accurate Compressible Flow Modelling of Liquid Shock Tube Problems



R. Jishnu Chandran, Risha Raju, A. Salih, and Senthil Kumar Arumugam

Abstract Studies and applications related to liquid shocks span over varied areas. This work intends to accurately model different liquid shock tube cases and to investigate the related flow characteristics. The work initially investigates the suitability of different liquid equations of state for modelling the compressible liquid shock tube physics. The shock tube with liquid water as the tube fluid is simulated for cases involving diverse diaphragm pressure ratios. The modified NASG is found to be the most appropriate EoS for modelling liquid water compressibility effects for the related class of flow problems because of its high accuracy and non-isothermal characteristic. The MUSCL-based HLLC algorithm with MC-type slope limiter is the numerical solver chosen for modelling the liquid shock scenarios. A liquid shock tube test case with slightly complex initial setup is also simulated to demonstrate the robustness of the numerical solver. Numerical results for all the liquid shock tube cases modelled showed excellent agreement with the corresponding analytical solutions. The MUSCL-based HLLC numerical solver algorithm along with the modified NASG EoS accurately simulated the compressible liquid shock tube physics for all the different cases considered. The test cases and solutions presented in the work could be used as benchmark results for the validation of numerical solvers.

Keywords Compressible liquid flow · Equation of state · HLLC · Liquid shock · Water shock tube

R. J. Chandran (✉)

School of Mechanical Engineering, Vellore Institute of Technology, Vellore, Tamil Nadu 632014, India

e-mail: jishnuchandran@gmail.com

R. Raju · A. Salih

Department of Aerospace Engineering, Indian Institute of Space Science and Technology, Thiruvananthapuram, Kerala 695547, India

S. K. Arumugam

School of Mechanical Engineering, VIT Bhopal University, Bhopal, Madhya Pradesh 466114, India

1 Introduction

There are several research available on the theory and applications of liquid shocks, spread over various fields. Campbell and Pitcher's [1] investigation of shock waves in a gas bubble-laden liquid as well as Campbell et al. [2]'s research of detonation in liquid explosives through shock initiation is among the earliest works on shocks in liquids. A reflecting shock wave-type experimental technique is described by Walsh and Rice [3] to measure some of the crucial thermodynamic variables at high pressures. Lyzenga et al. [4] experimentally measured the temperature variations in the shock-compressed water using the optical pyrometry technique. Li et al. [5] used a nonlinear wave model to numerically simulate the shock propagation into the liquid interior following the collision with a solid surface and suggested the prominence of the liquid compressibility effects for high-impact speeds. A review of the different techniques used for the estimation of viscosity of shock-compressed fluids, including liquids, is presented by Al'Tshuler et al. [6]. Cooke and Chen [7] used a generic equation of state to investigate the shock capturing in pure water. In the case of shock wave lithotripsy, the extracorporeal acoustic shock causes high positive pressures in the liquid media through which it propagates [8]. The electronic conduction studies and the Hugoniot relation for water from the shock velocity measurements are reported by Celliers et al. [9] for shock-compressed high-pressure water. Dolan et al. [10] carried out studies on water samples undergoing compression from multiple shock waves in nanosecond duration, leading to ultra-fast freezing of the liquid. Various researches on underwater shock waves applied to the development of different therapeutic devices are outlined by Takayama et al. [11]. Batani et al. [12] studied the variations in the liquid refractive index associated with the compression of liquid water to megabar pressure range by using laser-driven shock waves.

Gojani et al. [13] provide accurate numerical simulations and experimental data for reliably calculating the shock-Hugoniot curves for liquid media. The shock wave generation in liquid water for various biological studies is explained in detail by Kang et al. [14]. The study by Biance et al. [15] explored the effects of the elasticity of inertial liquid shocks. Spiller et al. [16] suggested shock wave modelling to accurately simulate the collapsed state of human veins with respect to the development of an exact solution to the resulting Riemann problem. Details of simulation studies on shock waves in water generated by a nanosecond laser pulse are outlined in Kubecka et al. [17]. Sharifi [18] studied the shock wave patterns in steam ejector flow using the two-phase non-equilibrium supersaturation model that considers the presence of liquid particles. The US patent [19] describes the use of shock waves to compress the liquid precursor jet for high-pressure material production. Song et al. [20] experimentally investigated the shock-induced liquid film breakup, while Debnath and Pandey [21] numerically analysed the detonation combustion wave in liquid kerosene-air mixture. Kaiser et al. [22] investigated the deformation of the interface of a droplet during its breakup by studying the pressure wave pattern formation that followed the shock propagation through the liquid. Li et al. [23] discuss

the behaviour of liquids under compression from shock and study the expansion wave dynamics in the liquid.

The present work intends to perform accurate compressible modelling of different liquid shock tube scenarios. This could be accomplished through the use of an efficient numerical algorithm along with an appropriate EoS to relate the fluid density variations with other thermodynamic parameters such as pressure and temperature. In the initial part of the study, the water shock tube problem setup is modelled using different liquid EoSs. The results are analysed to conclude on the relative merits and demerits of each of these state equations for modelling the compressibility effects in the liquid for the selected class of problems. The most suitable liquid EoS is further applied to model more cases of the liquid shock tube involving different diaphragm pressure ratios and operating temperature ranges. Numerical results obtained for each of the shock tube cases modelled are checked for consistency against their respective analytical solution. Further in the study, a water shock tube problem with a different initial flow setup is also modelled to investigate the versatility of the proposed solver.

2 Mathematical Model and Computational Strategy

The water shock tube problem (WSTP) that uses liquid water as the tube fluid is a modified variant of the Sod’s [24] gas shock tube test case. The schematic of the initial problem setup is as shown in Fig. 1.

A diaphragm is initially positioned at 2 m from the left boundary of a straight tube that has a total length 3 m. This diaphragm separates the high-pressure fluid in the driver section from the low-pressure fluid in the driven section. The main assumptions are that the fluid is non-viscous and non-heat conducting. For this problem, the compressibility effects of liquid water are taken into consideration. The one-dimensional compressible flow equations form the governing equation system for flow physics. The one-dimensional Euler equations that include the mass, the momentum, and the energy conservation relations are shown below in the conservative differential form.

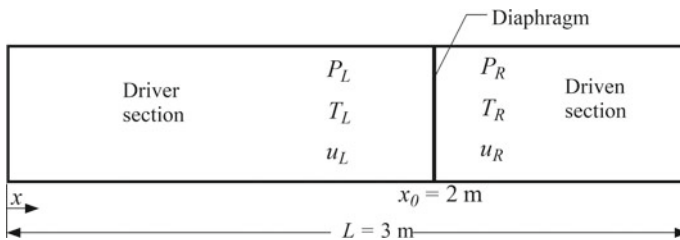


Fig. 1 1D schematic of the liquid shock tube problem test case

$$\frac{\partial \mathbf{U}}{\partial t} + \frac{\partial \mathbf{F}}{\partial x} = 0 \tag{1}$$

The vectors \mathbf{U} and \mathbf{F} in Eq. (1) are:

$$\mathbf{U} = \begin{bmatrix} \rho \\ \rho u \\ \rho e \end{bmatrix} \text{ and } \mathbf{F} = \begin{bmatrix} \rho \\ \rho u^2 + p \\ u(\rho e + p) \end{bmatrix} \tag{2}$$

where ρ is the density, u is the velocity, p the pressure, and e is the specific total internal energy. The total energy e and the internal energy, ε , of the fluid are related as:

$$e = \varepsilon + \frac{1}{2}u^2 \tag{3}$$

The closure of the mathematical system requires an additional relation that connects the pressure, density, and internal energy of the fluid. A suitable equation of state for the operating fluid needs to be employed to achieve this closure. The governing relations form a system of nonlinear PDEs that needs to be numerically solved. The one-dimensional computational domain of 3 m length is partitioned into 600 equally sized control volumes. Beginning with the event of the instantaneous rupture of the diaphragm, the transient computation is carried out up to a flow time of 200 microseconds. The numerical solver used for the computational modelling of the WSTP is the MUSCL-HLLC flux with MC-type slope limiter. All the flow variables are assumed to have only one-dimensional fluctuations, and the diaphragm rupture is treated as an instantaneous event.

Six different cases of the water shock tube problem are simulated to cover sufficiently wide pressure and temperature ranges. Three configurations are chosen in the first set, with the initial water pressure in the driver section on the left side chosen as $P_L = 10, 100, \text{ and } 1000 \text{ MPa}$. The relatively lower pressure in the right chamber is $P_R = 0.1 \text{ MPa}$ for all the three configurations. Prior to the diaphragm rupture, the fluid is considered to be stationary across the whole computational domain, i.e. the velocities $u_L = u_R = 0$. The fluid temperature on either side of the diaphragm is initially the same and at the value $T_L = T_R = 300 \text{ K}$. In the second set, three more configurations are selected where the driver and driven chamber pressures are initially fixed at $P_L = 500 \text{ MPa}$ and $P_R = 0.1 \text{ MPa}$, respectively, for all the cases. The assumption of zero initial fluid velocity is also valid for all three cases in the second set. However, these three cases correspond to three different initial operating temperatures of 280, 325, and 370 K in the shock tube domain. The details of the six different cases selected are shown in Table 1.

Table 1 Details of the water shock tube cases selected for the numerical modelling

Case no	P_L (MPa)	P_R (MPa)	T_L (K)	T_R (K)	u_L (m/s)	u_R (m/s)
1	10	0.1	300	300	0	0
2	100	0.1	300	300	0	0
3	1000	0.1	300	300	0	0
4	500	0.1	280	280	0	0
5	500	0.1	325	325	0	0
6	500	0.1	370	370	0	0

3 Evaluation of Equations of State for Water Shock Tube Simulation

The analytical solution to the WSTP has high dependency on the state equation used to relate the different properties of the fluid. However, it is a tedious task to derive the analytical solution based on each of the EoS because they involve a lot of rearrangements and new variable definitions. In this regard, the numerical solver can be used as an efficient tool to predict and understand the solution for the problem using different EoSs. This section explains the numerical solution of the WSTP, where four different equations of state for water will be used to model the fluid compressibility effects. Further, the results will be analysed to understand the merits and demerits of each EoS to arrive at the most suitable one for the selected class of problem. The initial problem setup for this study is as shown in Fig. 2.

The driver chamber pressure of 100 MPa, driven chamber pressure of 0.1 MPa, an operating temperature of 300 K, and the fluid initially at zero velocity constitute the problem setup. The Tait [25, 26] and the stiffened-gas [27] EoSs are among the most frequently used for liquid water. These two are studied along with the NASG [28] and the modified NASG [29] EoSs. The structural simplicity and the ease of inclusion into the flow model form the basis of selection for these EoSs.

The accuracy of the density prediction varies for each EoS and is dependent on the range of application. The density values of water at the temperature of 300 K and for the pressures 0.1 and 100 MPa from the NIST database are respectively 996.56

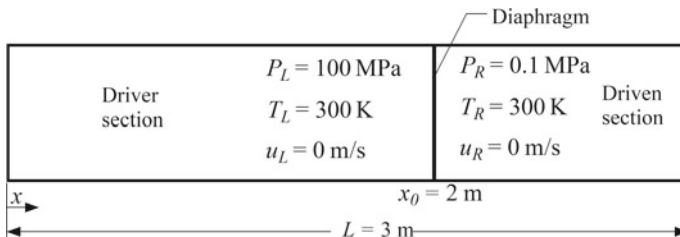


Fig. 2 WSTP test case for comparing liquid EoSs

and 1037.20 kg/m³. The percentage error in the density prediction associated with each EoS against the NIST data is presented in Table 2.

The Tait equation and the stiffened-gas equation respectively provide the most and the least accurate density estimates for liquid water. At higher pressure ranges, the error associated with the stiffened-gas EoS is too large to recommend its use. The Tait equation, irrespective of its high accuracy, has the limitation that it is an isothermal EoS. The NASG equation is observed to perform midway between these two choices. For the NASG EoS, the error diminishes with an increase in the pressure range, and the maximum error reported is 5.29% for the pressure of 0.1 MPa. The NASG EoS is originally introduced for the saturation states of water and is expected to show deviations in the density estimates while modelling liquid water away from the saturation conditions. The modified NASG equation is an improved version of the NASG EoS defined for high accuracy density estimate of the liquid water away from the saturation conditions. The error in the density estimates reducing from 5.29% to 0.044% at the lower pressure range of 0.1 MPa and from 5.18% to 0.72% at the higher pressure range of 100 MPa, with the modified version of NASG strengthens this claim.

The effect of the advantages and shortcomings associated with each of the EoS could be better perceived by observing the solution profiles obtained using them. Figure 3 displays the numerical solution profiles for the WSTP obtained with each of these liquid EoSs.

Significant variations are observed between the solution profiles obtained with the different state equations. These variations are more prominent with the density and the temperature. The density profile corresponding to the Tait equation does not exhibit any variation across the contact discontinuity, which is observable otherwise with the remaining EoSs. As already mentioned, this limitation is attributed to the isothermal nature of the Tait EoS that decouples the state and the caloric relations. The density profiles estimated using the stiffened-gas EoS and that with the NASG EoS are distinctly apart from the density profile corresponding to the Tait EoS because of the high errors associated with these EoSs. However, the density profile generated with the help of the modified NASG is close to that from the Tait EoS, and this profile also shows the discontinuity in the liquid density across the contact surface. The modified NASG is thus an EoS with an accuracy comparable to that of the Tait equation, with the clear advantage of the properly coupled state and caloric relations.

The velocity profiles predicted by the Tait, the stiffened gas, and the modified NASG EoSs exhibit a close agreement, as seen in Fig. 3a. However, the NASG equation predicts a slightly lower value of velocity. Figure 3b shows that the pressure estimated using all the four EOSs for the central region between the expansion fan

Table 2 Percentage error in density from each EoS compared to NIST data

Pressure range (MPa)	Tait	Stiffened gas	NASG	Modified NASG
0.1	0.044	3.32	5.29	0.044
100	0.155	11.18	5.18	0.72

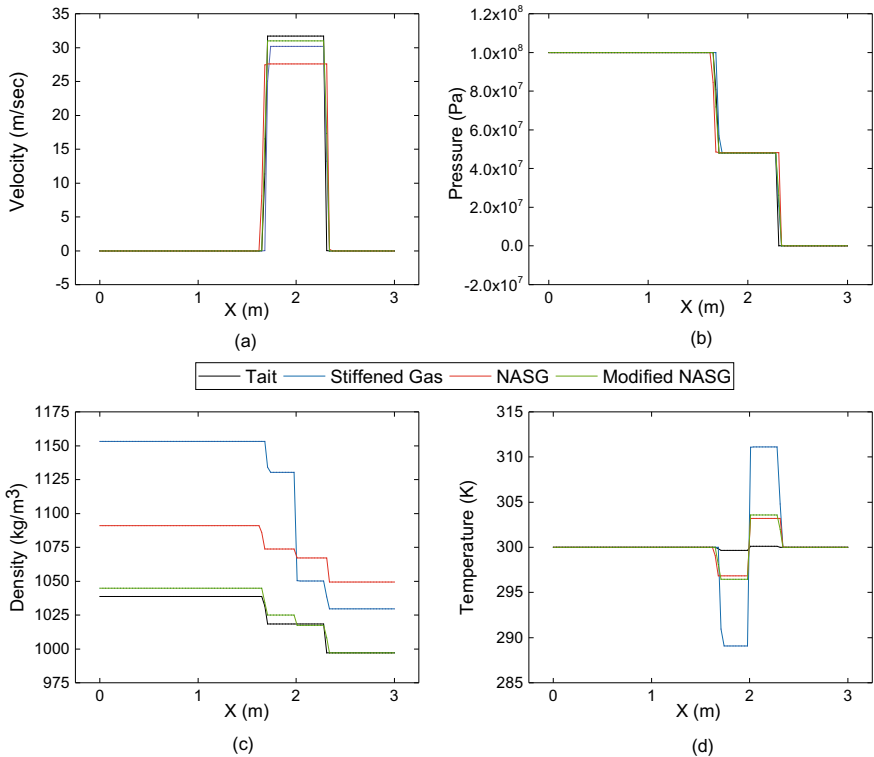


Fig. 3 Solution profiles for the liquid shock tube problem using the different EoSs of water

and the shock varies within a very narrow range, and this rounded-off value of the pressure is around 48 MPa. The temperature profiles also exhibit notable variations based on the EOS used. The Tait EoS predicted the temperature variation in the narrow range of 299.66–300.12 K. The stiffened-gas EoS reported the widest range of temperature variation, extending between 289.10 and 311.13 K. The stiffened gas is an EoS with inherent inaccuracies in the specific heat value of water, and this leads to the excessive estimation of temperature range by this EoS. The NASG EoS predicted the temperature between 296 and 302.44 K, and the modified NASG’s temperature estimates are in the range of 296.45 to 303.58 K.

Another main observation from the solution profiles is the variation in the extent of the central zone bounded by the expansion wave and the shock. This variation is because of the difference in speed of sound estimates by the different EoSs. The signal propagation speed determines the expanse over which the initial flow conditions are disturbed, and this value can vary over time.

The capability of the modified NASG EoS to correctly model the entire physics of the WSTP with minimum error in the density estimates is demonstrated here. Therefore, this EoS is recommended for use in the modelling of the related flow scenarios where both the compressible effects and the thermal effects in the liquid are

significant. The state relation of the modified NASG EoS that relates the pressure, P , the fluid specific volume v , and the specific internal energy, ε , is Eq. (4). The relation for the sound speed for the EoS is Eq. (5).

$$P = (\gamma - 1) \frac{(\varepsilon - q)}{(v - b)} - \gamma P_\infty \quad (4)$$

$$c = \left[\frac{\gamma v^2 (P + P_\infty)}{v - b} \right]^{1/2} \quad (5)$$

where γ is the ratio of specific heat, P_∞ is the stiffening parameter of the EoS, q is the heat bond, and b is the fluid co-volume.

4 Results and Discussion

Different cases of the WSTP corresponding to varied sets of initial conditions are numerically solved, and the results are checked for consistency by comparing with the respective analytical solution. Based on the study reported in the previous section, the modified NASG EoS is applied to model the compressibility effects in the fluid in the numerical simulations. The complete procedure for obtaining the analytical solution to the WSTP using the modified NASG EoS is available in [30].

A. Consistency Check of the Numerical Solver

The different property profiles in the solution to the WSTP for the driver pressures of 10, 100, and 1000 MPa are shown in Figs. 4, 5, and 6, respectively. The grid-independent numerical profiles are displayed using 100 data points in each of these figures. The most appropriate value of CFL is found to be close to 0.5 for the cases simulated.

The numerical solution profiles clearly indicate the formation of flow features in the domain such as a moving contact discontinuity, a shock, and an expansion fan, resulting from the rupture of the diaphragm. These are typical observations in the solution profiles of a gas shock tube problem. The scale over which each of the properties varies for the WSTP is different from those observed for the gas shock tube; however, the overall structure of the profiles is preserved. Scattered symbols are used to plot the numerical data points, and the continuous black curves represent the analytical solutions.

The numerical results for all driver pressures show a high degree of agreement with the analytical results. This close match of the numerical solutions is not limited to the estimated values of properties over different zones. The numerically predicted locations of all the important flow features in the shock tube domain are also in great conformity with the analytical results. The close agreement between the results indicates the effectiveness of the mathematical model in capturing the complete WSTP physics as described by the analytical solution.

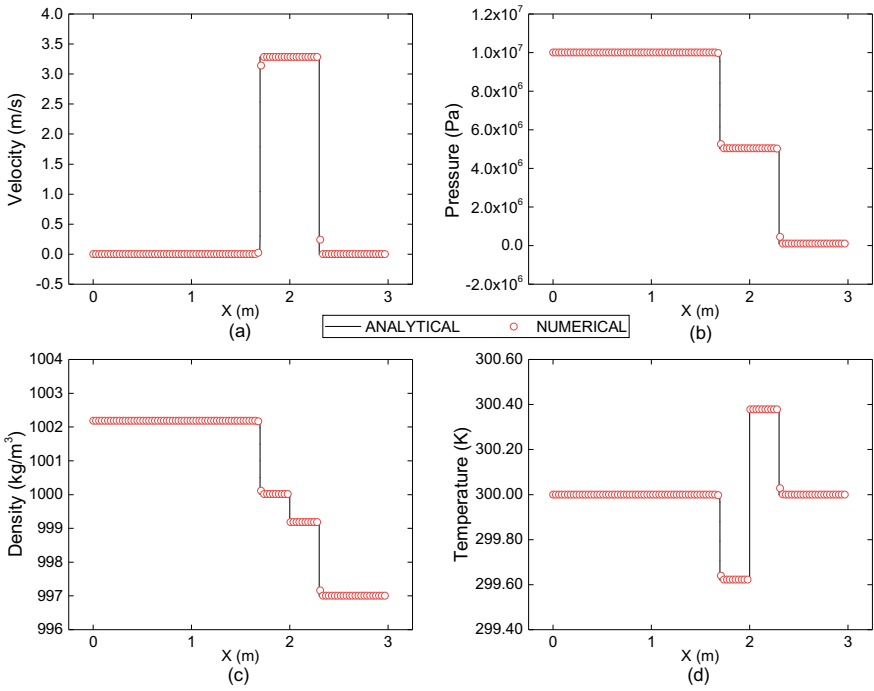


Fig. 4 Numerical and analytical solution profiles for Case 1 ($P_L = 10$ MPa, $P_R = 0.1$ MPa at $T = 300$ K)

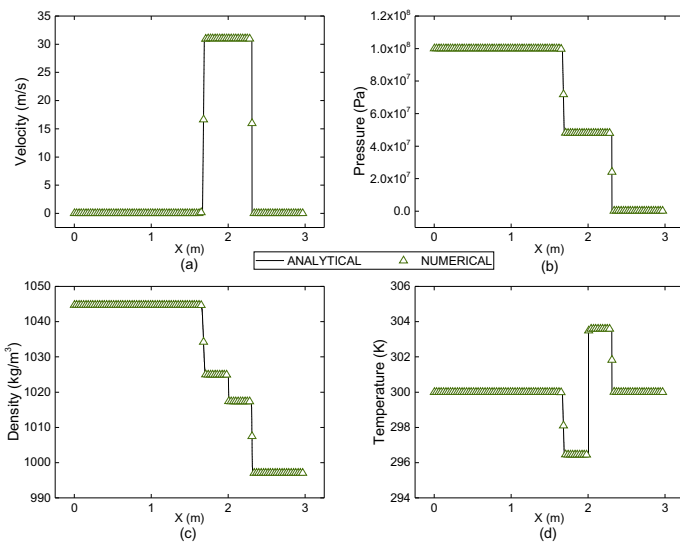


Fig. 5 Numerical and analytical solution profiles for Case 2 ($P_L = 100$ MPa, $P_R = 0.1$ MPa at $T = 300$ K)

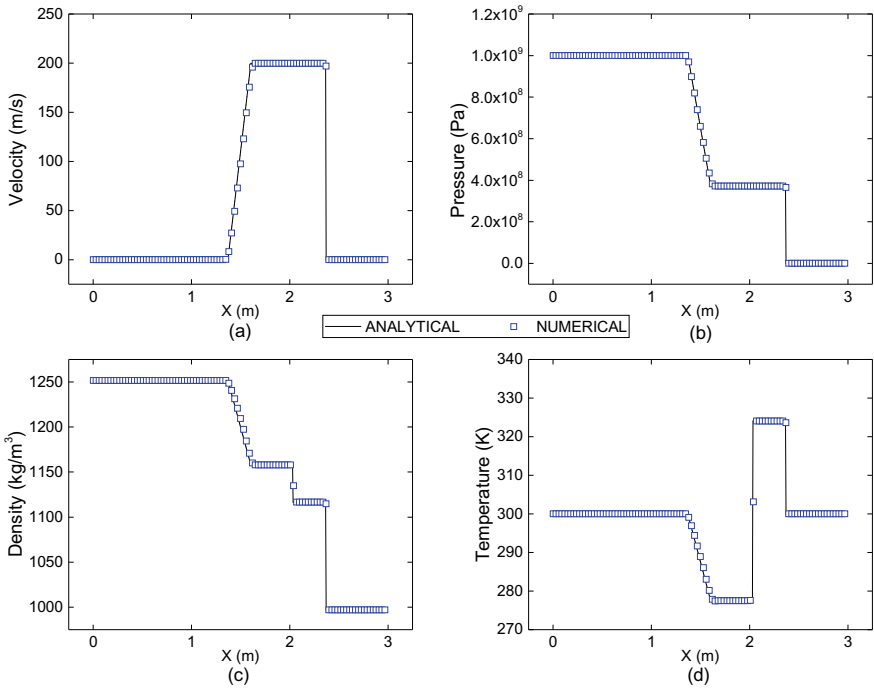


Fig. 6 Numerical and analytical solution profiles for Case 3 ($P_L = 1000$ MPa, $P_R = 0.1$ MPa at $T = 300$ K)

The equation of state used for the liquid and its non-isothermal character is critical to the mathematical system’s closure. While the analytical model involves a set of fundamental thermodynamic relations that govern the different physical processes in a shock tube, the solution of a system of PDEs is the basis for the numerical model. The excellent conformance observed between the numerical and the analytical results, obtained through completely different approaches, implies the dependability of the solution.

Figure 7 displays the numerical and analytical solution profiles for the WSTP for the initial system temperatures of 280, 325, and 370 K. As already mentioned, these cases correspond to the driver and driven chamber pressures of 500 MPa and 0.1 MPa, respectively. For all of the different operating temperatures considered, the numerical results are in excellent match with the analytical solution. Some variations were observed in the structure of the solution profiles between the cases involving different diaphragm pressure ratios. These variations were predominant over the spread of the expansion fans because of the large variation in the scale of the pressure ratio between cases. There are no such visible variations in the solution structure between the cases with different operating temperature ranges, especially because of the narrower variation in the scale of this property.

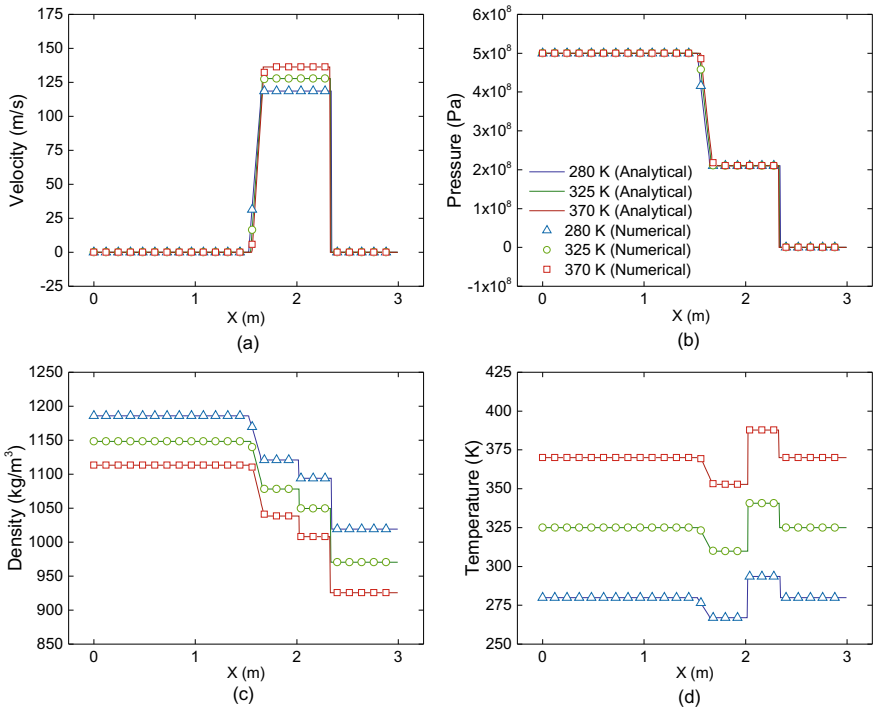


Fig. 7 Numerical and analytical solution for different operating temperatures (Cases 4, 5, and 6)

One can make the following observations from the property values reported over the various zones in the solution profiles for the varied configurations of the WSTP modelled. The flow velocity attained between the shock and the expansion fan increases with the rise in the diaphragm pressure ratio, as a result of the increase in the driving pressure difference. For a fixed diaphragm pressure ratio, the flow velocity increases with an increase in the operating temperature because of the lower fluid density resulting from the liquid expansion. The pressure in the zone bound by the shock and expansion fan is dependent on both the initial chamber pressures and on the diaphragm pressure ratio. It is evident from Fig. 7b that when the diaphragm pressure ratio is maintained as a constant, the pressure values over this zone remain nearly the same, irrespective of the variations in the operating temperature. The highest fluid density reported in the study is 1251.6 kg/m³ corresponding to a pressure of 1000 MPa and temperature of 300 K.

The increase in the diaphragm pressure ratio widens the range over which the liquid temperature varies inside the shock tube. However, as seen from Fig. 7d, such notable variations in the span of the temperature range are not observed between the cases with different operating temperatures. Instead, a complete upward shift of the span of variation of temperature is observed with the increase in the operating temperature. Along with the qualitative analysis of the results, this section confirms

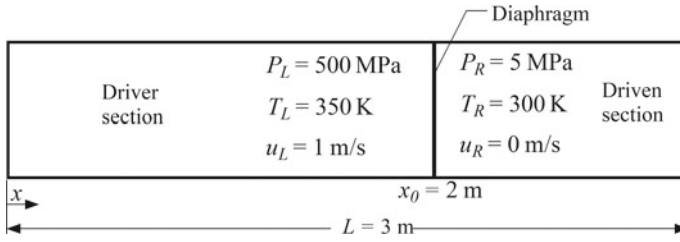


Fig. 8 WSTP test case with the varied setup

the consistency of the numerical results by demonstrating their close agreement with the respective analytical solutions.

B. Solver Consistency for a Complex Test Case Simulation

All the test cases of the WSTP discussed previously are based on the difference in either the driver pressure or the operating temperature. To explore the behaviour of the solution for complex initial conditions and to showcase the robustness of the numerical solver, a fresh case of the WSTP with a distinct problem setup is introduced. In this new test case, all the three properties, viz., the pressure, temperature, and velocity are initially discontinuous across the diaphragm. The initial setup of this problem is shown in Fig. 8.

The pressure in the driver and the driven sections is 500 and 5 MPa, respectively. The driver section is initially at 350 K with the velocity of 1 m/s, while the driven section temperature is 300 K with stationary fluid (0 m/s). The shock tube geometry is unaltered from the previous cases. In Fig. 9, the numerical solution profiles from the test case simulation are compared against the analytical results. There are a few notable variations observed in these profiles compared to those of the standard WSTP setup.

The pressure profiles do not show any difference; however, the remaining property profiles exhibit some variations in their structure. The temperature profile shows a piecewise decreasing pattern along the 1D domain. The typical temperature profile for a shock tube problem shows the temperature in the zone between the contact surface and shock to be greater than that in the zone between the expansion fan and the contact surface. However, the trend observed here is the reverse for the temperature values. Though the rarefaction waves tend to decrease the temperature and the shock wave induces a temperature rise, these are insufficient to overcome the initial temperature difference.

There are also notable variations in the density profiles for this problem. The fluid density over the region through which the expansion wave has traversed is typically lower than that of the region over which the shock has propagated. The results here are different from this typical observation, where the density is higher in the region over which the rarefaction has propagated. While the high pressure to the left of the contact surface tends to increase the fluid density, the high initial temperature has the opposite effect on fluid density over this region. The expansion of the liquid induced

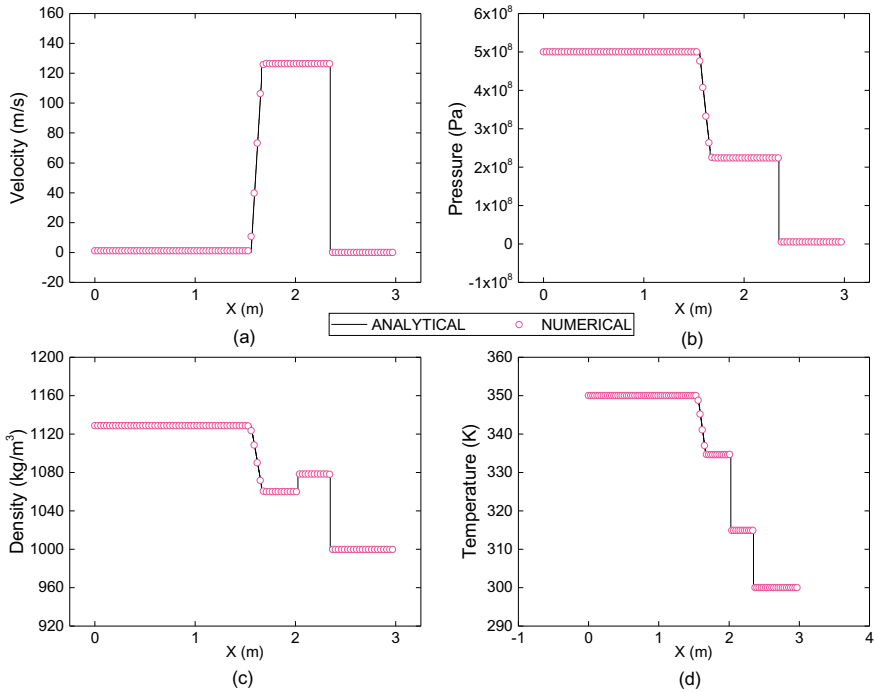


Fig. 9 Solution profiles for the WSTP test case with varied problem setup

by the high temperature ultimately results in a lower fluid density in this region compared to that on the right of the contact surface. The velocity profile also shows variation in the left-most and the right-most zones based on the initial conditions.

The close agreement between the numerical and analytical results depicted in Fig. 9 suggests the adequacy of the numerical solver to model the flow physics with high accuracy. The robustness of the computational solver that makes it easy to model varied flow cases is also demonstrated through this study.

5 Conclusions

The main aim of the work was to accurately model the liquid shock tube problem considering the compressibility effects in the fluid. The initial level of study evaluated the suitability of different equations of state of water to model the liquid compressibility effects in the WSTP simulation. This study showed the non-suitability of the stiffened-gas EoS for modelling the water shock tube problem because of its inaccuracy and the incapability of the Tait EoS to model the non-isothermal flow cases despite its high accuracy. The results also established the superiority of the modified NASG EoS for its accurate modelling of the compressibility effects in liquid water

under both isothermal and non-isothermal conditions. The MUSCL-based HLLC flux with the MC-type slope limiter was the numerical solver algorithm adopted.

The consistency of the compressible solver for modelling the liquid shock tube problem with the selected liquid EoS was tested through the simulation of six different cases of the water shock tube problem. The numerical results for all the six cases showed excellent agreement with the available analytical solutions. The results showed that the widely differing diaphragm pressure ratios could lead to variations in the structure of the solution. Also, a shift is observed in the temperature and the density profiles corresponding to different operating temperatures. The robustness of the solver was further tested and established by accurately simulating a newly introduced flow setup of the WSTP, having a different initial condition from the conventional problem setup.

The work recommends the MUSCL-HLLC flux with MC-type limiter as an appropriate numerical solver for modelling the governing equation system for the class of problems and the modified NASG as the most appropriate EoS for modelling the liquid water compressibility effects. The test cases and the results reported in this study could serve as benchmarking tools for the evaluation of numerical solvers, which are particularly developed for the simulation of liquid shocks and other compressible liquid flows.

References

1. Campbell IJ, Pitcher AS (1958) Shock waves in a liquid containing gas bubbles. *Proc Roy Soc London Ser A Math Phys Sci* 243(1235):534–545
2. Campbell AW, Davis WC, Travis JR (1961) Shock initiation of detonation in liquid explosives. *Phys Fluids* 4(4):498–510
3. Walsh JM, Rice MH (1957) Dynamic compression of liquids from measurements on strong shock waves. *J Chem Phys* 26(4):815–823
4. Lyzenga GA, Ahrens TJ, Nellis WJ, Mitchell AC (1982) The temperature of shock-compressed water. *J Chem Phys* 76(12):6282–6286
5. Li N, Zhou Q, Chen X, Xu T, Hui S, Zhang D (2008) Liquid drop impact on solid surface with application to water drop erosion on turbine blades, Part I: nonlinear wave model and solution of one-dimensional impact. *Int J Mech Sci* 50(10–11):1526–1542
6. Al'Tshuler LV, Doronin GS, Kim GK (1986) Viscosity of shock-compressed fluids. *J Appl Mech Techn Phys* 27(6):887–894
7. Cooke CH, Chen TJ (1992) On shock capturing for pure water with general equation of state. *Commun Appl Numer Methods* 8(4):219–233
8. Cheing GLY, Chang H (2003) Extracorporeal shock wave therapy. *J Orthop Sports Phys Ther* 33(6):337–343
9. Celliers PM, Collins GW, Hicks DG, Koenig M, Henry E, Benuzzi-Mounaix A, Batani D, Bradley DK, Da Silva LB, Wallace RJ et al (2004) Electronic conduction in shock-compressed water. *Phys Plasmas* 11(8):L41–L44
10. Dolan DH, Gupta YM (2004) Nanosecond freezing of water under multiple shock wave compression: optical transmission and imaging measurements. *J Chem Phys* 121(18):9050–9057
11. Takayama K, Yamamoto H, Shimokawa H (2013) Underwater shock wave research applied to therapeutic device developments. *J Eng Phys Thermophys* 86(4):963–975

12. Batani D, Jakubowska K, Benuzzi-Mounaix A, Cavazzoni C, Danson C, Hall T, Kimpel M, Neely D, Pasley J, Le Gloahec MR, Telaro B. Refraction index of shock compressed water in the megabar pressure range. *EPL Europhys Lett* 112(3):36001
13. Gojani AB, Ohtani K, Takayama K, Hosseini SHR (2016) Shock hugoniot and equations of states of water, castor oil, and aqueous solutions of sodium chloride, sucrose and gelatin. *Shock Waves* 26(1):63–68
14. Kang D, Nah JB, Cho M, Xiao S (2014) Shock wave generation in water for biological studies. *IEEE Trans Plasma Sci* 42(10):3231–3238
15. Biance AL, Chevy F, Clanet C, Lagubeau G, Quéré D (2006) On the elasticity of an inertial liquid shock. *J Fluid Mech* 554:47–66
16. Spiller C, Toro EF, Vázquez-Cendón ME, Contarino C (2017) On the exact solution of the Riemann problem for blood flow in human veins, including collapse. *Appl Math Comput* 303:178–189
17. Kubecka M, Obrusník A, Bonaventura Z (2018) Simulation of shockwaves in water induced by nanosecond-laser pulse, p P4.3006
18. Sharifi N (2020) Numerical study of non-equilibrium condensing supersonic steam flow in a jet-pump based on supersaturation theory. *Int J Mech Sci* 165:105221
19. Armstrong M, Bastea S (2021) System and method for rapid, high throughput, high pressure synthesis of materials from a liquid precursor, 5 Jan 2021, US Patent 10,882,017
20. Song X, Li B, Xie L (2020) Experimental investigation on the properties of liquid film breakup induced by shock waves. *Chin Phys B* 29(8):086201
21. Debnath P, Pandey KM (2021) Numerical analysis of detonation combustion wave in pulse detonation combustor with modified ejector with gaseous and liquid fuel mixture. *J Therm Anal Calorim* 145(6):3243–3254
22. Kaiser JW, Winter JM, Adami S, Adams NA (2020) Investigation of interface deformation dynamics during high-Weber number cylindrical droplet breakup. *Int J Multiph Flow* 132:103409
23. Li L, Lu XX, Ren XB, Ren YJ, Zhao ST, Yan XF. (2021) The mechanism of liquid dispersing from a cylinder driven by central dynamic shock loading. *Defence Technol* 17(4):1313–1325
24. Sod GA (1978) A survey of several finite difference methods for systems of nonlinear hyperbolic conservation laws. *J Comput Phys* 27(1):1–31
25. Saurel R, Cocchi JP, Butler PB (1999) Numerical study of cavitation in the wake of a hypervelocity underwater projectile. *J Propul Power* 15(4):513–522
26. Chandran J, Salih A (2017) Water shock tube simulation with Tait equation of state. In: Proceedings of the 24th national and 2nd international ISHMT-ASTFE heat and mass transfer conference (IHMTTC-2017) (United States), Begel House Inc.
27. Flåtten T, Morin A, Munkejord ST (2011) On solutions to equilibrium problems for systems of stiffened gases. *SIAM J Appl Math* 71(1):41–67
28. Le Métayer O, Saurel R (2016) The Noble-Abel stiffened-gas equation of state. *Phys Fluids* 28(046102)
29. Chandran J, Salih A (2019) A modified equation of state for water for a wide range of pressure and the concept of water shock tube. *Fluid Phase Equilibria* 483:182–188
30. Jishnu Chandran R, Salih A (2022) Development of a benchmark solution in compressible liquid flows: analytical solution to the water shock tube problem. *J Therm Anal Calorim* 147(8):5279–5292

Numerical Simulation of Compressible Multiphase Flows with Phase Change Using Two-Fluid Approach



Mansu Navaneethan, T. Sundararajan, and T. Jayachandran

Abstract The present study is a numerical approach for modelling compressible multiphase flows using two-fluid formulations. Two-fluid indicates two phases where separate governing equations are considered for both phases. The two phases considered can be gas–liquid, gas–solid or liquid–solid. The present study is focussed on combination of liquid and gas. A finite volume solver is developed based on AUSM⁺-up scheme which is efficient for all-speed computations. Results obtained from the code were validated with literature available for shock tube problems. Effects of initial conditions were also studied for air–water and water–air problems considering the need for extending the two-fluid concept for wide problems in various fields. The practical application of the model is also discussed in the study by considering a major and useful scenario of liquid film cooling from rocket propulsion systems. The results obtained considering phase change from liquid to vapour are also included and discussed towards the final sections.

Keywords Compressible · Multiphase · Two-fluid · AUSM⁺-up · Phase change

Nomenclature

t	Time [s]
x	X coordinate [m]
y	Y coordinate [m]
Q	Conserved variables [–]
E/G	Convective/viscous flux in x [–]

M. Navaneethan (✉)

Vikram Sarabhai Space Centre, Thiruvananthapuram 695022, India

e-mail: mansu.999@gmail.com

T. Sundararajan

Department of Mechanical Engineering, IIT Palakkad, Palakkad 678557, India

T. Jayachandran

Department of Aerospace Engineering, IIT Madras, Chennai 600036, India

F/H	Convective/viscous flux in y [-]
k	Fluid: liquid/gas [-]
S	Source term [-]
k	Turbulent kinetic energy [m^2/s^2]
ϵ	Turbulent dissipation rate [m^2/s^3]
ρ	Density [kg/m^3]
u, v	Velocity in x, y [m/s]
P, P^{int}	Pressure [Pa]
\dot{m}_v/\dot{m}_v	Evaporated mass flux [kg/sm^2]
\bar{u}, \bar{v}	Average velocity in x, y [m/s]
α	Volume fraction [-]
h	Heat transfer coefficient [$\text{W}/\text{m}^2 \text{ K}$]

1 Introduction

Many engineering applications involve combination of incompressible and compressible fluids such as cavitation problems, film cooling in propulsion systems and particle laden flows. Numerical model for obtaining solutions to these problems is an important research area in computational fluid mechanics. Treating compressible and incompressible regions with separate sets of governing equations with treatment for incompressibility effects poses great challenge numerically. In these problems, a development of unified solver with similar conservation equations is preferred where incompressible medium is assumed to be compressible, thus framing it as a compressible multiphase problem. The present study discusses the numerical approach for modelling compressible multiphase flows using two-fluid formulations. Two-fluid indicates two phases where separate governing equations are considered for both phases. Phase considered can be gas or liquid, gas or solid and finally liquid or solid. The compressibility of phases is introduced by appropriate equation of state for phases considered. Simple shock tube problems are solved using AUSM⁺-up scheme for air–water and water–air problems. One-dimensional shock tube problems are also solved for different initial conditions for either fluids especially velocity, pressure and temperature—which is a reality in many applications. Towards the end, a section is included for modelling phase change problems using two-fluid formulations by computing the mass loss through evaporation from liquid.

2 Literature Review and Objective

Computation on multiphase compressible flows is a widely used research area in many areas for decades [1]. Also a few studies are being done to extend incompressible flow methods for modelling compressible flows. For compressible multiphase

flows, approach proposed by Liou et al. [2, 3] is used, where AUSM⁺-up scheme was used by extending the single-phase model for two-fluid version instead of exact Riemann solver which is computationally expensive. AUSM schemes for calculating convective fluxes are very efficient in both low speed and hypersonic regimes in a given computational field. Studies were also done for extension of flux functions of AUSM schemes to compare performance in various multiphase problems. Studies done by Kitamura et al. [4, 5] considered different versions of AUSM schemes for obtaining solution to shock tube problems. Advection Upstream Splitting Method (AUSM) is based on upwind concept, and inviscid flux is considered as consisting of two convective and pressure fluxes where the former is associated with the flow speed and the latter with the acoustic speed.

It is seen that in most of the literature, application of two-fluid formulation mainly confined to cavitation problems. In the present study, a case more relevant in heat transfer process in propulsion systems is considered for studying application of the model. In heat transfer process associated with propulsion systems, it is required that two phases be treated to have different temperatures. A case of liquid film cooling, where the liquid is injected along the wall, to protect the wall from hot combustion gas, is considered here. In addition to these, in real applications such as in rocket thrust chambers, treatment of turbulence effects is important. Effect of turbulence in two-fluid formulation is also not accounted in most of literature. Thus the objective of the present study is formulated to investigate the application of two-fluid compressible flow model for practical applications involving heat transfer and phase change with turbulent effects.

3 Methodology

In this section, the governing equation used in the numerical simulation, discretization of fluxes and solution marching is presented. As the flow conditions for nozzle flows in practical applications are turbulent in nature, the governing equations considered RNG *k*-epsilon model for two-fluid as shown below

$$\frac{\partial Q_k}{\partial t} + \frac{\partial E_k}{\partial x} + \frac{\partial F_k}{\partial y} = P_k^{\text{int}} + \frac{\partial G_k}{\partial x} + \frac{\partial H_k}{\partial y} + S, \quad (1)$$

$k = 1, 2$ indicate the two fluids

$$Q_k = \begin{bmatrix} \alpha\rho \\ \alpha\rho u \\ \alpha\rho v \\ \alpha\rho E \\ \alpha\rho k \\ \alpha\rho\varepsilon \end{bmatrix}_k, E_k = \begin{bmatrix} \alpha\rho u \\ \alpha\rho u^2 + \alpha p \\ \alpha\rho uv \\ \alpha\rho uH \\ \alpha\rho uk \\ \alpha\rho u\varepsilon \end{bmatrix}_k, F_k = \begin{bmatrix} \alpha\rho v \\ \alpha\rho uv \\ \alpha\rho v^2 + \alpha p \\ \alpha\rho vH \\ \alpha\rho vk \\ \alpha\rho v\varepsilon \end{bmatrix}_k, P_k^{\text{int}} = \begin{bmatrix} 0 \\ p^{\text{int}} \frac{\partial\alpha}{\partial x} \\ p^{\text{int}} \frac{\partial\alpha}{\partial y} \\ -p^{\text{int}} \frac{\partial\alpha}{\partial t} \\ 0 \\ 0 \end{bmatrix}_k$$

$$G_k = \begin{bmatrix} 0 \\ \alpha\sigma_{xx} \\ \alpha\sigma_{yy} \\ \alpha q_x \\ \alpha\mu_k \frac{\partial k}{\partial x} \\ \alpha\mu_\varepsilon \frac{\partial \varepsilon}{\partial x} \end{bmatrix}_k, H_k = \begin{bmatrix} 0 \\ \alpha\sigma_{xy} \\ \alpha\sigma_{yy} \\ \alpha q_y \\ \alpha\mu_k \frac{\partial k}{\partial y} \\ \alpha\mu_\varepsilon \frac{\partial \varepsilon}{\partial y} \end{bmatrix}_k, S = \begin{bmatrix} \dot{m}_v \\ \dot{m}_v \bar{u} \\ \dot{m}_v \bar{v} \\ \dot{m}_v L \\ \alpha S_k \\ \alpha S_\varepsilon \end{bmatrix}_k$$

Pressure equilibrium is assumed for two fluids in a given cell. Relation between p and p^{int} is expressed such that p^{int} differ from p by δp^* [6]. The system of equation is closed by two equation of state (EoS) for each phase. The equations written above also account for phase change effects.

In the above set of equations, $\dot{m}_l = -\dot{m}_v$.

In the case of evaporation, $\dot{m}_l L = hA_{\text{int}}(T_g - T_l)$.

Computation of mass loss by evaporation is discussed in later sections.

For 1D problem, neglecting diffusion and turbulence effects, for each phase $k = 1$ or 2, application of finite volume scheme results in the following form:

$$\frac{V_i}{\Delta t} \Delta Q_i + E_{i+1/2} S_{i+1/2} - E_{i-1/2} S_{i-1/2} = p_i^{\text{int}} \begin{bmatrix} 0 \\ \alpha_{i+1/2,L} - \alpha_{i-1/2,L} \\ \frac{V_i(\alpha_i^{n+1} - \alpha_i^n)}{\Delta t} \end{bmatrix} \quad (2)$$

V_i represents volume of the cell and $i + 1/2$ and $i - 1/2$ stand for cell interfaces. S is area of cell interfaces. Volume fraction at interface is computed through MUSCL scheme, a 2nd-order accurate in space [7], with Van Albada’s limiter [8]. Time marching is performed through three-stage, 3rd-order time variation diminishing (TVD) Runge–Kutta method, and details will be presented in section. The convective terms were discretized using AUSM⁺-up suggested by Liou et al. [3]. For gas phase, ideal gas equation of state is employed, whereas stiffened-gas model is used for describing the state of liquid phase. The system in Eq. (1) is marched in time using three-stage TVD Runge–Kutta [9]. The 1D system in Eq. (2) is marched in time using three-stage TVD Runge–Kutta.

$$\hat{Q}_i^{(1)} = \hat{Q}_i^n + \frac{\Delta t}{V_j} R_i^n \quad (3)$$

$$\hat{Q}_i^{(2)} = \frac{3}{4} \hat{Q}_i^n + \frac{1}{4} \hat{Q}_i^{(1)} + \frac{1}{4} \frac{\Delta t}{V_i} R_i^{(1)} \quad (4)$$

$$\hat{Q}_i^{n+1} = \frac{1}{3} \hat{Q}_i^n + \frac{2}{3} \hat{Q}_i^{(2)} + \frac{2}{3} \frac{\Delta t}{V_i} R_i^{(2)} \quad (5)$$

$$\hat{Q}_i \equiv Q_i + \begin{bmatrix} 0 \\ 0 \\ p_i^{\text{int}} \alpha_i \end{bmatrix} = \begin{bmatrix} \hat{Q}_1 \\ \hat{Q}_2 \\ \hat{Q}_3 \end{bmatrix} \quad (6)$$

$$R_i \equiv -[E_{i+1/2}S_{i+1/2} - E_{i-1/2}S_{i-1/2}] + \begin{bmatrix} 0 \\ p_i^{\text{int}}(\alpha_{i+1/2,L} - \alpha_{i-1/2,R}) \\ 0 \end{bmatrix}$$

In the time marching steps defined by Eq. 3-5, p^{int} is frozen in given time step in all three stages. From value of \hat{Q}_i^{n+1} , value of p and α at $n + 1$ is computed through following steps:

$$p = \frac{1}{2} \left(B + \sqrt{B^2 + 4C} \right)$$

$$\alpha_k = \frac{\hat{A}_k}{p + \hat{a}_k}$$

The terms appearing in above equation is evaluated as follows:

$$\hat{A}_k = (\gamma_k - 1) \left(\hat{Q}_{3,k} - \frac{\hat{Q}_{2,k}^2}{2\hat{Q}_{1,k}} \right)$$

$$B = \sum_{k=1}^2 (\hat{A}_k - \hat{a}_k)$$

$$C = \hat{a}_1\hat{A}_2 + \hat{a}_2\hat{A}_1 - \hat{a}_1\hat{a}_2$$

$$\hat{a}_k = \gamma_k p_{k,\infty} + (\gamma_k - 1) p^{\text{int}}$$

Simultaneous computation of p and α is achieved through application of Newton iteration method on the system of equations given below.

$$\begin{cases} F_g = (p + \hat{a}_g)\alpha_g - \hat{A}_g \\ F_l = (p + \hat{a}_l)\alpha_l - \hat{A}_l \end{cases}$$

The concept of vanishing phase as described by Paillère et al. [10] is incorporated in present work. To enhance stability, the volume fraction is assumed to have a minimum and maximum cut-off values and blended with volume fraction of dominant fluid. Based on computed volume fraction values computed for a cell, velocity and temperature is re-evaluated as follows.

In compressible multiphase flow simulations, a cut-off, ϵ_{min} , is defined for volume fraction in each cell. If α is less than ϵ_{min} , $\alpha = \epsilon_{\text{min}}$.

Similarly, a parameter ϵ_{max} is also prescribed. If $\epsilon_{\text{min}} < \alpha < \epsilon_{\text{max}}$,

$$\xi = \frac{\alpha - \epsilon_{\text{min}}}{\epsilon_{\text{max}} - \epsilon_{\text{min}}}$$

From value of ζ ,

$$u'_1 = [-\xi_1^2(2\xi_1 - 3)]u_1 + [1 - [-\xi_1^2(2\xi_1 - 3)]]u_2$$

$$T'_1 = [-\xi_1^2(2\xi_1 - 3)]T_1 + [1 - [-\xi_1^2(2\xi_1 - 3)]]T_2$$

4 Results and discussion

4.1 Validation

The validation of in-house code was carried out using numerical experiments [5] conducted on shock tube. In shock tube experiments, two main cases are studied; (a) air–water and (b) water–air problems, with air and water at higher pressure respectively for either cases. For both cases, initial conditions reported in literature were considered, and unsteady computation was done to obtain the variation of parameters after 2 ms. Shock tube length is 10 m, and initial position of contact discontinuity is at $x = 5$ m. Conditions on left and right of the discontinuity are indicated as ‘L’ and ‘R’ labels; the values of pressure (Pa), volume fraction, velocity (m/s) and temperature (K) are given.

Air-water shock tube problem

The initial conditions for problem shown in Fig. 1 are listed below.

$$L(p, \alpha_g, u_k, T_k)_L = (10^9, 1 - \varepsilon, 0, 308.15).$$

$$R(p, \alpha_g, u_k, T_k)_R = (10^5, \varepsilon, 0, 308.15).$$

In air–water problem, air is at higher pressure causing movement of shock from air to water. Variation of pressure, average velocity and average temperature at end of 2 ms is plotted in Figs. 2, 3 and 4, respectively.

Fig. 1 Shock tube problem

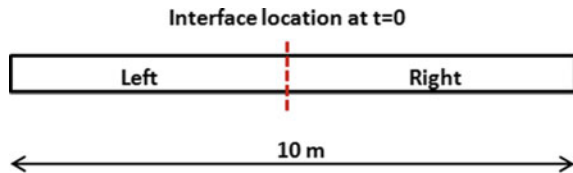


Fig. 2 Pressure along length

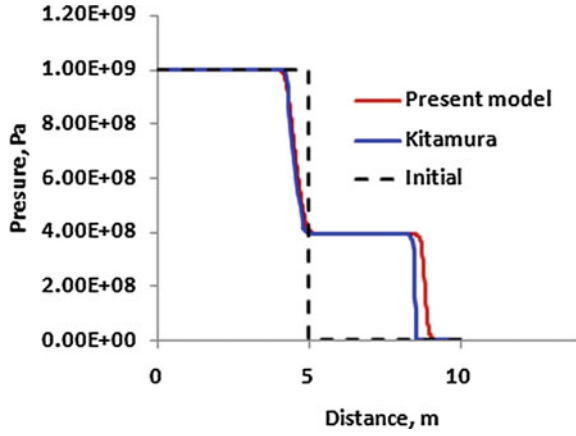


Fig. 3 Average temperature

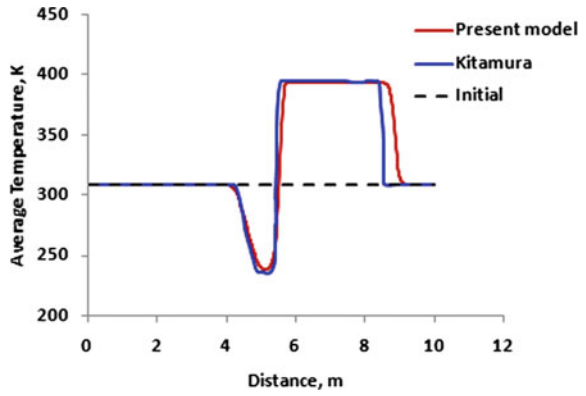


Fig. 4 Average velocity along length

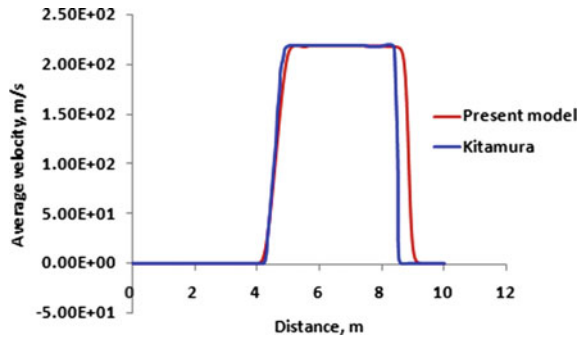
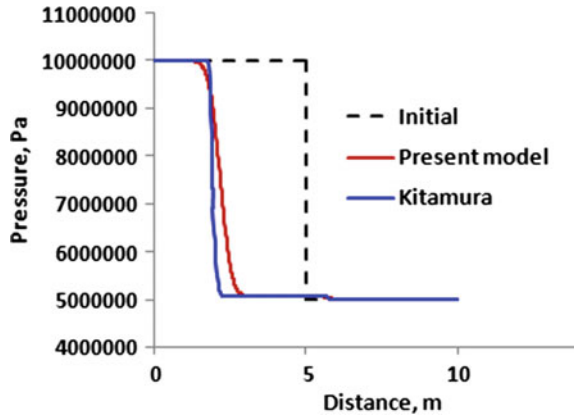


Fig. 5 Pressure along length



Initial temperature is indicated as 308.15 K. Near the contact discontinuity, there is decrease in pressure causing decrease in temperature, and further increase in temperature is due to higher pressure in region of water traversed by shock. Further, temperature decreases to initial value. Similarly velocity increases due to expansion near interface and remains constant till the pressure decreases to initial value in water.

Water-air shock tube problem

The initial conditions are listed below.

$$L = (1 \times 10^7, \varepsilon, 0, 308.15)$$

$$R = (5 \times 10^6, 1 - \varepsilon, 0, 308.15)$$

Variation of pressure, average velocity and average temperature at end of 2 ms is plotted in Figs. 5, 6 and 7, respectively. Water to air shock tube problem is considered as a challenging problem to validate various schemes in simulation of compressible multiphase flows.

The validation shows that the results from code implemented in-house are showing good comparison with literature data.

4.2 Effect of Initial Conditions

As seen from the literature, in most of the schemes for shock tube simulations, two-fluid formulations were applied with same initial temperature on both sides of the shock tube. However, it is required to study the compatibility of a scheme

Fig. 6 Average temperature along length

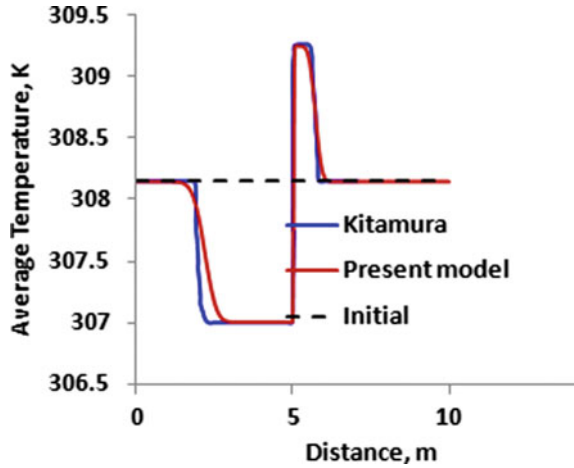
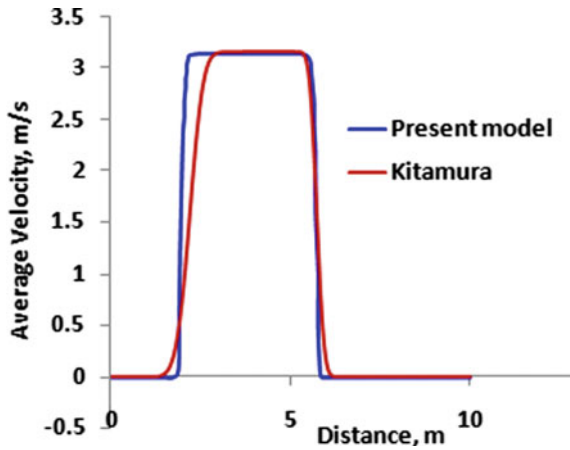


Fig. 7 Average velocity along length



for different initial condition on either side of the shock tube filled with liquid and gas, as discussed in coming sections so as to study the capability of the scheme to capture applications considered in present study. For the indented application, it is required that considerable velocity and temperature difference exist combined with minor difference in pressure. In film cooling application, liquid is injected at higher pressure and lower temperature than the hot gas. Thus, the scheme AUSM⁺-up scheme was applied to investigate the effect of variations in initial conditions across both the different fluids so as to ensure robustness of numerical scheme as considered in cases discussed as follows.

Case 1: Here, pressure for water is maintained at 60 bar, whereas in air side, 50 bar was assumed. The initial temperature for water and air was maintained at 300 K and 3000 K, respectively. Velocity on either sides of the interface was assumed to be zero.

The computation for one-dimensional problem was run for 2 ms with a time step of 0.000002 s. The variation of parameters such as pressure and mixture temperature/mixture velocity is shown in Figs. 8 and 9, respectively.

$$\text{Water: } (p, \alpha_g, u_k, T_k)_L = (6 \times 10^6, \varepsilon, 0, 300)$$

$$\text{Air: } (p, \alpha_g, u_k, T_k)_R = (5 \times 10^6, 1 - \varepsilon, 0, 3000)$$

Fig. 8 Pressure variation

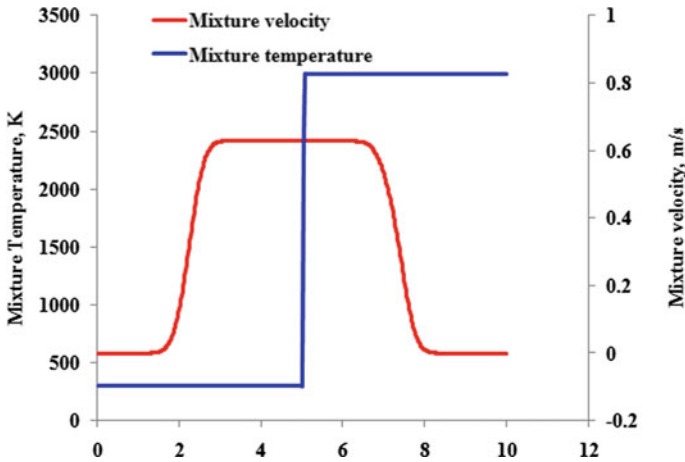
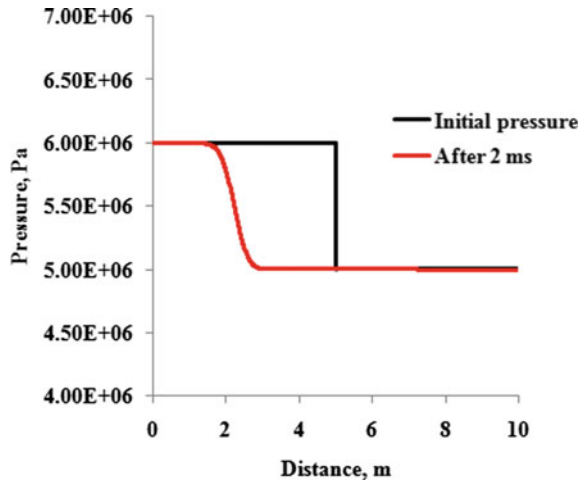


Fig. 9 Mixture temperature/velocity

Case 2: The pressure jump across the interface was maintained as in Case 1. Instead of different values of temperature on either side, the velocity was assumed to be 100 m/s on water side and air side was initially assumed to have velocity of 10 m/s. Temperatures at all locations were set as 300 K. Computational time and time step also remain the same as in Case 1. The variation of parameters such as pressure and mixture temperature/mixture velocity is shown in Figs. 10 and 11, respectively.

Fig. 10 Pressure variation

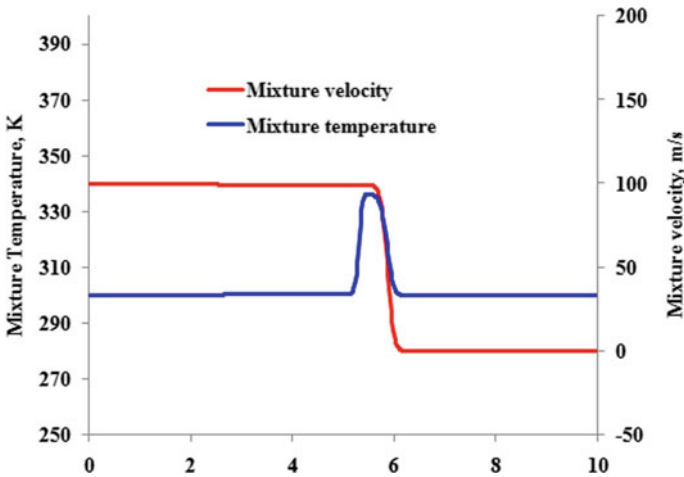
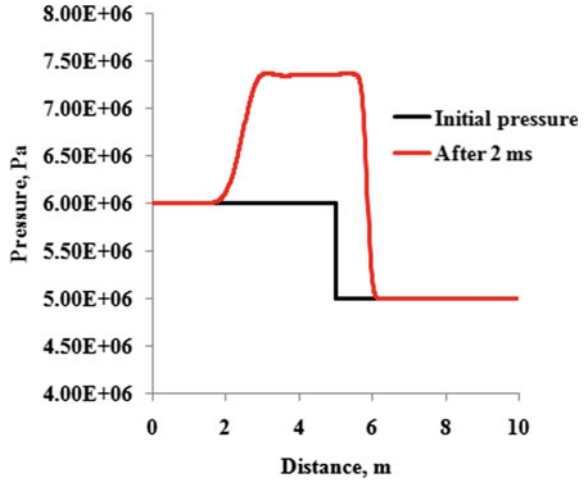


Fig. 11 Mixture temperature/velocity

$$\text{Water: } (p, \alpha_g, u_k, T_k)_L = (6 \times 10^6, \varepsilon, 100, 300)$$

$$\text{Air: } (p, \alpha_g, u_k, T_k)_R = (5 \times 10^6, 1 - \varepsilon, 10, 300)$$

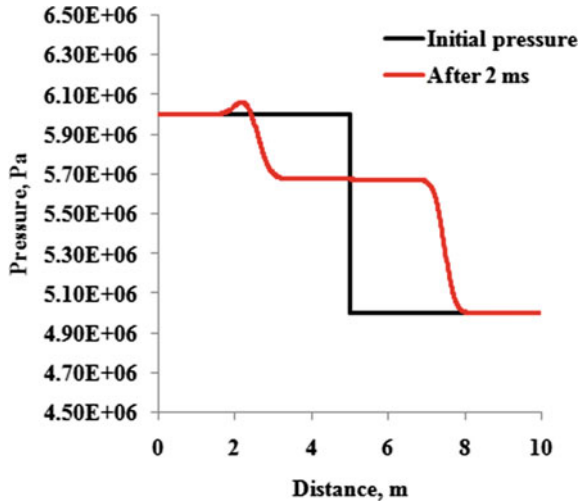
Case 3: Maintaining the same pressure jump, time step and interface locations, in Case 3, both velocity and temperature were initialized with different values across the interface. The variation of parameters such as pressure, mixture temperature and mixture velocity is shown in Figs. 12 and 13, respectively.

$$\text{Water: } (p, \alpha_g, u_k, T_k)_L = (6 \times 10^6, \varepsilon, 100, 300)$$

$$\text{Air: } (p, \alpha_g, u_k, T_k)_R = (5 \times 10^6, 1 - \varepsilon, 10, 3000)$$

In all the cases discussed here, no numerical errors were evident in the computation till 2 ms. The initial conditions were set similar to the values expected in actual problem for 2D geometry. No divergence was seen till the end of computations indicating that scheme is able to handle temperature jump across the interface.

Fig. 12 Pressure variation



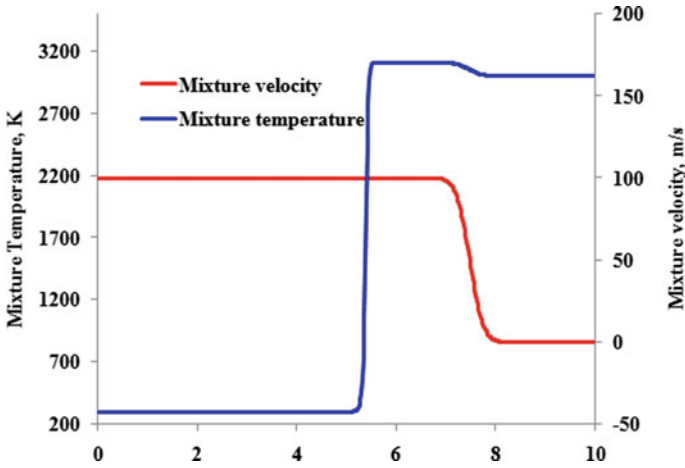


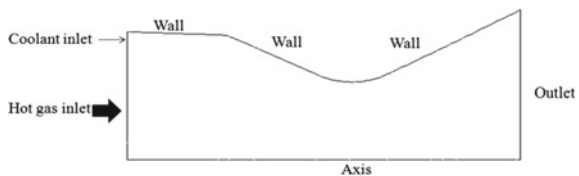
Fig. 13 Mixture temperature/velocity

4.3 Studies in Nozzle Flow Using AUSM Scheme

In the earlier section, application of schemes for problems with different initial condition was discussed. Based on numerical schemes detailed in previous sections, compressible multiphase flow approach was applied to a typical nozzle problem with liquid injected along the wall as in Fig. 14. In the present case study, AUSM⁺-up scheme was used for discretization of the convective terms. Stagnation pressure and temperature for the gas flow at inlet were maintained as 58 bar and 3000 K, respectively. At the inlet face of computational domain, injection of gas and liquid was considered. The total number of cells was 5850. For gas and coolant flow, subsonic inlet boundary condition was prescribed in terms of stagnation pressure and stagnation temperature. The evaporated mass flow rate is calculated by equating the energy transfer at interfaces by considering the convective heating to liquid and mass loss due to latent heating effects.

It is assumed that phase change occurs when liquid reaches the saturation temperature at the given local pressure. Nusselt number correlation for turbulent flow is used to compute heat transfer coefficient. Interface is assumed to be straight within a cell. Cells with temperature greater than saturation temperature are identified. Nodal values of volume fraction of inert gas are computed from neighbouring cell centre

Fig. 14 Tracking of interface



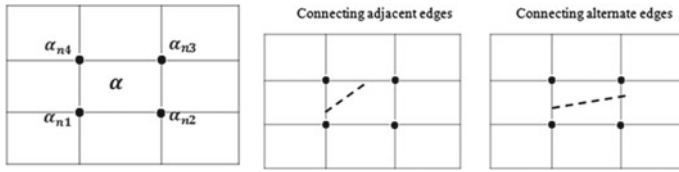


Fig. 15 Tracking of interface

values as shown in Fig. 15. Once the nodal values are obtained, the interface has to be reconstructed from bounding nodes of the cell. As the interface is considered as straight, interface will exist for a given edge if two nodes of the edge have one value > 0.5 and other value < 0.5 . From the figure, if $\alpha_{n1} > 0.5$ and $\alpha_{n2} < 0.5$, the interface exists on the line connecting nodes with α_{n1} and α_{n2} . Two possibilities of interface orientation within a cell considered are as shown in the figure. In either cases from the values of coordinates for the corresponding nodes and their respective mass fraction values, the intersection point is obtained from simple line intersection formula. The intersection point is obtained from the coordinates of the corner nodes. Once the interface is defined within the cell, the length of the interface is computed for calculation of interface area.

The results of the computation performed are discussed as follows. The wall is assumed to be adiabatic. The results for volume fraction of liquid with inclusion of phase change effects are shown in Fig. 16. It is seen from the results that the injected liquid is confined to wall boundary. The average temperature was computed from individual volume fraction, density and temperatures of each phase, and distribution is shown in Fig. 17. The pressure which is assumed same for both gas and liquid for a given cell is as given in Fig. 18. The evaporated mass flow rate computed from equation is depicted in Fig. 19. The phase change is evident at the interface between gas and liquid. Maximum evaporated mass at each axial location is plotted along the axis as in Fig. 20. It is mostly invariant in the combustion chamber; however, once the convergent region is reached, the evaporated mass shows fluctuations in the final phase of the portion where evaporation takes place. This is due to variation in flow parameters due to change in flow boundary. Most of the results indicate that there is less diffusion of liquid into the gas domain, and the liquid is confined to the region very near to wall. The presence of liquid is seen till the convergent portion of the nozzle.

5 Conclusions

Model based on two-fluid formulation was studied through series of validation cases and effects of initial conditions. Robustness of model for latter was also brought out from the study. Then, application of two-fluid model was studied for film cooling with gas and liquid as working fluid. Phase change effects were modelled through

Fig. 16 Liquid volume fraction

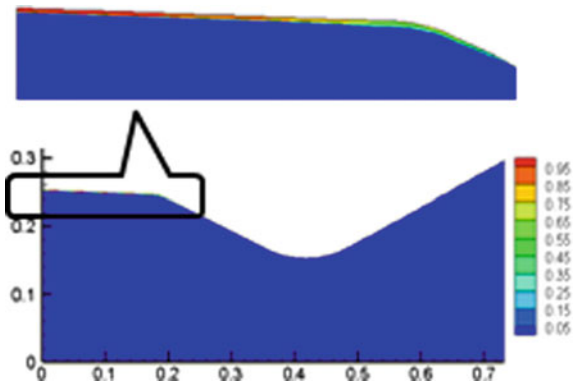


Fig. 17 Average temperature

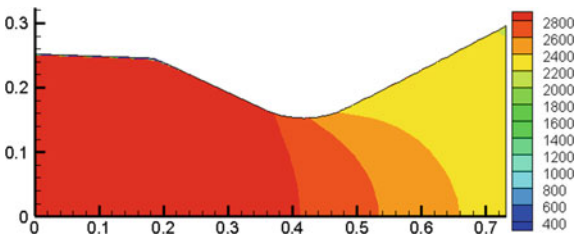


Fig. 18 Pressure distribution

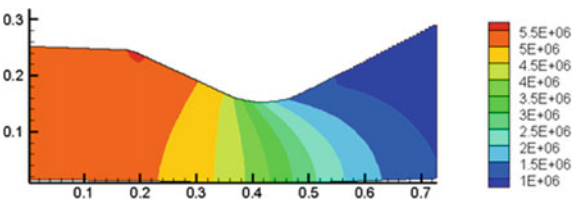
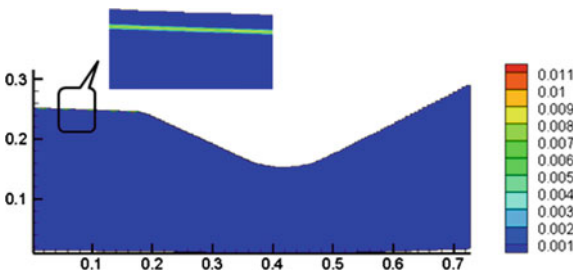
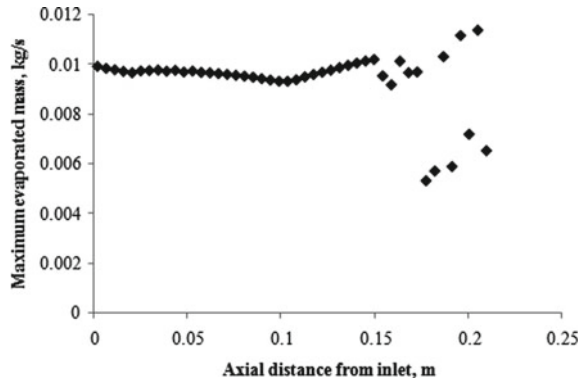


Fig. 19 Evaporated mass



heat transfer coefficient and interface area. There are other numerical techniques reported in literature to model phase change such as with rate constant and relaxation techniques, but applicability of those to any problem requires more detailed investigation. Phase change modelled in present paper is simple and more realistic

Fig. 20 Evaporated mass along axial distance



for phase change problems that involve mass loss from the interface. Introduction of film cooling will protect the cylindrical region of thrust chamber as found in actual operation of engine. And this fact is clearly established from the model which indicates that the liquid is able to protect the cylindrical region of combustion chamber from hot gas.

References

1. Osher SJ, Sethian JA (1988) Fronts propagation with curvature dependent speed: algorithms based on Hamilton Jacobi formulations. *J Comput Phys* 79:12–49
2. Liou MS (2006) A sequel to AUSM, Part II: AUSM⁺-up for all speeds *J Comput Phys* 214:137–170
3. Liou MS (1996) A sequel to AUSM: AUSM⁺. *J Comput Phys* 129:364–382
4. Kitamura K, Liou MS, Chang C (2014) Extension and comparative study of AUSM-family schemes for compressible multiphase flow simulations. *Commun Comput Phys* 16:632–674
5. Kitamura K, Liou MS (2012) Comparative study of AUSM-family schemes in compressible multiphase flow simulations. In: 7th International conference on computational fluid dynamics (ICCFD7), Hawaii
6. Liou MS, Nguyen L, Chang C, Theofanous T (2008) How to solve compressible multifluid equations: a simple, robust and accurate method. *AIAA J* 46:2345–2356
7. Van Leer B (1979) Towards the ultimate conservative difference scheme. V. A second-order sequel to Godunov's method. *J Comput Phys* 32:101–136
8. Van Albada GD, Van Leer B, Roberts WW Jr (1982) A comparative study of computational methods in cosmic gas dynamics. *Astron Astrophys* 108:76–84
9. Gottlieb S, Shu CW (1998) Total variation diminishing Runge-Kutta schemes. *Math Comput* 67:73–85
10. Paillère H, Corre C, Cascales JRG (2003) On the extension of the AUSM⁺ scheme to compressible two-fluid models. *Comput Fluids* 32:891–916